

Estimation of Partial Charges in Small Zeolite Imidazolate Frameworks from Density Functional Theory Calculations

Malay Kumar Rana

Dipartimento di Chimica, Università degli Studi di Sassari, Via Vienna 2, 07100 Sassari, Italy

Federico Giovanni Pazzona, Giuseppe Baldovino Suffritti, and Pierfranco Demontis

Dipartimento di Chimica, Università degli Studi di Sassari, and Consorzio Interuniversitario Nazionale per la Scienza e Tecnologia dei Materiali (INSTM), Unità di Ricerca di Sassari, Via Vienna 2, 07100 Sassari, Italy

Marco Masia*

Dipartimento di Chimica, Università degli Studi di Sassari, Istituto Officina dei Materiali del CNR, UOS SLACS, Via Vienna 2, 07100 Sassari, Italy

ABSTRACT: Zeolitic Imidazolate Frameworks (ZIFs) are the new frontier in the field of metal–organic materials. They incorporate the confining properties of the more traditional aluminosilicate zeolites together with the catalytic activity provided by transition metal ions and organic links. Computation of atomic point charges for these hybrid materials is important in the field of molecular simulations for substantial prediction of experimental results. However, due to the structural complexity of advanced materials in general, studies involving derivation of point charges for these materials are truly scarce. In this article, we have derived the atomic point charges of ZIF–8 through fitting of the quantum electrostatic potential obtained systematically from density functional theory (DFT) calculations both on finite clusters of increasing size and on the periodic system. For the periodic system, fluctuations on the atomic charges have been studied through ab initio molecular dynamics simulations. Using the latter approach, we have extended the study to ZIF–2 and ZIF–3, where it has been found that charge fluctuations are, as well as for ZIF–8, very narrow, therefore justifying the use of the point charge approximation for these materials.

I. INTRODUCTION

Microporous and nanoporous materials like zeolites are capturing increasingly large interest, especially in recent times, due to their high relevance in environmental, technological, and chemical applications. Among these nanoporous materials, Metal Organic Frameworks (MOFs)¹ are devised with tetrahedrally coordinated transition metal ions (e.g., Co, Cu, Zn, etc.) bridged by organic ligands. Covalent Organic Frameworks (COFs)² are also relatively new nanoporous materials where the nonmetal atoms (like B, C, O, Si, H, etc.) are linked by strong covalent bonds. Because of the wide choice of possible metal ions and organic ligands, the porosity and functionality of these materials can be tuned. As a drawback of their high tunability, performing an exhaustive experimental study of their gas adsorption/separation properties is not always an easy process. Metal–organic frameworks where zinc is tetrahedrally connected to imidazolate ligands, known as Zeolitic Imidazolate Frameworks (ZIFs), resemble zeolites but offer wider porosity and exceptional thermal and chemical stability and are very promising for gas storage and separation.^{3–6}

Molecular simulation methods represent a relevant investigation tool in the research of these materials, since they support advanced experimental applications. In simulation methods, a proper choice of force field parameters and site partial charges is important to mimic the true adsorbate–adsorbent interactions and hence the adsorption properties of these materials.⁷ In addition,

to get a transferable set of force field parameters, one has to rely on the accurate treatment of electrostatic interactions. In fact, computational simulations not considering accurate partial charges on the whole framework may yield unrealistic results.

Model force fields with fixed partial atomic charges have been proposed for simple molecular systems, whereas they are scarce for supramolecular systems such as ZIFs. Since long-range electrostatic interactions significantly contribute to the total interaction energy, robust numerical methods for computing partial charges in ZIFs are needed. Partial charges convey a chemically intuitive picture of how the electronic density within a molecule is distributed and are fundamental to describing the electrostatic interaction in classical simulations. Nevertheless, it should be noticed that they do not correspond to any quantum mechanical observable; thus there are many methods to partition the density into localized partial charges, some of them being more successful in reproducing the system properties in the simulations. In recent studies, Rankin et al.⁸ and Liu et al.^{9,10} have computed the charges on ZIF–68, ZIF–69, and ZIF–70 using, respectively, the Bader charge decomposition method¹¹ and the Mulliken charge partitioning scheme¹² from periodic density functional theory (DFT) calculations. It should be noticed though that the

Received: November 26, 2010

Published: April 29, 2011

Bader theory of atoms in molecules¹³ could be sensitive to substituents and structural modifications in supramolecular structures; a comparison between the cluster-based charge calculation of atomic charges and periodic DFT calculation employing the Bader charge decomposition method¹¹ has shown a substantial error for the MOF HKUST-1.¹⁴ Furthermore, it is known that the Mulliken charge analysis method based on periodic DFT calculation is highly sensitive toward the basis set,^{15,16,9} and hence care should be taken in handling the values of the resulting charges.

Numerical methods have been developed for fitting the partial charges to atomic sites to reproduce the quantum chemical electrostatic potential (ESP), considering grid points lying outside the molecule.^{17–20} Nonetheless, it should be stressed that the ESP charge analysis technique, usually applicable to molecular systems, suffers from serious technical faults for buried atoms. This is particularly true for atomically dense lattices, in which the shortage of empty volume makes difficult the definition of valid grid points outside the van der Waals radii. To eliminate this problem, the RESP method¹⁹ introduces a penalty term in the fitting procedure. In this context, several sampling schemes,^{21–24} e.g., MK, CHELP, and CHELPG, allow one to find the set of point charges or multipoles capable of most closely reproducing the electrostatic potential obtained from quantum chemical calculations. Framework charges have also been derived from the fragments of the periodic lattice through ESP fitting;^{25,26} special care has to be taken to fulfill the valency of all atoms or charge neutrality of the isolated fragment. It is worth mentioning that the potential derived from charge calculation using MK, CHELP, and CHELPG methods has been tested by Maciel and Garcia²⁷ who pointed out that CHELPG and MK outperform CHELP. Subsequently, the CHELPG scheme has widely been used in charge calculations for various molecular and lattice substances.^{28–30,14,8}

When dealing with periodic electronic structure calculation, a fundamental problem arises since the electrostatic potential for infinite periodic systems is ill-defined. Only recently has a method to overcome this flaw been developed (REPEAT: Repeating Electrostatic Potential Extracted Atomic—*vide infra*),³¹ which allows for RESP-like charge fits in DFT periodic calculations. As we will show in this article, it is a robust and relatively cheap method to also extract indirect information about the electronic density fluctuations in the framework.

The scope of this contribution is two-fold: first, we compare the results of some of the above-mentioned methods on the experimental X-ray structure of ZIF-8, a well studied porous material for the absorption of H₂ and CO₂ and other flue gases;^{32–39} then, we look into partial charge fluctuation during MD simulations of ZIF-8, ZIF-2, and ZIF-3. The manuscript is organized as follows: in section II, the computational approach used is explained; in section III, the results are shown, followed by our conclusions in section IV.

II. MODEL AND SIMULATION DETAILS

The reference structure for ZIFs have been reconstructed from the X-ray crystal data collected from the Cambridge Crystallographic Data Centre. The building unit for the fragments of ZIF-8 is a methyl-imidazolate group (mIm) coordinating two Zn atoms; hence, the nomenclature of atoms in the supramolecular structure is straightforward. The methyl-imidazolate ring has three types of carbon atom differing in bonding connectivity: the sp² carbon atom attached to the CH₃ group (hereby denoted as C1), two (chemically equivalent) sp² carbons belonging to the

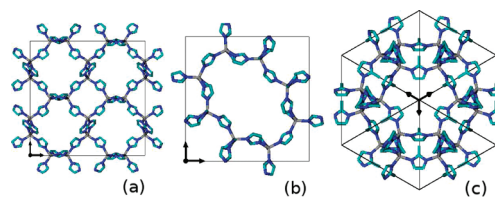


Figure 1. Unit cells for (a) ZIF-2, (b) ZIF-3, and (c) ZIF-8.

ring (C2), and the sp³ carbon atom of the methyl group (C3). H2 and H3 refer to the hydrogen atoms bonded respectively to C2 and C3 carbons. Nitrogen and zinc atoms do not need any kind of special numbering because they are unique.

The building unit of ZIF-2 and ZIF-3 is an imidazolate group (Im) coordinating two Zn atoms. Similarly to the mIm group in ZIF-8, the Im group in ZIF-2 and ZIF-3 has atom types named C1 and C2 to which H1 and H2 are bonded.

A. Cluster Calculations. Cluster calculations have been performed on fragments of ZIF-8. The crystal is characterized by the presence of square and hexagonal windows around the main cavity (see Figure 1). Thus, we considered portions of the periodic lattice located around these two types of windows. The rationale behind the choice of studying clusters of increasing size is that we aim to look for the minimum dimension of an isolated fragment to get converged values for the charges. In our study, Zn atoms at the vertices of square or hexagonal windows are bonded either to mIm groups or to NH₃ molecules. The need of using different groups coordinating zinc atoms originates from the fact that all of the fragments are charged. The overall charge cannot be neutralized while keeping the symmetry of the fragments at the same time; conserving the symmetry is of high importance because it allows the electronic density to be evenly shared on the core atoms, thus leading to more reliable results on the computed charges. On the other hand, it could be argued that the resulting charges would be affected by the total charge being different from zero. This considerations led us to perform calculations also on the periodic system, which is completely uncharged (see below). The clusters have been built up in such a way that the cleaved square (hexagonal) fragments can be grown symmetrically by adding further square (hexagonal) windows; a graphical intuitive representation of the systems studied is shown in Figure 2. For the sake of clarity, we name the fragments F-N_{Zn}^{tot}-N_{Zn}^{core}-L, where N_{Zn}^{tot} is the total number of Zn atoms in the cluster, N_{Zn}^{core} is the number of core Zn atoms (with the respective methyl-imidazolate group) considered for computing the charge, and L is the name of the terminal ligand (either mIm or NH₃). For example, the F-4-4-mIm cluster is the square fragment formed by four Zn atoms, all of them considered in charge calculation.

DFT and ab initio calculations on supramolecular fragments have been performed using the Gaussian 03⁴⁰ (only for the building unit) and Turbomole^{41,42} (for all fragments) software packages. The meta-GGA TPSS functional⁴³ was used together with Gaussian basis sets; considering that big clusters imply a high computational cost, the SVP basis set was used for all fragments studied. The convergence of results was assessed against calculations on small clusters with the TZVP and QZVP basis sets. The atomic charges were computed after having relaxed all structures to their equilibrium geometries. In all calculations, we used the Multipole Accelerated Resolution of the Identity (MARI-J), which involves the evaluation of the Coulomb interaction using auxiliary basis sets through the multipole expansion for

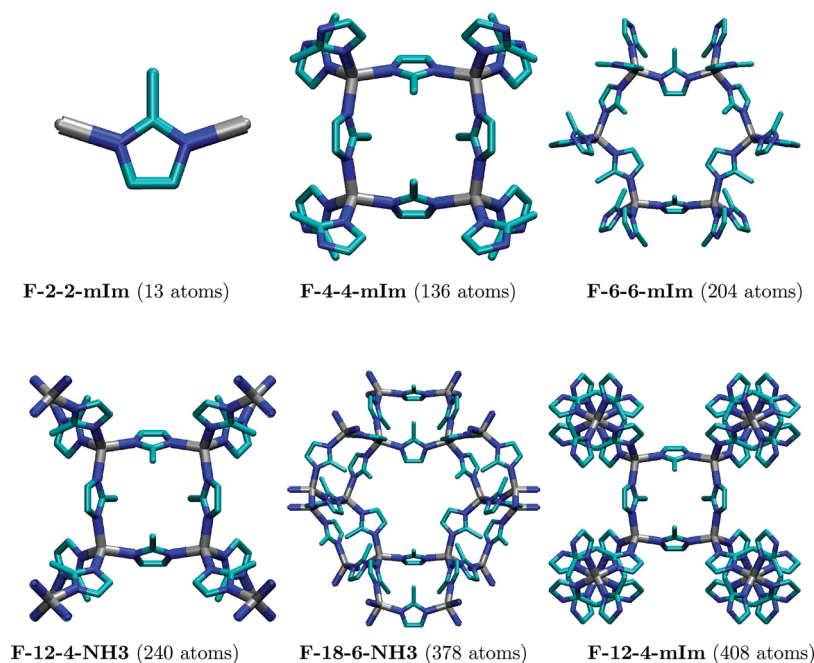


Figure 2. Structures of the clusters studied using a minimal representation for atoms and bonds. In the second and third clusters, the appearance of square and hexagonal windows can be appreciated.

nonoverlapping charge distributions without any significant loss of accuracy.^{44,45}

The sampling of the points at which ESPs are evaluated is accomplished using the spherical shells at specified multiples of an atom's van der Waals radius around each atom and with a density of 1 point/Å², as described in the MK sampling scheme.^{21,22} ESP calculations have been performed with the same programs used for the electronic structure calculations. The van der Waals radii for Turbomole calculations are 1.39 Å, 1.55 Å, 1.70 Å, and 1.09 Å, respectively, for Zn, N, C, and H, as taken from <http://www.ccdc.cam.ac.uk/products/csd/radii/>.

B. Periodic Structure. Periodic DFT calculations have been carried out for infinite crystalline ZIFs. The CPMD⁴⁶ (only for ZIF-8) and cp2k⁴⁷ packages have been used in order to explore two different types of basis function, namely, plane waves and Gaussian basis sets. The electronic structure calculations were done using both the BLYP^{48,49} and PBE⁵⁰ functionals. Norm-conserving Troullier–Martins⁵¹ (TM), Goedecker–Teter–Hutter^{52–54} (GTH), and Vanderbilt ultrasoft⁵⁵ (VDB) pseudopotentials were tested for single point calculations. As in a recent article on MOFs,⁵⁶ we used the TZV2P basis set for C, N, and H atoms, and the TZV for Zn. Molecular dynamics simulations were run for 1 ps in the microcanonical ensemble, after having equilibrated the system with massive Nose–Hoover⁵⁷ chain (NHC) thermostats at 300 K for 1 ps; massive thermostating consists of applying a NHC to each degree of freedom of the system, thus yielding to energy equipartition in a short time.

Both Car–Parrinello (CP) and Born–Oppenheimer (BO) molecular dynamics^{58,59} were run. In the former case, a time step of 4 au was used, and the fictitious mass of electron was set to 400 au. In the latter case, the time step was set to 0.5 fs. The orbital transformation (OT) minimizer⁶⁰ was used in wave function optimization for BO calculations.

During production runs, the electrostatic potential was stored for subsequent analysis with the REPEAT method³¹ (see below),

allowing us to compute the atomic charges and their time evolution along the simulation. The REPEAT author's code was used to evaluate the REPEAT charges. In the fitting procedure, we have not used any rescaling factor. The van der Waals radii used are 1.38 Å, 1.83 Å, 1.93 Å, and 1.44 Å, respectively, for Zn, N, C, and H, as taken from Universal Force Field.⁶¹ The FFT grid meshes used for the fitting are the defaults from periodic DFT calculations. The valid grid points are always considered outside the unscaled van der Waals radii for each atom.

C. Computation of Atomic Charges. The method used for evaluating the atomic charges for both types of systems studied is based on the restrained fitting of the DFT electrostatic potential. Let us indicate as Ψ_{qm} the electrostatic quantum potential and as Ψ_{cal} the electrostatic potential obtained iteratively from the initial guess of atomic point charges through the Coulomb equation by minimizing the following functional form in least-squares fit:

$$\Phi(q_i) = \sum_{\text{grid}} (\Psi_{\text{qm}}^{\text{grid}} - \Psi_{\text{cal}}^{\text{grid}})^2 + \lambda (\sum_i q_i - q_{\text{total}}) \quad (1)$$

where q_i is the set of N point charges, q_{total} is the total molecular charge, and λ is the Lagrange multiplier, ensuring that the sum of atomic charges is equal to the total charge of the system. The Coulomb interaction for infinite periodic replicas of point charges is handled by using the Ewald method.^{62–64} The conventional ESP charge fitting procedure for molecular systems, eq 1, yields unsatisfactory charges for periodic systems.⁶⁵ Taking into consideration the wide charge fluctuations of buried atoms due to the ill-defined reference state, a modified penalty function is adopted in the least-squares fit technique. This is expressed in the following form:

$$\Phi(\{q_i, \delta\psi_j\}) = \sum_{\text{grid}} (\Psi_{\text{qm}}^{\text{grid}} - \Psi_{\text{cal}}^{\text{grid}} + \delta\psi_j)^2 + \lambda (\sum_i q_i - q_{\text{total}}) + \sum_i \xi_i p_i \quad (2)$$

Table 1. Partial Charges on All Atoms for the Building Unit of ZIF-8 Computed with Different Methods

method	Zn	N	C1	C2	C3	H2	H3
HF-MK	1.78	-1.10	1.02	0.22	-0.91	0.12	0.27
HF-CHELPG	1.77	-1.10	1.09	0.24	-0.91	0.10	0.26
MP2-MK	1.74	-1.10	1.01	0.30	-0.91	0.09	0.27
MP2-CHELPG	1.72	-1.07	1.04	0.30	-0.90	0.08	0.26
DFT-MK	1.67	-0.98	0.92	0.25	-0.86	0.11	0.27
DFT-CHELPG	1.66	-0.94	0.94	0.24	-0.84	0.10	0.26

where ξ_i and P_i are respectively the Lagrange multiplier and the penalty function for buried atoms (the latter is given by expanding the energy of an atom as a function of charge up to the second order) and δ_{ψ} is the difference between the quantum chemical electrostatic potential and calculated electrostatic potential based on atom centered point charges, averaged over grid points. This is the basis for the REPEAT method.³¹

III. RESULTS AND DISCUSSIONS

A. Clusters. As a first step for the study of increasing size fragments, we validated the density functional calculations against Hartree-Fock and MP2 ab initio calculations on the building block (F-2-2-mIm). Atomic charges were derived using both the MK^{21,22} and the CHELPG²⁴ sampling schemes. The results are shown in Table 1. It can be seen that charges obtained with DFT calculations are slightly shifted (ca. 5%) with respect to the values obtained with ab initio methods. Similar results were obtained with both hybrid and non-hybrid functionals using both the TZVP and 6-311++g(d,p) basis sets. In passing, we would like to highlight that the differences between the MK and CHELPG schemes are always negligible. Thus, we are confident that any of the two methods together with DFT calculations are capable of giving reliable results. This is of the utmost importance for this study since it provides us with sound machinery to study huge fragments, without losing accuracy and increasing computer time. Before showing the results on the clusters, we should mention that the results shown proved to be highly dependent on the cluster structure. Geometry and wave function optimizations have been done with strict convergence criteria using fine grids for DFT calculations. This has caused the calculations to be very time-consuming, mainly for bigger fragments where the number of atoms is higher than 400.

As a first approach, we computed the charges on small systems formed by one zinc atom and two or four mIm molecules (respectively in a linear and tetrahedral arrangement). Though such a small size allowed us to perform calculations with large basis sets, the results were not reliable; in fact, the atoms of mIm experience an inhomogeneous environment which does not resemble the crystal structure situation, causing the charges on chemically equivalent atoms to be highly different. Hence, the main problem in this kind of calculation is to compute the charges on atoms which “experience” a coordination structure similar to that of the crystal. For this reason, we build up highly symmetric fragments of increasing size. In Table 2, we show the atomic site charges for various molecular ion fragments of ZIF-8, namely, F-4-4-mIm, F-6-6-mIm, F-12-4-NH₃, F-18-6-NH₃, and F-12-4-mIm, estimated through the MK method. Unfortunately, we were not able to converge the calculations on F-18-6-mIm given the high number of atoms (546).

Table 2. Partial Charges on Core Atoms of the Fragments of Increasing Size Grown on Square and Hexagonal Windows

fragment	Zn	N	C1	C2	C3	H2	H3
F-4-4-mIm	0.3961	-0.2402	0.3699	-0.1849	-0.5943	0.1302	0.1685
F-12-4-NH ₃	0.4995	-0.2530	0.3371	-0.1829	-0.4239	0.1672	0.1273
F-12-4-mIm	0.6955	-0.3294	0.3822	-0.1554	-0.4115	0.1393	0.1136
F-6-6-mIm	0.3130	-0.1120	0.1434	-0.2102	-0.5168	0.1497	0.1480
F-18-6-NH ₃	0.4691	-0.1876	0.2227	-0.1997	-0.3884	0.1726	0.1207

A distinguishable trend can be identified in the results. If we consider fragments built on square windows, we can see that the charge on Zn steadily increases, as well as on C2 and C3 atoms, while that for N and H3 decreases; the behavior of C1 and H2 is not as linear as for the other atoms. If we focus only on zinc, it can be seen how the value of the charge is almost doubled on passing from the small cluster to the big one. It should be stressed that, only in case of F-12-4-L fragments have we considered the core atoms; we think that this situation would be more comparable to the case of zinc atoms in the crystal, which experience a symmetric electron cloud distribution. According to this point of view, the results of the F-12-4-mIm fragment should be considered more reliable than those of F-12-4-NH₃, given that the species bonded to external zinc atoms resemble those of the crystal. A similar trend is also evident for the clusters with hexagonal windows. The values of the charges show the same trend, and we expect that, if we would have been able to compute them for the F-18-6-mIm cluster, we would have obtained results similar to those of F-12-4-mIm. The values obtained for the latter fragment are in fair agreement with the ones obtained in the calculations of the periodic system (see below), the largest difference being the charge on C3.

Care should be taken, though, in considering these results as being conclusive; in fact, we should stress that the overall charge of the biggest fragments is ± 12 , depending on the nature of terminal ligand L (the sign is positive for L = NH₃, while it is negative for L = mIm). From the analysis of localized charges, we have found that the excess charge is localized at the periphery of the cluster. In the case of the F-12-4-mIm, for example, the sum of the charges on the 48 core atoms is 1.26e, while the charges on the rest of atoms adds up to -13.26e. Although from this analysis we get insight into the way the excess charge is being distributed within the cluster, we are not aware of any straightforward method to verify the effect of such an excess charge on the electronic density distribution on core atoms. Hence, we are not able to claim with certainty that the computed charges on core atoms actually resemble those in the neutral crystal structure. These doubts on the reliability of our results move us to the following subsection where calculations on the fully periodic structure have been performed; the results will be useful also to assess the problem of computing partial charges on electrically charged clusters.

B. Periodic System. DFT calculations have been performed on the periodic structure using both plane waves and Gaussian basis sets.

We first tested for different pseudopotentials and functionals only with plane waves; single point energy calculations on the crystal structure were done using either PBE and BLYP functionals with TM, GTH, and VDB pseudopotentials. The average value of the charge of an atom type and the standard error were calculated as a function of the pseudopotential cutoff for the wave

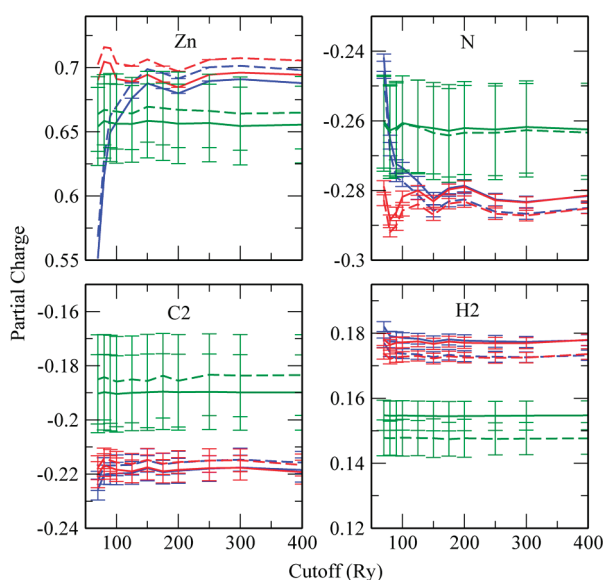


Figure 3. Values of the point charges for representative atoms as a function of the cutoff for the functional and pseudopotentials tested. Blue, red, and green are used respectively for GTH, TM, and VDB pseudopotentials. Solid lines: PBE functional. Dashed lines: BLYP functional.

function. The results are reported in Figure 3; it can be noticed that the difference among the results obtained with two functionals while using the same pseudopotentials is less than 1%. The standard error for most calculations is negligible (on the scale used for representing the results for Zn, it is even not distinguishable from the thickness of the line!); only when VDB pseudopotentials are used did we obtain huge error bars, hinting that these calculations with these pseudopotentials do not guarantee reliable results. All of the charge values converge to a stable value for a cutoff of 150 Ry, which coincides with the values for energy convergence; hence, the convergence of charges at this value of cutoff is related to the convergence of DFT calculations and not with the grid point used for the REPEAT fit. This analysis suggests that both GTH and TM pseudopotentials together with PBE and BLYP yield converged results for the charges with a small error. Using Gaussian basis sets, we have tested again the convergence of the charges with the pseudopotential cutoff for the density; in this case, only PBE with GTH pseudopotentials was tested in a cutoff range between 320 and 3000 Ry. We found that the convergence of atomic charge (as well as of total energy) is attained at 700 Ry; this result is in agreement with a recent study on MOFs.⁵⁶

We would like to highlight that the values of the charges obtained with the REPEAT method are similar to the ones computed on the biggest cluster (F-12-4-mIm), as discussed in the previous section. In Table 3, we show the absolute difference Δq between the charges computed with REPEAT and the respective entries in Table 2 for the F-12-4-mIm cluster. It can be seen that the only noticeable deviation between the two methods is found for the charge on C3, which differs by ca. $0.19e$. The differences in all of the other charges are negligible. The fact that the two methods converge to similar values is an important check of their reliability. Moreover, it seems that the calculation of partial charges on core atoms of highly charged clusters is not affected by the presence of the

Table 3. Partial Charges \bar{q} of ZIF-8 from Gaussian and Plane Wave Periodic DFT Calculations with the Relative Standard Errors ($S_{\bar{q}}$)^a

	Zn	N	C1	C2	C3	H2	H3
CPMD							
\bar{q}	0.6894	-0.2800	0.4184	-0.1910	-0.5726	0.1536	0.1481
$S_{\bar{q}}$	0.0016	0.0017	0.0027	0.0011	0.0025	0.0007	0.0007
Δq	0.0061	0.0494	0.0362	0.0356	0.1611	0.0143	0.0345
BOMD							
\bar{q}	0.7362	-0.3008	0.4339	-0.1924	-0.6042	0.1585	0.1572
$S_{\bar{q}}$	0.0014	0.0014	0.0024	0.0008	0.0021	0.0005	0.0005
Δq	0.0407	0.0286	0.0517	0.0370	0.1927	0.0192	0.0436

^a For each method, the difference $\Delta q = |\bar{q} - q(\text{F-12-4-mIm})|$ is also reported.

excess charge, thus confirming that the core atoms of big clusters experience an electronic environment similar to that of the neutral crystal structure. Although the two approaches give similar results, it should be noticed that the computational cost for the evaluation of atomic charges from calculations on large clusters is more than 1 order of magnitude higher, compared to the DFT plus REPEAT calculations on the periodic structure. This feature, besides rendering the REPEAT method an optimal choice for this type of calculation, makes it a suitable technique for addressing other issues, such as charge fluctuations during dynamics (see below).

Up to now, methods used to compute partial charges for molecules or for supramolecular assemblies have always relied on static ab initio calculations for the minimum energy structure. Though, at the condensed phase, many-body interactions could cause the electronic density to be polarized and to heavily fluctuate around an average value; this has been recently shown for halide ions in water.⁶⁶ Accounting for electron cloud polarization in classical molecular dynamics simulations implies the use of multipolar expansions or fluctuating charges, with a noticeable computational overhead. Nevertheless, there are cases where a simple point charge approximation gives a fair representation of the system. DFT-based molecular dynamics simulations are the ideal test tool to look into electronic density fluctuations in the system. To get a deeper insight into this issue, we computed the atomic charges every 10 fs during a 1 ps simulation; in this case, GTH pseudopotentials were used because they guarantee reliable results at a lower computational cost than TM pseudopotentials. Average charges \bar{q} and standard error $S_{\bar{q}}$ have been computed for all atom types with both PBE and BLYP functionals. The results for PBE using both CP and BO molecular dynamics are shown in Table 2. In Table 4, we also report results for ZIF-2 and ZIF-3, for which we used the same setup for the calculations on ZIF-8. Results of CPMD with the BLYP functional are in agreement (within the error) with the ones obtained with PBE and are not shown here. It can be seen that the values of the atomic charges converge to similar values, the largest differences being around 5%. Moreover, the fluctuations are almost negligible, hinting that using a simple point charge approximation for classical molecular dynamics simulations of ZIFs is sensible. We would like to notice that the calculations with plane waves (CPMD) and with Gaussian basis sets (BOMD) give basically the same results. Thus, both of them constitute sound methods to compute electrostatic potentials inside ZIFs. A comparison of the results obtained for the three different ZIFs considered here immediately highlights that

Table 4. Partial Charges \bar{q} with the Relative Standard Errors ($S_{\bar{q}}$) of ZIF-2 and ZIF-3 Born–Oppenheimer Molecular Dynamics Simulations

	Zn	N	C1	C2	H1	H2
ZIF-2						
\bar{q}	0.6100	-0.1798	-0.0384	-0.1341	0.1042	0.1285
$S_{\bar{q}}$	0.0021	0.0006	0.0014	0.0006	0.0003	0.0015
ZIF-3						
\bar{q}	0.6082	-0.1913	0.0208	-0.1511	0.0823	0.1388
$S_{\bar{q}}$	0.0011	0.0011	0.0018	0.0005	0.0006	0.0003

the values for the point charges are quite different. Therefore, it is advisable that, to perform molecular dynamics calculations on these materials, instead of taking standard values from generic force fields, point charges should be carefully calculated for any of them.

While this manuscript was under revision, a similar study was published where point charges were computed with the REPEAT method on ZIF-8.⁶⁷ By applying different scaling factors γ to the van der Waals radii, the authors found that the value of the point charges varies over a large interval, ranging, in the case of Zn, from $0.69e$ for $\gamma = 1$ to $-2.58e$ for $\gamma = 2$. Although the authors conclude that it is hard to attach any physical interpretation to the REPEAT charges, nevertheless, it should be considered that large values of exclusion radii, such as the ones just mentioned, are never used in ESP charge methods. In addition, it should be noted that, by using $\gamma = 1$, the values of point charges are in good agreement with our cluster calculations, with recent calculations made on biosystems containing building blocks similar to that of ZIF-8,^{69,68} and with DDEC and CBAC results reported in the same article of Watanabe and co-workers.⁶⁷ Therefore, we recommend the use of the REPEAT method with $\gamma = 1$.

It is interesting to notice that, from the latter study, it seems that the adsorption isotherms calculated with Grand Canonical Monte Carlo simulations are independent of the values chosen for charges. Considering this result, it is certainly of interest to assess the role played by the point charges in driving the dynamics of the system and in reproducing other experimental properties. In our group, we have started to address this issue with the use of force field molecular dynamics simulations.

IV. CONCLUDING REMARKS

Force-field-based calculations (Monte Carlo or molecular dynamics) rely on a reduced description of the system electronic density by means of atomic partial charges. In our study, we explored different approaches to derive them for zeolite imidazolate frameworks (ZIFs). The usual approach to compute partial charges for molecular systems is based on ab initio calculations on small clusters, followed by a fitting of the quantum chemical electrostatic potential. Among the many methods, we chose the Merz–Kollman sampling scheme, which has been shown to give reliable results; we also found that, for computing partial charges, density functional theory calculations yield values comparable to the ones obtained with Hartree–Fock and perturbative methods.

Partial charges computed for molecules give a fair description of the electronic density of the isolated system, which is considered to be slightly perturbed in the condensed phase; thus, values calculated for the isolated systems are transferred to liquid/solid simulation with a negligible loss of accuracy. This approximation does not hold for crystal systems such as ZIFs; in fact, every

atom/molecule in the supramolecular structure feels the crystalline environment, which should be somehow included in the description. Thus, for example, computing partial charges on the cluster formed by one zinc atom coordinated by four methylimidazolium molecules would make sense if we were interested only in the zinc charge. On the other hand, if we need to know the charges on N, we should consider a symmetric structure around the molecule.

To this end, we have explored two different methodological approaches to compute partial charges on ZIF-8 from first principles calculations. The first approach has been based on the building up of isolated clusters resembling the structure and symmetry of the crystal. We have observed that, in order to obtain converged results, the size of the cluster should be around 400–500 atoms, which renders this approach extremely computationally expensive. The second method is based on evaluating the REPEAT charges on the periodic crystal structure. In order to define an operative protocol to compute partial charges on ZIF-8 (which would be extended to similar materials), we compared the results obtained with two different functionals and six pseudopotentials. We found that ultrasoft Vanderbilt pseudopotentials give larger errors compared to norm-conserving Troullier–Martins or Goedecker–Teter–Hutter pseudopotentials. The results obtained with both PBE and BLYP functionals are in fair agreement, hinting that the computed properties are well described with the two of them. The convergence of results has been checked against the value of the pseudopotentials' cutoff. In the case of plane wave calculations, the partial charges converge at 150 Ry for the wave function cutoff, while for a mixed plane wave and Gaussian basis sets treatment, we found a density cutoff of 700 Ry to be the ideal choice. In passing, we notice that the values obtained for Zn and N are in agreement with those from recent studies^{67–69} on ZIFs and on systems of biological interest.

The values of REPEAT charges are also in agreement with those computed, at a much higher computational cost, on large isolated clusters. Given the reliability of the method, and considering its relatively low computational overhead, in the second part of the article, we looked into the fluctuations of charges, by propagating the system with DFT-based molecular dynamics simulations of the periodic structure. REPEAT charges have been computed for many configurations of three zeolite imidazolate frameworks, slightly differing among them in the structure and substituents: ZIF-8, ZIF-2, and ZIF-3.

For ZIF-8, both Car–Parrinello and Born–Oppenheimer molecular dynamics simulations show that the value obtained in single point calculations are in agreement with the average value during the time evolution of the system. The common feature to the three ZIFs studied is that the fluctuations in the charges of every atom are small. To our knowledge, this represents the first study of atomic partial charges where the fluctuations are taken into account; our results justify the choice of using the point charge approximation for these kinds of materials, given that the fluctuations are negligible. Nevertheless, if highly charged or polarizable adsorbates interact with the framework, the inclusion of polarization could be important in the description of physical chemical properties of ZIFs. Further studies in this direction are now in progress in our group.

■ AUTHOR INFORMATION

Corresponding Author

*E-mail: marco.masia@uniss.it.

ACKNOWLEDGMENT

The authors thankfully acknowledge C. Campaña, B. Mussard, and T. K. Woo for having kindly provided us with their code for computing REPEAT charges. This research has been funded by the European–Indian research project AMCOS (Advanced Materials Computational Study), NMP3-SL-2009-233502. The authors thankfully acknowledge the computer resources, technical expertise, and assistance provided by CASPUR within the Standard HPC grant Project std09-373 and by CINECA for the ISCRA project AIMD–ZIF (HP10AU2801). The “Consorzio COSMOLAB” is also acknowledged for the resources provided within the *Cybersar Project*. F.G.P. is thankful for the Master and Back fellowship provided by Regione Autonoma della Sardegna.

REFERENCES

- (1) James, S. L. *Chem. Soc. Rev.* **2003**, 32, 276.
- (2) Côté, A. P.; Benin, A. I.; Ockwig, N. W.; O’Keeffe, M.; Matzger, A. J.; Yaghi, O. M. *Science* **2005**, 310, 1166.
- (3) Park, K. S.; Ni, Z.; Côté, A. P.; Choi, J. Y.; Huang, R.; Uribe-Romo, F. J.; Chae, H. K.; O’Keeffe, M.; Yaghi, O. M. *Proc. Natl. Acad. Sci. U.S.A.* **2006**, 103, 10186.
- (4) Tian, Y. Q.; Zhao, Y. M.; Chen, Z. X.; Zhang, G. N.; Weng, L. H.; Zhao, D. Y. *Chem.—Eur. J.* **2007**, 13, 4146.
- (5) Banerjee, R.; Phan, A.; Wang, B.; Knobler, C.; Furukawa, H.; O’Keeffe, M.; Yaghi, O. M. *Science* **2008**, 319, 939.
- (6) Banerjee, R.; Furukawa, H.; Britt, D.; Knobler, C.; O’Keeffe, M.; Yaghi, O. M. *J. Am. Chem. Soc.* **2009**, 131, 3875.
- (7) Tafipolsky, M.; Amirjalayer, S.; Schmid, R. *Microporous Mesoporous Mater.* **2010**, 129, 304.
- (8) Rankin, R. B.; Liu, J.; Kulkarni, A. D.; Johnson, J. K. *J. Phys. Chem. C* **2009**, 113, 16906.
- (9) Liu, D.; Zheng, C.; Yang, Q.; Zhong, C. *J. Phys. Chem. C* **2009**, 113, 5004.
- (10) Liu, B.; Smit, B. *J. Phys. Chem. C* **2010**, 114, 8515.
- (11) Henkelman, G.; Arnaldsson, A.; Jonsson, H. *Comput. Mater. Sci.* **2006**, 36, 354.
- (12) Mulliken, R. S. *J. Chem. Phys.* **1955**, 23, 1833.
- (13) Bader, R. F. W. In *Atoms in Molecules*; Clarendon: Oxford, U. K., 1990.
- (14) Liu, J.; Rankin, R. B.; Johnson, J. K. *Mol. Simul.* **2009**, 35, 60.
- (15) Astrand, P. O.; Ruud, K.; Mikkelsen, K. V.; Helgaker, T. *J. Phys. Chem. A* **1998**, 102, 7686.
- (16) Salles, F.; Ghoufi, A.; Maurin, G.; Bell, R. G.; Mellot-Draznieks, C.; Ferey, G. *Angew. Chem., Int. Ed.* **2008**, 47, 8487.
- (17) Momany, F. A. *J. Phys. Chem.* **1978**, 82, 592.
- (18) Cox, S. R.; Williams, D. E. *J. Comput. Chem.* **1981**, 2, 304.
- (19) Bayly, C. I.; Cieplak, P.; Cornell, W. D.; Kollman, P. A. *J. Phys. Chem.* **1993**, 97, 10269.
- (20) Laio, A.; VandeVondele, J.; Rothlisberger, U. *J. Phys. Chem. B* **2002**, 106, 7300.
- (21) Singh, U. C.; Kollman, P. A. *J. Comput. Chem.* **1984**, 5, 129.
- (22) Besler, B. H.; Merz, K. M.; Kollman, P. A. *J. Comput. Chem.* **1990**, 11, 431.
- (23) Chirlian, L. E.; Francl, M. M. *J. Comput. Chem.* **1987**, 8, 894.
- (24) Breneman, C. M.; Wiberg, K. B. *J. Comput. Chem.* **1990**, 11, 361.
- (25) Dubbeldam, D.; Walton, K. S.; Ellis, D. E.; Snurr, R. Q. *Angew. Chem., Int. Ed.* **2007**, 46, 4496.
- (26) Greathouse, J. A.; Allendorf, M. D. *J. Phys. Chem. C* **2008**, 112, 5795.
- (27) Maciel, G. S.; Garcia, E. *Chem. Phys. Lett.* **2005**, 409, 29.
- (28) Heinz, H.; Suter, U. W. *J. Phys. Chem. B* **2004**, 108, 18341.
- (29) Martin, F.; Zipse, H. *J. Comput. Chem.* **2005**, 26, 97.
- (30) Yang, Q.; Zhong, C. *ChemPhysChem* **2006**, 7, 1417.
- (31) Campaña, C.; Mussard, B.; Woo, T. K. *J. Chem. Theory Comput.* **2009**, 5, 2866.
- (32) Moggach, S. A.; Bennett, T. D.; Cheetham, A. K. *Angew. Chem., Int. Ed.* **2009**, 48, 7087.
- (33) Wu, H.; Zhou, W.; Yildirim, T. *J. Am. Chem. Soc.* **2007**, 129, 5314.
- (34) Venna, S. R.; Carreon, M. A. *J. Am. Chem. Soc.* **2010**, 132, 76.
- (35) Liu, Y.; Liu, H.; Hu, Y.; Jiang, J. *J. Phys. Chem. B* **2009**, 113, 12326.
- (36) Zhou, M.; Wang, Q.; Zhang, L.; Liu, Y.; Kang, Y. *J. Phys. Chem. B* **2009**, 113, 11049.
- (37) Pantatosaki, E.; Pazzona, F. G.; Megariotis, G.; Papadopoulos, G. K. *J. Phys. Chem. B* **2010**, 114, 2493.
- (38) Liu, Y.; Liu, H.; Hu, Y.; Jiang, J. *J. Phys. Chem. B* **2010**, 114, 2820.
- (39) Pérez-Pellitero, J.; Amrouche, H.; Siperstein, F. R.; Pirngruber, G.; Nieto-Draghi, C.; Chaplais, G.; Simon-Masseron, A.; Bazer-Bachi, D.; Peralta, D.; Bats, N. *Chem.—Eur. J.* **2010**, 16, 1560.
- (40) Frisch, M. J.; Trucks, G. W.; Schlegel, H. B.; Scuseria, G. E.; Robb, M. A.; Cheeseman, J. R.; Montgomery, J. A., Jr.; Vreven, T.; Kudin, K. N.; Burant, J. C.; Millam, J. M.; Iyengar, S. S.; Tomasi, J.; Barone, V.; Mennucci, B.; Cossi, M.; Scalmani, G.; Rega, N.; Petersson, G. A.; Nakatsuji, H.; Hada, M.; Ehara, M.; Toyota, K.; Fukuda, R.; Hasegawa, J.; Ishida, M.; Nakajima, T.; Honda, Y.; Kitao, O.; Nakai, H.; Klene, M.; Li, X.; Knox, J. E.; Hratchian, H. P.; Cross, J. B.; Bakken, V.; Adamo, C.; Jaramillo, J.; Gomperts, R.; Stratmann, R. E.; Yazyev, O.; Austin, A. J.; Cammi, R.; Pomelli, C.; Ochterski, J. W.; Ayala, P. Y.; Morokuma, K.; Voth, G. A.; Salvador, P.; Dannenberg, J. J.; Zakrzewski, V. G.; Dapprich, S.; Daniels, A. D.; Strain, M. C.; Farkas, O.; Malick, D. K.; Rabuck, A. D.; Raghavachari, K.; Foresman, J. B.; Ortiz, J. V.; Cui, Q.; Baboul, A. G.; Clifford, S.; Cioslowski, J.; Stefanov, B. B.; Liu, G.; Liashenko, A.; Piskorz, P.; Komaromi, I.; Martin, R. L.; Fox, D. J.; Keith, T.; Al-Laham, M. A.; Peng, C. Y.; Nanayakkara, A.; Challacombe, M.; Gill, P. M. W.; Johnson, B.; Chen, W.; Wong, M. W.; Gonzalez, C.; Pople, J. A. *Gaussian 03, Revision B.03*; Gaussian, Inc.: Wallingford, CT, 2004.
- (41) Ahlrichs, R.; Bär, M.; Häser, M.; Horn, H.; Kölmel, C. *Chem. Phys. Lett.* **1989**, 162, 165.
- (42) *TURBOMOLE V6.0 2007*, a development of University of Karlsruhe and Forschungszentrum Karlsruhe GmbH, 1989–2007, TURBOMOLE GmbH, since 2007; available from <http://www.turbomole.com>.
- (43) Tao, J.; Perdew, J. P.; Staroverov, V. N.; Scuseria, G. E. *Phys. Rev. Lett.* **2003**, 91, 146041.
- (44) Vahtras, O.; Almlöf, J.; Feyereisen, M. *Chem. Phys. Lett.* **1993**, 213, 514.
- (45) Sierka, M.; Hogekamp, A.; Ahlrichs, R. *J. Chem. Phys.* **2003**, 118, 9136.
- (46) *CPMD*, version 3.13; Copyright IBM Corp. 1990–2008 (MPI für Festkörperforschung Stuttgart 1997–2001).
- (47) Lippert, G.; Hutter, J.; Parrinello, M. *Mol. Phys.* **1997**, 92, 477.
- (48) Becke, A. D. *Phys. Rev. A* **1988**, 38, 3098.
- (49) Lee, C.; Yang, W.; Parr, R. G. *Phys. Rev. B* **1988**, 37, 785.
- (50) Perdew, J. P.; Burke, K.; Ernzerhof, M. *Phys. Rev. Lett.* **1996**, 77, 3865.
- (51) Troullier, N.; Martins, J. L. *Phys. Rev. B* **1991**, 43, 1993.
- (52) Goedecker, S.; Teter, M.; Hutter, J. *Phys. Rev. B* **1996**, 54, 1703.
- (53) Hartwigsen, C.; Goedecker, S.; Hutter, J. *Phys. Rev. B* **1998**, 58, 3641.
- (54) Krack, M. *Theor. Chem. Acc.* **2005**, 114, 145.
- (55) Vanderbilt, D. *Phys. Rev. B* **1990**, 41, 7892.
- (56) Kosa, M.; Tan, J.; Merrill, C. A.; Krack, M.; Cheetham, A. K.; Parrinello, M. *ChemPhysChem* **2010**, 11, 2332.
- (57) Martyna, G.; Klein, M.; Tuckerman, M. *J. Chem. Phys.* **1992**, 97, 2635.
- (58) Car, R.; Parrinello, M. *Phys. Rev. Lett.* **1985**, 55, 2471.
- (59) VandeVondele, J.; Krack, M.; Mohamed, F.; Parrinello, M.; Chassaing, T.; Hutter, J. *Comput. Phys. Commun.* **2005**, 167, 103.
- (60) VandeVondele, J.; Hutter, J. *J. Chem. Phys.* **2003**, 118, 4365.
- (61) Rappe, A. K.; Casewit, C. J.; Colwell, K. S.; Goddard, W. A., III; Skiff, W. M. *J. Am. Chem. Soc.* **1992**, 114, 10024.

- (62) Ewald, P. P. *Ann. Phys.* **1921**, *64*, 253.
- (63) Allen, M. P.; Tildesley, D. J. In *Computer Simulations of Liquids*; Oxford University Press: Oxford, U. K., 1987.
- (64) Sola, J; Guàrdia, E.; Masia, M. *J. Chem. Phys.* **2010**, *133*, 234101.
- (65) Sagara, T.; Klassen, J.; Ganz, E. *J. Chem. Phys.* **2004**, *121*, 12543.
- (66) Guàrdia, E.; Skarmoutsos, I.; Masia, M. *J. Chem. Theory Comput.* **2009**, *5*, 1449.
- (67) Watanabe, T.; Manz, T. A.; Sholl, D. S. *J. Phys. Chem. C* **2011**, *115*, 4824.
- (68) Lin, F.; Wang, R. *J. Chem. Theory Comput.* **2010**, *6*, 1852.
- (69) Xu, Q.; Zhong, C. *J. Phys. Chem. C* **2010**, *114*, 5035.

Use of Umbrella Sampling to Calculate the Entrance/Exit Pathway for Z-Pro-Prolinal Inhibitor in Prolyl Oligopeptidase

Jean-François St-Pierre,[†] Mikko Karttunen,[‡] Normand Mousseau,^{*,†} Tomasz Róg,[§] and Alex Bunker^{||,⊥}

[†]Département de Physique and Regroupement Québécois sur les Matériaux de Pointe, Université de Montréal, C.P. 6128, succursale centre-ville, Montréal (Québec), Canada H3C 3J7

[‡]Department of Applied Mathematics, The University of Western Ontario, 1151 Richmond Street North, London (Ontario), Canada N6A 5B7

[§]Department of Physics, Tampere University of Technology, P.O. Box 692, FI-33101 Tampere, Finland

^{||}Centre for Drug Research, Faculty of Pharmacy, University of Helsinki, P.O. Box 56, FI-00014, University of Helsinki, Finland

[⊥]Department of Chemistry, Aalto University, PO Box 6100, FI-02015, Aalto, Finland

ABSTRACT: Prolyl oligopeptidase (POP), a member of the prolyl endopeptidase family, is known to play a role in several neurological disorders. Its primary function is to cleave a wide range of small oligopeptides, including neuroactive peptides. We have used force biased molecular dynamics simulation to study the binding mechanism of POP. We examined three possible binding pathways using Steered Molecular Dynamics (SMD) and Umbrella Sampling (US) on a crystal structure of porcine POP with bound Z-pro-prolinal (ZPP). Using SMD, an exit pathway between the first and seventh blade of the β -propeller domain of POP was found to be a nonviable route. US on binding pathways through the β -propeller tunnel and the TYR190-GLN208 flexible loop at the interface between both POP domains allowed us to isolate the flexible loop pathway as the most probable. Further analysis of that pathway suggests a long-range covariation of the interdomain H-bond network, which indicates the possibility of large-scale domain reorientation observed in bacterial homologues and hypothesized to also occur in human POP.

1. INTRODUCTION

Endopeptidases are a class of proteases that hydrolyze internal, i.e., nonterminal, peptide bonds. Prolyl oligopeptidase (POP) is a proline-specific endopeptidase that cleaves oligopeptides (<30-mer) at the C-side of an internal proline. *In vitro* analysis found that a wide variety of neuroactive peptides substrates can be cleaved by POP,^{1–5} and *in vivo* analysis indicates that these are its actual metabolic substrates.² It has been found, although somewhat inconsistently, that certain POP inhibitors can reverse memory loss caused by amnesic agents, neurological disorders, and aging, making POP an important drug target.^{6,7} In addition, an alteration in POP enzyme activity has been measured in serum samples taken from patients suffering from Parkinson's and Alzheimer's disease⁸ and multiple sclerosis.⁹ Experimental evidence exists that POP might have a role beyond its peptidase function. Examples of this include protein–protein interactions,^{2,10} intracellular transport,¹¹ inflammation,^{12,13} angiogenesis,¹⁴ and cancer development.^{14,15} The biochemical role of POP and its inhibitors has been reviewed in refs 1–5, 7, and 16.

Several fundamental questions regarding access to the active site, gating, selection, and the detailed inhibition mechanisms remain unanswered. Recent studies have combined a number of experimental and simulation techniques to address the details of inhibition mechanisms¹⁷ as well as binding and gating mechanisms,¹⁸ and progress has been made in developing combinatorial libraries for POP.¹⁹

In this paper, our focus is on the active site access (exit) pathways. This is a fundamental question in understanding the peptidase function. What makes this question particularly

challenging is its dynamic nature: entry and exit involve dynamic response. Hence, docking studies and short time-scale density functional calculations are not able to address this question. We study porcine POP, crystallized with a bound ZPP inhibitor described by Fülöp et al.²⁰ (PDB database ID 1QFS). The structure is composed of two domains: the protease catalytic domain with an α – β hydrolase fold composed of amino acids 1–71 and 436–710 and the seven-bladed β -propeller, comprised of amino acids 72–435. The active site is on the surface of an internal cavity between the two protein domains. The ZPP inhibitor has a hydrophobic head that sterically blocks the active site and an aldehyde tail that forms a reversible covalent hemiacetal bond with the SER554 residue of the catalytic domain. The β -propeller domain has an unusual, mostly hydrophobic interaction between the first and seventh blades. This is called the “velcro rip” and has been proposed to act as a filter to the active site.^{20–23} Later studies have demonstrated that the domain by itself is more stable than in conjunction with the catalytic domain.²⁴ This finding is in agreement with a small scale computational study carried out by Fuxreiter et al.²⁵ and our previous computational work on POP with an unbound inhibitor in the binding cavity:²⁶ both indicate that the β -propeller is a highly stable structure. It was suggested that the entry point is most likely through the H-bonded network of loosely structured loops that connect the two protein domains, in particular the location of the TYR190-GLN208 flexible loop.

Received: December 8, 2010

Published: April 29, 2011

Recent electron microscopy experiments suggest that the interdomain region offers a wider entry point than the β -propeller tunnel.¹⁸ For example, Shan and collaborators find that the crystal structure of a distant POP relative, *Sphingomonas capsulata* (SC; PDB database ID 1YRZ), displays an open conformation in absence of the inhibitor, where the two domains are separated, exposing the catalytic triad to the solvent.²⁷ Experimental evidence of an open form of a homologous protein has also been captured by X-ray diffraction crystallography of *Aeromonas punctata* prolyl endopeptidase.²⁸ In that study, Li et al. captured the closed form of the protein after soaking the open form of the crystallized protein in a bath of the inhibitor. By maintaining the protein in this open form using glutaraldehyde driven lysine cross-linking, they obtained a complete absence of activity. This interdomain large-scale motion has not yet been observed in experiments performed on mammalian POP. Cysteine cross-linking experiments binding the two domains together have, however, been shown to lead to strongly reduced protein activity.²⁹

Elucidating the mechanism through which substrates gain access to the active site, i.e., identifying the ligand entry pathway, would be beneficial for the development of new classes of inhibitors for mammalian POP. It is important to perform full MD simulations with explicit solvent since water can access the active site and in some cases even have a decisive role.³⁰ To study the entry pathways, it is necessary to test the various possible trajectories directly. In this paper, we use SMD and US to measure the free energies of the three postulated exit/entry pathways of the ZPP inhibitor. Once we have determined the correct entry/exit pathway, we then study the interaction between inhibitor and the elements of the protein structure that comes in contact with it. Although SMD is first used to generate rough pathways, the bulk of our results are obtained using US. Using these methods, we determine that the most probable exit pathway is through the loosely structured loops between the two domains opposite the interdomain hinge.

2. METHODS

2.1. Software, Model, and Simulation Parameters. All simulations were performed using the GROMACS 4.0 simulation package³¹ at constant pressure (1 bar) and temperature (310 K; NPT). Temperature was maintained using the Nosé–Hoover thermostat^{32,33} and pressure using the Parrinello–Rahman barostat.³⁴ The coupling time constants were set to 0.1 and 1.0 ps for thermostat and barostat, respectively, and the protein and solvent were thermalized separately. Electrostatic interactions were computed using the Particle-Mesh-Ewald method (PME).^{35,36} The Lennard-Jones interactions were cut off at 1.0 nm. The same cutoff was used for the real-space part of PME. Charge groups were chosen to be small to avoid artifacts that may arise if the charge groups are spatially too large.³⁷

To parametrize the POP and ZPP molecules and the solution ions, we used the OPLS-AA (Optimized Parameters for Liquid Simulations, AA stands for all-atom) potential set.³⁸ Partial charges on ZPP were taken from our previous work.²⁶ For water, the TIP3P model was used.³⁹

The initial structure was taken from our previous 100 ns MD study of POP with the ZPP inhibitor unbound in the active site.²⁶ POP was solvated in a box of water of size $10 \times 10 \times 10$ nm. Potassium and chlorine ions were added to neutralize the system

to model physiological conditions (140 mM salt concentration). The solvated simulation box contained a total of 100 468 atoms.

Analysis and visualization were performed using the VMD (Visual Molecular Dynamics) package⁴⁰ and GROMACS^{31,41} analysis tools. Pathways were generated and evaluated using SMD and US, as described in the following sections.

2.2. SMD and US. In SMD, an external force, called force bias, F_{fb} , is applied to a single atom or a group of chosen atoms, through their center of mass. SMD is an irreversible approach, and its use is based on the Jarzynski equality $\langle \exp[-W/k_{\text{B}}T] \rangle = \exp[-\Delta G/k_{\text{B}}T]$, where k_{B} is the Boltzmann constant, T is temperature, and W is the total nonreversible work done on the system by F_{fb} during a nonequilibrium transition between two states connected by a reaction coordinate λ .^{42–44} The free energy difference between these two states is given by $\Delta G \equiv \Delta G(\lambda)$. The angular brackets stand for an ensemble average taken by repeating the simulation many times along the path connecting the initial and final states, λ_1 and λ_2 . The essence of the Jarzynski equality is that it links rigorously the work done in a nonequilibrium process to the change in the equilibrium free energy difference. This method has been used in small systems, e.g., single molecule conformational changes,^{45–47} and, more rarely, in larger systems involving, e.g., protein–protein interactions.⁴⁸

We define the direction of F_{fb} as \hat{r}_{fb} . All other degrees of freedom are allowed to react freely to this force. To drive the system, we apply a harmonic force

$$\vec{F}_{\text{fb}}(\lambda) = k_{\text{fb}}(\lambda \vec{r}_{\text{fb}} - \vec{r}_{\text{cm}}) \quad (1)$$

where k_{fb} is the force constant and \vec{r}_{cm} is the center of mass. A force bias with a fixed value of k_{fb} is introduced with λ increasing from zero to one at a continuous rate as the simulation proceeds. This rate is known as the *pulling rate*.

It has been shown by Park and Schulten⁴⁹ that the Jarzynski equality is equivalent to calculating the free energy difference from the first and the second-order cumulants of the work done by the biasing force:

$$\Delta G = \langle W \rangle - \frac{\langle W^2 \rangle - \langle W \rangle^2}{2k_{\text{B}}T} \quad (2)$$

While both the Jarzynski equality and eq 2 are formally correct in the thermodynamic limit, finite sampling leads to potential problems since ΔG depends exponentially on W ; the result is easily dominated by the extremal values of the distribution.^{50,51} The impact of this sensitivity to rare pathways can be evaluated by comparing results obtained from these two methods.

US^{52,53} obtains the free-energy difference between two states from a set of equilibrated simulations. Like in SMD, a force bias is applied. However, now the configuration is equilibrated at each step, which we refer to as window. The value of the harmonic force constant used for each window is independent and can be set to a value that optimizes the efficiency with which the phase space is sampled. Parameters k_i and λ must be selected in such a way as to ensure that the phase space sampled by adjacent windows overlaps sufficiently, forming a continuous pathway between the initial and the final state. Results from all windows can then be combined using the weighted histogram analysis method (WHAM)⁵⁴ to provide the full thermodynamical evolution along the reaction coordinate.

Examples exist of systems where US has been successfully applied to include ion channels,^{55,56} unfolding of the I27 titin domain,⁵⁷ and the evaluation lipid transfer and peptide penetration

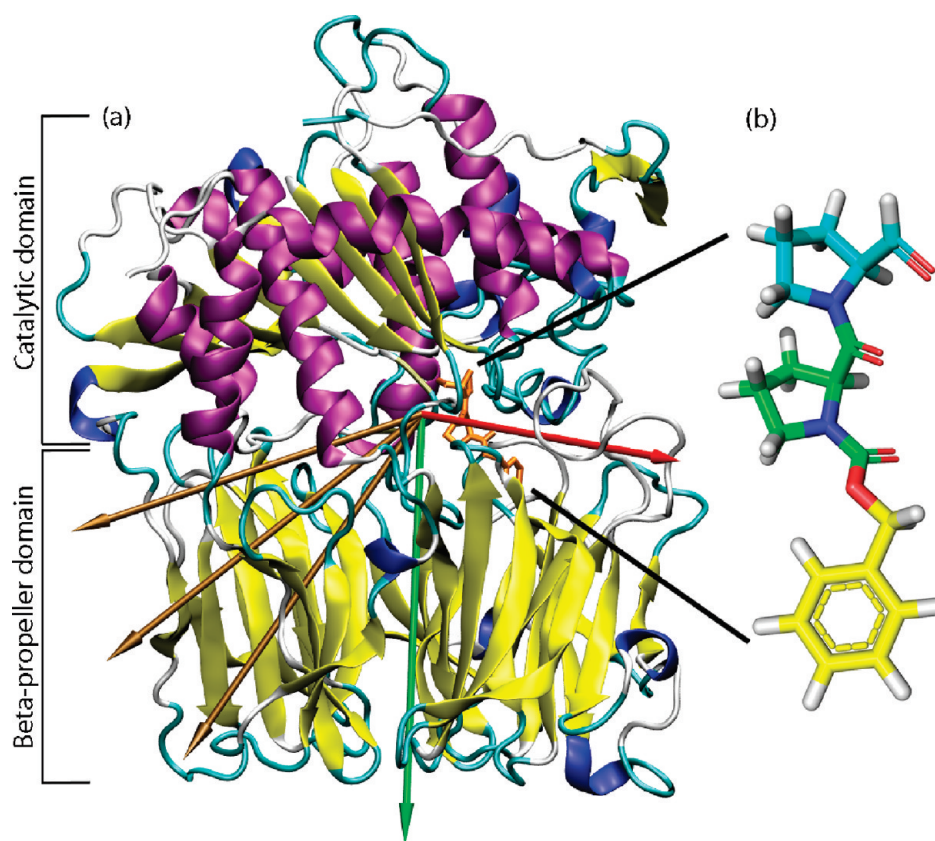


Figure 1. (a) SMD ZPP-pulling vectors for the flexible loop exit (red), the β -propeller tunnel exit (green), and three possible exits through the velcro-rip of the β -propeller (golden arrows). The ZPP inhibitor inside is in orange. (b) Zoom on the ZPP with carbons colored by our definition of its three regions: PHE (yellow), PRO1 (green), and PRO2 (cyan) groups. In its inhibition mode, the PRO2 aldehyde group is involved in a covalent bond to the SER554 of the protein. Oxygen and nitrogen atoms are left in red and dark blue, respectively.

in cellular membranes.^{58,59} SMD and US have been compared for ligand binding in the gramicidin A channel and Kv11.1 (also known as hERG) potassium channel.⁶⁰ Several comprehensive reviews are available.^{61,62}

2.3. Application of SMD and US to the Study of Our System. SMD employing the Jarzynski equality was performed on the system with the applied bias force dislocating the ZPP molecule from the binding pocket along the three proposed pathways shown in Figure 1a. We generated one pull vector each for the pathways through the β -propeller tunnel and the flexible loop. For the third pathway, the velcro-rip junction between the first and seventh blade of the β -propeller, three different pull vectors (see Figure 1a) were attempted to test this suggested exit pathway.^{20–23}

Since the center of mass and the orientation of the protein are not inherently conserved properties for the simulated system (protein + ZPP + solvent), it was necessary to add restraints to conserve the position and orientation of the protein. This was achieved by restraining the positions of a small number of α -carbon atoms positioned far from the sampled ZPP exit pathway with harmonic restoring forces with a force constant of 10 kJ/(mol \times nm²). Two sets of weak restraints were selected, for the flexible loop exit and β -propeller tunnel pathways, and in both cases the harmonic force constant on these restraints was 2–3 orders of magnitude smaller than the restraining force bias applied to the ZPP ligand. For the β -propeller tunnel pathway, the restrained residues PRO7-ASP35, ASP431-GLY464,

TYR510-LYS546, and ILE610-GLN629 were all located on the catalytic domain and did not form part of the inner cavity. For the flexible loop exit, the atoms selected for restraint span both domains: on the catalytic domain, the α -carbon atoms of the residues VAL427-LYS458 were restrained, and on the beta-propeller, they were placed on amino acids TYR73-GLY108 and GLY288-LYS458. Although, formally, this position on both domains affects allosteric communication between the two domains, the restraints are weak enough and dispersed enough to minimize this possibility. With the orientation of the protein maintained, the force bias is relative to the center of mass of the protein, and the expression for the force bias vector becomes

$$\vec{F}_{\text{fb}} = k_{\text{fb}}(\lambda \vec{r}_{\text{fb}} - (\vec{r}_{\text{cm-ZPP}} - \vec{r}_{\text{cm-protein}})) \quad (3)$$

Following the work of Tskhovrebova et al.,⁶³ we first computed the free-energy barriers for the different exit pathways using SMD. This was performed with a harmonic force constant $k_{\text{fb}} = 5$ MJ/(mol \times nm²) and pulling rates of 0.5 nm/ns, as was used in previous work,⁶⁴ and also of 0.1 nm/ns. To make it possible for the ZPP to exit POP, the simulation box was extended by 2.0 nm in the direction of the force bias for the β -propeller tunnel pulling vector, which brings the total number of atoms in the periodic box to 130 004.

For our US, we used states obtained from the SMD as starting configurations. For each window, we selected a state where the value of the component of the displacement vector (the vector

Table 1. Umbrella Sampling Windows Parameters for the Flexible Loop Exit^a

window	<i>z</i> (nm)	<i>T</i> (ns)	<i>k</i> _{fb} (MJ/(mol × nm ²))	source	window	<i>z</i> (nm)	<i>T</i> (ns)	<i>k</i> _{fb} (MJ/(mol × nm ²))	source
1	0.3	10	2.5	SMD	18b	1.95	7.2	10	18
2	0.4	10.1	2.5	SMD	19	2.1	10.1	2.5	SMD
3	0.5	10	2.5	SMD	20	2.2	10.1	2.5	SMD
4	0.6	10.1	2.5	SMD	20b	2.14	10.1	10	20
5	0.7	10	2.5	SMD	21	2.3	10.1	2.5	SMD
6	0.8	10	2.5	SMD	22	2.4	5	2.5	SMD
7	0.9	10	2.5	SMD	23	2.5	10	2.5	SMD
8	1	10	2.5	SMD	24	2.6	10	2.5	SMD
8b	1	8.4	10	8	25	2.7	10.1	2.5	SMD
9	1.1	10	2.5	SMD	26	2.8	10.1	2.5	SMD
9b	1.05	8.4	10	9	27	2.9	7	2.5	SMD
9c	1.1	7.1	10	9	28	3	10	2.5	SMD
10	1.2	10.1	2.5	SMD	29	3.1	10	2.5	SMD
10b	1.15	8.4	10	10	30	3.2	10	2.5	SMD
10c	1.2	8.4	10	10	31	3.3	10	2.5	SMD
11	1.3	10	2.5	SMD	32	3.4	10	2.5	SMD
12	1.4	10	2.5	SMD	33	3.5	10	2.5	SMD
13	1.5	10	2.5	SMD	34	3.6	10	2.5	SMD
13b	1.47	10	10	13	35	3.7	10	2.5	SMD
14	1.6	10.1	2.5	SMD	36	3.8	10	2.5	SMD
15	1.7	10.1	2.5	SMD	37	3.9	10	2.5	SMD
15b	1.65	8.4	10	15	38	4	10	2.5	SMD
15c	1.7	8.5	10	15	39	4.1	10	2.5	SMD
16	1.8	10	2.5	SMD	40	4.2	10	2.5	SMD
16b	1.75	7.1	10	16	41	4.3	11	2.5	SMD
16c	1.8	8.5	10	16	42	4.4	10	2.5	SMD
17	1.9	10	2.5	SMD	43	4.5	10	2.5	SMD
17b	1.85	7.2	10	17	44	4.6	10	2.5	SMD
17c	1.9	7.1	10	17	45	4.7	10	2.5	SMD
18	2	10	2.5	SMD	46	4.8	10	2.5	SMD

^a *z* is the reaction coordinate, the equilibrium distance between the ZPP and protein's center of mass for each window. *k*_{fb} is the force constant of the spring restraining the ZPP at distance *z*. *T* is the length of time of the window's MD simulation. The "source" column indicates what was the source of the initial conformation of the window, where SMD means it was extracted from the close position in the steered molecular dynamics and where a number points to the US window for which the last conformation was extracted.

connecting the centers of mass of the POP and ZPP along the direction of the force bias) matched the value of λ for the window.

Only the flexible loop and the β -propeller exit pathways were studied with US. The pathways were divided into 46 and 48 windows, respectively, with the reaction coordinate values separated by 0.1 nm. In each window, $k_{fb} = 2.5$ MJ/(mol × nm²), and force biased MD was performed for 10 ns and 8–9 ns, respectively. These initial simulations were started using conformations obtained from the SMD, as shown in Tables 1 and 2. To ensure sufficient overlap between distributions sampled in adjacent windows, undersampled regions were identified, and simulations were launched in these windows.

For the loop opening, 14 extension windows were added in regions where the resistance to sampling was particularly high (energy barrier regions); the sampling was extended by 5–8 ns, performed with a higher force constant of 5–10 MJ/(mol × nm²) to obtain a minimum sampling of 50 000 conformations per bin of size 0.01 nm along the reaction coordinate. For the β -propeller tunnel exit, 20 extension simulations with a force constant of 5 MJ/(mol × nm²) of length 5 ns each were

added to reach a minimum sampling of 100 000 conformations per bin of size 0.0095 nm. From this data, the free energy difference profile of ZPP-POP unbinding was computed using WHAM,⁵⁴ as implemented in GROMACS 4.5.3.⁶⁵ These extension windows were initiated with the last conformation of a nearby window, as indicated by the "source" columns of Tables 1 and 2.

3. RESULTS

In order to describe the ZPP molecule and its interactions with its environment, we use the same formalism as in our previous publication²⁶ to define the structure of the ZPP molecule in terms of three atomic groups. As shown in Figure 1b, PHE represents the aromatic phenyl head, PRO1 the middle proline, and PRO2 the terminal proline containing the aldehyde group (involved in the hemiacetal bond with SER554). In the following section, we describe our SMD results followed by the US results, and an analysis of the exit pathway.

3.1. Exploration of the Exit Pathways Using SMD. As the first attempt to estimate the free energy barriers associated with the exit pathways, we conducted a set of three SMD simulations

Table 2. Umbrella Sampling Windows Parameters for the β -Propeller Exit^a

window	<i>z</i> (nm)	<i>T</i> (ns)	<i>k</i> _{fb} (MJ/(mol × nm ²))	source	window	<i>z</i> (nm)	<i>T</i> (ns)	<i>k</i> _{fb} (MJ/(mol × nm ²))	source
1	−0.15	9.1	2.5	SMD	27b	2.19	9.5	5	27
2	−0.05	9.7	2.5	SMD	28	2.35	5	2.5	SMD
3	0.05	8.6	2.5	SMD	29	2.45	7.3	2.5	SMD
4	0.15	9.4	2.5	SMD	29b	2.36	8.3	5	29
5	0.25	9.3	2.5	SMD	30	2.55	8.3	2.5	SMD
5b	0.2	5	5	5	30b	2.48	5	5	30
6	0.35	9.3	2.5	SMD	31	2.65	7.9	2.5	SMD
7	0.45	9.3	2.5	SMD	31b	2.59	5	5	31
8	0.55	9	2.5	SMD	32	2.75	6.3	2.5	SMD
9	0.65	9.4	2.5	SMD	33	2.85	7.8	2.5	SMD
10	0.59	5	5	SMD	34	2.95	8.7	2.5	SMD
11	0.75	8.5	2.5	SMD	34b	2.88	5	5	34
12	0.85	8.1	2.5	SMD	35	3.05	8.6	2.5	SMD
12b	0.8	5	5	12	35b	3	5	5	35
13	0.95	8.2	2.5	SMD	36	3.15	8.6	2.5	SMD
14	1.05	7.8	2.5	SMD	37	3.25	8.3	2.5	SMD
15b	1	5	5	15	38	3.35	8.5	2.5	SMD
16	1.15	9.2	2.5	SMD	38b	3.31	5	5	38
17	1.25	7.9	2.5	SMD	39	3.45	8.2	2.5	SMD
18	1.35	8.1	2.5	SMD	39b	3.5	5	5	39
18b	1.3	5	5	18	40	3.55	8.6	2.5	SMD
19	1.45	8.2	2.5	SMD	40b	3.6	5	5	40
20	1.55	7.7	2.5	SMD	41	3.65	8.4	2.5	SMD
21	1.65	5	2.5	SMD	41b	3.7	5	5	41
21b	1.6	8.2	5	21	42	3.75	8.5	2.5	SMD
22	1.75	5	2.5	SMD	42b	3.8	5	5	42
22b	1.72	9.2	5	22	43	3.85	8.7	2.5	SMD
23	1.85	8.9	2.5	SMD	44	3.95	8.8	2.5	SMD
24	1.95	5	2.5	SMD	45	4.05	8.5	2.5	SMD
24b	1.95	9.3	5	24	45b	4.05	5	5	45
25	2.05	5	2.5	SMD	46	4.15	8.5	2.5	SMD
25b	2.05	8.4	5	25	47	4.25	8.8	2.5	SMD
26	2.15	9.3	2.5	SMD	48	4.35	8.6	2.5	SMD
27	2.25	5	2.5	SMD					

^a *z* is the reaction coordinate, the equilibrium distance between the ZPP and protein's center of mass for each window. *k*_{fb} is the force constant of the spring restraining the ZPP at distance *z*. *T* is the length of time of the window's MD simulation. The "source" column indicates what was the source of the initial conformation of the window, where SMD means it was extracted from the close position in the steered molecular dynamics and where a number points to the US window for which the last conformation was extracted.

with a pulling rate of 0.1 nm/ns and 35 SMD simulations at a rate of 0.5 nm/ns for both the flexible loop and the β -propeller exit pathways with a total simulation time near 250 ns per pulling direction. The work (*W*) required to move the ZPP over the entire path was calculated for each run. We computed the free energy difference from the distribution of *W* values using the two separate methods discussed previously and found a significant discrepancy between their results. The pull rate was found to strongly influence the sampled pathways: in all 35 SMD trajectories with the higher pulling rate along the loop exit pathway, the ligand exited either around or through the TYR190–GLN208 flexible loop, while two of the three slower SMD pathways favored a concerted opening of the same loop. Moreover, the orientation of the ZPP at the exit of these two trajectories was reversed. The trajectory requiring the lowest work had ZPP oriented such that the phenyl group PHE was directed toward the catalytic domain and the PRO2 proline group toward the β -propeller.

The second trajectory showing a concerted opening of the flexible loop had a value of *W* that was greater by 40 kJ/mol than the previous pathway. In this case, ZPP exited the protein in a reversed orientation with the PHE and PRO2 groups directed toward the β -propeller and catalytic domain, respectively. The lack of convergence in the sampled work obtained at the slow pulling rate of 0.1 nm/ns indicates that a slower pulling rate would be required for the ZPP to adopt the preferred conformation in most pulling trials. Given the large number of trials necessary for sufficient statistics, and the high computational cost of each pulling trial, this option was not retained.

We also used SMD to investigate a third possible exit pathway proposed by a number of groups, which involves ZPP moving through the velcro-rip between the first and seventh blades of the β -propeller domain (see Figure 1).^{20–23} We generated three SMD simulations using three different pulling vectors (gold vectors in Figure 1) and a pulling rate of 0.5 nm/ns. In all three

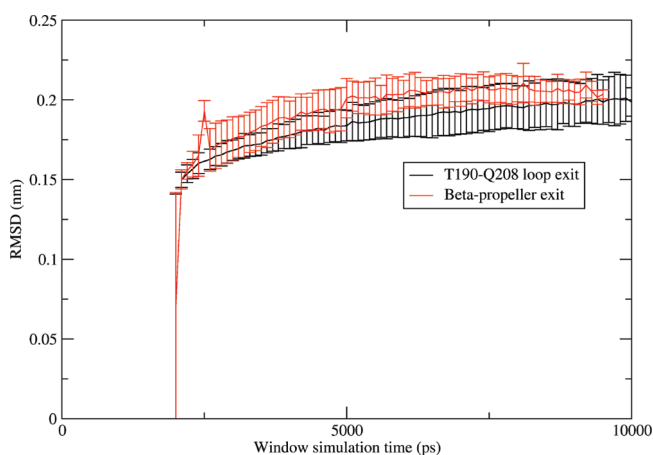


Figure 2. Average root-mean-square deviation evolution in the loop exit (black) and the β -propeller (red) as a function of displacement from the binding site. Error bars express the standard deviation.

cases, the ZPP molecule failed to pass through the velcro rip, either exiting by the β -propeller exit or through the hinge region linking the catalytic and the β -propeller domains. Clearly, the velcro-rip is extremely stable. This result is consistent with previous simulation results that indicated that the β -propeller domain is highly stable.^{26,25} Thus, this exit pathway was ruled out and the rest of our analysis focused only on the two remaining candidate pathways.

While SMD can serve to rule out a proposed exit pathway, this method requires too many simulations to converge. We did, however, use the configurations from generated pathways as starting points for US trajectories.

3.2. Free Energy Difference Calculations with US. The initial configurations for launching MD in all of the US windows were obtained from the SMD pathways. US for both the flexible loop and the β -propeller exit pathways was performed as described previously. The sum of all simulation times (i.e., including all windows) is equivalent to 539 ns of MD for the loop exit and 499 ns for the β -propeller exit. In all individual simulation windows, statistics were accumulated after an initial 2 ns equilibration with positions, simulation times, and force constants as listed in Tables 1 and 2. To evaluate convergence toward equilibrium, we computed the root-mean-square deviation (rmsd) of the protein for each window. After 4 ns, the rmsd values converged, on average, to 0.20 nm \pm 0.02 nm for the loop exit and 0.20 nm \pm 0.01 nm for the β -propeller pathway Figure 2.

Figure 3 shows the number of configurations sampled along the reaction coordinate for the loop and the β -propeller exit pathways, respectively, with bins of sizes 0.01 and 0.0095 nm. The smallest count for the loop exit is 50 585 conformations at $z = 1.45$ nm and 122 193 conformations at $z = 1.27$ nm for the β -propeller. They correspond to visiting times of 101 and 245 ps, respectively.

The resulting potential of mean force obtained from WHAM for the loop exit and β -propeller exit is presented in Figure 4. The error bars give the standard deviation as calculated using 100 iterations of statistical bootstrapping using the histogram Bayesian bootstrap available in Gromacs version 4.5.3.⁶⁵ For the loop exit, we find the lowest free energy at position 0.8 nm in the cavity, the transition peak at 1.8 nm, and the solvated free energy at 4.15 nm in the reaction coordinate. This reveals a free energy difference between the bound and free ZPP conformations of

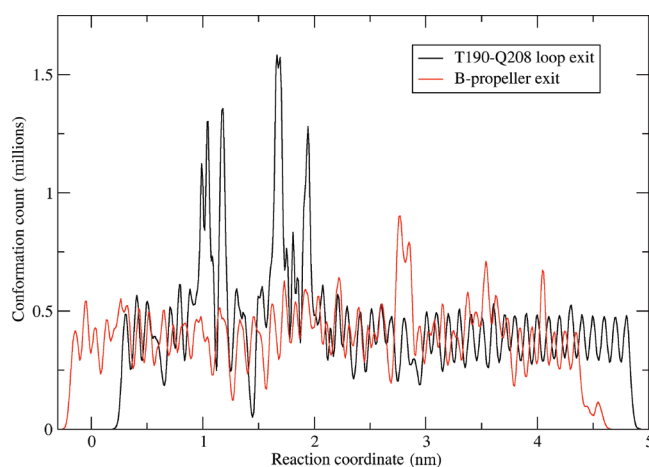


Figure 3. Histogram of the reaction coordinate along the loop exit as a function of displacement from the binding site using a bin size of 0.01 nm (black) and along the β -propeller tunnel exit using a bin size of 0.0095 nm (red).

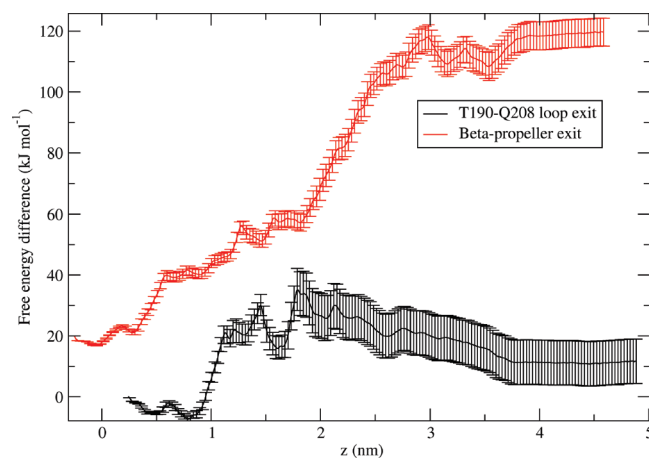


Figure 4. Potential of mean force for the loop exit (black) and β -propeller tunnel exit (red) as a function of displacement from the binding site. The red curve was shifted vertically for better legibility. Error bars express the standard deviation.

-18.5 ± 8.2 kJ/mol with a transition energy barrier of 25.1 ± 8.1 kJ/mol in the entry direction. For this interaction, we can calculate a constant of inhibition $K_i = 0.8$ mM using the formula:

$$K_i = [1M] e^{-\Delta G/RT} \quad (4)$$

where R is the perfect gas constant and T is the absolute temperature. The accuracy of ΔG was calculated to be ± 8.2 kJ/mol, on the basis of one standard deviation on the binding free energy difference; thus our the confidence interval for K_i is [32 μ M, 18 mM]. This inhibition constant is much weaker than the empirical value of $K_i = 0.35$ nM⁶⁶ since it does not include the formation of the favorable hemiacetal bond, an event not simulated in our study. However, the K_i found in our study is on the same order as other inhibitors who do not form a hemiacetal bond like suc-Gly-Pro-Nan with a $K_i = 0.278 \pm 0.35$ mM at pH 5.6 and Z-Gly-Pro-OH with a $K_i = 0.253 \pm 0.18$ mM at pH 8 or $K_i = 21.2 \pm 0.5$ μ M at pH 7.35.⁶⁷

For the β -propeller tunnel exit, a WHAM analysis performed on the US data (Figure 4 in red) yielded a free energy minimum at -0.05 nm and a transition free energy of -101.6 ± 4.7 kJ/mol, corresponding to a plateau starting at $z = 4.0$ nm, at which point the ZPP is free in the solvent. Contrary to the loop exit, this pathway shows no global minimum, rising systematically as the

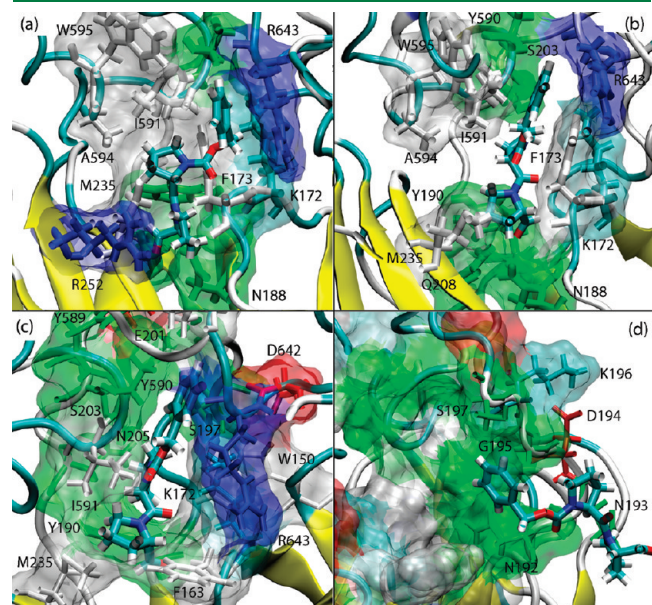


Figure 5. Main amino acids (colored by type) making contact with ZPP from the windows. $z = 1.0$ nm (a), $z = 1.3$ nm (b), $z = 1.6$ nm (c), and $z = 3.0$ nm (d).

ZPP moves out of the protein. Furthermore, the free energy barrier corresponds to a K_i of 7.6×10^{-18} M with a confidence interval [1.2 aM, 50 aM] based on one standard deviation of the free energy difference, 9 orders of magnitude smaller than the experimental value, hence very strong binding.

These two observations suggest that the β -propeller exit is not sampled sufficiently, in spite of a total of 499 ns of MD simulation dedicated to this pathway. We hypothesize that the cause of this undersampling is the pathway's extreme constriction, which leads to very low mobility of the ZPP in the windows, with a ZPP position ranging from $z = 1.95$ nm to $z = 2.95$ nm, presented in Figure 6, making it almost impossible to fully sample the accessible conformations along the trajectory. Thus, even though the displacement may vary and overlap with neighboring windows, the phase space along the exit path is not properly sampled due to the strong dependence on initial conditions for the MD run in each window. To verify this hypothesis, we compared the average radius of gyration of ZPP for both the loop and the β -propeller pathways, the number of conformation clusters adopted by ZPP based on a rmsd clustering and the standard deviation of the angular distribution of ZPP as a function of the position along the reaction coordinate (Figure 7).

The above quantities are associated with the mobility and the conformational entropy for ZPP as each new window is explored. For all three properties, the window-to-window fluctuations are 20 to 30% larger for the β -propeller exit than the flexible-loop exit. Since there is sufficient overlap between neighboring windows, we would expect that these three properties evolve smoothly from window to window, along the reaction coordinate. The large fluctuations observed for the β -propeller exit indicate rather that there is an imperfect overlap in the

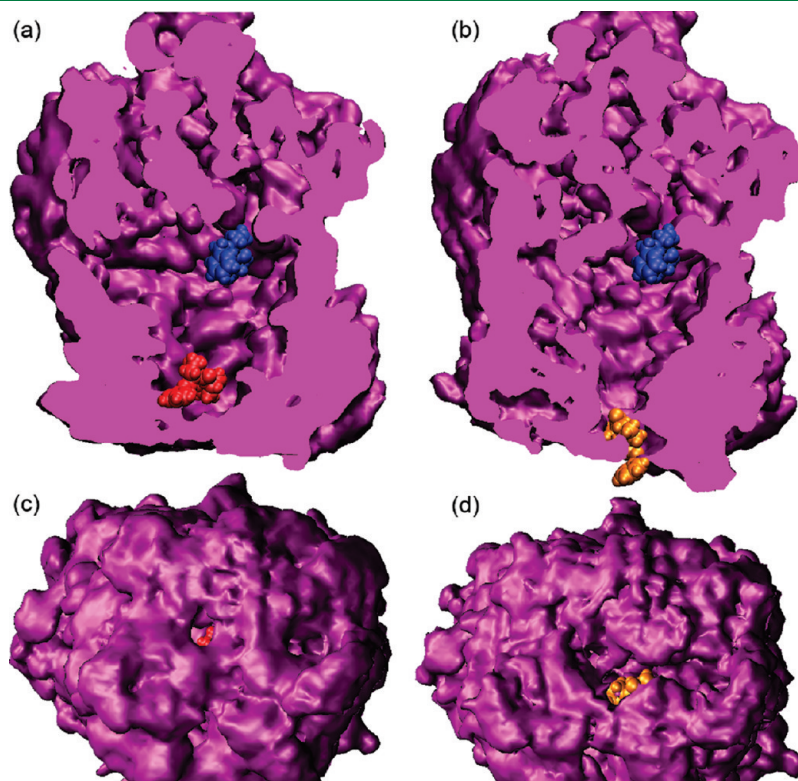


Figure 6. Constriction of the β -propeller exit pathway. Position of the ZPP is presented (a) in red for window $z = 1.95$ nm and (b) in orange for $z = 2.95$ nm, with the ZPP from window $z = -0.15$ nm in blue as a reference to the starting position. The bottom view of the β -propeller tunnel is presented in c and d, respectively. The protein's surface was computed from a volumetric density map averaged over the trajectory of the respective window.

configuration samples within adjacent windows leading to sharp conformational transitions between windows. The overlap of the position of the center of mass of ZPP between neighbor windows does not translate to a POP–ZPP complex conformation overlap of the same windows. This suggests that the visited states are strongly influenced by the initial configuration selected for each window. While we cannot, under these conditions, extract an accurate free-energy barrier for the β -propeller exit pathway, the sampling difficulties observed can be directly associated with the presence of a significant free-energy barrier. This suggests that the pathway is significantly less favorable than the loop exit. It is thus not unreasonable to conclude that this will not be the access pathway to the active site, leaving the loop exit as the only feasible pathway.

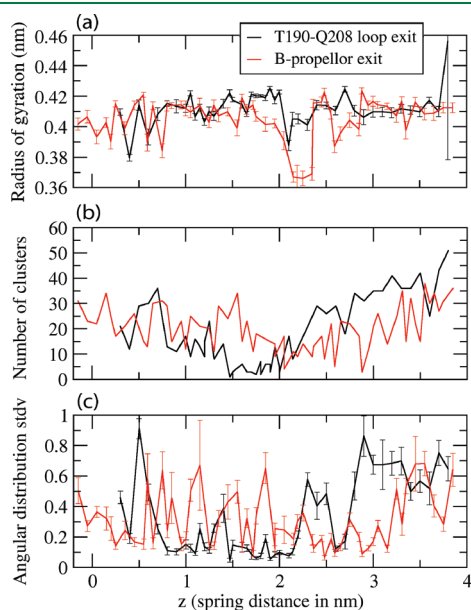


Figure 7. (a) Average radius of gyration of ZPP as a function of the displacement from the binding site. (b) Average number of conformation clusters using a rmsd clustering algorithm of cluster size 0.07 nm. (c) Standard deviation of the angular distribution of ZPP as a function of displacement. Error bars in a and c are obtained through a 5000 bootstrap evaluation of 10% of the available data and a confidence probability of 95%.

3.3. Interaction between ZPP Inhibitor and POP in Loop-Exit Pathway. Now that the loop exit, associated with three loosely structured loops between the two protein domains, has been identified as the most probable entrance/exit pathway, we investigate this pathway in further detail.

We investigated the relation between the free energy as a function of displacement z along the pathway with various structural properties to understand the nature of the energy barrier. As seen in Figure 4, two free energy peaks exist, at $z = 1.46$ and 1.8 nm, of approximately the same height, separated by a relatively deep local free-energy minimum at $z = 1.65$ nm. While it is difficult to determine the exact nature of these free-energy features, they are well correlated with specific alterations in the contacts and the H-bond network. Variation in the amino acids making contact with the different parts of ZPP can be linked to these transitions and are listed for the PRO2 (Table 3), PRO1 (Table 4), and PHE (Table 5) groups. As the ZPP moves out of the protein, and z approaches 1.3 nm, it comes into contact with the cavity wall, in particular, a group of hydrophobic side chains: MET235, ILE591, PHE173, and TRP595. ZPP makes contact predominantly with positively charged ARG252 and ARG643, positioned on each side of the ligand (see Figure 5a). As it moves through this constrained region, however, the ligand also forms contact with hydrophobic amino acids PHE173, ILE591, and MET235 Figure 5b, as well as with hydrophilic amino acids of the TYR190–GLN208 flexible loop (Figure 5c), strongly reducing ZPP's access to the solvent.

The ligand's outward displacement along the reaction coordinate is sterically constricted by a group of amino acids that block ZPP's direct access to the flexible loop. Looking more specifically at the configurations sampled around the free energy peak at $z = 1.46$ nm, we see that ZPP is sterically constrained between THR590 on one side of the PHE group and TRP150, LYS172, and ARG643 on the other side. This reduces significantly the PRO1 and PRO2 groups' conformation flexibility, thus lowering the entropy available to the ZPP and raising the free energy difference.

The drop in free energy, as ZPP moves past $z = 1.46$, is associated with a decrease in the average number of H bonds of 1.6 ± 0.4 (relative to the average number of H bonds for the region $z = 0.3$ to $z = 1.25$ nm) between the whole protein and its TYR190–GLN208 loop, easing ZPP's diffusion pathway

Table 3. Average Probability of Existence of the Most Persistent Contacts in Three Regions of the Reaction Coordinate z for the PRO2-Body Contacts and PRO2-Loop Contacts

PRO2-body		PRO2-loop									
region	0.3–1.3 nm	region	1.4–2.0 nm	region	2.1–3.7 nm	region	0.3–1.3 nm	region	1.4–2.0 nm	region	2.1–3.7 nm
MET235	0.62	PHE173	0.85	PHE173	0.42	TYR190	0.41	TYR190	0.84	GLN192	0.42
PHE173	0.44	MET235	0.79	MET235	0.34	GLN208	0.32	ALA189	0.45	SER197	0.34
ILE591	0.35	ILE591	0.61	LYSH172	0.27	ASN205	0.15	ASN205	0.43	GLY195	0.30
ASN188	0.32	LYSH172	0.45	ILE591	0.26	SER203	0.06	GLN192	0.33	LYSH196	0.23
ARG252	0.31	ASN188	0.28	TRP150	0.19	LEU206	0.03	GLN208	0.31	ASP194	0.23
GLY236	0.26	SER174	0.20	ARG170	0.16	ALA189	0.01	SER203	0.18	GLN193	0.23
CYSH175	0.20	TRP234	0.19	ASN188	0.12			GLY195	0.04	ASP198	0.17
SER174	0.19	TRP150	0.15	SER174	0.09						
TRP234	0.19	ALA594	0.14	TRP234	0.06						
ALA594	0.18	TRP595	0.05	VAL171	0.04						
GLY237	0.17	LYSH233	0.02	ALA594	0.04						
LYSH172	0.15			GLU169	0.03						

Table 4. Average Window Probability of Existence of the Most Persistent Contacts in Three Regions of the Reaction Coordinate z for the PRO1-Body Contacts and PRO1-Loop Contacts

PRO1-body						PRO1-loop					
region	0.3–1.3 nm	region	1.4–2.0 nm	region	2.1–3.7 nm	region	0.3–1.3 nm	region	1.4–2.0 nm	region	2.1–3.7 nm
ILE591	0.67	ASN205	0.77	TRP150	0.25	TYR190	0.092	SER203	0.75	GLN192	0.44
MET235	0.56	TRP150	0.70	ASN205	0.14	LEU206	0.048	TYR190	0.57	LYSH196	0.40
TRP595	0.48	LYSH172	0.66	PHE173	0.10	SER203	0.031	GLN192	0.51	GLY195	0.36
PHE173	0.46	THR590	0.51	LYSH172	0.07			SER197	0.50	SER197	0.34
ALA594	0.36	ILE591	0.45	ILE591	0.05			GLU201	0.32	ASP198	0.18
ILE478	0.26	PHE173	0.29	VAL171	0.04			THR204	0.13	ARG170	0.18
ARG252	0.21	MET235	0.11	MET235	0.04			ASP194	0.13	ASP194	0.18
PHE476	0.16	TYR589	0.03	THR590	0.01			LYSH196	0.10	TYR190	0.16

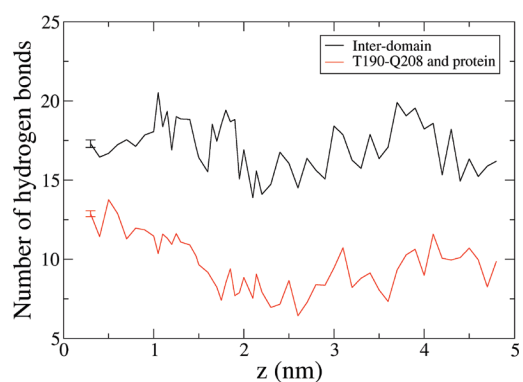
Table 5. Average Window Probability of Existence of the Most Persistent Contacts in Three Regions of the Reaction Coordinate z for the PHE-Body Contacts and PHE-Loop Contacts

PHE-body						PHE-loop			
region	0.3–1.3 nm	region	1.4–2.0 nm	region	2.1–3.7 nm	region	1.4–2.0 nm	region	2.1–3.7 nm
ILE591	0.84	THR590	0.92	TRP150	0.17	SER197	0.68	LYSH196	0.38
ARG643	0.87	LYSH172	0.81	ARG170	0.12	GLY199	0.61	SER197	0.38
PHE173	0.57	VAL645	0.56	PHE173	0.08	SER203	0.30	GLN192	0.32
TRP595	0.46	PHE173	0.53	THR590	0.06	ASP198	0.28	ASP198	0.31
THR590	0.36	ILE591	0.47	LYSH172	0.05	GLU201	0.23	GLY195	0.29
ASN555	0.24	ASP642	0.40	TYR589	0.03	THR202	0.12	SER203	0.24
HISB680	0.24	ARG643	0.36	LYSH23	0.03	THR200	0.08	GLU201	0.22
ASP149	0.23	TYR589	0.33			LYSH196	0.06	ASP194	0.18
LYSH172	0.22	VAL644	0.29			GLN192	0.05	ASN205	0.17
PHE476	0.21	VAL580	0.21						
ILE478	0.11	TRP150	0.19						
SER554	0.11	TRP595	0.06						

(Figure 8). Table 6 gives a list of H bonds between the above loop and the rest of the protein that are modulated by the passage of ZPP through position $z \geq 1.46$ nm. For $z < 1.46$, the TYR190–GLN208 loop maintains an average of 11.75 ± 0.12 H bonds with the rest of the protein. There are only 17 pairs of atoms forming H bonds between the above loop and the protein that exist for more than 25% of the simulation time and another 28 pairs of atoms present between 5% and 25% of that simulation time.

The second free energy barrier ($z = 1.8$ nm) can be linked with the breaking of H bonds that connect the β -propeller and catalytic domains. The average number of H bonds between these two domains increases from 15.5 ± 0.22 at $z = 1.6$ nm to 19.4 ± 0.15 at $z = 1.8$ nm and falling back to 15.1 ± 0.26 at $z = 1.95$ nm (Figure 8), which correlates well with the observed energy peak at $z = 1.8$ nm. The bulk of the variation in the H-bond network between the two domains is not directly linked to the opening of the flexible loop into the solvent since we can see that the number of H bonds between the TYR190–GLN208 loop and the catalytic domain varies only slightly, going from 1.5 ± 0.1 H bonds at $z = 1.6$ nm to 1.8 ± 0.1 at $z = 1.8$ nm and decreases to 1.3 ± 0.1 at $z = 1.95$ nm (data not presented).

To identify the H bonds modulated by the position of ZPP, we calculated the correlation coefficient between the average

**Figure 8.** Number of H bonds formed between the two domains of POP (black) and between the TYR190–GLN208 flexible loop and the protein body (red) as a function of the spring equilibrium length. Maximum errors evaluated to ± 0.26 and ± 0.18 , respectively, are obtained through a 5000 bootstrap evaluation of 10% of the available data and a confidence probability of 95%.

number of H bonds per US window and the probability of existence of each individual H bond for that window. We define this probability of existence as the percentage of time over the length of a window for which the H bond exists. Table 7 presents

those H bonds with (absolute value) minimum correlation coefficients of 0.4 for windows around the energy peaks. When combined, the fluctuations of this group of H bonds (including those with negative correlation coefficients) explains 75% of all of the interdomain H-bond fluctuations. Although a few H bonds are formed and broken in the vicinity of the ZPP (SER148–ASP642, ARG128–ASP641, LYSH172–ASP642), many are located opposite the loop opening in the interface region near the velcro-rip (THR686–ASN96, LYSH75–TYR71, LEU94–ASP72, LYSH428–GLU69 in Figure 9).

Once the ZPP has moved past the second free energy maximum, it gradually loses contact with the body of the protein, only keeping contact with the TYR190–GLN208 loop (Figure 5d). Due to the higher mobility of the solvent-exposed ZPP, no strong contact dominates in this region. As the ZPP is pulled outward, the flexible loop adopts an extended conformation to maintain contacts with it. The amino acids having the most frequent contacts with the ligand are those situated on the 192–198 segment of the loop, which can conformationally extend the furthest into the solvent.

When examining the evolution of the H-bond network between the two domains of POP, we can see a drop in the average number of H bonds as the ZPP moves outward from the second free energy peak ($z = 1.8$ nm), starting from 19.4 ± 0.15

and decreasing to 13.9 ± 0.17 at $z = 2.1$ nm. This number then increases as the ZPP moves further along the trajectory up to a value of 18.4 ± 0.22 at $z = 3.0$ nm. This increase of 4.5 ± 0.4 H bonds from $z = 2.1$ nm to $z = 3.0$ nm is mainly due to an increase of 1.9 ± 0.3 H bonds between the flexible loop and the catalytic domain, indicating that the TYR190–GLN208 loop is folding back onto the protein. A correlation analysis between the presence of each individual H bond and the average number of H bonds (Table 8) shows fewer H bonds forming atom pairs with high correlations: Specifically, all of the H-bond forming pairs with an absolute value minimum correlation of 0.3 had to be selected to explain 75% of the variation of the average number of H bonds.

Interestingly, we observed a prolonged interaction between the TYR190–GLN208 loop and ZPP in the z window, where the inhibitor is completely solvated. Starting from a ZPP–POP distance of $z = 2.7$ nm, and moving further outward from the protein, the large majority of the ligand's contacts are with amino acids on the flexible loop, even though ZPP's motion is only constrained along the reaction coordinates and the ligand can move freely in the perpendicular hyperplane. For example, in the $3.2 < z < 3.7$ nm region, ZPP makes contacts with 5.4 amino acids compared to 12.6 contacts on average for the $0.3 < z < 2.0$ nm region of the trajectory (data not presented). Small in number, these interactions are nevertheless sufficient to stabilize ZPP's position and keep it in contact with the loop for at least 80% of the simulation time. This suggests that the role of the flexible loop is not simply to open up and leave a pathway open for the ZPP entrance. The TYR190–GLN208 loop could play an active role in recruiting the ZPP ligand by binding to it in the solvent and directing it to the entry pathway, helping the ZPP to go through a first free energy barrier at $z = 1.8$ nm.

Table 6. Average Window Probability of Existence of the Most Persistent H Bonds between the TYR190–GLN208 Loop and Protein Body in the 0.3 nm to 1.8 nm Section of the Loop Exit Pathway

donor	acceptor	presence time ratio
SER203N	LYS588O	0.42
HIS593N	THR204OG	0.37
TYR190O	TRP234O	0.36
GLN208NE	TRP234O	0.33
LYS196NZ	GLU169O	0.31
ASN188ND2	GLN208OE1	0.30
SER203OG	THR590O	0.30
TRP234N	TYR190O	0.28
LYS196NZ	TRP150O	0.28

4. DISCUSSION

In this work, we identify the most probable pathway for binding ZPP to POP. Using SMD and US simulations, we eliminated two proposed pathways: first, through the velcro-rip and, second, through the β -propeller tunnel. The first pathway is ruled out because we were unable to even generate a pathway using SMD, demonstrating the extreme resistance to this path.

Table 7. Hydrogen Bonds Located at the Interdomain Interface with Activity Modulated by the Position of Zpp on the Reaction Coordinate As Identified by the Pearson's Correlation Coefficient against the Average Number of H Bonds for Two Regions, $z = [1.3, 2.0]$ and $z = [1.05, 2.1]$ ^a

Hydrogen bond	Region $z = [1.3, 2.0]$			Region $z = [1.05, 2.1]$		
	Correl.(p-val.)	Prob.	Std-dev	Correl.(p-val.)	Prob.	Std-dev
GLN439NE2-GLN439HE22-ASP356O	0.51(0.044)	0.30	0.08	0.39(0.060)	0.32	0.09
THR597OG1-THR597HG1-GLY254O	0.50(0.049)	0.16	0.34	0.33(0.115)	0.11	0.28
THR686OG1-THR686HG1-ASN96OD1	0.45(0.080)	0.34	0.42	0.52(0.009)	0.32	0.42
SER148OG-SER148HG-ASP642OD2	0.44(0.088)	0.29	0.31	0.31(0.140)	0.27	0.35
LYSH75NZ-LYSH75HZ3-TYR71OH	0.43(0.096)	0.28	0.42	0.39(0.060)	0.27	0.42
SER148OG-SER148HG-ASP642OD1	0.41(0.114)	0.26	0.35	0.20(0.349)	0.26	0.32
LYSH677NZ-LYSH677HZ3-ASP122OD1	0.40(0.125)	0.33	0.37	0.26(0.220)	0.36	0.38
ARG128NH1-ARG128HH12-ASP641OD1	-0.40(0.125)	0.16	0.33	-0.40(0.053)	0.16	0.30
LYSH172NZ-LYSH172HZ3-ASP642OD2	-0.43(0.096)	0.16	0.27	0.07(0.745)	0.22	0.32
LYSH428NZ-LYSH428HZ3-GLU69OE1	-0.54(0.031)	0.77	0.31	-0.31(0.140)	0.81	0.26
LEU94N-LEU94H-ASP72OD1	-0.54(0.031)	0.19	0.35	-0.06(0.780)	0.23	0.38

^aIn both cases, the average probability of existence and standard deviation of each h-bond in their respective subset of windows is also given.

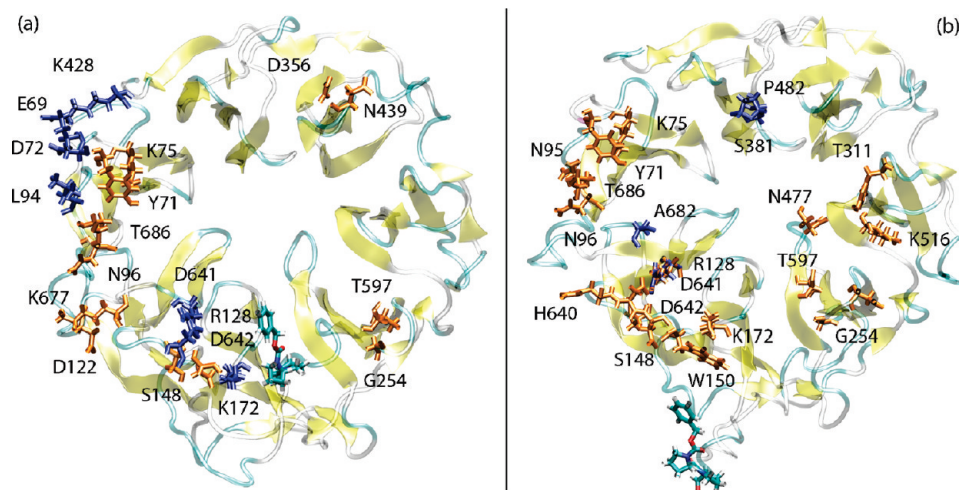


Figure 9. View of the amino acids forming interdomain H bonds modulated by the position of ZPP on the reaction coordinate as identified by Pearson's correlation coefficient of the involved H bond against the average number of H bonds. Amino acids in orange are positively correlated with the average number of H bonds, while those in blue are negatively correlated. The catalytic domain is hidden to facilitate the view. ZPP crossing $z = 1.3$ nm (a) and $z = 3.0$ nm (b).

Table 8. Hydrogen Bonds Located at the Inter-Domain Interface with Activity Modulated by the Position of ZPP on the Reaction Coordinate As Identified by the Pearson's Correlation Coefficient against the Average Number of H Bonds for the Hydrogen Bonds with the Highest Correlation for the Region $z = [1.75, 3.7]$ ^a

hydrogen bond	correl (p-val.)	prob.	std-dev
THR597OG1–THR597HG1–GLY254O	0.50 (0.008)	0.14	0.29
TRP150N–TRP150H–ASP642OD2	0.48 (0.011)	0.15	0.29
THR686OG1–THR686HG1–ASN96OD1	0.48 (0.012)	0.34	0.40
LYSH516NZ–LYSH516HZ3–ASP256OD1	0.43 (0.025)	0.13	0.23
THR686OG1–THR686HG1–GLN95O	0.41 (0.031)	0.11	0.27
ASN477ND2–ASN477HD22–TYR311OH	0.38 (0.051)	0.21	0.18
THR686N–THR686H–ASN96OD1	0.38 (0.051)	0.26	0.35
LYSH75NZ–LYSH75HZ3–TYR71O	0.37 (0.058)	0.31	0.40
SER148N–SER148H–HISA640O	0.36 (0.066)	0.19	0.22
ARG128NH2–ARG128HH22–ASP641OD1	0.32 (0.099)	0.19	0.31
LYSH172NZ–LYSH172HZ3–ASP642OD1	0.32 (0.106)	0.14	0.24
ARG128NH2–ARG128HH22–ALA682O	−0.31 (0.113)	0.08	0.19
SER381N–SER381H–PRO482O	−0.34 (0.086)	0.18	0.34

^aAlso included are the average probability of existence and standard deviation of each H bond in the selected subset of windows.

The resulting β -propeller exit trajectory free energy difference profile was unphysical. Detailed analysis suggests that this unphysical profile is associated with very constrained regions of the pathways where sampling is particularly difficult. On the basis of this evidence, we were also able to eliminate this pathway. The appropriate behavior of the ZPP when pulled through the flexible loop region and the physical nature of the free energy difference profile indicate that this is the correct access pathway.

Whether or not the access to the binding cavity involves a large domain reconfiguration could not be definitively resolved by our study. The natural substrates of POP, peptides of length <30 residues, are much larger than the ZPP inhibitor. Thus, the access mechanism of ZPP may not be the general pathway involved in its catalytic activity. The long-range destabilization of the H-bond network that was seen to occur as the ZPP left the binding cavity

could possibly be interpreted as evidence of the large scale interdomain motion²⁷ that has been hypothesized to play a role in the access pathway. In addition, the prolonged association of the TYR190–GLN208 loosely structured loop with the ZPP as it left the protein provides evidence that this region of the protein could possibly have a role in ligand recognition and recruitment.

AUTHOR INFORMATION

Corresponding Author

*E-mail: normand.mousseau@umontreal.ca.

ACKNOWLEDGMENT

This work was supported by the Natural Sciences and Engineering Research Council of Canada (M.K., N.M.), the Academy of Finland (T.R., M.K.), Canada Research Foundation (N.M.), and the GALENOS program (J.-F.S.-P.). We are grateful to the Réseau québécois de calcul de haute performance (RQCHP), SharcNet, and the Finnish IT Centre for Science for their generous allocation of computer time.

REFERENCES

- (1) Polgár, L. *Cell. Mol. Life Sci.* **2002**, *59*, 349–362.
- (2) Garcia-Horsman, J. A.; Männistö, P. T.; Venäläinen, J. I. *Neuropeptides* **2007**, *41*, 1–24.
- (3) Rea, D.; Fülöp, V. *Cell Biochem. Biophys.* **2006**, *44*, 349–365.
- (4) Brandt, I.; Scharpé, S.; Lampier, A.-M. *Clin. Chim. Acta* **2007**, *377*, 50–61.
- (5) Szeltner, Z.; Polgár, L. *Curr. Prot. Pept. Sci.* **2008**, *9*, 96–107.
- (6) Yoshimoto, Y.; Kado, K.; Matsubara, F.; Koriyama, N.; Kaneto, H.; Tsura, D. *J. Pharmacobiodyn.* **1987**, *10*, 730–735.
- (7) Männistö, P. T.; Venäläinen, J. I.; Jalkanen, A.; Garcia-Horsman, J. A. *Drug News Perspect.* **2007**, *20*, 293–305.
- (8) Mantle, D.; Falkous, G.; Ishiura, S.; Blanchard, P. J.; Perry, E. K. *Clin. Chim. Acta* **1996**, *249*, 129–139.
- (9) Tenorio-Laranga, J.; Coret-Ferrer, F.; Casanova-Estruch, B.; Bursal, M.; Garcia-Horsman, J. A. *J. Neuroinflammation* **2010**, *7*, 23.

- (10) Di Daniel, E.; Glover, C. P.; Grot, E.; Chan, M. K.; Sanderson, T. H.; White, J. H.; Ellis, C. L.; Gallagher, K. T.; Uney, J.; Thomas, J.; Maycox, P. R.; Mudge, A. W. *Mol. Cell. Neurosci.* **2009**, *41*, 373–382.
- (11) Schulz, I.; Zeitschel, U.; Rudolph, T.; Ruiz-Carrillo, D.; Rahfeld, J.-U.; Gerhartz, B.; Bigl, V.; Demuth, H.-U.; Rossner, S. *J. Neurochem.* **2005**, *94*, 970–979.
- (12) O'Reilly, P. J.; Hardison, M. T.; Jackson, P. L.; Xu, X.; Snelgrove, R. J.; Gaggar, A.; Galin, F. S.; Blalock, J. E. *J. Neuroimmunol.* **2009**, *217*, 51–54.
- (13) Gaggar, A.; Jackson, P. L.; Noerager, B. D.; O'Reilly, P. J.; McQuaid, D. B.; Rowe, S. M.; Clancy, J. P.; Blalock, J. E. *J. Immunol.* **2008**, *180*, 5662–5669.
- (14) Liu, J.-M.; Kusinski, M.; Ilic, V.; Bignon, J.; Hajem, N.; Komorowski, J.; Kuzdaz, K.; Stepien, H.; Wdziedzick-Bakala, J. *Anticancer Res.* **2008**, *28*, 2813–2817.
- (15) van Gool, A. R.; Verkerk, R.; Fekkes, D.; Sleijfer, S.; Bannink, M.; Kruit, W. H.; van der Holt, B.; Scharpé, S.; Eggermont, A. M. M.; Stoter, G.; Hengeveld, M. W. *J. Interferon Cytokine* **2008**, *28*, 283–286.
- (16) Lawandi, J.; Gerber-Lemaire, S.; Juillerat-Jeannere, L.; Moitessier, N. *J. Med. Chem.* **2010**, *53*, 3423–3438.
- (17) Lawandi, J.; Toumieux, S.; Seyer, V.; Campbell, P.; Thielges, S.; Juillerat-Jeanneret, L.; Moitessier, N. *J. Med. Chem.* **2009**, *52*, 6672–6684.
- (18) Tarrago, T.; Martin-Benito, J.; Sabido, E.; Claasen, B.; Madurga, S.; Gairi, M.; Valpeusta, J. M.; Giralt, E. *FEBS Lett.* **2009**, *583*, 3344–3348.
- (19) Comellas, G.; Kaczmarzka, Z.; Tarrago, T.; Teixidó, M.; Giralt, E. *PLoS One* **2009**, *4*, e6222.
- (20) Fülöp, V.; Böcskei, Z.; Polgár, L. *Cell* **1998**, *94*, 161–170.
- (21) Fülöp, V.; Jones, D. T. *Curr. Opin. Struct. Biol.* **1999**, *9*, 715–721.
- (22) Fülöp, V.; Szeltner, Z.; Polgár, L. *EMBO Rep.* **2000**, *1*, 277–281.
- (23) Szeltner, Z.; Renner, V.; Polgár, L. *J. Biol. Chem.* **2000**, *275*, 15000–15005.
- (24) Juhász, T.; Szeltner, Z.; Fulop, V.; Polgár, L. *J. Mol. Biol.* **2005**, *346*, 907–917.
- (25) Fuxreiter, M.; Magyar, C.; Juhász, T.; Szeltner, Z.; Polgár, L.; Simon, I. *Proteins Struct. Funct. Bioinf.* **2005**, *60*, 504–512.
- (26) Kaszuba, K.; Róg, T.; St. Pierre, J.-F.; Männistö, P. T.; Karttunen, M.; Bunker, A. *SAR QSAR Environ. Res.* **2009**, *20*, 595–609.
- (27) Shan, L.; Mathews, I. L.; Khosla, C. *Proc. Natl. Acad. Sci. U.S.A.* **2005**, *102*, 3599–3604.
- (28) Li, M.; Chen, C.; Davies, D. R.; Chiu, T. K. *J. Biol. Chem.* **2010**, *285*, 21487–95.
- (29) Szeltner, Z.; Rea, D.; Juhász, T.; Renner, V.; Fülöp, V.; Polgár, L. *J. Mol. Biol.* **2004**, *340*, 627–637.
- (30) Kaszuba, K.; Rog, T.; Bryl, K.; Vattulainen, I.; Karttunen, M. *J. Phys. Chem. B* **2010**, *114*, 8374–8386.
- (31) Hess, B.; Kutzner, C.; van der Spoel, D.; Lindahl, E. *J. Chem. Theory Comput.* **2008**, *4*, 435–447.
- (32) Nosé, S. *Mol. Phys.* **1984**, *52*, 255–268.
- (33) Hoover, W. G. *Phys. Rev. A* **1985**, *31*, 1695–1697.
- (34) Parrinello, M.; Rahman, A. *J. Appl. Phys.* **1981**, *52*, 7182–7190.
- (35) Darden, T.; York, D.; Pedersen, L. *J. Chem. Phys.* **1993**, *98*, 10089–10092.
- (36) Karttunen, M.; Rottler, J.; Vattulainen, I.; Saguí, C. *Curr. Top. Membr.* **2008**, *60*, 49–89.
- (37) Wong-ekkabut, J.; Miettinen, M. S.; Dias, C.; Karttunen, M. *Nat. Nanotechnol.* **2010**, *5*, 555–557.
- (38) Jorgensen, W.; Tirado-Rives, J. *J. Am. Chem. Soc.* **1988**, *110*, 1657–1666.
- (39) Jorgensen, W. L.; Chandrasekhar, J.; Madura, J. D.; Impey, R. W.; Klein, M. L. *J. Chem. Phys.* **1983**, *79*, 926–935.
- (40) Humphrey, W.; Dalke, A.; Schulten, K. *J. Mol. Graphics* **1996**, *14*, 33–38.
- (41) Lindahl, E.; Hess, B.; van der Spoel, D. *J. Mol. Model.* **2001**, *7*, 306–317.
- (42) Jarzynski, C. *J. Stat. Phys.* **2000**, *98*, 77–102.
- (43) Jarzynski, C. *Phys. Rev. E* **1997**, *56*, 5018–5035.
- (44) Park, S.; Schulten, K. *J. Chem. Phys.* **2004**, *120*, 5946–5961.
- (45) Sun, S. X. *J. Chem. Phys.* **2003**, *118*, 5769–5775.
- (46) Xiong, H.; Crespo, A.; Marti, M.; Estrin, D.; Roitberg, A. E. *Theor. Chem. Acc.* **2006**, *116*, 338–346.
- (47) Ytreberg, F. M.; Zuckerman, D. M. *J. Chem. Phys.* **2004**, *120*, 10876.
- (48) Cuendet, M. A.; Michielin, O. *Biophys. J.* **2008**, *95*, 3575–3590.
- (49) Park, S.; Schulten, K. *J. Chem. Phys.* **2004**, *120*, 5946–5961.
- (50) Oberhofer, H.; Dellago, C.; Geissler, P. L. *J. Phys. Chem. B* **2005**, *109*, 6902–15.
- (51) Baştuğ, T.; Kuyucak, S. *Chem. Phys. Lett.* **2007**, *436*, 383–387.
- (52) Torrie, G. M.; Valleau, J. P. *J. Comput. Phys.* **1977**, *23*, 187–199.
- (53) Roux, B. *Comput. Phys. Commun.* **1995**, *91*, 275–282.
- (54) Kumar, S.; Bouzida, D.; Swendsen, R. H.; Kollman, P. A.; Rosenberg, J. M. *J. Comput. Chem.* **1992**, *13*, 1011–1021.
- (55) Chen, P.-C.; Kuyucak, S. *Biophys. J.* **2009**, *96*, 2577–88.
- (56) Mustafa, M.; Henderson, D. J.; Busath, D. D. *Proteins* **2009**, *76*, 794–807.
- (57) Mills, M.; Andricioaei, I. *J. Chem. Phys.* **2008**, *129*, 114101.
- (58) Xing, C.; Faller, R. *J. Chem. Phys.* **2009**, *131*, 175104.
- (59) Yesylevskyy, S.; Marrink, S.-J.; Mark, A. E. *Biophys. J.* **2009**, *97*, 40–9.
- (60) Baştuğ, T.; Chen, P.-C.; Patra, S. M.; Kuyucak, S. *J. Chem. Phys.* **2008**, *128*, 155104.
- (61) Rodriguez-Gomez, D.; Darve, E. *J. Chem. Phys.* **2004**, *120*, 3563–3578.
- (62) Ytreberg, F. M.; Swendsen, R. H.; Zuckerman, D. M. *J. Chem. Phys.* **2006**, *125*, 184114.
- (63) Tskhovrebova, L.; Trinick, J.; Sleep, J. A.; Simmons, R. M. *Nature* **1997**, *387*, 308–312.
- (64) Liu, M.; Sun, T.; Hu, J.; Chen, W.; Wang, C. *Biophys. Chem.* **2008**, *135*, 19–24.
- (65) Hub, J. S.; de Groot, B. L.; van der Spoel, D. *J. Chem. Theory Comput.* **2010**, *6*, 3713–3720.
- (66) Bakker, A. V.; Jung, S.; Spencer, R. W.; Vinick, F. J.; Faraci, W. S. *Biochem. J.* **1990**, *271*, 559–562.
- (67) Szeltner, Z.; Renner, V.; Polgár, L. *Protein Sci.* **2000**, *9*, 353–360.

Accelerating All-Atom Normal Mode Analysis with Graphics Processing Unit

Li Liu,^{†,‡} Xiaofeng Liu,[†] Jiayu Gong,[‡] Hualiang Jiang,^{†,§} and Honglin Li^{*,†}

[†]State Key Laboratory of Bioreactor Engineering, Shanghai Key Laboratory of Chemical Biology, School of Pharmacy, East China University of Science and Technology, Shanghai 200237, China

[‡]School of Information Science and Engineering, East China University of Science and Technology, Shanghai 200237, China

[§]Drug Discovery and Design Center, Shanghai Institute of Materia Medica, Chinese Academy of Sciences, Shanghai 201203, China

ABSTRACT: All-atom normal mode analysis (NMA) is an efficient way to predict the collective motions in a given macromolecule, which is essential for the understanding of protein biological function and drug design. However, the calculations are limited in time scale mainly because the required diagonalization of the Hessian matrix by Householder-QR transformation is a computationally exhausting task. In this paper, we demonstrate the parallel computing power of the graphics processing unit (GPU) in NMA by mapping Householder-QR transformation onto GPU using Compute Unified Device Architecture (CUDA). The results revealed that the GPU-accelerated all-atom NMA could reduce the runtime of diagonalization significantly and achieved over 20× speedup over CPU-based NMA. In addition, we analyzed the influence of precision on both the performance and the accuracy of GPU. Although the performance of GPU with double precision is weaker than that with single precision in theory, more accurate results and an acceptable speedup of double precision were obtained in our approach by reducing the data transfer time to a minimum. Finally, the inherent drawbacks of GPU and the corresponding solution to deal with the limitation in computational scale are also discussed in this study.

INTRODUCTION

Predicting collective structural changes in biological macromolecules is essential in the understanding of protein function and drug design.¹ In addition to the experimental approaches such as X-ray crystallography,² NMR spectroscopy,³ and single-molecule biophysical techniques,⁴ some theoretical methods including molecular dynamics (MD) simulations⁵ and normal mode analysis (NMA)⁶ are available to explore the protein motions. Compared to MD simulation, NMA eliminates time-integration and explicit solvent degrees of freedom with a considerable computational advantage.⁷ This enables NMA to be used for much larger systems⁸ including viral capsids,⁹ molecular motors,¹⁰ and the ribosome.¹¹ Except for prediction of macromolecules' dynamic motions, another important application of NMA is to calculate the entropy change in the well-known MM/PBSA method, which is a relatively accurate but computationally expensive approach to calculate the binding free energy of the protein–protein or protein–ligand complex and is deemed more accurate than conventional scoring functions for molecular docking.^{12–14}

Classical all-atom NMA assumes that protein motions, including large-scale/low-frequency and small-scale/high-frequency motions, can be described by a quasi-harmonic approximation around a local minimum on the protein energy surface,¹⁵ and the low frequency modes can well describe large conformational changes relevant to protein function that are observed experimentally, such as the hinge opening and closing motions.¹⁶ The approach of NMA is to diagonalize the Hessian matrix, of which $3N \times 3N$ (N is the number of atoms) elements represent the second derivative of the potential energy function along the Cartesian coordinates.^{17,18} However, the application of

all-atom NMA has been limited due to intensive memory consumption ($O(N^2)$) and cubic CPU time complexity ($O(N^3)$) in the case of a protein with N atoms and the resulting dramatic increase in sampling time. Even though the storage of a Hessian matrix has become less of an obstacle due to the introduction of sparse matrix techniques, the diagonalization of the all-atom matrix is still a challenge to date. Therefore, all-atom NMA is normally applied to protein systems containing at most a few hundred residues. On the other hand, the entropy change calculation is often ignored in the application of the large-scale virtual screening with MM/PBSA approach because of the repeated and extremely time-consuming NMA calculation for all of the protein–ligand complexes during the process of molecular docking,¹⁹ which undermines the accuracy of the calculated binding free energies as well as the ranks of the hit compounds.

To solve the time-consumption problem, several coarse-grain methods, such as block normal mode (BNM)²⁰ and elastic network model (ENM),²¹ have been put forward to reduce the size of Hessian matrix and the computational time. The BNM starts from an energy-minimized system described by an all-atom force field but considers each residue as a rigid block²⁰ with six translation–rotation degrees of freedom, which reduces the size of the Hessian matrix to $6N \times 6N$ in the case of a protein with N residues.^{22,23} The ENM approximation regards the protein as an elastic network,^{24–26} and only the C α atoms of the individual residues are considered as nodes and connected by uniform springs.^{21,22} On the basis of ENM, the size of the Hessian matrix

Received: December 20, 2010

Published: May 13, 2011

is reduced to only $3N \times 3N$ in the case of a protein with N residues. In spite of outstanding computational efficiency, the accuracy of the coarse-grained NMA result is undermined because the modes with high frequencies are eliminated.²² Therefore, more efforts have been made to improve the computational efficiency for all-atom NMA to preserve the explicit representation of atomic degrees of freedom through reducing the time of diagonalizing the all-atom Hessian matrix.⁷

It is well-known that conventional supercomputers are typically large in size and very expensive in terms of manufacturing and maintenance. Fortunately, over the past few years, the graphics processor unit (GPU), which has tremendous raw computing power, has been rapidly evolving from a fixed-function pipeline into a programmable processor.²⁷ A contemporary GPU can achieve as much as 1000 GFLOPS peak performance²⁸ and a 1 order of magnitude speedup for single-precision arithmetic over corresponding CPU code. Due to the advantages of speed, cost, and accessibility, GPUs have been applied in many scientific computation fields, such as electrostatics,²⁹ molecular dynamics,³⁰ quantum chemistry,³¹ and so on. The GPU is suitable for handling problems involving large data sets and computationally intensive calculations³² and has the potential to revolutionize computational biology by changing the conventional batch-mode computational jobs into interactive tasks.³³

The Householder-QR transformation algorithm is generally used to find the eigenvalues and eigenvectors of a real matrix. This algorithm has been implemented in successive parallel versions of popular linear algebra libraries such as Linear Algebra Package (LAPACK), Parallel Linear Algebra for Scalable Multicore Architectures (PLASMA), and so on. The Householder-QR transformation implemented in LAPACK leverages the idea of blocking to limit the amount of bus traffic in favor of a high reuse of the data that is present in the higher level memories, which are also the fastest ones.³⁴ In PLASMA, the algorithm can be represented as a sequence of small tasks that operate on square blocks of data. These tasks can be dynamically scheduled for execution based on the dependencies among them and on the availability of computational resources.³⁵ In this study, the Householder-QR transformation algorithm for the Hessian matrix in GROMACS was reimplemented to map onto a GPU which is amenable to parallelization on single-instruction multiple-data (SIMD) architectures using the CUDA programming toolkit.³⁶ CUDA adopts an extension of the C/C++ programming language, which consists of a set of keywords and a runtime library to allow the execution of parallel code and memory control on the GPU. Through evaluating the performance of GPU-accelerated NMA on some benchmark molecules with various numbers of atoms and comparing the runtimes against the single-core CPU-based NMA in GROMACS, the GPU-accelerated NMA outperforms the CPU-based one with a higher computational efficiency and achieves over $20\times$ speedup with competitive accuracy, which highlights the GPU's potential to perform all-atom NMA on a desktop workstation in a fast and accurate way.

MATERIALS AND METHODS

Graphics Processing Unit Overview. A typical parallel program can be generalized in three parts in CUDA: (1) apply and release the memory storage; (2) execute the parallel parts as so-called kernel functions; (3) transfer data between host memory and device memory.³⁷ There is a scalable number of streaming multiprocessors (SMs) on a GPU, each containing

eight streaming processor (SP) cores. The SMs execute a data-parallel problem which is decomposed into independent work items called threads in CUDA.

Threads are executed together in cooperative work groups called blocks, which are grouped into grids. The computation of a grid corresponds to exactly one GPU kernel invocation.^{28,38} To achieve a decent performance increase compared to a CPU calculation, it is important to take three aspects into account. First, in order to fully occupy the device and provide sufficiently many threads of execution to hide various sources of latency, it requires a huge data parallel workload.³³ Second, memory access is much slower than arithmetic calculations on a GPU, and the data transfer between the host and the device has to be minimized. Third, to maximize the number of simultaneous running threads, appropriate thread usage of registers and synchronization between threads have to be determined due to the limitation of the memory size of local registers, which is only 64 KB per SM in the NVIDIA Geforce series of GPUs.³⁹

Normal Mode Analysis. The harmonic approximation of the potential energy function around a minimum energy conformation is the underlying hypothesis in normal mode calculations.⁴⁰ The quadratic form of the potential energy function $V(\mathbf{r})$ can be obtained by a Taylor expansion using \mathbf{r}^0 (a vector consisting of the $3N$ atomic Cartesian coordinates):^{24,41–43}

$$V(\mathbf{r}) \approx V(\mathbf{r}^0) + \sum_{i=1}^{3N} \left(\frac{\partial V}{\partial r_i} \right) (r_i - r_i^0) + \frac{1}{2} \sum_{i,j=1}^{3N} \left(\frac{\partial^2 V}{\partial r_i \partial r_j} \right) (r_i - r_i^0)^T (r_j - r_j^0) \quad (1)$$

The reference point \mathbf{r}^0 is chosen to correspond to a minimum of the potential energy function, where $(\partial V / \partial r_i) = 0$. In addition, the potential energy can be defined relative to this reference point, and the constant term $V(\mathbf{r}^0)$ can be taken as zero. As a result, eq 1 in matrix notation can be expressed as follows:

$$V(\mathbf{r}) \approx \frac{1}{2} \mathbf{r}^T \mathbf{H} \mathbf{r} \quad (2)$$

where $\mathbf{H} = \sum_{i,j=1}^{3N} (\partial^2 V / \partial r_i \partial r_j)$, $\mathbf{r} = (r_i - r_i^0)$.

At the same time, the kinetic energy K also has a quadratic form, which can be expressed as

$$K = \frac{1}{2} \dot{\mathbf{r}}^T \mathbf{M} \dot{\mathbf{r}} \quad (3)$$

where \mathbf{M} is a diagonal matrix of $3N \times 3N$ atomic masses and $\dot{\mathbf{r}}$ is the time derivative of \mathbf{r} . The equations of motions of a molecule in a harmonic well can be inferred from eqs 2 and 3:

$$\mathbf{M} \ddot{\mathbf{r}} = -\mathbf{H} \mathbf{r} \quad (4)$$

where $\ddot{\mathbf{r}}$ is the second time derivative of \mathbf{r} , and the vector \mathbf{r} can be resolved by adopting the general form, which can be expressed as a function of time:

$$r(t) = r^0 + A \cos(\nu t) \quad (5)$$

ν is the fundamental vibration frequency, and A is the amplitude of the vibration. Taking the second derivative of the extension gives

$$\nu^2 \mathbf{M} \mathbf{A} = \mathbf{H} \mathbf{A} \quad (6)$$

where \mathbf{M} consists of a diagonal matrix whose elements are the atomic masses, and ν^2 and \mathbf{A} are the eigenvalues and eigenvectors, respectively. The eigenvectors of this matrix are the normal

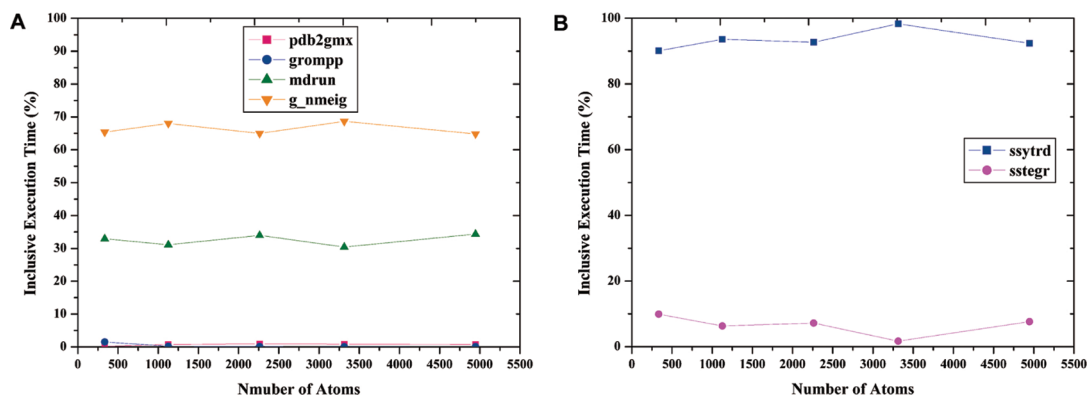


Figure 1. Runtime decomposition results of (A) the modules in the NMA calculation and (B) the subroutines of the Hessian matrix eigenvalues calculation in GROMACS 4.0. The protein test systems are 2WFU, 3CLN, 1A7R, 4AKE, and 1ATN.

modes, and the eigenvalues are the squares of the associated frequencies. Notice that when expressed in Cartesian space, a normal coordinate describes an internal collective change of the structure, except for the first six modes that correspond to global translations and rotations of the molecule with eigenvalues equal to zero.²¹ Therefore, the calculation of NMA is reduced to the diagonalization of the Hessian matrix H .

Hessian Matrix Diagonalization. Generally speaking, an efficient algorithm for the diagonalization of a symmetric matrix usually consists of the following two stages: the original matrix is first reduced to a tridiagonal matrix T , which is also called the Hessenberg matrix, by a sequence of orthogonal similarity transformed as follows:

$$\begin{bmatrix} \times & \times & \times & \times \\ \times & \times & \times & \times \\ \times & \times & \times & \times \\ \times & \times & \times & \times \end{bmatrix} \xrightarrow{Q_1} \begin{bmatrix} \times & \times & 0 & 0 \\ \times & \times & \times & \times \\ 0 & \times & \times & \times \\ 0 & \times & \times & \times \end{bmatrix} \xrightarrow{Q_2} \begin{bmatrix} \times & \times & 0 & 0 \\ \times & \times & \times & 0 \\ 0 & \times & \times & \times \\ 0 & 0 & \times & \times \end{bmatrix} \quad (7)$$

$A \qquad Q_1 A Q_1 \qquad Q_2 Q_1 A Q_1 Q_2$

Then, we need to accurately calculate its eigenvalues and eigenvectors based on QR, bisection, or divide-and-conquer algorithms etc.

The general scheme of Householder transformation method is as follows:^{44,45}

Step 1 Establish symmetric matrix $A = \{a_{ij} | a_{ij} = a_{ji} \text{ and } i, j \in [1, n]\}$.

Step 2 Iterate from eq 8 to 12 with $k = 1, 2, 3, \dots, n - 1$.

$$\sigma_{k+1} = \text{sign}(a_{k+1,k}) \left(\sum_{i=k+1}^n (a_{ik})^2 \right)^{1/2} \quad (8)$$

$$\rho_{k+1} = \sigma_{k+1} (\sigma_{k+1} + a_{k+1,k}) \quad (9)$$

$$U^{(k+1)} = (0, \dots, 0, \sigma_{k+1} + a_{k+1,k}, a_{k+2,k}, \dots, a_{nk}) \quad (10)$$

$$Q_{k+1} = I - \frac{1}{\rho_{k+1}} U^{(k+1)} (U^{(k+1)})^T \quad (11)$$

$$Q_{k+1} A Q_{k+1} = A \quad (12)$$

The first step establishes the raw Hessian matrix, which is tridiagonalized by multiplying it with the orthogonal matrix Q_i calculated in the second step.

Implementation Details. In order to accelerate NMA utilizing GPU, the primary step is to verify the time distribution in each part of the whole process in NMA. In GROMACS 4.0,⁴⁶ the process can be divided into four subroutines, and the corresponding runtimes against five protein systems with various numbers of atoms are shown in Figure 1A. The “pdb2gms” and “grompp” modules (preparation of coordinates and topology files) only occupy a small fraction of the overall computational time (less than 1.5%). Though the “mdrun” module (energy minimization and building a Hessian matrix from single conformation) costs about 30% of the computational time, it can be accelerated in parallel with conventional Parallel Virtual Machine (PVM) or Message Passing Interface (MPI) mechanisms across multiple CPUs.⁴⁷ The profiles of the five benchmark cases illustrate that the “g_nmeig” module (calculation of a Hessian matrix’s eigenvalues) is the most computationally expensive part, which accounts for over 64% of the inclusive execution time.

The calculation of the Hessian matrix eigenvalues can be further divided into two steps, whose runtime profiling against the five benchmark systems is shown in Figure 1B. The tridiagonalization process (ssytrd module) costs the dominant fraction of the computational time (over 90%) in the Hessian matrix eigenvalues calculation process. So far, it can be concluded that the most time-consuming part in NMA is the Householder transformation, which reduces the Hessian matrix to the tridiagonal form. For this reason, the NMA calculation on GPU is reduced to the determination of the Hessian matrix eigenvalues and further to the tridiagonalization according to the characteristics of CUDA technically.

Algorithm 1. Orthogonal vector construction on CPU

set N as the order of matrix A

for $i = 1$ to N

//Compute the norm of vector in row i , column i to N of matrix A .

$r_i = \text{sign}(a_{i,j+1}) \|A[i][i+1:N]\|$;

//Compute the orthogonal vector U

$U[0:i-1] = 0$;

$U[i] = U[i] + \text{sqrt}(r_i)$;

$U[i+1:N] = A[i][i+1:N]$;

//Compute the adjusted parameter t .

$t = 1/\text{sqrt}(r_i + \text{sqrt}(r_i)U[i])$;

Execute tridiagonalization function on GPU;

//Replace the vector in matrix A needed in next iteration.

$A[i+1][i+1:N] = U[i+1:N]$;

end for

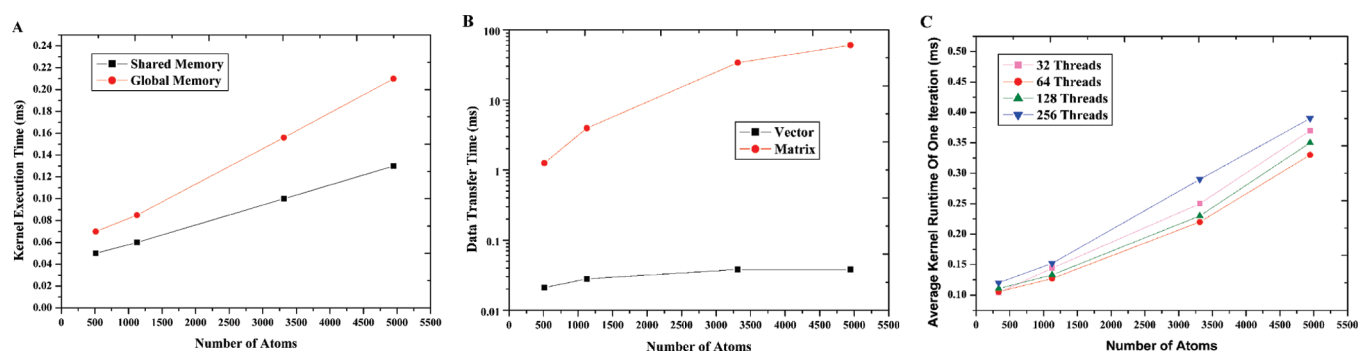


Figure 2. Optimization results of the GPU-accelerated QR Householder decomposition: (A) kernel runtimes with different memory locations for data storage, (B) kernel runtimes with different data structure for transfer (the vertical axis is scaled in log–linear coordinates), and (C) kernel runtimes with varying numbers of threads per block.

The details of Householder transformation implemented on a hybrid GPU-based architecture are described in Algorithms 1 and 2. Algorithm 1 gives the pseudocode for the orthogonal vector construction on the CPU. The orthogonal vector is used to create the reflector, which is essential in the tridiagonalization process. Algorithm 2 gives the tridiagonalization process implemented on CUDA, which completes the reflector and converts the original matrix into the tridiagonal form. The instructions in Algorithm 2 are operated on a number of threads within all of the blocks scheduled on each stream processor in parallel.

Algorithm 2. Tridiagonalization function on GPU

```

set block_size = 64; //64 threads per block.
number_of_blocks = N/block_size;
//All blocks on SMs executed in parallel.
for each block do
  set shared_memory_size = block_size;
  Load vector  $\mathbf{U}_i$  to shared memory of block;  

 $\mathbf{U}'_i = (\mathbf{U}_i)^T$ ; //Compute the transpose of the orthogonal  

  vector.  

  Load vector  $\mathbf{U}'_i$  to shared memory of block;  

 $\mathbf{H}_i = t(\mathbf{U}'_i \mathbf{U}'_i)$ ;  

 $\mathbf{H}_i = \mathbf{I}_i - \mathbf{H}_i$ ; //Compute the reflector.  

  Load matrix  $\mathbf{A}_i$  and  $\mathbf{H}_i$  to shared memory of block;  

 $\mathbf{A}_i = \mathbf{A}_i \mathbf{H}_i$ ; //Tridiagonalize the original matrix.
until all blocks are traversed;
 $\mathbf{U}[i + 1 : N] = \mathbf{A}[i + 1][i + 1 : N]$ ; //Return the vector  

needed in next iteration.

```

The CUDA implementation of the Householder transformation was executed on a single NVIDIA GeForce GTX295 (1.2 GHz), which held 480 stream processors to compute in parallel.⁴⁸ For comparison, the NMA module of GROMACS 4.0 (built with GCC 4.3.2 compilers in serial mode) was performed on a 2.50 GHz Quad-Core Intel Xeon E5420 CPU (running RedHat AS 6.0). The frequency of the CPU is more than twice higher than that of the GPU, so that it has a much better performance than a GPU on single-instruction single-data (SISD) architectures, and the random access memory (RAM) size (8 GB) is nearly 4 times larger than that of the GPU (1.7 GB). Meanwhile, we also compared the peak performance of the QR factorizations implemented in LAPACK, PLASMA, and CUDA. The block size was set to 64 in LAPACK and CUDA implementation to achieve the best performance. The number of cores in PLASMA was set to 16 with respect to the sizes of the test systems.

RESULTS AND DISCUSSION

Optimization of the Implementation. The GPU implementation was optimized from three perspectives which utilize higher level memories, minimize the amount of data transferred, and select the appropriate thread block size. In kernel functions, reading or writing global memory incurs about 400–600 clock cycles of latency, while it just needs one clock cycle of latency in shared memory.⁴⁹ In order to reduce the frequency of global memory access, we divided the huge matrix into submatrices which can be stored in the shared memory with a size of 16 KB per SM.⁵⁰ However, the maximum number of threads per block is reduced to 256 in our method, which is one-third of the maximum value in principle due to the limited size of the register memory.⁵¹ Subsequently, only the lower triangle (or upper triangle) in eq 11 needs to be calculated, which can effectively enhance the computational speed and save the memory size, utilizing the symmetrical property of the initial matrix and the orthogonal matrix. The loop sequence should be recorded in the kernel function to get the new temporary vector generated by the tridiagonalization process. We measured the kernel runtime of different GPU implementations with different memory accessing types (as shown in Figure 2A). The performance of the shared memory implementation did not improve remarkably (by only twice compared with the global memory implementation) because the load latency was covered by intensive arithmetic calculations of abundant threads.

On the other hand, since data transfer incurs many more clock cycles than arithmetic calculations on GPU threads, it would be effective to minimize the data transfer between the host and the GPU to increase speed performance. The Household-QR algorithm implemented on GPU consists of $n-1$ loops (n is the matrix order), each of which calculates one row/column in the Hessenberg matrix. Though the Hessian matrix is totally changed after one loop, only one vector of the Hessian matrix is needed in the next loop. A temporary vector storing the results from the previous loop is set to avoid transferring the whole matrix and minimize the time spent in data transfer between the GPU and CPU. Therefore, we also measured the time needed to transfer a whole matrix and a vector between the host and GPU (Figure 2B). The cost of transferring a whole matrix is much higher than that of transferring a vector decomposed from the same matrix, which cost over 60 and 0.038 ms, respectively, resulting in transferring of the vector alone between the device memory, and the host memory can improve the performance significantly.

Furthermore, the number of local registers in each thread is very limited, and they are often used as the index of blocks and threads, which are essential for kernel functions' ability to control each thread. However, in the process of transposing the vector, we import the argument ρ_i in eq 9 to occupy one register of each thread. Then, we complete the argument and vector multiplication on the GPU for the purpose of reducing the time complexity from $O(2n)$ to $O(1)$ by duplicating the argument to each thread. It is important to synchronize all threads in the same block if there are conditional statements and loops in kernel functions on the GPU. The transposing operations on GPU are complemented by exchanging the horizontal coordinates and vertical coordinates of elements in each thread. This section also reduces the time complexity from $O(n)$ to $O(1)$ for n elements in the vector U .

In addition, the block size of the threads also impacts the performance of kernel implementation on the GPU. The number of threads per block should be chosen as much as possible for better time slicing and full usage of computing resources. However, the more threads per block, the fewer registers that are available per thread. In addition, the size of shared memory per stream multiprocessor (SM) is 16 KB, which is organized into 16 banks.⁵² If all running threads access different banks, there are no bank conflicts, and the shared memory is the same speed as the register. If multiple threads access the same bank, the shared memory accessing time will be as long as the time required for the maximum number of threads simultaneously accessed to a single bank.⁵³ In order to avoid memory bank conflicts, the number of threads per block has to be set as a multiple of 32 (32, 64, 128, and 256 threads in our test), which is the minimum value of task scheduling and executing on SMs. The active thread block size cannot exceed 512 due to insufficient register memory size (64 KB per SM).⁵⁴ The blocks of 256 threads cost the most kernel runtime (see Figure 2C). The implementation with the blocks of 32 threads performed better than the one with 128 threads in the case of a smaller system, but the superiority got weaker when the test system grew larger. However, the effects on the kernel execution time are not obvious because the kernel execution time only occupies a small fraction of the total runtime. The final size of threads per block was set to 64 to achieve the best performance by avoiding the bank conflicts of shared memory and covering the load latency by assigning several active blocks on each SM.

Performance and Speedup. First, we compared the peak performance of GPU-accelerated Householder-QR factorizations with conventional (LAPACK) and parallel (PLASMA) implementation in the popular linear algebra libraries on the CPU (as shown in Figure 3). The peak performance Householder-QR factorizations implemented in CUDA can reach up to 180.6 Gflop/s on a single NVIDIA GeForce GTX295 on the average, which is much higher than that of LAPACK and PLASMA on a single CPU (the peak performances of LAPACK and PLASMA are 2.2 Gflop/s and 23.8 Gflop/s, respectively). The performance deteriorated slightly to 109.6 Gflop/s when the size of the matrix was below 3000, but it is still remarkably superior to LAPACK and PLASMA. The results indicated that the CUDA implementation of Householder-QR factorizations is much faster than conventional serial (LAPACK) and parallel (PLASMA) CPU implementations and lays a promising foundation for NMA acceleration on the GPU architecture.

To investigate the performance of the GPU-accelerated NMA calculation, five proteins were selected as the benchmark

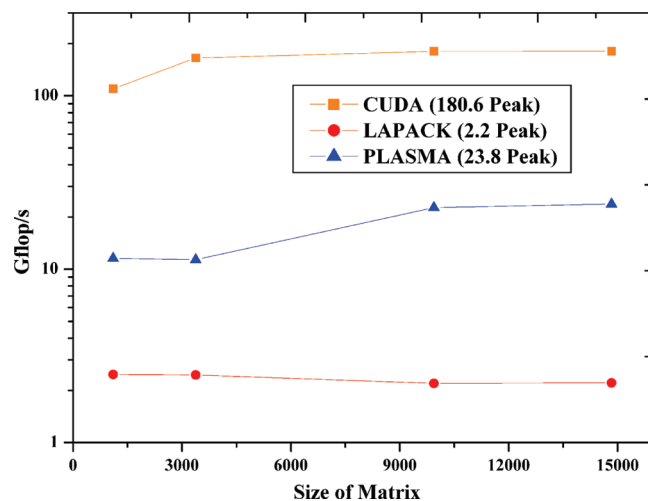


Figure 3. Comparing the peak performances of the QR factorization algorithm implemented in LAPACK, PLASMA, and CUDA. The vertical axis is scaled in log-linear coordinates.

systems: the D14A variant of the *Drosophila* insulin-like peptide 5 (2WFU, 335 atoms), calmodulin (3CLN, 1126 atoms), adenylylate kinases (4AKE, 3313 atoms), actin (1ATN, 4946 atoms), and alcohol dehydrogenase (1ADB, 6783 atoms). Table 1 summarizes the execution time of GROMACS 4.0 on a CPU in serial mode and our GPU implementation at both single and double data precisions. The benchmark results revealed that the GPU-accelerated Householder transformation did not show a performance advantage over the CPU for the small systems (2WFU) with 335 atoms, which can be attributed to the fact that for such a small protein system, the computational resources of GPU are not fully utilized, and the extra cost of multithread scheduling and synchronization occupies a relatively large fraction of the overall runtime. However, the GPU code achieved a more than 20 \times speedup over the CPU for the Householder transformation of larger systems in the cases of 4AKE, 1ATN, and 1ADB. Unfortunately, the NVIDIA GeForce GTX295 used in our study can only access a maximum of 1.7 GB VRAM, which limits the upper size of the simulation system to 7000 atoms with single precision and 5000 atoms with double precision, correspondingly. The tridiagonalization process of the largest protein 1ADB in the test with single precision costs more than 1.6 h on the CPU in serial mode, but it only costs about 219 s on the GPU in the multithread parallel mode. At the same time, the second largest protein 1ATN with double precision costs more than 1.1 h on the CPU, while it costs only 165 s on the GPU in our study. Although the 20 \times speedup of our GPU NMA implementation is not as high as those observed for GPU-accelerated MD simulations and may not be enough to make an abiding difference in NMA calculation for single protein systems, the speed advantage of GPU-accelerated NMA is promising for repeated and intensive NMA calculations involved in the MM/PBSA approach for large-scale virtual screening.

One of the determinants of the GPU-accelerated performance was the size of the intensive data. The speedup of GPU calculation increased with increasing size of the matrix for single and double precisions because a huge workload can fully utilize the computational resources of the GPU and hide various sources of latency including memory access and thread synchronization. Although the benchmark system size is limited by the global memory size in our study, the scale of the performance can

Table 1. Performance Comparison of the Runtime of Householder Transformation with Single and Double Precision on the CPU and GPU

PDB ID	number of residues	number of atoms	single precision			double precision		
			CPU runtime (s)	GPU runtime (s)	speedup	CPU runtime (s)	GPU runtime (s)	speedup
2WFU	46	335	1.031	2.491	<1	2.167	2.699	<1
3CLN	143	1126	44.584	10.127	4.402	63.542	15.103	4.207
4AKE	428	3313	1774.563	82.119	21.609	2162.016	103.157	20.959
1ATN	630	4946	2881.651	114.558	25.155	4029.183	164.954	24.426
1ADB	748	6783	5943.227	219.386	27.09			

The speedup is the runtime of Householder transformation on the GPU versus the runtime of the Householder transformation routines in GROMACS on the CPU. The GPU runtime was measured from the CUDA implementation of the Householder transformation (the double-type version was compiled by the nvcc compiler using option `-arch compute_13, -code sm_13`). The CPU runtime was measured by Householder transformation subroutines “`ssytrd`” with single precision and “`dsytrd`” with double precision in the lapack library of GROMACS 4.0.

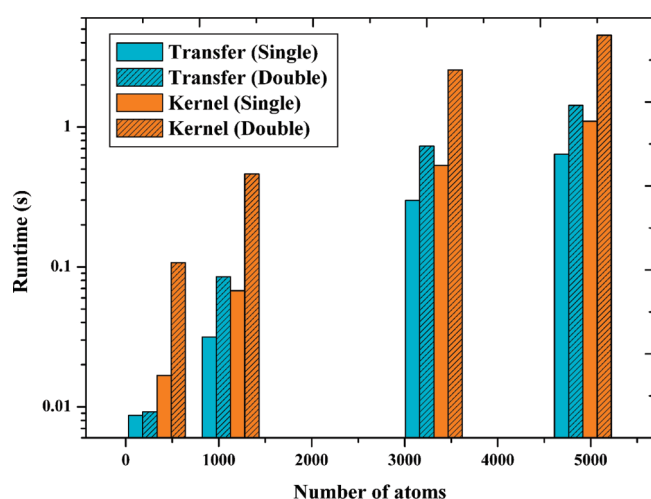


Figure 4. The distribution of data transfer and kernel runtime of the single (float) and double precision Householder transformation implementation on GPU. Note that the vertical axis is scaled in log–linear coordinates.

be maintained for larger protein systems on more powerful GPU cards with larger global memory as the latest Fermi architecture provided by NVIDIA (as many as 6 GB). Actually, the speedup of the GPU implementation over the CPU one could be even greater for larger systems in principle because the performance cannot be simply scaled by the number of atoms between the GPU and the CPU calculations. For the CPU case, the scaling is very close to $O(N^3)$, indicating that Householder transformation of the Hessian matrix is the dominant cost. However, the speedup of the GPU over the CPU increased faster than linearly with the number of atoms, which can be attributed to the time complexity of $O(1)$ as mentioned above if the latencies incurred from data transfer are ignored because the intensive data were loaded to the GPU and operated across all available cores simultaneously regardless of the data size involved.

The double precision code is expected to be more time-consuming because the number of single precision cores (32 bits) on the GPU is about 8 times more than that of the double precision cores (64 bits).⁵⁵ As shown in Figure 4, the transfer time of the double precision implementation increases almost twice, and the kernel runtime costs about 5–8 times more than the single precision one. The differences became more apparent

for larger test systems. The differences in speed for the single and double codes are reasonable given that the double type is twice longer than the single one in storage and transfer, and there are 8 times more single precision cores in the GPU. However, as shown in Table 1, the speedup for double precision only descends slightly compared with the single precision, which can be attributed to the fact that the kernel execution time on GPU only occupies a very small fraction in the overall program runtime, especially with larger protein systems.

Accuracy. Another important consideration in evaluating all-atom NMA implementation is the accuracy of the modes it produces. Previous work has shown that single precision float point is sufficient to produce high quality results in molecular dynamics,⁵⁶ but in practice, double precision is always used in the calculations in a way that avoids an unnecessary loss of accuracy. Since double precision code reduced the performance by about 8 times compared to the single precision one, as expected, it is worth investigating whether any potential error may have resulted from the precision truncation to make a compromise between the efficiency and accuracy.

To test the accuracy of our CUDA implementation, we performed the Householder transformation calculation of the Hessian matrix from the NMA of adenylate kinase (4AKE) with single and double precisions and generated the structural snapshots of corresponding modes with GROMACS from the decomposition results. The root-mean-square deviation (RMSD) between the snapshots of corresponding modes from the GPU code and GROMACS calculated on CPU were compared to evaluate the accuracy of the GPU implementation. Thirty snapshots from the 10 lowest-frequency vibration modes (modes 7–16) calculated by GROMACS were chosen as the reference of the NMA results. The average RMSD values of the 30 snapshots in each mode between single/double precision code and the reference structures were calculated. The average RMSDs between the modes generated by double precision code and GROMACS are in the range of 0.0021–0.042 Å (Figure 5A), and most of the heavy atoms' position deviations between the most different snapshot conformations of node 8 from the GPU and CPU are below 0.1 Å (as shown in Figure 5B). Considering that the resolution of the crystal structure (4AKE) is as high as 2.20 Å, the tiny structural deviations between the GPU and CPU NMA calculation results can be almost ignored. However, the average RMSDs calculated from single precision modes are higher than the double precision one and up to about 0.25 Å.

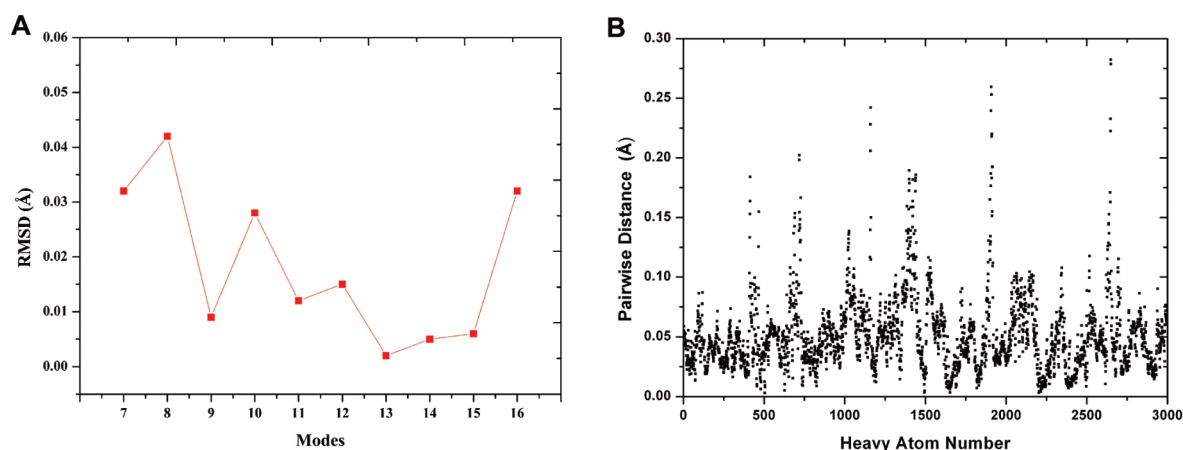


Figure 5. Accuracy comparison of *t* NMA calculation on GPU and CPU. (A) Average RMSD values of the top 10 modes of 4AKE (modes 7–16) between the results of GPU (double precision) and CPU implementation. (B) Distribution of pairwise distances for the heavy atoms between the most different snapshot conformations in mode 8 of 4AKE from GPU and CPU.

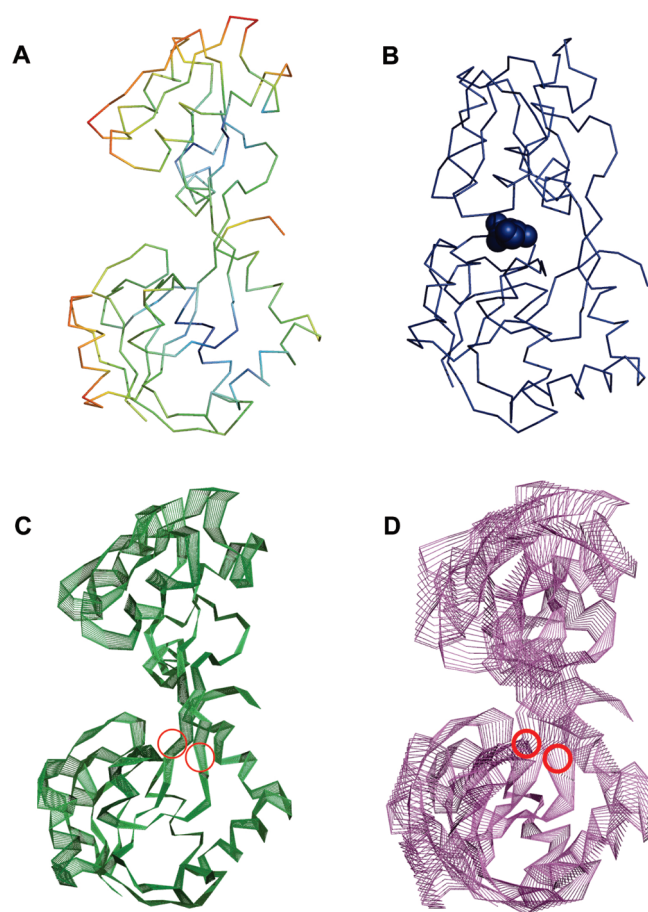


Figure 6. Collective motion prediction results for the allosteric conformational changes observed between (A) free (1GGG) and (B) substrate-bound (1WDN) forms of the glutamine-binding protein with (C) GPU-accelerated all-atom NMA and (D) ENM. The structure of the free glutamine-binding protein is colored according to the atom position deviations aligned onto the substrate-bound form: red color for deviation as high as 14.4 Å and blue color for deviation as low as 0.7 Å. The glutamine is represented in the sphere model. The superposition of intermediate structures for modes 7 from the GPU and ENM calculation are displayed. The two hinge regions are shown circled in red.

Although the accuracy of the faster single precision code is about 100 times lower than the double precision one, the errors of the results are still acceptable considering the resolutions of most of the crystal structures used for NMA calculation are higher than 1.0 Å, indicating that the results obtained from GPU with both single and double precisions are as accurate as the equivalent calculated from common CPU implementation in GROMACS.

Application. NMA is widely applied to predict the functional collective motions of the large macromolecules. Although the previous study of Tirion evidenced that a hypothetical force field with uniform (single-parameter) harmonic potentials (like ENM) yields global modes, which are almost indistinguishable from those obtained from a detailed force field with specific nonlinear terms,⁴⁸ all-atom NMA is still considered more accurate than the coarse-grained one because the magnitude of the excursions along the normal modes is almost unknown, and more attention must be paid when interpreting the resulted motions.⁸ We analyzed the allosteric conformational changes observed between the free (1GGG) and substrate-bound (1WDN) forms of the glutamine-binding protein with GPU-accelerated all-atom NMA.^{57,58} This ellipsoidal protein has two globular domains connected by two hinges and exhibits a large-scale movement of the two hinges connecting the two globular domains upon glutamine binding (as shown in Figure 6A and B). From the superposition of intermediate structures for mode 7 of the ligand-free structure (as shown in Figure 6C), the collective motion trend of the two domains around the hinges can be apparently observed to close the deep binding cleft for glutamine binding, which corresponds well with the most deviated regions between the ligand-free and ligand-bound regions, as shown in Figure 6A. Moreover, the hinge regions with less structural excursion variances are also apparent and coincide well with the crystal structures, which is more accurate and distinct than that of the ENM results (as shown in Figure 6C and D).

CONCLUSION AND FUTURE WORK

We have implemented Householder-QR transformation for Hessian matrix on GPU, which is the most time-consuming step in all-atom NMA. As expected, GPU implementation achieved an acceptable speedup compared with CPU. The results revealed

that the performance of GPU improved with the increasing computational workload, which can fully occupy the idle computational units and hide various sources of latency. At the same time, the influence of the data precision was also verified from the perspectives of both speed and accuracy. Data transfer and the amount of processing cores significantly impacted the performance of GPU when the precision of data type increases. The results of our calculations illustrate that all-atom NMA may be suitable for GPU acceleration for large systems without any coarse-grained approximation. The GPU code has been integrated into the GROMACS package as a standalone module to provide seamless acceleration of all-atom NMA for the molecular modeling community, which can be provided on request.

AUTHOR INFORMATION

Corresponding Author

*Phone/Fax: +86-21-64250213. E-mail: hlli@ecust.edu.cn.

ACKNOWLEDGMENT

This work was supported by the Special Fund for Major State Basic Research Project (Grants 2009CB918501 and 2011CB910200), the National Natural Science Foundation of China (Grants 20803022), the Shanghai Committee of Science and Technology (Grants 09dz1975700 and 10431902600), the Major National Scientific and Technological Project of China (Grants 2011ZX09307-002-03, 2009ZX09501-001, and 2009ZX09301-001), and the Fundamental Research Funds for the Central Universities. H.L. is also sponsored by the Shanghai Rising-Star Program (Grant 10QA1401800) and Program for New Century Excellent Talents in University. We also thank Prof. Rolf Hilgenfeld from University of Lübeck for the careful reading and polishing of this manuscript when he held a Chinese Academy of Sciences (CAS) Professorship.

ABBREVIATIONS

BNM, Block Normal Mode; CPU, Central Processing Unit; CUDA, Compute Unified Device Architecture; ENM, Elastic Network Model; GPU, Graphics Processing Unit; LAPACK, Linear Algebra Package; MD, Molecular Dynamics; MPI, Message Passing Interface; NMA, Normal Mode Analysis; PLASMA, Parallel Linear Algebra for Scalable Multicore Architectures; PVM, Parallel Virtual Machine; RAM, Random Access Memory; RMSD, Root Mean Square Deviation; SIMD, Single-Instruction Multiple-Data; SISD, Single-Instruction Single-Data; SM, Stream Multiprocessor; SP, Streaming Processor

REFERENCES

(1) Lindahl, E.; Azuara, C.; Koehl, P.; Delarue, M. NOMAD-Ref: visualization, deformation and refinement of macromolecular structures based on all-atom normal mode analysis. *Nucleic Acids Res.* **2006**, *34*, 52–56.

(2) Smyth, M. S.; Martin, J. H. J. X-Ray crystallography. *J. Clin. Pathol.* **2000**, *53*, 8–14.

(3) Wishart, D. S.; Sykes, B. D.; Richards, F. M. The chemical shift index: a fast and simple method for the assignment of protein secondary structure through NMR spectroscopy. *Biochemistry* **1992**, *31*, 1647–1651.

(4) Ritchie, K.; Iino, R.; Fujiwara, T.; Murase, K.; Kusumi, A. The fence and picket structure of the plasma membrane of live cells as revealed by single molecule techniques (Review). *Mol. Membr. Biol.* **2003**, *20*, 13–18.

(5) Karplus, M.; Petsko, G. A. Molecular dynamics simulations in biology. *Nature* **1990**, *347*, 631–639.

(6) Tama, F.; Sanejouand, Y. H. Conformational change of proteins arising from normal mode calculations. *Protein Eng.* **2001**, *14*, 1–6.

(7) Sedeh, R. S.; Bathe, M.; Bathe, K. J. The subspace iteration method in protein normal mode analysis. *J. Comput. Chem.* **2010**, *31*, 66–74.

(8) Bahar, I.; Lezon, T. R.; Bakan, A.; Shrivastava, I. H. Normal mode analysis of biomolecular structures: functional mechanisms of membrane proteins. *Chem. Rev.* **2010**, *110*, 1463–1497.

(9) Tama, F.; Valle, M.; Frank, J.; Brooks, C. L., III. Dynamic reorganization of the functionally active ribosome explored by normal mode analysis and cryo-electron microscopy. *Proc. Natl. Acad. Sci. U. S. A.* **2003**, *100*, 9319–9323.

(10) Ma, J. Usefulness and limitations of normal mode analysis in modeling dynamics of biomolecular complexes. *Structure* **2005**, *13*, 373–380.

(11) Tama, F.; Brooks, C. L., III. Symmetry, form, and shape: guiding principles for robustness in macromolecular machines. *Annu. Rev. Biophys. Biomol. Struct.* **2006**, *35*, 115–133.

(12) Kuhn, B.; Kollman, P. A. Binding of a diverse set of ligands to avidin and streptavidin: an accurate quantitative prediction of their relative affinities by a combination of molecular mechanics and continuum solvent models. *J. Med. Chem.* **2000**, *43*, 3786–3791.

(13) Swanson, J. M.; Henschman, R. H.; McCammon, J. A. Revisiting free energy calculations: a theoretical connection to MM/PBSA and direct calculation of the association free energy. *Biophys. J.* **2004**, *86*, 67–74.

(14) Obiol-Pardo, C.; Rubio-Martinez, J. Comparative evaluation of MMPBSA and XSCORE to compute binding free energy in XIAP-peptide complexes. *J. Chem. Inf. Model.* **2007**, *47*, 134–142.

(15) Brooks, B.; Karplus, M. Harmonic dynamics of proteins: normal modes and fluctuations in bovine pancreatic trypsin inhibitor. *Proc. Natl. Acad. Sci. U. S. A.* **1983**, *80*, 6571–6575.

(16) Delarue, M.; Sanejouand, Y. H. Simplified normal mode analysis of conformational transitions in DNA-dependent polymerases: the elastic network model. *J. Mol. Biol.* **2002**, *320*, 1011–1024.

(17) Marechal, J. D.; Perahia, D. Use of normal modes for structural modeling of proteins: the case study of rat heme oxygenase 1. *Eur. Biophys. J.* **2008**, *37*, 1157–1165.

(18) Suhre, K.; Sanejouand, Y. H. ElNemo: a normal mode web server for protein movement analysis and the generation of templates for molecular replacement. *Nucleic Acids Res.* **2004**, *32*, 610–614.

(19) Brown, S. P.; Muchmore, S. W. Rapid estimation of relative protein-ligand binding affinities using a high-throughput version of MM-PBSA. *J. Chem. Inf. Model.* **2007**, *47*, 1493–1503.

(20) Tama, F.; Gadea, F. X.; Marques, O.; Sanejouand, Y. H. Building-block approach for determining low-frequency normal modes of macromolecules. *Proteins* **2000**, *41*, 1–7.

(21) Hollup, S. M.; Salensminde, G.; Reuter, N. WEBnm@: a web application for normal mode analyses of proteins. *BMC Bioinf.* **2005**, *6*, 52–60.

(22) Bahar, I.; Rader, A. J. Coarse-grained normal mode analysis in structural biology. *Curr. Opin. Struct. Biol.* **2005**, *15*, 586–592.

(23) Tama, F.; Brooks, C. L., III. Diversity and identity of mechanical properties of icosahedral viral capsids studied with elastic network normal mode analysis. *J. Mol. Biol.* **2005**, *345*, 299–314.

(24) Hinsen, K. Analysis of domain motions by approximate normal mode calculations. *Proteins: Struct., Funct., Bioinf.* **1998**, *33*, 417–429.

(25) Yang, L.; Song, G.; Jernigan, R. How well can we understand large-scale protein motions using normal modes of elastic network models? *Biophys. J.* **2007**, *93*, 920–929.

(26) Zadra, A.; Brunet, G.; Derome, J. An empirical normal mode diagnostic algorithm applied to NCEP reanalyses. *J. Atmos. Sci.* **2002**, *59*, 2811–2829.

(27) Haque, I. S.; Pande, V. S. PAPER--accelerating parallel evaluations of ROCS. *J. Comput. Chem.* **2010**, *31*, 117–132.

(28) Owens, J.; Houston, M.; Luebke, D.; Green, S.; Stone, J.; Phillips, J. GPU computing. *Proc. IEEE* **2008**, *96*, 879–899.

- (29) Hardy, D. J.; Stone, J. E.; Schulten, K. Multilevel Summation of Electrostatic Potentials Using Graphics Processing Units. *Parallel Comput.* **2009**, *35*, 164–177.
- (30) Phillips, J. C.; Braun, R.; Wang, W.; Gumbart, J.; Tajkhorshid, E.; Villa, E.; Chipot, C.; Skeel, R. D.; Kale, L.; Schulten, K. Scalable molecular dynamics with NAMD. *J. Comput. Chem.* **2005**, *26*, 1781–1802.
- (31) Anderson, A. G.; Goddard, W. A.; Schroder, P. Quantum Monte Carlo on graphical processing units. *Comput. Phys. Commun.* **2007**, *177*, 298–306.
- (32) Che, S.; Boyer, M.; Meng, J. Y.; Tarjan, D.; Sheaffer, J. W.; Skadron, K. A performance study of general-purpose applications on graphics processors using CUDA. *J. Parallel. Distr. Comput.* **2008**, *68*, 1370–1380.
- (33) Stone, J. E.; Hardy, D. J.; Ufimtsev, I. S.; Schulten, K. GPU-accelerated molecular modeling coming of age. *J. Mol. Graphics Model.* **2010**, *29*, 116–125.
- (34) Buttari, A.; Langou, J.; Kurzak, J.; Dongarra, J. A class of parallel tiled linear algebra algorithms for multicore architectures. *Parallel Comput.* **2009**, *35*, 38–53.
- (35) Buttari, A.; Langou, J.; Kurzak, J.; Dongarra, J. Parallel tiled QR factorization for multicore architectures. *Concur. Comput.—Pract. E* **2008**, *20*, 1573–1590.
- (36) Belleman, R.; Bédorf, J.; Portegies Zwart, S. High performance direct gravitational N-body simulations on graphics processing units II: An implementation in CUDA. *New. Astron.* **2008**, *13*, 103–112.
- (37) Hong, S.; Kim, H. An analytical model for a GPU architecture with memory-level and thread-level parallelism awareness. *SIGARCH Comput. Archit. News* **2009**, *37*, 152–163.
- (38) Lindholm, E.; Nickolls, J.; Oberman, S.; Montrym, J. NVIDIA Tesla: A Unified Graphics and Computing Architecture. *IEEE Micro* **2008**, *28*, 39–55.
- (39) Nickolls, J.; Buck, I.; Garland, M.; Skadron, K. Scalable parallel programming with CUDA. *Queue* **2008**, *6*, 40–53.
- (40) Ghysels, A.; Van Speybroeck, V.; Pauwels, E.; Catak, S.; Brooks, B. R.; Van Neck, D.; Waroquier, M. Comparative study of various normal mode analysis techniques based on partial Hessians. *J. Comput. Chem.* **2010**, *31*, 994–1007.
- (41) Case, D. Normal mode analysis of protein dynamics. *Curr. Opin. Struct. Biol.* **1994**, *4*, 285–290.
- (42) Tirion, M. Large amplitude elastic motions in proteins from a single-parameter, atomic analysis. *Phys. Rev. Lett.* **1996**, *77*, 1905–1908.
- (43) Ma, J. New advances in normal mode analysis of supermolecular complexes and applications to structural refinement. *Curr. Protein Pept. Sci.* **2004**, *5*, 119–123.
- (44) Martin, R.; Wilkinson, J. Similarity reduction of a general matrix to Hessenberg form. *Numer. Math.* **1968**, *12*, 349–368.
- (45) Dongarra, J. J.; van de Geijn, R. A. Reduction to condensed form for the Eigenvalue problem on distributed memory architectures. *Parallel Comput.* **1992**, *18*, 973–982.
- (46) Lange, O. F.; Schafer, L. V.; Grubmuller, H. Flooding in GROMACS: accelerated barrier crossings in molecular dynamics. *J. Comput. Chem.* **2006**, *27*, 1693–1702.
- (47) Berendsen, H.; van der Spoel, D.; Van Drunen, R. GROMACS: a message-passing parallel molecular dynamics implementation. *Comput. Phys. Commun.* **1995**, *91*, 43–56.
- (48) Gao, W.; Huyen, N.; Loi, H.; Kemaq, Q. Real-time 2D parallel windowed Fourier transform for fringe pattern analysis using Graphics Processing Unit. *Opt. Express.* **2009**, *17*, 23147–23152.
- (49) Levy, T.; Cohen, G.; Rabani, E. Simulating Lattice Spin Models on Graphics Processing Units. *J. Chem. Theory Comput.* **2010**, *6*, 3293–3301.
- (50) Tunbridge, I.; Best, R. B.; Gain, J.; Kuttel, M. M. Simulation of Coarse-Grained Protein-Protein Interactions with Graphics Processing Units. *J. Chem. Theory Comput.* **2010**, *6*, 3588–3600.
- (51) Garland, M.; Le Grand, S.; Nickolls, J.; Anderson, J.; Hardwick, J.; Morton, S.; Phillips, E.; Zhang, Y.; Volkov, V. Parallel computing experiences with CUDA. *IEEE Micro.* **2008**, *28*, 13–27.
- (52) Yasuda, K. Accelerating density functional calculations with graphics processing unit. *J. Chem. Theory Comput.* **2008**, *4*, 1230–1236.
- (53) Zhang, Y.; Cohen, J.; Owens, J. D. Fast Tridiagonal Solvers on the GPU. *Acm. Sigplan. Notices* **2010**, *45*, 127–136.
- (54) Harvey, M. J.; De Fabritiis, G. An implementation of the smooth particle mesh Ewald method on GPU hardware. *J. Chem. Theory Comput.* **2009**, *5*, 2371–2377.
- (55) Manavski, S.; Valle, G. CUDA compatible GPU cards as efficient hardware accelerators for Smith-Waterman sequence alignment. *BMC Bioinf.* **2008**, *9*, 10–19.
- (56) Friedrichs, M. S.; Eastman, P.; Vaidyanathan, V.; Houston, M.; Legrand, S.; Beberg, A. L.; Ensign, D. L.; Bruns, C. M.; Pande, V. S. Accelerating molecular dynamic simulation on graphics processing units. *J. Comput. Chem.* **2009**, *30*, 864–872.
- (57) Hsiao, C. D.; Sun, Y. J.; Rose, J.; Wang, B. C. The crystal structure of glutamine-binding protein from *Escherichia coli*. *J. Mol. Biol.* **1996**, *262*, 225–242.
- (58) Sun, Y. J.; Rose, J.; Wang, B. C.; Hsiao, C. D. The structure of glutamine-binding protein complexed with glutamine at 1.94 Å resolution: comparisons with other amino acid binding proteins I. *J. Mol. Biol.* **1998**, *278*, 219–229.

Ab Initio Molecular Dynamics Simulations of (101) Surfaces of Potassium Dihydrogenphosphate

Damien J. Carter^{†,‡} and Andrew L. Rohl^{†,‡,*}

[†]Nanochemistry Research Institute, Department of Chemistry, Curtin University of Technology, GPO Box U1987, Perth, WA, Australia, 6845

[‡]iVEC, “The Hub of Advanced Computing in Western Australia”, Technology Park, Kensington, WA, Australia

ABSTRACT: We present an *ab initio* molecular dynamics study of bare and hydrated (101) surfaces of KDP. We examine the dynamical nature of the hydrogen bonding in the high and low temperature phases of bulk KDP and find evidence to support the theory that hydrogen atoms oscillate between two off-center positions in the high-temperature phase. We report the translational relaxation of the surface species on the (101) surface and find good agreement with experimental results, particularly with reference to the direction of the relaxation. We find a strongly hydrogen bound water layer close to the KDP surface, comparing closely to a highly ordered water layer observed experimentally. Overall, there is good agreement with the results of nanoscale experimental studies, demonstrating the effectiveness of *ab initio* molecular dynamics calculations at simulating bulk and surface properties.

INTRODUCTION

Potassium dihydrogenphosphate (KDP) is one of the first materials to be used and exploited for its nonlinear optical properties.¹ At room temperature, KDP forms a paraelectric phase in the tetragonal $I42d$ space group.² KDP undergoes a phase transition at 122 K³ to a ferroelectric phase in the orthorhombic C_{2v} 1-setting space group, as described by Baur.⁴ The structure of KDP and its phase change from a ferroelectric to a paraelectric material has been the subject of numerous diffraction and scattering studies, as reviewed elsewhere.^{2,5} Surface X-ray diffraction (SXRD) studies have examined the relaxation of atoms on the (101) surfaces of KDP.^{6–8} The surface structure under aqueous conditions suggests that there are several “ice-like” ordered water layers on the surface.⁸ The ice-like phenomena of water adsorption on surfaces has been reported in a wide range of mineral systems, such as mica.^{9,10} In recent years, Vlieg and co-workers^{11–13} have further examined the (101) and (100) surfaces of KDP with SXRD to determine the affect of pH on the surface structure and relaxations. They find the (100) surface is insensitive to pH, but the (101) surface is pH dependent, with a competition between K^+ and H_3O^+ .

On-going advances in parallel efficiency and linear scaling algorithms now make it possible to simulate larger and more complex systems using quantum mechanics. There have only been a limited number of quantum mechanical studies of bulk KDP.^{1,14–18} A number of these studies have examined the nature of the ferroelectric–paraelectric phase transition and attribute the ferroelectricity of KDP as predominantly a redistribution of charge density caused by a change of the P–O distance and a coupled P–O motion, and also a coordinated motion of the heavier P and K atoms. There are very few theoretical studies of the surfaces of KDP. Stack et al.¹⁹ have used DFT to study the (100) surface of KDP, in particular relating to the adsorbing/detaching of growth units. We have previously published a density functional theory study of (101) surfaces of KDP.¹⁸ In this previous work, we employed static surface calculations of

(101) surfaces under vacuum, nitrogen, and aqueous conditions. In general, we found good agreement with the results from experimental SXRD studies.

There is still a large gap in understanding between our static model used to examine surfaces of KDP and the experimental surface studies. Molecular dynamics provides us with another step of complexity toward a better description of the interactions that determine the surface structure of KDP. In this work, we present an *ab initio* molecular dynamics (MD) study of both the bare and hydrated (101) surfaces of KDP.

METHODOLOGY

Ab initio density functional theory (DFT) calculations were carried out using the SIESTA code.²⁰ A double- ζ basis set with polarization functions was used for all atoms except oxygen, which had a triple- ζ basis set with polarization functions. Core electrons are represented by norm-conserving pseudopotentials,²¹ and electron exchange–correlation was treated using the generalized gradient approximation (GGA:PBE²²). For potassium atoms, we explicitly include the 3p orbital in the valence configuration of the pseudopotential. Hartree and exchange–correlation energies were evaluated on a uniform real space grid of points with a defined maximum kinetic energy of 200 Ry. The numerical atomic orbitals were confined to an extent that induces an energy shift in each orbital of 0.01 Ry.

We used *ab initio* molecular dynamics (MD) calculations to examine both the high and low temperature phases of KDP. We generated a $2 \times 2 \times 2$ supercell of bulk KDP and used a $3 \times 3 \times 3$ Monkhorst Pack k-grid for reciprocal space integration. A temperature of 20 K was used to simulate the low temperature ferroelectric phase and 298 K for the high temperature paraelectric phase. Variable cell dynamics were performed with the temperature controlled Nose thermostat, enabling us to optimize

Received: December 24, 2010

Published: April 29, 2011

Table 1. Calculated Cell Parameters and Bond Lengths, Distances, and Angles for Ferroelectric and Paraelectric KDP

	ferroelectric		paraelectric		ferroelectric		
	MD	Expt.	MD	expt.	static calculations		
	20 K	102 K ^a	298 K	293 K ^a	0 K ^b	0 K ^c	0 K ^d
<i>a</i> (Å)	7.40	7.46	7.43	7.45	7.60	7.52	7.56
<i>b</i> (Å)	7.39	7.40	7.43	7.45	7.58	7.45	7.55
<i>c</i> (Å)	6.85	6.93	6.91	6.97	6.98	7.01	6.93
P–O (Å)	1.60	1.52	1.59	1.54	1.57	1.49	1.56
P–O _H (Å)	1.65	1.58	1.59	1.54	1.63	1.55	1.63
O _H –H (Å)	1.11	1.10	1.22	1.07	1.08	1.06	1.07
O _H ···H (Å)	1.38	1.44	1.22	1.43	1.39	1.42	1.42
O _H ···O (Å)	2.51	2.49	2.44	2.49	2.48	2.48	2.49
O _H –P–O _H (deg)	107.7	106.9	109.5	110.5	106.1	106.5	105.8
O–P–O (deg)	111.8	114.8	109.5	110.5	114.3	114.8	115.7
O _H –H···O (deg)	178.8	177.6	178.6	177.2	177.1		178.3

^a Results from Nelmes et al.² ^b DFT GGA-PBE results from Koval et al.¹⁴ ^c DFT GGA-PBE results from Zhang et al.²³ ^d DFT GGA-PBE results from Carter et al.¹⁸

the lattice vectors at internal coordinates of the low and high temperature phases. A step size of 1×10^{-15} s was used for all MD calculations, with each simulation running for approximately 10 000 steps. In all cases, dynamical equilibrium (based on energies and/or volume) appeared to be reached in typically 500–2000 steps. Time-averaged MD structures were generated by averaging the coordinates of each atom over approximately 2000 fs for surface calculations and 5000 fs for bulk calculations.

Using the averaged cell parameters and atomic positions of the high temperature 298 K phase, we then cleaved a (101) surface of KDP. There are two possible ways to cut the (101) surface: one produces a cation (K^+) terminated surface, and the other produces a dihydrogenphosphate ($H_2PO_4^-$) terminated surface. From our previous *ab initio* density functional calculations,¹⁸ we have shown that the K^+ terminated surface is significantly more stable than the $H_2PO_4^-$ surface. Surface X-ray diffraction studies of KDP by de Vries et al.^{6,7} have also confirmed this. As a result, we only consider the K^+ terminated (101) surface in our *ab initio* molecular dynamics calculations. Constant temperature (fixed cell) MD calculations were performed on the pure (101) surface with a temperature of 298 K, controlled by the Nose thermostat. The simulation was run for approximately 10 000 steps. Using the relaxed surface, the simulation cell was then filled with water molecules, and the MD calculation was repeated with the simulation running for approximately 10 000 steps.

Note that these calculations are extremely computer intensive, which severely restricts the time frame that can be accessed with *ab initio* molecular dynamics calculations compared to molecular dynamics calculations using interatomic potentials.

RESULTS AND DISCUSSION

The calculated lattice parameters of KDP at 20 and 298 K are compared to those of the experimentally observed paraelectric and ferroelectric phases, and other theoretical studies in Table 1.

From the results in Table 1, we find the calculated cell parameters of the low temperature ferroelectric phase and the high temperature paraelectric phase compare closely to experimentally reported cell parameters. In both cases, the calculated structures are slightly smaller than experimental results. GGA

functionals of inorganic solids typically lead to an overestimation of cell volumes by a few percent; however, GGA functionals are also known to overestimate the strength of hydrogen bonds in strongly hydrogen-bonded systems.²⁴ This overestimation of the strength of hydrogen bonds between the $H_2PO_4^-$ groups leads to a slight contraction in the cells.

There has been debate over the KDP ferroelectric–paraelectric phase transition relating to the ordering of the hydrogen in the high temperature phase. Neutron diffraction studies show that in the paraelectric structure, hydrogen atoms occupy two off-center site positions between the oxygen atoms on neighboring phosphates, with 50% probability.²⁵ The debate relates to how this 50% occupation occurs. One common theory is that above the phase transition temperature there is a disordered arrangement of $H_2PO_4^-$ groups, while below there is an ordered arrangement.² The other main theory is that the protons oscillate between the two equivalent sites between the oxygen atoms.²⁶ Recent neutron Compton scattering studies of KDP²⁷ show clearly that the proton is coherent over both sites in the paraelectric phase, a result that invalidates the commonly accepted disorder–order picture of the transition. Using our molecular dynamics results from the low and high temperature phases, we have investigated the nature of the occupation of hydrogen atoms in the off-center positions. We first examine the time-averaged MD high and low temperature structures and calculate the radial distribution function ($g(r)$) for oxygen to hydrogen distances. This is illustrated in Figure 1.

The low temperature ferroelectric phase (20 K) shows two distinct peaks/regions in Figure 1a. The smaller region from 1.0 to 1.2 Å corresponds to O–H bonds in the KDP, while the 1.3–1.5 Å region corresponds to the hydrogen bond O···H distances. As expected, the two peaks in the time-averaged MD structure are sharper than the peaks for the MD structure over the 5000 fs, due to the dynamical nature of the calculations. The high temperature paraelectric phase (Figure 1b) shows a single broad peak/region from 1.15 to 1.3 Å for the time-averaged MD structure. The MD structure shows a broad hump extending approximately 1.0 to 1.6 Å. There are small crests in this broad hump at approximately 1.1 Å and 1.4 Å, which correspond to typical O–H bond and O–H hydrogen distances. The broad

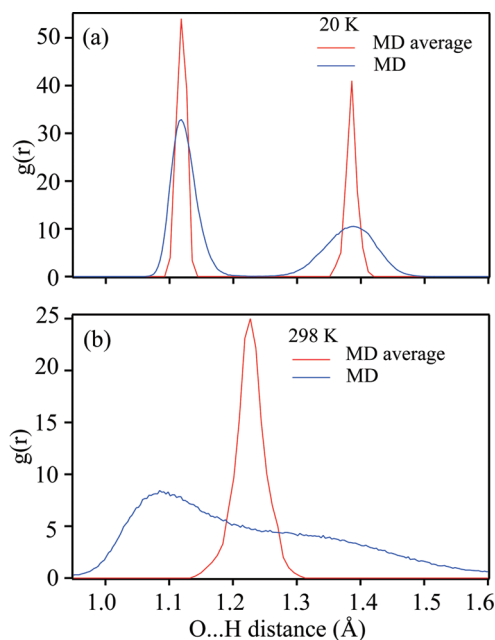


Figure 1. Radial distribution function ($g(r)$) of oxygen to hydrogen distances over 5000 fs (MD) and the time-averaged molecular dynamics structure for the (a) low (20 K) and (b) high (298 K) temperature phases of bulk KDP.

hump in the paraelectric phase is caused by the dynamical nature of the simulations, and in particular the oscillation of the hydrogen atom between the two equivalent off-center positions. If there was a simple disorder mechanism in the paraelectric phase, Figure 1b for the MD structure would have shown two distinct peaks (similar to that observed for the ferroelectric phase at 20 K).

The O–H bond length and O···H hydrogen bond distances of 1.22 Å for the 298 K MD structure differ from the experimental structure reported in Table 1. As discussed above, the position of the hydrogen atom is dynamical and typically occupies two off-center positions and can oscillate between them throughout the course of simulation. So to calculate the O–H bond and O···H hydrogen bond distances for the 298 K structure, we use the time-average MD structure (as illustrated in Figure 1b).

To further illustrate the dynamical behavior of the hydrogen atom position, in Figure 2, we illustrate the positions of oxygen and hydrogen atoms along an O···H···O bond/hydrogen bond over a simulation time of 5000 fs, for the 20 and 298 K structures. From Figure 2, one can see that the hydrogen atom in the low temperature (20 K) ferroelectric phase oscillates about its equilibrium off-center position along the O···H···O hydrogen bond, at approximately 1.1 Å from the nearest oxygen atom. The hydrogen atom in the high temperature (298 K) paraelectric phase exhibits much larger oscillations about its equilibrium position. These oscillations correspond to the hydrogen atom oscillating from one equivalent off-center site to the other (i.e., oscillating from $\text{P}=\text{O}\cdots\text{H}-\text{O}-\text{P}$ to $\text{P}-\text{O}-\text{H}\cdots\text{O}=\text{P}$). If the ferroelectric–paraelectric mechanism was an order–disorder reaction, then the 298 K paraelectric results would have looked very much like the low temperature results with only minimal oscillations around the equilibrium value. The MD results support the theory that hydrogen atoms oscillate between the two off-center positions in the paraelectric phase and are the

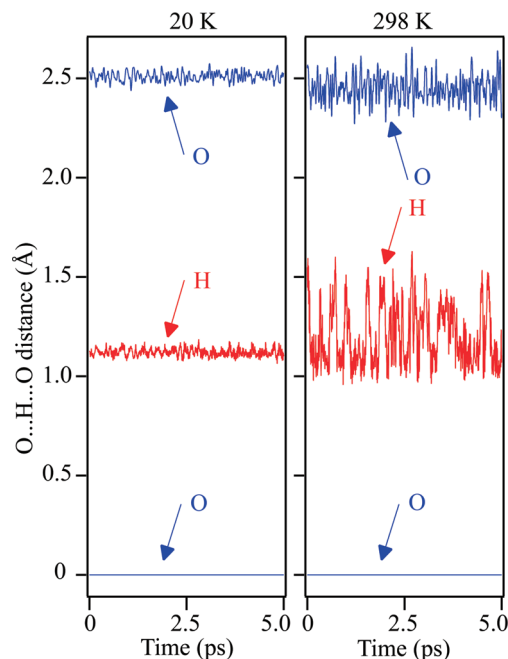


Figure 2. Displacement of a hydrogen atom between two oxygen atoms over 5000 fs for the low (20 K) and high (298 K) temperature phases of bulk KDP.

cause of the observed 50% occupation of the off-center positions in this phase.

The paraelectric–ferroelectric transition in KDP is not just related to the hydrogen ordering, but in the low temperature ferroelectric phase, there are also small displacements of potassium and phosphorus atoms along the c axis. For the KDP bulk at 20 K, the average displacement in the c direction is 0.04 Å for both the phosphorus and the potassium atoms. Neutron diffraction studies by Nelmes et al.² report that the experimental displacements for the low temperature phase of KDP of potassium and phosphorus at 102 K are approximately 0.05 Å. Energy minimization density functional calculations by Zhang et al.²³ report the displacement of phosphorus is 0.06 Å and that of potassium is 0.03 Å. Thus, the calculated displacements of potassium and phosphorus closely match the experimental values from neutron diffraction studies and the calculated values from planewave density functional calculations.

We also examined the electronic structure of the MD averaged paraelectric temperature phase. Examining the band structure, we find an insulator with a band gap of 5.54 eV. Density functional studies of bulk KDP have previously reported band gaps ranging from 4.2 to 6.0 eV.^{17,23,28} The band gap of KDP has also been determined experimentally to have values ranging from 7.0–8.8 eV.²⁹ In general, band gaps calculated using density functional theory are systematically underestimated when compared to experimental values, and this is the case again here.

To quantify the surface relaxations in our simulations of the cation terminated surface, we use the approach taken in the experimental studies of de Vries et al.,^{6,7} where a H_2PO_4^- ion is treated essentially as a fixed group, and movements of the central atom in this group (phosphorus) were measured. The displacements of atoms (in the z direction) are then calculated by comparing the positions in the relaxed and unrelaxed surfaces.

Table 2. Translational Relaxations of Species Perpendicular to the (101) Surface of KDP from Static and Molecular Dynamics Calculations

relaxations (Å)	vacuum surface		hydrated surface	
	static ^a	MD	static ^a	MD
	K^+			
layer 1	-0.25 (-0.29, -0.25)	+0.06 ± 0.05	+0.14 (+0.17, +0.11)	+0.25 ± 0.12
layer 2	-0.01 (-0.02, +0.01)	+0.11 ± 0.05	+0.05 (+0.08, +0.02)	+0.13 ± 0.05
layer 3	0.00 (-0.01, +0.01)	+0.13 ± 0.05	-0.01 (-0.02, 0.00)	+0.13 ± 0.04
layer 4	0.00 (-0.01, +0.01)	+0.00 ± 0.02	0.00 (-0.01, +0.01)	0.00 ± 0.03
	$H_2PO_4^-$			
layer 1	+0.12 (+0.18, +0.06)	+0.26 ± 0.10	+0.08 (0.00, +16.00)	+0.24 ± 0.09
layer 2	-0.06 (-0.07, -0.05)	+0.10 ± 0.03	-0.03 (-0.06, 0.00)	+0.18 ± 0.08
layer 3	0.00 (-0.01, +0.01)	0.04 ± 0.03	+0.01 (-0.02, +0.04)	+0.04 ± 0.06
layer 4	0.00 (-0.01, +0.01)	0.00 ± 0.03	0.00 (-0.01, +0.01)	0.00 ± 0.04

^a Results from Carter et al.¹⁸**Table 3. Translational Relaxations of K^+ and $H_2PO_4^-$ Ions at the (101) Surface of KDP from Theoretical and Experimental Studies**

relaxations (Å)	K^+	$H_2PO_4^-$
	experimental studies	
aqueous solution ^a	+0.10 ± 0.05	+0.04 ± 0.05
	static calculations ^b	
0 K vacuum	-0.25 (-0.27, -0.23)	+0.12 (+0.18, +0.06)
0 K hydrated	+0.14 (+0.17, +0.11)	+0.08 (+0.16, +0.00)
	molecular dynamics	
298 K vacuum	+0.06 ± 0.05	+0.26 ± 0.10
298 K hydrated	+0.25 ± 0.12	+0.24 ± 0.09

^a Results from de Vries et al.^{6,7} ^b Results from Carter et al.¹⁸

The 3D periodic simulation cells contain eight layers of K^+ and $H_2PO_4^-$ ions but have two surfaces (in the z direction); hence for each species, there are four unique layers (layers 1 and 8 are equivalent, 2 and 7 are equivalent, etc.). The surface relaxations are reported in Table 2 with a negative (-) displacement referring to inward relaxation and a positive (+) displacement referring to an outward relaxation. In Table 2, we compare the layer by layer relaxation for our molecular dynamics calculations versus the results for static surface calculations from our previous study.¹⁸ In Table 2, layer 1 refers to the outermost layer and layer 4 refers to the layer closest to the center of the KDP slab, and error ranges are shown as one standard deviation of the mean value. In experimental SXRD studies, a single site model is used for each surface layer; however, for the static calculations, there are two symmetry-unique positions for each layer, so we report an average relaxation value in Tables 2 and 3 (with the actual values given in parentheses). In the molecular dynamics calculations reported here, there are no longer two symmetry-unique positions for each layer, so we use a single site model for each layer.

One of the most obvious differences in the surface relaxation values for the vacuum surface in Table 2 is the direction of the K^+ species in the outermost layer (layer 1), with static calculations producing a large inward relaxation and MD calculations producing

a small outward relaxation. The (101) surfaces are terminated with K^+ ions, so the outermost $H_2PO_4^-$ layer (layer 1) is below the surface of the outermost K^+ layer. Under vacuum conditions and at 0 K, the K^+ ions have to contract inward toward the surface. When the temperature is 298 K and the surface is allowed to evolve over time using molecular dynamics, the outermost K^+ layer has a small expansion from its initial configuration. Coupled with this, we also see in MD calculations that there is an outward relaxation of the second and third layers, in contrast to the static calculations where there is negligible change. The relaxations of the $H_2PO_4^-$ layers for the static and MD calculations are similar in both magnitude and direction.

The layer-by-layer relaxations for the hydrated surfaces in Table 2 show similar trends for the static and MD calculations in terms of the direction of the translational relaxations, although the actual magnitudes do vary. The static calculations of K^+ and $H_2PO_4^-$ layers only appear to be significant in the outermost layer (layer 1), with the other layers having a negligible change. This was also observed in the vacuum surface calculations. In MD calculations of the hydrated surface, the second $H_2PO_4^-$ layer and the second and third K^+ layers also show a noticeable relaxation. The static and MD calculations on the hydrated surface both show an outward movement of the outermost (layer 1) K^+ and $H_2PO_4^-$ layers (see Figure 3 for MD averaged hydrated surface of KDP). The magnitudes of the relaxations of both species in the MD calculations are slightly larger than for static calculations. The static 0 K calculations consisted of 12 explicit water molecules above a surface and a simple geometry minimization to find a minimum energy. In MD calculations, the surface structure and interactions with the water molecules are allowed to time-evolve at a finite temperature, and thus we expect that the magnitudes of the surface relaxations will vary compared to the static calculations. Lateral relaxations of surface atoms in the directions parallel to the surface are approximately 0.04 Å and suggest that there are no large excited surface phonons.

MD simulations enable us to further examine the dynamical behavior of the (101) surface and its interactions with the water molecules. Examining the hydrated surfaces, we find a number of strong hydrogen bonds between the closest water molecules and the (101) surface with typical values of 1.4–1.7 Å. We also examined the position of the hydrogen atoms of surface

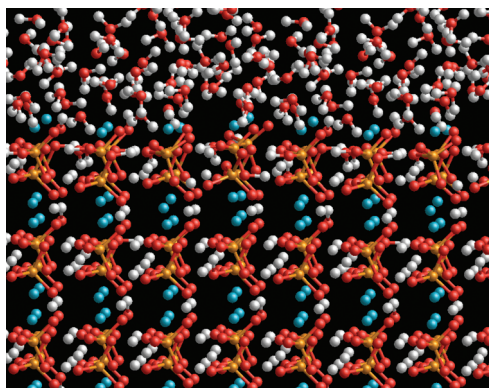


Figure 3. MD averaged hydrated surface of KDP. Oxygen, hydrogen, potassium, and phosphorus atoms are represented by red, white, blue, and orange colored spheres, respectively.

H_2PO_4^- groups to see if they dissociate into the water molecules or stay in their original positions. Analysis of their locations suggests that the hydrogen atoms of H_2PO_4^- do not exchange with water molecules under the finite temperature dynamics considerations but do form strong hydrogen bonds to the neighboring water layer.

In Table 3, we compare the surface relaxations from our static and MD calculations to the experimental results of de Vries et al.^{6,7} The surface relaxations in Table 3 are for the outermost K^+ and H_2PO_4^- layers. As described above, a negative (−) displacement refers to inward relaxation and a positive (+) displacement refers to an outward relaxation. Error ranges are shown as one standard deviation of the mean value.

We previously reported¹⁸ that surface relaxations from static calculations of the KDP (101) surfaces under nitrogen conditions compare closely (in direction and magnitude) to the experimental results of Reedjik.³⁰ Unfortunately, there are no experimental results for (101) surfaces under high vacuum conditions, as the surface quality was found to change over time, making it impossible to accurately determine the surface relaxations.⁷ Comparing the surface relaxations in Table 3, both static and MD calculations predict an outward displacement of the K^+ and H_2PO_4^- layers, matching the experimental trends, although there is some variation in the magnitudes of these relaxations. The calculated surface relaxations for the hydrated surfaces are larger than the experimental values, with the static 0 K results actually closer to those from experiments. As mentioned before, DFT calculations are known to overestimate the strength of hydrogen bonds. Examining the hydrated surfaces, we find that a number of strong hydrogen bonds with typical values of 1.4–1.7 Å have formed between the H_2PO_4^- layer and the neighboring water molecules. There is also an attraction between the K^+ ions and the water molecules. These interactions could account for the larger surface relaxations observed in our static and MD calculations.

The position of the water atoms above the (101) surface gives insight into the nature of the interactions of water with the surface. Experimental surface XRD studies by Reedjik et al.⁸ suggest that there are two well-ordered “ice-like” layers closest to the surface, then several quasi-ordered layers adjacent to these layers. The two well-ordered layers are predicted to have strong interactions with the (101) surface species. The oxygen atom positions in the first ordered water layer are predicted to be at the extrapolated position of a next potassium layer. Reedjik et al.⁸

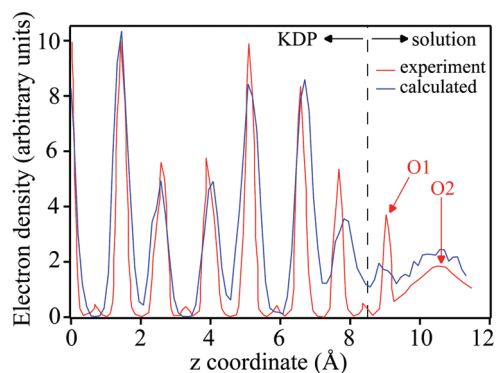


Figure 4. Electron density normal to the (101) surface from MD calculations of hydrated surfaces and experimental values extracted from Figure 8 of Vlieg et al.¹³ O1 and O2 refer to the positions of the first and second ordered water layers from experimental studies of Vlieg et al.¹³

report that the first ordered oxygen layer is approximately 1.3 Å above the surface K^+ layer. Using the molecular dynamics results, we extracted the “z” coordinates of the water oxygen atoms and the potassium atoms to compare to the experimental values. As noted above, we find strong hydrogen bonds, typically 1.4–1.7 Å, between the layer of water molecules closest to the surface and the H_2PO_4^- ions.

A convenient way to visualize the molecular dynamics results of the hydrated surface is by projecting the electron density normal to the (101) surface. In Figure 4, we plot the electron density normal to the (101) surface for the hydrated MD surface and compared this to the experimental results extracted from Figure 8 of Vlieg et al.¹³ In Figure 4, the sharp peaks at approximately 0, 1.3, 5.1, and 6.4 Å correspond to layers containing P atoms in H_2PO_4^- , and the sharp peaks at approximately 2.7, 4.0, and 7.8 Å correspond to K^+ layers (with 7.8 being the outermost layer). Experimental SXR results¹³ show a sharp oxygen peak at approximately 9.1 Å, corresponding to the first ordered water layer located approximately 1.3 Å above the surface K^+ layer, labeled O1 in Figure 4. Experimental results also show a second quasi-ordered (and much broader) water layer peak, labeled O2 in Figure 4, a similar distance farther out from the first ordered water. Our MD results in Figure 4 show a small peak corresponding to the first ordered water layer at approximately the same location as found experimentally. The MD results in Figure 4 also show a similar broad peak for the quasi-ordered second water layer, matching well with experimental findings.

Using the translational and lateral displacements of the ice-like O1 layer, it is possible to calculate the mean squared deviation for this layer. A comprehensive molecular dynamics study of hexagonal ice by Tanaka and Mohanty³¹ reports that the mean square deviation in the quantum harmonic approximation varies from 0.06 to 0.12 Å² for temperatures ranging from 150 to 250 K. The calculated mean square displacement for the ice-like O1 layer studied here is approximately 0.06 Å² in both the translational and lateral directions. Given the limited time frame accessible to this study (10 ps), compared to the classical molecular dynamics calculations of hexagonal ice, which uses a minimum of 15 ns of simulation time, the calculated mean square displacement compares quite favorably with the classical molecular dynamics study, strongly suggesting the O1 layer on the (101) surface exhibits ice-like behavior.

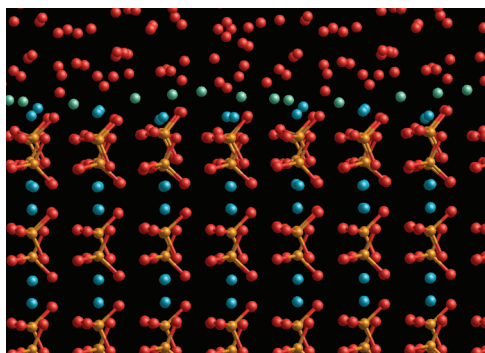


Figure 5. MD averaged hydrated surface of KDP. Hydrogen atoms have been removed for clarity. The green colored spheres represent oxygen atoms in water molecules that have two hydrogen bonds to the KDP surface and correspond to the 1st ordered water layer illustrated in Figure 4. Oxygen, potassium, and phosphorus atoms are represented by red, blue, and orange colored spheres, respectively.

To further illustrate the first ordered water on the KDP surface, in Figure 5, we show the MD averaged surface with water molecules highlighted (colored green), that form at least two hydrogen bonds to the KDP surface. The first ordered water layer indeed appears to correspond to water atoms that form multiple strong hydrogen bonds to the KDP surface. The location of this strongly bound water at the KDP surface in Figure 5 would thus correspond to the O1 peak in the Figure 4 density plot.

CONCLUSIONS

We performed *ab initio* molecular dynamics calculations of the high- and low-temperature phases of bulk KDP. For the high temperature phase, we find evidence to support the theory that hydrogen atoms oscillate between two off-center positions in the high temperature phase. We have for the first time presented the results for *ab initio* molecular dynamics calculations on (101) surfaces of KDP. In general, we find good agreement with our previous study using static calculations,¹⁸ and with the experimental results from SXR D studies, in particular with reference to the direction of the relaxation, although there is some variation in the magnitudes of the relations. We find a water layer that is strongly hydrogen bound to the KDP surface corresponding to a first ordered water layer, matching closely to experimental results. We also find a second quasi-ordered water region further out from the surface, also in agreement with experimental results. In the future, the next step would be to include the effect of ions in the solution of water to study the effect of pH on the surface relaxations. SXR D studies^{11,12} show that the (100) surface is insensitive to pH, but the (101) surface is affected by the pH, so molecular dynamics simulations could provide insight into the interactions between the surface and the solvent.

AUTHOR INFORMATION

Corresponding Author

*E-mail: a.rohl@curtin.edu.au.

ACKNOWLEDGMENT

The authors thank iVEC and the NCI for the provision of computational resources.

REFERENCES

- (1) Lin, Z.; Wang, Z.; Chen, C.; Lee, M. H. *J. Chem. Phys.* **2003**, *118*, 2349–2356.
- (2) Nelmes, R. J.; Tun, Z.; Kuhs, W. F. *Ferroelectrics* **1987**, *71*, 125–141.
- (3) Bastie, P.; Lajzerowicz, J.; Schneider, J. R. *J. Phys. C: Solid State Phys.* **1978**, *11*, 1203–1216.
- (4) Baur, W. H. *Acta Crystallogr., Sect. B* **1973**, *29*, 2726–2731.
- (5) Nelmes, R. J. *Ferroelectrics* **1987**, *71*, 87–123.
- (6) De Vries, S. A.; Goedtkindt, P.; Bennett, S. L.; Huisman, W. J.; Zwanenburg, M. J.; Smilgies, D. M.; De Yoreo, J. J.; van Enckevort, W. J. P.; Bennema, P.; Vlieg, E. *Phys. Rev. Lett.* **1998**, *80*, 2229–2232.
- (7) De Vries, S. A.; Goedtkindt, P.; Huisman, W. J.; Zwanenburg, M. J.; Feidenhans'l, R.; Bennett, S. L.; Smilgies, D. M.; Stierle, A.; De Yoreo, J. J.; Van Enckevort, W. J. P.; Bennema, P.; Vlieg, E. *J. Cryst. Growth* **1999**, *205*, 202–214.
- (8) Reedijk, M. F.; Arsic, J.; Hollander, F. F. A.; De Vries, S. A.; Vlieg, E. *Phys. Rev. Lett.* **2003**, *90*, 066103.
- (9) Odelius, M.; Bernasconi, M.; Parrinello, M. *Phys. Rev. Lett.* **1997**, *78*, 2855–2858.
- (10) Thiel, P. A.; Madey, T. E. *Surf. Sci. Rep.* **1987**, *7*, 211–385.
- (11) Kaminski, D.; Radenovic, N.; Deij, M. A.; Van Enckevort, W. J. P. *Phys. Rev. B* **2005**, *72*, 245404.
- (12) Kaminski, D.; Radenovic, N.; Deij, M. A.; Van Enckevort, W. J. P.; Vlieg, E. *Cryst. Growth Des.* **2006**, *6*, 588–591.
- (13) Vlieg, E.; Deij, M. A.; Kaminski, D.; Meekes, H.; Van Enckevort, W. J. P. *Faraday Discuss.* **2007**, *136*, 57–69.
- (14) Koval, S.; Kohanoff, J.; Migoni, R. L.; Bussmann-Holder, A. *Comput. Mater. Sci.* **2001**, *22*, 87–93.
- (15) Koval, S.; Kohanoff, J.; Migoni, R. L.; Tosatti, E. *Phys. Rev. Lett.* **2002**, *89*, 187602.
- (16) Zhang, Q.; Kiousis, N.; Demos, S. G.; Radousky, H. B. *J. Phys.: Condens. Matter* **2002**, *14*, L89–93.
- (17) Wang, K.; Fang, C.; Zhang, J.; Liu, C. S.; Boughton, R. I.; Wang, S.; Zhao, X. *Phys. Rev. B* **2005**, *72*, 184105.
- (18) Carter, D. J.; Rohl, A. L.; Gale, J. D. *J. Chem. Theory Comput.* **2006**, *2*, 797–800.
- (19) Stack, A. G.; Rustad, J. R.; De Yoreo, J. J.; Land, T. A.; Casey, W. H. *J. Phys. Chem. B* **2004**, *108*, 18284–18290.
- (20) Soler, J. M.; Artacho, E.; Gale, J. D.; Garcia, A.; Junquera, J.; Ordejon, P.; Sanchez-Portal, D. *J. Phys.: Condens. Matter* **2002**, *14*, 2745–2779.
- (21) Troullier, N.; Martins, J. L. *Phys. Rev. B* **1991**, *43*, 1993–2006.
- (22) Perdew, J. P.; Burke, K.; Ernzerhof, M. *Phys. Rev. Lett.* **1996**, *77*, 3865–3868.
- (23) Zhang, Q.; Chen, F.; Kiousis, N.; Demos, S. G.; Radousky, H. B. *Phys. Rev. B* **2001**, *65*, 024128.
- (24) Koch, W.; Holthausen, M. C. *A Chemist's Guide to Density Functional Theory*, 2nd ed.; Wiley-VCH Verlag GmbH: Weinheim, Germany, 2001.
- (25) Bacon, G. E.; Pease, R. S. *Proc. R. Soc. London, Ser. A* **1955**, *230*, 359–381.
- (26) Blinc, R. J. *Phys. Chem. Solids* **1960**, *13*, 204–211.
- (27) Reiter, G. F.; Mayers, J.; Platzman, P. *Phys. Rev. Lett.* **2002**, *89*, 135501.
- (28) Liu, C. S.; Kiousis, N.; Demos, S. G.; Radousky, H. B. *Phys. Rev. Lett.* **2003**, *91*, 015505.
- (29) Ogorodnikov, I. N.; Pustovarov, V. A.; Shul'gin, B. V.; Kuanyshev, V. T.; Satybaldieva, M. K. *Opt. Spectrosc.* **2001**, *91*, 224–231.
- (30) Reedijk, M. F. *Ordering at solid-liquid interfaces*. PhD Thesis, University of Nijmegen, The Netherlands, 2003.
- (31) Tanaka, H.; Mohanty, U. *J. Am. Chem. Soc.* **2002**, *124*, 8085–8089.

On the Efficiency of Algorithms for Solving Hartree–Fock and Kohn–Sham Response Equations

Joanna Kauczor,^{*,†} Poul Jørgensen,[†] and Patrick Norman[‡]

[†]Lundbeck Foundation Center for Theoretical Chemistry, Department of Chemistry, Aarhus University, Langelandsgade 140, Dk-8000 Aarhus C, Denmark

[‡]Department of Physics, Chemistry, and Biology, Linköping University, Se-581 83 Linköping, Sweden

ABSTRACT: The response equations as occurring in the Hartree–Fock, multiconfigurational self-consistent field, and Kohn–Sham density functional theory have identical matrix structures. The algorithms that are used for solving these equations are discussed, and new algorithms are proposed where trial vectors are split into symmetric and antisymmetric components. Numerical examples are given to compare the performance of the algorithms. The calculations show that the standard response equation for frequencies smaller than the highest occupied molecular orbital–lowest unoccupied molecular orbital gap is best solved using the preconditioned conjugate gradient or conjugate residual algorithms where trial vectors are split into symmetric and antisymmetric components. For larger frequencies in the standard response equation as well as in the damped response equation in general, the preconditioned iterative subspace approach with symmetrized trial vectors should be used. For the response eigenvalue equation, the Davidson algorithm with either paired or symmetrized trial vectors constitutes equally good options.

1. INTRODUCTION

Molecular properties are fundamental quantities underlying the macroscopic behavior of matter and their determination constitutes one of the most fruitful areas of interplay between experiment and theory. From a theoretical point of view, the determination of molecular properties can be achieved by calculations of response functions that express the responses of a molecular system toward weak perturbing fields, such as internal magnetic moments or externally applied electric and magnetic fields.¹ By considering poles and residues of response functions, it is also possible to evaluate energy separations and various couplings between specific states and molecular properties of excited states.¹

In approximate state electronic structure theory, the major task when calculating response functions and their poles and residues translates into solving sets of response equations, and the key module in programs devoted to the determination of molecular properties therefore is the response equation solver. The large dimensionality of the response equations imposes the use of iterative algorithms, and the two criteria against which such solver routines should be judged are stability and efficiency. We consider the solution of response equations for variational wave functions, such as Hartree–Fock (HF), multiconfiguration self-consistent field (MCSCF), and Kohn–Sham (KS) density functional theory (DFT). The overall structure of the response equations is identical for these wave functions, and our discussion will be relevant to all these cases. We will propose new algorithms based on a splitting of trial vectors into symmetric and antisymmetric components and, by numerical examples, compare them to the conventional algorithms that have been used for solving response equations.

For a real unperturbed reference state, three different types of response equations will be considered:

- Standard response equation: The standard response equation determines the responses in the wave function parameters

(collected as a vector \mathbf{X}_S) toward an off-resonance time-dependent perturbing field oscillating with frequency ω :

$$(\mathbf{E}^{[2]} - \omega \mathbf{S}^{[2]})\mathbf{X}_S = \mathbf{G} \quad (1)$$

where $\mathbf{E}^{[2]}$ and $\mathbf{S}^{[2]}$ are the generalized Hessian and metric matrix, respectively, and \mathbf{G} is a generalized gradient for the operator describing the coupling between the perturbing field and the molecular system—we refer to ref 1 for the definition of the response matrices in the HF and MCSCF theory and to ref 2 in the case of KS theory. We note that eq 1 represents a set of linear equations for a real symmetric matrix.

- Damped response equation: In near-resonance and resonance regions of the spectrum, eq 1 no longer provides a reasonable description of the induced polarization. However, in a situation with fast relaxation channels that depopulates the manifold of excited states, perturbation theory may still be applicable as long as relaxation parameters (here represented by a single parameter γ) are introduced:^{3–5}

$$(\mathbf{E}^{[2]} - (\omega + i\gamma)\mathbf{S}^{[2]})\mathbf{X}_D = \mathbf{G} \quad (2)$$

The damping parameters are associated with the inverse (finite) lifetimes of the excited states.^{6,7} In this case, the solution vector \mathbf{X}_D is complex with real and imaginary components describing dispersion and absorption processes, respectively. We note that eq 2 represents a set of linear equations for a complex non-Hermitian matrix.

- Response eigenvalue equation: Excitation energies occur at the poles of the linear response function and can be determined by solving the generalized eigenvalue equation:

$$(\mathbf{E}^{[2]} - \omega_f \mathbf{S}^{[2]})\mathbf{X}_f = 0 \quad (3)$$

Received: December 20, 2010

Published: April 29, 2011

where ω_f is the transition frequency between the reference state $|0\rangle$ and excited state $|f\rangle$, and X_f is the excitation vector. Since the metric $S^{[2]}$ is not positive definite, eq 3 represents a non-Hermitian eigenvalue equation.

In the early days of quantum chemistry only small molecular systems were considered, and the response matrices in eqs 1–3 were set up explicitly. The solutions to these equations were obtained by applying standard algorithms of numerical analysis. The standard response equation (eq 1) was for example solved using diagonalization and triangularization methods, e.g., using Gauss–Jordan elimination or LU factorization.^{8–10} The response eigenvalue equation (eq 3) was solved using standard algorithms for a non-Hermitian eigenvalue problem. However, since solving a Hermitian eigenvalue equation is simpler and, from an algorithmic point of view, more robust as compared to solving a non-Hermitian eigenvalue equation, eq 3 was expressed in a Hermitian form that involved the diagonalization of two Hermitian matrices of half the dimension of the $E^{[2]}$ and $S^{[2]}$ matrices.¹¹

For larger molecular systems it has become a standard practice in quantum chemistry to use iterative subspace algorithms. For example, Pople et al.¹² solved the coupled HF equations (eq 1) and Purvis and Bartlett¹³ the coupled cluster singles and doubles amplitude equations using iterative subspace algorithms. Wormer et al.¹⁴ recognized that both these algorithms lead to an iteration sequence identical to the one obtained using the conjugate gradient (CG) algorithm.¹⁵ The advantage of using a CG formulation,^{15–18} and similar for the conjugate residual (CR) algorithm,¹⁹ is that only the last three trial vectors are necessary to store the information content of all previous trial vectors. In a subspace approach the last three trial vectors together with their linear transformed vectors need to be stored on disk. In a unidirectional formulation of the CG and CR algorithms, the number of vectors that needs to be stored on disk in each iteration is reduced to three and four, respectively. The handling and storage of trial vectors therefore become simplified in the CG algorithm compared to an iterative subspace formulation. In Appendix A, the connection between the CG and subspace algorithms will be discussed. Our discussion will be referring to system sizes that prohibit the explicit formation of the Hessian matrix but yet small enough to allow the Fock/KS matrix transformations needed to achieve a preconditioning in the canonical self-consistent field (SCF) orbital basis. Using current standard mathematical library routines, diagonalization of Fock matrices of dimensions up to ca. 5×10^4 can straightforwardly be performed, but we acknowledge that in order to reach significantly larger system sizes the orbital transformation becomes a bottleneck, and “orbital-free” approaches have to be used, as has been demonstrated for time-independent²⁰ as well as time-dependent response theory.²¹

The Davidson algorithm²² is an iterative subspace algorithm for solving a standard Hermitian eigenvalue equation. It has been generalized to the non-Hermitian response eigenvalue equation (eq 3).²³ However, this generalization turned out unsuccessful because the non-Hermitian character of the response eigenvalue equation may introduce complex eigenvalues in the reduced subspace eigenvalue equations, which, in turn, made it difficult to generate new trial vectors and converge the response eigenvalue equation.²⁴ A remedy to this problem was proposed by Olsen et al.,²⁵ who for ground-state calculations recognized that the response eigenvalue equation could be viewed as a Hermitian

eigenvalue equation because the generalized Hessian $E^{[2]}$ is positive definite and therefore could be viewed as a metric with the inverse of the excitation energies as eigenvalues. Olsen et al. further recognized that the response eigenvalue equation has paired eigenvalues and that it is important to keep the paired structure of the eigenvalues in the reduced space eigenvalue equations. Paired eigenvalues can be obtained by adding paired trial vectors to the subspace in the iterative procedure. With these advances the Davidson algorithm was successfully applied.²⁵ We analyze the theoretical background for adding paired trial vectors. We also discuss the Olsen algorithm²⁶ in comparison with the Davidson algorithm, for the generation of new trial vectors in the iterative subspace algorithm.

From the linear transformation of $E^{[2]}$ and $S^{[2]}$ on a trial vector, the linear transformation on its paired counterpart can be generated at no additional cost. This suggests that it may be advantageous to solve also the standard response equation using the iterative subspace algorithm where trial vectors are added in pairs to the reduced subspace. In doing so, however, the attractive feature of the CG algorithm to keep the information from the entire trial vector space in the last three vectors is lost. But, as we shall see in the present work, by invoking an algorithm with symmetrized trial vectors, this feature can be retained while keeping the improved convergence rate seen when paired trial vectors are used.

In 1990, Casida suggested to solve the standard response and response eigenvalue equations by means of a block diagonalization of the Hessian (see ref 2) using an approach similar to the one described in ref 11. This algorithm is briefly discussed in Appendix D.

Saue and co-workers^{27–29} introduced a symmetry division of trial vectors for solving the standard response and eigenvalue equations in the four-component HF and DFT approximations. In their approach, trial vectors are split according to their Hermiticity and time-reversal symmetry, which are the two fundamental operator symmetries in a relativistic framework. The trial vectors are complex due to the complex nature of the four-component wave function, however, the reduced subspace equations remain real, due to the symmetry properties of $E^{[2]}$ and $S^{[2]}$. Recently, Villaume et al.³⁰ have generalized this approach to solve the damped response equation, including a presentation of a highly efficient preconditioner. This development represented a significant improvement of the original algorithm for the solution of damped response equations presented by Norman et al.^{3,4} (with computational improvements by Kristensen et al.),⁵ in which the complex response equation was considered as two coupled real equations.

In the spirit of the work by Villaume et al.,³⁰ we introduce an algorithm for solving response equations (eqs 1–3) in a non-relativistic framework (in a basis of real orbitals) where the solution vectors are expressed in terms of symmetric and antisymmetric components constituting the real and imaginary parts of Hermitian and anti-Hermitian vectors. We show that the standard response equation within this framework for frequencies smaller than the highest occupied molecular orbital–lowest unoccupied molecular orbital (HOMO–LUMO) gap may be solved using the preconditioned CG/CR algorithm, while for larger frequencies the preconditioned iterative subspace algorithm with symmetrized trial vectors should be used. We also show that the damped response equation (eq 2) may be expressed in terms of a set of linear equations for a symmetric but not positive definite matrix. These algorithms may be supplemented

with an efficient preconditioner, analogous to the one proposed by Villaume et al.³⁰ However, since this preconditioner is not positive definite, the preconditioned CR algorithm cannot be safely used, as discussed in Appendix B, and the damped response equation is therefore best solved using the preconditioned iterative subspace approach with symmetrized trial vectors.

In the next section, the structure of the response matrices in a basis of nonrelativistic real orbitals will be discussed. In Section 3, the standard iterative subspace algorithms are discussed for solving the three categories of response equations. In Section 4 iterative subspace methods with paired trial vectors are considered, and in Section 5 the advantages of using symmetrized trial vectors are discussed. In Section 6, we provide numerical examples to illustrate the efficiency of the various algorithms, and Section 7 contains the concluding remarks.

2. STRUCTURES OF RESPONSE MATRICES

The response equations are often written in a 2×2 matrix blocked form referencing the excitation and deexcitation spaces.¹ In this form, $\mathbf{E}^{[2]}$ and $\mathbf{S}^{[2]}$ have the structure:

$$\mathbf{E}^{[2]} = \begin{pmatrix} \mathbf{A} & \mathbf{B} \\ \mathbf{B} & \mathbf{A} \end{pmatrix}, \quad \mathbf{S}^{[2]} = \begin{pmatrix} \Sigma & \Delta \\ -\Delta & -\Sigma \end{pmatrix} \quad (4)$$

where

$$\begin{aligned} A_{pq} &= \langle 0 | [[Q_p, \hat{H}_0], Q_q^\dagger] | 0 \rangle \\ B_{pq} &= \langle 0 | [[Q_p, \hat{H}_0], Q_q] | 0 \rangle \\ \Sigma_{pq} &= \langle 0 | [Q_p, Q_q^\dagger] | 0 \rangle \\ \Delta_{pq} &= \langle 0 | [Q_p, Q_q] | 0 \rangle \end{aligned} \quad (5)$$

where $|0\rangle$ is the reference state, \hat{H}_0 is the nonrelativistic Hamiltonian, and Q_p^\dagger and Q_p are excitation and deexcitation operators, respectively. Both $\mathbf{E}^{[2]}$ and $\mathbf{S}^{[2]}$ are symmetric matrices. \mathbf{A} , \mathbf{B} , and Σ are symmetric, and Δ is antisymmetric.¹

For a closed shell system and a HF reference state $|0\rangle = |\text{HF}\rangle$, the excitation operator Q_p^\dagger becomes

$$Q_p^\dagger = Q_{AI}^\dagger = \frac{1}{\sqrt{2}}(a_{A\alpha}^\dagger a_{I\alpha} + a_{A\beta}^\dagger a_{I\beta}) \quad (6)$$

where I and A refer to occupied and unoccupied molecular orbital (MO) indices, respectively. In the canonical SCF basis, the elements of \mathbf{A} , \mathbf{B} , Σ , and Δ become¹¹

$$\begin{aligned} A_{pq} &= A_{AI, BJ} = \langle \text{HF} | [[Q_p, \hat{H}_0], Q_q^\dagger] | \text{HF} \rangle \\ &= \delta_{AB} \delta_{IJ} (\varepsilon_A - \varepsilon_I) + (AI|JB) - (AB|IJ) \end{aligned} \quad (7)$$

$$\begin{aligned} B_{pq} &= B_{AI, BJ} = \langle \text{HF} | [[Q_p, \hat{H}_0], Q_q] | \text{HF} \rangle \\ &= (AI|BJ) - (AJ|BI) \end{aligned} \quad (8)$$

$$\Sigma_{pq} = \langle \text{HF} | [Q_p, Q_q^\dagger] | \text{HF} \rangle = \delta_{AB} \delta_{IJ} \quad (9)$$

$$\Delta_{pq} = \langle \text{HF} | [Q_p, Q_q] | \text{HF} \rangle = 0 \quad (10)$$

respectively. ε_A and ε_I refer to orbital energies, and the Mulliken notation is used for the two-electron integrals. In KS theory, the two-electron integrals in eqs 7 and 8 have to be modified, and an exchange–correlation contribution added.² In MCSCF wave function theory, the explicit expressions for the matrix elements

in the electronic Hessian and overlap matrices are significantly more complicated, but the form is identical to that in single determinant theory.¹ Our present considerations regarding response equation solvers will be valid also in the case of MCSCF theory but with use of MCSCF specific approximations of the Hessians and overlap matrices for the construction of preconditioners.

A Møller–Plesset perturbation analysis shows that the $\mathbf{E}^{[2]}$ matrix can be split into the zeroth and the first order contribution:

$$\mathbf{E}^{[2]} = \mathbf{E}_0^{[2]} + \mathbf{E}_1^{[2]} \quad (11)$$

where $\mathbf{E}_0^{[2]}$ is a diagonal matrix containing the orbital energy differences:

$$\mathbf{E}_0^{[2]} = \begin{pmatrix} \Delta\varepsilon & 0 \\ 0 & \Delta\varepsilon \end{pmatrix} \quad (12)$$

where the elements of $\Delta\varepsilon$ are given by

$$\Delta\varepsilon_{AI, BJ} = \delta_{AB} \delta_{IJ} (\varepsilon_A - \varepsilon_I) \quad (13)$$

$\mathbf{E}_1^{[2]}$ contains the electron–electron repulsion contributions to $\mathbf{E}^{[2]}$, as can be seen from eqs 7 and 8. In KS theory, an exchange–correlation contribution has to be added to $\mathbf{E}_1^{[2]}$. The metric matrix $\mathbf{S}^{[2]}$ in the canonical SCF representation becomes

$$\mathbf{S}^{[2]} = \begin{pmatrix} \mathbf{1} & \mathbf{0} \\ \mathbf{0} & -\mathbf{1} \end{pmatrix} \quad (14)$$

The solution vectors \mathbf{X} in eqs 1–3 can also be written in the blocked form as

$$\mathbf{X} = \begin{pmatrix} \mathbf{x}_{AI} \\ \mathbf{x}_{JB} \end{pmatrix} \quad (15)$$

where \mathbf{x}_{AI} and \mathbf{x}_{JB} are the excitation and deexcitation components,¹ respectively.

Using the above notation, the response eigenvalue equation in the canonical SCF representation may be expressed as

$$\begin{pmatrix} \mathbf{A} & \mathbf{B} \\ \mathbf{B} & \mathbf{A} \end{pmatrix} \begin{pmatrix} \mathbf{x}_{AI, f} \\ \mathbf{x}_{JB, f} \end{pmatrix} = \omega_f \begin{pmatrix} \mathbf{1} & \mathbf{0} \\ \mathbf{0} & -\mathbf{1} \end{pmatrix} \begin{pmatrix} \mathbf{x}_{AI, f} \\ \mathbf{x}_{JB, f} \end{pmatrix} \quad (16)$$

where the eigenvector satisfies the positive normalization condition

$$\begin{pmatrix} \mathbf{x}_{AI, f}^T & \mathbf{x}_{JB, f}^T \end{pmatrix} \begin{pmatrix} \mathbf{1} & \mathbf{0} \\ \mathbf{0} & -\mathbf{1} \end{pmatrix} \begin{pmatrix} \mathbf{x}_{AI, f} \\ \mathbf{x}_{JB, f} \end{pmatrix} = 1 \quad (17)$$

Together with the positive $\mathbf{S}^{[2]}$ -normed solution $\mathbf{X}_{f+} = \begin{pmatrix} \mathbf{x}_{AI, f} \\ \mathbf{x}_{JB, f} \end{pmatrix}$, the response eigenvalue equation has a paired solution $\mathbf{X}_{f-} = \begin{pmatrix} \mathbf{x}_{JB, f} \\ \mathbf{x}_{AI, f} \end{pmatrix}$, with the eigenvalue $-\omega_f$.

$$\begin{pmatrix} \mathbf{A} & \mathbf{B} \\ \mathbf{B} & \mathbf{A} \end{pmatrix} \begin{pmatrix} \mathbf{x}_{JB, f} \\ \mathbf{x}_{AI, f} \end{pmatrix} = -\omega_f \begin{pmatrix} \mathbf{1} & \mathbf{0} \\ \mathbf{0} & -\mathbf{1} \end{pmatrix} \begin{pmatrix} \mathbf{x}_{JB, f} \\ \mathbf{x}_{AI, f} \end{pmatrix} \quad (18)$$

where the eigenvector satisfies the negative normalization condition:

$$\begin{pmatrix} \mathbf{x}_{B,f}^T & \mathbf{x}_{A,f}^T \end{pmatrix} \begin{pmatrix} 1 & 0 \\ 0 & -1 \end{pmatrix} \begin{pmatrix} \mathbf{x}_{B,f} \\ \mathbf{x}_{A,f} \end{pmatrix} = -1 \quad (19)$$

The excitation vectors may be collected as the columns of an eigenvector matrix \mathbf{X} with the positive $\mathbf{S}^{[2]}$ -normed eigenvectors collected first $\mathbf{X}_+ = \{\mathbf{X}_{1+}, \mathbf{X}_{2+}, \dots, \mathbf{X}_{f+}, \dots\}$, followed by the negative $\mathbf{S}^{[2]}$ -normed vectors $\mathbf{X}_- = \{\mathbf{X}_{1-}, \mathbf{X}_{2-}, \dots, \mathbf{X}_{f-}, \dots\}$.³¹

$$\mathbf{X} = (\mathbf{X}_+ \quad \mathbf{X}_-) \quad (20)$$

In matrix form the response matrices may be expressed as¹

$$\mathbf{X}^\dagger \mathbf{E}^{[2]} \mathbf{X} = \begin{pmatrix} \boldsymbol{\omega}_{\text{exc}} & 0 \\ 0 & \boldsymbol{\omega}_{\text{exc}} \end{pmatrix}; \quad \mathbf{X}^\dagger \mathbf{S}^{[2]} \mathbf{X} = \begin{pmatrix} 1 & 0 \\ 0 & -1 \end{pmatrix} \quad (21)$$

where $\boldsymbol{\omega}_{\text{exc}}$ is a diagonal matrix containing the excitation energies $\{\omega_1, \omega_2, \dots, \omega_f, \dots\}$.

For the ground state, $\mathbf{E}^{[2]}$ is a positive definite matrix. To see this, $\mathbf{E}^{[2]}$ may be transformed to block diagonal form using the unitary matrix \mathbf{U} :

$$\mathbf{U} = \frac{1}{\sqrt{2}} \begin{pmatrix} 1 & -1 \\ 1 & 1 \end{pmatrix} \quad (22)$$

giving

$$\mathbf{U}^\dagger \mathbf{E}^{[2]} \mathbf{U} = \begin{pmatrix} \mathbf{A} + \mathbf{B} & 0 \\ 0 & \mathbf{A} - \mathbf{B} \end{pmatrix} \quad (23)$$

Submatrices $\mathbf{A} + \mathbf{B}$ and $\mathbf{A} - \mathbf{B}$ represent the stability conditions³² in the wave function $|0\rangle$ with respect to imaginary and real variations, respectively. For a ground state, both $\mathbf{A} - \mathbf{B}$ and $\mathbf{A} + \mathbf{B}$ have to be positive definite, implying that $\mathbf{E}^{[2]}$ is positive definite. For a ground state, $\mathbf{E}^{[2]}$ may thus be viewed as a positive definite metric matrix, and the response eigenvalue equation, eq 3, may be expressed as

$$\begin{pmatrix} 1 \\ \omega_f \end{pmatrix} \mathbf{E}^{[2]} - \mathbf{S}^{[2]} \mathbf{X}_f = 0 \quad (24)$$

which is a standard symmetric eigenvalue equation where $(\omega_f)^{-1}$ are the eigenvalues.

In the following discussion, we will focus on HF and KS theory and assume that we are using a canonical SCF representation, where the generalized metric $\mathbf{S}^{[2]}$ has the structure in eq 14, and the generalized Hessian $\mathbf{E}^{[2]}$ can be split into the zeroth and the first order contribution as in eq 11. However, in the practical calculations, we evaluate the linear transformations of $\mathbf{E}^{[2]}$ and $\mathbf{S}^{[2]}$ on trial vectors in the atomic orbital (AO) representation, as discussed in detail in refs 21 and 33. The detailed structure of $\mathbf{E}^{[2]}$ and $\mathbf{S}^{[2]}$ in the AO representation is described in ref 31. We note that the preconditioning of the response equations is always most efficiently performed in the canonical SCF representation where $\mathbf{S}^{[2]}$ has a particular structure (eq 14), which allows an exact treatment of this matrix and where the access to orbital energy differences enables a representation of the $\mathbf{E}^{[2]}$ matrix that is superior to available approximations in the AO basis.

3. SOLVING RESPONSE EQUATIONS USING STANDARD ITERATIVE METHODS

In electronic structure theory, the response equations (eqs 1–3) are conventionally solved using subspace iterative algorithms. In the subspace iterative algorithms, it is assumed that the linear transformations of the generalized Hessian $\mathbf{E}^{[2]}$ and metric $\mathbf{S}^{[2]}$ matrices on a trial vector \mathbf{b} can be carried out

$$\boldsymbol{\sigma} = \mathbf{E}^{[2]} \mathbf{b}, \quad \boldsymbol{\rho} = \mathbf{S}^{[2]} \mathbf{b} \quad (25)$$

The solution to the response equations is obtained from a sequence of linear transformations on trial vectors giving gradually improved solutions to the response equations.

3.1. General Subspace Iterative Algorithm. The solution to the response equations may be obtained using an iterative subspace algorithm. After iteration n of an iterative subspace algorithm we have n trial vectors:

$$\mathbf{b}^n = \{\mathbf{b}_1, \mathbf{b}_2, \dots, \mathbf{b}_n\} \quad (26)$$

and the linear transformed vectors

$$\boldsymbol{\sigma}^n = \{\boldsymbol{\sigma}_1, \boldsymbol{\sigma}_2, \dots, \boldsymbol{\sigma}_n\}, \quad \boldsymbol{\rho}^n = \{\boldsymbol{\rho}_1, \boldsymbol{\rho}_2, \dots, \boldsymbol{\rho}_n\} \quad (27)$$

Reduced response equations are then set up in the subspace \mathbf{b}^n giving

$$(\mathbf{E}_R^{[2]} - \omega \mathbf{S}_R^{[2]})(\mathbf{X}_S)_R = \mathbf{G}_R \quad (28)$$

$$[\mathbf{E}_R^{[2]} - (\omega + i\gamma) \mathbf{S}_R^{[2]}](\mathbf{X}_D)_R = \mathbf{G}_R \quad (29)$$

$$(\mathbf{E}_R^{[2]} - \omega_f^R \mathbf{S}_R^{[2]})(\mathbf{X}_f)_R = 0 \quad (30)$$

for the standard, damped, and eigenvalue equation, respectively, where

$$(\mathbf{E}_R^{[2]})_{ij} = \mathbf{b}_i^\dagger \boldsymbol{\sigma}_j, \quad (\mathbf{S}_R^{[2]})_{ij} = \mathbf{b}_i^\dagger \boldsymbol{\rho}_j \quad (31)$$

and

$$(\mathbf{G}_R)_i = \mathbf{b}_i^\dagger \mathbf{G} \quad (32)$$

Equations 28–30 determine the optimal solution vector \mathbf{X}_{n+1} in the subspace \mathbf{b}^n

$$\mathbf{X}_{n+1} = \sum_{i=1}^n (\mathbf{X}_R)_i \mathbf{b}_i \quad (33)$$

The residuals for the response equations are given as

$$\begin{aligned} \mathbf{R}_{n+1} &= (\mathbf{E}^{[2]} - \omega \mathbf{S}^{[2]})(\mathbf{X}_S)_{n+1} - \mathbf{G} \\ &= \sum_{i=1}^n [(\mathbf{X}_S)_R]_i (\boldsymbol{\sigma}_i - \omega \boldsymbol{\rho}_i) - \mathbf{G} \end{aligned} \quad (34)$$

$$\begin{aligned} \mathbf{R}_{n+1} &= \mathbf{E}^{[2]} - (\omega + i\gamma) \mathbf{S}^{[2]} (\mathbf{X}_D)_{n+1} - \mathbf{G} \\ &= \sum_{i=1}^n [(\mathbf{X}_D)_R]_i [\boldsymbol{\sigma}_i - (\omega + i\gamma) \boldsymbol{\rho}_i] - \mathbf{G} \end{aligned} \quad (35)$$

$$\begin{aligned} \mathbf{R}_{n+1} &= (\mathbf{E}^{[2]} - \omega_f^R \mathbf{S}^{[2]})(\mathbf{X}_f)_{n+1} \\ &= \sum_{i=1}^n [(\mathbf{X}_f)_R]_i (\boldsymbol{\sigma}_i - \omega_f^R \boldsymbol{\rho}_i) \end{aligned} \quad (36)$$

for the standard, damped, and eigenvalue equation, respectively. To improve the convergence of the standard and damped response equations they may be preconditioned.³⁴ The new trial vector is then obtained from the preconditioned residual:

$$\mathbf{b}_{n+1} = \mathbf{L}^{-1} \mathbf{R}_{n+1} \quad (37)$$

where the preconditioner \mathbf{L} is an approximation to $(\mathbf{E}^{[2]} - \omega \mathbf{S}^{[2]})$ for the standard response equation and $[\mathbf{E}^{[2]} - (\omega + i\gamma) \mathbf{S}^{[2]}]$ for the damped response equation. Due to the fact that $\mathbf{S}^{[2]}$ is a diagonal matrix (see eq 14) and $\mathbf{E}^{[2]}$ is a diagonally dominant matrix (see eq 11), $(\mathbf{E}_0^{[2]} - \omega \mathbf{S}^{[2]})$ and $[\mathbf{E}_0^{[2]} - (\omega + i\gamma) \mathbf{S}^{[2]}]$ may be used as preconditioners for the standard and damped response equations, respectively. The improvement in convergence obtained when preconditioning is introduced will be discussed in more detail in Section 3.3 and the subsequent sections.

When the eigenvalue equation (eq 3) is solved, new trial vectors may be obtained either using the Davidson²² algorithm or the Olsen²⁶ algorithm, see details in the subsequent section. The new trial vector \mathbf{b}_{n+1} is added to the subspace in eq 26, and the iteration procedure is continued until convergence is obtained. The iterative scheme is converged when the residual Euclidean norm $\|\mathbf{R}\|$ is smaller than a preset threshold.

3.2. Response Eigenvalue Equation. In this section we describe how new trial vectors are generated when solving the response eigenvalue equation, using the Davidson²² and the Olsen²⁶ algorithms. Both these algorithms were originally designed for solving Hermitian eigenvalue equations. We discuss the problems that may occur when the Davidson and the Olsen algorithms are applied to the non-Hermitian response eigenvalue equation.

3.2.1. Davidson Algorithm. In the Davidson algorithm a new trial vector is obtained as for the preconditioned standard and damped response equations, according to eq 37, where the matrix \mathbf{L} is a diagonal approximation to $(\mathbf{E}^{[2]} - \omega_f^R \mathbf{S}^{[2]})$

$$\mathbf{b}_{n+1} = (\mathbf{E}_0^{[2]} - \omega_f^R \mathbf{S}^{[2]})^{-1} \mathbf{R}_{n+1} \quad (38)$$

For the linear equation improved convergence is obtained when $\mathbf{E}_0^{[2]}$ becomes an improved approximation to the $\mathbf{E}^{[2]}$ matrix. In fact, when $\mathbf{E}_0^{[2]}$ is replaced by $\mathbf{E}^{[2]}$, the converged solution is obtained right away for a set of linear equations. However, when the eigenvalue equation is solved using the Davidson algorithm, a problem arises in the limit where $\mathbf{E}_0^{[2]}$ is approaching $\mathbf{E}^{[2]}$ as no new direction is generated. To see this, we replace $\mathbf{E}_0^{[2]}$ with $\mathbf{E}^{[2]}$ in eq 38 and introduce the definition of the residual in eq 36, giving

$$\begin{aligned} \mathbf{b}_{n+1} &= (\mathbf{E}^{[2]} - \omega_f^R \mathbf{S}^{[2]})^{-1} (\mathbf{E}^{[2]} - \omega_f^R \mathbf{S}^{[2]}) (\mathbf{X}_f)_{n+1} \\ &= (\mathbf{X}_f)_{n+1} \end{aligned} \quad (39)$$

The proposed new trial vector is therefore equal to the subspace solution to eq 30, so in effect, no new trial vector is obtained using the Davidson algorithm.³⁵ This may be cumbersome when improved preconditioners are used, and a remedy to this problem is provided in the Olsen algorithm.²⁶

3.2.2. Olsen Algorithm. In the Olsen algorithm, it is assumed that we know an approximate solution to the response eigenvalue equation. This may be the optimal solution vector $(\mathbf{X}_f)_{n+1}$ of eq 33, for convenience denoted as \mathbf{X}^0 , which satisfies the normalization condition in eq 17. The zeroth order eigenvalue

ω_f^0 associated with \mathbf{X}^0 is obtained by projecting the eigenvalue equation in eq 3 with $(\mathbf{X}^0)^T$

$$(\mathbf{X}^0)^T (\mathbf{E}^{[2]} - \omega_f^0 \mathbf{S}^{[2]}) \mathbf{X}^0 = 0 \quad (40)$$

Note that ω_f^0 obtained from eq 40 is identical to ω_f^R in eq 30.

To get an improved solution vector in the Olsen algorithm, we express eq 3 in terms of the zeroth order and the correction components:

$$\omega_f = \omega_f^0 + \omega_f^1 \quad (41)$$

$$\mathbf{X}_f = \mathbf{X}^0 + \mathbf{X}^1 \quad (42)$$

where ω_f^1 and \mathbf{X}^1 are correction terms to the eigenvalue ω_f^0 and the eigenvector \mathbf{X}^0 , respectively. The $\mathbf{E}^{[2]}$ matrix may also be written in terms of a zeroth order and a correction component as in eq 11. Inserting eqs 11, 41, and 42 into eq 3 gives

$$[(\mathbf{E}_0^{[2]} + \mathbf{E}_1^{[2]}) - (\omega_f^0 + \omega_f^1) \mathbf{S}^{[2]}] (\mathbf{X}^0 + \mathbf{X}^1) = 0 \quad (43)$$

Neglecting terms that are quadratic in the corrections, we get

$$(\mathbf{E}_0^{[2]} - \omega_f^0 \mathbf{S}^{[2]}) \mathbf{X}^1 = -(\mathbf{E}^{[2]} - \omega_f^0 \mathbf{S}^{[2]}) \mathbf{X}^0 + \omega_f^1 \mathbf{S}^{[2]} \mathbf{X}^0 \quad (44)$$

and \mathbf{X}^1 can be determined as

$$\mathbf{X}^1 = -(\mathbf{E}_0^{[2]} - \omega_f^0 \mathbf{S}^{[2]})^{-1} [(\mathbf{E}^{[2]} - \omega_f^0 \mathbf{S}^{[2]}) \mathbf{X}^0 - \omega_f^1 \mathbf{S}^{[2]} \mathbf{X}^0] \quad (45)$$

By requiring that the eigenvector correction \mathbf{X}^1 is orthogonal to \mathbf{X}^0 in the generalized metric $\mathbf{S}^{[2]}$

$$(\mathbf{X}^1)^T \mathbf{S}^{[2]} \mathbf{X}^0 = 0 \quad (46)$$

we may determine ω_f^1 by multiplying eq 45 with $(\mathbf{X}^0)^T \mathbf{S}^{[2]}$

$$\omega_f^1 = \frac{(\mathbf{X}^0)^T \mathbf{S}^{[2]} (\mathbf{E}_0^{[2]} - \omega_f^0 \mathbf{S}^{[2]})^{-1} (\mathbf{E}^{[2]} - \omega_f^0 \mathbf{S}^{[2]}) \mathbf{X}^0}{(\mathbf{X}^0)^T \mathbf{S}^{[2]} (\mathbf{E}_0^{[2]} - \omega_f^0 \mathbf{S}^{[2]})^{-1} \mathbf{S}^{[2]} \mathbf{X}^0} \quad (47)$$

The inverse matrix $(\mathbf{E}_0^{[2]} - \omega_f^0 \mathbf{S}^{[2]})^{-1}$ is readily constructed as both $\mathbf{E}_0^{[2]}$ and $\mathbf{S}^{[2]}$, which are diagonal matrices. Once the linear transformations $\mathbf{E}^{[2]} \mathbf{X}^0$ and $\mathbf{S}^{[2]} \mathbf{X}^0$ are known, we may determine ω_f^1 from eq 47, and then the correction vector \mathbf{X}^1 may be obtained from eq 45. The new trial vector $\mathbf{b}_{n+1} = \mathbf{X}^1$ is added to the trial vector subspace in eq 26, and the iteration procedure is continued until convergence.

Note that the first term in eq 45 gives the Davidson correction in eq 38. The second term in eq 45 thus ensures that a new improved trial vector is obtained also when $\mathbf{E}_0^{[2]}$ is approaching $\mathbf{E}^{[2]}$. In fact, when $\mathbf{E}_0^{[2]}$ in the Olsen algorithm is replaced by $\mathbf{E}^{[2]}$, we establish the inverse-iteration method with the Rayleigh quotient.^{16,35,36} Note that new trial vectors are obtained using the Olsen algorithm without carrying out new linear transformations compared to the Davidson algorithm.

3.2.3. Problems When Solving the Response Eigenvalue Equation. Due to the fact that $\mathbf{S}^{[2]}$ is an easily invertible matrix $[(\mathbf{S}^{[2]})^{-1} = \mathbf{S}^{[2]}]$, the response eigenvalue equation may be expressed as

$$\mathbf{S}^{[2]} \mathbf{E}^{[2]} \mathbf{X} = \omega \mathbf{X} \quad (48)$$

eq 48 was used in early iterative subspace algorithms to obtain the solution to the response eigenvalue equation.²⁴ However, $(\mathbf{S}^{[2]} \mathbf{E}^{[2]})$ is a non-Hermitian matrix, and eq 48 therefore represents a non-Hermitian eigenvalue equation. When a non-Hermitian rather than

a standard Hermitian eigenvalue equation is solved using an iterative subspace algorithm, some difficulties may occur. For a Hermitian eigenvalue equation, the subspace eigenvalue equation is guaranteed to have real eigenvalues. Also monotonic convergence is obtained to the lowest eigenvalues due to MacDonald's theorem.³⁷ In contrast, when a non-Hermitian eigenvalue equation is solved the eigenvalues of the reduced generalized eigenvalue equation may be complex. Then new trial vectors cannot be obtained neither using the Davidson nor the Olsen algorithms because, in both cases, it is assumed that ω_f^R is real. Bouman et al.²⁴ encountered this problem when the Davidson algorithm was applied to eq 48. Also the monotonic convergence to the lowest eigenvalues is lost.

In eq 24, it is shown that for the ground state, the non-Hermitian response eigenvalue equation may be transformed into a Hermitian eigenvalue equation. In Section 4, we discuss how this Hermitian eigenvalue equation may be solved using a generalization of the Davidson iterative subspace algorithm, by imposing the paired structure of the response matrices $\mathbf{E}^{[2]}$ and $\mathbf{S}^{[2]}$ on their subspace counterparts.

3.3. Standard Response Equation. The standard response equation in eq 1 represents a set of linear equations with a symmetric matrix. For angular frequencies ω that are smaller than the lowest excitation energy, the response matrix $(\mathbf{E}^{[2]} - \omega\mathbf{S}^{[2]})$ is also positive definite. In Appendix A, it is described how, for a positive definite symmetric matrix, the subspace iterative algorithm described in Section 3.1 and the CG algorithm^{15–18} lead to the same iteration sequence.¹⁴ This is obtained because the residuals in the subspace algorithm and the optimal directions in the CG method span the same space. The CG algorithm is designed such that the set of vectors stored on disk may be truncated to the three vectors, so the storing and the manipulation of the large amount of directions (trial vectors) that is required to set up the reduced space equations in the subspace algorithm can be avoided. For angular frequencies ω larger than the lowest excitation energy, $(\mathbf{E}^{[2]} - \omega\mathbf{S}^{[2]})$ is not positive definite but still symmetric, and the CR algorithm may, in principle, be applied. To improve convergence the CG and CR algorithms are used with the diagonal preconditioner $(\mathbf{E}_0^{[2]} - \omega\mathbf{S}^{[2]})$. However, this preconditioner is positive definite only for ω smaller than the HOMO–LUMO gap, and the preconditioned CR algorithm can therefore be safely used to solve the standard response equation for ω smaller than the HOMO–LUMO gap (see Appendix B). For larger ω the preconditioned iterative subspace algorithm is the best option.

In the absence of a preconditioner, the convergence rate for an iterative solution of the standard response equation is determined by the condition number of the response matrix $(\mathbf{E}^{[2]} - \omega\mathbf{S}^{[2]})$, i.e., the ratio between the smallest and largest eigenvalues of the response matrix $\omega_f^{\max}/\omega_f^{\min}$. This condition number is typically large since there are very large eigenvalues in the Hessian referring to, e.g., core excitations as well as nonphysical excitations into the continuum energy spectrum that appear as discrete levels due to the use of a localized atomic orbital basis. However, by using $(\mathbf{E}_0^{[2]} - \omega\mathbf{S}^{[2]})$ as preconditioner, the convergence rate is instead determined by the condition number of the matrix:

$$\begin{aligned} & (\mathbf{E}_0^{[2]} - \omega\mathbf{S}^{[2]})^{-1}(\mathbf{E}^{[2]} - \omega\mathbf{S}^{[2]}) \\ &= (\mathbf{E}_0^{[2]} - \omega\mathbf{S}^{[2]})^{-1}[(\mathbf{E}_0^{[2]} - \omega\mathbf{S}^{[2]}) + \mathbf{E}_1^{[2]}] \\ &= 1 + (\mathbf{E}_0^{[2]} - \omega\mathbf{S}^{[2]})^{-1}\mathbf{E}_1^{[2]} \end{aligned} \quad (49)$$

and the condition number is therefore greatly reduced since all the large eigenvalues discussed above (e.g., as due to core excitations) are scaled more or less to unity by the preconditioner. We note, however, that, when the optical frequency ω is in close resonance with excitation energies of the system or rather with orbital energy differences, the matrix inverse $(\mathbf{E}_0^{[2]} - \omega\mathbf{S}^{[2]})^{-1}$ becomes nearly singular, and the preconditioning will give rise to an increase in the condition number for these near resonance excitation energies. This will result in a slower convergence rate as compared to the nonresonant case. It is also clear that the higher the density of states in the region of the optical frequency, the worse the convergence rate we expect, simply since there are a larger number of eigenvalues that will be scaled poorly by the preconditioner.

3.4. Damped Response Equation. The damped response equation of the form in eq 2 represents a set of linear equations for a non-Hermitian complex matrix. We will now describe how eq 2 may be transformed to a set of linear equations for a real symmetric matrix, thereby avoiding complex algebra.

The solution to eq 2 may be expressed in terms of the solution for the real and the imaginary component of eq 2. This results in two coupled real equations

$$(\mathbf{E}^{[2]} - \omega\mathbf{S}^{[2]})\mathbf{X}_D^R = \mathbf{G}^R - \gamma\mathbf{S}^{[2]}\mathbf{X}_D^I \quad (50)$$

$$(\mathbf{E}^{[2]} - \omega\mathbf{S}^{[2]})\mathbf{X}_D^I = \mathbf{G}^I + \gamma\mathbf{S}^{[2]}\mathbf{X}_D^R \quad (51)$$

where \mathbf{G}^R and \mathbf{G}^I is the real and the imaginary component of the gradient vector \mathbf{G} , respectively. When eqs 50 and 51 are solved separately without explicit coupling between the two equations, this may lead to divergence in the resonance regions where the solution vector has a large eigenvector component in both \mathbf{X}_D^R and \mathbf{X}_D^I . The coupling between \mathbf{X}_D^R and \mathbf{X}_D^I can be considered explicitly by expressing eqs 50 and 51 in the matrix form:

$$\begin{pmatrix} \mathbf{E}^{[2]} - \omega\mathbf{S}^{[2]} & \gamma\mathbf{S}^{[2]} \\ -\gamma\mathbf{S}^{[2]} & \mathbf{E}^{[2]} - \omega\mathbf{S}^{[2]} \end{pmatrix} \begin{pmatrix} \mathbf{X}_D^R \\ \mathbf{X}_D^I \end{pmatrix} = \begin{pmatrix} \mathbf{G}^R \\ \mathbf{G}^I \end{pmatrix} \quad (52)$$

that represents a set of linear equations for a nonsymmetric matrix. However, since it is advantageous to solve the set of linear equation for a symmetric matrix, by reversing the sign of the second row, we express eq 52 as

$$\begin{pmatrix} \mathbf{E}^{[2]} - \omega\mathbf{S}^{[2]} & \gamma\mathbf{S}^{[2]} \\ \gamma\mathbf{S}^{[2]} & -(\mathbf{E}^{[2]} - \omega\mathbf{S}^{[2]}) \end{pmatrix} \begin{pmatrix} \mathbf{X}_D^R \\ \mathbf{X}_D^I \end{pmatrix} = \begin{pmatrix} \mathbf{G}^R \\ -\mathbf{G}^I \end{pmatrix} \quad (53)$$

which represents a standard set of linear equations for a symmetric, indefinite, and real matrix.

The residuals of eq 53 are given by

$$\mathbf{R}_{n+1}^R = (\mathbf{E}^{[2]} - \omega\mathbf{S}^{[2]})\mathbf{X}_{n+1}^R - \mathbf{G}^R + \gamma\mathbf{S}^{[2]}\mathbf{X}_{n+1}^I \quad (54)$$

$$\mathbf{R}_{n+1}^I = -(\mathbf{E}^{[2]} - \omega\mathbf{S}^{[2]})\mathbf{X}_{n+1}^I + \mathbf{G}^I + \gamma\mathbf{S}^{[2]}\mathbf{X}_{n+1}^R \quad (55)$$

and may be used to check for convergence. In the preconditioned iterative subspace algorithm, new trial vectors are obtained by

preconditioning the residuals:

$$\begin{pmatrix} \mathbf{b}_{n+1}^R \\ \mathbf{b}_{n+1}^I \end{pmatrix} = [(\mathbf{E}_0^{[2]} - \omega \mathbf{S}^{[2]})^2 + \gamma^2 \mathbf{1}]^{-1} \otimes \begin{pmatrix} \mathbf{E}_0^{[2]} - \omega \mathbf{S}^{[2]} & \gamma \mathbf{S}^{[2]} \\ \gamma \mathbf{S}^{[2]} & -(\mathbf{E}_0^{[2]} - \omega \mathbf{S}^{[2]}) \end{pmatrix} \begin{pmatrix} \mathbf{R}_{n+1}^R \\ \mathbf{R}_{n+1}^I \end{pmatrix} \quad (56)$$

where we have introduced a direct matrix product according to

$$\mathbf{c} = \mathbf{a} \otimes \begin{pmatrix} \mathbf{b}_{11} & \mathbf{b}_{12} \\ \mathbf{b}_{21} & \mathbf{b}_{22} \end{pmatrix} = \begin{pmatrix} \mathbf{ab}_{11} & \mathbf{ab}_{12} \\ \mathbf{ab}_{21} & \mathbf{ab}_{22} \end{pmatrix} \quad (57)$$

It can be seen by inspection that the inverse preconditioner in eq 56 is the inverse matrix to the matrix in eq 53, where $\mathbf{E}^{[2]}$ is replaced by $\mathbf{E}_0^{[2]}$.

Since eq 53 represents a set of linear equations for a symmetric, indefinite matrix, it cannot be solved using the CG algorithm, but the CR algorithm^{19,38} may be applied. However, the preconditioner in eq 56 is not positive definite, and therefore the preconditioned CR algorithm cannot be safely used (see Appendix B). When solving eq 53 using preconditioning, the iterative subspace algorithm therefore becomes the best option.

The condition number is significantly reduced by preconditioning for similar reasons as presented in Section 3.3 for the standard response equation, as the dominant contributions to the large eigenvalues are removed. The condition number will increase when $[(\mathbf{E}_0^{[2]} - \omega \mathbf{S}^{[2]})^2 + \gamma^2 \mathbf{1}]^{-1}$ is approaching a singularity, and a slower convergence will be observed. Since the γ parameter is small, the condition number of the preconditioned standard response equation and the preconditioned damped response equation will be similar, and similar convergence will be observed for the preconditioned standard and damped response equations.

The preconditioned iterative subspace approach presented in this section, represents a simple and straightforward scheme for solving the damped response equation, using a real trial vector space. In Section 5.3, we show that introducing symmetrized trial vectors leads to an improved efficiency with respect to solving the damped response equation.

4. ITERATIVE METHODS WITH PAIRED TRIAL VECTORS

In the previous section, we discussed how iterative algorithms may be used to solve the response equations, where the response matrices $\mathbf{E}^{[2]}$ and $\mathbf{S}^{[2]}$ were considered to be standard symmetric matrices. As discussed in Section 2, the response matrices have a 2×2 matrix block structure (see eq 4), which imposes that the response eigenvalue equation has paired eigensolutions (see eqs 17–21). When the response equations are solved using the general subspace iterative approach described in Section 3.1, this paired structure is lost in the reduced space equations. However, preserving the 2×2 block structure in the reduced space equations in eqs 28–30, leads to improvement in convergence.²⁵ This paired structure may be recovered in the reduced space by adding trial vectors in the iterative subspace algorithm in pairs²⁵ as will be described below.

In paired iterative algorithms, together with a trial vector \mathbf{b}

$$\mathbf{b} = \begin{pmatrix} \mathbf{b}_{AI} \\ \mathbf{b}_{BI} \end{pmatrix} \quad (58)$$

the paired vector \mathbf{b}^P

$$\mathbf{b}^P = \begin{pmatrix} \mathbf{b}_{BI} \\ \mathbf{b}_{AI} \end{pmatrix} \quad (59)$$

is added to the subspace in each iteration of the iterative procedure. From the linear transformations of $\mathbf{E}^{[2]}$ and $\mathbf{S}^{[2]}$ on \mathbf{b} in eq 25, the linear transformations on the corresponding paired trial vector can be obtained without significant computational cost, as

$$\mathbf{E}^{[2]}\mathbf{b}_i^P = \boldsymbol{\sigma}_i^P, \quad \mathbf{S}^{[2]}\mathbf{b}_i^P = -\boldsymbol{\rho}_i^P \quad (60)$$

where we have used eqs 4, 58, and 59.

After n iterations in the paired iterative subspace algorithm, the reduced space \mathbf{b}^{2n} consists of $2n$ trial vectors:

$$\mathbf{b}^{2n} = \{\mathbf{b}_1, \mathbf{b}_2, \dots, \mathbf{b}_n, \mathbf{b}_1^P, \mathbf{b}_2^P, \dots, \mathbf{b}_n^P\} \quad (61)$$

and the associated spaces of linear transformed vectors $\boldsymbol{\sigma}^{2n}$ and $\boldsymbol{\rho}^{2n}$ are also known. The reduced matrix equations of the form depicted in eq 28–30 may now be set up, and the matrix elements of the reduced space generalized Hessian and metric matrices are given as

$$(\mathbf{E}_R^{[2]})_{ij} = (\mathbf{b}_i^{2n})^T \boldsymbol{\sigma}_j^{2n}, \quad (\mathbf{S}_R^{[2]})_{ij} = (\mathbf{b}_i^{2n})^T \boldsymbol{\rho}_j^{2n} \quad (62)$$

respectively. In matrix block form $\mathbf{E}_R^{[2]}$ and $\mathbf{S}_R^{[2]}$ may be expressed as

$$\mathbf{E}_R^{[2]} = \begin{pmatrix} \mathbf{A}_R & \mathbf{B}_R \\ \mathbf{B}_R & \mathbf{A}_R \end{pmatrix}, \quad \mathbf{S}_R^{[2]} = \begin{pmatrix} \Sigma_R & \Delta_R \\ -\Delta_R & -\Sigma_R \end{pmatrix} \quad (63)$$

where \mathbf{A}_R , \mathbf{B}_R , and Σ_R are symmetric, and Δ_R is an antisymmetric matrix of the dimension n . The reduced subspace matrices thus have the same paired structure as their full matrix counterparts in eq 4. The reduced space right-hand sides in eqs 28 and 29 are given by

$$(\mathbf{G}_R)_i = (\mathbf{b}_i^{2n})^T \mathbf{G} \quad (64)$$

Solving the reduced response equations (eqs 28–30) yields a solution vector $(\mathbf{X})_{n+1}$ in the subspace according to

$$(\mathbf{X})_{n+1} = \sum_{i=1}^{2n} (\mathbf{X}_R)_i \mathbf{b}_i^{2n} \quad (65)$$

The residuals for $(\mathbf{X})_{n+1}$ become equal to

$$\begin{aligned} \mathbf{R}_{n+1} &= (\mathbf{E}^{[2]} - \omega \mathbf{S}^{[2]})(\mathbf{X}_S)_{n+1} - \mathbf{G} \\ &= \sum_{i=1}^{2n} [(\mathbf{X}_S)_R]_i (\boldsymbol{\sigma}_i^{2n} - \omega \boldsymbol{\rho}_i^{2n}) - \mathbf{G} \end{aligned} \quad (66)$$

$$\begin{aligned} \mathbf{R}_{n+1} &= (\mathbf{E}^{[2]} - \omega_f^R \mathbf{S}^{[2]})(\mathbf{X}_f)_{n+1} \\ &= \sum_{i=1}^{2n} [(\mathbf{X}_f)_R]_i (\boldsymbol{\sigma}_i^{2n} - \omega_f^R \boldsymbol{\rho}_i^{2n}) \end{aligned} \quad (67)$$

for the standard and eigenvalue response equation, respectively. For the damped response equations the real and imaginary

components of the residual are given as

$$\begin{aligned} \mathbf{R}_{n+1}^{\text{R}} &= (\mathbf{E}^{[2]} - \omega \mathbf{S}^{[2]})(\mathbf{X}_{\text{D}}^{\text{R}})_{n+1} - \mathbf{G}^{\text{R}} + \gamma \mathbf{S}^{[2]}(\mathbf{X}_{\text{D}}^{\text{I}})_{n+1} \\ &= \sum_{i=1}^{4n} [(\mathbf{X}_{\text{D}}^{\text{R}})_{\text{R}}]_i (\boldsymbol{\sigma}_i^{4n} - \omega \boldsymbol{\rho}_i^{4n}) - \mathbf{G}^{\text{R}} + \gamma \mathbf{S}^{[2]}(\mathbf{X}_{\text{D}}^{\text{I}})_{n+1} \end{aligned} \quad (68)$$

and

$$\begin{aligned} \mathbf{R}_{n+1}^{\text{I}} &= (\mathbf{E}^{[2]} - \omega \mathbf{S}^{[2]})(\mathbf{X}_{\text{D}}^{\text{I}})_{n+1} - \mathbf{G}^{\text{I}} - \gamma \mathbf{S}^{[2]}(\mathbf{X}_{\text{D}}^{\text{R}})_{n+1} \\ &= \sum_{i=1}^{4n} [(\mathbf{X}_{\text{D}}^{\text{I}})_{\text{R}}]_i (\boldsymbol{\sigma}_i^{4n} - \omega \boldsymbol{\rho}_i^{4n}) - \mathbf{G}^{\text{I}} - \gamma \mathbf{S}^{[2]}(\mathbf{X}_{\text{D}}^{\text{R}})_{n+1} \end{aligned} \quad (69)$$

respectively. When the damped response equation is solved, the reduced subspace has a dimension $4n$, as it contains trial vectors for both the real and imaginary components of the solution vector together with their paired counterparts.^{3,5}

The residual norm is calculated to check for convergence. A new trial vector \mathbf{b}_{n+1} is obtained from the preconditioned residuals according to eq 37. The new trial vector, together with its paired counterpart $\mathbf{b}_{n+1}^{\text{P}}$, are added to the reduced subspace in eq 61, and the iterative procedure is continued until convergence.

When the response eigenvalue equation in eq 24 is solved using the algorithm with paired trial vectors, the reduced subspace matrices thus have the 2×2 block structure similar to their exact counterparts. For a ground-state response calculation, $\mathbf{E}_{\text{R}}^{[2]}$ is also positive definite, and the reduced eigenvalue equations will therefore have paired real eigenvalues with positive eigenvalues for the positive $\mathbf{S}^{[2]}$ -normed eigensolutions. It was stated in ref 25 that the lowest positive eigenvalue will converge monotonically toward the full space lowest positive eigenvalue,³⁷ e.g., the lowest positive eigenvalue of iterations n and $n+1$, satisfies $(\omega_1^{\text{R}})_n \geq (\omega_1^{\text{R}})_{n+1}$. This statement is proven in the present work in Appendix C. When the response eigenvalue equation is solved using the subspace algorithm with paired trial vectors, the Davidson algorithm may straightforwardly be applied as for a Hermitian eigenvalue equation, and monotonic convergence will be obtained toward the full space lowest eigenvalue.

For the standard response equation, Olsen et al.²⁵ demonstrated an improved convergence using an iterative subspace algorithm with paired trial vectors. When the standard response equation (eq 1) is solved without pairing, an identical iteration sequence is obtained for ω smaller than the HOMO–LUMO gap regardless of whether the iterative subspace or the CG algorithm is used (see Appendix A). But when paired trial vectors are employed, the reduction in the number of subspace vectors is not obtained for the CG algorithm. We shall see in Section 5.2, however, that this reduction is retained in the CG algorithm when symmetrized trial vectors are used.

5. ITERATIVE METHODS WITH SYMMETRIZED TRIAL VECTORS

In the previous section, we discussed advantages of using paired trial vectors to solve response equations. In this section, we consider the advantages that may be obtained by splitting trial vectors into symmetric and antisymmetric components.

A real symmetric (g) and antisymmetric (u) trial vector may be written as

$$\mathbf{b}_g = \begin{pmatrix} \mathbf{b}_{\text{IA}} \\ \mathbf{b}_{\text{IA}} \end{pmatrix} \quad (70)$$

and

$$\mathbf{b}_u = \begin{pmatrix} \mathbf{b}_{\text{IA}} \\ -\mathbf{b}_{\text{IA}} \end{pmatrix} \quad (71)$$

respectively.

A set of paired trial vectors, as given in eqs 58 and 59, may be represented by the symmetric and antisymmetric components of the vector \mathbf{b} according to

$$\mathbf{b}_g = \frac{1}{2}(\mathbf{b} + \mathbf{b}^{\text{P}}) = \frac{1}{2} \begin{pmatrix} \mathbf{b}_{\text{AI}} + \mathbf{b}_{\text{JB}} \\ \mathbf{b}_{\text{JB}} + \mathbf{b}_{\text{AI}} \end{pmatrix} \quad (72)$$

$$\mathbf{b}_u = \frac{1}{2}(\mathbf{b} - \mathbf{b}^{\text{P}}) = \frac{1}{2} \begin{pmatrix} \mathbf{b}_{\text{AI}} - \mathbf{b}_{\text{JB}} \\ \mathbf{b}_{\text{JB}} - \mathbf{b}_{\text{AI}} \end{pmatrix} \quad (73)$$

Adding always one symmetric and one antisymmetric trial vector in a subspace algorithm is thus equivalent to adding a set of paired vectors, and it will ensure an implicit paired structure of the reduced space equations.

The symmetry of a trial vector is conserved for the linear transformation with respect to $\mathbf{E}^{[2]}$:

$$\boldsymbol{\sigma}_g = \mathbf{E}^{[2]}\mathbf{b}_g, \quad \boldsymbol{\sigma}_u = \mathbf{E}^{[2]}\mathbf{b}_u \quad (74)$$

and reversed for the linear transformation with respect to $\mathbf{S}^{[2]}$:

$$\boldsymbol{\rho}_g = \mathbf{S}^{[2]}\mathbf{b}_u, \quad \boldsymbol{\rho}_u = \mathbf{S}^{[2]}\mathbf{b}_g \quad (75)$$

From the linear transformation of $\mathbf{E}^{[2]}$ on the sum of one symmetric and one antisymmetric trial vector (\mathbf{b}_g and \mathbf{b}_u of eqs 70 and 71), we may determine the linear transformations on the individual components in eq 74 as the linear transformation conserves the symmetry of a trial vector. Similar arguments hold for linear transformation involving the $\mathbf{S}^{[2]}$ matrix. The computational cost of the linear transformation on a general trial vector and on its symmetric and antisymmetric components is thus identical.

A subspace representation of the $\mathbf{E}^{[2]}$ matrix for a set of symmetric vectors \mathbf{b}_g gives a subspace representation for the $\mathbf{A} + \mathbf{B}$ matrix

$$\mathbf{b}_{ig}^{\text{T}} \mathbf{E}^{[2]} \mathbf{b}_{jg} = \mathbf{b}_{ig}^{\text{T}} \boldsymbol{\sigma}_{jg} = 2(\mathbf{A} + \mathbf{B})_{ij}^{\text{R}} \quad (76)$$

where \mathbf{b}_{ig} is the i 'th element of the vector subspace

$$\mathbf{b}_g^n = \{\mathbf{b}_{1g}, \mathbf{b}_{2g}, \dots, \mathbf{b}_{ng}\} \quad (77)$$

and $\boldsymbol{\sigma}_{jg}$ is the j 'th element of the $\mathbf{E}^{[2]}$ linear transformed vector subspace

$$\boldsymbol{\sigma}_g^n = \{\boldsymbol{\sigma}_{1g}, \boldsymbol{\sigma}_{2g}, \dots, \boldsymbol{\sigma}_{ng}\} \quad (78)$$

A similar subspace representation of the $\mathbf{E}^{[2]}$ matrix for the antisymmetric \mathbf{b}_u vectors gives a subspace representation of the $\mathbf{A} - \mathbf{B}$ matrix.

The symmetries of the $\mathbf{E}^{[2]}$ and $\mathbf{S}^{[2]}$ matrices in eqs 74 and 75 make it advantageous to split the solution to the response

equations into symmetric and antisymmetric components. For the standard response equation and the eigenvalue equation, we express the solution vectors as

$$\mathbf{X}_S = \mathbf{X}_g + \mathbf{X}_u \quad (79)$$

$$\mathbf{X}_f = \mathbf{X}_{g,f} + \mathbf{X}_{u,f} \quad (80)$$

respectively. The solution to the damped response equation is written in terms of the Hermitian and anti-Hermitian components

$$\mathbf{X}_D = \mathbf{X}^H + \mathbf{X}^A \quad (81)$$

where

$$\mathbf{X}^H = \mathbf{X}_g^R + i\mathbf{X}_u^I \quad (82)$$

$$\mathbf{X}^A = \mathbf{X}_u^R + i\mathbf{X}_g^I \quad (83)$$

and \mathbf{X}_g^R , \mathbf{X}_g^I , \mathbf{X}_u^R , and \mathbf{X}_u^I are real. Introducing \mathbf{X}_S , \mathbf{X}_f , and \mathbf{X}_D of eqs 79–81 in the response equations (in eqs 1–3) simplifies the solving of these equations, as will be demonstrated below.

5.1. Response Eigenvalue Equation. Employing the symmetries of the $\mathbf{E}^{[2]}$ and $\mathbf{S}^{[2]}$ matrices and expressing the solution vector as in eq 80, the response eigenvalue equation in eq 3 may be written in matrix blocked form, according to

$$\begin{pmatrix} \mathbf{E}^{[2]} & -\omega_f \mathbf{S}^{[2]} \\ -\omega_f \mathbf{S}^{[2]} & \mathbf{E}^{[2]} \end{pmatrix} \begin{pmatrix} \mathbf{X}_{g,f} \\ \mathbf{X}_{u,f} \end{pmatrix} = \begin{pmatrix} 0 \\ 0 \end{pmatrix} \quad (84)$$

where the coupling that occurs between the two components $\mathbf{X}_{g,f}$ and $\mathbf{X}_{u,f}$ is introduced explicitly. Equation 84 may be written in the form of a generalized, non-Hermitian, eigenvalue equation:

$$\begin{pmatrix} \mathbf{E}^{[2]} & 0 \\ 0 & \mathbf{E}^{[2]} \end{pmatrix} \begin{pmatrix} \mathbf{X}_{g,f} \\ \mathbf{X}_{u,f} \end{pmatrix} = \omega_f \begin{pmatrix} 0 & \mathbf{S}^{[2]} \\ \mathbf{S}^{[2]} & 0 \end{pmatrix} \begin{pmatrix} \mathbf{X}_{g,f} \\ \mathbf{X}_{u,f} \end{pmatrix} \quad (85)$$

where the generalized indefinite overlap matrix is viewed as metric. If instead the generalized, positive definite Hessian is viewed as metric, then eq 85 represents a standard eigenvalue equation for a Hermitian matrix, with eigenvalues $(\omega_f)^{-1}$, analogous to eq 24.

Equation 84 may be solved using an iterative subspace algorithm where in each iteration a symmetric and an antisymmetric trial vector is added. In iteration n , we therefore have two sets of trial vectors:

$$\mathbf{b}_g^n = \{\mathbf{b}_{1g}, \mathbf{b}_{2g}, \dots, \mathbf{b}_{ng}\} \quad (86)$$

$$\mathbf{b}_u^n = \{\mathbf{b}_{1u}, \mathbf{b}_{2u}, \dots, \mathbf{b}_{nu}\} \quad (87)$$

and the corresponding sets of linear transformed vectors $\sigma_{g'}^n$, σ_w^n , ρ_{iw}^n , and ρ_g^n ; the i^{th} vector in these latter sets is referred to as $\sigma_{ig'}$, σ_{iw} , ρ_{iu} , and ρ_{ig} , respectively. Equation 84 is solved in the subspace given by eqs 86 and 87 yielding a reduced space equation:

$$\begin{pmatrix} \mathbf{E}_{R,gg}^{[2]} & -\omega_f^R \mathbf{S}_{R,gu}^{[2]} \\ -\omega_f^R \mathbf{S}_{R,ug}^{[2]} & \mathbf{E}_{R,uu}^{[2]} \end{pmatrix} \begin{pmatrix} (\mathbf{X}_{g,f})_R \\ (\mathbf{X}_{u,f})_R \end{pmatrix} = \begin{pmatrix} 0 \\ 0 \end{pmatrix} \quad (88)$$

where

$$\begin{aligned} \mathbf{E}_{R,gg}^{[2]} &= \mathbf{b}_g^T \mathbf{E}^{[2]} \mathbf{b}_g, & \mathbf{E}_{R,uu}^{[2]} &= \mathbf{b}_u^T \mathbf{E}^{[2]} \mathbf{b}_u, \\ \mathbf{S}_{R,gu}^{[2]} &= \mathbf{b}_g^T \mathbf{S}^{[2]} \mathbf{b}_u, & \mathbf{S}_{R,ug}^{[2]} &= \mathbf{b}_u^T \mathbf{S}^{[2]} \mathbf{b}_g \end{aligned} \quad (89)$$

The optimal vectors in the subspace in eqs 86 and 87 have a form

$$\mathbf{X}_{n+1,g,f} = \sum_{i=1}^n [(\mathbf{X}_{g,f})_R]_i \mathbf{b}_{ig} \quad (90)$$

$$\mathbf{X}_{n+1,u,f} = \sum_{i=1}^n [(\mathbf{X}_{u,f})_R]_i \mathbf{b}_{iu} \quad (91)$$

From the solution vectors, the residuals are obtained

$$\begin{aligned} \mathbf{R}_{n+1,g} &= \mathbf{E}^{[2]} \mathbf{X}_{n+1,g,f} - \omega_f^R \mathbf{S}^{[2]} \mathbf{X}_{n+1,u,f} \\ &= \sum_{i=1}^n [(\mathbf{X}_{g,f})_R]_i \sigma_{ig} - \omega_f^R \sum_{i=1}^n [(\mathbf{X}_{u,f})_R]_i \rho_{ig} \end{aligned} \quad (92)$$

$$\begin{aligned} \mathbf{R}_{n+1,u} &= \mathbf{E}^{[2]} \mathbf{X}_{n+1,u,f} - \omega_f^R \mathbf{S}^{[2]} \mathbf{X}_{n+1,g,f} \\ &= \sum_{i=1}^n [(\mathbf{X}_{u,f})_R]_i \sigma_{iu} - \omega_f^R \sum_{i=1}^n [(\mathbf{X}_{g,f})_R]_i \rho_{iu} \end{aligned} \quad (93)$$

that are used to check for convergence.

New trial vectors $\mathbf{b}_{n+1,g}$ and $\mathbf{b}_{n+1,u}$ may be obtained from the optimal solution vectors $\mathbf{X}_{n+1,g}$ and $\mathbf{X}_{n+1,u}$ using either the Davidson or the Olsen algorithm, discussed in Sections 3.2.1 and 3.2.2, respectively. As discussed in Section 3.2.2, the Olsen algorithm is used to resolve the problem that arises when $\mathbf{E}_0^{[2]}$ is approaching $\mathbf{E}^{[2]}$. When the response eigenvalue equations are solved, $\mathbf{E}_0^{[2]}$ is about equally good approximation to $\mathbf{E}^{[2]}$ in the whole frequency range, and the Davidson algorithm can therefore safely be used to generate new trial vectors. In the Davidson algorithm, new trial vectors are constructed from eq 38, which by writing the residuals and trial vectors in terms of a symmetric and an antisymmetric component may be expressed as

$$(\mathbf{b}_{n+1,g} + \mathbf{b}_{n+1,u}) = (\mathbf{E}_0^{[2]} - \omega_f^R \mathbf{S}^{[2]})^{-1} (\mathbf{R}_{n+1,g} + \mathbf{R}_{n+1,u}) \quad (94)$$

To obtain trial vectors that are symmetric and antisymmetric, we use that

$$\begin{aligned} (\mathbf{E}_0^{[2]} - \omega_f^R \mathbf{S}^{[2]})^{-1} &= (\mathbf{E}_0^{[2]} - \omega_f^R \mathbf{S}^{[2]})^{-1} (\mathbf{E}_0^{[2]} + \omega_f^R \mathbf{S}^{[2]})^{-1} (\mathbf{E}_0^{[2]} + \omega_f^R \mathbf{S}^{[2]}) \\ &= [(\mathbf{E}_0^{[2]})^2 - (\omega_f^R)^2 \mathbf{1}]^{-1} (\mathbf{E}_0^{[2]} + \omega_f^R \mathbf{S}^{[2]}) \end{aligned} \quad (95)$$

Equation 94 may now be expressed in the matrix blocked form according to

$$\begin{pmatrix} \mathbf{b}_{n+1,g} \\ \mathbf{b}_{n+1,u} \end{pmatrix} = [(\mathbf{E}_0^{[2]})^2 - (\omega_f^R)^2 \mathbf{1}]^{-1} \otimes \begin{pmatrix} \mathbf{E}_0^{[2]} & \omega_f^R \mathbf{S}^{[2]} \\ \omega_f^R \mathbf{S}^{[2]} & \mathbf{E}_0^{[2]} \end{pmatrix} \begin{pmatrix} \mathbf{R}_{n+1,g} \\ \mathbf{R}_{n+1,u} \end{pmatrix} \quad (96)$$

giving directly new trial vectors that are symmetric and antisymmetric, respectively. The new trial vectors are added to the reduced subspaces in eqs 86 and 87, and the iterative procedure is repeated until convergence.

5.2. Standard Response Equation. Inserting eq 79 into eq 1, we may write eq 1 in the matrix blocked form

$$\begin{pmatrix} \mathbf{E}^{[2]} & -\omega\mathbf{S}^{[2]} \\ -\omega\mathbf{S}^{[2]} & \mathbf{E}^{[2]} \end{pmatrix} \begin{pmatrix} \mathbf{X}_g \\ \mathbf{X}_u \end{pmatrix} = \begin{pmatrix} \mathbf{G}_g \\ \mathbf{G}_u \end{pmatrix} \quad (97)$$

where \mathbf{G}_g and \mathbf{G}_u are the symmetric and antisymmetric components, respectively, of the gradient vector \mathbf{G} . Equation 97 may be solved using a subspace algorithm, as for the response eigenvalue equation. Assuming that after iteration n , the trial vector subspaces of the forms given in eqs 86 and 87 are known, we obtain a reduced standard response equation according to

$$\begin{pmatrix} \mathbf{E}_{R,gg}^{[2]} & -\omega\mathbf{S}_{R,gu}^{[2]} \\ -\omega\mathbf{S}_{R,ug}^{[2]} & \mathbf{E}_{R,uu}^{[2]} \end{pmatrix} \begin{pmatrix} \mathbf{X}_{R,g} \\ \mathbf{X}_{R,u} \end{pmatrix} = \begin{pmatrix} \mathbf{G}_{R,g} \\ \mathbf{G}_{R,u} \end{pmatrix} \quad (98)$$

where the reduced Hessian and metric matrices are given in eq 89, and the reduced right-hand side has the form

$$\mathbf{G}_{R,g} = \mathbf{b}_g^T \mathbf{G}_g, \quad \mathbf{G}_{R,u} = \mathbf{b}_u^T \mathbf{G}_u \quad (99)$$

Solving eq 98 leads to the optimal solution vectors of the form given in eqs 90 and 91, and the residuals $\mathbf{R}_{n+1,g}$ and $\mathbf{R}_{n+1,u}$ may then be obtained as

$$\begin{aligned} \mathbf{R}_{n+1,g} &= \mathbf{E}^{[2]} \mathbf{X}_{n+1,g} - \omega\mathbf{S}^{[2]} \mathbf{X}_{n+1,u} - \mathbf{G}_g \\ &= \sum_{i=1}^n (\mathbf{X}_{R,g})_i \boldsymbol{\sigma}_{ig} - \omega \sum_{i=1}^n (\mathbf{X}_{R,u})_i \boldsymbol{\rho}_{ig} - \mathbf{G}_g \end{aligned} \quad (100)$$

$$\begin{aligned} \mathbf{R}_{n+1,u} &= \mathbf{E}^{[2]} \mathbf{X}_{n+1,u} - \omega\mathbf{S}^{[2]} \mathbf{X}_{n+1,g} - \mathbf{G}_u \\ &= \sum_{i=1}^n (\mathbf{X}_{R,u})_i \boldsymbol{\sigma}_{iu} - \omega \sum_{i=1}^n (\mathbf{X}_{R,g})_i \boldsymbol{\rho}_{iu} - \mathbf{G}_u \end{aligned} \quad (101)$$

From the residuals the new trial vectors may be constructed by using a preconditioner similar to the one in eq 95

$$\begin{pmatrix} \mathbf{b}_{n+1,g} \\ \mathbf{b}_{n+1,u} \end{pmatrix} = [(\mathbf{E}_0^{[2]})^2 - \omega^2 \mathbf{1}]^{-1} \otimes \begin{pmatrix} \mathbf{E}_0^{[2]} & \omega\mathbf{S}^{[2]} \\ \omega\mathbf{S}^{[2]} & \mathbf{E}_0^{[2]} \end{pmatrix} \begin{pmatrix} \mathbf{R}_{n+1,g} \\ \mathbf{R}_{n+1,u} \end{pmatrix} \quad (102)$$

The iterative sequence is continued until convergence.

For frequencies smaller than the HOMO–LUMO gap, both the matrix in eq 97 and the preconditioner in eq 102 are positive definite, and the preconditioned CG/CR algorithms may therefore be used. For larger frequencies neither of these matrices are positive definite, and therefore the CG/CR algorithms cannot safely be applied. Equation 97 then has to be solved using the preconditioned subspace algorithm.

For small ω the condition number is significantly reduced by the preconditioning in eq 102, as the dominant contribution to the large eigenvalues is removed. However, when ω becomes larger and approaches an orbital energy difference, the preconditioning matrix will approach a singularity leading to an increased condition number and poor convergence. Note that the preconditioner in eq 102 is identical to the one used in the algorithm with paired trial vectors described in Section 4, as in eq 102 we have exploited the symmetry properties of $\mathbf{E}^{[2]}$ and $\mathbf{S}^{[2]}$ matrices in eqs 74 and 75.

5.3. Damped Response Equation. *5.3.1. Symmetric and Antisymmetric Trial Vectors.* When the damped response

equation in eq 2 is solved, we write the solution vector in the form of eq 81. This gives a set of linear equations for each of the four components

$$\begin{aligned} \mathbf{E}^{[2]} \mathbf{X}_g^R - \omega\mathbf{S}^{[2]} \mathbf{X}_u^R + \gamma\mathbf{S}^{[2]} \mathbf{X}_u^I &= \mathbf{G}_g^R \\ \mathbf{E}^{[2]} \mathbf{X}_u^R - \omega\mathbf{S}^{[2]} \mathbf{X}_g^R + \gamma\mathbf{S}^{[2]} \mathbf{X}_g^I &= \mathbf{G}_u^R \\ \mathbf{E}^{[2]} \mathbf{X}_u^I - \omega\mathbf{S}^{[2]} \mathbf{X}_g^I - \gamma\mathbf{S}^{[2]} \mathbf{X}_g^R &= \mathbf{G}_u^I \\ \mathbf{E}^{[2]} \mathbf{X}_g^I - \omega\mathbf{S}^{[2]} \mathbf{X}_u^I - \gamma\mathbf{S}^{[2]} \mathbf{X}_u^R &= \mathbf{G}_g^I \end{aligned} \quad (103)$$

where \mathbf{G}_g^R and \mathbf{G}_u^R (\mathbf{G}_g^I and \mathbf{G}_u^I) are the symmetric and antisymmetric components of the real (imaginary) part of the gradient vector \mathbf{G} . When expressed in matrix form, eq 103 is represented by a set of linear equations for a nonsymmetric matrix. Equation 103 may alternatively be expressed in terms of a coupled set of linear equations for a real symmetric matrix (as in Section 3.4):

$$\begin{pmatrix} \mathbf{E}^{[2]} & -\omega\mathbf{S}^{[2]} & \gamma\mathbf{S}^{[2]} & 0 \\ -\omega\mathbf{S}^{[2]} & \mathbf{E}^{[2]} & 0 & \gamma\mathbf{S}^{[2]} \\ \gamma\mathbf{S}^{[2]} & 0 & -\mathbf{E}^{[2]} & \omega\mathbf{S}^{[2]} \\ 0 & \gamma\mathbf{S}^{[2]} & \omega\mathbf{S}^{[2]} & -\mathbf{E}^{[2]} \end{pmatrix} \begin{pmatrix} \mathbf{X}_g^R \\ \mathbf{X}_u^R \\ \mathbf{X}_u^I \\ \mathbf{X}_g^I \end{pmatrix} = \begin{pmatrix} \mathbf{G}_g^R \\ \mathbf{G}_u^R \\ -\mathbf{G}_u^I \\ -\mathbf{G}_g^I \end{pmatrix} \quad (104)$$

The complex non-Hermitian damped response equation (eq 2) is thus transformed to a set of linear equations for a real symmetric but indefinite matrix, where the coupling between the different components is considered explicitly. In iteration n , the residuals of eq 104 are given by

$$\begin{aligned} \mathbf{R}_{n+1,g}^R &= \mathbf{E}^{[2]} \mathbf{X}_{n+1,g}^R - \omega\mathbf{S}^{[2]} \mathbf{X}_{n+1,u}^R + \gamma\mathbf{S}^{[2]} \mathbf{X}_{n+1,u}^I - \mathbf{G}_g^R \\ \mathbf{R}_{n+1,u}^R &= \mathbf{E}^{[2]} \mathbf{X}_{n+1,u}^R - \omega\mathbf{S}^{[2]} \mathbf{X}_{n+1,g}^R + \gamma\mathbf{S}^{[2]} \mathbf{X}_{n+1,g}^I - \mathbf{G}_u^R \\ \mathbf{R}_{n+1,u}^I &= -\mathbf{E}^{[2]} \mathbf{X}_{n+1,u}^I + \omega\mathbf{S}^{[2]} \mathbf{X}_{n+1,g}^I + \gamma\mathbf{S}^{[2]} \mathbf{X}_{n+1,g}^R + \mathbf{G}_u^I \\ \mathbf{R}_{n+1,g}^I &= -\mathbf{E}^{[2]} \mathbf{X}_{n+1,g}^I + \omega\mathbf{S}^{[2]} \mathbf{X}_{n+1,u}^I + \gamma\mathbf{S}^{[2]} \mathbf{X}_{n+1,u}^R + \mathbf{G}_g^I \end{aligned} \quad (105)$$

where $\mathbf{X}_{n+1,g}^R$, $\mathbf{X}_{n+1,u}^R$, $\mathbf{X}_{n+1,u}^I$ and $\mathbf{X}_{n+1,g}^I$ are the optimal solution vectors in iteration n . The residual may be used to check for convergence. In the preconditioned iterative subspace approach, new trial vectors are obtained by preconditioning the residuals:

$$\begin{pmatrix} \mathbf{b}_{n+1,g}^R \\ \mathbf{b}_{n+1,u}^R \\ \mathbf{b}_{n+1,u}^I \\ \mathbf{b}_{n+1,g}^I \end{pmatrix} = \mathcal{P} \otimes \begin{pmatrix} \mathcal{A} & \mathcal{B} & \mathcal{C} & \mathcal{D} \\ \mathcal{B} & \mathcal{A} & \mathcal{D} & \mathcal{C} \\ \mathcal{C} & \mathcal{D} & -\mathcal{A} & -\mathcal{B} \\ \mathcal{D} & \mathcal{C} & -\mathcal{B} & -\mathcal{A} \end{pmatrix} \begin{pmatrix} \mathbf{R}_{n+1,g}^R \\ \mathbf{R}_{n+1,u}^R \\ \mathbf{R}_{n+1,u}^I \\ \mathbf{R}_{n+1,g}^I \end{pmatrix} \quad (106)$$

where \mathcal{P} , \mathcal{A} , \mathcal{B} , \mathcal{C} , and \mathcal{D} are given as

$$\begin{aligned} \mathcal{P} &= [(\mathbf{E}_0^{[2]})^2 - (\omega^2 - \gamma^2)\mathbf{1}]^2 + 4\omega^2\gamma^2\mathbf{1}]^{-1} \\ \mathcal{A} &= \mathbf{E}_0^{[2]} [(\mathbf{E}_0^{[2]})^2 - (\omega^2 - \gamma^2)\mathbf{1}] \\ \mathcal{B} &= \omega\mathbf{S}^{[2]} [(\mathbf{E}_0^{[2]})^2 - (\omega^2 + \gamma^2)\mathbf{1}] \\ \mathcal{C} &= \gamma\mathbf{S}^{[2]} [(\mathbf{E}_0^{[2]})^2 + (\omega^2 + \gamma^2)\mathbf{1}] \\ \mathcal{D} &= 2\omega\gamma\mathbf{E}_0^{[2]} \end{aligned}$$

The preconditioner in eq 106 is an approximation to the symmetric matrix in eq 104 with $\mathbf{E}^{[2]}$ replaced by $\mathbf{E}_0^{[2]}$.

The condition number of eq 104 is significantly reduced by the preconditioning in eq 106, since the dominant component to the large eigenvalues is removed, as described in Section 3.3, and the convergence is therefore radically improved. However, for small values of γ , the condition number of the preconditioning matrix will increase significantly when the optical frequency approaches an orbital energy difference resulting in a slower rate of convergence. In the resonance region, the extent to which the rate of convergence is reduced depends on the density of states at the optical frequency of interest, since none of the eigenvalues in the resonance region are brought close to unity by the preconditioning matrix. Another issue with calculations of response properties in the resonance regions is concerned with the fact that the preconditioner in eq 106 is not positive definite, and as a consequence, the preconditioned CR algorithm cannot be safely applied (see Appendix B). We therefore conclude that the preconditioned iterative subspace algorithm is the best option for solving eq 104.

5.3.2. Damped Response Equations using Hermitian and Anti-Hermitian Trial Vectors. Villaume et al.³⁰ have described how the response equations within relativistic theory may be efficiently solved using an algorithm where the solution vectors are split according to their Hermiticity and the time-reversal symmetry. It is beyond the scope of the present work to give a detailed review of the solution of response equations within a relativistic theory, but it is clear that the structure of the relativistic and nonrelativistic equations are similar differing mainly in the fact that electronic wave functions (molecular orbitals) in a relativistic theory are complex and of two- or four-component forms. Matrix representations of operators are consequently complex and characterized by Hermiticity. The introduction of spin-adapted excitation operators in the non-relativistic realm (see eq 6) finds its correspondence in the exploitation of time-reversal symmetry. The equations presented in the previous section represent a nonrelativistic adaptation of the response equations presented in ref 30 with the requirement of using real trial vectors. We will here give a brief description of how the two representations are connected.

The independent variables in the relativistic formulation of damped response theory were chosen as $\{x^H, i\bar{x}^A, x^A, i\bar{x}^H\}$, representing Hermitian and anti-Hermitian matrices (or vectors) and their complex conjugates. These variables can, however, be divided into symmetric and antisymmetric components according to

$$\begin{aligned} x^H &= x_g^R + ix_u^I, & x^A &= x_u^R + ix_g^I \\ ix^H &= -x_u^R + ix_g^I = -(x^A)^*, & ix^A &= -x_g^R + ix_u^I = -(x^H)^* \end{aligned} \quad (107)$$

where the set $\{x_g^R, x_u^R, x_u^I, x_g^I\}$ contains the real variables employed in the previous section. We note that either set may be used to span the solution space as there is a nonsingular transformation connecting them according to

$$\begin{aligned} x_g^R &= \frac{1}{2}(x^H + (x^H)^*), & x_u^I &= -\frac{i}{2}(x^H - (x^H)^*) \\ x_u^R &= \frac{1}{2}(x^A + (x^A)^*), & x_g^I &= -\frac{i}{2}(x^A - (x^A)^*). \end{aligned} \quad (108)$$

With use of the set of complex variables, Villaume et al. obtained a damped response equation that can be written

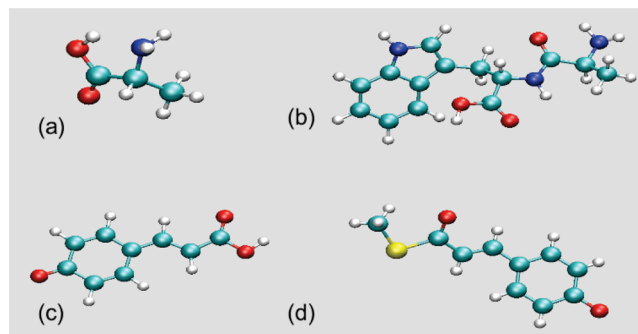


Figure 1. Molecular structures of: (a) alanine, (b) Ala-Trp, (c) pCA⁻, and (d) pCT⁻.

in the form

$$\begin{pmatrix} \mathbf{E}^{[2]} & -\omega\mathbf{S}^{[2]} & \gamma\mathbf{S}^{[2]} & 0 \\ -\omega\mathbf{S}^{[2]} & \mathbf{E}^{[2]} & 0 & \gamma\mathbf{S}^{[2]} \\ -\gamma\mathbf{S}^{[2]} & 0 & \mathbf{E}^{[2]} & -\omega\mathbf{S}^{[2]} \\ 0 & -\gamma\mathbf{S}^{[2]} & -\omega\mathbf{S}^{[2]} & \mathbf{E}^{[2]} \end{pmatrix} \begin{pmatrix} \mathbf{X}^H \\ \mathbf{X}^A \\ \bar{\mathbf{X}}^A \\ \bar{\mathbf{X}}^H \end{pmatrix} = \begin{pmatrix} \mathbf{G}^H \\ 0 \\ 0 \\ 0 \end{pmatrix} \quad (109)$$

where all components of the solution vector, i.e., \mathbf{X}^H , \mathbf{X}^A , $\bar{\mathbf{X}}^A$, and $\bar{\mathbf{X}}^H$, are complex. The 4×4 blocked matrix in eq 109 is not symmetric, but it can be made symmetric by reversing signs of rows three and four, in analogy to what we did to arrive at eq 104.

6. NUMERICAL EXAMPLES

All calculations have been carried out using a local version of DALTON.³⁹ For all reported results, preconditioning is used in the canonical SCF orbital basis.

6.1. Standard Response Equation. In this section, we compare the convergence of the various algorithms for solving the standard response equation in eq 1 with a property gradient referring to the electric dipole operator and to a residual norm of 10^{-4} au. Our calculation refers to alanine (see Figure 1a) at the HF level of theory with use of the 6-31G basis set,⁴⁰ and the performance of the algorithms is compared at the two frequencies of 0.1 and 0.4 au corresponding to the nonresonance and resonance regions of the spectrum, respectively. The adopted molecular geometry is taken from the NIST online database (ref 41).

In Table 1, we compare the convergence of the standard response equation in the nonresonance region, at $\omega = 0.1$ au, using five different iterative algorithms (the transition frequency of the lowest singlet excited state of alanine in the present wave function parametrization is 0.2129 au). In the column order of the table, the presented results refer to the following algorithms: (i) the general subspace approach (discussed in Section 3.3); (ii) the subspace algorithm with paired trial vectors (discussed in Section 4); (iii) the subspace algorithm with symmetrized trial vectors (discussed in Section 5.2); (iv) the CG algorithm with symmetrized trial vectors (discussed in Section 5.2 and Appendix A); and (v) the CR algorithm with symmetrized trial vectors (discussed in Section 5.2 and Appendix B). Residuals \mathbf{R} for the general subspace approach and the algorithm with paired trial vectors are given in eqs 34 and 66, respectively. Residuals \mathbf{R}_g and \mathbf{R}_u in the algorithms with the symmetrized trial vectors are given in eqs 100 and 101, respectively. For all algorithms, one

Table 1. Residual Norms (in au) for Solving the Standard Response Equation with $\omega = 0.1$ au (See eq 1) Using Different Iterative Approaches^a

iteration number	iterative approach with trial vectors of the type:						
	general	paired	symmetrized				
			subspace		CG	CR	
$\ R\ $	$\ R\ $	$\ R_g\ $	$\ R_u\ $	$\ R_g + R_u\ $	$\ R_g + R_u\ $	$\ R_g + R_u\ $	
1	4.51473	1.81777	0.12568	1.81342	1.81777	0.81189	0.71915
2	1.85994	0.68841	0.04235	0.68710	0.68841	0.23247	0.22109
3	0.47364	0.18677	0.02104	0.18558	0.18677	0.09411	0.08346
4	0.17550	0.08252	0.01044	0.08186	0.08252	0.05206	0.04005
5	0.08012	0.04116	0.00363	0.04100	0.04116	0.03190	0.02242
6	0.04412	0.02368	0.00180	0.02361	0.02368	0.01961	0.01384
7	0.03078	0.00933	0.00076	0.00930	0.00933	0.00698	0.00591
8	0.01389	0.00399	0.00045	0.00396	0.00399	0.00364	0.00301
9	0.00523	0.00178	0.00014	0.00177	0.00178	0.00151	0.00133
10	0.00198	0.00050	0.00004	0.00050	0.00050	0.00047	0.00043
11	0.00084	0.00018	0.00001	0.00018	0.00018	0.00018	0.00017
12	0.00054	0.00004	0.00001	0.00004	0.00004	0.00005	0.00005
13	0.00019						
14	0.00005						

^aThe calculations refer to the alanine molecule at the HF/6-31G level of theory.

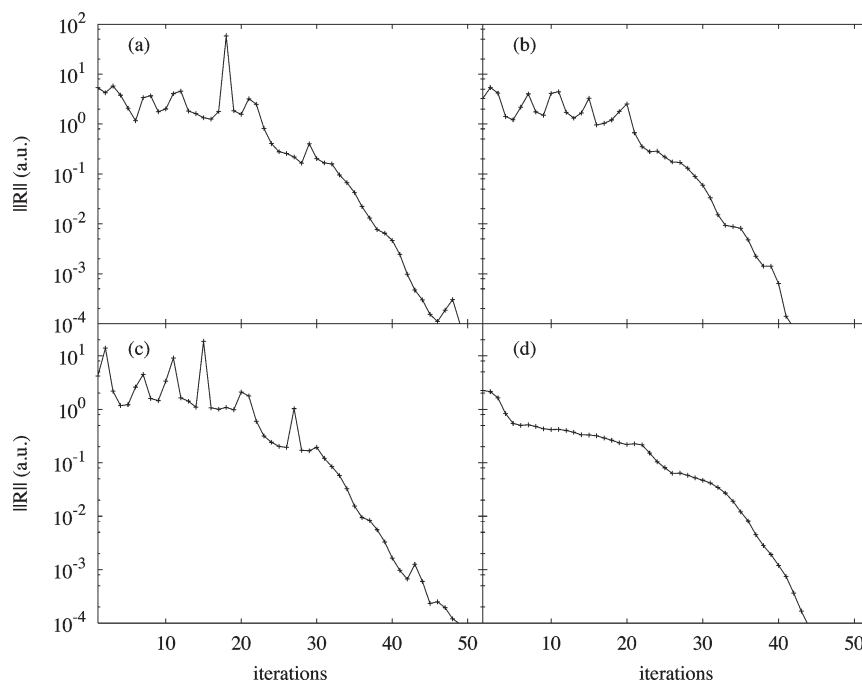


Figure 2. Convergence of the standard response equation for alanine in the resonance region ($\omega = 0.4$ au) using different response solver algorithms: (a) general subspace approach, (b) subspace approach with symmetrized trial vectors, (c) CG approach with symmetrized trial vectors and (d) CR approach with symmetrized trial vectors. Calculations refer to the HF level of theory using basis set 6-31G.

linear transformation of $E^{[2]}$ (and $S^{[2]}$) on a trial vector is required in each iteration.

To begin with, we remark that for ω smaller than the HOMO–LUMO gap results obtained using the general subspace approach (second column) are identical to those obtained when the CG algorithm is applied (see Appendix C), and such a

comparison is therefore left out in the table. When comparing the results obtained using the general subspace approach (second column) with the ones for the subspace algorithm with paired trial vectors (third column), a small reduction in the number of iterations is observed. This is due to the fact that a larger subspace is spanned when paired trial vectors are used. The obtained

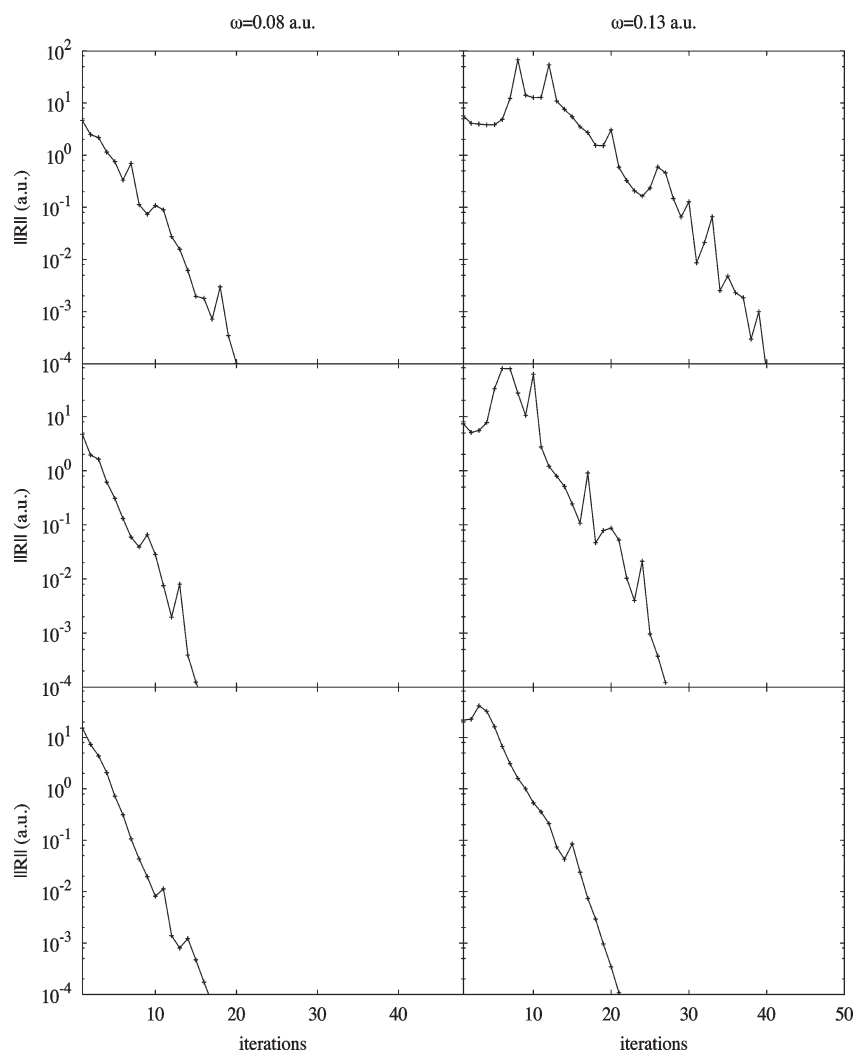


Figure 3. Convergence of damped response equation for pCA^- at frequencies 0.08 (nonresonance region) and 0.13 au (resonance region) employing a damping parameter $\gamma = 0.005$ au. Adopted algorithms are (top) CR with general vectors, (middle) CR with symmetrized trial vectors and (bottom) subspace algorithm with symmetrized trial vectors. Calculations refer to CAM-B3LYP level of theory using basis set cc-pVDZ.

improvement is not dramatic in the present case, but we recall that it is obtained without additional computational cost (see eq 60). The iteration sequences obtained using the algorithm with symmetrized trial vectors (sixth column) and the algorithm with paired trial vectors (third column) are identical. This is related to the fact that the symmetrized trial vectors may be considered as a special set of paired trial vectors, as described in Section 5. When the subspace approach is used, both paired and symmetrized vectors span identical subspaces in any given iteration, and for this reason, their respective iteration sequences become identical, as is seen from Table 1.

Comparing the sixth and the seventh column in Table 1, we see that the iteration sequence for the subspace algorithm with symmetrized trial vectors differs slightly from its CG counterpart. This is due to the fact that, in the CG algorithm, optimal coefficients are determined for vectors of the form $\mathbf{b} = (\mathbf{b}_g, \mathbf{b}_u)^T$ (see eqs 138–140), while in the subspace approach optimal coefficients are obtained for the individual components \mathbf{b}_g and \mathbf{b}_u (see eq 98). However, this difference only has a minor effect on the rate of convergence. By comparing the seventh and the eighth column in Table 1, we see that the convergence rate of the CG

and CR algorithms is similar in accordance with theoretical findings.³⁸ For ω smaller than the HOMO–LUMO gap, we have found that the standard response equation is best solved using the preconditioned CG or CR algorithm, thereby avoiding the storing and the manipulation of a large set of trial vectors needed to set up the reduced space equations.

In Figure 2, we compare the convergence behavior for solving the standard response equation at a near resonant frequency of $\omega = 0.4$ au. In the present wave function parametrization, this frequency is close to the two spin-allowed transition frequencies at 0.4042 and 0.4097 au, respectively. We compare the convergence behavior of four different iterative algorithms: (a) the general subspace approach, (b) the subspace algorithm with symmetrized trial vectors, (c) the CG algorithm with symmetrized trial vectors, and (d) the CR algorithm with symmetrized trial vectors. The results obtained using the algorithm with paired trial vectors are not presented, since, as shown in Table 1, the iteration sequence is identical to the one obtained using the algorithm with symmetrized vectors (plotted in Figure 2b). By comparing results presented in Figure 2 to those listed in Table 1, we see that more iterations are needed to converge the standard

response equation in the resonance region. This is due to the fact that when the frequency ω is close to a transition frequency, the preconditioning of the response equations becomes less efficient as discussed in Section 3.3.

A convergence improvement occurs when the standard response equation is solved using the subspace algorithm with symmetrized trial vectors compared to the general subspace approach (see Figure 2a and b), as discussed above. In Figure 2c and d, the performance of the CG algorithm and the CR algorithm is also displayed. Neither the CG or the CR algorithm can be safely applied for $\omega = 0.4$ au, since neither the matrix in eq 97 nor the preconditioner in eq 102 is positive definite. In the CG algorithm the minimization of the quadratic function (see eqs 111 and 112) is only uniquely defined for an equation with a positive definite matrix. In the CR algorithm the minimization of the preconditioned residual (see eq 156) is only uniquely defined for a positive definite preconditioner. In contrast, in the subspace algorithm the optimal solution is determined by solving a reduced subspace equation and is therefore uniquely determined. In Figure 2, only a small degradation in the convergence is seen when the CG and the CR algorithms are applied in regions where the minimization in the CG and the CR algorithms is not uniquely defined. In other cases the degradation may be much larger, e.g., for $\omega = 0.6$ au the convergence has not been obtained when the CR algorithm has been applied.

For all reported results preconditioning is used. For calculations performed without preconditioning, the convergence has been obtained in 187 and 351 iterations, for $\omega = 0.1$ and 0.4 au, respectively. However, we note that the convergence is rather poor due to the fact that calculations have been performed in the AO representation. In the MO representation (traditionally used), much faster convergence of nonpreconditioned response equations is observed.

The convergence behavior reported above for the general subspace approach and the subspace algorithm with symmetrized trial vectors has been found for calculations on a large variety of molecular systems and also using more extended basis sets as well as at the KS level of theory. The standard response equation for ω larger than the HOMO–LUMO gap is thus best solved using the iterative subspace algorithm with symmetrized trial vectors.

6.2. Damped Response Equation. In this section, we compare the convergence of the various algorithms for solving the damped response equation in eq 2 with a property gradient referring to the electric dipole operator and to a residual norm of 10^{-4} au. In addition to alanine, we will consider three other molecules (see Figure 1), namely: (i) the model dipeptide alanine-tryptophan (Ala-Trp), (ii) deprotonated *trans-p*-coumaric acid (pCA⁻), and (iii) deprotonated *trans*-thiomethyl-*p*-coumarate (pCT⁻). The adopted molecular structures have different sources. The structure of Ala-Trp is obtained by use of the MAESTRO program⁴² without carrying out any additional optimization. The structure of pCA⁻ is that optimized at the KS level of theory using the B3LYP^{43,44} exchange–correlation functional and the aug-cc-pVDZ basis set.⁴⁵ The structure of pCT⁻, which is a model for the protein chromophore PYP (the photoactive yellow protein), is taken from experiment.⁴⁶ The presented response calculations are carried out at the HF and KS levels of theory, in the latter case with employment of the Coulomb attenuated B3LYP exchange–correlation functional (CAM-B3LYP).⁴⁷

In Figure 3, we present the convergence of the damped response equation for calculations on pCA⁻ at the CAM-B3LYP/

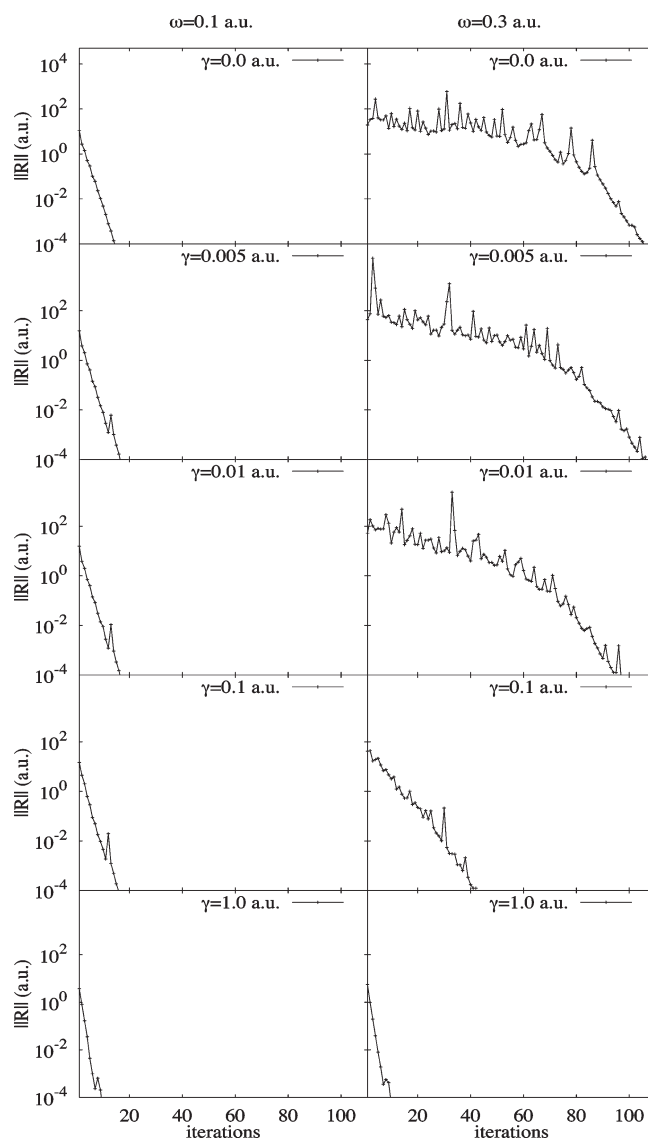


Figure 4. Convergence of the damped response equation for the Ala-Trp molecule at frequencies 0.1 (nonresonance region) and 0.3 au (resonance region) employing damping parameters 0.0, 0.005, 0.01, 0.1, and 1.0 au, respectively. Calculations refer to use of the subspace algorithm with symmetrized trial vectors and are carried out at the CAM-B3LYP level of theory using basis set 6-31G.

cc-pVDZ level of theory. In these calculations, we have adopted a damping parameter of $\gamma = 0.005$ au, and we present the norm of the residual as obtained with (i) the CR algorithm with general vectors (discussed in Section 3.4 and Appendix B), (ii) the CR algorithm with symmetrized trial vectors (discussed in Section 5.3 and Appendix B) and (iii) the subspace algorithm with symmetrized trial vectors (discussed in Section 5.3). The left panels correspond to an optical frequency in the nonresonant region ($\omega = 0.08$ au), whereas the right panels correspond to $\omega = 0.13$ au, which is close to the calculated lowest spin-allowed transition frequency $\omega_1 = 0.1321$ au. In the upper and middle panels, where the CR algorithm is used, the preconditioners in eqs 56 and 106 are not positive definite, and the preconditioned CR algorithm is therefore not uniquely defined. In both the upper and middle panels, we therefore observe a significant degradation in the convergence compared to the subspace

approach (lower panel) in particular for the calculations in the resonance region. The convergence obtained with the CR algorithm is also rather erratic because the preconditioner is not positive definite, while a monotonic convergence would be obtained if the preconditioner was positive definite. In the subspace approach with symmetrized trial vectors in the lower panel, we see only a small degradation in the convergence when the frequency is increased.

In Figure 4, we present calculations for Ala-Trp at the CAM-B3LYP/6-31G level of theory using the subspace algorithm with symmetrized trial vectors presented in Section 5.3. The damped response equation was solved at two different frequencies namely $\omega = 0.1$ (left panels) and $\omega = 0.3$ au (right panels) and five different values of the damping parameter namely γ equal to 0.0, 0.005, 0.01, 0.1, and 1.0 au. Note that results obtained with the last two values of γ do not have any physical meaning and are given here only to demonstrate the robustness of our algorithm toward large γ values. We can conclude that, in the nonresonant

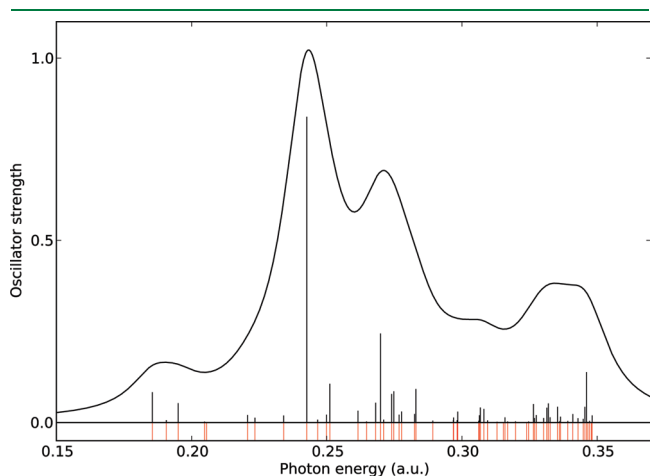


Figure 5. Excitation spectrum for the Ala-Trp molecule at the CAM-B3LYP/6-31G level of theory. Bar heights represent oscillator strengths. All singlet excited states in the spectral region up to 0.3481 au are indicated by red bars below the spectrum.

region, the convergence is independent of the damping parameter γ , owing to the fact that preconditioner given in eq 106 is very efficient. By comparing the left and the right panels of Figure 4, we see that significantly more iterations are needed to converge the damped response equation in the resonance region. This is due to the fact that in the higher frequency region, there is a relatively high density of excited states as seen in Figure 5, and the preconditioning therefore becomes less efficient as these states will interact strongly in this frequency region. For small values of the γ parameter, the preconditioner in eq 106 becomes nearly singular in the higher frequency region, and therefore slow convergence is observed in the top panels in Figure 4. For unphysically large values of γ , on the other hand, the convergence is fast (as can be seen in the bottom panels in Figure 4) due to the fact that the γ contribution becomes the dominant contribution in the preconditioner.

In Figure 6, we report HF/6-31G calculations of the absorptive part (imaginary part) of the electric dipole polarizability of the pCT⁻ molecule—we here adopt a damping parameter γ equal to 0.005 au. In ref 5, it was demonstrated that, for response theory calculations on pCT⁻, the preconditioned two-level subspace approach represented a significant improvement in convergence rate with respect to the complex response equation solver described in ref 3. We here compare the convergence of the preconditioned two-level subspace approach with the convergence obtained using the subspace algorithm with symmetrized trial vectors, as described in Section 5.3. The algorithmic efficiency is depicted in terms of the number of iterations that are needed to obtain a solution vector at each spectral point. In each iteration, linear transformations of trial vectors by $E^{[2]}$ are carried out. The linear transformation requires that a Fock matrix is set up where the computationally expensive two-electron integrals have to be constructed. At the time the calculations presented in ref 5 had been performed, in each iteration of the preconditioned two-level subspace approach, two linear transformations (and therefore two Fock matrices) for the real and the imaginary component of the trial vector were carried out sequentially. However, in an improved implementation, linear transformations are carried simultaneously, and the cost in one iteration is independent of the number of trial vectors, and therefore we compare the

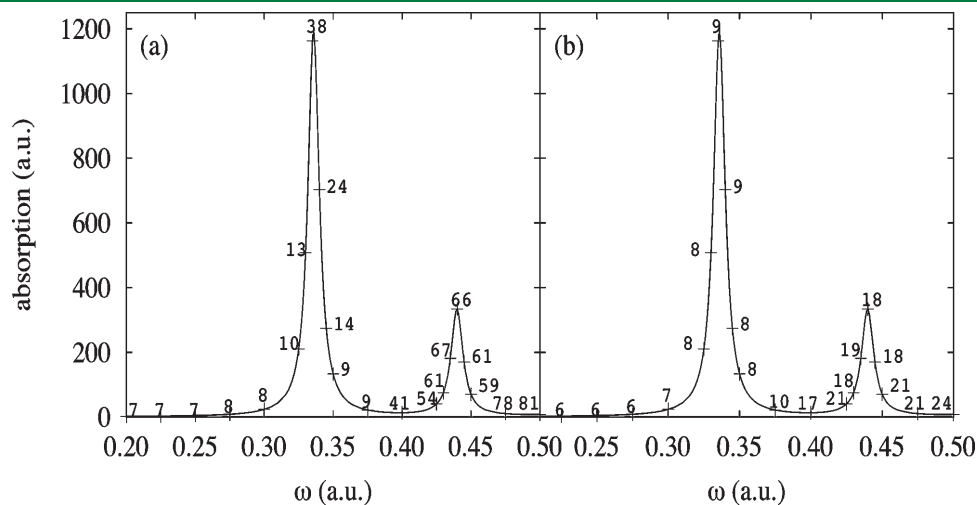


Figure 6. Absorptive part of the electric dipole polarizability determined for pCT⁻ with $\gamma = 0.005$ au. Number of iterations required to reach convergence (residual threshold of 10^{-4} au) is given at spectral points. Comparison is made of (a) response solver proposed in ref 5 and (b) response solver with symmetrized trial vectors proposed in the present work. Calculations refer the HF level of theory using basis set 6-31G.

total number of iterations instead of the total number of Fock matrices constructed during the calculations as was done in ref 5. As seen in Figure 6a and as discussed in the previous section, the computational cost depends on the closeness of the optical frequency to resonances and also on the density of excited states. In the nonresonance region, rapid convergence is observed due to a small coupling between the real and the imaginary component of the solution vectors, but in the resonance region, where there are large couplings between the real and the imaginary components, the convergence is considerably slower. In Figure 6a, the computational cost in the region above $\omega = 0.4$ au is therefore also significantly higher than in the region below (even though there is one strong excitation at around $\omega = 0.33$ au).

When comparing the total number of iterations in the calculations using the preconditioned two-level subspace approach (Figure 6a) and the subspace algorithm with the symmetrized trial vectors (Figure 6b), we see that the performance of the latter represents a clear improvement. In the region of the lowest excitation (around $\omega = 0.33$ au), the algorithm with symmetrized trial vectors requires only two to three more iterations to converge eq 2, as compared to the case in the nonresonance region. In the region with a high density of excited states (above $\omega = 0.4$ au), the number of iterations increases but not as drastically as when the preconditioned two-level subspace approach is used. In comparison to employment of the preconditioned two-level subspace approach⁵ in spectral resonant regions, the computational cost associated with use of the proposed symmetrized trial vector approach is substantially lower—at times the computational cost is reduced by as much as a factor of 4. This is due to the very efficient way of obtaining new trial vectors in the approach with the symmetrized trial vectors using a preconditioner that includes the coupling between vectors explicitly. It should also be noted that in the preconditioned two-level subspace approach, all the trial vectors (from so-called micro- and macroiterations) are stored on disk; that makes this approach inefficient for treating large molecular systems. When the approach with the symmetrized trial vectors is used, the storage requirements are reduced.

6.3. Response Eigenvalue Equation. In Table 2, the convergence behavior of the response eigenvalue equation (eq 3) is shown. The calculations are carried out for the Ala-Trp molecule at the CAM-B3LYP level of theory using the 6-31G basis set. The response eigenvalue equation was solved for the first eigenvalue to a residual norm of 10^{-4} au, and three different iterative algorithms were used (i) the Davidson algorithm with paired trial vectors (discussed in Section 4); (ii) the Davidson algorithm with symmetrized trial vectors (discussed in Section 5.1); and (iii) the Olsen algorithm (discussed in Section 3.2.2) with symmetrized trial vectors. The residual \mathbf{R} for the Davidson algorithm with paired trial vectors is given in eq 67, whereas residuals \mathbf{R}_g and \mathbf{R}_u in the algorithms with the symmetrized trial vectors are given in eqs 100 and 101, respectively.

As discussed in Sections 5 and 6.1, the symmetrized vectors may be considered as a special set of paired vectors. Therefore the Davidson algorithm, both with paired and with symmetrized trial vectors, will in each iteration span the same subspace, and identical iteration sequences are thus obtained. Since the paired structure of the reduced Hessian and metric matrices ($\mathbf{E}_R^{[2]}$ and $\mathbf{S}_R^{[2]}$) is preserved during the iterative procedure in both algorithms, paired eigenvalues are obtained in the reduced subspace in both cases.

Table 2. Residual Norms (in au) for Determination of the Lowest Root of the Eigenvalue Equation (See eq 3) Using Different Iterative Approaches^a

iteration number	Davidson alg.		Olsen alg.
	paired	symmetrized	symmetrized
	$\ \mathbf{R}\ $	$\ \mathbf{R}_g + \mathbf{R}_u\ $	$\ \mathbf{R}_g + \mathbf{R}_u\ $
1	0.11663	0.11663	0.11663
2	0.03819	0.03819	0.03819
3	0.02775	0.02775	0.02782
4	0.01723	0.01723	0.01725
5	0.02148	0.02148	0.02149
⋮	⋮	⋮	⋮
18	0.00146	0.00146	0.00144
19	0.00134	0.00134	0.00132
20	0.00068	0.00068	0.00068
21	0.00045	0.00045	0.00045
22	0.00030	0.00030	0.00030
23	0.00018	0.00018	0.00018
24	0.00008	0.00008	0.00008

^aThe calculations refer to the Ala-Trp molecule at the CAM-B3LYP/6-31G level of theory.

From the third and the fourth column of Table 2, we see that the iteration sequence obtained using the Olsen algorithm is nearly identical to the one obtained using the Davidson algorithms. The Olsen algorithm does not give a significant improvement unless $\mathbf{E}_0^{[2]}$ is approaching $\mathbf{E}^{[2]}$, and this is generally not the case when response eigenvalue equations are solved. Therefore response eigenvalue equations may safely be solved using the Davidson algorithm with paired or symmetrized trial vectors.

7. CONCLUSIONS

The response equations in Hartree–Fock, multiconfigurational self-consistent field, and Kohn–Sham density functional theory have identical structure. We have discussed the algorithms that have been used for solving these equations, and introduced new, efficient, algorithms based on the splitting of trial vectors into symmetric and antisymmetric components. We have used that, upon linear transformation by the generalized Hessian $\mathbf{E}^{[2]}$ (generalized metric $\mathbf{S}^{[2]}$), the symmetry of a trial vector is preserved (reversed). By introducing symmetrized trial vectors, the response equations are transformed to a form which allows them to be solved efficiently, in particular due to the fact that very efficient preconditioners are used with an exact treatment of the $\mathbf{S}^{[2]}$ matrix.

We have demonstrated that the most efficient algorithm for solving the standard and damped response equation is the preconditioned iterative subspace algorithm with symmetrized trial vectors. For the standard response equation at optical frequencies smaller than the HOMO–LUMO gap, the use of symmetrized trial vectors enables the employment of the preconditioned CG or CR algorithms, and one thereby avoids the storing and the handling of a large set of trial vectors to set up the reduced space equations.

For solving the response eigenvalue equations, it is equally efficient to use algorithms with paired²⁵ as with symmetrized trial vectors, and no improvement is obtained by using the Olsen

algorithm.²⁶ We have explicitly proven that, when the Davidson algorithm is applied, the lowest eigenvalue of the reduced subspace equation converges monotonically toward the exact eigenvalue.

APPENDIX A. CONJUGATE GRADIENT (CG) ALGORITHM

The CG algorithm¹⁵ is an iterative method for solving a set of linear equations:

$$\mathbf{Ax} = \mathbf{b} \quad (110)$$

where \mathbf{A} is a symmetric and positive definite matrix. The minimization of the quadratic function:

$$f(\mathbf{x}) = \frac{1}{2}\mathbf{x}^T\mathbf{Ax} - \mathbf{x}^T\mathbf{b} \quad (111)$$

gives

$$\frac{\partial f(\mathbf{x})}{\partial \mathbf{x}} = \mathbf{Ax} - \mathbf{b} = 0 \quad (112)$$

that is a solution to eq 110. Note that the residual of eq 111 may be expressed as

$$\mathbf{r} = -\frac{\partial f(\mathbf{x})}{\partial \mathbf{x}} = \mathbf{b} - \mathbf{Ax} \quad (113)$$

In iteration $n+1$ of the CG algorithm the trial solution \mathbf{x}_{n+1} is parametrized as a linear combination of the residual \mathbf{r}_n of iteration n and the optimal search directions $\{\mathbf{p}_0, \mathbf{p}_1, \dots, \mathbf{p}_{n-1}\}$ of the previous iterations:

$$\mathbf{x}_{n+1} = \mathbf{x}_n + \sum_{i=0}^{n-1} \alpha_i^{(n)} \mathbf{p}_i + \alpha_n^{(n)} \mathbf{r}_n \quad (114)$$

where $\alpha_n^{(n)}$ is determined by applying eq 112. The idea of the CG algorithm is to identify an optimal search direction \mathbf{p}_n and replacing the multiple search direction in eq 114 by a single search direction:

$$\mathbf{x}_{n+1} = \mathbf{x}_n + \alpha_n^{(n)} \mathbf{p}_n \quad (115)$$

such that minimization of the function $f(\mathbf{x}_{n+1})$ calculated from eqs 114 or 115 gives a mathematically identical result. In the CG algorithm, all but the last direction may be discarded without loss of convergence rate.

We will now present the development of the CG algorithm with special emphasis on the developments that allow us to connect the solution that is obtained in the CG algorithm with the one obtained using the subspace iterative algorithm, that is commonly used in quantum chemistry.

A.1. First Iteration. Let us assume that \mathbf{x}_0 is our starting guess. In the first iteration we have a single search direction

$$\mathbf{r}_0 = \mathbf{b} - \mathbf{Ax}_0 \quad (116)$$

which therefore is optimal, i.e., $\mathbf{p}_0 = \mathbf{r}_0$. The solution vector at iteration 1 has therefore a form

$$\mathbf{x}_1 = \mathbf{x}_0 + \alpha_0^{(0)} \mathbf{p}_0 \quad (117)$$

Minimization of $f(\mathbf{x}_1)$ in the direction \mathbf{p}_0 gives

$$\frac{\partial f(\mathbf{x}_1)}{\partial \alpha_0^{(0)}} = \alpha_0^{(0)} \mathbf{p}_0^T \mathbf{Ap}_0 - \mathbf{p}_0^T \mathbf{r}_0 = 0 \quad (118)$$

that determines the optimal step length in the direction \mathbf{p}_0 :

$$\alpha_0^{(0)} = \frac{\mathbf{p}_0^T \mathbf{r}_0}{\mathbf{p}_0^T \mathbf{Ap}_0} \quad (119)$$

The residual at \mathbf{x}_1 :

$$\mathbf{r}_1 = \mathbf{b} - \mathbf{Ax}_1 \quad (120)$$

is orthogonal to the search direction \mathbf{p}_0 :

$$\mathbf{p}_0^T \mathbf{r}_1 = \mathbf{r}_0^T \mathbf{r}_1 = 0. \quad (121)$$

A.2. Second Iteration. The trial vector now has components along \mathbf{p}_0 and \mathbf{r}_1

$$\mathbf{x}_2 = \mathbf{x}_1 + \alpha_0^{(1)} \mathbf{p}_0 + \alpha_1^{(1)} \mathbf{r}_1 \quad (122)$$

Minimization of $f(\mathbf{x}_2)$, with respect to coefficients $\alpha_0^{(1)}$ and $\alpha_1^{(1)}$, gives the subspace equations:

$$\begin{pmatrix} \mathbf{p}_0^T \mathbf{Ap}_0 & \mathbf{p}_0^T \mathbf{Ar}_1 \\ \mathbf{r}_1^T \mathbf{Ap}_0 & \mathbf{r}_1^T \mathbf{Ar}_1 \end{pmatrix} \begin{pmatrix} \alpha_0^{(1)} \\ \alpha_1^{(1)} \end{pmatrix} = \begin{pmatrix} \mathbf{p}_0^T \mathbf{r}_1 \\ \mathbf{r}_1^T \mathbf{r}_1 \end{pmatrix} = \begin{pmatrix} 0 \\ \mathbf{r}_1^T \mathbf{r}_1 \end{pmatrix} \quad (123)$$

where in the first row of eq 123 the coefficient $\alpha_0^{(1)}$ may be written in terms of $\alpha_1^{(1)}$:

$$\alpha_0^{(1)} = -\alpha_1^{(1)} \frac{\mathbf{p}_0^T \mathbf{Ar}_1}{\mathbf{p}_0^T \mathbf{Ap}_0} \quad (124)$$

The trial vector \mathbf{x}_2 may be expressed as a unidirectional search:

$$\mathbf{x}_2 = \mathbf{x}_1 + \alpha_1^{(1)} \mathbf{p}_1 \quad (125)$$

where the direction \mathbf{p}_1 is

$$\mathbf{p}_1 = \mathbf{r}_1 - \frac{\mathbf{p}_0^T \mathbf{Ar}_1}{\mathbf{p}_0^T \mathbf{Ap}_0} \mathbf{p}_0 \quad (126)$$

The optimal step length in the direction \mathbf{p}_1 becomes

$$\alpha_1^{(1)} = \frac{\mathbf{r}_1^T \mathbf{p}_1}{\mathbf{p}_1^T \mathbf{Ap}_1} \quad (127)$$

The residual at \mathbf{x}_2 becomes

$$\mathbf{r}_2 = \mathbf{b} - \mathbf{Ax}_2 \quad (128)$$

or

$$\mathbf{r}_2 = \mathbf{r}_1 - \alpha_1^{(1)} \mathbf{Ap}_1 \quad (129)$$

It can be shown that

$$\mathbf{p}_0^T \mathbf{Ap}_1 = 0, \quad \mathbf{r}_2^T \mathbf{Ap}_0 = 0 \quad (130)$$

$$\mathbf{r}_2^T \mathbf{p}_1 = 0, \quad \mathbf{r}_2^T \mathbf{r}_1 = 0, \quad \mathbf{r}_2^T \mathbf{p}_0 = 0, \quad \mathbf{r}_2^T \mathbf{r}_0 = 0 \quad (131)$$

A.3. $n + 1$ th Iteration. The previous directions and residuals fulfill the relations

$$\mathbf{r}_i^T \mathbf{p}_j = 0, \quad \mathbf{r}_i^T \mathbf{r}_j = 0, \quad i, j = 0, 1, \dots, n, \quad i > j \quad (132)$$

$$\mathbf{r}_i^T \mathbf{Ap}_j = 0, \quad i, j = 0, 1, \dots, n, \quad i > j + 1 \quad (133)$$

$$\mathbf{p}_i^T \mathbf{A} \mathbf{p}_j = \mathbf{p}_i^T \mathbf{A} \mathbf{p}_j \delta_{ij}, \quad i, j = 0, 1, \dots, n-1 \quad (134)$$

The new trial vector is initially written as a general vector in the space spanned by the previous search directions $\{\mathbf{p}_0, \mathbf{p}_1, \dots, \mathbf{p}_{n-1}\}$ and the current residual \mathbf{r}_n :

$$\mathbf{x}_{n+1} = \mathbf{x}_n + \sum_{i=0}^{n-1} \alpha_i^{(n)} \mathbf{p}_i + \alpha_n^{(n)} \mathbf{r}_n \quad (135)$$

Minimizing $f(\mathbf{x}_{n+1})$ with respect to the $n+1$ free parameters one obtains the subspace equation:

$$\begin{pmatrix} \mathbf{p}_0^T \mathbf{A} \mathbf{p}_0 & \mathbf{p}_0^T \mathbf{A} \mathbf{p}_1 & \dots & \dots & \mathbf{p}_0^T \mathbf{A} \mathbf{p}_{n-1} & \mathbf{p}_0^T \mathbf{A} \mathbf{r}_n \\ \mathbf{p}_1^T \mathbf{A} \mathbf{p}_0 & \mathbf{p}_1^T \mathbf{A} \mathbf{p}_1 & \dots & \dots & \mathbf{p}_1^T \mathbf{A} \mathbf{p}_{n-1} & \mathbf{p}_1^T \mathbf{A} \mathbf{r}_n \\ \dots & \dots & \dots & \dots & \dots & \dots \\ \dots & \dots & \dots & \dots & \dots & \dots \\ \mathbf{p}_{n-1}^T \mathbf{A} \mathbf{p}_0 & \mathbf{p}_{n-1}^T \mathbf{A} \mathbf{p}_1 & \dots & \dots & \mathbf{p}_{n-1}^T \mathbf{A} \mathbf{p}_{n-1} & \mathbf{p}_{n-1}^T \mathbf{A} \mathbf{r}_n \\ \mathbf{r}_n^T \mathbf{A} \mathbf{p}_0 & \mathbf{r}_n^T \mathbf{A} \mathbf{p}_1 & \dots & \dots & \mathbf{r}_n^T \mathbf{A} \mathbf{p}_{n-1} & \mathbf{r}_n^T \mathbf{A} \mathbf{r}_n \end{pmatrix} \begin{pmatrix} \alpha_0^{(n)} \\ \alpha_1^{(n)} \\ \vdots \\ \vdots \\ \alpha_{n-1}^{(n)} \\ \alpha_n^{(n)} \end{pmatrix} = \begin{pmatrix} \mathbf{p}_0^T \mathbf{r}_n \\ \mathbf{p}_1^T \mathbf{r}_n \\ \vdots \\ \vdots \\ \mathbf{p}_{n-1}^T \mathbf{r}_n \\ \mathbf{r}_n^T \mathbf{r}_n \end{pmatrix} \quad (136)$$

that is equivalent to

$$\begin{pmatrix} \mathbf{p}_0^T \mathbf{A} \mathbf{p}_0 & 0 & \dots & 0 & 0 & 0 \\ 0 & \mathbf{p}_1^T \mathbf{A} \mathbf{p}_1 & \dots & 0 & 0 & 0 \\ \dots & \dots & \dots & \dots & \dots & \dots \\ \dots & \dots & \dots & \dots & \dots & \dots \\ 0 & 0 & \dots & \mathbf{p}_{n-2}^T \mathbf{A} \mathbf{p}_{n-2} & 0 & 0 \\ 0 & 0 & \dots & 0 & \mathbf{p}_{n-1}^T \mathbf{A} \mathbf{p}_{n-1} & \mathbf{p}_{n-1}^T \mathbf{A} \mathbf{r}_n \\ 0 & 0 & \dots & 0 & \mathbf{r}_n^T \mathbf{A} \mathbf{p}_{n-1} & \mathbf{r}_n^T \mathbf{A} \mathbf{r}_n \end{pmatrix} \begin{pmatrix} \alpha_0^{(n)} \\ \alpha_1^{(n)} \\ \vdots \\ \vdots \\ \alpha_{n-2}^{(n)} \\ \alpha_{n-1}^{(n)} \\ \alpha_n^{(n)} \end{pmatrix} = \begin{pmatrix} 0 \\ 0 \\ \vdots \\ \vdots \\ 0 \\ 0 \\ \mathbf{r}_n^T \mathbf{r}_n \end{pmatrix} \quad (137)$$

where eqs 132–134 were used. It can be seen from eq 137 that solving the reduced space equation can be avoided, due to the fact that all the information necessary to obtain the optimal solution vector is contained in the last three trial vectors.

Due to the form of the subspace equation the optimal solution vector \mathbf{x}_{n+1} may be expressed in terms of a single search direction \mathbf{p}_n and the optimal step length $\alpha_n^{(n)}$ as

$$\mathbf{x}_{n+1} = \mathbf{x}_n + \alpha_n^{(n)} \mathbf{p}_n \quad (138)$$

where

$$\mathbf{p}_n = \mathbf{r}_n - \frac{\mathbf{p}_{n-1}^T \mathbf{A} \mathbf{r}_n}{\mathbf{p}_{n-1}^T \mathbf{A} \mathbf{p}_{n-1}} \mathbf{p}_{n-1} \quad (139)$$

$$\alpha_n^{(n)} = \frac{\mathbf{p}_n^T \mathbf{r}_n}{\mathbf{p}_n^T \mathbf{A} \mathbf{p}_n} \quad (140)$$

Therefore only three vectors: \mathbf{x}_n , \mathbf{r}_n and \mathbf{p}_{n-1} need to be stored in each iteration. Equations 132–134 are valid for n increased by one, and the iteration procedure of the CG algorithm is established.

The CG algorithm in iteration $n+1$ may be viewed as an iterative subspace algorithm that uses the basis of the trial vectors $\{\mathbf{p}_0, \mathbf{p}_1, \dots, \mathbf{p}_{n-1}, \mathbf{r}_n\}$. The iterative subspace algorithm in eq 28 is set up in terms of trial vectors consisting of $\{\mathbf{r}_0, \mathbf{r}_1, \dots, \mathbf{r}_{n-1}, \mathbf{r}_n\}$. From eqs 114 and 115 it is seen that these two sets of trial vectors span the same space and that the CG and the iterative subspace algorithms of eq 28 therefore give the same iteration sequence.

APPENDIX B. CONJUGATE RESIDUAL ALGORITHM AND ITS PRECONDITIONING

B.1. Conjugate Residual (CR) Algorithm. In this section, the CR algorithm¹⁹ is discussed (described in detail in ref 38). The CR algorithm is an iterative method for solving a set of linear equations of a form in eq 110, where \mathbf{A} is a symmetric but not necessarily positive definite matrix. The residual for a general vector \mathbf{x} is given as

$$\mathbf{r} = \mathbf{b} - \mathbf{A} \mathbf{x} \quad (141)$$

The solution to eq 110 is obtained by minimization of the squared residual norm:

$$g(\mathbf{x}) = \mathbf{r}^T \mathbf{r} \quad (142)$$

as

$$\frac{\partial g(\mathbf{x})}{\partial \mathbf{x}} = 2\mathbf{A}(\mathbf{A} \mathbf{x} - \mathbf{b}) = 0 \quad (143)$$

We shortly summarize the CR algorithm with emphasis on the development that allows us to connect to iterative subspace algorithms that are used in quantum chemistry. We refer to the paper by Ziólkowski et al.,³⁸ where a more thorough development of CR is given, and the connection to the DIIS algorithm^{48,49} (that is commonly used in quantum chemistry) is presented.

After n iterations of the CR algorithm, the optimal solution vector \mathbf{x}_n , n residuals \mathbf{r}_i , and n optimal directions \mathbf{p}_i are known. It may be shown that the previous optimal directions and residuals fulfill the relations:³⁸

$$\mathbf{r}_i^T \mathbf{A} \mathbf{p}_j = 0, \quad \mathbf{r}_i^T \mathbf{A} \mathbf{r}_j = 0, \quad i, j = 0, 1, \dots, n, \quad i > j \quad (144)$$

$$\mathbf{r}_i^T \mathbf{A}^2 \mathbf{p}_j = 0, \quad i, j = 0, 1, \dots, n, \quad i > j + 1 \quad (145)$$

$$\mathbf{p}_i^T \mathbf{A}^2 \mathbf{p}_j = \mathbf{p}_i^T \mathbf{A}^2 \mathbf{p}_j \delta_{ij}, \quad i, j = 0, 1, \dots, n-1 \quad (146)$$

In iteration $n+1$, the new trial vector may be written as a general vector in the space spanned by the previous optimal search directions $\{\mathbf{p}_0, \mathbf{p}_1, \dots, \mathbf{p}_{n-1}\}$, and the current residual \mathbf{r}_n :

$$\mathbf{x}_{n+1} = \mathbf{x}_n + \sum_{i=0}^{n-1} \alpha_i^{(n)} \mathbf{p}_i + \alpha_n^{(n)} \mathbf{r}_n \quad (147)$$

Minimizing $g(\mathbf{x}_{n+1})$ with respect to the $n+1$ free parameters leads to a subspace equation:

$$\begin{pmatrix} \mathbf{p}_0^T \mathbf{A}^2 \mathbf{p}_0 & \mathbf{p}_0^T \mathbf{A}^2 \mathbf{p}_1 & \dots & \dots & \mathbf{p}_0^T \mathbf{A}^2 \mathbf{p}_{n-1} & \mathbf{p}_0^T \mathbf{A}^2 \mathbf{r}_n \\ \mathbf{p}_1^T \mathbf{A}^2 \mathbf{p}_0 & \mathbf{p}_1^T \mathbf{A}^2 \mathbf{p}_1 & \dots & \dots & \mathbf{p}_1^T \mathbf{A}^2 \mathbf{p}_{n-1} & \mathbf{p}_1^T \mathbf{A}^2 \mathbf{r}_n \\ \dots & \dots & \dots & \dots & \dots & \dots \\ \dots & \dots & \dots & \dots & \dots & \dots \\ \mathbf{p}_{n-1}^T \mathbf{A}^2 \mathbf{p}_0 & \mathbf{p}_{n-1}^T \mathbf{A}^2 \mathbf{p}_1 & \dots & \dots & \mathbf{p}_{n-1}^T \mathbf{A}^2 \mathbf{p}_{n-1} & \mathbf{p}_{n-1}^T \mathbf{A}^2 \mathbf{r}_n \\ \mathbf{r}_n^T \mathbf{A}^2 \mathbf{p}_0 & \mathbf{r}_n^T \mathbf{A}^2 \mathbf{p}_1 & \dots & \dots & \mathbf{r}_n^T \mathbf{A}^2 \mathbf{p}_{n-1} & \mathbf{r}_n^T \mathbf{A}^2 \mathbf{r}_n \end{pmatrix} \begin{pmatrix} \alpha_0^{(n)} \\ \alpha_1^{(n)} \\ \vdots \\ \vdots \\ \alpha_{n-1}^{(n)} \\ \alpha_n^{(n)} \end{pmatrix} = \begin{pmatrix} \mathbf{p}_0^T \mathbf{A} \mathbf{r}_n \\ \mathbf{p}_1^T \mathbf{A} \mathbf{r}_n \\ \vdots \\ \vdots \\ \mathbf{p}_{n-1}^T \mathbf{A} \mathbf{r}_n \\ \mathbf{r}_n^T \mathbf{A} \mathbf{r}_n \end{pmatrix} \quad (148)$$

that is equivalent to

$$\begin{pmatrix} \mathbf{p}_0^T \mathbf{A}^2 \mathbf{p}_0 & 0 & \dots & 0 & 0 & 0 & 0 \\ 0 & \mathbf{p}_1^T \mathbf{A}^2 \mathbf{p}_1 & \dots & 0 & 0 & 0 & 0 \\ \dots & \dots & \dots & \dots & \dots & \dots & \dots \\ \dots & \dots & \dots & \dots & \dots & \dots & \dots \\ 0 & 0 & \dots & \mathbf{p}_{n-1}^T \mathbf{A}^2 \mathbf{p}_{n-2} & 0 & 0 & 0 \\ 0 & 0 & \dots & 0 & \mathbf{p}_{n-1}^T \mathbf{A}^2 \mathbf{p}_{n-1} & \mathbf{p}_{n-1}^T \mathbf{A}^2 \mathbf{r}_n & \alpha_{n-1}^{(n)} \\ 0 & 0 & \dots & 0 & \mathbf{r}_n^T \mathbf{A}^2 \mathbf{p}_{n-1} & \mathbf{r}_n^T \mathbf{A}^2 \mathbf{r}_n & \alpha_n^{(n)} \end{pmatrix} \begin{pmatrix} \alpha_0^{(n)} \\ \alpha_1^{(n)} \\ \vdots \\ \vdots \\ \alpha_{n-2}^{(n)} \\ \alpha_{n-1}^{(n)} \\ \alpha_n^{(n)} \end{pmatrix} = \begin{pmatrix} 0 \\ 0 \\ \vdots \\ \vdots \\ 0 \\ 0 \\ \mathbf{r}_n^T \mathbf{A} \mathbf{r}_n \end{pmatrix} \quad (149)$$

where relations eqs 144–146 were used. From eq 149 it may be seen that also in the CR algorithm only the three last trial vectors are necessary to obtain the optimal solution vector in iteration $n+1$.

The optimal solution vector \mathbf{x}_{n+1} may be expressed in terms of a single search direction \mathbf{p}_n and of the optimal step length $\alpha_n^{(n)}$ as

$$\mathbf{x}_{n+1} = \mathbf{x}_n + \alpha_n^{(n)} \mathbf{p}_n \quad (150)$$

where

$$\mathbf{p}_n = \mathbf{r}_n - \frac{\mathbf{p}_{n-1}^T \mathbf{A}^2 \mathbf{r}_n}{\mathbf{p}_{n-1}^T \mathbf{A}^2 \mathbf{p}_{n-1}} \mathbf{p}_{n-1} \quad (151)$$

$$\alpha_n^{(n)} = \frac{\mathbf{p}_n^T \mathbf{A} \mathbf{r}_n}{\mathbf{p}_n^T \mathbf{A}^2 \mathbf{p}_n} \quad (152)$$

and

$$\mathbf{r}_{n+1} = \mathbf{r}_n - \alpha_n^{(n)} \mathbf{A} \mathbf{p}_n \quad (153)$$

Equations 144–146 are valid for n increased by one, and the iteration procedure of the CR algorithm is established.

In the CR algorithm, we may thus discard all but the last direction without information lost, similarly to what is found in the CG algorithm. The main difference between the CG and the CR algorithms is that step lengths in the CG algorithm are determined from a minimization of $f(\mathbf{x})$ in eq 111, whereas in the CR algorithm the step length is determined from a minimization of $g(\mathbf{x})$ in eq 143. The minimization of $f(\mathbf{x})$ is only unique for a symmetric positive matrix \mathbf{A} , while the minimization of $g(\mathbf{x})$ is unique also for a nonsingular symmetric but not necessarily positive definite matrix. The CG algorithm therefore can only be safely applied for a positive definite matrix \mathbf{A} , while the CR algorithm can also be applied when the matrix \mathbf{A} is not positive definite.

B.2. Preconditioned CR Algorithm. To improve the convergence of the CR algorithm, the set of linear equations in eq 110 may be solved in a preconditioned form, where a coordinate transformation is introduced to produce a new set of linear equations which has a lower condition number. To carry out this transformation, eq 110 is multiplied with the transpose of a nonsingular matrix: \mathcal{P}

$$\mathcal{P}^T \mathbf{A} \mathcal{P} \mathbf{Y} - \mathcal{P}^T \mathbf{b} = 0 \quad (154)$$

where $\mathbf{Y} = \mathcal{P}^{-1} \mathbf{x}$. We may now solve eq 154 using the CR algorithm and transform the solution to the original coordinates. Alternatively, eq 154 may be solved in the original basis using modified CR equations. To do this, we write the residual in the \mathbf{Y} basis as

$$\mathbf{r}^{\mathcal{P}} = \mathcal{P}^T \mathbf{b} - \mathcal{P}^T \mathbf{A} \mathcal{P} \mathbf{Y} = \mathcal{P}^T \mathbf{r} \quad (155)$$

Optimal directions are now determined by minimizing

$$\mathbf{g}^{\mathcal{P}}(\mathbf{x}) = (\mathbf{r}^{\mathcal{P}})^T \mathbf{r}^{\mathcal{P}} = \mathbf{r}^T \mathcal{P} \mathcal{P}^T \mathbf{r} = \mathbf{r}^T \mathbf{C}^{-1} \mathbf{r} \quad (156)$$

where

$$\mathbf{C}^{-1} = \mathcal{P} \mathcal{P}^T \quad (157)$$

The preconditioned analogue to eqs 150–153 becomes³⁸

$$\mathbf{x}_{n+1} = \mathbf{x}_n + \alpha_n^{(n)} \mathbf{C}^{-1} \mathbf{p}_n \quad (158)$$

where

$$\mathbf{p}_n = \mathbf{r}_n - \frac{\mathbf{p}_{n-1}^T \mathbf{C}^{-1} \mathbf{A} \mathbf{C}^{-1} \mathbf{A} \mathbf{C}^{-1} \mathbf{r}_n}{\mathbf{p}_{n-1}^T \mathbf{C}^{-1} \mathbf{A} \mathbf{C}^{-1} \mathbf{A} \mathbf{C}^{-1} \mathbf{p}_{n-1}} \mathbf{p}_{n-1} \quad (159)$$

$$\alpha_n^{(n)} = \frac{\mathbf{p}_n^T \mathbf{C}^{-1} \mathbf{A} \mathbf{C}^{-1} \mathbf{r}_n}{\mathbf{p}_n^T \mathbf{C}^{-1} \mathbf{A} \mathbf{C}^{-1} \mathbf{A} \mathbf{C}^{-1} \mathbf{p}_n} \quad (160)$$

and

$$\mathbf{r}_{n+1} = \mathbf{r}_n - \alpha_n^{(n)} \mathbf{A} \mathbf{C}^{-1} \mathbf{p}_n \quad (161)$$

Choosing \mathcal{P}^T such that \mathbf{C} is a good approximation to \mathbf{A} ensures that the linear equations are solved in a basis where the matrix \mathbf{A} has a lower condition number.

From eqs 158 and 159, it seems like the preconditioned CR algorithm may be applied whenever an easily invertible matrix \mathbf{C} that is a good approximation to the \mathbf{A} matrix can be identified. However, the step lengths in the preconditioned CR algorithm are determined from a minimization of $\mathbf{g}^{\mathcal{P}}(\mathbf{x})$ in eq 156, and this minimization is uniquely defined only when \mathbf{C}^{-1} corresponds to a coordinate transformation and can be decomposed as in eq 157. The decomposition in eq 157 requires that \mathbf{C}^{-1} is positive

definite, and we thus conclude that the CR preconditioned equations in eqs 158–161 can be safely applied only for a positive definite preconditioner \mathbf{C} .

APPENDIX C. MACDONALD'S THEOREM FOR THE GROUND-STATE RESPONSE EIGENVALUE EQUATION

For a ground state, the response eigenvalue equation may be expressed as

$$\mathbf{E}^{[2]}\mathbf{X} = \mathbf{S}^{[2]}\mathbf{X}\boldsymbol{\omega} \quad (162)$$

where the positive $\mathbf{S}^{[2]}$ -norm eigensolutions $\mathbf{X}_+ = \{\mathbf{X}_{1+}, \mathbf{X}_{2+}, \dots, \mathbf{X}_{p+}, \dots\}$ are associated with positive eigenvalues $\{\omega_1, \omega_2, \dots, \omega_p, \dots\}$. We assume that the eigenvalues are sorted in ascending order. Similarly, the negative $\mathbf{S}^{[2]}$ -normed eigensolutions $\mathbf{X}_- = \{\mathbf{X}_{1-}, \mathbf{X}_{2-}, \dots, \mathbf{X}_{p-}, \dots\}$ are associated with the negative eigenvalues $\{-\omega_1, -\omega_2, \dots, -\omega_p, \dots\}$. The matrix \mathbf{X} is the collection of positive and negative eigenvectors $[\mathbf{X}_+, \mathbf{X}_-]$, and $\boldsymbol{\omega}$ is a diagonal matrix collecting the eigenvalues in corresponding order.

Let us now compare the solution to eq 162 for two paired subspaces:

$$\mathbf{b}' = \{\mathbf{b}_1, \mathbf{b}_2, \dots, \mathbf{b}_N, \mathbf{b}_1^p, \mathbf{b}_2^p, \dots, \mathbf{b}_N^p\} \quad (163)$$

$$\mathbf{b}'' = \{\mathbf{b}_1, \mathbf{b}_2, \dots, \mathbf{b}_N, \mathbf{b}_{N+1}, \mathbf{b}_1^p, \mathbf{b}_2^p, \dots, \mathbf{b}_N^p, \mathbf{b}_{N+1}^p\} \quad (164)$$

where \mathbf{b}'' is obtained from \mathbf{b}' by adding the paired vectors \mathbf{b}_{N+1} and \mathbf{b}_{N+1}^p . The solution to eq 162 in \mathbf{b}' and \mathbf{b}'' spaces may be expressed as (see eq 21):

$$(\mathbf{X}')^\dagger \mathbf{E}^{[2]}\mathbf{X}' = \begin{pmatrix} \boldsymbol{\omega}'_{\text{exc}} & 0 \\ 0 & \boldsymbol{\omega}'_{\text{exc}} \end{pmatrix}; \quad (\mathbf{X}')^\dagger \mathbf{S}^{[2]}\mathbf{X}' = \begin{pmatrix} \mathbf{1} & 0 \\ 0 & -\mathbf{1} \end{pmatrix} \quad (165)$$

$$(\mathbf{X}'')^\dagger \mathbf{E}^{[2]}\mathbf{X}'' = \begin{pmatrix} \boldsymbol{\omega}''_{\text{exc}} & 0 \\ 0 & \boldsymbol{\omega}''_{\text{exc}} \end{pmatrix}; \quad (\mathbf{X}'')^\dagger \mathbf{S}^{[2]}\mathbf{X}'' = \begin{pmatrix} \mathbf{1} & 0 \\ 0 & -\mathbf{1} \end{pmatrix} \quad (166)$$

where \mathbf{X}' contains N paired eigenvectors in the \mathbf{b}' subspace and \mathbf{X}'' contains $(N+1)$ paired eigenvectors in the \mathbf{b}'' subspace. The positive eigenvalues are collected in the diagonal matrices $\boldsymbol{\omega}'_{\text{exc}}$ and $\boldsymbol{\omega}''_{\text{exc}}$ and represent subspace approximations to the eigenvalues $\boldsymbol{\omega}$ in eq 162. Since \mathbf{b}' is a subset of \mathbf{b}'' , we may express the eigenvectors in the \mathbf{b}' subspace in terms of the eigenvectors of the \mathbf{b}'' subspace as

$$\mathbf{X}'_{p+} = \sum_{q=1}^{N+1} [a_{p+q+}\mathbf{X}''_{q+} + a_{p+q-}\mathbf{X}''_{q-}] \quad (167)$$

where the normalization of \mathbf{X}'_{p+} in the $\mathbf{S}^{[2]}$ -norm implies

$$\sum_{q=1}^{N+1} [|a_{p+q+}|^2 - |a_{p+q-}|^2] = 1 \quad (168)$$

The lowest positive eigenvalue in \mathbf{b}' is equal to

$$\omega'_{1+} = (\mathbf{X}'_{1+})^\dagger \mathbf{E}^{[2]}\mathbf{X}'_{1+} \quad (169)$$

However, by means of eq 167, the same eigenvalue can also be expressed as

$$\begin{aligned} \omega'_{1+} &= \sum_{n,m=1}^{N+1} [a_{1+n+}\mathbf{X}''_{n+} + a_{1+n-}\mathbf{X}''_{n-}]^\dagger \mathbf{E}^{[2]} [a_{1+m+}\mathbf{X}''_{m+} + a_{1+m-}\mathbf{X}''_{m-}] \\ &= \sum_m^{N+1} \omega''_{m+} [|a_{1+m+}|^2 + |a_{1+m-}|^2] \\ &\geq \sum_m^{N+1} \omega''_{1+} [|a_{1+m+}|^2 + |a_{1+m-}|^2] \\ &\geq \omega''_{1+} \sum_m^{N+1} [|a_{1+m+}|^2 + |a_{1+m-}|^2] \\ &= \omega''_{1+} \end{aligned} \quad (170)$$

We have thus shown that $\omega'_{1+} \geq \omega''_{1+}$ for iterative solutions of the response eigenvalue equation. This result represents a generalization of MacDonald's theorem for a symmetric positive definite eigenvalue equation with a positive definite metric.

APPENDIX D. ALGORITHMS BASED ON BLOCK DIAGONALIZATION OF THE HESSIAN

Another approach for solving the standard response equations has been presented by Casida.² This approach is analogous to the approach introduced by Jørgensen et al. in ref 11. In the approach in ref 2, the standard response equation:

$$\left[\begin{pmatrix} \mathbf{A} & \mathbf{B} \\ \mathbf{B} & \mathbf{A} \end{pmatrix} - \omega \begin{pmatrix} \boldsymbol{\Sigma} & 0 \\ 0 & -\boldsymbol{\Sigma} \end{pmatrix} \right] \begin{pmatrix} \mathbf{X} \\ \mathbf{Y} \end{pmatrix} = \begin{pmatrix} \mathbf{G}_1 \\ \mathbf{G}_2 \end{pmatrix} \quad (171)$$

is transformed by means of the unitary transformation \mathbf{U} in eq 22, to become equal to

$$\left[\begin{pmatrix} \mathbf{A} + \mathbf{B} & 0 \\ 0 & \mathbf{A} - \mathbf{B} \end{pmatrix} - \omega \begin{pmatrix} 0 & -\boldsymbol{\Sigma} \\ -\boldsymbol{\Sigma} & 0 \end{pmatrix} \right] \begin{pmatrix} \mathbf{X}' \\ -\mathbf{Y}' \end{pmatrix} = \begin{pmatrix} \mathbf{G}'_1 \\ -\mathbf{G}'_2 \end{pmatrix} \quad (172)$$

where

$$\begin{aligned} \mathbf{X}' &= \mathbf{X} + \mathbf{Y}; \quad \mathbf{Y}' = \mathbf{X} - \mathbf{Y}; \quad \mathbf{G}'_1 = \mathbf{G}_1 + \mathbf{G}_2; \\ \mathbf{G}'_2 &= \mathbf{G}_1 - \mathbf{G}_2 \end{aligned} \quad (173)$$

From eq 172 two separate equations are obtained namely:

$$\begin{aligned} [(\mathbf{A} + \mathbf{B}) - \omega^2 \mathbf{S}(\mathbf{A} - \mathbf{B})^{-1} \boldsymbol{\Sigma}] \mathbf{X}' \\ = \mathbf{G}'_1 + \omega \boldsymbol{\Sigma}(\mathbf{A} - \mathbf{B})^{-1} \mathbf{G}'_2 \end{aligned} \quad (174)$$

and

$$\begin{aligned} [(\mathbf{A} - \mathbf{B}) - \omega^2 \boldsymbol{\Sigma}(\mathbf{A} + \mathbf{B})^{-1} \boldsymbol{\Sigma}] \mathbf{Y}' \\ = \mathbf{G}'_2 - \omega \boldsymbol{\Sigma}(\mathbf{A} + \mathbf{B})^{-1} \mathbf{G}'_1 \end{aligned} \quad (175)$$

The solution to the standard response equation is thus replaced by solving two sets of linear equations of half the dimension. When solving eqs 174 and 175, the inverse matrices $(\mathbf{A} - \mathbf{B})^{-1}$ and $(\mathbf{A} + \mathbf{B})^{-1}$ are required. When the matrices $(\mathbf{A} - \mathbf{B})$ and $(\mathbf{A} + \mathbf{B})$ are constructed explicitly, the inverse matrices may be obtained straightforwardly. But, when the matrix dimension is large and the iterative subspace algorithms need to

be used, the separation of eq 172 into eqs 174 and 175 becomes prohibitively inefficient. The response equations are better solved in a form referencing the double dimension in eq 172, as in eq 97, thereby separating the determination of the symmetric and antisymmetric components of the solution vector and maintaining the full coupling between the symmetric and antisymmetric components.

AUTHOR INFORMATION

Corresponding Author

*E-mail: joaka@ifm.liu.se.

ACKNOWLEDGMENT

J.K. and P.J. acknowledge Dr. Jeppe Olsen for very helpful and constructive discussions. J.K. and P.J. acknowledge support from the Lundbeck Foundation and the Danish Center for Scientific Computing. P.N. acknowledges financial support from the Swedish Research Council (grant no. 621-2010-5014).

REFERENCES

- (1) Olsen, J.; Jørgensen, P. *J. Chem. Phys.* **1985**, *82*, 3235–3264.
- (2) Casida, M. E. In *Recent Advances in Density Functional Methods*, Part 1; Chong, D. P., Ed.; World Scientific: Singapore, 1995; Vol. 1; Chapter 5, pp 155–192.
- (3) Norman, P.; Bishop, D. M.; Jensen, H. J. A.; Oddershede, J. *J. Chem. Phys.* **2001**, *115*, 10323–10334.
- (4) Norman, P.; Bishop, D. M.; Jensen, H. J. A.; Oddershede, J. *J. Chem. Phys.* **2005**, *123*, 194103–194120.
- (5) Kristensen, K.; Kauczor, J.; Kjergaard, T.; Jørgensen, P. *J. Chem. Phys.* **2009**, *131*, 044112(33).
- (6) Orr, B. J.; Ward, J. F. *Mol. Phys.* **1971**, *20*, 513–526.
- (7) Boyd, R. W. *Nonlinear Optics*, 3rd ed.; Academic Press: Burlington, MA, 2008; pp 155–157.
- (8) Bunch, J. R.; Hopcroft, J. E. *Math. Comp.* **1974**, *28*, 231–236.
- (9) Atkinson, K. A. *An Introduction to Numerical Analysis*, 2nd ed.; John Wiley & Sons: New York, 1989; pp 511–525.
- (10) Trefethen, L. N.; Bau, D., III *Numerical Linear Algebra*; SIAM: Philadelphia, PA, 1997; pp 172–178.
- (11) Jørgensen, P.; Linderberg, J. *Int. J. Quantum Chem.* **1970**, *4*, 587–602.
- (12) Pople, J. A.; Krishnan, R.; Schlegel, H.; Binkley, J. S. *Int. J. Quantum Chem.* **1979**, *13*, 225–241.
- (13) Purvis, G. D.; Bartlett, R. J. *J. Chem. Phys.* **1981**, *75*, 1284–1292.
- (14) Wormer, P. E. S.; Visser, F.; Paldus, J. J. *Comput. Phys.* **1982**, *48*, 23–44.
- (15) Hestenes, M. R.; Stiefel, E. *J. Res. Natl. Bur. Stand., Sect. A* **1952**, *49*, 409–436.
- (16) Press, W. H.; Teukolsky, S. A.; Vetterling, W. T.; Flannery, B. P. *Numerical Recipes in C++: The Art of Scientific Computing*, 3rd ed.; Cambridge University Press: Cambridge, U.K., 2007; pp 87–92.
- (17) Shewchuk, J. R. *An Introduction to the Conjugate Gradient Method Without the Agonizing Pain*; Carnegie Mellon University: Pittsburgh, PA, 1994.
- (18) Saad, Y. *Iterative Methods for Sparse Linear Systems*; SIAM: Philadelphia, PA, 2003; pp 187–194.
- (19) Stiefel, E. *Comment. Math. Helv.* **1955**, *29*, 157–179.
- (20) Niklasson, A. M. N.; Challacombe, M. *Phys. Rev. Lett.* **2004**, *92*, 193001(4).
- (21) Coriani, S.; Høst, S.; Jansik, B.; Thøgersen, L.; Olsen, J.; Jørgensen, P.; Reine, S.; Pawłowski, F.; Helgaker, T.; Sałek, P. *J. Chem. Phys.* **2007**, *126*, 154108(11).
- (22) Davidson, E. R. *J. Comput. Phys.* **1975**, *17*, 87–94.
- (23) Flament, J. P.; Gervais, H. P. *Int. J. Quantum Chem.* **1979**, *16*, 1347–1356.
- (24) Hansen, A. E.; Voigt, B.; Rettrup, S.; Bouman, T. D. *Int. J. Quantum Chem.* **1983**, *23*, 595–611.
- (25) Olsen, J.; Jensen, H. J. A.; Jørgensen, P. *J. Comput. Phys.* **1988**, *74*, 265–282.
- (26) Olsen, J.; Jørgensen, P.; Simons, J. *Chem. Phys. Lett.* **1990**, *169*, 463–476.
- (27) Saue, T. In *Relativistic Electronic Structure Theory - Part 1: Fundamentals*; Schwerdtfeger, P., Ed.; Elsevier, Amsterdam, The Netherlands, 2002; Chapter 7, pp 332–400.
- (28) Saue, T.; Jensen, H. J. A. *J. Chem. Phys.* **2003**, *118*, 522–536.
- (29) Bast, R.; Jensen, H. J. A.; Saue, T. *Int. J. Quantum Chem.* **2009**, *109*, 2091–2112.
- (30) Villaume, S.; Saue, T.; Norman, P. *J. Chem. Phys.* **2010**, *133*, 064105(10).
- (31) Kjergaard, T.; Jørgensen, P.; Olsen, J.; Coriani, S.; Helgaker, T. *J. Chem. Phys.* **2008**, *129*, 054106(23).
- (32) Čížek, J.; Paldus, J. *J. Chem. Phys.* **1967**, *47*, 3976–3985.
- (33) Larsen, H.; Jørgensen, P.; Olsen, J.; Helgaker, T. *J. Chem. Phys.* **2000**, *113*, 8908–8917.
- (34) Axelsson, O. *Iterative Solution Methods*; Cambridge University Press: Cambridge, U.K., 1996; pp 252–254.
- (35) Helgaker, T.; Jørgensen, P.; Olsen, J. *Molecular Electronic Structure Theory*; Wiley: Chichester, U.K., 2000; pp 543–548.
- (36) Parlett, B. N. *The Symmetric Eigenvalue Problem*; Prentice Hall: Englewood Cliff, New Jersey, 1980; pp 75–80.
- (37) MacDonald, J. K. L. *Phys. Rev.* **1933**, *43*, 830–833.
- (38) Ziolkowski, M.; Weijo, V.; Jørgensen, P.; Olsen, J. *J. Chem. Phys.* **2008**, *128*, 204105(12).
- (39) Helgaker, T.; Jensen, H. J. A.; Jørgensen, P.; DALTON an ab initio electronic structure program, release 2.0, 2005; <http://www.kjemi.uio.no/software/dalton/dalton.html>.
- (40) Hehre, W. J.; Ditchfield, R.; Pople, J. A. *J. Chem. Phys.* **1972**, *56*, 2257–2261.
- (41) NIST Standard Reference Database Number 69; NIST: Gaithersburg, MD; <http://webbook.nist.gov/chemistry>.
- (42) Maestro, v. 8.5; Schrodinger, LLC: Cambridge, MA, 2008; <http://www.schrodinger.com>.
- (43) Becke, A. D. *J. Chem. Phys.* **1993**, *98*, 5648–5652.
- (44) Stephens, P. J.; Devlin, F. J.; Chabalowski, C. F.; Frisch, M. J. *J. Phys. Chem.* **1994**, *98*, 11623–11627.
- (45) Dunning, T. H. *J. Chem. Phys.* **1989**, *90*, 1007–1023.
- (46) Genick, U. K.; Soltis, S. M.; Kuhn, P.; Canestrelli, I. L.; Getzoff, E. D. *Nature* **1998**, *392*, 206–209.
- (47) Yanai, T.; Tew, D. P.; Handy, N. C. *Chem. Phys. Lett.* **2004**, *393*, 51–57.
- (48) Pulay, P. *Chem. Phys. Lett.* **1980**, *73*, 393–398.
- (49) Pulay, P. *J. Comput. Chem.* **1982**, *3*, 556–560.

Placing Rigorous Bounds on Numerical Errors in Hartree–Fock Energy Computations

Pete P. Janes and Alistair P. Rendell*

Research School of Computer Science, The Australian National University, Canberra, Australia

ABSTRACT: The accuracy of electronic structure calculations are affected to some degree by numerical errors. Assessing whether these errors are at an acceptable level for chemical accuracy is difficult. This paper demonstrates how interval arithmetic can be used to address this issue in the context of a Hartree–Fock computation. Using the method proposed here, the effect of system size and basis set type on the overall numerical accuracy of the Hartree–Fock total energy is studied. Consideration is also given to the impact of various algorithmic design decisions. Examples include the use of integral screening, computing some integrals in single precision, and reducing the accuracy of the interpolation tables used to compute the reduced incomplete Gamma function required by some integral evaluation algorithms. All of these issues have relevance to the use of novel computing devices such as graphics processing units (GPU) and the Sony Toshiba IBM Cell Broadband, to exascale and green computing, and to the exploitation of the emerging generation of massively multicore processors.

1. INTRODUCTION

During the past 20 years, the vast majority of computational chemistry programs have been written to use IEEE 754 double precision floating point arithmetic.¹ This was motivated both by the perception that double precision was required in order to obtain sufficiently accurate results and the fact that efficient implementations of this standard were available on all commonly used high performance microprocessors. With a few notable exceptions,^{2,3} relatively little attention was given to using alternative levels of numerical precision. In the past few years, this situation has changed dramatically. This has been largely prompted by the move by manufacturers of graphics and gaming hardware into the general purpose computing market, the ability of this new hardware to perform floating point computations at a rate that was significantly higher than that of contemporary general purpose microprocessors, and the fact that this was (initially) only possible when using single precision arithmetic with rounding modes that were not entirely IEEE 754 compliant. Two high profile early examples are the Sony Toshiba IBM (STI) Cell Broadband Engine⁴ that forms the basis for the Playstation 3 and the NVIDIA GTX8800 CUDA based graphics card.⁵

More recently, initiatives in exascale computing, green computing, and many-core architectures have provided added impetus for reconsidering the role of numerical precision in computational chemistry codes. In these cases, the sheer number of operations performed, the energy required to perform the operations, and the available bandwidth for moving data on and off the processor chip are all causes for wanting to represent data with the minimal number of bytes possible. Also, developments in field programmable gate array (FPGA) technology mean that computational devices can now be constructed on the fly to use arbitrary levels of precision that may not be standard single or double precision.

Mindful of the above, we have developed a Hartree–Fock code that uses interval arithmetic to place rigorous bounds on the numerical errors associated with computing the total electronic

energy. Our aim is to build a tool that can be used to explore the effects of numerical precision and various other underlying numerical approximations on the quality of the final result. Examples considered here include the effects of basis set and system size, as well as “hidden” issues such as the use of different levels of integral prescreening and the choice of different interpolation schemes for evaluating the base quantities from which all two-electron integrals are assembled.

In *interval analysis*,⁶ a quantity is represented as an interval $X = [\underline{X}, \bar{X}]$, which contains the set of all real numbers between a *lower bound* \underline{X} and an *upper bound* \bar{X} . Intervals can be used to bound all uncertainties and errors, including those caused by rounding to finite precision, truncation or approximating a series, limits in the accuracy of a measured quantity, etc. When computing with intervals, the uncertainties encapsulated within each interval are propagated on to the final result. That is, the final result is an interval which rigorously bounds the entire range of possible results when all of those uncertainties are taken into account. Inferences can then be made about the errors associated with the result based on the width of the final interval.

In comparison to a traditional code that represents a data quantity using a single floating point number, an interval code will use two floating point numbers, one representing the lower bound and one representing the upper bound. Where a traditional floating point code rounds the result of a floating point operation to a machine representable number, an interval code must broaden the interval result to the nearest machine representable interval that includes the exact interval result. Interval codes should also take care to include errors associated with truncating infinite series when reporting the result, e.g., in functions to compute e^x , $\log(x)$, $\sin(x)$, etc. Needless to say, the goal in an interval code is to minimize the width of the final interval.

Received: January 12, 2011

Published: May 13, 2011

The work reported here follows on from a number of related works. Specifically, Takashima et al.⁷ investigated whether large scale Hartree–Fock energy (E_{HF}) calculations were chemically accurate given a potentially large accumulation of numerical errors. Their study focused on the calculation of E_{HF} , given an initial set of integrals and a density matrix. Error contaminated data were simulated by uniformly perturbing each double precision floating point quantity involved in the Fock matrix construction step at the last bit of the mantissa. The error was measured by comparing E_{HF} calculated using contaminated data with E_{HF} calculated using uncontaminated data, calculating both cases using double precision floating point arithmetic. This approach can be implemented using existing quantum chemistry software, although it makes the broad assumption that the errors in the initial data are uniformly perturbed. By contrast, when using intervals, errors are modeled without making such assumptions. In the same study, the authors applied a technique known as partial summation to improve the accuracy of E_{HF} and used linear regression to predict errors for very large problems involving 10 000 basis functions.

Ramdas et al.³ proposed the use of interval arithmetic as an *off-line design space tool* to experiment with different arithmetic unit configurations. In particular, they were interested in whether a mix of different arithmetic precisions could be used for calculating the Hartree–Fock energy on an FPGA, while maintaining an acceptable degree of chemical accuracy. Their work adopted the same approach as Yasuda:² determining which integral or batches of integrals to calculate using single precision based on its Schwarz⁸ upper bound, the assumption being that smaller integrals can be calculated in single precision without substantially affecting the accuracy of the final result. The investigation in Ramdas et al. was, however, confined to a single H₂O molecule using the 6-31G** basis set.

The rest of this paper is organized as follows. Section 2 gives a more detailed description of interval analysis and how it can be used as an error analysis tool. Section 3 outlines the interval implementation of the Hartree–Fock method, while section 4 details the experimental methodology used and presents and discusses the results. Section 5 concludes the paper and discusses future work.

2. INTERVAL ANALYSIS

Interval arithmetic was proposed by Ramon Moore in 1959.⁹ It represents numerical quantities in terms of closed intervals $X = [\underline{X}, \bar{X}]$, where each interval represents the set of all real numbers between the lower bound $\underline{X} \in \mathbb{R}$ and upper bound $\bar{X} \in \mathbb{R}$. The set of interval numbers is denoted as $I(\mathbb{R})$, whereas the set of n dimensional vectors with interval elements is denoted as $I(\mathbb{R}^n)$.

Intervals were first proposed as a tool for bounding rounding errors;⁹ however, in practice, an interval can be used to bound any uncertain quantity. This includes any combination of rounding errors, truncation errors, measurement errors, unknown/poorly understood parameters, etc.

2.1. Interval Arithmetic. The set of basic arithmetic operations, $\bullet = +, -, \times$, between two intervals is defined such that

$$X \bullet Y = \{x \bullet y | x \in X, y \in Y\} \quad (1)$$

By this definition, the arithmetic operations between two intervals $X \in I(\mathbb{R})$ and $Y \in I(\mathbb{R})$ result in another interval that contains the results of operations between all possible combinations of real values contained in X and Y . This property is generally

referred to as the *containment property* for interval arithmetic operations.¹⁰

For practical purposes, interval arithmetic operations are almost always carried out using IEEE 754 floating point arithmetic, referred to as *Floating Point Interval Arithmetic*.⁶ To ensure containment, both upward and downward rounding modes (instead of round to nearest) are used:

$$\begin{aligned} X + Y &= [\oplus_{\nabla}(\underline{X}, \underline{Y}), \oplus_{\Delta}(\bar{X}, \bar{Y})] && \text{addition} \\ X - Y &= [\ominus_{\nabla}(\underline{X}, \bar{Y}), \oplus_{\Delta}(\bar{X}, \underline{Y})] && \text{subtraction} \\ X \times Y &= [a, b] && \text{multiplication} \\ a &= \min(\otimes_{\nabla}(\underline{X}, \underline{Y}), \otimes_{\nabla}(\underline{X}, \bar{Y}), \\ &\quad \otimes_{\nabla}(\bar{X}, \underline{Y}), \otimes_{\nabla}(\bar{X}, \bar{Y})) \\ b &= \max(\otimes_{\Delta}(\underline{X}, \underline{Y}), \otimes_{\Delta}(\underline{X}, \bar{Y}), \\ &\quad \otimes_{\Delta}(\bar{X}, \underline{Y}), \otimes_{\Delta}(\bar{X}, \bar{Y})) \\ 1/Y &= [\oslash_{\nabla}(1, \bar{Y}), \oslash_{\nabla}(1, \underline{Y})] && \text{division} \\ X/Y &= X \times 1/Y && (2) \end{aligned}$$

where the subscripts Δ and ∇ refer respectively to upward and downward rounding. With no specific hardware support, interval arithmetic requires more instructions and storage to implement than floating point arithmetic.

2.2. Interval Functions. An *interval function* is a function which takes a set of intervals as input and returns a set of intervals as output.⁶ The containment principle is extended to interval functions. We say that an interval function $\mathbf{F}: I(\mathbb{R}^m) \rightarrow I(\mathbb{R}^n)$ is an *interval extension*⁶ of a function $\mathbf{f}: \mathbb{R}^m \rightarrow \mathbb{R}^n$ if

$$\mathbf{F}(\mathbf{X}) \supseteq \{\mathbf{f}(\mathbf{x}) | \mathbf{x} \in \mathbf{X}\} \quad (3)$$

An interval extension of \mathbf{f} therefore contains the range of \mathbf{f} over the domain spanned by $\mathbf{X} \in I(\mathbb{R}^m)$. Furthermore, if $\mathbf{g}(\mathbf{x})$ is an approximation function of $\mathbf{f}(\mathbf{x})$ and ε is the maximum truncation error in \mathbf{X} , then if $\mathbf{G}(\mathbf{X})$ is the interval extension of $\mathbf{g}(\mathbf{x})$, we can write the interval extension of $\mathbf{f}(\mathbf{x})$ as $\mathbf{F}(\mathbf{X}) = [\mathbf{G}(\mathbf{X}) - \varepsilon, \mathbf{G}(\mathbf{X}) + \varepsilon]$.

The interval extension of standard mathematical functions such as e^X , $\log(X)$, $\sin(X)$, and $\cos(X)$ are relatively straightforward to implement, e.g., $e^X = [e^{\underline{X}}, e^{\bar{X}}]$. For *rational functions*⁶ whose expression consists entirely of the four basic arithmetic operations, interspersed with standard mathematical functions for which an interval extension is known, there is a also relatively straightforward procedure to obtain an interval extension: first, write the mathematical expression for the function; then, replace each elementary arithmetic operation by its equivalent interval arithmetic operation and each standard function by its interval extension, and then replace each variable by an interval. An interval extension formulated using this procedure is known as a *natural interval extension*.⁶

2.3. Interval Arithmetic for Error Analysis. Interval extensions provide a way to calculate rigorous bounds on the range of function values due to uncertain inputs. In combination with interval arithmetic, it allows uncertainties caused by rounding and truncation errors to be propagated toward the final result.

The final interval will almost always overestimate the actual numerical errors due to the fact that interval arithmetic must account for the worst possible interaction between the interval quantities involved in the calculation. The problem of finding the exact range over a given domain of uncertainty is generally an NP-Hard problem. This implies that interval arithmetic can only provide a *worst-case error analysis* of the calculation in question.

Therefore, we can only rigorously state what set of factors can or cannot guarantee accuracy within a given threshold. However, other useful inferences can be made about the behavior of numerical errors, albeit with the above caveat in mind.

Another issue that also causes interval error overestimation is the *dependency problem*.¹⁰ Interval arithmetic assumes all quantities are independent of one another. Ignoring the dependencies between quantities leads to illogical results. For example, suppose $X = [0,1]$; then using interval arithmetic, $X - X$ returns $[-1,1]$ instead of $[0,0]$. It is not difficult to deduce that this problem is likely to affect most interval calculations, except those involving expressions where each variable occurs only once, such as $X_1 + X_2 + X_3 + \dots$. In this work, however, the dependency effects will be small, as we mainly deal with near-degenerate intervals containing relatively small rounding and truncation errors.

Similar approaches which allow errors to be propagated exist in uncertainty and sensitivity analysis,¹¹ almost all of these involve extensively sampling the domain of uncertain variables in order to obtain a statistical representation of variations in the result. However, this approach is difficult to apply for larger models with many uncertain quantities. In Takashima et al.,⁷ the errors in the Hartree–Fock total energy due to numerical errors in the input (the one and two electron integrals) are estimated by comparing the results calculated from a set of perturbed inputs to those calculated from a set of unperturbed inputs. This is not as rigorous as a sampling based approach but reflects the difficulties involved in effectively sampling a large set of uncertain parameters which exists in a typical Hartree–Fock calculation.

3. INTERVAL HARTREE–FOCK

Hartree–Fock theory provides an *ab initio* model of the interactions between particles on the molecular scale. Although not a particularly accurate model, it provides the framework from which many other, more advanced, methods are derived. For this reason, Hartree–Fock theory is still widely used as a starting point for studies of electronic structure. The Hartree–Fock energy for a closed shell molecular system with n electrons can be expressed as

$$E_{\text{HF}} = V_{nn} + 2 \sum_{\mu}^{n/2} H_{\mu} + \sum_{\mu}^{n/2} \sum_{\nu}^{n/2} (2J_{\mu,\nu} - K_{\mu,\nu}) \quad (4)$$

where V_{nn} is the nuclear repulsion energy and H_{μ} , $J_{\mu,\nu}$, and $K_{\mu,\nu}$ are integrals over the *Core-Hamiltonian*, *Coulomb*, and *Exchange* operators. The latter are defined in terms of the molecular orbitals (Φ) as

$$\begin{aligned} H_{\mu} &= (\Phi_{\mu} | H_{\text{core}} | \Phi_{\mu}) \\ J_{\mu,\nu} &= (\Phi_{\mu} \Phi_{\mu} | \Phi_{\nu} \Phi_{\nu}) \\ K_{\mu,\nu} &= (\Phi_{\mu} \Phi_{\nu} | \Phi_{\mu} \Phi_{\nu}) \end{aligned} \quad (5)$$

with the Coulomb and Exchange integrals collectively referred to as the two-electron repulsion integrals (ERI).

Normally, the set of molecular orbitals $\{\phi\}$ is expanded in terms of a linear combination of N atomic orbitals $\{\chi\}$:

$$\phi_{\mu} = \sum_{a=1}^N C_{\mu a} \chi_a \quad (6)$$

where $\mathbf{C} = \{C_{\mu a}\}$, $\forall \mu, a \in \{1, 2, 3, \dots, N\}$ are the *molecular orbital coefficients*.

For most practical purposes, the atomic orbitals in the LCAO are represented by *Contracted Gaussian Functions* (CGF):

$$\begin{aligned} \chi_a(r) &= \sum_{k=1}^{K_a} D_{ak} \chi_{ak}(r), \text{ where} \\ \chi_{ak}(r) &= (X - X_a)^{x_a} (Y - Y_a)^{y_a} (Z - Z_a)^{z_a} e^{\alpha_{ak}|r - r_a|^2} \end{aligned} \quad (7)$$

where K_a is the degree of contraction for function a , D_{ak} is a contraction coefficient, and $\chi_{ak}(r)$ is a *Primitive Gaussian Function* (PGF) with exponent $\{\alpha_{ai}\}$, coordinates $r_a = (X_a, Y_a, Z_a)$, and angular components $l_a = \{x_a, y_a, z_a\}$.

A Self-Consistent Field (SCF) calculation involves minimizing the value of E_{HF} with respect to the molecular orbital coefficients \mathbf{C} to produce the ground state energy, E_0 . This problem can be solved iteratively by reformulating the minimization problem as a nonlinear eigenvalue problem known as the *Roothaan equations*

$$\mathbf{FC} = \mathbf{SC}\epsilon \quad (8)$$

where $\mathbf{F} \in \mathbb{R}^{N \times N}$ is the *Fock matrix* that represents the one and two-electron interactions, $\mathbf{S} \in \mathbb{R}^{N \times N}$ is the *overlap matrix* that represents the overlap between atomic orbitals, and $\epsilon \in \mathbb{R}^{N \times N}$ is the *molecular orbital energies*.

In this paper, we focus on evaluating the numerical errors in the ground state Hartree–Fock total energy E_{HF} —using as input the set of ground state molecular orbital coefficients calculated using a conventional floating point SCF code. The interval bounds of the total energy reflect errors propagated from (i) the one- and two-electron integrals, (ii) the construction of the Fock matrix, (iii) the calculation of the nuclear repulsion, and (iv) the calculation of the total energy. The three latter steps are implicit in eq 4.

Of the various operations performed during a Hartree–Fock/self-consistent field calculation, evaluating the ERIs is by far the most computationally demanding.¹² It is also the aspect of the calculation that requires the most attention when developing an interval Hartree–Fock code.

A primitive ERI involving four atomic orbitals is given by

$$[\chi_a \chi_b | \chi_c \chi_d] \equiv \int \int \frac{\chi_a(r_1) \chi_b(r_1) \chi_c(r_2) \chi_d(r_2) \, dr_1 \, dr_2}{|r_1 - r_2|} \quad (9)$$

while a contracted ERI is given by

$$[\chi_a \chi_b | \chi_c \chi_d] \equiv \sum_{i=1}^{K_i} \sum_{j=1}^{K_j} \sum_{k=1}^{K_k} \sum_{l=1}^{K_l} D_{ai} D_{bj} D_{ck} D_{dl} [\chi_{ai} \chi_{bj} | \chi_{ck} \chi_{dl}] \quad (10)$$

with the number of ERIs required for a given problem scaling as $O(N^4)$ in the problem size.

There are a number of numerical approaches for evaluating primitive ERIs. Some of the most widely used are by *McMurchie–Davidson*¹³ (MD), *Obara–Saika*¹⁴ (OS), *Rys–Depuis–King*¹⁵ (RDK), and *Head-Gordon–Pople*¹⁶ (HGP). All of these schemes use recursion relations to assemble the final integral from some very simple integrals. In the case of the MD, OS, and HGP schemes, the simple integrals are *Reduced Incomplete Gamma Functions*¹⁷ which are denoted as $F_m(T)$:

$$F_m(T) = \int_0^1 t^{2m} e^{-Tt} \, dt \quad (11)$$

In the above, T is a real non-negative number with a value that is dependent on the distance between the basis function centers and

Table 1. Decimal Digits of Precision of E_{HF} for TIP4P Water Clusters of n Water Molecules Computed Using 3-21G, 6-31G**, cc-pVDZ, 6-31G++**, and 6-311G(2df,2pd) Basis Sets^a

$(\text{H}_2\text{O})_n$	N	3-21G	N	6-31G**	N	cc-pVDZ	N	6-31++G**	N	6-311G(2df,2pd)
2	26	12.63	50	12.26	50	12.14	62	11.98	130	11.48
3	39	12.30	75	11.92	75	11.76	93	11.63	195	11.12
4	52	12.08	100	11.69	100	11.57	124	11.41	260	10.88
5	65	11.87	125	11.48	125	11.31	155	11.19	325	10.56
6	78	11.70	150	11.29	150	11.16	186	11.01		
7	91	11.56	175	11.15	175	11.04	217	10.85		
8	104	11.41	200	11.00	200	10.85	248	10.69		
9	117	11.28	225	10.88	225	10.73	279	10.58		
10	130	11.17	250	10.77	250	10.64	310	10.46		
11	143	11.08								
12	156	11.00								
13	169	10.92								
14	182	10.84								
15	195	10.77								

^a N is the number of basis functions.

the values of their exponents, while m is an integer with a value that depends on the total angular momentum of all of the Gaussian functions in the ERI.

There are no general analytical approaches for evaluating $F_m(T)$. Many years ago, Shavitt presented a scheme for evaluating $F_m(T)$ that used either a series or an asymptotic approximation depending on the value of T .¹⁸ This approach was subsequently refined to involve precomputing a select number of values for $F_m(T)$ using the Shavitt scheme and then using Taylor or Chebyshev polynomial interpolation to compute specific values.¹⁹ Truncation errors arise in both the Shavitt scheme and in the interpolation, and it is important that any interval scheme to evaluate ERIs correctly bounds both of these sources of errors. We discuss how to achieve this in a previous paper.²⁰

3.1. Implementation Details. The interval extension of the Hartree–Fock energy (eq 4) was formulated as a natural interval extension using the procedure described in section 2.2. For this study, ERIs are evaluated using a natural interval extension of the Head-Gordon–Pople (HGP) algorithm,¹⁶ with values of $F_m(T)$ evaluated by default using sixth-degree Chebyshev polynomial interpolation. Truncation errors in $F_m(T)$ were manually bounded and propagated.

4. COMPUTATIONAL RESULTS

The following experiments investigate the numerical errors in E_{HF} as the size and complexity of the molecular problem increases, and when different algorithms are used. We focus particularly on issues relevant to the use of Graphics Processing Units (GPUs). It is important to note, however, that all the results given here are obtained using the interval HF code run on a conventional CPU; that is, we are using the interval code to pose “what-if” questions without needing to have access to hardware that supports that “what-if” scenario. Before considering the experiments in detail, it is pertinent first to define and discuss the error terminology used.

Supposing that E_{HF}^{I} is the interval bound of E_{HF} , the relative numerical error is expressed as

$$\text{err} = 2.0 \times \frac{\overline{E_{\text{HF}}^{\text{I}}} - \underline{E_{\text{HF}}^{\text{I}}}}{\overline{E_{\text{HF}}^{\text{I}}} + \underline{E_{\text{HF}}^{\text{I}}}}$$

This is equivalent to dividing the width of E_{HF}^{I} by its midpoint. For clarity, we will often state the result in terms of *precision* instead of error, where $-\log_{10}(\text{err})$ is used to indicate the number of *decimal digits of precision* in the result. For instance, $\text{err} = 1 \times 10^{-13}$ implies 13 decimal digits of precision. If the computation is implemented in double precision, there are a maximum of 16 decimal digits, so a relative error of 1×10^{-13} implies that three decimal digits have been lost due to numerical errors. The results should be construed as an estimate of errors in the *worst case*, since we are using interval arithmetic.

The total electronic energy is generally regarded to be *chemically accurate* if its error is no greater than 0.01 kcal/mol or around 1.59×10^{-5} Hartree.⁷ As a consequence, larger systems with larger total energies will require more digits of precision in order to be chemically accurate. However, calculations on large molecules also require more operations to be performed so there is greater potential for accumulating errors. As interval arithmetic bounds the numerical errors, it can be used to rigorously guarantee that chemical accuracy is achieved.

Experimental Platform. All experiments were conducted on a Sun Microsystems V1280 UltraSPARCIIIICu System with 12×900 MHz cores, using the Solaris 10 operating system.²¹ All programs were implemented in either C++ or SPARC assembler and compiled using SunStudio 11 compilers at patch level 20060426.²² The build options used are

```
-fast -xopenmp -xia -xtarget=ultra3 -
xarch=v9b -xlic_lib=sunperf
```

where the `-xia` flag enables the interval arithmetic library.²³ Source code for all the interval SCF programs used here is available at the authors' Web site.²⁴

4.1. Effect of System Size and Basis Set. To study the effects of system and basis set size, we have used H_2O clusters of varying size and basis sets that range from the near minimal 3-21G set to the extensive 6-311G(2df,2pd) basis set. The geometries used are those of the TIP4P water clusters at the Cambridge Cluster Database.²⁵

Results are shown in Table 1 for systems with total basis set sizes of up to around 325 basis functions. As expected, increasing the number of atoms and/or the basis set size decreases the number of decimal digits of precision. Use of the 3-21G basis set

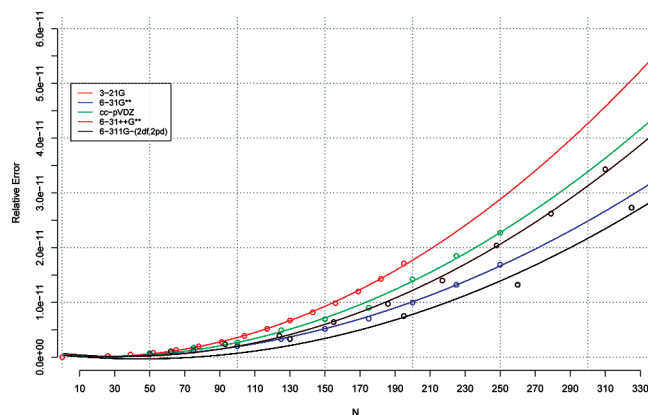


Figure 1. Relative error of E_{HF} for water clusters fitted against the number of basis functions N using second degree polynomial regression.

and going from 2 to 15 water molecules results in a loss of two significant figures in the total energy. In terms of chemical accuracy, another significant figure is effectively lost as the total energy also increases by more than 1 order of magnitude on going from 2 to 15 water molecules. With 15 water molecules and a total energy on the order of 10^3 , 10.77 digits of decimal precision are still, however, enough to give total energies accurate to 10^{-5} Hartrees.

For the smaller systems, increasing the basis set size from 3-21G to 6-311G (2df,2pd) also results in a loss of more than one decimal digit of precision in E_{HF} . Comparing the 6-31G** and cc-pVDZ basis sets, both of which have the same number of contracted functions but were achieved using different contraction schemes, reveals that the cc-pVDZ correlation consistent basis set gives slightly fewer digits of precision. Adding diffuse functions to the 6-31G** basis gives a slight further loss in precision. Interestingly, the number of digits of precision appears to be relatively constant for a given total number of functions regardless of whether this results from a large number of atoms or from a large basis set.

To explore the latter point further, we plot in Figure 1 the relative errors from Table 1 as a function of N . A second-degree polynomial regression was used to fit the data for each basis set type. The R^2 (coefficient of determination) values of the regressions were found to be 0.9989, 0.9983, 0.9958, 0.9977, and 0.9841 for the 3-21G, 6-31G**, cc-pVDZ, 6-31++G, and 6-311G (2df,2pd) basis sets, respectively. This strongly suggests that a second-degree polynomial model is sufficient to explain the variation of numerical errors with N . Linear regression was also considered, but it was found not to yield as good a fit. The success of the second polynomial is likely to be related to the numerical complexity of the Hartree–Fock method. For example, in an N -term summation of $O(N)$ complexity, the growth in numerical errors is on the order $O(N)$ but also depends on the type of terms involved.²⁶ In the Hartree–Fock method, the numerical complexity grows as $O(N^4)$. For real systems, however, larger problem sizes mean larger spatial extent, and since the Coulombic interaction decreases with distance, it is not surprising to find that the numerical errors increase in a nonlinear fashion, but at a rate that is less than quartic. Finally, aggregating together the results for all basis set types and then applying regression also leads to a poorer fit.

While the least precise result found in Table 1 is still well within chemical accuracy, the loss of precision will become an

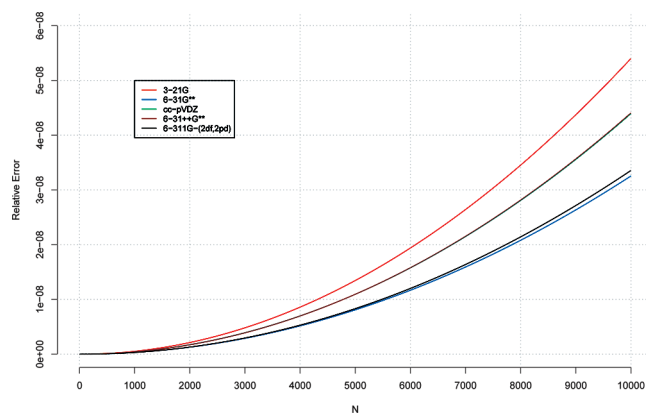


Figure 2. Predicted relative error of E_{HF} for water clusters of size up to $N = 10\,000$ using second degree polynomial regression models derived from existing data.

Table 2. Predicted Relative Numerical Error at $N = 10\,000$ for TIP4P Water Clusters Computed Using Different Types of Basis Sets

3-21G	6-31G**	cc-pVDZ	6-31++G**	6-311G(2df,2pd)
5.39×10^{-8}	3.25×10^{-8}	4.39×10^{-8}	4.40×10^{-8}	3.35×10^{-8}

issue in larger clusters and/or with larger basis sets. The polynomial regression models shown in Figure 1 can be used to predict errors for larger values of N . This is shown in Figure 2 for the four basis sets used. The plot indicates that relative numerical errors are on the order of 1×10^{-8} when $N = 10\,000$, with the specific values given in Table 2.

The largest system considered in the experiment above was $(\text{H}_2\text{O})_5$ 6-311G(2df,2pd) with 325 basis functions. The system sizes that can be studied are limited by the performance of the interval code. Interval computation is inherently slower than floating point computation due to the additional storage requirement and the additional number of floating operations required to achieve a single interval arithmetic operation (eq 2). The code implemented for this paper is also experimental in nature and therefore not optimized to the same degree as better established floating point codes. Moreover, in order to guarantee rigorous bounds on numerical errors, time saving heuristics such as two-electron integral screening cannot be used as with floating point codes. In fact, all $O(N^4)$ two-electron integrals were calculated using interval arithmetic in our implementation. In actual experiments, the interval Hartree–Fock code was observed to be around 10 to 25 times slower than its floating point equivalent.

4.2. Effect of Two-Electron Integral Screening. It is customary in HF calculations to prescreen the ERIs and only compute those with a magnitude greater than some threshold. The most widely used screening technique is based on the Schwartz test.⁸ This sets the following upper bound for value of an ERI:

$$|\langle \chi_a \chi_b | \chi_c \chi_d \rangle| \leq \kappa_{ab} \kappa_{cd}, \text{ where } \kappa_{ab} = \sqrt{\langle \chi_a \chi_b | \chi_a \chi_b \rangle} \quad (12)$$

Use of Schwartz screening requires precomputation of two center ERIs of the form $\langle \chi_a \chi_b | \chi_a \chi_b \rangle$. Before computing a specific integral, the value of $\kappa_{ab} \kappa_{cd}$ is computed and compared against the screening threshold τ . If $\kappa_{ab} \kappa_{cd} > \tau$, the actual integral is

Table 3. Decimal Digits of Precision of E_{HF} for Different ERI Screening Thresholds^a

system	N	no. ERI ($\times 10^6$)	ϵ	τ		
				1×10^{-12}	1×10^{-8}	1×10^{-4}
(H ₂ O) ₄	100	11.29	11.69	11.59 [13.74%]	8.43 [34.84%]	4.05 [68.93%]
alanine	125	29.11	11.41	11.34 [5.80%]	8.07 [17.65%]	3.44 [50.31%]
serine	140	44.77	11.30	11.24 [7.94%]	7.98 [21.73%]	3.40 [54.73%]
cytoccine	145	59.77	11.24	11.18 [9.08%]	7.91 [23.27%]	3.37 [53.30%]
(H ₂ O) ₈	200	154.91	11.00	10.90 [23.92%]	7.90 [53.02%]	3.60 [85.60%]

^aThe entries inside the square brackets indicate the percentage of unique ERI that is screened with respect to each cut-off.

evaluated; otherwise, it is neglected. For efficiency, Schwartz screening is usually performed for batches of integrals, not for individual integrals.

In Schwartz screening, choosing a value for τ represents a trade-off between speed and accuracy: set too high and the accuracy will be affected, set too low and the time to solution increases but with insignificant improvement in numerical accuracy. Interval arithmetic can be used to quantify the numerical error that results from using different values of τ , and to determine rigorously the maximum value of τ possible while still maintaining chemical accuracy. To do this, we assign each screened integral an interval value of $[-K_{ab}K_{cd}, K_{ab}K_{cd}]$.

In Table 3, we show the number of digits of precision in E_{HF} for ERI screening thresholds ranging from the machine epsilon (ϵ) to 1×10^{-4} for computations performed using a 6-31G** basis set. Five different systems are considered, two water clusters and three amino acid systems. The values in square brackets denote the percentage of unique nonzero ERIs that are screened away.

The results show that when using screening at machine epsilon, E_{HF} is accurate to between 11 and 12 significant digits. When using a screening value of 1×10^{-12} , there is minimal effect on the number of significant digits in E_{HF} , but the number of computed integrals decreases by between 6 and 24%. Increasing the screening value to 1×10^{-8} results in a significantly larger loss of precision and values for E_{HF} that are now barely accurate to 10^{-5} Hartrees. Further increasing the value of τ clearly gives unsatisfactory results.

4.3. Effect of Using Mixed Precision. While general purpose CPUs have traditionally provided strong double precision performance, this has not always been the case for GPUs and other specialized processors. For example, the high end NVIDIA GTX280 GPU is capable of 933 GFLOP/s in single precision, but only 78 GFLOP/s in double precision. Similarly the CellBE PowerXCell 8i is capable of 230.4 GLOP/s in single precision, but only 108.8 GFLOP/s in double precision.

To early users, it was clear that in order to harness the full potential of these systems, single precision arithmetic must be prioritized over double precision arithmetic. Yasuda² sought to address this issue by partitioning integrals based on their Schwarz upper bounds: computing all integrals below some bound (λ_{GPU}) in single precision on the GPU, while other integrals greater than λ_{GPU} were calculated in double precision on the host CPU. The larger the value of λ_{GPU} , the greater the proportion of the ERIs calculated in single precision and the faster the overall computation, but the lower the overall accuracy of the result. Yasuda showed that evaluating integrals entirely in single precision was not accurate enough for production runs.

Ufimtsev and Martinez,²⁷ while accepting Yasuda's approach, questioned whether mixing different floating point precisions

was worthwhile given the arrival of double precision capable GPUs designed specifically for scientific computing. It can be argued, however, that GPUs first emerged as a cost-effective solution not for scientific computing but for an entirely different market segment where double precision is not important. This market segment is considerably larger than for scientific computing and will continue to only require single precision floating point and integer arithmetic for the foreseeable future. Thus, the demands of scientific computing are always going to come second in driving GPU innovation. However, and as discussed in the Introduction, there are a number of other factors that motivate the use of short data types where possible.

Interval arithmetic can be used to model the numerical errors in E_{HF} due to different thresholds for λ_{GPU} . This differs from previously published work that compares single precision results to double precision results in that the intervals rigorously bound interactions with other sources of errors, not only those due to the value of λ_{GPU} . To do this, all integrals with a Schwarz upper bound below λ_{GPU} are calculated using single precision interval arithmetic, while the rest are calculated using the default double precision interval arithmetic.

Results obtained with different values of λ_{GPU} are given in Table 4 for some of the water cluster systems using the 6-31G** basis set. Values for λ_{GPU} of 10^{-12} , 10^{-8} , 10^{-4} , and 1 are used. The columns labeled D.P and S.P correspond to results calculated using solely double or single precision arithmetic, respectively. The values in the square brackets denote the percentage of the unique nonzero ERIs that were evaluated using single precision arithmetic.

As expected, the number of decimal digits of precision in E_{HF} generally decreases as the problem size increases. An exception is for (H₂O)₃, where the results obtained using $\lambda_{\text{GPU}} = 1 \times 10^{-4}$ are less precise than the equivalent numbers for the larger (H₂O)₄ and (H₂O)₅ systems. This is due to the composition of the ERIs: (H₂O)₃ has more ERIs with magnitudes between 1×10^{-6} and 1×10^{-4} (38%) compared to (H₂O)₄ (26%) and (H₂O)₅ (20%). Thus, a disproportionately large number of integrals near the threshold are calculated in single precision for the (H₂O)₃ case. This shows that while partitioning between single and double precision calculation based solely on the Schwarz upper bound of the ERI is generally reliable, the specific distribution of integral values can also be a factor for some systems. Since the magnitude of a two electron integral is determined by the distance between each electron, we can expect denser molecular systems to have higher concentrations of large integrals.

The results also show that numerical errors increase as the cutoff is relaxed and more integrals are calculated in single precision. For the problems considered, using a λ_{GPU} value as large as 10^{-2} still provides sufficient precision to give E_{HF} values

Table 4. Decimal Digits of Precision of E_{HF} for TIP4P Water Clusters Using the 6-31G Basis Set, with Different Cutoff Points (λ_{GPU}) Where ERIs Are Evaluated Using Single Precision Instead of Double Precision Floating Point.^a**

$(\text{H}_2\text{O})_n$	N	D.P	λ_{GPU}					S.P
			1×10^{-12}	1×10^{-8}	1×10^{-4}	1×10^{-2}	$1 \times 10^{+0}$	
2	50	12.26	12.26 [3.61%]	12.26 [14.95%]	10.81 [42.89%]	8.52 [67.20%]	6.15 [99.90%]	6.02
3	75	11.92	11.92 [5.98%]	11.92 [21.86%]	10.36 [56.79%]	8.17 [81.86%]	6.07 [99.95%]	5.95
4	100	11.69	11.68 [13.74%]	11.68 [34.84%]	10.56 [68.93%]	8.29 [87.73%]	6.03 [99.97%]	5.91
5	125	11.48	11.46 [21.87%]	11.46 [47.38%]	10.39 [77.97%]	8.11 [91.31%]	6.01 [99.98%]	5.88
6	150	11.29	11.20 [17.14%]	11.20 [42.81%]	10.12 [78.74%]	7.93 [93.51%]	5.97 [99.99%]	5.84
7	175	11.15	11.05 [21.18%]	11.05 [49.75%]	10.14 [82.80%]	7.94 [94.86%]	5.94 [99.99%]	5.82
8	200	11.00	10.98 [23.92%]	10.90 [53.02%]	9.88 [85.60%]	7.70 [96.15%]	5.90 [99.99%]	5.78

^aD.P stands for a fully double precision ERI calculation, and S.P stands for a fully single precision ERI calculation, with cutoff points of various magnitudes in between (the numbers in the square brackets indicate the percentage of single precision ERIs).

Table 5. Predicted Relative Numerical Error at $N = 10\,000$ for TIP4P Water Clusters for Different λ_{GPU} 's

D.P	λ_{GPU}					S.P
	1×10^{-12}	1×10^{-8}	1×10^{-4}	1×10^{-2}	$1 \times 10^{+0}$	
3.25×10^{-8}	3.02×10^{-8}	4.16×10^{-8}	2.68×10^{-7}	3.07×10^{-5}	5.40×10^{-5}	7.13×10^{-5}

that are chemically accurate, while using a value for λ_{GPU} of 1 is clearly inadequate. Alternatively, setting a λ_{GPU} threshold of 10^{-8} gives results that are almost as precise as exclusively using double precision.

In section 4.1, we used a second-degree polynomial regression model to predict numerical errors when $N = 10\,000$. If we apply the same approach to the data in Table 4, we find the projections given in Table 5. The columns show the predicted (relative) numerical errors for each respective λ_{GPU} value. If only single precision is used, the predicted error is on the order of 1×10^{-5} , which is not chemically accurate.

4.4. Effect of $F_m(T)$ Interpolation Table Size. Memory management is one of the most important factors affecting the performance of CPUs, GPUs, and special purpose processors. This can mean managing a complex cache hierarchy, small amounts of user controlled local memory, or a combination of both. For example, the NVIDIA GTX280 has 16 KB of fast local shared memory available to each thread block,²⁸ the synergistic processing elements (SPE) on the STI CellBE each have 256 KB of local memory for SPE instructions and data,⁴ and the SPARC VIIIfx CPU has a user controlled on-chip memory that can be cache, local memory, or a combination of both.²⁹

How to use small fast on-chip memory is therefore an increasingly important question for program developers. In ERI evaluation, the $F_m(T)$ interpolation table is a good candidate for storage in fast memory. Use of interpolation gives rise to a significant reduction in floating point operations, but this is only beneficial if the data that comprise the interpolation table can be accessed quickly. So an issue is how small can the $F_m(T)$ interpolation table be made while still obtaining sufficiently accurate results. For the purpose of this study, we will assume an ERI evaluation scheme similar to that employed by Ufimtsev and Martinez, where each thread or thread block on a GPU calculates a single primitive integral or contracted integral, with the $F_m(T)$ interpolation table replicated for each thread block in the fast local memory.

The size of the interpolation table depends on the interpolation scheme used, the degree of the polynomial interpolation, the

Table 6. Chebyshev Interpolation Table Sizes (KB) for Different Integral Types and Truncation Error Tolerances

integral	degree	$e_{F_m(T)}$			
		ε	1×10^{-12}	1×10^{-8}	1×10^{-4}
(ss ss)	3	1134	138	13	1
	6	25	7	2	<1
(pp pp)	3	1581	193	19	1
	6	35	10	2	<1
(dd dd)	3	1925	235	23	2
	6	43	12	3	1
(ff ff)	3	2269	277	27	2
	6	50	15	4	1
(gg gg)	3	2544	310	31	3
	6	56	17	4	1

largest total angular momentum of any ERI, and the truncation error tolerance. Table 6 shows the amount of memory required to represent a third and sixth degree Chebyshev polynomial interpolation table for integrals of type (ss|ss) through (gg|gg) when using different $F_m(T)$ truncation error tolerances. Third degree polynomials require larger interpolation tables than sixth degree polynomials but require less operations to evaluate each subsequent $F_m(T)$ value. Thus, the choice of whether to use a third or sixth order polynomial involves a trade-off between floating point operation count and memory usage. For GPUs and the CellBT systems, memory size is probably the major bottleneck; thus, sixth degree interpolation appears to be the best choice. The results in Table 6 show that keeping truncation error around machine precision requires an interpolation table much larger than that which can be stored in the shared memory on a current GPU system. However, by relaxing the error tolerances, it is possible to fit the interpolation table in fast shared memory. Supposing that 8 KB is the maximum table size allowed, then using sixth-degree Chebyshev polynomials, (ss|ss) type integrals

Table 7. Decimal Digits of Precision of E_{HF} for Different $F_m(T)$ Truncation Error Tolerances (e_{FMT})^a

system	basis	N	$e_{F_m(T)}$			
			ϵ	1×10^{-12}	1×10^{-8}	1×10^{-4}
(H ₂ O) ₄	6-31G**	100	11.69	11.68	9.05	4.97
alanine	6-31G**	125	11.41	11.37	8.40	4.22
serine	6-31G**	140	11.30	11.27	8.39	4.19
cytosin	6-31G**	145	11.24	11.21	8.31	4.14
(H ₂ O) ₈	6-31G**	200	11.00	11.00	8.85	4.74
	table size (KB)	43	12	3	1	

^a The last row indicates the interpolation table sizes associated with each tolerance.

can be calculated with errors on the order of 10^{-12} and $(pp|pp)$, $(dd|dd)$, $(ff|ff)$, and $(gg|gg)$ integrals with errors on the order of 10^{-8} .

Using intervals, we can place rigorous bounds on the effect of varying the interpolation table sizes on the final value of E_{HF} . This is shown in Table 7 when using sixth-degree Chebyshev polynomial interpolation and a range of different $F_m(T)$ thresholds. The results show that the precision of E_{HF} is decreased when the error tolerance is relaxed and that chemical accuracy is maintained in all cases except when the $F_m(T)$ threshold is 10^{-4} . Interestingly, and in a similar manner to what was observed in section 4.3, when using error tolerances of 10^{-8} and 10^{-4} , the precision for (H₂O)₈ is greater than for any of the amino acid cases despite the fact the total number of basis functions (N) is greater. This is again because there is a higher proportion of large magnitude ERIs for the amino acids than for (H₂O)₈.

5. CONCLUSION AND FUTURE WORK

In this paper, interval arithmetic is used as an error analysis tool to explore the effect of numerical errors in calculating the Hartree–Fock total energy under a variety of scenarios. The results highlight the fact that under certain conditions chemical accuracy can still be achieved even when the Hartree–Fock energy is calculated using relatively unconventional parameters, for example, (i) by varying the integral screening threshold, (ii) by varying the numerical precision between single and double precision, and (iii) by varying the granularity of integral interpolation tables. This result gives reasonable grounds to suggest that some key modifications to existing evaluation schemes can be made while maintaining chemical accuracy. This is especially relevant when looking to circumvent the limitations of specialized processing hardware in regard to double precision performance and fast memory capacity.

The results also highlight the gradual accumulation of numerical errors with increasing basis set and system sizes, which will eventually reach a stage where chemical accuracy can no longer be guaranteed. Another significant finding is that the estimated growth in numerical errors can be accurately modeled by regressing the number of basis functions against the width of the interval bound E_{HF} . The best fit was achieved using second degree polynomials. Nonlinear scaling is expected as the number of ERIs scales nonlinearly with basis set size, but the number of ERIs scales as $O(N^4)$ not $O(N^2)$. This finding supports the generally accepted view that it is possible to use integral screening to significantly reduce the computational scaling of large HF computations. On a cautionary note, the results also show that

there are other factors that affect accuracy, such as the density of the molecular system.

The main drawback of using interval arithmetic for numerical accuracy studies is that it provides a worst-case error analysis. The fact that interval results get rounded out to the nearest larger machine representable interval and the dependency problem means that these results are almost always overly pessimistic. That said, when the interval result is within the accuracy required, we do have guaranteed assurance of the numerical accuracy.

The current results also rely on a conventional Self-Consistent-Field (SCF) calculation to find the ground state molecular orbitals from a fixed atomic geometry. From the results of this calculation, the interval total energy is then calculated. This work does not consider how accurate a solution these coefficients are to the SCF problem, or indeed whether the solution represents the true ground state. Interval methods can be extended to address both issues, as will be discussed in another upcoming publication.

Finally, the results presented are confined to a limited set of small- and medium-sized systems. Another next step is to consider larger systems involving a larger variety of atoms, molecules, and basis set types, in particular, to test further the effectiveness of the polynomial regression model and to explore further other factors that affect numerical accuracy such as near linearly dependent basis sets.

AUTHOR INFORMATION

Corresponding Author

*E-mail: Alistair.Rendell@anu.edu.au.

ACKNOWLEDGMENT

This work was supported in part by Australian Research Council grant DP0558228.

REFERENCES

- (1) IEEE Computer Society Standards Committee. Working group of the Microprocessor Standards Subcommittee, American National Standards Institute. *IEEE standard for binary floating-point arithmetic, ANSI/IEEE Std 754–1985*; IEEE Computer Society Press: Silver Spring, MD, 1985; p 18.
- (2) Yasuda, K. *J. Comput. Chem.* **2008**, *29*, 334–342.
- (3) Ramdas, T.; Egan, G.; Abramson, D.; Baldrige, K. *Theor. Chem. Acc.* **2008**, *120*, 133–153.
- (4) Kahle, J. A.; Day, M. N.; Hofstee, H. P.; Johns, C. R.; Maeurer, T. R.; Shippy, D. *IBM J. Res. Dev.* **2005**, *49*, 589–604.
- (5) Zein, A.; Mccreath, E.; Rendell, A.; Smola, A. Performance Evaluation of the NVIDIA GeForce 8800 GTX GPU for Machine Learning. http://dx.doi.org/10.1007/978-3-540-69384-0_52 (accessed April 2011).
- (6) Caprani, O.; Madsen, K.; Nielsen, H. B. *Introduction to Interval Analysis*; Danmarks Tekniske Universitet: Copenhagen, Denmark, 2002.
- (7) Takashima, H.; Kitamura, K.; Tanabe, K.; Nagashima, U. *J. Comput. Chem.* **1999**, *20*, 443–454.
- (8) Almlöf, J. In *Modern Electronic Structure Theory Part II*; Yarkony, D. R., Ed.; World Scientific: Singapore, 1995; Vol. 1, Chapter: Direct Methods in Electronic Structure Theory, pp 110–151.
- (9) Moore, R. E. *Automatic Error Analysis in Digital Computation*; Technical Report Space Div. Report LMSD84821, Lockheed Missiles and Space Co.: Sunnyvale, CA, 1959
- (10) Hansen, E. R. *Global optimization using interval analysis*; Marcel Dekker, Inc.: New York, 1992; pp 1–21.

- (11) Saltelli, A.; Ratto, M.; Tarantola, S.; Campolongo, F. *RESS* **2006**, *91*, 1109–1125, The Fourth International Conference on Sensitivity Analysis of Model Output (SAMO 2004)—SAMO 2004.
- (12) Lindh, R. Integrals of Electron Repulsion. *Encyclopaedia of Computational Chemistry*; John Wiley and Sons: New York, 1998; p 1337.
- (13) McMurchie, L. E.; Davidson, E. R. *J. Chem. Phys.* **1988**, *89*, 5777–5786.
- (14) Obara, S.; Saika, A. *J. Chem. Phys.* **1986**, *84*, 3963.
- (15) Rys, J.; Dupuis, M.; King, H. *J. Comput. Chem.* **1983**, *4*, 154–157.
- (16) Head-Gordon, M.; Pople, J. A. *J. Comput. Phys.* **1978**, *26*, 218–231.
- (17) Gill, P. M. W. *Adv. Quantum Chem.* **1994**, *25*, 141–205.
- (18) Shavitt, I. *Meth. Comput. Phys.* **1963**, *2*, 1–44.
- (19) Gill, P. M.; Johnson, B. G.; Pople, J. A. *Int. J. Quantum Chem.* **1991**, *40*, 745–752.
- (20) Janes, P. P.; Rendell, A. P. *CSE* **2008**, *0*, 75–82.
- (21) Sun Microsystems Inc. *The Sun Fire V1280 Server Architecture*. http://www.sun.com/servers/midrange/pdfs/V1280_wp_final.pdf (accessed Jan 9, 2011).
- (22) Sun Microsystems Inc. *SunStudio 11: C++ User's Guide*. <http://download.oracle.com/docs/cd/E19422-01/819-3690-10/819-3690-10.pdf> (accessed Feb 6, 2011).
- (23) Sun Microsystems Inc. *Sun Studio 11: C++ Interval Arithmetic Programming Reference*. <http://download.oracle.com/docs/cd/E19422-01/819-3696-10/819-3696-10.pdf> (accessed Feb 6, 2011).
- (24) <http://cs.anu.edu.au/people/Pete.Janes/applications/> (accessed Jan 11, 2011).
- (25) Wales, D.; Doye, J.; Dullweber, A.; Hodges, M.; Naumkin, F.; Calvo, F.; Hernández-Rojas, J.; Middleton, T. *The Cambridge Cluster Database*. <http://www-wales.ch.cam.ac.uk/CCD.html> (accessed Jan 2, 2011).
- (26) Higham, N. J. *Accuracy and Stability of Numerical Algorithms*, 2nd ed.; Society for Industrial and Applied Mathematics: Philadelphia, PA, 2002; pp 79–92.
- (27) Ufimtsev, I. S.; Martinez, T. J. *J. Chem. Theory Comput.* **2008**, *4*, 222–231.
- (28) *NVIDIA CUDA Programming Guide*, Version 3.0; NVIDIA: Santa Clara, CA, 2010.
- (29) Maruyama, T.; Yoshida, T.; Kan, R.; Yamazaki, I.; Yamamura, S.; Takahashi, N.; Hondou, M.; Okano, H. *IEEE Micro* **2010**, *30*, 30–40.

Complete vs Restricted Active Space Perturbation Theory Calculation of the Cr₂ Potential Energy Surface

Fernando Ruipérez,[†] Francesco Aquilante,[‡] Jesus M. Ugalde,[†] and Ivan Infante^{*†}[†]Kimika Fakultatea, Euskal Herriko Unibertsitatea, and Donostia International Physics Center (DIPC), P. K. 1072, 20080 Donostia, Euskadi, Spain[‡]Department of Physical Chemistry, University of Geneva Chemical Center, 30 Quai Ernest-Ansermet, CH-1211, Geneva, Switzerland

ABSTRACT: In this paper, we calculate the potential energy surface (PES) and the spectroscopic constants of the chromium dimer using the recently developed restricted active space second-order perturbation (RASPT2) method. This approach is benchmarked against available experimental measurements and the complete active space second-order perturbation theory (CASPT2), which is nowadays established as one of the most accurate theoretical models available. Dissociation energies, vibrational frequencies, and bond distances are computed at the RASPT2 level using several reference spaces. The major advantage of the RASPT2 method is that with a limited number of configuration state functions, it can reproduce well the equilibrium bond length and the vibrational frequency of the Cr dimer. On the other hand, the PES is well described only at short distances, while at large distances, it compares very poorly with the CASPT2. The dissociation energy is also ill-behaved, but its value can be largely improved using a simple workaround that we explain in the text. In the paper, we also address the effect of the Ionization Potential Electron Affinity (IPEA) shift (a parameter introduced in the zeroth-order Hamiltonian in the CASPT2 method to include the effect of two-electron terms) and show how its default value of 0.25 is not suitable for a proper description of the PES and of the spectroscopic parameters and must be changed to a more sound value of 0.45.

1. INTRODUCTION

The interest in small transition metal (TM) clusters has grown rapidly in recent years because of their wide range of applications in different fields, such as catalysis, optics, biomedicine, environment.^{1–5} TM clusters also serve as a bridge between bulk materials and nanomaterials, since they are experimentally accessible and, at the same time, still tractable with very accurate theoretical models.

From a theoretical standpoint, the description of transition metal elements and their compounds is particularly challenging due to the presence of a dense manifold of low-lying states generated by the partial occupation of the *nd* and (*n* + 1)*s* shells. These factors can lead to ground state (or excited state) wave functions of multireference character, where a large number of configurations is needed to properly account for *static* correlation effects, of fundamental importance for the accurate description of potential energy surfaces and dissociation energies. This precludes in many cases the use of post-Hartree–Fock methods and poses great challenges to density functional theory (DFT), as these approaches work best for the accurate description of solely the *dynamic* correlation. Under these circumstances, a multiconfigurational model such as the complete active space self-consistent field method followed by second-order perturbation theory, CASSCF/CASPT2,^{6–10} is particularly attractive to achieve a proper description of both types of correlation energy.

The recent development of the so-called *ab initio* density fitting and Cholesky-based algorithms^{11–14} has expanded considerably the range of molecular sizes for which CASSCF/CASPT2 calculations are feasible. A number of insightful studies of diverse chemical problems^{15–18} has been possible as a result of these improvements in theory and algorithms. Unfortunately, the

application of CASSCF/CASPT2 is still limited by the solution of the configuration interaction (CI) problem, a step where the computational cost increases factorially with the size of the active space. This adverse circumstance prevents its use for the study of TM clusters with more than two atoms. In order to overcome such limitation, new theoretical models have been introduced^{19–21} to reduce drastically the number of configuration state functions (CSFs) in the CI step. In particular, the restricted active space self-consistent field method, followed by second-order perturbation theory, RASSCF/RASPT2,^{19–22} is emerging as a promising alternative. Although the RASSCF method was developed 20 years ago,^{19,20} its extension to include dynamical correlation, the so-called RASPT2 method,²¹ was successfully established only recently. A few applications can be found already in the literature with encouraging results.^{21,23–25}

To achieve the goal of studying TM clusters of increasing size, we decided to assess the performance of RASSCF/RASPT2 on a small albeit complex transition metal molecule: the chromium dimer.

The Cr₂ molecule poses a big challenge from a theoretical standpoint because its ground state presents one of the most complicated electronic structures that can be found among metal dimers. The ¹Σ_g⁺ electronic ground state is highly multiconfigurational, and the dominant CSF, 4sσ_g²3dσ_g²3dπ_u⁴3dδ_g⁴, weighs only 47% (this work). Also, the experimental potential energy surface (PES) shows, in addition to the relatively deep minimum at approximately 1.68 Å corresponding to the 3d–3d interaction, a rather flat, shelf-like region, at about 2.5 Å, where the interaction

Received: January 21, 2011

Published: April 14, 2011

between the diffuse 4s orbitals is dominant.²⁶ As a further complication, the dimer dissociates into two chromium atoms whose ground state has a high-spin open-shell electronic configuration 7S , with six unpaired electrons distributed as $3d^5 4s^1$. This means that the static electron correlation becomes dramatically important along the potential energy surface.

Popular exchange-correlation (xc) functionals, within the framework of DFT, have been demonstrated to poorly describe the PES and some of the spectroscopic constants. Only the BLYP functional is capable of reproducing the first minimum and the shelf-like potential along the PES, while traditional hybrid functionals like B3LYP and B3PB86 fail to show the region at 2.5 Å.²⁷ For all xc functionals used, the stretching vibrational frequency is computed at about 800 cm^{-1} , almost 2 times larger than the experimental value, 481 cm^{-1} . Furthermore, spin contamination affects all DFT results, pinpointing the fact that a single closed-shell configuration represents a too simplistic description of the bonding pattern in the Cr dimer.

A variety of post-HF calculations have been employed to study the Cr_2 PES;^{28,29} however, for the purposes of this paper, we focus on the ones based on the CASSCF/CASPT2 method. The first of these calculations showed severe problems with intruder states, and the calculations were not able to reproduce the shallow region at 2.5 Å in the potential energy surface.³⁰ Years later, several improvements were included in the computational model, regarding basis sets, active space, and the zeroth-order Hamiltonian. The first attempt to solve the problem of the intruder states involved the use of a modified zeroth-order Hamiltonian, called $g1$, and significant improvement was achieved. A deep inspection of the CASPT2 wave function revealed that the 4p orbitals were playing a major role in removing the intruder states; hence, the original active space, which included 12 electrons in 12 orbitals (the 3d and 4s orbitals of the two atoms), called CAS(12/12), was extended to include four extra orbitals of 4p character, more precisely the three bonding combination $4p_\sigma$ and $4p_\pi$ and the antibonding $4p_\sigma^*$. Using this big active space, it was possible to reproduce satisfactorily the shape of the potential energy surface, and the intruder-state problem was corrected applying a level shift of 0.3 au.³¹

In this work, we show that it is possible to represent correctly the spectroscopic constants and the shape of the potential energy surface for Cr_2 using the original (12/12) active space that includes the 3d and 4s orbitals, provided that an optimal value of the IPEA shift (vide infra) is chosen. Moreover, with this value of the IPEA shift, we have investigated the possibility of using the less computationally intensive RASSCF/RASPT2 method to determine the electronic structure and PES of Cr_2 . Our results also provide insight into how to use the method and what its limitations are if applied to the study of bigger systems such as small metal clusters.

2. DETAILS OF THE CALCULATIONS

All-electron spin-free relativistic calculations were carried out using the Douglas–Kroll–Hess Hamiltonian.^{32,33} In the first step, complete active space self-consistent field calculations (CASSCF)^{6–8} are performed choosing an active space in which 12 electrons are distributed in the following 12 molecular orbitals, $4s\sigma_g$, $3d\sigma_g$, $3d\pi_u$, $3d\delta_g$, $4s\sigma_u^*$, $3d\sigma_u^*$, $3d\pi_g^*$, and $3d\delta_u^*$, composed of the 3d and 4s atomic orbitals of each Cr atom. Using this wave function, dynamical correlation effects are included through complete active space second-order perturbation theory calculations (CASPT2)^{9,10}

using the ionization potential electron affinity (IPEA)-corrected zeroth-order Hamiltonian³⁴ and the so-called $g1$ modified zeroth-order Hamiltonian.³⁵ The use of an imaginary shift³⁶ of 0.2 au was necessary in order to avoid the presence of intruder states in the CASPT2 step, where the 3s and 3p closed shells are also correlated dynamically. In the (IPEA)-corrected calculations, different values of the IPEA shift, ϵ , were tested. Moreover, we have also performed calculations at the RASSCF/RASPT2^{19–22} level of theory, in which the zeroth-order wave function is obtained in a restricted active space (RAS). In the RASSCF method, the active space is divided into three subspaces: RAS1, RAS2, and RAS3. RAS2 is identical to the CAS, where all possible spin- and symmetry-adapted configuration state functions are constructed, i.e., a full CI within the selected space, while RAS1 and RAS3 are subspaces originally containing doubly occupied and empty orbitals, respectively. These two subspaces allow the generation of additional configuration state functions with the restriction that a maximum number of excitations may occur from RAS1 (to RAS2 and RAS3) and a maximum number of excitations may occur into RAS3 (from RAS1 and RAS2). This model can handle larger active spaces than regular CAS, provided that the resulting number of CSFs does not exceed the present limits. All calculations were performed with MOLCAS 7.4 code³⁷ and using C_{2h} symmetry. We used the basis set developed by Roos³¹ for this system, which is obtained from the primitive basis set 21s15p10d6f4g of Pou-Amerigo et al.³⁸ contracted to 10s10p8d6f4g.

The potential energy surface of the Cr dimer is scanned using the VIBROT program.³⁷ This program fits the potential to an analytical form using cubic splines and solves the ro-vibrational Schrödinger equation numerically. The energies are then analyzed in terms of spectroscopic constants, namely, equilibrium bond length (R_e), dissociation energy (D_e and D_0), and fundamental vibrational frequency ($\Delta G_{1/2}$). The dissociation energy of the molecule can be also calculated by subtracting the ground state energy of the dimer at the equilibrium to the energy of the isolated atoms in their ground state calculated at the full CASPT2 level: $D'_e = 2 \times E[\text{Cr}(^7S)] - E[\text{Cr}_2(^1\Sigma_g^+)]$. Although this dissociation energy should be the same as the one computed with VIBROT, CASPT2 calculations lead to subtle differences due to possible numerical inconsistencies. For the sake of clarity, we show both types of dissociation throughout the paper.

The effect of counterpoise correction is minimal: 0.002 Å on the bond distance, 0.03 eV on the dissociation energy, and 10 cm^{-1} on the vibrational frequency. For this reason, we consider the BSSE noninfluential for the overall discussion, and we decided to avoid its computation for all the PESs presented in this article.

3. RESULTS

3.1. Effect of the Zeroth-Order Hamiltonian and IPEA Shift. In the original formulation of the zeroth-order Hamiltonian in the CASPT2 method, a systematic error is introduced by defining a generalized effective one-electron Fock operator that does not include explicitly two-electron terms in the Hamiltonian. In this simplified framework, a nonbalanced description of bond energies and electronic excitation energies can occur once the states that are compared have different spin-multiplicity, in particular when one of the states is a closed-shell.³⁹

In order to correct this systematic error, Ghigo et al.³⁴ proposed a modification of the zeroth-order Hamiltonian by introducing a shift operator, the so-called Ionization Energy (IP)–Electron

Affinity (EA) shift, or more simply IPEA shift, ϵ , which modifies the diagonal elements of the generalized one-electron Fock matrix. Basically, in partially filled orbitals like the active orbitals in the CASSCF method, the shift modifies the diagonal elements of the Fock matrix in such a way that the energies of the active orbitals become closer to $-IP$, when an electron is excited out of these orbitals, and closer to $-EA$, when one electron is excited into one of them. This shift can be determined either using experimental results or by comparison with highly accurate calculations. For transition metals, the value of ϵ varies between 0.2 and 0.4 au, with an average value of 0.25 au, which is currently the default value used in the present implementation of the zeroth-order Hamiltonian in MOLCAS.³⁷ The addition of this parameter considerably reduces the previously mentioned systematic errors found in CASPT2 calculations; however, few studies carried out in some test cases have revealed that this is not the most appropriate value in every case.^{40–42}

In this work, we study how the variation of this parameter, ϵ , drastically affects not only the potential energy surface but also the equilibrium bond length, the dissociation energy, and the vibrational frequency of the Cr dimer. A summary of the results is shown in Table 1 and in Figure 1.

The theoretical potential energy surface calculated using the original g1 zeroth-order Hamiltonian is shown in Figure 1, together with the experimental curve. It is interesting to include the g1 result, as it is the one based on previous calculations by Roos³¹ where a bigger active space was needed together with a level shift of 0.3 au in order to accurately describe the experimental PES. In our work, for consistency with the IPEA curves, we employed an active space that includes only 3d and 4s orbitals and an imaginary level shift of 0.2 au. Under these conditions, this Hamiltonian generates a curve that agrees reasonably well with the experiment regarding the overall shape, as it reproduces the shelf-like region (see green line in Figure 1). However the first minimum, located in the 3d–3d region is much deeper than it should be and is about 0.6 eV more binding than the experimental value. Clearly, this approach is flawed since $\Delta G_{1/2}$ is also overestimated by about 100 cm^{-1} as compared to the experiment. See Table 1 for more details.

When the IPEA Hamiltonian is employed, some very interesting results are obtained. Starting with $\epsilon = 0.25$, which is the default value, we notice that the shape of the curve around the 3d minimum is rather shallow, while the behavior of the curve is preserved in the 4s region (see red line in Figure 1). What is most important here is that the 3d–3d interaction is so weak that the actual bond occurs at longer distances, in the 4s–4s area. This may lead to serious errors in the geometry of the dimer, but especially in larger clusters in which the 4s interaction would always be the leading one and the clusters would show unusually large bond lengths among distinct Cr–Cr sites. To make things worse, the fundamental vibrational frequency of the Cr dimer is computed at 70 cm^{-1} , about 400 wavenumbers lower than the experimental result. It is evident from what is described above that with the default choice for the IPEA shift, we are unable to reproduce our PES, and therefore a new value of this parameter must be sought.

For $\epsilon = 0.10$, the potential surface reproduces the experimental flat region, corresponding to the 4s–4s interaction; however, in the region of the 3d minimum, only a small shoulder is observed (see orange line in Figure 1). When the IPEA shift is increased to higher values, the shape of the 3d minimum is improved, while the behavior in the 4s region remains almost well-described. This means that the IPEA modifies mainly the 3d–3d interaction,

Table 1. Spectroscopic Constants Obtained with the (IPEA-) Corrected Zeroth-Order Hamiltonian for Different Values of IPEA Shift (ϵ) and with the Modified g1 Zeroth-Order Hamiltonian^a

ϵ	R_e	D_e	D'_e	D_0	$\Delta G_{1/2}$	IP
0.00			0.608			
0.25	1.736	1.15	1.38	1.14	70	7.13
0.40	1.696	1.45	1.42		468	7.12
0.45	1.687	1.52		1.50	516	7.12
0.50	1.681	1.60	1.98	1.56	542	
0.75			2.41			
1.00			2.73			
g1 ^b	1.682	2.12	2.13	2.09	551	7.08
g1 ^c	1.662			1.65	413	
exp.	1.679 ^d	1.56		1.53 ^e	452 ^d	6.9988 ^e

^aThe dissociation energies are calculated from the potential energy surfaces (D_e) and from 2 times the energy of the isolated atoms (D'_e). The vertical ionization potential and the experimental data are also shown. Distances in Å, vibrational frequencies in cm^{-1} , and energies in eV. ^bThis work. ^cFrom ref 31. ^dFrom ref 43. ^eFrom ref 44.

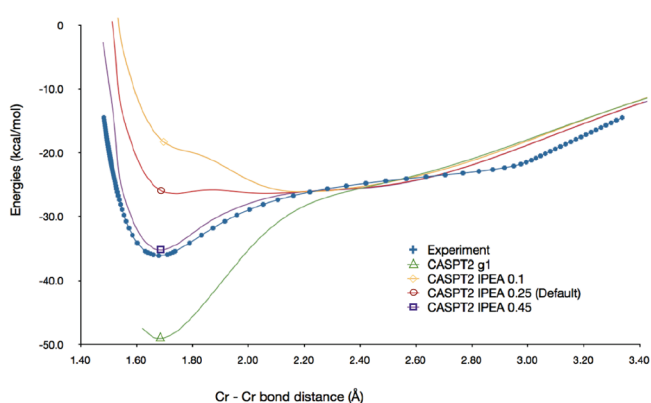


Figure 1. Potential energy surfaces obtained with different values of IPEA shift, ϵ , and using the modified g1 Hamiltonian, together with the experimental curve. Bond distances in Å and energies in kcal/mol. The asymptotic zero energy taken as reference is the total energy of the Cr atoms at a distance of 10 Å.

while the 4s–4s is properly accounted for and rather independent from this parameter. Finally, we find that the best agreement with the experiment is achieved at a value of about $\epsilon = 0.45$ (see purple line in Figure 1) where the shape of the curve reproduces accurately the region around the first minimum, both the shape and the energy, as well as the small minimum at longer distances.

Regarding bond lengths, we find that they are decreased with increasing IPEA shift, and the best agreement with the experiment corresponds to $\epsilon = 0.50$ (1.681 Å calculated and 1.679 Å experimental). The g1 Hamiltonian also leads to satisfactory values of R_e (1.682 and 1.662 Å). The dissociation energy increases with higher values of IPEA, and the best result corresponds to $\epsilon = 0.45$ (1.50 eV calculated and 1.53 eV experimental). Finally, the best agreement with experimental results for $\Delta G_{1/2}$ is obtained with $\epsilon = 0.40$ (468 cm^{-1}), compared to the experimental 452 cm^{-1} .

On the basis of the above results, we decided to proceed with an IPEA shift parameter value of 0.45, which gives the best

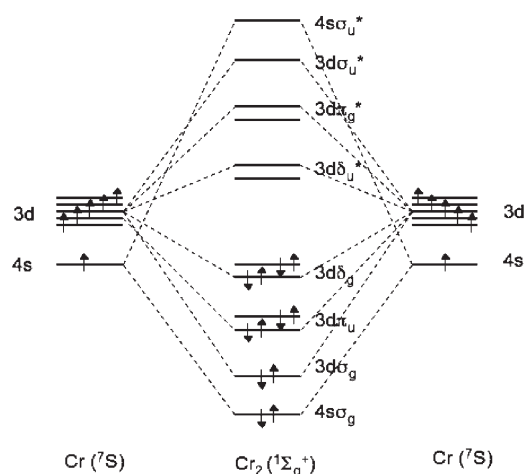


Figure 2. Schematic representation of the molecular orbital diagram for the chromium dimer. The energy ordering is arbitrary and only for didactical purposes.

compromise in terms of PES facets, dissociation energy, equilibrium bond length, and fundamental vibrational frequency.

3.2. Accuracy of Quantum Chemical Calculations: RASPT2 vs CASPT2 Results. The previous part of this work was devoted to the analysis of the effects of the IPEA shift on some properties of the chromium dimer, using high level CASSCF/CASPT2 calculations. However, as was mentioned earlier, the main goal of this paper is to benchmark the capabilities of the recently proposed RASPT2 method, which has been previously successfully employed.^{21,23–25} In this part of the work, we would like to check the performance of the RASPT2 method on some properties of the Cr₂ dimer, and in order to do so, we decided to probe in a consistent way the size of the RAS subspaces (RAS1, RAS2, RAS3) with respect to the CASPT2 results.

In Figure 2, we represent a qualitative molecular orbital diagram for the dimer. This diagram will guide us in the distribution of the molecular orbitals in the different RAS subspaces. The nomenclature used in these calculations is the following: $(n_e \text{ in } n_o)/(n_{e2} \text{ in } n_{o2})/n$, where n_e in n_o is the total number of electrons distributed in the total number of orbitals in the whole active space, n_{e2} in n_{o2} corresponds to the electrons and orbitals in the RAS2 space, and, finally, n is the number of excitations allowed from RAS1 and into RAS3. The calculations performed are the following:

CAS(12/12). The CAS contains all bonding and antibonding combinations arising from the interaction of the five 3d and the 4s atomic orbitals of the two Cr atoms at the equilibrium bond length. The following molecular orbitals are obtained (Figure 2): $4s\sigma_g$, $3d\sigma_g$, $3d\pi_u$, $3d\delta_g$, $4s\sigma_u^*$, $3d\sigma_u^*$, $3d\pi_u^*$, and $3d\delta_u^*$. This level of calculation is the most accurate and will be used as a reference for RASSCF and RASPT2. In Figure 3, we immediately notice that in the CASSCF potential, the 3d–3d bond is virtually absent and is represented by a very small shoulder at about 1.80 Å. At increased distances, the energy profile becomes more stabilizing, with a large shallow minimum at about 3 Å. The facets of the PES change drastically with the inclusion of the dynamic correlation energy, thanks to the formation of a deep well in the 3d–3d bonding energy (Figure 4). This allows one to obtain the correct form of the potential, which leads to a correct description of the spectroscopic parameters in the CASPT2 results.

CAS(10/10). In this calculation, we remove from the active space the $4s\sigma_g$ bonding and $4s\sigma_u^*$ antibonding orbitals, and we

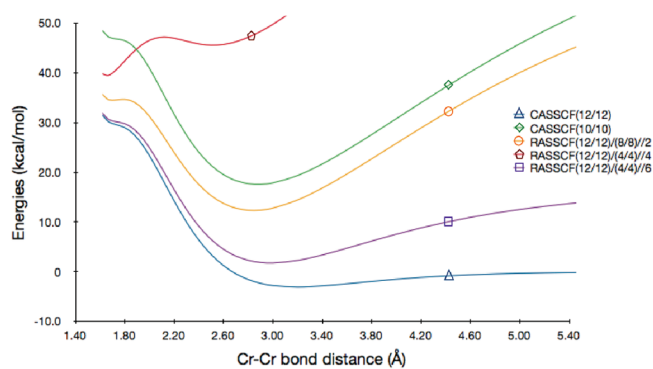


Figure 3. Potential energy surfaces calculated at CASSCF and RASSCF levels of theory. Bond distances in Å and energies in kcal/mol. For simplicity, the asymptotic zero energy taken as a reference is the total energy of the Cr atoms at a distance of 10 Å and computed at the CASSCF(12/12) level of theory. All other binding energies are depicted with respect to this value.

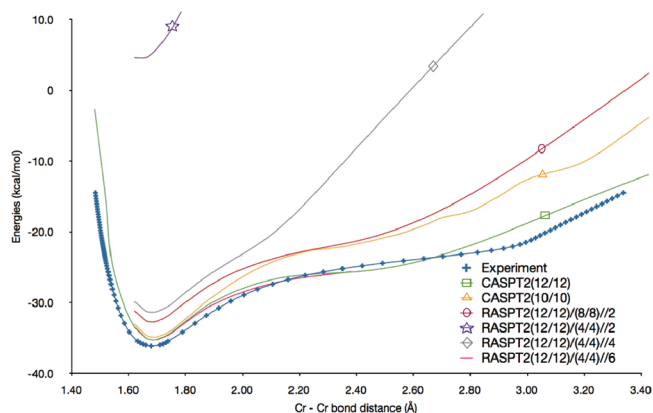


Figure 4. Potential energy surfaces calculated at different levels of theory, together with the experimental curve. Bond distances in Å and energies in kcal/mol. For simplicity, the asymptotic zero energy taken as reference here is the total energy of the Cr atoms at a distance of 10 Å and computed at the CASPT2(12/12) level of theory. All other binding energies are depicted with respect to this value. For this reason, the binding energies expressed in the figure are not equal (with the exception of the full CASPT2) to the D_e given in the tables throughout the text.

correlate them perturbatively in the CASPT2 step. This gives rise to an erratic PES for both the CASSCF and CASPT2, since the effect of the CSFs produced by excitations from (into) $4s\sigma_g$ ($4s\sigma_u^*$) is treated only perturbatively and, therefore, not accurately enough to describe the 4s–4s bond breaking. As a result, large deviations are seen in the 2.5 Å region, where the 4s–4s interaction is dominant. At short distances, the CASPT2 curve behaves accurately. The spectroscopic parameters are affected dramatically (see Table 2), with the exception of the equilibrium bond length. The dissociation energy is more binding by 2 eV, and the vibrational frequency is reduced by about 30 cm^{-1} .

RAS(12/12)/(10/10)/2. In this first RASSCF/RASPT2 calculation, the 4s bonding orbital ($4s\sigma_g$) is included in RAS1 and the corresponding antibonding ($4s\sigma_u^*$) in RAS3. Single and double excitations are allowed from $4s\sigma_g$ and into $4s\sigma_u^*$. This active space is actually equivalent to the CAS(12/12), since RAS2 produces up to 10-fold excitations that can combine with the singles and doubles from RAS1 and into RAS3, therefore reaching 12-fold

Table 2. Spectroscopic Constants and Number of Configuration State Functions (CSF) for Different Levels of Calculation Using the IPEA Shift Value $\epsilon = 0.45^a$

calculation	CSF	R_e	D_e	D_0	D'_e	$\Delta G_{1/2}$
CASPT2(10/10)	4956	1.689	3.40	3.37	1.10	389
CASPT2(12/12)	57168	1.687	1.53	1.50	1.53	516
RASPT2(12/12)/(10/10)//2	57168	1.687	1.53	1.50	1.53	516
RASPT2(12/12)/(8/8)//2	29244	1.682	4.26	4.23	1.41	515
RASPT2(12/12)/(8/8)//4	57168	1.687	1.53	1.50	1.53	516
RASPT2(12/12)/(4/4)//2	2298	1.641	4.17	4.15	0.30	208
RASPT2(12/12)/(4/4)//4	29164	1.681	5.94	5.90	1.35	502
RASPT2(12/12)/(4/4)//6	55126	1.687	2.33	2.30	1.53	504
RASPT2(12/12)/(4/4)//8	57168	1.687	1.53	1.50	1.53	516
RASPT2(12/12)/(0/0)//2 ^b	199					
RASPT2(12/12)/(0/0)//4	7206	1.638	10.82	10.80	0.39	212
RASPT2(12/12)/(0/0)//6	37122	1.678	5.54	5.51	1.37	516
RASPT2(12/12)/(0/0)//8	55629	1.687	2.38	2.35	1.53	512
RASPT2(12/12)/(0/0)//10	57155	1.687	1.58	1.55	1.53	510
RASPT2(12/12)/(0/0)//12	57168	1.687	1.53	1.50	1.53	516
experiment		1.679		1.53		452

^a Rows in italics denote calculations that reproduce the full CASPT2 results with the same number of CSFs. Experimental values are also included. Distances in Å, vibrational frequencies in cm^{-1} , and energies in eV. The D_e is computed following the PES from the Cr_2 ground state to the separated fragments in their ground states at the given level of theory. The D'_e is computed with respect to the isolated fragments at the full CASPT2. ^b In this RAS space, most of the calculations have diverged, and a complete description of the spectroscopic parameters is not possible.

excitations. This equivalence is obviously reflected in the number of CSFs used to build the wave function in each of the two methods, as seen in Table 2.

RAS(12/12)/(8/8)//2,4. The composition of the different spaces is as follows: RAS1 ($4s\sigma_g$, $3d\sigma_g$), RAS3 ($4s\sigma_w^*$, $3d\sigma_w^*$) and RAS2 ($3d\pi_w$, $3d\delta_g$, $3d\pi_g^*$, $3d\delta_u^*$). Basically, we exclude the most bound 3d orbital, i.e., the $3d\sigma_g$, and its antibonding counterpart from the RAS2 space. We calculated the effect of double and quadruple excitations from RAS1 and into RAS3. The latter one is equivalent to the full CASSCF/CASPT2(12/12). With the double excitations, the number of CSFs is reduced by about half, from 57 168 to 29 244. The CASPT2 PES is well described up to 2.5 Å. After this point, the curve moves upward compared to the correct behavior, and higher excitations are needed for a proper description of these long-range interactions. The RASPT2 equilibrium bond length and vibrational frequency (1.682 Å and 515 cm^{-1} , respectively) are in good agreement with the CASPT2 values (1.687 Å and 516 cm^{-1}); nevertheless, the dissociation energy is largely overestimated (4.23 eV compared to 1.50 eV). We can conclude that this level of approximation is accurate enough to describe the geometry of the dimer and the vibrational frequency, but not the dissociation energy.

RAS(12/12)/(4/4)//2,4,6,8. In this calculation, RAS1 includes $4s\sigma_g$, $3d\sigma_g$, and $3d\pi_u$ orbitals; RAS3 includes $4s\sigma_w^*$, $3d\sigma_w^*$ and $3d\pi_g^*$; and finally RAS2 contains $3d\delta_g$ and $3d\delta_u^*$. Up to octuple excitations are allowed from RAS1 and into RAS3. As in the former cases, the highest order of excitations corresponds to the full CASSCF/CASPT2. For the rest, we notice some interesting things for the RASPT2 results: the number of excitations influences slightly the equilibrium bond lengths—1.641 Å for doubles, 1.681 Å for quadruples, and 1.687 Å for sextuples—and the

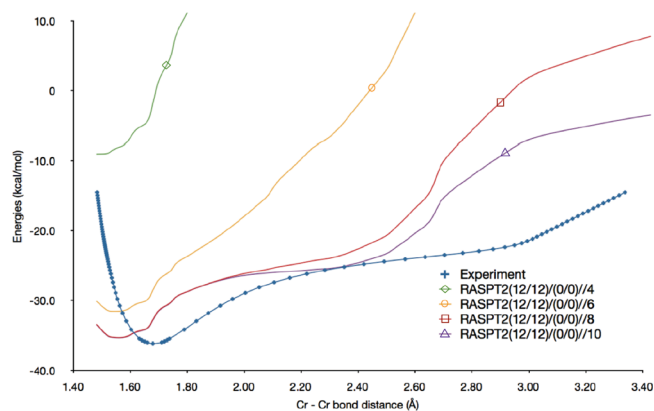


Figure 5. Potential energy surfaces calculated at RASPT2(12/12)(0/0)//2,4,6,8,10,12 levels of theory, together with the experimental curve. Bond distances in Å and energies in kcal/mol. For simplicity, the asymptotic zero energy taken as a reference is the total energy of the Cr atoms at a distance of 10 Å and computed at the CASPT2(12/12) level of theory. All other binding energies are depicted with respect to this value. For this reason, the binding energies expressed in the figure are not equal (with the exception of the full CASPT2) to the D_e given in the tables throughout the text.

comparison with the experiment (1.679 Å) or the CASPT2 (1.687 Å) is satisfactory. In particular, in the calculation with doubles that has only 2298 CSFs, about 20 times less than those of the full CASPT2, the geometry is reasonably well reproduced. Unfortunately, the dissociation energy is affected to a greater extent for almost all RAS spaces, showing important discrepancies with the experimental values (see Table 2). In Figure 4, it is possible to see the trends just described: in the region of the first minimum, all of the RAS spaces compare well with the experimental curve, but at longer distances, only the one including sextuple excitations shows an acceptable behavior.

RAS(12/12)(0/0)//2,4,6,8,10,12. In this calculation, RAS1 includes the following orbitals: $4s\sigma_g$, $3d\sigma_g$, $3d\pi_u$ and $3d\delta_g$, and RAS3 includes $4s\sigma_w^*$, $3d\sigma_w^*$, $3d\pi_g^*$, and $3d\delta_u^*$ orbitals. The RAS2 subspace is empty, which means that these calculations are similar to multireference CI, except for the fact that the coefficients of the molecular orbitals are also optimized variationally. Here, we perform up to 12-ple excitations between RAS1 and into RAS3 subspaces, with this latter one corresponding to a full CASPT2(12/12). For the sake of clarity, the results are represented in Figure 5. All orders of excitations from RAS1 and into RAS3 produce reasonable results regarding equilibrium bond lengths (see Table 2); however, the dissociation energies are quite poor at first but improved notably with increasing degrees of excitation. For example, with quadruple excitations, D_e is 10.80 eV and with 10-plex is 1.55 eV, very close to the CASPT2 value (1.50 eV). The vibrational frequencies are satisfactory from sextuple excitations and up. Obviously, the best RASPT2 space is the one that includes 10-ple excitations. However, this level of calculation generates roughly the same number of configuration state functions (57155) as CASPT2 (57168), and there is no real computational advantage. A reasonable compromise is the RASPT2(12/12)(0/0)//6 space, with 37 122 CSFs, and very good equilibrium bond length and vibrational frequency are obtained.

Vibrational Levels. As a further litmus test for the RASPT2 method, we decided to compare higher vibrational levels with the

Table 3. Calculated Vibrational Frequencies^a

ν	CASA0	CASA1	CASA2	RASB//2	RASC//2	RASC//4	RASC//6	RASD//4	RASD//6	RASD//8	RASD//10	exp.
$\Delta G_{\nu+1/2} = G_{\nu+1} - G_{\nu}$												
0	413	516	389	515	208	502	504	212	516	512	510	452
1	439	477	140	436	171	442	443	178	452	452	450	423
2	428	431	130	371	156	382	381	161	396	391	391	405
3	401	373	146	336	148	340	326	150	356	338	340	365
4	370	322	153	300	144	313	284	142	320	297	299	340
5	335	281	156	270	140	289	250	136	296	265	266	315
6	298	244	159	243	137	271	222	131	280	237	236	280
7	259	204	161	221	133	258	198	128	264	214	208	250
8	218	151	162	201	130	249	173	125	254	192	176	210
MUE	22	38	160	33	186	25	45	186	23	36	37	
$G_{\nu+1} - G_0$												
0	413	516	389	515	208	502	504	212	516	512	510	452
1	852	993	529	951	379	944	947	390	968	964	960	875 ± 10
2	1279	1424	659	1322	535	1326	1328	551	1364	1355	1351	1280 ± 10
3	1681	1797	805	1658	683	1666	1654	701	1720	1693	1691	1645 ± 10
4	2050	2119	958	1958	827	1979	1938	843	2040	1990	1990	1985 ± 15
5	2385	2400	1114	2228	967	2268	2188	979	2336	2255	2256	2300 ± 15
6	2683	2644	1273	2471	1104	2539	2410	1110	2616	2492	2492	2580 ± 20
7	2942	2848	1434	2692	1237	2797	2608	1238	2880	2700	2700	2830 ± 20
8	3160	2999	1596	2893	1367	3046	2781	1363	3134	2876	2876	3040 ± 20
MUE	65	93	914	76	1076	34	110	1067	65	75	77	

^aNomenclature: CAS and RAS stand for CASPT2 and RASPT2, respectively. A1 and A2 stand for active spaces of types (12/12) and (10/10). A0 results are taken from ref 31. B for (12/12)/(8/8). C for (12/12)/(4/4), and D for (12/12)/(0/0). Experimental data are taken from ref 26. Mean unsigned error (MUE) is given in the last row.

available experimental values, from $\nu = 0$ to $\nu = 8$, for $\Delta G_{\nu+1/2}$ and $G_{\nu+1} - G_0$.²⁶ In Table 3, we report a summary of all the results. The last row identifies the mean unsigned error, MUE. The first eye-catching feature is that the previous results by Roos carry an overall error lower than the present calculations, including our full CASPT2. This is probably due to the fact that to describe with even more accuracy the upper vibrational levels, we would need to include the 4p orbitals in the active space. Moreover, apart from the RAS spaces with the lowest number of excitations (in the table, referred to as A2, C//2, and D//4), we obtain a satisfactory agreement between the RASPT2 values and the experiment, with MUE varying between 23 and 45 cm^{-1} for $\Delta G_{\nu+1/2}$ and between 34 and 77 cm^{-1} for $G_{\nu+1} - G_0$. It is noteworthy that cancellation of errors makes some of the RASPT2 active spaces more accurate than the full CASPT2.

3.3. Discussion and Conclusions. The RASPT2 method carries limited advantages over CASPT2 in the specific case of the Cr dimer. The best compromise of accuracy vs computational advantage is obtained by RASPT2(12/12)/(8/8)//2, which describes quite well the equilibrium bond length and the vibrational frequency. Unfortunately, the dissociation energy is somewhat off, as it is in most of the RAS spaces we have chosen. To fix this problem and to get more accurate values for the dissociation, we then decided to make use of a simple workaround. Instead of taking the atoms at large distances and computing the energy with the same RAS space used at the equilibrium, we used the energy of the isolated atoms computed at the full CASPT2 level of theory. This energy is cheap to calculate because the atom has a reduced active space, i.e., (6/6), and a full CASPT2 accounts for only a small number of CSFs. If we take this CASPT2 energy as a

reference for the atomic fragments, the RASPT2 dissociation energies are improved. In Table 2, they are represented with the acronym D'_c . The maximum error is contained within about 1.2 eV, while already with some higher order of excitations from RAS1 and into RAS3, this error can be contained within the 0.2–0.3 eV. It is evident that the improvement is huge, as the error is drastically reduced by a factor of 3 to 5. This way of proceeding, however, introduced an imbalance between the active space used for the atomic fragments and that for the dimer at the equilibrium. This imbalance holds at the CASSCF (or RASSCF) step, but it is virtually canceled out at the PT2 level, when also the 3s and 3p orbitals are perturbatively correlated using all virtual orbitals, restoring in this way a numerical size consistency.

In conclusion, if one would like to study a cluster with more Cr atoms, it is wise to proceed with a balanced RASPT2 space, not necessarily too big, to obtain reasonable geometries and frequencies. For the dissociation energy, as explained above, it is always better to take the fragments computed with the most accurate method available, keeping the size consistency at the PT2 step.

We must also consider that in this paper we have chosen to benchmark an extremely complicated molecule that shows a heavy multiconfigurational character and a complicated potential energy surface. This had repercussions, as we have seen, not only on the RASPT2 method but also on the IPEA shift, which we had to tune to a value of 0.45 for a correct description of the potential energy surface and the spectroscopic constants. It may be interesting to apply the RASPT2 method and check the default value of the IPEA shift for other transition metal dimers, where these limitations can be less pronounced and where RASPT2

may show significant computational advantages over CASPT2, contrary to what observed for the Cr dimer.

Overall, RASPT2 appears as a computationally viable alternative to CASPT2 for studying stationary points on a PES, but it may fail to reproduce some details of the surface, as shown by the peculiar case of Cr₂.

AUTHOR INFORMATION

Corresponding Author

*Fax: +34-943-015270. E-mail: iinfant76@gmail.com.

ACKNOWLEDGMENT

Financial support comes from Eusko Jaurlaritza and the Spanish Office for Scientific Research. The SGI/IZO-SGIker UPV/EHU is gratefully acknowledged for generous allocation of computational resources. I.I. would like to thank the Spanish Ministry of Science and Innovation for a Juan de la Cierva fellowship.

REFERENCES

- (1) Baletto, F.; Ferrando, R. *Rev. Mod. Phys.* **2005**, *77*, 371.
- (2) Barden, C. J.; Rienstra-Kiracofe, J. C.; Schaefer, H. F. *Chem. Rev.* **2000**, *100*, 637.
- (3) Morse, M. D. *Chem. Rev.* **1986**, *86*, 1049.
- (4) Caada-Vilalta, C.; O'Brien, T. A.; Brechin, E. K.; Pink, M.; Davidson, E. R.; Christou, G. *Inorg. Chem.* **2004**, *43*, 5505.
- (5) Gutsev, G. L.; Bauschlicher, C. W., Jr. *J. Phys. Chem. A* **2003**, *107*, 7013.
- (6) Roos, B. O.; Taylor, P. R.; Siegbahn, P. E. M. *Chem. Phys.* **1980**, *48*, 157.
- (7) Siegbahn, P. E. M.; Heiberg, A.; Roos, B. O.; Levy, B. *Phys. Scr.* **1980**, *21*, 323.
- (8) Siegbahn, P. E. M.; Heiberg, A.; Almlöf, J.; Roos, B. O. *J. Chem. Phys.* **1981**, *74*, 2384.
- (9) Andersson, K.; Malmqvist, P.-Å.; Roos, B. O.; Sadlej, A. J.; Wolinski, K. *J. Phys. Chem.* **1990**, *94*, 5483.
- (10) Andersson, K.; Malmqvist, P.-Å.; Roos, B. O. *J. Chem. Phys.* **1992**, *96*, 1218.
- (11) Pedersen, T. B.; Aquilante, F.; Lindh, R. *Theor. Chem. Acc.* **2009**, *124*, 1.
- (12) Aquilante, F.; Todorova, T.; Pedersen, T. B.; Gagliardi, L.; Roos, B. O. *J. Chem. Phys.* **2009**, *131*, 34113.
- (13) Aquilante, F.; Pedersen, T. B.; de Meras, A. S.; Koch, H. *J. Chem. Phys.* **2008**, *129*, 24113.
- (14) Aquilante, F.; Malmqvist, P.-Å.; Pedersen, T. B.; Ghosh, A.; Roos, B. O. *J. Chem. Theory Comput.* **2008**, *4*, 694.
- (15) Srncic, M.; Aquilante, F.; Ryde, U.; Rulisek, L. *J. Phys. Chem. B* **2009**, *113*, 6074.
- (16) Huber, S. M.; Ertem, M. Z.; Aquilante, F.; Gagliardi, L.; Tolman, W. B.; Cramer, C. J. *Chem.—Eur. J.* **2009**, *15*, 4886.
- (17) La Macchia, G.; Li Manni, G.; Todorova, T. K.; Brynda, M.; Aquilante, F.; Roos, B. O.; Gagliardi, L. *Inorg. Chem.* **2010**, *49*, 5216.
- (18) Sala, X.; Ertem, M. Z.; Vigara, L.; Todorova, T. K.; Chen, W.; Rocha, R. C.; Aquilante, F.; Cramer, C. J.; Gagliardi, L.; Llobet, A. *Angew. Chem., Int. Ed.* **2010**, *49*, 7745.
- (19) Olsen, J.; Roos, B. O.; Jørgensen, P.; Jensen, H. J. A. *J. Chem. Phys.* **1988**, *89*, 2185.
- (20) Malmqvist, P.-Å.; Rendell, A.; Roos, B. O. *J. Phys. Chem.* **1990**, *94*, 5477.
- (21) Malmqvist, P.-Å.; Pierloot, K.; Shahi, A. R. M.; Cramer, C. J.; Gagliardi, L. *J. Chem. Phys.* **2008**, *128*, 204109.
- (22) Li Manni, G.; Aquilante, F.; Gagliardi, L. *J. Chem. Phys.* **2011**, *134*, 034114.
- (23) Shahi, A. R. M.; Cramer, C. J.; Gagliardi, L. *Phys. Chem. Chem. Phys.* **2009**, *11*, 10964.
- (24) Infante, I.; Kovacs, A.; La Macchia, G.; Shahi, A. R. M.; Gibson, J. K.; Gagliardi, L. *J. Phys. Chem. A* **2010**, *114*, 6007.
- (25) Sauri, V.; Serrano-Andrés, L.; Shahi, A. R. M.; Gagliardi, L. *Phys. Chem. Chem. Phys.* **2009**, *11*, 10964.
- (26) Casey, S. M.; Leopold, D. G. *J. Phys. Chem.* **1993**, *97*, 816.
- (27) Bauschlicher, C. W., Jr.; Partridge, H. *Chem. Phys. Lett.* **1994**, *231*, 277.
- (28) Müller, T. *J. Phys. Chem. A* **2009**, *113*, 12729.
- (29) Celani, P.; Stoll, H.; Werner, H. J.; Knowles, P. *J. Mol. Phys.* **2004**, *102*, 2369.
- (30) Andersson, K.; Roos, B. O.; Malmqvist, P.-Å.; Widmark, P.-O. *Chem. Phys. Lett.* **1994**, *230*, 391.
- (31) Roos, B. O. *Collect. Czech. Chem. Commun.* **2003**, *68*, 265.
- (32) Douglas, M.; Kroll, N. M. *Ann. Phys. (N.Y.)* **1974**, *82*, 89.
- (33) Hess, B. A. *Phys. Rev. A* **1986**, *33*, 3742.
- (34) Ghigo, G.; Roos, B. O.; Malmqvist, P.-Å. *Chem. Phys. Lett.* **2004**, *396*, 142.
- (35) Andersson, K. *Theor. Chim. Acta* **1995**, *91*, 31.
- (36) Forsberg, N.; Malmqvist, P.-Å. *Chem. Phys. Lett.* **1997**, *274*, 196.
- (37) Aquilante, F.; De Vico, L.; Ferré, N.; Ghigo, G.; Malmqvist, P.-Å.; Neogrady, P.; Pedersen, T. B.; Pitonak, M.; Reiher, M.; Roos, B. O.; Serrano-Andrés, L.; Urban, M.; Veryazov, V.; Lindh, R. *Comput. Chem.* **2010**, *31*, 224.
- (38) Pou-Amerigo, R.; Merchán, M.; Widmark, P.-O.; Roos, B. O. *Theor. Chim. Acta* **1995**, *92*, 149.
- (39) Andersson, K.; Roos, B. O. *Int. J. Quantum Chem.* **1993**, *45*, 591.
- (40) Queralt, N.; Taratiel, D.; de Graaf, C.; Caballol, R.; Cimiraglia, R.; Angeli, C. *J. Comput. Chem.* **2008**, *29*, 994.
- (41) Suaid, N.; Bonet, M.-L.; Boilleau, C.; Labèguerie, P.; Guihéry, N. *J. Am. Chem. Soc.* **2009**, *131*, 715.
- (42) Kepenekian, M.; Robert, V.; Le Guennic, B. *J. Chem. Phys.* **2009**, *131*, 114702.
- (43) Bondybey, V. E.; English, J. H. *Chem. Phys. Lett.* **1983**, *94*, 443.
- (44) Simard, B.; Lebeault-Dorget, M. A.; Marijijnissen, A.; ter Meulen, J. J. *J. Chem. Phys.* **1998**, *108*, 9668.

Embedding vs Supermolecular Strategies in Evaluating the Hydrogen-Bonding-Induced Shifts of Excitation Energies

Georgios Fradelos,[†] Jesse J. Lutz,[‡] Tomasz A. Wesolowski,^{*,†} Piotr Piecuch,^{*,†} and Marta Włoch[§]

[†]Département de Chimie Physique, Université de Genève, 30, quai Ernest-Ansermet, CH-1211 Genève 4, Switzerland

[‡]Department of Chemistry, Michigan State University, East Lansing, Michigan 48824, United States

[§]Department of Chemistry, Michigan Technological University, Houghton, Michigan 49931, United States

 Supporting Information

ABSTRACT: Shifts in the excitation energy of the organic chromophore, *cis*-7-hydroxyquinoline (*cis*-7HQ), corresponding to the $\pi \rightarrow \pi^*$ transition in *cis*-7HQ and induced by the complexation with a variety of small hydrogen-bonded molecules, obtained with the frozen-density embedding theory (FDET), are compared with the results of the supermolecular equation-of-motion coupled-cluster (EOMCC) calculations with singles, doubles, and noniterative triples, which provide the reference theoretical data, the supermolecular time-dependent density functional theory (TDDFT) calculations, and experimental spectra. Unlike in the supermolecular EOMCC and TDDFT cases, where each complexation-induced spectral shift is evaluated by performing two separate calculations, one for the complex and another one for the isolated chromophore, the FDET shifts are evaluated as the differences of the excitation energies determined for the same many-electron system, representing the chromophore fragment with two different effective potentials. By considering eight complexes of *cis*-7HQ with up to three small hydrogen-bonded molecules, it is shown that the spectral shifts resulting from the FDET calculations employing nonrelaxed environment densities and their EOMCC reference counterparts are in excellent agreement with one another, whereas the analogous shifts obtained with the supermolecular TDDFT method do not agree with the EOMCC reference data. The average absolute deviation between the complexation-induced shifts, which can be as large, in absolute value, as about 2000 cm^{-1} , obtained using the nonrelaxed FDET and supermolecular EOMCC approaches that represent two entirely different computational strategies, is only about 100 cm^{-1} , i.e., on the same order as the accuracy of the EOMCC calculations. This should be contrasted with the supermolecular TDDFT calculations, which produce the excitation energy shifts that differ from those resulting from the reference EOMCC calculations by about 700 cm^{-1} on average. Among the discussed issues are the choice of the electronic density defining the environment with which the chromophore interacts, which is one of the key components of FDET considerations, the basis set dependence of the FDET, supermolecular TDDFT, and EOMCC results, the usefulness of the monomer vs supermolecular basis expansions in FDET considerations, and the role of approximations that are used to define the exchange-correlation potentials in FDET and supermolecular TDDFT calculations.

1. INTRODUCTION

Accurately predicting the effect of a hydrogen-bonded environment on the electronic structure of embedded molecules represents a challenge for computational chemistry. In spite of being relatively weak, noncovalent interactions with the environment, such as hydrogen bonds, can qualitatively affect the electronic structure and properties of the embedded molecules. Among such properties, electronic excitation energies are of great interest in view of the common use of organic chromophores as probes in various environments.^{1–4} Typically, hydrogen bonding results in shifts in the positions of the maxima of the absorption and emission bands anywhere between a few hundred and about 3000 cm^{-1} .⁵ Thus, in order to be able to use computer modeling for the interpretation of experimental data, the intrinsic errors of the calculated shifts must be very small, on the order of 100 cm^{-1} or less.

Unfortunately, the brute force application of the supermolecular strategy to an evaluation of the excitation energy shifts due to the formation of weakly bound complexes with environment molecules, in which one determines the shift as a difference between the excitation energy for a given electronic transition in

the complex and the analogous excitation energy characterizing the isolated chromophore, has a limited range of applicability. The supermolecular approach hinges on a condition that many of the existing quantum chemistry approaches struggle with, namely, the ability of a given electronic structure method to provide an accurate and well-balanced description of excitation energies in systems that have different sizes, which in the specific case of spectral shifts induced by complexation are the total system consisting of the chromophore and environment molecules and the system representing the isolated chromophore. *Ab initio* methods based on the equation-of-motion (EOM)^{6–10} or linear-response^{11–16} coupled-cluster (CC)^{17–22} theories (cf. refs 23–25 for selected reviews), including, among many schemes proposed to date, the basic EOMCC approach with singles and doubles (EOMCCSD)^{7–9} and the suitably modified variant of the completely renormalized (CR) EOMCC theory with singles, doubles, and noniterative triples, abbreviated as δ -CR-EOMCC(2,3), which is based on the CR-CC(2,3)^{26–28} and CR-EOMCC(2,3)^{29,30}

Received: February 10, 2011

Published: May 02, 2011

methods and which is used in the present study to provide the reference data, or the closely related EOMCCSD(2)_T³¹ and EOMCCSD(\hat{T})³² approximations, satisfy this condition, since they provide an accurate and systematically improvable description of the electronic excitations in molecular systems and satisfy the important property of size-intensivity,^{16,33} but their applicability is limited to relatively small molecular problems due to the CPU steps that typically scale as \mathcal{N}^6 – \mathcal{N}^7 with the system size \mathcal{N} . In recent years, progress has been made toward extending the EOMCC and response CC methods to larger molecules through the use of local correlation techniques^{34–37} and code parallelization, combined, in analogy to the widely used QM/MM techniques, with molecular mechanics,^{38–42} and we hope to be able to extend our own, recently developed, local correlation cluster-in-molecule CC algorithms^{43–45} to excited states as well, but in spite of these advances, none of the resulting approaches is as practical, as far as computer costs are concerned, as methods based on the time-dependent density functional theory (TDDFT).⁴⁶ Unfortunately, the existing TDDFT approaches, although easily applicable to large molecular systems due to low computer costs, are often not accurate enough to guarantee a robust description of the complexation-induced spectral shifts in weakly bound complexes when the supermolecular approach is employed, due to their well-known difficulties with describing dispersion and charge-transfer interactions, and other intrinsic errors.

Methods employing the embedding strategy, including those based on the frozen-density embedding theory (FDET)^{47–50} that interests us in this work, provide an alternative strategy to the supermolecular approach for evaluating the excitation energy shifts. In embedding methods, of both empirical (QM/MM, for instance) and FDET types, the effect of the environment is not treated explicitly but, rather, by means of the suitably designed embedding potential. Thus, instead of solving the electronic Schrödinger equation for the total ($N_A + N_B$)-electron system AB consisting of the N_A -electron chromophore A and N_B -electron environment B , i.e.

$$\hat{H}^{(AB)}|\Psi^{(AB)}\rangle = E^{(AB)}|\Psi^{(AB)}\rangle \quad (1)$$

where $\hat{H}^{(AB)}$ is the Hamiltonian of the total system AB , and the electronic Schrödinger equation for the isolated chromophore A

$$\hat{H}^{(A)}|\Psi^{(A)}\rangle = E^{(A)}|\Psi^{(A)}\rangle \quad (2)$$

where $\hat{H}^{(A)}$ is the Hamiltonian of the chromophore in the absence of environment, and then calculating the shift in an observable of interest associated with an operator \hat{O} by forming the difference of the expectation values of \hat{O} computed for two systems that have different numbers of electrons,

$$\Delta\langle\hat{O}\rangle = \langle\Psi^{(AB)}|\hat{O}|\Psi^{(AB)}\rangle - \langle\Psi^{(A)}|\hat{O}|\Psi^{(A)}\rangle \quad (3)$$

as one would have to do in supermolecular calculations, one solves two many-electron problems characterized by the same number of electrons, namely, eq 2 and

$$[\hat{H}^{(A)} + \hat{V}_{\text{emb}}^{(A)}]|\Psi_{\text{emb}}^{(A)}\rangle = E_{\text{emb}}^{(A)}|\Psi_{\text{emb}}^{(A)}\rangle \quad (4)$$

where $|\Psi_{\text{emb}}^{(A)}\rangle$ is the auxiliary N_A -electron wave function describing the effective state of the chromophore A in the presence of environment B and $\hat{V}_{\text{emb}}^{(A)} = \sum_{i=1}^{N_A} v_{\text{emb}}(\vec{r}_i)$ is the suitably designed embedding operator defined in terms of the effective one-electron potential $v_{\text{emb}}(\vec{r})$. As a result, the

complexation-induced shift in an observable represented by an operator \hat{O} is evaluated in the embedding strategy as

$$\Delta\langle\hat{O}\rangle = \langle\Psi_{\text{emb}}^{(A)}|\hat{O}|\Psi_{\text{emb}}^{(A)}\rangle - \langle\Psi^{(A)}|\hat{O}|\Psi^{(A)}\rangle \quad (5)$$

i.e., by using the many-electron wave functions $|\Psi^{(A)}\rangle$ and $|\Psi_{\text{emb}}^{(A)}\rangle$ that represent two different physical states of system A corresponding to the same number of electrons, the state of the isolated chromophore A and the state of A embedded in the environment B . This has two immediate advantages over the supermolecular approach. First, the embedding strategy does not require the explicit consideration of the total ($N_A + N_B$)-electron system consisting of the interacting complex of chromophore and environment. This may lead to a significant cost reduction in the computer effort in applications involving larger environments. Second, by determining the complexation-induced shift $\Delta\langle\hat{O}\rangle$ using the wave functions $|\Psi^{(A)}\rangle$ and $|\Psi_{\text{emb}}^{(A)}\rangle$ corresponding to the same number of electrons, the errors due to approximations used to solve the N_A -electron problems represented by eqs 2 and 4 largely cancel out, as we do not have to worry too much about the possible dependence of the error on the system size. In the calculations of the shifts in excitation energies using the size-intensive EOMCC methods, one does not have to worry about the size dependence of the error resulting from the calculations either, but the supermolecular EOMCC approach requires an explicit consideration of the ($N_A + N_B$)-electron system consisting of the chromophore and environment, which may lead to a significant cost increase when N_B is larger.

The above description implies that the accuracy of the complexation-induced shifts obtained in embedding calculations largely depends on the quality of the embedding operator $\hat{V}_{\text{emb}}^{(A)}$ or the underlying one-electron potential $v_{\text{emb}}(\vec{r})$ that defines it. Thus, when compared with the supermolecular approach, the challenge is moved from assuring the cancellation of errors in approximate solutions of two Schrödinger equations for systems that differ in the number of electrons to developing a suitable form of the embedding potential that can accurately describe the state of the chromophore in the weakly bound complex with environment. As already mentioned above, the practical advantage of the embedding strategy (provided a sufficiently accurate approximation for the embedding potential is employed) is the fact that it can be used for much larger systems than the supermolecular one and can even be applied in multiscale molecular simulations.^{48,51–53} As formally demonstrated in our previous studies,^{47–50} the embedding operator can be represented in terms of a local potential $v_{\text{emb}}(\vec{r})$ (orbital-free embedding potential), which is determined by the pair of electron densities, ρ_A , describing the embedded system A and constructed using the $|\Psi_{\text{emb}}^{(A)}\rangle$ wave function, and ρ_B , representing the electron density of the environment B . Unfortunately, except for some analytically solvable systems,⁵⁴ the precise dependence of $v_{\text{emb}}(\vec{r})$ on ρ_A and ρ_B is not known. Only its electrostatic component is known exactly. The nonelectrostatic component, which arises from the nonadditivity of the density functionals for the exchange-correlation and kinetic energies, must be approximated or reconstructed, either analytically (if possible)⁵⁴ or numerically.^{55–57} In the case of the hydrogen-bonded environments that interest us in this study, the electrostatic component of the exact embedding potential can be expected to dominate and the overall accuracy of the environment-induced changes of the electronic structure of embedded

species can be expected to be accurately described. Indeed, a number of our previous studies^{58,59} show that the currently known approximants to the relevant functional representations of $v_{\text{emb}}(\vec{r})$ in terms of ρ_A and ρ_B are adequate.

Our past examinations of the formal and practical aspects of the FDET methodology have largely focused on model systems or direct comparisons with experimental results. Analytically solvable model systems (see ref 54) are especially important, since, as pointed out above, they enable one to develop ideas about the dependence of the embedding potential $v_{\text{emb}}(\vec{r})$ on densities ρ_A and ρ_B , but real many-electron systems may be quite different than models. A comparison with experimental results is clearly the ultimate goal of any modeling technique, and FDET is no different in this regard, but it often happens that experiments have their own error bars and their proper interpretation may require additional considerations and the incorporation of physical effects that are not included in the purely electronic structure calculations. This study offers an alternative way of testing the FDET techniques. Thus, the main objective of the present work is to make a direct comparison of the benchmark results obtained in the high-level, supermolecular, wave function-based EOMCC calculations, using the aforementioned size-intensive modification of the CR-EOMCC(2,3) method,^{29,30} designated as δ -CR-EOMCC(2,3), with those produced by the embedding-theory-based FDET approach^{47–50} and the supermolecular TDDFT methodology. To this end, we obtain the δ -CR-EOMCC(2,3)-based shifts in the vertical excitation energy corresponding to the $\pi \rightarrow \pi^*$ transition in the organic chromophore, *cis*-7-hydroxyquinoline (*cis*-7HQ), induced by formation of hydrogen-bonded complexes with eight different environments defined by the water, ammonia, methanol, and formic acid molecules and their selected aggregates consisting of up to three molecules, for which, as shown in this work, reliable EOMCC data can be generated and which were previously examined using laser resonant two-photon UV spectroscopy,^{5,59} and we use the resulting reference shift values to assess the quality of the analogous spectral shifts obtained in the FDET and supermolecular TDDFT calculations.

Having access to accurate reference EOMCC data enables us to explore various aspects of the FDET methodology and approximations imposed within. For example, in addition to the approximations used for the nonelectrostatic component of the embedding potential $v_{\text{emb}}(\vec{r})$, the FDET techniques exploit various forms of the electron density of the environment ρ_B . Since ρ_B is an assumed quantity in the FDET considerations, its choice may critically affect the calculated environment-induced shifts in observables.^{60,61} The dependence of the FDET values of the shifts in the excitation energy of *cis*-7HQ induced by the complexation with hydrogen-bonded molecules on the form of ρ_B represents one of the most important aspects of the present study. Among other issues discussed in this work are the basis set dependence of the FDET, supermolecular TDDFT, and EOMCC results, the usefulness of the monomer vs supermolecular basis expansions in the FDET calculations, and the role of approximations that are used to define the exchange-correlation potentials in the FDET and supermolecular TDDFT calculations.

Although the main focus of this work is a comparison of the embedding-theory-based FDET and supermolecular TDDFT results with the high-level *ab initio* EOMCC data to demonstrate the advantages of the FDET approach over the conventional supermolecular TDDFT methodology in a realistic application, a

comparison of the theoretical shifts with the corresponding experimental data^{5,59} is discussed as well. The gas-phase complexes examined in this paper have been intensely studied, both experimentally and theoretically, since some of these complexes, particularly the larger ones, can be viewed as models of proton-transferring chains in biomolecular systems.^{1,62}

2. METHODS

As explained in the Introduction, the main goal of this study is a comparison of the shifts in the excitation energy corresponding to the $\pi \rightarrow \pi^*$ transition in the *cis*-7HQ system, induced by the formation of hydrogen-bonded complexes of *cis*-7HQ with a number of small molecules, resulting from the embedding-theory-based FDET approach and supermolecular TDDFT calculations, with those obtained with the EOMCC-based δ -CR-EOMCC(2,3) scheme that provides the theoretical reference data. This section provides basic information about the electronic structure theories exploited in this work. Since the supermolecular TDDFT approach is a well-established methodology, our description focuses on the FDET and EOMCC methods used in our calculations.

2.1. Frozen-Density Embedding Theory. The FDET formalism^{47–50,63} provides basic equations for the variational treatment of a quantum-mechanical subsystem embedded in a given electronic density. Various FDET-based approaches developed by us^{47–50,54,58,64} and others,^{65–69} differing in the way the environment density is generated, the choice made for the approximants for the relevant density functionals, or the choice for the quantum-mechanical descriptors for the embedded subsystem, are in use today. Below, we outline the basic elements of the FDET methodology.

1. Basic Variables. The total system *AB*, consisting of a molecule or an aggregate of molecules of interest, *A*, embedded in the environment *B* created by the other molecule(s), is characterized by two types of densities. The first one is the density of the embedded molecule(s), $\rho_A(\vec{r})$, which is typically represented using one of the following auxiliary quantities: (i) the occupied orbitals of a noninteracting reference system $\{\phi_i^{(A)}(\vec{r})\}$, $i = 1, \dots, N_A\}$,⁴⁷ (ii) the occupied and unoccupied orbitals of a noninteracting reference system,⁶³ (iii) the interacting wave function,⁴⁹ or (iv) the one-particle density matrix.⁵⁰ The second one is the density of the environment, $\rho_B(\vec{r})$, which is fixed for a given electronic problem (“frozen density”).

2. Constrained Search. The optimum density $\rho_A(\vec{r})$ of the system *A* embedded in the environment *B*, represented by the fixed density $\rho_B(\vec{r})$ satisfying

$$\int \rho_B(\vec{r}) \, d\vec{r} = N_B \quad (6)$$

is obtained by performing the following constrained search:

$$E_{\text{emb}}^{(A)}[\rho_B] = \min_{\rho \geq \rho_B} E_{\text{HK}}[\rho] = \min_{\rho_A} E_{\text{HK}}[\rho_A + \rho_B] \quad (7)$$

subject to the conditions

$$\int \rho(\vec{r}) \, d\vec{r} = N_A + N_B \quad (8)$$

and

$$\int \rho_A(\vec{r}) \, d\vec{r} = N_A \quad (9)$$

where $E_{HK}[\rho]$ in eq 7 is the usual Hohenberg–Kohn energy functional.

3. *Constrained Search by Modifying the External Potential.* In practice, the search for the optimum density ρ_A , defined by eq 7, is conducted by solving eq 4, in which $\hat{H}^{(A)}$ is the environment-free Hamiltonian of the isolated system A and $\hat{V}_{\text{emb}}^{(A)} = \sum_{i=1}^{N_A} v_{\text{emb}}(\vec{r})$, where $v_{\text{emb}}(\vec{r})$ has the form of a local, orbital-free, embedding potential $v_{\text{emb}}^{\text{eff}}(\vec{r})$, determined by the pair of densities $\rho_A(\vec{r})$ and $\rho_B(\vec{r})$ and designated by $v_{\text{emb}}^{\text{eff}}[\rho_A, \rho_B; \vec{r}]$.

4. *Orbital-Free Embedding Potential.* As shown earlier,⁴⁹ the relationship between the local potential $v_{\text{emb}}^{\text{eff}}[\rho_A, \rho_B; \vec{r}]$ and densities $\rho_A(\vec{r})$ and $\rho_B(\vec{r})$ depends on the quantum-mechanical descriptors that are used as the auxiliary quantities for defining $\rho_A(\vec{r})$. If we use the orbitals of a noninteracting reference system, the wave function of the full configuration interaction form, or the one-particle density matrix as the descriptors to define $\rho_A(\vec{r})$, the local, orbital-free, embedding potential reads as follows:

$$v_{\text{emb}}^{\text{eff}}[\rho_A, \rho_B; \vec{r}] = v_{\text{ext}}^B(\vec{r}) + \int \frac{\rho_B(\vec{r}')}{|\vec{r}' - \vec{r}|} d\vec{r}' + v_{\text{xc}}^{\text{nad}}[\rho_A, \rho_B](\vec{r}) + v_t^{\text{nad}}[\rho_A, \rho_B](\vec{r}) \quad (10)$$

where

$$v_{\text{xc}}^{\text{nad}}[\rho_A, \rho_B](\vec{r}) = \left. \frac{\delta E_{\text{xc}}[\rho]}{\delta \rho} \right|_{\rho = \rho_A + \rho_B} - \left. \frac{\delta E_{\text{xc}}[\rho]}{\delta \rho} \right|_{\rho = \rho_A} \quad (11)$$

and

$$v_t^{\text{nad}}[\rho_A, \rho_B](\vec{r}) = \left. \frac{\delta T_s[\rho]}{\delta \rho} \right|_{\rho = \rho_A + \rho_B} - \left. \frac{\delta T_s[\rho]}{\delta \rho} \right|_{\rho = \rho_A} \quad (12)$$

As we can see, the above equation for $v_{\text{emb}}^{\text{eff}}[\rho_A, \rho_B; \vec{r}]$ involves the external and Coulomb potentials due to the environment B and the $v_{\text{xc}}^{\text{nad}}[\rho_A, \rho_B](\vec{r})$ and $v_t^{\text{nad}}[\rho_A, \rho_B](\vec{r})$ components that arise from the nonadditivities of the exchange–correlation and kinetic energy functionals of the Kohn–Sham formulation⁷⁰ of DFT,⁷¹ $E_{\text{xc}}[\rho]$ and $T_s[\rho]$, respectively.

5. *Kohn–Sham Equations with Constrained Electronic Density.* Once $v_{\text{emb}}^{\text{eff}}[\rho_A, \rho_B; \vec{r}]$ is defined, as in eq 10, and if we use a noninteracting reference system to perform the constrained search given by eq 7, the corresponding orbitals $\phi_i^{(A)}$, $i = 1, \dots, N_A$, of the system A embedded in the environment B are obtained from the following Kohn–Sham-like equations [cf. eqs 20 and 21 in our earlier work⁴⁷]:

$$\left[-\frac{1}{2}\nabla^2 + v_{\text{KS}}^{\text{eff}}[\rho_A; \vec{r}] + v_{\text{emb}}^{\text{eff}}[\rho_A, \rho_B; \vec{r}] \right] \phi_i^{(A)} = \varepsilon_i^{(A)} \phi_i^{(A)} \quad (13)$$

where $v_{\text{KS}}^{\text{eff}}[\rho_A; \vec{r}]$ is the usual expression for the potential of the Kohn–Sham DFT for the isolated system A . After obtaining the orbitals $\phi_i^{(A)}$ and the corresponding orbital energies $\varepsilon_i^{(A)}$ by solving eq 13, we proceed to the determination of the ground- and excited-state energies and properties, which in this case describe the system A embedded in the environment B , in a usual manner, using standard techniques of DFT or TDDFT.

The effectiveness of methods based on eq 13, with $v_{\text{emb}}^{\text{eff}}[\rho_A, \rho_B; \vec{r}]$ determined using eq 10, in the calculations of changes in the electronic structure arising due to the interactions between the embedded system and its environment was

demonstrated in a number of applications, including vertical excitation energies,^{59,63} ESR hyperfine coupling constants,^{72,73} ligand-field splittings of f levels in lanthanide impurities,⁶⁰ NMR shieldings,⁷⁴ dipole and quadrupole moments, and electronic excitation energies and frequency-dependent polarizabilities.⁷⁵ The FDET strategy, as summarized above, is expected to calculate the shifts in the vertical excitation energy corresponding to the $\pi \rightarrow \pi^*$ transition in the *cis*-7HQ system due to its environment in a reasonable manner,⁵² and the present paper verifies if this is indeed the case by comparing the results of the FDET and δ -CR-EOMCC(2,3)-based EOMCC calculations.

In this context, it is useful to mention two other approaches related to FDET that aim at the description of a system consisting of subsystems, including the situation of a molecule or a molecular complex embedded in an environment which interests us here, namely, the subsystem formulation of DFT (SDFT)^{76,77} and the recently developed partition DFT (PDFT).⁷⁸ In analogy to FDET, in the SDFT approach, the charge of each subsystem is assumed to be an integer, whereas PDFT allows for fractional subsystem charges. In the exact limit, both SDFT and PDFT lead to the exact ground-state electronic density and energy of the total system under investigation, providing an alternative to the conventional supermolecular Kohn–Sham framework. This should be contrasted with the FDET approach, which does not target the exact ground-state electronic density of the total system AB but, rather, the density of subsystem A that minimizes the Hohenberg–Kohn energy functional of the total system, $E_{HK}[\rho_A + \rho_B]$, using a fixed form of the environment density ρ_B in the presence of constraints, as in eqs 6–9. Thus, FDET may lead to the same total ground-state density as SDFT, Kohn–Sham DFT, or PDFT, but only when the specific set of additional assumptions and constraints is employed.⁴⁸ Indeed, in the case of the total system AB consisting of two subsystems A and B , where A is a molecular system embedded in environment B , the SDFT approach searches for the pure-state, noninteracting, ν -representable subsystem densities ρ_A and ρ_B that minimize the Hohenberg–Kohn energy functional $E_{HK}[\rho_A + \rho_B]$

$$E^{(AB)} = \min_{\rho_A, \rho_B} E_{HK}[\rho_A + \rho_B] \quad (14)$$

subject to the constraints given by eqs 6–9. Thus, the sufficient condition for reaching the exact ground-state density of the total system AB , ρ_{AB} , in SDFT is the decomposability of ρ_{AB} into a sum of two pure-state, noninteracting, ν -representable densities ρ_A and ρ_B representing subsystems A and B consisting of the integer numbers of electrons, N_A and N_B , respectively (see the discussion in ref 48). The FDET approach does not search for the exact ground-state density ρ_{AB} of the total system AB . It uses the variational principle described by eq 7 to find the density, which minimizes the total ground-state energy in the presence of the constraint

$$\rho \geq \rho_B \quad (15)$$

with the subsystem density ρ_B given in advance. As a result, the total density obtained with FDET is not equal to the exact ground-state density ρ_{AB} except for one specific case where the difference between $\rho_{AB}(\vec{r})$ and the assumed density $\rho_B(\vec{r})$ is representable using one of the aforementioned auxiliary descriptors, including orbitals of the noninteracting reference system,⁴⁷ interacting wave function,⁴⁹ or one particle-density matrix.⁵⁰ Thus, by the virtue of the Hohenberg–Kohn theorem, unless

$\rho_B(\vec{r})$ is representable using the above auxiliary descriptors, the FDET approach can only give the upper bound to the exact ground-state energy of the total system AB ,

$$E_{\text{emb}}^{(A)}[\rho_B] \geq E^{(AB)} \quad (16)$$

Although there are differences between SDFT and FDET, as pointed out above, both methodologies have a lot in common as well. In particular, any computer implementation of the FDET approach can easily be converted into the SDFT algorithm. For example, as shown in the original numerical studies based on SDFT concerning atoms in solids^{76,77} and in the recent implementation of SDFT for molecular liquids,⁷⁹ in the SDFT approach one has to solve a system of coupled Kohn–Sham equations, which is similar to the system represented by eq 13. One of the most efficient schemes for solving such systems is the “freeze-and-thaw” iterative procedure introduced in ref 80. The “freeze-and-thaw” algorithm was exploited in a number of SDFT studies, including those reported in refs 81–83, and the same algorithm is used in the present work to carry out the FDET calculations for the hydrogen-bonded complexes of the *cis*-7HQ system. The “freeze-and-thaw” scheme for solving the coupled Kohn–Sham-like equations of FDET and SDFT was previously used by us in the methodological studies on approximants to the bifunctional of the nonadditive kinetic energy potential $v_i^{\text{nad}}[\rho_A, \rho_B](\vec{r})$ (see, e.g., refs 64, 84, and 85) and in the preparatory stages for the large-scale FDET simulations, in which the search defined by eq 7 is initially performed for smaller model systems in order to establish the adequacy of the simplified form of $\rho_B(\vec{r})$ to be used in the subsequent calculations for the target large system. We also demonstrated that the “freeze-and-thaw” procedure for solving the coupled Kohn–Sham-like equations of the type seen in eq 13 can be performed simultaneously with displacing nuclear positions, accelerating the SDFT-based geometry optimizations.⁸⁶

Finally, it should be noted that the relaxation of the environment density ρ_B during the SDFT “freeze-and-thaw” iterations is accompanied by errors which are introduced by the approximant to the bifunctional of the nonadditive kinetic energy potential $v_i^{\text{nad}}[\rho_A, \rho_B](\vec{r})$, eq 12, and which can artificially be enhanced by the relaxation of ρ_B . Thus, when the expected polarization effects are small, the relaxation of ρ_B during the SDFT iterations should be avoided, and the results presented in section 4 clearly show this. This problem does not enter the nonrelaxed FDET considerations, in which one fixes the form of ρ_B prior to FDET iterations. On the other hand, one needs to be aware of the fact that if the electronic polarization effects are strong or if the goal is to obtain embedding potentials that mimic supermolecular TDDFT calculations, one should use the fully relaxed “freeze-and-thaw” iterations to optimize both components of the total electronic density ρ_{AB} , i.e., ρ_A and ρ_B , not just ρ_A . Indeed, as shown in section 4, the FDET results for the spectral shifts in the *cis*-7HQ chromophore induced by complexation, in which ρ_B is allowed to relax, are quite close to the results of supermolecular TDDFT calculations, even though the latter results are generally poor and far from the EOMCC benchmark values and the corresponding experimental data. The fact that the relaxed FDET calculations lead to a considerably worse description of the complexation-induced shifts in *cis*-7HQ than the nonrelaxed ones has several reasons. One of them is the aforementioned problem of the errors introduced by the approximants used to represent $v_i^{\text{nad}}[\rho_A, \rho_B](\vec{r})$, which penalize the overlap between ρ_A

and ρ_B . Another is the realization of the fact that the relaxation of ρ_B in the FDET considerations is not necessarily the same as the physical effect of the electronic polarization of the environment B by subsystem A , i.e., one cannot expect automatic improvements in the results of the FDET calculations when ρ_B is allowed to relax, particularly when the polarization effects are small. The relaxation of the environment density ρ_B within the FDET framework is related to a complex notion of the pure-state noninteracting ν -representability of the target subsystem density ρ_A , which does not automatically translate into the physical polarization of B by A . Indeed, let $\rho_{B,\text{iso}}$ designate the exact ground-state density of the isolated species B and let $\rho_{B,\text{fro}}$ be a particular choice of ρ_B used in FDET. If $\rho_{B,\text{fro}}$ is chosen in such a way that the density difference $\bar{\rho}_A \equiv \rho_{AB} - \rho_{B,\text{fro}}$, where ρ_{AB} represents the exact ground-state density of the total system AB , is pure-state ν -representable, we can obtain this $\bar{\rho}_A$ by solving the Kohn–Sham system given by eq 13. Most likely, there is an infinite number of densities $\rho_{B,\text{fro}}$ that lead to the pure-state ν -representable $\bar{\rho}_A$. Each one of them will result in a different solution for $\bar{\rho}_A$ and, what is more important here, in a different relaxation, as measured by the difference $\Delta\rho_B \equiv \rho_{B,\text{fro}} - \rho_{B,\text{iso}}$. In particular, if $\rho_{B,\text{iso}}$ is one of the densities $\rho_{B,\text{fro}}$ that guarantees the pure-state noninteracting ν -representability of $\bar{\rho}_A$, there is no physical relaxation at all ($\Delta\rho_B = 0$), and the “freeze-and-thaw” calculations are not needed, regardless of whether the physical polarization of B by A is significant or not. It is also worth mentioning that although the pure-state noninteracting ν -representability of $\bar{\rho}_A$ cannot be *a priori* assured, there are strong indications from the recent studies of exactly solvable systems⁵⁴ that even if the N -representable density $\bar{\rho}_A$ associated with a given $\rho_{B,\text{fro}}$ is not pure-state ν -representable, it can be approached arbitrarily closely by a solution of eq 13 obtained with a suitably chosen smooth embedding potential. All of this demonstrates that the connection between the mathematical (in practice, numerical) relaxation of ρ_B in the FDET considerations and the physical polarization of the environment B by subsystem A is far from obvious. For this reason, comparing the results of the nonrelaxed and relaxed FDET calculations with the independent high-level *ab initio* data obtained with the carefully validated wave function theory is very important. The main objective of the present study is to demonstrate that when the polarization of the environment is small, as is the case when the weakly bound complexes of the *cis*-7HQ molecule are examined, one is better off by using a simplified FDET procedure in which the relaxation of the *a priori* determined environment density ρ_B is neglected, as this leads to a considerably better agreement with the results of the converged EOMCC calculations and the experiment.

2.2. Equation-of-Motion Coupled-Cluster Calculations.

The main goal of the present work is to compare the shifts in the $\pi \rightarrow \pi^*$ excitation energy of the *cis*-7HQ system, induced by the complexation of *cis*-7HQ with small hydrogen bonded molecules, obtained with the FDET approach, with the results of the supermolecular EOMCC calculations with singles, doubles, and noniterative triples, exploiting the size-intensive modification of the CR-EOMCC(2,3) approach,^{29,30} abbreviated as δ -CR-EOMCC(2,3), which is used to provide the required reference theoretical data. The basic idea of the EOMCC formalism is the following wave function ansatz:^{6–9}

$$|\Psi_\mu\rangle = R_\mu e^T |\Phi\rangle \quad (17)$$

where $|\Psi_\mu\rangle$ is the ground ($\mu = 0$) or excited ($\mu > 0$) state, $|\Phi\rangle$ is the reference determinant, which usually is the Hartree–Fock state [in all of the EOMCC calculations reported in this work, the restricted Hartree–Fock (RHF) configuration], and R_μ is the linear excitation operator which generates the excited-state wave functions $|\Psi_\mu\rangle$ from the CC ground state $|\Psi_0\rangle = e^T|\Phi\rangle$. Here and elsewhere in this article, we use a convention in which the $\mu = 0$ excitation operator $R_{\mu=0}$ is defined as a unit operator, $R_{\mu=0} = \mathbf{1}$, to incorporate the ground- and excited-state cases within a single set of formulas. The T operator entering the above definitions is the usual cluster operator of the ground-state CC theory, which is typically obtained by truncating the corresponding many-body expansion

$$T = \sum_{n=1}^N T_n \quad (18)$$

where

$$T_n = \sum_{i_1 < \dots < i_n, a_1 < \dots < a_n} t_{a_1 \dots a_n}^{i_1 \dots i_n} a^{a_1} \dots a^{a_n} a_{i_1} \dots a_{i_n} \quad (19)$$

is the n -body component of T , at some, preferably low, excitation level $M < N$, and by solving the nonlinear system of equations for cluster amplitudes $t_{a_1 \dots a_n}^{i_1 \dots i_n}$ with $n \leq M$, which define the truncated form of T , designated as $T^{(M)}$, resulting from the substitution of the CC wave function ansatz into the electronic Schrödinger equation and the projection of the resulting equation on the excited determinants $|\Phi_{i_1 \dots i_n}^{a_1 \dots a_n}\rangle$ that correspond to the many-body components T_n included in $T^{(M)}$. Here and elsewhere in the present article, we use a standard notation in which i_1, i_2, \dots or i, j, \dots and a_1, a_2, \dots or a, b, \dots are the occupied and unoccupied spin-orbitals, respectively, and a^{a_k} (a_{i_k}) designate the usual creation (annihilation) operators. Once the ground-state operator T and the corresponding ground-state CC energy E_0 are determined, one obtains the many-body components

$$R_{\mu, n} = \sum_{i_1 < \dots < i_n, a_1 < \dots < a_n} r_{\mu, a_1 \dots a_n}^{i_1 \dots i_n} a^{a_1} \dots a^{a_n} a_{i_1} \dots a_{i_n} \quad (20)$$

of the linear excitation operator

$$R_\mu = r_{\mu, 0} \mathbf{1} + \sum_{n=0}^N R_{\mu, n} \quad (21)$$

which is typically truncated at the same excitation level M as the cluster operator T , and the corresponding vertical excitation energies

$$\omega_\mu = E_\mu - E_0 \quad (22)$$

by solving the EOMCC eigenvalue problem involving the similarity-transformed Hamiltonian $\bar{H}^{(M)} = e^{-T^{(M)}} H e^{T^{(M)}}$ in the subspace of the N -electron Hilbert space spanned by the excited determinants $|\Phi_{i_1 \dots i_n}^{a_1 \dots a_n}\rangle$ that correspond to the many-body components $R_{\mu, n}$ included in R_μ .

The basic EOMCC approximation, in which $M = 2$, so that $T \approx T^{(2)} = T_1 + T_2$ and $R_\mu \approx R_\mu^{(2)} = r_{\mu, 0} \mathbf{1} + R_{\mu, 1} + R_{\mu, 2}$, defining the EOMCCSD approach,^{7–9} in which one diagonalizes the similarity-transformed Hamiltonian of CCSD, $\bar{H}^{(2)} = e^{-T^{(2)}} H e^{T^{(2)}}$, in the space spanned by singly and doubly excited determinants $|\Phi_i^a\rangle$ and $|\Phi_{ij}^{ab}\rangle$, and its linear-response CCSD counterpart^{15,16} have been successful in describing excited states dominated by one-electron transitions, but this success does not automatically extend to the more complicated, more

multireference excited electronic states, such as those characterized by a significant two-electron excitation nature (cf. refs 29, 30, 87–93 for examples). There also are cases of excited states dominated by singles, where the EOMCCSD theory level may be insufficient to obtain high-quality results.^{94,95} Thus, particularly in the context of this study, where we expect the EOMCC theory to provide accurate reference data for the FDET and TDDFT calculations, it is important to examine if the EOMCC results used by us are reasonably well converged with the truncations in T and R_μ . Ideally, one would like to perform the full EOMCCSDT (EOMCC with singles, doubles, and triples) calculations^{96–98} and compare them with the corresponding EOMCCSD results to see if the latter results are accurate enough. Unfortunately, it is virtually impossible to carry out the full EOMCCSDT calculations for the *cis*-7HQ system and its complexes investigated in this work due to a steep increase of the CPU time and storage requirements characterizing the EOMCCSDT approach that scale as $n_o^3 n_u^5$ and $\sim n_o^3 n_u^5$ with the numbers of occupied and unoccupied orbitals, n_o and n_u , respectively, as opposed to the $n_o^2 n_u^4$ CPU time and $\sim n_o^2 n_u^2$ storage requirements of EOMCCSD. Thus, one has to resort to one of the approximate treatments of triple excitations in EOMCC that replace the prohibitively expensive iterative CPU steps of EOMCCSDT that scale as \mathcal{N}^8 with the system size \mathcal{N} to the more manageable \mathcal{N}^6 – \mathcal{N}^7 steps.

A large number of approximate EOMCCSDT approaches and their linear-response analogs have been proposed to date.^{29–32,87–89,91,92,96,97,99–106} The noniterative EOMCC methods, in which one adds corrections due to triples to the EOMCCSD energies, such as EOM-CC(2)PT(2)¹⁰⁰ and its size-intensive EOM-CCSD(2)_T³¹ analog, CCSDR3,^{102,103} EOMCCSD(T),¹⁰¹ EOMCCSD(\tilde{T}),³² EOMCCSD(T'),³² CR-EOMCCSD(T)^{87,88,91,92} and the related N-EOMCCSD(T) approach,¹⁰⁶ and CR-EOMCC(2,3),^{29,30} including the spin-flip variant of the CR-EOMCC(2,3) approach of refs 29 and 30 considered in ref 107, are particularly promising in this regard, since they represent computational black boxes similar to those of the popular CCSD(T) ground-state approach¹⁰⁸ or its CR-CC(2,3) extension.^{26–28} All of the above methods greatly reduce the computer costs of full EOMCCSDT calculations, while improving the EOMCCSD results. The improvements are particularly significant for the excited states characterized by significant double-excitation components, but they are often non-negligible for states dominated by one-electron transitions. For example, the most promising EOM-CCSD(2)_T, CCSDR3, EOMCCSD(\tilde{T}), CR-EOMCCSD(T), N-EOMCCSD(T), and CR-EOMCC(2,3) approaches are characterized by the iterative $n_o^2 n_u^4$ steps of EOMCCSD and the noniterative $n_o^3 n_u^4$ steps needed to construct the triples corrections to the EOMCCSD energies, while eliminating the need for storing the $\sim n_o^3 n_u^3$ triply excited amplitudes defining the T and R_μ operators. This makes these methods applicable to much larger problems than those that can be handled by full EOMCCSDT, including the hydrogen-bonded complexes of the *cis*-7HQ system considered in this work.

In this paper, we focus on the size-intensive modification of the CR-EOMCC(2,3) method of refs 29 and 30 defining the δ -CR-EOMCC(2,3) approach implemented in this work. The CR-EOMCC(2,3) approach and the underlying ground-state CR-CC(2,3) approximation^{26–28} are examples of the renormalized CC/EOMCC schemes, which are based on the idea of adding the *a posteriori*, noniterative, and state-specific corrections

δ_μ due to higher-order excitations, neglected in the conventional CC/EOMCC calculations defined by some truncation level M , such as CCSD or EOMCCSD, to the corresponding CC/EOMCC energies. The formal basis for deriving the computationally manageable expressions for corrections δ_μ is provided by one of the forms^{26,27,87–89,109–111} of the expansion describing the difference between the full CI and CC/EOMCC energies in terms of the generalized moments of the CC/EOMCC equations characterizing the truncated CC/EOMCC method we want to correct. If we are interested in correcting the results of the CC/EOMCC calculations truncated at M -tuple excitations, the moments that enter the expressions for the relevant energy corrections δ_μ are defined as projections of the CC/EOMCC equations with T and R_μ truncated at M -body components on the excited determinants $|\Phi_{i_1 \dots i_n}^{a_1 \dots a_n}\rangle$ with $n > M$ that are disregarded in the conventional CC/EOMCC considerations, i.e.

$$\mathcal{M}_{\mu, a_1 \dots a_n}^{i_1 \dots i_n}(M) = \langle \Phi_{i_1 \dots i_n}^{a_1 \dots a_n} | (\bar{H}^{(M)} R_\mu^{(M)}) | \Phi \rangle \quad (23)$$

[$R_\mu^{(M)}$ in eq 23 is the R_μ operator truncated at the M -body component $R_{\mu, M}$]. All of the resulting moment expansions of the full CI energy of the μ th electronic state can be cast into the generic form

$$\delta_\mu = \sum_{n=M+1}^{N_{\mu, M}} \sum_{i_1 < \dots < i_n, a_1 < \dots < a_n} \mathcal{L}_{\mu, i_1 \dots i_n}^{a_1 \dots a_n} \mathcal{M}_{\mu, a_1 \dots a_n}^{i_1 \dots i_n}(M) \quad (24)$$

with $N_{\mu, M}$ representing the highest value of n for which $\mathcal{M}_{\mu, a_1 \dots a_n}^{i_1 \dots i_n}(M)$ is still nonzero, and the only essential difference between various approximations based on eq 24 is in the way one handles the coefficients $\mathcal{L}_{\mu, i_1 \dots i_n}^{a_1 \dots a_n}$.

In the specific case of the CR-EOMCC(2,3) approach that interests us here, one calculates the energies of the ground and excited states as

$$E_\mu = E_\mu^{(\text{CCSD})} + \sum_{i < j < k, a < b < c} \mathcal{L}_{\mu, ijk}^{abc} \mathcal{M}_{\mu, abc}^{ijk}(2) \quad (25)$$

where $E_\mu^{(\text{CCSD})}$ are the CCSD ($\mu = 0$) and EOMCCSD ($\mu > 0$) energies, $\mathcal{M}_{\mu, abc}^{ijk}(2)$ are the moments of the CCSD/EOMCCSD equations corresponding to triple excitations, which are defined by eq 23 in which $M = 2$, and $\mathcal{L}_{\mu, ijk}^{abc}$ are the deexcitation amplitudes that one can calculate using the quasi-perturbative expressions shown in refs 29 and 30. The $\mathcal{L}_{\mu, ijk}^{abc}$ amplitudes used in the CR-EOMCC(2,3) considerations are expressed in terms of the one- and two-body components of the deexcitation operator defining the left EOMCCSD eigenstate,⁹ and the one-body, two-body, and—in the full implementation of CR-EOMCC(2,3) defining variant D of it designated as CR-EOMCC(2,3),D—selected three-body components of the similarity-transformed Hamiltonian of CCSD, $\bar{H}^{(2)}$. The latter components enter the Epstein–Nesbet-like denominator for triples defining the $\mathcal{L}_{\mu, ijk}^{abc}$ amplitudes in the CR-EOMCC(2,3),D approach. In the simplified variant A of CR-EOMCC(2,3), abbreviated as CR-EOMCC(2,3),A and equivalent to the EOM-CC(2)PT(2) method of ref 100, one replaces the Epstein–Nesbet-like denominator defining $\mathcal{L}_{\mu, ijk}^{abc}$ which in variant D of CR-EOMCC(2,3) is calculated as $\omega_\mu^{(\text{CCSD})} - (\langle \Phi_{ijk}^{abc} | \bar{H}_1^{(2)} | \Phi_{ijk}^{abc} \rangle + \langle \Phi_{ijk}^{abc} | \bar{H}_2^{(2)} | \Phi_{ijk}^{abc} \rangle + \langle \Phi_{ijk}^{abc} | \bar{H}_3^{(2)} | \Phi_{ijk}^{abc} \rangle)$, where $\omega_\mu^{(\text{CCSD})}$ is the EOMCCSD excitation energy and $\bar{H}_n^{(2)}$ is the n -body component of $\bar{H}^{(2)}$, by the simplified form of it,

which represents the Møller–Plesset-like denominator for triple excitations, $\omega_\mu^{(\text{CCSD})} - (\varepsilon_a + \varepsilon_b + \varepsilon_c - \varepsilon_i - \varepsilon_j - \varepsilon_k)$. The differences between variants A and D are substantial, in favor of CR-EOMCC(2,3),D, when the excited states of interest are dominated by two-electron transitions. When the excited states in question are dominated by one-electron transitions, as is the case when we examine the $\pi \rightarrow \pi^*$ excitations in *cis*-7HQ and its complexes, the CR-EOMCC(2,3),A and CR-EOMCC(2,3),D approaches provide similar results. We refer the reader to the original work on the CR-EOMCC(2,3) approach and its variants^{29,30} for further details. The similarity of the CR-EOMCC(2,3),A and CR-EOMCC(2,3),D excitation energies for the *cis*-7HQ system and its hydrogen-bonded complexes examined in this study is shown in section 4.1.

Before discussing the computational details of the FDET, TDDFT, and EOMCC calculations reported in this work, we must explain how one obtains the desired δ -CR-EOMCC(2,3) results. As shown in refs 30 and 31, although the ground-state CR-CC(2,3),D energy and its CR-CC(2,3),A analog, which is equivalent to the CCSD(2)_T approach of ref 112, are size extensive, being ideally suited for examining the weakly bound complexes involving larger molecules,^{43–45} such as those studied in this work, their excited state CR-EOMCC(2,3),D and CR-EOMCC(2,3),A [or EOM-CC(2)PT(2)] analogs do not satisfy the property of size intensivity satisfied by EOMCCSD,^{16,33} i.e., the vertical excitation energy of a noninteracting system $A + B$, in which fragment A is excited, resulting from the CR-EOMCC(2,3) or EOM-CC(2)PT(2) calculations, is not the same as that obtained for the isolated system A . Although the departure from strict size intensivity in the CR-EOMCC calculations of vertical and adiabatic excitation energies is in many cases of relatively minor significance when compared to other sources of errors,⁹² this may be a more serious issue when examining the shifts in the excitation energy due to the formation of weakly bound complexes. The lack of size intensivity of the CR-EOMCC(2,3) and EOM-CC(2)PT(2) excitation energies can be traced back to the presence of the size-extensive contribution

$$\beta_\mu = \sum_{i < j < k, a < b < c} (r_{\mu, 0}^{abc} \mathcal{L}_{\mu, ijk}^{abc} - \mathcal{L}_{0, ijk}^{abc}) \mathcal{M}_{0, abc}^{ijk}(2) \quad (26)$$

in the vertical excitation energy

$$\omega_\mu^{(\text{CR-EOMCC}(2,3))} = E_\mu^{(\text{CR-EOMCC}(2,3))} - E_0^{(\text{CR-CC}(2,3))} \quad (27)$$

Indeed, using the above equations for the CR-EOMCC(2,3) energies, particularly eq 25, we can decompose the CR-EOMCC(2,3) excitation energy as follows:^{30,31}

$$\omega_\mu^{(\text{CR-EOMCC}(2,3))} = \omega_\mu^{(\text{CCSD})} + \alpha_\mu + \beta_\mu \quad (28)$$

Here, $\omega_\mu^{(\text{CCSD})}$ is the vertical excitation energy of EOMCCSD,

$$\alpha_\mu = \sum_{i < j < k, a < b < c} \mathcal{L}_{\mu, ijk}^{abc} \tilde{\mathcal{M}}_{\mu, abc}^{ijk}(2) \quad (29)$$

where $\tilde{\mathcal{M}}_{\mu, abc}^{ijk}(2) = \langle \Phi_{ijk}^{abc} | \bar{H}^{(2)} (R_{\mu, 1} + R_{\mu, 2}) | \Phi \rangle$ is the contribution to the triply excited moment $\mathcal{M}_{\mu, abc}^{ijk}(2)$ of EOMCCSD due to the one- and two-body components of $R_\mu^{(2)}$, and β_μ is the quantity defined by eq 26. Since the EOMCCSD approach is rigorously size intensive and, as shown in ref 31, the α_μ term is size intensive as well, the $[\omega_\mu^{(\text{CCSD})} + \alpha_\mu(2,3)]$ part of the

CR-EOMCC(2,3) excitation energy $\omega_{\mu}^{(\text{CR-EOMCC}(2,3))}$ is a size-intensive quantity. Unfortunately, the β_{μ} term defined by eq 26, being a size-extensive contribution that does not cancel out, grows with the size of the system,^{30,31} destroying the size intensity of $\omega_{\mu}^{(\text{CR-EOMCC}(2,3))}$. In order to address this concern and following the discussion in refs 30 and 31 in this work, we have implemented the rigorously size-intensive variant of CR-EOMCC(2,3), designated as δ -CR-EOMCC(2,3), by neglecting the problematic β_{μ} term in eq 28 and redefining the excitation energy as follows:

$$\omega_{\mu}^{(\delta\text{-CR-EOMCC}(2,3))} = \omega_{\mu}^{(\text{CCSD})} + \alpha_{\mu} \quad (30)$$

with α_{μ} given by eq 29. The resulting δ -CR-EOMCC(2,3) approach provides a size-intensive description of the excitation energies and, by defining the total energy of a given electronic state μ , i.e., E_{μ} , as a sum of the size-extensive ground-state CR-CC(2,3) energy and size-intensive excitation energy $\omega_{\mu}^{(\delta\text{-CR-EOMCC}(2,3))}$, eq 30, so that

$$\begin{aligned} E_{\mu} &= E_0^{(\text{CR-CC}(2,3))} + \omega_{\mu}^{(\delta\text{-CR-EOMCC}(2,3))} \\ &= E_{\mu}^{(\text{CCSD})} + \sum_{i < j < k, a < b < c} \langle 0, ijk | \hat{V}^{ijk} | 0, abc \rangle (2) \\ &\quad + \sum_{i < j < k, a < b < c} \langle \mu, ijk | \hat{V}^{ijk} | \mu, abc \rangle (2) \end{aligned} \quad (31)$$

the size extensive description of state μ , assuming that the electronic excitation in AB is either in A or in B , but not in both fragments simultaneously (cf. refs 16, 33, and 92). Again, as in the regular CR-EOMCC(2,3) approach, we can distinguish between the full variant D of $\omega_{\mu}^{(\delta\text{-CR-EOMCC}(2,3))}$ and its various approximations, including variant A. The δ -CR-EOMCC(2,3)A method is equivalent to the EOMCCSD(2)_T approach of ref 31 and, if we limit ourselves to the vertical excitation energies only, to the EOMCCSD(\bar{T}) approach of ref 32. As shown in section 4.1, variants A and D provide nearly identical results for the vertical excitation energies in the *cis*-7HQ chromophore and its complexes, corresponding to the lowest $\pi \rightarrow \pi^*$ transition, which seem to be in good agreement with the experimental data reported in refs 5 and 59.

3. COMPUTATIONAL DETAILS

In order to examine the performance of the FDET approach and to demonstrate its advantages when compared with the results of supermolecular TDDFT calculations, both benchmarked against the high-level EOMCC data of δ -CR-EOMCC(2,3) quality, we have investigated the shifts in the vertical excitation energy $\omega_{\pi \rightarrow \pi^*}$ corresponding to the lowest $\pi \rightarrow \pi^*$ transition in the *cis*-7HQ chromophore induced by the formation of hydrogen-bonded complexes shown in Figure 1, which were previously examined using laser resonant two-photon UV spectroscopy.^{5,59} The eight complexes considered in this work include the *cis*-7HQ $\cdots B$ systems, where B represents one of the following environments: a single water molecule, a single ammonia molecule, a water dimer, a single molecule of methanol, a single molecule of formic acid, a trimer consisting of ammonia and two water molecules, a trimer consisting of ammonia, water, and ammonia, and a trimer consisting of two ammonia and one water molecules (see Figure 1). For each *cis*-7HQ $\cdots B$ complex and for each electronic structure approach employed in this study, the corresponding environment-induced shift $\Delta\omega_{\pi \rightarrow \pi^*}$

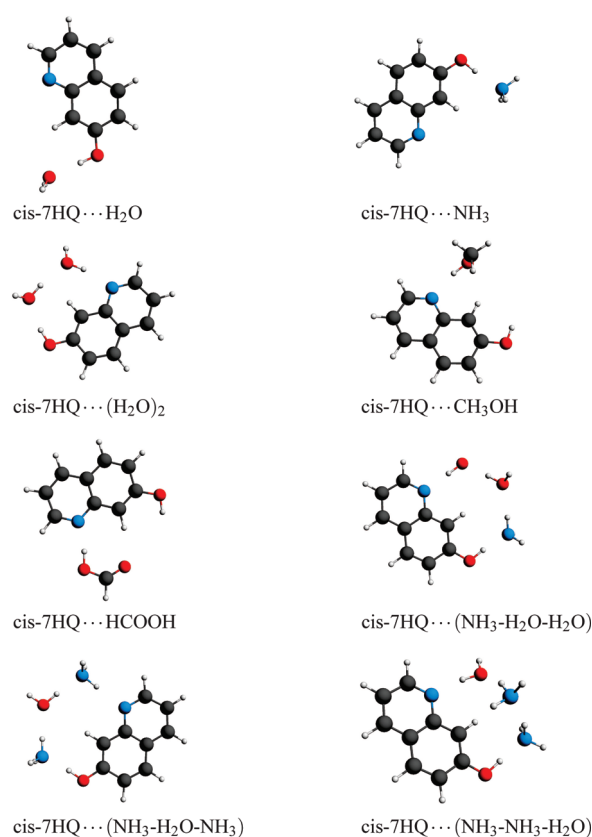


Figure 1. The eight hydrogen-bonded complexes of the *cis*-7HQ molecule studied in the present work.

was calculated as a difference between the value of $\omega_{\pi \rightarrow \pi^*}$ characterizing the complex and that obtained for the isolated *cis*-7HQ molecule, using the nuclear geometries of *cis*-7HQ $\cdots B$ and *cis*-7HQ optimized in the second-order Møller–Plesset perturbation theory (MP2)¹¹³ calculations employing the aug-cc-pVTZ basis set.^{114,115} The optimizations of nuclear geometries of the *cis*-7HQ and *cis*-7HQ $\cdots B$ systems were performed using the analytic gradients of MP2 available in the Gaussian 03 package.¹¹⁶ As in all other post-Hartree–Fock wave function calculations discussed in this article, the lowest-energy core molecular orbitals (MOs) correlating with the 1s shells of the C, N, and O atoms were frozen in these optimizations.

Once the nuclear geometries of the *cis*-7HQ and *cis*-7HQ $\cdots B$ systems were determined, we performed the desired FDET and supermolecular TDDFT and EOMCC calculations of the vertical excitation energies $\Delta\omega_{\pi \rightarrow \pi^*}$ and the environment-induced shifts $\Delta\omega_{\pi \rightarrow \pi^*}$. The most essential information about these calculations, including basis sets, key algorithmic details, and computer codes used to perform them, is provided below.

3.1. Reference EOMCC Calculations. In order to establish the reference EOMCC values of the environment-induced shifts $\Delta\omega_{\pi \rightarrow \pi^*}$, we performed a series of EOMCCSD calculations for the *cis*-7HQ, 7HQ \cdots H₂O, and 7HQ \cdots NH₃ systems using five different basis sets, including 6-31+G(d),^{117–119} 6-31++G(d,p),^{117–119} 6-311+G(d),^{119,120} aug-cc-pVDZ,^{114,115} and the [5s3p2d/3s2p] basis of Sadlej,¹²¹ designated as POL, followed by the EOMCCSD and δ -CR-EOMCC(2,3) computations for all eight *cis*-7HQ $\cdots B$ complexes examined in this work using the largest basis sets that we could afford, namely,

6-311+G(d) in the EOMCCSD case and 6-31+G(d) in the case of the δ -CR-EOMCC(2,3) approach. The main purpose of all of these calculations was to examine the stability of the final EOMCC values of the $\Delta\omega_{\pi\rightarrow\pi^*}$ shifts, recommended for use in benchmarking the FDET and supermolecular TDDFT data, with respect to the choice of the basis set and higher-order correlation effects neglected in EOMCCSD, but included in δ -CR-EOMCC(2,3). As explained in section 4.1, the final EOMCC values of the vertical excitation energies $\omega_{\pi\rightarrow\pi^*}$ that are used in this paper to benchmark the FDET and supermolecular TDDFT methods were obtained using the composite approach, in which we augment the EOMCCSD/6-311+G(d) results by the triples corrections to EOMCCSD energies extracted from the δ -CR-EOMCC(2,3)/6-31+G(d) calculations, as in the following formula:

$$\begin{aligned} \omega_{\pi\rightarrow\pi^*}(\text{EOMCC}) &= \omega_{\pi\rightarrow\pi^*}(\text{EOMCCSD}/6-311+G(d)) \\ &+ [\omega_{\pi\rightarrow\pi^*}(\delta\text{-CR-EOMCC}(2,3)/6-31+G(d)) \\ &- \omega_{\pi\rightarrow\pi^*}(\text{EOMCCSD}/6-31+G(d))] \quad (32) \end{aligned}$$

All of the EOMCC calculations reported in this work were carried out with the programs developed at Michigan State University described, for example, in refs 26, 30, 91, and 92, that form part of the GAMESS package.^{122,123} In order to obtain the final δ -CR-EOMCC(2,3) results, we had to modify the previously developed^{26,30} CR-CC(2,3)/CR-EOMCC(2,3) GAMESS routines, since we had to replace the vertical excitation energy of CR-EOMCC(2,3) given by eq 28 with its size-intensive δ -CR-EOMCC(2,3) counterpart defined by eq 30. Thanks to this effort, the present GAMESS code enables the calculations of three different types of triples corrections to EOMCCSD energies, including CR-EOMCCSD(T),^{87,88,91,92} CR-EOMCC(2,3),^{29,30} and δ -CR-EOMCC(2,3), as defined by eqs 30 and 31. The corresponding ground-state CCSD calculations, which precede the determination of the left CCSD and right and left EOMCCSD eigenstates that enter the formulas for the triples corrections of δ -CR-EOMCC(2,3) and the steps needed to compute the triples corrections of the ground-state CR-CC(2,3) and excited-state CR-EOMCC(2,3) and δ -CR-EOMCC(2,3) approaches, were performed with the routines described in ref 124, which form part of GAMESS as well. The RHF orbitals were employed throughout, and as pointed out above, the lowest-energy core MOs that correlate with the 1s shells of the non-hydrogen atoms were frozen in the CCSD, EOMCCSD, and δ -CR-EOMCC(2,3) calculations. The CCSD/EOMCCSD energies were converged to 10^{-7} Hartree. We refer the reader to refs 26, 30, 91, and 92 for further details of the EOMCC computer codes and algorithms exploited in this work.

3.2. FDET and Supermolecular TDDFT Calculations. All of the FDET and supermolecular TDDFT calculations reported in this article were performed using the linear-response TDDFT routines available in the ADF2009.01 code.¹²⁵ In particular, the FDET calculations followed the general protocol introduced in ref 58 in which the occupied and unoccupied orbitals for the embedded chromophore that are obtained by solving the Kohn–Sham-like system defined by eq 13 are subsequently used within the linear-response TDDFT framework⁴⁶ to obtain excitation energies.

In order to examine the effect of the basis set on the complexation-induced shifts $\Delta\omega_{\pi\rightarrow\pi^*}$, three STO-type basis sets¹²⁵ were employed in the FDET and supermolecular TDDFT calculations: STO DZP (double- ζ basis with one set of

polarization functions), STO TZ2P (triple- ζ basis with two sets of polarization functions), and STO ATZ2P, which includes all TZ2P functions plus one set of diffuse s-STO and p-STO functions.

The environment density ρ_B used in the FDET calculations was either nonrelaxed, i.e., constructed using the ground-state electronic density of the environment obtained by solving the conventional Kohn–Sham equations for the environment molecules in the absence of the chromophore, or relaxed, i.e., obtained with the aforementioned “freeze-and-thaw” procedure.⁸⁰ We also examined two types of basis expansions to represent the occupied and unoccupied orbitals of the chromophore A embedded in the environment B and densities ρ_A and ρ_B in the FDET calculations. In the supermolecular expansion approach, all atomic centers of the total system AB were used to represent the orbitals and densities. In the monomer-expansion FDET calculations, the orbitals of the chromophore A embedded in B and the corresponding density ρ_A were represented using the atomic centers of A, whereas the environment density ρ_B was represented using the atomic centers of B (see refs 80 and 126 for further information). The monomer-expansion technique using nonrelaxed ρ_B , which is the recommended variant of FDET for the type of applications reported in this article, relies on the approximation, referred to as the Neglect of Dynamic Response of the Environment (NDRE), in which we assume that the dynamic response of the whole system AB to the process of electronic excitation is limited to chromophore A and that the coupling between the excitations in the embedded system and in its environment can be neglected. A comparison of the complexation-induced shifts $\Delta\omega_{\pi\rightarrow\pi^*}$ in the *cis*-7HQ ··· B systems resulting from the FDET and EOMCC calculations, discussed in the next section, clearly shows that such coupling can indeed be neglected, as the spectral overlap between *cis*-7HQ and the environment molecules bound to it is negligible. The NDRE approximation and the monomer-expansion-based FDET approach that results from it are very effective in eliminating spurious electronic excitations involving the environment (see the discussion in ref 52). If the coupling between the excitations in the embedded system and in its environment could not be neglected, we would have to rely on the more general formalism introduced in ref 127 (for the additional discussion of the importance of such couplings in FDET calculations, see ref 128).

In both the FDET and supermolecular TDDFT calculations, we used the SAOP scheme¹²⁹ to approximate the relevant exchange-correlation potential contributions for the isolated and embedded chromophore (the FDET case) and for the total system (the supermolecular TDDFT case). The nonadditive kinetic energy potential $v_i^{\text{nad}}[\rho_A, \rho_B](\vec{r})$, eq 12, that forms part of the local, orbital-free embedding potential $v_{\text{emb}}^{\text{eff}}[\rho_A, \rho_B; \vec{r}]$, eq 10, used in the FDET calculations was approximated using the generalized gradient approximation (GGA97),¹²⁶ whereas the nonadditive exchange-correlation component of $v_{\text{emb}}^{\text{eff}}[\rho_A, \rho_B; \vec{r}]$, eq 11, was approximated using the Perdew–Wang (PW91) functional. We also performed calculations in which the nonadditive kinetic energy potential $v_i^{\text{nad}}[\rho_A, \rho_B](\vec{r})$ was approximated with the help of the recently developed NDSD approximant,⁶⁴ which takes into account the exact conditions that become relevant for the proper behavior of $v_i^{\text{nad}}[\rho_A, \rho_B](\vec{r})$ in the vicinity of nuclei, but we do not show these results in this article, since they are very similar to those obtained with GGA97. Because of the small energy differences that define the spectral shifts examined in this work, we used

Table 1. Basis-Set Dependence of the Vertical Excitation Energies $\omega_{\pi \rightarrow \pi^*}$ and the Environment-Induced Shifts $\Delta\omega_{\pi \rightarrow \pi^*}$ (in cm^{-1}) Obtained with the EOMCCSD Approach Corresponding to the Lowest $\pi \rightarrow \pi^*$ Transition in the *cis*-7HQ Chromophore and Its Complexes with the Water and Ammonia Molecules

basis set	$\omega_{\pi \rightarrow \pi^*}$			$\Delta\omega_{\pi \rightarrow \pi^*}$	
	7HQ	7HQ...H ₂ O	7HQ...NH ₃	7HQ...H ₂ O	7HQ...NH ₃
6-31+G(d)	35171	34643	34396	-528	-775
6-31++G(d,p)	35120	34597	34351	-523	-769
6-311+G(d)	35046	34500	34263	-546	-783
aug-cc-pVDZ	34707	34182	33923	-525	-784
POL	34596	34077	33819	-519	-777

Table 2. Vertical Excitation Energies $\omega_{\pi \rightarrow \pi^*}$ and the Environment-Induced Shifts $\Delta\omega_{\pi \rightarrow \pi^*}$ (in cm^{-1}) Obtained with the EOMCCSD/6-31+G(d), EOMCCSD/6-311+G(d), δ -CR-EOMCC(2,3),A/6-31+G(d), and δ -CR-EOMCC(2,3),D/6-31+G(d) Approaches, and Their Composite EOMCC,A and EOMCC,D Analogs Defined by eq 32, Corresponding to the Lowest $\pi \rightarrow \pi^*$ Transition in the *cis*-7HQ Chromophore and Its Various Complexes

environment	EOMCCSD/ 6-31+G(d)	EOMCCSD/ 6-311+G(d)	δ -CR-EOMCC(2,3),A/ 6-31+G(d)	δ -CR-EOMCC(2,3),D/ 6-31+G(d)	EOMCC,A ^a	EOMCC,D ^b	Exp. ^c
	$\omega_{\pi \rightarrow \pi^*}$						
none	35171	35046	31103	30711	30977	30586	30830
H ₂ O	34643	34500	30558	30199	30415	30056	30240
NH ₃	34396	34263	30291	29922	30157	29788	29925
2H ₂ O	33867	33699	29700	29378	29532	29210	29193
CH ₃ OH	34830	34695	30717	30428	30582	30293	30363
HCOOH	34505	34371	30368	30056	30235	29922	29816
NH ₃ -H ₂ O-H ₂ O	33381	33218	29171	28863	29008	28701	28340
NH ₃ -H ₂ O-NH ₃	33542	33385	29355	29036	29197	28879	28694
NH ₃ -NH ₃ -H ₂ O	33302	33136	29088	28812	28922	28646	28348
$\Delta\omega_{\pi \rightarrow \pi^*}$							
H ₂ O	-528	-546	-544	-512	-562	-530	-590
NH ₃	-775	-783	-812	-789	-820	-797	-905
2H ₂ O	-1304	-1347	-1403	-1333	-1446	-1376	-1637
CH ₃ OH	-341	-351	-386	-283	-396	-292	-467
HCOOH	-666	-675	-734	-655	-743	-664	-1014
NH ₃ -H ₂ O-H ₂ O	-1790	-1828	-1932	-1847	-1969	-1885	-2490
NH ₃ -H ₂ O-NH ₃	-1629	-1661	-1748	-1675	-1780	-1707	-2136
NH ₃ -NH ₃ -H ₂ O	-1869	-1910	-2014	-1899	-2055	-1940	-2482

^a Defined by eq 32, in which variant A of CR-EOMCC(2,3) is employed. ^b Defined by eq 32, in which variant D of CR-EOMCC(2,3) is employed. ^c Obtained with laser resonant two-photon ionization UV spectroscopy.⁵

tight convergence criteria when solving the Kohn–Sham and linear-response TDDFT equations (10^{-10} hartree).

4. RESULTS AND DISCUSSION

The results of our FDET, supermolecular TDDFT, and EOMCC calculations for the shifts in the vertical excitation energy $\omega_{\pi \rightarrow \pi^*}$ corresponding to the lowest $\pi \rightarrow \pi^*$ transition in the *cis*-7HQ chromophore induced by the formation of the eight complexes shown in Figure 1 are summarized in Tables 1–8 and Figures 2–5. We begin our discussion with the analysis of the EOMCCSD and δ -CR-EOMCC(2,3) calculations aimed at establishing the reference EOMCC values for benchmarking purposes. The comparison of the FDET shifts $\Delta\omega_{\pi \rightarrow \pi^*}$ with the reference EOMCC, supermolecular TDDFT, and experimental

data is presented immediately afterward. Among the key discussed aspects are the basis set dependence of the FDET and supermolecular TDDFT results, the issues created by relaxing the environment density ρ_B in the FDET calculations, the usefulness of the monomer vs supermolecular basis expansions in the FDET considerations, and the effect of the approximations that are used for the exchange-correlation potentials on the FDET and supermolecular TDDFT results.

4.1. Reference EOMCC Results. In order to establish the level of EOMCC theory that would be appropriate for serving as a reference for the FDET and supermolecular TDDFT calculations reported in this work, we first examine the dependence of the environment-induced shifts $\Delta\omega_{\pi \rightarrow \pi^*}$ resulting from the EOMCCSD calculations on the basis set. In Table 1, we compare the results of the EOMCCSD calculations obtained with the

Table 3. Comparison of the Environment-Induced Shifts $\Delta\omega_{\pi\rightarrow\pi^*}$ (in cm^{-1}) of the Vertical Excitation Energy Corresponding to the Lowest $\pi\rightarrow\pi^*$ Transition in the *cis*-7HQ Chromophore Resulting from the Monomer-Expansion-Based FDET and Supermolecular TDDFT Calculations Using the STO ATZ2P Basis Set with the Reference EOMCC,A Data

environment	supermolecular		FDET	
	EOMCC,A	TDDFT	nonrelaxed ρ_B	relaxed ρ_B
H ₂ O	-562	-944	-645	-768
NH ₃	-820	-1222	-816	-1005
2H ₂ O	-1446	-2280	-1624	-1975
CH ₃ OH	-396	-805	-454	-625
HCOOH	-743	-1569	-972	-1312
NH ₃ -H ₂ O-H ₂ O	-1969	-2838	-1863	-2342
NH ₃ -H ₂ O-NH ₃	-1780	-2594	-1791	-2232
NH ₃ -NH ₃ -H ₂ O	-2055	-2899	-1890	-2436
av. dev. from EOMCC,A	0	-673	-36	-366
av. abs. dev. from EOMCC,A	0	673	104	366

Table 4. Environment-Induced Shifts $\Delta\omega_{\pi\rightarrow\pi^*}$ (in cm^{-1}) of the Vertical Excitation Energy Corresponding to the Lowest $\pi\rightarrow\pi^*$ Transition in the *cis*-7HQ Chromophore Resulting from the Supermolecular-Expansion-Based FDET and Supermolecular TDDFT Calculations Using the STO ATZ2P Basis Set, along with the Average Errors Relative to the Reference EOMCC,A Data

environment	supermolecular	FDET	
	TDDFT	nonrelaxed ρ_B	relaxed ρ_B
H ₂ O	-944	-529	-840
NH ₃	-1222	-849	-1082
2H ₂ O	-2280	-1659	-2032
CH ₃ OH	-805	-474	-698
HCOOH	-1569	-1025	-1587
NH ₃ -H ₂ O-H ₂ O	-2838	-1933	-2526
NH ₃ -H ₂ O-NH ₃	-2594	-1859	-2372
NH ₃ -NH ₃ -H ₂ O	-2899	-1940	-2524
av. dev. from EOMCC,A	-673	-62	-486
av. abs. dev. from EOMCC,A	673	108	486

6-31+G(d), 6-31++G(d,p), 6-311+G(d), aug-cc-pVDZ, and POL basis sets for the two smallest complexes, 7HQ···H₂O and 7HQ···NH₃, for which we could afford the largest number of computations. The results in Table 1 indicate that although the vertical excitation energies $\omega_{\pi\rightarrow\pi^*}$ in the bare *cis*-7HQ system and its complexes with the water and ammonia molecules vary with the basis set (for the basis sets tested here by as much as about 600 cm^{-1}), the environment-induced shifts $\Delta\omega_{\pi\rightarrow\pi^*}$ are almost insensitive to the basis set choice. Although we were unable to perform a similarly thorough analysis for the remaining complexes due to prohibitive computer costs, we were able to obtain the EOMCCSD $\omega_{\pi\rightarrow\pi^*}$ and $\Delta\omega_{\pi\rightarrow\pi^*}$ values for all of the complexes examined in this study using the 6-31+G(d) and 6-311+G(d) basis sets. As shown in Table 2, the differences between the EOMCCSD/6-31+G(d) and EOMCCSD/6-311+G(d) values

Table 5. Environment-Induced Shifts $\Delta\omega_{\pi\rightarrow\pi^*}$ (in cm^{-1}) of the Vertical Excitation Energy Corresponding to the Lowest $\pi\rightarrow\pi^*$ Transition in the *cis*-7HQ Chromophore Resulting from the Monomer-Expansion-Based FDET and Supermolecular TDDFT Calculations Using the STO TZ2P Basis Set, along with the Average Errors Relative to the Reference EOMCC,A Data

environment	supermolecular	FDET	
	TDDFT	nonrelaxed ρ_B	relaxed ρ_B
H ₂ O	-876	-636	-757
NH ₃	-1227	-849	-1016
2H ₂ O	-2298	-1635	-1962
CH ₃ OH	-847	-491	-665
HCOOH	-1602	-1012	-1334
NH ₃ -H ₂ O-H ₂ O	-2811	-1911	-2355
NH ₃ -H ₂ O-NH ₃	-2519	-1806	-2177
NH ₃ -NH ₃ -H ₂ O	-2871	-1896	-2370
av. dev. from EOMCC,A	-660	-58	-358
av. abs. dev. from EOMCC,A	660	113	358

Table 6. Environment-Induced Shifts $\Delta\omega_{\pi\rightarrow\pi^*}$ (in cm^{-1}) of the Vertical Excitation Energy Corresponding to the Lowest $\pi\rightarrow\pi^*$ Transition in the *cis*-7HQ Chromophore Resulting from the Monomer-Expansion-Based FDET and Supermolecular TDDFT Calculations Using the STO DZP Basis Set, along with the Average Errors Relative to the Reference EOMCC,A Data

environment	supermolecular	FDET	
	TDDFT	nonrelaxed ρ_B	relaxed ρ_B
H ₂ O	-884	-641	-764
NH ₃	-1220	-832	-1014
2H ₂ O	-2324	-1653	-1956
CH ₃ OH	-884	-525	-678
HCOOH	-1644	-1027	-1321
NH ₃ -H ₂ O-H ₂ O	-2862	-1925	-2364
NH ₃ -H ₂ O-NH ₃	-2546	-1787	-2160
NH ₃ -NH ₃ -H ₂ O	-2886	-1896	-2353
av. dev. from EOMCC,A	-685	-64	-355
av. abs. dev. from EOMCC,A	685	115	355

of the environment-induced shifts $\Delta\omega_{\pi\rightarrow\pi^*}$ remain small for all complexes of interest, ranging from 8 cm^{-1} in the 7HQ···NH₃ case to 43 cm^{-1} in the case of 7HQ···(H₂O)₂, or 1–3%. Thus, we can conclude that the choice of the basis set, although important for obtaining the converged $\omega_{\pi\rightarrow\pi^*}$ values, is of relatively little significance when the environment-induced shifts in the vertical excitation energy corresponding to the lowest $\pi\rightarrow\pi^*$ transition in the *cis*-7HQ chromophore are considered.

Although the EOMCCSD approach is known to provide an accurate description of excited states dominated by one-electron transitions, such as the $\pi\rightarrow\pi^*$ transition in *cis*-7HQ and its complexes, there have been cases of similar states reported in the literature, where the EOMCCSD level has not been sufficient to obtain high-quality results.^{94,95} Moreover, our interest in this study is in the small energy differences defining the

Table 7. Dependence of the Vertical Excitation Energy Corresponding to the Lowest $\pi \rightarrow \pi^*$ Transition in *cis*-7HQ Resulting from the Supermolecular TDDFT Calculations Using the STO TZ2P Basis Set (in cm^{-1}) on the Position of Ghost Functions

position of ghost functions	excitation energy
none	30494
H ₂ O	30470
NH ₃	30503
2H ₂ O	30536
CH ₃ OH	30478
HCOOH	30500
(NH ₃ -H ₂ O-H ₂ O)	30468
(NH ₃ -H ₂ O-NH ₃)	30516
(NH ₃ -NH ₃ -H ₂ O)	30454

Table 8. Effect of the Approximation Used for the Exchange-Correlation Energy Functional on the Environment-Induced Shifts $\Delta\omega_{\pi \rightarrow \pi^*}$ (in cm^{-1}) of the Vertical Excitation Energy Corresponding to the Lowest $\pi \rightarrow \pi^*$ Transition in the *cis*-7HQ Chromophore Calculated Using the FDET and Supermolecular TDDFT Methodologies and the STO ATZ2P Basis Set

environment	FDET ^d			supermolecular		
	PW91 ^b	LDA ^c	SAOP ^d	PW91 ^b	LDA ^c	SAOP ^d
H ₂ O	-724	-718	-645	-1031	-1014	-944
NH ₃	-933	-922	-816	-1415	-1405	-1222
2H ₂ O	-1767	-1756	-1624	-2440	-2480	-2280
CH ₃ OH	-465	-461	-454	-856	-895	-805
HCOOH	-1007	-998	-972	-1578	-1611	-1569
NH ₃ -H ₂ O-H ₂ O	-2030	-2017	-1863	-3143	-3162	-2838
NH ₃ -H ₂ O-NH ₃	-1975	-1960	-1791	-2899	-2930	-2594
NH ₃ -NH ₃ -H ₂ O	-2065	-2050	-1890	-3145	-3204	-2899
av. dev. from EOMCC,A	-149	-139	-36	-842	-866	-673
av. abs. dev. from EOMCC,A	149	140	104	842	866	673

^aIn FDET calculations, PW91, LDA, and SAOP refer to three different approximations for the exchange-correlation potential evaluated at the chromophore density ρ_A . The nonadditive contributions to the orbital-free embedding potential use the same approximants in all cases (PW91 for exchange-correlation and GGA97 for the kinetic energy). The FDET calculations use the nonrelaxed environment density ρ_B and the monomer basis expansion. ^bRef 136. ^cRef 135. ^dRef 129.

environment-induced shifts $\Delta\omega_{\pi \rightarrow \pi^*}$, which may be sensitive to the higher-order correlation effects neglected in the EOMCCSD calculations. For this reason, we also examined the effect of triples corrections to EOMCCSD energies on the calculated $\omega_{\pi \rightarrow \pi^*}$ and $\Delta\omega_{\pi \rightarrow \pi^*}$ values by performing the δ -CR-EOMCC(2,3) calculations with the 6-31+G(d) basis set. The results of these calculations, shown in Table 2, indicate that triple excitations have a significant effect on the vertical excitation energies $\omega_{\pi \rightarrow \pi^*}$, reducing the 4000–5000 cm^{-1} differences between the EOMCCSD and experimental data to no more than about 800 cm^{-1} , when the δ -CR-EOMCC(2,3),A/6-31+G(d)

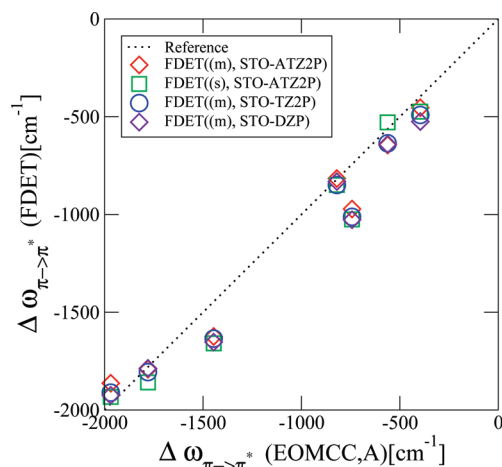


Figure 2. The dependence of the environment-induced shifts $\Delta\omega_{\pi \rightarrow \pi^*}$ of the vertical excitation energy corresponding to the lowest $\pi \rightarrow \pi^*$ transition in the *cis*-7HQ chromophore on the STO-type basis set used in the FDET calculations employing the monomer (m) and supermolecular (s) expansions and nonrelaxed ρ_B , and a comparison of the resulting FDET shifts with the reference EOMCC,A data.

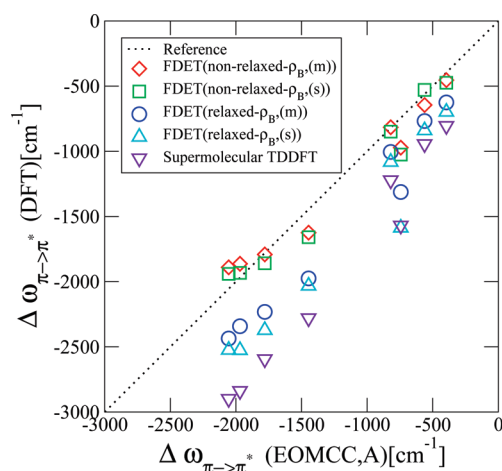


Figure 3. The dependence of the environment-induced shifts $\Delta\omega_{\pi \rightarrow \pi^*}$ of the vertical excitation energy corresponding to the lowest $\pi \rightarrow \pi^*$ transition in the *cis*-7HQ chromophore on the type of the frozen electron density ρ_B used in the FDET calculations employing the STO ATZ2P basis set and the monomer (m) and supermolecular (s) expansions, and a comparison of the resulting shifts with the reference EOMCC,A and supermolecular TDDFT data.

calculations are performed, and no more than about 500 cm^{-1} when the δ -CR-EOMCC(2,3),D/6-31+G(d) approach is employed, while bringing the $\Delta\omega_{\pi \rightarrow \pi^*}$ values closer to the experimentally observed shifts when compared with EOMCCSD. Although the differences between the δ -CR-EOMCC(2,3) and EOMCCSD values of the environment-induced shifts $\Delta\omega_{\pi \rightarrow \pi^*}$ resulting from the calculations with the 6-31+G(d) basis set do not exceed 15–16% of the EOMCCSD values, triples corrections improve the EOMCCSD results and, as such, are useful for the generation of the reference EOMCC data.

Ideally, one would like to perform the δ -CR-EOMCC(2,3) calculations for basis sets larger than 6-31+G(d), such as 6-311+G(d), but complexes of *cis*-7HQ examined in this study

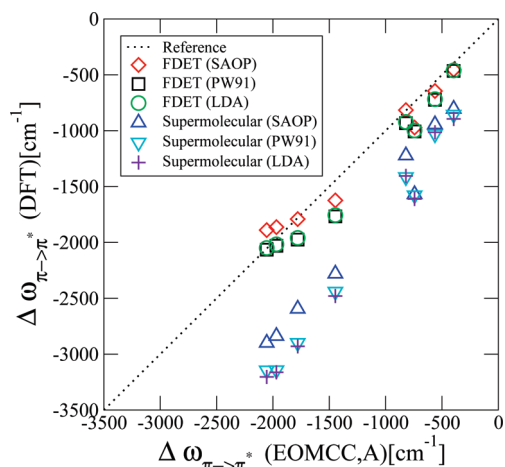


Figure 4. The dependence of the environment-induced shifts $\Delta\omega_{\pi\rightarrow\pi^*}$ of the vertical excitation energy corresponding to the lowest $\pi\rightarrow\pi^*$ transition in the *cis*-7HQ chromophore and resulting from the FDET and supermolecular TDDFT calculations with the STO ATZ2P basis set on the form of the exchange-correlation functional of the effective Kohn–Sham potential, and a comparison of the resulting shifts with the reference EOMCC,A data.

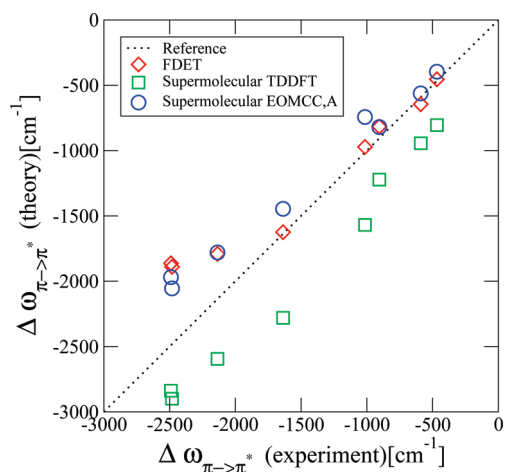


Figure 5. A comparison of the environment-induced shifts $\Delta\omega_{\pi\rightarrow\pi^*}$ of the vertical excitation energy corresponding to the lowest $\pi\rightarrow\pi^*$ transition in the *cis*-7HQ chromophore and resulting from the FDET with nonrelaxed- ρ_B and supermolecular TDDFT calculations using the STO ATZ2P basis set, with the reference supermolecular EOMCC,A and experimental⁵ data (the latter obtained with laser resonant two-photon ionization UV spectroscopy).

are too large for performing such calculations on our computers. Thus, in the absence of the δ -CR-EOMCC(2,3) larger basis set data and considering the fact that the triples corrections to the environment-induced shifts $\Delta\omega_{\pi\rightarrow\pi^*}$ are relatively small when compared to the EOMCCSD $\Delta\omega_{\pi\rightarrow\pi^*}$ values, we have decided to combine the EOMCCSD/6-311+G(d) results with the triples corrections to EOMCCSD energies extracted from the δ -CR-EOMCC(2,3)/6-31+G(d) calculations, as in eq 32. As shown in Table 2, the resulting composite EOMCC,A and EOMCC,D approaches provide vertical excitation energies $\omega_{\pi\rightarrow\pi^*}$ that are in excellent agreement with the experimental excitation energies, while offering further improvements in the

environment-induced shifts $\Delta\omega_{\pi\rightarrow\pi^*}$ when compared with the EOMCCSD/6-311+G(d) and δ -CR-EOMCC(2,3)/6-31+G(d) calculations. Indeed, the EOMCC,A approach, which adds the triples correction extracted from the δ -CR-EOMCC(2,3),A/6-31+G(d) calculation to the EOMCCSD/6-311+G(d) energy, gives errors in the calculated excitation energies $\omega_{\pi\rightarrow\pi^*}$ relative to experimental results that range between 147 cm^{-1} in the case of the bare *cis*-7HQ system and 668 cm^{-1} in the case of the $7\text{HQ}\cdots(\text{NH}_3\text{-H}_2\text{O-H}_2\text{O})$ complex, never exceeding 2% of the experimental excitation energies. The EOMCC,D approach, which adds the triples correction obtained in the δ -CR-EOMCC(2,3),D/6-31+G(d) calculation to the EOMCCSD/6-311+G(d) energy, gives errors in the calculated excitation energies $\omega_{\pi\rightarrow\pi^*}$ relative to experimental results that range between 17 cm^{-1} in the case of the $7\text{HQ}\cdots(\text{H}_2\text{O})_2$ complex and 361 cm^{-1} for $7\text{HQ}\cdots(\text{NH}_3\text{-H}_2\text{O-H}_2\text{O})$, or no more than 1% of the experimental values. These results should be compared to the much larger differences between the EOMCCSD/6-311+G(d) and experimental excitation energies that range between 14 and 17%. The complexation-induced spectral shifts $\Delta\omega_{\pi\rightarrow\pi^*}$ resulting from the EOMCC,A and EOMCC,D calculations agree with their experimental counterparts to within 5–27% or 15% on average in the case of EOMCC,A and 10–37% or 22% on average in the EOMCC,D case. The EOMCC,D approach, while bringing the excitation energies $\omega_{\pi\rightarrow\pi^*}$ to a much closer agreement with experimental results than the EOMCCSD/6-311+G(d) calculations, does not offer improvements in the calculated shifts $\Delta\omega_{\pi\rightarrow\pi^*}$. The composite EOMCC,A approach provides additional small improvements in the calculated $\Delta\omega_{\pi\rightarrow\pi^*}$ values, reducing the 7–33% errors relative to experiment obtained in the EOMCCSD/6-311+G(d) calculations to 5–27%. For this reason, we consider the EOMCC,A values of the spectral shifts $\Delta\omega_{\pi\rightarrow\pi^*}$ as the theoretical reference values for assessing the quality of the FDET and supermolecular TDDFT calculations, although the use of EOMCC,D would not change any of our main conclusions.

Clearly, a comparison of the purely electronic EOMCC and experimental data discussed above has limitations, since we would have to examine the effect of nuclear motion on the calculated EOMCCSD and δ -CR-EOMCC(2,3) excitation energies and use basis sets larger than 6-31+G(d) in the δ -CR-EOMCC(2,3) calculations to make more definitive statements, which we cannot do at this time within the EOMCC framework due to the size of systems examined in this work. To overcome this difficulty, we could try to combine the EOMCC and TDDFT or FDET data, using TDDFT or FDET to examine the role of nuclear geometries and vibrational motions and δ -CR-EOMCC(2,3) to provide electronic excitation energies. The problem is that this would defeat the main purpose of the present study, in which we want to objectively compare the purely electronic FDET and supermolecular TDDFT results for the complexation-induced spectral shifts $\Delta\omega_{\pi\rightarrow\pi^*}$ with the corresponding, also purely electronic, EOMCC data, using the best EOMCC approach we can afford and using the same nuclear geometries in all calculations. Thus, although there are limitations in our EOMCC calculations when compared with experimental results which the present study cannot completely overcome, we believe that the EOMCC,A results obtained by combining the EOMCCSD/6-311+G(d) excitation energies with the triples corrections extracted from the δ -CR-EOMCC(2,3),A/6-31+G(d) calculations, as in eq 32, are of sufficiently high quality to allow us to assess the quality of the FDET and supermolecular TDDFT methods in applications involving the environment-induced spectral shifts in complexes of *cis*-7HQ.

4.2. A Comparison of the Excitation Energy Shifts from the FDET Calculations Using Nonrelaxed Environment Densities with the Reference EOMCC Data. As shown in Table 2 and in agreement with the experimental data,⁵ the excitation energy shifts $\Delta\omega_{\pi\rightarrow\pi^*}$ for the hydrogen-bonded $7\text{HQ}\cdots B$ complexes examined in this work resulting from the EOMCC calculations are always negative. Although this is not a strict rule, the magnitude of $\Delta\omega_{\pi\rightarrow\pi^*}$ correlates, to a large extent, with the size of the hydrogen-bonded environment B in the *cis*- $7\text{HQ}\cdots B$ complex. According to the reference EOMCC,A calculations, the shifts in the vertical excitation energy $\omega_{\pi\rightarrow\pi^*}$ corresponding to the lowest $\pi\rightarrow\pi^*$ transition in the *cis*- 7HQ chromophore vary from -396 to -820 cm^{-1} in the case of the smaller $7\text{HQ}\cdots B$ complexes involving the CH_3OH , H_2O , HCOOH , and NH_3 monomers, through -1446 cm^{-1} in the case of the $7\text{HQ}\cdots(\text{H}_2\text{O})_2$ complex involving the water dimer, to -1780 to -2055 cm^{-1} in the case of the largest $7\text{HQ}\cdots B$ systems involving the $(\text{NH}_3-\text{H}_2\text{O}-\text{NH}_3)$, $(\text{NH}_3-\text{H}_2\text{O}-\text{H}_2\text{O})$, and $(\text{NH}_3-\text{NH}_3-\text{H}_2\text{O})$ trimers. It is interesting to examine how well the FDET and supermolecular TDDFT calculations reproduce these data.

We begin our discussion by assessing the quality of the FDET results employing the nonrelaxed density ρ_B , which is obtained by solving the Kohn–Sham equations for the environment molecule(s) in the absence of the *cis*- 7HQ chromophore, with a focus on the results obtained with the monomer basis expansions to represent the chromophore density ρ_A and the environment density ρ_B . As explained in section 3.2, the combined use of the nonrelaxed environment density ρ_B and monomer expansions in the FDET calculations relies on the simplifying assumptions that the response of system AB to the process of electronic excitation is limited to chromophore A , that the coupling between the excitations in the embedded system and its environment can be neglected, and that the polarization of the environment molecules by the chromophore is of no importance. The supermolecular EOMCC calculations performed in this work do not rely on any of these assumptions, so a comparison of the FDET results employing the nonrelaxed density ρ_B and monomer expansions of ρ_A and ρ_B with the EOMCC data is particularly interesting.

As shown in Table 3 and Figure 2, the overall agreement of the monomer-expansion-based FDET/ATZ2P data using the nonrelaxed ρ_B with the reference EOMCC,A data is excellent. The absolute values of the deviations between the $\Delta\omega_{\pi\rightarrow\pi^*}$ values resulting from the nonrelaxed, monomer-expansion-based FDET/ATZ2P and supermolecular EOMCC,A calculations range from 4 cm^{-1} in the case of the $7\text{HQ}\cdots\text{NH}_3$ complex, where the EOMCC,A shift is -820 cm^{-1} , to 229 cm^{-1} in the case of the $7\text{HQ}\cdots\text{HCOOH}$ system, where the EOMCC,A result for $\Delta\omega_{\pi\rightarrow\pi^*}$ is -743 cm^{-1} . The mean signed and unsigned errors in the nonrelaxed, monomer-expansion-based FDET/ATZ2P results for the environment-induced shifts $\Delta\omega_{\pi\rightarrow\pi^*}$ relative to the EOMCC,A reference data are -36 and 104 cm^{-1} , respectively, or 11%, if we average the individual relative errors. On the basis of the analysis of the EOMCCSD and δ -CR-EOMCC(2,3) calculations presented in section 4.1, the deviations between the nonrelaxed, monomer-expansion-based FDET/ATZ2P and reference EOMCC,A data shown in Table 3 and Figure 2 are well within the accuracy of the EOMCC calculations, indicating the excellent performance of the nonrelaxed FDET approach.

Remarkably, the nonrelaxed, monomer-expansion-based FDET values of the $\Delta\omega_{\pi\rightarrow\pi^*}$ shifts do not vary with the basis

set (see Table 3–6), allowing us to obtain reasonably well converged results with the relatively small basis sets, such as STO DZP (cf. Table 6). Moreover, although we prefer to use the monomer expansion within the FDET approach, where the orbitals of the chromophore A and the corresponding density ρ_A are represented using the atomic centers of A , whereas the environment density ρ_B is represented using the atomic centers of B , the use of the supermolecular expansion within the FDET methodology employing the nonrelaxed ρ_B does not seem to change the calculated shift values. For example, as a comparison of the results shown in Tables 3 and 6 demonstrates, the average deviation from EOMCC,A characterizing the nonrelaxed, monomer-expansion-based FDET calculations using the smallest STO DZP basis set, of 115 cm^{-1} , is virtually identical to the analogous average deviation characterizing the nonrelaxed, supermolecular-expansion-based FDET calculations using the largest STO ATZ2P basis (108 cm^{-1}). It is also worth mentioning that the quality of the shifts calculated with the FDET approach using the nonrelaxed environment density ρ_B does not diminish with or significantly depend on the size of the environment. For example, the absolute value of the difference between the $\Delta\omega_{\pi\rightarrow\pi^*}$ values resulting from the nonrelaxed, monomer-expansion-based FDET/ATZ2P and supermolecular EOMCC,A calculations for the smallest $7\text{HQ}\cdots\text{H}_2\text{O}$ complex is 83 cm^{-1} or 15%. The analogous difference characterizing the considerably larger $7\text{HQ}\cdots(\text{NH}_3-\text{H}_2\text{O}-\text{NH}_3)$ complex is 11 cm^{-1} or 1%.

All of the above observations show that the FDET approach employing the nonrelaxed environment densities ρ_B , including its simplest, monomer-expansion-based variant, is as accurate in describing complexation-induced shifts as the high-level EOMCC approach with singles, doubles, and noniterative triples, represented here by the composite EOMCC,A approximation. The FDET results with relaxed densities ρ_B are discussed next.

4.3. The Dependence of the FDET Shifts on the Choice of ρ_B . By determining the environment density ρ_B in the absence of the chromophore, the nonrelaxed FDET model examined in section 4.2 ignores the complexation-induced changes in the electronic density of the environment, such as polarization of the environment molecule(s) by the chromophore. Furthermore, the use of monomer basis expansions to represent the chromophore density ρ_A and the environment density ρ_B does not allow for a penetration of the region of space occupied by the chromophore by the electronic density of the environment or for a penetration of space occupied by the environment by the electronic density of the chromophore. These simplifying assumptions make the nonrelaxed, monomer-expansion-based FDET approach computationally very attractive, as the costs of such calculations are defined by the size of the chromophore only. However, they represent an arbitrary choice, prompting the question of whether relaxing the environment density ρ_B in the presence of the chromophore would help the FDET results.

As explained in section 3.2, for a given choice of approximants for the functionals used in the FDET calculations, one can optimize the environment density ρ_B , adjusting it to the density of the chromophore ρ_A , when solving the Kohn–Sham-like system for the chromophore A embedded in the environment B defined by eq 13, by exploiting the “freeze-and-thaw” procedure.⁸⁰ One might think that such relaxed FDET calculations should be more accurate than the nonrelaxed ones in which ρ_B is not adjusted, since relaxation of ρ_B takes into account the effect of electronic polarization of the environment by the chromophore. Unfortunately, this is not necessarily the case

because of the inaccuracies in describing the nonadditive kinetic energy potential $v_t^{\text{nad}}[\rho_A, \rho_B](\vec{r})$, eq 12, that couples the two densities and that enters eq 13, especially when the full, supermolecular set of atomic orbitals, including those centered on *A* and those centered on *B*, is used to represent the chromophore density ρ_A and the environment density ρ_B .^{64,84,130,131} It is usually impossible to *a priori* determine which effect is numerically more important in a molecular system of interest, the neglect of the electronic polarization of the environment by the chromophore or the errors produced by the approximations used to define the $v_t^{\text{nad}}[\rho_A, \rho_B](\vec{r})$ potential. In order to examine this issue, we performed the FDET calculations in which the environment density ρ_B was relaxed in the iterative process of solving eq 13 for the orbitals of the *cis*-7HQ chromophore.

As shown in Tables 3–6 and Figure 3, the relaxation of the environment density ρ_B in the FDET calculations for each of the eight complexes examined in this study substantially worsens the results for the $\Delta\omega_{\pi\rightarrow\pi^*}$ shifts when compared with the EOMCC,A reference data. The differences between the $\Delta\omega_{\pi\rightarrow\pi^*}$ values resulting from the relaxed FDET calculations using the STO ATZ2P basis set and the corresponding EOMCC,A data range, in absolute value, from 185 cm^{-1} in the case of the 7HQ $\cdot\cdot\cdot\text{NH}_3$ complex, where the EOMCC,A shift is -820 cm^{-1} , to 569 cm^{-1} , in the case of the 7HQ $\cdot\cdot\cdot\text{HCOOH}$ system, where the EOMCC,A result for $\Delta\omega_{\pi\rightarrow\pi^*}$ is -743 cm^{-1} . These are much larger differences when compared with the corresponding non-relaxed FDET calculations, which, as pointed out in section 4.2, give substantially smaller differences with the EOMCC,A data that range from 4 to 229 cm^{-1} when the same basis set is employed. As shown in Table 3, the mean signed and unsigned errors in the relaxed FDET/ATZ2P results for the environment-induced shifts $\Delta\omega_{\pi\rightarrow\pi^*}$ relative to the EOMCC,A reference data are -366 and 366 cm^{-1} , respectively, or, if we average the individual relative errors, 37%. This should be contrasted with the mean signed error of -36 cm^{-1} , mean unsigned error of 104 cm^{-1} , and average relative error of 11% in the analogous nonrelaxed FDET calculations. In some cases, the effect of relaxing ρ_B in the FDET calculations on the calculated $\Delta\omega_{\pi\rightarrow\pi^*}$ shifts is enormous, e.g., 546 cm^{-1} in the 7HQ $\cdot\cdot\cdot(\text{NH}_3-\text{NH}_3-\text{H}_2\text{O})$ case. As in the case of the FDET calculations using the nonrelaxed densities ρ_B , neither the type of the basis expansion used to represent densities ρ_A and ρ_B (monomer or supermolecular) nor the computational basis set used in the calculations affect the above observations (see Tables 3–6), although the use of the supermolecular expansion to represent ρ_A and ρ_B in the context of the relaxed FDET calculations with the STO ATZ2P basis set seems to worsen the results, increasing the mean unsigned error in the calculated $\Delta\omega_{\pi\rightarrow\pi^*}$ values relative to EOMCC,A from 366 cm^{-1} in the monomer-expansion case to 486 cm^{-1} , when the supermolecular expansion is employed (cf. the results in Tables 3 and 4), bringing the relaxed FDET results closer to the supermolecular TDDFT data (cf. the discussion below).

The substantial increase in the differences between the FDET and EOMCC,A shift values due to the relaxation of the environment densities ρ_B may be related to the fact that the Kohn–Sham-type methods applying semilocal approximants to the exchange–correlation energy used in this work tend to overestimate molecular polarizabilities in organic molecules.^{132,133} The exaggerated polarizability values would certainly lead to the overestimated chromophore polarization effects that could result in the artificially enhanced effects of relaxation of environment

densities on the calculated $\Delta\omega_{\pi\rightarrow\pi^*}$ values observed in our calculations. We must remember though that this argument, although reasonable here, may not be generally applicable, since going to the left-hand side of the periodic table shows that the same functionals underestimate polarizabilities.¹³⁴

It is worth pointing out that the result of the “freeze-and-thaw” FDET calculations employing the complete supermolecular basis expansion to represent the ρ_A and ρ_B densities, in which the environment density ρ_B is allowed to relax when solving eq 13 for the orbitals of *A*, represents the variational limit for a given approximant to the nonadditive kinetic energy potential $v_t^{\text{nad}}[\rho_A, \rho_B](\vec{r})$. If such an approximant were exact and if the same approximant were used to represent all of the exchange–correlation contributions in both supermolecular TDDFT and FDET calculations, the total electron density obtained in the relaxed “freeze-and-thaw” FDET calculations and its analog obtained in the supermolecular TDDFT calculations would be identical (see ref 48 and the references therein). This explains why the results of the relaxed FDET calculations using the supermolecular basis expansions to represent the ρ_A and ρ_B densities and their supermolecular TDDFT analogs shown in Table 4 and Figure 3 are so similar. Indeed, by relaxing the ρ_A and ρ_B densities simultaneously and by allowing them to penetrate both subsystems *A* and *B* when solving eq 13, we produce the situation in which the differences between the supermolecular and embedding strategies for calculating the $\Delta\omega_{\pi\rightarrow\pi^*}$ shifts become small. We must remember though that by relaxing the environment densities in the FDET approach or by performing the supermolecular TDDFT calculations with the functionals that are certainly imperfect, we introduce new errors, such as the inadequacy of the representation of the nonadditive kinetic energy potential $v_t^{\text{nad}}[\rho_A, \rho_B](\vec{r})$ in the FDET considerations that may be significantly enhanced when ρ_B is relaxed or the difficulties with maintaining a balanced treatment of the chromophore and its complex with the environment within the supermolecular TDDFT framework. These are the reasons why the nonrelaxed FDET approach may represent a better computational strategy in determining the excitation energy shifts in weakly bound systems of the type of complexes examined in this work, when compared with the relaxed FDET and supermolecular TDDFT methodologies, as the results in Tables 3–6 and Figures 2–5 clearly illustrate.

4.4. A Comparison of the Excitation Energy Shifts from the Supermolecular TDDFT Calculations with the Nonrelaxed FDET and Reference EOMCC Data. As already alluded to above, the excitation energy shifts in the eight complexes of *cis*-7HQ examined in this study resulting from the supermolecular TDDFT calculations are a lot less accurate than their FDET counterparts employing the nonrelaxed environment densities, when both types of calculations are compared with the reference EOMCC,A data. They are also less accurate than the FDET results obtained with the relaxed environment densities, although, as pointed out at the end of section 4.3, the differences between the $\Delta\omega_{\pi\rightarrow\pi^*}$ values obtained in the supermolecular TDDFT and relaxed FDET calculations are smaller than the analogous differences between the results of the supermolecular TDDFT and nonrelaxed FDET calculations. Indeed, as shown in Table 3 (cf. also, Figure 3), the differences between the $\Delta\omega_{\pi\rightarrow\pi^*}$ shift values obtained in the supermolecular TDDFT calculations using the STO ATZ2P basis set and their reference EOMCC,A counterparts range, in absolute value, from 382 cm^{-1} in the case of the 7HQ $\cdot\cdot\cdot\text{H}_2\text{O}$ complex, where the EOMCC,A shift

is -562 cm^{-1} , to 869 cm^{-1} , in the case of the $7\text{HQ}\cdots(\text{NH}_3-\text{H}_2\text{O}-\text{H}_2\text{O})$ system, where the EOMCC,A $\Delta\omega_{\pi\rightarrow\pi^*}$ value is -1969 cm^{-1} . The mean unsigned error in the supermolecular TDDFT/ATZ2P values of the $\Delta\omega_{\pi\rightarrow\pi^*}$ shifts relative to EOMCC,A is 673 cm^{-1} or, if we average the individual relative errors, 65%. These clearly are much larger differences when compared with the corresponding nonrelaxed, monomer-expansion-based FDET calculations that give the $4\text{--}229\text{ cm}^{-1}$ deviations from the EOMCC,A data and the differences, which are about twice as large as those characterizing the relaxed, monomer-expansion-based FDET approach. The 65% average relative error characterizing the $\Delta\omega_{\pi\rightarrow\pi^*}$ values resulting from the supermolecular TDDFT/ATZ2P calculations is 6 times bigger than the analogous error characterizing the nonrelaxed, monomer-expansion-based FDET/ATZ2P calculations. On the basis of the analysis of the EOMCC calculations performed in this work presented in section 4.1, the differences between the supermolecular TDDFT and reference EOMCC,A data are well outside the accuracy of the EOMCC calculations for the $\Delta\omega_{\pi\rightarrow\pi^*}$ shifts, indicating the poor performance of the supermolecular TDDFT approach. Unlike in the FDET case, the differences between the supermolecular TDDFT and EOMCC,A $\Delta\omega_{\pi\rightarrow\pi^*}$ values increase with the size of the environment bound to the *cis*-7HQ chromophore. This indicates the difficulties with obtaining the balanced description of excitation energies in systems that have different sizes in the supermolecular TDDFT calculations, which are not present in the FDET and EOMCC calculations.

The large inaccuracies in the supermolecular TDDFT results might be due to various reasons. One possibility might be the basis set superposition error (BSSE), which could potentially be well pronounced due to the difficulties the supermolecular TDDFT approach has with obtaining a balanced description of excitation energies in systems that have different sizes, but, as shown in Table 7, the $\pi\rightarrow\pi^*$ excitation energy in the isolated *cis*-7HQ system is barely affected by the position of ghost basis functions centered on the atoms of environment molecules. Another possibility might be a particular choice of the approximation used to determine the exchange-correlation potential contributions in the TDDFT calculations (the SAOP scheme¹²⁹). To investigate this issue, we performed additional supermolecular TDDFT calculations using two other treatments of the exchange-correlation contributions, namely, the local density approximation (LDA)¹³⁵ and the PW91 functional,¹³⁶ which is a representative functional from the GGA family. The results of these additional calculations are shown in Table 8 and Figure 4. It is quite clear that the use of the LDA and PW91 functionals to treat the exchange-correlation contributions does not help the supermolecular TDDFT results, making them, in fact, even less accurate than in the SAOP case. Interestingly, the use of the LDA and PW91 functionals in the nonrelaxed FDET calculations has a small effect on these calculations, increasing the mean unsigned errors relative to EOMCC,A characterizing the SAOP-based nonrelaxed, monomer-expansion-based FDET/ATZ2P calculations of 104 cm^{-1} to 140 cm^{-1} in the LDA case and 149 cm^{-1} in the PW91 case. This makes us believe that the primary reason for the poor performance of the supermolecular TDDFT approach is the difficulty with obtaining a balanced description of excitation energies in systems that have different sizes in the supermolecular TDDFT calculations, which are not present in the size-intensive FDET and EOMCC calculations and which are only enhanced in the supermolecular TDDFT calculations by incorrect asymptotic behavior of the LDA and PW91

(GGA) potentials, critical for the determination of the relatively small spectral shifts in weakly bound molecular clusters. This is yet another argument in favor of the embedding strategy represented here by the FDET approach, which is much less sensitive to the asymptotic behavior of the exchange-correlation potentials.

4.5. A Comparison of the Excitation Energy Shifts from the FDET Calculations Using Nonrelaxed Environment Densities with the Experimental Data. Although the main goal of this work is to compare the FDET and supermolecular TDDFT values of the vertical excitation energy shifts characterizing the hydrogen-bonded complexes of the *cis*-7HQ system with the corresponding EOMCC,A data, all obtained using the same nuclear geometries, it is useful to comment on the quality of the shifts resulting from our best FDET calculations employing the nonrelaxed environment densities, when compared with the available experimental data.⁵ In analogy to the EOMCC,A results discussed in section 4.1, a comparison of the purely electronic FDET and experimental data discussed above has limitations, since one cannot measure vertical excitation energies obtained in a direct manner. The experimental shifts reported in ref 5 that we refer to in this work correspond to the complexation-induced shifts in the maxima of the $\pi\rightarrow\pi^*$ absorption band in the *cis*-7HQ chromophore. Thus, although the experimental shifts reported in ref 5 are closely related to the theoretical shifts obtained in this study, the two types of quantities differ because of the following factors: (i) the maxima of the absorption bands characterizing the isolated *cis*-7HQ system and its complexes may not occur between the same vibrational levels as a result of the geometry relaxation in the excited states of the *cis*-7HQ $\cdots B$ complexes when compared to the corresponding ground electronic states, and (ii) the MP2/aug-cc-pVTZ geometries of *cis*-7HQ and its complexes used in this work, although probably quite reasonable, are not the experimental geometries. All of these factors certainly contribute to the deviations between the theoretical shifts calculated in this study and their experimental counterparts reported in ref 5.

On the other hand, the careful EOMCC calculations reported in this work which, as analyzed in section 4.1, closely follow the experimental excitation energies corresponding to the lowest $\pi\rightarrow\pi^*$ transition in the *cis*-7HQ and *cis*-7HQ $\cdots B$ systems, particularly when the EOMCC,A and EOMCC,B approaches corrected for triple excitations are employed (see Table 2), seem to indicate that all of the above factors, although important, lead to a relatively small overall effect. It is, therefore, interesting to compare our best FDET results for the excitation energy shifts $\Delta\omega_{\pi\rightarrow\pi^*}$, obtained in the nonrelaxed, monomer-expansion-based FDET calculations employing the STO ATZ2P basis set, given in Table 3, which are in excellent agreement with the reference EOMCC,A data, with the experimentally derived shifts reported in ref 5 and listed in Table 2. This comparison is shown in Figure 5. As one can see by inspecting Tables 2 and 3 and Figure 5, the $\Delta\omega_{\pi\rightarrow\pi^*}$ values obtained in the nonrelaxed, monomer-expansion-based FDET/ATZ2P calculations are in very good agreement with the shifts in the experimental UV absorption spectra. The mean unsigned error in the $\Delta\omega_{\pi\rightarrow\pi^*}$ values resulting from the nonrelaxed, monomer-expansion-based FDET/ATZ2P calculations, relative to the spectral shifts observed in experiment, is 222 cm^{-1} , in excellent agreement with the EOMCC,A approach, which gives 244 cm^{-1} . The analogous mean unsigned error characterizing the supermolecular TDDFT calculations is twice as large (429 cm^{-1}), demonstrating once

again the advantages of the embedding vs supermolecular strategy within the TDDFT framework. It is clearly very encouraging that the nonrelaxed FDET approach, which can be applied to large molecular systems, can provide shifts in the excitation energy corresponding to the lowest $\pi \rightarrow \pi^*$ transition in the *cis*-7HQ system due to the formation of hydrogen-bonded complexes involving *cis*-7HQ and a variety of small molecules that can compete with the results of the considerably more expensive EOMCC calculations.

5. SUMMARY AND CONCLUSIONS

We used the embedding FDET approach to determine the shifts in the excitation energy corresponding to the lowest $\pi \rightarrow \pi^*$ transition in *cis*-7-hydroxyquinoline (*cis*-7HQ), induced by the formation of hydrogen-bonded complexes of *cis*-7HQ with a number of small molecules, and compared the resulting shift values with the reference EOMCC data and the analogous shifts obtained in the conventional supermolecular TDDFT calculations. The main difference between the embedding strategy, represented in the present study by the FDET method, and the conventional supermolecular approach is in the fact that in the former case one evaluates the excitation energy shifts induced by the interactions of the chromophore with its molecular environment as the differences of the excitation energies of the same many-electron system, representing the chromophore fragment with two different effective potentials, whereas in the latter case one has to perform calculations for two systems that differ in the number of electrons, the complex formed by the chromophore and its molecular environment, and the isolated chromophore.

By considering eight complexes of *cis*-7HQ with up to three small hydrogen-bonded molecules, we demonstrated that the spectral shifts resulting from the FDET calculations with the *a priori* determined nonrelaxed environment densities are in excellent agreement with the reference EOMCC data obtained in the supermolecular, rigorously size-intensive EOMCC calculations with singles, doubles, and noniterative triples, whereas the analogous shifts obtained with the supermolecular TDDFT approach are far from those obtained with EOMCC. The nonrelaxed FDET calculations provide shifts that agree with their EOMCC analogs to within about 100 cm^{-1} or 10% on average, where the absolute values of the excitation energy shifts in the complexes of *cis*-7HQ examined in this study resulting from the EOMCC calculations range between about 500 and 2000 cm^{-1} . As shown in the present study, the accuracy of the FDET shift calculations employing nonrelaxed environment densities is on the order of the accuracy of the high-level EOMCC calculations. This should be contrasted with the excitation energy shifts obtained with the supermolecular TDDFT approach, which differ from the reference EOMCC values reported in this work by about 700 cm^{-1} or 65% on average and which are well outside the accuracy of the EOMCC calculations. We demonstrated that none of the above findings are significantly affected by the type of basis expansion used in the FDET calculations (monomer or supermolecular), by the computational basis set used in the FDET and supermolecular TDDFT calculations, or by the approximations applied to the exchange-correlation potentials in the FDET and supermolecular TDDFT calculations, although it is quite clear that better approximations for the exchange-correlation potential would help the supermolecular TDDFT approach. One of the key

findings of the present study is the fact that the FDET methodology, particularly the nonrelaxed form of it, works well even with the functionals that are characterized by the relatively poor long-range behavior, offering results that are competitive with the high-level EOMCC approaches.

We demonstrated that the relaxation of the environment density in the FDET calculations worsens the quality of the calculated spectral shifts, although the shifts resulting from the relaxed FDET calculations are typically somewhat more accurate than those obtained with the supermolecular TDDFT approach. Among the reasons that may contribute to the worsening of the results obtained with the FDET approach using relaxed environment densities are the difficulties the Kohn–Sham-type methods applying semilocal approximants to the exchange-correlation energy, used in this work, have with describing molecular polarizabilities and the inadequacies in representing the non-additive kinetic energy potential in the FDET considerations that may be significantly enhanced when the environment density is allowed to relax when solving a coupled system of Kohn–Sham-like equations defining the FDET approach and involving the chromophore and environment densities. Our calculations strongly suggest that at least in the applications involving shifts in the electronic spectrum due to the formation of weakly bound complexes, where the electronic excitation is localized on the absorbing chromophore, the neglect of the electronic polarization of the environment by the chromophore, implicitly assumed in the FDET calculations using nonrelaxed environment densities, is of much lesser significance than the errors that result from the approximations used to define the nonadditive kinetic energy potential, which can be quite substantial. On the basis of a direct comparison of the FDET results obtained with nonrelaxed and relaxed environment densities, the nonrelaxed FDET approach is a preferred strategy for the embedding calculations if the polarization of the environment by the chromophore is small, as is the case when the weakly bound complexes of *cis*-7HQ are examined. On the other hand, if one is interested in generating results that are similar to those obtained with the supermolecular TDDFT methodology, relaxing environment density in the FDET calculations may be more appropriate. We demonstrated that the fully relaxed FDET calculations are capable of producing spectral shifts that are quite close to the results of the supermolecular TDDFT calculations, even though both sets of calculations led to results that are quite far from the benchmark EOMCC and experimental data.

As shown in our study, the FDET approach with nonrelaxed environment densities represents a robust computational methodology, which works much better than the FDET methods with relaxed densities and supermolecular TDDFT schemes and which can provide complexation-induced spectral shifts that can compete with the high-quality *ab initio* data resulting from EOMCC calculations, as long as one can neglect the polarization of the environment by the chromophore. This is very encouraging from the point of view of spectroscopic applications involving large weakly bound molecular complexes, since the FDET approach with nonrelaxed environment densities is less expensive than its relaxed and supermolecular TDDFT counterparts, not to mention the EOMCC methods. In the FDET calculations employing nonrelaxed environment densities, one obtains these densities only once and *a priori* by solving the ground-state Kohn–Sham equations for the environment molecule(s) in the absence of the absorbing chromophore. This should be contrasted with the relaxed FDET calculations, where

the environment density is allowed to vary during the Kohn–Sham-like calculations for the orbitals of the chromophore embedded in the environment, and with the supermolecular TDDFT and EOMCC calculations, where one has to consider larger many-electron systems corresponding to the chromophore complexes that do not have to be considered in the FDET calculations. The latter is challenging for the supermolecular TDDFT approaches, since they have difficulties with balancing accuracies involving systems of different sizes, and for methods based on the EOMCC theory, which can balance these accuracies, but are often prohibitively expensive.

Although the main focus of this study was the comparison of the FDET and supermolecular TDDFT results for the complexation-induced shifts in the excitation energy corresponding to the lowest $\pi \rightarrow \pi^*$ transition in *cis*-7HQ with the EOMCC data, we also compared the FDET, supermolecular TDDFT, and reference EOMCC shift values with the experimental shifts reported in ref 5. Although, as explained in the previous sections, such comparison has obvious limitations due to the neglect of the effect of nuclear motion on photoabsorption spectra in our purely electronic calculations, the spectral shifts obtained with the FDET approach using nonrelaxed environment densities and those obtained with the EOMCC methodology agree with the experimental shifts quite well, whereas the supermolecular TDDFT calculations produce once again very large errors. This confirms the superiority of the FDET strategy when compared with the conventional supermolecular TDDFT approach in applications involving complexation-induced spectral shifts.

■ ASSOCIATED CONTENT

Supporting Information. The nuclear geometries of the *cis*-7HQ molecule and its complexes examined in this study along with the vertical excitation energies $\omega_{\pi \rightarrow \pi^*}$ resulting from the FDET and supermolecular TDDFT calculations. This material is available free of charge via the Internet at <http://pubs.acs.org/>.

■ AUTHOR INFORMATION

Corresponding Authors

*E-mail: tomasz.wesolowski@unige.ch; piecuch@chemistry.msu.edu.

■ ACKNOWLEDGMENT

This work has been supported by the Chemical Sciences, Geosciences and Biosciences Division, Office of Basic Energy Sciences, Office of Science, U.S. Department of Energy (Grant No. DE-FG02-01ER15228; P.P.) and Fonds National Suisse de la Recherche Scientifique (Grant No. 200020-124817; T.A.W.).

■ REFERENCES

- (1) Tanner, C.; Manca, C.; Leutwyler, S. *Science* **2003**, *302*, 1736.
- (2) Bruhwiler, D.; Calzaferri, G.; Torres, T.; Ramm, J. H.; Gartmann, N.; Dieu, L.-Q.; Lopez-Duarte, I.; Martinez-Diaz, M. V. *J. Mater. Chem.* **2009**, *19*, 8040.
- (3) Hernandez, F. E.; Yu, S.; Garcia, M.; Campiglia, A. D. *J. Phys. Chem. B* **2005**, *109*, 9499.
- (4) Goldberg, J. M.; Batjargal, S.; Petersson, E. J. *J. Am. Chem. Soc.* **2010**, *132*, 14719.
- (5) Thut, M.; Tanner, C.; Steinlin, A.; Leutwyler, S. *J. Phys. Chem. A* **2008**, *112*, 5566.
- (6) Emrich, K. *Nucl. Phys. A* **1981**, *351*, 379.
- (7) Geertsen, J.; Rittby, M.; Bartlett, R. J. *Chem. Phys. Lett.* **1989**, *164*, 57.
- (8) Comeau, D. C.; Bartlett, R. J. *Chem. Phys. Lett.* **1993**, *207*, 414.
- (9) Stanton, J. F.; Bartlett, R. J. *J. Chem. Phys.* **1993**, *98*, 7029.
- (10) Piecuch, P.; Bartlett, R. J. *Adv. Quantum Chem.* **1999**, *34*, 295.
- (11) Monkhorst, H. *Int. J. Quantum Chem. Symp.* **1977**, *11*, 421.
- (12) Dalgaard, E.; Monkhorst, H. *Phys. Rev. A* **1983**, *28*, 1217.
- (13) Mukherjee, D.; Mukherjee, P. K. *Chem. Phys.* **1979**, *39*, 325.
- (14) Takahashi, M.; Paldus, J. J. *Chem. Phys.* **1986**, *85*, 1486.
- (15) Koch, H.; Jørgensen, P. *J. Chem. Phys.* **1990**, *93*, 3333.
- (16) Koch, H.; Jensen, H. J. A.; Jørgensen, P.; Helgaker, T. *J. Chem. Phys.* **1990**, *93*, 3345.
- (17) Coester, F. *Nucl. Phys.* **1958**, *7*, 421.
- (18) Coester, F.; Kümmel, H. *Nucl. Phys.* **1960**, *17*, 477.
- (19) Čížek, J. *J. Chem. Phys.* **1966**, *45*, 4256.
- (20) Čížek, J. *Adv. Chem. Phys.* **1969**, *14*, 35.
- (21) Čížek, J.; Paldus, J. *Int. J. Quantum Chem.* **1971**, *5*, 359.
- (22) Paldus, J.; Shavitt, I.; Čížek, J. *Phys. Rev. A* **1972**, *5*, 50.
- (23) Gauss, J. In *Encyclopedia of Computational Chemistry*; Schleyer, P. v. R., Allinger, N. L., Clark, T., Gasteiger, J., Kollman, P. A., Schaefer, H. F., III, Schreiner, P. R., Eds.; Wiley: Chichester, U. K., 1998; Vol. 1; pp 615–636.
- (24) Paldus, J.; Li, X. *Adv. Chem. Phys.* **1999**, *110*, 1.
- (25) Bartlett, R. J.; Musiał, M. *Rev. Mod. Phys.* **2007**, *79*, 291.
- (26) Piecuch, P.; Włoch, M. *J. Chem. Phys.* **2005**, *123*, 224105.
- (27) Piecuch, P.; Włoch, M.; Gour, J. R.; Kinal, A. *Chem. Phys. Lett.* **2006**, *418*, 467.
- (28) Włoch, M.; Gour, J. R.; Piecuch, P. *J. Phys. Chem. A* **2007**, *111*, 11359.
- (29) Włoch, M.; Lodriguito, M. D.; Piecuch, P.; Gour, J. R. *Mol. Phys.* **2006**, *104*, 2149.
- (30) Piecuch, P.; Gour, J. R.; Włoch, M. *Int. J. Quantum Chem.* **2009**, *109*, 3268.
- (31) Shiozaki, T.; Hirao, K.; Hirata, S. *J. Chem. Phys.* **2007**, *126*, 244106.
- (32) Watts, J. D.; Bartlett, R. J. *Chem. Phys. Lett.* **1996**, *258*, 581.
- (33) Meissner, L.; Bartlett, R. J. *J. Chem. Phys.* **1995**, *102*, 7490.
- (34) Korona, T.; Werner, H.-J. *J. Chem. Phys.* **2003**, *118*, 3006.
- (35) Korona, T.; Schütz, M. *J. Chem. Phys.* **2006**, *125*, 104106.
- (36) Kats, D.; Korona, T.; Schütz, M. *J. Chem. Phys.* **2007**, *127*, 064107.
- (37) Crawford, T. D.; King, R. A. *Chem. Phys. Lett.* **2002**, *366*, 611.
- (38) Fan, P.-D.; Valiev, M.; Kowalski, K. *Chem. Phys. Lett.* **2008**, *458*, 205.
- (39) Valiev, M.; Kowalski, K. *J. Chem. Phys.* **2006**, *125*, 211101.
- (40) Valiev, M.; Kowalski, K. *J. Phys. Chem. A* **2006**, *110*, 13106.
- (41) Kowalski, K.; Valiev, M. *J. Phys. Chem. A* **2008**, *112*, 5538.
- (42) Epifanovsky, E.; Kowalski, K.; Fan, P.-D.; Valiev, M.; Matsika, S.; Krylov, A. I. *J. Phys. Chem. A* **2008**, *112*, 9983.
- (43) Li, W.; Gour, J. R.; Piecuch, P.; Li, S. *J. Chem. Phys.* **2009**, *131*, 114109.
- (44) Li, W.; Piecuch, P. *J. Phys. Chem. A* **2010**, *114*, 8644.
- (45) Li, W.; Piecuch, P. *J. Phys. Chem. A* **2010**, *114*, 6721.
- (46) Casida, M. E. In *Recent Advances in Density-Functional Methods, Part-I*; Chong, D. P., Ed.; World Scientific: Singapore, 1995; pp 155–192.
- (47) Wesolowski, T. A.; Warshel, A. *J. Phys. Chem.* **1993**, *97*, 8050.
- (48) Wesolowski, T. A. In *Computational Chemistry: Reviews of Current Trends*; Leszczyński, J., Ed.; World Scientific: Singapore, 2006; Vol. 10; pp 1–82.
- (49) Wesolowski, T. A. *Phys. Rev. A* **2008**, *77*, 012504.
- (50) Pernal, K.; Wesolowski, T. A. *Int. J. Quantum Chem.* **2009**, *109*, 2520.
- (51) Wesolowski, T. A.; Warshel, A. *J. Phys. Chem.* **1994**, *98*, 5183.
- (52) Neugebauer, J.; Louwse, M. J.; Baerends, E. J.; Wesolowski, T. A. *J. Chem. Phys.* **2005**, *122*, 094115.
- (53) Kaminski, J. W.; Gusarov, S.; Kovalenko, A.; Wesolowski, T. A. *J. Phys. Chem. A* **2010**, *114*, 6082.

- (54) Savin, A.; Wesolowski, T. A. In *Advances in the Theory of Atomic and Molecular Systems: Conceptual and Computational Advances in Quantum Chemistry*; Piecuch, P., Maruani, J., Delgado-Barrio, G., Wilson, S., Eds.; Progress in Theoretical Chemistry and Physics; Springer: Dordrecht, The Netherlands, 2009; Vol. 19; pp 327–339.
- (55) Roncero, O.; de Lara-Castells, M.; Villarreal, P.; Flores, F.; Ortega, J.; Paniagua, M.; Aguado, A. *J. Chem. Phys.* **2008**, *129*, 184104.
- (56) Fux, S.; Jacob, C.; Neugebauer, J.; Visscher, L.; Reiher, M. *J. Chem. Phys.* **2010**, *132*, 164101.
- (57) Goodpaster, J. D.; Ananth, N.; Manby, F. R.; Miller, T. F., III. *J. Chem. Phys.* **2010**, *133*, 084103.
- (58) Wesolowski, T. *J. Am. Chem. Soc.* **2004**, *126*, 11444.
- (59) Fradelos, G.; Kaminski, J. W.; Wesolowski, T. A.; Leutwyler, S. *J. Phys. Chem. A* **2009**, *19*, 9766.
- (60) Zbiri, M.; Atanasov, M.; Daul, C.; Garcia-Lastra, J. M.; Wesolowski, T. A. *Chem. Phys. Lett.* **2004**, *397*, 441.
- (61) Fradelos, G.; Wesolowski, T. A. *J. Chem. Theory Comput.* **2011**, *7*, 213.
- (62) Domcke, W.; Sobolewski, A. L. *Science* **2003**, *302*, 1963.
- (63) Wesolowski, T. A. *J. Am. Chem. Soc.* **2004**, *126*, 11444.
- (64) Lastra, J. M. G.; Kaminski, J. W.; Wesolowski, T. A. *J. Chem. Phys.* **2008**, *129*, 074107.
- (65) Stefanovich, E. V.; Truong, T. N. *J. Chem. Phys.* **1996**, *104*, 2946.
- (66) Govind, N.; Wang, Y. A.; Carter, E. A. *J. Chem. Phys.* **1999**, *110*, 7677.
- (67) Neugebauer, J.; Jacob, C. R.; Wesolowski, T. A.; Baerends, E. J. *J. Phys. Chem. A* **2005**, *109*, 7805.
- (68) Hodak, M.; Lu, W.; Bernholc, J. *J. Chem. Phys.* **2008**, *128*, 014101.
- (69) Gomes, A. S. P.; Jacob, C. R.; Visscher, L. *Phys. Chem. Chem. Phys.* **2008**, *10*, 5353.
- (70) Kohn, W.; Sham, L. J. *Phys. Rev.* **1965**, *140*, A1133.
- (71) Hohenberg, P.; Kohn, W. *Phys. Rev.* **1964**, *136*, B864.
- (72) Wesolowski, T. A. *Chem. Phys. Lett.* **1999**, *311*, 87.
- (73) Neugebauer, J.; Louwerse, M. J.; Belanzoni, P.; Wesolowski, T. A.; Baerends, E. J. *J. Chem. Phys.* **2005**, *123*, 114101.
- (74) Jacob, C. R.; Visscher, L. *J. Chem. Phys.* **2006**, *125*, 194104.
- (75) Jacob, C. J.; Neugebauer, J.; Jensen, L.; Visscher, L. *Phys. Chem. Chem. Phys.* **2006**, *8*, 2349.
- (76) Cortona, P. *Phys. Rev. B* **1991**, *44*, 8454.
- (77) Senatore, G.; Subbaswamy, K. *Phys. Rev. B* **1986**, *34*, 5754.
- (78) Elliott, P.; Cohen, M. H.; Wasserman, A.; Burke, K. *J. Chem. Theory Comput.* **2009**, *5*, 827.
- (79) Iannuzzi, M.; Kirchner, B.; Hutter, J. *Chem. Phys. Lett.* **2006**, *421*, 16.
- (80) Wesolowski, T. A.; Weber, J. *Chem. Phys. Lett.* **1996**, *248*, 71.
- (81) Wesolowski, T. A.; Tran, F. *J. Chem. Phys.* **2003**, *118*, 2072.
- (82) Kevorkyants, R.; Dulak, M.; Wesolowski, T. A. *J. Chem. Phys.* **2006**, *124*, 024104.
- (83) Dulak, M.; Kaminski, J. W.; Wesolowski, T. A. *J. Chem. Theory Comput.* **2007**, *3*, 735.
- (84) Wesolowski, T. A.; Weber, J. *Int. J. Quantum Chem.* **1997**, *61*, 303.
- (85) Bernard, Y. A.; Dulak, M.; Kaminski, J. W.; Wesolowski, T. A. *J. Phys. A* **2008**, *41*, 0553902.
- (86) Dulak, M.; Kaminski, J. W.; Wesolowski, T. A. *Int. J. Quant. Chem.* **2009**, *109*, 1886.
- (87) Piecuch, P.; Kowalski, K.; Pimienta, I. S. O.; McGuire, M. J. *Int. Rev. Phys. Chem.* **2002**, *21*, 527.
- (88) Piecuch, P.; Kowalski, K.; Pimienta, I. S. O.; Fan, P.-D.; Lodriguito, M.; McGuire, M. J.; Kucharski, S. A.; Kuš, T.; Musiał, M. *Theor. Chem. Acc.* **2004**, *112*, 349.
- (89) Kowalski, K.; Piecuch, P. *J. Chem. Phys.* **2001**, *115*, 2966.
- (90) Kowalski, K.; Piecuch, P. *J. Chem. Phys.* **2002**, *116*, 7411.
- (91) Kowalski, K.; Piecuch, P. *J. Chem. Phys.* **2004**, *120*, 1715.
- (92) Włoch, M.; Gour, J. R.; Kowalski, K.; Piecuch, P. *J. Chem. Phys.* **2005**, *122*, 214107.
- (93) Kowalski, K.; Hirata, S.; Włoch, M.; Piecuch, P.; Windus, T. L. *J. Chem. Phys.* **2005**, *123*, 074319.
- (94) Coussan, S.; Ferro, Y.; Trivella, A.; Roubin, P.; Wieczorek, R.; Manca, C.; Piecuch, P.; Kowalski, K.; Włoch, M.; Kucharski, S. A.; Musiał, M. *J. Phys. Chem. A* **2006**, *110*, 3920.
- (95) Kowalski, K.; Krishnamoorthy, S.; Villa, O.; Hammond, J. R.; Govind, N. *J. Chem. Phys.* **2010**, *132*, 154103.
- (96) Kowalski, K.; Piecuch, P. *J. Chem. Phys.* **2001**, *115*, 643.
- (97) Kowalski, K.; Piecuch, P. *Chem. Phys. Lett.* **2001**, *347*, 237.
- (98) Kucharski, S. A.; Włoch, M.; Musiał, M.; Bartlett, R. J. *J. Chem. Phys.* **2001**, *115*, 8263.
- (99) Kowalski, K.; Piecuch, P. *J. Chem. Phys.* **2000**, *113*, 8490.
- (100) Hirata, S.; Nooijen, M.; Grabowski, I.; Bartlett, R. J. *J. Chem. Phys.* **2001**, *114*, 3919; **2001**, *115*, 3967 [Erratum].
- (101) Watts, J. D.; Bartlett, R. J. *Chem. Phys. Lett.* **1995**, *233*, 81.
- (102) Christiansen, O.; Koch, H.; Jørgensen, P. *J. Chem. Phys.* **1996**, *105*, 1451.
- (103) Christiansen, O.; Koch, H.; Jørgensen, P.; Olsen, J. *Chem. Phys. Lett.* **1996**, *256*, 185.
- (104) Koch, H.; Christiansen, O.; Jørgensen, P.; Olsen, J. *Chem. Phys. Lett.* **1995**, *244*, 75.
- (105) Christiansen, O.; Koch, H.; Jørgensen, P. *J. Chem. Phys.* **1995**, *103*, 7429.
- (106) Kowalski, K. *J. Chem. Phys.* **2009**, *130*, 194110.
- (107) Manohar, P. U.; Krylov, A. I. *J. Chem. Phys.* **2008**, *129*, 194105.
- (108) Raghavachari, K.; Trucks, G. W.; Pople, J. A.; Head-Gordon, M. *Chem. Phys. Lett.* **1989**, *102*, 479.
- (109) Piecuch, P.; Kowalski, K. In *Computational Chemistry: Reviews of Current Trends*; Leszczyński, J., Ed.; World Scientific: Singapore, 2000; Vol. 5; pp 1–104.
- (110) Kowalski, K.; Piecuch, P. *J. Chem. Phys.* **2000**, *113*, 18.
- (111) Kowalski, K.; Piecuch, P. *J. Chem. Phys.* **2005**, *122*, 074107.
- (112) Hirata, S.; Fan, P.-D.; Auer, A. A.; Nooijen, M.; Piecuch, P. *J. Chem. Phys.* **2004**, *121*, 12197.
- (113) Møller, C.; Plesset, M. S. *Phys. Rev.* **1934**, *46*, 618.
- (114) Dunning, T. H., Jr. *J. Chem. Phys.* **1989**, *90*, 1007.
- (115) Kendall, R. A.; Dunning, T. H., Jr.; Harrison, R. J. *J. Chem. Phys.* **1992**, *96*, 6796.
- (116) Frisch, M. J.; Trucks, G. W.; Schlegel, H. B.; Scuseria, G. E.; Robb, M. A.; Cheeseman, J. R.; Montgomery, J. A., Jr.; Vreven, T.; Kudin, K. N.; Burant, J. C.; Millam, J. M.; Iyengar, S. S.; Tomasi, J.; Barone, V.; Mennucci, B.; Cossi, M.; Scalmani, G.; Rega, N.; Petersson, G. A.; Nakatsuji, H.; Hada, M.; Ehara, M.; Toyota, K.; Fukuda, R.; Hasegawa, J.; Ishida, M.; Nakajima, T.; Honda, Y.; Kitao, O.; Nakai, H.; Klene, M.; Li, X.; Knox, J. E.; Hratchian, H. P.; Cross, J. B.; Adamo, C.; Jaramillo, J.; Gomperts, R.; Stratmann, R. E.; Yazyev, O.; Austin, A. J.; Cammi, R.; Pomelli, C.; Ochterski, J. W.; Ayala, P. Y.; Morokuma, K.; Voth, G. A.; Salvador, P.; Dannenberg, J. J.; Zakrzewski, V. G.; Dapprich, S.; Daniels, A. D.; Strain, M. C.; Farkas, O.; Malick, D. K.; Rabuck, A. D.; Raghavachari, K.; Foresman, J. B.; Ortiz, J. V.; Cui, Q.; Baboul, A. G.; Clifford, S.; Cioslowski, J.; Stefanov, B. B.; Liu, G.; Liashenko, A.; Piskorz, P.; Komaromi, I.; Martin, R. L.; Fox, D. J.; Keith, T.; Al-Laham, M. A.; Peng, C. Y.; Nanayakkara, A.; Challacombe, M.; Gill, P. M. W.; Johnson, B.; Chen, W.; Wong, M. W.; Gonzalez, C.; Pople, J. A. *Gaussian 03*, Revision B.03; Gaussian, Inc., Pittsburgh, PA, 2003.
- (117) Hehre, W. J.; Ditchfield, R.; Pople, J. A. *J. Chem. Phys.* **1972**, *56*, 2257.
- (118) Hariharan, P. C.; Pople, J. A. *Theor. Chim. Acta* **1973**, *28*, 213.
- (119) Clark, T.; Chandrasekhar, J.; Spitznagel, G. W.; Schleyer, P. v. R. *J. Comput. Chem.* **1983**, *4*, 294.
- (120) Krishnan, R.; Binkley, J. S.; Seeger, R.; Pople, J. A. *J. Chem. Phys.* **1980**, *72*, 650.
- (121) Sadlej, A. J. *Collect. Czech. Chem. Commun.* **1988**, *53*, 1995.
- (122) Schmidt, M. W.; Baldridge, K. K.; Boatz, J. A.; Elbert, S. T.; Gordon, M. S.; Jensen, J. H.; Koseki, S.; Matsunaga, N.; Nguyen, K. A.; Su, S. J.; Windus, T. L.; Dupuis, M.; Montgomery, J. A. *J. Comput. Chem.* **1993**, *14*, 1347.

- (123) Gordon, M. S.; Schmidt, M. W. In *Theory and Applications of Computational Chemistry: The First Forty Years*; Dykstra, C. E., Frenking, G., Kim, K. S., Scuseria, G. E., Eds.; Elsevier: Amsterdam, 2005; pp 1167–1190.
- (124) Piecuch, P.; Kucharski, S. A.; Kowalski, K.; Musiał, M. *Comput. Phys. Commun.* **2002**, *149*, 71.
- (125) ADF2009 suite of programs. Theoretical Chemistry Department, Vrije Universiteit, Amsterdam. <http://www.scm.com>
- (126) Wesolowski, T. A.; Chermette, H.; Weber, J. J. *Chem. Phys.* **1996**, *105*, 9182.
- (127) Casida, M. E.; Wesolowski, T. A. *Int. J. Quantum Chem.* **2004**, *96*, 577.
- (128) Neugebauer, J. J. *Chem. Phys.* **2007**, *134*, 134116.
- (129) Gritsenko, O. V.; Schipper, P. R. T.; Baerends, E. J. *Chem. Phys. Lett.* **1999**, *302*, 199.
- (130) Dulak, M.; Wesolowski, T. A. *J. Chem. Phys.* **2006**, *124*, 164101.
- (131) Jacob, C. R.; Beyhan, S. M.; Visscher, L. *J. Chem. Phys.* **2007**, *126*, 234116.
- (132) McDowell, S. A. C.; Amos, R. D.; Handy, N. C. *Chem. Phys. Lett.* **1995**, *235*, 1.
- (133) van Gisbergen, S. J. A.; Osinga, V. P.; Gritsenko, O. V.; van Leeuwen, R.; Snijders, J. G.; Baerends, E. J. *J. Chem. Phys.* **1996**, *105*, 3142.
- (134) Guan, J.; Casida, M. E.; Köster, A. M.; Salahub, D. R. *Phys. Rev. B* **1995**, *52*, 2184.
- (135) Vosko, S. H.; Wilk, L.; Nusair, M. *Can. J. Phys.* **1980**, *58*, 1200.
- (136) Perdew, J. P.; Chevary, J. A.; Vosko, S. H.; Jackson, K. A.; Pederson, M. R.; Singh, D. J.; Fiolhais, C. *Phys. Rev. B* **1993**, *48*, 4978.

How Well Can Modern Density Functionals Predict Internuclear Distances at Transition States?

Xuefei Xu, I. M. Alecu, and Donald G. Truhlar*

Department of Chemistry and Supercomputing Institute, University of Minnesota, Minneapolis, Minnesota 55455-0431, United States

ABSTRACT: We introduce a new database called TSG48 containing 48 transition state geometrical data (in particular, internuclear distances in transition state structures) for 16 main group reactions. The 16 reactions are the 12 reactions in the previously published DBH24 database (which includes hydrogen transfer reactions, heavy-atom transfer reactions, nucleophilic substitution reactions, and association reactions plus one unimolecular isomerization) plus four H-transfer reactions in which a hydrogen atom is abstracted by the methyl or hydroperoxyl radical from the two different positions in methanol. The data in TSG48 include data for four reactions that have previously been treated at a very high level in the literature. These data are used to test and validate methods that are affordable for the entire test suite, and the most accurate of these methods is found to be the multilevel BMC-CCSD method. The data that constitute the TSG48 database are therefore taken to consist of these very high level calculations for the four reactions where they are available and BMC-CCSD calculations for the other 12 reactions. The TSG48 database is used to assess the performance of the eight Minnesota density functionals from the M05–M08 families and 26 other high-performance and popular density functionals for locating transition state geometries. For comparison, the MP2 and QCISD wave function methods have also been tested for transition state geometries. The MC3BB and MC3MPW doubly hybrid functionals and the M08-HX and M06-2X hybrid meta-GGAs are found to have the best performance of all of the density functionals tested. M08-HX is the most highly recommended functional due to the excellent performance for all five subsets of TSG48, as well as having a lower cost when compared to doubly hybrid functionals. The mean absolute errors in transition state internuclear distances associated with breaking and forming bonds as calculated by the B2PLYP, MP2, and B3LYP methods are respectively about 2, 3, and 5 times larger than those calculated by MC3BB and M08-HX.

1. INTRODUCTION

Computational thermochemical kinetics is an important branch of theoretical chemistry focused on the prediction of thermal rate constants of chemical reactions. Reliable transition state properties (e.g., geometry and vibrational frequencies) and reaction barrier heights are indispensable information for calculating rate constants by transition state theory. Therefore, the reliability of the electronic structure method chosen for locating transition states and calculating their barrier heights will directly affect the quality of thermochemical kinetics calculations.

In the past 20 years, Kohn–Sham density functional theory (DFT) has become a workhorse of computational thermochemistry and thermochemical kinetics due to its lower computational cost compared to wave function theory (WFT) and to the continuing improvement of exchange–correlation functionals. However, the appropriate choice of functional is still a key issue for getting accurate results. Some benchmark databases^{1–10} of barrier heights for diverse types of reactions have been established for the assessment of DFT functionals. DBH24/08¹⁰ is of special interest because it was designed as a representative database, and it includes 24 accurate barrier heights for 12 reactions: three hydrogen transfer reactions, three heavy-atom transfer reactions, three nucleophilic substitution reactions of anions, and three unimolecular and association reactions. Recently, the DBH24/08 database was used¹⁰ to assess 348 model chemistries. Several hybrid density functionals, in particular, M08-SO,¹¹ M06-2X,^{12,13} M08-HX,¹¹ BB1K,¹⁴ BMK,¹⁵ PWB6K,¹⁶ MPW1K,¹⁷ BHandHLYP,^{18c,d} and TPSS25B95,¹⁹ were recommended for calculations of barrier heights.

Although considerable attention has been paid to the performance of DFT for barrier heights, the ability of density functionals to accurately calculate transition state geometries has been less well investigated. Inaccurate calculations of transition state geometries could lead to unrealistic potential energy surfaces, unreliable vibrational frequencies, and inaccurate predictions of rate constants and kinetic isotope effects. By 1998, it had already been learned that even the most successful functional (at that time), B3LYP,^{18a,b,20} is quantitatively unreliable for transition state geometries and energies for a number of cases.²¹ In 2001, the performance of four hybrid density functionals (MPW1K, mPW1PW91,²² B3LYP, and BHandHLYP) was tested for predicting the transition state geometries of five reactions, as compared to very high-level calculations,²³ and only the MPW1K functional, which was optimized for kinetics, was recommended for locating transition state geometries. In 2005,²⁴ some newer DFT methods were tested for the transition state geometries and energetics of the hydrogen abstraction reaction from methanol by a hydrogen atom. The MC3BB doubly hybrid DFT method²⁵ and the BB1K hybrid meta-GGA, which was specially optimized for kinetics, were suggested as reasonably accurate DFT methods.

Since 2005, some new functionals have been developed, and we are especially concerned here with the Minnesota functionals,^{26,27} which were designed for broad applicability in chemistry. As mentioned above, the Minnesota family of density

Received: February 14, 2011

Published: April 26, 2011

Table 1. The TSG48 Database

reactions		R_1	R_2	R_3
HTG9: Hydrogen Transfer				
R1	$\text{OH} + \text{CH}_4 \rightarrow \text{CH}_3 + \text{H}_2\text{O}$	1.341	1.192	2.530
R2	$\text{H} + \text{OH} \rightarrow \text{O} + \text{H}_2$	0.894 (0.892) ^a	1.215 (1.216) ^a	2.109 (2.107) ^a
R3	$\text{H} + \text{H}_2\text{S} \rightarrow \text{H}_2 + \text{HS}$	1.160	1.426	2.578
HATG9: Heavy-Atom Transfer				
R4	$\text{H} + \text{N}_2\text{O} \rightarrow \text{OH} + \text{N}_2$	1.431	1.226	2.187
R5	$\text{H} + \text{ClH} \rightarrow \text{HCl} + \text{H}$	1.480 (1.485) ^a	1.480 (1.485) ^a	2.960 (2.970) ^a
R6	$\text{CH}_3 + \text{FCl} \rightarrow \text{CH}_3\text{F} + \text{Cl}$	2.047	1.767	3.814
NSG9: Nucleophilic Substitution of Anion				
R7	$\text{Cl}^- \cdots \text{CH}_3\text{Cl} \rightarrow \text{ClCH}_3 \cdots \text{Cl}^-$	2.305 (2.303) ^a	2.305 (2.303) ^a	4.610 (4.605) ^a
R8	$\text{F}^- \cdots \text{CH}_3\text{Cl} \rightarrow \text{FCH}_3 \cdots \text{Cl}^-$	2.020	2.114	4.134
R9	$\text{OH}^- + \text{CH}_3\text{F} \rightarrow \text{HOCH}_3 + \text{F}^-$	1.988	1.758	3.745
UAG9: Unimolecular and Association				
R10	$\text{H} + \text{N}_2 \rightarrow \text{HN}_2$	1.439	1.127	2.201
R11	$\text{H} + \text{C}_2\text{H}_4 \rightarrow \text{CH}_3\text{CH}_2$	1.925	1.351	2.662
R12	$\text{HCN} \rightarrow \text{HNC}$	1.183 (1.188) ^a	1.387 (1.378) ^a	1.187 (1.194) ^a
MHTG12: Methanol Hydrogen Transfer				
R13	$\text{CH}_3\text{OH} + \text{HO}_2 \rightarrow \cdot\text{CH}_2\text{OH} + \text{HOOH}$	1.240	1.289	2.501
R14	$\text{CH}_3\text{OH} + \text{CH}_3 \rightarrow \cdot\text{CH}_2\text{OH} + \text{CH}_4$	1.398	1.301	2.697
R15	$\text{CH}_3\text{OH} + \text{HO}_2 \rightarrow \text{CH}_3\text{O}\cdot + \text{HOOH}$	1.103	1.246	2.337
R16	$\text{CH}_3\text{OH} + \text{CH}_3 \rightarrow \text{CH}_3\text{O}\cdot + \text{CH}_4$	1.248	1.248	2.490

^a For the cases where we use accurate values from refs 2 and 28, the BMC-CCSD value is given in parentheses for comparison.

functionals, especially the Minnesota 2008 functionals M08-HX and M08-SO, were found to perform well for calculating barrier heights.¹⁰ Here, we test the performance of the Minnesota functionals and other popular (and a few interesting but not so popular) DFT functionals for calculating transition state geometries for a variety of reactions. To accomplish this, we present a database, called TSG48, of 48 data for transition state geometries.

2. TSG48 DATABASE

The 16 reactions in the TSG48 database are listed in Table 1. The database consists of five subdatabases: HTG9 for three hydrogen transfer reactions in DBH24, HATG9 for three heavy-atom transfer reactions in DBH24, NSG9 for three nucleophilic substitution reactions of anions in DBH24, UAG9 for three unimolecular and association reactions in DBH24, and MHTG12 for four H-transfer reactions in which an H atom is abstracted by the methyl or hydroperoxyl radical from the two different positions in methanol. For each reaction, we consider three geometrical data for transition state structures, in particular, three internuclear distances labeled R_1 , R_2 , and R_3 . For each transition state, these are the three key distances involving the breaking and forming of bonds. For atom transfer reactions, $\text{A} + \text{X}-\text{D} \rightarrow \text{A}-\text{X} + \text{D}$, where A is the acceptor, D is the donor, and X is the transferred atom; R_1 , R_2 , and R_3 are respectively the a-X, X-d, and a-d distances, where a is the accepting atom in the acceptor molecule or group A and d is the donating atom in the donor molecule or group D. For three $\text{S}_{\text{N}}2$ reactions, which are all methyl cation transfers, the three distances are a-C, C-d, and a-d, where C is the carbon of the methyl cation. For the R10 and R12 reactions, we consider all three distances with the order being H-N, N-N', and N'-H for R10 and C-H, N-H, and

C-N for R12. For reaction R11, namely, $\text{H} + \text{C}_2\text{H}_4 \rightarrow \text{CH}_3\text{CH}_2$, R_1 , R_2 , and R_3 are the three distances between the attached H atom and/or the two carbon atoms, with the order being H-C, C-C', and C'-H.

Accurate transition state geometries^{2,28} are available for four of the reactions (R2, R5, R7, and R12) in the TSG48 database. For reaction R2, the accurate values^{28b} are based on an internally contracted multireference configuration interaction including all single and double excitations (with the 1s core of oxygen frozen) from a CASSCF reference space that was extended from the full-valence reference space by adding orbitals that are nominally $3p\pi$ orbitals on O. The basis set was aug-cc-pVQZ. For reaction R5, the accurate values^{28a} are based on internally contracted multireference configuration interaction including all single and double excitations (with the 1s, 2s, and 2p core electrons of Cl frozen) from a full-valence CASSCF reference space followed by scaling the external correlation-energy (SEC^{28d}). The basis set was aug-cc-pV5Z, excluding h functions for Cl and aug-cc-pVQZ for H. They obtained an H-Cl bond length in the transition state of 1.480 Å, which is only 0.001 Å larger than an earlier^{28e} calculation employing the SEC method with a smaller basis set. For reaction R7, the accurate values² are from CCSD(T)//cc-pVQZ+1 calculations. For reaction R12, the accurate values^{28c} are based on the CCSD(T) method and exponential extrapolation to a complete basis set from optimizations with the cc-pCVDZ to cc-pCVQZ basis sets.

The four accurate values discussed in the previous paragraph were used to test the potential accuracy of nine wave function methods that have a lower cost than the methods used for the four accurate values. The nine wave function methods are multilevel BMC-CCSD,²⁹ the best N^6 method for barrier height calculations,¹⁰ multireference second-order Møller-Plesset theory MRMP2³⁰ in combination with the MG3S³¹ and aug-cc-pVTZ³² basis sets,

Table 2. The Mean Unsigned Deviations MUD (in Å) of Transition State Geometries Obtained by Wave Function Methods for the Four Selected Reactions in TSG48 Database, Compared to the Best Estimated Geometries from refs 2 and 28

method	R2 ^a	R5 ^b	R7 ^c	R12 ^d	AMUD ^e
BMC-CCSD	0.002	0.007	0.003	0.007	0.005
MRMP2/ <i>nom</i> -CPO/MG3S ⁴⁰	0.011	0.003	0.004	0.009	0.007
QCISD/MG3	0.017	0.008	0.023	0.003	0.013
MP2/6-31+G(d,p)	0.018	0.013	0.008	0.021	0.015
MRMP2/ <i>nom</i> -CPO/aug-cc-pVTZ ⁴⁰	0.016	0.003	0.038	0.008	0.016
MP2/def2-TZVP	0.019	0.013	0.028	0.013	0.018
MP2/MG3S	0.024	0.016	0.023	0.013	0.019
MP2/ma-TZVP	0.020	0.017	0.027	0.013	0.019
MP2/maug-cc-pV(T+d)Z	0.022	0.027	0.038	0.016	0.026

^a Accurate values from ref 28b. ^b Accurate values from ref 28a. ^c Accurate values from ref 2. ^d Accurate values from ref 28c. ^e Average deviation from 12 accurate transition state internuclear distances.

quadratic configuration interaction with single and double excitations³³ (QCISD with the MG3^{31a–e,34} basis set), and second-order Møller–Plesset theory³⁵ (MP2) with five different basis sets: MG3S, ma-TZVP,³⁶ def2-TZVP,³⁷ maug-cc-pV(T+d)Z,^{32,38} and 6-31+G(d,p).³⁹ The tests are given in Table 2. The mean unsigned deviation (MUD, where the deviation is the difference from the accurate value) of the three key bond lengths R_1 , R_2 , and R_3 for each of the four reactions are given in the table, which also shows the average MUD (AMUD) in the three internuclear distances over the four reactions for each wave function method. Table 2 shows that the BMC-CCSD method gives the most accurate transition state structures with an AMUD of only 0.005 Å, and it even performs better than MRMP2 using nominal correlated participating orbitals (*nom*-CPO) as an active space in combination with the MG3S basis set, as reported in a previous study.⁴⁰ It also performs better than the more expensive QCISD/MG3 method. The MP2 method is sensitive to the basis set, and its combination with 6-31+G(d,p) gives good results, which are comparable with those obtained by the MRMP2/*nom*-CPO/aug-cc-pVTZ method.⁴⁰ However, it is broadly appreciated that the tendency of MP2 to give better results with small basis sets results from a cancellation of errors.

As a result of its good performance in the test of Table 2, we shall use BMC-CCSD geometries for the other 12 reactions. All 36 geometrical data for the 12 reactions obtained by BMC-CCSD and 12 geometrical data from the literature for the four reactions with accurate values are shown in Table 1, and the 48 geometrical data constitute the TSG48 database. For comparison, the BMC-CCSD results for the four reactions with accurate values are also shown in Table 1.

3. COMPUTATIONAL DETAILS

For both wave function and density functional methods, the transition state geometries of the 16 reactions in TSG48 have been located and confirmed by frequency calculations. The wave function methods employed include MP2, QCISD, and BMC-CCSD, and the DFT functionals include four generalized gradient approximations (GGAs), MOHLYP,⁴¹ MOHLYP2,¹⁰ BLYP,^{18a,b} and SOGGA;⁴² one meta-GGA, M06-L;^{12,26} 12 hybrid GGAs, ω B97,⁴³ ω B97X,⁴³ ω B97X-D,⁴⁴ MPW1K, PBE0,⁴⁵

mPW1PW,²² B97-3,⁴⁶ B97-D,⁴⁷ B98,⁴⁸ B1LYP,⁴⁹ BHandHLYP, and B3LYP; 14 hybrid meta-GGAs: M08-HX, M08-SO, M06-2X, PWB6K, BB1K, MPWB1K,⁵⁰ PW6B95,¹⁶ BMK, TPSS25B95, M05-2X,⁵¹ M06-HF,⁵² M06,¹³ M05,⁵³ and τ HCTHhyb;⁵⁴ and three doubly hybrid functionals, MC3BB, MC3MPW,²⁵ and B2PLYP.⁵⁵ Note that the hybrid GGAs may be further classified: MPW1K, PBE0, mPW1PW, B97-3, B98, B1LYP, BHandHLYP, and B3LYP are global hybrid GGAs; B97-D is a global hybrid GGA combined with molecular mechanics; ω B97 and ω B97X are range-separated hybrid GGAs; and ω B97X-D is a range-separated hybrid GGA combined with molecular mechanics. Note that hybrid and doubly hybrid functionals include a nonzero percentage of Hartree–Fock exchange, and other functionals do not; the latter functionals are called local and are less expensive for geometry optimizations of large systems.

The MG3S basis set has been used for all DFT and MP2 calculations except for BMC-CCSD, MC3BB, and MC3MPW, in which particular basis sets are specified for the components in these calculations by the definitions of the methods. For the QCISD calculations, in which the transition state geometries of the 12 reactions in DBH24 are taken from ref 8, the MG3 basis set was used. Other basis sets, in particular, ma-TZVP, def2-TZVP, maug-cc-pV(T+d)Z, and 6-31+G(d,p), have also been tested for several selected functionals to confirm that MG3S is a good choice for the optimization of transition state geometries.

For some model chemistries, the exoergic direction of some reactions, in particular R6, R8, and R15, appears to proceed without a barrier. In such cases, the energetic transition state is technically predicted to be located at the reactant asymptote by that model chemistry, and the error in some of the internuclear distances is therefore infinite. Thus, we could have listed the mean error for such model chemistries as infinite, but we thought it would be more informative to assign a large finite error in such cases. Therefore, for such bond lengths, in order to compute the MUD, the deviation was set not to infinity but rather to the largest deviation for that bond length in any of the model chemistries that have a finite error for that bond length.

All calculations were performed using Gaussian09.a02,⁵⁶ Gaussian03.d01,⁵⁷ or a locally modified version of Gaussian03.e01. MNGFM4.1⁵⁸ that contains additional Minnesota functionals. For the multilevel BMC-CCSD and doubly hybrid MC3BB and MC3MPW methods, the MLGauss2.0⁵⁹ program was used.

Note that all transition states discussed in this article are conventional transition states, i.e., saddle points, not variational transition states.

4. RESULTS AND DISCUSSION

Table 3 shows the average MUD in the three internuclear distances of transition state geometries as compared to the ones in the TSG48 database for each of the five subsets: HTG9, HATG9, NSG9, UAG9, and MHTG12. All density functional results in Table 3 were obtained with the MG3S basis set (except for the MC3BB and MC3MPW results, as discussed above). Table 3 also gives the AMUDs over all 48 geometrical data in TSG48. For comparison, the AMUDs for the MP2/MG3S and QCISD/MG3 methods are also included in Table 3.

4.1. The Performance over the 16 Reactions of TSG48. Overall, the MC3BB doubly hybrid functional, the M08-HX hybrid meta-GGA, and the MC3MPW doubly hybrid functional perform best when all 16 reactions in TSG48 are considered.

Table 3. The Average Mean Unsigned Deviations (AMUD, in Å) of Transition State Geometries Obtained Using 36 Model Chemistries, Compared to the TSG48 Database

method	type ^a	HTG9	HATG9	NSG9	UAG9	MHTG12	TSG48	TSG39 ^b
QCISD/MG3	WFT	0.020	0.013	0.015	0.014	0.014	0.015	0.014
MP2/MG3S	WFT	0.038	0.067	0.017	0.041	0.025	0.037	0.034
MC3BB	DHDFT	0.011	0.020	0.009	0.018	0.009	0.013	0.013
M08-HX/MG3S	H-m	0.016	0.012	0.013	0.016	0.014	0.014	0.015
MC3MPW	DHDFT	0.012	0.027	0.012	0.023	0.009	0.016	0.015
M06-2X/MG3S	H-m	0.021	0.013	0.017	0.025	0.012	0.017	0.018
M08-SO/MG3S	H-m	0.018	0.022	0.030	0.017	0.020	0.021	0.020
ω B97/MG3S	H	0.030	0.025	0.013	0.034	0.011	0.022	0.023
PWB6K/MG3S	H-m	0.028	0.022	0.015	0.031	0.021	0.023	0.024
B2PLYP/MG3S	DHDFT	0.019	0.029	0.042	0.017	0.015	0.024	0.018
BB1K/MG3S	H-m	0.030	0.024	0.014	0.038	0.018	0.025	0.025
ω B97X/MG3S	H	0.034	0.026	0.014	0.040	0.013	0.025	0.025
MPWB1K/MG3S	H-m	0.029	0.022	0.018	0.037	0.019	0.025	0.026
M05-2X/MG3S	H-m	0.041	0.022	0.015	0.056	0.006	0.027	0.028
BMK/MG3S	H-m	0.034	0.039	0.013	0.039	0.016	0.028	0.027
MPW1K/MG3S	H	0.029	0.021	0.018	0.058	0.017	0.028	0.030
ω B97X-D/MG3S	H	0.036	0.035	0.021	0.046	0.015	0.030	0.029
BHandHLYP/MG3S	H	0.043	0.023	0.023	0.051	0.021	0.032	0.031
M06-HF/MG3S	H-m	0.044	0.019	0.045	0.030	0.032	0.034	0.035
PW6B95/MG3S	H-m	0.038	0.048	0.025	0.045	0.021	0.034	0.030
PBE0/MG3S	H	0.037	0.041	0.016	0.068	0.023	0.036	0.033
M06/MG3S	H-m	0.044	0.047	0.033	0.051	0.016	0.037	0.033
mPW1PW/MG3S	H	0.036	0.042	0.021	0.068	0.022	0.037	0.033
TPSS25B95/MG3S	H-m	0.048	0.050	0.032	0.043	0.024	0.038	0.031
B97-3/MG3S	H	0.039	0.045	0.034	0.053	0.024	0.038	0.035
M05/MG3S	H-m	0.042	0.048	0.041	0.078	0.021	0.044	0.040
B98/MG3S	H	0.058	0.076	0.047	0.071	0.028	0.054	0.046
B1LYP/MG3S	H	0.059	0.071	0.066	0.069	0.024	0.056	0.049
B3LYP/MG3S	H	0.065	0.095	0.069	0.080	0.029	0.065	0.054
M06-L/MG3S ^c	m	0.070	0.100	0.069	0.081	0.039	0.070	0.057
τ HCTHhyb/MG3S ^c	H-m	0.084	0.107	0.059	0.087	0.040	0.073	0.058
SOGGA/MG3S ^d	GGA	0.132	0.032	0.043	0.159	0.069	0.086	0.091
MOHLYP2/MG3S	GGA	0.074	0.101	0.199	0.056	0.072	0.099	0.082
BLYP/MG3S ^{c,d,e}	GGA	0.163	0.125	0.148	0.133	0.065	0.123	0.108
MOHLYP/MG3S ^{c,d}	GGA	0.205	0.117	0.126	0.137	0.076	0.129	0.121
B97-D/MG3S ^{c,d,e}	H	0.285	0.117	0.149	0.168	0.054	0.148	0.140

^a Abbreviations: WFT, wave function theory; DHDFT, doubly hybrid DFT; H-m, hybrid meta-GGA; H, hybrid GGA; m, meta-GGA; GGA, generalized gradient approximation. ^b TSG39 is the same as TSG48 except that R6, R8, and R15 are omitted. ^c The transition state of reaction R6 cannot be located. The largest deviations of the three key bond lengths obtained using other model chemistries were used to calculate the MUD in such cases. ^d The transition state of reaction R15 cannot be located. The largest deviations of the three key bond lengths obtained using other model chemistries were used to calculate the MUD in such cases. ^e The transition state of reaction R8 cannot be located. The largest deviations of the three key bond lengths obtained using other model chemistries were used to calculate the MUD in such cases.

First, we consider the two doubly hybrid DFT methods. MC3BB performs best of all; it does even better than the more expensive QCISD/MG3 method. MC3BB includes kinetic energy density, while MC3MPW does not. Thus, MC3MPW would be an alternative choice for users of computer programs that do not include functionals with kinetic energy density. The third doubly hybrid DFT method we tested, B2PLYP, does not perform as well as either MC3BB or MC3MPW. The MP2 components in MC3BB and MC3MPW are obtained with the basis set 6-31+G(d,p), which has been found to yield better results than MG3S in section 2. This could be one of the reasons that MC3-type methods do better than B2PLYP/MG3S, although a more likely

reason is that MC3BB and MC3MPW are parametrized for use with specific basis sets. Incidentally, we note that a timing analysis in which the relative computational cost associated with MC3BB, MC3MPW, and B2PLYP/MG3S was estimated by taking the average of the total CPU times required for the single-point energy calculation of each of the four transition states in reactions 13–16, and dividing this quantity by exactly the same quantity obtained from HF/MG3S single-point calculations, using the same computational software and the same computer, revealed that these three model chemistries have comparable computational costs for single-point energies—each being on average 3–4 times more expensive than HF/MG3S. However, for

geometry optimization, the more relevant cost is that for a single-point gradient, by which we mean a gradient at a single geometry (this includes the computer time to calculate one energy and a gradient at the same geometry as the energy), and a comparison like that just described, but for single-point gradients, reveals that MC3BB, MC3MPW, and B2PLYP/MG3S single-point gradients are respectively 4.6, 3.9, and 4.5 times more expensive (averaged over the four transition states) than single-point HF/MG3S gradients.

Most of the hybrid meta-GGAs predict better transition state geometries than GGAs and hybrid GGAs. The two best hybrid meta-GGAs are M08-HX and M06-2X, and their AMUDs are 0.014 Å and 0.017 Å, respectively, over the 16 reactions, which is similar in quality to MC3BB and MC3MPW. The range-separated ω B97 functional is the best hybrid GGA we tested. Twelve hybrid meta-GGAs (M08-HX, M06-2X, M08-SO, PWB6K, BB1K, MPWB1K, M05-2X, BMK, PW6B95, M06-HF, M06, and TPSS25B95) and eight hybrid GGAs (ω B97, ω B97X, MPW1K, ω B97X-D, BHandHLYP, PBE0, mPW1PW, and B97-3) have a better or similar performance to that of MP2 with the MG3S basis set, but with less cost. The hybrid B3LYP functional is very widely used but is found to perform poorly here.

The τ HCTHhyb and B97-D functionals are respectively the worst hybrid-meta GGA and worst hybrid GGA for the 16 reactions explored here. These two functionals, along with the GGA functionals we tested, are not good enough for reliable optimizations of transition state geometries; some transition states for reactions (R6, R8, and R15) with low reaction barriers cannot even be located successfully because, when using the functionals mentioned above, there is no barrier. The M06-L meta-GGA performs better than any other tested functional that has no Hartree–Fock exchange. MOHLYP2 is the only GGA that can locate all transition state structures for the 16 reactions explored here, although it has a large AMUD.

4.2. The Performance for the Subsets of TSG48. For the hydrogen atom transfer reactions in HTG9, the superiority of the doubly hybrid DFT methods is especially remarkable, and all three doubly hybrid methods, namely, MC3BB, MC3MPW, and B2PLYP, perform better than QCISD/MG3. The three best hybrid meta-GGAs (M08-HX, M06-2X, and M08-SO) have similar performance to the more expensive B2PLYP.

Due to the worse performance of the MP2 component, the doubly hybrid DFT methods give worse results than many hybrid meta-GGAs for the heavy atom transfer reactions of HATG9. In this case, M08-HX, QCISD/MG3, and M06-2X become the three best methods. M06-HF and SOGGA are found to perform better in HATG9 than in other subsets; M06-HF gives a better result than doubly hybrid functionals for this subset.

Many of the model chemistries tested in the present work are suitable for locating the transition states of the anionic nucleophilic substitution reactions in NSG9. Again, MC3BB and MC3MPW perform better than QCISD/MG3, and MP2/MG3S is almost as good. It is perhaps surprising to find that B2PLYP has poor performance for this subset; the relatively poor behavior of B2PLYP in predicting barrier heights for nucleophilic substitution reactions¹⁰ could be the main reason.

None of the DFT methods perform better than QCISD/MG3 for the UAG9 subset (unimolecular and association reactions). Most of the density functionals tested have the worst performance for this subset; this could result from the transition states of the reactions in UAG9 all having significant multireference character.⁴⁰ The four best DFT methods over these three reactions are M08-HX, M08-SO,

B2PLYP, and MC3BB. M06-2X, which is usually among the top performers for other reaction types, performs relatively worse but still reasonably well. Other functionals with performances significantly above average for this difficult set are MC3MPW, M06-HF, and PWB6K.

All DFT-based electronic model chemistries performed relatively well for the hydrogen transfer reactions from methanol to the methyl or hydroperoxyl radicals in the MHTG12 subset, except for the GGA methods. Hydrogen bonding plays an important role in stabilizing the transition states for R13 and R15. The best performance for the MHTG12 subset is for M05-2X (which is reasonably accurate for systems characterized by hydrogen bonding and other weak noncovalent interactions¹³), which attains an AMUD of just 0.006 Å.

4.3. Dependence on Basis Set. In this section, we consider the dependence of the results on basis set. The goal is not a study of basis set convergence (where one might, for example, systematically look at changes in going from double- ζ to triple- ζ to quadruple- ζ in a convergent sequence of basis sets) but rather a study of how accurate the results are when one uses the basis sets that have become popular because of their favorable general performance/cost ratio and their affordability for large systems. Such basis sets are of special interest because they have stood the test of being widely applied, which in practice is a form of broad testing. This is necessarily unsystematic because these broadly tested basis sets are not themselves systematic, but we chose basis sets for the present study on the basis of our previous experiences in basis set selection for transition state calculations, for example refs 10, 36, and 38b.

MG3S is a minimally augmented triple- ζ basis set that is highly recommended for kinetics based on our previous studies. However the double- ζ 6-31+G(d,p) basis set was found to be a better basis set for the MP2 method for four reactions discussed in section 2 due to cancellation of errors. It is well-known that MP2 results often become worse as the basis set is increased, and similar deterioration is often seen for density functional calculations using relatively inaccurate functionals, such as B3LYP. Thinking along these lines, one might ask which double- or triple- ζ basis set is most suitable for density functional studies of transition state geometry and how much does the quality of the result depend on the specific choice of basis. To answer this, MG3S, 6-31+G(d,p), and three additional triple- ζ basis sets, def2-TZVP, ma-TZVP, and maug-cc-pV(T+d)Z, were tested for selected methods (MP2, B2PLYP, M08-HX, M06-2X, MPW1K, B3LYP, and τ HCTHhyb) over the 12 reactions in the DBH24 database. The 6-31+G(d,p) basis set is chosen for this study because we and others have found for numerous applications that it is a good general choice for DFT calculations at the double- ζ level. The ma-TZVP and maug-cc-pV(T+d)Z basis sets are chosen because they are examples of minimally augmented basis sets, which have been highly recommended for general applications of DFT.^{36,38b,60,61} The ma-TZVP basis set is a modification of the def2-TZVP basis set³⁷ minimally augmented by one diffuse s function and one diffuse p subshell on all non-hydrogenic atoms. The maug-cc-pV(T+d)Z basis set is the aug-cc-pV-(T+d)Z basis set with the set of diffuse basis functions truncated to only the s and p functions on non-hydrogenic atoms. The corresponding calculated average mean unsigned deviations (AMUDs) for these basis sets for the TSG48 database are shown in Table 4.

Table 4 provides yet another example where MP2's performance is not improved by using better basis sets, and the best results are obtained with the smallest basis set examined. Since it is known that

Table 4. The Average Mean Unsigned Deviations (AMUD, in Å) of Transition State Geometries Obtained Using MP2 and Six DFT Methods in Combination with Five Basis Sets, for Subdatabases of the TSG48 Database

method	HTG9	HATG9	NSG9	UAG9	TSG36 ^d	TSG30 ^d
M06-2X/MG3S	0.021	0.013	0.017	0.025	0.019	0.020
M06-2X/ma-TZVP	0.024	0.011	0.014	0.025	0.019	0.020
M06-2X/def2-TZVP	0.025	0.013	0.020	0.024	0.021	0.021
M06-2X/maug-cc-pV(T+d)Z	0.021	0.012	0.014	0.028	0.019	0.020
M06-2X/6-31+G(d,p)	0.030	0.036	0.022	0.035	0.031	0.029
M08-HX/MG3S	0.016	0.012	0.013	0.016	0.014	0.014
M08-HX/ma-TZVP	0.018	0.011	0.012	0.017	0.015	0.015
M08-HX/def2-TZVP	0.019	0.013	0.008	0.017	0.014	0.016
M08-HX/maug-cc-pV(T+d)Z	0.018	0.010	0.013	0.019	0.015	0.015
M08-HX/6-31+G(d,p)	0.021	0.029	0.017	0.021	0.022	0.021
B3LYP/MG3S	0.065	0.095	0.069	0.080	0.077	0.061
B3LYP/ma-TZVP	0.072	0.082	0.068	0.081	0.076	0.063
B3LYP/def2-TZVP ^b	0.076	0.079	0.107	0.079	0.085	0.064
B3LYP/maug-cc-pV(T+d)Z	0.069	0.083	0.064	0.084	0.075	0.063
B3LYP/6-31+G(d,p) ^c	0.081	0.119	0.087	0.106	0.098	0.080
MPW1K/MG3S	0.029	0.021	0.018	0.058	0.032	0.033
MPW1K/ma-TZVP	0.035	0.018	0.020	0.059	0.033	0.035
MPW1K/def2-TZVP	0.037	0.017	0.028	0.058	0.035	0.036
MPW1K/maug-cc-pV(T+d)Z	0.030	0.019	0.020	0.062	0.033	0.035
MPW1K/6-31+G(d,p)	0.038	0.035	0.019	0.071	0.041	0.039
τ HCTHhyb/MG3S ^c	0.084	0.107	0.059	0.087	0.084	0.065
τ HCTHhyb/ma-TZVP ^c	0.088	0.107	0.057	0.088	0.085	0.066
τ HCTHhyb/def2-TZVP ^{b,c}	0.088	0.108	0.097	0.087	0.095	0.067
τ HCTHhyb/maug-cc-pV(T+d)Z ^b	0.086	0.106	0.053	0.089	0.084	0.066
τ HCTHhyb/6-31+G(d,p) ^b	0.104	0.119	0.075	0.105	0.101	0.083
B2PLYP/MG3S	0.019	0.029	0.042	0.017	0.026	0.020
B2PLYP/ma-TZVP	0.019	0.025	0.039	0.016	0.025	0.019
B2PLYP/def2-TZVP	0.022	0.025	0.054	0.015	0.029	0.020
B2PLYP/maug-cc-pV(T+d)Z	0.020	0.025	0.034	0.020	0.025	0.020
B2PLYP/6-31+G(d,p)	0.025	0.051	0.055	0.026	0.039	0.030
MP2/MG3S	0.038	0.067	0.017	0.041	0.041	0.036
MP2/ma-TZVP	0.037	0.069	0.018	0.041	0.042	0.036
MP2/def2-TZVP	0.037	0.066	0.026	0.042	0.043	0.036
MP2/maug-cc-pV(T+d)Z	0.037	0.073	0.028	0.039	0.044	0.038
MP2/6-31+G(d,p)	0.033	0.051	0.012	0.032	0.032	0.028

^a TSG36 is the same as TSG48 except that R13–R16 are omitted; TSG30 is the same as TSG36 except that R6 and R8 are omitted. ^b The transition state of reaction R8 cannot be located. The largest deviations of the three key bond lengths obtained using other model chemistries were used to calculate the MUD in such cases. ^c The transition state of reaction R6 cannot be located. The largest deviations of the three key bond lengths obtained using other model chemistries were used to calculate the MUD in such cases.

MP2 requires large basis sets for convergence of energies, this clearly results from a cancellation of errors. However, density functional theory does not benefit from such cancellation, and the double- ζ basis set 6-31+G(d,p) is clearly not good enough for reliable density functional calculations of transition state geometries. All four triple- ζ basis sets studied in Table 4 have similar performances for the typical density functionals when the R6 and R8 reactions are excluded. B3LYP and τ HCTHhyb failed to locate the transition state with the less diffuse def2-TZVP basis set for reaction R8, and B3LYP/6-31+G(d,p) also failed for R6. The functionals with relatively poor performance for barrier heights need more diffuse and larger basis sets.

Table 4 shows that MG3S, maug-cc-pV(T+d)Z, and ma-TZVP are equally well suited for DFT studies of transition state geometries. This confirms the reasonableness of using the MG3S

basis set in the tests in Table 3 for evaluating the performance of density functionals.

4.4. The Relationship between Good Performance for Barrier Heights and That for Transition State Geometries. On the basis of the present investigation, the hybrid functionals that were recommended for the calculations of barrier heights,¹⁰ M08-HX, M08-SO, M06-2X, BB1K, BMK, PWB6K, MPW1K, BHandHLYP, and TPSS25B95, can all obtain comparable or more reliable transition state geometries than those obtained by MP2. Figure 1 provides a more thorough test of the question: is good performance for locating transition state geometries associated with smaller errors for barrier heights? Figure 1 includes all methods applied to the entire TSG48 database in this article that were also evaluated for predicting barrier heights in the DBH24/08 article,¹⁰ except that the methods that failed to

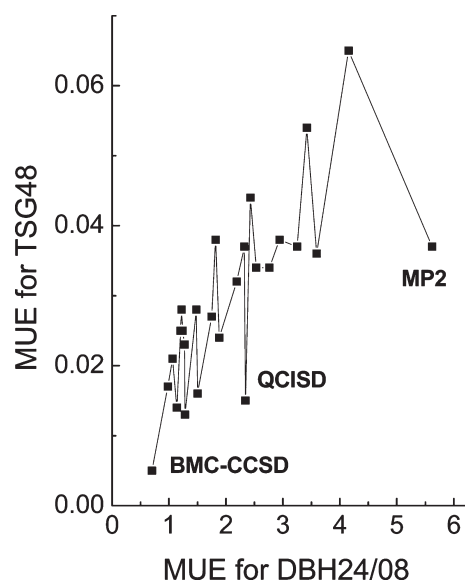


Figure 1. Plot of MUE (in Å) for TSG48 vs MUE (in kcal/mol) for DBH24/08 for various methods. The three results for wave function methods are labeled, and the unlabeled points all correspond to density functional theory. From left to right, the complete set of points corresponds to BMC-CCSD, M06-2X/MG3S, M08-SO/MG3S, M08-HX/MG3S, BB1K/MG3S, BMK/MG3S, MPWB1K/MG3S, PWB6K/MG3S, MC3BB, MPW1K/MG3S, MC3MPW, M05-2X/MG3S, B97-3/MG3S, B2PLYP/MG3S, BHandHLYP/MG3S, M06/MG3S, QCISD/MG3, M05/MG3S, M06-HF/MG3S, PW6B95/MG3S, TPS-S25B95/MG3S, mPW1PW/MG3S, B98/MG3S, PBE0/MG3S, B3LYP/MG3S, and MP2/MG3S. Since the BMC-CCSD data are used as reference data for part of TSG48, the value plotted is based on only the reactions where a more accurate value is available; that is, it is based on Table 2 or 5, whereas the other values in the plot are based on Table 3.

predict a finite-distance transition state for any of the low-barrier reactions are excluded from the plot. The figure shows that there is indeed a correlation of error in bond length with error in barrier height if one compares density functional methods to one another or if one compares wave function methods to one another, but for a given accuracy in barrier heights, wave function methods predict more accurate transition state geometries. This is perhaps surprising since a strategy employed by many workers (including us) since the early days of DFT applications in chemistry has been to use DFT for geometries and WFT for energies, but one should keep in mind that the reason for using DFT for geometries is its lower cost. One can obtain more accurate geometries for a given cost with DFT.

Although the methods that failed to predict a finite-distance TS for any of the low-barrier reactions are left out of Figure 1, they generally also follow the correlation of large errors in barrier heights being associated with large errors in transition state geometries in that they have high average errors for the reactions where they do predict a transition state, and except for MOHLYP, they have high MUEs in barrier heights. For example, BLYP and SOGGA have MUEs for DBH24/08 of 8–10 kcal/mol.

For the reactions with a low reaction barrier, functionals that usually underestimate barrier heights are not well suited to locating transition state geometries. As already mentioned, reaction R15 is a good example of this, and it is interesting to further examine this case. The reaction is endoergic, and the barrier in the reverse direction is therefore the intrinsic barrier.

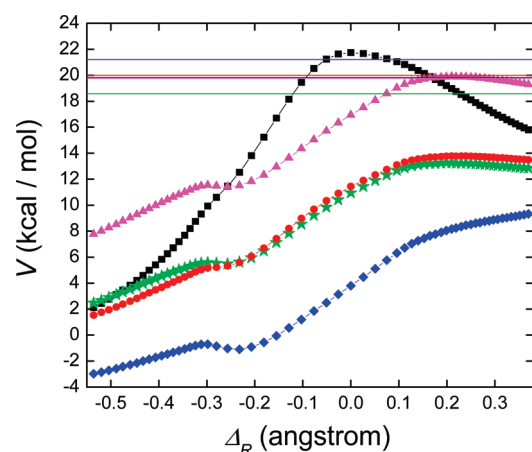


Figure 2. Potential energy curves $V(\Delta_R)$ for reaction R15 generated by single-point energy calculations along a fixed reaction path. For all five curves, the reaction path is the M08-SO/MG3S minimum-energy path in isoinertial coordinates, and Δ_R is a measure of the reaction progress defined in the text. The curves correspond to five different density functional methods: BLYP/MG3S (green stars), B97-D/MG3S (red circles), SOGGA/MG3S (blue diamonds), MOHLYP/MG3S (magenta triangles), and M08-SO/MG3S (black squares). In each case, the potential curve is normalized relative to its value for the reactants at the M08-SO/MG3S geometry. The value of the reaction energy (to which each curve would tend if extended to the right) are also shown for each of the five density functional methods, in corresponding colors; these values are calculated, for the purposes of this figure, by using the M08-SO/MG3S geometries for the reactants and products in all cases and have values of 18.57, 20.00, 21.20, 19.76, and 19.81 kcal/mol for BLYP/MG3S, B97-D/MG3S, SOGGA/MG3S, MOHLYP/MG3S, and M08-SO/MG3S, respectively (therefore, the magenta and black horizontal lines are hard to distinguish visually because they are almost on top of one another).

Given that the barrier height for the reverse of R15 is quite small,^{62,63} it is no surprise that it has vanished completely in calculations using density functionals like BLYP, B97-D, SOGGA, and MOHLYP that tend to significantly underestimate barrier heights; i.e., the potential energy decreases monotonically for the reverse reaction. To illustrate the shape of the energy profile in these cases, potential energy curves $V(\Delta_R)$, where Δ_R is a reaction coordinate defined below, were generated for reaction R15 by single-point BLYP/MG3S, B97-D/MG3S, SOGGA/MG3S, and MOHLYP/MG3S energy calculations along a fixed reaction path. The fixed reaction path corresponds to the M08-SO/MG3S minimum-energy path (MEP). The results are plotted as functions of Δ_R , which is defined as

$$\Delta_R \equiv \begin{cases} R_1 - R_1' & \text{before the saddle} \\ R_2' - R_2 & \text{after the saddle} \end{cases}$$

where R_1' and R_2' respectively correspond to the values (in angstroms) for the forming bond and the breaking bond for nonstationary points along the M08-SO/MG3S MEP. We have chosen M08-SO/MG3S to construct the MEP because this electronic model chemistry has been shown to accurately characterize the reaction energetics for hydrogen atom transfer reactions involving similar oxygenated hydrocarbons.⁶⁴ In each case, the potential curve was normalized relative to its value for the reactants. In addition, the reaction energy for R15 was also

Table 5. The Mean Unsigned Deviations (MUD, in Å) of Transition State Geometries for the Four Selected Reactions in TSG48 Database, Compared to the Best Estimated Geometries from refs 2 and 28 for the Three Wave Function Methods and Five Best DFT Methods over 16 Reactions in Table 3

method	R2 ^a	R5 ^b	R7 ^c	R12 ^d	AMUD ^e
BMC-CCSD	0.002	0.007	0.003	0.007	0.005
MRMP2/ <i>nom</i> -CPO/MG3S ⁴⁰	0.011	0.003	0.004	0.009	0.007
QCISD/MG3	0.017	0.008	0.023	0.003	0.013
MC3BB	0.012	0.012	0.009	0.016	0.012
MC3MPW	0.016	0.014	0.013	0.015	0.014
M06-2X/MG3S	0.024	0.009	0.006	0.025	0.016
M08-HX/MG3S	0.040	0.011	0.000	0.025	0.019
M08-SO/MG3S	0.024	0.011	0.030	0.022	0.022

^a Accurate values from ref 28b. ^b Accurate values from refs 28a. ^c Accurate values from ref 2. ^d Accurate values from ref 28c. ^e Average deviation from 12 accurate transition state internuclear distances.

calculated with each of the five density functional methods. The results of this analysis are depicted in Figure 2.

Figure 2 shows that while the TS for M08-SO/MG3S is higher in energy than that for the products (as expected), the reaction-path potential energies computed by the BLYP/MG3S, B97-D/MG3S, and SOGGA/MG3S electronic model chemistries are all significantly lower than that of the products. In the case of MOHLYP/MG3S, there are a few points along the potential energy curve that are slightly (up to 0.14 kcal/mol) higher in energy than the products. Interestingly, the potential curves obtained with BLYP/MG3S, B97-D/MG3S, MOHLYP/MG3S, and SOGGA/MG3S show mildly oscillatory behavior. In each of these cases, attempts were made to locate saddle points for R15 using the geometries of the higher-energy points as initial guesses as well as other initial geometry guesses, but no saddle points were found—we concluded that there is no saddle point in these cases. This illustrates how, for reactions with low intrinsic barriers, density functionals that tend to appreciably underestimate barrier heights not only are unsuitable for quantitative calculations of saddle point geometries, but, in some cases, fail to even predict the existence of a saddle point.

4.5. Comparison to MRMP2. The methods tested so far are single-reference methods, which are more convenient than multi-reference methods. One additional issue that is worth discussing, therefore, is whether it is advantageous to use multireference methods for even greater accuracy. It is well-known that complete-active-space self-consistent-field (CASSCF) theory^{65,66} does not provide a reliable scheme for calculating transition state geometries because it neglects dynamical correlation energy. The next multireference level in terms of higher cost and higher accuracy is multireference second-order perturbation theory based on a CASSCF reference state. There is more than one version of this approach (e.g., MRMP2⁶⁷ and CASPT2⁶⁸), and they are expected to give similar results if a similar selection is made for the active space. In recent work,⁴⁰ a well-defined choice of active space for atom transfer reactions, called the nominal correlated participating orbitals scheme (*nom*-CPO), was presented and used to optimize four of the transition states considered here for which we have more accurate results than BMC-CCSD. The mean unsigned deviations from the benchmark results and the average mean unsigned deviations from the benchmark results are presented in Table 5, where they are compared with the seven most accurate methods tested in earlier sections of this paper.

Table 5 shows that BMC-CCSD and MRMP2/*nom*-CPO have AMUDs in the 0.005–0.007 Å range, whereas the best of the other methods tested have AMUDs no smaller than 0.012 Å for these four reactions. Thus, we recommend both BMC-CCSD and MRMP2/*nom*-CPO when one wants higher accuracy than is afforded by MC3BB and M08-HX.

5. CONCLUDING REMARKS

In the present work, a database called TSG48 containing 48 transition state geometrical data for 16 reactions is introduced to assess the performance of density functionals for locating transition state geometries. The MC3BB and MC3MPW doubly hybrid functionals and the M08-HX and M06-2X hybrid meta-GGAs are found to have the best performance. M08-HX is the most highly recommended functional due to the excellent performance for all five subsets of TSG48, as well as having a lower cost when compared to doubly hybrid functionals. Functionals with good performance for barrier heights usually predict accurate transition state geometries, and similarly, bad performance for barrier heights is associated with less reliable prediction of transition state structures. Therefore, all local functionals tested in the present work, in particular, GGAs and meta-GGAs, and some hybrid density functionals, such as B97-D, τ HCTHhyb, B3LYP, B1LYP, B98, and M05, are not recommended for locating transition states due to errors in geometry associated in part with the underestimation of the barrier height.

Due to a cancellation of errors, the 6-31+G(d,p) basis set gives better results than large basis sets for MP2, but 6-31+G(d,p) is not good enough for the best performance attainable with DFT methods. A minimally augmented triple- ζ basis set, such as MG3S, ma-TZVP, or maug-cc-pV(T+d)Z, is recommended.

AUTHOR INFORMATION

Corresponding Author

*E-mail: truhlar@umn.edu.

ACKNOWLEDGMENT

The authors are grateful to Jingjing Zheng for helpful assistance. This work was supported in part by the U.S. Department of Energy, Office of Science, Office of Basic Energy Sciences, under grant no. DE-FG02-86ER13579, and as part of the Combustion Energy Frontier Research Center under Award Number DE-SC0001198.

GLOSSARY

Density Functionals

See the last 34 rows of Table 2 for a list of density functionals included in the present study; references for these density functionals are cited at their first mention in the text in sections 1 and 3

Types of Density Functionals

GGA	generalized gradient approximation to the density functional, which is a type of density functional in which the exchange-correlation energy density at a point in space depends on the local values of the up-spin and down-spin electron densities and their reduced gradients
m	meta generalized gradient approximation to the density functional, which is like a GGA but the

exchange-correlation energy density at a point in space also depends on the local values of the up-spin and down-spin electron kinetic energy densities

H hybrid GGA in which the exchange energy also has a nonlocal component, which is Hartree–Fock exchange in the cases considered in this article

H–m hybrid meta-GGA in which the exchange energy also has a nonlocal component, which is Hartree–Fock exchange in the cases considered in this article

DHDFFT doubly hybrid density functional, which is like a hybrid functional with the addition of a nonlocal component to the correlation energy as well as the exchange energy. In the cases considered in this article, this is an orbital-dependent term with the form of the MP2 correlation energy, computed using either the Hartree–Fock orbitals or the Kohn–Sham orbitals, which are both functionals of the electron density

Basis Sets

References explaining basis sets are given in section 2

Databases

DBH24 original database of 24 diverse barrier heights, with subdatabases explained in Table 1

DBH24/08 database of 24 diverse barrier heights, with the same reactions and subdatabases as DBH24 but with the majority of the barrier heights updated in 2008

MHTG12 database of 12 transition state geometrical data for methanol hydrogen transfer data, in particular, internuclear distances involving atoms in breaking and making bonds at transition state structures of four reactions involving abstraction of H from methanol

TSG48 database of 48 transition state geometrical data, in particular, internuclear distances involving atoms in breaking and making bonds at transition state structures of 16 reactions, with MHTG12 and four other subdatabases explained in section 2

Wave Function Methods

BMC-CCSD balanced multicoefficient method based on coupled cluster theory with single and double excitations and a basis set especially balanced for extrapolation; the coefficients are used to extrapolate toward the complete configuration interaction limit

CASPT2 MRMP2 based on a CASSCF reference state

CASSCF complete-active-space self-consistent-field

MP2 Møller–Plesset second-order perturbation theory based on a single-configuration wave function as the zero-order reference state

MRMP2 multireference MP2, that is, second-order perturbation theory based on a multiple-configuration wave function as the zero-order reference state

nom-CPO nominal correlated participating orbitals, which is a way to specify the active space for MRMP2

QCISD quadratic configuration interaction with single and double excitations

Mean Errors

MUD mean unsigned deviation (i.e., mean absolute value of the deviation) from most accurate available reference data

AMUD average MUD, that is, average over all of the reactions in a database of the MUD for the three key internuclear distances of each reaction

REFERENCES

- (1) Baker, J.; Muir, M.; Andzelm, J.; Scheiner, A. *ACS Symp. Ser.* **1996**, *629*, 342.
- (2) Parthiban, S.; de Oliveira, G.; Martin, J. M. L. *J. Phys. Chem. A* **2001**, *105*, 895.
- (3) Lynch, B. J.; Truhlar, D. G. *J. Phys. Chem. A* **2003**, *107*, 3898.
- (4) Lynch, B. J.; Truhlar, D. G. *J. Phys. Chem. A* **2003**, *107*, 8996.
- (5) Guner, V.; Khuong, K. S.; Leach, A. G.; Lee, P. S.; Bartberger, M. D.; Houk, K. N. *J. Phys. Chem. A* **2003**, *107*, 11445.
- (6) Zhao, Y.; Gonzalez-Garcia, N.; Truhlar, D. G. *J. Phys. Chem. A* **2005**, *109*, 2012.
- (7) Ess, D. H.; Houk, K. N. *J. Phys. Chem. A* **2005**, *109*, 9542.
- (8) Zheng, J.; Zhao, Y.; Truhlar, D. G. *J. Chem. Theory Comput.* **2007**, *3*, 569.
- (9) Karton, A.; Tarnopolsky, A.; Lamre, J.-F.; Schatz, G. C.; Martin, J. M. L. *J. Phys. Chem. A* **2008**, *112*, 12868.
- (10) Zheng, J.; Zhao, Y.; Truhlar, D. G. *J. Chem. Theory Comput.* **2009**, *5*, 808.
- (11) Zhao, Y.; Truhlar, D. G. *J. Chem. Theory Comput.* **2008**, *4*, 1849.
- (12) Zhao, Y.; Truhlar, D. G. *J. Chem. Phys.* **2006**, *125*, 194101.
- (13) Zhao, Y.; Truhlar, D. G. *Theor. Chem. Acc.* **2008**, *120*, 215.
- (14) Zhao, Y.; Lynch, B. J.; Truhlar, D. G. *J. Phys. Chem. A* **2004**, *108*, 2715.
- (15) Boese, A. D.; Martin, J. M. L. *J. Chem. Phys.* **2004**, *121*, 3405.
- (16) Zhao, Y.; Truhlar, D. G. *J. Phys. Chem. A* **2005**, *109*, S656.
- (17) Lynch, B. J.; Fast, P. L.; Harris, M.; Truhlar, D. G. *J. Phys. Chem. A* **2000**, *104*, 4811.
- (18) (a) Becke, A. D. *Phys. Rev. A* **1988**, *38*, 3098. (b) Lee, C. T.; Yang, W. T.; Parr, R. G. *Phys. Rev. B* **1988**, *37*, 785. (c) Becke, A. D. *J. Chem. Phys.* **1993**, *98*, 1372. (d) Note that the BHandHLYP functional, explained in detail in the manual of the *Gaussian* computer program (ref 58), is similar in spirit to Becke's half-and-half functional of part c of this ref but not identical to it.
- (19) Quintal, M. M.; Karton, A.; Iron, M. A.; Boese, A. D.; Martin, J. M. L. *J. Phys. Chem. A* **2006**, *110*, 709.
- (20) Stephens, P. J.; Devlin, F. J.; Chabalowski, C. F.; Frisch, M. J. *J. Phys. Chem.* **1994**, *98*, 11623.
- (21) Truhlar, D. G. *Faraday Discuss.* **1998**, *110*, 362.
- (22) Adamo, C.; Barone, V. *J. Chem. Phys.* **1998**, *108*, 664.
- (23) Lynch, B. J.; Truhlar, D. G. *J. Phys. Chem. A* **2001**, *105*, 2936.
- (24) Pu, J.; Truhlar, D. G. *J. Phys. Chem. A* **2005**, *109*, 773.
- (25) Zhao, Y.; Lynch, B. J.; Truhlar, D. G. *J. Phys. Chem. A* **2004**, *108*, 4786.
- (26) Zhao, Y.; Truhlar, D. G. *Acc. Chem. Res.* **2008**, *41*, 157.
- (27) Zhao, Y.; Truhlar, D. G. *Chem. Phys. Lett.* **2011**, *502*, 1.
- (28) (a) Bian, W.; Werner, H.-J. *J. Chem. Phys.* **2000**, *112*, 220. (b) Peterson, K. A.; Dunning, T. H., Jr. *J. Phys. Chem. A* **1997**, *101*, 6280. (c) Van Mourik, T.; Harris, G. J.; Polyansky, O. L.; Tennyson, J.; Császár, A.; Knowles, P. J. *J. Chem. Phys.* **2001**, *115*, 3706. (d) Brown, F. B.; Truhlar, D. G. *Chem. Phys. Lett.* **1985**, *117*, 307. (e) Schwenke, D. W.; Tucker, S. C.; Steckler, R.; Brown, F. B.; Lynch, G. C.; Truhlar, D. G.; Garrett, B. C. *J. Chem. Phys.* **1989**, *90*, 3110.
- (29) Lynch, B. J.; Zhao, Y.; Truhlar, D. G. *J. Phys. Chem. A* **2005**, *109*, 1643.
- (30) Hirao, K. *Quantum Chem. Int. J.* **1992**, *517*. Hirao, K. *Chem. Phys. Lett.* **1992**, *196*, 397.
- (31) (a) Krishnan, R.; Binkley, J. S.; Seeger, R.; Pople, J. A. *J. Chem. Phys.* **1980**, *72*, 650. (b) Clark, T.; Chandrasekhar, J.; Spitznagel, G. W.;

- Schleyer, P. v. R. *J. Comput. Chem.* **1983**, *4*, 294. (c) Frisch, M. J.; Pople, J. A.; Binkley, J. S. *J. Chem. Phys.* **1984**, *80*, 3265. (d) Curtiss, L. A.; Raghavachari, K.; Redfern, C.; Rassolov, V.; Pople, J. A. *J. Chem. Phys.* **1998**, *109*, 7764. (e) Fast, P. L.; Sanchez, M. L.; Truhlar, D. G. *Chem. Phys. Lett.* **1999**, *306*, 407. (f) Lynch, B. J.; Zhao, Y.; Truhlar, D. G. *J. Phys. Chem. A* **2003**, *107*, 1384.
- (32) (a) Kendall, R. A.; Dunning, T. H., Jr.; Harrison, R. J. *J. Chem. Phys.* **1992**, *96*, 6796. (b) Woon, D. E.; Dunning, T. H., Jr. *J. Chem. Phys.* **1993**, *98*, 1358.
- (33) Pople, J. A.; Head-Gordon, M.; Raghavachari, K. *J. Chem. Phys.* **1987**, *87*, 5968.
- (34) Tratz, C.; Fast, P. L.; Truhlar, D. G. *Phys. Chem. Comm.* **1999**, *2*, 14.
- (35) Møller, C.; Plesset, M. S. *Phys. Rev.* **1934**, *46*, 618.
- (36) Zheng, J.; Xu, X.; Truhlar, D. G. *Theor. Chem. Acc.* **2011**, *128*, 295.
- (37) Weigend, F.; Ahlrichs, R. *Phys. Chem. Chem. Phys.* **2005**, *7*, 3297.
- (38) (a) Dunning, T. H., Jr. *J. Chem. Phys.* **1989**, *90*, 1007. (b) Papajak, E.; Leverentz, H. R.; Zheng, J.; Truhlar, D. G. *J. Chem. Theory Comput.* **2009**, *5*, 1197.
- (39) (a) Hariharan, P. C.; Pople, J. A. *Theor. Chem. Acta* **1973**, *28*, 213. (b) Frandl, M. M.; Pietro, W. J.; Hehre, W. J.; Binkley, J. S.; Gordon, M. S.; DeFrees, D.; Pople, J.; Pople, A. *J. Chem. Phys.* **1982**, *77*, 3654.
- (40) Tishchenko, O.; Zheng, J.; Truhlar, D. G. *J. Chem. Theory Comput.* **2008**, *4*, 1208.
- (41) Schultz, N.; Zhao, Y.; Truhlar, D. G. *J. Phys. Chem. A* **2005**, *109*, 11127.
- (42) Zhao, Y.; Truhlar, D. G. *J. Chem. Phys.* **2008**, *128*, 184109.
- (43) Chai, J.-D.; Head-Gordon, M. *J. Chem. Phys.* **2008**, *128*, 084106.
- (44) Chai, J.-D.; Head-Gordon, M. *Phys. Chem. Chem. Phys.* **2008**, *10*, 6615.
- (45) (a) Perdew, J. P.; Burke, K.; Ernzerhof, M. *Phys. Rev. Lett.* **1996**, *77*, 3865. (b) Adamo, C.; Cossi, M.; Barone, V. *THEOCHEM* **1999**, *493*, 145.
- (46) Keal, T. W.; Tozer, D. J. *J. Chem. Phys.* **2005**, *123*, 121103.
- (47) Grimme, S. *J. Comput. Chem.* **2006**, *27*, 1787.
- (48) Schmider, H. L.; Becke, A. D. *J. Chem. Phys.* **1998**, *108*, 9624.
- (49) Adamo, C.; Barone, V. *Chem. Phys. Lett.* **1997**, *274*, 242.
- (50) Zhao, Y.; Truhlar, D. G. *J. Phys. Chem. A* **2004**, *108*, 6908.
- (51) Zhao, Y.; Schultz, N. E.; Truhlar, D. G. *J. Chem. Theory Comput.* **2006**, *2*, 364.
- (52) Zhao, Y.; Truhlar, D. G. *J. Phys. Chem. A* **2006**, *110*, 13126.
- (53) Zhao, Y.; Schultz, N. E.; Truhlar, D. G. *J. Chem. Phys.* **2005**, *123*, 161103.
- (54) Boese, A. D.; Handy, N. C. *J. Chem. Phys.* **2002**, *116*, 9559.
- (55) Grimme, S. *J. Chem. Phys.* **2006**, *124*, 034108.
- (56) Frisch, M. J.; Trucks, G. W.; Schlegel, H. B.; Scuseria, G. E.; Robb, M. A.; Cheeseman, J. R.; Scalmani, G.; Barone, V.; Mennucci, B.; Petersson, G. A.; Nakatsuji, H.; Caricato, M.; Li, X.; Hratchian, H. P.; Izmaylov, A. F.; Bloino, J.; Zheng, G.; Sonnenberg, J. L.; Hada, M.; Ehara, M.; Toyota, K.; Fukuda, R.; Hasegawa, J.; Ishida, M.; Nakajima, T.; Honda, Y.; Kitao, O.; Nakai, H.; Vreven, T.; Montgomery, J. A., Jr.; Peralta, J. E.; Ogliaro, F.; Bearpark, M.; Heyd, J. J.; Brothers, E.; Kudin, K. N.; Staroverov, V. N.; Kobayashi, R.; Normand, J.; Raghavachari, K.; Rendell, A.; Burant, J. C.; Iyengar, S. S.; Tomasi, J.; Cossi, M.; Rega, N.; Millam, N. J.; Klene, M.; Knox, J. E.; Cross, J. B.; Bakken, V.; Adamo, C.; Jaramillo, J.; Gomperts, R.; Stratmann, R. E.; Yazyev, O.; Austin, A. J.; Cammi, R.; Pomelli, C.; Ochterski, J. W.; Martin, R. L.; Morokuma, K.; Zakrzewski, V. G.; Voth, G. A.; Salvador, P.; Dannenberg, J. J.; Dapprich, S.; Daniels, A. D.; Farkas, Ö.; Foresman, J. B.; Ortiz, J. V.; Cioslowski, J.; Fox, D. J. *Gaussian 09*, Revision A.02; Gaussian, Inc.: Wallingford, CT, 2009.
- (57) Frisch, M. J.; Trucks, G. W.; Schlegel, H. B.; Scuseria, G. E.; Robb, M. A.; Cheeseman, J. R.; Scalmani, G.; Barone, V.; Mennucci, B.; Petersson, G. A.; Nakatsuji, H.; Caricato, M.; Li, X.; Hratchian, H. P.; Izmaylov, A. F.; Bloino, J.; Zheng, G.; Sonnenberg, J. L.; Hada, M.; Ehara, M.; Toyota, K.; Fukuda, R.; Hasegawa, J.; Ishida, M.; Nakajima, T.; Honda, Y.; Kitao, O.; Nakai, H.; Vreven, T.; Montgomery, J. A., Jr.; Peralta, J. E.; Ogliaro, F.; Bearpark, M.; Heyd, J. J.; Brothers, E.; Kudin, K. N.; Staroverov, V. N.; Kobayashi, R.; Normand, J.; Raghavachari, K.; Rendell, A.; Burant, J. C.; Iyengar, S. S.; Tomasi, J.; Cossi, M.; Rega, N.; Millam, N. J.; Klene, M.; Knox, J. E.; Cross, J. B.; Bakken, V.; Adamo, C.; Jaramillo, J.; Gomperts, R.; Stratmann, R. E.; Yazyev, O.; Austin, A. J.; Cammi, R.; Pomelli, C.; Ochterski, J. W.; Martin, R. L.; Morokuma, K.; Zakrzewski, V. G.; Voth, G. A.; Salvador, P.; Dannenberg, J. J.; Dapprich, S.; Daniels, A. D.; Farkas, Ö.; Foresman, J. B.; Ortiz, J. V.; Cioslowski, J.; Fox, D. J. *Gaussian 03*, Revision D.01; Gaussian, Inc.: Wallingford, CT, 2003.
- (58) (a) Frisch, M. J.; Trucks, G. W.; Schlegel, H. B.; Scuseria, G. E.; Robb, M. A.; Cheeseman, J. R.; Scalmani, G.; Barone, V.; Mennucci, B.; Petersson, G. A.; Nakatsuji, H.; Caricato, M.; Li, X.; Hratchian, H. P.; Izmaylov, A. F.; Bloino, J.; Zheng, G.; Sonnenberg, J. L.; Hada, M.; Ehara, M.; Toyota, K.; Fukuda, R.; Hasegawa, J.; Ishida, M.; Nakajima, T.; Honda, Y.; Kitao, O.; Nakai, H.; Vreven, T.; Montgomery, J. A., Jr.; Peralta, J. E.; Ogliaro, F.; Bearpark, M.; Heyd, J. J.; Brothers, E.; Kudin, K. N.; Staroverov, V. N.; Kobayashi, R.; Normand, J.; Raghavachari, K.; Rendell, A.; Burant, J. C.; Iyengar, S. S.; Tomasi, J.; Cossi, M.; Rega, N.; Millam, N. J.; Klene, M.; Knox, J. E.; Cross, J. B.; Bakken, V.; Adamo, C.; Jaramillo, J.; Gomperts, R.; Stratmann, R. E.; Yazyev, O.; Austin, A. J.; Cammi, R.; Pomelli, C.; Ochterski, J. W.; Martin, R. L.; Morokuma, K.; Zakrzewski, V. G.; Voth, G. A.; Salvador, P.; Dannenberg, J. J.; Dapprich, S.; Daniels, A. D.; Farkas, Ö.; Foresman, J. B.; Ortiz, J. V.; Cioslowski, J.; Fox, D. J. *Gaussian 03*, Revision E.01; Gaussian, Inc.: Wallingford, CT, 2003. (b) Zhao, Y.; Truhlar, D. G. *MN-GFM: Minnesota Gaussian Functional Module*, version 4.1; University of Minnesota: Minneapolis, MN, 2008.
- (59) Zhao, Y.; Truhlar, D. G. *MLGAUSS*, version 2.0; University of Minnesota: Minneapolis, MN, 2006.
- (60) Lynch, B. J.; Zhao, Y.; Truhlar, D. G. *J. Phys. Chem. A* **2003**, *107*, 1384.
- (61) Papajak, E.; Truhlar, D. G. *J. Chem. Theory Comput.* **2010**, *6*, 597.
- (62) Klippenstein, S. J.; Harding, L. B.; Davis, M. J.; Tomlin, A. S.; Skodje, R. T. *Proc. Combust. Inst.* **2011**, *33*, 351.
- (63) Skodje, R. T.; Tomlin, A. S.; Klippenstein, S. J.; Harding, L. B.; Davis, M. J. *J. Phys. Chem. A* **2010**, *114*, 8286.
- (64) Zheng, J.; Truhlar, D. G. *Phys. Chem. Chem. Phys.* **2010**, *12*, 7782.
- (65) Ruedenberg, K.; Sundberg, K. R. In *Quantum Science: Methods and Structure*; Calais, J.-L., Goscinski, O., Linderberg, J., Ohrn, Y., Eds.; Plenum: New York, 1976; p 505.
- (66) Roos, B. O.; Taylor, P. R.; Siegbahn, P. E. M. *Chem. Phys.* **1980**, *48*, 157.
- (67) Nakano, H.; Nakajima, T.; Tsuneda, T.; Hirao, K. In *Theory and Applications of Computational Chemistry: The First Forty Years*; Dykstra, C. E., Frenking, G., Kim, K. S., Scuseria, G. E., Eds.; Elsevier: Amsterdam, 2005; p 507.
- (68) Roos, B. O. In *Theory and Applications of Computational Chemistry: The First Forty Years*; Dykstra, C. E., Frenking, G., Kim, K. S., Scuseria, G. E., Eds.; Elsevier: Amsterdam, 2005; p 725.

A Locality Analysis of the Divide–Expand–Consolidate Coupled Cluster Amplitude Equations

Kasper Kristensen,^{†,*} Marcin Ziólkowski,^{‡,†} Branislav Jansík,[†] Thomas Kjærgaard,^{§,†} and Poul Jørgensen[†]

[†]Lundbeck Foundation Center for Theoretical Chemistry, Department of Chemistry, University of Aarhus, DK-8000 Århus C, Denmark

ABSTRACT: We present a thorough locality analysis of the divide–expand–consolidate amplitude equations for second-order Møller–Plesset perturbation theory and the coupled cluster singles doubles (CCSD) model, which demonstrates that the amplitude equations are local when expressed in terms of a set of local occupied and local unoccupied Hartree–Fock orbitals, such as the least-change molecular basis. The locality analysis thus shows that a CC calculation on a large molecular system may be carried out in terms of CC calculations on small orbital fragments of the total molecular system, where the sizes of the orbital fragment spaces are determined in a black box manner to ensure that the CC correlation energy is calculated to a preset energy threshold. A practical implementation of the locality analysis is described, and numerical results are presented, which demonstrate that both the orbital fragment sizes and the relative energy error compared to a full CC calculation are independent of the molecular system size.

1. INTRODUCTION

A coupled cluster (CC) calculation¹ starts out with a mean field Hartree–Fock (HF) calculation,^{2,3} which gives the total HF energy and a set of occupied and unoccupied HF molecular orbitals. The CC wave function is expanded in the HF orbital basis, and the CC amplitudes are determined by solving sets of nonlinear amplitude equations. From the CC amplitudes the correlation energy is determined. The total CC energy is the sum of the HF energy and the correlation energy.

The mean field HF calculation gives a good description of the long-range interaction between the electrons, while the interaction for shorter distances is described with less accuracy. The major task of a CC calculation is therefore to describe these short-ranged electron–electron interactions. Using a simplistic physical picture, this interaction may be expressed in terms of the very short-ranged interaction leading to coulomb holes in the wave function and the longer ranged interaction leading to dispersion effects. Both these effects describe local phenomena.

Standard CC calculations are expressed in the canonical HF basis which is a nonlocal basis, where the individual HF orbitals extend over the whole molecular system. The description of local phenomena using a nonlocal basis will inherently lead to a scaling wall for the standard CC calculations. To circumvent this scaling wall, it has been attempted to express the CC wave function in a basis of local HF orbitals.⁴

Local occupied HF orbitals have been obtained by localizing the canonical HF orbitals using various standard techniques.^{5–7} However, none of these techniques have been able to yield a set of local unoccupied HF orbitals.⁸ Projected atomic orbitals (PAOs), where the occupied HF orbital space is projected out of the atomic basis, have been used to span the unoccupied HF orbital space. The PAOs constitute a redundant set, but a more severe drawback in a local wave function context is that the locality of the PAOs is much less pronounced than the locality of the localized occupied HF orbitals.

The local correlation wave function method development was pioneered by Pulay⁴ and Saebø and Pulay,⁹ and the local CC

method of Hampel and Werner¹⁰ and Schütz and Werner^{11–13} constitutes a prominent early contribution. Many other local CC methods have been proposed,^{14–25} including atomic orbital-based CC,^{14–16} the natural linear scaling approach,¹⁸ the cluster-in-molecule approach,^{19–21} the divide-and-conquer approach,²² the fragment molecular orbital approach,²³ and the incremental scheme.^{24,25} For the simplest correlation method, second-order Møller–Plesset perturbation theory (MP2), other approaches have also been proposed where linear scaling have been obtained²⁶ with Laplace transformations of the energy denominator and applying state-of-the-art integral screening techniques.^{27–29}

We have recently described how a local HF orbital basis—the least-change molecular (LCM) basis³⁰—can be obtained for both the occupied and the unoccupied HF orbital spaces. In particular, we have found that the locality of the unoccupied HF orbitals is not very different from the locality of the occupied HF orbitals for standard basis sets, such as cc-pVDZ and cc-pVTZ. By applying this local HF basis and restructuring the CC equations, we have developed the linear-scaling and embarrassingly parallel divide–expand–consolidate (DEC) CC method.³¹ The DEC method is on par with the standard CC method in the sense that the precision of the correlation energy is defined by a preset threshold. Specifically, in a standard CC calculation the precision is specified by a preset threshold for the residual norm for the CC amplitude equations, and in a DEC calculation the precision is specified by a preset threshold for the atomic fragment energies, which directly reflects the accuracy in the total correlation energy (provided that a tight residual threshold is used in the amplitude equations for the fragment calculations). In short, the accuracy in standard CC and DEC CC is defined prior to the calculation.

In the Laplace integral screening AO-MP2 approach the error compared to a full MP2 calculation can also be controlled in a precise manner,^{27–29} while in existing local CC methods the standard CC correlation energy is an asymptotic limit, which is

Received: February 17, 2011

Published: April 18, 2011

obtained when all thresholds are removed. However, in practice, ad hoc approximations to the standard CC method are introduced in the local CC methods, where the effects of these approximations on the correlation energy and the molecular properties are not known. The approximations include a priori assignments of local orbital spaces, which introduce local correlation errors, e.g., when the completeness criterion of Boughton and Pulay³² is used to assign a priori fixed orbital excitation spaces to localized occupied HF orbitals. Some approximations also include nonphysical bond cuts of the molecular system. At the end of a local CC calculation, where ad hoc approximations have been introduced, the precision of the calculation compared to a full CC calculation is in general unknown.

One could argue that compared to the large errors in CC calculations due to the basis set incompleteness and the approximate CC wave function model, the approximations that are introduced in the local CC methods are acceptable. However, in chemistry we are typically interested in the energy differences for molecular conformers, for example, reaction enthalpies, interaction energies of van der Waals complexes, excitation energies, and geometrical energy derivatives. These energy differences are small compared to total energies, and to obtain a reliable and accurate description of these small differences, it is necessary to know the errors introduced by the local approximations.

Comparing the DEC approach to existing local CC methods, we conclude that using the DEC approach, the accuracy in the energy is defined prior to the calculation, and the sizes of the orbital spaces are adjusted during the calculation according to this accuracy. In this way the DEC scheme ensures that the standard CC energy is reproduced to the requested accuracy using as small orbital spaces as possible. Existing local CC approaches in general lack the flexibility to allow the sizes of the orbital spaces to adjust to an energy threshold, and therefore the error compared to the standard CC energy is in general unknown.

The DEC energy equations have previously been presented.³¹ In this paper we perform a thorough locality analysis of the MP2 and CC singles doubles (CCSD) amplitude equations, which demonstrate that the amplitude equations are indeed local when expressed in the LCM basis,³⁰ where both the occupied and the virtual orbitals are local. The locality analysis shows that a CC calculation on a molecular system may be carried out in terms of CC calculations on small orbital fragments of the total molecular system, when the fragmentation of the orbital spaces is carried out as in the DEC CC method. We also present a practical implementation of the DEC method. In particular, we discuss the removal of orbital tail coefficients to obtain more local molecular orbitals (and thus smaller atomic orbital spaces for evaluating two-electron integrals), how orbital spaces are determined according to a predefined energy accuracy, and how to avoid wave function superposition errors when pair interaction energies are calculated. Numerical results are given, which demonstrate that the sizes of the fragment orbital spaces are independent of the molecular system size—in agreement with the theoretical locality analysis—and that the standard CC correlation energy can be recovered to a predefined accuracy using relatively small orbital fragment spaces.

In the next section we derive the basic equations of the DEC model. In Sections 3 and 4 we perform a locality analysis for the MP2 and CCSD amplitude equations. In Section 5 the computational scaling in DEC calculations is discussed, and Section 6 contains implementation details for the DEC method. In Section 7 we present some illustrative DEC calculations. Finally, in Section 8 we give a short summary of the DEC model and some concluding remarks.

2. DEC MODEL

2.1. CC Energy. For a closed shell molecule the total energy E_{CC} for a CC wave function model may be expressed as³³

$$E_{CC} = E_{HF} + E_{corr} \quad (1)$$

where E_{HF} is the HF total energy, and the correlation energy E_{corr} is obtained as

$$E_{corr} = \sum_{ijab} (t_{ij}^{ab} + t_i^a t_j^b) (2g_{iajb} - g_{ibja}) \quad (2)$$

where t_i^a and t_{ij}^{ab} are the cluster singles and doubles amplitudes, respectively. Indices i, j, \dots refer to occupied HF orbitals and a, b, \dots to unoccupied HF orbitals, and g_{iajb} is a two-electron integral in the HF orbital basis using the Mulliken notation. The correlation energy expression in eq 2 applies to all standard CC models. The singles contribution vanishes for MP2.

In a conventional CC calculation the CC wave function is expanded in the nonlocal canonical HF orbital basis, and therefore all integrals and cluster amplitudes in E_{corr} are nonvanishing. The evaluation of E_{corr} therefore has a fourth power scaling in system size. When a local HF orbital basis is used the correlation energy can be expressed in terms of orbital spaces which reference only local parts of the molecular system. We describe in the following sections how this may be accomplished.

2.2. CC Energy for Local HF Orbitals. For each local HF orbital the Mulliken charge is determined, and the HF orbital is assigned to the atomic site with the largest Mulliken charge. In this way each atomic site gets assigned a set of local occupied and local unoccupied HF orbitals. The set of occupied HF orbitals assigned to atomic site P is denoted \underline{P} , and the set of unoccupied HF orbitals assigned to atomic site P is denoted \bar{P} . A cartoon illustrating how a model one-dimensional molecular system is divided into atomic sites and assigned a set of occupied and unoccupied HF orbitals is given in Figure 1A. As a specific example we present the orbital assignment for the $C_{14}H_2$ molecule (LCM molecular orbitals using a cc-pVDZ basis set) in Figure 1B. (In Section 7.1.1 we elaborate on the assignment of orbitals in Figure 1B.) In Table 1 we give an overview of the notation for orbital spaces and energies used for describing the DEC model.

Having assigned the local HF orbitals to atomic sites, the correlation energy in eq 2 can be expressed in terms of atomic fragment energies E_P and atomic pair fragment energies E_{PQ} :

$$E_P = \sum_{\substack{ij \in \underline{P} \\ ab}} (t_{ij}^{ab} + t_i^a t_j^b) (2g_{iajb} - g_{ibja}) \quad (3)$$

$$E_{PQ} = \sum_{\substack{ij \in \underline{P} \cup \underline{Q} \\ ab}} (t_{ij}^{ab} + t_i^a t_j^b) (2g_{iajb} - g_{ibja}) \quad (4)$$

giving

$$E_{corr} = \sum_P E_P + \sum_{P > Q} \Delta E_{PQ} \quad (5)$$

where the sum runs over all atomic sites, and the pair interaction energy ΔE_{PQ} is given as

$$\Delta E_{PQ} = E_{PQ} - E_P - E_Q \quad (6)$$

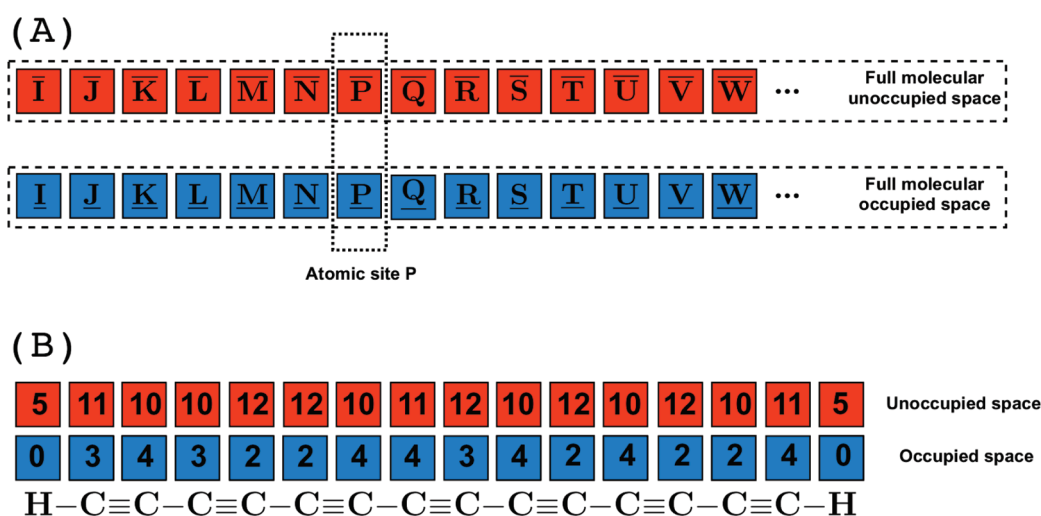


Figure 1. (A) Molecular system divided into atomic sites I, J, ..., P, ..., where each site has been assigned a set of occupied (blue) and unoccupied (red) HF orbitals. (B) Example of orbital assignments for the C₁₄H₂ molecule (LCM molecular orbitals using a cc-pVDZ basis set). The values above each atom denote the number of occupied and virtual orbitals assigned to that atom.

Table 1. Overview of Notation for Atomic Sites, Energies, And Orbitals Spaces

symbol	short description
P, Q, R, ...	labels for atomic sites
E_P	atomic fragment energy
E_{PQ}	atomic pair fragment energy
ΔE_{PQ}	pair interaction energy
\mathcal{E}_P	energy orbital space (EOS) for evaluating E_P
\mathcal{A}_P	amplitude orbital space (AOS) for calculating CC amplitudes
$\{\mathcal{A}_P\}$	atomic fragment extent where MO coefficients are expanded
\underline{P}	set of occupied orbitals assigned to site P (occupied orbitals in \mathcal{E}_P)
\overline{P}	set of unoccupied orbitals assigned to site P
$[P]$	set of occupied orbitals local to P
$\overline{[P]}$	set of unoccupied orbitals local to P (unoccupied orbitals in \mathcal{E}_P)
$[P]_2$	set of occupied orbitals local to $[P]$ (including $[P]$)
$\overline{[P]}_2$	set of unoccupied orbitals local to $\overline{[P]}$ (including $\overline{[P]}$)
\mathcal{B}	occupied buffer orbital space
$\overline{\mathcal{B}}$	unoccupied buffer orbital space

No approximations have been made in eq 5, where the sum over the two occupied orbital indices in eq 2 has been replaced by sums over the occupied orbitals of the atomic fragments and atomic pair fragments. The first term in eq 5 describes the coulomb holes in the wave function, while the second term for larger PQ distances mainly describes dispersion effects.

In the local HF orbital basis the integral g_{iajb} is nonvanishing only if the orbital pair indices ia refer to the same atomic site or to neighboring atomic sites and similarly for jb . Therefore the integral g_{iajb} is nonvanishing only if $i \in \underline{P}$ and $a \in \overline{[P]}$, where $\overline{[P]}$ refers to the unoccupied HF orbital space local to \overline{P} (including \overline{P}) and similarly for jb . The requirements for a nonvanishing integral may thus be summarized as

$$g_{iajb} : i \in \underline{P}, \quad a \in \overline{[P]}, \quad j \in \underline{Q}, \quad b \in \overline{[Q]} \quad (7)$$

When the atomic fragment energy E_P in eq 3 is calculated, both occupied indices belong to atomic site P [$P = Q$ in eq 7]. Since the integral $(2g_{iajb} - g_{ibja})$ in E_P is nonvanishing only if $a, b \in \overline{[P]}$, we may restrict the virtual index summation in eq 3 and evaluate

E_P as

$$E_P = \sum_{\substack{ij \in \underline{P} \\ ab \in \overline{[P]}}} (t_{ij}^{ab} + t_i^a t_j^b) (2g_{iajb} - g_{ibja}) \quad (8)$$

where the summation over the unoccupied indices has been restricted to atomic sites, which are local to P. Similarly, the locality of the integral $(2g_{iajb} - g_{ibja})$ in eq 4 implies that the atomic pair fragment energy E_{PQ} may be evaluated as

$$E_{PQ} = \sum_{\substack{ij \in \underline{P} \cup \underline{Q} \\ ab \in \overline{[P]} \cup \overline{[Q]}}} (t_{ij}^{ab} + t_i^a t_j^b) (2g_{iajb} - g_{ibja}) \quad (9)$$

where the unoccupied index summation has been restricted to the union of unoccupied spaces which are local to \overline{P} and \overline{Q} using eq 7. The total orbital space required for evaluating E_{PQ} is thus the union of orbital spaces for evaluating E_P and E_Q .

Disregarding singles the atomic fragment energy E_P depends on the doubles amplitudes:

$$t_{ij}^{ab} : i, j \in \underline{P}, \quad a, b \in \overline{[P]} \quad (10)$$

The orbital space defined by eq 10 will be denoted the atomic fragment energy orbital space (EOS) \mathcal{E}_P . The atomic pair fragment energy E_{PQ} depends on the doubles amplitudes

$$t_{ij}^{ab} : i, j \in \underline{P} \cup \underline{Q}, \quad a, b \in \overline{[P]} \cup \overline{[Q]} \quad (11)$$

and the orbital space defined by eq 11 is denoted the atomic pair fragment EOS $\mathcal{E}_{PQ} = \mathcal{E}_P \cup \mathcal{E}_Q$.

A CC calculation carried out in terms of atomic fragment and pair fragment calculations will be denoted a DEC calculation because it follows the following procedure:

- Divide the orbital space among the atomic sites.
- Expand the orbital space of the individual atomic fragments to obtain converged fragment energies.

- Consolidate the fragment energies according to eq 5 to get the correlation energy for the full molecular system.

3. DEC-MP2 AMPLITUDE EQUATIONS

In this section the MP2 amplitude equations are analyzed in the local HF basis to understand how the atomic fragment and the atomic pair fragment energies can be determined from calculations referencing only small fragments of the full molecular orbital space. In the next section a similar analysis will be performed for the CCSD amplitude equations.

The locality analysis of the amplitude equations demonstrates that a full MP2 calculation can be carried out in terms of small independent fragment calculations. The actual fragment sizes are determined during the DEC calculation in order to ensure that the fragment energies are determined to a given threshold, as will be discussed in Section 6.2.

3.1. MP2 Amplitude Equations. Using standard notation³³ the MP2 amplitude equations may be expressed as

$$\Omega_{abj} = \left\langle \begin{array}{c} \overline{ab} \\ ij \end{array} \left| \hat{H} \right| \text{HF} \right\rangle + \left\langle \begin{array}{c} \overline{ab} \\ ij \end{array} \left| [\hat{F}, \hat{T}_2] \right| \text{HF} \right\rangle = 0 \quad (12)$$

where \hat{H} is the Hamiltonian:

$$\hat{H} = \sum_{rs} h_{rs} E_{rs} + \frac{1}{2} \sum_{rstu} g_{rstu} (E_{rs} E_{tu} - \delta_{st} E_{ru}) \quad (13)$$

\hat{T}_2 is the cluster doubles operator:

$$\hat{T}_2 = \frac{1}{2} \sum_{abij} t_{ij}^{ab} E_{ai} E_{bj} \quad (14)$$

and $\left\langle \begin{array}{c} \overline{ab} \\ ij \end{array} \right|$ is a doubles bra state in the biorthonormal basis. \hat{F} is the Fock operator:

$$\hat{F} = \sum_{pq} F_{pq} E_{rs}$$

where the Fock matrix elements are given as

$$F_{pq} = h_{pq} + \sum_i (2g_{pqi} - g_{piqi}) \quad (15)$$

The Fock matrix has vanishing matrix elements between occupied and unoccupied HF orbitals and therefore has a block diagonal structure:

$$\mathbf{F} = \begin{pmatrix} \mathbf{F}^{oo} & \mathbf{0} \\ \mathbf{0} & \mathbf{F}^{vu} \end{pmatrix} \quad (16)$$

where \mathbf{F}^{oo} and \mathbf{F}^{vu} denote the occupied–occupied and unoccupied–unoccupied blocks of the Fock matrix, respectively. The MP2 amplitude equation in eq 12 may be evaluated as

$$\Omega_{abj}^{\text{MP2}} = g_{abj} + \sum_c t_{ij}^{cb} F_{ac} + \sum_c t_{ij}^{ac} F_{bc} - \sum_k t_{kj}^{ab} F_{ki} - \sum_k t_{ik}^{ab} F_{kj} = 0 \quad (17)$$

and becomes a set of linear equations which determine the cluster amplitudes.

In the canonical HF basis where \mathbf{F}^{oo} and \mathbf{F}^{vu} are diagonal matrices with orbital energies on the diagonal ($F_{ij}^{oo} = \delta_{ij} \varepsilon_j$, $F_{ab}^{vu} = \delta_{ab} \varepsilon_a$), the amplitude equations in eq 17 decouple, and the solution to eq 17 becomes trivial:

$$t_{ij}^{ab} = -g_{abj} (\varepsilon_a + \varepsilon_b - \varepsilon_i - \varepsilon_j)^{-1} \quad (18)$$

However, in the canonical basis, where the HF orbitals are nonlocal, all integrals g_{abj} and therefore also all amplitudes t_{ij}^{ab} are, in general, nonvanishing. The canonical basis is therefore not suited for a DEC calculation.

3.2. Orbital Spaces for Evaluating E_p and E_{pQ} for MP2. For a local HF basis the correlation energy is obtained as a sum of the atomic fragment and the pair fragment energies in eqs 8 and 9, which are determined from the amplitudes of the EOSs defined by eqs 10 and 11. We describe below how the amplitudes of the EOS can be determined from MP2 calculations, which reference only a small fragment of the full molecular orbital space. The selection of the orbital spaces for the small orbital fragment calculations is performed based on a locality analysis of the MP2 amplitude equations in a local HF basis. Since we are interested in determining the EOS amplitudes in eqs 10 and 11, we consider the propagation of the amplitude equations in eq 17 for $i \in \underline{P}$ and $j \in \underline{Q}$.

The amplitude equations in eq 17 constitute a set of linear equations, which can be ordered to give a positive definite coefficient matrix:

$$\sum_c t_{ij}^{cb} F_{ac} + \sum_c t_{ij}^{ac} F_{bc} - \sum_k t_{kj}^{ab} F_{ki} - \sum_k t_{ik}^{ab} F_{kj} = -g_{abj} \quad (19)$$

Equation 19 may be solved using standard iterative algorithms, such as the conjugate gradient or conjugate residual methods. When solving eq 19 using one of these methods, a new direction for the $(n + 1)$ th iteration is determined from the residual containing the amplitudes of the n th iteration $t_{ij}^{n,ab}$:

$$t_{ij}^{n+1,ab} = t_{ij}^{n,ab} + R_{abj}^{n,\text{MP2}}(t^n) \quad (20)$$

where $R_{abj}^{n,\text{MP2}}(t^n)$ is the residual of eq 19 for iteration n :

$$\begin{aligned} R_{abj}^{n,\text{MP2}}(t^n) &= -\Omega_{abj}^{n,\text{MP2}}(t^n) \\ &= -g_{abj} - \sum_c t_{ij}^{n,cb} F_{ac} - \sum_c t_{ij}^{n,ac} F_{bc} + \sum_k t_{kj}^{n,ab} F_{ki} \\ &\quad + \sum_k t_{ik}^{n,ab} F_{kj} \end{aligned} \quad (21)$$

In the conjugate gradient or the conjugate residual methods, a line search is performed along the residual direction. Furthermore, the convergence may be improved by preconditioning the linear equations. Both line search and preconditioning will affect the convergence rate of the algorithm, but they will have no effect on how new orbital spaces are introduced in each iteration, starting from $i \in \underline{P}$ and $j \in \underline{Q}$. Since the focus in this analysis is on the propagation of orbital spaces, we choose to carry out the analysis using the simplified algorithm outlined above without line search and preconditioning. We note that in practice we use the conjugate residual algorithm and precondition the equation using the diagonal elements of the Fock matrix.

Before carrying out the locality analysis it is instructive to demonstrate that for a diagonal Fock matrix the simple algorithm outlined above converges to the trivial solution in eq 18. Schematically, eq 19 may then be written as

$$\varepsilon t = -g \quad (22)$$

where $\varepsilon = \varepsilon_a + \varepsilon_b - \varepsilon_i - \varepsilon_j$ is positive. The residual in eq 21 now becomes

$$R^n = -g - \varepsilon t^n \quad (23)$$

In each iteration the t amplitudes are updated as described in eq 20:

$$t^{n+1} = t^n + R^n = -g + (1 - \varepsilon)t^n \quad (24)$$

where we have inserted eq 23. Starting out with $t^1 = 0$ we thus obtain

$$t^2 = -g \quad (25)$$

$$t^3 = -g[1 + (1 - \varepsilon)] \quad (26)$$

$$t^4 = -g[1 + (1 - \varepsilon) + (1 - \varepsilon)^2] \quad (27)$$

$$\dots \quad (28)$$

$$t^{n+1} = -g[1 + (1 - \varepsilon) + (1 - \varepsilon)^2 + \dots + (1 - \varepsilon)^{n-1}] \quad (29)$$

Noting that for $0 > \varepsilon > 1$, we may expand $1/\varepsilon$ as

$$\frac{1}{\varepsilon} = 1 + (1 - \varepsilon) + (1 - \varepsilon)^2 + \dots \quad (0 < \varepsilon < 1) \quad (30)$$

it is seen that the amplitude update in eq 20 indeed converges to solution of eq 22:

$$t^\infty = -g[1 + (1 - \varepsilon) + (1 - \varepsilon)^2 + \dots] = -\frac{g}{\varepsilon} \quad (31)$$

Let us now return to analyzing the propagation of the amplitude equations in eq 19 in a local HF basis. We start out by considering $i \in \underline{P}$ and $j \in \underline{Q}$ in the first iteration to investigate how the EOS amplitudes in eqs 10 and 11 couple to other amplitudes at different stages of the iteration sequence. In particular, we will investigate the local orbital spaces entering iterations two, three, and four, i.e., we consider the local amplitude analogues of the diagonal expressions in eqs 25–27. First we note that the coupling of amplitudes in eq 19 occurs via the off-diagonal elements in F^{oo} and F^{vv} , in contrast to the simple diagonal case above, where the amplitudes are uncoupled. The Fock matrix in the local basis in eq 14 is, however, diagonally dominant in the sense that the largest elements of F^{oo} and F^{vv} occur for pair indices ij or ab , where the orbital indices refer to the same atomic site. Furthermore, the magnitudes of the off-diagonal Fock matrix elements decrease with an increasing distance between the atomic sites. Non-negligible off-diagonal Fock matrix elements are therefore encountered only if

$$F_{kl}^{oo}; k \in \underline{P}, l \in [\underline{P}] \quad \text{or} \quad k \in [\underline{P}], l \in \underline{P} \quad (32)$$

$$F_{ab}^{vv}; a \in \bar{P}, b \in [\bar{P}] \quad \text{or} \quad a \in [\bar{P}], b \in \bar{P} \quad (33)$$

The iterative algorithm is started by setting the amplitudes $t^1 = 0$, which, using eq 21, gives the residual

$$R_{aibj}^{1,MP2}(t^1) = -g_{aibj} \quad (34)$$

For $i \in \underline{P}$ and $j \in \underline{Q}$ the integrals g_{aibj} are nonvanishing only if $a \in [\bar{P}]$ and $b \in [\bar{Q}]$, see eq 7. In the first iteration we therefore consider only the residuals for the orbital space:

$$R_{aibj}^{1,MP2}(t^1) : i \in \underline{P}, a \in [\bar{P}], j \in \underline{Q}, b \in [\bar{Q}] \quad (35)$$

which is identical to the EOS orbital space \mathcal{E}_{PQ} in eq 11. The amplitudes of the second iteration therefore become

$$t_{ij}^{2,ab} = t_{ij}^{1,ab} + R_{aibj}^{1,MP2}(t^1) = R_{aibj}^{1,MP2}(t^1) \quad (36)$$

and are nonvanishing only for the EOS:

$$t_{ij}^{2,ab} : i \in \underline{P}, a \in [\bar{P}], j \in \underline{Q}, b \in [\bar{Q}] \quad (37)$$

When the residual in the EOS vanishes, the amplitudes that determine E_{PQ} are converged. Carrying out an iterative procedure the convergence of the residual in the EOS is fast due to the diagonal dominance of the Fock matrix. New orbital spaces are introduced during the iterative procedure, however the most important effect for the convergence of the residual for the EOS is the relaxation of the amplitudes for the orbital spaces already considered.

In the second iteration the orbital space which interacts directly with the EOS is determined. The residual in the second iteration becomes

$$R_{aibj}^{2,MP2}(t^2) = -g_{aibj} - \sum_{c \in [\bar{P}]} t_{ij}^{2,cb} F_{ac} - \sum_{c \in [\bar{Q}]} t_{ij}^{2,ac} F_{bc} \\ + \sum_{k \in \underline{P}} t_{kj}^{2,ab} F_{ki} + \sum_{k \in \underline{Q}} t_{ik}^{2,ab} F_{kj} \quad (38)$$

For the second term in eq 38, the summation index is restricted to $c \in [\bar{P}]$ due to the restrictions on the amplitudes in eq 37. The second term thus gives a nonvanishing residual for $i \in \underline{P}, a \in [\bar{P}]_2, j \in \underline{Q}, b \in [\bar{Q}]$, where we have used eq 33 to restrict the a index such that $[\bar{P}]_2$ refers to unoccupied orbitals assigned to atoms that are local to $[\bar{P}]$ (including $[\bar{P}]$ itself). (Similarly, $[\bar{P}]_3$ is the unoccupied space local to $[\bar{P}]_2$ and so on.) The integral contribution ($-g_{aibj}$) to the residual is vanishing for the extended orbital space $i \in \underline{P}, a \in [\bar{P}]_2 - [\bar{P}], j \in \underline{Q}, b \in [\bar{Q}]$, see eq 7, and therefore the residual in this extended orbital space is small. The third term may be treated similarly as the second term. For the fourth term in eq 38 the summation is restricted to $k \in \underline{P}$ due to the restrictions on the amplitudes in eq 37. The fourth term therefore gives a nonvanishing residual contribution for the orbital space $i \in \underline{P}, a \in [\bar{P}], j \in \underline{Q}, b \in [\bar{Q}]$, where we have also used eq 32 to restrict the i index. In this case the extended orbital space $i \in [\underline{P}] - \underline{P}, a \in [\bar{P}], j \in \underline{Q}, b \in [\bar{Q}]$ has a nonvanishing integral contribution to the residual, and the residual may therefore be of the same magnitude as the residual in the first iteration. The last term in eq 38 may be treated similarly as the fourth term. In conclusion, nonvanishing residuals are obtained in the second iteration for the orbital spaces:

$$R_{aibj}^{2,MP2} : i \in [\underline{P}], a \in [\bar{P}]_2, j \in [\underline{Q}], b \in [\bar{Q}]_2 \quad (39)$$

where residuals for the extended spaces $i \in [\underline{P}] - \underline{P}, a \in [\bar{P}], j \in [\underline{Q}] - \underline{Q}, b \in [\bar{Q}]$ have both an integral and a coupling term contribution, while the residual for the extended spaces $i \in \underline{P}, a \in [\bar{P}]_2 - [\bar{P}], j \in \underline{Q}, b \in [\bar{Q}]_2 - [\bar{Q}]$ only has a coupling term contribution.

The amplitudes of the third iteration becomes

$$t_{ij}^{3,ab} = t_{ij}^{2,ab} + R_{aibj}^{2,MP2}(t^2) \quad (40)$$

where nonvanishing amplitudes $t_{ij}^{3,ab}$ are obtained for the nonvanishing residuals in eq 39:

$$t_{ij}^{3,ab} : i \in [\underline{P}], a \in [\bar{P}]_2, j \in [\underline{Q}], b \in [\bar{Q}]_2 \quad (41)$$

Iteration 2 thus introduces a first-order interaction (FOI) space to the EOS containing the amplitudes:

$$t_{ij}^{3,ab} : i \in [\underline{P}] - \underline{P}, a \in [\bar{P}]_2 - [\bar{P}], j \in [\underline{Q}] - \underline{Q}, \\ b \in [\bar{Q}]_2 - [\bar{Q}] \quad (42)$$

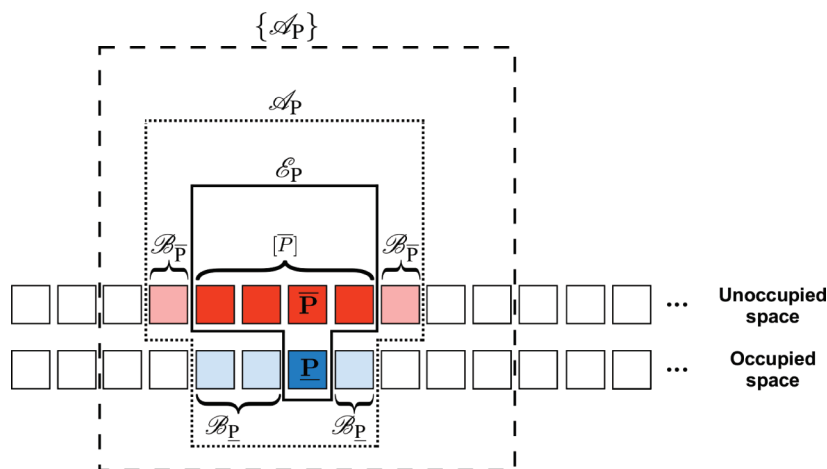


Figure 2. Atomic fragment P . The correlated wave function calculation is carried out using the amplitude orbital space \mathcal{A}_P (dark-blue, light-blue, red, and pink markings), while the atomic fragment energy E_P is evaluated using the energy orbital space \mathcal{E}_P (dark-blue and red markings). The orbitals in the molecular fragment P are confined to the atoms in the atomic fragment extent $\{\mathcal{A}_P\}$. Thus, two-electron integrals in the AO basis need to be calculated for atoms in the $\{\mathcal{A}_P\}$ space.

The FOI space in eq 42 is the difference between the space for the third iteration amplitudes in eq 41 and the second iteration amplitudes in eq 37. The t^3 amplitudes referencing only the indices $a \in [\bar{P}]_2 - [\bar{P}]$ and $b \in [\bar{Q}]_2 - [\bar{Q}]$ of the FOI space are small because the residuals in eq 38 have no integral contribution, while the amplitudes referencing the indices $i \in [\underline{P}] - \underline{P}$ and $j \in [\underline{Q}] - \underline{Q}$ of the FOI space may be of the same size as the amplitudes of the first iteration because the residual had an integral contribution.

Using a similar analysis for the fourth iteration, nonvanishing amplitudes may be obtained for the orbital space:

$$t_{ij}^{4,ab} : i \in [\underline{P}]_2, a \in [\bar{P}]_3, j \in [\underline{Q}]_2, b \in [\bar{Q}]_3 \quad (43)$$

Iteration three thus introduces a second-order interaction (SOI) space relative to the EOS containing the amplitudes:

$$t_{ij}^{4,ab} : i \in [\underline{P}]_2 - [\underline{P}], a \in [\bar{P}]_3 - [\bar{P}]_2, j \in [\underline{Q}]_2 - [\underline{Q}], b \in [\bar{Q}]_3 - [\bar{Q}]_2 \quad (44)$$

The SOI space is the difference between the spaces in eqs 43 (iteration four) and 41 (iteration three). The SOI space does not interact directly with the amplitudes of the EOS, and its effect on the residual of the EOS is therefore small, in particular for the interaction, which goes through the virtual FOI space, where the amplitudes are small. The effect of the SOI space on the amplitudes of the EOS can therefore in most cases be neglected. Continuing the iteration procedure leads to fast convergence of the amplitudes for the EOS, and the effect of new orbital spaces on the amplitudes of the EOS becomes insignificant.

The above development can be used to set up orbital spaces for the calculations which determine the amplitudes that are used for evaluating E_P and E_{PQ} . For E_P (corresponding to $P = Q$ in the above analysis) the amplitudes of eq 10 are required, and the orbital space therefore has to include the atomic fragment EOS $\mathcal{E}_P : ij \in \underline{P}$ and $a, b \in [\bar{P}]$. Iteration two shows that the EOS interacts directly with the FOI space in eq 42. This interaction can be taken into account by introducing buffer spaces for the occupied ($\mathcal{B}_P = [\underline{P}] - \underline{P}$) and for the unoccupied ($\mathcal{B}_{\bar{P}} = [\bar{P}]_2 - [\bar{P}]$) orbital spaces. The orbital space \mathcal{A}_P which is used for solving the amplitude equations required to determine E_P therefore becomes

$$\mathcal{A}_P = \underline{P} + [\bar{P}] + \mathcal{B}_{\underline{P}} + \mathcal{B}_{\bar{P}} \quad (45)$$

where the two first terms denote the spaces involved directly in the calculation of E_P (i.e., the atomic fragment EOS \mathcal{E}_P , see eq 8). The last two terms contain the amplitudes outside this space, which are necessary for determining the EOS amplitudes with high precision due to coupling of the amplitudes. The orbital space defined by eq 45 will be denoted the amplitude orbital space (AOS) of an atomic fragment calculation. In general, the indirect interactions on the residual of the EOS introduced in the third and higher iterations may be considered by having flexible buffer spaces, where the buffer spaces are extended until the atomic fragment energy is unaffected by further extensions. The determination of the sizes of the fragment spaces will be detailed in Section 6.2. An illustration of the orbital spaces that are in use when the atomic fragment energy E_P is evaluated is displayed in Figure 2 for a one-dimensional system. The $\{\mathcal{A}_P\}$ space will be discussed in Section 6.1.

For E_{PQ} we need the amplitudes of eq 11. The orbital space therefore has to include the atomic pair fragment EOS $\mathcal{E}_{PQ} : ij \in \underline{P} \cup \underline{Q}$ and $a, b \in [\bar{P}] \cup [\bar{Q}]$. The FOI space introduces the occupied buffer

$$\mathcal{B}_{\underline{PQ}} = [\underline{P} \cup \underline{Q}] - \underline{P} \cup \underline{Q}$$

and the unoccupied buffer

$$\mathcal{B}_{\bar{PQ}} = [\bar{P}]_2 \cup [\bar{Q}]_2 - [\bar{P}] \cup [\bar{Q}]$$

orbital spaces, and the indirect interaction to the SOI and the higher order spaces is considered using the union of buffer orbital spaces for evaluating E_P and E_Q . The atomic pair fragment AOS used for evaluating E_{PQ} therefore becomes

$$\begin{aligned} \mathcal{A}_{PQ} &= \mathcal{A}_P \cup \mathcal{A}_Q \\ &= \underline{P} \cup \underline{Q} + [\bar{P}] \cup [\bar{Q}] + \mathcal{B}_{\underline{PQ}} + \mathcal{B}_{\bar{PQ}} \end{aligned} \quad (46)$$

where the two first terms denote the spaces required for determining the atomic pair fragment energy, see eq 9, and the last two terms are the occupied and virtual buffer spaces. The orbital spaces used for the atomic pair fragment PQ calculation are thus formed as unions of orbital spaces for atomic fragments P and Q . The locality of a DEC pair fragment calculation is therefore determined by the orbital spaces that are obtained in the atomic fragment calculations.

3.3. Summary of MP2 Locality Analysis. Using an iterative algorithm analysis we have shown that the equations for the EOS amplitudes required to determine E_P and E_{PQ} in eqs 8 and 9 may be solved in small fragment orbital spaces (see eqs 45 and 46). The analysis thus demonstrates that locality may be exploited to divide a full MP2 calculation into small orbital fragment calculations, which may be carried out independently. The locality of an MP2 calculation is determined by the locality of the atomic fragment calculations, while the atomic pair fragment energies are obtained from calculations involving the union of spaces for the corresponding atomic fragment calculations. The optimal sizes of the fragment orbital spaces, i.e., $[\bar{P}]$, \mathcal{B}_P , and $\mathcal{B}_{\bar{P}}$, are of course not known a priori. In Section 6.2 we discuss how these spaces are determined in a DEC calculation.

4. DEC-CCSD AMPLITUDE EQUATIONS

4.1. CCSD Amplitude Equations. We now consider the amplitude equations for the CCSD model for a closed-shell molecule. Following the notation of ref 33, the cluster amplitudes are obtained by solving the cluster amplitude equations:

$$\Omega_{ai} = \left\langle \bar{a}_i \left| \exp(-\hat{T}_2) \hat{H} \exp(\hat{T}_2) \right| \text{HF} \right\rangle = 0 \quad (47)$$

and

$$\Omega_{aij} = \left\langle \bar{ab}_{ij} \left| \exp(-\hat{T}_2) \hat{H} \exp(\hat{T}_2) \right| \text{HF} \right\rangle = 0 \quad (48)$$

where $\langle \bar{a}_i |$ and $\langle \bar{ab}_{ij} |$ are single and double bra states in the biorthonormal basis. The cluster doubles operator \hat{T}_2 is given in eq 14, and the singles operator \hat{T}_1 is given as

$$\hat{T}_1 = \sum_{ai} t_i^a E_{ai} \quad (49)$$

\hat{H} refers to the \hat{T}_1 transformed Hamiltonian:

$$\begin{aligned} \hat{H} &= \exp(-\hat{T}_1) \hat{H} \exp(\hat{T}_1) \\ &= \hat{H}_1 + \hat{H}_2 = \sum_{rs} \tilde{h}_{rs} E_{rs} + \frac{1}{2} \sum_{rstu} \tilde{g}_{rstu} (E_{rs} E_{tu} - \delta_{st} E_{ru}) \end{aligned} \quad (50)$$

Above we have introduced the \hat{T}_1 transformed integrals:

$$\tilde{h}_{rs} = \sum_{\mu\nu} X_{\mu r} Y_{\nu s} h_{\mu\nu}, \quad (51)$$

$$\tilde{g}_{pqrs} = \sum_{\mu\nu\sigma\omega} X_{\mu p} X_{\sigma r} Y_{\nu q} Y_{\omega s} g_{\mu\nu\sigma\omega}, \quad (52)$$

where the transformation matrices \mathbf{X} and \mathbf{Y} are defined as

$$\mathbf{X} = \mathbf{C}(1 - \mathbf{t}_1^T) \quad (53)$$

and

$$\mathbf{Y} = \mathbf{C}(1 + \mathbf{t}_1) \quad (54)$$

where \mathbf{C} is the transformation matrix from the AO basis to the local HF basis.

Table 2. Explicit Form of the CCSD Singles and Doubles Equations

contributions to singles residual	
Ω_{ai}^{A1}	$= \sum_{ckd} t_{ki}^{cd} \tilde{g}_{adkc}$
Ω_{ai}^{B1}	$= -\sum_{ckl} t_{kl}^{ac} \tilde{g}_{kila}$
Ω_{ai}^{C1}	$= \sum_{ck} {}^I \tilde{F}_{kc} t_{ik}^{ac}$
Ω_{ai}^{D1}	$= {}^I \tilde{F}_{ai}$
contribution to doubles residual	
Ω_{aij}^{A2}	$= \tilde{g}_{aijb} + \sum_{cd} t_{ij}^{cd} \tilde{g}_{acbd}$
Ω_{aij}^{B2}	$= \sum_{kl} t_{kl}^{ab} (\tilde{g}_{klaj} + \sum_{cd} t_{ij}^{cd} \tilde{g}_{kcdl})$
Ω_{aij}^{C2}	$= -\frac{1}{2} \sum_{ck} t_{kj}^{bc} \left(\tilde{g}_{kiac} - \frac{1}{2} \sum_{dl} t_{li}^{ad} \tilde{g}_{kald} \right) - \sum_{ck} t_{ki}^{bc} \left(\tilde{g}_{kjac} - \frac{1}{2} \sum_{dl} t_{ij}^{ad} \tilde{g}_{kdcl} \right)$
Ω_{aij}^{D2}	$= \frac{1}{2} \sum_{ck} t_{jk}^{bc} \left(\tilde{L}_{aikc} + \frac{1}{2} \sum_{dl} t_{il}^{ad} \tilde{L}_{ldkc} \right)$
Ω_{aij}^{E2}	$= \sum_c t_{ij}^{ac} ({}^I \tilde{F}_{bc} - \sum_{dkl} t_{kl}^{bd} \tilde{g}_{ldkc}) - \sum_k t_{ik}^{ab} ({}^I \tilde{F}_{kj} + \sum_{cdl} t_{ij}^{cd} \tilde{g}_{kdcl})$
defined intermediates	
u_{ij}^{ab}	$= 2t_{ij}^{ab} - t_{ji}^{ab}$
\tilde{L}_{pqrs}	$= 2\tilde{g}_{pqrs} - \tilde{g}_{psrq}$
${}^I \tilde{F}_{rs}$	$= \tilde{h}_{rs} + \sum_i (2\tilde{g}_{rsii} - \tilde{g}_{riis})$

The CCSD amplitude equations in eqs 47 and 48 may be expressed in terms of the \hat{T}_1 transformed integrals as

$$\Omega_{ai}^{\text{CCSD}} = \Omega_{ai}^{A1} + \Omega_{ai}^{B1} + \Omega_{ai}^{C1} + \Omega_{ai}^{D1} = 0 \quad (55)$$

and

$$\Omega_{aij}^{\text{CCSD}} = \Omega_{aij}^{A2} + \Omega_{aij}^{B2} + P_{ij}^{ab} (\Omega_{aij}^{C2} + \Omega_{aij}^{D2} + \Omega_{aij}^{E2}) = 0 \quad (56)$$

where the explicit expressions for the individual terms in eqs 55 and 56 are given in Table 2, and where the P_{ij}^{ab} operator carries out the following permutation of pair indices:

$$P_{ij}^{ab} A_{ij}^{ab} = A_{ij}^{ab} + A_{ji}^{ba} \quad (57)$$

The amplitude equations in eqs 55 and 56 constitute a set of nonlinear equations.

4.2. CCSD Amplitude Equations for Local HF Orbitals. We will now examine the locality of the CCSD amplitude equations in eqs 55 and 56. The CCSD amplitude equations are expressed in terms of \hat{T}_1 transformed integrals, which are defined in terms of the transformation matrices in eqs 53 and 54 involving the singles amplitudes. The singles amplitudes are small, and initially we ignore these amplitudes in the locality analysis. The CCSD amplitude equations in eqs 55 and 56 will thus be viewed as referencing conventional integrals in the local HF basis. Of course, when atomic fragment and atomic pair fragment energies are determined the \hat{T}_1 transformed integrals have to be considered. We elaborate on this point in Section 4.2.3 below.

A Møller–Plesset perturbation analysis shows that through first order in the fluctuation potential the singles equation vanishes and the doubles equation reduces to the MP2 amplitude equation in eq 17 (the first term in Ω_{aij}^{A2} and the terms containing the Fock

Table 3. Locality Restrictions on the Summation Indices in the CCSD Equations^a

contributions to singles residual	
$\Omega_{ai}^{A1} = 2\sum_{ckd} t_{ki}^{cd} g_{adkc} - \sum_{ckd} t_{ik}^{cd} g_{adkc}$	$a \in [\bar{P}]_2, c \in [\bar{R}], d \in [\bar{P}], k \in R; a \in [\bar{P}]_4, c \in [\bar{P}], d \in [\bar{P}]_3, k \in [\underline{P}]_2$
$\Omega_{ai}^{B1} = -2\sum_{ckl} t_{ki}^{cl} g_{kilc} + \sum_{ckl} t_{ik}^{cl} g_{kilc}$	$a \in [\bar{P}]_2, c \in [\bar{R}], l \in R, k \in [\underline{P}]; a \in [\bar{P}]_4, c \in [\bar{P}]_2, k \in [\underline{P}], l \in [\underline{P}]_3$
$\Omega_{ai}^{C1} = 2\sum_{ck} t_{ki}^{ac} \tilde{F}_{ck} - \sum_{ck} t_{ik}^{ac} \tilde{F}_{ck}$	$a \in [\bar{P}], c \in [\bar{R}], k \in R; a \in [\bar{P}]_3, c \in [\bar{P}], k \in [\underline{P}]_2$
$\Omega_{ai}^{D1} = t_{ai}^{\tilde{F}}$	$a \in [\bar{P}]$
contributions to doubles residual	
$\Omega_{aijb}^{A2} = \tilde{g}_{aijb} + \sum_{cd} t_{ij}^{cd} g_{acbd}$	$a \in [\bar{P}], b \in [\underline{Q}]; a \in [\bar{P}]_2, b \in [\underline{Q}]_2, c \in [\bar{P}], d \in [\underline{Q}]$
$\Omega_{aijb}^{B2} = \sum_{kl} t_{ij}^{ab} g_{klij} + \sum_{kl} t_{ij}^{ab} \sum_{cd} t_{cd}^{ij} g_{ckld}$	$a \in [\bar{P}]_2, b \in [\underline{Q}]_2, k \in [\underline{P}], l \in [\underline{Q}]; a \in [\bar{P}]_3, b \in [\underline{Q}]_3, c \in [\bar{P}], d \in [\underline{Q}], k \in [\underline{P}]_2, l \in [\underline{Q}]_2$
$\Omega_{aijb}^{C2} = -(1/2)\sum_{ck} t_{kj}^{bc} g_{kiaac} + 1/4\sum_{ck} t_{kj}^{bc} \sum_{ad} t_{li}^{ad} g_{kdalc} - \sum_{ck} t_{kj}^{bc} g_{kjac} + 1/2\sum_{ck} t_{kj}^{bc} \sum_{ad} t_{li}^{ad} g_{kdalc}$	$a \in [\underline{Q}]_2, b \in [\bar{P}]_2, c \in [\underline{Q}], k \in [\underline{P}]; a \in [\underline{Q}]_3, b \in [\bar{P}]_3, c \in [\underline{Q}], d \in [\bar{P}], k \in [\underline{P}]_2, l \in [\underline{Q}]_2; a \in [\bar{P}]_2, b \in [\underline{Q}]_2, c \in [\bar{P}], k \in [\underline{Q}], b \in [\underline{Q}]_3, c \in [\bar{P}], d \in [\underline{Q}], k \in [\underline{Q}]_2, l \in [\underline{P}]_2$
$\Omega_{aijb}^{D2} = 2\sum_{ck} t_{kj}^{bc} g_{aick} - \sum_{ck} t_{kj}^{bc} g_{acki} - \sum_{ck} t_{kj}^{bc} g_{aick} + 1/2\sum_{ck} t_{kj}^{bc} g_{acki} + 2\sum_{ck} t_{kj}^{bc} \sum_{ad} t_{li}^{ad} g_{ldack} - \sum_{ck} t_{kj}^{bc} \sum_{ad} t_{li}^{ad} g_{ldack} - \sum_{ck} t_{kj}^{bc} \sum_{ad} t_{li}^{ad} g_{ldack} + 1/2\sum_{ck} t_{kj}^{bc} \sum_{ad} t_{li}^{ad} g_{ldack} - \sum_{ck} t_{kj}^{bc} \sum_{ad} t_{li}^{ad} g_{ldack} + 1/2\sum_{ck} t_{kj}^{bc} \sum_{ad} t_{li}^{ad} g_{ldack} + 1/2\sum_{ck} t_{kj}^{bc} \sum_{ad} t_{li}^{ad} g_{ldack} - 1/4\sum_{ck} t_{kj}^{bc} \sum_{ad} t_{li}^{ad} g_{ldack}$	$a \in [\bar{P}], b \in [\underline{Q}], c \in [\bar{R}], k \in R; a \in [\bar{P}]_3, b \in [\underline{Q}], c \in [\bar{P}]_2, k \in [\underline{P}]; a \in [\bar{P}], b \in [\underline{Q}]_3, c \in [\underline{Q}], k \in [\underline{Q}]_2; a \in [\underline{Q}]_2, b \in [\bar{P}]_2, c \in [\underline{Q}], k \in [\underline{P}]; a \in [\bar{P}], b \in [\underline{Q}], c \in [\bar{R}], d \in [\underline{S}], k \in R, l \in S; a \in [\bar{P}], b \in [\underline{Q}], c \in [\bar{R}], k \in R, l \in [\underline{R}]_2, d \in [\bar{R}]; a \in [\bar{P}]_3, b \in [\underline{Q}], c \in [\bar{R}], d \in [\bar{P}], k \in R, l \in [\underline{P}]_2; a \in [\bar{P}]_3, b \in [\underline{Q}], c \in [\bar{P}]_3, d \in [\bar{P}], k \in [\underline{P}]_2, l \in [\underline{P}]_4; a \in [\bar{P}], b \in [\underline{Q}]_3, c \in [\underline{Q}], d \in [\bar{R}], k \in [\underline{Q}]_2, l \in R; a \in [\bar{P}], b \in [\underline{Q}]_3, c \in [\underline{Q}], d \in [\underline{Q}]_3, k \in [\underline{Q}]_4, l \in [\underline{Q}]_2; a \in [\bar{P}]_3, b \in [\underline{Q}]_3, c \in [\underline{Q}], d \in [\bar{P}], k \in [\underline{Q}]_2, l \in [\underline{P}]_2; a \in [\underline{Q}]_3, b \in [\bar{P}]_3, c \in [\underline{Q}], d \in [\bar{P}], k \in [\underline{P}]_2, l \in [\underline{Q}]_2$
$\Omega_{aijb}^{E2} = +\sum_{ck} t_{ij}^{ac} \tilde{F}_{bc} - \sum_{ck} t_{ij}^{ac} \tilde{F}_{bc} - 2\sum_{ck} t_{ij}^{ac} \sum_{dl} t_{kl}^{bd} g_{ldack} + \sum_{ck} t_{ij}^{ac} \sum_{dl} t_{kl}^{bd} g_{ldack} - 2\sum_{ck} t_{ij}^{ac} \sum_{dl} t_{kl}^{bd} g_{ldack} + \sum_{ck} t_{ij}^{ac} \sum_{dl} t_{kl}^{bd} g_{ldack}$	$a \in [\bar{P}], b \in [\underline{Q}]_2, c \in [\underline{Q}]; a \in [\bar{P}], b \in [\underline{Q}]_2, k \in [\underline{Q}]; a \in [\bar{P}], b \in [\underline{Q}]_3, c \in [\underline{Q}], d \in [\bar{R}], k \in [\underline{Q}]_2, l \in R; a \in [\bar{P}], b \in [\underline{Q}]_3, c \in [\underline{Q}], d \in [\underline{Q}]_3, k \in [\underline{Q}]_2, l \in [\underline{Q}]_4; a \in [\bar{P}], b \in [\underline{Q}]_3, c \in [\bar{R}], d \in [\underline{Q}], k \in [\underline{Q}]_2, l \in R; a \in [\bar{P}], b \in [\underline{Q}]_3, c \in [\underline{Q}], d \in [\underline{Q}]_3, k \in [\underline{Q}]_4, l \in [\underline{Q}]_2$

^a More precisely, the locality restrictions refer to the second CCSD iteration, but for clarity, the iteration number has been omitted from the amplitudes. In all terms it is assumed that $i \in \underline{P}$ and $j \in \underline{Q}$ and the remaining index restrictions have been derived based on this assumption. In some terms the k and l indices belong to general atomic sites R and S . However, R and S may also be restricted to indices local to P and Q without introducing significant errors, see the discussion in the text. In this way all terms may be evaluated in a local fragment orbital space. The locality constraints referencing different terms are separated by semicolons.

matrix in Ω^{E2} , see Table 2). Neglecting the second and higher order CCSD terms in the amplitude equations in eqs 55 and 56, the CCSD amplitude equations become identical to the MP2 amplitude equations, and these terms will therefore have the locality of the MP2 equations. In the following we examine how the second and higher order CCSD terms affect the locality of the MP2 amplitude equations, which was discussed in Section 3.

The first MP2 iteration determines the cluster amplitudes of the EOS: $i \in \underline{P}$, $a \in [\bar{P}]$, $j \in \underline{Q}$, $b \in [\underline{Q}]$. These amplitudes are used in the second iteration to determine the residual $R_{aijb}^{2,MP2}(t^2)$ in eq 38 and to identify the FOI space. We now discuss the extensions of the FOI space that are required when the second and higher order terms in the CCSD amplitude equations are added to the MP2 residual $R_{aijb}^{2,MP2}(t^2)$ in eq 38. In short, we examine the nonvanishing contributions to the residual, which originate from the second and higher order terms in $\Omega_{ai}^{CCSD}(t^2)$ and $\Omega_{aijb}^{CCSD}(t^2)$.

Using the locality restrictions for t_{ij}^{ab} in eq 37 as a starting point, we may carry out a locality analysis for the CCSD equations in a similar manner as was done for the MP2 equations in Section 3. The results are summarized in Table 3, where for simplicity the iteration number for t^2 has been omitted from the amplitudes. From a locality perspective the residual terms in Table 3 can be divided into three types:

- Type 1: Terms where the locality is straightforwardly accounted for through the locality of the MP2 equations. These terms involve only P and possibly Q sites in Table 3.
- Type 2: Terms where the locality is accounted for through the locality in the MP2 equation but where the terms

contain summation indices referencing contributions that are long ranged. These are terms involving other sites than P and Q in Table 3, i.e., sites R and possibly also S . The long-ranged decay, however, does not follow the behavior of a Coulombic potential, which decays with inverse distance between the atomic sites P and R and between atomic sites Q and R . Rather it follows an inverse cubed distance behavior as we discuss in more detail below.

- Type 3: Terms involving the \hat{T}_1 transformed Fock matrix \tilde{F} .
- 4.2.1. *Type 1 Terms.* These terms include most of the second and higher order terms in eqs 55 and 56. An example is the second term in $\Omega^{A2} (\sum_{cd} t_{ij}^{cd} g_{acbd})$ which may be expressed as

$$t_{ij}^{ab} = \sum_{c \in [\bar{P}], d \in [\underline{Q}]} t_{ij}^{cd} g_{acbd}; \quad i \in \underline{P}, j \in \underline{Q}, a \in [\bar{P}]_2, b \in [\underline{Q}]_2 \quad (58)$$

To obtain eq 58 the summation indices have been restricted to $c \in [\bar{P}]$, $d \in [\underline{Q}]$ using eq 37 and a nonvanishing integral \tilde{g}_{acbd} then implies that $a \in [\bar{P}]_2$ and $b \in [\underline{Q}]_2$. The locality analysis for the MP2 amplitude equations ensures that this term is properly treated.

For some terms of type 1 the coupling to neighboring sites is more extensive than for MP2, e.g., for the second term in B2 where $a \in [\bar{P}]_3$ and $b \in [\underline{Q}]_3$. However for this term the more extensive coupling is due to a term that is of third order in Møller–Plesset perturbation theory and therefore has a very small effect on the solution of the amplitude equations in the

EOS. If it does have a nonvanishing effect, then it is taken into account through our way of determining orbital buffer spaces.

4.2.2. Type 2 Terms. An example of these terms is the first term in Ω^{D2} ($1/2\sum_{ck}t_{jk}^{bc}\tilde{L}_{aikc}$) which has a contribution:

$$J_{ij}^{ab} = \sum_R \sum_{c \in [\bar{R}], k \in \underline{R}} t_{jk}^{bc} g_{aikc}; \quad i \in \underline{P}, \quad j \in \underline{Q}, \quad a \in [\bar{P}], \quad b \in [\bar{Q}] \quad (59)$$

where the c summation has been restricted because \tilde{g}_{aikc} has to be nonvanishing. In principle, the R summation runs over all atomic sites, however, the integrals \tilde{g}_{aikc} and the amplitudes t_{jk}^{bc} both have a cubic decay with respect to the distance between the atomic sites P and R and between the atomic sites Q and R , respectively. The cubic decay of integrals and amplitudes is due to the fact that when a multipole expansion of the integral \tilde{g}_{aikc} is carried out, the monopole integral contribution vanishes.³⁴ This happens because the charge distributions carry no charge as the occupied, and virtual orbitals are orthogonal. Furthermore, we recall that this term is second order in the fluctuation potential and therefore not one of the main contributors to the total residual. For these reasons it is well-justified to restrict the R summation in eq 59 to include only atoms local to P and Q .

For other doubles amplitude terms in Table 3 (e.g., $2\sum_{ck}t_{jk}^{bc}\sum_{dl}t_{il}^{ad}\tilde{g}_{ldkc}$ in Ω^{D2}), the summations occur over two atomic sites R and S . The cubic decay of amplitudes and integrals and the fact that these terms are only third-order in the fluctuation potential justify that they can be evaluated within a local fragment orbital space.

For the singles amplitude contributions (e.g., $2\sum_{ckd}t_{ki}^{cd}\tilde{g}_{adkc}$ in Ω^{A1}) the integral only has a quadratic inverse decay because the $\phi_a\phi_d$ distribution does carry a charge. The t_{ki}^{cd} amplitudes, however, have cubic decay with respect to the distance between the charge distributions $\phi_k\phi_c$ and $\phi_l\phi_d$ due to orthogonality.

4.2.3. Type 3 Terms. When carrying out the fragment calculations the \hat{T}_1 -transformed Fock matrix ${}^1\tilde{F}$:

$${}^1\tilde{F}_{rs} = \tilde{h}_{rs} + \sum_i (2\tilde{g}_{rsii} - \tilde{g}_{riis}) \quad (60)$$

has long-range contributions as a result of the \hat{T}_1 transformation, see eqs 51 and 52.

When evaluating atomic fragment and atomic pair fragment energies we may introduce the following approximation to the \hat{T}_1 -transformed Fock matrix:

$${}^1\tilde{F}_{pq} \rightarrow {}^1\tilde{F}_{pq}^{\mathcal{L}} - {}^1F_{pq}^{\mathcal{L}} + {}^1F_{pq} \quad (61)$$

where ${}^1F_{pq}^{\mathcal{L}}$ is a nontransformed Fock matrix element referencing only the orbitals of the fragment orbital space, and ${}^1\tilde{F}_{pq}^{\mathcal{L}}$ is defined in the same way but with \hat{T}_1 -transformed integrals. Within this approximation we have thus only included the effect of the \hat{T}_1 transformation inside the fragment, whereas the polarization from orbitals outside the fragment orbital space has been neglected.

The solution to this problem is to save all singles amplitudes when carrying out the atomic fragment and the atomic pair fragment calculations for all fragments in the molecule. In this first calculation we use the Fock matrix in eq 61. After all fragment calculations have been carried out we may use the stored singles amplitudes to construct the fully \hat{T}_1 -transformed Fock matrix ${}^1\tilde{F}$, which include the polarization of all orbitals. A new calculation may then be carried out using the fully transformed Fock matrix instead of eq 61. In this second calculation the long-ranged polarization effects described by the singles amplitudes are treated to a high precision. An even more elaborate treatment of the singles polarization effect is to use eq 61,

where ${}^1F_{pq}$ and ${}^1F_{pq}^{\mathcal{L}}$ are replaced by the one-index transformed Fock matrix with t -amplitudes from the first calculation.

4.3. Summary of CCSD Locality Analysis. Even though the CCSD locality analysis is much more cumbersome than the corresponding analysis for MP2, our analysis shows that it is indeed possible to carry out a full CCSD calculation in terms of small independent fragment calculations. In other words, the analysis substantiates from a theoretical point of view that the CCSD fragment calculations may be carried out in orbital spaces of limited size. More precisely, all terms in the CCSD residual are local in the sense that the effects on the t_{ij}^{ab} amplitudes required for pair fragment PQ (i.e., $i \in \underline{P}$ and $j \in \underline{Q}$) rapidly decrease as the summation indices in the individual residual contributions move away from atomic sites P and Q . One should also keep in mind that the first-order residual terms (MP2) are the dominating ones, and the main effect of the second and higher order CCSD terms is to relax the amplitudes. The sizes of the EOSs will be similar for MP2 and CCSD, because they are basically obtained by requiring nonzero overlap distributions for the integrals entering the fragment energies, see eqs 8 and 9. However, the CCSD fragments will in general require larger buffer orbital spaces than MP2 fragments due to a more extensive coupling of amplitudes in CCSD.

The analysis above is carried out for an atomic pair fragment ($i \in \underline{P}$ and $j \in \underline{Q}$). It follows that for an atomic fragment (corresponding to $P = Q$) the effects of the CCSD residual contributions diminish with increasing distance between the atomic site P and the orbital summation indices in the CCSD residual. In an atomic fragment calculation, we gradually extend the orbital fragment sizes to include orbitals located still further away from atomic site P (to be detailed in Section 6.2). Since all contributions fall off rapidly with increasing distance to the P center, each step of the fragment expansion procedure will include orbitals with still smaller effects on the fragment energy. This orbital expansion procedure can therefore be repeated until the atomic fragment energy has been converged to a predefined threshold. Of course we do not know, for a given orbital space expansion, which of the individual CCSD residual terms have the largest effect on the atomic fragment energy, but the fragment expansion procedure ensures that the orbital spaces are large enough that only the truly small terms are neglected. If the optimal orbital spaces for atomic fragments P and Q have been determined, the analysis above then substantiates that the corresponding pair fragment PQ can be formed from the union of orbital spaces for P and Q .

5. COMPUTATIONAL SCALING IN DEC CC CALCULATIONS

Within the DEC model a CC calculation is carried out in terms of atomic fragment and atomic pair fragment calculations. The locality of the CC calculation is determined by the atomic fragment calculations. The sizes of the amplitude orbital spaces are determined in a black box manner in a way that ensures that the atomic fragment energies are calculated to a preset threshold. The orbital spaces employed for evaluating atomic pair fragment energies are determined as unions of the orbital spaces for the two atomic fragments involved.

Since the major task of a CC calculation is to describe short-ranged phenomena associated with Coulomb holes in the wave function and the dispersion effects, the fragment sizes are to a large extent system independent. The number of atomic fragments scales as the number of atoms in the molecular system, and the calculation of atomic fragment energies is therefore linearly scaling. The number of atomic pair fragment energies in eq 5 has a quadratic scaling with system size, but this scaling is reduced to linear for large systems

because the pair fragment calculations only need to be carried out for pair atomic distances, where the dispersion forces are non-negligible.

The DEC scheme is embarrassingly parallelizable. The evaluation of the atomic fragment energies may first be done independently; second the atomic pair fragment energies that are needed may also be calculated independently. Provided that a sufficient number of processors are available, the wall time for a parallelized correlated wave function calculation is therefore the sum of a single atomic fragment calculation and a single atomic pair fragment energy calculation, not considering the time for the initial HF calculation, whose efficient evaluation has been discussed previously, and may be done using a linear-scaling algorithm.^{35–38}

6. DETAILS ABOUT THE DEC MODEL

In Section 6.1 we discuss how to improve the locality of the molecular orbitals (MOs) used in a DEC fragment calculation. In Section 6.2 we discuss how the sizes of the EOS and AOS are determined. The fragment calculations are carried out as standard MP2 and CCSD calculations, as we detail in Section 6.3. In Section 6.4 we discuss how errors similar to basis set superposition errors (BSSE) may be avoided when calculating pair interaction energies ΔE_{PQ} . Finally, in Section 6.5 we summarize the various spaces employed in a DEC fragment calculation.

6.1. Defining Locality of MOs and Atomic Fragment Extents. Even though the LCM HF orbitals³⁰ are local, the orthonormal character of this basis causes small but nonvanishing coefficients on atoms located some distance away from the atomic site where the HF orbital was assigned. In this section we discuss how this tail region may be treated without considering explicitly the atomic sites at which the small expansion coefficients are situated. This development will be used to reduce the number of atomic sites where the atomic orbital integrals have to be evaluated.

A normalized HF orbital associated with atomic site P :

$$\varphi_r^P = \sum_{\mu} \chi_{\mu} c_{\mu r}^P \quad (62)$$

may be approximated in the following way:

$$\tilde{\varphi}_r^P = \sum_{\tilde{\mu}} \tilde{\chi}_{\tilde{\mu}} \tilde{c}_{\tilde{\mu} r}^P \quad (63)$$

where the $\tilde{\mu}$ -summation is restricted to atomic sites, which in some sense are neighboring the atomic site P (to be detailed below). For example, the tail region of φ_r^P may be excluded. The expansion coefficients of $\tilde{\varphi}_r^P$ may be determined from a least-squares fit of

$$f(\tilde{c}^P) = \|\tilde{\varphi}_r^P - \varphi_r^P\| \quad (64)$$

giving the expansion coefficients

$$\tilde{c}_{\tilde{\mu} r}^P = \sum_{\tilde{\nu} \eta} \tilde{S}_{\tilde{\mu} \tilde{\nu}}^{-1} \tilde{S}_{\tilde{\nu} \eta} c_{\eta r}^P \quad (65)$$

where the dimensions of the overlap matrices are defined by the restrictions that are imposed on the AO indices:

$$\tilde{S}_{\tilde{\mu} \tilde{\nu}} = \langle \tilde{\chi}_{\tilde{\mu}} | \tilde{\chi}_{\tilde{\nu}} \rangle \quad (66)$$

$$S_{\tilde{\nu} \eta} = \langle \tilde{\chi}_{\tilde{\nu}} | \chi_{\eta} \rangle \quad (67)$$

We note that an equation similar to eq 65 was also used by Usvyat and Schütz³⁹ for obtaining localized Wannier functions. We now discuss how the $\tilde{\mu}$ -summation in eq 63 may be restricted to exclude the tail region of atomic fragments. An HF orbital φ_r^P was assigned to atomic site P because its largest Mulliken charge was situated on

atomic site P . For φ_r^P all nonvanishing Mulliken charges may be determined and arranged in order of decreasing size to prioritize the importance of the atomic sites. We may then restrict $\tilde{\mu}$ to the atomic sites which have a Mulliken charge larger than a given threshold and determine the expansion coefficients $\tilde{c}_{\tilde{\mu} r}^P$ from eq 65. Using $(1 - \langle \tilde{\varphi}_r^P | \varphi_r^P \rangle)$ as a measure of the quality of the least-squares fit, we identify the largest Mulliken charge threshold for which

$$1 - \langle \tilde{\varphi}_r^P | \varphi_r^P \rangle = 1 - \sum_{\tilde{\mu} \tilde{\nu}} \tilde{c}_{\tilde{\mu} r}^P \tilde{S}_{\tilde{\mu} \tilde{\nu}} \tilde{c}_{\tilde{\nu} r}^P < \delta \quad (68)$$

where δ is a small prefixed number. The atomic sites defined by the Mulliken charge threshold determine the orbital extent of $\tilde{\varphi}_r^P$. The union of extents for all HF orbitals assigned to atomic site P is denoted the atomic extent $\{\mathcal{P}\}$. We note that a screening of atomic centers in accordance with eq 68 was used by Boughton and Pulay³² as a completeness criteria for the assignment of excitation spaces for the occupied HF orbitals.

When solving the amplitude equations for the atomic fragment P calculation we use the MOs in the AOS \mathcal{A}_P in eq 45. The MOs have expansion coefficients on atomic sites outside the \mathcal{A}_P space. The atomic sites, where atomic integrals have to be evaluated to ensure that the MO integrals in \mathcal{A}_P are properly evaluated, consist of the union of atomic extents for all atoms in \mathcal{A}_P . We denote this space the atomic fragment extent $\{\mathcal{A}_P\}$. If for example we consider the case where \mathcal{A}_P contains the atomic sites L, M, N, P, Q, and R, then

$$\{\mathcal{A}_P\} = \{\text{L}\} \cup \{\text{M}\} \cup \{\text{N}\} \cup \{\text{P}\} \cup \{\text{Q}\} \cup \{\text{R}\} \quad (69)$$

We have now defined the amplitude orbital space \mathcal{A}_P , where the amplitude calculation is carried out, and the atomic centers in terms of which the MOs are expanded $\{\mathcal{A}_P\}$. The MOs that are used in an atomic fragment calculation are then obtained from an expansion of the form

$$\tilde{\varphi}_r^X = \sum_{\tilde{\mu} \in \{\mathcal{A}_P\}} \tilde{\chi}_{\tilde{\mu}} \tilde{c}_{\tilde{\mu} r}^X; \quad (X \in \mathcal{A}_P) \quad (70)$$

where the summation is restricted to $\{\mathcal{A}_P\}$. The expansion coefficients in eq 70 may be determined from eq 65, giving the best uniform description of the MOs in \mathcal{A}_P confined to the space $\{\mathcal{A}_P\}$. The quality of the least-squares fit, which determine the MOs, depends on the parameter δ in eq 68. Reducing the size of δ will lead to an extension of $\{\mathcal{A}_P\}$ and thus a better least-squares fit.

We may also require that the approximated orbitals in eq 70 are normalized

$$\langle \tilde{\varphi}_r^X | \tilde{\varphi}_r^X \rangle = \sum_{\tilde{\mu} \tilde{\nu}} \tilde{c}_{\tilde{\mu} r}^X \tilde{S}_{\tilde{\mu} \tilde{\nu}} \tilde{c}_{\tilde{\nu} r}^X = 1 \quad (71)$$

by multiplying $\tilde{\varphi}_r^X$ by an appropriate constant such that eq 71 is satisfied.

We have now established the locality of an atomic fragment calculation in terms of the spaces \mathcal{A}_P and $\{\mathcal{A}_P\}$ and identified the MOs that should be used in the amplitude calculations. For clarity let us summarize the main steps for constructing the approximate MOs $\tilde{\varphi}$:

- Choose a δ value which is a measure of how much the approximated orbitals $\tilde{\varphi}$ deviate from the original orbitals φ .
- For each approximated orbital add atoms based on their Mulliken charge until eq 68 is satisfied. This newly generated list of atoms constitutes the orbital extent for each orbital.
- For each atom P construct the atomic extent as the union of orbital extents for all orbitals assigned to that atom.

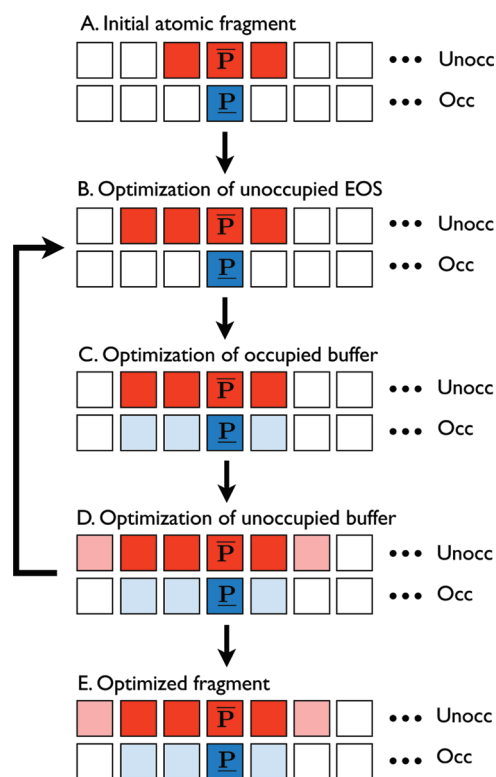


Figure 3. Main steps in the fragment optimization procedure. (A) Initially a starting guess is made for the size of the molecular fragment for evaluating E_P . The unoccupied energy orbital space (red) is then determined (B) followed by an optimization of the occupied (light blue) and unoccupied (pink) buffer spaces (C and D). It is then checked that the spaces are still optimal going through the steps in B–D again until the sizes of all spaces remain unchanged to yield the optimized fragment (E).

- Construct the atomic fragment extent $\{\mathcal{A}_P\}$ as the union of atomic extents for the atomic sites in \mathcal{A}_P .
- Determine the local MOs using eq 70, where the MO coefficients are determined from eq 65. Subsequently the MOs may be normalized by enforcing eq 71.

The above development may be viewed as an effective integral screening technique which allows atomic sites that reference small molecular orbital expansion coefficients to be removed from the atomic integral evaluation. The screening depends on the single parameter δ in eq 68.

6.2. Optimization of Fragment Orbital Spaces. An atomic fragment calculation for fragment P is carried out using the atomic fragment AOS \mathcal{A}_P in Figure 2, and the atomic fragment energy is calculated from the amplitudes referencing the atomic fragment EOS \mathcal{S}_P , i.e., \underline{P} and $[\overline{P}]$ for the occupied and unoccupied spaces, respectively. The orbital spaces $[\overline{P}]$, $\mathcal{B}_{\underline{P}}$, and $\mathcal{B}_{\overline{P}}$ are determined from a sequence of calculations, where the sizes of these spaces are gradually increased until the atomic fragment energy E_P in eq 8 is converged to a preset energy threshold. In Figure 3A–D we have illustrated how the unoccupied EOS $[\overline{P}]$ (red) and the buffer spaces $\mathcal{B}_{\underline{P}}$ (light blue) and $\mathcal{B}_{\overline{P}}$ (pink) may gradually be increased to ensure that E_P is determined to a preset energy tolerance, the fragment optimization threshold (FOT). When the change in the atomic fragment energy is larger than the FOT, the step is accepted, otherwise it is rejected. Continuing in this manner the cycle in

Figure 3B–D is repeated until we have carried through one full optimization round where the sizes of the unoccupied EOS, occupied buffer, and unoccupied buffer spaces all remain unchanged.

In practice the sizes of the unoccupied EOS, occupied buffer, and unoccupied buffer spaces are defined by three orbital space radii. For example, if the distance between atomic site P and an atomic site R is smaller than the unoccupied EOS radius for P , then the unoccupied orbitals assigned to R are included in the unoccupied EOS $[\overline{P}]$. The increment of orbital spaces may thus be controlled by adding a fixed orbital space step size parameter to the existing orbital space radii.

The atomic pair fragment orbital space for evaluating E_{PQ} is formed as the union of the atomic fragment orbital spaces for evaluating E_P and E_Q . The locality analysis in Sections 3.2 and 4.2 substantiates that it is not necessary to carry out additional fragment size optimizations for the combined PQ space, as the locality is defined by the atomic fragment calculations on P and Q . The numerical results presented in Section 7 also support this.

The fragment optimization procedure discussed above applies both to MP2 and CCSD fragment calculations. In a CCSD calculation we may take advantage of the fact that the locality of the CCSD amplitude equations is similar to the one for MP2 equations, except for a more extensive coupling among the amplitudes. Therefore the optimized MP2 fragment spaces serve as good starting guesses for the optimal CCSD fragment orbital spaces.

6.3. CC Calculations on Atomic Fragments and Atomic Pair Fragments. The MP2 and CCSD atomic fragment and atomic pair fragment calculations are carried out as standard MP2 and CCSD calculations using the local HF orbitals and the atomic fragment or atomic pair fragment orbital spaces. The MP2 amplitude equations constitute a set of linear equations with a symmetric matrix and are solved using the conjugate residual with optimal trial vectors (CROP) algorithm, where only the last three trial vectors need to be stored to maintain the information content of all previous trial vectors (see ref 40). For CCSD we solve nonlinear amplitude equations using the CROP algorithm. The nonlinearity of the CCSD amplitude equations generally requires more than three trial vectors to be stored.⁴⁰

6.4. Avoiding Wave Function Superposition Problems in Pair Energy Calculations. The calculation of pair interaction energies requires special attention because the equations presented in Section 2.2 may be subject to errors which are similar to BSSE. We now demonstrate how this problem may easily be circumvented.

The nontruncated expression for the pair interaction energy is given in eq 6:

$$\begin{aligned} \Delta E_{PQ} &= E_{PQ} - E_P - E_Q \\ &= \sum_{\substack{ij \in \underline{P} \cup \underline{Q} \\ ab}} (t_{ij}^{ab} + t_i^a t_j^b) (2g_{iajb} - g_{ibja}) \\ &\quad - \sum_{\substack{ij \in \underline{P} \\ ab}} (t_{ij}^{ab} + t_i^a t_j^b) (2g_{iajb} - g_{ibja}) \\ &\quad - \sum_{\substack{ij \in \underline{Q} \\ ab}} (t_{ij}^{ab} + t_i^a t_j^b) (2g_{iajb} - g_{ibja}) \end{aligned} \quad (72)$$

where we have inserted the expressions for the atomic fragment and the atomic pair fragment energies in eqs 3 and 4. No approximations have been introduced in eq 72 since the virtual summation indices run over the full molecular system.

In DEC fragment calculations we may evaluate ΔE_{PQ} in two different ways: (i) the simple approach or (ii) the counterpoise-corrected approach.

For case (i) we simply insert the approximate expressions for E_P , E_Q , and E_{PQ} in eqs 8 and 9 into eq 6:

$$\begin{aligned} \Delta E_{PQ} &= E_{PQ} - E_P - E_Q \\ &= \sum_{\substack{ij \in \underline{P} \cup \underline{Q} \\ ab \in [\overline{P}] \cup [\overline{Q}]}} (t_{PQ,ij}^{ab} + t_{PQ,i}^a t_{PQ,j}^b) (2g_{iajb} - g_{ibja}) \\ &\quad - \sum_{\substack{ij \in \underline{P} \\ ab \in [\overline{P}]}} (t_{P,ij}^{ab} + t_{P,i}^a t_{P,j}^b) (2g_{iajb} - g_{ibja}) \\ &\quad - \sum_{\substack{ij \in \underline{Q} \\ ab \in [\overline{Q}]}} (t_{Q,ij}^{ab} + t_{Q,i}^a t_{Q,j}^b) (2g_{iajb} - g_{ibja}) \quad (73) \end{aligned}$$

where we have added P , Q , and PQ subscripts to emphasize which fragment space is used for determining the amplitudes. The problem with eq 73 is that the amplitudes used for determining E_P , E_Q and E_{PQ} are obtained from fragment calculations in different AOSs, i.e., \mathcal{A}_P , \mathcal{A}_Q and $\mathcal{A}_{PQ} = \mathcal{A}_P \cup \mathcal{A}_Q$. The orbital space employed for the atomic pair fragment PQ calculation is thus larger than the orbital spaces used for the P and Q atomic fragment calculations. This means that the amplitudes used to determine E_{PQ} are determined slightly more accurately than the amplitudes used to determine E_P and E_Q , and therefore BSSE-like errors will be introduced when the pair interaction energy is calculated according to eq 73.

For case (ii), to avoid BSSE-like errors, we may calculate a counterpoise-corrected pair interaction energy by using only amplitudes from the pair fragment calculation and letting all virtual summations run over the unoccupied EOS in the pair fragment:

$$\begin{aligned} \Delta E_{PQ} &= \sum_{\substack{ij \in \underline{P} \cup \underline{Q} \\ ab \in [\overline{P}] \cup [\overline{Q}]}} (t_{PQ,ij}^{ab} + t_{PQ,i}^a t_{PQ,j}^b) (2g_{iajb} - g_{ibja}) \\ &\quad - \sum_{\substack{ij \in \underline{P} \\ ab \in [\overline{P}] \cup [\overline{Q}]}} (t_{PQ,ij}^{ab} + t_{PQ,i}^a t_{PQ,j}^b) (2g_{iajb} - g_{ibja}) \\ &\quad - \sum_{\substack{ij \in \underline{Q} \\ ab \in [\overline{P}] \cup [\overline{Q}]}} (t_{PQ,ij}^{ab} + t_{PQ,i}^a t_{PQ,j}^b) (2g_{iajb} - g_{ibja}) \quad (74) \end{aligned}$$

We thereby determine ΔE_{PQ} in line with a counterpoise-corrected interaction energy.

6.5. Overview of the Spaces Employed in a DEC Calculation. It is now in place to summarize the various spaces employed in the atomic fragment and atomic pair fragment calculations.

In Table 1 we summarize the notation used for the various energies and orbital spaces used in a DEC calculation, while Figure 2 gives an illustrative overview of the orbital spaces used in an atomic fragment calculation. The amplitude equation for atomic fragment P is solved for MOs assigned to atoms in the AOS \mathcal{A}_P in eq 45, and the fragment energy E_P is calculated using only the EOS orbitals, see eq 8. \mathcal{E}_P and \mathcal{A}_P are optimized during the calculation as discussed in Section 6.2. The MOs in atomic fragment P have nonvanishing expansion coefficients only for the atomic sites in the $\{\mathcal{A}_P\}$ space. Thus, when solving the amplitude equations in the \mathcal{A}_P space, we need two-electron integrals in the AO basis for atomic sites in the $\{\mathcal{A}_P\}$ space to properly describe the necessary MO integrals.

For the atomic pair fragment calculations we employ the union of spaces from the atomic fragment calculations as discussed in Section 3.2. The amplitude equations are solved using the $\mathcal{A}_P \cup \mathcal{A}_Q$ AOS space, and the pair interaction energy ΔE_{PQ} is calculated in the $\mathcal{E}_P \cup \mathcal{E}_Q$ EOS space as described in Section 6.4. The MOs are expanded in terms of atoms in the $\{\mathcal{A}_P\} \cup \{\mathcal{A}_Q\}$ space, and two-electron integrals in the AO basis are therefore calculated in that space.

7. ILLUSTRATIVE RESULTS

In Section 7.1 we present calculations demonstrating that the total MP2 and CCSD correlation energies may be determined from DEC fragment calculations with control of the errors introduced compared to a full molecular calculation. In Section 7.2 we show that the fragment sizes and the relative energy errors in DEC-MP2 calculations are independent of the size of the molecular system.

7.1. DEC-MP2 and DEC-CCSD Calculations on $C_{14}H_2$. Using the $C_{14}H_2$ molecule as a test system we now compare DEC-MP2 and DEC-CCSD calculations to full molecular MP2 and CCSD calculations. We first discuss the assignment of orbitals in Section 7.1.1. In Section 7.1.2 we discuss the energy errors compared to a full molecular calculation as a function of the FOT. We demonstrate the importance of using counterpoise-corrected pair interaction energies in Section 7.1.3, and in Section 7.1.4 we discuss the sizes of the orbital spaces employed. Finally, in Section 7.1.5 we show that the total correlation energy is very insensitive to the choice of δ parameter. For the calculations in Sections 7.1.2–7.1.4 we have used $\delta = 0.01$ and imposed the normalization condition in eq 71. Furthermore, we have used orbital space step size parameters of 3.0 au for all orbital spaces (see Section 6.2),

7.1.1. Assignment of Orbitals. The number of occupied and virtual orbitals assigned to each atomic site in the $C_{14}H_2$ molecule are given in Figure 1B. The virtual orbitals are evenly distributed among the different atomic sites, while the distribution is less even for the occupied orbitals. The hydrogen atoms in general have no occupied orbitals assigned, whereas the carbon atoms have between two and four occupied orbitals assigned. This orbital partitioning may seem counterintuitive as we are considering a highly symmetric molecule. It is, however, not surprising, because the LCM orbitals do not reflect the molecular point group symmetry and are simply assigned to atoms based on the largest Mulliken charge. Therefore, if for a given molecular orbital two atoms have roughly the same Mulliken charge, then

the assignment of that orbital is quite arbitrary. However, the precise assignment does not affect the total correlation energy. The DEC algorithm automatically adjusts the size of the virtual orbital space for an uneven assignment of occupied orbitals through the way orbital spaces are selected (see Figure 3). For example, in Figure 1B, a carbon atom with four occupied orbitals assigned will, in general, require a larger virtual orbital space than a carbon atom with only two occupied orbitals assigned.

7.1.2. Energy Errors. In Table 4 we have listed the total energy errors (fourth column) compared to a full molecular calculation for various FOTs for MP2 and CCSD. It is seen that in general the errors decrease by an order of magnitude when the FOT is lowered by an order of magnitude, even though some deviance from this general result is observed for CCSD (to be explained below).

The second and third columns in Table 4 contain the sums of the single atomic fragment and the atomic pair interaction energy errors compared to a full space calculation. We henceforth denote $\Sigma_P E_P$ as the total single energy and $\Sigma_{P>Q} \Delta E_{PQ}$ as the total pair interaction energy. For both MP2 and CCSD, the total single energy and the total pair interaction energy errors systematically decrease when tightening the FOT. Furthermore, total single and total pair interaction energy errors are of similar

Table 4. Energy Errors [au] Compared to a Full Molecular Calculation for Single, Pair, And Total Correlation Energies as a Function of Fragment Optimization Thresholds^a

threshold	$\Delta(\Sigma_P E_P)$	$\Delta(\Sigma_{P>Q} \Delta E_{PQ})$	ΔE_{corr}	% of E_{corr}
	MP2			
10^{-3}	0.013063	0.016875	0.029938	98.278
10^{-4}	0.001601	0.001775	0.003377	99.806
10^{-5}	0.000121	0.000139	0.000260	99.985
10^{-6}	0.000023	0.000014	0.000037	99.998
	CCSD			
10^{-3}	-0.000811	0.000369	-0.000442	100.025
10^{-4}	-0.000255	0.000067	-0.000189	100.011
10^{-5}	-0.000059	0.000046	-0.000013	100.001
10^{-6}	-0.000021	0.000006	-0.000015	100.001

^aThe calculations were carried out on the $C_{14}H_2$ molecule at the MP2 and CCSD levels of theory using the cc-pVDZ basis.

magnitude, substantiating that pair fragments may be determined as unions of atomic fragments without carrying out additional fragment optimizations.

In general, all MP2 errors are positive, i.e., the fragment energies calculated using the DEC scheme are larger than fragment energies calculated in the total orbital space. Therefore the total energy error ΔE_{corr} compared to a full molecular calculation also decreases systematically when the FOT is lowered. In contrast, for CCSD the total single energy errors are negative, whereas the total pair interaction energy errors are positive. This leads to cancellation of errors for CCSD, and therefore the total energy errors for CCSD are smaller than those for MP2. This cancellation of errors is also the reason why the error (accidentally) is smaller when the FOT is 10^{-5} than 10^{-6} for the CCSD case, although the total single and total pair interaction energy errors both decrease when lowering the threshold. A closer look at the individual atomic fragment energy errors reveals that these are always positive for MP2, whereas their signs vary for CCSD. This will in general lead to cancellation of errors for DEC-CCSD compared to DEC-MP2. Thus, DEC-MP2 shows the “worst case scenario”, where all individual fragment errors are added, whereas DEC-CCSD in general give smaller errors due to cancellation of errors. However, if the amplitudes are used to evaluate for example molecular gradients, errors of similar size will be obtained for MP2 and CCSD, as the cluster amplitudes are of similar quality.

In summary, it is a crucial feature of the DEC model that the full molecular correlation energy may be determined to any desired accuracy simply by choosing the appropriate FOT. It should be noted though that for CCSD, the error may be smaller than expected due to fortuitous cancellation of fragment energy errors.

7.1.3. Counterpoise Corrections. In the calculations presented so far we have calculated the pair interaction energies using the counterpoise-corrected expression in eq 74. In Figure 4 we have plotted the total pair interaction energy error against the FOT using the counterpoise-corrected expression (red solid curve) and using the simple expression in eq 73 (green dashed curve), which is prone to BSSE-like errors. The counterpoise-corrected strategy is clearly superior to the simple approach, and we therefore use counterpoise-corrected pair interaction energies in the calculations presented in this paper.

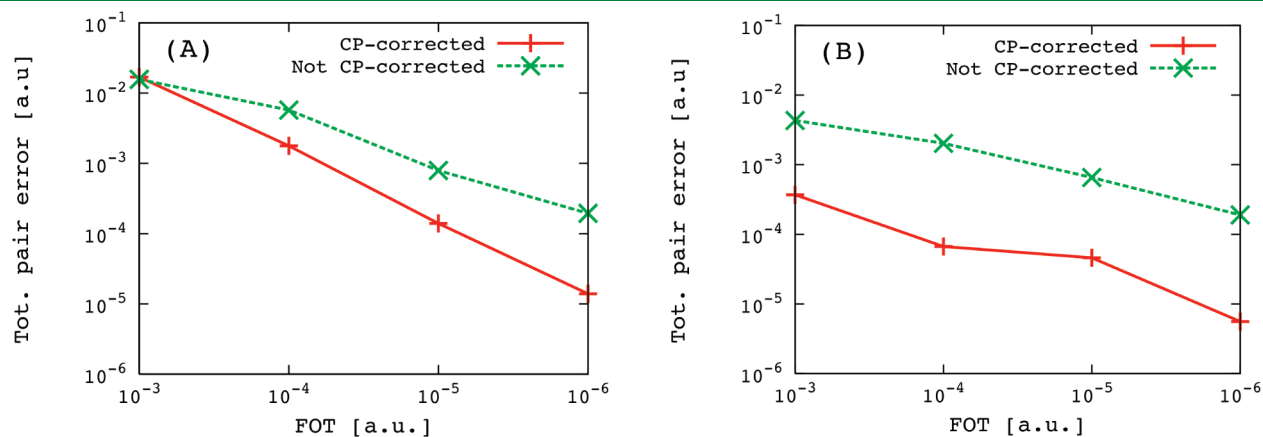


Figure 4. Errors of the total pair interaction energy $\Sigma_{P>Q} \Delta E_{PQ}$ compared to a full molecular calculation as a function of the FOT for MP2/cc-pVDZ (A) and CCSD/cc-pVDZ (B) calculations on the $C_{14}H_2$ molecule. Red solid curve: counterpoise-corrected (CP) pair interaction energies, see eq 74. Green dashed curve: pair interaction energies obtained by simple subtraction of atomic fragment energies from pair energies, see eq 73.

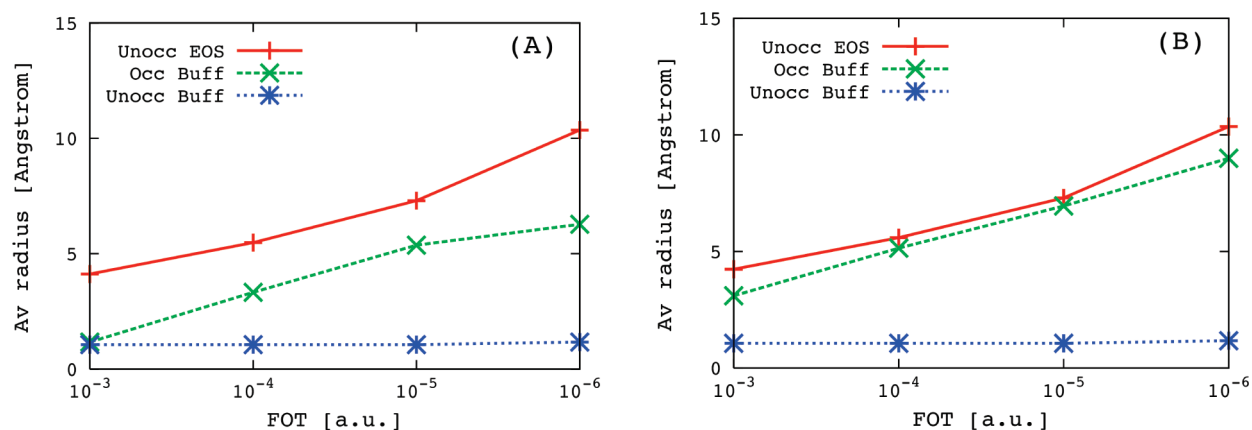


Figure 5. Average orbital space radii for DEC-MP2/cc-pVDZ (A) and DEC-CCSD/cc-pVDZ (B) calculations on the $C_{14}H_2$ molecule. Red solid curve: unoccupied energy orbital space. Green dashed curve: occupied buffer space. Blue dotted curve: buffer unoccupied space.

7.1.4. Sizes of Orbital Spaces. In Figure 5 we have plotted the average orbital space radii for various FOTs. Recall that the orbital space radii define the number of MOs in the atomic fragments, see the discussion in Section 6.2. To avoid confusion we note that the unoccupied buffer space radius refers only to the buffer space, i.e., the total unoccupied space radius is the sum of the unoccupied EOS radius and the unoccupied buffer radius. As expected the orbital space radii in Figure 5 increases when the FOT is lowered, i.e., the lower the FOT, the more orbitals are included in the atomic fragment. In other words, the fragment sizes are systematically increased (Figure 5) to yield increasingly accurate energies (Table 4). We also note that the sizes of the unoccupied spaces are very similar for the MP2 and CCSD calculations, whereas a larger occupied buffer is required for the CCSD case due to a more extensive coupling of amplitudes, in accordance with the locality analysis in Section 4.2.

7.1.5. The δ Parameter. Let us finally comment on the value of the δ parameter, which has been set to 0.01 in all calculations presented above. In Figure 6 we have plotted the error in the total MP2 correlation energy compared to a full molecular MP2 calculation for various FOTs and δ parameters. The error in the total energy decreases by roughly an order of magnitude when decreasing the FOT by an order of magnitude, as discussed in Section 7.1.2, whereas the errors are practically independent of the choice of δ parameter in eq 68 (the lines in Figure 6 are almost horizontal). In general we may therefore control the error in the total correlation energy by tightening the FOT for a fixed value of δ . Even though $\delta = 0.01$ was used in the calculations presented above, even $\delta = 0.1$ seems to be sufficient for a proper description of the orbitals. To understand why a value of $\delta = 0.1$ is sufficient, recall that the atomic fragment orbital space $\{\mathcal{A}_p\}$ is the union of atomic extents for all atoms in the AOS \mathcal{A}_p (see the discussion in Section 6.1). Since the EOS orbitals used for evaluating the atomic fragment energy are assigned to atoms in the central part of the fragment (see Figure 2) and are expanded on all atoms in the atomic fragment extent (including buffer regions), a very accurate description of the EOS orbitals is obtained, even for $\delta = 0.1$. The MOs in the buffer space are described less accurately for $\delta = 0.1$, but this has a very small indirect effect on the atomic fragment energy.

7.2. DEC-MP2 Calculations on Polyalanine Strings. In the previous section we demonstrated that for a given molecule the correlation energy error in a DEC calculation may be

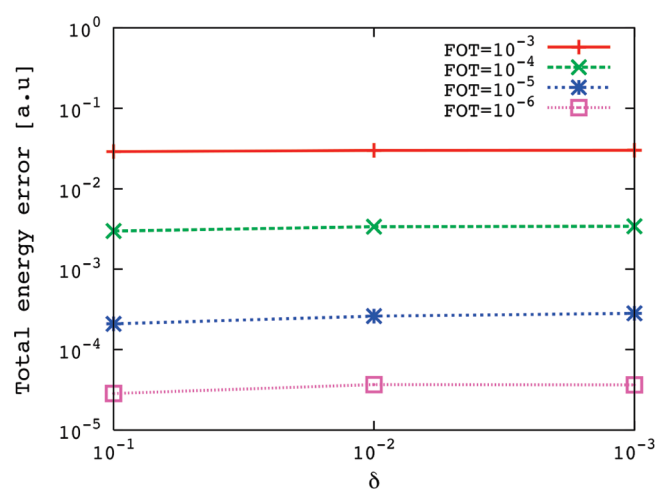


Figure 6. Total energy errors for various fragment optimization thresholds (FOTs) and δ values. In general, the energy error is proportional to the FOT, whereas it is very insensitive to the value of δ . The calculations have been carried out on the $C_{14}H_2$ molecule at the MP2/cc-pVDZ level of theory.

controlled by varying the FOT. In this section we investigate how the correlation energy error and the fragment sizes are affected when we systematically increase the molecular size using a fixed FOT.

The molecules under investigation are extended peptide chains containing 2, 4, 6, 8, or 10 alanine residues, see Figure 7. The geometries were obtained using extended peptide chains in the Maestro program⁴¹ without carrying out any additional optimizations. We thus have a set of molecular structures where the size is systematically increased. All DEC calculations presented in this section were carried out at the MP2/cc-pVDZ level of theory using a FOT of 10^{-4} , $\delta = 0.1$, orbital step size parameters of 2.0 au, and normalization of the orbitals. The validity of using $\delta = 0.1$ was discussed in Section 7.1.5. We shall not go into any detail about the choice of step size parameter, as we are currently developing a more sophisticated fragment optimization algorithm which does not involve any orbital step size radii.

7.2.1. Energy Errors. In Table 5 we present the correlation energy errors obtained in DEC-MP2 calculations compared to

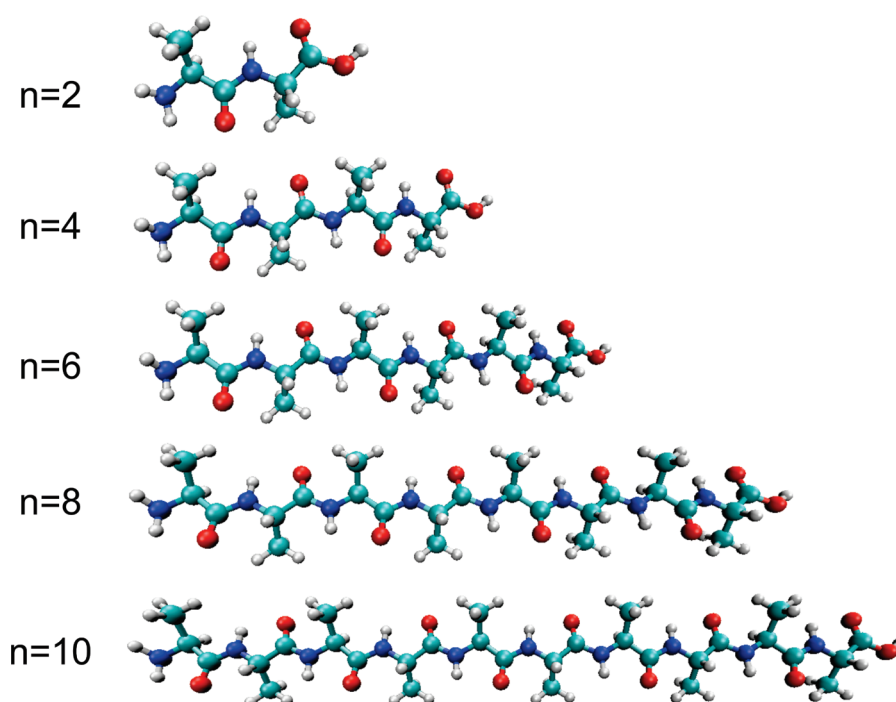


Figure 7. Extended polyaniline structures, and n is the number of alanine residues.

full molecular MP2 calculations. As expected the total correlation energy (E_{corr}) increases linearly with molecular size. The absolute energy errors (third column of Table 5) also roughly increase linearly with system size, although slight deviation from this behavior is observed, in particular for the alanine string with eight residues. The fact that the absolute error increases with molecular size can be understood by recalling that the total correlation energy is calculated as a sum of atomic fragment and atomic pair fragment interaction energies, see eq 5. For MP2 calculations we have observed that the fragment energy errors are all positive (see also the discussion in Section 7.1.2), and the errors therefore accumulate instead of canceling each other, such that the total absolute energy error increases with system size. In other words, the absolute MP2 energy errors are positive and size extensive. However, the percentage of E_{corr} that is recovered (fourth column of Table 5) remains roughly constant at approximately 99.93% as we increase the molecular size. The relative energy error is thus independent of the size of the molecule under investigation, i.e., regardless of the system size, the DEC scheme ensures control of the relative energy error. Cluster amplitudes, and therefore also molecular properties (e.g., molecular gradients), are thus determined with about equal accuracy independently of the system size.

7.2.2. Locality of Orbitals and Orbital Spaces. We now consider the sizes of the spaces employed in the DEC-MP2 calculations on the molecules in Figure 7. Let us first consider the locality of the LCM basis³⁰ which ultimately defines the locality of the DEC calculations. In the fifth column in Table 5 we have plotted the maximum orbital spread for the LCM orbitals employed in the calculation. The orbital spread is a measure of the locality of the orbitals (see ref 30 for a more thorough discussion of orbital spreads). It is clear that the maximum orbital spread is independent of the molecular size. The locality of the LCM orbitals is manifested in the sizes of the DEC orbital fragments as may be seen from Figure 8, where we

Table 5. Absolute (ΔE_{corr}) and Relative (% E_{corr}) Energy Errors of DEC-MP2/cc-pVDZ Calculations on Polyaniline Strings of Increasing Lengths Compared to Full Molecular Calculations^a

no. alanines	E_{corr} (au)	ΔE_{corr} (au)	% of E_{corr}	orb. spread (Å)
2	-1.737622	0.0015	99.92	1.91
4	-3.278702	0.0020	99.94	1.92
6	-4.819890	0.0034	99.93	1.90
8	-6.361143	0.0035	99.95	1.89
10	-7.902389	0.0056	99.93	1.95

^a Also shown is the maximum orbital spread (orb. spread) which is a measure of the locality of the least-change molecular (LCM) basis.

have plotted the average (A) and maximum (B) sizes of the orbital space radii in the DEC atomic fragment calculations as a function of the number of alanine residues. As we increase the size of the molecular system, the average and maximum orbital space radii become independent of the system size, in accordance with the locality analysis in Section 3.2. This is crucial for the applicability of the DEC scheme to calculate correlation energies for large molecular systems: regardless of the total molecular size the individual (independent) fragment calculations are small enough that they may be carried out using standard quantum chemical techniques (see Section 6.3). Thus, provided that a sufficient number of processors is available, the total wall time for carrying out an MP2 calculation for a large molecule system is defined by the largest fragment involved in the calculation.

7.2.3. Sizes of Atomic Fragment Extents. In a DEC fragment calculation the molecular integrals are calculated only for atoms in the atomic fragment extent (see Section 6.1 and Figure 2). In Figure 9 we have plotted the average (green dashed line) and the maximum (blue dotted line) number of atoms in the atomic

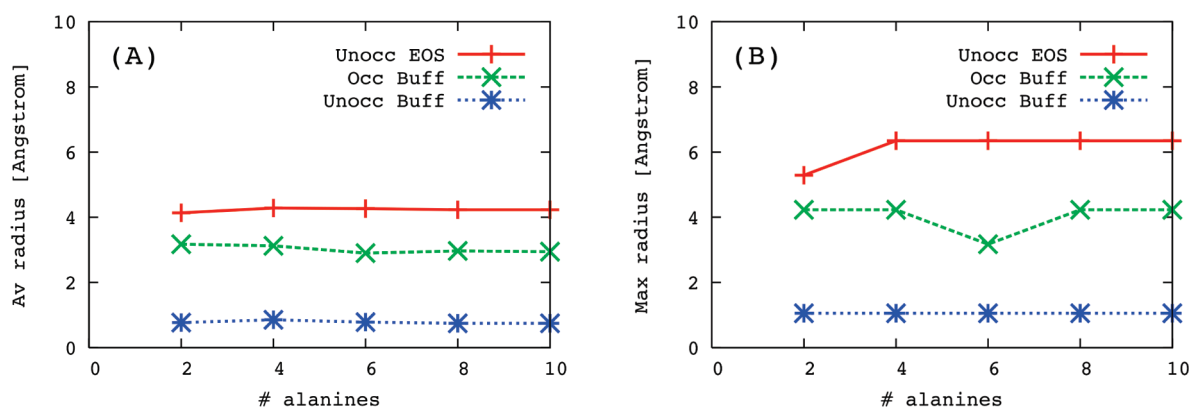


Figure 8. Average (A) and maximum (B) unoccupied energy (red solid curve), occupied buffer (green dashed curve), and unoccupied buffer (blue dotted curve) orbital space radii in DEC atomic fragment calculations as a function of the number of alanine residues.

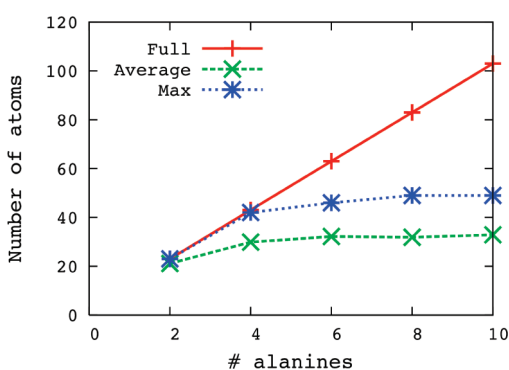


Figure 9. Average (green dashed) and maximum (blue dotted) number of atoms in the atomic fragment extent $\{\mathcal{A}_P\}$ in DEC atomic fragment calculations as a function of the number of alanine residues. For comparison the number of atoms in the corresponding full molecular calculations (red solid) is also plotted.

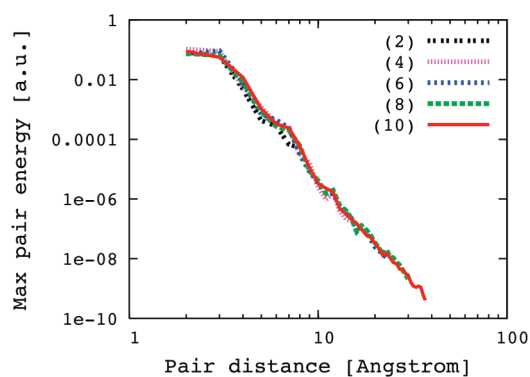


Figure 10. Maximum pair interaction energies (absolute values) against pair distance for polyaniline strings with 2, 4, 6, 8, and 10 alanine residues as indicated in the figure.

fragment extent $\{\mathcal{A}_P\}$ in DEC atomic fragment calculations as a function of the number of alanine residues. For comparison, we have also plotted the total number of atoms in the polyaniline molecules (red solid line). For the smallest polyanilines all atoms in the molecule are included in some of the atomic fragment extents. However, as the molecular size increases, the average and maximum sizes of the atomic fragment extents approach a

Table 6. Total Pair Interaction Energy ($\Sigma_{P>Q}\Delta E_{PQ}$) for Different Pair Distance Cutoffs^a

distance thr. (Å)	$\Sigma_{P>Q}\Delta E_{PQ}$ (au)
all pairs	-2.53084
30.0	-2.53084
25.0	-2.53084
20.0	-2.53084
15.0	-2.53084
10.0	-2.53077
5.0	-2.52383

^aThe calculations were carried out on a polyaniline string with 10 alanine residues at the DEC-MP2/cc-pVDZ level of theory.

constant value of roughly 35 and 50 atoms, respectively. This is in line with that we observed in Figure 8: for “large” molecules the fragment sizes are independent of the molecular size.

7.2.4. Pair Interaction Energies for Polyanilines. Let us also comment on the pair distance dependence of the pair interaction energies ΔE_{PQ} for the polyaniline strings. In Figure 10 we have plotted the maximum pair interaction energies (absolute values) against the pair distance for polyaniline strings with 2, 4, 6, 8, and 10 alanine residues. The fact that the different polyaniline plots almost coincide show that the pair interaction energies, which represent dispersion interactions for larger pair distances, are of similar sizes in all molecules. This is hardly surprising as the molecules are of similar structure, see Figure 7. The magnitude of the pair interaction energies rapidly decreases with pair distance, since dispersion forces ideally depend on the inverse pair distance R_{PQ} to the sixth power.⁴² In fact, the (almost) straight line in the double logarithmic plot in Figure 10B does indicate a power dependence, i.e., $\Delta E_{PQ} \propto R_{PQ}^{-n}$. A regression plot for the polyaniline string containing 10 alanine residues yields $n \approx 7.1$. The idealized case where $n = 6$ occurs for two relatively distant atoms and assumes that higher order interactions (i.e., terms proportional to R_{PQ}^{-n} with $n > 6$) can be neglected. What we observe in Figure 10 is a mixture of pair interactions referencing localized orbitals centered on different atom types in different environments and also includes higher order interactions. It is therefore not surprising that our power exponent differs slightly from six.

From a practical point of view the rapid decrease of pair interaction energies with pair distance implies that pairs separated by more than some pair distance cutoff may be omitted from the DEC calculation without affecting the total correlation

energy. To quantify the contributions of distant atomic pairs to the correlation energy, we have in Table 6 given the total pair interaction energy ($\sum_{P>Q} \Delta E_{PQ}$) for different values of the pair distance cutoff for a polyaniline string containing 10 alanine residues. It is seen that atomic pairs separated by more than, say, 10 Å do not contribute significantly to the total pair energy considering that the atomic fragment energies were only calculated to a threshold of 10^{-4} au. Pairs separated by more than 10 Å may therefore be omitted from the DEC calculation. Thus, for a large molecule the number of pair interaction energies that needs to be calculated does indeed scale linearly with the size of the molecule.

In a practical calculation, where the total pair energy with all pairs included is not known, a pair distance cutoff of 10 Å seems reasonable for a general nonmetallic molecular system, whereas 15 Å is a more conservative value.

The short version of this discussion is that pair interaction energies describe dispersion effects, which is the same physical effect for all molecules. The threshold for neglecting pair interactions can thus be set based on the distance dependence of this interaction.

8. SUMMARY

We have presented a locality analysis of the MP2 and CCSD amplitude equations which demonstrate that—assuming that a set of local HF orbitals is available, such as the LCM basis,³⁰—a full CC calculation can be divided into a set of small independent atomic fragment and atomic pair fragment calculations, where the fragment orbital spaces constitute small subsets of the total orbital space. This is possible because, using a local HF basis, the contributions to the MP2 and CCSD amplitude equations rapidly decrease with increasing spatial distance between the central atom(s) in the atomic (pair) fragment and the orbitals referencing the summation indices in the residual expression.

In a practical calculation, the optimal sizes of the atomic fragment orbital spaces are not known a priori. Rather, they have to be determined during the calculation to ensure that the atomic fragment energies are determined to a preset threshold. Subsequently the atomic pair fragments are formed from unions of atomic fragments to determine the pair interaction energies. A CC calculation on a large molecular system may thus be carried out in terms of CC calculations on small orbital fragments of the total molecular system, where the sizes of the orbital fragments are determined in a black box manner during the calculation to ensure that the total CC correlation energy is calculated to a preset energy threshold.

In summary, a DEC calculation consists of a series of independent atomic fragment calculations followed by a series of independent atomic pair fragment calculations. Pairs which are widely separated in space may be neglected, as their corresponding pair interaction energies (representing dispersion interactions) are exceedingly small. Thus, for large molecules the number of pair fragments with nonvanishing contributions to the correlation energy scales linearly with the number of atoms in the system. The DEC scheme is therefore linearly scaling and embarrassingly parallelizable with roughly the same wall time for small and large molecular systems provided that a sufficient number of processors are available.

Numerical results demonstrate that the energy errors in a DEC-MP2 or DEC-CCSD calculation compared to a full molecular calculation may be defined by the FOT parameter prior to the calculation. We have also demonstrated that the absolute energy errors in a DEC-MP2 calculation compared to a full

calculation are size extensive, whereas the relative energy errors are independent of the system size. Thus, in a relative sense, small and large molecules are treated with equal precision in DEC-MP2 calculations. Furthermore, it has been shown that the fragment sizes are independent of the molecular system size and that the fragments are small enough to be treated using standard quantum chemical implementations. Therefore, a DEC correlation energy calculation for a general molecule can be carried out provided that the HF calculation can be carried out and that a local HF basis can be determined.

AUTHOR INFORMATION

Corresponding Author

*E-mail: kasperk@chem.au.dk.

Present Addresses

[‡]Department of Chemistry, Northwestern University, Evanston, Illinois 60208–3113, United States

[§]Department of Chemistry, Oslo University, P.O. Box 1033, Blindern, 0315 Oslo, Norway

ACKNOWLEDGMENT

This work has been supported by the Lundbeck Foundation and the Danish Center for Scientific Computing (DCSC).

REFERENCES

- (1) Shavitt, I.; Bartlett, R. J. *Many-Body Methods in Chemistry and Physics. MBPT and Coupled-Cluster Theory*; Cambridge University Press: Cambridge, U.K., 2009.
- (2) Hartree, D. R. *Proc. Cambridge Philos. Soc.* **1928**, *24*, 89.
- (3) Fock, V. Z. *Phys.* **1930**, *61*, 126.
- (4) Pulay, P. *Chem. Phys. Lett.* **1983**, *100*, 151.
- (5) Boys, S. F. *Rev. Mod. Phys.* **1960**, *32*, 296.
- (6) Edmiston, C.; Ruedenberg, K. *Rev. Mod. Phys.* **1963**, *35*, 457–464.
- (7) Pipek, J.; Mezey, P. G. *J. Chem. Phys.* **1989**, *90*, 4916.
- (8) Subotnik, J. E.; Dutoi, A. D.; Head-Gordon, M. *J. Chem. Phys.* **2005**, *123*, 114108.
- (9) Saebo, S.; Pulay, P. *Annu. Rev. Phys. Chem.* **1993**, *44*, 213–236.
- (10) Hampel, C.; Werner, H.-J. *J. Chem. Phys.* **1996**, *104*, 6286–6297.
- (11) Schütz, M.; Hetzer, G.; Werner, H.-J. *J. Chem. Phys.* **1999**, *111*, 5691–5705.
- (12) Schütz, M. *J. Chem. Phys.* **2000**, *113*, 9986.
- (13) Schütz, M.; Werner, H.-J. *J. Chem. Phys.* **2001**, *114*, 661–681.
- (14) Scuseria, G. E.; Ayala, P. Y. *J. Chem. Phys.* **1999**, *111*, 8330–8343.
- (15) Christiansen, O.; Manninen, P.; Jørgensen, P.; Olsen, J. *J. Chem. Phys.* **2006**, *124*, 084103.
- (16) Weijs, V.; Manninen, P.; Jørgensen, P.; Christiansen, O.; Olsen, J. *J. Chem. Phys.* **2007**, *127*, 074106.
- (17) Subotnik, J. E.; Sodt, A.; Head-Gordon, M. *J. Chem. Phys.* **2006**, *125*, 074116.
- (18) Flocke, N.; Bartlett, R. J. *J. Chem. Phys.* **2004**, *121*, 10935–10944.
- (19) Li, S.; Ma, J.; Jiang, Y. *J. Comput. Chem.* **2001**, *23*, 237.
- (20) Li, W.; Piecuch, P.; Gour, J. R.; Li, S. *J. Chem. Phys.* **2009**, *131*, 114109.
- (21) Li, W.; Piecuch, P. *J. Phys. Chem. A* **2010**, *114*, 8644.
- (22) Kobayashi, M.; Nakai, H. *J. Chem. Phys.* **2008**, *129*, 044103.
- (23) Fedorov, D. G.; Kitaura, K. *J. Chem. Phys.* **2005**, *123*, 134103.
- (24) Stoll, H. *Chem. Phys. Lett.* **1992**, *191*, 548.

- (25) Friedrich, J.; Hanrath, M.; Dolg, M. *J. Chem. Phys.* **2007**, *126*, 154110.
- (26) Almlöf, J. *Chem. Phys. Lett.* **1991**, *181*, 319.
- (27) Ayala, P. Y.; Scuseria, G. E. *J. Chem. Phys.* **1999**, *110*, 3660–3671.
- (28) Lambrecht, D. S.; Doser, B.; Ochsenfeld, C. *J. Chem. Phys.* **2005**, *123*, 184102.
- (29) Ochsenfeld, C.; Kussmann, J.; Lambrecht, D. S. *Reviews in computational chemistry*; VCH Publishers, Inc.: New York, 2007; Vol. 23, p 1.
- (30) Ziolkowski, M.; Jansik, B.; Jørgensen, P.; Olsen, J. *J. Chem. Phys.* **2009**, *131*, 124112.
- (31) Ziolkowski, M.; Jansik, B.; Kjærgaard, T.; Jørgensen, P. *J. Chem. Phys.* **2010**, *133*, 014107.
- (32) Boughton, J. W.; Pulay, P. *J. Comput. Chem.* **1993**, *14*, 736.
- (33) Helgaker, T.; Jørgensen, P.; Olsen, J. *Molecular Electronic-Structure Theory*; John Wiley & Sons: Chichester, U.K., 2002.
- (34) Hetzer, G.; Pulay, P.; Werner, H.-J. *Chem. Phys. Lett.* **1998**, *290*, 143–149.
- (35) Goedecker, S. *Rev. Mod. Phys.* **1999**, *71*, 1085.
- (36) Goedecker, S.; Scuseria, G. E. *Comp. Sci. Eng.* **2003**, *5*, 14.
- (37) Polly, R.; Werner, H.-J.; Manby, F. R.; Knowles, P. J. *Mol. Phys.* **2004**, *102*, 2311.
- (38) Ochsenfeld, C.; Kussmann, J.; Lambrecht, D. S. In *Reviews in computational chemistry*; Lipkowitz, K. B., Cundari, T. R., Eds.; VCH Publishers, Inc.: New York, 2007, Vol. 23.
- (39) Usvyat, D.; Schütz, M. *Theo. Chem. Acc.* **2005**, *114*, 7.
- (40) Ziolkowski, M.; Weijo, V.; Jørgensen, P.; Olsen, J. *J. Chem. Phys.* **2008**, *128*, 204105–12.
- (41) *Maestro*, v. 8.5; Schrödinger, LLC: Cambridge, MA, 2008; <http://www.schrodinger.com>.
- (42) Sakurai, J. J. *Modern Quantum Mechanics*, revised ed.; Addison-Wesley Publishing Company: New York, 1994.

Selection and Validation of Charge and Lennard-Jones Parameters for QM/MM Simulations of Hydrocarbon Interactions with Zeolites

Paul M. Zimmerman,[†] Martin Head-Gordon,^{*,†} and Alexis T. Bell[‡]

[†]Department of Chemistry, University of California, Berkeley, California 94720-1461, United States

[‡]Department of Chemical and Biomolecular Engineering, University of California, Berkeley, California 94720-1462, United States

ABSTRACT: Quantum mechanics/molecular mechanics (QM/MM) models are an appealing method for performing zeolite simulations. In QM/MM, a small cluster chosen to encompass the active center is described by QM, while the rest of the zeolite is described by MM. In the present study, we demonstrate that the charges and Lennard-Jones parameters on Si and O must be chosen properly for QM/MM calculations of adsorption energies and activation energies to agree closely with full QM calculations. The selection of parameters for Si and O is based on using the ω B97X-D functional for DFT calculations of the QM region, which is effective in capturing the effects of van der Waals interactions. A comparison of the heats of adsorption for a variety of adsorbates and activation energies for the cracking of propane and butane reveals that energies derived from QM/MM calculation carried out with appropriately selected MM parameters agree to within an rms error of ~ 1.5 kcal/mol with QM calculations. To avoid reparametrization for new substrates, Lennard-Jones zeolite parameters are chosen to be compatible with existing CHARMM parameters. Transferability of these parameters is demonstrated by tests utilizing the B3LYP density functional and simulations of MFI and FAU zeolites. Moreover, the computational time for QM/MM calculations is considerably lower than that for QM calculations, and the ratio of computational times decreases rapidly with increasing size of the cluster used to represent the zeolite.

INTRODUCTION

Zeolites are crystalline microporous solids composed of corner-sharing, tetrahedrally coordinated silicate (SiO_4) units. Isomorphic substitution of Si atoms by Al atoms and a charge-compensating proton (HAlO_4) introduces Brønsted acidic bridge-bonded hydroxyl groups. Zeolites in this form are solid acids widely used to catalyze a variety of reactions, e.g., cracking, isomerization, and alkylation, involved in the conversion of petroleum to transportation fuels and the production of commodity and specialty chemicals.^{1–4} Substitution of the Brønsted-acid protons by metal cations enables zeolites to serve as catalysts for other reactions, such as the selective reduction of NO, the decomposition of N_2O , oxidation of olefins, the carbonylation of alcohols, etc.⁵ In these reactions, the metal cation acts as either a Lewis acid or a redox center. Experimental studies have shown that the activity and selectivity of both Brønsted-acid and metal-containing zeolites are strong functions of their architecture and Si/Al ratio.⁴ Since the number of possible zeolite structures exceeds those used commercially by several orders of magnitude,^{6–10} it would be highly desirable to predict how zeolite structure and composition affect the activity and selectivity of zeolite catalysts. An attractive approach to this end is the use of quantum chemical calculations to describe the electronic and catalytic properties of catalytically active sites located within the pores and channels of zeolites. Molecular-scale information that is often difficult, and sometimes not possible, to obtain otherwise can be obtained by this means.^{11,12} Examples include the geometry, energy, and vibrational spectrum of ground and transition states, and the dynamics of elementary processes involved in the transformation of reactants to products. Such calculations are also useful for confirming interpretations of adsorbate structure and reaction mechanisms

deduced from experimental evidence and for assessing the impact of zeolite architecture and composition on catalyst activity and selectivity.

The application of quantum mechanics to chemical reactions occurring in zeolites is particularly challenging because of the large number of atoms required to capture the long-range Coulombic and van der Waals interactions. Ab initio wave function theories (MP2, CCSD(T), etc.) cannot be carried out for such systems because they scale with the fifth power or more of the number of atoms in the system. Consequently, most investigations of reactions occurring in zeolites are based on density functional theory¹³ (DFT), which scales with no worse than the third order of the number of atoms. While the computational cost of DFT calculations is acceptable for many applications, the accuracy of the method depends on the exchange-correlation functional. Recent work has demonstrated that the popular B3LYP functional¹⁴ does not capture the effects of dispersive interactions adequately, leading to significantly inaccurate heats of adsorption and activation energies.^{15,16} Of the various functionals developed over the last several years, the two that have been demonstrated to be most effective in capturing van der Waals interactions in zeolites are MO6-2X¹⁷ and ω B97X-D.¹⁸

Recent studies utilizing density functional theory (DFT) have shown that in order to achieve results consistent with experimental results, it is necessary to use large cluster representations of the active center and surrounding portion of the zeolite framework as well as a functional that properly accounts for dispersion. Although DFT is much more efficient computationally relative to other

Received: March 9, 2011

Published: May 20, 2011

Table 1. Sampling of Charges Used for Si in QM/MM Simulations of Zeolites in the Literature

Si charge (au)	explanation	reference
0.0	mechanical embedding	48
1.0	Mulliken from DFT	39
1.2	potential derived charge from DFT	49
1.2	taken from MM parameter set	50
1.84	fit to Hartree–Fock	51
2.0	one-half of formal charge	26, 52
4.0	formal charge	53

electronic structure theories, its $\sim N^3$ scaling means that computations with the large clusters required to capture the effects of dispersive and electrostatic interactions are prohibitively slow. For this reason, it is very difficult to achieve convergence of calculated thermochemical properties to values observed experimentally with increasing cluster size.¹⁹ To overcome the electrostatic issue, some researchers have utilized periodic boundary conditions to represent the extended framework.^{20,21} However, these simulations remain computationally intractable for large zeolite unit cells. Periodic simulations of the active site and associated molecules can result in the experience of dipole–dipole interactions with periodic images, which may influence the quality of the results. An additional limitation of periodic boundary simulations is that the algorithms used for such calculations cannot readily utilize advanced functionals, such as ω B97X-D, due to difficulties in computing exact exchange.

Several authors have explored the option of carrying out hybrid quantum mechanical/molecular mechanical (QM/MM) simulations as a means for balancing accuracy and computational time for very large systems.^{22–27} In this formalism, reactive atoms (the active site and reagents) are represented by DFT (or other *ab initio* method), and nonreacting atoms are represented by a molecular mechanics (MM) force field. This division is natural in zeolites and allows for bond-breaking to be described in the QM region and other important, but more distant, interactions to be captured by interactions with the MM region. QM/MM is vastly more computationally efficient than QM and therefore well suited for investigating large zeolite frameworks.^{24–30} However, it must be recognized that the accuracy of QM/MM simulations depends critically on the functional used for the DFT calculations and also the choice of charges and Lennard-Jones parameters used for the MM calculations. Surprisingly, this issue has not been investigated in a systematic manner. As may be seen from Table 1, a wide range of charge parameters have been used by different authors. In some cases, formal charges have been used, while in other cases charges were adjusted to replicate the results of Hartree–Fock calculations. It should also be noted that, in some simulations, MM–QM electrostatics have been neglected, even though this mechanical embedding poorly represents the polarized Si–O bonding.

In this paper, we describe the selection and validation of MM parameters tailored for zeolite QM/MM simulations. Using the parameters determined in this study, QM/MM is shown to reproduce accurately QM geometries and QM energetics to within ~ 2 kcal/mol. Furthermore, these parameters work well with both ω B97X-D and B3LYP functionals. In our QM/MM implementation, we employ static point charges in an electrostatically embedded model with Lennard-Jones potentials to

account for dispersion interactions. The Lennard-Jones parameters are chosen such that the adsorbate Lennard-Jones parameters can be taken directly from the existing CHARMM parameters. Because this is a simple electrostatic embedding model with a standard form of empirical dispersion, we anticipate that the parameter set will be highly useful for existing QM/MM implementations.

COMPUTATIONAL METHODS

Zeolite Geometries. The crystallographic structures of MFI³¹ and FAU³² were used to determine the positions of all atoms in the zeolites. Although Al can be located in 12 symmetrically distinct positions in MFI, different in energy by only a small amount, there is evidence that the T12 position is favored.^{33,34} Therefore, the T12 site was chosen for the calculations reported here. Zeolite clusters with 23 and 44 tetrahedral atoms (T23 and T44) were generated for MFI. Calculations were done for FAU using a T52 cluster. Since all T sites have the same symmetry in FAU, the placement of the Al atom is not critical for FAU. Each of the clusters was terminated with hydrogen atoms positioned on the vector between the terminal Si atoms and the replaced O atoms, located 1.47 Å away from the terminal Si atoms. During geometry optimizations, the lattice atoms away from the T5 region were kept frozen at their crystallographic positions.

QM Computations. Calculations were performed with DFT/ ω B97X-D in order to provide benchmarks for verifying the results of QM/MM. Geometries were optimized using the ω B97X-D functional and the double- ζ , polarized 6-31G* basis set, and single point DFT energies were then determined with the augmented, polarized 6-31+G** basis set. Geometries were reoptimized with B3LYP and 6-31G* for the B3LYP test set. All QM computations were performed using Q-Chem.³⁵

QM/MM Setup. Multiple strategies exist for implementing QM/MM simulations,^{22–27} all of which begin by dividing the atoms of the system into QM and MM regions. Notable for zeolite simulations are Sauer's QM/shell model^{28,29} and Morokuma's ONIOM method.³⁰ These two approaches involve mechanical embedding of the QM region and can include empirical dispersion interactions between the regions. Since MM–QM electrostatic interactions are not considered, polarization of the active site by the lattice is, therefore, excluded. Our QM/MM implementation follows the method of ref 36, where both dispersion and electrostatics are treated between the QM and MM regions (i.e., electrostatic embedding²²).

The division between QM and MM regions is described in Figure 1. To divide the QM and MM regions smoothly, a single hydrogen link atom is used to replace a Si–O bond at the terminus of the QM cluster.³⁷ The terminating H atoms were placed along each of the terminal Si–O bonds at a distance of 0.92 R(Si–O) from the terminal Si atom. Typical Si–H link atom bond lengths were approximately 1.47 Å. To achieve charge neutrality of the MM subsystem, a fraction of the link atom charge was added to its covalently bonded neighbor, and the charge on the link atom was set to zero. Failure to neutralize the MM region caused significant errors in the absorption energies of polar species; therefore, neutrality of the MM region was maintained for all simulations. Except where noted, the QM region was a T5 cluster centered on the zeolite acid site. While other strategies have been used for QM/MM simulations,^{38,39} these approaches are more complicated and require additional parametrization.

The MM region was described by a standard force field of the CHARMM type.⁴⁰ The most important terms in the force field are the electrostatic energy,

$$E_{\text{ES}} = \sum_{ij} \frac{q_i q_j}{4\pi\epsilon_0 r_{ij}} \quad (1)$$

and the Lennard-Jones potential energy

$$E_{\text{LJ}} = \sum_{ij} \epsilon_{ij} \left[\left(\frac{R_{ij}}{r_{ij}} \right)^{12} - 2 \left(\frac{R_{ij}}{r_{ij}} \right)^6 \right] \quad (2)$$

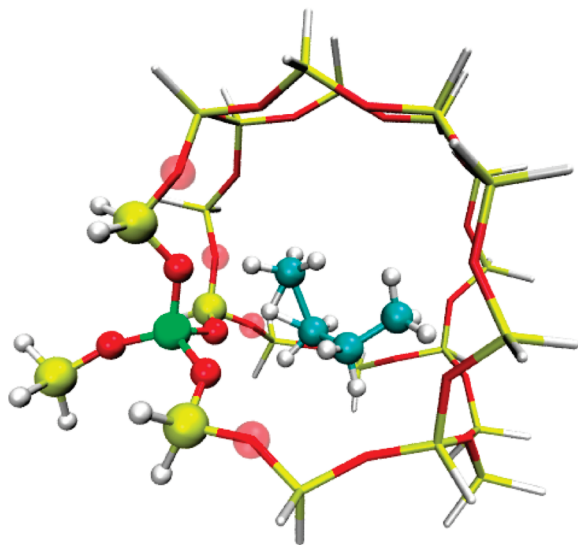


Figure 1. Schematic of the division between QM and MM regions. Spherical atoms are QM, and transparent atoms are link atoms. The QM region is polarized by atomic partial charges in the MM region. The immediate Si neighbors to the link atoms are assigned a smaller charge to create an overall neutral MM region. Lennard-Jones potentials are applied to pairs of atoms that include at least one MM atom to account for dispersion.

where $\epsilon_{ij} = (\epsilon_i \epsilon_j)^{1/2}$ and $R_{ij} = (R_i + R_j)/2$. These expressions require three parameters for each atom type: q_i , the atomic partial charge; R_i , the van der Waal's radius; and ϵ_i , the characteristic energy for the Lennard-Jones potential. A point charge model was used instead of more sophisticated polarizable models to allow compatibility with existing electrostatically embedded QM/MM implementations. While simple, this approach yielded results of sufficiently high accuracy. To avoid modifying parameters of nonzeolite molecules, CHARMM parameters were utilized for the atoms of the molecules interacting with the zeolite. QM/MM simulations were performed utilizing a development version of the Q-Chem software package.³⁵

PARAMETER SELECTION

Because most of the atoms in the zeolite lattice were kept frozen at their crystallographic positions, we focused on determining reliable atomic charges and Lennard-Jones parameters for Si and O, while the MM bonding parameters remain unchanged. Since our approach selects MM parameters specifically for QM/MM use, we used the CHARMM parameters for silica⁴¹ as a reasonable starting point. This set of parameters (referred to below as parameter set P1) was developed using the standard CHARMM procedure that ensures consistency with existing CHARMM parameter sets.⁴⁰ While the parameters for Si and O determined by this means are suitable for CHARMM MM simulations, they are not necessarily reliable for use in QM/MM simulations.

Selection of a satisfactory set of charge and Lennard-Jones parameters for Si and O was done by reducing the error between QM/MM and QM calculations carried out for three test sets. For each one, the van der Waals radii, R_i , for Si and O in CHARMM were maintained, and only the energy parameters, ϵ_i , were adjusted along with the charge parameters. The first test set examines the adsorption of methane, ethane, propane, and butane in purely siliceous MFI (silicalite), represented by a T23 cluster. For this set of molecules, adsorbate–zeolite interactions are dominated by dispersive forces. The second test set examines the interactions of propane, CO, acetonitrile, NH_3 , and

Table 2. Quantum Mechanical Absorption Energies and Apparent Activation Energies from ω B97X-D and Experiments (kcal/mol)

		B3LYP	ω B97X-D	ω B97X-D		
		6-31G*	6-31G*	6-31+G**	exp. ΔH_{abs}	ref.
T23 MFI (all silica)	methane	1.3	−4.2	−3.8	−4.8	54
	ethane	−0.7	−7.7	−7.8	−7.9	54
	propane	−0.4	−10.9	−9.3	−9.6	54
	butane	−2.6	−14.7	−13.9	−11.7	54
T44 H-MFI	propane	−0.4	−12.2	−13.7	−11.0	55
	CO	−7.4	−10.8	−10.2	−6.3, −8.0	56, 57
	acetonitrile	−16.8	−25.8	−24.7	−26.3	58
	NH_3	−28.3	−33.6	−30.0	−34.7	59
	pyridine	−27.2	−42.9	−46.8	−47.6	59
		6-31G*	6-31G*	6-31+G**	exp. apparent ΔH^\ddagger	
T23 H-MFI	propane cracking	45.2	32.0	30.7	37.0, 35.1	60, 61
	propane H-exchange	28.3	22.8	20.3	n/a	
	butane cracking 1	42.2	26.8	26.2	32.3	60
	butane cracking 2	42.1	26.2	25.3	32.3	60

pyridine with a Brønsted acid site in H-MFI, represented by a T44 cluster. This group contains larger molecules that are more sensitive to long-range charge interactions with the lattice and molecules such as NH_3 and pyridine that can interact strongly with the Brønsted acid proton of the zeolite. The third test set examines the activation barriers for hydrogen exchange and cracking of propane, and for *n*-butane cracking at the C1 and C2 positions. A T23 H-MFI cluster was used for these calculations.

The accuracy of the QM calculations was established by comparison with experimental values. As seen in Table 2, the QM calculations carried out at the $\omega\text{B97X-D}/6\text{-}31\text{G}^*$ and $\omega\text{B97X-D}/6\text{-}31+\text{G}^{**}$ levels for the first test set agree closely with the experimental values of the heats of adsorption for methane, ethane, propane, and butane. However, similar calculations carried out with B3LYP/6-31G* yield heats of adsorption that are consistently lower than those calculated with $\omega\text{B97X-D}/6\text{-}31\text{G}^*$ and those observed experimentally, confirming the superior performance of the $\omega\text{B97X-D}$ functional for describing dispersive interactions. Similar conclusions can be drawn by examining the results for a second test set. It is also noted that the strong interactions of pyridine, acetonitrile, and ammonia with the Brønsted acid site are well described using the $\omega\text{B97X-D}$ functional. For the third test set, QM calculations carried out at the $\omega\text{B97X-D}/6\text{-}31\text{G}^*$ and $\omega\text{B97X-D}/6\text{-}31+\text{G}^{**}$ levels underpredict the experimentally observed apparent activation barriers by about 5–6 kcal/mol (i.e., the energy difference between the transition state and the molecule in the gas phase), but are consistently better than calculations done at the B3LYP/6-31G* level, which tend to overpredict activation barriers by about 10 kcal/mol.

Because the $\omega\text{B97X-D}$ functional produced results in good agreement with experimental ones, QM/MM parameters were selected to reproduce these QM results. Figure 2 outlines a general methodology for generating reliable charge and L-J parameters for zeolites. After comparing the results from QM to QM/MM with the CHARMM parameter set (P1), the L-J parameters are modified. QM/MM computations are repeated holding the charge constant until a small value of rms error is

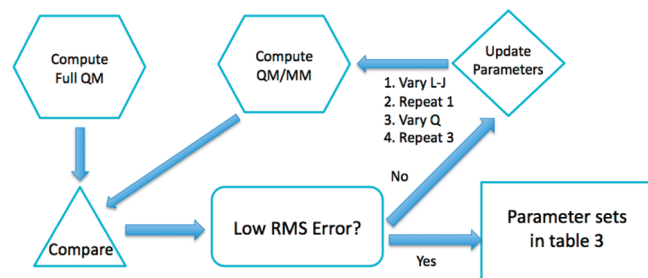


Figure 2. Schematic for generating Lennard-Jones and charge parameters.

achieved. This procedure produces the P2 parameter set. Having determined the L-J parameters, these are fixed and a similar iterative procedure evaluates the charge parameters. The lowest rms errors resulted from parameter sets P3 and P4. Finally, a mechanically embedded parameter set, P5, is constructed by setting the charge to zero.

These sets, presented in Table 3, are P1, the CHARMM set of charges and Lennard-Jones parameters for Si and O determined for silica ($Q_{\text{Si}} = 1.08$, $Q_{\text{O}} = -0.54$, $\epsilon_{\text{Si}} = 0.6$ kcal/mol, and $\epsilon_{\text{O}} = 0.1521$ kcal/mol); P2, the CHARMM charges for Si and O and the new set of Lennard-Jones parameters found in this work ($Q_{\text{Si}} = 1.08$, $Q_{\text{O}} = -0.54$, $\epsilon_{\text{Si}} = 0.2$ kcal/mol, and $\epsilon_{\text{O}} = 0.075$ kcal/mol); P3, the first set of reduced charges on Si and O and the new set of Lennard-Jones parameters ($Q_{\text{Si}} = 0.80$, $Q_{\text{O}} = -0.40$, $\epsilon_{\text{Si}} = 0.2$ kcal/mol, and $\epsilon_{\text{O}} = 0.075$ kcal/mol); P4, the second set of reduced charges on Si and O and the new set of Lennard-Jones parameters ($Q_{\text{Si}} = 0.70$, $Q_{\text{O}} = -0.35$, $\epsilon_{\text{Si}} = 0.2$ kcal/mol, and $\epsilon_{\text{O}} = 0.075$ kcal/mol); and P5, no charges on Si and O and the new set of Lennard-Jones parameters ($Q_{\text{Si}} = 0.0$, $Q_{\text{O}} = 0.0$, $\epsilon_{\text{Si}} = 0.2$ kcal/mol, and $\epsilon_{\text{O}} = 0.075$ kcal/mol), which corresponds to mechanical embedding of the QM region. Reference to Table 1 shows that the charges on Si and O used here are significantly smaller than those previously reported.

QM/MM VALIDATION

Figures 3–5 show the difference between the energy (adsorption energy or activation energy) determined by QM/MM and full QM for each member of the three test sets. The difference between the adsorption or activation energies determined from QM/MM and full QM calculations is sensitive in general to the choice of charges placed on Si and O and to the parameters of the Lennard-Jones potential. However, the sensitivity to the choices of charges and Lennard-Jones parameters depends on the test set examined. Figure 3 reveals that the heats of adsorption of C_1 – C_4 alkanes are insensitive to the choice of the charges placed on Si and O but quite sensitive to the choice of Lennard-Jones parameters. When the values of these parameters found in the present study are used, the rms error between QM/MM and full QM is 0.3 kcal/mol for parameter set P5 (i.e., mechanical embedding) and is 0.4 kcal/mol for parameter set P3 ($Q_{\text{Si}} = 0.8$ and $Q_{\text{O}} = -0.4$).

By contrast for the second test set (shown in Figure 4), in which electrostatic adsorbate–zeolite interactions are significant, the difference in the adsorption energies determined from QM/MM and full QM calculation is sensitive to both the charges placed on the Si and O atoms of the zeolite lattice and the corresponding Lennard-Jones parameters. The smallest difference is obtained using parameter set P4; however, using parameter set P3 yields only slightly larger errors. It is also apparent that exclusion of electrostatic interactions (P5) leads to large

Table 3. Charge and Lennard-Jones Parameters for O and Si Used in This Work^a

parameter set	Q_{Si}	Q_{O}	ϵ_{Si} (kcal/mol)	R_{Si} (Å)	ϵ_{O} (kcal/mol)	R_{O} (Å)	$\Delta E_{\text{rms}}/6\text{-}31+\text{G}^{**}$ (kcal/mol)
P1	1.08	−0.54	0.6	2.2	0.1521	1.77	6.2
P2	1.08	−0.54	0.2	2.2	0.075	1.77	3.7
P3	0.8	−0.4	0.2	2.2	0.075	1.77	1.4
P4	0.7	−0.35	0.2	2.2	0.075	1.77	1.5
P5	0.0	0.0	0.2	2.2	0.075	1.77	8.1

^a Adsorbate Lennard-Jones parameters are from the CHARMM force field.⁴⁰

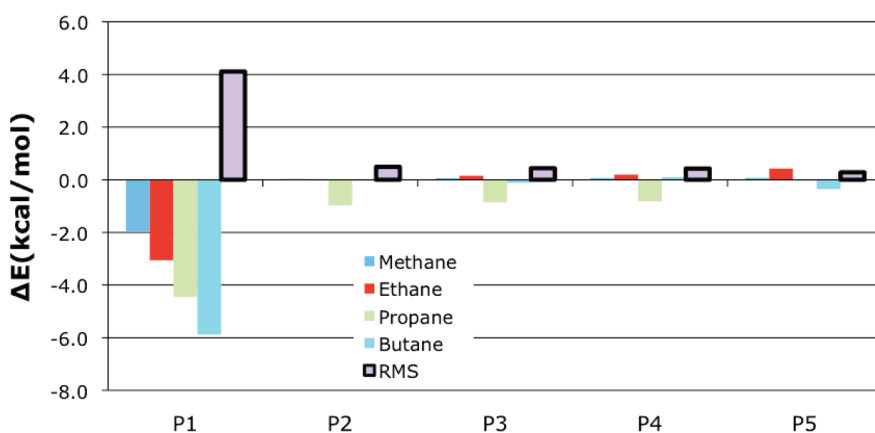


Figure 3. Energy differences between QM/MM and QM results (6-31+G** basis) for alkanes adsorbed in all-silica T23 MFI. Alkane absorption is sensitive to Lennard-Jones parameters but insensitive to MM charges.

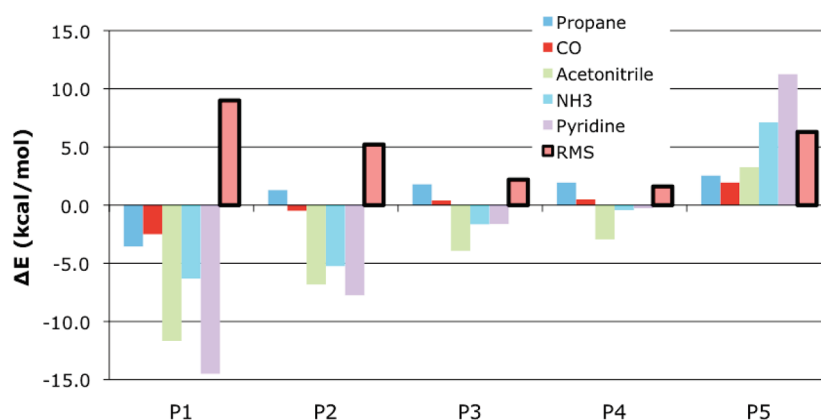


Figure 4. Energetic differences between QM/MM and QM results (6-31+G** basis) for molecules adsorbed in T44 H-MFI. These adsorbed molecules are sensitive to both Lennard-Jones parameters and MM charges.

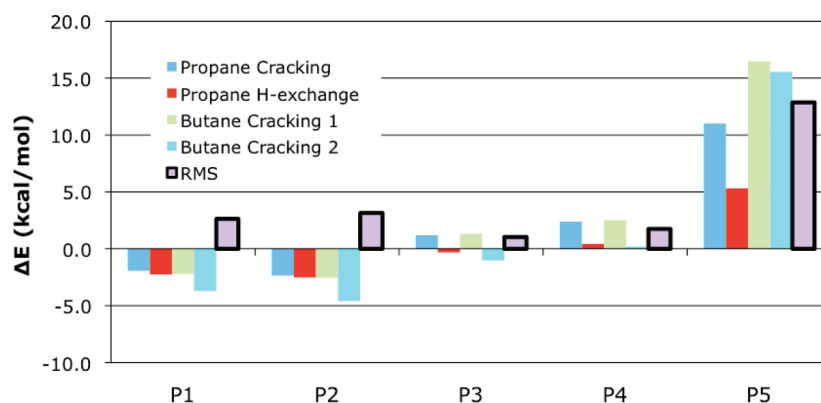


Figure 5. Energetic differences between QM/MM and QM results (6-31+G** basis) for alkane activation in T23 H-MFI. Transition states are most sensitive to MM charge parameters, and mechanical embedding (P5) fails to reproduce QM results.

differences in the energies calculated from QM/MM and full QM. An even stronger effect of the charges placed on Si and O is evident for the calculation of activation energies for reactions involving propane and butane. In this case, the best agreement between QM/MM and full QM calculations is obtained using parameter set P3. When all three test sets are examined together, Figure 6 demonstrates that the

smallest rms difference in energies between the two computational strategies is obtained using parameter set P4.

QM/MM calculations carried out with the new charge and Lennard-Jones parameters also reproduced geometries obtained from full QM calculations. When single-point full QM energies were determined using fully converged QM/MM geometries,

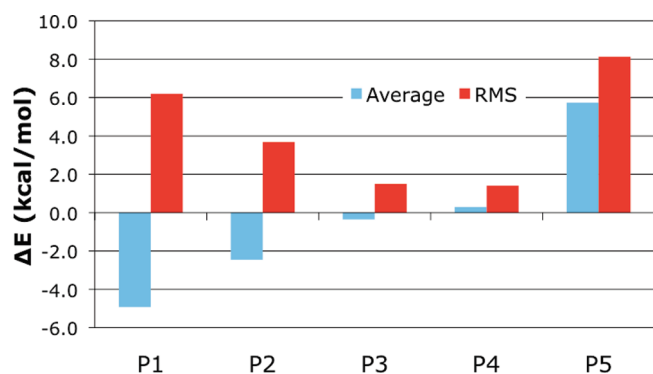


Figure 6. Energetic differences between QM/MM and QM results (6-31+G** basis) averaged over the entire test set. The largest errors occur when mechanical embedding (zero charge in MM region, P5) is used and when charge and Lennard-Jones parameters are taken directly from an MM force field (P1).

Table 4. Difference in Energy from QM Single Points at QM/MM Optimized Geometries Compared to QM Optimized Geometries

		P3		P4	
		6-31G*	6-31+G**	6-31G*	6-31+G**
T23 MFI	methane	0.0	0.0	0.0	0.0
(all silica)	ethane	-0.5	-0.5	-0.5	-0.5
	propane	-0.3	-0.3	-0.3	-0.3
	butane	-0.2	-0.2	-0.1	-0.1
T44	propane	0.0	1.1	0.0	1.1
H-MFI	CO	0.0	0.4	0.0	0.2
	acetonitrile	1.7	0.6	1.7	0.6
	NH ₃	-0.7	0.3	-0.7	0.2
	pyridine	0.0	0.5	0.0	0.5
T23	propane cracking	-1.9	-0.6	-2.0	-0.7
H-MFI	propane H exchange	-2.5	-1.0	-2.4	-1.0
	butane cracking 1	1.3	0.5	1.2	0.4
	butane cracking 2	0.9	0.3	0.9	0.3
overall	average	-0.2	0.1	-0.2	0.1
	rms	1.0	0.6	1.1	0.6

the rms difference between QM energies at the full converged QM geometry and QM at the QM/MM geometry was less than 1 kcal/mol (see Table 4).

Parameter Transferability. To determine the transferability of the selected parameters, two additional tests were done. First, the entire test set was repeated with B3LYP and the 6-31G* basis (see Table 2). To ensure a reasonable comparison, Lennard-Jones energies were removed from the QM/MM results because, as discussed earlier, the B3LYP functional does not account for dispersive interactions. Across the entire test set, QM/MM reproduces B3LYP energies with an rms difference of 1.8 kcal/mol with parameter set P4 and an rms difference of 2.2 kcal/mol with parameter set P3. In comparison, QM/MM with ω B97X-D reproduces the QM energies with a 1.5 kcal/mol rms error, indicating that these parameters are likely transferable to other density functionals.

To test the transferability of the charges and Lennard-Jones parameters found to be best-suited for MFI, calculations were

Table 5. Single Point Energy Times from QM and QM/MM for Propane Adsorption

	time/SCF cycle		
	QM	QM/MM	QM/MM speedup
T5	9.2	N/A	1×
T23	769.2	14.6	53×
T44	9212.0	13.4	687×
	in seconds		

carried out for the adsorption of CO, pyridine, and NH₃ at Brønsted acid sites in FAU. For these calculations, the framework of FAU was represented by a T52 cluster. For DFT calculations carried out at the ω B97X-D/6-31G* level, the rms errors in absorption energies obtained from QM and QM/MM were 2.0 kcal/mol for parameter set P4 and 3.7 kcal/mol for parameter set P3. Therefore, the charge and Lennard-Jones parameters that give accurate results for MFI are transferable to FAU and, by extension, to other zeolites.

As demonstrated by the current study, QM/MM calculations of adsorption and reaction occurring in cluster representations of zeolites can achieve accuracies rivaling those obtained from full QM calculations for clusters of the same size as that used for the QM/MM calculations. The significant difference, though, is that QM calculations in the QM/MM approach are done for only a T5 cluster electrostatically embedded in the remainder of the model cluster. This difference enables substantially faster computational times than can be achieved using a full QM approach. To demonstrate this point, Table 5 lists the times required for single point calculations of the energy for propane adsorption in MFI determined by QM and QM/MM as a function of the cluster size. It is evident that for a T23 cluster, QM/MM is over 50 times faster than QM, and for a T44 cluster, QM/MM is over 600 times faster than QM. This means that the QM/MM approach can be used to carry out calculations of adsorption and reaction processes using a very large overall cluster, which may contain multiple active sites.

■ ALKANE ACTIVATION IN LARGE ZEOLITE LATTICE

To demonstrate the lattice size approachable by QM/MM, parameter set P4 was used to investigate the cracking in MFI of *n*-alkanes^{42–47} containing up to 18 carbon atoms. A cluster of about 1000 atoms (T356) was required to represent the straight channel of MFI so as to capture the effects of dispersive interactions for alkanes containing up to 18 carbon atoms (see Figure 7). The MFI zeolite includes a single acid site at the T12 position. The reacting molecules and a T5 active site are placed in the QM region of QM/MM. If a smaller cluster had been used, a part of the largest alkanes in the series would have spilled out of the cluster, and a similar problem would have arisen if we had tried to use a small repeated cell for periodic boundary calculations. Therefore, neither QM cluster simulations nor periodic simulations can handle the size of the cluster required to study linear alkanes with 18 carbon atoms. With $\sim N^3$ scaling for DFT, such a large cluster would require approximately 5000 times the computational time required for a T23 cluster and hence would be prohibitive.

This setup is designed to demonstrate the ability of QM/MM to describe chemistries that require a large model zeolite, but we do not suggest that the absorption and cracking of C12 and C18 alkanes in the zeolite straight channel specifically represent the physical process in MFI. Instead, if C₁₂H₂₆ or C₁₈H₃₈ were to

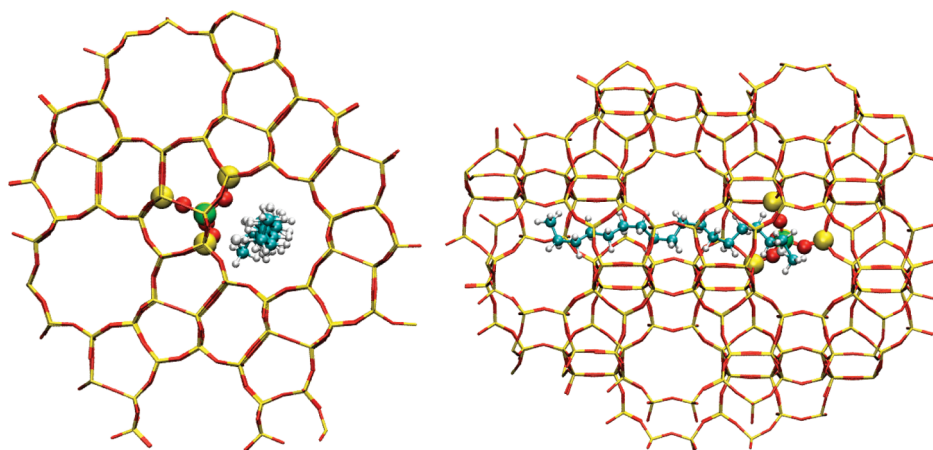


Figure 7. T356 MFI zeolite used for investigating the cracking of long alkanes. C18 is shown in the straight channel. The T5 QM region centered on the Al site is highlighted (view down straight channel on left, side view on right).

Table 6. Intrinsic Activation Barriers (ΔH_{773K}^\ddagger) for Terminal Carbon Cracking of C_3 – C_8 Alkanes Determined via QM/MM ω B97X-D/6-31G* Using a T356 Representation of the Straight Channel in MFI with the Acid Site Located at the T12 Position

	Intrinsic Cracking Barrier, ΔH_{773K}^\ddagger (kcal/mol)	
	T356	exp.
C_3H_8	40.4	46.1, ⁶¹ 47.3 ⁶⁰
C_6H_{14}	36.3	47.1 ⁶⁰
$C_{12}H_{22}$	35.1	N/A
$C_{18}H_{38}$	37.3	N/A

diffuse into MFI, cracking may begin prior to complete absorption. For this reason, we emphasize that the following results are specifically based on the assumption that the long chain alkanes diffuse to an absorption site in a zeolite straight channel without being cracked prior to absorption.

Table 6 lists the intrinsic activation enthalpy for C_3 through C_{18} for terminal C–C bond cracking determined at the ω B97X-D/6-31G* level of theory. The intrinsic activation enthalpy for propane cracking (i.e., the energy difference between the transition state and propane absorbed at the acid site) is 40.4 kcal/mol. This value is 4.8 kcal/mol lower than that determined at the same level of theory using a T23 cluster. The lower barrier height determined for the larger cluster is due to the additional electrostatic stabilization of the separated charges in cracking TSs and indicates the significance of long-range interactions that are missed by small cluster models. For cracking at an acid site positioned at T12, QM/MM with ω B97X-D/6-31G* underestimates the experimentally determined intrinsic barrier heights for cracking of terminal C–C bonds in propane and hexane by 7–10 kcal/mol. To determine how sensitive the cracking barrier was to the acid site position, the cracking barriers for propane and hexane were determined with the acid site positioned at T3. With this acid site, the intrinsic activation barriers rose by 3.2 and 5.8 kcal/mol, for propane and hexane, respectively, indicating significant variance due to acid site position. These barriers therefore come within about 4 kcal/mol of the experimental

Comparison of atomic distances calculated by QM/MM using T23 and T356 cluster representations of MFI

C_3H_8	Distance in Å	
	T23 Cluster	T356 Cluster
C1-C2	1.808	1.755
C1-H1	1.244	1.303
C2-H1	1.314	1.333
O1-H1	1.873	1.709

Effect of alkane length on bond distances determined by QM/MM using a T356 representation of MFI

	Distance in Å			
	C_3H_8	C_6H_{14}	$C_{12}H_{26}$	$C_{18}H_{38}$
C1-C2	1.755	1.730	1.780	1.788
C1-H1	1.303	1.327	1.293	1.287
C2-H1	1.333	1.318	1.268	1.269
O1-H1	1.709	1.698	1.860	1.858

Figure 8. Geometric distances for cracking reactions in T23 MFI cluster compared to the large (T356) MFI cluster. Both zeolites contain the acid site at the T12 position. Only the T5 QM region is shown, and geometries are qualitatively similar for cracking of the longer alkanes.

values. This is by no means a complete sampling of the variety of acid sites in MFI, so a complete theoretical study of alkane activation will require systematic investigation of the effect of the acid site to provide a quantitative comparison to experimental results.

The geometries for cracking reactions are somewhat dependent on the size of the zeolite cluster model and the alkane length. Figure 8 shows a comparison of cracking geometries from T23 and the large zeolite for reactions with the T12 acid site. These geometries are compared via examination of the distances between the acid active site oxygen, the proton, and the two carbon atoms undergoing cracking. While the smaller T23 zeolite qualitatively reproduces the larger zeolite's cracking geometries for propane, the O–H distance at the TS is longer by about 0.16 Å. This indicates that the missing long-range electrostatics cause an approximate description of the TS geometry. This suggests that previous simulations with smaller clusters (i.e., T23, T44) can yield useful information about zeolite reactivity but are still incomplete descriptions of chemistries like alkane cracking. Furthermore, smaller model clusters will inevitably leave out the

shape selectivity inherent to the zeolite structure and cannot model any reactivity that depends on extended zeolite structure.

There is a small but significant difference in the alkane cracking geometries when comparing the shorter alkanes to the longer alkanes. Specifically, the O–H distance for the shorter alkanes is about 0.15 Å shorter than in the longer alkanes. This difference can be attributed to the steric constraints of adsorbing and cracking C12 and C18 in the straight channel. The longer alkanes do not have the same degree of steric flexibility as C3 and C6, forcing the proton to be slightly further away from the acid site at the cracking geometry. Because the potential energy surface in zeolites is relatively flat due to the long-range electrostatics and dispersion of the lattice, multiple minima corresponding to the same TS may be present. To determine whether this was true, we reoptimized the TSs for C12 and C18 starting from geometries with quantitatively similar bond lengths as C3. However, the TS searches resulted in the same geometries as determined previously, indicating that the shorter and longer alkanes can be differentiated on the basis of the steric properties of their absorption in the large zeolite lattice.

CONCLUSIONS

Hybrid QM/MM simulations that provide similar accuracy to full QM simulations have been achieved over a diverse test set of zeolite interactions and reactions. Although QM/MM has been known to be a computationally efficient method (about 50× faster than QM for a T23 zeolite compared to QM/MM with a T5 QM region, 700× faster for T44), its accuracy is shown to be highly dependent on the quality of the MM parameters. As Table 1 shows, there is no agreement in the literature on the appropriate atomic partial charges, and up to this point, no systematic testing has been done to validate charge parameters for QM/MM. In QM/MM simulations, utilizing charge parameters designed for MM is inappropriate without careful validation.

Parameters specifically selected for QM/MM in zeolites are provided herein (see Table 5) and are useful for electrostatically embedded QM/MM implementations. The Lennard-Jones parameters are chosen for compatibility with CHARMM adsorbate parameters. The selected parameters provide an accuracy of about 1.5 kcal/mol and reproduce QM structures to within 1.0 kcal/mol when a T5 cluster is used for the QM region. These errors are quite low and demonstrate the applicability of static point charges and single hydrogen link atoms for QM/MM simulations. This accuracy, however, could still be improved by accounting for polarization in the MM region or improved link atom representations. Because the parameters are applicable to ω B97X-D and B3LYP functionals as well as MFI and FAU zeolites, we anticipate that they will be generally useful for QM/MM zeolite simulations.

The accuracy of zeolite simulations depends strongly on the quality of the density functional as well as the MM parameters. The results of this study suggest that density functionals that capture dispersion interactions should be used whenever possible, and dispersion corrections should also be applied between MM–QM atom pairs. This is exemplified in Table 2, where B3LYP poorly reproduces experimental heats of absorption and apparent activation energies. Furthermore, examination of Table 3 and Figure 6 shows that neglect of electrostatics (i.e., $Q_{\text{Si}} = Q_{\text{O}} = 0$ mechanical embedding) outside of the T5 cluster produces results that are far from convergence. QM/MM simulations that reproduce the results of density functionals such as ω B97X-D provide an efficient avenue for examining complex shape-selective reactivity in zeolites.

AUTHOR INFORMATION

Corresponding Author

*E-mail: mhg@ccchem.berkeley.edu.

REFERENCES

- (1) Corma, A. *Chem. Rev.* **1995**, *95*, 559–614.
- (2) Smit, B.; Maesen, T. L. M. *Chem. Rev.* **2008**, *108*, 4125–4184.
- (3) Vermeiren, W.; Gilson, J.-P. *Top. Catal.* **2009**, *52*, 1131–1161.
- (4) Yu, J.; Xu, R. *Acc. Chem. Res.* **2010**, *43* (9), 1195–1204.
- (5) Traa, Y.; Burger, B.; Weitkamp, J. *Microporous Mesoporous Mater.* **1999**, *30*, 3–41.
- (6) Marcilly, C. R. *Top. Catal.* **2000**, *13*, 357–366.
- (7) Ribeiro, M.F., J. M. *J. Mol. Cat. A* **1995**, *96*, 245–270.
- (8) Rigutto, M. S. In *Zeolites and Related Materials: Trends, Targets and Challenges*; Gedeon, A., Massania, P., Babonneau, F., Eds; Elsevier: Amsterdam, 2008; Vol 174, pp 43–52.
- (9) Sastre, G.; Corma, A. *J. Mol. Cat. A* **2009**, *305*, 3–7.
- (10) Ribeiro, M. F. R.; Alvarez, F.; Henriques, C.; Lemos, F.; Lopes, J. M.; Ribeiro, M. F. *J. Mol. Cat. A* **1995**, *96*, 245–270.
- (11) Broadbelt, L. J.; Snurr, R. Q. *App. Catal. A* **2000**, *200*, 23–46.
- (12) Tafipolsky, M.; Amirjalayer, S.; Schmid, R. *Microporous Mesoporous Mater.* **2010**, *129*, 304–318.
- (13) (a) Hohenberg, P.; Kohn, W. *Phys. Rev.* **1964**, *136*, B864. (b) Kohn, W.; Sham, L. J. *Phys. Rev.* **1965**, *140*, A1133.
- (14) (a) Becke, A. D. *Phys. Rev. A* **1988**, *38*, 3098–3100. (b) Lee, C. T.; Yang, W. T.; Parr, R. G. *Phys. Rev. B* **1988**, *37*, 785–789.
- (15) Zhao, Y.; Truhlar, D. G. *J. Phys. Chem. C* **2008**, *112* (17), 6860–6868.
- (16) Zhao, Y.; Truhlar, D. G. *Org. Lett.* **2006**, *8* (25), 5753–5755.
- (17) Zhao, Y.; Truhlar, D. G. *Theor. Chem. Acc.* **2008**, *120*, 215.
- (18) (a) Chai, J.-D.; Head-Gordon, M. *Phys. Chem. Chem. Phys.* **2008**, *10*, 6615–6620. (b) Chai, J.-D.; Head-Gordon, M. *J. Chem. Phys.* **2008**, *128*, 084106.
- (19) (a) Blaszkowski, S. R.; Nascimento, M. A. C.; van Santen, R. A. *J. Phys. Chem.* **1996**, *100* (9), 3463–3472. (b) Boronat, M.; Viruela, P.; Corma, A. *J. Phys. Chem. A* **1998**, *102*, 982–989.
- (20) Hansen, N.; Kerber, T.; Sauer, J.; Bell, A. T.; Keil, F. J. *J. Am. Chem. Soc.* **2010**, *132*, 11525–11538.
- (21) Tuma, C.; Kerber, T.; Sauer, J. *Angew. Chem., Int. Ed.* **2010**, *49*, 4678–4680.
- (22) Lin, H.; Truhlar, D. G. *Theor. Chem. Acc.* **2007**, *117*, 185–199.
- (23) Bakowies, D.; Thiel, W. *J. Phys. Chem.* **1996**, *100*, 10580–10594.
- (24) de Vries, A. H.; Sherwood, P.; Collins, S. J.; Rigby, A. M.; Rigutto, M.; Kramer, G. J. *J. Phys. Chem. B* **1999**, *103*, 6133–6141.
- (25) Clark, L. A.; Sierka, M.; Sauer, J. *J. Am. Chem. Soc.* **2004**, *126*, 936–947.
- (26) Lomratsiri, J.; Probst, M.; Limtrakul, J. *J. Mol. Graphics Model.* **2006**, *25*, 219–225.
- (27) Shor, A. M.; Ivanova Shor, E. A.; Laletina, S.; Naslusov, V. A.; Vayssilov, G. N.; Rosch, N. *Chem. Phys.* **2009**, *363*, 33–41.
- (28) Sierka, M.; Sauer, J. *Faraday Disc.* **1997**, *106*, 41–62.
- (29) Sauer, J.; Sierka, M. *J. Comput. Chem.* **2000**, *21* (16), 1470–1493.
- (30) Svensson, M.; Humbel, S.; Froese, R. D. J.; Matsubara, T.; Sieber, S.; Morokuma, K. *J. Phys. Chem.* **1996**, *100* (50), 19357–19363.
- (31) Olson, D. H.; Koktailo, G. T.; Lawton, S. L.; Meier, W. M. *J. Phys. Chem. B* **1981**, *85*, 2238–2243.
- (32) Olson, D. H. *Zeolites* **1995**, *15*, 439–443.
- (33) Olson, D. H. *J. Phys. Chem. B* **2000**, *104*, 4844–4848.
- (34) Mentzen, B. F.; Sacerdoteperonnet, M. *Mater. Res. Bull.* **1994**, *29*, 1341–1348.
- (35) Shao, Y.; *Phys. Chem. Chem. Phys.* **2006**, *8*, 3172–3191.
- (36) Woodcock, H. L.; Hodoscek, M.; Gilbert, A. T. B.; Gill, P. M. W.; Schaefer, H. F.; Brooks, B. R. *J. Comput. Chem.* **2007**, *28* (9), 1485–1502.

- (37) Field, M. J.; Bash, P. A.; Karplus, M. *J. Comput. Chem.* **1990**, *11*, 700.
- (38) Shao, Y.; Kong, J. *J. Phys. Chem. A* **2007**, *111*, 3661.
- (39) Ferre, N.; Assfeld, X. *THEOCHEM* **2003**, *632*, 83–90.
- (40) (a) Foloppe, N.; Mackerell, A. D. *J. Comput. Chem.* **2000**, *21* (2), 86–104. (b) Yin, D.; Mackerell, A. D. *J. Comput. Chem.* **1998**, *19* (3), 334–348. (c) Vanommeslaeghe, K.; Hatcher, E.; Acharya, C.; Kundu, S.; Zhong, S.; Shim, J.; Darian, E.; Guvench, O.; Lopes, P.; Vorobyov, I.; Mackerell, A. D. *J. Comput. Chem.* **2009**, *31* (4), 671.
- (41) Lopes, P. E. M.; Murashov, V.; Tazi, M.; Demchuk, E.; Mackerell, A. D. *J. Phys. Chem. B* **2006**, *110*, 2782–2792.
- (42) Swisher, J. A.; Hansen, N.; Maesen, T.; Keil, F. J.; Smit, B.; Bell, A. T. *J. Phys. Chem. C* **2010**, *114*, 10229–10239.
- (43) Kottrel, S.; Knozinger, H.; Gates, B. C. *Microporous Mesoporous Mater.* **2000**, *35–36*, 11–20.
- (44) Haag, W. O. *Stud. Surf. Sci. Catal.* **1994**, *84*, 1375.
- (45) Kottrel, S.; Rosynek, M. P.; Lunsford, J. H. *J. Phys. Chem. B* **1999**, *103*, 818–824.
- (46) Katada, N.; Suzuki, K.; Noda, T.; Miyatani, W.; Taniguchi, F.; Niwa, M. *Appl. Catal. A: Gen.* **2010**, *373*, 208–213.
- (47) Babitz, S. M.; Williams, B. A.; Miller, J. T.; Snurr, R. Q.; Haag, W. O.; Kung, H. H. *Appl. Catal. A: Gen.* **1999**, *179*, 71–86.
- (48) Pantu, P.; Boekfa, B.; Limtrakul, J. *J. Mol. Cat. A* **2007**, *277*, 171–179. (b) Kasuriya, S.; Namuangruk, S.; Treesukol, P.; Tirtowidjojo, M.; Limtrakul, J. *J. Catal.* **2003**, *219*, 320–328. (c) Sung, C.-Y.; Broadbelt, L. J.; Snurr, R. Q. *J. Phys. Chem. C* **2009**, *113*, 15643–15651.
- (49) Nasluzov, V. A.; Ivanova, E. A.; Shor, A. M.; Vayssilov, G. N.; Birkenheuer, U.; Rosch, N. *J. Phys. Chem. B* **2003**, *107*, 2228–2241.
- (50) Shor, A. M.; Ivanova Shor, E. A.; Laletina, S.; Nasluzov, V. A.; Vayssilov, G. N.; Rosch, N. *Chem. Phys.* **2009**, *363*, 33–41.
- (51) Sherwood, P.; de Vries, A. H.; Collins, S. J.; Greatbanks, S. P.; Burton, N. A.; Vincent, M. A.; Hillier, I. H. *Faraday Discuss* **1997**, *106*, 79–92.
- (52) Injan, N.; Pannorad, N.; Probst, M.; Limtrakul, J. *Int. J. Quantum Chem.* **2005**, *105*, 898–905.
- (53) Stefanovich, E. V.; Truong, T. N. *J. Phys. Chem. B* **1998**, *102*, 3018–3022.
- (54) Sun, M. S.; Shah, D. B.; Xu, H. H.; Talu, O. *J. Phys. Chem. B* **1998**, *102*, 1466–1473.
- (55) Eder, F.; Stockenhuber, M.; Lercher, J. A. *J. Phys. Chem. B* **1997**, *101*, 5414–5419.
- (56) Savitz, S.; Myers, A. L.; Gorte, R. J. *J. Phys. Chem. B* **1999**, *103*, 3687–3690.
- (57) Szanyi, J.; Paffett, M. T. *Microporous Mater.* **1996**, *7*, 201–218.
- (58) Lee, C.-C.; Gorte, R. J.; Farneth, W. E. *J. Phys. Chem. B* **1997**, *101*, 3811–3817.
- (59) Parrillo, D. J.; Gorte, R. J. *Appl. Catal. A: Gen.* **1994**, *110*, 67–74.
- (60) Narbeshuber, T. F.; Vinek, H.; Lercher, J. A. *J. Catal.* **1995**, *157*, 388–395.
- (61) Xu, B.; Sievers, C.; Hong, S. B.; Prins, R.; van Bokhoven, J. A. *J. Catal.* **2006**, *244*, 163–168.

Nature of Chemical Interactions from the Profiles of Electron Delocalization Indices

Marco García-Revilla,[†] Paul L. A. Popelier,[‡] Evelio Francisco,[†] and Ángel Martín Pendás^{*,†}

[†]Departamento de Química Física y Analítica, Facultad de Química, Universidad de Oviedo, E-33006-Oviedo, Spain

[‡]Manchester Interdisciplinary Biocentre (MIB), 131 Princess Street, Manchester M1 7DN, United Kingdom and School of Chemistry, University of Manchester, Oxford Road, Manchester M13 9PL, United Kingdom

ABSTRACT: We analyze the behavior of the profiles of delocalization indices (DIs) between relevant pairs of atoms along reaction coordinates for a set of model chemical processes. A relationship between the topology of the DI and the nature of the underlying chemical change is reported. As shown, exponential shapes correspond to the traditional category of repulsive/nonbonded interactions, while sigmoidal profiles signal the formation/breaking of chemical links.

1. INTRODUCTION

The concept of the chemical bond, central to the science of chemistry, is still a matter of lively debate among scholars almost 95 years after Lewis's insights¹ and 50 years after Pauling² laid the modern foundations of the field. At the very heart of the problem lies the fact that establishing both when two atoms are bonded or not and when their interaction stabilizes the energy of a molecule are not easy tasks for polyatomics. In fact, they require either techniques to describe atoms in molecules or ways to partition molecular energies into atomic or pair contributions.

In the past few decades, real space theories of the chemical bond have provided an alternative to the molecular orbital (MO)³ paradigm that has dominated the field. The best known approaches are based on partitioning the real space through the gradient operating on some scalar field endowed with chemical content and are collectively known as Quantum Chemical Topology (QCT).^{4,5} Among them, the Quantum Theory of Atoms in Molecules (QTAIM) developed by Bader⁶ stands out. In its basic mode of operation, a set of indicators based on reduced density matrices (like the density itself, ρ , the laplacian of the density, $\nabla^2\rho$, the energy density, H , and many others) are obtained at the finite set of distinguished points in space where $\nabla\rho = 0$. These are the critical points (CPs) of the ρ field, and their set of indicators is used to build correlations to chemically important concepts, ranging from bond order and bond type to basicity or reactivity indices.

Recently, one of the best known results of the QTAIM, the identification between bond critical points (BCPs) at stationary molecular configurations⁷ and pairs of bonded atoms, has been put into question. In short, BCPs are found where chemists will not place them and vice versa.^{8–11} The situation has led to a particularly intense debate regarding the meaning of BCPs in situations that are usually understood as nonbonding (steric, repulsive).^{11–16} Examples of this discussion may be found in the recent work of Grimme et al. about the nonexistence of a bonded interaction between the bay moiety hydrogens in phenanthrene¹⁷ and in the study of Henn et al. on the absence of BCPs in HS(CH)(CH₂) and F(CH₂)₄F.¹⁸ The debate is in

our opinion far from over, and radically opposite interpretations are offered by the supporters of both positions.

Some of us have previously contributed to this discussion by noticing that alternative interpretations to the meaning of BCPs exist.¹⁹ According to our proposal, on the basis of the interacting quantum atoms approach (IQA),^{20–23} bond paths signal privileged exchange-correlation (xc) channels between pairs of atoms, thus always providing a locally stabilizing V_{xc} term to the total energy. Since V_{xc} is just one of the terms in the IQA energetic decomposition, this view makes the presence of BCPs fully compatible with global destabilizations. The close relationship of BCPs to the energetic properties of a system connects two paradigmatic views of the chemical bond, the molecular structure due to the topology of $\rho(r)$ and the energetic behavior associated with a bonded system. Such a connection between the structure and the energetics gives an important contribution to the physical meaning of the BCPs and to the partitioning of space provided by the QTAIM.

It is becoming increasingly clear that a common source of this and other criticisms made to QCT resides in its local operating mode. By restricting QCT analyses to examining properties at CPs, we unfortunately subject our description to the lability of these positions in space, which appear and disappear catastrophically upon geometrical rearrangements of the nuclei. Such a sensitivity is absent if QCT focuses on global (i.e., domain-integrated) properties. Global descriptors may involve not only one basin but two, as in the calculation of V_{xc} , or even many, being perfectly suited to identifying relations among atoms. We firmly believe that by using global descriptors, useful insights about the nature of chemical interactions will be found.

In this work, we examine the behavior of one of the simplest two-basin indices, the shared electron delocalization index (SEDI), or delocalization index (DI) for short, and uncover an interesting link between the topology of the DI profile along a reaction coordinate and the nature of the chemical change associated with it. The close algebraic proximity between SEDIs

Received: March 17, 2011

Published: May 13, 2011

(see eq 1 below) and V_{xc} 's²⁰ pushes us to do so, the latter being an energetic signature of the former. Thus, as the competition of different exchange-correlation energetic contributions between a given atom and its neighbors determines the existence or not of BCPs, DIs may hold interesting information that may be masked in V_{xc} due to the intrinsic dependence on interelectron distances of the latter. As it will show up in the following, the new insights cannot be obtained directly from either V_{xc} or the local values of scalars fields, i.e., densities, laplacians, etc., at BCPs.

Although QCT DI profiles are not new,²⁴ they have been scarcely used in the literature up to now. For instance, their evolution along reaction paths has been used to study the reactivity and aromaticity in model chemical reactions.^{25–29} Similarly, Poater and co-workers²⁵ have proposed that the changes in the DI are evidence of the reorganization of the electron pairing along the reaction path. Within this interpretation, a DI profile agrees with the predictions of the traditional Lewis model. Another related study was presented by Matito and co-workers,²⁸ where the behavior of DI and localization index profiles was used to visualize quantitatively the problems of the restricted Hartree–Fock method in reproducing homolitic dissociations. In addition, Ponc and Cooper²⁶ reported the presence of inflection points in DI profiles for bonded systems, finding no molecule-specific significance to the location of such points. They did not compare bonded and nonbonded systems.

In summary, a literature survey shows that the different shapes of the DI profiles are related to the bonding or nonbonding nature of the interaction that is being followed but that this link has not been explored explicitly up to now. Here, we examine a number of simple, prototypical chemical changes modeled at different levels of theory to substantiate our findings.

2. METHODS, SYSTEMS, AND COMPUTATIONAL DETAILS

The delocalization index between two quantum groups A and B , δ^{AB} , was introduced by Bader and Stephens³⁰ as a measure of the number of electron pairs delocalized between the groups. Since then, it has been used as a real space measure of the covalent bond order³¹ and has been shown to correspond to the real space analogue of the commonly used Wiberg–Mayer bond index.^{32,33} δ^{AB} is obtained by a two-electron, two-basin integration of the exchange-correlation density, $\rho_{xc}(1,2) = \rho(1)\rho(2) - \rho_2(1,2)$, where ρ_2 is the second order reduced density matrix:

$$DI = \delta^{AB} = 2 \int_A d1 \int_B d2 \rho_{xc}(1,2) \quad (1)$$

In the case of single determinant (SD) wave functions, ρ_{xc} may be factorized in terms of the nondiagonal first order density matrix:

$$\begin{aligned} \rho_{xc}(1,2) &= \rho(1;2)\rho(2;1) \\ &= \sum_{i,j} \phi_i(1)\phi_j(1)\phi_i(2)\phi_j(2) \end{aligned} \quad (2)$$

where the sums run over all of the occupied spin orbitals ϕ . In this way, the DI is written in terms of domain-restricted overlap integrals, or atomic overlap matrices (AOM), $\delta^{AB} = 2 \sum_{i,j} C_{ij}^A C_{ij}^B$. This expression has many times been taken as the definition of the DI but is rigorously valid only in the Hartree–Fock approximation. If correlation is deemed important, as in many of the cases we are going to present, then the full four-index representation of the second order density has to be used, and more cumbersome expressions appear. Nevertheless, the DI may

always be written as a linear combination of AOM elements, and thus no true 6D integrations are actually needed for its evaluation. With this 3D factorization, the computational complexity of obtaining DIs is not larger than that in the usual 3D integrations of the QTAIM. This is no longer true for other two-electron indices like V_{xc} . As a consequence, DIs are among the only two-electron properties that are commonly obtained in standard QTAIM packages, at least for SD wave functions. We have developed efficient methods to compute DIs in the case of multideterminant expansions of Ψ ,³⁴ and expressions based on density matrix functional theory approximations to ρ_{xc} have also been developed.^{35,36}

A connection between the DI and the fluctuation of the basin populations exists.^{30,37–39} It may be shown that the covariance of the joint probability distribution for the number of electrons in the basins A and B is given by the DI:

$$\delta^{AB} = -2\text{cov}(n_A, n_B) = -2[\langle n_A n_B \rangle - \langle n_A \rangle \langle n_B \rangle] \quad (3)$$

where $\langle n_A n_B \rangle = \sum_{n_A, n_B} n_A n_B p(n_A, n_B)$ and $\langle n_A \rangle = \sum_{n_A} n_A p(n_A)$. In these expressions, $p(n_A)$ and $p(n_A, n_B)$ are electron number distribution functions (EDFs). The first provides the probabilities of observing an exactly integer number of electrons n_A in basin A and the second, the joint probability of finding n_A electrons in basin A and n_B electrons in basin B . Since there are now efficient methods to construct such EDFs,^{40–42} an interesting interpretation is emerging in which chemical bonding is interpreted in terms of the fluctuation in the number of electrons associated with quantum atoms. In a diatomic, for instance, the constancy of the total number of electrons $N = n_A + n_B$ forces any change in the population of one basin to be accompanied by a symmetric (and opposite in sign) change in the other. The DI (minus covariance) in such a case is a necessarily positive quantity, a property that does not necessarily hold in general polyatomic systems. DIs are (contrarily to other atomic expectation values, like the kinetic energy) perfectly defined for any pair of nonoverlapping regions of the 3D space. They will be positive-definite if the integrand is positive-definite. This is not true, for ρ_{xc} may take negative values whenever the Coulomb correlation contribution dominates over the Fermi one. This means that we may in principle find two regions of space with negative ρ_{xc} that will give a negative DI. What is necessarily true is that the sum of all delocalization and localization values, i.e., the integral over the full 6D space of ρ_{xc} , must be positive and equal to N , the number of electrons in the molecule. We think that it is very unlikely that a negative DI will show up between two entire atomic regions. This would mean that the Coulomb correlation overcomes the Fermi contribution over large regions, something not very plausible, but not impossible. In any case, positive values will arise whenever the populations of two basins are negatively correlated. In other words, whenever there is a direct physical exchange of electrons between the basins. Using this kind of insight, we have shown⁴¹ how the bond order may be interpreted in terms of the number of electrons of one basin that may be exchanged with the other, providing an intuitive view of well-known traditional concepts.

Following some reported observations based on the shape of both Wiberg indices^{43,44} and QCT DIs,^{24,45} we have selected a number of simple chemical processes and studied the behavior of DIs along their intrinsic reaction coordinates (IRC). The use of IRCs allows us to map the complex geometric rearrangements following a reaction onto a unique scalar parameter. The processes examined include dissociations, atomic exchanges,

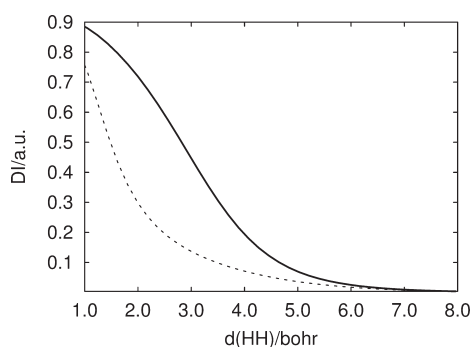


Figure 1. Delocalization index versus HH distance for the dissociation of singlet (full line) and triplet (dotted line) H_2 .

migrations, intramolecular rearrangements, and a few of the controversial systems commented on before. Some of these processes are well represented at the Hartree–Fock (HF) level, and since our purpose here is not quantitative, we present such low level calculations. Other dissociations, particularly open-shell ones, cannot be adequately described if correlation is not taken into account. In such cases, appropriate multideterminant calculations will be reported, either at the CAS or CISD level.

All electronic structure calculations, including optimizations, transition state (TS) searches, and constrained optimizations, have been performed with the GAMESS⁴⁶ code using the 6-311++G(d,p) basis set. DIs have been obtained with our PROMOLDEN code.

3. RESULTS

We will begin our discussion by examining the dissociation of simple bonded and nonbonded diatomics, starting with H_2 . We have previously reported⁴⁷ an EDF/IQA analysis in this system to which the reader is referred for further insights, but no explicit account of the behavior of DIs was given there.

3.1. The Dissociation of Diatomics. We have examined the formation and breaking of several homo- and heteronuclear diatomics. Here, we report on the dissociation of H_2 , N_2 , He_2 , Ar_2 , and LiH .

The breaking of the first molecule is the paradigm of an open-shell process, so we will use a CAS[2,2] description. It provides the simplest wave function that fully describes the process. Figure 1 shows the variation of DI(HH) with the internuclear separation for both the $X^1\Sigma_g^+$ and $b^3\Sigma_u^+$ states. The optimization of the former gives rise to the ground state of H_2 at an internuclear distance of about $d = 1.4$ bohr, while the latter is a repulsive state. The effect of correlation in the singlet is essential, since a SD description provides $DI = 1$ at any internuclear distance. This may be interpreted as a result of the statistical independence of α and β electrons at the HF level that leads, through eq 3, to a binomial distribution of the electron populations in both basins. Thus, the probabilities of finding simultaneously n_A and n_B electrons in each basin becomes $p(2,0) = p(0,2) = 0.25$ and $p(1,1) = 0.5$.⁴⁷ Introduction of α,β correlation partially localizes both electrons, and $p(1,1)$ increases so that $DI = 2 - 2p(1,1)$ decreases. The two α electrons are always correlated in the triplet state, even in a SD description.

The DI profiles for the H_2 dissociation of the singlet and triplet states are shown in Figure 1, the singlet profile is similar to that reported by Matito and co-workers.²⁸ As we can observe, the topology of the DI profiles is qualitatively different in both cases,

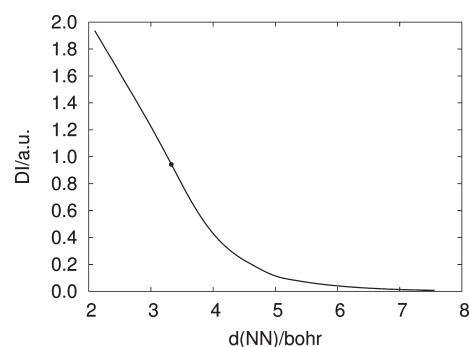


Figure 2. Delocalization index versus NN distance for the dissociation of N_2 . The inflection point has been highlighted.

the singlet displaying a clearly developed inflection point that is absent in the triplet. As we will illustrate throughout this work, this property seems rather general. Another interesting aspect is the position of the inflection point. A polynomial fit determines it occurring at $d \approx 2.90 \pm 0.1$ bohr, where $DI = 0.5 \pm 0.1$.

There are several possible interpretations for this $DI = 1/2$ value, and the simplest one relates it to a half-formed (or broken) bond. In the independent electron approximation, a full covalent ($2c,2e$) symmetric link with $DI = 1$ is the result of two completely delocalized electrons, each of them displaying a probability $1/2$ of being found in any of the atoms. Similarly, two isolated electrons, one found exclusively in basin A and the other in basin B, are the signature of a noninteracting system. A 50/50 statistical mixture of both descriptions gives rise to the EDF $p(2,0) = p(0,2) = 0.125$, $p(1,1) = 0.75$, which is that found at $DI = 0.5$. Finally, the sigmoidal shape of the DI profile in the singlet curve points toward a kind of cooperative transition in which the internuclear distance plays the role of an order parameter. It is the presence or absence of this transition that seems to distinguish the nature of the process.

The H_2 example shows very clearly why the information introduced by DI profiles is new, not contained in other quantities explored up to now. First, it is not contained in the variation of V_{xc} 's with interbasin distance. For both the singlet and triplet states, V_{xc}^{AB} decreases exponentially in H_2 . It is also not contained in local scalars computed at BCPs. Given that there is no V_{xc} competition in this diatomic system, a BCP is present at any internuclear separation. The density, for instance, decays exponentially, in both states, although it is larger in the singlet. Similarly, the laplacian becomes negative for both the singlet and the triplet at distances smaller than a given (of course, different) threshold value. The DI profiles are, nevertheless, qualitatively different.

We have also studied the dissociation of the dinitrogen molecule at the CAS[10,8] level, with $r_c = 2.10$ bohr, and our results are shown in Figure 2. The sigmoidal shape is qualitatively similar to the one displayed in Figure 1. The inflection point is located at $d \approx 3.3 \pm 0.1$ bohr, where $DI = 0.9 \pm 0.1$. Such a behavior is thus related with the breaking of the covalent interaction along the process, as was pointed out in the case of H_2 dissociation. Notice how the value of the DI at the inflection point is again located at about half the DI value attained at the equilibrium geometry.

Other simple dissociations have also been considered. In bonded homodiatomics, the results are completely equivalent to those found in H_2 and N_2 and do not deserve further

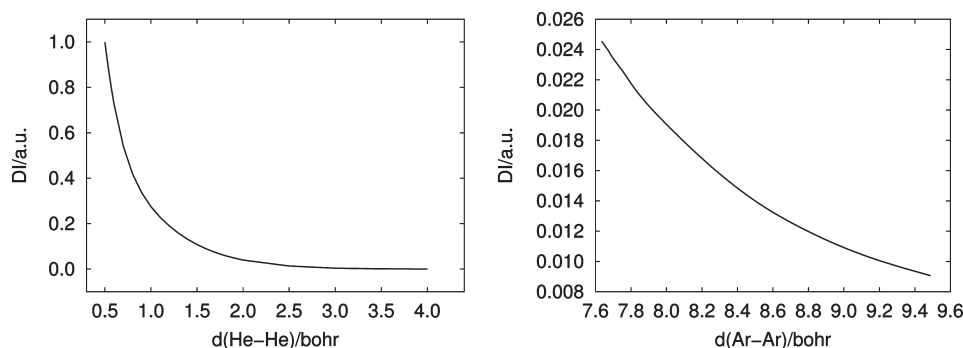


Figure 3. Delocalization index versus internuclear distance for the dissociation of ground state He_2 and Ar_2 molecules.

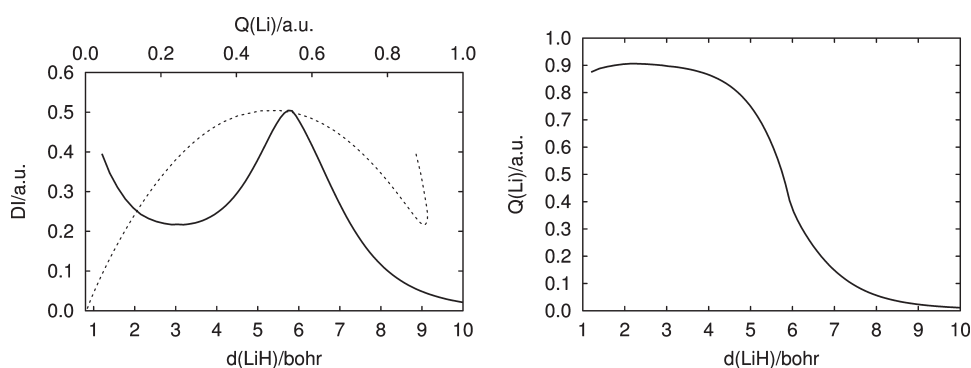


Figure 4. DI profiles in the dissociation of LiH at the CAS[2,2] level. (Left) DI versus the LiH internuclear distance (full line). The same DI profile is also shown versus the topological charge of Li (dotted line). Charge values less than 0.5 are related to the covalent regime, and values close to 1.0 are located in the ionic regime. (Right) Sigmoidal shape of the variation of the topological charge of Li versus the internuclear separation.

comment. More interesting is an examination of traditionally nonbonded interactions. Figure 3 contains the DI profiles for the dissociation of He_2 and Ar_2 , calculated at the CISD. In both cases, the results are qualitatively similar, and the DI grows more or less exponentially as the internuclear distance decreases. Notice how the nonbonded/repulsive character of the interactions is mapped onto a monotonous profile both for an excited state of a bound system (triplet H_2) and for the ground states of unbound diatomics.

Dissociation processes in heterodiatomics are more interesting, particularly when avoided crossings occur. Figure 4 shows the DI for the dissociation of LiH in a CAS[2,2] calculation. Similar results have already been reported.^{26,29,45} An avoided crossing between the ionic and neutral states is found at about $d = 5.5$ bohr, closely corresponding to the maximum in the DI profile and to the region where $\text{DI} = 0.5$.

The basic characteristics of this shape may be easily modeled as a unidirectional charge transfer (CT) of one electron from H to Li. Actually, from $d = 3$ to $d = 10$ bohr, the EDF of the system is reproduced to better than 1% by just two contributions, $p(2,2)$ and $p(3,1)$, where the first figure corresponds to the number of electrons in the Li basin. Were the process a linear transfer of the electron from H to Li, going from $p(2,2) = 1$ (and $p(3,1) = 0$) to $p(2,2) = 0$, the DI would show an inverted parabolic shape starting and ending at $\text{DI} = 0$, and peaking at $\text{DI} = 0.5$ when half an electron had been transferred. The results shown in the figure display very good quadratic behavior, except in the vicinity of the equilibrium geometry.

This tells us that the nonparabolic variation of the DI with internuclear distance is due to the nonlinear character of charge

transfer, which is depicted on the right side of Figure 4. The variation of CT with d is again sigmoidal,⁴⁵ with an inflection point at about the avoided crossing (or DI maximum). It is also worth noticing that the equilibrium geometry, $d \approx 3.0$ bohr, is close to the DI minimum shown in the figure. At smaller distances, another delocalization channel appears: $p(1,3)$ starts to increase, and so does the DI in a nonbonding manner. DI profiles with a local maximum thus indicate charge transfers or ionic interactions.

The sigmoidal variation of $Q(\text{Li})$ with distance reinforces the idea that cooperative phenomena underlie bonding landscapes. This may be worked out in slightly more detail by noticing that general $(2c,2e)$ symmetric delocalizations, as well as $(2c,1e)$ CTs, may be modeled with a single electron transfer coordinate $t \in [0,1]$ that measures the degree of delocalization or CT, respectively. In a homodiatomic case like H_2 , the two electron EDF may always be written as the direct product of two symmetric one-electron distributions: for the first electron, $p(1,0) = t/2$ and $p(0,1) = 1 - t/2$; for the second, $p(1,0) = 1 - t/2$ and $p(0,1) = t/2$. Notice that t values $\in [1,2]$ simply correspond to a basin exchange and need not be considered. With this model, $\delta^{AB} = t$, and the transfer parameter behaves sigmoidally. In the ionic case, the parameter is just the probability that the transferred electron lies in the final basin, so $t = p(1,0) = Q(\text{Li})$ is sigmoidal. In both cases, the inflection point of the t curves is very close to $t = 1/2$. Further work related to the possible universal behavior of the t versus distance curve clearly needs to be done.

3.2. Other Dissociations. We have examined other bonded and nonbonded dissociations. The first category is represented

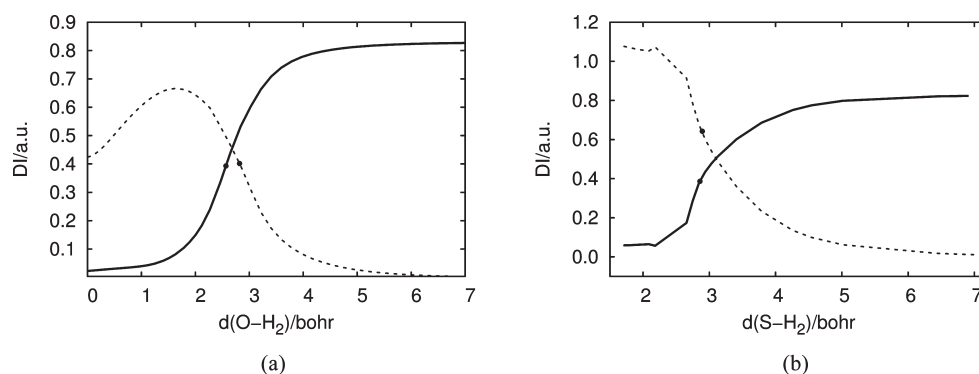


Figure 5. DI profiles for the $\text{H}_2\text{X} \rightleftharpoons \text{H}_2 + \text{X}$ dissociations: H_2O (a) and H_2S (b). Both δ^{HX} (dotted lines) and δ^{HH} (full lines) are shown. The inflection points of the curves are marked with filled circles, and d is the perpendicular distance from the X atom to the H_2 axis.

by the approach of $\text{X} = \text{O}$ and S atoms in their ^1D state to a ground state H_2 molecule to form a H_2X molecule. These are well studied processes that may also be described as H_2 subtractions from H_2X systems, which are recognized as emblematic examples of the change in connectivity along a chemical reaction in the QTAIM.⁶ The C_{2v} symmetry has been maintained at all points, such that the X atom evolves along a line perpendicular to the H_2 axis passing through its center. Let us call d the perpendicular distance between X and the H–H axis.

The case of H_2O was used in our previous study on the reinterpretation of bond paths as privileged exchange channels.¹⁹ There, the behavior of V_{xc} was examined, while we focus here on the relevant DIs. To follow this dissociation channel, a size-consistent CAS[6,8] level has been selected. At the H_2X equilibrium configurations, $d = 1.138$ and 1.710 bohr in water and H_2S , respectively.

Figure 5 displays our computed DI profiles using d as a reaction coordinate. A simple consideration of their shape allows us to neatly classify the underlying chemistry. For instance, in the H_2O case, we distinguish a covalent one-parameter dissociation for the H–H pair as d decreases coupled to a mixture of covalent association and charge transfer processes for O–H. We identify the presence of a mixture by the peak DI value, $\delta^{\text{OH}} \approx 0.65$. Any value of DI larger than 0.5 cannot be attained via a one-electron transfer. It is possible to model the shapes of these DIs with two parameters, and on doing so one may justify the deviation in the position of the inflection point (or the DI maximum) with respect to the one parameter ideal values shown in the last subsection. However, since our purpose is to qualitatively show the link between the DI shape and the nature of an interaction, we will not pursue this here. The situation in H_2S is similar, although the HS covalency is considerably larger in this case, and the charge transfer maximum is barely visible. The H_2S dissociation was calculated at the CAS[6,8] level of theory.

At the beginning of the reaction the sulfur shares a bit more than one electron pair with each hydrogen, and at the end the hydrogens share a correlated value of about 0.8. A fitted polynomial locates the inflection point at $d \approx 2.85 \pm 0.01$ bohr with $\text{DI} \approx 0.40 \pm 0.01$ for the H–H interaction and at $d \approx 2.89 \pm 0.01$ bohr with $\text{DI} \approx 0.64 \pm 0.01$ for the H–S interaction. As in the H_2O case, these values are related to the mixing of covalent and ionic terms.

Finally, let us briefly show a repulsive/nonbonded polyatomic case. Figure 6 displays the evolution of the DI between the two clashing hydrogens in the head to head approach (or dissociation) of two methane molecules $\text{H}_3\text{C}-\text{H} \cdots \text{H}-\text{CH}_3$ such that the C_{3v} axis is preserved. This is a closed-shell

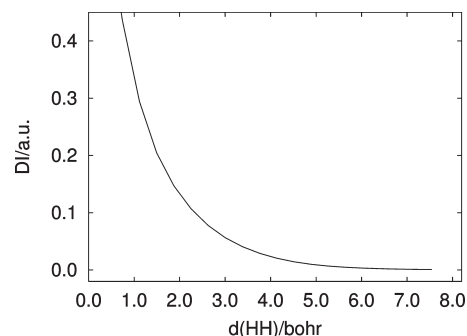


Figure 6. DI profile for the $\text{H}_3\text{C}-\text{H} \cdots \text{H}-\text{CH}_3$ process examined in this work. d is the distance between the head-on approaching hydrogens.

interaction that is qualitatively well described at the RHF level. The distance between the approaching hydrogens at the equilibrium geometry is about 7.92 bohr. As seen, there is no hint of inflection point, and the delocalization index falls off exponentially as the two hydrogens separate, being practically zero at the equilibrium geometry.

3.3. Atomic (or Bond) Exchanges. Processes in which bonds are broken at the expense of the formation of others are also interesting and worth studying. The simplest one is the linear exchange of H with a H_2 (or D_2) molecule, $\text{H1} + \text{H2}-\text{H3} \rightarrow \text{H1}-\text{H2} + \text{H3}$, which is correctly described by even a single-determinant high-spin wave function. This type of change has been studied by Yamasaki and Goddard^{43,44} using the equivalent to DIs in Fock space with Mulliken and Löwdin charge operators. Their correlation analysis for chemical bonds (CACB) technique gave rise to fairly similar results to those found here. Figure 7a shows the $\text{H2}-\text{H3}$ and $\text{H1}-\text{H2}$ DIs along the IRC. Since the reaction is completely symmetric, we find a concerted mechanism in which one bond is being formed while the other is being broken. Correspondingly, the DIs of both pairs are sigmoidal and symmetric, with their inflection points coinciding exactly with the transition state at $\text{IRC} = 0$.

Since the hydrogen exchange may be understood as a bond exchange process, it is also interesting to examine the behavior of the sum of both DIs. Figure 7 shows how, apart from a small rise in the transition state region, the sum turns out to be essentially constant. This supports⁴⁴ the use of the sum of the DIs involving a given atom A , $\sum_X \delta^{\text{AX}}$, as a measure of its free valence or bonding capacity. The wave functions were obtained with the ROHF level of theory.

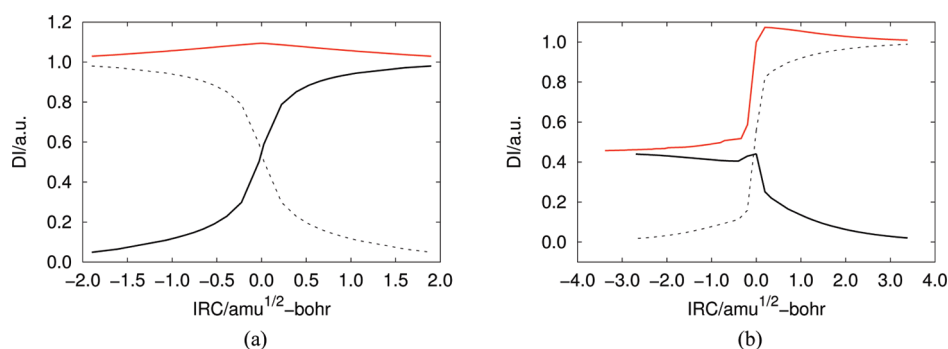


Figure 7. DI profiles for hydrogen exchange reactions. Left, $\text{H1} + \text{H2-H3} \rightarrow \text{H1-H2} + \text{H3}$. Dashed and full lines are used for the H2-H3 and H1-H2 pairs, respectively. Right, $\text{H1} + \text{F-H2} \rightarrow \text{H1-H2} + \text{F}$. Dashed and full lines are used for the HH and the HF pairs. For both systems, the sum of the DIs is shown in red.

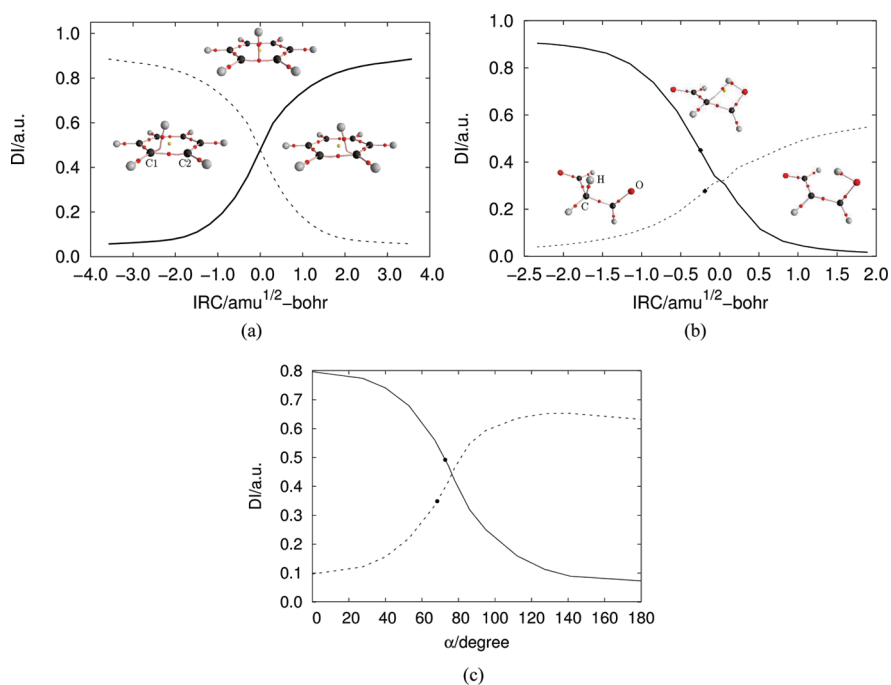


Figure 8. DI profiles for the intramolecular migrations studied in this work. In part a, we show the symmetric DIs for the HC_1 and HC_2 pairs in the benzenium cation 1–2 hydrogen migration. In part b, the malonaldehyde keto–enol tautomerism is examined, with the HO and HC pairs indicated by a dashed and full line, respectively. In part c, we show the HCN to CNH isomerization, using as IRC the angle α between the H to center-of-mass line and the CN internuclear axis. The HC and HN pairs are marked with dashed and full lines, respectively.

A more complex, interesting case is the fluorine–hydrogen exchange $\text{H1} + \text{F-H2} \rightarrow \text{H1-H2} + \text{F}$ presented in Figure 7b, also at the ROHF level. The H1-H2 DI displays the same shape shown in the $\text{H} + \text{H}_2$ system, while the H1-F does not. As H1 approaches the F-H2 molecule, the F-H2 DI starts to decrease slowly from its leftmost IRC value, 0.45. This small value indicates a rather large ground state ionicity, and the topological net charges at this stage are $q(\text{H2}) = 0.743$, $q(\text{H1}) = 0.008$, and $q(\text{F}) = -0.750$. As the reaction progresses, δ^{FH2} displays a shallow minimum around -0.5 IRC, and an inverted parabolic shape peaking at about the TS followed by a more or less exponential decrease toward the F dissociation. Notice how the region around the TS coincides with the relevant chemical changes, in agreement with intuition. At the peak of the F-H2 DI curve, $q(\text{H1}) = 0.120$, $q(\text{H2}) = 0.008$, and $q(\text{F}) = -0.128$, and we clearly see the transition between the starting and the final bonding situation. We may therefore follow

the chemical changes easily from reading the DI figure: a covalent HH link is formed at the expense of the HF bond in the first stage. This is followed by a charge transfer process in the vicinity of the TS. Once this process is completed, the fluorine is expelled as the HH link consolidates.

As in the previous case, we have also considered the sum of both DIs, which is well described as a sudden jump between two rather well-defined values. If this jump is washed out from Figure 7b, the behavior of the DI sum is pretty similar to that in the $\text{H} + \text{H}_2$ case, being constant apart from a small increase in the TS region. The jump is to be associated with the sudden availability of an electron for the construction of a covalent bond H-H , and thus to the transfer of that electron from the F basin toward the H_2 one.

3.4. Migrations. Intramolecular migrations are good examples of coupled formation and breaking of chemical bonds. In

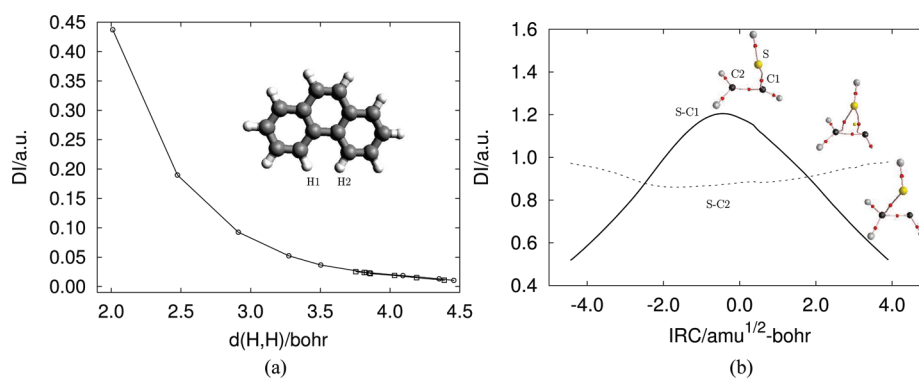


Figure 9. (a) DI evolution of the symmetric (open circles) and asymmetric (open squares) modes for the H1–H2 interaction in the bay moiety of phenanthrene. (b) DI profile and structural change graphs during the CH rotation in CHCH₂SH. The ring structure ephemerally exists close to the rightmost line crossing.

topological terms, they are accompanied by the transformation of bond critical points using either the conflict or the bifurcation mechanisms, using the terminology of catastrophe theory as applied to chemical structural change.⁶ We have studied three DI profiles of prototropic migrations: the 1–2 intramolecular hydrogen migration of the benzenium cation,⁴⁸ the keto–enol tautomerism in malonaldehyde,⁴⁹ and the H–C≡N ⇌ H–N≡C isomerization.

Figure 8a contains the relevant DIs in the 1–2 hydrogen migration process in the benzenium cation, calculated at the CAS[6,6] level. The graph shows the DI of the migrating hydrogen with the two carbons directly involved in the reaction. As in the H + H₂ case, the reaction is symmetric, and the inflection point is located exactly at the TS. At the beginning of the reaction, the DI between the migrating H and the C1 is 0.9 and decreases as the hydrogen moves to the TS. This process is synchronically coupled to the increase in the HC2 DI and shows that our expectations based on the argument explored in this work are again fulfilled. At the inflection point, DI ≈ 0.5, and we have a rather standard covalent-to-covalent transition that may be modeled uniparametrically.

We have obtained the profiles for the malonaldehyde keto–enol tautomerism at the RHF level and plotted them in Figure 8b. As shown, the behavior is basically the same as in the benzenium cation case, the differences associated to the change in ionicity, much larger in the final situation where a HO link is present than in the initial one, which is characterized by a rather covalent HC bond. This forcibly leads to a rather large H–C DI of about 0.9, to be compared with its H–O equivalent, about 0.5. The inflection points are placed to the left of the TS. It is to be noticed that in both cases, the inflection points are located at about half the total height of the sigmoids, and that the HO curve displays it at a very small DI value, about 0.25. This half-width position is quite general in all of the cases examined.

Finally, the HCN isomerization is examined in Figure 8c, again at the RHF level. The behavior is similar, but this time we may appreciate a shallow maximum in the HN DI that offers a clear indication of partial charge transfer.

3.5. Controversial Cases. In order to include systems where bond paths cause controversy, two systems have been studied: the normal modes assigned to the stretching of the HC bonds for the hydrogen atoms located in the bay moiety of the phenanthrene molecule and the rotation of the CH fragment in CHCH₂SH. The first system has been used by Grimme et al.¹⁷ to purportedly show that both theoretical models and the

spectroscopic assignment of the experimental IR stretching modes are in agreement with a repulsive H1H2 interaction in the bay moiety of phenanthrene. Thus, the role of the BCP that is found between both hydrogens in QTAIM analyses is put into question. The second has been presented by Henn et al.¹⁸ as an example of a molecule where a chemical bond is absent between two atoms (the SC1 pair), while other theoretical tools, like the natural bond orbital formalism of Weinhold and Landis,⁵⁰ state that it is present. We have computed DI profiles in both systems at the RHF level.

The DI between the H1 and H2 atoms in phenanthrene at selected geometries has been constructed following the eigenvectors of their HC stretching normal modes. Figure 9a shows its evolution in the symmetric and asymmetric cases. The distance between the bay moiety hydrogens at the equilibrium geometry is about 3.83 bohr. According to the experience gained with the previous examples, the absence of inflection points along the symmetric-mode coordinate is compatible with a nonbonded/repulsive process, as observed throughout this work. Since the H1–H2 distance hardly varies along the asymmetric motion, the DI evolution in this normal mode is difficult to interpret and will not be pursued anymore.

In our second example, a bond path is expected between the sulfur and the C1 carbon, but topological analyses reported at several levels of theory¹⁸ do not find it at the equilibrium geometry. To further investigate this problem, we have computed the TS and IRC along the rotation of the C1H between two quasi-degenerate conformers that differ in the position of the C1 hydrogen. In this transition, see Figure 9b, the system evolves between the conformers by passing through two three-centered ring regions where SC1 BCPs exist. These BCPs are broken through a bifurcation mechanism. Along the process, δ^{SC2} oscillates in a small window with a width equal to 0.1 around a clearly covalent value of about 0.9, but the SC1 DI widely changes between 0.5 and more than 1.2. According to the insights developed in this work, it is rather clear that the SC1 interaction is basically electrostatic in both conformers and that only in configurations where the hydrogen atom linked to the C1 carbon is close to coplanar with the SC1C2 plane do we find delocalization indices compatible with a SC1 bond.

4. CONCLUDING REMARKS

In this work, we have shown compelling evidence that the topology of the profiles of QTAIM delocalization indices in simple chemical processes keeps information about the nature of

the chemical changes that are taking place. Three basic modes have been uncovered. For repulsive/nonbonded cases, the evolution of the DI turns out to be exponential. In bonded interactions, two extreme cases appear. In the first, associated to covalent or shared interactions, the DI shape is sigmoidal. Contrarily, a bell-like profile is found when charge transfers are involved. We have also shown how one-parameter models for the ideal electron distribution functions in covalent and ionic cases are compatible with these findings if the charge transfer parameter evolves sigmoidally with the reaction coordinate. We think that this points to cooperative phenomena as major players in the formation or breaking of chemical bonds. Interestingly, the information provided by DI profiles seems not to be present in the variation of local scalar fields at bond critical points.

The behavior here uncovered seems of fairly general validity. Dissociations, both in diatomics and polyatomics, bond exchanges, and inter- and intramolecular migrations seem to follow it, and the qualitative pattern is quite independent of the theoretical level used in the computations. Since calculating DIs is considerably cheaper than performing a full QTAIM energy partitioning analysis, the use of the correlations proposed here may help in discerning the nature of chemical interactions in controversial cases, as we have tried to show by examining a few recent examples. We want to stress, however, that as with many other findings in real space theories of chemical bonding, the relationships here explored are empirical and that we are not aware of any formal justification of them. Further work in this direction is welcome.

AUTHOR INFORMATION

Corresponding Author

*E-mail: angel@fluor.quimica.uniovi.es.

ACKNOWLEDGMENT

The authors are thankful for the financial support from the Spanish MICINN, Project No. CTQ2009-08376, the European Union FEDER funds, the MALTA-Consolider program (CSD2007-00045), and FICYT Project No. IB09-019.

REFERENCES

- (1) Lewis, G. N. *J. Am. Chem. Soc.* **1916**, *38*, 762.
- (2) Pauling, L. *The Nature of the Chemical Bond*, 3rd ed.; Cornell Univ. Press.: Ithaca, NY, 1960.
- (3) Gimarc, B. M. *Molecular structure and bonding. The qualitative molecular orbital approach*; Academic Press: New York, 1979.
- (4) Popelier, P. L. A.; Brémond, E. A. G. *Int. J. Quantum Chem.* **2009**, *109*, 2542.
- (5) Popelier, P. L. A.; Aicken, F. M. *Chem. Phys. Chem.* **2003**, *4*, 824.
- (6) Bader, R. F. W. *Atoms in Molecules*; Oxford University Press: NY, 1990.
- (7) Bader, R. F. W. *J. Phys. Chem. A* **1998**, *102*, 7314.
- (8) Cioslowski, J.; Mixon, S. T. *J. Am. Chem. Soc.* **1992**, *114*, 4382.
- (9) Haaland, A.; Shorokhov, D. J.; Tverdova, N. V. *Chem.—Eur. J.* **2004**, *10*, 4416.
- (10) Farrugia, L. J.; Evans, C.; Tegel, M. *J. Phys. Chem. A* **2006**, *110*, 7952.
- (11) Haaland, A.; Shorokhov, D. J.; Tverdova, N. V. *Chem.—Eur. J.* **2004**, *10*, 4416.
- (12) Bader, R. F. W.; Fang, D.-C. *J. Chem. Theory Comput.* **2005**, *1*, 403.
- (13) Poater, J.; Solà, M.; Bickelhaupt, F. M. *Chem.—Eur. J.* **2006**, *12*, 2889.
- (14) Poater, J.; Solà, M.; Bickelhaupt, F. M. *Chem.—Eur. J.* **2006**, *12*, 2902.
- (15) Bader, R. F. W. *Chem.—Eur. J.* **2006**, *12*, 2902.
- (16) Poater, J.; Visser, R.; Solà, M.; Bickelhaupt, F. M. *J. Org. Chem.* **2007**, *72*, 1134.
- (17) Grimme, S.; Mück-Lichtenfeld, C.; Erker, G.; Kehr, G.; Wang, H.; Beckers, H.; Willner, H. *Angew. Chem., Int. Ed.* **2009**, *48*, 2592.
- (18) Henn, J.; Leusser, D.; Stalke, D. *J. Comput. Chem.* **2007**, *28*, 2317.
- (19) Martín Pendás, A.; Francisco, E.; Blanco, M. A.; Gatti, C. *Chem.—Eur. J.* **2007**, *13*, 9362.
- (20) Francisco, E.; Martín Pendás, A.; Blanco, M. A. *J. Chem. Theory Comput.* **2006**, *2*, 90.
- (21) Martín Pendás, A.; Blanco, M. A.; Francisco, E. *J. Comput. Chem.* **2007**, *28*, 161.
- (22) Blanco, M. A.; Martín Pendás, A.; Francisco, E. *J. Chem. Theory Comput.* **2005**, *1*, 1096.
- (23) Francisco, E.; Martín Pendás, A.; Blanco, M. A. *J. Chem. Theory Comput.* **2006**, *2*, 90.
- (24) Ángyán, J. G.; Loos, M.; Mayer, I. *J. Phys. Chem.* **1994**, *98*, 5244.
- (25) Poater, J.; Solà, M.; Duran, M.; Fradera, X. *J. Phys. Chem.* **2001**, *105*, 2052.
- (26) Ponc, R.; Cooper, D. L. *THEOCHEM* **2005**, *727*, 133.
- (27) Matito, E.; Poater, J.; Duran, M.; Solà, M. *THEOCHEM* **2005**, *727*, 165.
- (28) Matito, E.; Duran, M.; Solà, M. *J. Chem. Educ.* **2006**, *83*, 1243.
- (29) Matito, E.; Solà, M.; Salvador, P.; Duran, M. *Faraday Discuss.* **2007**, *135*, 325.
- (30) Bader, R. F. W.; Stephens, M. E. *J. Am. Chem. Soc.* **1975**, *97*, 7391.
- (31) Fradera, X.; Austen, M. A.; Bader, R. F. W. *J. Phys. Chem. A* **1999**, *103*, 304.
- (32) Wiberg, K. B. *Tetrahedron* **1968**, *24*, 1083.
- (33) Mayer, I. *Chem. Phys. Lett.* **1983**, *97*, 270.
- (34) Martín Pendás, A.; Francisco, E.; Blanco, M. A. *J. Comput. Chem.* **2004**, *26*, 344.
- (35) Fulton, R. L. *J. Phys. Chem.* **1993**, *97*, 7516.
- (36) Wang, Y. G.; Werstiuk, N. H. *J. Comput. Chem.* **2003**, *24*, 379.
- (37) Bader, R. F. W.; Stephens, M. E. *Chem. Phys. Lett.* **1974**, *26*, 445.
- (38) Chamorro, E.; Fuentealba, P.; Savin, A. *Electron J. Comp. Chem.* **2003**, *24*, 496.
- (39) Savin, A. *Probability Distributions and Valence Shells in Atoms. In Reviews of Modern Quantum Chemistry*; Sen, K. D., Ed.; World Scientific Publishing: Singapore, 2002; Vol. 1, pp 43–62.
- (40) Francisco, E.; Martín Pendás, A.; Blanco, M. A. *J. Chem. Phys.* **2007**, *126*, 094102.
- (41) Martín Pendás, A.; Francisco, E.; Blanco, M. A. *J. Chem. Phys.* **2007**, *127*, 144103.
- (42) Martín Pendás, A.; Francisco, E.; Blanco, M. A. *Phys. Chem. Chem. Phys.* **2007**, *9*, 1087.
- (43) Yamasaki, T.; Goddard, W. A., III. *J. Phys. Chem. A* **1998**, *102*, 2919.
- (44) Yamasaki, T.; Mainz, D. T.; Goddard, W. A., III. *J. Phys. Chem. A* **2000**, *104*, 2221.
- (45) Martín Pendás, A.; Francisco, E.; Blanco, M. A. *Faraday Discuss.* **2007**, *135*, 423.
- (46) Schmidt, M. W.; Baldrige, K. K.; Boatz, J. A.; Elbert, S. T.; Gordon, M. S.; Jensen, J. H.; Koseki, S.; Matsunaga, N.; Nguyen, K. A.; Su, S. J.; Windus, T. L.; Dupuis, M.; Montgomery, J. A. *J. Comput. Chem.* **1993**, *14*, 1347.
- (47) Martín Pendás, A.; Francisco, E.; Blanco, M. A. *Chem. Phys. Lett.* **2007**, *437*, 287.
- (48) Garcia-Revilla, M.; Hernandez-Trujillo, J. *Phys. Chem. Chem. Phys.* **2009**, *11*, 8425.
- (49) Delchev, V. B.; Nikolov, G. S. *Monatsh. Chem.* **2000**, *131*, 99.
- (50) Weinhold, F.; Landis, C. *Valency and Bonding. A Natural Bond Orbital Donor-Acceptor Perspective*; Cambridge Univ. Press: Cambridge, U.K., 2005.

Nonorthogonality Problem and Effective Electronic Coupling Calculation: Application to Charge Transfer in π -Stacks Relevant to Biochemistry and Molecular Electronics

Agostino Migliore^{*,†}[†]School of Chemistry, Tel Aviv University, Tel Aviv 69978, Israel

Supporting Information

ABSTRACT: A recently proposed method for the calculation of the effective electronic coupling (or charge-transfer integral) in a two-state system is discussed and related to other methods in the literature. The theoretical expression of the coupling is exact within the two-state model and applies to the general case where the charge transfer (CT) process involves nonorthogonal initial and final diabatic (localized) states. In this work, it is shown how this effective electronic coupling is also the one to be used in a suitable extension of Rabi's formula to the nonorthogonal representation of two-state dynamical problems. The formula for the transfer integral is inspected in the regime of long-range CT and applied to CT reactions in redox molecular systems of interest to biochemistry and/or to molecular electronics: the guanine–thymine stack from regular B-DNA, the polyaromatic perylene diimide stack, and the quinol–semiquinone couple. The calculations are performed within the framework of the Density Functional Theory (DFT), using hybrid exchange–correlation (XC) density functionals, which also allowed investigation of the appropriateness of such hybrid-DFT methods for computing electronic couplings. The use of the recently developed M06-2X and M06-HF density functionals in appropriate ways is supported by the results of this work.

1. INTRODUCTION

The recent progress in molecular electronics fostered a considerable increase in experimental,^{1–7} and theoretical,^{2,3,8–14} investigations of CT in molecular systems. From a theoretical point of view, many efforts have been devoted to the understanding and quantification of the CT efficiency in molecular systems, which depends crucially on the reorganization energy (that is, the free energy change caused by the nuclear rearrangement that follows a CT process) and the charge-transfer integral between the hole or electron donor and acceptor groups.^{11,15} This is particularly evident within the framework of Marcus electron transfer theory,^{16,17} where the transfer rate constant is expressed as¹⁸

$$k_{\text{ET}} = \kappa(V_{\text{IF}})\nu \exp\left[-\frac{(\Delta G^0 + \lambda)^2}{4\lambda k_{\text{B}}T}\right] \quad (1)$$

In eq 1, κ is the electronic transmission coefficient, which depends on the effective electronic coupling V_{IF} and is proportional to the mean-square value of V_{IF} in the nonadiabatic limit (i.e., for suitably weak coupling between the charge donor and acceptor species¹⁹). ν is an effective frequency that characterizes the nuclear motion along the reaction coordinate, λ is the reorganization energy, ΔG^0 is the reaction free energy, k_{B} is Boltzmann's constant, and T is the temperature. λ is the only relevant parameter in the exponential nuclear factor for self-exchange reactions, where ΔG^0 is zero. Depending on the system, eq 1 yields, indeed, the rate constant for electron or hole transfer reactions, the latter being described, in all respects considered in this paper, as electron transitions in the reverse direction of the hole transfer in a system with a net positive charge.

The rate in eq 1 is an important quantity not only for CT reactions between redox molecular centers but also in molecular electronics, where it is strictly related to the electrical conductance through metal–molecule–metal junctions, especially in the regime of weak molecule–metal couplings,^{9,18,20} from whence comes the importance of accurate calculations of the involved physical parameters. As shown by eq 1, V_{IF} can play a crucial role in determining the value of k_{ET} and also provides a compact link between k_{ET} and the electronic properties of the system.

Disparate approaches to accurate calculation of transfer integrals have been used in the literature,^{8,21–34} with an increasing presence of DFT or hybrid-DFT approaches.^{14,33–37} This trend relies on (i) the fact that DFT computational schemes include electron correlation and can be applied to larger systems than those allowed by reliable *ab initio* approaches other than Hartree–Fock (HF). On the other hand, the HF approach does not include the so-called correlation energy. Thus, DFT offers the best compromise between accuracy and feasibility for the study of most (bio)molecular systems of relevance to nanoelectronics.³⁸ The trend also relies on (ii) the elaboration of new hybrid XC functionals, with continuous improvement in their ability to correct for the presence of unphysical electron self-interaction. Indeed, hybrid functionals mostly perform better than self-interaction corrected DFT schemes.³⁹ Moreover, correcting their residual self-interaction errors does not necessarily improve their description of molecular properties.³⁹

Most quantum chemical methods for the computation of transfer integrals need to cope with a suitable definition of the

Received: March 21, 2011

Published: April 26, 2011

involved diabatic states that describe the different localization of the transferring charge before and after the hole or electron transition. Ref 34 provides an expression of the effective electronic coupling, which is exact within the two-state model and does not make any assumption about the overlap between the diabatic electronic states. Such formulation is in harmony with the fact that in most physical situations¹⁵ the localization of the (transferring) excess charge in different redox sites leads to electronic distributions with nonzero spatial overlap. Thereby, its application can help physical interpretation (see, e.g., section 2.4) and lead to practical advantages. On the other hand, the same V_{IF} value is obtained by using diabatic states with different overlaps (or orthogonal ones), as long as the two-state approximation is satisfied, a sufficiently accurate computational level is used, and the different diabatic representations are suitably related, as discussed in the next section.

The method in ref 34 is a generalization of that in ref 33. The relation between both approaches and previous literature^{15,40–42} is discussed in sections 2.1 and 2.2. It is worth mentioning, in this regard, that ref 43 calculates, within a two-electron valence bond model, and compares coupling matrix elements between the electronic states of diatomic systems in different representations (the adiabatic representation, a nonorthogonal diabatic representation, and a symmetrically orthogonalized diabatic representation). The role of V_{IF} in the transition probability at fixed nuclear coordinates is investigated in section 2.3. Sections 2.2 and 2.3 provide a full analytical basis for the correct form of the “effective” coupling or perturbation to be used in nonorthogonal representations of the two-state dynamics. The investigation of the long-range behavior of V_{IF} in section 2.4 contributes to an exhaustive analysis of the role played by the overlap between the diabatic states in determining the effective electronic coupling. Then, the systems under consideration and the used computational setups are described in section 3. Applications follow in section 4. The V_{IF} calculations provided in this work highlight limitations, advantages, and suitable uses of the considered hybrid-DFT implementations. The comparison with previous results in the literature using Hartree–Fock (HF), multireference,⁴⁴ DFT,^{14,30} and other constrained DFT³⁷ approaches contributes to restricting the ranges of expectation values of V_{IF} in the studied systems, in view of future experimental validation and applications.

2. THEORY

2.1. Effective Electronic Coupling Calculations Using Diabatic States with Zero and Nonzero Overlap. Within the two-state model, the ground-state vector of a system is written as

$$|\psi\rangle = a|\psi_I\rangle + b|\psi_F\rangle = a_0|\chi_I\rangle + b_0|\chi_F\rangle \quad (2)$$

where the nonorthogonal wave functions ψ_I and ψ_F , or the orthogonal ones χ_I and χ_F , represent the reactant and product states, respectively, as introduced in the diabatic picture of charge transfer. In these diabatic states, the excess charge is localized on the donor and acceptor, respectively, at any value of the chosen reaction coordinate Q ⁴⁵ (see Figure 1). The energy profile shows a splitting between the adiabatic ground and first excited states at the transition state coordinate (here called Q_t), where the diabatic states are degenerate. At such a coordinate, both the requirement of energy conservation and the Franck–Condon principle⁴⁶ are satisfied in the transition from a diabatic state to the other, and the corresponding Franck–Condon factor takes its maximum.

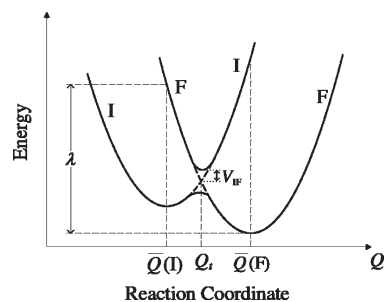


Figure 1. Cross-section of the (free) energy profile for the initial (I) and final (F) electronic states of a typical electron transfer reaction. The solid and dashed curves describe the adiabatic and diabatic states, respectively. $Q(I)$ and $Q(F)$ are the equilibrium coordinates of states I and F, respectively. Q_t is the transition state coordinate, which corresponds to the lowest energy on the crossing seam surface. The reorganization energy λ is also shown.

The separation ΔE_v of the adiabatic energies at Q_t gives a measure of the effective electronic coupling V_{IF} between $|\psi_I\rangle$ and $|\psi_F\rangle$. This splitting can be easily obtained from the secular equation

$$\begin{vmatrix} H_{II} - \varepsilon & H_{IF} - \varepsilon S_{IF} \\ H_{IF} - \varepsilon S_{IF} & H_{FF} - \varepsilon \end{vmatrix} = 0 \quad (3)$$

where H is the Hamiltonian of the two-state system, ε is the energy eigenvalue, $H_{II} = \langle\psi_I|H|\psi_I\rangle$ and $H_{FF} = \langle\psi_F|H|\psi_F\rangle$ are the energies of the diabatic states, $H_{IF} = \langle\psi_I|H|\psi_F\rangle$ is their electronic coupling, and $S_{IF} = \langle\psi_I|\psi_F\rangle$ is their overlap. The eigenvalues of eq 3 can be written in the implicit form⁴⁷

$$E_{\pm} = \frac{1}{2}[H_{II} + H_{FF} \pm \sqrt{\Delta E_{IF}^2 + 4(H_{IF} - E_{\pm} S_{IF})^2}] \quad (4)$$

where $\Delta E_{IF} = E_I - E_F \equiv H_{II} - H_{FF}$ is the energy difference, at the given nuclear configuration, between the CT initial (I) and final (F) diabatic states. Then, the vertical excitation energy can be written as^{34,48}

$$\Delta E_v \equiv E_+ - E_- = \sqrt{\frac{\Delta E_{IF}^2}{1 - S_{IF}^2} + 4V_{IF}^2} \quad (5)$$

(so that $\Delta E_v = 2V_{IF}$ at $Q = Q_t$, where $E_I = E_F$ ⁴⁹), where

$$V_{IF}(Q) \equiv \frac{1}{1 - S_{IF}^2(Q)} \left| H_{IF}(Q) - S_{IF}(Q) \frac{H_{II}(Q) + H_{FF}(Q)}{2} \right| \quad (6)$$

is the CT matrix element or effective electronic coupling or transfer integral.⁸ According to the Condon approximation,¹⁸ the dependence of V_{IF} on the nuclear degrees of freedom, which is explicitly shown in eq 6, is neglected all along the Q axis. When such approximation is not fulfilled, a meaningful value of $V_{IF}(Q)$ to be inserted into eq 1 for calculating the CT rate needs to be obtained close enough to Q_t , i.e., in the proximity of the crossing seam point of Figure 1. The possible dependence on Q is not explicitly shown in the next equations. If orthogonal diabatic states are used (e.g., the localized states are obtained by suitable rotation of the adiabatic states), then $V_{IF} = H_{IF}$, and the effective electronic coupling can be written in terms of a_0 and b_0 as

$$V_{IF} = H_{IF} = a_0 b_0 \Delta E_v \quad (7)$$

This formula appears in ref 41, besides another original approach that makes use of the quasi-degenerate perturbation theory and where the determination of the adiabatic energies or diabatic wave functions is not compulsory, as only electron correlation contributions to H_{IF} are explicitly computed.

By using eq 5 for zero S_{IF} and relating a_0 and b_0 to the adiabatic and diabatic dipole moments, under the assumption of weakly interacting diabatic states connected by a zero transition dipole moment (thus, first order perturbation theory can be used), eq 7 becomes^{22,42,50,51}

$$V_{\text{IF}} = \frac{|\mu_{-+}|\Delta E_{\text{IF}}}{|\Delta\mu_{\text{IF}}|} \quad (8)$$

where μ_{-+} is the transition dipole moment that connects the adiabatic states and $\Delta\mu_{\text{IF}}$ is the difference between the dipole moments of the diabatic states. Equation 8 represents the Mulliken–Hush approach to the calculation of $V_{\text{IF}} = H_{\text{IF}}$. As shown in refs 42 and 50d, eq 8 may be extended to the nonperturbative regime by replacing ΔE_{IF} with ΔE_{v} . In ref 22a, the generalized Mulliken–Hush (GMH) model is introduced, which (i) retains the assumption that the diabatic states localized at different sites have zero off-diagonal dipole moment matrix elements, (ii) is not restricted to a perturbative treatment within the state space of interest, and (iii) does not require approximation of $\Delta\mu_{\text{IF}}$ using structural data. In a two-state system, by expressing $\Delta\mu_{\text{IF}}$ in terms of the adiabatic dipole moments μ_{-} and μ_{+} , and their difference $\Delta\mu_{-+}$, the following result is obtained²²

$$V_{\text{IF}} = \frac{\Delta E_{\text{v}}|\mu_{-+}|}{\sqrt{(\Delta\mu_{-+})^2 + 4\mu_{-+}^2}} \quad (9)$$

where also eq 5 written for zero overlap is exploited.

Contrary to the GMH method, in ref 33, the transfer integral V_{IF} is expressed exclusively in terms of quantities that pertain to diabatic states with generally nonzero overlap, as

$$V_{\text{IF}} = \left| \frac{ab}{a^2 - b^2} \Delta E_{\text{IF}} \right| \quad (10)$$

This also avoids calculation of the vertical excitation energy, with evident advantages for the application of eq 10 in DFT schemes, e.g., for the *ab initio* study of large portions of biochemical systems. Moreover, it provides a useful link, for $Q \rightarrow Q_{\text{t}}$ (where eq 10 has an eliminable discontinuity), with the concept of resonance energy widely used in valence bond theory (cf. eqs 8 and 11 in ref 34 with eq 10 in ref 52). In ref 33, eq 10 was derived from the secular equation, eq 3, in the presence of a suitably small overlap. In ref 34, it is shown that, irrespective of the values of S_{IF} and Q , V_{IF} is exactly given by (wave function overlap method)

$$V_{\text{IF}} = \left| \frac{ab}{a^2 - b^2} \Delta E_{\text{IF}} \left(1 + \frac{a^2 + b^2}{2ab} S_{\text{IF}} \right) \frac{1}{1 - S_{\text{IF}}^2} \right| \quad (11a)$$

or, equivalently,

$$V_{\text{IF}} = \left| \frac{AB}{A^2 - B^2} \Delta E_{\text{IF}} \left(1 - \frac{A^2 + B^2}{2AB} S_{\text{IF}} \right) \frac{1}{1 - S_{\text{IF}}^2} \right| \quad (11b)$$

where the overlap integrals $A \equiv \langle \psi_1 | \psi \rangle = a + bS_{\text{IF}}$ and $A \equiv \langle \psi_{\text{F}} | \psi \rangle = b + aS_{\text{IF}}$ have been inserted. In the same work, it is shown that eq 10 can indeed be used as an approximation of

eqs 11, at any coordinate Q and in terms of either a and b or A and B , if S_{IF} is much smaller than $2ab$ or $2AB$. Such a condition is much weaker than neglecting S_{IF} . In fact, it allows S_{IF} values that can lead to a considerable difference between the effective electronic coupling V_{IF} and the electronic coupling H_{IF} ,^{18,30,36,53} related as in eq 6. For $S_{\text{IF}} \ll 2ab$, the insertion of eq 11 into eq 5 and the Taylor expansion of eq 5 up to the zero-order term in $S_{\text{IF}}/(2ab)$ gives

$$\Delta E_{\text{v}} = \left| \frac{a^2 + b^2}{a^2 - b^2} \Delta E_{\text{IF}} \right| \quad (12)$$

By combining eqs 10 and 12, it is seen that the right-most term of eq 7 still provides a formal expression for V_{IF} after replacement of a_0 and b_0 with a and b , respectively, while $V_{\text{IF}} \neq H_{\text{IF}}$. In other words, whereas for zero overlap eqs 7 and 10 are equivalent solutions of the secular equation and essentially differ by the respectively required computational approaches, for $S_{\text{IF}}/(2ab) = o(1) \neq 0$ (as it is in several cases^{11,30,34,48,53–56}), the use of nonorthogonal diabatic states for the direct (i.e., without prior and suitable orthogonalization) computation of V_{IF} is allowed only by eq 10 or, within the limits of applicability of eq 12, by a modified eq 7 where the overlap-dependent coefficients

$$a = \frac{A - BS_{\text{IF}}}{1 - S_{\text{IF}}^2}, \quad b = \frac{B - AS_{\text{IF}}}{1 - S_{\text{IF}}^2} \quad (13)$$

are employed. In many other cases,^{8,15,34,40,57–59} the diabatic states that rely on physically meaningful approximations (e.g., the valence bond structures that correspond to the reactants and products of the CT reaction^{15,59}) have an overlap that is not negligible compared to $2ab$ or is even larger than this quantity. For example, the value of S_{IF} can be an appreciable fraction of unity in short-range CT reactions, or, for weakly coupled redox sites, the valence charge in the ground state can be mostly localized around one of them, so that a or b is almost unity and the other coefficient is much less than unity. In all such cases, the modified eq 7 and eq 10 are not equivalent approximations to the exact analytical solution of the secular equation provided by eq 11, and both fail in quantifying the transfer integral from nonorthogonal states, for which eq 11 can be used. Ultimately, eqs 9 and 11 represent alternative theoretical approaches to the calculation of effective electronic couplings in the adiabatic and diabatic representations, respectively.

2.2. Wave Function Overlap Method and Diabatic States. As discussed in the previous literature,^{15,40,59,60} the definition of effective diabatic states is not unique. Thus, the use of a given set of diabatic states to describe the CT reaction under investigation generally needs to rely on physical grounds. This point was, e.g., considered in refs 34 and 48, where different sets of diabatic states were selected, on the basis of the structure of the system and the localization of the charge in the donor and acceptor centers, in order to describe hole transfer through DNA nucleobase stacks. Often, the I and F diabatic electronic states are constructed as the valence bond structures of the involved reactants and products.^{15,59} For instance, ref 59 provides an interesting model for deriving effective diabatic states using *ab initio* self-consistent field bond theory. An interesting and fruitful DFT approach to charge localization is provided by constrained DFT (CDFT),³² where the addition of a suitable external effective potential to the Hamiltonian of the CT system allows one to obtain self-consistently the lowest-energy I and F states, under the approximations of the given XC functional and the basis set used to expand the electron wave functions. The uncertainty

in the definition of the CDFT diabatic states in general decreases with the separation of the charge donor and acceptor groups.³² Nevertheless, eq 11 suggests the possibility of using CDFT diabatic states also in various short-range (and intramolecular) CT processes. The appropriateness of the CDFT approach to charge localization in such contexts is mainly the subject of future work. In this paper, the investigation of this point is limited to (i) a guanine–thymine base stack from regular DNA, which is characterized by the largest intrastrand effective electronic coupling among the DNA nucleobase stacks and a related large overlap integral between CDFT-type diabatic states,³⁴ and (ii) the quinol–semiquinone redox couple, on the short-distance side of Figure 4.

In this paper, the use of eq 11 with CDFT diabatic states, and a suitable choice of basis set and hybrid XC density functional, is proposed as an efficient hybrid-DFT theoretical-computational method for the first-principles calculation of the effective electronic coupling in various molecular systems of interest to biochemistry and nanoelectronics. Also, other valuable methods for the construction of diabatic states^{15,30,53,61} can be combined indeed with the use of eq 11. Such implementations can be fruitful and are desirable, but they are out of the scope of the present work. On the other hand, tensor product (TP) diabatic states are also employed in section 4.1. In general, such states can be used for separated redox sites and in very accurate computational schemes (see, e.g., Table 1, where the largest Pople-style basis set is used).^{34,48}

The consistency of using sets of diabatic states characterized by different overlaps can be investigated and rationalized by exploiting the Löwdin transformation.^{40,43} In particular, it is important to understand to what extent orthogonal and non-orthogonal diabatic representations can be consistently adopted in order to calculate the charge-transfer integral for a given redox system. To this aim, consider first the general case where physically meaningful assumptions (e.g., based on the involved

valence bond structures) lead to diabatic wave functions ψ_I and ψ_F ⁶² with appreciable overlap S_{IF} that provide a good description of the CT reaction under investigation, as validated by comparison with relevant experimental data. I will call $\Psi = (\psi_I \psi_F)$ the reference diabatic set. An equivalent orthonormal diabatic set is obtained using the Löwdin transformation⁴⁰

$$\chi = \Psi S^{-1/2} \quad (14)$$

where $\chi = (\chi_I \chi_F)$ and S is the overlap matrix defined as

$$S = \begin{pmatrix} 1 & S_{IF} \\ S_{IF} & 1 \end{pmatrix} \quad (15)$$

The insertion of χ in eq 7 or eq 10 with $a = a_0$ and $b = b_0$ leads to the same V_{IF} value that results from the application of eq 11 in the Ψ representation. In fact, as shown by eq 48 (see Appendix), insertion of eq 14 into eq 10 leads to eq 11. Considering that χ can also be obtained by rotation of the adiabatic states,²⁷ eq 14 fixes the rotation angle that relates the suitable diabatic representation to the adiabatic one in any direct use of eq 7 by exploiting orthogonal diabats. On the other hand, eq 11 provides a general expression of the effective electronic coupling in terms of a few electronic quantities that characterize the orthogonal diabatic representation (in this case, the overlap in the expression of V_{IF} is zero) or any nonorthogonal diabatic representation, which is related to χ by the Löwdin orthogonalization in eq 14 and to the reference representation by the equation (see Appendix)

$$\bar{\Psi} = \Psi M \quad (16)$$

where M is the symmetric matrix

$$M = \frac{1}{2} \begin{pmatrix} \sqrt{(1 + \bar{S}_{IF})/(1 + S_{IF})} + \sqrt{(1 - \bar{S}_{IF})/(1 - S_{IF})} & \sqrt{(1 + \bar{S}_{IF})/(1 + S_{IF})} - \sqrt{(1 - \bar{S}_{IF})/(1 - S_{IF})} \\ \sqrt{(1 + \bar{S}_{IF})/(1 + S_{IF})} - \sqrt{(1 - \bar{S}_{IF})/(1 - S_{IF})} & \sqrt{(1 + \bar{S}_{IF})/(1 + S_{IF})} + \sqrt{(1 - \bar{S}_{IF})/(1 - S_{IF})} \end{pmatrix} \quad (17)$$

and $\bar{S}_{IF} = \langle \bar{\psi}_I | \bar{\psi}_F \rangle$. Equation 14 is clearly the special case of eq 16 for $\bar{S}_{IF} = 0$.

In many circumstances, different diabatic sets can provide convenient representations of the given CT system (e.g., this can be the case in section 4.1). Even if these diabatic representations are related as in eq 17, various sources of error can clearly lead to different values of the effective electronic coupling and/or the vertical excitation energy or to consistently wrong results. For example, DFT calculations are generally affected by the presence of spurious electron self-interaction,⁶³ although hybrid XC functionals can yield optimal correction, also depending on the system.³⁹ Then, since different sets of diabatic states correspond to diverse electron localizations, the corresponding energies may differently suffer from self-interaction, thus leading to different values of V_{IF} even if eq 17 is fulfilled and eq 11 is employed. On the contrary, but for analogous reasons, similar values can arise from diabatic sets which are not related as in eq 17. At any rate, eq 17 can generally provide a helpful check of the consistency and robustness of the computational results. Then, differences in the results can even become a source of useful information.

Finally, it is worth noting that the connection between eq 11 and the Löwdin transformation can be reformulated in terms of

the Hamiltonian operator H of the CT system. In fact, the relation between the orthogonal and nonorthogonal diabatic sets is an expression of the fact that the algebraic problem of the secular equation including the S_{IF} terms is reduced to the zero overlap form if the matrix H is replaced by the self-adjoint matrix^{40,64}

$$H' = S^{-1/2} H S^{-1/2} \quad (18)$$

The insertion of eq 41 from the Appendix into eq 18 and comparison with eq 6 yields

$$|H'_{IF}| = \left| H_{IF} - \frac{H_{II} + H_{FF}}{2} S_{IF} + H_{IF} S_{IF}^2 - \dots \right| = V_{IF} \quad (19)$$

which reduces to the usually adopted small-overlap Löwdin transformation,^{30,40,53}

$$V_{IF} = H_{IF} - \frac{H_{II} + H_{FF}}{2} S_{IF} \quad (20)$$

when the terms nonlinear in S_{IF} can be disregarded. Alternatively, eq 19 is indeed formulated by eq 48 in the Appendix. In conclusion, (i) the exact expression of the effective electronic

coupling in terms of a few electronic quantities that characterize the diabatic states and their connection with the ground state was obtained in ref 34 by direct solution of the secular equation, using the definition (eq 6) of V_{IF} ; (ii) it is^{33,34,41,42}

$$V_{IF} = \begin{cases} \langle \chi_I | H_{IF} | \chi_F \rangle = |a_0 b_0 \Delta E_v| = \left| \frac{a_0 b_0}{a_0^2 - b_0^2} \Delta E_{IF}^0 \right| & S_{IF} = 0 \\ \langle \psi_I | H'_{IF} | \psi_F \rangle \cong \left| \frac{ab}{a^2 - b^2} \Delta E_{IF} \right| & S_{IF} = o(2ab) \leq o(1) \\ \langle \psi_I | H'_{IF} | \psi_F \rangle = \left| \frac{ab}{a^2 - b^2} \Delta E_{IF} \left(1 + \frac{a^2 + b^2}{2ab} S_{IF} \right) \frac{1}{1 - S_{IF}^2} \right| & \forall S_{IF} \end{cases} \quad (21)$$

where ΔE_{IF}^0 is the diabatic energy difference between χ_I and χ_F ; (iii) V_{IF} is invariant under the Löwdin transformation, hence, in general, under the change of representation defined by the \mathbf{M} matrix in eq 17.

In ref 34, I stressed that the calculation of V_{IF} directly from eq 6 or 20 is generally very sensitive to the value of S_{IF} , especially if the involved matrix elements are computed in a multielectron scheme. In fact, in this case, the right-hand side of eq 6 involves a delicate numerical difference of two energy quantities much larger than their difference (see also p 28 of ref 18). Equation 11 allows one to avoid this critical point. On the other hand, both the numerator and the denominator of eq 11 tend to zero at the transition state coordinate Q_t . However, as is demonstrated in ref 34, the expression of V_{IF} in eq 11 (i) has an eliminable discontinuity at Q_t , (ii) has the correct behavior for $Q \rightarrow Q_t$, and (iii) allows calculation of V_{IF} with high accuracy even when Q is very close to Q_t , as quantified by the fact that $\Delta E_{IF}(Q) \ll 2V_{IF}(Q)$ and thus the relative difference between $2V_{IF}(Q)$ and $\Delta E_v(Q)$ is correspondingly small. Point iii was noticed in ref 48 and is strongly supported by the cogent computational test in section 4.2 of this work.

2.3. Electron Transition Probability at Fixed Nuclear Coordinates. As shown by eq 1, V_{IF} plays a crucial role in determining the electronic transmission coefficient κ that appears in the electron transfer rate. Near the transition state coordinate, the electron transitions that can be caused by this coupling are mixed with the nuclear dynamics, which, overall, leads to the expression of κ . While the interplay of the electron and nuclear dynamics has been treated in different, though related, ways in the literature,^{16,17,19,65–67} common appreciation of those treatments is that the nuclear coordinates can be taken as external parameters at the short times when a single electron transfer event occurs. This leads to tackling the time-dependent Schrödinger equation for the electronic state of the system. The electron distributions before and after a CT event are clearly not eigenstates of the overall system and represent, in general,^{18,66} nonorthogonal states. This is, e.g., explicitly considered in ref 66, where the ground-state wave function at a generic time t is expanded on two nonorthogonal wave functions

$$\psi(t) = C_I(t)\psi_I + C_F(t)\psi_F \quad (22)$$

with $\langle \psi_I | \psi_F \rangle = S_{IF}$, and the time-dependent Schrödinger equation

$$i\hbar \frac{\partial}{\partial t} [C_I(t)\psi_I + C_F(t)\psi_F] = H[C_I(t)\psi_I + C_F(t)\psi_F] \quad (23)$$

is solved under the initial conditions

$$C_I(0) = 1; C_F(0) = 0. \quad (24)$$

This led to an expression of $|C_F(t)|^2$ (used as an expression of the probability of electron transfer at the given nuclear

coordinates) that extended Rabi's formula for this square coefficient to the nonorthogonal set of electronic states, and where the "effective" coupling or perturbation is not symmetric with respect to the two diabatic states. In fact, it appears in the form $H_{FI} - H_{IF}S_{FI}$, which is different from that in eq 6 and is an off-diagonal element of the Hamiltonian matrix \mathbf{H} in the $\Psi = (\psi_I, \psi_F)$ representation. \mathbf{H} is non-Hermitian for $H_{II} \neq H_{FF}$ ⁶⁸ and is obtained by multiplying eq 23 by ψ_S^* ($S = I, F$; a standard notation for complex conjugate quantities is used) and integrating it over the spatial coordinates, which gives⁶⁶

$$i\hbar \frac{\partial}{\partial t} \mathbf{C}(t) = \mathbf{H}\mathbf{C}(t) \quad (25a)$$

where \mathbf{C} is the column vector of components C_I and C_F and⁶⁹

$$\mathbf{H} = \frac{1}{1 - S_{IF}^2} \begin{pmatrix} H_{II} - H_{IF}S_{IF} & H_{IF} - H_{FF}S_{IF} \\ H_{IF} - H_{II}S_{IF} & H_{FF} - H_{IF}S_{IF} \end{pmatrix} \quad (25b)$$

Various devices were conceived to achieve the desired Hermitian behavior within a purely electronic framework.¹⁵ In ref 18, it is argued that the off-diagonal terms of the \mathbf{H} operator in eq 25b include two contributions: "part of the perturbation induces the transition while other parts distort the zero order states to be coupled".¹⁸ Now, I decompose the Hamiltonian in eq 25b as follows:

$$\mathbf{H} = \begin{pmatrix} \frac{1}{1 - S_{IF}^2} (H_{II} - H_{IF}S_{IF}) & V_{IF} \\ V_{IF} & \frac{1}{1 - S_{IF}^2} (H_{FF} - H_{IF}S_{IF}) \end{pmatrix} + \frac{1}{1 - S_{IF}^2} \begin{pmatrix} 0 & \frac{\Delta E_{IF}}{2} S_{IF} \\ -\frac{\Delta E_{IF}}{2} S_{IF} & 0 \end{pmatrix} \quad (26)$$

where V_{IF} and ΔE_{IF} are defined as above. The first matrix is Hermitian, and its off-diagonal element V_{IF} is the effective electronic coupling that determines, essentially, the probability of transition. To see this, it is necessary to recognize that, since ψ_I and ψ_F , though nonorthogonal, are the initial and final states, the probabilities of interest are given by $|\langle \psi_{I,F} | \psi(t) \rangle|^2$. According to eq 24, the system is initially in state $|\psi_I\rangle$, which does not entail zero probability of finding the system in state $|\psi_F\rangle$, because of the nonzero overlap between the two electronic states. In fact, $|\langle \psi_F | \psi(0) \rangle|^2 = S_{IF}^2$. Note that this probability is well-defined irrespective of the partner wave function chosen to expand $\psi(0)$. In fact, it results also from the decomposition of $\psi(0)$ in ψ_F and the wave function orthogonal to ψ_F , i.e., $\psi(0) = S_{IF}\psi_F + (1 - S_{IF}^2)^{1/2}\bar{\psi}_I$ with $\bar{\psi}_I = (\psi_I - S_{IF}\psi_F)/(1 - S_{IF}^2)^{1/2}$. Then, one is interested in the probability that the system is in state ψ_F at a later time t , that is, $|\langle \psi_F | \psi(t) \rangle|^2$. The fact that $S_{IF} \neq 0$ means, simply, that the probability of finding the system in ψ_I at time t , given by $|\langle \psi_I | \psi(t) \rangle|^2$, is not equal to $1 - |\langle \psi_F | \psi(t) \rangle|^2$. In order to calculate the transition probability $|\langle \psi_F | \psi(t) \rangle|^2$, first I consider that eq 22 and the normalization condition on ψ give

$$|\langle \psi_F | \psi(t) \rangle|^2 = 1 - (1 - S_{IF}^2)|C_I(t)|^2 \quad (27)$$

Insertion of eq 26 into eq 25a and application of the Laplace transform method yields

$$C_1(t) = \frac{1}{2} \left[(e^{u_+t} + e^{u_-t}) - \frac{1}{1 - S_{\text{IF}}^2} \frac{\Delta E_{\text{IF}}}{\Delta E_{\text{v}}} (e^{u_+t} - e^{u_-t}) \right] \quad (28a)$$

where ΔE_{v} is given by eq 5 and

$$u_{\pm} = -\frac{i}{\hbar} \left[\frac{1}{1 - S_{\text{IF}}^2} \left(\frac{H_{\text{II}} + H_{\text{FF}}}{2} - S_{\text{IF}} H_{\text{IF}} \right) \mp \frac{\Delta E_{\text{v}}}{2} \right] \quad (28b)$$

Finally, insertion of eqs 28 into eq 27 gives

$$\begin{aligned} |\langle \psi_{\text{F}} | \psi(t) \rangle|^2 &= S_{\text{IF}}^2 \cos^2 \left(\frac{\Delta E_{\text{v}}}{2\hbar} t \right) + \frac{4V_{\text{IF}}^2}{(\Delta E_{\text{v}})^2} \sin^2 \left(\frac{\Delta E_{\text{v}}}{2\hbar} t \right) \\ &= S_{\text{IF}}^2 + \left[\frac{4V_{\text{IF}}^2}{(\Delta E_{\text{v}})^2} - S_{\text{IF}}^2 \right] \sin^2 \left(\frac{\Delta E_{\text{v}}}{2\hbar} t \right) \end{aligned} \quad (29)$$

The probability oscillates between S_{IF}^2 and $4V_{\text{IF}}^2/(\Delta E_{\text{v}})^2$. As expected, also in the presence of S_{IF} , unity is attained only if $H_{\text{II}} = H_{\text{FF}}$. Equation 29 shows that V_{IF} , which is defined as in eq 6 and is the off-diagonal element of the Hermitian component of the \mathbf{H} operator in eq 26, is the effective coupling that appears in the probability of transition between nonorthogonal states, which is an electron transition probability when ψ_{I} and ψ_{F} are the diabatic (or localized) states of a typical CT reaction. Notice that, although the decomposition in eq 26 is not necessary for the solution of eq 25a, it turned out to be useful to obtain the transition probability directly in terms of V_{IF} and ΔE_{v} and thereby to identify the effective perturbation that plays a crucial role in the amplitude of oscillation of eq 29.

Indeed, because of the overlap between ψ_{I} and ψ_{F} , there is a nonzero transition probability also for $V_{\text{IF}} = 0$. In this case, eq 29 becomes

$$|\langle \psi_{\text{F}} | \psi(t) \rangle|^2 = S_{\text{IF}}^2 \cos^2 \left(\frac{\Delta E_{\text{IF}}}{2\hbar \sqrt{1 - S_{\text{IF}}^2}} t \right) \quad (30)$$

so that the transition probability oscillates between zero and a maximum of S_{IF}^2 . Such values correspond to $\psi = \bar{\psi}_{\text{I}} = (\psi_{\text{I}} - S_{\text{IF}}\psi_{\text{F}})/(1 - S_{\text{IF}}^2)^{1/2}$, that is, the state orthogonal to ψ_{F} , and $\psi = \psi_{\text{I}}$. In fact, ψ_{I} is not an eigenstate of the Hamiltonian; thus the system evolves from it and, given the zero effective electronic coupling between ψ_{I} and ψ_{F} , the amplitude of the transition probability cannot overcome the initial value of S_{IF} , while it can reach zero. To understand it analytically, it is necessary to consider also the coefficient $C_2(t)$, which is provided in ref 66. By rearranging it in terms of V_{IF} , ΔE_{IF} , and ΔE_{v} (or, equivalently, proceeding as above), and choosing a phase factor consistent with the choice in eqs 28, the following is written:

$$C_2(t) = -\frac{H_{\text{IF}} - H_{\text{II}}S}{(1 - S_{\text{IF}}^2)\Delta E_{\text{v}}} (e^{u_+t} - e^{u_-t}) \quad (31)$$

By evaluating eqs 28 and 31 for $V_{\text{IF}} = 0$ and inserting them into eq 22, the following is obtained:

$$\psi = \cos \left(\frac{\Delta E_{\text{IF}}}{2\hbar \sqrt{1 - S_{\text{IF}}^2}} t \right) \psi_{\text{I}} - i \sin \left(\frac{\Delta E_{\text{IF}}}{2\hbar \sqrt{1 - S_{\text{IF}}^2}} t \right) \bar{\psi}_{\text{I}} \quad (32)$$

that is, an oscillation between ψ_{I} and $\bar{\psi}_{\text{I}}$ in a wave function subspace where the maximum overlap of ψ with ψ_{F} is given by

S_{IF} , as stated above. A nonzero effective electronic coupling between ψ_{I} and ψ_{F} allows the system to go out of this subspace, which can be defined as a space “quasi-orthogonal” to ψ_{F} for small S_{IF} values. Then, the maximum transition probability is given by $4V_{\text{IF}}^2/(\Delta E_{\text{v}})^2$, which has the same formal expression as in Rabi’s formula but with new definitions for the involved quantities as in eqs 5 and 6. In conclusion, the above equations fully characterize V_{IF} with the symmetric expression in eq 6 as the “effective” electronic coupling in the Ψ representation, without the use of any *ad hoc* device.

2.4. Overlap between the Diabatic States and Effective Electronic Coupling in Long-Range CT. The relation between effective electronic coupling and diabatic state overlap approximately reduces to a linear one in diverse circumstances:^{70,71}

$$V_{\text{IF}} = CS_{\text{IF}} \quad (33)$$

where C is a suitable constant for the system under consideration. Relations of this form have been used to calculate the interatomic resonance integral⁷⁰ and also the effective electronic coupling at larger interatomic distances.⁷¹ For CT between off-resonance states (as is the case, e.g., in DNA base stacks¹¹), the long-range behavior of V_{IF} can be easily obtained without using empirical parameters, which can have useful implications for the study of many biochemical processes. If the given donor and acceptor centers are far enough, V_{IF} (as well as S_{IF}) is very small and the electron is almost completely localized on one redox site, e.g., $\psi = \psi_{\text{I}}$. Then, $a \cong 1$, and the normalization constraint $\langle \psi | \psi \rangle = a^2 + b^2 + 2\text{Re}(ab^*)S_{\text{IF}}$ yields $b = 0$, which would give zero effective coupling, or $b \cong -2\text{sgn}(a)S_{\text{IF}}$. Moreover, at a large enough distance, it is $V_{\text{IF}} \leq \Delta E_{\text{IF}} \cong \Delta E_{\text{v}}$, and the diabatic energy difference essentially arises from the distribution of the excess charge in different local environments, at the given internal coordinates of the two redox sites. This difference approaches the value $\Delta E_{\text{IF}}^{(0)}$ for infinitely separated redox sites. Thus, on the basis of the above considerations, eq 11 leads to

$$V_{\text{IF}} \cong \frac{3}{2} |\Delta E_{\text{IF}}| S_{\text{IF}} \cong \frac{3}{2} |\Delta E_{\text{v}}| S_{\text{IF}} \cong \frac{3}{2} |\Delta E_{\text{IF}}^{(0)}| S_{\text{IF}} \quad (34)$$

which fixes the constant C in eq 33 at the value $3/2|\Delta E_{\text{IF}}^{(0)}|$. The diabatic energy difference mainly determines the electron localization on one molecular site. If two diverse redox couples have the same value of $\Delta E_{\text{IF}}^{(0)}$ at suitable nuclear coordinates, different S_{IF} values indicate different effective electronic couplings, hence different abilities to spread the excess charge out of the occupied site. Before concluding this section, it is also worth noting the similarity between the expression (eq 34) of the transfer integral in terms of the vertical excitation energy, within the context of long-distance CT, and the relation between resonance energy and atomic orbital overlap in ref 70, where the resonance energy is written in a form similar to the off-diagonal elements in the \mathbf{H} matrix of eq 25b and is set proportional to the ionization energy for the appropriate valence atomic orbital.

3. SYSTEMS AND COMPUTATIONAL METHODS

3.1. Systems and Purposes. The first system under investigation is a guanine–thymine (GT) stack from ideal B-DNA (Figure 2a). The hole transfer between G and T is reconsidered, after its study in ref 34 with the Becke-half a d-half⁷² (BHH) hybrid XC functional, to test the performance of the recently developed M06-2X and M06-HF XC density functionals.^{73–75} In fact, GT is the nucleobase stack with the largest intrastrand V_{IF}

and is a paradigmatic case of relevance to theoretical studies on CT through DNA strands. Moreover, since the influence of the sugar–phosphate backbone on the electronic coupling between the stacked nucleobases is negligible,¹¹ the backbone can be excluded from the first-principles calculation of V_{IF} . Thus, both the TP and CDFT diabatic states can be used to describe the through-space hole transfer between G and T.

The perylenediimide (PDI; Figure 2b) belongs to a class of polycyclic aromatic molecules that are promising materials for nanoelectronics (e.g., for organic photovoltaics and thin film transistors), due to their ability to organize in well-ordered π stacks and to support hole or electron transport.^{14,76,77} Hence, the charge transfer integrals for hole and electron transfer through stacked PDI molecules are parameters of practical relevance. The calculations performed in this work pursue the following main objectives: (i) test the performance of the M06-2X and M06-HF functionals, once used in combination with eq 11, in this kind of extended aromatic system, where the high-nonlocality character of the functional can play an important role; (ii) verify the (high) accuracy of the proposed theoretical-computational approach also very near the transition state coordinate, where the Condon approximation can be safely assumed; (iii) contribute to identify, or restrict, the maximal range of reliable values for the involved hole and electron transfer integrals. In a similar fashion to previous works on DNA stacks,⁴⁸ this is done calculating the V_{IF} values at different levels of computational accuracy and comparing the results with valuable ones in the previous literature.¹⁴

The distance dependence of the transfer integral and the fulfillment of eq 34 are investigated on the electron transfer between a quinol and a semiquinone function in a face-to-face arrangement. Apart from the importance of the redox reactions involving this system in biology and medicine,^{78,79} it was chosen as a paradigmatic case for testing the performance of the M06-HF density functional.

3.2. TP and CDFT Diabatic States. The DNA stack can be easily separated into a donor group \mathcal{D} (i.e., one of the two nucleobases), where the hole is initially localized, and an acceptor group \mathcal{A} , receiving the transferring hole. Hence, the I and F electronic states can be conveniently defined as $|\psi_{\text{I}}\rangle = |\mathcal{D}^+\rangle|\mathcal{A}\rangle$ and $|\psi_{\text{F}}\rangle = |\mathcal{D}\rangle|\mathcal{A}^+\rangle$, respectively, where the charge localized on each base has been explicitly indicated. They are obtained as tensor products of reference states for the isolated \mathcal{D} and \mathcal{A} groups in the initial and final charge states. The necessary electronic wave functions are built as single Slater determinants of the lowest-lying occupied Kohn–Sham spin orbitals. The feasibility of this procedure also regarding the spin contamination problem⁶³ has been discussed in ref 33 (see also ref 80 and references therein). The A , B , and S_{IF} overlaps are obtained by exploiting the ET module in the NWChem computational chemistry package.^{8,81} The ET module is not used otherwise. Afterward, the a and b coefficients are derived from eq 13. The energy difference between the TP diabatic states is obtained from

$$\Delta E_{\text{IF}} = (E_{\text{D}^+} + E_{\text{A}}) - (E_{\text{D}} + E_{\text{A}^+}) + W_{\text{D}^+-\text{A}} - W_{\text{D}-\text{A}^+} \quad (35)$$

$E_{\mathcal{D}^+}$, $E_{\mathcal{A}^+}$, $E_{\mathcal{D}}$, and $E_{\mathcal{A}}$ are the ground-state energies of the isolated subsystems in the indicated charge states, which are directly provided by self-consistent field DFT calculations on such subsystems. $W_{\mathcal{D}^+-\mathcal{A}}$ and $W_{\mathcal{D}-\mathcal{A}^+}$ are the interaction energies between \mathcal{D} and \mathcal{A} in states $|\psi_{\text{I}}\rangle$ and $|\psi_{\text{F}}\rangle$, respectively, which are computed as energies of electrostatic interaction by

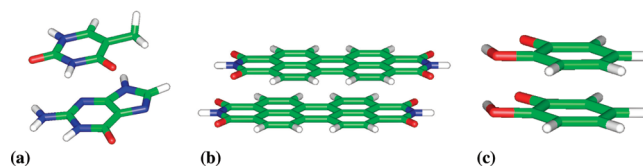


Figure 2. Molecular systems under consideration: (a) guanine-thymine (GT) stack from ideal B-DNA, (b) perylenediimide (PDI) stack, and (c) quinol–semiquinone redox couple.

using restraint electrostatic potential (RESP) charges that fit the quantum mechanical electrostatic potential on a specified grid. This is performed through the ESP module in the NWChem program,⁸¹ with hyperbolic restraining on the partial atomic charges. After suitable testing, the maximum distance between a grid point and any of the atomic centers was set at the value 0.5 nm, and a grid spacing of 0.008 nm was used.

Alternatively (and exclusively for the other two systems), the diabatic electronic states $|\psi_{\text{I}}\rangle$ and $|\psi_{\text{F}}\rangle$ are obtained from CDFT³² calculations on the overall system, performed using NWChem. The CDFT approach consists of finding an effective external potential to add to the Hamiltonian in order to get the electronic state of lowest energy under the specified density constraint.³² In hole (electron) transfer processes, a unit positive (negative) charge is localized in \mathcal{D} (\mathcal{A}) for the initial (final) state. ΔE_{IF} is directly given by the difference between the energies E_{I} and E_{F} of the CDFT states. Hence, the approximations inherent in the partition scheme of eq 35 and consequent evaluation of $W_{\mathcal{D}^+-\mathcal{A}}$ and $W_{\mathcal{D}-\mathcal{A}^+}$ are avoided. The Löwdin population scheme was used in all of the CDFT calculations, whereas the Becke scheme turned out not to be feasible for the considered systems and hybrid-DFT approaches.

4. COMPUTATIONAL RESULTS AND DISCUSSION

4.1. Effective Electronic Coupling in the Guanine–Thymine Dimer. The charge-transfer and spatial overlap integrals for the GT nucleobase stack calculated in this work are reported in Table 1 (top panel). They are compared with previous results in the literature (bottom panel) based on the same set of atomic coordinates.⁴⁴

Table 1 shows that the hole transfer integrals obtained by using the M06-2X functional are consistently overestimated ($\sim 40\%$) compared to those calculated in ref 34 with the BHH functional and the values from refs 30 and 44 which use the DFT fragment-orbital (FO) method and the GMH method combined with Koopmans' theorem⁸² approximation (KTA),²⁶ respectively. Thus, on the basis of these results, the M06-2X functional should not be used for quantitative calculations of effective electronic couplings in DNA systems involving the GT stack.

On the contrary, the M06-HF functional, which uses full HF exchange, gives results that (i) are almost insensitive to the employed basis set and (ii) are in excellent agreement with the value of V_{IF} obtained in ref 44 by means of the second-order perturbation formulation (CAS-PT2) of the complete active space self-consistent field (CASSCF) method. In the reported multireference calculations, the full active space is indeed reduced to include 11 electrons in 12 π orbitals. Moreover, dynamic correlation is not included in the CASSCF approach. However, the CAS-PT2 calculations include the multistate formulation,

Table 1. (Upper Panel) Diabatic Energy Difference (ΔE_{IF}), Effective Electronic Coupling (V_{IF}) from eq 11, Overlap Integral (S_{IF}), and Vertical Excitation Energy (ΔE_{v}) from eq 5 for the 5'-GT-3' Nucleobase Stack from Regular B-DNA, Calculated in This Work Using Both CDFT and TP Diabatic Electronic States^a (Bottom Panel) Results from Hybrid-DFT,³⁴ DFT (with eq 20),³⁰ HF and Multireference⁴⁴ Calculations^b

XC functional	basis set	ΔE_{IF}	V_{IF}	S_{IF}	ΔE_{v}	$\Delta E_{\text{IF}}^{(\text{TP})}$	$V_{\text{IF}}^{(\text{TP})}$	$S_{\text{IF}}^{(\text{TP})} \equiv \bar{S}_{\text{IF}}$
This Work								
M06-2x	6-31 g*	1.210	0.197	0.0629	1.274			
	6-311 g**	1.230	0.179	0.0761	1.284			
	cc-pVTZ	1.230	0.169	0.0826	1.280	1.248	0.1701	0.0171
	cc-pVTZ–BSSE					1.248	0.1701	0.0171
	6-311++g(3df,3pd)					1.217	0.168	0.0183
M06-HF	6-31 g*	1.207	0.078	0.0514	1.218			
	6-311 g**	1.232	0.077	0.0600	1.244			
	cc-pVTZ	1.258	0.078	0.0630	1.270	1.278	0.0804	0.0177
	cc-pVTZ–BSSE					1.281	0.0806	0.0177
	6-311++g(3df,3pd)					1.222	0.075	0.0195
Ref 34								
BHH	6-31 g*	1.271	0.135	0.053	1.300	1.305	0.140	0.012
	6-311 g**	1.290	0.128	0.064	1.317	1.307	0.132	0.015
	cc-pVTZ	1.284	0.126	0.070	1.311	1.300	0.129	0.016
	6-311++g(3df,3pd)					1.272	0.127	0.017
Ref 30								
DFT, FO	TZ2P		0.334			0.141		0.023
Ref 44								
GMH-KTA	6-31 g*				0.137			1.574
CASSCF(7,8)	6-31 g*				0.098			1.799
CASSCF(11,12)	6-31 g*				0.097			1.415
CAS-PT2(11,12)	6-31 g*				0.081			1.175

^a Use of the latter ones is explicitly indicated. ^b All energy quantities are expressed in eV.

MS-PT2, and tend to overcome these shortcomings. While, as discussed in ref 34, the comparison between the results from BHH and multireference calculations does not allow one to draw definitive conclusions in favor of either approach, my current results using eq 11 and the M06-HF functional clearly support the post-HF data. Furthermore, the results in Table 1 confirm the conclusions in ref 75 about the ability of this hybrid XC functional to correct for the unphysical electron self-interaction⁶³ and its considerable improvement on HF. In the M06-HF approximation,⁷³ the XC energy is obtained by adding the nonlocal HF exchange energy, as computed from the occupied Kohn–Sham orbitals, to XC energy with the same local functional form as for M06-L but different values of the parameters that enforce its compatibility with the presence of full HF exchange. Ultimately, M06-HF includes both local and nonlocal exchange, but only the latter survives at large enough distances, thereby providing the correct asymptotic behavior. Moreover, it satisfies the uniform-electron-gas limit at both the short and long range, which is an important formal property, and includes short-range static-correlation effects that are missing in hybrid functionals where the HF exchange is added to pure correlation energy. Such features can also lead, on the average, to a better

description of the ground-state energetics than that given by the popular B3LYP functional.⁷³ By considering the ingredients in eq 11, the optimal performance of the M06-HF functional might be attributed to an equilibrated description of the ground state, with a good medium–long-range behavior of the exchange in the considered GT system. This avoids an excessive spread of the valence charge over the two nucleobases, which would otherwise amount to exceedingly similar values of a and b in eqs 11 and a correspondingly overestimated transfer integral. The investigation of other DNA nucleobase stacks is however necessary to confirm this indication and is the subject of future work, also considering the low computational cost of the hybrid-DFT implementation of eq 11. In this regard, it is noteworthy that the M06-HF functional shows an optimal performance even at the 6-31g* level of computation, which is an important point for first-principles calculations of charge-transfer integrals on large-scale systems.

Note that in eq 11 the DFT energies appear only in ΔE_{IF} , that is, the difference between the energies of the whole system in the two diabatic states for the given nuclear coordinates. Hence, the addition of the dispersion terms according to the recipes allowed by the employed computational chemistry package⁸¹ does not

Table 2. Quality of the Two-State Approximation Using TP and CDFT Diabatic States, Quantified in the First Two Data Columns via the Square Modulus of the Ground-State Wave Function That Results from the First Expansion in eq 2, and the Overlap Integrals of the Diabatic States Belonging to the TP and CDFT Sets (C_{ij}) Obtained from eqs 36a and 36b, by Inserting the Values of S_{IF} and \bar{S}_{IF} from the Calculations (First Line for Each Functional) or Directly from the Computed Wave Functions (Second Line)

		$\langle\psi \psi\rangle_{\text{CDFT}}$	$\langle\psi \psi\rangle_{\text{TP}}$	C_{11}	C_{22}	C_{12}	C_{21}	$(C_{12} + C_{21})/2$
M06-2x	eqs 36a and 36b			0.9995	0.9995	0.0499	0.0499	0.0499
	computation	0.9983	0.9917	0.9930	0.9910	0.0508	0.0488	0.0498
M06-HF	eqs 36a and 36b			0.9997	0.9997	0.0404	0.0404	0.0404
	computation	0.9995	0.9934	0.9940	0.9910	0.0395	0.0410	0.0403

change the value of the charge-transfer integral resulting from eq 11. Furthermore, as discussed elsewhere,⁴⁸ the approach is also robust against the basis set superposition error (BSSE). In this work, it is shown by the data at the M06-2x/cc-pVTZ and M06-HF/cc-pVTZ computational levels in Table 1, which were obtained using the counterpoise method.⁸³

The cc-pVTZ basis set⁸⁴ was used to compute V_{IF} with both the TP and CDFT diabatic states. The two diabatic sets lead to very similar V_{IF} values against significantly different overlaps S_{IF} in either M06-2X or M06-HF calculations. Indeed, the differences in the transfer integral values can be essentially ascribed to the slight overestimation of ΔE_{IF} by eq 35. The similarity of the V_{IF} values, the fulfillment of the two-state approximation regarding the values of⁸⁵ $\langle\psi|\psi\rangle = a^2 + b^2 + 2abS_{\text{IF}}$ (Table 2), and the nature of the system, where the D and A groups are spatially well separated, support the use of both TP and CDFT states, which are then expected to satisfy eqs 16 and 17. To see this, the quantities (obtained from eq 16)

$$C_{11} \equiv \langle\psi_1|\bar{\psi}_1\rangle = C_{22} \equiv \langle\psi_F|\bar{\psi}_F\rangle = \frac{1}{2} \left[\sqrt{\frac{1+\bar{S}_{\text{IF}}}{1+S_{\text{IF}}}} + \sqrt{\frac{1-\bar{S}_{\text{IF}}}{1-S_{\text{IF}}}} + \left(\sqrt{\frac{1+\bar{S}_{\text{IF}}}{1+S_{\text{IF}}}} - \sqrt{\frac{1-\bar{S}_{\text{IF}}}{1-S_{\text{IF}}}} \right) S_{\text{IF}} \right] \quad (36a)$$

$$C_{12} \equiv \langle\psi_1|\bar{\psi}_F\rangle = C_{21} \equiv \langle\psi_F|\bar{\psi}_1\rangle = \frac{1}{2} \left[\sqrt{\frac{1+\bar{S}_{\text{IF}}}{1+S_{\text{IF}}}} - \sqrt{\frac{1-\bar{S}_{\text{IF}}}{1-S_{\text{IF}}}} + \left(\sqrt{\frac{1+\bar{S}_{\text{IF}}}{1+S_{\text{IF}}}} + \sqrt{\frac{1-\bar{S}_{\text{IF}}}{1-S_{\text{IF}}}} \right) S_{\text{IF}} \right] \quad (36b)$$

are considered. The overlaps between the CDFT and TP diabatic wave functions (identified with Ψ and $\bar{\Psi}$, respectively) obtained from the M06-2x and M06-HF calculations are compared in Table 2 with the values obtained by insertion of S_{IF} and \bar{S}_{IF} (see Table 1) into eqs 36a and 36b. The agreement is good, thus confirming the expectation. Notice that, although the \bar{S}_{IF} values are smaller than the S_{IF} ones, and much smaller than unity, eq 11 (or its approximation in eq 10) must be used to obtain V_{IF} from nonorthogonal diabatic states. The corresponding value of H_{IF} can be obtained from eq 6 and is generally very different from V_{IF} , even if the involved energy quantities are computed in a one-orbital picture, as in ref 30 (see the H_{IF} and V_{IF} values reported in Table 1).

The assessment of the V_{IF} value for the hole transfer through the GT stack around 0.08 eV by both the CAS-PT2 method in ref 44 and the hybrid-DFT one at the M06-HF level in this work is in my opinion a useful step toward a systematic and consistent

quantification of hole-transfer integrals between stacked nucleobases. This consistency needs to be assessed at a more extended level in future works, including calculations with the complementary nucleobases for the GT stack and on other DNA stacks. It is worth noticing that in the Marcus nonadiabatic regime, where the CT rate has a quadratic dependence on V_{IF} ,¹⁷ a transfer integral of ~ 0.08 eV rather than ~ 0.13 eV amounts to a difference by a factor of ~ 2.64 in the estimate of the CT rate, which brings about an important difference if hopping transport through a strand is considered. Anyway, if either hopping of localized charges^{86,87} or polaron diffusive motion^{88,89} is the effective transport mechanism, the charge transfer integral between neighboring units plays an important role in the electrical conduction through DNA systems.⁹⁰

It is worth noting that all hybrid-DFT implementations lead to values of the vertical excitation energy between the CASSCF-(11,12) and CAS-PT2(11,12) values, closer to the latter. In particular, while M06-2X appears to overestimate V_{IF} , it provides ΔE_v values that are located between the M06-HF and BHH ones. Indeed, a recent study⁹¹ shows that M06-2X performs better than M06-HF, and widely used hybrid XC functionals such as B3LYP and PBE0, for the description of other types of excitations, i.e., vertical singlet excitations of adenine–thymine and guanine–cytosine base stacks. On the other hand, the M06-HF functional was designed⁷³ for accurate predictions of long-range CT excited states. Future studies with the most recent Minnesota hybrid meta density functionals (i.e., M08-HX and M08-SO,⁹² which may be considered as improved versions of M06-2X,⁹³ also with reference to the self-interaction term in the correlation functional⁹²) are desirable on the basis of the above results and discussion.

4.2. Hole and Electron Transfer Integrals in the Perylene-diimide Dimer. The hole and electron transfer integrals are calculated for the PDI-H (or simply PDI) dimer, with a hydrogen atom at the imide position. The geometry of the monomer was drawn from the Supporting Information of ref 14, and the dimer was built with the same shift parameters used in ref 14 for the CH_3 derivative. In particular, the stacking distance was fixed at 3.4 Å.⁹⁴ In order to move the dimer slightly away from the transition state coordinate Q_t , the H atoms in one of the monomers were further relaxed. The resulting geometry of the dimer corresponds to a value Q of the reaction coordinate very close to Q_t ($Q = Q_t + \delta Q$), as quantified by the fact that $\Delta E_{\text{IF}}(Q) \ll 2V_{\text{IF}}(Q)$ (see Table 3 and also Table S1 in the Supporting Information).

Considering that the PDI molecule is a kind of cyclic polyene, the M06-2X functional was first used in the calculations, thereby following the indications that result from ref 75 and the excellent performance achieved in ref 14. The hole-transfer ($V_{\text{IF}}^{(h)}$) and electron-transfer ($V_{\text{IF}}^{(e)}$) integrals obtained using the 6-311g** basis set are reported in the first row of Table 3 (values of the

Table 3. Hole ($V_{\text{IF}}^{(\text{h})}$) and Electron ($V_{\text{IF}}^{(\text{e})}$) Transfer Integrals and Corresponding Diabatic Energy Differences ($\Delta E_{\text{IF}}^{(\text{h})}$ and $\Delta E_{\text{IF}}^{(\text{e})}$) in the PDI Dimer, Using CDFT Diabatic Electronic States^a

XC functional	basis set	$V_{\text{IF}}^{(\text{h})}$	$\Delta E_{\text{IF}}^{(\text{h})}$	$V_{\text{IF}}^{(\text{e})}$	$\Delta E_{\text{IF}}^{(\text{e})}$
M06-2x	6-311 g**	35.2–35.9	0.04–0.40	127.6–129.7	0.10–0.95
	6-311 g**/6-311++g*	41.5		138.2	
BHH	6-311 g**/6-311++g*			112.9	

^a First row: ranges of values corresponding to different geometries (see main text) and using the M06-2X hybrid functional. Second and third rows: values at the nuclear coordinates $Q_t + \delta Q$, using the M06-2X and BHH XC functionals, respectively, with the mixed 6-311g**/6-311++g* basis set. All quantities are expressed in meV.

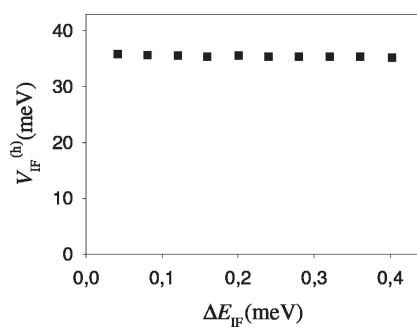


Figure 3. Effective electronic coupling for hole transfer in a PDI-H stack (x shift = 1.60 Å, y shift = 0.94 Å, z shift = 3.40 Å). The y axis starts from 0 meV to point up the small relative spread of the data points.

effective electronic coupling and the diabatic energy difference at the left and right sides, respectively, of each reported interval). They are close to the effective couplings for the CH₃ derivative provided in ref 14.

By assuming the Condon approximation in $[Q_t, Q_t + \delta Q]$, the computational accuracy allowed by eq 11 near Q_t was tested by calculating $V_{\text{IF}}^{(\text{h})}$ also at the atomic positions $Q_j = Q_t + j\delta Q/10$, with $j = 1$ to 9. A further test was performed on $V_{\text{IF}}^{(\text{e})}$, at nuclear coordinates $Q_j = Q_t + j\delta Q/10$, with $j = 1$ and 5. The ranges of values in the first line of Table 3 were thus obtained (see individual values in Table S1 of the Supporting Information). Such narrow ranges, with a maximum difference of less than 2%, show the high accuracy of the transfer integral calculation using eq 11, irrespective of the fact that the differences in the values may actually be ascribed to computational uncertainty or small deviation from the Condon approximation. The small spread in the $V_{\text{IF}}^{(\text{h})}$ values is also displayed in Figure 3. ΔE_{IF} ⁹⁵ is chosen as the reaction coordinate, which highlights the proximity to Q_t (cf. the energy ranges on the two axes).

The values of $V_{\text{IF}}^{(\text{h})}$ and $V_{\text{IF}}^{(\text{e})}$ were also calculated by using a composite 6-311g**/6-311++g* basis set. To obtain a proper spanning of the intermolecular space, despite the limited amount of diffuse functions allowed by the available CDFT implementation, the basis set was augmented on O and N atoms, and the C atoms mainly involved in the spatial distributions of the frontier orbitals according to the calculations at the M06-2X/6-311g** level. The $V_{\text{IF}}^{(\text{h})}$ and $V_{\text{IF}}^{(\text{e})}$ values remain close to those for the CH₃ derivative in ref 14. In particular, the large value of the electron-transfer integral is confirmed.

The calculation at the BHH/6-311g**/6-311++g* level confirms the high value of $V_{\text{IF}}^{(\text{e})}$. Hence, the PDI system, without a specific substituent at the imide position, is also a promising candidate for incorporation into electronic devices where excess electron transport is exploited. BHH yields a value of $V_{\text{IF}}^{(\text{e})}$ that is

about 20% smaller than that provided by M06-2X. Indeed, any XC density functional is an approximation of the unknown exact one and can be affected by spurious electron self-interaction,⁶³ with consequent errors in electronic coupling valuations. Thus, the difference in the BHH and M06-2X values of $V_{\text{IF}}^{(\text{e})}$ is the result of different approximations to the exact XC functional, and both values can be, in principle, affected by errors. However, for the same reason that BHH and M06-2X are quite different approximations, the two values contribute to identify a probable range for the value of $V_{\text{IF}}^{(\text{e})}$, whence comes the order of magnitude of its uncertainty. This is valuable information, all the more so that the size of the system is prohibitive for multireference calculations.

The above comparison and the consistency of the M06-2X values near Q_t denote good performance of the M06-2X hybrid XC functional for the PDI system. This is an important point in favor of M06-2X compared to many other XC functionals, which for large and complicated electronic systems often suffer from fundamental problems that may lead to divergence or convergence to an energy saddle point rather than to the ground-state minimum.⁹⁶ Indeed, the considered PDI system at the given nuclear coordinates offers a paradigmatic case in this respect. In fact, the calculations of $V_{\text{IF}}^{(\text{h})}$ using BHH and of $V_{\text{IF}}^{(\text{e})}$ using both BHH and M06-HF showed problematic convergence and led to broken-symmetry charge-localized solutions for the ground-state wave function, which did not allow suitable computation of $V_{\text{IF}}^{(\text{h})}$ and $V_{\text{IF}}^{(\text{e})}$.

4.3. Long-Range Electron Transfer in the Quinol-Semiquinone Redox Couple. Following refs 73 and 75, the M06-HF density functional was used to study the dependence of the charge-transfer integral on the distance between donor and acceptor. Similarly to recent results,³⁷ the transfer integral values in a semilog plot lie approximately on a straight line (see black data points and best-fit line in Figure 4); thus

$$V_{\text{IF}} \cong V_0 \exp(-\beta R_{\mathcal{D}\mathcal{A}}) \quad (37)$$

where V_0 is a suitable constant, $R_{\mathcal{D}\mathcal{A}}$ is the donor–acceptor distance, and β is the decay factor. On the basis of the whole set of data points, the decay factor is $\beta = 2.07 \text{ \AA}^{-1}$, which is larger than the value of 1.7 \AA^{-1} predicted by the pathway model.⁹⁷ However, if the fit is performed for $\mathcal{D}\text{--}\mathcal{A}$ separations between 3 and 6 Å, where eq 37 turns out to be well-satisfied, a decay factor $\beta = 1.64 \text{ \AA}^{-1}$ is obtained (gray line). On the other hand, eq 34 turns out to be valid at large enough $\mathcal{D}\text{--}\mathcal{A}$ distances ($R_{\mathcal{D}\mathcal{A}} \geq 3.5 \text{ \AA}$ in the graph of Figure 4). In particular, the red squares are computed using the first approximate equality in eq 34.

The results in Figure 4 support the use of the full-HF-exchange M06-HF hybrid functional over a large range of $\mathcal{D}\text{--}\mathcal{A}$ separations. Indeed, for the face-to-face quinol–semiquinone system, the implementation of eq 11 using CDFT diabatic states and the M06-HF functional appears to perform reasonably well even at

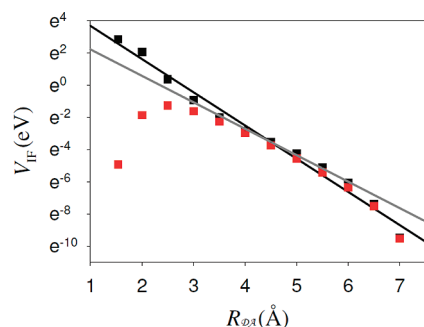


Figure 4. Electron transfer integral (on a natural logarithm scale) vs the donor–acceptor distance $R_{\mathcal{D},\mathcal{A}}$, obtained using eq 11 (black) and the first equality in eq 34 (red), which clearly fails at small distances. A mixed cc-pVTZ/aug-cc-pVTZ basis set is used, with diffuse functions added on the O atoms for a proper spanning of the intermolecular space. The black and gray best-fit lines are described in the main text.

the shortest explored distance $R_{\mathcal{D},\mathcal{A}} = 1.54 \text{ \AA}$, where the overlap integral is unduly large, $S_{\text{IF}} = 0.949$ (Table S2 in the Supporting Information), so that the definition of the CDFT states reaches the largest uncertainty.³² Yet, the value of V_{IF} is 17.2 eV and differs by about 2% from the value of 17.6 eV in ref 37. Clearly, both values can, in principle, be wrong. However, they are obtained from different theoretical-computational setups (except for the common use of CDFT diabatic states), and hence the similarity of the results gives support to their reliability. The results in this section also support the use of CDFT diabatic states in short-range and/or intramolecular CT, but in the latter case, the donor and acceptor groups are not separated, so it is important to check that any reliable electron density constraint, which includes the atoms of a redox site dictated by suitable chemical reasons, leads to the same value of the effective electronic coupling.

5. CONCLUDING REMARKS

I recently proposed³⁴ a formula (i.e., eq 11 in this paper) for the calculation of charge-transfer integrals using a few electronic quantities that characterize the diabatic states and that can be easily obtained from *ab initio* computation. Equation 11 applies to both orthogonal and nonorthogonal diabatic states and is exact within the two-state model. This is useful in all of those cases where the nature of the CT system suggests the use of a nonorthogonal diabatic representation. Moreover, the results of this work markedly indicate that the quantities involved in eq 11 can be obtained from CDFT³² diabatic states, even if such states are characterized by a relatively large overlap (or a large one, e.g., for the quinol–semiquinone redox system at short distance). This is to be considered also in future studies of short-range intramolecular CT reactions.

From an exquisitely theoretical point of view, this work (i) relates eq 11 to previous approaches to V_{IF} calculation, (ii) establishes its connection with Löwdin's transformation, (iii) fully characterizes V_{IF} , as defined⁸ in eq 6 (thereby, also as expressed by eq 11), as the effective electronic coupling or perturbation that is involved in the probability of transition between nonorthogonal electronic states, and (iv) establishes the relation between charge-transfer and overlap integrals in the long-range CT between off-resonance diabatic states, without the use of empirical parameters.

As shown in section 2.2, the application of eq 11 to non-orthogonal diabatic states is equivalent to the exact Löwdin

transformation⁴⁰ of such states and use of the same eq 11 or eq 10 (for zero overlap) with the Löwdin orthogonal states. Anyhow, given a physically meaningful set of nonorthogonal diabatic states, eq 11 can be directly used by calculating the necessary quantities on these states without a need for their prior orthogonalization or any approximation based on the magnitude of the overlap.

On the one hand, the analysis in section 2.2 and the Appendix clarifies the relation between eq 11 and other methods in the previous literature^{22,27,41,42} that use orthogonal diabatic electronic states and where the latter can be obtained from rotation of the diabatic states.²⁷ In particular, it is observed that, once an appropriate nonorthogonal diabatic representation of the CT reaction under consideration is known, the correct rotation of the adiabatic states must lead to orthogonal diabats related to the nonorthogonal ones by the Löwdin transformation. Thus, any criterion for obtaining the diabatic states directly by rotation of the adiabatic ones should be confronted with indications resulting from the nature of the CT system and the way it is initially prepared (e.g., depending on the initial localization of the charge in a redox moiety and the distance between donor and acceptor, hence the spread of the initial electron charge distribution on a near redox site). In this respect, in my opinion, the CDFT approach affords a “natural” localization of the transferring electron charge, since it searches for the charge distribution of minimum energy under the constraint of charge localization around a given set of atoms which can be inferred and thus selected on the basis of chemical grounds. Then, eq 11 allows the use of the CDFT diabatic states without approximations, within the two-state model.

On the other hand, since eq 11 is obtained by direct solution of the two-state secular equation by using the definition of V_{IF} in eq 6, working with nonorthogonal states requires that eq 6 indeed provides the effective coupling in the nonorthogonal representation of a two-state dynamical problem. This is not a trivial point considering that the effective Hamiltonian is represented by a non-Hermitian matrix (see eq 25b), whereas V_{IF} from eq 6 is the off-diagonal element of a Hermitian operator. In order to extricate this delicate conceptual problem, eq 29 of this paper shows that V_{IF} from eq 6 gives, as desired, the effective perturbation involved in the transition between two nonorthogonal electronic states at any fixed nuclear coordinates. Equation 29 can be considered as an appropriate extension of Rabi's formula to the case of nonorthogonal electronic states. In particular, similarly to the latter, it gives the maximum oscillation of the transition probability for isoenergetic initial and final electronic states. Ultimately, although the effective Hamiltonian for the two-state model using nonorthogonal diabatic states is, in general, represented by a non-Hermitian operator and various devices have been used to regain the desired Hermitian behavior,¹⁵ eqs 26 and 29 yield the role of the perturbation term in the Hermitian component of the Hamiltonian. Therefore, with reference to CT processes, eq 6, hence its expression in eq 11, provides the appropriate expression of the effective coupling between nonorthogonal states, and not just an *ad hoc* symmetrized expression of such coupling.

The computational results of this work contribute to delimiting the theoretical expectation values of the effective electronic coupling for the considered CT reactions and support selective use of the Minnesota hybrid meta density functionals⁷⁵ for the study of diverse kinds of CT systems. However, in general, the results of this work, in agreement with previous ones,^{34,48} stress the importance of using different hybrid XC functionals and basis

sets as a crucial rule in order to identify reliable DFT values or probable ranges of values for the charge-transfer integral in many redox systems.

The BHH functional performs better than the M06-2X one for the computation of the charge-transfer integral in the guanine–thymine stack, if the results from multireference calculations⁴⁴ reported in Table 1 are taken as reference values. On the contrary, M06-HF gives values of the charge-transfer integral and the vertical excitation energy very close to those from the multireference calculations.⁴⁴ This fosters use of this hybrid functional in other DNA stacks, and also further investigation into the presence of complete Watson–Crick pairs. Moreover, M06-HF is expected to be particularly useful for studying triplets of base pairs, where long-range CT is also involved. On the basis of the current and previous^{34,48} results, M06-HF and BHH may provide the best set of hybrid functionals to be applied in the investigation of the hole transfer through nucleobase stacks. Nevertheless, it is worth noting that the M06-2X density functional shows optimal performance in the calculation of the vertical excitation energy for the GT stack.

Overall, M06-2X does much better than all other XC functionals tested on the perylenediimide stack. The analysis of this large π -electron system points to M06-2X as the most robust XC functional against convergence problems in the iterative solution of Kohn–Sham equations. It allowed the calculation of the hole and electron transfer integrals in the PDI stack very close to its transition state coordinate with high computational accuracy.

Finally, long-range CT has been studied in the quinol–semiquinone redox couple, for which M06-HF gives a V_{IF} decay factor in the expected range^{37,97} and confirms the theoretical expectation of eq 34.

Ultimately, the computational results of this paper suggest BHH, M06-2X, and M06-HF as a good set of hybrid functionals for charge-transfer integral calculations in various molecular systems. Clearly, future investigation of the most recent M08-HX and M08-SO⁹² Minnesota functionals is desirable.

APPENDIX

Wave Function Overlap Method and Löwdin Transformation. The row matrix $\Psi = (\psi_1 \ \psi_F)$ is related to the orthogonal set $\chi = (\chi_1 \ \chi_F)$ by the equation

$$\chi = \bar{\Psi} \bar{S}^{-1/2} \quad (38)$$

where

$$\bar{S} = \begin{pmatrix} 1 & \bar{S}_{\text{IF}} \\ \bar{S}_{\text{IF}} & 1 \end{pmatrix} \quad (39)$$

By equating the right-hand sides of eqs 14 and 38, and multiplying on the right by the matrix $\bar{S}^{1/2}$, the following is obtained:

$$\bar{\Psi} = \Psi \bar{S}^{-1/2} \bar{S}^{1/2} \quad (40)$$

The matrix $\bar{S}^{-1/2}$ is given by^{60,98}

$$\bar{S}^{-1/2} = \frac{1}{2} \begin{pmatrix} 1/\sqrt{1+\bar{S}_{\text{IF}}} + 1/\sqrt{1-\bar{S}_{\text{IF}}} & 1/\sqrt{1+\bar{S}_{\text{IF}}} - 1/\sqrt{1-\bar{S}_{\text{IF}}} \\ 1/\sqrt{1+\bar{S}_{\text{IF}}} - 1/\sqrt{1-\bar{S}_{\text{IF}}} & 1/\sqrt{1+\bar{S}_{\text{IF}}} + 1/\sqrt{1-\bar{S}_{\text{IF}}} \end{pmatrix} \quad (41)$$

and

$$\bar{S}^{1/2} = \frac{1}{2} \begin{pmatrix} \sqrt{1+\bar{S}_{\text{IF}}} + \sqrt{1-\bar{S}_{\text{IF}}} & \sqrt{1+\bar{S}_{\text{IF}}} - \sqrt{1-\bar{S}_{\text{IF}}} \\ \sqrt{1+\bar{S}_{\text{IF}}} - \sqrt{1-\bar{S}_{\text{IF}}} & \sqrt{1+\bar{S}_{\text{IF}}} + \sqrt{1-\bar{S}_{\text{IF}}} \end{pmatrix} \quad (42)$$

The insertion of eqs 41 and 42 into eq 40 gives eq 17. Moreover, the comparison of eqs 17 and 41 shows that $\mathbf{M} = \bar{S}^{-1/2}$ when \bar{S} is the identity matrix, i.e., when $\bar{S}_{\text{IF}} = 0$, which gives eq 14 as a special case of eq 16.

Finally, I wish to show how the insertion of eq 14 into eq 10 leads to eq 11. According to eqs 14 and 41, the energies of the orthogonal states χ_1 and χ_F are related to those of the non-orthogonal ones ψ_1 and ψ_F by

$$E(\chi_1) = (\mathbf{S}^{-1/2})_{11}^2 E(\psi_1) + (\mathbf{S}^{-1/2})_{12}^2 E(\psi_F) + 2(\mathbf{S}^{-1/2})_{11}(\mathbf{S}^{-1/2})_{12} \langle \psi_1 | H | \psi_F \rangle \quad (43)$$

and

$$E(\chi_F) = (\mathbf{S}^{-1/2})_{12}^2 E(\psi_1) + (\mathbf{S}^{-1/2})_{11}^2 E(\psi_F) + 2(\mathbf{S}^{-1/2})_{11}(\mathbf{S}^{-1/2})_{12} \langle \psi_1 | H | \psi_F \rangle \quad (44)$$

where the symmetry of $\mathbf{S}^{-1/2}$ has been exploited. Therefore, the corresponding diabatic energy differences $\Delta E_{\text{IF}}(\chi) \equiv E(\chi_1) - E(\chi_F)$ and $\Delta E_{\text{IF}}(\Psi) \equiv E(\psi_1) - E(\psi_F)$ satisfy the equation

$$\Delta E_{\text{IF}}(\chi) = [(\mathbf{S}^{-1/2})_{11}^2 - (\mathbf{S}^{-1/2})_{12}^2] \Delta E_{\text{IF}}(\Psi) = \frac{\Delta E_{\text{IF}}(\Psi)}{\sqrt{1 - S_{\text{IF}}^2}} \quad (45)$$

Alternatively, this result can be obtained by equating the expressions of the vertical excitation energy for the two diabatic sets. The wave function overlaps are related by the equations

$$A(\chi) \equiv \langle \chi_1 | \psi \rangle = (\mathbf{S}^{-1/2})_{11} A(\psi) + (\mathbf{S}^{-1/2})_{12} B(\psi) \quad (46)$$

and

$$B(\chi) \equiv \langle \chi_F | \psi \rangle = (\mathbf{S}^{-1/2})_{12} A(\psi) + (\mathbf{S}^{-1/2})_{11} B(\psi) \quad (47)$$

Then,

$$V_{\text{IF}} = \left| \frac{A(\chi)B(\chi)}{A^2(\chi) - B^2(\chi)} \Delta E_{\text{IF}}(\chi) \right| = \left| \frac{[(\mathbf{S}^{-1/2})_{11}^2 + (\mathbf{S}^{-1/2})_{12}^2] A(\Psi)B(\Psi) + (\mathbf{S}^{-1/2})_{11}(\mathbf{S}^{-1/2})_{12} [A^2(\Psi) + B^2(\Psi)]}{[(\mathbf{S}^{-1/2})_{11}^2 - (\mathbf{S}^{-1/2})_{12}^2] [A^2(\Psi) - B^2(\Psi)]} \times \frac{\Delta E_{\text{IF}}(\Psi)}{\sqrt{1 - S_{\text{IF}}^2}} \right| = \left| \frac{A(\Psi)B(\Psi)}{A^2(\Psi) - B^2(\Psi)} \Delta E_{\text{IF}}(\Psi) \left[1 - \frac{A^2(\Psi) + B^2(\Psi)}{2A(\Psi)B(\Psi)} S_{\text{IF}} \right] \frac{1}{1 - S_{\text{IF}}^2} \right| \quad (48)$$

that is the expression in eq 11b.

ASSOCIATED CONTENT

S Supporting Information. Table S1, which contains the values of the effective electronic couplings and diabatic energy differences in the PDI stack at the coordinates Q_j ($j = 1$ to 10), and Table S2, which includes the effective electronic couplings, diabatic energy differences, and overlaps for the quinol-semiquinone system

at the considered distances. This material is available free of charge via the Internet at <http://pubs.acs.org>.

AUTHOR INFORMATION

Corresponding Author

*Phone: +972-3-6407634. Fax: +972-3-6409293. E-mail: migliore@post.tau.ac.il

ACKNOWLEDGMENT

I am thankful to Abraham Nitzan for his scientific and human support during the elaboration of this work. I thank Stefano Corni, Rosa Di Felice, and Joseph Subotnik for useful discussions. I acknowledge support of this research from the Israel Science Foundation and the European Science Council (FP7/ERC grant number 226628).

REFERENCES

- (1) Slowinski, K.; Chamberlain, R. V.; Miller, C. J.; Majda, M. *J. Am. Chem. Soc.* **1997**, *119*, 11910–11919.
- (2) Napper, A. M.; Liu, H.; Waldeck, D. H. *J. Phys. Chem. B* **2001**, *105*, 7699–7707.
- (3) Chi, Q.; Zhang, J.; Jensen, P. S.; Christensen, H. E. M.; Ulstrup, J. *Faraday Discuss.* **2006**, *131*, 181–195.
- (4) Sek, S.; Palys, B.; Bilewicz, R. *J. Phys. Chem. B* **2002**, *106*, 5907–5914.
- (5) Jensen, P. S.; Chi, Q.; Zhang, J.; Ulstrup, J. *J. Phys. Chem. C* **2009**, *113*, 13993–14000.
- (6) Chi, Q.; Zhang, J.; Arslan, T.; Borg, L.; Pedersen, G. W.; Christensen, H. E. M.; Nazmudtinov, R. R.; Ulstrup, J. *J. Phys. Chem. B* **2010**, *114*, 5617–5624.
- (7) Feng, X.; Marcon, V.; Pisula, W.; Hansen, M. R.; Kirkpatrick, J.; Grozema, F.; Andrienko, D.; Kremer, K.; Müllen, K. *Nat. Mater.* **2009**, *8*, 421–426.
- (8) Farazdel, A.; Dupuis, M.; Clementi, E.; Aviram, A. *J. Am. Chem. Soc.* **1990**, *112*, 4206–4214.
- (9) Nitzan, A. *Annu. Rev. Phys. Chem.* **2001**, *52*, 681–750.
- (10) Tong, G. S. M.; Kurnikov, I. V.; Beratan, D. N. *J. Phys. Chem. B* **2002**, *106*, 2381–2392.
- (11) Rösch, N.; Voityuk, A. A. *Top. Curr. Chem.* **2004**, *237*, 37–72 and references therein.
- (12) Corni, S. *J. Phys. Chem. B* **2005**, *109*, 3423–3430.
- (13) Kuznetsov, A. M.; Medvedev, I. G.; Ulstrup, J. *J. Chem. Phys.* **2009**, *131*, 164703.
- (14) Vura-Weis, J.; Ratner, M. A.; Wasielewski, M. R. *J. Am. Chem. Soc.* **2010**, *132*, 1738–1739.
- (15) Newton, M. D. *Chem. Rev.* **1991**, *91*, 767–792 and references therein.
- (16) Marcus, R. A. *J. Chem. Phys.* **1956**, *24*, 966–978. **1956**, *979*–989.
- (17) Marcus, R. A.; Sutin, N. *Biochim. Biophys. Acta* **1985**, *811*, 265–322.
- (18) Kuznetsov, A. M.; Ulstrup, J. *Electron Transfer in Chemistry and Biology*; John Wiley & Sons: New York, 1999.
- (19) (a) Landau, L. D. *Phys. Z. Sowjetunion* **1932**, *1*, 88. **1932**, *2*, 46. (b) Zener, C. *Proc. R. Soc. London, Ser. A* **1932**, *137*, 696–702. **1933**, *140*, 660–668.
- (20) Marcus, R. A. *Annu. Rev. Phys. Chem.* **1964**, *15*, 155–196.
- (21) Zhang, L. Y.; Friesner, R. A.; Murphy, R. B. *J. Chem. Phys.* **1997**, *107*, 450–459.
- (22) (a) Cave, R. J.; Newton, M. D. *Chem. Phys. Lett.* **1996**, *249*, 15–19. (b) *J. Chem. Phys.* **1997**, *106*, 9213–9226.
- (23) Skourtis, S. S.; Beratan, D. N. *Adv. Chem. Phys.* **1999**, *106*, 377–452.
- (24) Regan, J. J.; Onuchic, J. N. *Adv. Chem. Phys.* **1999**, *107*, 497–553.
- (25) Prezhdo, O. V.; Kindt, J. T.; Tully, J. C. *J. Chem. Phys.* **1999**, *111*, 7818–7827.
- (26) Voityuk, A.; Rösch, N.; Bixon, M.; Jortner, J. *J. Phys. Chem. B* **2000**, *104*, 9740–9745.
- (27) Voityuk, A. A.; Rösch, N. *J. Chem. Phys.* **2002**, *117*, 5607–5616.
- (28) Zheng, X. H.; Stuchebrukhov, A. A. *J. Phys. Chem. B* **2003**, *107*, 9579–9584.
- (29) Bredas, J. L.; Beljonne, D.; Coropceanu, V.; Cornil, J. *Chem. Rev.* **2004**, *104*, 4971–5003.
- (30) Senthilkumar, K.; Grozema, F. C.; Fonseca Guerra, C.; Bickelhaupt, F. M.; Lewis, F. D.; Berlin, Y. A.; Ratner, M. A.; Siebbeles, L. D. A. *J. Am. Chem. Soc.* **2005**, *127*, 14894–14903.
- (31) Nishioka, H.; Kimura, A.; Yamato, T.; Kawatsu, T.; Kakitani, T. *J. Phys. Chem. B* **2005**, *109*, 1978–1987.
- (32) (a) Wu, Q.; Van Voorhis, T. *Phys. Rev. A* **2005**, *72*, 024502. (b) *J. Chem. Phys.* **2006**, *125*, 164105.
- (33) Migliore, A.; Corni, S.; Di Felice, R.; Molinari, E. *J. Chem. Phys.* **2006**, *124*, 064501.
- (34) Migliore, A. *J. Chem. Phys.* **2009**, *131*, 114113.
- (35) Glaesemann, K. R.; Govind, N.; Krishnamoorthy, S.; Kowalski, K. *J. Phys. Chem. A* **2010**, *114*, 8764–8771.
- (36) Mikołajczyk, M. M.; Zalesny, R.; Czyżnikowska, Ż.; Toman, P.; Leszczynski, J.; Bartkowiak, W. *J. Mol. Model.* [Online] DOI: 10.1007/s00894-010-0865-7.
- (37) de la Lande, A.; Salahub, D. R. *THEOCHEM* **2010**, *943*, 115–120.
- (38) Nowak, M. J.; Lapinski, L.; Kwiatkowski, J. S.; Leszczynski, J. *Computational Chemistry: Reviews of Current Trends*; Leszczynski, J., Ed.; World Scientific: Singapore, 1997; Vol. 2, pp 140–216.
- (39) Cremer, D. *Mol. Phys.* **2001**, *99*, 1899–1940.
- (40) Löwdin, P. O. *J. Chem. Phys.* **1950**, *18*, 365–375.
- (41) Sanz, J. F.; Malrieu, J.-P. *J. Phys. Chem.* **1993**, *97*, 99–106.
- (42) Creutz, C.; Newton, M. D.; Sutin, N. *J. Photochem. Photobiol. A: Chem.* **1994**, *82*, 47–59.
- (43) Numrich, R. W.; Truhlar, D. G. *J. Phys. Chem.* **1975**, *79*, 2745–2766.
- (44) Blancafort, L.; Voityuk, A. A. *J. Phys. Chem. A* **2006**, *110*, 6426–6432.
- (45) Nakamura, H.; Truhlar, D. G. *J. Chem. Phys.* **2001**, *115*, 10353–10372.
- (46) (a) Franck, J.; Dymond, E. G. *Trans. Faraday Soc.* **1926**, *21*, 536–542. (b) Condon, E. U. *Phys. Rev.* **1926**, *28*, 1182–1201.
- (47) Weissbluth, M. *Atoms and Molecules*; Academic Press: New York, 1978; p 587.
- (48) Migliore, A.; Corni, S.; Varsano, D.; Klein, M. L.; Di Felice, R. *J. Phys. Chem. B* **2009**, *113*, 9402–9415.
- (49) A careful discussion of the relations among the crossing of the diabatic energy surfaces, the transfer integral, and the minimum adiabatic energy splitting when other electronic states are involved, and thus an effective two-state model is usually employed, can be found in ref 15.
- (50) (a) Mulliken, R. S. *J. Am. Chem. Soc.* **1952**, *74*, 811–824. (b) Hush, N. S. *Prog. Inorg. Chem.* **1967**, *8*, 391–444. (c) Hush, N. S. *Electrochim. Acta* **1968**, *13*, 1005–1023. (d) Reimers, J. R.; Hush, N. S. *J. Phys. Chem.* **1991**, *95*, 9773–9781.
- (51) Mulliken, R. S.; Person, W. B. *Molecular Complexes*; Wiley: New York, 1969.
- (52) Valero, R.; Song, L.; Gao, J.; Truhlar, D. G. *J. Chem. Theory Comput.* **2009**, *5*, 1–22.
- (53) Kubař, T.; Woiczikowski, P. B.; Cuniberti, G.; Elstner, M. *J. Phys. Chem. B* **2008**, *112*, 7937–7947.
- (54) Migliore, A.; Corni, S.; Di Felice, R.; Molinari, E. *J. Phys. Chem. B* **2006**, *110*, 23796–23800.
- (55) Migliore, A.; Corni, S.; Di Felice, R.; Molinari, E. *J. Phys. Chem. B* **2007**, *111*, 3774.
- (56) Migliore, A.; Sit, P. H.-L.; Klein, M. L. *J. Chem. Theory Comput.* **2009**, *5*, 307–323.
- (57) Wolfsberg, M.; Helmholz, L. *J. Chem. Phys.* **1952**, *20*, 837–843.
- (58) Stuchebrukhov, A. A. *J. Chem. Phys.* **2003**, *118*, 7898–7906.
- (59) Song, L.; Gao, J. *J. Phys. Chem. A* **2008**, *112*, 12925–12935.
- (60) Rossi, M.; Sohlberg, K. *J. Phys. Chem. C* **2009**, *113*, 6821–6831.
- (61) Sit, P. H.-L.; Cococcioni, M.; Marzari, N. *Phys. Rev. Lett.* **2006**, *97*, 028303.

(62) The electron wave functions considered in ref 40 are, indeed, atomic orbitals. Full-electron states are used in the present discussion in harmony with the computation methods employed in this paper.

(63) Koch, W.; Holthausen, M. C. *A Chemist's Guide to Density Functional Theory*; Wiley: New York, 2000; pp 53–54 (spin contamination), Chapters 2 and 6 (self-interaction).

(64) Note that the overlap matrix S defined in this paper, as well as in ref 58, corresponds to the sum of S and the identity matrix in ref 40.

(65) Dogonadze, R. R.; Urushadze, Z. D. *J. Electroanal. Chem.* **1971**, *32*, 235–245.

(66) Efrima, S.; Bixon, M. *J. Chem. Phys.* **1976**, *64*, 3639–3647.

(67) Bixon, M.; Jortner, J. *Adv. Chem. Phys.* **1999**, *106*, 35–202 and references therein.

(68) Cave, R. J.; Baxter, D. V.; Goddard, W. A., III; Baldeschwieler, J. D. *J. Chem. Phys.* **1987**, *87*, 926–935 proposes an effective electronic coupling of the form $[(H_{IF} - H_{II}S_{IF})(H_{IF} - H_{FE}S_{IF})]^{1/2}/(1 - S_{IF}^2)$ where symmetry is achieved by means of geometric average. Also, other devices have been employed, as discussed in ref 15.

(69) Real wave functions are assumed here for the sake of simplicity, so that $S_{FI} = S_{IF}$ and $H_{FI} = H_{IF}$, as in eqs 3–6 and section 2.4. The relevant conclusions are not affected by this choice.

(70) Mulliken, R. S. *J. Phys. Chem.* **1952**, *56*, 295–311.

(71) Troisi, A.; Orlandi, G. *J. Phys. Chem. B* **2002**, *106*, 2093–2101.

(72) Becke, A. D. *J. Chem. Phys.* **1993**, *98*, 1372–1377.

(73) Zhao, Y.; Truhlar, D. G. *J. Phys. Chem. A* **2006**, *110*, 13126–13130.

(74) Zhao, Y.; Truhlar, D. G. *J. Chem. Phys.* **2006**, *125*, 194101.

(75) Zhao, Y.; Truhlar, D. G. *Theor. Chem. Acc.* **2008**, *120*, 215–241 and references therein.

(76) van der Boom, T.; Hayes, R. T.; Zhao, Y.; Bushard, P. J.; Weiss, E. A.; Wasielewski, M. R. *J. Am. Chem. Soc.* **2002**, *124*, 9582–9590.

(77) Bao, Z.; Locklin, J. J. *Organic Field-Effect Transistors*; CRC Press: Boca Raton, FL, 2007.

(78) Forquer, I.; Covian, R.; Bowman, M. K.; Trumpower, B. L.; Kramer, D. M. *J. Biol. Chem.* **2006**, *281*, 38459–38465.

(79) Grimaldi, S.; Arias-Cartin, R.; Lanciano, P.; Lyubenova, S.; Endeward, B.; Prisner, T. F.; Magalon, A.; Guigliarelli, B. *J. Biol. Chem.* **2010**, *285*, 179–187.

(80) Stowasser, R.; Hoffmann, R. *J. Am. Chem. Soc.* **1999**, *121*, 3414–3420.

(81) (a) Straatsma, T. P.; Aprà, E.; Windus, T. L.; Bylaska, E. J.; de Jong, W.; Hirata, S.; Valiev, M.; Hackler, M.; Pollack, L.; Harrison, R. *NWChem, A Computational Chemistry Package for Parallel Computers*, Version 5.1.1; Pacific Northwest National Laboratory: Richland, WA, 2008. (b) Kendall, R. A.; Apra, E.; Bernholdt, D. E.; Bylaska, E. J.; Dupuis, M.; Fann, G. I.; Harrison, R. J.; Ju, J.; Nichols, J. A.; Nieplocha, J.; Straatsma, T. P.; Windus, T. L.; Wong, A. T. *Comput. Phys. Commun.* **2000**, *128*, 260–283.

(82) Koopmans, T. *Physica* **1934**, *1*, 104.

(83) van Duijneveldt, F. B.; van Duijneveldt-van de Rijdt, J. G. C. M.; van Lenthe, J. H. *Chem. Rev.* **1994**, *94*, 1873–1885.

(84) Dunning, T. H., Jr. *J. Chem. Phys.* **1989**, *90*, 1007–1023.

(85) Normalized diabatic states and real a and b coefficients are obtained from the computation.

(86) Giese, B.; Amaudrut, J.; Köhler, A.-K.; Spormann, M.; Wessely, S. *Nature* **2001**, *412*, 318–320.

(87) Bixon, M.; Jortner, J. *J. Am. Chem. Soc.* **2001**, *123*, 12556–12567.

(88) Liu, C.-S.; Hernandez, R.; Schuster, G. B. *J. Am. Chem. Soc.* **2004**, *126*, 2877–2884.

(89) Conwell, E. M.; Bloch, S. M.; McLaughlin, P. M.; Basko, D. M. *J. Am. Chem. Soc.* **2007**, *129*, 9175–9181.

(90) Grozema, F. C.; Tonzani, S.; Berlin, Y. A.; Schatz, G. C.; Siebbeles, L. D. A.; Ratner, M. A. *J. Am. Chem. Soc.* **2008**, *130*, 5157–5166.

(91) Aquino, A. J. A.; Nachtigallova, D.; Hobza, P.; Truhlar, D. G.; Hättig, C.; Lischka, H. *J. Comput. Chem.* **2011**, *32*, 1217–1227.

(92) Zhao, Y.; Truhlar, D. G. *J. Chem. Theory Comput.* **2008**, *4*, 1849–1868.

(93) Zhao, Y.; Truhlar, D. G. *Chem. Phys. Lett.* **2011**, *502*, 1–13.

(94) Liu, S.-G.; Sui, G.; Cormier, R. A.; Leblanc, R. M.; Gregg, B. A. *J. Phys. Chem. B* **2002**, *106*, 1307–1315.

(95) Warshel, A. *J. Phys. Chem.* **1982**, *86*, 2218–2224.

(96) Høst, S.; Jansík, B.; Olsen, J.; Jørgensen, P.; Reine, S.; Helgaker, T. *Phys. Chem. Chem. Phys.* **2008**, *10*, 5344–5348.

(97) Jones, M. L.; Kurnikov, I. V.; Beratan, D. N. *J. Phys. Chem. A* **2002**, *106*, 2002–2006.

(98) Mayer, I. *Simple Theorems, Proofs, and Derivations in Quantum Chemistry*; Kluwer Academic/Plenum Publishers: New York, 2003; p 60.

Electron Attachment to Diselenides Revisited: Se–Se Bond Cleavage Is Neither Adiabatic nor the Most Favorable Process

José A. Gámez and Manuel Yáñez*

Departamento de Química, Módulo 13, Facultad de Ciencias, Universidad Autónoma de Madrid, Campus de Excelencia UAM-CSIC, Cantoblanco, 28049-Madrid, Spain

ABSTRACT: Up to now it has been generally assumed that the electron capture on diselenides $XSeSeX'$ produces a fragmentation of the Se–Se bond. However, our high-level ab initio calculations indicate that this is the case only when the substituents X and X' attached to the diselenide bridge have low electronegativity. Also importantly, even when the two substituents are of similar electronegativity, the Se–Se bond cleavage rarely is an adiabatic process. For low-electronegative X substituents, the extra electron is placed in the $\sigma^*(Se-Se)$ antibonding orbital, and the cleavage of the Se–Se bond is the most favorable process. However, the mechanism of this bond breaking is more intricate than previously assumed, and for asymmetric derivatives it proceeds through a conical intersection (CI). These findings emphasize the importance of using accurate ab initio calculations, rather than the usually employed density functional theory approaches, when dealing with reactions in biochemistry and organometallic chemistry, because the characterization of a CI requires the use of multireference methods to account for the mixing of states. When X is highly electronegative, the $\sigma^*(Se-X)$ antibonding orbital becomes highly stabilized with respect to the $\sigma^*(Se-Se)$ strongly favoring the cleavage of the Se–X bond, whereas the Se–Se remains practically unperturbed. Finally, when comparing the present results on diselenides with those of the disulfide analogues, it is apparent that the activation barriers and the final products of the different unimolecular reactions are higher in energy for the diselenides, in spite of the higher antioxidant strength of diselenides. This seems to indicate that the electron detachment process, less favorable for diselenides than for disulfides, competes with the electron-capture dissociation process and therefore should also be considered to explain the different antioxidant ability of these compounds.

INTRODUCTION

Selenium is an essential trace element which has received an increased interest as it has been identified in a large range of living beings, including humans.¹ It is primarily present in proteins, mainly under the form of the amino acids selenocysteine (Sec) and selenomethionine. Selenoproteins have been reported to play important and diverse roles in organisms, like elimination of peroxides and other oxidant agents, cancer prevention, and inflammation protection.^{2–4} Besides, sulfur and selenium share many physicochemical properties, and consequently, selenium usually accompanies or even substitutes sulfur in organisms. Indeed, the mutation of cysteine (Cys) to Sec has been proved to be very conservative, preserving the structure and the biological functionality of the selenomutant.^{5–15} Nevertheless, the substitution of Cys by Sec may bring significant advantages as it is the case for some oxidoreductases containing catalytic redox-active Sec,¹⁶ whose Cys mutants are typically 100–1000 times less active.¹⁷

Diselenide compounds are of special interest within the huge family of selenium derivatives for their applications in organic synthesis^{18–20} and as therapeutic drugs.^{21,22} Besides, they are also found in proteins as diselenide bridges,²³ in a similar fashion to sulfur-containing peptides. Diselenides are well-known for their high antioxidant activity,^{24–26} which is actually higher than that of disulfides, so the study of their reductive cleavage has attracted considerable attention.^{27–30} However, there is not enough information to fully understand the mechanism of this process. In the present contribution we would like to shed some light on this open question by modeling the reductive cleavage of

diselenides with the electron-capture dissociation (ECD) reaction, a process largely investigated for disulfides^{31–36} but which has not received such attention in the case of diselenides. Previous studies on dimethyldiselenide^{37,38} indicate that electron attachment yields mainly the breaking of the Se–Se linkage since the extra electron is accommodated in the $\sigma^*(Se-Se)$ antibonding orbital, like for disulfides, although these results are not sufficient to get a general picture of the electron-capture process in diselenides.

When an electron is added to a bond A–B, it may happen that the bond is preserved, a two-center, three-electron (2c3e) A...B bond being established, or that the bond gets broken, the centers being bound by means of charge–dipole interactions. A previous study in our group has shown that both situations are encountered when an extra electron is added to a diselenide depending on the electronegativity of the substituent of the diselenide bond.³⁹ The distinction about the nature of the activated bonds is of great relevance from the mechanistic point of view. The 2c3e bonds are characterized by a charge fluctuation between the bonding centers, rendering a nearly equal sharing of the unpaired charge.⁴⁰ However, as the bond stretches, it may happen that the extra charge and spin density, both initially delocalized throughout the bond, separate and localize into different fragments, a phenomenon known as charge–spin separation. For this reason several authors^{41,42} have pointed out that a proper description of the dissociation of 2c3e linkages has to appropriately account for

Received: April 4, 2011

Published: May 13, 2011

a delocalized covalent ground state for the minimum and a localized ionic one for the broken fragments, with the consequent (avoided) crossing of such states at certain bond distances.

The theoretical treatment of several electronic states simultaneously requires the use of special methodology, mainly when they are quite close in energy or even cross. Density functional theory (DFT) is frequently used in biochemistry, but it is inadequate to describe situations of near degeneracy or states crossing. Moreover it is well-known that standard DFT dramatically fails to describe the dissociation of odd-electron bonds.^{41–44} This failure is attributed, in part, to the self-interaction error (SIE), an unbalanced description of the exchange and correlation terms in approximate DFT functionals. SIE can be alleviated with a certain amount of HF exchange, i.e., with hybrid functionals,⁴⁵ but, since the extent of the SIE varies along the potential energy surface (PES),^{43,44} a hybrid functional properly describing a particular region of the PES is likely to fail at other regions, so they do not provide a general solution to the problem. Many SIE-free functionals have been developed following the recipe proposed by Perdew and Zunger,⁴⁶ although they are still not well suited to describe the dissociation of 2c3e bonds.⁴³ Other corrections, like the one proposed by Chermette et al.,⁴⁷ show also good results but depend on nuclear charges, which are not physically observable and are difficult to accurately determine.

As DFT provides a troublesome description of the dissociation of odd-electron bonds, wave function methods seem a more reliable alternative. However, previous theoretical studies on the cleavage of diselenides by electron attachment were performed with DFT or other unsuitable methods, and their conclusions may be compromised. Moreover, such works were based on symmetric molecules or systems bearing low-electronegative substituents. These situations are far from reality as proteins are highly asymmetric, and also, they create an environment where diselenides are exposed to substituents with varying electron-withdrawing strength, distorting the electronic density along the bond. The aim of the present contribution is to fully determine how these two factors: the electronegativity of the substituents and the asymmetry of the system influence the ECD reaction of diselenides, as some preliminary results⁴⁸ suggest that they do play an important role in the dissociation process. For this purpose, the CH₃SeSeX (X = NH₂, OH, and F) set of molecules has been chosen as representative of asymmetric diselenides with substituents of increasing electronegativity, which can be compared with HSeSeH and CH₃SeSeCH₃ to determine the influence of the asymmetry in the Se–Se bond cleavage.

COMPUTATIONAL METHODS

Throughout the Introduction Section we mentioned the inadequacy of standard DFT-based methods to describe the dissociation of odd-electron systems. This failure has been traditionally attributed to the SIE, which has been renamed more recently as delocalization error,⁴⁹ present when, due to delocalization, atomic centers bear fractional charges. Both approaches lead to the same behavior: Approximate functionals tend to underestimate the energy of systems with fractional charges. Consequently, MP2 perturbation theory was preferred for geometry optimizations and is able to recover enough electronic correlation at a computational affordable cost for the systems here considered. It is noteworthy, nevertheless, that MP2 can lead to erroneous geometries in the case of asymmetric 2c3e

Table 1. Se–Se and Se–X Bond Lengths (in Å) for the Neutral (CH₃SeSeX) and Most Stable Radical–Anionic ([CH₃SeSeX][−]) Diselenide Derivatives Calculated at the MP2/6-31++G(d,p) Level of Theory^a

X species	H	CH ₃	NH ₂	OH	F	
CH ₃ SeSeX	2.340	2.322	2.331	2.295	2.262	<i>d</i> (Se–Se)
[CH ₃ SSX] [−]	2.948	2.929	2.957	2.529	2.428	
CH ₃ SSX	1.484	1.966	1.847	1.833	1.803	<i>d</i> (Se–X)
[CH ₃ SSX] [−]	1.483	1.958	1.905	2.016	2.050	

^a (for X = H, the system is HSeSeH).

bonds.⁵⁰ However, in a previous publication³⁹ we have checked the MP2 estimates against more accurate methods, like coupled-cluster singles and doubles (CCSD), at predicting the geometries of the systems here considered. In addition to this comparison, it has also been proposed a rule to assess the validity of the MP2 geometries.⁵⁰ In all cases, MP2 performs pretty well, showing that it can accurately describe the geometries of the diselenides under study. Once a reliable method is decided, the 6-31++G(d,p) (BS1) expansion has been employed as the basis set, as it is flexible enough to describe the bonding situations we deal with. Since we are describing anions, with an electron placed far from the nuclei, the use of diffuse functions is almost compulsory. The optimized geometries were identified as real minima of the potential energy surface by evaluation of the Hessian matrix. Final energies have been corrected with the CCSD(T) approach, able to recover correlation effects beyond second order, and a more extended basis set, namely aug-cc-pVTZ (BS2). Geometry optimizations and Hessian evaluations with BS1 have been performed with the Gaussian03 suite of programs,⁵¹ while the single point calculations with BS2 at the CCSD(T) level were carried out with the MOLPRO 2009.01 package.⁵²

As mentioned above, some of the reactions may involve the crossing of different PESs, what makes mandatory the use of multireference methods, among which the most reliable ones are⁵³ the multireference configuration interaction (MRCI)⁵⁴ or the CASSCF/CASPT2⁵⁵ methods. In our study the CASSCF/CASPT2 approach has been chosen because it is less computationally demanding than the MRCI approach and it has been shown to produce reliable results.^{53,56} Geometries were optimized, when needed, at the CASSCF level with the atomic natural orbital (ANO) basis set described by Pierloot et al.⁵⁷ contracted to Se[5s4p3d]/C,N,O,F[3s2p1d]/H[2s1p] (BS3). With these geometries, high-level energies were obtained with the multireference second-order perturbation CASPT2 method and the aforementioned BS2 expansion. The active space was constructed by distributing 10 electrons (11 in the case of anions) in 8 orbitals (9 for the anions), which showed good results in a similar study involving disulfides.⁵⁸ The multireference calculations were performed with the MOLCAS 7.2 package of programs.⁵⁹

RESULTS AND DISCUSSION

Cleavage of the Se–Se Bond. Previous studies on electron capture of diselenides or their reactions with nucleophiles focused on the breaking of the Se–Se linkage. This cleavage seems quite favorable for X = H, CH₃, and NH₂ considering the geometrical changes triggered upon electron capture (see Table 1), with a remarkable increase of the Se–Se distance, while the rest

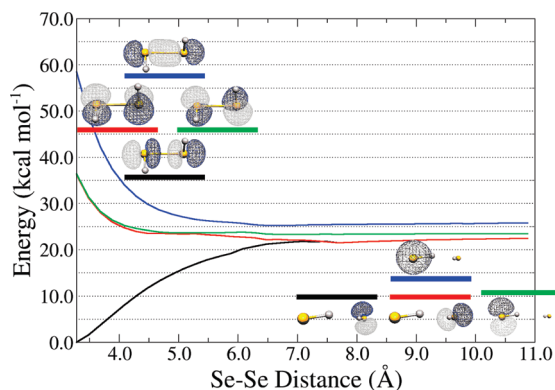


Figure 1. Relative energy (calculated at the CASSCF(11,9)/aug-cc-pVDZ level) of the four lowest states of $[\text{HSeSeH}]^-$ with respect to the Se–Se bond distance. To better understand the nature of these states, in the top left corner of the graph the SOMO of each state for $d(\text{Se–Se}) = 3.280 \text{ \AA}$ are depicted. In the bottom right corner, the same diagram can be found for $d(\text{Se–Se}) = 10.680 \text{ \AA}$. Note that the upper three excited states can be viewed as core excited states.

of the molecule remains practically unperturbed. However, as the electronegativity of X increases, like for X = OH or F, the activation of the Se–Se bond is less and less important with respect to that of the Se–X linkage, and actually for the anion $[\text{CH}_3\text{SeSeF}]^-$, the $\text{Se}\cdots\text{F}$ interaction has greatly lost its covalent character.³⁹ Based on this, the electron-capture process would yield two different types of fragmentations depending on which of the two linkages Se–Se or Se–X actually cleaves, as a function of the nature of X. Consequently, we will start by studying the Se–Se bond fission in the subset of molecules which seems more prone to it: HSeSeH , $\text{CH}_3\text{SeSeCH}_3$, and $\text{CH}_3\text{SeSeNH}_2$.

In the anionic form of these three molecules, the extra electron occupies the $\sigma^*(\text{Se–Se})$ antibonding orbital being delocalized between both selenium atoms. Therefore, the Se–Se linkage can be viewed as a typical 2c3e bond. As mentioned earlier, the dissociation of the Se–Se bond may involve a crossing between two different states, necessary to connect the reactants, with an unpaired electron delocalized between the two Se atoms, with the products, in which that extra charge will be localized on a particular fragment. However, such a state crossing does not occur for $[\text{HSeSeH}]^-$, as shown in Figure 1, which represents the variation of the energy of the four lowest states of $[\text{HSeSeH}]^-$ along the Se–Se coordinate.

For the anion in its ground state and in its equilibrium conformation, $d(\text{Se–Se}) = 3.280 \text{ \AA}$, the extra electron occupies the $\sigma^*(\text{Se–Se})$ orbital. Higher in energy there are two degenerate states whose single occupied molecular orbitals (SOMOs) are π -type linear combinations of the other two p orbitals of selenium. Finally, still higher in energy, there is a fourth state where the extra electron is allocated in the $\sigma(\text{Se–Se})$ MO. The last three states can be considered as core excited states, since they can be seen as the result of the attachment of the extra electron to an excited state of the neutral system. As shown in Figure 1 they lie very high in energy at the equilibrium distance of the anion, and although they can participate in dissociative electron attachment (DEA) processes when the anion is generated in crossed electron/molecular beams experiments,^{60,61} the important point here is that as the Se–Se bond is stretched, these four states come closer in energy until being degenerate at infinite Se–Se distance,

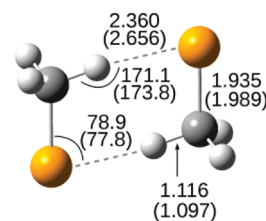


Figure 2. Post-dissociation minimum formed by dissociation of the Se–Se bond in $[\text{CH}_3\text{SeSeCH}_3]^-$, calculated at the MP2/6-31++G(d,p) (CASSCF/BS3 in parentheses) level of theory. Bond lengths are given in \AA and angles, in degrees ($^\circ$).

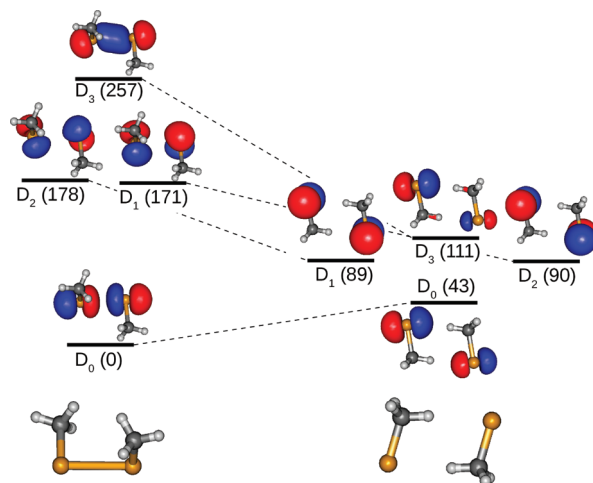


Figure 3. Correlation diagram of the electronic states of the $[\text{CH}_3\text{SeSeCH}_3]^-$ anion (left-hand side) and the post-dissociation minimum (right-hand side), where each state is represented by its SOMO. The numbers in parentheses correspond to the relative energies (in kJ mol^{-1}) of the states calculated at the MS-CASPT2/aug-cc-pVTZ level.

since each HSe moiety has two symmetry-equivalent p orbitals (four if the two equivalent HSe fragments are considered). We will show in forthcoming sections that when the system is asymmetric, there is indeed a two-state crossing between the ground state and one of the core excited states characterized by a $\sigma(\text{Se–Se})$ SOMO. For HSeSeH^- , as shown on the bottom right corner of Figure 1, already at large Se–Se internuclear distances, the electron is localized either on the right HSe moiety (black and red state) or on the left one (green and blue states), situations which will be strictly equivalent at infinite distance. Consequently, due to the symmetry of the $[\text{HSeSeH}]^-$ molecule, the cleavage of the Se–Se bond is a typical adiabatic process. It should be noted that after the Se–Se bond fission a weakly bound complex between the two moieties, SeX^\cdot and SeX^\cdot , is formed. This stationary point of the PES will be named hereafter post-dissociation minimum.

A similar situation is found for the also symmetric $[\text{CH}_3\text{SeSeCH}_3]^-$ anion. In this case a clearer picture can be obtained by using, instead of the potential energy curves of Figure 1, a correlation diagram between the states of the anion in its equilibrium conformation and the states of the post-dissociation minimum (see Figure 2). The description at the MP2 and CASSCF levels of theory of this post-dissociation minimum, where the two SeCH_3 moieties are bound together by means of

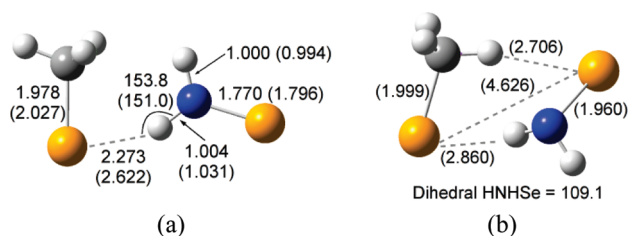


Figure 4. (a) Post-dissociation minimum formed after dissociation and (b) MECP encountered in the Se–Se bond cleavage of the $[\text{CH}_3\text{SeSeNH}_2]^-$ anion, calculated at the MP2/6-311+G(d,p) (CASSCF/BS3 in parentheses) level of theory. Bond lengths are given in Å and angles, in degrees ($^\circ$).

two weak C–H···Se interactions, forcing the Se, C, and two H atoms to lie in the same plane in a C_{2h} structure, is rather similar. With this structure, we can now build a correlation diagram between the states of the anion and those of this post-dissociation minimum. An inspection of Figure 3 shows that, as for the HSeSeH system, the Se–Se bond cleavage does not involve the crossing of two different states. Due to the symmetry of the post-dissociation minimum, the extra electron is delocalized between both Se atoms, like in the radical anion. Actually, the structures of the electronic states in both the anion and the post-dissociation minimum are quite similar, although these four states become closer for the post-dissociation minimum, being degenerate at infinite distance like in $[\text{HSeSeH}]^-$.

The results obtained for the symmetric HSeSeH and $\text{CH}_3\text{SeSeCH}_3$ make it interesting to investigate the cleavage of the Se–Se linkage when the symmetry is broken by introducing two substituents with different electronegativity, like in $\text{CH}_3\text{SeSeNH}_2$. In this case, the most favorable dissociation process leads $[\text{SeCH}_3]^- + [\text{SeNH}_2]^\cdot$, while the $[\text{SeCH}_3]^\cdot + [\text{SeNH}_2]^-$ dissociation channel lies 40 kJ mol^{-1} higher in energy. This finding seems to be counterintuitive, since from the electronegativity difference between the methyl and the amino group, one would expect the second dissociation limit to be lower in energy than the first one. However this is not so because the electron affinity (EA) of $[\text{SeCH}_3]^\cdot$ is larger than that of $[\text{SeNH}_2]^\cdot$. In the former, the lowest unoccupied molecular orbital (LUMO) corresponds to a nonbonding 4p AO of selenium, while for $[\text{SeNH}_2]^\cdot$ the LUMO is a $\pi^*(\text{Se-N})$ MO, arising from a combination between the 4p AO of Se and the lone pair of N, which necessarily rises the energy of the LUMO and, consequently, decreases the EA of the system. The enhanced stability of the $[\text{SeCH}_3]^\cdot + [\text{SeNH}_2]^\cdot$ products with respect to $[\text{SeCH}_3]^- + [\text{SeNH}_2]^-$ is also reflected in the structure of the post-dissociation minimum (Figure 4a). Since in the $[\text{SeNH}_2]^\cdot$ radical the $\pi^*(\text{Se-N})$ antibonding is only singly occupied, the Se–N bond retains some double-bond character, and actually the SeNH_2 fragment of the post-dissociation minimum (Figure 4a) is planar, the HNH bond angle (115.7°) being close to a pure sp^2 hybridization. Conversely, for the $[\text{SeNH}_2]^-$ anion the structure is far from being planar, and the Se–N distance is much longer because the extra electron doubly occupies the $\pi^*(\text{Se-N})$ antibonding MO. Note that in the post-dissociation minimum both subunits are held together by a $\text{Se}\cdots\text{HN}$ weak interaction in a way that the SeNH_2 fragment is coplanar to the Se and C atoms of the other fragment.

How the extra electron gets localized in the SeCH_3 moiety is the question which needs to be answered now because, different

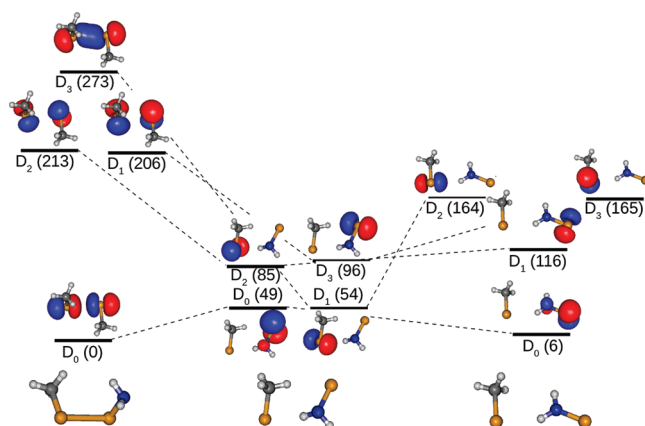


Figure 5. Correlation diagram of the electronic states of the $[\text{CH}_3\text{SeSeNH}_2]^-$ anion (left-hand side), the post-dissociation minimum (right-hand side), and the MECP (middle part) connecting them. Each state is characterized by its SOMO and its relative energy (in kJ mol^{-1}) in parentheses calculated at the MS-CASPT2/aug-cc-pVTZ level.

from $[\text{HSeSeH}]^-$ and $[\text{CH}_3\text{SeSeCH}_3]^-$, analyzed above, this process cannot be adiabatic. In the $[\text{CH}_3\text{SeSeNH}_2]^-$ anion in its equilibrium conformation, as in the previous cases, the extra charge is delocalized between both Se, and therefore the charge localization on the SeCH_3 moiety can only be accomplished if the $\sigma^*(\text{Se-Se})$ and $\sigma(\text{Se-Se})$ MOs strongly interact so that their combination would recover the p orbitals on each selenium, enabling the aforementioned charge localization. Thus, the ground state and one of the core excited states, whose SOMOs are the $\sigma^*(\text{Se-Se})$ and $\sigma(\text{Se-Se})$ orbitals, respectively, have to cross. The corresponding minimum-energy crossing point (MECP) structure, which is displayed in Figure 4b, is rather similar to the final post-dissociation minimum since the Se–Se bond is already practically broken, although the nitrogen still exhibits some sp^3 character as suggested by the HNHSe dihedral angle. The localization of this late barrier for the Se–Se bond fission of $[\text{CH}_3\text{SeSeNH}_2]^-$ contrasts with what has been found for the analogous S–S bond cleavage of the $[\text{CH}_3\text{SSNH}_2]^-$ anion.⁶² For the sulfur derivative, the MECP has a shorter S–S distance and is more similar to that in the equilibrium conformation of the anion. Such an early barrier has been also found for $[\text{CH}_3\text{SeSeNH}_2]^-$ but about 50 kJ mol^{-1} above the late MECP barrier displayed in Figure 4b.

The correlation diagram between the states of the anion and the post-dissociation minimum connected through the MECP is shown in Figure 5.

The low-lying states for the $[\text{CH}_3\text{SeSeNH}_2]^-$ anion (left-hand side of the diagram) are similar to those found for $[\text{HSeSeH}]^-$ and $[\text{CH}_3\text{SeSeCH}_3]^-$ anions, i.e., in the ground state the unpaired electron is placed in the $\sigma^*(\text{Se-Se})$ orbital, higher in energy there are two quasidegenerate states with the p nonbonding orbitals on each Se as SOMOs, while for the highest one the SOMO is the $\sigma(\text{Se-Se})$ MO. On going to the MECP, the interaction between this latter state (initially D_3) and the ground state (D_0) results in an energy lowering of the former until crossing with the ground state at the MECP. This produces two degenerate states (D_0, D_1) which, on their evolution toward the post-dissociation products, split apart as a consequence of the privileged charge localization on the SeCH_3 moiety. Consequently, the two lowest states (D_0, D_1) of the post-dissociation

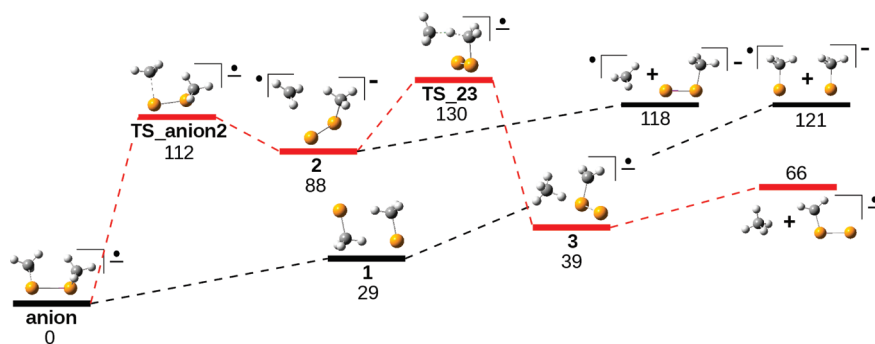


Figure 6. Energy profile associated with the main fragmentations of $[\text{CH}_3\text{SeSeCH}_3]^-$. The path leading to the loss of CH_4 is highlighted in red. Relative ΔH values (in kJ mol^{-1}) calculated at the CCSD(T)/aug-cc-pVTZ level are displayed under each structure.

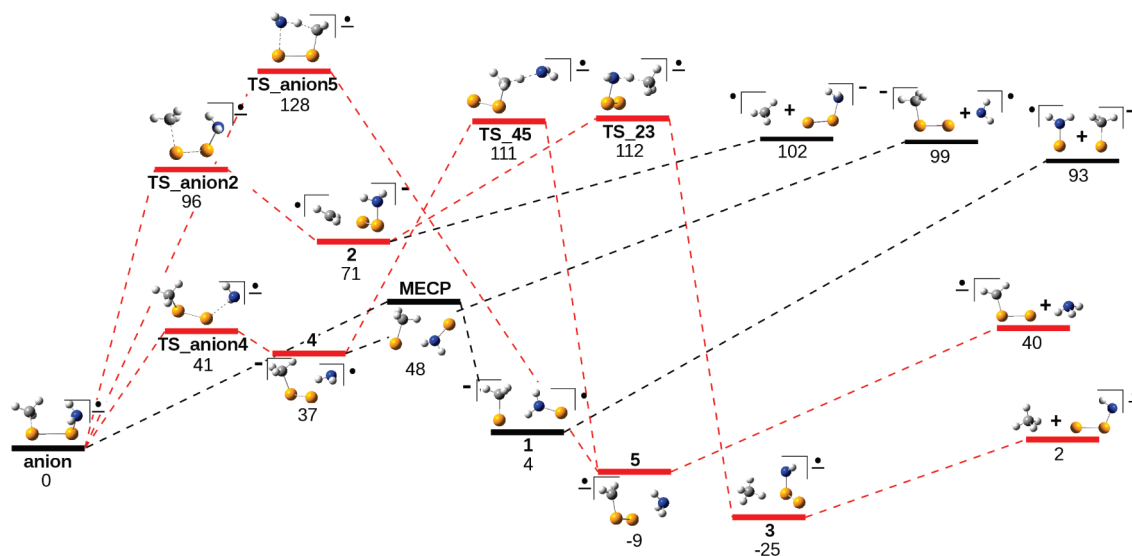


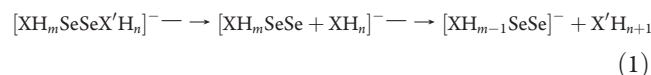
Figure 7. Energy profile associated with the main fragmentations of $[\text{CH}_3\text{SeSeNH}_2]^-$. The paths leading to the loss of CH_4 and NH_3 are highlighted in red. Relative ΔH values (in kJ mol^{-1}) calculated at the CCSD(T)/aug-cc-pVTZ level are displayed under each structure. For the MECP structure, the CASPT2 method was used instead.

minimum localize the unpaired electron at the SeNH_2 fragment and the negative charge at the SeCH_3 moiety. The fact that these two states are not degenerate reflects the aforementioned resonance between one of these 3p orbitals of selenium and the lone pair of nitrogen in D_0 . The most important conclusion is that for strongly asymmetric systems, such as $[\text{CH}_3\text{SeSeNH}_2]^-$, the cleavage of the Se–Se bond goes necessarily through a conical intersection in order to localize the extra charge on a particular fragment.

Other Fragmentation Products. However, the picture presented in the previous sections for the ECD of diselenides is only a partial one since other fragmentations products are possible. As a matter of fact, for both systems, $[\text{CH}_3\text{SeSeCH}_3]^-$ and $[\text{CH}_3\text{SeSeNH}_2]^-$, the most stable fragmentations from the thermodynamic point of view are not the ones discussed so far but the release of neutral molecules: CH_4 and NH_3 . To understand why these latter molecules experimentally appear only as secondary products, it is necessary to explore the PES associated with these bond fragmentations (See Figures 6 and 7, respectively).

Both PESs show that, although the release of neutrals is by far the most favorable process from the thermodynamic point of

view, due to the significant stability of both CH_4 and NH_3 , it has to overcome higher reaction barriers than those associated with the Se–Se bond fission. Besides, the loss of CH_4 and NH_3 is a two-step process (eq 1), which will surely have a negative influence in the rate of the overall reaction.



As a matter of fact as shown in Figure 6 and 7, in the first step the $[\text{CH}_3\text{SeSeX}'\text{H}_n]^-$ anion leads to a complex between a methyl radical and a $[\text{SeSeX}'\text{H}_n]^-$ anion (structure 2), which may dissociate into the two constituents or undergo a hydrogen transfer which would yield $\text{CH}_4 + [\text{SeSeX}'\text{H}_{n-1}]^-$ as final products.

In the case of methyl-amino derivative ($X = \text{C}$, $X' = \text{N}$), a transition structure (TS_anion5) connecting directly the anion with complex 5 ($[\text{SeSeCH}_2]^- \cdots \text{NH}_3$) has been located. Although the corresponding activation barrier is still too high to render the latter fragmentation channel kinetically favorable with respect to the Se–Se bond cleavage, it is noteworthy that a similar transition structure was not found for the fragmentation

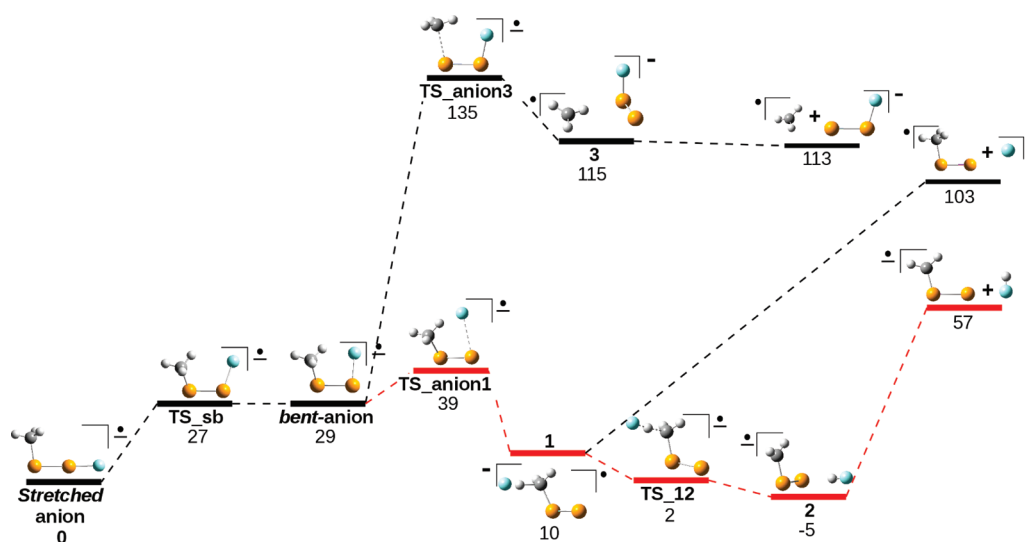


Figure 8. Energy profile associated with the main fragmentations of $[\text{CH}_3\text{SeSeF}]^-$. The paths leading to the loss of HF is highlighted in red. Relative ΔH values (in kJ mol^{-1}) calculated at the CCSD(T)/aug-cc-pVTZ level are displayed under each structure.

of the $[\text{CH}_3\text{SSNH}_2]^-$ analogue,⁶² and hence, the release of NH_3 would be more probable in the diselenide than in the disulfide. These differences between diselenide and disulfide could be due to the more extended orbitals of selenium, causing the Se–N bonds being longer than the S–N ones favoring the proximity of the NH_2 and the CH_3 groups and therefore the H shift between them. However, for $X' = \text{C}$, all the efforts to find a similar late-transition structure failed, likely reflecting the lower basicity of the methyl group with respect to that of the amino one.

Preliminary results also suggested that the electronegativity of the substituents has an important influence in the ECD process of diselenides.⁴⁸ This effect can be assessed by considering CH_3SeSeF . Recalling the results of Table 1, the electron attachment produces a much larger activation of the Se–F bond than of the Se–Se one, so the $[\text{SeCH}_3]^\cdot + [\text{SeF}]^-$ dissociation limit lies above in energy than the $[\text{CH}_3\text{SeSe}]^\cdot + \text{F}^-$ one. More importantly, the energy barrier associated to the cleavage of the Se–F bond is quite low (see Figure 8). In particular, the release of HF is the most likely process since the barrier of the Se–F bond fission is of ca. 10 kJ mol^{-1} , and the proton transfer from $[\text{CH}_3\text{SeSe}]^\cdot$ to F^- is practically barrierless. Actually, although in terms of electronic energies, TS_12 lies above 1 and 2, when the zero point energy correction is included, it passes below 1 indicating that in practice the process is barrierless. Regarding the $[\text{CH}_3]^\cdot + [\text{SeSeF}]^-$ exit channel, which is the third most stable, it is noteworthy that the value of the T_1 diagnosis of the CCSD(T) method (0.03), indicates that the TS_anion3 has a non-negligible multireference character. When its energy is recalculated with CASPT2, the value obtained (172 kJ mol^{-1}) suggests that this barrier is even higher than shown in Figure 8.

So far, two types of systems have been presented, depending whether the Se–Se or Se–X bond fissions are the most favorable process. The $[\text{CH}_3\text{SeSeOH}]^-$ radical-anion represents an intermediate situation since the transition states involved in both Se–Se and Se–O bond cleavages, TS_b3 and MECP2, respectively (Figure 9), are of comparable relative energies. It can be observed that this PES is much more intricate than the ones previously discussed. Starting from the most stable anionic isomer, namely stretched-anion, two other isomers can be

formed, bent-anion and book-anion,³⁹ which are better prepared for the breaking of the Se–O and Se–Se linkages, respectively. From the book-anion, the Se–Se bond fission goes through a two-state crossing (MECP2), as previously described for $\text{CH}_3\text{SeSeNH}_2$, to yield structure 6, where the $[\text{SeCH}_3]^\cdot$ and $[\text{SeOH}]^\cdot$ moieties are bound together by a $\text{Se} \cdots \text{HO}$ weak interaction. This intermediate can give rise to two different products: $[\text{SeCH}_3]^- + [\text{SeOH}]^\cdot$ or $\text{CH}_3\text{SeH} + [\text{SeO}]^-$, which in this case are practically degenerate. The bent-anion can undergo the cleavage of the Se–C bond through the transition structure TS_b1 to yield structure 1, which can directly lead to $[\text{CH}_3]^\cdot + [\text{SeSeOH}]^-$ or $\text{CH}_4 + [\text{SeO}]^-$ through a hydrogen transfer. More favorable is, nevertheless, the breaking of the Se–O bond to yield structure 3. This intermediate species can directly lead to $[\text{CH}_3\text{SeSe}]^- + [\text{OH}]^\cdot$ or, more interestingly, undergo an internal charge transfer through MECP1 to end up in 4, which is similar to 3 but with an inverse charge polarization. Structure 4 is better prepared to yield, the final products $[\text{CH}_2\text{SeSe}]^- + \text{H}_2\text{O}$, through a proton transfer (TS_45). The higher energy of $[\text{CH}_3\text{SeSe}]^\cdot + [\text{OH}]^-$ exit channel with respect to $[\text{CH}_3\text{SeSe}]^- + [\text{OH}]^\cdot$ explains why the rupture of the Se–O bond in (3) produces a hydroxyl radical. Consequently, the release of H_2O and HSeCH_3 , which are among the most stable products, is significantly hindered by the high barrier needed to convert 3 into 4. Conversely, for the analogous disulfide,⁶² $[\text{CH}_3\text{SSOH}]^-$, the $[\text{CH}_3\text{SS}]^\cdot + [\text{OH}]^-$ exit channel was found to be lower in energy, and accordingly, no charge transfer was needed to obtain H_2O and HSCH_3 . A similar discrepancy is found between the S and Se derivatives as far as the relative stabilities of the $[\text{CH}_3\text{X}]^\cdot + [\text{XOH}]^-$ and $\text{CH}_3\text{XH} + [\text{XO}]^-$ ($X = \text{S}, \text{Se}$) products is concerned. According to the more reliable CCSD(T) estimates both exit channels are equally stable when $X = \text{Se}$, whereas for $X = \text{S}$ the latter products are ca. 50 kJ mol^{-1} lower in energy.

Comparison between Diselenides and Disulfides. The full mechanisms of the different unimolecular reactions triggered by electron attachment to diselenides can be used to get some insight into the redox strength of sulfur- and selenium-containing proteins. Although sulfur and selenium share many physico-chemical properties, valence orbitals of Se are more diffuse than

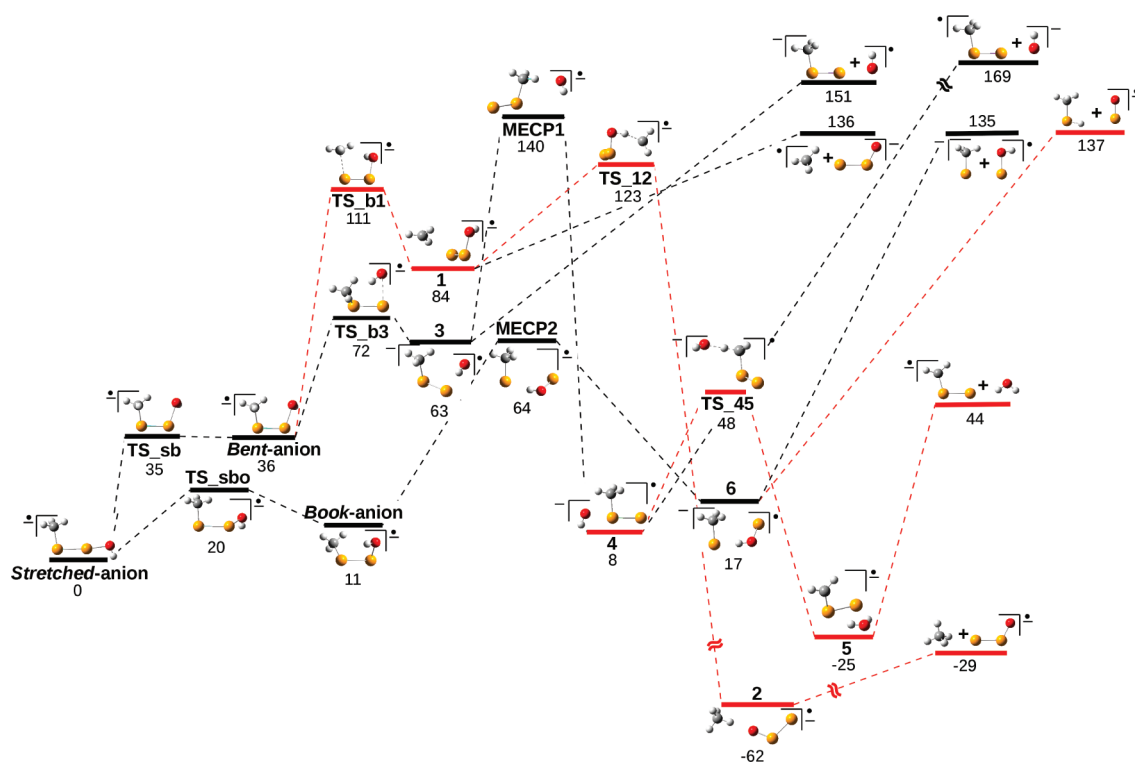


Figure 9. Energy profile associated with the main fragmentations of $[\text{CH}_3\text{SeSeOH}]^-$. The paths leading to the loss of CH_4 and H_2O are highlighted in red. Relative ΔH values (in kJ mol^{-1}) calculated at the CCSD(T)/aug-cc-pVTZ level are displayed under each structure. For the MECP1, MECP2, TS_b3, and 3 structures, the CASPT2 method was used instead.

those of S, which explains some of the differences between the mechanisms of the ECD of disulfides and diselenides described so far. For instance, the fact that Se–N bonds are larger than S–N ones may rationalize the existence of a direct unimolecular process for the release of NH_3 in $[\text{CH}_3\text{SeSeNH}_2]^-$, which is absent in $[\text{CH}_3\text{SSNH}_2]^-$.

More interesting are the differences between $[\text{CH}_3\text{SSOH}]^-$ and $[\text{CH}_3\text{SeSeOH}]^-$ regarding the fission of the A–O bond (A = S, Se). As mentioned above, the cleavage of the Se–O linkage produces $[\text{CH}_3\text{SeSe}]^- + [\text{OH}]^\cdot$, while for the disulfide $[\text{CH}_3\text{SS}]^\cdot + [\text{OH}]^-$ is obtained. This is so because the EA of the $[\text{OH}]^\cdot$ radical (1.74 eV) is slightly higher than that of $[\text{CH}_3\text{SS}]^\cdot$ (1.72 eV) but significantly lower than that of $[\text{CH}_3\text{SeSe}]^\cdot$ (1.91 eV), likely reflecting a smaller interelectronic repulsion, due to the more diffuse orbitals of Se. The different EA of the $[\text{CH}_3\text{SS}]^\cdot$, $[\text{CH}_3\text{SeSe}]^\cdot$ and $[\text{OH}]^\cdot$ radicals also helps us to rationalize the different mechanism of the S–O and Se–O bond cleavage. Due to the similar EA of the $[\text{CH}_3\text{SS}]^\cdot$ and $[\text{OH}]^\cdot$ fragments, the extra electron is nearly delocalized between both moieties (their NBO charges being 0.48 and 0.52 e, respectively), and a conical intersection is needed to accomplish the charge localization after bond breaking, in a similar fashion as in the cleavage of the Se–Se bond previously described. However, the dissimilar EA of the $[\text{CH}_3\text{SeSe}]^\cdot$ and $[\text{OH}]^\cdot$ produces the extra electron to be more localized on the former (the NBO charges being 0.60 and 0.40 e, respectively), favoring its dissociation into $[\text{CH}_3\text{SeSe}]^- + [\text{OH}]^\cdot$ through TS_b3 (See Figure 9). Although for both $[\text{CH}_3\text{SSOH}]^-$ and $[\text{CH}_3\text{SeSeOH}]^-$ the most favorable process from a thermodynamical viewpoint is the release of H_2O (see Figure 9 for the diselenide and Figure 10 of ref 54 for the disulfide), the mechanisms behind are significantly different. In

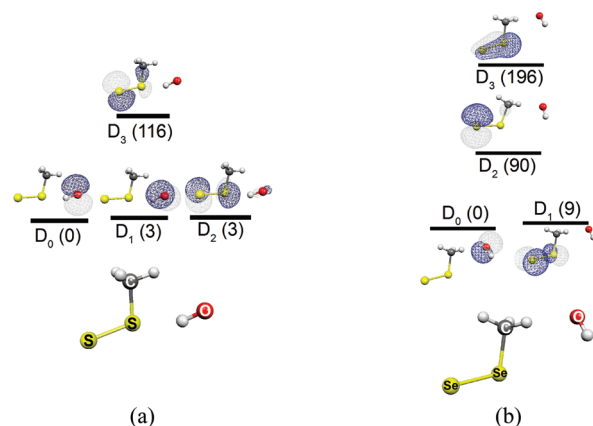


Figure 10. Four lowest states of the MECP structures corresponding to the transition between the $[\text{CH}_3\text{AA}]^- + [\text{OH}]^\cdot$ and $[\text{CH}_3\text{AA}]^\cdot + [\text{OH}]^-$ products for (a) $[\text{CH}_3\text{SSOH}]^-$ and (b) $[\text{CH}_3\text{SeSeOH}]^-$. Each state is characterized by its SOMO and its relative energy (in kJ mol^{-1}) in parentheses calculated at the MS-CASPT2/aug-cc-pVTZ level.

both cases water is formed by a proton transfer from $[\text{CH}_3\text{AA}]^\cdot$ toward $[\text{OH}]^-$, but the mechanism by which these two species are formed is different if A = S or Se. While in the case of $[\text{CH}_3\text{SSOH}]^-$ the breaking of the S–O bond directly leads to $[\text{CH}_3\text{SS}]^\cdot + [\text{OH}]^-$, the same process for $[\text{CH}_3\text{SeSeOH}]^-$ leads to $[\text{CH}_3\text{SeSe}]^\cdot$ and $[\text{OH}]^\cdot$, and a subsequent charge transfer to produce $[\text{OH}]^-$ through a quite high barrier (MECP1 of Figure 9) associated with a conical intersection is needed. As a result, the production of water should be much more likely to occur in $[\text{CH}_3\text{SSOH}]^-$ than in $[\text{CH}_3\text{SeSeOH}]^-$.

Table 2. Reaction Barriers (B) and Dissociation Energies (DE) of the Cleavage of the A–A and A–X Bonds and the Subsequent Hydrogen-/Proton-Transfer Process (H_{transf}) to Lead to the Loss of Neutrals (CH_4 , NH_3 , H_2O , and HF) for the CH_3AAXH_n (A = S, Se; X = CH_3 , NH_2 , OH, F) Systems^a

barriers / X		B(A–A)	DE(A–A)	B(A–X)	DE(A–X)	H_{transf}	AA + XH_{n+1}	EA
C	S		83 ^b	111 ^b	80 ^b	116 ^b	16 ^b	23 ^c
	Se		121	112	118	130	66	53 ^d
N	S	33	35 ^b	32 ^b	52 ^b	78 ^b	–20 ^b	0 ^c
	Se	48	93	41	99	111	40	49 ^d
O	S	33	83 ^b	56 ^b	90 ^b	4 ^b	–37 ^b	11 ^c
	Se	64	135	54	151	140	44	73 ^d
F	S			21 ^b	63 ^b	0 ^b	23 ^b	77 ^c
	Se			39	103	0	57	124 ^d

^aThe adiabatic EA of the neutral systems is also displayed. All values are in kJ mol^{-1} . ^bTheoretical values taken from ref 62. ^cTheoretical values taken from ref 58. ^dTheoretical values taken from ref 39.

Interestingly, for $[\text{CH}_3\text{SSOH}]^-$ is its dissociation into $[\text{CH}_3\text{SS}]^- + [\text{OH}]^\cdot$ the one that occurs through a CI involving D_0 , D_1 , and D_2 (See Figure 10), which constitutes the first example of a three state crossing in a thermal reaction occurring in the ground state.⁶³ These three states correspond to one allocating the unpaired electron in a $\pi^*(\text{S}–\text{S})$ orbital (ground state of $[\text{CH}_3\text{SS}]^\cdot$) and another two where the unpaired electron is in a p orbital of O (the $^2\Pi$ ground state of $[\text{OH}]^\cdot$) (see Figure 10a). In contrast, for the diselenide analogue the C–H \cdots O interaction, which stabilizes MECPI, breaks the degeneracy of the two p orbitals of O (see Figure 10b).

However, the mechanism of the ECD of disulfides and diselenides shows many more differences from a quantitative point of view. As previously mentioned, diselenides are better prepared to accommodate the extra charge due to the more extended orbitals of selenium. Consequently, their unimolecular fragmentations show higher reaction barriers than disulfides, and the final products also lie higher in energy (see Table 2). Experimentally, however, diselenides are stronger reductants than disulfides.^{17,64,65} The conciliation between this experimental evidence and the fact that the activation barriers for the unimolecular fragmentation of diselenides are higher than for the disulfide analogues suggests that other processes, such as the ejection of the extra electron, may compete with the ECD. Indeed the EA of these systems (see Table 2) is smaller than the energy required to break the A–A and A–X bonds. This means that a complete picture of the reductive ability of disulfides and diselenides should consider the electron detachment reaction. A first estimate about the extent of this reaction can be obtained from the EA values, which indicate that the electron release process should be less important for diselenides than for disulfides, which would be coherent with the higher reductant strength of the former.

CONCLUSIONS

Based on what has been generally assumed for disulfides and some experimental results on simple diselenides, like dimethyl-diselenide, one might expect that the electron capture on diselenides XSeSeX' produces a fragmentation of the Se–Se bond. However, our results indicate that this is the case only when the substituents X and X' attached to the diselenide linkage have low electronegativity. Also importantly, even when the two substituents are of similar electronegativity, the Se–Se bond cleavage rarely is an adiabatic process.

In our detailed mechanistic study of the different unimolecular reactions triggered by electron attachment to CH_3SeSeX diselenides, we have found that, quite surprisingly, the most favorable processes, from a thermodynamic point of view, correspond to the release of neutral molecules: CH_4 , NH_3 , H_2O , and HF . Nevertheless, these products are only likely to be observed for very high electronegative substituents X such as F due to two factors: (i) the occupation of the $\sigma^*(\text{Se}–\text{X})$ antibonding MO by the extra electron is favored when X is a very electronegative element, facilitating the breaking of the Se–X bond and (ii) the activation barrier associated to the proton transfer which produces HF is rather low. Although both conditions (i) and (ii) are fulfilled for X = O, the release of H_2O is disfavored because the breaking of the Se–O bond produces a hydroxyl radical (3), which has to undergo an internal charge transfer through a very high conical intersection barrier to obtain a precursor (4) with the proper charge distribution to produce $[\text{CH}_2\text{SeSe}]^\cdot + \text{H}_2\text{O}$.

For low-electronegative X substituents, the extra electron is placed in the $\sigma^*(\text{Se}–\text{Se})$ antibonding orbital, and the cleavage of the Se–Se bond is the most favorable process. However, the mechanism of this bond breaking is more intricate than previously assumed since, although for symmetric systems, such as HSeSeH or $\text{CH}_3\text{SeSeCH}_3$, it is strictly adiabatic, for the asymmetric $\text{CH}_3\text{SeSeNH}_2$ it proceeds through a CI. This crossing between two states is necessary to localize in one of the two fragment products the extra electron, which in the anion is delocalized in the $\sigma^*(\text{Se}–\text{Se})$ antibonding MO. These findings emphasize the importance of using accurate ab initio calculations for the study of electron attachment dissociations of diselenides and, perhaps, other related processes. Many reactions in biochemistry and organometallic chemistry are usually investigated by DFT-based methods due to the size of the systems. However, the characterization of a CI requires the use of multireference methods to account for the mixing of states. This methodological problem has recently been addressed by Shaik and co-workers⁶⁶ in the study of the active site of enzymes cytochromes P450 and chloroperoxidase, where the use of CASPT2/MM calculations might change the multistate reactivity of these systems by including some states not present in the DFT/MM picture.

When X is highly electronegative, the $\sigma^*(\text{Se}–\text{X})$ antibonding orbital becomes highly stabilized with respect to the $\sigma^*(\text{Se}–\text{Se})$ strongly favoring the cleavage of the Se–X bond.

Finally, when comparing the present results on diselenides with those of the disulfide analogues, it is apparent that the activation barriers and the final products of the different

unimolecular reactions are higher in energy for the diselenides, in spite of their higher antioxidant strength. This seems to indicate that the electron detachment process, less favorable for diselenides than for disulfides, competes with the ECD process and therefore should also be considered. However, a more detailed study of the electron detachment process needs to be carried out to validate this hypothesis.

AUTHOR INFORMATION

Corresponding Author

*E-mail: manuel.yanez@uam.es.

ACKNOWLEDGMENT

This work has been partially supported by the DGI Project NO CTQ2006-08558/BQU, Project MADRID SOLAR2, ref.: P2009/PPQ-1533 of the Comunidad Autónoma de Madrid, by Consolider on Molecular Nanoscience CSC2007-00010 and by the COST Action COST CM0702. A generous allocation of computer time at the CCC of the UAM is also acknowledged. J.A.G. acknowledges a contract from the Comunidad Autónoma de Madrid.

REFERENCES

- Castellano, S.; Lobanov, A. V.; Chapple, C.; Novoselov, S. V.; Albercht, M.; Hua, D.; Lescure, A.; Lengauer, T.; Krol, A.; Gladyshev, V. N.; Guigo, R. *Proc. Nat. Acad. Sci. U.S.A.* **2005**, *102*, 16188.
- Rayman, M. P. *Lancet* **2000**, 356, 233.
- Chen, J.; Berry, M. J. *J. Neurochem.* **2003**, *86*, 1.
- Schomburg, L.; Schweizer, U.; Koehle, J. *Cell. Mol. Life Sci.* **2004**, *61*, 1988.
- Frank, W. Z. *Physiol. Chem.* **1964**, 339, 222.
- Walter, R.; du Vigneaud, V. *J. Am. Chem. Soc.* **1965**, *87*, 4192.
- Walter, R.; du Vigneaud, V. *J. Am. Chem. Soc.* **1966**, *88*, 1331.
- Hartrodt, B.; Neubert, K.; Bierwolf, B.; Blech, W.; Jakubke, H. D. *Tetrahedron Lett.* **1980**, *21*, 2393.
- Besse, D.; Budisa, N.; Karnbrock, W.; Minks, C.; Musiol, H. J.; Pegararo, S.; Siedler, F.; Weyher, E.; Moroder, L. *J. Biol. Chem.* **1997**, *378*, 211.
- Koider, T.; Itoh, H.; Otaka, A.; Furuya, M.; Kitajima, Y.; Fujii, N. *Chem. Pharm. Bull.* **1993**, *46*, 5382.
- Rajaratnam, K.; Sykes, B. D.; Dewald, B.; Baggolini, M.; Clark-Lewis, I. *Biochemistry* **1999**, *38*, 7653.
- Metanis, N.; Keinan, E.; Dawson, P. E. *J. Am. Chem. Soc.* **2006**, *128*, 16684.
- Armishaw, C. J.; Daly, N. T.; Adams, D. J.; Craik, D. J.; Alewook, P. F. *J. Biol. Chem.* **2006**, *281*, 14136.
- Fori, S.; Pegararo, S.; Rudolph-Böhner, S.; Cramer, J.; Moroder, L. *Biopolymers* **2000**, *53*, 550.
- Hondal, R. J.; Nilsson, B. L.; Raines, R. T. *J. Am. Chem. Soc.* **2001**, *123*, 5140.
- Jacob, C.; Giles, G. I.; Giles, N. M.; Sies, H. *Angew. Chem., Int. Ed.* **2003**, *42*, 4742.
- Johansson, I.; Gafvelin, G.; Amér, E. S. *Biochim. Biophys. Acta* **2005**, *1726*, 1.
- Sheu, C.; Sobkowiak, A.; Zhang, L.; Ozbalik, N.; Barton, D. H. R.; Sawyer, D. T. *J. Am. Chem. Soc.* **1989**, *111*, 8030.
- Tian, F.; Yu, Z.; Lu, S. *J. Org. Chem.* **2004**, *69*, 4520.
- Degrad, C.; Nour, M. *J. Electroanal. Chem.* **1984**, *190*, 213.
- Barbosa, N. B. V.; Rocha, J. B. T.; Wondracek, D. C.; Pettroni, J.; Zeni, G.; Nogueira, C. W. *Chem.-Biol. Interact.* **2006**, *3*, 230.
- de Freitas, A. S.; Funck, V. R.; Rotta, M. d. S.; Bohrer, D.; Mörschbacher, V.; Puntel, R. L.; Nogueira, C. W.; Farina, M.; Aschner, M.; Rocha, J. B. T. *Brain Res. Bull.* **2009**, *79*, 77.
- Shchedrina, V. A.; Novoselov, S. V. *Proc. Nat. Acad. Sci. U.S.A.* **2007**, *104*, 13919.
- Arteel, G. E.; Sies, H. *Environ. Toxicol. Pharmacol.* **2001**, *10*, 153.
- Meotti, F. C.; Stangherlin, E. C.; Zeni, G.; Nogueira, C. W.; Rocha, J. B. T. *Environ. Res.* **2004**, *94*, 276.
- Kumar, B. S.; Kunwar, A.; Ahmad, A.; Kumbhare, L. B.; Jain, V. K.; Priyadarsini, K. I. *Radiat. Environ. Biophys.* **2009**, *48*, 379.
- Pearson, J. K.; Boyd, R. J. *J. Phys. Chem. A* **2007**, *111*, 3152.
- Movassagh, B.; Shamsipoor, M.; Joshaghani, M. *J. Chem. Res.* **2004**, 148.
- Russavskaya, N. V.; Levanova, E. P.; Sukhomazova, E. N.; Grabel'nykh, V. A.; Klyba, L. V.; Zhanchipova, E. R.; Albanov, A. I.; Korchervin, N. A. *Russ. J. Gen. Chem.* **2006**, *76*, 229.
- Zhang, S. L.; Tian, F. S. *J. Chem. Res.* **2001**, 198.
- Uggerund, E. *Int. J. Mass Spectrom.* **2004**, *234*, 45.
- Antonello, S.; Daasbjerg, K.; Jensen, H.; Taddei, F.; Maran, F. *J. Am. Chem. Soc.* **2003**, *125*, 14905.
- Sobczyk, M.; Simons, J. *Int. J. Mass Spectrom.* **2006**, *253*, 274.
- Anusiewicz, I.; Berdys-Kochanska, J.; Simons, J. *J. Phys. Chem. A* **2005**, *109*, 5801.
- Modelli, A.; Jones, D. *J. Phys. Chem. A* **2006**, *110*, 13195.
- Yamaji, M.; Tojo, S.; Takehira, K.; Tobita, S.; Fujitsuka, M.; Majima, T. *J. Phys. Chem. A* **2006**, *110*, 13487.
- Meija, J.; Beck, T. L.; Caruso, J. A. *J. Am. Soc. Mass Spectrom.* **2004**, *15*, 1325.
- Modelli, A.; Jones, D.; Distefano, G.; Tronc, M. *Chem. Phys. Lett.* **1991**, *181*, 361.
- Gámez, J. A.; Yáñez, M. *J. Chem. Theory Comput.* **2010**, *6*, 3102.
- Hiberty, P. C.; Humbel, S.; Archirel, P. *J. Phys. Chem. A* **1994**, *98*, 11697.
- Bally, T.; Sastry, G. N. *J. Phys. Chem. A* **1997**, *101*, 7923.
- Chermette, H.; Ciofini, I.; Mariotti, F.; Daul, C. *J. Chem. Phys.* **2001**, *114*, 1447.
- Gräfenstein, J.; Kraka, E.; Cremer, D. *Phys. Chem. Chem. Phys.* **2004**, *6*, 1096.
- Gräfenstein, J.; Kraka, E.; Cremer, D. *J. Chem. Phys.* **2004**, *120*, 524.
- Braida, B.; Hiberty, P. C.; Savin, A. *J. Phys. Chem. A* **1998**, *102*, 7872.
- Perdew, J. P.; Zunger, A. *Phys. Rev. B* **1984**, *23*, 5048.
- Chermette, H.; Ciofini, I.; Mariotti, F.; Daul, C. *J. Chem. Phys.* **2001**, *115*, 11068.
- Gámez, J. A.; Yáñez, M. *Chem. Commun.* **2011**, *47*, 3939.
- Cohen, A.; Mori-Sánchez, P.; Yang, W. *Science* **2008**, *321*, 792.
- Braida, B.; Hiberty, P. C. *J. Phys. Chem. A* **2000**, *104*, 4618.
- Frisch, M. J.; Trucks, G. W.; Schlegel, H. B.; Scuseria, G. E.; Robb, M. A.; Cheeseman, J. R.; Montgomery, J. A., Jr.; Vreven, T.; Kudin, K. N.; Burant, J. C.; Millam, J. M.; Iyengar, S. S.; Tomasi, J.; Barone, V.; Mennucci, B.; Cossi, M.; Scalmani, G.; Rega, N.; Petersson, G. A.; Nakatsuji, H.; Hada, M.; Ehara, M.; Toyota, K.; Fukuda, R.; Hasegawa, J.; Ishida, M.; Nakajima, T.; Honda, Y.; Kitao, O.; Nakai, H.; Klene, M.; Li, X.; Knox, J. E.; Hratchian, H. P.; Cross, J. B.; Bakken, V.; Adamo, C.; Jaramillo, J.; Gomperts, R.; Stratmann, R. E.; Yazyev, O.; Austin, A. J.; Cammi, R.; Pomelli, C.; Ochterski, J. W.; Ayala, P. Y.; Morokuma, K.; Voth, G. A.; Salvador, P.; Dannenberg, J. J.; Zakrzewski, V. G.; Dapprich, S.; Daniels, A. D.; Strain, M. C.; Farkas, O.; Malick, D. K.; Rabuck, A. D.; Raghavachari, K.; Foresman, J. B.; Ortiz, J. V.; Cui, Q.; Baboul, A. G.; Clifford, S.; Cioslowski, J.; Stefanov, B. B.; Liu, G.; Liashenko, A.; Piskorz, P.; Komaromi, I.; Martin, R. L.; Fox, D. J.; Keith, T.; Al-Laham, M. A.; Peng, C. Y.; Nanayakkara, A.; Challacombe, M.; Gill, P. M. W.; Johnson, B.; Chen, W.; Wong, M. W.; Gonzalez, C.; Pople, J. A. *Gaussian Gaussian Inc., Wallingford, CT*, 2004.
- Werner, H.-J.; Knowles, P. J.; Lindh, R.; Manby, F. R.; Schütz, M.; Celani, P.; Korona, T.; Mitrushenkov, A.; Rauhut, G.; Adler, T. B.; Amos, R. D.; Bernhardsson, A.; Berning, A.; Cooper, D. L.; Deegan, M. J. O.; Dobbyn, A. J.; Eckert, F.; Goll, E.; Hampel, C.; Hetzer, G.; Hrenar, T.; Knizia, G.; Köppl, C.; Liu, Y.; Lloyd, A. W.; Mata, R. A.; May,

A. J.; McNicholas, S. J.; Meyer, W.; Mura, M. E.; Nicklass, A.; Palmieri, P.; Pflüger, K.; Pitzer, R.; Reiher, M.; Schumann, U.; Stoll, H.; Stone, A. J.; Tarroni, R.; Thorsteinsson, T.; Wang, M.; Wolf, A. *MOLPRO 2009.01*; University College Cardiff Consultants Limited: Cardiff, U.K., 2009.

(53) Sherrill, C. D. *J. Chem. Phys.* **2010**, *132*, 110902.

(54) Werner, H.-J.; Knowles, P. J. *J. Chem. Phys.* **1988**, *89*, 5803.

(55) Andersson, K.; Roos, B. O. In *Advanced Series in Physical Chemistry*; Yarkony, D. R., Ed.; World Scientific: Singapore, 1995; Vol. 2.

(56) Abrams, M. L.; Sherrill, C. D. *J. Phys. Chem. A* **2003**, *107*, 5611.

(57) Pierloot, K.; Dumez, B.; Widmark, P.-O.; Roos, B. O. *Theor. Chem. Acta* **1995**, *90*, 87.

(58) Gámez, J. A.; Serrano-Andrés, L.; Yáñez, M. *Phys. Chem. Chem. Phys.* **2010**, *5*, 1042.

(59) Veryazov, V.; Widmark, P.-O.; Serrano-Andrés, L.; Lindh, R.; Roos, B. O. *Int. J. Quantum Chem.* **2004**, *100*, 626.

(60) Sulzer, P.; Ptasinska, S.; Zappa, F.; Mielewska, B.; Milosavljevic, A. R.; Scheier, P.; Mark, T. D.; Bald, I.; Gohlke, S.; Huels, M. A.; Illenberger, E. *J. Chem. Phys.* **2006**, *125*, 044304.

(61) Papp, P.; Urban, J.; Matejcek, S.; Stano, M.; Ingolfsson, O. *J. Chem. Phys.* **2006**, *125*, 204301.

(62) Gámez, J. A.; Serrano-Andrés, L.; Yáñez, M. *ChemPhysChem* **2010**, *11*, 2530.

(63) Gámez, J. A.; Serrano-Andrés, L.; Yáñez, M. *Int. J. Quantum Chem.*, DOI: 10.1002/qua.23015.

(64) Roussyn, I.; Briviba, K.; Masumoto, H.; Sies, H. *Arch. Biochem. Biophys.* **1996**, *330*, 216.

(65) Briviba, K.; Roussyn, I.; Sharov, V. S.; Sies, H. *Biochem. J.* **1996**, *319*, 13.

(66) Chen, H.; Song, J. S.; Lai, W. Z.; Wu, W.; Shaik, S. J. *Chem. Theory Comput.* **2010**, *6*, 940.

A Long-Range Electric Field Solver for Molecular Dynamics Based on Atomistic-to-Continuum Modeling

Jeremy A. Templeton,^{*,†} Reese E. Jones,[‡] Jonathan W. Lee,^{†,||} Jonathan A. Zimmerman,[‡] and Bryan M. Wong[§]

[†]Thermal/Fluids Science and Engineering, [‡]Mechanics of Materials Department, and [§]Materials Chemistry Department, Sandia National Laboratories, Livermore, California 94551-0969, United States

ABSTRACT: Understanding charge transport processes at a molecular level is currently hindered by a lack of appropriate models for incorporating nonperiodic, anisotropic electric fields in molecular dynamics (MD) simulations. In this work, we develop a model for including electric fields in MD using an atomistic-to-continuum framework. This framework provides the mathematical and the algorithmic infrastructure to couple finite element (FE) representations of continuous data with atomic data. Our model represents the electric potential on a FE mesh satisfying a Poisson equation with source terms determined by the distribution of the atomic charges. Boundary conditions can be imposed naturally using the FE description of the potential, which then propagate to each atom through modified forces. The method is verified using simulations where analytical solutions are known or comparisons can be made to existing techniques. In addition, a calculation of a salt water solution in a silicon nanochannel is performed to demonstrate the method in a target scientific application in which ions are attracted to charged surfaces in the presence of electric fields and interfering media.

1. INTRODUCTION

The application of molecular dynamics (MD) simulations for understanding complex processes at the atomic scale has witnessed a radical improvement in the past three decades.¹ At present, however, most MD simulations are still performed in periodic domains due to the difficulty of accurately prescribing boundary conditions that break the spatial symmetries and enable many problems of scientific and technological interest to be examined. For example, simulating the electric double layer that forms at the interfaces of charged surfaces and ionic solutions is difficult to model with conventional techniques based on periodic boundaries in applications where the domain is anisotropic or the application of boundary conditions is required. The recent United States Department of Energy Basic Energy Sciences report² on research needs in electrical energy storage devices points to the inability to represent inhomogeneous electric fields within MD as one of the most important barriers to MD playing a role in modeling charge transport in batteries and supercapacitors. This statement is a direct consequence of the aforementioned difficulty in breaking spatial symmetries in MD simulations. By examining the current methods for incorporating long-range electric field effects in MD, the limitation can be better understood.

MD simulations achieve their computational efficiency by using a cutoff radius, r_c , such that any two distinct atoms α and β only interact if the distance between them, $r_{\alpha\beta}$, is such that $r_{\alpha\beta} < r_c$. The forces that convey the interactions are determined by the potential energy of the system comprised of empirical functions dependent on interatomic distances. The functional form of most MD potentials is such that the decay rate with distance is fast, implying the cutoff radius approximation is appropriate. However, the electric potential between two charged particles only decays as $r_{\alpha\beta}^{-1}$, so possibly an infinite amount of energy will be artificially removed from the system if this interaction

is truncated. Because including an interaction between any two atoms requires both additional memory storage and increased computational time, directly simulating charged atoms is intractable for all but the smallest systems. Therefore, algorithms which can approximate the Coulombic interaction between particles have been developed to model charged systems while retaining the scalability and the efficiency of MD. Two common approaches for computing long-range electrical interactions are Ewald summations³ and the particle–particle/particle–mesh (PPPM) method.⁴ Other notable long-range interaction methods are the particle–mesh Ewald technique⁵ (similar to the PPPM method), charge sheets,⁶ and the fast multipole method⁷ for long-range Coulombic forces and the Ewald method for long-range dispersion forces.⁸

Long-range methods for calculating electrical forces are often derived from the following decomposition of the electric potential due to point charges:

$$\begin{aligned}
 U &= k \sum_{\alpha \in -\ell} \sum_{\substack{\beta \in -\ell \\ \beta \neq \alpha}} \left(\frac{q^\alpha q^\beta}{r_{\alpha\beta}} \right) \\
 &= k \sum_{\alpha \in -\ell} \sum_{\substack{\beta \in -\ell \\ \beta \neq \alpha}} \left(\frac{q^\alpha q^\beta}{r_{\alpha\beta}} - \int \int \frac{\rho^\alpha(\mathbf{r}) \rho^\beta(\mathbf{r}')}{|\mathbf{r} - \mathbf{r}'|} \mathrm{d}\mathbf{r} \mathrm{d}\mathbf{r}' \right) \\
 &+ k \sum_{\alpha \in -\ell} \sum_{\beta \in -\ell} \int \int \frac{\rho^\alpha(\mathbf{r}) \rho^\beta(\mathbf{r}')}{|\mathbf{r} - \mathbf{r}'|} \mathrm{d}\mathbf{r} \mathrm{d}\mathbf{r}' - k \sum_{\alpha \in -\ell} \int \int \frac{\rho^\alpha(\mathbf{r}) \rho^\alpha(\mathbf{r}')}{|\mathbf{r} - \mathbf{r}'|} \mathrm{d}\mathbf{r} \mathrm{d}\mathbf{r}'
 \end{aligned} \tag{1}$$

Received: December 19, 2010

Published: May 05, 2011

where continuous charge densities ρ^α are introduced based on the idea that long-range forces are less sensitive to the location of the charges. In eq 1, U is the total electrostatic potential energy of the system as a function of all the atoms in the system, denoted by the set \mathcal{A} and indexed by α and β (separated by distance $r_{\alpha\beta}$) with each atom having a charge q^α . Coulomb's constant is represented by k . The first term accounts for short-range interactions between particles, while the remaining terms describe the long-range effects of smooth charge distributions associated with each atom, ρ^α . In both the PPPM and Ewald methods, the short-range sum is truncated to include only near neighbors, while ρ^α is represented using a Gaussian distribution as a finite-width approximation to the Dirac δ function (although this is not strictly required by the PPPM method). While the terms based on ρ^α appear redundant, this form of the equation is amenable to separation between short- and long-ranged interactions based on a cutoff radius. In this mode, the first term accounts for the electrostatic interaction between two charges within the cutoff radius. It is corrected by the second term, which is needed when the charge density of every atom is used to compute the third term in eq 1 for the long-range interactions. Ewald sums analytically solve this equation using the Fourier space representation of the convolution of each ρ^α . The PPPM method instead restricts ρ^α to a grid and then computes its Fourier transform to quickly solve for the total electrostatic potential. Of the two, the PPPM approach is more widely used than the older Ewald sum, particularly for large systems.⁹ It can be further accelerated by choosing "assignment functions" narrower than ρ^α to interpolate the forces and correcting the potential solve with a modified Coulomb Green's function.⁴

Despite the differences in performance that drive the preference of one method over the other, both use analysis in Fourier space to solve eq 1 and thus are applicable for systems containing at least one periodic direction. Further, there is no mechanism within the methods to assign commonly needed, general boundary conditions associated with continuous potential fields. Methods to enable these types of simulations have been successfully developed for specialized geometries. For example, two-dimensional Ewald sums have been used in slab geometries.^{10–12} An alternative is to use the full three-dimensional Ewald sums and extend the computational domain in the nonperiodic direction,¹³ although the domain may need to be enlarged three to five times in extent, thus increasing the computational expense and introducing Gibbs artifacts.¹⁴ These approaches have been used to simulate a variety of physically important systems. Examples include a silicon nanochannel with dissolved NaCl¹⁵ (a correction term is used to account for the channel's dipole moment),¹⁶ biological membranes,^{17,18} and ions at liquid/gas interfaces for systems with a net charge.¹⁹ In addition, a great deal of expertise using these methods has been developed in the research community, and they have been extensively compared against each other to determine the most appropriate long-range electric field model for a particular problem.^{9,20,21}

While much work has been done to examine fully periodic and slab periodic systems, the authors are unaware of any general formulation applicable to systems without periodicity. The present work aims to provide such a framework by developing a new method for computing the electric field within an atomistic-to-continuum (AtC) framework. AtC methods involve coupling the discrete atomic dynamics in MD to spatially continuous processes represented by finite elements (FE). See

the review article of Miller and Tadmor²² for a comparison of AtC approaches for mechanics simulations in which the FE represents continuous displacements and stresses. For this application, however, the FE will compute the long-range electric field, while the MD calculates the atomic motion. Shape functions associated with the elements enable projection of the atomic point charges to a continuous function spanned by the FE basis. In this way, the present AtC approach can be thought of as extending the PPPM method to a general basis set beyond harmonic functions. The next section describes the mathematical formulation required to apply AtC techniques to resolving electronic interactions of particles over distances longer than the cutoff radius of their Coulombic interactions. The algorithmic framework used in this work is based on multiscale AtC coupling²³ as implemented in the MD code LAMMPS (see ref 24 and <http://lammps.sandia.gov> for more details about LAMMPS). The theory section is followed by Section 3 which presents some example calculations to demonstrate the method's performance and applications. Finally, some conclusions are offered in Section 4.

2. MATHEMATICAL FORMULATION

2.1. Mathematical Framework for Multiscale Modeling.

The multiscale modeling framework used in this work is based on approximate FE projections of MD data to restrict atomic quantities to a FE mesh and corresponding interpolation operators to compute FE quantities on atoms.²³ The FE method is founded on approximating arbitrary integrable functions with a subset of functions contained in a space \mathcal{W} . In the case of a continuous charge density field $\rho(\mathbf{x})$ for $\mathbf{x} \in \Omega \subset \mathbb{R}^3$, ρ is weakly equivalent to a function $\hat{\rho}(\mathbf{x}) \in \mathcal{W}$ if

$$\int \hat{w} \rho \, dV = \int w \rho \, dV, \quad \forall w \in \mathcal{W} \quad (2)$$

Now assume that the space \mathcal{W} can be spanned by a finite number of basis functions, denoted shape functions, with the I th function written as N_I , where indices I are in the finite set \mathcal{F} . Then the approximate charge density field can be written as

$$\hat{\rho} = \sum_{I \in \mathcal{F}} N_I(\mathbf{x}) \rho_I, \quad \forall \mathbf{x} \in \Omega \quad (3)$$

where ρ_I is the nodal charge density associated with the I th shape function. In order to determine the nodal charge densities ρ_I , the function ρ is projected onto \mathcal{W} in the least-squares sense according to the Bubnov–Galerkin formulation:

$$\sum_{J \in \mathcal{F}} \rho_J \int_{\Omega} N_I N_J \, dV = \int_{\Omega} N_I \rho(\mathbf{x}) \, dV, \quad \forall I \in \mathcal{F} \quad (4)$$

In standard FE notation, $\int_{\Omega} N_I N_J$ is the IJ th entry of the "mass matrix", while $\int_{\Omega} N_I \rho(\mathbf{x}) \, dV$ is the inner product of the continuous function ρ and the I th FE basis function.

With this formulation, the set of equations, eqs 2–4, is strictly only appropriate for reducing the dimensionality of continuous functions, so it must be modified to account for the discrete nature of atomic quantities in MD. Typically, FE data take the form of nodal densities (i.e., charge density), while the atomic data are primitive variables (i.e., charge). These distinct quantities can be related by defining atomic densities using a small but finite associated volume, ΔV_ρ^α (to be determined later). In this work, it is assumed that the MD and FE domains exactly coincide.

Because continuous integration is not well-defined over the discrete atomic locations, the projection of a continuous function onto its FE representation is performed in this work by summation over the atomic charges q^α :

$$\sum_{J \in \mathcal{F}} \rho_J \int_{\Omega} N_I N_J dV = \sum_{\alpha \in \mathcal{A}} N_I^\alpha \frac{q^\alpha}{\Delta V_\rho^\alpha} \Delta V^\alpha, \quad \forall I \in \mathcal{F} \quad (5)$$

using the approximation:

$$\rho(\mathbf{x}^\alpha) \equiv \rho^\alpha = \frac{q^\alpha}{\Delta V_\rho^\alpha} \quad (6)$$

following the ideas introduced by Wagner et al.²³

In eq 5, two notions of associated atomic volume are present. The physically motivated ΔV_ρ^α is a measure of the space occupied by atom α such that ρ^α is an approximation of the true bulk density. In contrast, ΔV^α is an integration quadrature weight used to make the discrete sum approximate the continuous integral. While there is no requirement that these two volumes associated with atom α be equal, equating the two atomic volumes, i.e., $\Delta V_\rho^\alpha = \Delta V^\alpha$, will prove advantageous. This equality enables the fundamental relationship between a continuous density and its associated atomic quantity to be derived as

$$\sum_{J \in \mathcal{F}} \rho_J \int_{\Omega} N_I N_J dV = \sum_{\alpha \in \mathcal{A}} N_I^\alpha q^\alpha, \quad \forall I \in \mathcal{F} \quad (7)$$

The notation used in these equations and the remainder of this work is as follows. Indices in the set \mathcal{F} are denoted by subscript Roman letters, while superscript Greek letters denote atomic indices from the set \mathcal{A} enumerating the atoms in the system. N_I^α then denotes the value of the shape function associated with node I at the position of atom α , i.e., $N_I(\mathbf{x}^\alpha)$. The variables ρ and q denote charge density and charge, respectively. In the sequel, all explicit set associations will be removed except where needed for clarity.

To verify the appropriateness of eq 7, it can be related to continuum models of fluid flow by differentiating it with respect to time. On the right-hand side, the result is

$$\frac{d}{dt} \sum_{\alpha} N_I^\alpha q^\alpha = \sum_{\alpha} q^\alpha \frac{d}{dt} N_I^\alpha = \sum_{\alpha} q^\alpha \nabla N_I^\alpha \cdot \mathbf{v}^\alpha \quad (8)$$

The time derivative of the left-hand side produces two terms:

$$\frac{d}{dt} \left[\sum_J \rho_J \int_{\Omega} N_I N_J dV \right] = \sum_J \left[\frac{d\rho_J}{dt} \int_{\Omega} (N_I N_J dV) + \rho_J \int_{\Omega} \frac{d}{dt} (N_I N_J dV) \right] \quad (9)$$

The term multiplying $d\rho_J/dt$ is the standard FE mass matrix while

$$\int_{\Omega} \frac{d}{dt} (N_I N_J dV) = \frac{d}{dt} \left(\int_{\Omega} N_I N_J dV \right) = 0 \quad (10)$$

because the shape functions are fixed in the spatial domain and do not change with the movement of the atoms. To get eq 8 into the appropriate form, consider

$$\begin{aligned} \sum_{\alpha} q^\alpha \nabla N_I^\alpha \cdot \mathbf{v}^\alpha &= \sum_{\alpha} \nabla N_I^\alpha \cdot (\rho^\alpha \mathbf{v}^\alpha) \Delta V^\alpha \\ &\approx \int_{\Omega} \nabla N_I \cdot (\rho \mathbf{v}) dV \end{aligned}$$

The accuracy of the approximation of this equation is a function only of the approximate MD quadrature with weights ΔV^α .

The standard, continuous time evolution equation for density ρ is

$$\frac{d\rho}{dt} + \nabla \cdot (\rho \mathbf{v}) = 0 \quad (11)$$

which has the usual FE approximation:

$$\sum_J \frac{d\rho_J}{dt} \int_{\Omega} N_I N_J dV = - \int_{\Omega} N_I \nabla \cdot (\rho \mathbf{v}) dV \quad (12)$$

$$= \int_{\Omega} \nabla N_I \cdot (\rho \mathbf{v}) dV - \int_{\Gamma} N_I (\rho \mathbf{v}) \cdot \mathbf{n} dS \quad (13)$$

where Γ is the boundary of the set Ω . Hence, if the atomic quadrature is exact and if there is no flux of atoms in or out of the system, then the standard FE approximation to the charge conservation equation is obtained which verifies the approach's consistency. The precision of the quadrature is related to the number of atoms in each element, so as the ratio of atoms per element becomes large, the correct continuous transport equation is recovered.

2.2. Electric Field Model. *2.2.1. Long-Range Electric Field.* The emphasis of this work is on the formulation of an AtC electric field in which long-range interactions are computed on a FE mesh and communicated to the atoms, while short-range interactions are modeled directly by Coulombic interactions to maintain high fidelity. Each charged atom contributes to the electric potential, and because the potential is long-range, a direct restriction of the electric potential would be prohibitively costly, just as direct computation of the long-range Coulombic interactions is costly. Instead, the equation governing the electric potential will be solved on the FE mesh. The continuous equation governing the electric potential is

$$\nabla^2 \phi = - \frac{1}{\epsilon_0} \rho \quad (14)$$

with ϵ_0 being the dielectric constant.

It is now necessary to determine what FE equations the electric potential should satisfy. Standard FE practice is to multiply by the shape functions and integrate by parts to reduce the smoothness requirements on the solution, a procedure which produces:

$$\int_{\Omega} \nabla N_I \cdot \nabla \phi dV = \frac{1}{\epsilon_0} \int_{\Omega} N_I \rho dV - \int_{\Gamma} N_I \mathbf{E} \cdot \mathbf{n} dS \quad (15)$$

Here, the electric field is given by $\mathbf{E} = -\nabla \phi$ and must be prescribed on boundaries with a free potential ϕ . If the FE electric potential is approximated by an expansion in the shape functions:

$$\hat{\phi}(\mathbf{x}) = \sum_I N_I(\mathbf{x}) \phi_I \quad (16)$$

and the continuous charge density is approximated by the FE projection in eq 7, the FE equation for the potential is

$$\sum_J \phi_J \int_{\Omega} \nabla N_I \cdot \nabla N_J dV = \frac{1}{\epsilon_0} \sum_J \rho_J \int_{\Omega} N_I N_J dV - \int_{\Gamma} N_I \mathbf{E} \cdot \mathbf{n} dS \quad (17)$$

where we recognize the first matrix $\int_{\Omega} \nabla N_I \cdot \nabla N_J dV$ as the usual "stiffness" matrix of FE and the second $\int_{\Omega} N_I N_J dV$ as the "mass"

matrix. In contrast to the AtC projection, continuous integrals are retained because all quantities involved are continuous. This difference highlights the contrast between intrinsic (atomic-based) and extrinsic (non-atomic-based) fields.

2.2.2. Atomic Electric Field. The equations described in the previous section provide a straightforward definition for the electric force on an atom due to the FE electric potential:

$$\mathbf{f}_{e,FE}^{\alpha} = q^{\alpha} \mathbf{E} = -q^{\alpha} \nabla \hat{\phi}(\mathbf{x}^{\alpha}) \equiv -q^{\alpha} \sum_I \nabla N_I^{\alpha} \varphi_I \quad (18)$$

While this force could account for the entirety of the electrical interactions present in a system of interest, it would be impractical because the FE mesh resolution would have to be such that there were more elements than atoms to obtain a grid-converged solution. Alternately, all the Coulombic interactions could be explicitly incorporated according to

$$\mathbf{f}_{e,C}^{\alpha} = \sum_{\substack{\beta \in \mathcal{N} \\ \beta \neq \alpha}} \frac{kq^{\alpha}q^{\beta}}{r_{\alpha\beta}^2} \mathbf{r}'_{\alpha\beta} \quad (19)$$

where $\mathbf{r}'_{\alpha\beta}$ is the unit vector in the direction of $\mathbf{r}_{\alpha\beta} = \mathbf{x}_{\beta} - \mathbf{x}_{\alpha}$.

In order to effectively blend eqs 18 and 19 into a unified formalism, the FE electric field must be split into two parts: $\hat{\phi} = \hat{\phi}^{l\alpha} + \hat{\phi}^{s\alpha}$. The first term, $\hat{\phi}^{l\alpha}$, represents the potential due to charges from all atoms outside of the cutoff radius, \mathcal{N}_{ω} and the imposed boundary conditions, i.e., the long-range interactions. It satisfies eq 17 with a modified nodal charge density $\rho_j^{l\alpha}$ given by

$$\sum_J \rho_j^{l\alpha} \int_{\Omega} N_I N_J dV = \sum_{\beta \in \mathcal{N}_{\omega}} N_I^{\beta} q^{\beta} \quad (20)$$

The second part of the decomposition, denoted by $\hat{\phi}^{s\alpha}$, accounts for the short-range contributions to the potential due to charges from individual atoms within the cutoff radius of atom α , i.e., $\beta \in \mathcal{N}_{\alpha}$, where \mathcal{N}_{α} is the set of neighbors of atom α (including α itself). It is computed by solving eq 17 with homogeneous boundary conditions and a nodal charge density $\rho_j^{s\alpha}$ defined with a modification of eq 17:

$$\sum_J \rho_j^{s\alpha} \int_{\Omega} N_I N_J dV = \sum_{\beta \in \mathcal{N}_{\alpha}} N_I^{\beta} q^{\beta} \quad (21)$$

Note that the decomposition is different for each atom and hence the dependence of the superscript on α .

While the equations discussed in the previous subsection describe the FE component of the electrical interaction, combining the Coulombic interactions with two components of the electric field decomposition will provide a mechanism to balance fidelity and cost of the method. Tractability implies that a finite cutoff distance is needed, as is standard in MD.³ Outside of this cutoff, the only information regarding charge interactions between two particles is provided by the large-scale electric field. However, inside this cutoff radius the electrostatic force is most accurately described by Coulomb's law. Within this framework, the total electrostatic force on atom i is

$$\mathbf{f}_e^{\alpha} = \sum_{\beta \in \mathcal{N}_{\alpha}} \frac{kq^{\alpha}q^{\beta}}{r_{\alpha\beta}^2} \mathbf{r}'_{\alpha\beta} - q^{\alpha} \nabla \hat{\phi}^{l\alpha}(\mathbf{x}^{\alpha}) \quad (22)$$

The force has been decomposed into a Coulombic and FE long-range force. Recall the potential decomposition implies:

$$\nabla \hat{\phi}^{l\alpha}(\mathbf{x}^{\alpha}) = \nabla \hat{\phi}(\mathbf{x}^{\alpha}) - \nabla \hat{\phi}^{s\alpha}(\mathbf{x}^{\alpha}) \quad (23)$$

Because the potential satisfies a linear equation, the short-range potential can be expressed as the sum of the electric potentials due to single atoms:

$$\hat{\phi}^{s\alpha}(\mathbf{x}^{\alpha}) = \sum_{\beta \in \mathcal{N}_{\alpha}} \hat{\phi}^{\beta} \quad (24)$$

where the notation $\hat{\phi}^{\beta}$ has been used to denote the potential arising from the charge associated with atom β only with homogeneous boundary conditions. By using eq 23 and eq 24, eq 22 can be rewritten as

$$\begin{aligned} \mathbf{f}_e^{\alpha} &= \sum_{\beta \in \mathcal{N}_{\alpha}} \frac{kq^{\alpha}q^{\beta}}{r_{\alpha\beta}^2} \mathbf{r}'_{\alpha\beta} - q^{\alpha} \left[\nabla \hat{\phi}(\mathbf{x}^{\alpha}) - \sum_{\beta \in \mathcal{N}_{\alpha}} \nabla \hat{\phi}^{\beta}(\mathbf{x}^{\alpha}) \right] \\ &= \sum_{\beta \in \mathcal{N}_{\alpha}} \frac{kq^{\alpha}q^{\beta}}{r_{\alpha\beta}^2} \mathbf{r}'_{\alpha\beta} - q^{\alpha} \nabla \hat{\phi}(\mathbf{x}^{\alpha}) + q^{\alpha} \sum_{\beta \in \mathcal{N}_{\alpha}} \nabla \hat{\phi}^{\beta}(\mathbf{x}^{\alpha}) \end{aligned} \quad (25)$$

Equation 25 partitions the total electrostatic force between the exact Coulombic part at short ranges and a corrected FE accounting for the long-range energy and boundary conditions.

Accounting for a smoothly decreasing Coulombic energy between particles as occurs in many MD potentials (e.g., CHARMM)²⁵ is straightforward in this approach. Equation 22 is modified as follows:

$$\begin{aligned} \mathbf{f}_e^{\alpha} &= \sum_{\beta \in \mathcal{N}_{\alpha}} h(\mathbf{x}^{\alpha}, \mathbf{x}^{\beta}) \frac{kq^{\alpha}q^{\beta}}{r_{\alpha\beta}^2} \mathbf{r}'_{\alpha\beta} - q^{\alpha} \nabla \hat{\phi}^{l\alpha}(\mathbf{x}^{\alpha}) \\ &\quad - q^{\alpha} \sum_{\beta \in \mathcal{N}_{\alpha}} [1 - h(\mathbf{x}^{\alpha}, \mathbf{x}^{\beta})] \nabla \hat{\phi}^{\beta}(\mathbf{x}^{\alpha}) \end{aligned}$$

where h is an arbitrary smoothing function. The resulting total force decomposition is

$$\mathbf{f}_e^{\alpha} = \sum_{\beta \in \mathcal{N}_{\alpha}} h(\mathbf{x}^{\alpha}, \mathbf{x}^{\beta}) \frac{kq^{\alpha}q^{\beta}}{r_{\alpha\beta}^2} \mathbf{r}'_{\alpha\beta} - q^{\alpha} \nabla \hat{\phi}(\mathbf{x}^{\alpha}) + q^{\alpha} \sum_{\beta \in \mathcal{N}_{\alpha}} h(\mathbf{x}^{\alpha}, \mathbf{x}^{\beta}) \nabla \hat{\phi}^{\beta}(\mathbf{x}^{\alpha})$$

Given the expression for the total electrostatic force acting on atom α in eq 25, the Coulombic interaction is computed from the MD, while the large-scale electric field is applied directly from the FE. It therefore remains to determine an effective manner in which to compute the contribution of the electric field at an atom strictly from its neighbors. Directly solving for the electric potential based on this set is a burdensome cost because it must be repeated over every atom and scales with the size of the FE mesh; a potentially significant burden for large three-dimensional grids. Instead, a method using Green's functions, $G^I(\mathbf{x}) = \sum_K N_K(\mathbf{x}) G_K^I$, computed on the FE mesh is preferable because it can be used to efficiently invert eq 17. The Green's function associated with the I^{th} node satisfies the system of equations:

$$\sum_K G_K^I \int_{\Omega} \nabla N_J \cdot \nabla N_K dV = \frac{1}{\epsilon_0} \delta_{IJ} \quad (26)$$

with δ_{IJ} being the Kronecker δ . Boundary conditions are taken to be homogeneous by definition in eq 26. The factor of $1/\epsilon_0$, while not necessary, is retained to facilitate later notation. The nodal variables G_J^I define the response of each mesh node, J ,

to an impulse at the I^{th} node, and can be recognized as scaled coefficients of the inverse stiffness matrix. A solution for the total potential at every node I can be written as

$$\varphi_I = \sum_J G_{IJ}^I f_J - \int_{\Gamma} N_I \mathbf{E} \cdot n dS \quad (27)$$

where

$$f_J = \sum_K \rho_K \int_{\Omega} N_J N_K dV \quad (28)$$

Using this formulation, the potential due to only the neighbors is defined by two operations:

$$\sum_J \rho_J^{\beta} \int_{\Omega} N_I N_J dV = N_I^{\beta} q^{\beta}, \quad \forall \beta \in \mathcal{N}_{\alpha} \quad (29)$$

$$\phi_I^{\beta} = \sum_J \rho_K^{\beta} \left(\sum_K \int_{\Omega} N_J N_K dV \right) G_I^J \quad (30)$$

This framework allows the potential at atom β due to its neighbors to be easily evaluated. However, rather than solving eq 30 directly, substituting into it the right-hand side of eq 29 yields

$$\phi_I^{\beta} = \sum_{J \in \mathcal{F}^{\beta}} N_J^{\beta} q^{\beta} G_I^J \quad (31)$$

obviating the need to solve eq 29 for ρ_J^{β} . In fact, making a similar substitution in eq 17:

$$\sum_J \varphi_J \int_{\Omega} \nabla N_I \cdot \nabla N_J dV = \frac{1}{\epsilon_0} \sum_{\alpha} N_I^{\alpha} q^{\alpha} + \int_{\Gamma} N_I \mathbf{E} \cdot n dS \quad (32)$$

means that $\hat{\rho}$ itself need never be computed except as required for postprocessing, saving the computational cost of a matrix inversion. More importantly, eq 31 has been “localized” such that rather than have every node J included in the sum, instead a much smaller set, denoted by \mathcal{F}^{β} , is required. It is the set of shape function indices whose support includes atoms in the set \mathcal{N}_{β} . A graphical example is shown in Figure 1, and an algorithm for its determination is provided in algorithm 1 (see Chart 1). This algorithm guarantees that all nodes with shape functions corresponding to atom pairs that could be neighbors, if one of them is in the support of node I , are included but no others are. If the mesh size is bounded below, then the number of nodes retained in each sparsity pattern is bounded above and is independent of the total number of nodes in a mesh. This allows the short-range interactions to be correctly accounted for in an efficient manner.

The operation count for computing the short-range FE field using eqs 31 and 32 scales as $O(n_{\mathcal{L}} n_{\mathcal{N}_{\alpha}})$, where $n_{\mathcal{L}}$ is the number of atoms, and $n_{\mathcal{N}_{\alpha}}$ is the average number of neighbors per atom because $n_{\mathcal{N}_{\alpha}}$ sums must be performed per atom. This is the same operation count as is needed to evaluate the long-range Coulombic interactions and naturally fits into the spatial decomposition mode of parallelism. However, the factor contained in the scaling itself depends on the number of FE nodes because each term in the sum involves a vector of data at each node. If a highly refined grid is used, the cost of evaluating the short-range FE electric forces will dominate the short-range Coulombic force computation.

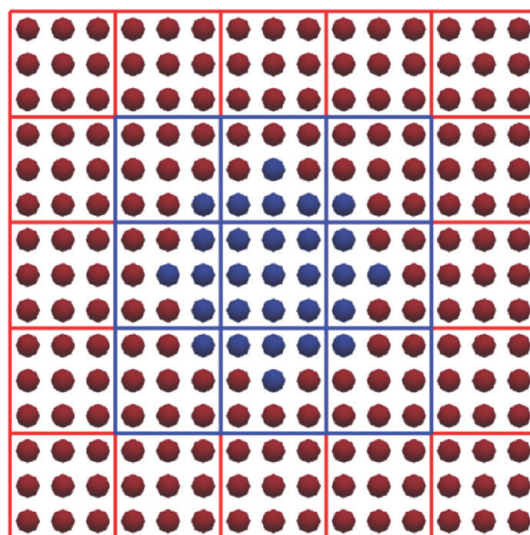


Figure 1. Schematic of the short-/long-range decomposition of the atoms within a cutoff radius and the nodes for which G_I^J is nonzero. Blue atoms are within the cutoff radius of the central atom, while red atoms are not. Similarly, the blue parts of the mesh denote the set of nodal Green's functions which must be retained for that atom, while the nodes in red part of the mesh will not contribute to the correction of the electric potential.

Chart 1. Determination of Green's Function Sparsity Pattern for node I

Algorithm 1 Determination of Green's Function Sparsity Pattern for node I

- 1: set $\mathcal{F}^{\beta} = \emptyset$
- 2: insert I into \mathcal{F}^{β}
- 3: list NEIGHBORS = set of all nodes $J \in \mathcal{F}$ such that $\int_{\Omega} N_I N_J dV \neq 0$
- 4: insert all nodes in NEIGHBORS into \mathcal{F}^{β}
- 5: enqueue nodes in NEIGHBORS into queue NEXT-NODES
- 6: **while** NEXT-NODES is not empty **do**
- 7: pop NEXT-NODES to node J
- 8: list NEXT-NEIGHBORS = set of all nodes $K \in \mathcal{F}$ such that $K \notin \mathcal{F}^{\beta}$ and $\int_{\Omega} N_J N_K dV \neq 0$
- 9: insert all nodes in NEXT-NEIGHBORS into \mathcal{F}^{β}
- 10: **if** node J is within the cutoff radius of any node in NEIGHBORS **then**
- 11: enqueue all nodes in NEXT-NEIGHBORS in NEXT-NODES
- 12: **end if**
- 13: **end while**
- 14: return \mathcal{F}^{β}

2.3. Boundary Condition Models. Imposing classical boundary conditions on MD systems presents a challenge because, at the scales of MD, boundary conditions are actually fluctuating quantities rather than fixed constraints. This section describes how some relevant types of boundary information can be applied within the present methodology. The first boundary conditions considered are Neumann conditions, which involve the normal derivatives that appear explicitly in eq 15. If the system is immersed in a strong and known electric field, setting \mathbf{E} at the boundaries to this quantity will impose the correct conditions. It can also be based on known currents because these are proportional to the electric field strength. If far-field data indicate there is no overall electric field or current, \mathbf{E} should be set to zero because that is correct on average. Accounting for the fluctuations in the boundary conditions as a result of the unsteadiness of the physics at the nanoscale is beyond the scope of this work.

The next case of interest is a charged infinite surface, which will occur in an MD calculation if one or two dimensions

parallel to the surface are periodic. Because an infinite surface carries infinite charge, a potential cannot be assigned to this surface. Rather, a bulk electric field should be applied perpendicular to the surface with strength based on the desired surface charge density. At the surface, the potential is set to zero so that the total electric potential is the superposition of two potentials arising from different sets of charge: (1) the charge that generates the bulk electric field and (2) the charged particles represented in the MD.

In addition to the surface charge, special considerations must be given for periodic boundaries. Within the current implementation, the potential is not computed in Fourier space and therefore cannot be determined to a global constant. Instead, a single (arbitrary) node is fixed to an arbitrary value, although other methods are possible (e.g., setting a global constraint on the average potential). A prerequisite for this approach is the net charge within the simulation box is zero, otherwise the spatially varying component of the potential due to point charges cannot be periodic. Further complications arise from the Green's function equation, eq 26. The Green's function of interest in this case is nonperiodic and infinite because the short-range charges should affect only interacting pairs rather than the infinite number of interactions of an atom with all the periodic images of its neighbors. Overcoming this challenge is possible, for example, the infinite Green's function can be approximated on a larger mesh or the analytic Green's function projected onto the existing basis. However, this approach will be deferred to future work. Instead the PPPM method is used to account for the electric forces in those directions, while the AtC approach only applies forces in the nonperiodic directions even though the electric potential is three-dimensional. A small error is introduced using this approach because the nonperiodic component will have a slight overcorrection due to the presence of its periodic images.

A final case of interest is the inclusion of a finite, fixed potential surface. For the purpose of developing appropriate models of such a surface in this work, a fixed potential surface is defined as a surface with a prescribed charge distribution such that the desired potential is the self-induced value everywhere on the surface. In contrast, a surface with a fixed charge will have a varying potential due to the presence of external charge sources, such as point charges. In large systems, it is reasonable to assume that an external voltage will maintain a potential roughly constant in time, but at the small time and length scales present in MD, this is an approximation. The surface charge would also depend on the electronic properties of the surface. For example, the surface charge in a conductor will vary to maintain the absence of an electric field inside the conducting body, while other surfaces would require a more complex relationship between surface charge and voltage. These effects are not included in the surface charge model that follows but are somewhat mitigated by the inclusion of short-range interactions with the wall.

Consider a fixed charged on a finite surface specified on a set of FE faces that must not be periodic in any direction. Because the faces are finite, a constant surface charge density will not maintain a constant potential. The potential due to a continuous charge $\sigma(\mathbf{x})$ on a surface can be determined by

$$V(\mathbf{x}) = \int_S \frac{k\sigma(s)}{\|\mathbf{x} - \mathbf{s}\|} dS \quad (33)$$

The FE projection for the voltage is

$$\begin{aligned} \sum_{J \in \mathcal{J}} V_J \int_S N_I N_J dS &= \int_S N_I V(\mathbf{s}) dS \\ &= \int_S N_I \left(\int_{S'} \frac{k\sigma(\mathbf{s}')}{\|\mathbf{s} - \mathbf{s}'\|} dS' \right) dS, \quad \forall I \in \mathcal{J} \end{aligned} \quad (34)$$

where \mathcal{J} is the set of FE nodes belonging to surface S . The integral on the right-hand side of eq 34 can be evaluated using standard FE face quadrature. As an aside, if the charge distribution is also defined by a FE expansion, then eq 34 becomes

$$\sum_{J \in \mathcal{J}} V_J \int_S N_I N_J dS = \sum_{J \in \mathcal{J}} \sigma_J \int_S N_I \left(\int_{S'} \frac{kN_J}{\|\mathbf{s} - \mathbf{s}'\|} dS' \right) dS, \quad \forall I \in \mathcal{J} \quad (35)$$

Equation 35 defines a linear relationship between the nodal potential on a surface and its associated nodal charge. The nodal charge for a fixed potential can be determined by solving eq 35 for σ_J while setting V_J to be fixed.

Within the multiscale framework for the electric potential, the surface charge will play a similar role to the atomic charges in that they both induce a long-range potential and provide short-range interactions. To consider these types of interactions, we further expand eq 25 by accounting for the surface charge in the electric potential:

$$\begin{aligned} \mathbf{f}_e^\alpha &= \sum_{\beta \in \mathcal{N}_\alpha} \frac{kq^\alpha q^\beta}{r_{\alpha\beta}^2} \mathbf{r}'_{\alpha\beta} + q^\alpha \sum_I \sigma_I \int_{S \cap B(\mathbf{x}^\alpha, r_c)} \frac{kN_I}{\|\mathbf{x}^\alpha - \mathbf{s}\|^2} \mathbf{r}'_{\alpha\beta} dS - q^\alpha \nabla \hat{\phi}^\alpha \\ &+ q^\alpha \sum_{\beta \in \mathcal{N}_\alpha} \nabla \hat{\phi}^\beta(\mathbf{x}^\alpha) + q^\alpha \int_{S \cap B(\mathbf{x}^\alpha, r_c)} \nabla \hat{\phi}_s^\alpha dS \end{aligned} \quad (36)$$

The first integral accounts for the exact short-range force exerted by the surface charge, while the second integral is a correction removing the effect of the surface charge through the FE potential on atom α . Both integrals can be evaluated directly using FE quadrature, although other quadrature schemes are possible (e.g., based on atoms contained in those faces). The potential induced by the surface charge can be determined by computing Green's functions for each of the quadrature points by first solving eq 35 for the induced surface potential of a unit charge and then solving the electric potential equation treating the surface as a fixed potential boundary. This results in additional Green's functions for each quadrature point in the surface.

In general, these Green's functions are highly nonlocal because charge at any point on a surface induces a nonzero potential everywhere on the surface, as shown in eq 35. However, the resulting short-range interactions can still be localized by truncating the Green's functions to only those nodes within a cutoff radius of the surface, in exactly the same manner as was done for the point charges. The surface Green's functions can also be computed and stored during a precomputation phase. This method is a low-storage, low-cost approach that accounts for accurate short- and long-range interactions between charged MD atoms and prescribed surface data. An important point to note is that for any quadrature scheme used to evaluate the surface integrals in eq 36, each quadrature point will require its own Green's function.

2.4. Implementation Details. The methods described above were implemented in LAMMPS within an existing AtC framework.

This framework generates a FE mesh overlaying a region of atoms and computes piecewise linear shape function values and derivatives at FE quadrature points and atomic locations. A preprocessing step first computes the list of neighboring nodes for each node based on the force cutoff radius according to algorithm 1 (see Chart 1). Then the stiffness matrix is set up for the electric potential, eq 32, and used to compute each Green's function according to eq 26. Green's functions are then truncated and stored in sparse vectors based on the nodal neighbor lists. At the same time, fixed potential boundary values are determined by eq 34. Then the Green's function for each surface quadrature point used to evaluate eq 34 is calculated by solving eq 32. The bulk of the work of this method occurs immediately after the LAMMPS force calculation step, which is between the two steps in the standard Verlet time integration scheme.¹ At each time step, the shape functions N_I^α used in the projection operation eq 7 must be updated to the new positions of the atoms.

After the shape function-related quantities are updated, the charges can be restricted using eq 7 with row–sum lumping to form the right-hand side for the FE electric potential, eq 32, enabling its calculation using the precomputed stiffness matrix. Neumann conditions are applied by adjusting the right-hand side during the solve, while Dirichlet conditions are satisfied by a penalty method. This method weights the diagonal entry of all fixed nodes with a value 10^4 greater than the maximum diagonal value in the left-hand side matrix. Correspondingly, the right-hand side is modified by adding the same penalty factor multiplying the desired potential value. It should be noted that other matrix solution schemes would perform adequately in this application.

LAMMPS adds in the Coulombic interaction before the present method is executed, so only the last two terms in eq 25 need to be accounted for. The first, accounting for the total FE electric field, is added to all atoms. Afterward, the truncated FE potential associated with each atom is computed using the Green's functions multiplied by the restricted atomic charges. This preprocessing step allows the neighbor FE potentials for each atom to be quickly calculated by summing over the FE potential contribution of all its neighbors. The potential is then corrected to result in the appropriate electric force at each atom using eq 25.

Charged surfaces are implemented in an approximate manner. In a preprocessing step, consistent with a form of row–sum lumping approximation of eq 34, the potential is determined from a fixed charge by

$$V_I = \sum_{y \in \mathcal{Q}} \frac{k\sigma(y)}{|\mathbf{x}_I - \mathbf{y}|} w(\mathbf{x}_I, \mathbf{y}) \quad (37)$$

where \mathcal{Q} denotes the location of the Gauss quadrature points on the face, and w is the associated quadrature weight. This approach ensures the denominator is always nonzero. To evaluate the short-range interactions, the nodes are used as effective charge locations with charge set to the shape-function weighted integral of the surface charge:

$$\eta_I = \int_{\Gamma} N_I \sigma(\mathbf{x}) dS \quad (38)$$

with the integral evaluated using the same Gaussian quadrature as eq 37. Note that η_I is the effective charge associated with node I and not a nodal value of a finite element representation of $\hat{\sigma}$.

When computing the short-range surface interactions and corrections in eq 36, only nodes within the cutoff radius of each atom are considered, and then their Green's functions are used to

remove the FE potential. As a simplifying approximation, face-specific Green's functions are not computed for the charge at each quadrature point that contributes to the charge at node I in eq 38. Instead, only their contributions to the potential at node I are considered, which allows the same Green's functions, as those used in eq 31, to be reused. The net effect of all these approximations is that low-order integration is used to evaluate the first integral in eq 36, while the correction from the second integral does not take into account all the long-range impact of local charge on the fixed potential boundary condition applied in eq 32.

Improvements to the surface charge fidelity can be made by improving the order of integration over the surface within the cutoff radius and more accurately estimating the impact of charge associated with quadrature points on the electric potential. A final improvement in performance can be realized by maintaining neighbor lists at each surface quadrature point to avoid the search over all atoms to determine those near a wall. (Walls are currently implemented in LAMMPS with this more expensive approach as well.) These improvements in the implementation of charged surfaces as well as more general models for other types of surfaces and periodic boundary corrections for eq 25 are deferred for future work.

3. COMPUTATIONAL RESULTS

3.1. Comparison with Analytic Results. To verify the basic correctness and implementation of the method, a simple stack of atoms was set up with fully periodic conditions along the span (y, z) . Periodic conditions on the atomic forces were also used along the length of the stack (x) to maintain the equilibrium structure. An FCC lattice structure with spacing 4.08 Å, resulting in 144 atoms, was used to develop a test case amenable to analytical solution. Around this lattice a FE mesh was constructed to represent the continuous charge distributions and electric field. While the elements have nonzero volume, periodicity in the y and z directions effectively makes the elements one-dimensional with length 2.04 Å. However the FE mesh is not periodic in the x direction so fixed potential and electric field boundary conditions can be applied. The overall structure is shown in Figure 2a.

The electric field in this case was driven by both boundary conditions and internal charges. Each atom was given a unit charge (equivalent of a proton) such that the system's charge density was uniform at 5.89×10^{-2} unit charges per Å³. The FE potential was fixed to zero at the left end. At the right end, either an insulating or a fixed electric field condition was used. The known boundary conditions and charge densities allow the analytic solution to Poisson's equation to be determined. All the calculations in Section 3 used a 10 Å cutoff radius. As shown in Figure 2, in both cases the analytic solution is recovered by the method. This case tests the Poisson solver and projection operations. The results verify their implementation and demonstrate that the overall mathematical formulation of the problem is reasonable given the behavior of the FE system.

3.2. Comparison with Existing Methods: PPPM and Ewald Sums. Providing a quantitative comparison of the present method with existing approaches for including long-range electrostatic forces in MD is an important aspect of verifying the technique. These are primarily PPPM and Ewald sums as described in Section 1. Since these methods are only appropriate for periodic systems, a fully periodic FCC lattice system is created

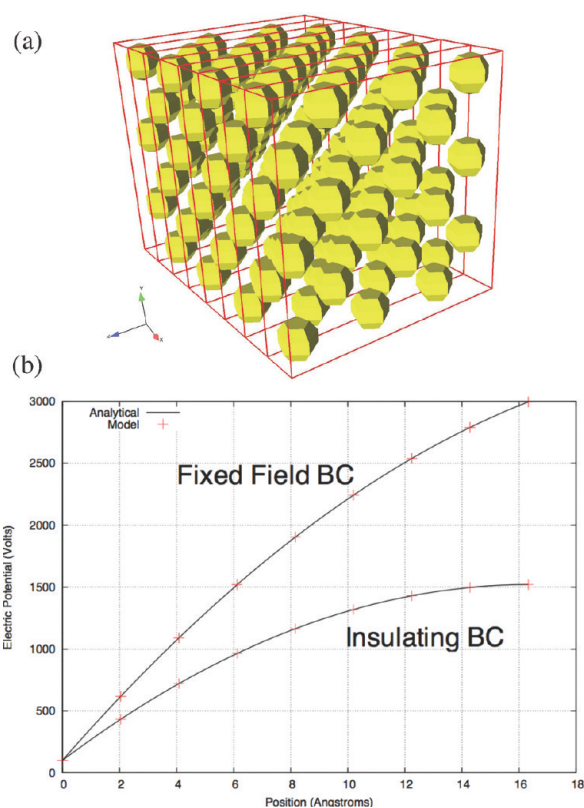


Figure 2. Basic verification test case: (a) shows the problem set up, while (b) presents the results for different boundary conditions.

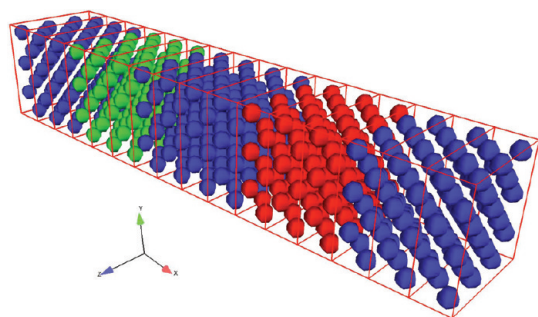


Figure 3. Schematic of the PPPM and Ewald comparison case with the present method. Red atoms are positively charged, green atoms are negatively charged, and blue atoms are neutral.

with dimensions $65.28 \times 12.24 \times 12.24 \text{ \AA}^3$ and lattice spacing of 4.08 \AA , composed of 576 atoms. The atoms are uncharged except for a group with a positive unit charge and a group with a negative unit charge, as shown in Figure 3 (which also shows the finest FE mesh). Initial computations were performed with the short-range Coulombic force disabled so that the only forces acting on the atoms are the long-range forces generated by the method. Hence the issues with periodicity affecting the short-range correction discussed in Section 2.3 do not affect this calculation. As shown in Table 1, the proposed AtC method produces forces similar to the other methods. In each case the force acting on the negatively charged atoms is presented because the net force was zero for all methods. To see how this is related to the FE fields, Figure 4 shows the FE charge density and the electric potential

Table 1. Comparison of the Force Computed by the Long-Range Electric Field^a

force (g ps/ \AA^2 mol)	method/mesh
8.49533×10^6	PPPM
8.49543×10^6	Ewald sums
4.71971×10^6	$8 \times 1 \times 1$ elements
8.49547×10^6	$16 \times 1 \times 1$ elements
8.49547×10^6	$32 \times 1 \times 1$ elements
8.49547×10^6	$32 \times 2 \times 2$ elements
8.49547×10^6	$32 \times 4 \times 4$ elements

^aThe present method, with entries denoted by the mesh size, is shown along with existing approaches. Execution times were also compared using software profiling tools. The $16 \times 1 \times 1$ element AtC computation was slightly more expensive than the PPPM method and considerably cheaper than the Ewald summations. As the grid is refined the cost increases, with the $32 \times 1 \times 1$ and $32 \times 2 \times 2$ element meshes bracketing the cost of the Ewald solution. Note the AtC electric field solver has not been optimized, while the existing methods in LAMMPS and their associated fast fourier transforms are highly optimized.

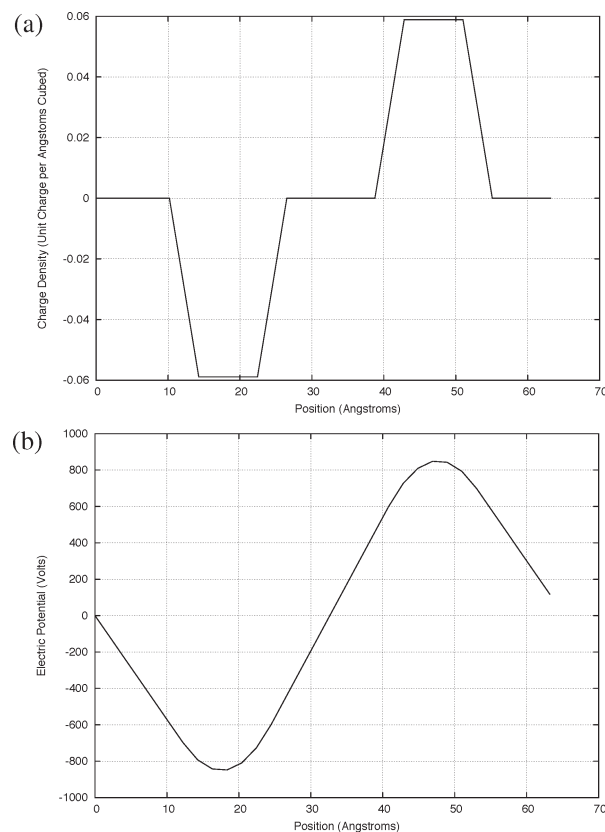


Figure 4. Finite element fields from the finest mesh used to compare against the PPPM method and Ewald Sums. (a) Charge density and (b) electric potential using this charge density as a source.

variables. The charge density is simply the approximate projection of the atomic state and enters into the right-hand side of the equation governing the electric potential. On the coarsest mesh, inadequate resolution exists to accurately solve the gradients needed in this equation, resulting in significant error in the solution.

This test demonstrates the correctness of the theory and implementation regarding the prolongation of the long-range

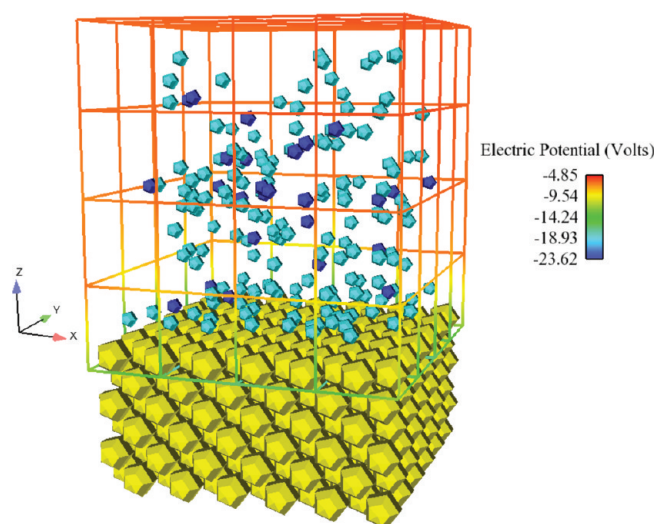


Figure 5. Schematic of the argon/gold configuration. Gold atoms are yellow, neutral argon atoms are light blue, and positively charged argon atoms are dark blue. Particles are kept in the box using 9-3 LJ walls at each unbounded side of the mesh, which is colored using the electric potential.

force from the FE to the atoms, including the use of FE shape functions to take derivatives of the electric potential. It further demonstrates that the method has accuracy comparable to existing methods, even though the finest FE grid had only 256 elements, while the automatically generated PPPM method required a grid of 2.592×10^6 ($320 \times 90 \times 90$) Fourier collocation points to achieve a relative error of 10^{-4} . This is the only case considered in this work in which a fully periodic system could be used because dynamics were not evaluated, and therefore the short-range FE correction was not needed (recall the current correction scheme is not designed for handling periodic directions). However, to use the FE method the node corresponding to the origin was fixed to have zero potential so the Poisson equation would be well-posed.

3.3. Comparison with Full Anisotropic Solution. For the purposes of comparing the proposed method to its alternatives, there is one other way to incorporate long-range electrical interactions between charged particles in MD: “brute force” calculation of the electric field using a finite MD simulation with a Coulombic cutoff distance greater than the maximum possible atomic separation. For most simulations, the cost of building the neighbor lists and computing the interatomic electrical interactions would prevent application of this method. Furthermore, it is inappropriate for periodic systems because an infinite cutoff radius would be required. While such limitations render such an approach impractical for computations of scientific interest, a small model problem has been developed that serves as a surrogate for an electric double layer. This problem also enables investigation of some of the complex boundary conditions that can be applied. At the wall, a fixed surface charge condition will be used, which introduces some error by transforming into a fixed potential boundary condition at long distances. Also, Neumann conditions will be used to prescribe the remaining boundary conditions on the electric field, but as will be shown, this is an approximation because there is no way of knowing what the normal component of the electric field should be.

The model system built to examine this case consists of an FCC gold lattice with spacing 4.08 \AA over a horizontal span of $22.44 \times 22.44 \text{ \AA}^2$. The lattice is not periodic in any direction, and these atoms are held fixed. They serve as an effective force field on a system of liquid argon on top of this structure to a height of 22.44 \AA . Dimensions of the box were selected to be the maximum size such that the neighbor lists could fit in the available memory and still be long enough for atoms at opposite ends of the box to be neighbors. The fluid used was argon, which was equilibrated at 300 K for 50 ps with a time step of 0.5 fs using the Nosé–Hoover thermostat.²⁶ A schematic of the system, including the FE mesh, is shown after the equilibration step in Figure 5. Upon creation, certain argon atoms were randomly chosen to have a positive unit charge so that during equilibration they tend to separate. Argon atoms were confined by 9-3 Lennard-Jones (LJ) walls along the five sides without gold, with the energy given by

$$E = \varepsilon_{93} \left[\frac{2}{15} \left(\frac{\sigma_{93}}{r} \right)^9 - \left(\frac{\sigma_{93}}{r} \right)^3 \right], \quad r < r_c \quad (39)$$

with $\varepsilon_{93} = 0.0195 \text{ eV}$ and $\sigma_{93} = 3.45 \text{ \AA}$. Interatomic forces were modeled using LJ interactions, i.e.:

$$E_i = 4\varepsilon_i \left[\left(\frac{\sigma_i}{r} \right)^{12} - \left(\frac{\sigma_i}{r} \right)^6 \right], \quad r < r_c \quad (40)$$

Parameters for LJ interactions are the energy depth of the well ε , the length scale σ , and the cutoff radius r_c . Gold–gold interactions use $\varepsilon = 0.724 \text{ eV}$ and $\sigma = 2.598 \text{ \AA}$, while the argon–argon model has $\varepsilon = 0.010 \text{ eV}$ and $\sigma = 3.405 \text{ \AA}$. A uniform cutoff radius of 13.0 \AA was used for the interatomic LJ interactions, while $r_c = 10 \text{ \AA}$ for the wall and short-range electrical interactions when using the AtC method. Cross-species interactions were parameterized by mixing the potential parameters according to the rules $\varepsilon_{ij} = (\varepsilon_i \varepsilon_j)^{1/2}$ and $\sigma_{ij} = (\sigma_i + \sigma_j)/2$.

After equilibration, the top layer of gold atoms is negatively charged so that it can be exactly screened by the ions. This configuration is run to a statistical steady state using either only Coulombic interactions with a long cutoff distance of 40 \AA or the present method with a much more modest cutoff of 13 \AA . As already mentioned, exactly resolving all long Coulombic interactions was the limiting factor in choosing this geometry. The FE mesh was created to cover the liquid using $7 \times 7 \times 7$ uniform elements of size approximately 48 \AA^3 . When using the AtC method the gold atom charge was removed and accounted for by use of a fixed charge boundary and its corresponding spatially varying surface potential, as described in the previous section. Fixing the gold atoms was chosen in order to remove surface deformation phenomena from the problem, with a consequence being that the wall acts as a cold surface. Zero normal electric field (Neumann) boundary conditions were used on all other sides, which serves as a rough approximation to the true electric field’s behavior when the long cutoff is used.

This case illustrates the difficulty in exactly translating continuous boundary conditions to an atomistic setting. An insulating condition is only appropriate in the limit of an infinitely small screening layer such that the electric field is zero outside of the domain of interest. This limit is violated even in the steady state of this solution and is clearly incorrect during the transient. Further, the charged surface is treated as a fixed potential surface by the FE electric potential, when in reality the potential varies based on the distribution of the atoms. In a true conductor, for

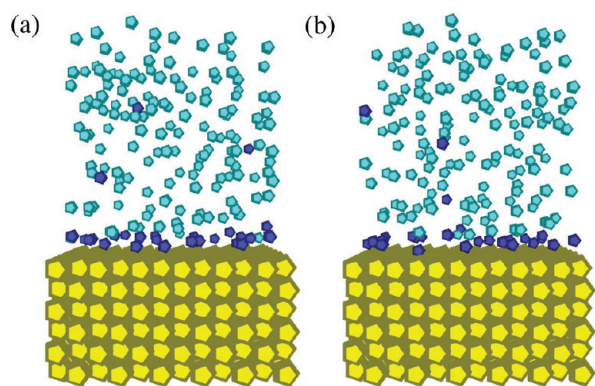


Figure 6. Comparison of the final MD state from: (a) the direct calculation and (b) the AtC method. See Figure 5 for the color legend.

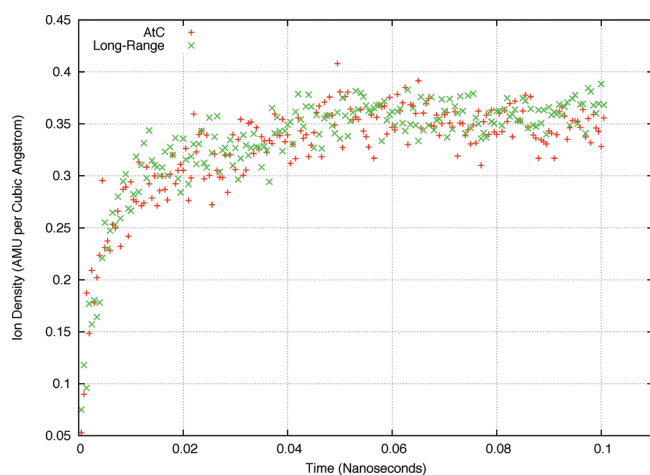


Figure 7. Time history of the plane-averaged charged argon density at the FE node adjacent to the gold.

example, the potential and surface charge would change to make the electric field in the conductor zero. Derivations in this work have focused on developing the general framework for the long-range potential in terms of solving an appropriately sourced Poisson equation in conjunction with the standard fixed potential and insulating boundary conditions encountered in electrostatics. While a few enhancements have been made to approximate surfaces with a fixed charge, boundary models to better account for the physics are left for future work.

Despite the inconsistency noted above, the exact MD solution can be compared against the MD solution using the long-range FE electric field. However, it is sufficient to obtain reasonable quantitative comparisons between the two solutions since the bulk of the potential drop occurs both very near and perpendicular to the gold surface. In both cases, 24 charged atoms lie in an immobile layer near the wall, while three remain mobile above this layer (based on the particles' trajectories, one of the free atoms is partially screened). By congregating near the wall, these atoms screen the electric field so it drastically reduces in magnitude away from the wall. The dynamics of these atoms indicate they are highly attracted to the charged wall as they experience only a vibrational motion after their adsorption, however there is a limit to how densely they can be packed.

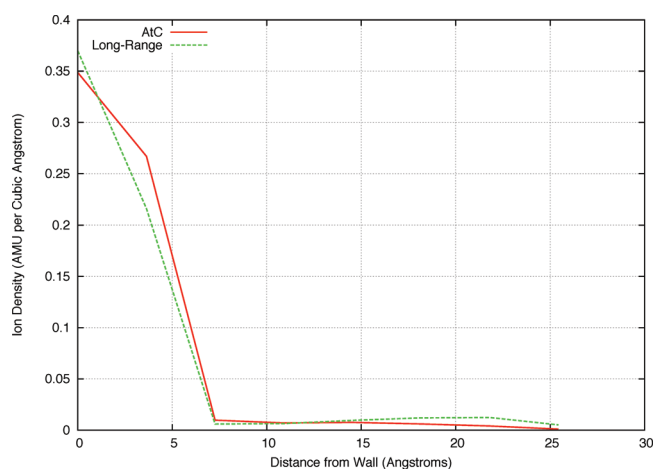


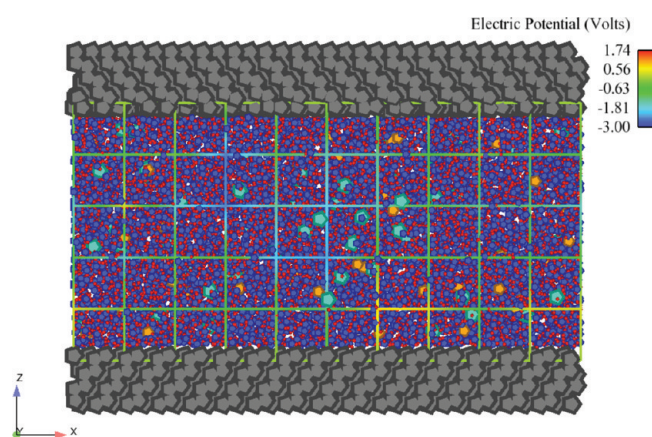
Figure 8. Time-averaged nodal charged argon densities at the steady state.

The AtC method can also be used to extract comparable quantitative data from the simulation. After the gold is charged, an initial transient occurs during which the free charged argon atoms form the immobile screening layer on the wall. It can be visualized by examining the time history of the nodal charged argon density adjacent to the wall. The atomic configuration is visualized in Figure 6, while Figure 7 shows this density averaged over the first node of the FE calculation (a similar mesh was set up over the long-range cutoff geometry for postprocessing only, exactly as in Figure 5). Both cases have nearly identical rise times with the density in the long-range case being slightly higher than the AtC case. Given how the data is partitioned in FE, this indicates the location of the layer is slightly closer to the wall when the long-range Coulombic cutoff is used. To determine precisely the difference in the height of the layers, the simulation is run for an additional nanosecond with the density data averaged over nodes at the same vertical distance from the gold. As shown in Figure 8, despite the approximate nature of the insulating FE boundary conditions and the low-order quadrature used to implement the charged surface, good agreement is obtained with the exact solution when using this method in both quantitative and qualitative senses.

3.4. Electrolyte Flow in a Silicon Nanochannel. In this case, flow in a nanofluidic device is considered. A full analysis of this configuration is beyond the scope of this work, but the case illustrates how to perform these types of technologically relevant simulations. Silicon crystals form walls at the top and the bottom of a region of salt water, which is free to flow in the wall-parallel directions. Periodic conditions are used to allow this flow, while the channel walls break the symmetry. Table 2 gives the potential type, coefficients, and source for each pair of interactions considered in the simulations. References refer to relevant simulations that used these parameters in similar physical situations, except for the Stillinger–Weber (SW), where the originating reference for this potential is provided. All short-range charged interactions were modeled using Coulombic interactions with a sharp cutoff at 10 Å. Water is modeled using the TIP3²⁸ set of pairwise LJ coefficients and with charges on the oxygen of -0.830 and the hydrogen of 0.415 in terms of fractions of a proton charge. For the Morse potential the parameters are the energy D_0 , inverse length scale

Table 2. Interaction Potential, Potential Coefficients, And References for Pairwise Interactions in the Silicon Nanochannel Simulation

atom 1	atom 2	potential	coefficients	source
O	O	LJ	$\epsilon = 0.006740, \sigma = 3.1650, r_c = 10$	28
O	Na	LJ	$\epsilon = 0.005348, \sigma = 3.24085, r_c = 10$	15
O	Cl	LJ	$\epsilon = 0.005348, \sigma = 3.77535, r_c = 10$	15
O	Si	Morse	$D_0 = 0.0668, \alpha = 1.3, r_0 = 3.7, r_c = 9$	15
Na	Na	LJ	$\epsilon = 0.004336, \sigma = 3.331, r_c = 10$	15
Na	Cl	LJ	$\epsilon = 0.004336, \sigma = 3.8655, r_c = 10$	15
Na	Si	LJ	$\epsilon = 0.0056043, \sigma = 2.9645, r_c = 10$	15
Cl	Cl	LJ	$\epsilon = 0.004336, \sigma = 4.4, r_c = 10$	15
Cl	Si	LJ	$\epsilon = 0.056043, \sigma = 3.499, r_c = 10$	15
Si	Si	SW	see ²⁷	27

**Figure 9.** Schematic of the silicon nanochannel simulation. Water is modeled using hydrogen atoms (red) bonded to oxygen atoms (blue). Other atoms are sodium ions (orange), chlorine ions (light blue), and silicon (gray). The FE mesh is overlaid and colored by the electric potential.

α , equilibrium distance r_0 , and cutoff radius r_c :

$$E = D_0[e^{-2\alpha(r-r_0)} - 2e^{-\alpha(r-r_0)}], \quad r < r_c \quad (41)$$

The units used are Å for length and eV for energy. Note that hydrogen atoms only interact with other atoms electrically. In general, interactions were chosen to match the model of Qiao and Aluru¹⁵ in the case of the silicon nanochannel.

Figure 9 illustrates the computational geometry. The silicon planes are initialized in a similar manner to the gold in Section 3.3 except for the periodic boundaries in the transverse direction. The silicon is arranged in a diamond lattice with the [111] face toward the water, and then the arrangement is adjusted to minimize the potential energy to account for the exposed $\pm z$ faces. A box of water containing 16 sodium and 16 chlorine ions dissolved in 1819 water molecules is initialized for 1 ns, using a time step of 0.5 fs, in a fixed region using the Nosé–Hoover thermostat to maintain a fixed temperature of 300 K and 9-3 LJ walls to contain the fluid in the wall-normal directions. After equilibration, the water (without the LJ walls) is inserted between the silicon planes and allowed to readjust for 1 ns. During this phase, the water was integrated using Newtonian dynamics, while the Nosé–Hoover thermostat was applied to

the silicon so it could thermally regulate the salt water. After the entire system comes into equilibrium, electric fields of strength -1 V/nm were applied in the x (wall-parallel) and z (wall-normal) directions. With these fields in place, ions of opposite charge are forced to flow along the channel in opposite directions as well as aggregate to opposite sides of the channel, resulting in shear flow in the channel. Statistics were captured after running for 0.1 ns using the method of Zimmerman et al.²⁹

A similar case was originally considered by Qiao and Aluru using a different methodology to account for the ionic electric field by applying a wall-normal correction to the Ewald summations used to compute the long-range electrostatic interactions in the periodic directions.¹⁶ In addition, the potential drop was applied by fictitiously charging the silicon atoms.

The present method instead decomposes the electric potential into three components and uses the most appropriate method for each. To account for the applied voltage drop in the wall-normal direction, a fixed electric field was used requiring minimal additional computation. Similarly, the wall-parallel flow was driven by a fixed electric field. Electrical interactions induced by water and ions in the wall-parallel directions were handled using the PPPM method in LAMMPS in a slab mode (and explicitly removing wall-normal forces). Motivating the use of PPPM for this component of the field is the fact that using the Fourier basis is more efficient than a general FE basis, whereas the AtC method's purpose is to account for inhomogeneous directions with Dirichlet and Neumann boundary conditions. The Green's functions used to correct the short-range interactions by the AtC method are nontrivial to implement correctly for periodic boundaries because if they account for the periodicity they will remove too much force, as noted in Section 2.3. Specifically, the long-range forces from periodic images of nearby atoms will be canceled. Note the short-range electrostatic interactions are handled using the standard Coulombic formulation implemented directly in LAMMPS.

As previously noted, the PPPM approach requires approximations in the wall-normal direction, which can be avoided by using the AtC method to compute the wall-normal electric potential. In order to have the correct total potential when each component is summed, fixed (zero) potential boundary conditions are used at the layer of silicon atoms adjacent to the salt water. Use of these boundary conditions also mitigates the numerical errors in the wall-normal direction of the periodic Green's functions. Grid spacing of the AtC FE mesh is chosen to be half the cutoff radius to minimize the impact of errors from the electric field solve on the atomic forces. In general, the grid spacing should be less than the cutoff radius because of the numerical errors associated with approximating the delta functions due to the point charges in the source term. However, within the present formulation, if a fixed cutoff radius is used, then the total electrical interactions will converge with mesh refinement. A fully three-dimensional grid is used for the AtC solve so that spatial variations in the electric field are accounted for in the wall-normal electric forces. Periodic boundary conditions are applied in the wall-parallel directions to the AtC FE solution to generate an accurate electric potential. This approach of decomposing the total potential therefore enables each method to be used to greatest effect.

The results of this calculation demonstrate the appropriateness of using the AtC electric potential in directions in which spatial symmetries are broken. In this case, an electric double layer forms on each surface mitigated by the wall-normal electric forces. As in the case of Qiao and Aluru, insufficient charge is

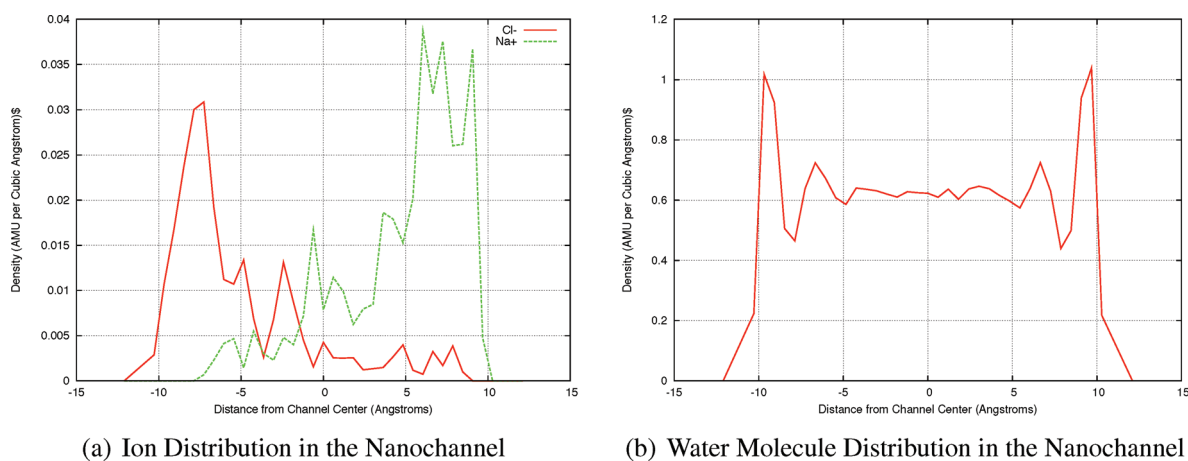


Figure 10. Plane-averaged wall-normal density profiles of the species present in the nanochannel: (a) charged ions and (b) water molecules.

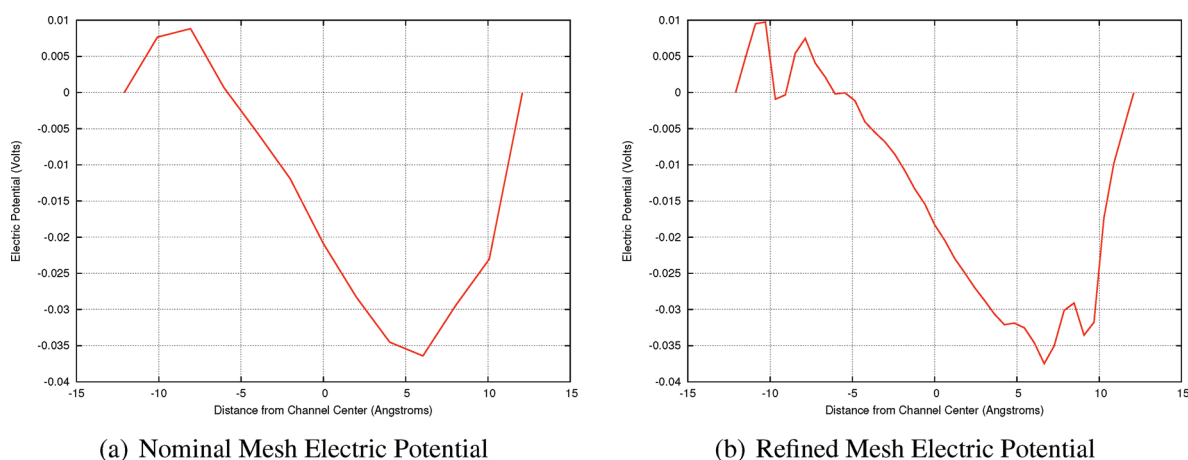


Figure 11. Plane-averaged wall-normal electric potential induced by ions in the nanochannel: (a) nominal mesh and (b) refined mesh.

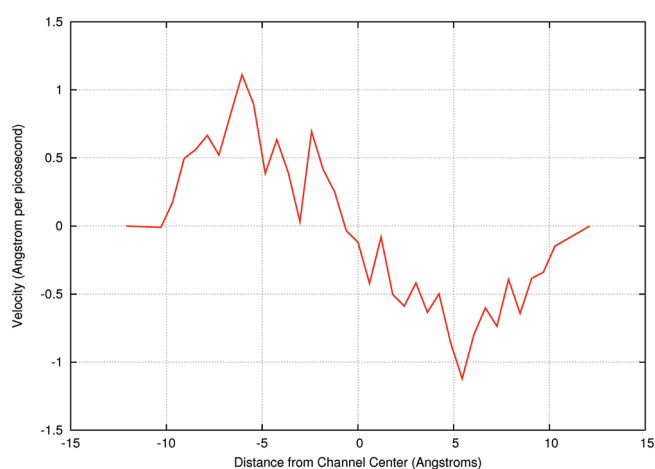


Figure 12. Plane-averaged wall-normal velocity profile of the water molecules.

included in the solution to fully screen the applied electric field. Some ions form an adsorbed layer adjacent to the wall, while others remain in solution but preferentially distributed based the electric field, as shown in Figure 10. Both the ions and water

demonstrate layering effects based on the electric field and nanoscale dimensions of the channel. Figure 11 illustrates how the electric potential induced by the ions reflects this structure with near wall extrema. The field is much smoother than the ionic distributions because the element size is greater than the layering size. Therefore short-range electrical interactions account for the ionic layering, while the long-range effects determine the interaction between the species segregated on opposite walls. Calculating this potential with sufficient fidelity to accurately capture the long-range interactions is critical. To demonstrate an appropriate mesh spacing exists, a further run was performed using an eight-fold mesh refinement in the wall-normal direction. The resulting potential, provided in Figure 11b, now has multiple near-wall extrema due to the layering. However, this structure is not needed for the long-range interactions, and the observation that the overall potential drop and the field structure are unchanged verifies the appropriateness of the original mesh. Finally, the resulting velocity profile is presented in Figure 12, confirming the flow is slower near the channel center as it is primarily driven by the ions in the double layers near the walls. In a technological application, this would be the relevant quantity determining device performance.

4. CONCLUSIONS AND FUTURE WORK

This work describes a method to apply consistent anisotropic electric fields, including prescribed boundary conditions, to molecular dynamics simulations. By using AtC coupling, the electric potential can be solved on a FE mesh using source terms arising from the atomistic charge distribution. The approach is a significant improvement over current schemes for incorporating long-range electrical interactions, which are restricted to periodic domains. By breaking this symmetry, the AtC electric field enables simulations of more technologically relevant configurations with applied electric fields or potential surfaces.

The AtC coupling methodology in this work can be thought of as a generalization of previous methods, such as PPPM, to a wider set of basis functions for representing the electric potential. By choosing appropriate functions from this set, a framework has been developed that does not rely upon periodic boundary conditions to compute long-range electrical interactions. Three core numerical techniques comprise the method. The first is restriction of atomic charge information to a continuous density fields represented on a FE mesh, similar to kernel estimation. Next, the electric potential is solved on the FE mesh using a Poisson equation with appropriate sources based on electrostatics. Finally, the electric forces due to this potential are computed on a per-atom basis and corrected based on resolved short-range interactions. The FE potential solve allows for standard fixed potential and fixed field boundary conditions. In addition, approximate boundary conditions for charged surfaces were also presented. Periodic boundaries are currently handled through combining this approach with existing long-range electric field methods.

To demonstrate the correctness of this method, four example simulations were performed. To verify the restriction of atomic information and the Poisson solution, including Dirichlet and Neumann boundary conditions, a simple block of charged atoms was considered. Excellent agreement between the resulting electric potentials with analytic solutions was obtained. Next, the method was compared with the PPPM and Ewald sum techniques implemented in LAMMPS using a charge neutral bar with blocks of opposite charge separated by more than the Coulombic interaction cutoff distance. All three methods computed the forces between the charged blocks to four significant digits, showing the accuracy of the atomic projection step. The case also demonstrated reasonable mesh size guidelines. A final verification problem examined a small box of fluid argon atoms, some charged, some not, in the presence of a charged surface. Direct MD computations were possible by retaining a very long cutoff radius for the Coulombic interactions. Comparison with the proposed method was possible by using approximate boundary conditions at the charged surface as well as zero-field conditions on the other sides of the box. Despite these approximations, good agreement was demonstrated between the method for both the transient development of the layer of charged argon near the surface and for the steady-state ion density profiles.

While the previous simulations compared the proposed method to existing analytical and numerical solutions, they did not examine the technique in one of its intended applications. Therefore, flow in a silicon nanochannel was modeled using the AtC method to compute shear flow in a NaCl solution between oppositely charged plates. This case demonstrates the steps that must be taken to perform these simulations by incrementally building and equilibrating the various components, such as silicon and water,

followed by applying separate models for the isotropic and anisotropic components of the electric field. As expected, ions congregated near oppositely charged walls, while a parallel electric field accelerated the ions, causing a shear flow to develop. These results show that information relevant to both scientific understanding and technological applications can be obtained using this formulation.

As demonstrated by the various simulations, this technique enables MD to be used to examine a new class of problems in which spatial symmetries are not present, making periodic boundary conditions inappropriate. The ability to prescribe boundary conditions means that interactions with the environment can be included in an approximate manner. However, defining physically appropriate boundary conditions for molecular systems is challenging and depends on the type of environment. Future work will enhance the method by developing appropriate boundary conditions for other types of physics, e.g., conducting and insulating surfaces. Error analysis, based on the FE mesh spacing, and the Coulombic cutoff radius will also be considered to automate the mesh generation process. Even without these features, the present method still represents an important improvement in MD capabilities by enabling long-range electric field effects to be incorporated in complex geometries with a generalized set of boundary conditions.

AUTHOR INFORMATION

Corresponding Author

*E-mail: jatempl@sandia.gov.

Present Addresses

^{||}Rice University, Department of Mechanical Engineering and Materials Science, Houston, Texas, United States.

ACKNOWLEDGMENT

Sandia National Laboratories is a multiprogram laboratory managed and operated by Sandia Corporation, a wholly owned subsidiary of Lockheed Martin Corporation, for the U.S. Department of Energy's National Nuclear Security Administration under contract DE-AC04-94AL85000. Funding for this work was provided by the Laboratory Directed Research and Development program at Sandia National Laboratories, and its support is gratefully acknowledged. The authors appreciate P. Crozier, G. Wagner, and S. James for providing helpful comments on a draft of this manuscript. The sparse vector software used in this work was implemented by J. Oswald.

REFERENCES

- (1) Frenkel, D.; Smit, B. *Understanding Molecular Simulation: From algorithms to applications*; Academic Press: San Diego, CA, 2002.
- (2) Goodenough, J.; et al. *Basic Research Needs for Electrical Energy Storage*; Technical Report; Office of Science, U.S. Department of Energy: Washington, DC, 2007.
- (3) Allen, M.; Tildesely, D. *Computer Simulation of Liquids*; Clarendon Press: Oxford, U.K., 1987.
- (4) Hockney, R.; Eastwood, J. *Computer Simulation using Particles*; Taylor & Francis Group: Bristol, PA, 1988.
- (5) Darden, T.; York, D.; Pedersen, L. *J. Chem. Phys.* **1993**, *98*, 10089–10092.
- (6) Torrie, G.; Valleau J. *Chem. Phys. Lett.* **1979**, *65*, 343.
- (7) Greengard, L.; Rokhlin, V. *J. Comput. Phys.* **1987**, *73*, 325–348.
- (8) in 't Veld, P. J.; Ismail, A. E.; Grest, G. S. *J. Chem. Phys.* **2007**, *127* 144711.

- (9) Pollock, E.; Glosli, J. *Comput. Phys. Commun.* **1996**, *95*, 93–110.
- (10) Parry, D. E. *Surf. Sci.* **1975**, *49*, 433–440.
- (11) Heyes, D.; Barber, M.; Clarke, J. H. R. *J. Chem. Soc., Faraday Trans. 2* **1977**, *73*, 1485–1496.
- (12) de Leeuw, S. W.; Perram, J. W. *Mol. Phys.* **1979**, *37*, 1313–1322.
- (13) Shelley, J.; Patey, G.; Berard, D.; Torrie, G. J. *J. Chem. Phys.* **1997**, *107*, 2122–2141.
- (14) Spohr, E. *J. Chem. Phys.* **1997**, *107*, 6342–6348.
- (15) Qiao, R.; Aluru, N. J. *J. Chem. Phys.* **2003**, *118*, 4692–4701.
- (16) Yeh, I.-C.; Berkowitz, M. J. *J. Chem. Phys.* **1999**, *111*, 3155.
- (17) Yang, Y.; Henderson, D.; Crozier, P.; Rowley, R.; Busath, D. *J. Chem. Phys.* **1983**, *79*, 926–935.
- (18) Sachs, J.; Crozier, P.; Woolf, T. *J. Chem. Phys.* **2004**, *121*, 10847–10851.
- (19) Ballenegger, V.; Arnold, A.; Cerda, J. *J. Chem. Phys.* **1983**, *79*, 926–935.
- (20) Crozier, P.; Rowley, R.; Spohr, E.; Henderson, D. *J. Chem. Phys.* **2000**, *112*, 9253–9257.
- (21) Patra, M.; Hyvonen, M.; Falck, E.; Sabouri-Ghomi, M.; Vattulainen, I.; Karttunen, M. *Comput. Phys. Commun.* **2007**, *176*, 14–22.
- (22) Miller, R.; Tadmor, E. *Model. Simul. Mater. Sci. Eng.* **2009**, *17*, 053001.
- (23) Wagner, G.; Jones, R.; Templeton, J.; Parks, M. *Comput. Meth. Appl. Mech. Eng.* **2008**, *197*, 3351–3365.
- (24) Plimpton, S. J. *Comput. Phys.* **1995**, *117*, 1–19.
- (25) MacKerell, A.; *J. Phys. Chem. B* **1998**, *102*, 3586–3616.
- (26) Hoover, W. *Phys. Rev. A* **1985**, *31*, 1695–1697.
- (27) Stillinger, F.; Weber, T. *Phys. Rev. B* **1985**, *31*, 5262–5271.
- (28) Jorgensen, W.; Chandrasekhar, J.; Madura, J.; Impey, R.; Klein, M. *J. Chem. Phys.* **1983**, *79*, 926–935.
- (29) Zimmerman, J.; Webb, E.; Hoyt, J.; Jones, R.; Klein, P.; Bammann, D. *Model. Simul. Mater. Sci. Eng.* **2004**, *12*, S319–S332.

The Significance of Parameters in Charge Equilibration Models

T. Verstraelen,^{*,†} P. Bultinck,[‡] V. Van Speybroeck,[†] P. W. Ayers,[§] D. Van Neck,[†] and M. Waroquier[†]

[†]Center for Molecular Modeling, QCMM Alliance Ghent-Brussels, Ghent University, Technologiepark 903, B-9052 Zwijnaarde, Belgium

[‡]Department of Inorganic and Physical Chemistry, QCMM Alliance Ghent-Brussels, Ghent University, Krijgslaan 281 (S-3), B-9000 Gent, Belgium

[§]Department of Chemistry, McMaster University, 1280 Main Street West, Hamilton, Ontario, Canada

S Supporting Information

ABSTRACT: Charge equilibration models such as the electronegativity equalization method (EEM) and the split charge equilibration (SQE) are extensively used in the literature for the efficient computation of accurate atomic charges in molecules. However, there is no consensus on a generic set of optimal parameters, even when one only considers parameters calibrated against atomic charges in organic molecules. In this work, the origin of the disagreement in the parameters is investigated by comparing and analyzing six sets of parameters based on two sets of molecules and three calibration procedures. The resulting statistical analysis clearly indicates that the conventional least-squares cost function based solely on atomic charges is in general ill-conditioned and not capable of fixing all parameters in a charge-equilibration model. Methodological guidelines are formulated to improve the stability of the parameters. Although in this case a simple interpretation of individual parameters is not possible, charge equilibration models remain of great practical use for the computation of atomic charges.

I. INTRODUCTION

A thorough understanding and efficient computation of molecular interactions is of fundamental importance in computational chemistry.¹ Electrostatic interactions are typically the strongest intermolecular interactions and therefore play a dominant role in many important processes in extended molecular systems such as drug-receptor interactions in proteins,² host-guest interactions in zeolites,^{3–5} reactions in solvents,^{6–8} and so on.

Molecular electrostatics can to a large extent be rationalized in terms of the molecular charge distribution condensed into the atoms that compose the molecule, i.e., through the assignment of effective atomic charges. Although the concept of charges on the atoms in the molecule (AIM) is evident for most chemists, it is far less obvious to define them in a quantum-mechanical context.^{9–11} AIM charges can be computed in a multitude of ways. One group of methods relies on the introduction of AIM subspaces within the molecule. Many such density or wave function partitioning schemes were proposed over the past 60 years to divide molecules into atomic parts, e.g., Mulliken population analysis (MPA),¹² Lowdin population analysis,¹³ Hirshfeld partitioning,¹⁴ natural population analysis (NPA),¹⁵ Bader's AIM scheme,¹⁶ Hirshfeld-I partitioning,¹⁷ and so on. Besides this class of methods, atomic charges can also be fitted to reproduce the electrostatic potential around a molecule,¹⁸ with for example the Merz–Kollman¹⁹ or RESP scheme.²⁰ Nevertheless, a quantum mechanically unique definition of the atom in the molecule, and thus the atomic charge, remains problematic.⁹ At best, one can test and assess a population scheme using as criteria its basis-set and geometry independence, and its accuracy with respect to the molecular electrostatic potential. Benchmark studies showed that the Hirshfeld-I¹⁷ scheme performs well in this regard.^{21–23} Despite its attractive features, both from the application and information

theoretical viewpoints, it is not feasible to compute Hirshfeld-I charges on extended systems with many thousands of atoms. The prerequisite for any type of charge population scheme is the computation of the total electron density of the molecular system with a reliable electronic structure method, which becomes prohibitive for large systems, or even for smaller systems when the molecular environment is included explicitly.

An alternative approach for the computation of effective atomic charges is through charge equilibration models.²⁴ These models are derived from rigorous density functional theory but are computationally much less demanding than full electronic structure computations. As a consequence, they are sometimes considered a kind of semiempirical density functional theory.²⁵ Charge equilibration models allow an efficient computation of the charge distribution in large molecular systems, while the corresponding electronic structure computation requires an enormous computational effort. This advantage of charge equilibration models enables many attractive applications, including high-throughput screening of drug candidates due to the possibility of computing diverse molecular properties very quickly.^{26,27} Moreover, charge equilibration models are a cornerstone in advanced molecular mechanics developments such as polarizable force fields^{28–30} and reactive force fields.³¹

Charge equilibration models have an intrinsic weakness: one needs to determine many model parameters with ad hoc calibration methods before one can actually apply charge equilibration models. Optimally, one could hope that the calibrated parameters have a clear physical interpretation, i.e., that one can find an ultimate set of parameters that both satisfy intuitive

Received: January 4, 2011

Published: May 02, 2011

Table 1. Non-Exhaustive Overview of EEM Parameters (in eV) Reported in the Literature^a

reference		H	C	N	O	F	S	Cl	Br
Mortier and Baekelandt (a): HF/STO-3G MPA	χ	4.4	5.7	10.6	8.5				
	η	27.6	18.2	26.4	22.2				
Rappe (b)	χ	4.5280	5.343	6.899	8.741	10.874	6.928	8.564	7.790
	η	13.8904	10.126	11.760	13.364	14.948	8.972	9.892	8.850
Menegon (c): PM3 CM1	χ	3.885	4.656	7.175	10.075				
	η	18.404	14.264	13.452	20.690				
Bultinck (d): B3LYP/6-31G* MPA	χ	1.0	5.25	8.80	14.75	15.0			
	η	35.9	18.0	18.78	28.68	39.54			
Bultinck (d): B3LYP/6-31G* NPA	χ	1.0	8.49	13.45	27.06	39.18			
	η	38.88	18.3	20.92	39.26	88.2			
Verstraelen (e): METS, MP2/Aug-cc-pVDZ MPA	χ	9.73	6.94	10.42	25.59	29.26	5.68	5.99	-3.84
	η	19.50	12.65	19.85	40.05	39.91	9.87	32.08	33.64
Verstraelen (e): NETS, MP2/Aug-cc-pVDZ NPA	χ	1.81	4.65	6.26	8.65	17.79	3.54	3.45	1.15
	η	19.36	11.47	12.18	14.92	39.32	8.24	33.09	32.77
Verstraelen (e): HETS, MP2/Aug-cc-pVDZ Hirshfeld-I	χ	6.37	7.37	8.03	9.23	16.31	6.98	10.19	8.11
	η	15.54	10.74	10.93	12.85	38.37	7.86	31.89	31.94

^a(a) Refs 32, 39. (b) Ref 35. (c) Ref 40. (d) Refs 26, 37, 38. (e) Ref 36. The acronyms METS, NETS, and HETS refer to calibrations of the EEM model as discussed in this work, using Mulliken, natural, and Hirshfeld-I charges, respectively.

expectations and reproduce a set of reference charges used for the calibration.

Two important charge equilibration models have been proposed in the literature: the electronegativity equalization method³² (EEM) and the split charge equilibration (SQE)³³ model. All of the model parameters in these models can be given a physical meaning. Since charge equilibration is fundamentally rooted in density functional theory, and the model parameters are closely related to properties of atoms in a vacuum³² and electrostatic properties of extended systems,³⁴ one would expect that the corresponding calibrated parameters can be given a physical interpretation and are unique. Unfortunately, the EEM parameter sets reported in the literature show large fluctuations. A nonexhaustive overview of EEM parameters^{32,35–40} calibrated for organic systems is given in Table 1. Even the electronegativity and hardness parameters of carbon are scattered over ranges of 4.65–8.49 eV and 10.13–18.30 eV, respectively. As shown below, part of the differences may be due to the use of different electrostatic interaction models, e.g., point charge versus Gaussian charge. This tabulation raises the concern that EEM parameters may not have any physical interpretation, simply because no consensus can be extracted from the sets of EEM parameters in the literature. This is also problematic from the practical perspective: which set of parameters is trustworthy for computational applications? A thorough analysis of the spread on the parameters and its origin is required to re-establish the credibility of charge equilibration models.

The primary objective of this work is therefore an in-depth investigation of the reasons underlying the spread in the reported EEM parameters, and a similar analysis for the SQE model. As a side effect, many practical guidelines will be formulated to improve the quality of calibrated charge equilibration parameters.

The paper is structured as follows: The EEM and SQE models are introduced in section II. The next section, section III, first reviews the conventional parameter calibration methods, which are also used in this work to investigate the spread in the calibrated parameters. Then, the various analysis techniques that

are introduced to understand the origin of the fluctuations in the parameters are highlighted. In section IV, we discuss the results of the parameter calibrations and analysis techniques. Finally, section V summarizes the findings of this work and formulates some guidelines for future EEM and SQE calibrations.

II. THEORETICAL CHARGE EQUILIBRATION MODELS

EEM. The EEM model describes charge equilibration in molecular systems based on the effective atomic charges, their electrostatic interaction, and additional local energy terms. It is basically a second order expansion of the molecular energy in terms of atomic partial charges and has the following general mathematical form:

$$E_{\text{EEM}} = v^T q + \frac{1}{2} q^T J q \quad (1)$$

In this expression, q is a column vector of length N containing the effective atomic charges, v is a column vector of length N containing the first-order coefficients, and J is an $N \times N$ matrix containing the second-order coefficients.

The electronegativity equalization method³² (EEM) postulates specific mathematical expressions for the elements J and v based on density functional theory. The diagonal elements of matrix J are the atomic hardness parameters, η_i . The off-diagonal elements model the electrostatic interactions between atom pairs. In the original work of Mortier et al.,³² a simple point charge model is used, leading to $J_{ij} = 1/r_{ij}$ for the off-diagonal elements, where r_{ij} is the distance between atoms i and j . (Atomic units are used throughout.) Smeared-charge electrostatic interactions were introduced in subsequent papers by various authors to account for the finite size of the atomic charge distribution.^{28,35,36,41,42} A particular advantage of the smeared-charge potentials is that one can introduce lower bounds for the hardness parameters to guarantee a positive definite matrix J .^{36,43} The elements in the vector v are the atomic electronegativity parameters, χ_i . Although the electronegativity and hardness parameters should correspond approximately to their gas-phase

values,^{32,44} they are in practice calibrated to quantum mechanical reference data (e.g., atomic charges from some AIM method or the molecular electrostatic potential from a quantum chemical calculation) for a large training set of molecules,^{26,36–38,45–48} as further discussed in section III.

The equilibrium charge distribution is the vector of atomic charges that minimizes the energy in eq 1 under a total charge constraint. The conventional approach is to introduce a Lagrange multiplier, λ , as follows:

$$\tilde{E}_{\text{EEM}} = v^T q + \frac{1}{2} q^T J q - \lambda (d^T q - Q_{\text{tot}}) \quad (2)$$

where d is a column vector with N elements, all equal to one. The equations for the equilibrium charges require that the derivatives of \tilde{E}_{EEM} toward the partial charges are zero and that the total charge constraint is satisfied, which leads to a set of linear equations. These equations are conveniently written in block matrix notation:

$$\begin{bmatrix} J & -d \\ -d^T & 0 \end{bmatrix} \begin{bmatrix} q \\ \lambda \end{bmatrix} = - \begin{bmatrix} v \\ Q_{\text{tot}} \end{bmatrix} \quad (3)$$

where dotted lines do not only separate block matrices but also vectors, as in $[q; \lambda]^T$. These equations reveal that the electronegativity of all atoms, $\partial E_{\text{EEM}}/\partial q_i$, must be equal to the Lagrange multiplier. Hence, one often uses the term *equalized electronegativity* or *molecular electronegativity* for the Lagrange multiplier, and one refers to this method as the *electronegativity equalization method*. In the remainder of the text, we will use the symbol χ_{mol} instead of λ .

It is clear that the charges minimizing the energy \tilde{E}_{EEM} in eq 2 are invariant when changing all electronegativity parameters by the same amount: $\chi_i \rightarrow \chi_i + \alpha$. Therefore, the individual χ_i 's are only determined up to an additive constant when only reference charges are used for the calibration. The following extension of the EEM model involving a charge bath is used in the calibration process to avoid serious deviations from the physical atomic electronegativities. A molecule is allowed to exchange charge with a charge bath that has an electronegativity, χ_{bath} , equal to the Mulliken electronegativity⁴⁹ of the molecule as derived from the quantum mechanical (QM) computation,

$$E_b = v^T q + \frac{1}{2} q^T J q - \chi_{\text{bath}} (d^T q - Q_0) + \frac{1}{2} \eta_{\text{bath}} (d^T q - Q_0)^2 \quad (4)$$

where Q_0 is the target value for the total charge of the molecule and η_{bath} determines the strength of the restraint penalty. The condition for a minimum is

$$v^T q + J q = \chi_{\text{bath}} d - \eta_{\text{bath}} (d^T q - Q_0) d \quad (5)$$

As one can see, the total charge constraint of the molecule, $d^T q - Q_0 = 0$, can only be realized when the atomic equalized electronegativities (left side of eq 5) are all equal to the bath electronegativity. Otherwise, the molecule would exchange charge with the bath. Conventional calibration methods try to reproduce QM atomic charges and are therefore sensitive to errors in the total charge as well. As a result, the optimized parameters will not show deviations between the QM Mulliken electronegativity⁴⁹ and the EEM equalized electronegativity. The hardness of the charge bath is used to control the relative importance of a correct

equalized electronegativity and the correct total charge. In the limit of a very high bath hardness, the restraint behaves like a conventional constraint, and the cost function becomes again insensitive to errors in the equalized electronegativity. In this work, a bath hardness of 5 eV is used, which results in a weak influence of the QM Mulliken electronegativities in the calibration procedure. In previous works, where a strict charge constraint is used during the calibration, the reference value for the electronegativity parameters is not determined by the training data. Instead, an arbitrary constraint on one of the atomic electronegativities is imposed.³⁷ We will demonstrate in section IV that the charge-bath approach indeed fixes the reference value for the atomic electronegativity parameters based on QM data.

One drawback of the EEM is that the model systematically overestimates the molecular polarizability of insulators in the limit of large molecules. In the macroscopic limit, the polarizability per unit volume of an insulator becomes constant, while the EEM predicts a quadratic increase with system size.^{29,33,43,50} One pernicious consequence is that EEM predicts vanishing multipole moments for large systems due to internal charge redistribution.⁴³ A solution is provided by the SQE model as introduced in the next section.

SQE. The second model relies on the introduction of a new set of variables, the so-called split-charges,³³ p_{ji} , which are linearly related to the effective charges as follows:

$$q_i = \frac{Q_{\text{tot}}}{N} + \sum_{j \neq i} p_{ji} \quad (6)$$

where the summation runs over all atoms j that are covalently bonded to atom i . The symbol p_{ji} stands for the charge transferred from atom j to atom i ; therefore, $p_{ji} = -p_{ij}$. This notation implicitly assumes that charge transfer is only possible between fragments that are connected through covalent bonds, which does not pose any difficulties for the molecules studied in this paper. The total charge constraint is realized by treating Q_{tot} as a constant after the transformation, or by using Q_{tot} as a variable in the charge bath approach. In the case of molecular ions, this approach assumes that the excess charge is distributed equally over the entire molecule. Although one may obtain a more accurate model by placing the excess charge in specific atoms, this choice is the simplest possible and does not introduce additional parameters.

For the remainder of the paper, it is convenient to introduce a matrix notation for the split charges, which allows for a straightforward substitution of eq 6 into the energy expression in eq 1. For each bond, we introduce an index k going from 1 to N_{cov} , where N_{cov} is the total number of covalent bonds. For each bond k that connects atom i_k and j_k , let $t_k = p_{j_k i_k}$ with $j_k < i_k$. This choice eliminates the need for the constraint $p_{ij} = -p_{ji}$. The matrix notation for eq 6 becomes

$$q = U u \quad \text{with} \quad U = \begin{bmatrix} T & \frac{d}{N} \end{bmatrix} \quad \text{and} \quad u = \begin{bmatrix} t \\ Q_{\text{tot}} \end{bmatrix} \quad (7)$$

where T is the transfer matrix with N rows and N_{cov} columns and t is the column vector with N_{cov} split charges. Each column k of matrix T contains only two nonzero elements corresponding to the atoms j_k and i_k that are connected by bond k . By construction, the first nonzero element of each column is +1 and the second is -1. For example, the matrix U of a water molecule, where the oxygen

atom comes first, has the following form:

$$\begin{bmatrix} 1 & 1 & 1/3 \\ -1 & 0 & 1/3 \\ 0 & -1 & 1/3 \end{bmatrix}$$

The split charge equilibration³³ (SQE) is an improvement of the EEM with an additional second-order term borrowed from the atom–atom charge transfer (AACT) model²⁹ to yield the correct trend of the polarizability for large systems, and with an extra first-order term to obtain an improved fitting of the equilibrium charges. When the parameters in the extra terms are set to zero, one retrieves the original EEM form. The additional second order term, $\sum_{k=1}^{N_{\text{cov}}} \kappa_k t_k^2$, is diagonal in the split charges and represents a harmonic energy term for the charge transferred through a chemical bond. The bond hardness parameter, κ_k , is a constant that depends on the type of bond. Bonds in conductor-like systems have a low bond hardness, while bonds in dielectric systems with low polarizability have a high bond hardness.³⁴ The linear term is a bond correction for the atomic electronegativity parameters. For each bond k , the electronegativity parameter of atom j_k is increased by $\Delta\chi_{j_k i_k}$ and the electronegativity parameter of i_k is decreased by the same amount. By construction, the correction parameters obey $\Delta\chi_{j_k i_k} = -\Delta\chi_{i_k j_k}$. The parameter $\Delta\chi_{j_k i_k}$ is a constant associated with the type of bond between atoms i_k and j_k . It mainly influences the charge distribution between bonded atoms and can be interpreted as an ad hoc correction to the atomic electronegativity parameters due to the direct molecular environment.

We must introduce a convention for the electronegativity correction parameters, in analogy with the definition of t_k to obtain a practical matrix notation for the SQE model. For every bond k , we define $c_k = \Delta\chi_{j_k i_k}$ with $j_k < i_k$, which is now a set of independent parameters. The vector with corrections to the atomic electronegativity parameters is written as

$$v' = Tc \quad (8)$$

where T is the transfer matrix and c is a vector of length N_{cov} with electronegativity correction parameters. In terms of the split charges and the total charge, one can write the EEM energy (eq 1) as

$$E_{\text{EEM}} = v^T U u + \frac{1}{2} u^T U^T J U u \quad (9)$$

The SQE energy,

$$E_{\text{SQE}} = (v + v')^T U u + \frac{1}{2} u^T (U^T J U + J') u \quad (10)$$

has a comparable form but contains an additional linear and quadratic term. The matrix J' is a diagonal matrix with $N_{\text{cov}} + 1$ rows and columns. The first N_{cov} diagonal elements are the bond hardness parameters; the last diagonal element is zero.

III. COMPUTATIONAL METHODS

Parameter Calibration. The parameters in the EEM (η_i and χ_i) and the SQE model (η_i , χ_i , κ_k and c_k) must be calibrated with respect to a set of training data in order to obtain a useful model. In this process, one has to introduce atom and bond types and associate unique parameters with atoms or bonds of the same type. Several papers in the literature have used atomic charges, based on QM computations for a set of organic molecules, as

Table 2. Main Characteristics of the Two Training Sets (P^{27,37,38} and T³⁶) Used for the Calibration of Charge Equilibration Parameters

	set P	set T
# molecules	166	500
# H atoms	1080	1899
# C atoms	714	1651
# N atoms	121	657
# O atoms	108	496
# F atoms	65	99
# S atoms		267
# Cl atoms	30	116
# Br atoms		44
# neutral	166	419
# positive		32
# negative		49

reference data.^{26,32,37–39,51} One postulates an objective function to measure the mismatch between the model charges and the QM charges:

$$X = \sum_{m=1}^M \sum_{i=1}^{N_m} w_{m,i} (q_{m,i}^{\text{QM}} - q_{m,i}^{\text{MODEL}})^2 \quad (11)$$

The first sum runs over the molecules in the set of training data for which QM computations have been carried out. The second sum runs over all atoms within molecule m . For each atom, the difference between the QM atomic charge, $q_{m,i}^{\text{QM}}$, and the charge obtained with the equilibration model for a given set of parameters, $q_{m,i}^{\text{MODEL}}$, is squared and multiplied with a weight $w_{m,i}$. In the conventional treatment of the least-squares procedure,⁵² the weights are related to the measurement error on the reference data. In this context, the reference data consists of theoretical numbers without measurement errors, and one must resort to ad hoc schemes to define the weights.^{36,37} Through the model charges, the cost function, X , becomes a function of the parameters. This cost can be minimized to find the parameters that result in an optimal performance for the selected training set.

A local minimization of the cost function (eq 11) may lead to multiple and disparate solutions for two reasons. Both may explain the large variety of EEM parameters reported in the literature. In the first place, due to the nonlinear dependence of the model charges on the second-order parameters, the cost function in eq 11 can in principle have multiple local minima. However, even if one finds the global minimum, the cost function may have (around the global minimum) a few directions of low curvature, which implies that very different sets of parameters are degenerate and thus equally good. The exact position of the minimum of the cost function along those directions is sensitive to small changes in the training data, and is therefore significantly affected by the model-development choices like the selection of molecules in the training set, the definition of atom types, and the population scheme used to define the QM atomic charges. We will investigate the relative importance of both mechanisms and their impact on the interpretation of calibrated parameters.

The calibration procedure used in this work is largely based on a previous EEM/SQE benchmark paper,³⁶ and we refer to that work for a detailed description. Our in-house code QFIT is used for the calibration of the parameters. The implementation of QFIT relies extensively on the MOLMOD library, which is also

Table 3. Summary of the Three Parameter Calibration Procedures

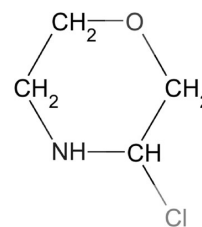
procedure	model	atom types	population scheme
1	EEM	element	Hirshfeld-I
2	EEM	element	Mulliken
3	SQE	force field	Hirshfeld-I

the basis for other software projects such as ZEOBUILDER,⁵³ MD-TRACKS,⁵⁴ and TAMKIN.⁵⁵ Below, we review the most important aspects of the calibration for this paper.

Two different sets of molecules are used for the calibration. The first set (P) consists of 166 organic molecules with elements H, C, N, O, F, and Cl; it is based on the work of Bultinck et al.^{26,37,38} The second set (T) contains 500 organic molecules comprising the elements H, C, N, O, F, S, Cl, and Br and is taken from the benchmark paper of Verstraelen et al.³⁶ A summary with the main characteristics of each set is given in Table 2. Lewis structures of each molecule are given in the first section of the Supporting Information. The geometry of each molecule is optimized at the MP2/CC-pVDZ level, followed by a single point calculation of the wave function at the MP2/Aug-CC-pVDZ level,^{56,57} using the Gaussian 03⁵⁸ program. Mulliken¹² and Hirshfeld-I¹⁷ charges are derived from the MP2/Aug-CC-pVDZ wave functions. For each molecule, the single point computation is repeated on the same geometry with one additional electron and one electron less to compute the molecular electronegativity with the Mulliken definition,⁴⁹ not to rely on Koopmans' theorem.⁵⁹ The parameters are calibrated in six different ways, using three different procedures applied to the sets P and T. The first two procedures are based on the EEM and group parameters per element, i.e., all atoms of a given element share the same parameters. The first procedure employs Hirshfeld-I charges as reference data, while the second uses Mulliken charges. The third procedure is based on the SQE and combines the atomic number and the number of bonds to define force-field atom (and bond) types and further uses Hirshfeld-I charges. Previous work showed that force-field atom types are only of fundamental importance in the context of the SQE model.^{36,37} The three different procedures are summarized in Table 3. The six combinations of training set and calibration procedure are denoted in the remainder of the text as P1, P2, P3, T1, T2, and T3. Note that T1, T2, and T3 correspond to calibrations HETS (Hirshfeld-I + EEM + trivial atom types + static cost function), METS (Mulliken + EEM + trivial atom types + static cost function), and HSFS (Hirshfeld-I + SQE + force field atom types + static cost function), respectively, in the benchmark paper of Verstraelen et al.³⁶ The parameters found in this work are slightly improved because of improvements in the conjugate gradient routine used to minimize the cost function. The prevalent atomic elements and force-field atom (and bond) types in both training sets are tabulated in the second section of the Supporting Information.

During the calibration, a lower bound is imposed on all second-order parameters to guarantee a positive definite matrix J in eq 1 for all possible molecular geometries.⁴³ The atoms in the EEM and SQE model in this paper are treated as Gaussian effective charge distributions. The distribution centered at the atom has the form of an S-type Gaussian:

$$\rho_i(\mathbf{r}) = q_i(R_i^2\pi)^{-3/2}\exp\left(-\frac{|\mathbf{r}-\mathbf{r}_i|^2}{R_i^2}\right) \quad (12)$$

**Figure 1.** The chemical structure of 3-chloromorpholine.

where R_i is the radius of atom i and \mathbf{r}_i , its position. The atomic radius parameters are based on the covalent radius of the atom.⁶⁰ For hydrogen three times the covalent bond radius is used. For all other atoms, 1.5 times the covalent bond radius is used. The minimal value for the atomic hardness parameter is equal to the self-interaction of the charge distribution of the atom divided by q_i^2 :

$$\eta_{i,\min} = \frac{1}{q_i^2} \int \frac{\rho_i(\mathbf{r}) \rho_i(\mathbf{r}')}{|\mathbf{r}-\mathbf{r}'|} d\mathbf{r} d\mathbf{r}' = \sqrt{\frac{2}{\pi}} \frac{1}{R_i} \quad (13)$$

The radii and minimal values for the atomic hardness parameters are tabulated in section 3 of the Supporting Information. The bond hardness parameters must be larger than zero. With these lower bounds, the hardness matrix is always positive definite.⁴³ This is not only interesting from a physical point of view, as it ensures that the energy function in eq 1 has a minimum. It also renders the calibration of the parameters more tractable, as the cost function in eq 11 diverges for parameters that make the hardness matrix singular for one of the molecules in the training set.^{61,62} The restriction of the parameters to positive definite hardness matrices therefore confines the parameters to the region where the cost function is well-behaved, which is beneficial for the optimization of the parameters.

Parameter Scans. The minimum of the cost function in eq 11 does not necessarily correspond to a sharply determined point in the multidimensional parameter space. The minimum may also lie in an elongated valley where many disparate parameter vectors lead to virtually the same (minimal) value of the cost function. Elongated valleys imply a low local curvature of the cost function at the position of the optimal parameters. Because the cost function is multidimensional, this local curvature is characterized by the Hessian, i.e., the symmetric matrix of second-order derivatives with respect to the parameters. Eigenvectors of the Hessian associated with relatively small eigenvalues correspond to displacements of the optimal parameters that lead to a relatively small increase in the cost function. The spectrum of the Hessian, computed from finite differences of the analytical first-order derivatives, is analyzed for all six calibrations in this paper. In general one can use the condition number of the Hessian, defined as the ratio of the highest over the lowest eigenvalue of the Hessian, to assess the presence of low-curvature eigenvectors at the minimum of the cost function and the resulting lack of robustness of the parameters toward changes in the training data.

In order to assess the impact of parameter displacements along a low eigenvector, we compute for a test molecule (3-chloromorpholine, see Figure 1) the AIM charges resulting from EEM and SQE, equalized electronegativity, and global hardness for different displacements of the optimal parameters along this low eigenvector. Specifically, we consider a series of parameter vectors along a line segment in the parameter space that is centered on the

optimal parameters, is parallel to an eigenvector, and has a length of 20 eV. The points on this line segment are characterized by the mathematical relation:

$$\mathbf{x}_{\text{scan},i}(\gamma) = \mathbf{x}_{\text{opt}} + \gamma \mathbf{a}_i \quad (14)$$

where \mathbf{x}_{opt} is the optimized parameter vector, \mathbf{a}_i is an eigenvector associated with the scan, and γ is the line parameter going from -10 eV to $+10$ eV. This type of analysis is only discussed for the calibration P1, but the same trends are present in the other calibrations.

Influence of the Training Set. There is a long history in computational chemistry of the use of low-frequency vibrational modes in molecular systems to search for or explain conformational changes.⁶³ For example, in biochemistry, one typically expands the relative vector of Cartesian coordinates of two protein conformers into the basis of lowest vibrational eigenmodes of one of the conformers to investigate if extended motion along these modes could lead to a transition of one conformer to the other.^{64–67} We use a similar analysis technique to compare two parameter vectors that are derived with the same procedure but based on different training sets, e.g., to compare P1 with T1. The difference between the two parameter vectors is expanded in the basis of eigenvectors of the Hessian of either P1 or T1. This allows one to compute, for each eigenvector, the percentage contribution to the difference between two parameter vectors. Because calibration T1 contains more atom types and hence more parameters, we restrict the relative parameter vector to the parameters that are present in both P1 and T1. Likewise, the Hessian of T1 is reduced to those parameters present in P1 by omitting the columns and rows that correspond to the parameters that are only present in T1.

Let the basis of eigenvectors be \mathbf{a}_i and let the parameter vectors be \mathbf{x}_{P1} and \mathbf{x}_{T1} ; then, the percentage contribution to the difference between two parameter vectors due to basis vector i , Pct_i , is defined as

$$\text{Pct}_i = \frac{((\mathbf{x}_{\text{P1}} - \mathbf{x}_{\text{T1}}) \cdot \mathbf{a}_i)^2}{\|\mathbf{x}_{\text{P1}} - \mathbf{x}_{\text{T1}}\|^2} \times 100\% \quad (15)$$

The same analysis is used to compare the parameters obtained with P2 versus T2 and P3 versus T3.

Influence of the Charge Population Scheme. Strictly speaking, there are no measurement errors on the QM atomic charges since all data are obtained from theoretical computations. Nevertheless, we do not expect the QM atomic charges to be totally robust with respect to the initial guess of the wave function, limited convergence criteria, numerical errors, and so on. This lack of robustness adds an unpredictable contribution to the atomic charges, which we can treat as measurement errors. Such errors on the training data will result in errors on the calibrated model parameters. This error will also contribute to the deviation between two parameters derived from different training sets. The norm of the difference between the parameters of P1 and T1 can be compared with the norm of the difference between parameters of P2 and T2. Because procedures 1 and 2 only differ in the choice of QM charge population scheme, the relative magnitude of the two norms is an indication for the relative robustness of the underlying population schemes.

Multiple Minima. In the present subsection, we introduce a method to provide an indication for the absence of multiple minima in the cost function of T1 when the second-order parameters are restricted to the region where the hardness matrix is guaranteed to be positive definite.

As argued before, AIM charges are contaminated to some extent by numerical errors. Even in the absence of these numerical errors, there will be a residual error between the charges predicted by the EEM or the SQE and the QM training data, simply because both equilibration models are approximations that cannot capture all features and trends in the QM computations.

Assume that the numerical errors and the elusive trends in the QM atomic charges can be modeled with a simple uncorrelated Gaussian error that is completely responsible for the deviation between the QM data and the model predictions. The variance of this Gaussian noise is not known a priori. This assumption is only an approximate description because elusive trends are not true random noise. However, it provides a useful statistical model for the errors between model and reference charges.

In the vicinity of the optimal parameters, we can approximate our cost function by a generalized linear least-squares cost function, except that our cost function (eq 11) contains weight factors that replace the measurement errors that are typically present in a χ^2 -type cost function.⁵² The propagation of errors from the training data to the estimated parameters is mathematically analogous, and therefore the inverse of the Hessian of our cost function is a model for the covariance matrix of the parameters,⁵² up to a constant factor because we do not know the variance of the error on the training data a priori.

We validate this hypothesis, i.e., the relation between the Hessian of the cost function and the uncertainty in the parameters, by studying the covariance of the parameter vectors obtained from 100 distinct cross-validation calibrations for T1. The difference between the 100 runs is the selection of the molecules in the training set: for each case, a random representative subset of 400 molecules is taken from the full set of 500 molecules. The same subsets are used as for the cross-validation in our EEM/SQE benchmark paper,³⁶ and we refer to that work for further details on the generation of the subsets. The covariance matrix of the 100 parameter vectors and the Hessian of the cost function in T1 can be compared in terms of eigenvalues and corresponding eigenvectors. The same analysis is carried out for T2, but not for T3. The latter calibration fits more than 100 parameters, which makes it impossible to estimate the covariance of the parameters using 100 samples.

One can further test whether the parameter vectors obey the multivariate normal distribution dictated by the Hessian of the cost function. One applies an affine transformation to the 100 parameter vectors that brings the average to the origin and turns the covariance matrix of the transformed parameter vectors into a unit matrix. In this new coordinate system, the squared norm of the parameter vectors should follow the χ^2 distribution with the number of degrees of freedom equal to the number of model parameters.

A strict validation of our statistical model for the training data is not the purpose of this analysis. We are rather interested in a procedure to examine and invalidate the existence of multiple minima for this type of cost function. The initial first-order parameters are sampled between -50 and $+50$ eV. The initial second-order parameters are selected randomly between 5 and 50 eV above their lower bound. This should be sufficient to trigger optimizations into different local minima if they would exist. The tests for the statistical model of the parameter distribution must fail dramatically if multiple minima are present in our cost function. The spread of the 100 parameter vectors over multiple minima cannot be predicted by the Hessian of the cost function

of calibration T1. By consequence, if the tests do not fail, it is very unlikely that multiple minima are present in the cost function of T1.

Parameter Correlations in EEM. In this subsection, we only consider the EEM model for a more detailed analysis of the statistical correlations between the atomic electronegativity and hardness parameters. Consider at first instance a molecule in which each atom has its own (η_i, χ_i) parameter pair. The equations to determine the charges, q_i in this molecule are given by

$$\chi_i + q_i \eta_i + \sum_{j=1, j \neq i}^N q_j J_{ij} = \chi_{\text{mol}} \text{ and } \sum_{j=1}^N q_j = Q_{\text{tot}} \quad (16)$$

where J_{ij} represents the electrostatic interaction between atoms i and j , χ_{mol} is the equalized electronegativity, and Q_{tot} is the total charge. Once these equations are solved, one can change the parameter χ_i of each atom and update the value of η_i according to

$$\eta_i = \frac{\chi_{\text{mol}} - \chi_i - \sum_{j=1, j \neq i}^N q_j J_{ij}}{q_i} \quad (17)$$

without changing the equilibrium charges.³⁷ If one substitutes the QM atomic charges and the molecular electronegativity into eq 17, one finds a linear relation for all possible optimal (η_i, χ_i) parameter pairs associated with atom i . It was to be expected that the optimal parameters are not unique, since there are twice as many parameters as there are atomic charges to be reproduced.

The statistical correlations so far consider independent parameters for each atom in the entire set of molecules, while in practice the same parameters are used for atoms with the same element (or force-field atom type). Therefore, we introduce a graphical representation for every element in scheme P1 to analyze the statistical correlation data of all of the corresponding independent atomic parameters. Given an element, we construct a plot in the (η_i, χ_i) plane with the lines according to eq 17 for all atoms alike in all of the molecules in the training set. When this bundle of lines features an approximate common intersection point, we expect that the calibrated P1 parameters for that pair to be close to the intersection. In other words, a contour plot of the cost function of P1 in the (η_i, χ_i) plane, keeping all other parameters constant at their optimal value, should reveal a minimum in the vicinity of the approximate intersection point of the bundle of lines. When a bundle of lines is almost parallel for a given element, the corresponding optimal (η_i, χ_i) parameter pair should be ill-defined, and the contour plot should reveal an elongated valley instead of a unique minimum. Note that our cost function is designed to take also into account the electronegativity of each molecule in the training set; otherwise one should not expect any correspondence between the contour plots and the lines defined by eq 17.

IV. RESULTS AND DISCUSSION

For ease of reference, results from the methods described in the various subsections of section III, are discussed in the corresponding subsections of section IV.

Parameter Calibration. In total, six calibrations were carried out with a subsequent detailed analysis of the significance of the parameters. The optimal parameters can be found in the Supporting Information, section 4. Before analyzing the results, we briefly review the main statistical properties of the calibrations.

The R^2 and RMSE values in Table 4 immediately reveal the major differences between the six calibrations. First of all: procedures 1 and 3 are superior in accuracy compared to procedure 2. The latter is based on Mulliken charges, while the former two use Hirshfeld-I charges. It is known that Mulliken charges are ill-behaved when large basis sets with diffuse functions are used,^{12,15,68} while Hirshfeld-I charges are much less basis set dependent.²³ The R^2 and RMSE values confirm that Mulliken charges have a larger degree of arbitrariness, which makes them more difficult to reproduce with charge equilibration models. A second observation is that the SQE (in procedure 3) is more accurate than the EEM (procedure 1). Both observations are in line with earlier work.^{33,36} When comparing results from training set P with those of T, the reference data based on set P are easier to reproduce. This is related to the fact that set P contains fewer molecules and that set T is generated with an algorithm that tries to maximize the diversity of chemical functional groups.

As discussed above, a high condition number is an indicator for less robust parameters, i.e., parameters that are more sensitive to irrelevant details in the training data. The optimal parameters are ill-conditioned in all six cases. All of the condition numbers of the Hessian are at about 5 or more orders of magnitude above the minimal and ideal value, i.e., 1. The condition number is clearly higher for calibration T3, and the Hessian is virtually singular in case P3. This is partly due to the larger number of parameters in the SQE model and to the introduction of multiple force-field atom types for the same element. Also note that set P is designed to be used for EEM calibrations without extensive use of force-field atom types,²⁶ while set T is specifically constructed with force-field atom and bond types in mind.³⁶ It is therefore expected that set P does not contain sufficient information to fix all of the parameters in procedure 3. This is also visible in the actual parameters of P3, e.g., the electronegativity parameter of atom type N1 is 24.53 eV, which is excessively high. The Hessians of T1, T2, and T3 are positive definite in this work, which was not the case in the EEM/SQE benchmark paper.³⁶ The conjugate gradient optimizer used in this work is extended with a diagonal preconditioner, which significantly improves the rate of convergence compared to a conventional conjugate gradient optimizer.

Calibrations P2, T2, and P3 clearly have weaknesses and should not be used for general applications. They are however interesting for this paper, revealing the typical problems inherent in calibrated EEM and SQE parameters.

Correlated Parameters in a Diatomic Molecule. It is instructive to show how the atomic charges are invariant to certain changes in parameters when the SQE model is applied to a neutral heteronuclear diatomic molecule. The charges are given by

$$q_1 = -q_2 = \frac{\chi_1 - \chi_2}{\eta_1 + \eta_2 + \kappa - \frac{2}{r_{ij}}} \quad (18)$$

where the last term in the denominator is twice the electrostatic interaction between the two atoms. As mentioned earlier, one can replace the electrostatic term by other functional forms, which will clearly affect the optimal values of the hardness parameters. There are in total five parameters to fix only one unknown, leaving four degrees of freedom in the parameters that cannot be fixed in a calibration where charges are used as reference data. The following degrees of freedom remain:

- 1 An arbitrary constant can be added to both electronegativity parameters without changing the charge q_1 . This was already

Table 4. Key Statistical Characteristics of Each Calibration (P1, T1, P2, T2, P3, and T3)^a

quantity	(a) R ² [%]		(b) RMSE [e]		(c) condition number		(d) # parameters	
	P	T	P	T	P	T	P	T
training set								
procedure 1	95.47	89.61	0.0646	0.1149	2.74×10^5	4.15×10^5	12	16
procedure 2	67.05	53.74	0.2674	0.3006	9.83×10^5	8.09×10^4	12	16
procedure 3	99.36	98.18	0.0242	0.0481		6.79×10^6	70	135

^a (a) The Pearson correlation coefficient between the QM and model charges, (b) the root-mean-square error (RMSE) between QM and model charges, (c) the condition number of the Hessian of the cost function (defined as the ratio of the highest over the lowest eigenvalue of the Hessian), and (d) the number of parameters in the charge equilibration model.

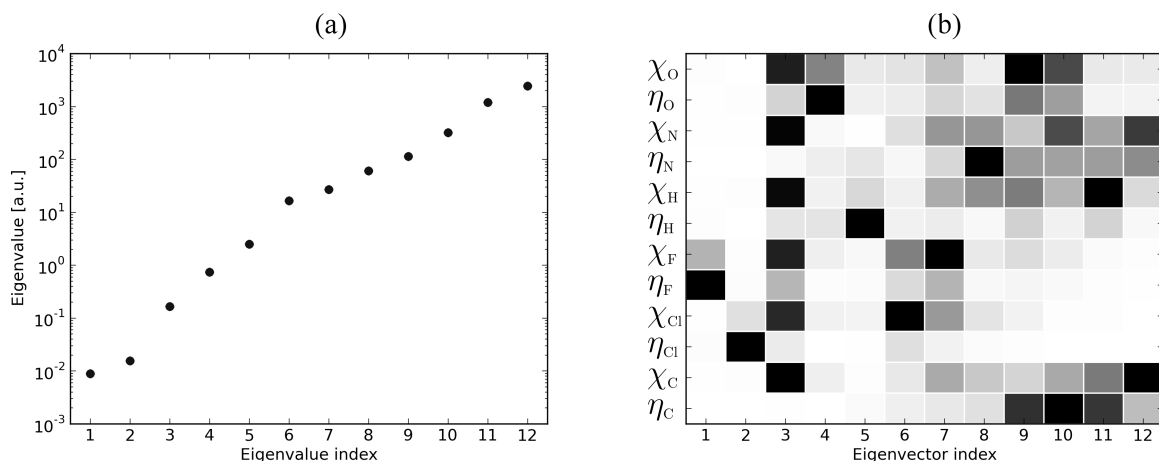


Figure 2. Graphical representation of the eigenvalues (a) and the eigenvectors (b) in calibration P1. Each column in part b corresponds to an eigenvector, and each row corresponds to a parameter. The cells are colored on the basis of the absolute value of the corresponding matrix element: the darker the color, the larger the absolute value.

mentioned in section II, and this invariant is also present in more general molecules.

- One can also increase the electronegativity difference and compensate for this by increasing the parameters in the denominator of eq 18. This type of parameter correlation is discussed at the end of section III and section IV when the EEM model is applied to more general molecules.
- The last two invariants consist of an increase (or decrease) in one hardness parameter that is exactly compensated with opposite changes in the other hardness parameters. In the case of the EEM, such problems were not observed, probably because the training sets contain a large set of molecules to which this invariant does not simply apply.

Parameter Scans. Before we proceed with the eigenvector-following analysis, we first examine the eigenvalue decomposition of the Hessian. The results for calibration P1 are depicted in Figure 2. Similar plots for all other calibrations are included in the Supporting Information, section 5. Note that the eigenvectors could not be properly visualized for P3 and T3 due to the large number of parameters. Figure 2b visualizes the eigenvectors as follows. Each column in the figure corresponds to an eigenvector of the Hessian of the cost function used in calibration P1, sorted from low to high eigenvalue. Each row corresponds to a parameter in the P1 calibration. The cells are colored on the basis of the absolute value of the corresponding coefficient of the eigenvector: the darker the color, the larger the absolute value. Figure 2 reveals the following two trends. First, the lowest two eigenvectors of the Hessian indicate that the P1 cost function is

not sensitive to a linear combination of the (η_i, χ_i) parameter pair of each halogen. To a lesser extent, the same problem is visible for oxygen. Similar conclusions can be drawn from the Hessian of T1. Second, the influence of the charge bath is visible in eigenvector 3; i.e., the cost function is (weakly) sensitive to a constant shift of all electronegativity parameters. If a strict total charge constraint was used during the parametrization, this eigenvector would have a corresponding eigenvalue of zero because the cost function is then completely insensitive to the reference value for the electronegativity parameters. Both observations also apply to the calibrations based on the Mulliken charges, P2 and T2.

Figure 3 contains the results for two linear scans through the parameter space in the context of calibration P1. The first scan (Figure 3a and b) is taken along the eigenvector with the lowest-but-one eigenvalue of the Hessian. The scan with the lowest eigenvalue is not used because it mainly affects the fluorine parameters, while there is no fluorine present in the test molecule (3-chloromorpholine, see Figure 1). The second scan is similar but based on the highest eigenvalue (Figure 3c and d). All 15 atomic charges (3a and c) and the molecular electronegativity and hardness^{69,70} (3b and d) are computed for the test molecule in both scans. The hatched region is excluded during the calibration due to the lower bounds on the second-order parameters. In the red region, the hardness matrix of the test molecule has at least one negative eigenvalue. The beginning, middle, and end point of each scan and the eigenvectors are given in section 6 of the Supporting Information.

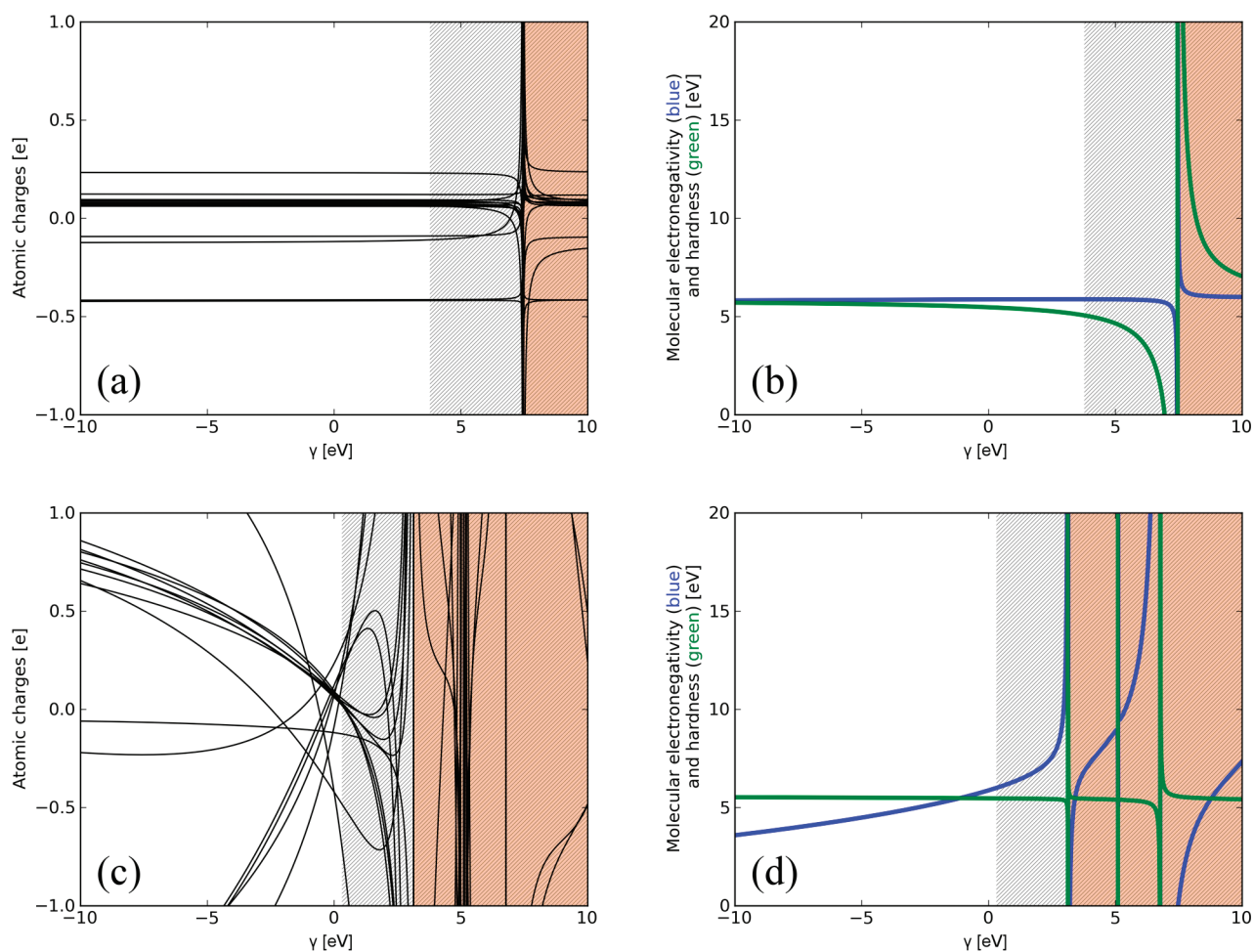


Figure 3. Evolution of the 15 atomic charges (parts a and c) and molecular electronegativity and hardness (blue and green respectively in parts b and d) during two linear scans through the parameter space for a test molecule (3-chloromorpholine, see Figure 1). The optimal P1 parameter vector corresponds to $\gamma = 0$ in each plot. In the top row (a,b) the scans are taken along the eigenvector of the P1 Hessian with the lowest-but-one eigenvalue. In the bottom row (c,d) the highest eigenvalue is used. The hatched region is excluded during the calibration due to the lower bounds on the second-order parameters. In the red region, the hardness matrix of the test molecule is no longer positive definite.

The first scan shows virtually no changes in atomic charges as the parameter vector is displaced in the region that is allowed during the calibration (see Figure 3a). Only when the parameters lead to a hardness matrix that is almost singular do the charges change significantly. At the edge of the red region, the hardness matrix has one zero eigenvalue; the charges (and therefore also the cost function) diverge.^{61,62} The molecular electronegativity shows the same behavior as the charges: it is practically constant except near the singularity in the hardness matrix. The molecular hardness is more sensitive than the electronegativity. The weak sensitivity of the charges along this eigenvector is a general feature for many molecules in the training set, which explains the low curvature of the cost function for this eigenvector.

The scan along the eigenvector with the largest eigenvalue goes through three points where the hardness matrix becomes singular (Figure 3d). At each of these three points, all computed quantities diverge. The charges show stronger fluctuations. The molecular electronegativity is sensitive, and the molecular hardness is not. The fact that the cost function has the highest curvature along this direction is solely due to high sensitivity of the atomic partial charges for changes in parameters along this direction.

The figures discussed above show that the parameter space is full of transitions where one of the eigenvalues of the hardness matrix (of one of the molecules in the training set) changes sign. Each of these transitions takes place at a hypersurface in the parameter space that separates feasible regions in which the atomic charges remain finite. At the boundary of each feasible region, the cost function diverges toward plus infinity, and consequently, each region contains at least one local minimum. However, there is only one feasible region for which all hardness matrices in the training set are positive definite, which will be denoted below as the *positive definite feasible region*. All other feasible regions are called *nonpositive definite*.

The contour plot of the cost function P1 in Figure 4 shows the multitude of feasible regions (for example, when $\eta_H < \eta_{H,\min}$ or $\eta_C < \eta_{C,\min}$). The region excluded during the calibration is darker and separated by a thick dashed line from the allowed region. From the practical point of view, one should avoid allowing the calibration algorithm to converge to parameters that are locally optimal in one of these tiny *nonpositive definite* feasible regions. It is not just that it is difficult to find the feasible region with the lowest minimum. The real problem is that one can always find a molecular structure that has a singular hardness matrix for those

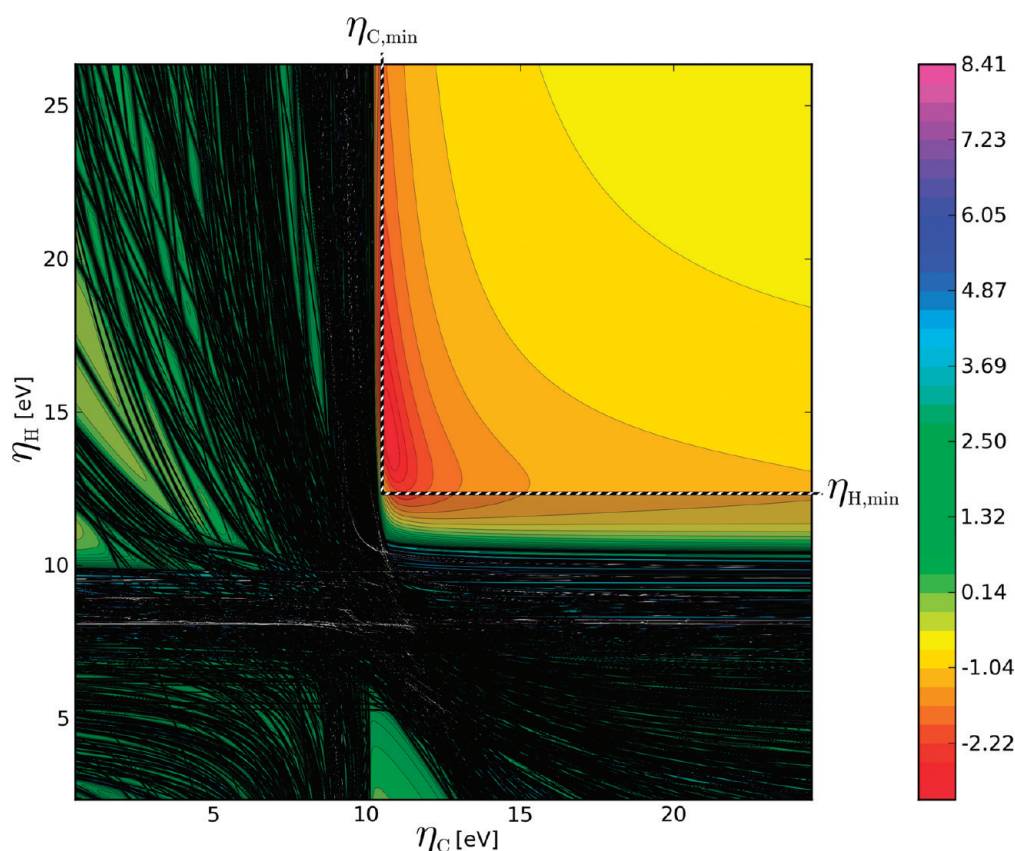


Figure 4. A contour plot of the cost function of P1 with two atomic hardness parameters as variables (η_C and η_H). All other parameters are kept at their optimal values. The allowed region during the calibration comprises the top-right corner of the scan, bordered by the dashed line. The contours represent iso-curves for the logarithm of the cost function.

Table 5. The Values of the Parameters Present in Both P1 and T1 and Their Differences^a

parameter	P1 [eV]	T1 [eV]	difference [eV]
χ_H	5.583	7.019	-1.436
χ_C	6.263	8.002	-1.738
χ_N	6.847	8.610	-1.763
χ_O	8.173	9.699	-1.525
χ_F	8.625	11.150	-2.525
χ_S		7.510	
χ_{Cl}	6.602	8.426	-1.823
χ_{Br}		7.769	
η_H	14.126	15.483	-1.357
η_C	10.743	10.718	0.025
η_N	10.887	10.877	0.010
η_O	13.068	12.724	0.344
η_F	17.235	21.199	-3.963
η_S		7.870	
η_{Cl}	11.266	15.291	-4.025
η_{Br}		18.933	

^a The norm of the difference is 7.354 eV.

locally optimal parameters. Note that all nonpositive definite feasible regions have at least one hardness parameter that is below its lower bound. In the allowed region, only one local minimum is visible, although this does not prove that there is

only one minimum in the positive definite feasible region when all degrees of freedom are considered.

Influence of the Training Set. The parameters for calibrations P1 and T1 are given in Table 5. They show that the same calibration procedure applied to two different sets of training data can lead to significant differences in the optimal parameters. Similar differences are present when comparing P3 with T3 and become even more pronounced in sets P2 and T2. This subsection relates such differences to the low eigenmodes of the Hessian belonging to the cost functions used for the calibration. The discussion and data in this subsection are based on calibrations P1 and T1, but the same explanation is valid for the other calibrations. The data for P2 versus T2 and P3 versus T3 are given in the Supporting Information, section 7.

The comparison between P1 and T1 is troubled by the sulfur and bromine parameters χ_S , η_S , χ_{Br} , and η_{Br} that are present in T1, but absent in P1. Set P does not contain molecules with sulfur or bromine. For this reason, the parameter vector of T1 is projected on the parameter space of P1 by simply omitting the additional four parameters. An analogous projection is applied to the Hessian of T1; i.e., all rows and columns corresponding to those four parameters are deleted. After the projection operations, one can compute the difference between the parameter vectors of P1 and T1 and expand the difference on the basis of eigenvectors of the Hessian of P1 or the projected Hessian of T1. The same type of projection must be carried out when comparing P2 with T2 or P3 with T3.

The results for the comparison of P1 and T1 are given in Tables 5, 6, and 7. Table 5 also reports the difference between the

Table 6. Decomposition of the Vector Representing the Difference between the P1 and T1 Parameters in the Basis of P1 Hessian Eigenvectors^a

index	relative eigenvalue	coefficient [eV]	contribution [%]
1	3.646e-6	-4.619e+0	39.44
2	6.341e-6	-4.117e+0	31.35
3	6.807e-5	-3.788e+0	26.52
4	3.053e-4	1.656e-1	0.05
5	1.017e-3	1.143e+0	2.41
6	6.794e-3	-5.107e-2	0.00
7	1.098e-2	3.133e-1	0.18
8	2.499e-2	1.175e-1	0.03
9	4.695e-2	-5.788e-2	0.01
10	1.322e-1	3.197e-3	0.00
11	4.907e-1	-3.959e-2	0.00
12	1.000e+0	-2.426e-2	0.00

^a The eigenvalues of the P1 Hessian are given relative to the highest eigenvalue.

Table 7. Decomposition of the Vector Representing the Difference between the P1 and T1 Parameters in the Basis of Projected T1 Hessian Eigenvectors^a

index	relative eigenvalue	coefficient [eV]	contribution [%]
1	4.636e-06	-4.470e+00	36.95
2	1.283e-05	-4.162e+00	32.02
3	1.213e-03	-2.614e-01	0.13
4	1.579e-03	1.401e+00	3.63
5	3.437e-03	-2.227e+00	9.17
6	3.970e-03	1.105e+00	2.26
7	1.920e-02	-2.828e+00	14.79
8	3.264e-02	-6.524e-01	0.79
9	6.963e-02	-3.314e-01	0.20
10	2.208e-01	-3.148e-02	0.00
11	3.544e-01	1.831e-01	0.06
12	1.000e+00	-5.094e-02	0.00

^a The eigenvalues of the projected T1 Hessian are given relative to the highest eigenvalue.

parameters of P1 and T1. Note that the significant differences fall into two categories: (i) all electronegativity parameters in T1 are about 1.8 eV higher than those in P1; (ii) the parameters of the halogens differ more than those of the other atoms. Tables 6 and 7 give the decomposition of the relative parameter vector in the basis of the Hessian of P1 and the projected Hessian of T1, respectively. The percentage contributions of the lowest three eigenmodes in case P1 (Table 6) add up to 97%. In Table 7, the first two eigenmodes only account for 69% of the difference, and some higher modes also have a non-negligible contribution. When comparing P2 with T2 or P3 with T3, the same pattern is found: at least one of the two Hessians has low eigenmodes that form a nearly complete basis for the differences between the parameters. We conclude that cost functions based on training set P or T essentially have the same ill-conditioned minimum, but due to the subtle differences in the reference data, the exact position of the optimal point is shifted along the directions of low curvature on the cost function surface.

Influence of the Charge Population Scheme. The norm of the difference between the parameters of P2 and T2 (83.164 eV) is much larger than the norm of the difference between P1 and T1 (7.354 eV). This means that the parameters obtained with procedure 2 are much more sensitive to the selection of molecules in the training set. The only difference between procedures 1 and 2 is that 1 uses Hirshfeld-I charges while 2 is based on Mulliken charges. The lack of robustness of the Mulliken charges when using large basis sets for the QM computation, i.e., its sensitivity to irrelevant details in the wave function,^{12,15,68} clearly causes two undesirable effects: (i) Mulliken charges are difficult to reproduce with equilibration models (as discussed above), and (ii) the position of optimal parameters along the directions of low curvature of the cost function are heavily scattered. In the context of generalized linear least squares methods, one can show that the noise on the parameters is a linear function of the noise on the training data.⁵² Because our cost function can be locally approximated as a linear least squares cost function, the same relation applies. Similar conclusions can be drawn for any QM population scheme that is not fully robust. For example, ESP fitted charges tend to be sensitive to the choice of grid points, while the choice of grid points is irrelevant from the physical perspective.¹⁸ Therefore, we expect that ESP-fitted charges are, just like Mulliken charges, of little use for the calibration of statistically sound EEM or SQE parameters.³⁸

Multiple Minima. The cross-validation runs for T1 and T2 confirm the reliability of the calibration procedure. For each run, RMSE and R^2 values are computed to test how well the parameters based on a selection of 400 (out of 500) molecules can reproduce the data of the 100 remaining molecules. In line with previous work,³⁶ the performance measures obtained in the cross-validation are very comparable to the numbers obtained in Table 4. The remainder of the discussion is limited to the results based on calibration T1. Similar data for calibration T2, leading to the same conclusions, are included in the Supporting Information in section 8.

The sampling covariance matrix of the 100 parameter vectors is closely related to the Hessian of the cost function. In principle, our covariance estimate does not converge to the true covariance of the parameters because each training subset of 400 molecules shares at least 300 molecules with all other subsets. Therefore, our current approach systematically underestimates the true covariance. This is of little concern because the model for the parameter covariance, based on the inverse of the Hessian of T1, is only known up to a constant factor. In Figure 5a, the square root of the sampling covariance eigenvalues are plotted in blue. The first eigenmode corresponds to a spread of about 1 eV on the parameters. The inverse of the square root of the Hessian eigenvalues are plotted as red dots. Both data series follow the same trend up to a constant factor, a first confirmation that the Hessian of the cost function minimum can be used to explain the fluctuations on the EEM parameters. The eigenvectors of the covariance and the Hessian are compared in Figure 5b, which is a visual representation of the overlap matrix of both sets of eigenvectors. Each cell of the overlap matrix is colored according to its absolute value: the darker the color, the larger the absolute value. In the ideal picture, only the diagonal elements would be 100% black, while all off-diagonal elements would remain white. Figure 5b reveals some contamination between eigenvectors with similar eigenvalues, but the overall correspondence between the two sets of eigenvectors is good.

The statistical explanation of the variation on the parameters can be further validated by studying the distribution of the

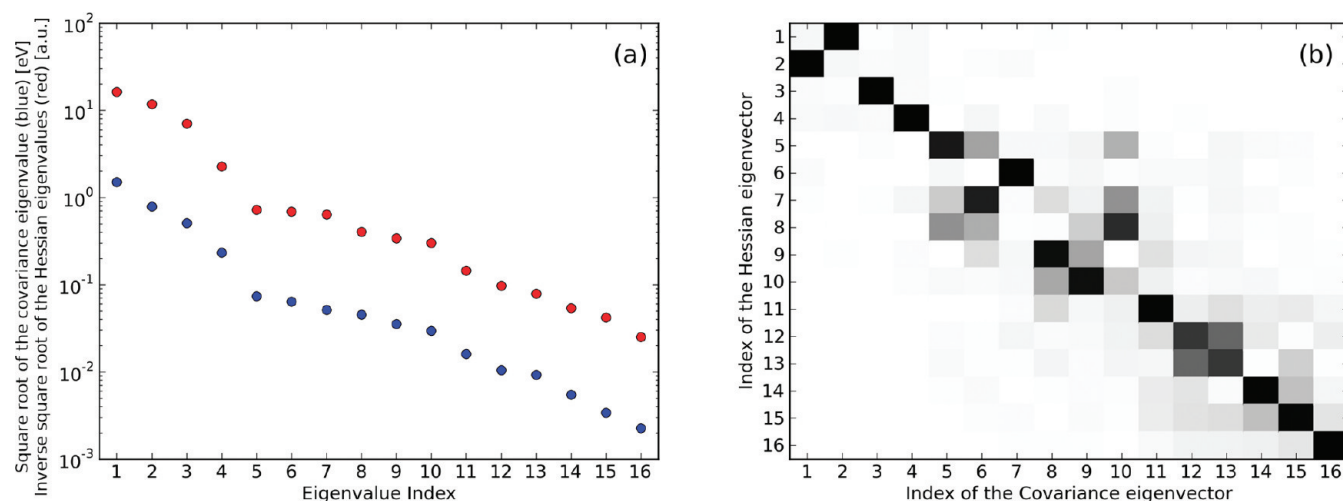


Figure 5. Comparison of the covariance of the 100 parameter vectors from the cross-validation of calibration T1 with the inverse of the Hessian of the cost function of T1. (a) The square roots of both matrices. Note the square root of a covariance eigenvalue can be interpreted as the standard deviation of the parameters along the corresponding eigenvector. (b) Visual representation of the overlap matrix of the eigenvectors of covariance and the Hessian. Each cell of the overlap matrix is colored on the basis of its absolute value: the darker the color, the larger the absolute value.

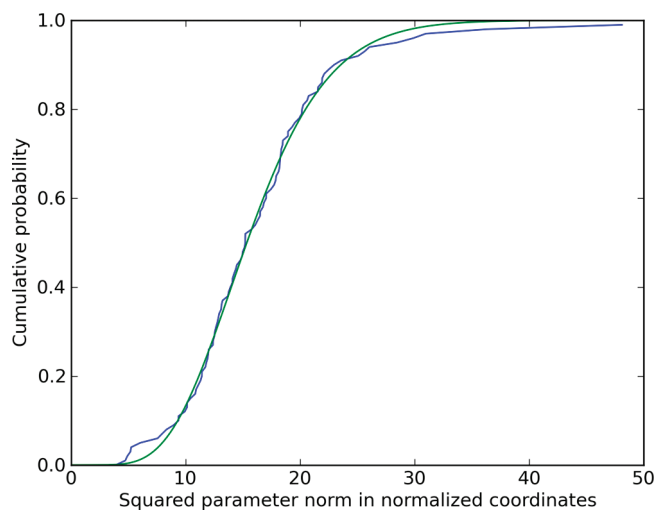


Figure 6. Comparison of the cumulative frequency distribution of the squared norm of the 100 parameter vectors from the cross-validation of T1 in normalized coordinates (blue) and the expected cumulative χ^2 distribution with 16 degrees of freedom (green).

distance of each parameter vector from the average. First, we apply an affine transformation to the parameters such that the average vector is zero and the covariance matrix becomes unity. The squared norm of the parameter vectors in these normalized coordinates should be distributed according to a χ^2 distribution with 16 degrees of freedom, i.e., the number of parameters in T1. A comparison of the cumulative frequency plot with the exact cumulative χ^2 distribution is presented in Figure 6. Small aberrations are found in the tails of the distribution, but there is no indication that firm outliers are present.

Both tests point out that the Hessian of the cost function explains the uncertainty on the parameters of T1. This is only possible if all 100 parameter vectors essentially describe the same minimum but are slightly displaced due to differences in the training data. If the 100 parameter vectors would be due to truly different minima in the cost function, one would not expect such

a good correspondence between the sampling covariance matrix and the inverse of the Hessian of T1. Therefore, we conclude that cost function T1 has only one minimum in the positive definite feasible region. This justifies the use of a local minimization algorithm for the calibration of the parameters instead of a computationally more expensive global minimizer.

Finally, we must stress that this analysis can only work under two important conditions. First, the calibration of the parameters must be restricted to one feasible region, e.g., by imposing lower bounds on the second-order parameters. Otherwise, one can find at least one minimum in the cost function for each feasible region. Second, one must use a training set for the calibration and the subsets for the cross-validation that contain sufficient information to determine all parameters. If not, the covariance of the parameters diverges.

Parameter Correlations in EEM. All results so far point out that parameters in the EEM and SQE models are inherently correlated to a high degree, even when the molecules in the training sets are carefully selected to contain sufficient information to estimate the parameters. In this subsection, we show that correlated parameters are practically unavoidable with cost functions that are based solely on atomic partial charges. The results in this subsection are based on calibration P1.

Figure 7a and b contain lines defined in eq 17, for carbon and fluorine atoms, respectively. The optimal parameters for carbon and fluorine are indicated with a black cross. The corresponding contour plots of the cost function in the same planes are shown in Figure 7c and d, respectively. The same color scale is used as in Figure 4. The plots for other elements (H, N, O, and Cl) are given in section 9 of the Supporting Information. As discussed in the methods, the optimal parameters for a given element should coincide with the approximate crossing point of the bundle. This is always the case, except for a constant shift of all of the electronegativity parameters of about +2 eV. Such a deviation is to be expected since our cost function is only weakly sensitive to the reference value for the electronegativity parameters. The correlation between the line plots and the corresponding contour plots is striking. Both the positions and the shapes of the minima in the contour plots have a surprising direct link with the reference data.

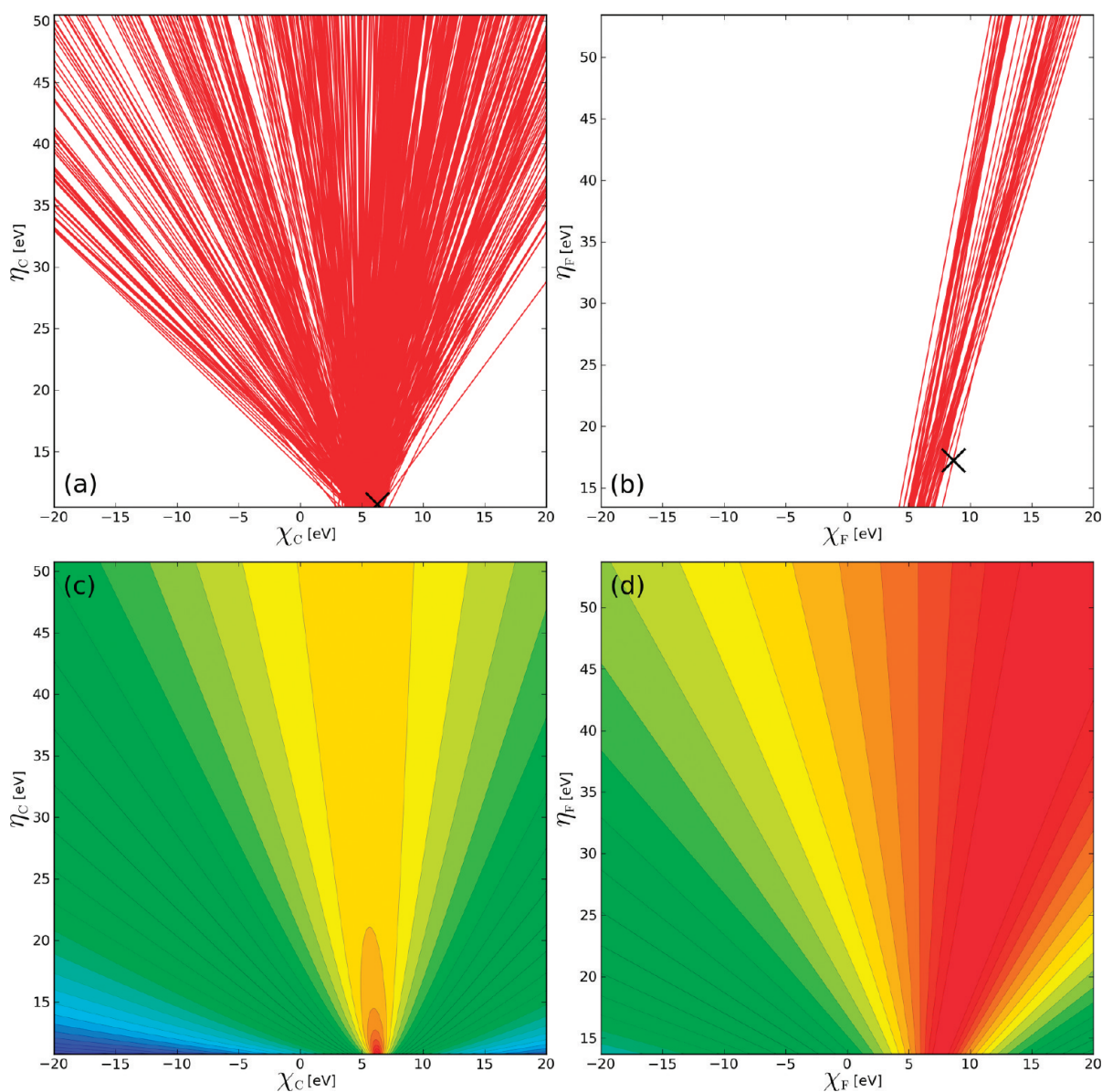


Figure 7. The lines for (a) carbon and (b) fluorine associated with the QM atomic charges in calibration P1. (See text for the definition of the lines.) The position of the optimal parameters for each element is indicated with a black cross. Parts c and d contain the corresponding contour plots of the cost function in the same planes, using the same ranges for χ_i and η_i . The color code for the contour plots is the same as in Figure 4.

This is not only useful to construct an initial guess for the parameters. It also shows why the parameters of the halogens can vary easily: all of the lines associated with fluorine (or chlorine) have approximately the same slope, and hence there is no clear intersection point. The slope of the lines is determined by the charge on the corresponding atoms, see eq 17, which implies that atoms with little variation in the partial charge are inherently difficult to parametrize.^{37,38}

Given these insights, one can think of potential improvements in the calibration procedures. (i) One could define a weight $w_{m,i}$ per element (or force-field atom type in the case of SQE) in the cost function (eq 11) that is inversely proportional to the variance on the atomic charges within the atom type.⁷¹ With this choice, atom types whose charges show little variation in the training set receive a much higher weight. This increases the curvature of the cost function, i.e., its sensitivity, for parameters

that are otherwise underdetermined. In this paper, the weights were still based on the prevalence of atomic elements or force-field atom types.³⁶ (ii) A second improvement is based on the observation that the parameter correlations are always found in pairs, i.e., the hardness and electronegativity parameters of the same element. One could use two separate cost functions: one to determine the second-order parameters (e.g., based on linear response data) and one for the linear parameters (e.g., based on equilibrium charge distributions). This is of course only helpful when both separate cost functions have a low condition number. An alternative remedy is tested in the benchmark paper of Verstraelen et al.:³⁶ an additional term is added to the cost function based on linear response data, which only depends on second-order parameters. The reduced condition number of the Hessian of such an extended cost function shows that this approach leads to less dispersed parameters.

V. CONCLUSION

Three sets of parameters for the EEM and SQE models are calibrated in this work using state-of-the-art methods and resulted in three practically useful calibrations (P1, T1, and T3). These three sets of parameters are calibrated with Hirshfeld-I charges for a sufficiently large set of molecules compared to the number of parameters in the corresponding models. Three other calibrations (P2, T2, and P3) are used to illustrate the typical problems that can arise in the calibration of charge equilibration parameters. Despite the careful calibration protocols, our analysis demonstrates that the EEM and SQE parameters are still statistically ill-defined numbers that have no absolute interpretation and can only be considered as regression parameters. Irrelevant details in the training set can lead to large fluctuations on the parameters, but cross-validation tests confirm that these fluctuations do not affect the charge distribution predicted by the EEM or SQE model.

Using a variety of analysis techniques, we investigated the two potential issues that may lead to parameters that are not unique: (i) the presence and nature of multiple minima in the cost function and (ii) directions of low curvature in the minimum of the cost function. Screened electrostatics combined with suitable and reasonable lower limits on the second-order parameters restrict the calibration to a single feasible region in the parameter space. Numerical tests indicate that this region contains only one local minimum, which leaves the lack of curvature of the cost function as the only potential difficulty. The lack of curvature is present in all six calibrations in this work and seems to be a general feature, which is not surprising given the large number of parameters. In practice, this means that there is a large hyper-ellipsoid in the parameter space that contains all of the parameter vectors that are nearly optimal. Every effort to find the true minimum in this ellipsoid is completely in vain, as its exact position is very sensitive to irrelevant details in the training set. It is therefore also impossible to give a physical interpretation to individual parameters.

A certain amount of noise on the calibrated EEM and SQE parameters is unavoidable, but several measures are proposed in the paper to improve their robustness. It is compulsory to design a well-balanced training set in which each atom (and bond) type is sufficiently prevalent. On the basis of the training data, one should construct a cost function that includes a maximum of information from the training data. In addition to the atomic charges, our cost function is also sensitive to the molecular electronegativity, and one can further enrich the cost function with linear response data. One should also try to reduce the noise in the training data; e.g., it is advantageous to use Hirshfeld-I charges instead of Mulliken charges because the former are less basis set dependent. We also expect that the cost function will become better behaved when the weights associated with the charges in the cost function are defined per element (or atom type) such that they are inversely proportional to the variance on the charge of all atoms within the same atom type.

Our investigation raises many issues in the calibration of EEM and SQE parameters, and even more so in the direct interpretation of the calibrated parameters. We hope our analysis of the calibration procedures will be a fruitful source of inspiration for future work on charge equilibration models.

■ ASSOCIATED CONTENT

S Supporting Information. The following are included: (1) Lewis structures of the molecules in set P and T; (2) prevalence of atomic elements and force-field atom types in

training sets P and T; (3) atomic radii used for the screened electrostatic interactions and corresponding minimum values for the atomic hardness parameters; (4) calibrated parameters for P1, T1, P2, T2, P3, and T3; (5) plots of eigenvalues (and eigenvectors) of the Hessians in T1, P2, T2, P3, and T3; (6) numerical description of the scans through the parameter space in case P1; (7) comparison of parameters of P2 with T2 and of P3 with T3 and the decomposition of the relative parameter vectors; (8) results for the covariance analysis based on the cross-validation data for calibration T2; (9) lines and contour plots similar to Figure 7, but for elements H, N, O, and Cl. This information is available free of charge via the Internet at <http://pubs.acs.org/>.

■ AUTHOR INFORMATION

Corresponding Author

*E-mail: Toon.Verstraelen@UGent.be.

■ ACKNOWLEDGMENT

This work is supported by the Fund for Scientific Research—Flanders (FWO), the Research Board of Ghent University (BOF), and BELSPO in the frame of IAP/6/27. Funding was also received from the European Research Council under the European Community's Seventh Framework Programme (FP7(2007-2013) ERC grant agreement number 240483). The authors would also like to thank the Ghent University for the computational resources (Stevin Supercomputer Infrastructure). P.W.A. thanks NSERC and the Canada Research Chairs for financial support.

■ REFERENCES

- (1) Politzer, P.; Murray, J. S. *Theor. Chem. Acc.* **2002**, *108*, 134–142.
- (2) Neves-Petersen, M. T.; Petersen, S. B. Protein electrostatics: A review of the equations and methods used to model electrostatic equations in biomolecules - Applications in biotechnology. In *Biotechnology Annual Review*; El-Gewely, M. R., Ed.; Elsevier: Amsterdam, The Netherlands, 2003; Vol. 9, pp 315–395.
- (3) Labat, F.; Fuchs, A. H.; Adamo, C. *J. Phys. Chem. Lett.* **2010**, *1*, 763–768.
- (4) Verstraelen, T.; Szyja, B. M.; Lesthaeghe, D.; Declerck, R.; Van Speybroeck, V.; Waroquier, M.; Jansen, A. P. J.; Aerts, A.; Follens, L. R. A.; Martens, J. A.; Kirschhock, C. E. A.; van Santen, R. A. *Top. Catal.* **2009**, *52*, 1261–1271.
- (5) Townsend, R. Ion Exchange in Zeolites. In *Introduction to Zeolite Science and Practice*; van Bekkum, H., Flanigen, E. M., Jansen, J., Eds.; Elsevier: Amsterdam, The Netherlands, 1991; Vol. 58, pp 359–390.
- (6) Maple, J. R.; Cao, Y.; Damm, W.; Halgren, T. A.; Kaminski, G. A.; Zhang, L. Y.; Friesner, R. A. *J. Chem. Theory Comput.* **2005**, *1*, 694–715.
- (7) McCreery, J. H.; Christoffersen, R. E.; Hall, G. G. *J. Am. Chem. Soc.* **1976**, *98*, 7191–7197.
- (8) Declerck, R.; De Sterck, B.; Verstraelen, T.; Verniest, G.; Manginckx, S.; Jacobs, J.; De Kimpe, N.; Waroquier, M.; Van Speybroeck, V. *Chem.—Eur. J.* **2009**, *15*, 580–584.
- (9) Parr, R. G.; Ayers, P. W.; Nalewajski, R. F. *J. Phys. Chem. A* **2005**, *109*, 3957–3959.
- (10) Matta, C. F.; Bader, R. F. W. *J. Phys. Chem. A* **2006**, *110*, 6365–6371.
- (11) Bultinck, P.; Popelier, P. Atoms in Molecules and Population Analysis. In *Chemical Reactivity Theory*; Chattaraj, P. K., Ed.; Taylor and Francis: Oxon, U. K., 2009; pp 215–227.
- (12) Politzer, P.; Mulliken, R. S. *J. Chem. Phys.* **1955**, *23*, 1833–1840.
- (13) Lowdin, P. *J. Chem. Phys.* **1950**, *18*, 365–375.

- (14) Hirshfeld, F. L. *Theor. Chem. Acta.* **1977**, *44*, 129–138.
- (15) Reed, A. E.; Weinstock, R. B.; Weinhold, F. J. *Chem. Phys.* **1985**, *83*, 735–746.
- (16) Bader, R. F. W. *Phys. Rev. B* **1994**, *49*, 13348.
- (17) Bultinck, P.; Van Alsenoy, C.; Ayers, P. W.; Carbo-Dorca, R. *J. Chem. Phys.* **2007**, *126*, 144111.
- (18) Francl, M. M.; Chirlian, L. E. The Pluses and Minuses of Mapping Atomic Charges to Electrostatic Potentials. In *Reviews in Computational Chemistry*; Lipkowitz, K. B., Boyd, D. B., Eds.; John Wiley & Sons, Inc.: New York, 2000; Vol. 14, pp 1–31.
- (19) Singh, U. C.; Kollman, P. A. J. *Comput. Chem.* **1984**, *5*, 129–145.
- (20) Bayly, C.; Cieplak, P.; Cornell, W.; Kollman, P. J. *Phys. Chem.* **1993**, *97*, 10269–10280.
- (21) Van Damme, S.; Bultinck, P.; Fias, S. J. *Chem. Theory Comput.* **2009**, *5*, 334–340.
- (22) Catak, S.; D'hooghe, M.; Verstraelen, T.; Hemelsoet, K.; Van Nieuwenhove, A.; Ha, H.; Waroquier, M.; De Kimpe, N.; Van Speybroeck, V. *J. Org. Chem.* **2010**, *75*, 4530–4541.
- (23) Bultinck, P.; Ayers, P. W.; Fias, S.; Tiels, K.; Van Alsenoy, C. *Chem. Phys. Lett.* **2007**, *444*, 205–208.
- (24) Mortier, W. Electronegativity equalization and its applications. In *Structure & Bonding*; Kali, S., Jørgensen, C., Eds.; Springer: Germany, 1987; Vol. 66, pp 125–143.
- (25) Parr, R. G.; Yang, W. Aspects of atoms and molecules. In *Density-Functional Theory of Atoms and Molecules*; Oxford University Press: New York, 1994; pp 218–236.
- (26) Bultinck, P.; Vanholme, R.; Popelier, P. L. A.; De Proft, F.; Geerlings, P. J. *Phys. Chem. A* **2004**, *108*, 10359–10366.
- (27) Bultinck, P.; Langenaeker, W.; Carbo-Dorca, R.; Tollenaere, J. P. J. *Chem. Inf. Comput. Sci.* **2003**, *43*, 422–428.
- (28) York, D. M.; Yang, W. J. *Chem. Phys.* **1996**, *104*, 159–172.
- (29) Chelli, R.; Procacci, P.; Righini, R.; Califano, S. J. *Chem. Phys.* **1999**, *111*, 8569–8575.
- (30) Warshel, A.; Kato, M.; Pislakov, A. V. J. *Chem. Theory Comput.* **2007**, *3*, 2034–2045.
- (31) van Duin, A. C. T.; Strachan, A.; Stewman, S.; Zhang, Q.; Xu, X.; Goddard, W. A. J. *Phys. Chem. A* **2003**, *107*, 3803–3811.
- (32) Mortier, W.; Ghosh, S.; Shankar, S. J. *Am. Chem. Soc.* **1986**, *108*, 4315–4320.
- (33) Nistor, R. A.; Polihronov, J. G.; Müser, M. H.; Mosey, N. J. *J. Chem. Phys.* **2006**, *125*, 094108.
- (34) Nistor, R. A.; Müser, M. H. *Phys. Rev. B* **2009**, *79*, 104303.
- (35) Rappe, A.; Goddard, W. J. *Phys. Chem.* **1991**, *95*, 3358–3363.
- (36) Verstraelen, T.; Van Speybroeck, V.; Waroquier, M. J. *Chem. Phys.* **2009**, *131*, 044127.
- (37) Bultinck, P.; Langenaeker, W.; Lahorte, P.; De Proft, F.; Geerlings, P.; Waroquier, M.; Tollenaere, J. P. J. *Phys. Chem. A* **2002**, *106*, 7887–7894.
- (38) Bultinck, P.; Langenaeker, W.; Lahorte, P.; De Proft, F.; Geerlings, P.; Van Alsenoy, C.; Tollenaere, J. P. J. *Phys. Chem. A* **2002**, *106*, 7895–7901.
- (39) Baekelandt, B.; Mortier, W.; Lievens, J.; Schoonheydt, R. J. *Am. Chem. Soc.* **1991**, *113*, 6730–6734.
- (40) Menegon, G.; Shimizu, K.; Farah, J. P. S.; Dias, L. G.; Chaimovich, H. *Phys. Chem. Chem. Phys.* **2002**, *4*, 5933–5936.
- (41) Chelli, R.; Procacci, P. J. *Chem. Phys.* **2002**, *117*, 9175–9189.
- (42) De Proft, F.; Langenaeker, W.; Geerlings, P. *THEOCHEM* **1995**, *339*, 45–55.
- (43) Warren, L. G.; Davis, J. E.; Patel, S. J. *Chem. Phys.* **2008**, *128*, 144110.
- (44) Parr, R.; Pearson, R. J. *Am. Chem. Soc.* **1983**, *105*, 7512–7516.
- (45) Gilson, M. K.; Gilson, H. S.; Potter, M. J. J. *Chem. Inf. Model.* **2003**, *43*, 1982–1997.
- (46) Varekova, R. S.; Jirouskova, Z.; Vanek, J.; Suchomel, S.; Koca, J. *I. J. Mol. Sci.* **2007**, *8*, 572–582.
- (47) Berente, I.; Czinkó, E.; Náráy-Szabó, G. J. *Comput. Chem.* **2007**, *28*, 1936–1942.
- (48) Njo, S. L.; Fan, J.; van de Graaf, B. J. *Mol. Cat. A* **1998**, *134*, 79–88.
- (49) Mulliken, R. S. J. *Chem. Phys.* **1934**, *2*, 782–793.
- (50) Smalø, H. S.; Åstrand, P.; Jensen, L. J. *Chem. Phys.* **2009**, *131*, 044101.
- (51) Chaves, J.; Barroso, J. M.; Bultinck, P.; Carbo-Dorca, R. *J. Chem. Inf. Model.* **2006**, *46*, 1657–1665.
- (52) Press, W. H.; Flannery, B. P.; Teukolsky, S. A.; Vetterling, W. T. General Linear Least Squares. In *Numerical Recipes in C: The Art of Scientific Computing*; Cambridge University Press: New York, 1992; pp 671–680.
- (53) Verstraelen, T.; Van Speybroeck, V.; Waroquier, M. J. *Chem. Inf. Model.* **2008**, *48*, 1530–1541.
- (54) Verstraelen, T.; Van Houteghem, M.; Van Speybroeck, V.; Waroquier, M. J. *Chem. Inf. Model.* **2008**, *48*, 2414–2424.
- (55) Ghysels, A.; Verstraelen, T.; Hemelsoet, K.; Waroquier, M.; Van Speybroeck, V. J. *Chem. Inf. Model.* **2010**, *50*, 1736–1750.
- (56) Møller, C.; Plesset, M. S. *Phys. Rev.* **1934**, *46*, 618–622.
- (57) Woon, D. E.; Dunning, T. H. J. *Chem. Phys.* **1993**, *98*, 1358–1371.
- (58) Frisch, M. J.; Trucks, G. W.; Schlegel, H. B.; Scuseria, G. E.; Robb, M. A.; Cheeseman, J. R.; Montgomery, J. A.; Vreven, T.; Kudin, K. N.; Burant, J. C.; Millam, J. M.; Iyengar, S. S.; Tomasi, J.; Barone, V.; Mennucci, B.; Cossi, M.; Scalmani, G.; Rega, N.; Petersson, G. A.; Nakatsuji, H.; Hada, M.; Ehara, M.; Toyota, K.; Fukuda, R.; Hasegawa, J.; Ishida, M.; Nakajima, T.; Honda, Y.; Kitao, O.; Nakai, H.; Klene, M.; Li, X.; Knox, J. E.; Hratchian, H. P.; Cross, J. B.; Bakken, V.; Adamo, C.; Jaramillo, J.; Gomperts, R.; Stratmann, R. E.; Yazyev, O.; Austin, A. J.; Cammi, R.; Pomelli, C.; Ochterski, J. W.; Ayala, P. Y.; Morokuma, K.; Voth, G. A.; Salvador, P.; Dannenberg, J. J.; Zakrzewski, V. G.; Dapprich, S.; Daniels, A. D.; Strain, M. C.; Farkas, O.; Malick, D. K.; Rabuck, A. D.; Raghavachari, K.; Foresman, J. B.; Ortiz, J. V.; Cui, Q.; Baboul, A. G.; Clifford, S.; Cioslowski, J.; Stefanov, B. B.; Liu, G.; Liashenko, A.; Piskorz, P.; Komaromi, I.; Martin, R. L.; Fox, D. J.; Keith, T.; Al-Laham, M. A.; Peng, C. Y.; Nanayakkara, A.; Challacombe, M.; Gill, P. M. W.; Johnson, B.; Chen, W.; Wong, M. W.; Gonzalez, C.; Pople, J. A. *Gaussian 03*, revision B.03; Gaussian, Inc.: Wallingford, CT, 2004.
- (59) Koopmans, T. *Physica* **1934**, *1*, 104–113.
- (60) Cordero, B.; Gomez, V.; Platero-Prats, A. E.; Reves, M.; Echeverria, J.; Cremades, E.; Barragan, F.; Alvarez, S. *Dalton Trans.* **2008**, 2832–2838.
- (61) Bultinck, P.; Carbo-Dorca, R. *J. Math. Chem.* **2003**, *34*, 67–74.
- (62) Bultinck, P.; Carbo-Dorca, R.; Langenaeker, W. J. *Chem. Phys.* **2003**, *118*, 4349–4356.
- (63) Simons, J.; Joergensen, P.; Taylor, H.; Ozment, J. J. *Phys. Chem.* **1983**, *87*, 2745–2753.
- (64) Brooks, B.; Karplus, M. *Proc. Natl. Acad. Sci. U.S.A.* **1985**, *82*, 4995–4999.
- (65) Nicolay, S.; Sanejouand, Y. *Phys. Rev. Lett.* **2006**, *96*, 078104.
- (66) Ghysels, A.; Van Speybroeck, V.; Pauwels, E.; Catak, S.; Brooks, B. R.; Van Neck, D.; Waroquier, M. J. *Comput. Chem.* **2010**, *31*, 994–1007.
- (67) Ghysels, A.; Van Speybroeck, V.; Pauwels, E.; Van Neck, D.; Brooks, B. R.; Waroquier, M. J. *Chem. Theory Comput.* **2009**, *5*, 1203–1215.
- (68) De Proft, F.; Martin, J. M. L.; Geerlings, P. *Chem. Phys. Lett.* **1996**, *250*, 393–401.
- (69) Bultinck, P.; Carbo-Dorca, R. *Chem. Phys. Lett.* **2002**, *364*, 357–362.
- (70) Baekelandt, B.; Mortier, W.; Schoonheydt, R. The EEM approach to chemical hardness in molecules and solids: Fundamentals and applications. In *Chemical Hardness; Structure & Bonding*; Springer: Berlin, 1993; Vol. 80, pp 187–227.
- (71) Acke, G. *Benaderende Elektrostatistische Potentialen via Atoms in Moleculen en Elektronegativiteitsequalizatie*; Ghent University: Gent, Belgium, 2010.

Optimized Potential of Mean Force Calculations for Standard Binding Free Energies

Ignasi Buch,[†] S. Kashif Sadiq,[†] and Gianni De Fabritiis*

Computational Biochemistry and Biophysics Laboratory (GRIB-IMIM), Universitat Pompeu Fabra, Barcelona Biomedical Research Park (PRBB), C/Doctor Aiguader 88, 08003 Barcelona, Spain

S Supporting Information

ABSTRACT: The prediction of protein–ligand binding free energies is an important goal of computational biochemistry, yet accuracy, reproducibility, and cost remain a problem. Nevertheless, these are essential requirements for computational methods to become standard binding prediction tools in discovery pipelines. Here, we present the results of an extensive search for an optimal method based on an ensemble of umbrella sampling all-atom molecular simulations tested on the phosphorylated tetrapeptide, pYEEI, binding to the SH2 domain, resulting in an accurate and converged binding free energy of -9.0 ± 0.5 kcal/mol (compared to an experimental value of -8.0 ± 0.1 kcal/mol). We find that a minimum of 300 ns of sampling is required for every prediction, a target easily achievable using new generation accelerated MD codes. Convergence is obtained by using an ensemble of simulations per window, each starting from different initial conformations, and by optimizing window-width, orthogonal restraints, reaction coordinate harmonic potentials, and window-sample time. The use of uncorrelated initial conformations in neighboring windows is important for correctly sampling conformational transitions from the unbound to bound states that affect significantly the precision of the calculations. This methodology thus provides a general recipe for reproducible and practical computations of binding free energies for a class of semirigid protein–ligand systems, within the limit of the accuracy of the force field used.

1. INTRODUCTION

Achieving a standard, reliable, and accurate protocol for the quantitative determination of protein–ligand binding affinities has remained one of the pivotal problems in computational biochemistry; its attainment is set to yield a tremendous gain in the basic understanding of molecular biological processes. Attempts to compute binding affinities have been made since near the inception of computational biomolecular modeling, and several notable methods involving molecular dynamics (MD) simulations have arisen.^{1,2} The underpinning problem circumvented by all of these methods is that unbiased equilibrium-based free ligand binding using an all-atom model (including solvent), although computationally possible in certain cases, is much more expensive than the present calculations. Another route is therefore employed in arriving at a quantitative determination of the binding free energy.

At the high-throughput end, empirically tuned methods such as linear interaction energy (LIE) methods^{3–5} are used with the forfeit of compromising some accuracy. One major strategy is to use implicit solvent MD,⁶ which drastically reduces the computational cost, sometimes at the expense of neglecting crucial structural water mediated interactions.⁷ Such continuum solvent methods are often used in conjunction with thermodynamic cycle methods, such as the molecular mechanics Poisson–Boltzmann/Generalized-Born solvent accessible surface area (MMPB/GBSA) methods,^{2,8–13} that indirectly compute the binding free energy in solution by separation of the solvation and *in vacuo* interaction components of the free energy. Other more accurate and computationally intensive methods involving “alchemical” mutations, such as free energy perturbation (FEP)^{14–16} and thermodynamic integration (TI),^{17–19} have been traditionally

employed for—but not limited to—calculating relative binding free energies between related protein–ligand combinations, being able to calculate absolute binding free energies.²⁰ The latter, however, has a much greater computational cost.

Methods involving the biased sampling along a set of pre-selected reaction coordinates that follow physically meaningful binding pathways have also found a measure of success. These include metadynamics,^{21,22} adaptive force bias,²³ the Jarzynski method,^{24,25} and umbrella sampling^{26,27} among others. For example, metadynamics approaches have been used to determine peptidic binding of highly flexible target proteins,²⁸ while biased umbrella sampling methods have shown that accurate binding free energies are indeed possible once conformational (rotational and translational) restraints are properly sampled.^{29–33} The overriding problem with such methods is that they require extensive knowledge of the specific system, in order to apply the relevant biases; they are thus costly in human resources, requiring informed and manual selection of appropriate restraints in the configurational space, and are thus not scalable in a standard way to the high-throughput domain. Recently, an unbiased umbrella sampling method was reported using only a one-dimensional potential of mean force (PMF) calculation³⁴ and the weighted histogram analysis method (WHAM).³⁵ Although only modestly precise when applied to the benzamidine–trypsin system, the method does away with conformational biasing and applies only generic restraints, orthogonal to the direction of binding. Furthermore, the ease of implementation of this method makes further evaluation of it an attractive

Received: January 26, 2011

Published: April 28, 2011

prospect for being an optimal method for high-throughput binding free energy determination, provided that the fundamental problem of sufficient sampling can be overcome.

The current age of micro- to millisecond MD brings with it the ability to test the hypothesis that current MD force fields are accurate enough to reproducibly attain accurate binding free energies, given enough sampling. Aggregate sampling across such time scales has been implemented by several groups,^{36–41} primarily with respect to conformational dynamics and protein folding, and lends itself naturally to distributed computing initiatives.⁴² Furthermore, the recent advances in programmable GPU technology^{43–45} have facilitated several initiatives, like ACEMD,⁴⁴ a new generation fast MD code exclusively running on GPUs, and GPU GRID, a distributed computing project⁴⁶ for molecular dynamics simulations. Using this resource, we have previously shown that extensive sampling (over 19 μ s of aggregate sampling) using the 1D-PMF method for a larger-ligand system than the benzamidine-trypsin, results in accurate binding free energies compared with experimental results,⁴⁶ while with the optimization reported here, only 300 ns are necessary.

In this paper, we investigate whether such a method can be made robust, convergent, and reproducible, while optimizing the protocol to minimize the amount of required computational cost and crucially retaining the accuracy of the result. To allow an optimal comparison to other methods²⁹ and our earlier investigations,⁴⁷ the method is applied to the Src homology 2 (SH2) domain binding to the phosphorylated tetrapeptide pYEEI. SH2 domains are noncatalytic domains⁴⁸ composed of approximately 100 amino acids,⁴⁹ involved in a large variety of tyrosine–kinase signal transduction pathways,^{50–52} and bind short peptidic sequences containing phosphorylated tyrosine residues.^{53,54} Furthermore, many pathological conditions, such as autoimmune diseases, cancer, and asthma, can be associated with the incorrect function of SH2-mediated processes, making them an attractive target for structure-based drug design.^{55–57} This ubiquitous role in cell function and regulation^{48,50} imposes conditions of high affinity and specificity for a range of peptides,^{58,63} making them an excellent template for differentiating various computational methodologies.^{29,47,64}

Here, we first reimplement our extensive 1D-PMF sampling protocol used previously,⁴⁶ analyzing its convergent properties. Second, we adapt the 1D-PMF protocol through a sequence of optimizations. These include window-width and thus corresponding harmonic restraint variation, the use of ensemble trajectory sampling, which has been shown to be advantageous over single trajectory sampling in other methods,¹³ and the use of multiple initial conditions. At each stage, the computational cost is reduced or the corresponding accuracy and convergence increased. As the sampling required to achieve convergence is related to the conformational freedom and thus the size of the system, the protocol that emerges from this optimization is capable of producing accurate and reproducible binding free energies up to the given size of the system implemented here. This result would allow a vast array of ligand–protein binding free energies up to the given molecular weight to be accurately and rapidly determined through high-throughput molecular simulation.

2. MATERIALS AND METHODS

2.1. System Preparation.

The input model is based on the bound crystallographic structure of the complex of the human

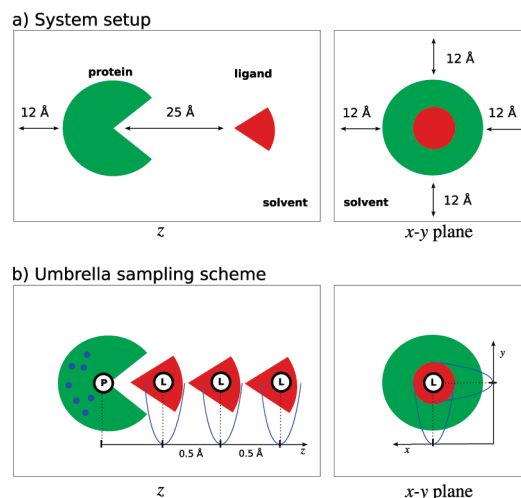


Figure 1. (a) Schematic representation of a system for the calculation of free-energy of binding. “P” and “L” are for protein and ligand, respectively. (b) Schematic visualization of the initial configurations for the US of the SH2 domain/pYEEI ligand complex (PDB: 1LKK) in the water box.

p56^{lck} domain and the peptide phosphotyrosine-Glu-Glu-Ile (pYEEI; PDB: 1LKK) using the CHARMM27⁶⁵ force field. The phosphotyrosine residue was assumed to be in its charged form $Y-PO_3^{2-}$ as experimentally determined.⁶⁰ Neutral acetylated N-terminus (ACE) and amidated C-terminus (CT2) residues were used to cap the peptide. The complex was solvated in a TIP3P⁶⁶ water box with a boundary at least 12 Å from the system in the x and y directions and at 52 Å in the z direction, giving a box size of $65 \times 62 \times 93 \text{ \AA}^3$, the z axis being larger to allow for the generation of several US initial configurations with the ligand at different distances from the protein (Figure 1a).

The ionic strength was set to 0.15 M Na^+ and Cl^- and the system charge neutralized. The final system comprised 38 655 atoms. The reaction coordinate z was set to be orthogonal to the plane formed by the binding interface of the complex; the protein was then rotated manually during system preparation with the aim of providing a large water reservoir in the direction of the ligand displacement.

The system was minimized and relaxed under NPT conditions at 1 atm and 298 K using a time step of 2 fs, a cutoff of 9 Å, with rigid bonds and PME for long-range electrostatics with a grid of $64 \times 64 \times 96$. During minimization and equilibration, the heavy protein atoms were restrained by a 10 kcal/mol/Å² spring constant. Two rounds of velocity reinitialization for 2 ps were performed under NVT conditions. The magnitude of the restraining spring constant was then reduced to 1 kcal/mol/Å² during 10 ps of NVT before the barostat was switched on at 1 atm for a further 10 ps of NPT simulation. A final 40 ps of NPT simulation was conducted with a restraint constant of 0.05 kcal/mol/Å². Finally, the volume was allowed to relax for 10 ns under NPT conditions. During this run, only C α atoms of the complex were restrained with a 1 kcal/mol/Å² constant in order to prevent reorientation.⁴⁶

Production simulations were run using ACEMD⁴⁴ over GPU GRID.net⁴⁶ with the same parameters used for the relaxation but a time step of 4 fs due to the use of the hydrogen mass repartition scheme⁶⁷ implemented in ACEMD. This elegant method⁶⁷ uses the mathematical property that individual atom masses do not

Table 1. Umbrella Sampling Simulation Parameter Variation^a

ID	N_r	N_w	Δw (Å)	t (ns)	k_{xy} (kcal/(mol·Å ²))	k_z (kcal/mol·Å ²)	IC	t_{tot} (μs)
set 1 ⁴⁶	1	381	0.1	50	0.1	10	IC1	19
set 2	10 × 3	51	0.5	80	0.1, 1	0.5, 1, 2.5, 5, 10	IC2	122.4
set 3	10	51	0.5	20	1	0.5	IC2	10.2
set 4	10	51	0.5	20	1	0.5	IC1	10.2

^a N_r , number of complete US replicas; N_w , number of windows per US replica; Δw , US window width; t , simulation time per US window; k_{xy} , force constant for orthogonal restraints; k_z , force constant for US restraints; IC, source of initial conformations; t_{tot} , total aggregate simulation time.

appear explicitly in the equilibrium distribution; therefore changing them only affects the transport properties of the system marginally but not the equilibrium distribution.⁴⁴

2.2. Initial Conformation Generation. The umbrella sampling (US) method requires the prior generation of initial conformations for each window of the production sampling. Window-centered initial conformations corresponding to the entire range of the reaction coordinate were generated via preliminary MD simulations in which the ligand was displaced by 25 Å along the z direction toward the bulk from $z = 0$ Å to $z = 25$ Å by applying a linear force $F = -k_d(z - vt)$ to all of its carbon atoms, where $k_d = 10$ kcal/mol/Å² and $v = 5$ Å/ns. A second biasing restraint of $k = 0.1$ kcal/mol/Å² was applied to the center of mass of the ligand to restrain to the xy plane (with respect to the initial bound position of the ligand). A harmonic restraint of $k = 1$ kcal/mol/Å² was applied to every C α atom residing in an α -helix or β -sheet of the protein further than 9 Å from the ligand. This prevented rotation and translation of the protein during ligand separation while preserving the flexibility of the binding pocket. Snapshots of the system coordinates (Figure 1b) were saved at constant intervals. Two sets of initial conformations were generated using this method. The first set (denoted IC1 hereafter) employed a single preliminary MD run, generating a single initial conformation for each window from that run. The second set (denoted IC2 hereafter) employed a total of 10 preliminary MD simulations, thus generating 10 initial conformations for each window. Initial conformations were then chosen by window-sequential selection across the set of 10 preliminary runs, thus ensuring that neighboring initial conformations were from different runs. Initial conformations derived from the same preliminary run thus had a 10-window spacing within the set.

2.3. Umbrella Sampling Optimization. A number of umbrella sampling (US) simulations were performed, each varying a protocol parameter, namely, window width (Δw) and, correspondingly, the number of windows, sample time per independent simulation per window (t), orthogonal restraints k_{xy} , force constant for the harmonic window potential k_z , the ensemble size or number of independent simulations (N_r), and finally whether the initial starting conformation set was IC1 or IC2 (IC). The reaction coordinate always extended from $z = 0$ Å to $z = 25$ Å with the bound configuration at position $z = 0$ Å used as a reference. The parameter sets for the full range of simulations performed here together with the total corresponding sampling time (t_{tot}) are listed in Table 1. All initial US windows were submitted to GPUGRID.net for execution of the US protocol. Each US window simulation was divided into several successive steps, with each step being 4 ns of duration. Each step was run as a separate GPUGRID work unit (WU), where each WU corresponded to about 6 h of continued computation for a typical GPUGRID volunteer computer, while ACEMD on a top GPU

like a GTX480 would perform 50 ns/day for this system. Preliminary runs to generate initial conformations were performed locally. The rationale for the different simulations is explained below.

Set 1 corresponded to the implementation of a previous exhaustive sampling simulation, reported previously,⁴⁶ using a small window width of 0.1 Å (381 windows) and a sampling time up to 50 ns per window. Initial conformations were generated from a single preliminary MD run (IC1).

Set 2 corresponded to the optimization procedure for the force constants for the harmonic potentials both for restraining diffusion in the xy plane (k_{xy}) and for the US potential (k_z). It employed a set of three US simulations each of up to 80 ns/window for a combination of 10 different permutations of k_{xy} and k_z listed in Table 1 and using a larger window width of 0.5 Å (51 windows). The optimal parameter set (OPS) was determined as $k_{xy} = 1$ kcal/mol/Å² and $k_z = 0.5$ kcal/mol/Å² (Figure 3). The initial conformation set was IC2.

Set 3 corresponded to the ensemble sampling procedure using the OPS. This entailed an ensemble of 10 identical US simulations for which the PMF and subsequent binding free energy were calculated in order to determine the convergence properties of the method. Initial conformations were generated as for set 2 (IC2).

Set 4 corresponded to the study of the effect of using a less varied initial conformation set across neighboring windows. A set of 10 identical US simulations were performed, similar to set 3 but using initial conformations generated in a more simple manner, from a single preliminary MD simulation (IC1).

2.4. Free-Energy Calculation. The PMF over the reaction coordinate for each replica was reconstructed using WHAM³⁵ with a convergence tolerance of 10^{-4} . From the PMF, the standard free energy of binding was computed using the expression given in³⁴

$$\Delta G^\circ = \Delta W_R - k_B T \ln \left(\frac{l_b A_{u,R}}{V^\circ} \right) + \Delta G_R \quad (1)$$

where ΔW_R is the PMF depth, k_B is the Boltzmann constant, T is the temperature, $l_b = \int_{\text{bound}} \exp(-W_R(z)/k_B T) dz$ is the integral of the PMF over the bound length, $A_{u,R} = 2\pi k_B T/k_{xy}$ is the area in the x and y directions of the unbound ligand, $V^\circ = 1661$ Å³ is the standard volume, and ΔG_R is the free energy to remove the orthogonal restraints (on x and y) when the ligand is bound. ΔG_R is obtained via a free energy perturbation approach from the exponential average.³⁴

In order to assess convergence, the sampling time per window used to construct the PMF and thus the free energy for each replica was increased up to the maximum sampling time across the 51 windows. The convergence of each replica with an

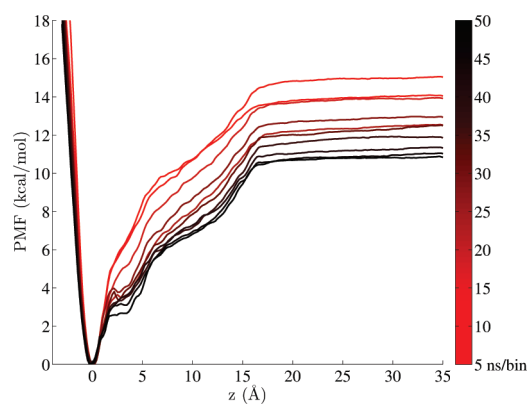


Figure 2. Reconstructed potential of mean force of the SH2 domain/pYEEI ligand complex along the reaction coordinate, calculated from 381 completed US configurations of 50 ns each. The PMF is reconstructed over increasing sample time windows along the US trajectories showing the long relaxation time of the US simulations. The reference ΔW_R value (PMF depth) computed from the last PMF is 10.8 kcal/mol, producing a standard free energy of binding of -8.5 ± 0.5 kcal/mol, accounting for the standard volume and biasing factors. The experimental value for this system is -8.0 kcal/mol. Simulation is termed set 1.

increase in time was then charted as well as the corresponding mean and standard deviation.

3. RESULTS AND DISCUSSION

We begin by analyzing the exhaustive umbrella sampling (US) method reported previously,⁴⁶ called set 1 here. Optimization of the method requires us to obtain convergent and accurate results with the minimum sampling time and proceeds via alteration of window width and a corresponding systematic parameter search with respect to harmonic restraint values (set 2). Convergence is investigated by employing an ensemble of simulations and analyzing across an increasing sampling time per window (set 3) and compared against a similar ensemble with the choice of using less varied initial conformations (set 4).

3.1. Exhaustive Umbrella Sampling. An exhaustive umbrella sampling method utilizing $19 \mu\text{s}$ aggregate sampling was used to determine the free energy of binding of SH2 to pYEEI (set 1⁴⁶ in Table 1, 1 run). The PMF depth (see Figure 2) is $\Delta W_R = -10.8$ kcal/mol, with a small variation for different times in the US runs. The bound distance is $l_b = 0.93$ Å, and the area explored by the ligand in the xy plane $A_{u,R} = 37.07$ Å². The free energy to remove the constraints have a negligible contribution $\Delta G_R = -0.0124$ kcal/mol due to the low restraint applied. The standard free energy of binding for the pYEEI ligand is computed from eq 1 as $\Delta G^\circ = -8.5$ kcal/mol, which compares with a reported experimental value of -8.0 kcal/mol.⁶¹

Construction of the PMF over the entire data set thus results in a single value for free energy without specification of the error. In order to compute the error, it is first instructive to determine the amount of sampling time per window required to stabilize the free energy. Computing the PMF for increasing sample time within each window (Figure 2), we see that convergence is achieved after approximately 50 ns with a value of -8.5 kcal/mol. This first indicates that the sampling can be reduced to $12 \mu\text{s}$ by considering a shorter (25 Å) reaction coordinate. However, it also indicates that a long equilibration time is necessary using an approach with a single simulation per window. An associated

error is then determined by discretizing the postequilibration region into 5 ns blocks and computing the block average (as done in previous studies³⁴). This results in a binding free energy of $\Delta G^\circ = -8.5 \pm 0.5$ kcal/mol and compares well with a reported experimental value of -8.0 kcal/mol.⁶¹ However, the accuracy of the above result comes at a substantial sampling cost ($19 \mu\text{s}$); it is thus desirable to lower these costs by optimizing the method.

3.2. Determining the Optimal Parameter Set (OPS). The first optimization strategy is to reduce the number of windows by increasing the window width to 0.5 Å. However, alteration of window width requires further optimization of harmonic restraints, in particular, that of the umbrella sampling potential (k_z). To determine the optimal choice of k_{xy} and k_z , an ensemble of three umbrella sampling simulations for every window is performed for each of 10 permutations of k_{xy} and k_z (set 2 in Table 1, 30 runs).

It is clear from Figure 3a and b that a stabilized PMF is exhibited for various selections of k_{xy} and k_z . For example, for $k_{xy} = 0.1$ kcal/mol/Å² and $k_z = 1$ kcal/mol/Å² (blue lines in Figure 3a), each of the three members of the ensemble show unchanging PMF values after 60 ns but vary among themselves over a range of 2.5 kcal/mol.

We have shown thus far that binding free energies attained using single runs exhibit stable PMFs with respect to themselves at 50 ns. However, convergence requires that multiple replicas of the same run converge to the same value. Here, even for 80 ns of sampling per window, no harmonic constraint permutation yields convergent results between the three members of its corresponding ensemble, except that of $k_{xy} = 1$ kcal/mol/Å² and $k_z = 0.5$ kcal/mol/Å² (green lines in Figure 3a). This set converges to within 0.5 kcal/mol within 50 ns of sampling per window at the given window width of 0.5 Å, establishing it as the optimal parameter set (OPS). After 50 ns of sampling, the OPS thus attains an accurate binding free energy of -9.0 ± 0.5 kcal/mol, within 1 kcal/mol of experiment.

The chosen OPS exhibits the best convergence but only for an ensemble of three. While sufficient to discriminate it from the other parameter sets, the convergence properties of the absolute binding free energy can be investigated better using a larger ensemble.

3.3. Convergence and Sampling Properties of the Optimal Parameter Set. Here, we perform a larger ensemble of simulations using the OPS (set 3 in Table 1, 10 runs) and analyze the corresponding convergence properties with an increase in sample time per window. We also investigate whether using less varied initial conformations across the US profile confers any difference to the accuracy or convergence properties of the binding free energy. This entails a second ensemble of similar size and sampling time (set 4 in Table 1, 10 runs).

The mean binding free energy across the ensemble set as a function of sample time is analyzed (Figure 4) for each. The free energy for set 3 exhibits convergence at 6 ns with a free energy of -9.0 ± 0.9 kcal/mol and convergence to within 0.4 kcal/mol at 20 ns. By contrast, set 4 does not exhibit true convergence, even up to 20 ns, even though it yields a flattened mean binding free energy of -8.7 ± 1 kcal/mol. This is because, unlike for set 3, the error does not diminish significantly with increased sampling. Examination of the convergence of each single US run with increasing sample time (see Supporting Information) shows that while all single runs converge to the same value for set 3, they do not for set 4. Instead, single runs stabilize on a particular binding

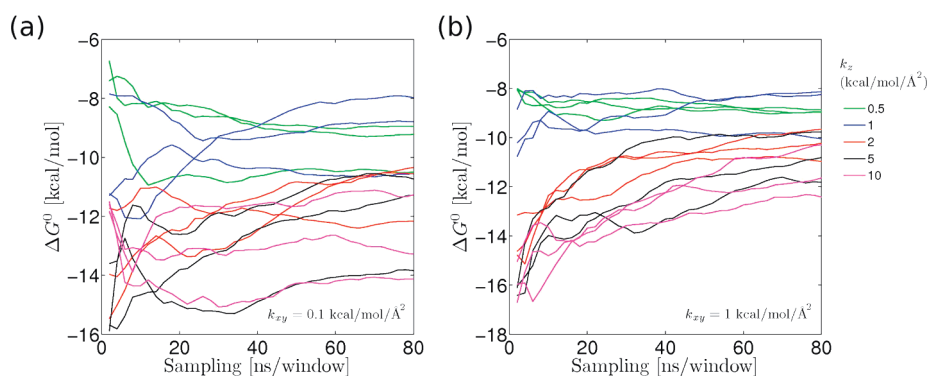


Figure 3. Harmonic constraint optimization over a range of $k_z = 0.5, 1, 2.5, 5, 10$ kcal/mol/Å² for $k_{xy} = 0.1$ (left) and $k_{xy} = 1$ kcal/mol/Å² (right). Simulation is termed set 2.

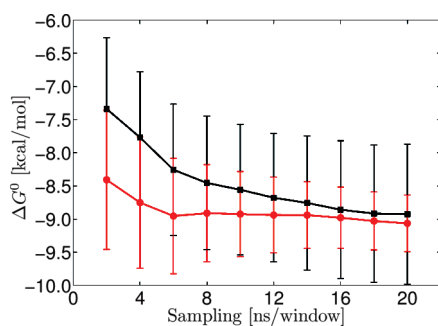


Figure 4. Comparison of two ensembles of 10 US simulations, one where each simulation was started from a different initial conformation per window (red), termed set 3, and the other where each simulation was started from a single initial conformation per window (black), termed set 4.

free energy, and this results in the error not diminishing for the latter while it does for the former.

The above analysis draws us to conclude that, provided convergence is demonstrated through an ensemble of runs, a single run using the OPS and an aggregate sampling time of 300 ns is sufficient to provide a result to within 1 kcal/mol accuracy and precision to within 1 kcal/mol and 1 μ s to within the same accuracy but a tighter convergence of within 0.5 kcal/mol. However, it is important to note that such an aggregate time scale also requires a sufficient relaxation time to be met within each window; in this case, relaxation leads to convergence of the binding free energy within 6 ns of sample time per window.

Furthermore, the analysis also demonstrates that the choice of initial conformations plays a significant role in the attainment of convergence. More specifically, it is the sensitivity to the correlation between the initial conformations along a single profile of US windows that affects the convergence of the binding free energy. Furthermore, deriving initial conformations from a single preliminary MD run would require marginally less computation; however, the loss of convergence due to the correlated nature of the initial conformations prevents such a choice being optimal.

3.4. Structural Correlates of Differential Sampling. Convergent sampling depends on the flexibility of the ligand and the protein across the reaction coordinate. Very flexible ligands/proteins or those capable of accessing multiple distinct conformations increase the convergence time because it requires sampling across all the relevant conformational degrees of freedom.

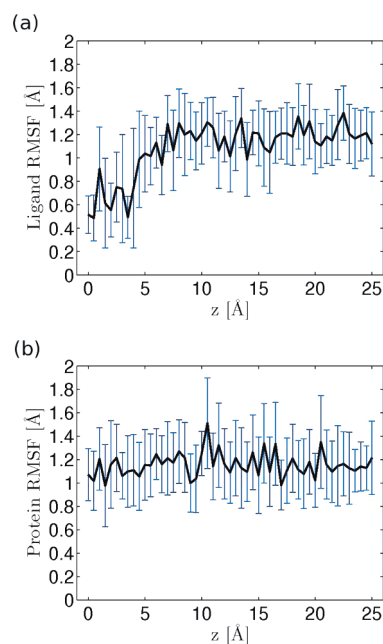


Figure 5. Backbone flexibility in terms of root mean squared fluctuations (RMSF) relative to the average structure in each window of the reaction coordinate. (a) The ligand is more rigid closer to the surface of the protein (RMSF ~ 0.6 Å) and more flexible in the unbound state (RMSF ~ 1.2 Å). A sharp transition in flexibility is seen between 4.5 and 5.5 Å along the reaction coordinate. Within a 1 Å distance, the ligand transits from being rigidly bound to being flexible and unbound. (b) The protein, instead, shows similar flexibility (RMSF ~ 1.3 Å) between its bound and unbound conformations.

The flexibility of both the protein and the ligand is thus assessed in terms of root mean squared fluctuations (RMSF) relative to the average structure in each window of the reaction coordinate (Figure 5).

In Figure 5, it is shown that the ligand is more rigid closer to the surface of the protein (RMSF ~ 0.6 Å) and more flexible in the unbound state (RMSF ~ 1.2 Å). The protein shows similar flexibility upon binding (RMSF ~ 1.3 Å) with the ligand to that when unbound. There is a sharp transition in flexibility in the ligand RMSF between 4.5 and 5.5 Å along the reaction coordinate, while the ligand transits from being bound at 4.5 Å to more flexible and unbound over a short distance of 1 Å.

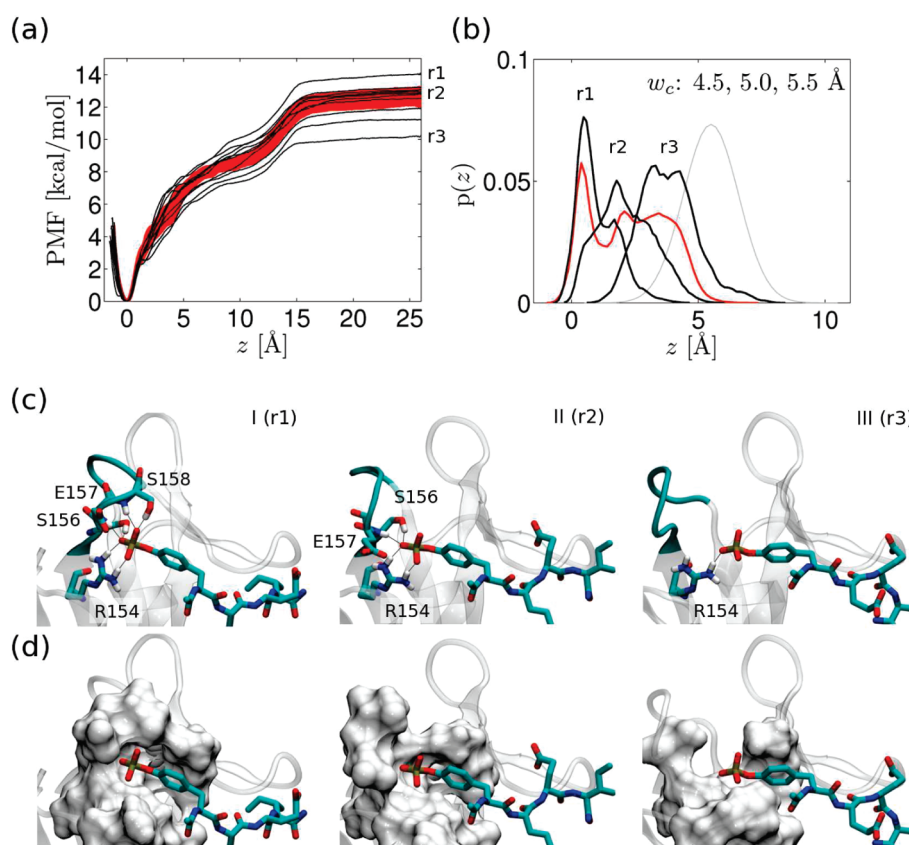


Figure 6. (a) PMF of all members of the set 4 ensemble (black lines) against the PMF range of set 3 (red band). Notable individual members corresponding to excessive, accurate, and underestimated binding free energies are denoted r1, r2, and r3, respectively. (b) Integrated probability distribution of r1, r2, and r3 for the differential sampling region exhibited in the PMF across windows centered at 4.5, 5, and 5.5 Å. The aggregate distribution of set 3 is also shown (red) as well as the theoretical distribution for a system acting only under the restraining potential (gray). (c) Principal structural correlates, corresponding to the three sampling peaks in b, showing pY interaction with R184, S156, E157, and S158 of SH2. The differential conformation of the flexible loop region (cyan) corresponds to the degree of hydrogen bonding exhibited. (d) Surface representation of the corresponding conformations.

The sensitivity of convergence to the correlation between initial conformations is investigated in more detail and the structural correlates pertaining to the variation of binding free energies for correlated PMF profiles determined. First, the PMF profiles (Figure 6a) of all individual US runs belonging to set 4 (black lines) show greater variability than the converged PMF profile range of set 3 (red band). It is this variation that causes the 3 kcal/mol deviation between the highest and the lowest value for the free energy. Crucially, significant variation with respect to the convergence band commences across windows centered at 4.5, 5, and 5.5 Å, corresponding to the sharp transition region exhibited in ligand flexibility, suggesting that it is in this region where orientational and conformational degrees of freedom play a more important role.

Three profiles from set 4, corresponding to the binding free energies of -6.7 kcal/mol, -9.2 kcal/mol, and -10.4 kcal/mol from individual simulations denoted r1, r2 and r3, respectively, are investigated more closely on the basis that the first underestimates the free energy, the second lies within the convergence band, and the third overestimates the free energy. An examination of the integrated normalized probability distribution of the ligand center of mass across the windows centered at 4.5 Å, 5 Å, and 5.5 Å (Figure 6b) shows substantially different sampling compared to set 3 (red). While the converged ensemble samples

a trimodal distribution consisting of a sharp peak at 0 Å, and two shallower peaks at 2.5 and 3.5 Å, respectively, the three individual simulations r1, r2, and r3 each predominantly simulate a different mode from each other. Each one, however, corresponds to a mode within the trimodal distribution of set 3. This confirms that the region with window centers between $z = 4.5$ Å and $z = 5.5$ Å thus corresponds to a sensitive transition region between bound and unbound states of pY for the two protocols.

The three sampling peaks exhibited along the reaction coordinate (Figure 6b) correspond to three distinct structural conformations (Figure 6c and d), which are all sampled correctly in the converged simulations but incorrectly in the individual runs. The most bound conformation (I), at $z = 0$ Å, consists of an extremely tight hydrogen bond network (six hydrogen bonds) between the phosphotyrosine (pY) of the ligand and the R154, S156, E157, and S158 residues in SH2. This is due to the favorable conformation of the flexible loop between residues 156 and 162 of SH2 (cyan). The second conformation (II), at $z = 2.5$ Å, corresponds to a slight retraction of the loop coupled with the increased separation of the ligand and results in the loss of two hydrogen bonds with S158. The third conformation (III) at $z = 3.5$ Å corresponds to a more significant retraction of the flexible loop region losing all of its hydrogen bonds with pY; only a single hydrogen bond is maintained with R154. The individual

run r1 thus oversamples the most bound conformation, increasing the PMF at that point and resulting in an excessive binding free energy. Conversely, r3 oversamples the more unbound conformation, flattening the PMF at that point and eventually resulting in a smaller free energy. Finally, r2 oversamples conformation II, which compensates the loss in bound-conformation sampling with a loss in more unbound sampling and results in a PMF change within the convergence band, leading to an accurate binding free energy.

The above analysis shows that the accuracy of the binding free energy calculation can be significantly affected by differently sampled structural events that occur in each window, especially in windows that correspond to sharp transitions in ligand flexibility and/or binding that have their root in discrete structural events such as hydrogen bonding. While both stably bound and unbound states are easier to sample correctly by several approaches, convergence is more profoundly tested in the transition region between the two. However, it is not only the occurrence of such events in each window that matters but the overall integration across a number of relevant neighboring windows. The use of correlated initial conformations increases the chance of maintaining insufficient sampling across a set of neighboring windows resulting in an incorrect shift in PMF depth (r1 and r3), which is then propagated along the reaction coordinate. Even though this can occur for uncorrelated neighboring windows too, the latter exhibit far more sampling across windows, resulting in a tighter convergence of the PMF.

4. CONCLUSIONS

In this work, we show that it is possible to determine accurate, reproducible, and scalable absolute protein–ligand binding free energies using molecular dynamics simulations, at least for the specific case used here. Our optimized protocol employs a simply biased 1D-PMF umbrella sampling method applied using an ensemble of simulations, initiated from uncorrelated initial conformations across neighboring windows and an optimal parameter set (OPS) describing orthogonal restraints, a force constant for the sampling potential, window width, and sampling time per window.

Applied to the SH2 domain binding to the pYEEI ligand, we obtain an absolute binding free energy of -9.0 ± 0.5 kcal/mol, in good agreement with experimental results (1 kcal/mol deviation), demonstrating the accuracy of the method. The minimum aggregate sampling time to compute an accurate result is 300 ns with the OPS, a significant improvement over the 19 μ s aggregate sampling of a previous method.

Our methodology is also demonstrated to be reproducible; that is, ensemble-based repetition of the calculation shows convergence to within 1 kcal/mol among independent simulations for the above-mentioned aggregate sampling time. Furthermore, we show that it is correct sampling of sensitive bound–unbound transition regions, corresponding to various phosphotyrosine interactions in the binding groove, that determine the convergence of the result. Structural correlates of differential sampling account for the discrepancies between different methodologies, and the optimal methodology presented here overcomes such sensitivities.

The protocol reported concerns the calculation of the PMF for systems where there is a direct path from the bulk to the binding site, thus making it amenable to the 1D-PMF method. Calculations for more complex binding processes that involve multiple reaction coordinates and/or significant protein–ligand conformational changes upon binding are beyond the remit of the method. Within the remit, however, as the protocol reported

here does away with system specific conformational restraints and the corresponding human choices of system construct, it is readily scalable to a large number of protein–ligand systems. There may be limits of transferability for the parameters optimized in this system when applied to other systems. A priori, it is difficult to determine whether certain classes of systems will exhibit transferable parameters, but it is likely that flexibility, ligand size, and binding pathway will play an important role. Cases where the protein is very flexible,⁶⁸ much more so than the SH2 domain, may cause a problem because the umbrella sampling would need to sample correctly all of the conformations. This was possible here where the conformational fluctuation was limited to a loop of the SH2 domain by properly sampling the initial conformations of the umbrella sampling. The same problem of conformational sampling applies for very flexible ligands. Also, if the exit pathway of the ligand is very narrow, care has to be used in the selection of the exit direction. In summary, we would expect this methodology and parameter set to work for semirigid proteins (small loop movements) and semirigid ligands with an easy access pathway to the binding site. In the case where these parameters may not be directly transferable (free energy of binding very different from the experimental value), we believe that a good approach is to enhance the creation of initial configurations for the umbrella sampling before undergoing any deep optimization study. Once the limit of this protocol is reached, additional optimization methods like Hamiltonian replica exchange⁶⁹ would need to be considered. Finally, as the accuracy and precision obtained is, in this case, very high, it supports the accuracy of the force field for the given ligand. However, ligand force field accuracy is not the general case, which means that the extensive and convergent sampling provided by this methodology may allow the validation and improvement of force field accuracy for different ligands.

■ ASSOCIATED CONTENT

Supporting Information. ΔG° evolution with increased sampling time per window. This material is available free of charge via the Internet at <http://pubs.acs.org/>.

■ AUTHOR INFORMATION

Corresponding Author

*E-mail: gianni.defabritiis@upf.edu.

Author Contributions

[†]These authors contributed equally to this work

■ ACKNOWLEDGMENT

The authors are grateful to the volunteers of GPUGRID who donate GPU computing time to the project. I.B. acknowledges support from the Obra Social Fundació “La Caixa”. S.K.S. acknowledges support from a European Commission FP7 Marie Curie IEF. G.D.F. acknowledges support from the Ramón y Cajal scheme and from the Spanish Ministry of Science and Innovation (ref. FIS2008-01040).

■ REFERENCES

- (1) Kollman, P. *Chem. Rev.* **1993**, *93*, 2395–2417.
- (2) Kollman, P. A.; Massova, I.; Reyes, C.; Kuhn, B.; Huo, S.; Chong, L.; Lee, M.; Lee, T.; Duan, Y.; Wang, W.; Donini, O.; Cieplak, P.;

- Srinivasan, J.; Case, D. A.; Cheatham, T. E. R. *Acc. Chem. Res.* **2000**, *33*, 889–897.
- (3) Wang, W.; Wang, J.; Kollman, P. A. *Proteins: Struct. Funct. Genet.* **1999**, *34*, 395–402.
- (4) Aqvist, J.; Medina, C.; Samuelsson, J.-E. *Protein Eng.* **1994**, *7*, 385–391.
- (5) Carlson, H. A.; Jorgensen, W. L. *J. Phys. Chem.* **1995**, *99*, 10667–10673.
- (6) Kuhn, B.; Kollman, P. A. *J. Med. Chem.* **2000**, *43*, 786–3791.
- (7) Wittayanarakul, K.; Hannongbua, S.; Feig, M. *J. Comput. Chem.* **2008**, *29*, 673–685.
- (8) Schwarzl, S. M.; Tschoopp, T. B.; Smith, J. C.; Fischer, S. *J. Comput. Chem.* **2002**, *23*, 1143–1149.
- (9) Rizzo, R. C.; Toba, S.; Kuntz, I. D. *J. Med. Chem.* **2004**, *47*, 3065–3074.
- (10) Wang, W.; Kollman, P. A. *J. Mol. Biol.* **2000**, *303*, 567–582.
- (11) Zoete, V.; Michielin, O.; Karplus, M. *J. Comput.-Aided Mol. Des.* **2003**, *17*, 861–880.
- (12) Stoica, I.; Sadiq, S. K.; Coveney, P. V. *J. Am. Chem. Soc.* **2008**, *130*, 2639–2648.
- (13) Sadiq, S. K.; Wright, D. W.; Kenway, O. A.; Coveney, P. V. *J. Chem. Inf. Model.* **2010**, *50*, 890–905.
- (14) Lu, N.; Singh, J. K.; Kofke, D. A. *J. Chem. Phys.* **2003**, *118*, 2977–2984.
- (15) Price, D.; Jorgensen, W. J. *Comput.-Aided Mol. Des.* **2001**, *15*, 681–695.
- (16) Reddy, M.; Erion, M. *J. Am. Chem. Soc.* **2001**, *123*, 6246–6252.
- (17) Shirts, M. R.; Pande, V. S. *J. Chem. Phys.* **2005**, *122* (144107), 1–16.
- (18) Fowler, P. W.; Jha, S.; Coveney, P. V. *Philos. Trans. R. Soc. London, Ser. A* **2005**, *363*, 1999–2015.
- (19) Wan, S.; Coveney, P. V.; Flower, D. R. *Philos. Trans. R. Soc. London, Ser. A* **2005**, *363*, 2037–2053.
- (20) Mobley, D. L.; Chodera, J. D.; Dill, K. A. *J. Chem. Phys.* **2006**, *125*, 084902.
- (21) Gervasio, F.; Laio, A.; Parrinello, M. *J. Am. Chem. Soc.* **2005**, *127*, 2600–2607.
- (22) Fidelak, J.; Juraszek, J.; Branduardi, D.; Bianciotto, M.; Gervasio, F. *J. Phys. Chem. B* **2010**, *114*, 9516–9524.
- (23) Babin, V.; Roland, C.; Sagui, C. *J. Chem. Phys.* **2008**, *128*, 134101.
- (24) Jarzynski, C. *Phys. Rev. E* **2002**, *65*, 046122.
- (25) Jarzynski, C. *Phys. Rev. Lett.* **1997**, *78*, 2690–2693.
- (26) Roux, B. *Comput. Phys. Commun.* **1995**, *91*, 275–282.
- (27) Virnau, P.; Müller, M. *J. Chem. Phys.* **2004**, *120*, 10925.
- (28) Pietrucci, F.; Marinelli, F.; Carloni, P.; Laio, A. *J. Am. Chem. Soc.* **2009**, *131*, 11811–11818.
- (29) Woo, H.-J.; Roux, B. *Proc. Natl. Acad. Sci. U. S. A.* **2005**, *102*, 6825–6830.
- (30) Wang, J.; Deng, Y.; Roux, B. *Biophys. J.* **2006**, *91*, 2798–2814.
- (31) Shivakumar, D.; Deng, Y.; Roux, B. *J. Chem. Theory Comput.* **2009**, *5*, 919–930.
- (32) Gan, W.; Roux, B. *Proteins: Struct., Funct. Bioinf.* **2009**, *74*, 996–1007.
- (33) Deng, Y.; Roux, B. *J. Phys. Chem. B* **2009**, *113*, 2234–2246.
- (34) Doudou, S.; Burton, N.; Henchman, R. *J. Chem. Theory Comput.* **2009**, *5*, 909–918.
- (35) Kumar, S.; Rosenberg, J.; Bouzida, D.; Swendsen, R.; Kollman, P. *J. Comput. Chem.* **1992**, *13*, 1011–1021.
- (36) Snow, C. D.; Nguyen, H.; Pande, V. S.; Gruebele, M. *Nature* **2002**, *420*, 102–106.
- (37) Fujitani, H.; Tanida, Y.; Ito, M.; Jayachandran, G.; Snow, C. D.; Shirts, M. R.; Sorin, E. J.; Pande, V. S. *J. Chem. Phys.* **2005**, *123*, 084108.
- (38) Jayachandran, G.; Vishal, V.; Pande, V. S. *J. Chem. Phys.* **2006**, *124*, 164902.
- (39) Voelz, V.; Bowman, G.; Beauchamp, K.; Pande, V. *J. Am. Chem. Soc.* **2010**, *132*, 1526–1528.
- (40) Shaw, D. E.; Maragakis, P.; Lindorff-Larsen, K.; Piana, S.; Dror, R. O.; Eastwood, M. P.; Bank, J. A.; Jumper, J. M.; Salmon, J. K.; Shan, Y.; Wriggers, W. *Science* **2010**, *330*, 341–346.
- (41) Klepeis, J.; Lindorff-Larsen, K.; Dror, R.; Shaw, D. *Curr. Opin. Struct. Biol.* **2009**, *19*, 120–127.
- (42) Shirts, M.; Pande, V. S. *Science* **2000**, *290*, 1903–1904.
- (43) Giupponi, G.; Harvey, M.; De Fabritiis, G. *Drug Discovery Today* **2008**, *13*, 1052–1058.
- (44) Harvey, M.; Giupponi, G.; Fabritiis, G. *J. Chem. Theory Comput.* **2009**, *5*, 1632–1639.
- (45) Harvey, M.; De Fabritiis, G. *J. Chem. Theory Comput.* **2009**, *5*, 2371–2377.
- (46) Buch, I.; Harvey, M.; Giorgino, T.; Anderson, D.; De Fabritiis, G. *J. Chem. Inf. Model.* **2010**, *50*, 397–403.
- (47) Fabritiis, G.; Geroult, S.; Coveney, P.; Waksman, G. *Proteins: Struct., Funct. Bioinf.* **2008**, *72*, 1290–1297.
- (48) Sadowski, I.; Stone, J.; Pawson, T. *Mol. Cell Biol.* **1986**, *6*, 4396.
- (49) Waksman, G.; Shoelson, S.; Pant, N.; Cowburn, D.; Kuriyan, J. *Cell* **1993**, *72*, 779–790.
- (50) Botfield, M.; Green, J. *Annu. Rep. Med. Chem.* **1995**, *30*, 227–237.
- (51) Bradshaw, J.; Mitaxov, V.; Waksman, G. *J. Mol. Biol.* **1999**, *293*, 971–985.
- (52) Tong, L.; Warren, T.; King, J.; Betageri, R.; Rose, J.; Jakes, S. *J. Mol. Biol.* **1996**, *256*, 601–610.
- (53) Zhou, S.; *Cell* **1993**, *72*, 767–778.
- (54) Sheinerman, F.; Al-Lazikani, B.; Honig, B. *J. Mol. Biol.* **2003**, *334*, 823–841.
- (55) Brugge, J. *Science* **1993**, *260*, 918–919.
- (56) Gibbs, J.; Oliff, A. *Cell* **1994**, *79*, 193–198.
- (57) Sawyer, T. *Peptide Sci.* **1998**, *47*, 243–261.
- (58) Morelock, M.; Ingraham, R.; Betageri, R.; Jakes, S. *J. Med. Chem.* **1995**, *38*, 1309–1318.
- (59) Cousins-Wasti, R.; Ingraham, R.; Morelock, M.; Grygon, C. *Biochemistry* **1996**, *35*, 16746–16752.
- (60) Bradshaw, J.; Waksman, G. *Biochemistry* **1998**, *37*, 15400–15407.
- (61) Lee, T.; Lawrence, D. *J. Med. Chem.* **2000**, *43*, 1173–1179.
- (62) Lubman, O.; Waksman, G. *J. Mol. Biol.* **2003**, *328*, 655–668.
- (63) Nam, N.; Ye, G.; Sun, G.; Parang, K. *J. Med. Chem.* **2004**, *47*, 3131–3141.
- (64) Fowler, P.; Geroult, S.; Jha, S.; Waksman, G.; Coveney, P. *J. Chem. Theory Comput.* **2007**, *3*, 1193–1202.
- (65) MacKerell, A., Jr.; Banavali, N.; Foloppe, N. *Biopolymers* **2000**, *56*, 257–265.
- (66) Jorgensen, W. L.; Chandrasekhar, J.; Madura, J. D.; Impey, R. W.; Klein, M. L. *J. Chem. Phys.* **1983**, *79*, 926–935.
- (67) Hess, K.; Berendsen, H. *J. Comput. Chem.* **1999**, *20*, 786–798.
- (68) Sadiq, S. K.; De Fabritiis, G. *Proteins* **2010**, *78*, 2873–2885.
- (69) Sindhikara, D.; Meng, Y.; Roitberg, A. E. *J. Chem. Phys.* **2008**, *128*, 024103.

Iterative Optimization of Molecular Mechanics Force Fields from NMR Data of Full-Length Proteins

Da-Wei Li and Rafael Brüschweiler*

Chemical Sciences Laboratory, Department of Chemistry and Biochemistry and National High Magnetic Field Laboratory, Florida State University, Tallahassee, Florida 32306, United States

ABSTRACT: High quality molecular mechanics force fields of proteins are key for the quantitative interpretation of experimental data and the predictive understanding of protein function based on computer simulations. A strategy is presented for the optimization of protein force fields based on full-length proteins in their native environment that is guided by experimental NMR chemical shifts and residual dipolar couplings (RDCs). An energy-based reweighting approach is applied to a long molecular dynamics trajectory, performed with a parent force field, to efficiently screen a large number of trial force fields. The force field that yields the best agreement with the experimental data is then used as the new parent force field, and the procedure is repeated until no further improvement is obtained. This method is demonstrated for the optimization of the backbone φ, ψ dihedral angle potential of the Amber ff99SB force field using six trial proteins and another 17 proteins for cross-validation using ^{13}C chemical shifts with and without backbone RDCs. The φ, ψ dihedral angle potential is systematically improved by the inclusion of correlation effects through the addition of up to 24 bivariate Gaussian functions of variable height, width, and tilt angle. The resulting force fields, termed ff99SB_ $\varphi\psi$ (g24;CS) and ff99SB_ $\varphi\psi$ (g8;CS,RDC), perform significantly better than their parent force field in terms of both NMR data reproduction and Cartesian coordinate root-mean-square deviations between the MD trajectories and the X-ray crystal structures. The strategy introduced here represents a powerful addition to force field optimization approaches by overcoming shortcomings of methods that are solely based on quantum-chemical calculations of small molecules and protein fragments in the gas phase.

INTRODUCTION

Molecular dynamics (MD) simulations of biomolecules play an important complementary role with respect to experiments. In principle, computer simulations can provide a complete time-resolved single-molecule picture of a protein's behavior in atomic detail. On the other hand, experimental studies are invariably incomplete since certain properties are hard to measure. In recent years, MD has been increasing in popularity in the study of protein behavior enabled by the continuing exponential increase in computational power¹ that allows the simulation of both larger systems and longer time scales and due to progress in the quality of the underlying molecular mechanics force fields.^{2,3} Indeed, critical assessment of protein force fields has greatly benefited from the ability to sample conformational space of proteins more thoroughly.⁴ Still, there remains much room for further improvement to enable increasingly accurate *in silico* studies of protein properties and function. Currently, MD simulations into the hundreds of nanoseconds regime are becoming routine, which permit a fully quantitative comparison between computation and certain types of experiments, such as heteronuclear NMR spin relaxation.^{4,5} Other NMR parameters, such as chemical shifts, scalar J couplings, and residual dipolar couplings (RDCs), reflect a wider range of time scales from picoseconds to milliseconds, covering motional regimes on which many biologically important events occur. In order to validate force fields on the full range of time scales, the use of longer simulations represents a natural choice.^{6–8}

The development of better force fields is a complex task that is both labor-intensive and time-consuming. Essentially, all modern

force fields have been parametrized on the basis of both extensive quantum-chemical calculations and experimental data.^{2,9–27} The complexity associated with the fitting of a large number (well over 100) of force field parameters is reflected in different parametrization philosophies for different force fields. A common approach is the fitting of force field parameters to gas-phase quantum-chemical calculations and experimental data of small molecules, including amino acid analogs and small peptides, in terms of average conformation, vibrational spectra, solvation free energies, and relative energies of different conformations. The fine-tuning of the CHARMM force field in the final step through MD simulations of protein crystals is an exception.³

Not only can NMR data of full-length proteins in their native environment be used to cross-validate MD trajectories, but these data can also serve to directly improve the molecular mechanics force field itself. Using an energy-based reweighting scheme, we recently demonstrated this strategy by improving the backbone dihedral angle potential of the Amber ff99SB^{2,28} force field using experimental NMR chemical shift data from a set of proteins.²⁹ The force field was improved through modification of the coefficients of a fourth order Fourier series expansion in the backbone dihedral angles. Here, we present an alternative strategy that uses a set of bivariate Gaussian functions that are added to the backbone dihedral angle potential to optimize agreement with respect to both protein ^{13}C chemical shifts and backbone RDCs measured in multiple alignment media.

Received: February 9, 2011

Published: May 05, 2011

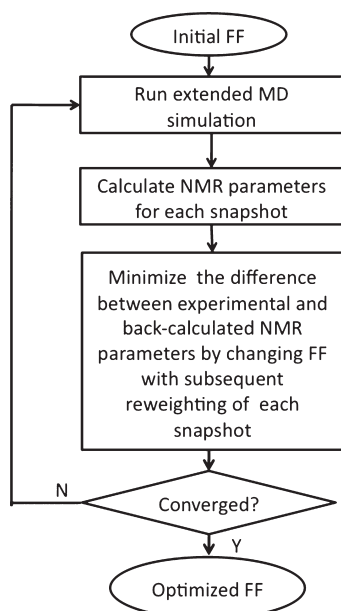


Figure 1. Schematic presentation of the iterative optimization procedure of protein molecular mechanics force fields using experimental data (in the present work, NMR chemical shifts or RDCs) of intact full-length proteins as input.

METHODS

Iterative Reweighting Strategy. The computational strategy used in this work is outlined in Figure 1. It starts with the back-calculation of experimental parameters, such as chemical shifts and RDCs, for each snapshot of the MD trajectory based on the parent force field (V_{old}) of one or several protein systems, which are stored for subsequent analysis. We use here $C\alpha$, $C\beta$, and C' chemical shifts predicted for each MD snapshot using the program SHIFTS^{30,31} as well as RDCs (see below). Time- and ensemble-averaged chemical shifts are calculated with equal weights, $p_{\text{old}}(i) = 1/N$, for all N snapshots and compared with the experimental chemical shifts by means of the root-mean-square deviation (RMSD) in units of parts per million. We then reweight a parent trajectory performed with the original force field V_{old} for a new test force field V_{new} by using Boltzmann's relationship:

$$p_{\text{new}}(i) = p_{\text{old}}(i) e^{-V_{\text{new}}(i)/kT} / e^{-V_{\text{old}}(i)/kT} \quad (1)$$

where $p_{\text{old}}(i)$ and $p_{\text{new}}(i)$ are the relative weights and $V_{\text{old}}(i)$ and $V_{\text{new}}(i)$ are the potential energies of snapshot i for the old and new force field, respectively, k is Boltzmann's constant, and T is the simulation temperature that is kept constant. The force field is then optimized iteratively as follows. For each new trial force field V_{new} , the new weights $p_{\text{new}}(i)$ are used to compute new NMR parameters. The optimized force field is the one that minimizes the overall discrepancy between the back-calculated and experimental parameters. In previous work,²⁹ we applied downhill simplex minimization for optimization. In order to search force field space more comprehensively, we use here a Monte Carlo simulated annealing method followed by simplex minimization.

Energy-based reweighting is a well-known tool in biomolecular simulations,³² whose utility for force field optimization has only been demonstrated recently.²⁹ Because reweighting does

not create new conformations, its effectiveness critically depends on the overlap of the parent trajectory with the reweighted trajectory. We therefore use a collectivity parameter³³

$$\kappa = \frac{100\%}{N} \exp\left[-\sum_{i=1}^N p_{\text{new}}(i) \log p_{\text{new}}(i)\right] \quad (2)$$

where $p_{\text{new}}(i)$ are the normalized populations of eq 1. $\kappa = 100\%$ indicates that all snapshots in the parent trajectory contribute equally to the reweighted trajectory, whereas a collectivity parameter near zero means that very few snapshots dominate the reweighted trajectory. The latter situation is undesirable, as it leads to a statistically poor representation of the native ensemble. Throughout this work, we require that $\kappa > 50\%$ to ensure that the parent and the reweighted trajectories significantly overlap. Since this requirement limits the allowed range of changes between the new and the parent force field, the above reweighting procedure is iteratively repeated (Figure 1) until no further improvement is achieved.

Local Reweighting Method. As every protein possesses a large number of degrees of freedom, even a moderately large change of a single force field term can produce a change in the potential energy that amounts to minimal overlap between the parent and the new trajectory (low κ value). To overcome this issue, we employ a local residue-based reweighting scheme. For the evaluation of the ensemble-averaged chemical shift of atom j from the reweighted trajectory, rescaled energy changes $\Delta E_j = \sum_{k=1}^{N_{\text{res}}} \exp(-r_{kj}/r_0) \Delta E_{kj}$ are used where ΔE_{kj} is the dihedral angle energy difference between the parent and trial force field of residue k with their $C\alpha$ atoms separated by the distance r_{kj} , N_{res} is the number of residues, and r_0 is set to 9 Å. This assumes that the effect of residue k on the local structure of atom j decreases with increasing distance. MD simulations with the new force field are then carried out to verify its performance.

Chemical Shift RMSD Calculations. The new predicted ensemble averaged chemical shifts $\langle \delta_m \rangle$ are calculated as

$$\langle \delta_m \rangle = \frac{\sum_{i=1}^N p_{\text{new}}(i) \delta_m(i)}{\sum_{i=1}^N p_{\text{new}}(i)} \quad (3)$$

where $\delta_m(i)$ is the chemical shift of a given nucleus m predicted for snapshot i . The root-mean-square deviation (RMSD) between predicted chemical shifts $\langle \delta_m \rangle$ and experimental chemical shifts $\delta_{m,\text{exp}}$ is given by

$$\text{RMSD} = \sqrt{\frac{1}{N_{\text{nuclei}}} \sum_{m=1}^{N_{\text{nuclei}}} (\langle \delta_m \rangle - \delta_{m,\text{exp}})^2} \quad (4)$$

in units of parts per million (ppm) where N_{nuclei} is the number of nuclei of each type, $C\alpha$, $C\beta$, or C' . Total RMSDs are obtained by averaging of the RMSDs of the different types of nuclei. All experimental chemical shifts were taken from the BioMagRes Bank³⁴ with the databank entry codes given in column 1 of Table 2.

Residual Dipolar Coupling Calculations. RDCs represent another type of NMR parameter, which reflects protein structure and dynamics in a way that is complementary to chemical shifts.^{35–38} RDCs are observed as cross-peak splittings due to weak alignment of the proteins in an anisotropic environment. The simple geometric dependence of RDCs on protein structure makes them suitable for the rigorous assessment of the quality of

MD trajectories.^{39,40} For the same reason, force-field optimization based on RDC information is attractive. However, extension of the residue-based local reweighting method from chemical shifts to RDCs is not straightforward because back-calculation of RDCs involves fitting of an alignment tensor by singular value decomposition,^{39,41} which simultaneously involves all RDCs across a protein. In analogy to the local chemical shift reweighting (see above), we assign a relative weight $\exp(-r/r_0)$ to each individual RDC in the global fitting when RDCs of internuclear vectors that belong to one particular residue are back-calculated from the MD trajectory where r is the distance between the C α atoms of the two residues and r_0 is set to 9 Å. The agreement between back-calculated RDCs, $D_{i,\text{back}}$, and experimental values, $D_{i,\text{exp}}$ ($i = 1, \dots, N_{\text{RDC}}$), is then expressed by the Q value:³⁹

$$Q = \left[\frac{\sum_{i=1}^{N_{\text{RDC}}} (D_{i,\text{back}} - D_{i,\text{exp}})^2}{\sum_{i=1}^{N_{\text{RDC}}} D_{i,\text{exp}}^2} \right]^{1/2} \quad (5)$$

Q values obtained for different alignments are linearly averaged, resulting in $\langle Q \rangle$. One limitation associated with force field optimization using RDCs only is that high-quality experimental data for proteins with known high-resolution 3D structures are presently available for only a few systems, which poses the risk of overfitting. Therefore, we combine RDCs with chemical shifts where the optimization target for force field improvement is the weighted sum of the average chemical shift RMSD and the average RDC-derived $\langle Q \rangle$, with weights of 1.0 and 2.5 for chemical shifts and RDCs, respectively.

Bivariate Gaussian Potential Dihedral Angle Energy Terms. In the course of force field optimization, backbone dihedral angle terms are often optimized in the final step because they do not directly affect the interaction between amino acids and between amino acids and explicit water. In our previous work,²⁹ we limited ourselves to the modification of individual backbone dihedral angle energy terms. Here, we explicitly include non-amino acid specific backbone dihedral angle *cross terms* involving $\varphi = \text{C}'-\text{N}-\text{C}\alpha-\text{C}\beta$ and $\psi = \text{C}\beta-\text{C}\alpha-\text{C}'-\text{N}$ (except for glycines) with the goal of further improving the force field quality. Cross terms between φ and ψ , which are part of the CMAP correction of the CHARMM 22 force field,^{3,42} have previously not been used in the Amber family of force fields. To keep the number of fitting parameters in our reweighting scheme reasonably small, we allow the addition of eight bivariate Gaussian potential energy terms (GPETs) to the 2D backbone dihedral angle energy surface where each GPET is defined as

$$\Delta V = f \cdot \exp\{-a(\varphi - d)^2 - b(\varphi - d)(\psi - e) - c(\psi - e)^2\} \quad (6)$$

where the parameters a , b , c , d , e , and f defining the center, widths, tilt angle, and height of each GPET are used as fitting parameters. Initially, three GPETs are placed in the α -helical region of φ, ψ space, three GPETs are placed in the β -strand region, and two GPETs are placed in the α_{R} regions. The half widths (standard deviations) of all GPETs are originally set to 10° along both φ and ψ , and all heights are set to zero. With each additional round of optimization, a new set of eight GPETs is added to the existing ones.

Protein Systems for Force Field Optimization and Validation. Protein GB3 (PDB code 1IGD) together with a pool of

22 proteins with variable sizes and topologies used previously²⁹ were selected for this study. GB3 is added because of its extensive set of backbone RDCs. All of these proteins were determined by X-ray crystallography (except for the NMR structure 2EA9) with a resolution of 2.1 Å or better, except for 1HIK and 3ILE. All NMR chemical shifts data are directly taken from the BMRB database.³⁴ The chemical shifts of GB1 were obtained from S. Grzesiek, and the ones of GB3 are taken from the examples provided with CS-ROSETTA.⁴³ Six proteins (1UBQ, 1IGD, 1HIK, 1ENH, 1SMX, and 1QZM) were selected as trial proteins in our force field optimization based on chemical shifts, while all others were used for validation. A comprehensive set of experimental backbone N–H^N residual dipolar couplings measured in 23 different alignment media for ubiquitin⁴⁴ and a set of backbone N–H^N, N–C α , C α –C', and C α –H^N RDCs measured in five different alignment media for GB3⁴⁵ have been reported in the literature. Backbone N–H^N RDCs in two different alignment media for GB1 were taken from the BMRB. Three proteins (1UBQ, 1IGD, and 1PGA) were selected for force field optimization based on RDCs.

To test the dynamics properties of the proteins under the new force field, NMR relaxation backbone N–H^N S² order parameters^{46,47} of the three proteins, ubiquitin (1UBQ), lysozyme (6LYT), and interleukin-4 (1HIK), are back-calculated and compared with experimental results using the iRED⁴⁸ approach (without correction for zero-point vibrations⁴⁹).

Unfolded Peptide System. To test the new force field on unfolded and intrinsically disordered polypeptides, the Ala₃ peptide was simulated at 300 K for 1 μs in explicit water, and back-calculated vicinal scalar J-coupling constants were compared with experimental results. Both termini of the Ala₃ peptide are protonated to be consistent with experimental conditions (pH 2).⁵⁰ Hence, the peptide has a net charge of + e , which is balanced by the addition of a Cl[−] ion during the simulation. Because the charge distribution for the protonated, uncapped C-terminus of Ala₃ is not available in the literature, charges of the carboxyl group were taken from the side-chain of protonated Glu in the Amber ff99SB force field, and the charge of the C-terminal C α atom was adjusted to ensure a total peptide charge of + e . We find that the details of the charge model of the C-terminus can have a significant influence on the structural propensity of this short peptide during the MD simulation.

As in previous work, the deviation between simulations and experiments is calculated as⁵¹

$$\chi^2 = N_{\text{Jcoupl}}^{-1} \sum_{i=1}^{N_{\text{Jcoupl}}} (\langle J_i \rangle_{\text{sim}} - J_{i,\text{exp}})^2 / \sigma_i^2 \quad (7)$$

where N_{Jcoupl} is the total number of J couplings, $\langle J_i \rangle_{\text{sim}}$ is the average coupling constant back-calculated from the MD trajectory, and $J_{i,\text{exp}}$ is the corresponding experimental value. The coupling constants used here are ${}^3J(\text{HN},\text{H}\alpha)$, ${}^3J(\text{HN},\text{C}')$, ${}^3J(\text{H}\alpha,\text{C}')$, ${}^3J(\text{C}',\text{C}')$, ${}^3J(\text{HN},\text{C}\beta)$, ${}^1J(\text{N},\text{C}\alpha)$, ${}^2J(\text{N},\text{C}\alpha)$, and ${}^3J(\text{HN},\text{C}\alpha)$. The ${}^1J(\text{N},\text{C}\alpha)$ coupling of the C-terminal residue was not included in eq 7 due to its strong sensitivity to the precise charges and their distribution in the C-terminus. The corresponding Karplus parameters, the experimental values, and errors σ_i included in eq 7 were directly taken from the literature.^{50–52}

MD Simulations. All MD simulations were performed using the Gromacs 4.5 package^{53–56} with its built-in support of dihedral angle cross terms. Backbone cross terms were added to the Gromacs topology file manually, after it was generated by

Table 1. Average Chemical Shift RMSDs (ppm) for the Six Trial Proteins after Each Round of Optimization for Both Reweighted Trajectories (“reweighted”) As Well As New MD Simulations (“new”)

PDB	99SB	round 1		round 2		round 3	
		reweighted MD	new MD	reweighted MD	new MD	reweighted MD	new MD
1UBQ	3.14	3.04	3.06	2.99	3.02	2.98	2.99
1IGD	3.43	3.39	3.43	3.41	3.39	3.38	3.36
1ENH	3.86	3.78	3.83	3.74	3.62	3.61	3.73
1HIK	3.30	3.17	3.09	3.08	3.23	3.21	3.26
1SMX	3.98	3.80	3.70	3.66	3.78	3.77	3.64
1QZM	2.13	1.97	2.02	1.96	1.91	1.87	1.93

Gromacs’ PDB2GMX module. All protein MD simulations (i.e., both parent trajectories and validation trajectories) were run for 100 ns at 300 K using the TIP3P water model. The simulation of the Ala₃ peptide was run for 1 μ s. The proteins as well as the peptide are uncapped. The integration time step was set to 2 fs with all bond lengths involving hydrogen atoms constrained by the SETTLE algorithm. Electrostatic interactions were cut off at 10 Å, and the long-range electrostatic interactions were calculated using the PME algorithm with 1.2 Å spacing. van der Waals interactions were cut off at 8 Å. The initial protein structures listed in Table 2 were taken from the Protein Data Bank.⁵⁷ The corresponding PDB codes are listed in the first column of Table 2. Standard minimization and heating procedures described previously⁵⁸ were applied before the final production runs at a constant temperature and pressure (NPT ensemble) of 300 K and 1 atm, respectively.

RESULTS

Force Field Optimization Using Chemical Shifts. Application of the reweighting strategy depicted in Figure 1 to the six trial proteins using only NMR chemical shift information leads to a significant drop in the chemical shift RMSD. Subsequent application of the modified force field to the validation set indicates that the force field has indeed improved. Further improvement is achieved by two additional rounds of optimization, but a fourth iteration did not yield any further improvement. The chemical shift RMSDs obtained from the reweighted trajectories as well as from new sets of MD runs are summarized in Table 1 for the first three rounds of optimization. The force field obtained after three rounds is named ff99SB $_{\varphi\psi}$ (g24;CS), where ff99SB indicates the parent force field, $\varphi\psi$ stands for “backbone dihedral potential”, g24 stands for the 24 Gaussian potential functions added, and CS stands for chemical shift information as input for refinement. (According to this terminology, the force field ff99SBnmr1²⁹ becomes ff99SB $_{\varphi\psi}$ (f32;CS), where f32 stands for the 32 Fourier series coefficients.)

The modification made to the backbone dihedral φ,ψ energy surface from the new ff99SB $_{\varphi\psi}$ (g24;CS) force field is shown in Figure 2A. The new force field fine-tunes the energy surface both in the α -helical and β -strand basins and makes the left-handed α -region (α_L) more stable. In the α -helical basin (α_R), the new force field renders conformations centered around $(\varphi,\psi) = (-50^\circ, -50^\circ)$ more stable, while it slightly destabilizes conformations centered around $(\varphi,\psi) = (-50^\circ, -25^\circ)$. In the β -strand basin, the new force field stabilizes both β -sheet conformations and polyproline II conformations while adding a small barrier between them.

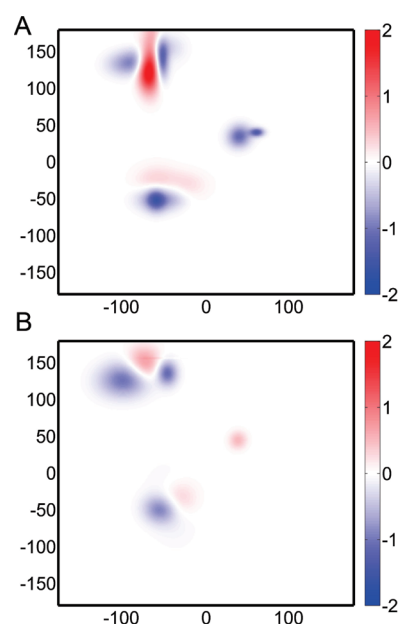


Figure 2. Optimization results following the scheme of Figure 1 for backbone φ,ψ dihedral angle potential modifications using $C\alpha$, $C\beta$, and C' chemical shifts of six proteins (1UBQ, 1IGD, 1ENH, 1HIK, 1QZM, and 1SMX) (A) without RDCs (force field ff99SB $_{\varphi\psi}$ (g24;CS)) and (B) with RDCs of three proteins (1UBQ, 1IGD, and 1PGA) as input (force field ff99SB $_{\varphi\psi}$ (g8;CS;RDC)).

Next, the new force field is validated with the 17 proteins that were excluded during optimization. As shown in Figure 3A, the average improvement found for the validation protein set is similar to that of the six trial proteins, which provides evidence that the new backbone dihedral cross term is (i) not the result of overfitting and (ii) is transferable to a broad range of globular proteins of variable topology and size, as illustrated in Figure 3D. It is noted that the overall improvement is larger than that obtained for ff99SBnmr1 (see Figure 4).²⁹ The only exception is protein 2RNJ, whose structure was determined by NMR. A comparison of the performance of ff99SB and its optimized variants is provided in Table 2.

Besides the accurate reproduction of chemical shifts, a favorable protein force field is expected to stabilize native state protein structure. This property of ff99SB $_{\varphi\psi}$ (g24;CS) is assessed here on the basis of average backbone RMSDs (excluding flexible N- and C-termini) of 100 ns MD trajectories with respect to initial PDB structures. A comparison of these results with the corresponding results obtained for ff99SB are shown in Figure 5A.

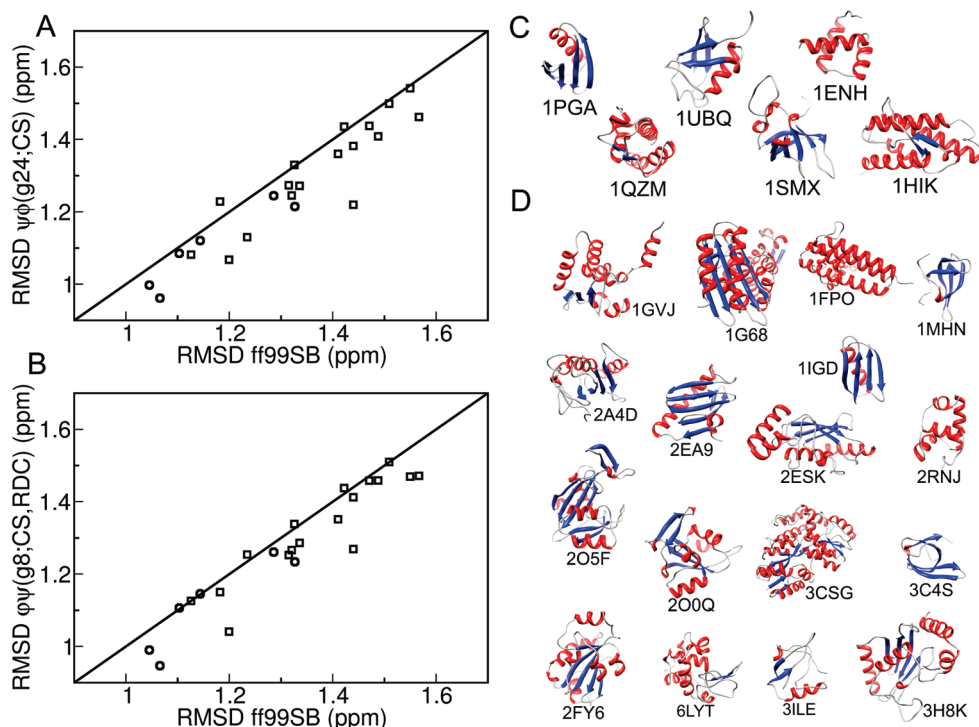


Figure 3. Test of the performance of the new force fields (A) $\text{ff99SB}_{\phi\psi}(g24;CS)$ and (B) $\text{ff99SB}_{\phi\psi}(g8;CS,RDC)$ using the combined $C\alpha$, $C\beta$, and C' chemical shift RMSD from 100 ns MD trajectories of 23 proteins shown in C and D. The average chemical shift RMSDs (eq 3) are compared with the ones obtained for the parent force field ff99SB . The circles belong to the six proteins used during optimization, and the 17 squares belong to proteins used only for validation. Proteins below the diagonal show improved performance with the new force field. Ribbon models of (C) six trial proteins and (D) 17 validation proteins together with PDB codes (α -helices are in red and β -strands in blue).

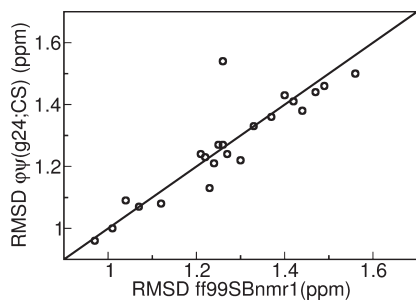


Figure 4. Comparison of the performance of the new force field $\text{ff99SB}_{\phi\psi}(g24;CS)$ and ff99SBnmr1^{29} (i.e., $\text{ff99SB}_{\phi\psi}(f32;CS)$) in terms of the combined $C\alpha$, $C\beta$, and C' chemical shift RMSD of the 23 proteins depicted in Figure 3C,D.

The new force field $\text{ff99SB}_{\phi\psi}(g24;CS)$ leads to a significantly reduced average RMSD: for 13 out of the 23 proteins, it yields an RMSD that is lower than for ff99SB , whereas only six proteins show a weak opposite trend.

The force field can be cross-validated also by RDC data, as such data were not used during optimization. For ubiquitin, the average Q value (excluding the flexible C-terminal residues 72–76) improves from $\langle Q \rangle = 0.27$ for ff99SB to $\langle Q \rangle = 0.22$ for $\text{ff99SB}_{\phi\psi}(g24;CS)$, confirming the improved performance of the new force field. Considering that dipolar couplings and NMR chemical shifts reflect protein geometry and fluctuations in highly complementary ways, this underscores that the new force field more accurately captures structural-dynamic properties of this protein. For GB3, back-calculation of the RDCs yields Q values

for $\text{ff99SB}_{\phi\psi}(g24;CS)$ (ff99SB) of 0.14 (0.12), 0.22 (0.21), 0.12 (0.11), and 0.23 (0.22) for $C\alpha-C'$, $C'-N$, $C\alpha-H\alpha$, and $N-H^N$ couplings, respectively. The new Q values are just slightly higher than the ones of ff99SB and on average are still very low. Similarly, back-calculated RDCs for GB1 yield a Q value of 0.14, which is only slightly larger than the original one of ff99SB , which is 0.12. Hence, the performance of the new force field is successful, as reflected by the low Q values when reproducing these RDCs.

Not only do modifications of force fields alter the distribution of conformer populations, but they can also affect the dynamics properties of proteins. NMR relaxation data, particularly S^2 order parameters, are very well-suited to evaluate the performance of the force field for protein dynamics on pico- to nanosecond time scales. Backbone $N-H^N$ S^2 order parameters are calculated for ubiquitin⁵⁹ (1UBQ), lysozyme⁶⁰ (6LYT), and interleukin-4⁶¹ (1HIK) for both ff99SB and $\text{ff99SB}_{\phi\psi}(g24;CS)$ using iRED,⁴⁸ with a detailed comparison shown in Figure 6. The overall level of agreement is almost identical for the two force fields, although relatively minor differences can be found for specific regions.

Combined Force Field Optimization Using Chemical Shifts and RDCs. Chemical shift and RDC information can be directly combined in the scheme of Figure 1 for the optimization of force fields. After one round of optimization with chemical shifts of the six proteins used above and RDCs of the three proteins with a total of eight bivariate Gaussian corrections, a modified ϕ, ψ energy surface is obtained, termed $\text{ff99SB}_{\phi\psi}(g8;CS,RDC)$, which is shown in Figure 2B. A second round of optimization did not yield further improvement. The changes are similar to the ones in Figure 2A, except that $\text{ff99SB}_{\phi\psi}(g8;$

Table 2. Comparison of the Performance of the ff99SB Force Field and Its Variants for the Prediction of ^{13}C Chemical Shifts, Expressed As RMSDs (eq 4), for Six Trial Proteins and 17 Validation Proteins

PDB code	resolution (Å)	BMRB code	ff99SB	ff99SB_φψ(g24;CS)	ff99SB_φψ(g8;CS,RDC)	ff99SBnmr1 (ff99SB_φψ(f32;CS))
1UBQ ^a	1.8	6475	1.04	1.00	0.99	1.01
1IGD ^a	1.1	n/a	1.14	1.12	1.14	n/a
1ENH ^a	2.1	15536	1.28	1.24	1.26	1.21
1HIK ^a	2.6	4094	1.10	1.09	1.11	1.04
1SMX ^a	1.8	6122	1.33	1.21	1.23	1.24
1QZM ^a	1.9	5107	1.07	0.96	0.95	0.97
1PGA	2.1	n/a	1.20	1.07	1.04	1.07
6LYT	1.9	4562	1.49	1.41	1.46	1.42
1G68	2.0	6838	1.44	1.38	1.41	1.44
1MHN	1.8	4899	1.18	1.23	1.15	1.22
2EA9	2.1	15088	1.51	1.50	1.51	1.56
2RNJ	NMR	11024	1.55	1.54	1.47	1.26
2ESK	1.4	6277	1.32	1.33	1.34	1.33
3CSG	1.8	4986	1.47	1.44	1.46	1.47
2FY6	1.9	6709	1.34	1.27	1.29	1.26
1GVJ	1.5	5991	1.41	1.36	1.35	1.37
3C4S	1.7	15604	1.32	1.24	1.27	1.27
3H8K	1.8	6711	1.31	1.27	1.25	1.25
3ILE	2.9	16325	1.23	1.13	1.25	1.23
1FPO	1.8	15541	1.13	1.08	1.12	1.12
2A4D	1.7	7219	1.44	1.22	1.27	1.30
2O0Q	1.8	15281	1.42	1.43	1.44	1.40
2O5F	1.9	5570	1.57	1.46	1.47	1.49

^a These proteins were used during force field optimization, while all others were strictly used for validation purposes only.

CS,RDC) slightly destabilizes the α_1 region. Under the new force field, the Q values of two proteins and chemical shifts RMSDs of four proteins drop significantly while the chemical shifts RMSDs of the remaining two proteins are essentially unchanged (Table 3a and b). (It is noted that the Q values obtained with local reweighting cannot be directly compared with Q values obtained from MD.)

Validation results with chemical shifts of proteins, not included during optimization, are given in Figure 3B and Table 2. They demonstrate the improvement of the new force field over ff99SB and a performance that is comparable to that of ff99SB_φψ(g24;CS). The protein stability test (Figure 5B) shows backbone RMSDs similar to ff99SB_φψ(g8;CS,RDC) and ff99SB. Backbone N–H^N S² order parameters calculated for ubiquitin (1UBQ), lysozyme (6LYT), and interleukin-4 (1HIK) are displayed in Figure 6. The overall quality of the agreement is remarkably high, similar to the trajectories obtained with ff99SB_φψ(g24;CS) and ff99SB.

Force Field Validation for Ala₃ Peptide. Modification of backbone dihedral angle terms is expected to significantly affect also the properties of intrinsically disordered proteins and short peptides, as these systems are less stabilized by other interactions such as intramolecular hydrogen bonds and hydrophobic interactions. Experimental J-coupling constants⁵⁰ of the Ala–Ala–Ala peptide are utilized to evaluate the three force fields. The χ^2 values (eq 7) obtained for a 1 μs trajectory of Ala₃ are 1.69, 1.55, and 1.88 for ff99SB, ff99SB_φψ(g24;CS), and ff99SB_φψ(g8;CS,RDC), respectively. A plot of the comparison between experimental and predicted J-scalar coupling constants in Figure 7 shows that for essentially all couplings the predictions fall within the experimental error bar, consistent with the low χ^2 values.

Considering this fact, together with the uncertainties of the associated Karplus parameters used for J-coupling back-calculation, the agreement is very good. This result demonstrates that the new force fields adequately represent the free energy balance between the different secondary structural basins.

DISCUSSION

The availability of better force fields is not only beneficial for computational chemists and biophysicists. Experimental structural biologists, in particular, protein X-ray crystallographers and NMR spectroscopists, have a longstanding tradition in using computer simulations of proteins that include energy restraints derived from experimental data to refine protein structures. Recently, an increasing number of experimental biochemists are using MD simulations as “*in silico* experiments” without experimental restraints, to interpret their experimental data from a variety of sources, including calorimetry, small-angle X-ray scattering, magnetic resonance, and optical spectroscopy.^{62–68} Taken together, these demands make the development of more accurate biomolecular force fields a timely task.

Traditionally, force field parametrizations have been primarily based on quantum-chemical energy calculations of peptide fragments in a vacuum.^{2,14,16} Despite the success of this approach in the past, the potential for further force field improvements using ever higher level quantum-chemical calculations and larger basis sets is unclear. An accurate representation of protein interactions in a vacuum does not guarantee that the energetics are correctly reproduced when the protein is placed in its native environment (water, ions, lipid bilayers, etc.). This obstacle can be overcome, in principle, by optimizing the force field directly

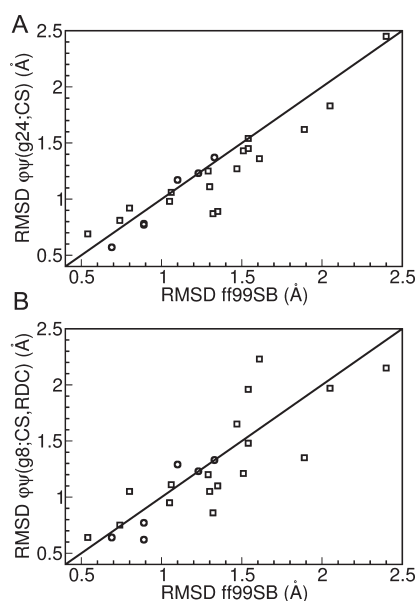


Figure 5. Test of the performance of the new force fields (A) ff99SB_φψ(g24;CS) and (B) ff99SB_φψ(g8;CS,RDC) relative to ff99SB by comparing the average Cartesian coordinate backbone RMSD of the 100 ns validation MD simulations with respect to the X-ray crystal structures. The circles belong to the six proteins used during optimization, and the squares belong to the 17 proteins used only for validation.

against experimental data of full-length proteins in the native environment.

This approach, which is pursued in this work using NMR data of intact globular proteins, permits by means of superposition of multiple bivariate Gaussian correction terms versatile and specific modifications of positions, shapes, and correlations of the favorable and unfavorable energy regions in φ, ψ space. On the other hand, it is unlikely that the method changes the relative average weights between distinct regions, because during the simulation of a globular protein it is quite rare that a residue visits both α and β regions. Hence, free energy differences between these regions are mostly inconsequential for the back-calculation of NMR data of globular proteins. The global balance between the α -helical and β -strand basins in the optimization of backbone dihedral angle terms is best achieved¹⁸ using experimental data of (partially) unfolded systems.

In our previous work,²⁹ the backbone dihedral angle potential was modified through adjustment of the Fourier series coefficients truncated at the fourth order. The truncation at relatively low order was imposed by practical considerations to keep the number of fitting parameters manageable. However, it gives each Fourier component, as well as any of their superpositions, a significant nonlocal character and thereby has the tendency to introduce unwanted “wiggles” in the φ, ψ energy map. For the present work, we therefore decided to allow a “basis set” of potential energy correction terms in the form of bivariate Gaussian functions that, depending on the widths, can have both a local as well as a more global character.

The chosen length of the protein MD trajectories, which has been set to 100 ns, strikes a balance between computational affordability and convergence. In previous work, the comparison between experimental ¹³C carbon chemical shifts and predicted ones from a microsecond MD simulation of ubiquitin showed the onset of convergence around 100 ns.⁶⁹ Moreover, the use of six to

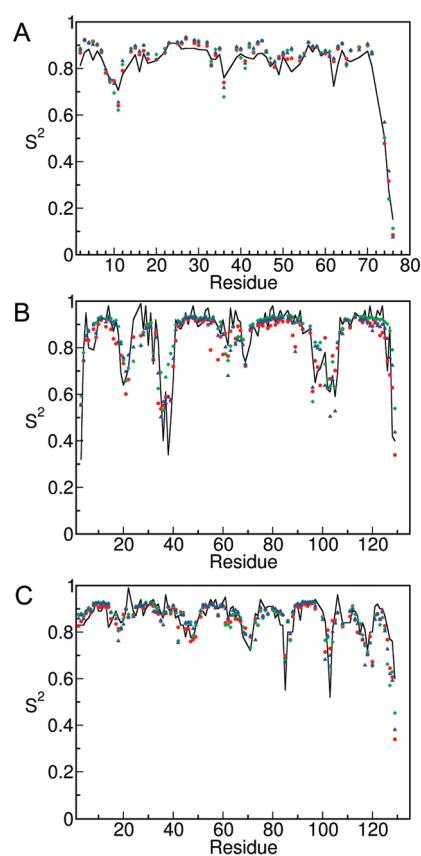


Figure 6. Comparison of the new force fields for the calculation of NMR N–H^N S^2 order parameters of (A) ubiquitin, (B) interleukin-4, and (C) lysozyme. The S^2 values were computed by iRED from 100 ns MD trajectories with averaging done over (A) 4, (B) 6, and (C) 8 ns time windows. Black lines belong to experimental values. Red circles, green diamonds, and blue triangles belong to ff99SB, ff99SB_ψφ(g24;CS), and ff99SB_ψφ(g8;CS,RDC), respectively.

eight proteins during optimization, as opposed to four proteins used previously, further enhances the stability of the force field parameter fitting. Chemical shifts represent the most abundant experimental NMR parameter of proteins. Their predictions from a given structural model (or ensemble) have dramatically improved over the past decade, but they are still not fully quantitative. This explains, at least in part, the observed RMSD offset observed even when the force field optimization protocol has converged. RDCs provide a complementary source of structural and dynamics information, and they are well suited for the optimization task at hand. However, the number of RDC sets reported in the literature for proteins for which a well-resolved X-ray crystal structure is available is still very sparse. Therefore, RDCs of only three proteins were included during optimization. The resulting force field ff99SB_φψ(g8;CS,RDC) performs similarly well to the one optimized with chemical shift data only. The average backbone RDC Q value of ubiquitin of a free MD simulation using this force field now drops to 0.19, which is only slightly higher than Q_{free} reported in an RDC optimized accelerated MD simulation.⁷⁰ As high-quality RDC sets of more proteins with known X-ray crystal structures are becoming available, their utility for force-field optimization holds significant promise.

Our optimization protocol can be further expanded to incorporate other NMR data, including T_1 , T_2 , and nuclear

Table 3. Force Field Optimization Results Using Both Chemical Shifts and RDCs for (a) Chemical Shift Agreement^a and (b) RDC Q Values for ff99SB Trajectories, Reweighted Trajectories, and New MD Simulations

PDB	(a) Chemical shift RMSDs		
	ff99SB	reweighted MD	new MD
1UBQ	3.14	3.03	2.97
GB3	3.43	3.40	3.44
1ENH	3.80	3.77	3.78
1HIK	3.30	3.20	3.32
1QZM	2.12	1.96	1.89
1SMX	3.98	3.86	3.70

PDB	(b) RDC Q Values			
	ff99SB	Q_{local} ff99SB	Q_{local} reweighted	Q_{new}
1UBQ	0.26	0.55	0.51	0.19
1PGA	0.12	0.32	0.31	0.13
1IGD	NH	0.12	0.42 ^b	0.12
	CH	0.21		0.20
	CN	0.22		0.18
	C α C	0.11		0.11

^a Average chemical shift RMSDs (ppm) for both reweighted trajectories (“reweighted”) and new MD simulations (“new”). ^b Q_{local} corresponds to the average over the 4 internuclear vectors.

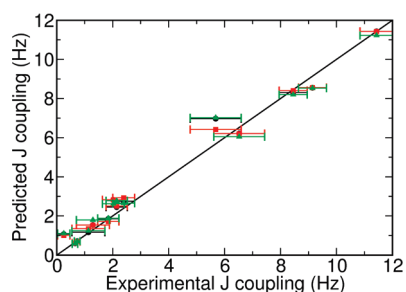


Figure 7. Comparison of back-calculated and experimental scalar J-coupling constants of Ala₃ listed below eq 7 for different force fields: ff99SB (black), ff99SB_φψ(g24;CS) (red), and ff99SB_φψ(g8;CS, RDC) (green).

Overhauser enhancement (NOE) spin-relaxation parameters of ¹⁵N spins,⁷¹ ¹³C spins,⁷² and ²H spin relaxation parameters⁷³ of ¹³C-D groups and partially deuterated ¹³CDH₂-methyl moieties of methyl-bearing side chains.^{74,75} These parameters can be expressed in terms of model-free S² order parameters and intramolecular correlations times τ in the pico- to nanosecond range, which can be used to actively guide force field improvements using methods similar to the ones presented here. Although we focused here on NMR data, obviously our approach can be combined with other types of experimental data too. The average Cartesian coordinate RMSD between the MD trajectory and the high-resolution X-ray structure has been found to correlate well with the quality of the force field. Although in Figure 5 this information serves for cross-validation purposes only, it can also be used to actively guide force field improvements. In this case, one should either simulate proteins in their full crystalline environment⁷⁶ or exclude during optimization those atoms that are significantly affected by crystal packing.⁷⁷

Hence, the Cartesian RMSD of selected sets of atoms can be employed as a metric to assess and improve force fields. Meanwhile, crystallographic B factors, which report on both dynamics and static disorder in protein crystals, represent another measure that is worth exploring for force field validation and refinement.

The present work focuses on backbone dihedral angles, although the extension to side chain dihedral angles is rather straightforward. Most side-chain potentials have not been updated for well over a decade. A recent quantum chemical study showed that amino acid specific potentials for ILDN residues can provide improvements.⁷⁸ Although NMR parameters of side-chains are less abundant than for the backbone, side-chain assignments (and thus chemical shifts) are becoming available for an increasing number of proteins and, thus, can be used in full analogy to backbone chemical shifts. Our optimization protocol can be also applied to force field terms other than backbone dihedral angle terms, such as Coulomb interactions, van der Waals interactions, and explicit hydrogen-bonding potentials. The latter terms were used in the early phase of force field development,¹¹ subsequently abolished, and have been revisited more recently.^{79,80} Similarly, it should be possible to further improve the parametrization of explicit water models to better reflect structural, dynamic, and thermodynamic properties of protein solutes in their native solvent. Finally, with the imminent advent of polarizable force fields^{81–84} for biomacromolecules, the optimization approach presented here should find useful application in this emerging field.

CONCLUSION

MD simulations have been limited in the past by the accuracy of force fields and limited sampling of conformational space.⁸⁵ While sampling improves with every new generation of computer hardware, the development of better force fields has been a relatively slow, labor-intensive task mostly based on small molecules and protein fragments in a vacuum. However, the performance of a force field when applied to an entire protein in explicit solvent is more than the sum of its isolated parts. The work presented here shows how the confluence of efficient optimization protocols and protein structural and NMR databases make the development of force fields on intact full-length proteins feasible and computationally tractable. These advances enable a plethora of opportunities to render current molecular mechanics force fields increasingly quantitative, which remains a key prerequisite for the predictive understanding of biomolecular properties and function.

AUTHOR INFORMATION

Corresponding Author

*Tel.: 850-644-1768. Fax: 850-644-8281. E-mail: bruschweiler@magnet.fsu.edu.

ACKNOWLEDGMENT

This work was supported by grant MCB-0918362 of the National Science Foundation.

REFERENCES

- (1) Klepeis, J. L.; Lindorff-Larsen, K.; Dror, R. O.; Shaw, D. E. *Curr. Opin. Struct. Biol.* **2009**, *19*, 120–127.
- (2) Hornak, V.; Abel, R.; Okur, A.; Strockbine, B.; Roitberg, A.; Simmerling, C. *Proteins* **2006**, *65*, 712–725.


- (3) Mackerell, A. D.; Feig, M.; Brooks, C. L. *J. Comput. Chem.* **2004**, *25*, 1400–1415.
- (4) Showalter, S. A.; Brüschweiler, R. *J. Chem. Theory Comput.* **2007**, *3*, 961–975.
- (5) Trbovic, N.; Cho, J. H.; Abel, R.; Friesner, R. A.; Rance, M.; Palmer, A. G. *J. Am. Chem. Soc.* **2009**, *131*, 615–622.
- (6) Freddolino, P. L.; Liu, F.; Gruebele, M.; Schulten, K. *Biophys. J.* **2008**, *94*, L75–L77.
- (7) Freddolino, P. L.; Park, S.; Roux, B.; Schulten, K. *Biophys. J.* **2009**, *96*, 3772–3780.
- (8) Shaw, D. E.; Maragakis, P.; Lindorff-Larsen, K.; Piana, S.; Dror, R. O.; Eastwood, M. P.; Bank, J. A.; Jumper, J. M.; Salmon, J. K.; Shan, Y. B.; Wrigger, W. *Science* **2010**, *330*, 341–346.
- (9) Jorgensen, W. L.; Tirado-Rives, J. *J. Am. Chem. Soc.* **1988**, *110*, 1657–1666.
- (10) Jorgensen, W. L.; Maxwell, D. S.; Tirado-Rives, J. *J. Am. Chem. Soc.* **1996**, *118*, 11225–11236.
- (11) Brooks, B. R.; Bruccoleri, R. E.; Olafson, B. D.; States, D. J.; Swaminathan, S.; Karplus, M. *J. Comput. Chem.* **1983**, *4*, 187–217.
- (12) MacKerell, A. D.; Bashford, D.; Bellott, M.; Dunbrack, R. L.; Evanseck, J. D.; Field, M. J.; Fischer, S.; Gao, J.; Guo, H.; Ha, S.; Joseph-McCarthy, D.; Kuchnir, L.; Kuczera, K.; Lau, F. T. K.; Mattos, C.; Michnick, S.; Ngo, T.; Nguyen, D. T.; Prodhom, B.; Reiher, W. E.; Roux, B.; Schlenkrich, M.; Smith, J. C.; Stote, R.; Straub, J.; Watanabe, M.; Wiorkiewicz-Kuczera, J.; Yin, D.; Karplus, M. *J. Phys. Chem. B* **1998**, *102*, 3586–3616.
- (13) MacKerell, A. D.; Banavali, N.; Foloppe, N. *Biopolymers* **2000**, *56*, 257–265.
- (14) Brooks, B. R.; Brooks, C. L.; Mackerell, A. D.; Nilsson, L.; Petrella, R. J.; Roux, B.; Won, Y.; Archontis, G.; Bartels, C.; Boresch, S.; Caffisch, A.; Caves, L.; Cui, Q.; Dinner, A. R.; Feig, M.; Fischer, S.; Gao, J.; Hodoscek, M.; Im, W.; Kuczera, K.; Lazaridis, T.; Ma, J.; Ovchinnikov, V.; Paci, E.; Pastor, R. W.; Post, C. B.; Pu, J. Z.; Schaefer, M.; Tidor, B.; Venable, R. M.; Woodcock, H. L.; Wu, X.; Yang, W.; York, D. M.; Karplus, M. *J. Comput. Chem.* **2009**, *30*, 1545–1614.
- (15) Cornell, W. D.; Cieplak, P.; Bayly, C. I.; Gould, I. R.; Merz, K. M.; Ferguson, D. M.; Spellmeyer, D. C.; Fox, T.; Caldwell, J. W.; Kollman, P. A. *J. Am. Chem. Soc.* **1995**, *117*, 5179–5197.
- (16) Wang, J. M.; Cieplak, P.; Kollman, P. A. *J. Comput. Chem.* **2000**, *21*, 1049–1074.
- (17) Duan, Y.; Wu, C.; Chowdhury, S.; Lee, M. C.; Xiong, G.; Zhang, W.; Yang, R.; Cieplak, P.; Luo, R.; Lee, T.; Caldwell, J.; Wang, J.; Kollman, P. *J. Comput. Chem.* **2003**, *24*, 1999–2012.
- (18) Best, R. B.; Hummer, G. *J. Phys. Chem. B* **2009**, *113*, 9004–9015.
- (19) Warshel, A. *Isr. J. Chem.* **1973**, *11*, 709–717.
- (20) Rappe, A. K.; Casewit, C. J.; Colwell, K. S.; Goddard, W. A.; Skiff, W. M. *J. Am. Chem. Soc.* **1992**, *114*, 10024–10035.
- (21) Levitt, M.; Hirshberg, M.; Sharon, R.; Daggett, V. *Comput. Phys. Commun.* **1995**, *91*, 215–231.
- (22) Halgren, T. A. *J. Comput. Chem.* **1996**, *17*, 490–519.
- (23) Arnautova, Y. A.; Jagielska, A.; Scheraga, H. A. *J. Phys. Chem. B* **2006**, *110*, 5025–5044.
- (24) Oostenbrink, C.; Villa, A.; Mark, A. E.; Van Gunsteren, W. F. *J. Comput. Chem.* **2004**, *25*, 1656–1676.
- (25) Christen, M.; Hunenberger, P. H.; Bakowies, D.; Baron, R.; Burgi, R.; Geerke, D. P.; Heinz, T. N.; Kastenholz, M. A.; Krautler, V.; Oostenbrink, C.; Peter, C.; Trzesniak, D.; Van Gunsteren, W. F. *J. Comput. Chem.* **2005**, *26*, 1719–1751.
- (26) Nevins, N.; Lii, J. H.; Allinger, N. L. *J. Comput. Chem.* **1996**, *17*, 695–729.
- (27) Langley, C. H.; Allinger, N. L. *J. Phys. Chem. A* **2003**, *107*, 5208–5216.
- (28) Hornak, V.; Okur, A.; Rizzo, R. C.; Simmerling, C. *Proc. Natl. Acad. Sci. U. S. A.* **2006**, *103*, 915–920.
- (29) Li, D. W.; Brüschweiler, R. *Angew. Chem., Int. Ed.* **2010**, *49*, 6778–6780.
- (30) Xu, X. P.; Case, D. A. *J. Biomol. NMR* **2001**, *21*, 321–333.
- (31) Xu, X. P.; Case, D. A. *Biopolymers* **2002**, *65*, 408–423.
- (32) Torrie, G. M.; Valleau, J. P. *J. Comput. Phys.* **1977**, *23*, 187–199.
- (33) Brüschweiler, R. *J. Chem. Phys.* **1995**, *102*, 3396–3403.
- (34) Ulrich, E. L.; Akutsu, H.; Doreleijers, J. F.; Harano, Y.; Ioannidis, Y. E.; Lin, J.; Livny, M.; Mading, S.; Mazziuk, D.; Miller, Z.; Nakatani, E.; Schulte, C. F.; Tolmie, D. E.; Kent Wenger, R.; Yao, H.; Markley, J. L. *Nucleic Acids Res.* **2008**, *36*, D402–408.
- (35) Tjandra, N.; Bax, A. *Science* **1997**, *278*, 1111–1114.
- (36) Prestegard, J. H.; Al-Hashimi, H. M.; Tolman, J. R. *Q. Rev. Biophys.* **2000**, *33*, 371–424.
- (37) Tolman, J. R.; Al-Hashimi, H. M.; Kay, L. E.; Prestegard, J. H. *J. Am. Chem. Soc.* **2001**, *123*, 1416–1424.
- (38) Meiler, J.; Prompers, J. J.; Peti, W.; Griesinger, C.; Brüschweiler, R. *J. Am. Chem. Soc.* **2001**, *123*, 6098–6107.
- (39) Showalter, S. A.; Brüschweiler, R. *J. Am. Chem. Soc.* **2007**, *129*, 4158–4159.
- (40) Lange, O. F.; van der Spoel, D.; de Groot, B. L. *Biophys. J.* **2010**, *99*, 647–655.
- (41) Losonczi, J. A.; Andrec, M.; Fischer, M. W.; Prestegard, J. H. *J. Magn. Reson.* **1999**, *138*, 334–342.
- (42) Buck, M.; Bouguet-Bonnet, S.; Pastor, R. W.; MacKerell, A. D. *Biophys. J.* **2006**, *90*, L36–L38.
- (43) Shen, Y.; Lange, O.; Delaglio, F.; Rossi, P.; Aramini, J. M.; Liu, G. H.; Eletsky, A.; Wu, Y. B.; Singarapu, K. K.; Lemak, A.; Ignatchenko, A.; Arrowsmith, C. H.; Szyperski, T.; Montelione, G. T.; Baker, D.; Bax, A. *Proc. Natl. Acad. Sci. U. S. A.* **2008**, *105*, 4685–4690.
- (44) Lakomek, N. A.; Walter, K. F. A.; Fares, C.; Lange, O. F.; de Groot, B. L.; Grubmüller, H.; Brüschweiler, R.; Munk, A.; Becker, S.; Meiler, J.; Griesinger, C. *J. Biomol. NMR* **2008**, *41*, 139–155.
- (45) Ulmer, T. S.; Ramirez, B. E.; Delaglio, F.; Bax, A. *J. Am. Chem. Soc.* **2003**, *125*, 9179–9191.
- (46) Lipari, G.; Szabo, A. *J. Am. Chem. Soc.* **1982**, *104*, 4559–4570.
- (47) Lipari, G.; Szabo, A. *J. Am. Chem. Soc.* **1982**, *104*, 4546–4559.
- (48) Prompers, J. J.; Brüschweiler, R. *J. Am. Chem. Soc.* **2002**, *124*, 4522–4534.
- (49) Brüschweiler, R. *J. Am. Chem. Soc.* **1992**, *114*, 5341–5344.
- (50) Graf, J.; Nguyen, P. H.; Stock, G.; Schwalbe, H. *J. Am. Chem. Soc.* **2007**, *129*, 1179–1189.
- (51) Wickstrom, L.; Okur, A.; Simmerling, C. *Biophys. J.* **2009**, *97*, 853–856.
- (52) Case, D. A.; Scheurer, C.; Brüschweiler, R. *J. Am. Chem. Soc.* **2000**, *122*, 10390–10397.
- (53) Berendsen, H. J. C.; van der Spoel, D.; van der Unen, R. *Comput. Phys. Commun.* **1995**, *91*, 43–56.
- (54) Lindahl, E.; Hess, B.; van der Spoel, D. *J. Mol. Model.* **2001**, *7*, 306–317.
- (55) van der Spoel, D.; Lindahl, E.; Hess, B.; Groenhof, G.; Mark, A. E.; Berendsen, H. J. C. *J. Comput. Chem.* **2005**, *26*, 1701–1718.
- (56) Hess, B.; Kutzner, C.; van der Spoel, D.; Lindahl, E. *J. Chem. Theory Comput.* **2008**, *4*, 435–447.
- (57) Berman, H. M.; Westbrook, J.; Feng, Z.; Gilliland, G.; Bhat, T. N.; Weissig, H.; Shindyalov, I. N.; Bourne, P. E. *Nucleic Acids Res.* **2000**, *28*, 235–242.
- (58) Li, D. W.; Meng, D.; Brüschweiler, R. *J. Am. Chem. Soc.* **2009**, *131*, 14610–14611.
- (59) Lienin, S. F.; Bremi, T.; Brutscher, B.; Brüschweiler, R.; Ernst, R. R. *J. Am. Chem. Soc.* **1998**, *120*, 9870–9879.
- (60) Buck, M.; Boyd, J.; Redfield, C.; Mackenzie, D. A.; Jeenes, D. J.; Archer, D. B.; Dobson, C. M. *Biochemistry* **1995**, *34*, 4041–4055.
- (61) Redfield, C.; Smith, L. J.; Smith, R. A. G.; Dobson, C. M. *Biochemistry* **1992**, *31*, 10431–10437.
- (62) Abbate, S.; Barlati, S.; Colombi, M.; Fornili, S. L.; Francescato, P.; Gangemi, F.; Lebon, F.; Longhi, G.; Manitto, P.; Recca, T.; Speranza, G.; Zoppi, N. *Phys. Chem. Chem. Phys.* **2006**, *8*, 4668–4677.
- (63) Lim, C. C.; Yang, H.; Yang, M.; Wang, C. K.; Shi, J.; Berg, E. A.; Pimentel, D. R.; Gwathmey, J. K.; Hajjar, R. J.; Helmes, M.; Costello, C. E.; Huo, S.; Liao, R. *Biophys. J.* **2008**, *94*, 3577–3589.

- (64) El-Turk, F.; Cascella, M.; Ouertatani-Sakouhi, H.; Narayanan, R. L.; Leng, L.; Bucala, R.; Zweckstetter, M.; Rothlisberger, U.; Lashuel, H. A. *Biochemistry* **2008**, *47*, 10740–10756.
- (65) Feng, J. W. A.; Kao, J.; Marshall, G. R. *Biophys. J.* **2009**, *97*, 2803–2810.
- (66) Pelikan, M.; Hura, G. L.; Hammel, M. *Gen. Physiol. Biophys.* **2009**, *28*, 174–189.
- (67) Daneshgar, P.; Moosavi-Movahedi, A. A.; Norouzi, P.; Ganjali, M. R.; Madadkar-Sobhani, A.; Saboury, A. A. *Int. J. Biol. Macromol.* **2009**, *45*, 129–134.
- (68) Lerbret, A.; Affouard, F.; Bordat, P.; Hedoux, A.; Guinet, Y.; Descamps, M. J. *Chem. Phys.* **2009**, 131.
- (69) Li, D. W.; Brüscheiler, R. *J. Phys. Chem. Lett.* **2010**, *1*, 246–248.
- (70) Markwick, P. R. L.; Bouvignies, G.; Salmon, L.; McCammon, J. A.; Nilges, M.; Blackledge, M. J. *Am. Chem. Soc.* **2009**, *131*, 16968–16975.
- (71) Jarymowycz, V. A.; Stone, M. J. *Chem. Rev.* **2006**, *106*, 1624–1671.
- (72) Igumenova, T. I.; Frederick, K. K.; Wand, A. J. *Chem. Rev.* **2006**, *106*, 1672–1699.
- (73) Sheppard, D.; Li, D. W.; Brüscheiler, R.; Tugarinov, V. J. *Am. Chem. Soc.* **2009**, *131*, 15853–15865.
- (74) Millet, O.; Muhandiram, D. R.; Skrynnikov, N. R.; Kay, L. E. *J. Am. Chem. Soc.* **2002**, *124*, 6439–6448.
- (75) Skrynnikov, N. R.; Millet, O.; Kay, L. E. *J. Am. Chem. Soc.* **2002**, *124*, 6449–6460.
- (76) Cerutti, D. S.; Freddolino, P. L.; Duke, R. E.; Case, D. A. *J. Phys. Chem. B* **2010**, *114*, 12811–12824.
- (77) Li, D. W.; Brüscheiler, R. *Biophys. J.* **2009**, *96*, 3074–3081.
- (78) Lindorff-Larsen, K.; Piana, S.; Palmo, K.; Maragakis, P.; Klepeis, J. L.; Dror, R. O.; Shaw, D. E. *Proteins* **2010**, *78*, 1950–1958.
- (79) Wroblewska, L.; Jagielska, A.; Skolnick, J. *Biophys. J.* **2008**, *94*, 3227–3240.
- (80) Huang, J.; Meuwly, M. J. *Chem. Theory Comput.* **2010**, *6*, 467–476.
- (81) Warshel, A.; Kato, M.; Pisiakov, A. V. *J. Chem. Theory Comput.* **2007**, *3*, 2034–2045.
- (82) Lopes, P. E. M.; Roux, B.; MacKerell, A. D. *Theor. Chem. Acc.* **2009**, *124*, 11–28.
- (83) Cieplak, P.; Dupradeau, F. Y.; Duan, Y.; Wang, J. M. *J. Phys.: Condens. Matter* **2009**, *21*, 333102.
- (84) Ponder, J. W.; Wu, C. J.; Ren, P. Y.; Pande, V. S.; Chodera, J. D.; Schnieders, M. J.; Haque, I.; Mobley, D. L.; Lambrecht, D. S.; DiStasio, R. A.; Head-Gordon, M.; Clark, G. N. I.; Johnson, M. E.; Head-Gordon, T. J. *J. Phys. Chem. B* **2010**, *114*, 2549–2564.
- (85) Yang, W.; Nymeyer, H.; Zhou, H. X.; Berg, B.; Brüscheiler, R. *J. Comput. Chem.* **2008**, *29*, 668–672.

Searching Peptide Conformational Space

Julie Grouleff and Frank Jensen*

Department of Chemistry, Aarhus University, DK-8000 Aarhus, Denmark

 Supporting Information

ABSTRACT: We have performed a near complete analysis of the conformational space in terms of minima and transition structures for four small peptide models with a force field energy function. There is a clear trend that minima having a large difference in structure, as measured by the distance in torsional space, are rarely connected by a single transition structure. There is a similar trend that activation energies for conformational transitions correlate with structure differences, such that small conformational changes occur with low energy barriers and vice versa. This suggests that a systematic search for low energy conformational transition structures should focus on pairs of minima that are structurally similar. Eigenvectors from diagonalization of force constant matrices at minima are better at describing conformational transitions than vibrational normal modes, as verified both by overlaps with geometry difference vectors and results from biased molecular dynamics simulations.

INTRODUCTION

Parameterized force field energy functions are at the core of all biomolecular simulations and determine the ultimate accuracy of the results.¹ The purpose of a molecular dynamics (MD) or Monte Carlo simulation is to sample the phase space, which for biomolecules is determined primarily by the torsional degrees of freedom. The force fields' ability to accurately represent the conformational space near minima and connecting transition structures (TSs) is thus an essential component for providing accurate simulation results. Commonly used force fields like MM2,² MM3,³ MMFF,⁴ AMBER,^{5,6} OPLS,⁷ and CHARMM27⁸ have been parametrized to reproduce the conformational minima for a set of small reference systems, but we envision that the next generation of force fields will require parametrization against a much larger training set of not only conformational minima but also connecting TSs.^{9–15} It is experimentally difficult to obtain such reference data, but it is relatively easy to generate quite accurate results by using electronic structure calculations.

The conformational minima on a given potential energy surface (PES) can be located by a random or systematic generation of many trial structures followed by minimization,¹⁶ but more sophisticated global search methods are also available.¹⁷ A brute force approach will for small systems enable the location of all minima. However, locating all connecting TSs is more difficult, and it is virtually impossible to establish that all TSs have been found. Several groups have developed methods aimed at establishing transition networks corresponding to a tabulation of minima and connecting saddle points.¹⁸ Saddle points are typically located by attempted uphill walking from a minimum¹⁹ or by using a chain-of-state method for each pair of minima.²⁰ The question of whether a given pair of minima is connected by a first order saddle point is of general interest, as it is unlikely that all pairs of minima are connected by a TS, and the fraction of minima pairs connected by a TS will decrease with increasing system size. In the present study, we investigate the conformational space of four peptide models by locating all minima and a large fraction of all of the connecting TSs by using a combination

of three TS search algorithms, of which one has the potential to locate all TSs. These data allow us to probe whether it is possible to deduce the existence of a TS connecting two conformations, using only information from the two minima, the efficiency of various algorithms for locating such TSs, and whether normal mode directions can be used to guide TS searches or bias MD simulations to achieve conformational transitions. For large systems, a complete enumeration of minima and saddle points is infeasible and unnecessary, and the focus is instead on an adequate sampling of the relevant phase space. Small systems with a well characterized energy surface, however, provide a platform for calibrating different methods for sampling the phase space.

All of the results have been generated using the OPLS force field, and other methods may generate a PES with a different topology, but the conclusions regarding connections between minima and TSs and associated properties should remain generally valid.

COMPUTATIONAL DETAILS

All force field calculations have been carried out using the Tinker²¹ and Macromodel²² programs and the OPLS²³ force fields using a dielectric constant of 1.0. Vibrational analyses have been performed in natural internal coordinates²⁴ using a locally modified version of the Gamess-US program package.²⁵ Internal coordinates offer a significant advantage over Cartesian coordinates for describing conformational transitions, as these primarily correspond to changes in torsional coordinates. Following a low-frequency normal mode in internal coordinates effectively only changes the torsional coordinates, while following the same normal mode in Cartesian coordinates also significantly changes bond lengths and angles.

The vibrational analysis corresponds to diagonalizing the force constant matrix in mass-weighted coordinates, which can be

Received: March 8, 2011

Published: May 17, 2011

either Cartesian or internal coordinates, and these eigenvectors are orthogonal. Transforming the eigenvectors from mass-weighted coordinates to non-mass-weighted coordinates, or from internal to Cartesian coordinates, destroys the orthogonality. In order to facilitate the data analysis, it is advantageous to reorthogonalize the transformed eigenvectors, which has been done by a frequency-weighted Löwdin procedure. In a traditional nonweighted Löwdin orthogonalization, a set of vectors is transformed by $S^{-1/2}$, where S is the overlap matrix between the nonorthogonal vectors, and this ensures the least change of all of the vectors. As we are primarily interested in the low frequency modes, we have employed a frequency-weighted version²⁶ where the transformation matrix is given by $W(WSW)^{-1/2}$, and W is a diagonal matrix containing the weights $w_i = \exp(-v_i/1000)$ based on the frequency v_i (in cm^{-1}). This ensures that the low frequency modes are changed as little as possible by the orthogonalization. For glycine, a typical overlap between modes before and after orthogonalization is 0.7.

Transition structure optimizations have been done using three different methods: quadratic synchronous transit (QST), growing string (GS), and scaled hypersphere search (SHS). The QST method²⁷ searches for a saddle point between two minima by a sequence of minimizations and maximizations using a quadratic interpolation between the two end points until a low energy intermediate geometry is located.

The GS method²⁸ is a version of the nudged elastic band method²⁹ where the points on the string connecting the two minima are placed sequentially and optimized before additional points are added. Both the QST and GS methods provide only a guess for the TS, which is refined using a Newton–Raphson algorithm. The combination of a nudged elastic band and a Newton–Raphson-based algorithm for locating saddle points has been used extensively by Wales and co-workers.³⁰ The images along the initial reaction path are usually generated by interpolation between the two end-points,³¹ and if used as a black-box method, it is only able to locate one connecting saddle point between each pair of minima.

The SHS³² method searches for TSs by performing a series of constrained optimizations on hyperspheres with increasing radii and the center at a single minimum, where the initial search direction is generated by perturbing along Hessian eigenvectors. The SHS has been claimed to be able to locate essentially all TSs on a given PES,³³ although numerical issues may prevent this in practice. To our knowledge, the present work is the first application of the SHS method for locating conformational TSs on a force field energy surface. The nature of all minima and TSs has been confirmed by diagonalization of the Hessian matrix as having zero or one negative eigenvalue, respectively.

MD simulations have been done in Cartesian coordinates at a temperature of 310 K using the NAMD program.³⁴ The bias force is taken as a normal mode in internal coordinates, and since the conversion from internal to Cartesian coordinates is non-linear, this necessitates a look-up table approach. Prior to a simulation, a table is constructed which links geometries along the bias normal mode in internal and Cartesian coordinates. At a given point in the simulation, the geometry change relative to the starting minimum along the bias normal mode is calculated in internal coordinates, and the bias force is the tangent direction in Cartesian coordinates, calculated as a finite difference from the tabulated values. The magnitude of the biasing force needs to be large enough for the bias to have effect but small enough that the temperature of the system does not increase significantly. This

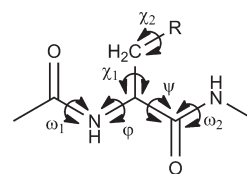


Figure 1. Notation for torsional angles.

Table 1. Calculated Relative Energies and Torsional Angles for Minima for Ace-Gly-NHMe

EQ <i>i</i>	class	$E_{\text{rel}}(\text{kJ/mol})$	ω_1	φ	ψ	ω_2
1	TT	0.0	-175.8	124.9	-143.0	-179.9
2	TT	3.6	176.4	109.7	-60.4	179.6
3	TC	13.3	-174.6	127.3	-157.5	0.2
4	CT	14.0	0.3	115.7	-11.2	179.7
5	CT	22.6	4.9	126.6	-145.2	180.0
6	TT	26.1	-180.0	0.0	0.0	180.0
7	CC	34.8	5.5	128.2	-161.4	-0.5
8	CC	43.9	-1.0	-119.9	-78.7	-1.4
9	CC	64.0	12.6	28.3	65.4	0.9

depends on the frequency of the given mode and thus has to be determined for each mode, which has been done by running test simulations with different force magnitude settings. In cases where the frequency is relatively high, the required magnitude of force is sufficiently large that the temperature of the system has to be damped additionally, which is done by increasing the Langevin damping coefficient for the system. The escape from the starting minimum is detected by collecting structures every 10th femtosecond and subsequently minimizing them in order to determine to which basin they belong. The first structure not equal to the starting minimum is the one listed in Table 3 along with the time for the transition.

RESULTS AND DISCUSSION

We have selected the glycine, alanine, serine, and cysteine amino acids as our trial set of systems, with side chains corresponding to H, CH₃, CH₂OH, and CH₂SH, respectively. Acetyl and N-methyl groups were added to the N- and C-termini to mimic the environment in longer peptide chains. The notation for the torsion angles is depicted in Figure 1. Conformations for peptides are commonly discussed in terms of a Ramachandran map with the backbone φ and ψ angles as the variables, where a positive sign indicates a clockwise rotation. The side chain and peptide bond torsional angles are labeled χ_i and ω_i , respectively.

Conformational minima have been located by an exhaustive Monte Carlo search. The OPLS PES for glycine contains nine minima, described in Table 1, as well as mirror images of eight of these. The minima are labeled according to energy such that EQ1 is the global minimum. On the basis of the configuration of the two peptide bonds, the minima can be separated into four groups. EQ1, EQ2, and EQ6 all have a *trans* configuration of both bonds and belong to a class labeled TT, and this is the configuration commonly found in peptides and proteins. The *trans,cis* class (TC) only consists of EQ3 while the *cis,trans* class (CT) contains EQ4 and EQ5. The structures with *cis,cis* configurations (CC) have the highest relative energies and include EQ7, EQ8, and EQ9. It should be noted that EQ9 is a very shallow minimum with a transition barrier to the mirror image of EQ8 of only 0.004 kJ/mol.

MP2 calculations for the TT class suggest that only EQ1 and EQ2 are genuine minima, while different force fields disagree on the existence of EQ6.¹⁰ With the employed OPLS force field, EQ6 is a weakly defined minimum with a barrier of only 1.6 kJ/mol for transition to EQ2.

The three TS search algorithms located a total of 66 unique TSs on the PES for glycine. TSs corresponding to methyl rotations are not included in these 66 TSs and are not part of the analysis. Graphical representations of a number of two-dimensional projections of the PES were examined to verify the existence of the found TSs, and these plots allowed us to locate an additional six TSs. Four of these correspond to transitions where two different TSs connect the same two minima, corresponding to short and long reaction pathways depending on the direction of rotation around the torsional angles. The four manually found TSs all belong to the long pathways and in all cases have the three search-algorithm located TSs corresponding to the short pathway. An additional two TSs were constructed by mirroring two already located TSs. On the basis of our analyses of two-dimensional projections of the PES, we believe that the 74 located TSs (Table S1, Supporting Information) represent all of the first order saddle point on the PES, although this is difficult to prove rigorously.

The three search methods display different performances. The GS algorithm locates only 16 TSs. The QST finds 42 TSs, while SHS is capable of locating 49 TSs. That is, none of the methods are able to locate all TSs even when all minima are known. The energy barriers for the found transitions are in the range of 0.004–122 kJ/mol, and all three methods locate TSs corresponding to both low and high energy transitions. None of the methods are particularly better than the others at locating the low energy TSs, which usually are the most interesting. While the SHS method in principle should be able to locate all TSs,³³ the numerical issues regarding the detection of branching points is quite delicate, and the present work suggests that there is still room for improvements.

Out of the 136 possible TSs connecting the 17 minima (including mirror images, assuming only one TS exists between each pair of minima), we have located 50, which indicates that approximately only one-third of the possible TSs exist for this system. In 24 cases, there are two different TSs connecting the same two minima, and including these higher energy dual-TSs accounts for a total of 74 TSs. The corresponding values for only the nine symmetry unique minima are 36 possible TSs, of which we have located 17 unique. The QST and SHS algorithms locate 15 and 14 of these TSs, respectively, while GS only finds eight TSs.

The QST algorithm only optimizes a single structure and is the computationally cheapest method. The GS algorithm performs a sequential optimization of an increasing number of structures (up to 21 in the present cases) and requires approximately two orders of magnitude more computer time. The SHS algorithm requires second derivatives and performs a sequence of constrained optimizations along a set of normal modes and is, further, one order of magnitude more expensive computationally. For the present small systems and simple energy function, the computational times vary from less than 1 s to minutes for each saddle point search.

Wales and co-workers have advocated the combination of a nudged elastic band and a Newton–Raphson-based algorithm for locating saddle points.³⁰ In our case, the GS variant of the nudged elastic band algorithm is the method displaying the

Table 2. Calculated Relative Energies and Torsional Angles for Minima for Ace-Ala-NHMe

EQ <i>i</i>	<i>E</i> _{rel} (kJ/mol)	class	ω_1	φ	ψ	ω_2
1	0.0	TT	−179.4	−79.4	61.6	179.9
2	4.1	TT	177.8	−152.0	158.3	179.8
3	10.4	TT	175.9	75.4	−48.9	179.8
4	12.8	TT	−177.8	−133.8	40.7	−179.6
5	16.1	CT	−2.8	−83.8	−6.1	179.8
6	18.8	TC	178.2	−151.1	151.7	−1.4
7	20.9	TC	175.5	−90.9	122.3	−3.2
8	21.3	CT	−1.2	−138.3	22.1	−179.5
9	25.1	CT	−1.6	−148.9	155.5	179.9
10	25.8	TT	176.1	−159.0	−49.6	178.9
11	28.0	CT	−2.5	82.3	6.7	−179.9
12	29.2	CT	−2.8	−88.8	137.0	−179.9
13	38.9	CC	−1.6	−148.5	150.3	−0.9
14	42.1	CC	−2.7	−88.5	141.4	0.1
15	44.0	CC	−2.0	−142.9	64.7	1.6
16	46.1	CT	−3.1	83.4	160.1	179.9
17	46.7	TC	176.9	−152.3	−44.8	−5.8
18	46.4	TC	179.9	−70.9	−33.2	−5.0
19	48.1	CC	−3.6	−71.5	−36.5	−3.5
20	51.2	TC	−178.3	98.8	−97.3	2.4
21	51.2	TC	−179.5	102.9	−67.4	−0.7
22	53.1	CC	−1.0	−145.5	−42.6	−5.3
23	54.2	TC	−174.6	93.8	162.4	−0.7
24	55.9	TC	178.0	71.8	43.4	4.8
25	56.7	CC	−1.3	74.6	52.1	2.7
26	61.2	CC	−1.8	85.2	143.8	−1.0
27	80.0	CC	−2.8	95.5	−121.0	1.0

poorest performance, but other implementations and/or use of other coordinates may display better performance. Dual TSs, however, cannot be located by methods relying on interpolating between the two minima but can be located by the SHS algorithm.

In terms of potential energy, the 32 TSs having both the lowest absolute energies and the lowest activation energies all belong to transitions within each of the four classes, meaning that only the φ and ψ torsional angles change significantly. The remaining 42 TSs all correspond to transitions between classes. In the TT, CT, and CC classes, the lowest transition corresponds to a rotation dominated by the ψ angle. This indicates that the rotation barrier for this torsion is lower than for φ , ω_1 , and ω_2 , respectively. As expected, the data also show that rotation around the φ angle is softer than rotation around either of the peptide bonds. Nine pairs of minima (including mirror images) are connected by two different TSs, corresponding to rotation in the two possible directions. The shortest pathway in all cases has the lowest energy barrier. Not surprisingly, the three TS search methods are much better at locating the TS corresponding to the shortest pathway than the longer one.

The alanine system has 27 minima, shown in Table 2, and the conformational space is spanned by the same four torsional angles as for the glycine system. The PES for glycine contains seven well-defined minima (EQ1, EQ2, EQ3, EQ4, EQ5, EQ7, EQ8), and minima similar to all of these can be found on the PES for alanine. The introduction of the side chain methyl group

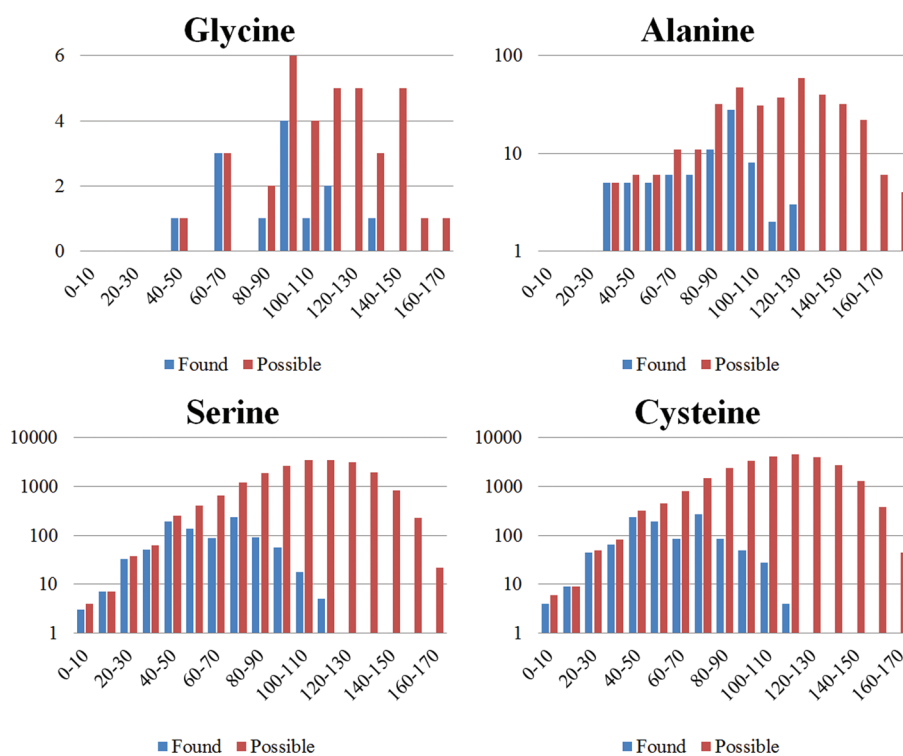


Figure 2. Comparison between the number of possible TSs and those actually located as a function of torsional RMS difference between the two connected minima.

causes some of the glycine energy minima to split up into two distinct minima for alanine. The presence of the methyl side chain introduces additional electrostatic and van der Waals interactions that results in a number of alanine minima which do not have a glycine equivalent.

MP2 calculations for the TT class suggest that there are seven minima,¹⁰ while the presently employed OPLS force field has five minima. These five structures are in agreement with the OPLS free energy surface obtained by metadynamics simulations.³⁵

The combination of the QST, GS, and SHS methods located a total of 97 TSs (excluding methyl group rotations) on the PES for alanine (Table S2, Supporting Information), of which 15 are dual TSs. On the basis of the results for the glycine system, we expect that there may be a few additional TSs which have not been found by the three automated methods, of which some represents additional dual TSs. Out of the 351 possible TSs connecting the 27 minima, the results thus suggest that only approximately one-fourth actually exist. In analogy with the glycine system, the 40 lowest energy TSs only connect conformations with a given subclass defined by two amide bonds. In terms of activation energy, the 44 lowest energy TSs correspond to transitions inside a given class, while the rest are transitions between subclasses. Out of the possible 10 TSs within the TT subclass, we have found seven.³⁶

The serine system has 202 minima, and we have located a total of 1108 TSs, while the cysteine system has 227 minima, and we have found 1251 TSs (Tables S3–S6, Supporting Information). On the basis of the results for glycine, we expect that these represent a large fraction of all of the possible TSs, and the numbers can be compared to the combinatorially possible 20 301 and 25 651 TSs for the two systems, respectively; i.e., only ~5% of the possible TSs actually exist. Within the TT subclass, the

number of minima for the two systems is 26 and 35, which can be compared to 39 and 47 found at the MP2 level of theory.¹⁰ Within this subclass, there are 325 and 595 possible TSs, respectively, and we have located 73 and 103.

For serine, the 497 lowest energy TSs all belong to transitions within each of the four classes, while the 671 TSs with lowest activation energies correspond to in-class transitions. The results for cysteine are similar: 584 lowest TSs if sorted by energy and 762 lowest TSs if sorted by activation energy. For both serine and cysteine, the TSs with a higher energy correspond to a mixture of transitions inside and between the classes.

Existence of Transition Structures. It seems intuitively reasonable that the probability of finding a TS between a pair of minima is higher for a pair of structurally similar minima than for a pair of structurally very different minima. To probe this hypothesis, we have calculated the torsional root-mean-square (RMS) deviation for all pairs of minima for all four systems and compared these values with the ratio between found and combinatorially possible TSs. In this analysis, the mirror images of the minima for glycine were not included. For glycine and alanine, the torsional RMS is calculated from the four backbone angles ($\omega_1, \varphi, \psi, \omega_2$). For serine and cysteine, the side chain torsions (χ_1, χ_2) are also included in the analyses. As can be seen from Figure 2 (note the logarithmic scale), there is a high possibility of finding a TS if the torsional RMS for the pair of minima is $<50^\circ$. The likelihood of finding a TS between the two minima falls significantly if the torsional RMS is greater than 80° , and this is especially clear for the cysteine and serine systems.

Figure 3 shows the connection between the torsional RMS deviation between two minima and the activation energy calculated relative to the lowest energy minimum. As expected, there is a general correlation between the two, such that transitions

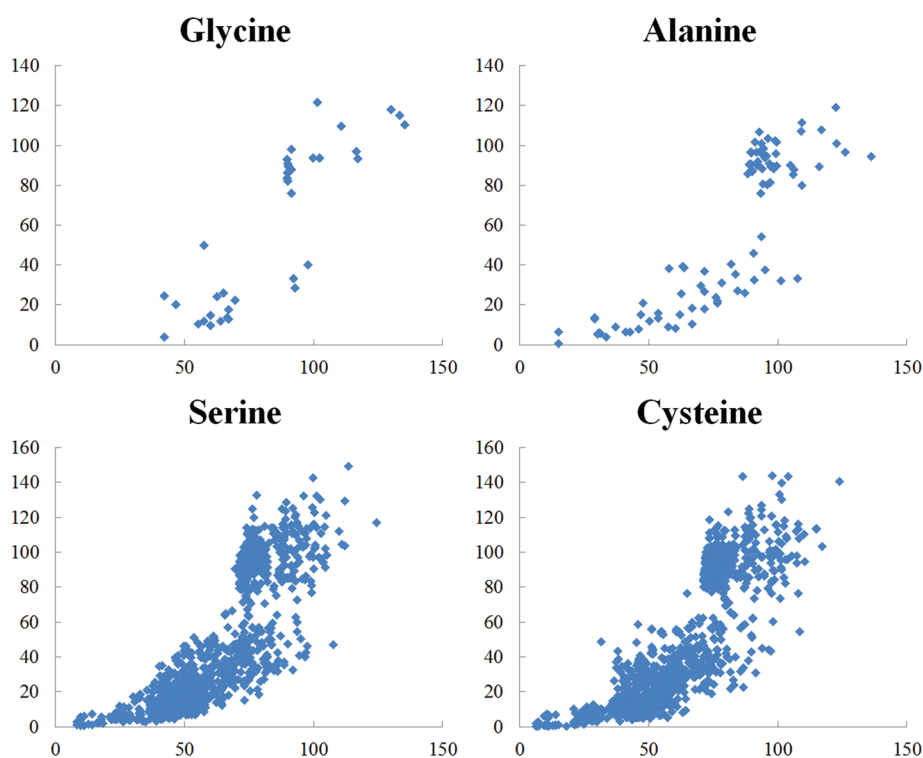


Figure 3. Correlation between activation energy (kJ/mol) and torsional RMS difference (degrees) between the two connecting minima.

involving large structural changes occur by TSs having relatively large activation energies.

The results shown in Figure 2 suggest that large structural changes rarely occur in a single step but rather as a sequence of transitions involving smaller changes. Figure 3 shows that transitions involving large structural changes that do occur in a single step tend to have high activation energies and are therefore less important from a dynamical point of view. The combination of these results suggests that a search for low energy conformational TSs can be focused on pairs of minima that are structurally similar. For the present systems, a torsional RMS less than $\sim 80^\circ$ would appear as a reasonable criterion, but such a threshold value is likely to be dependent on the system size.

Use of Normal Modes for Predicting Transition Structures.

The eigenvectors from diagonalization of the force constant matrix contain information about the curvature of the PES, where the eigenvector associated with the lowest eigenvalue points in the direction where the energy increases least. If the force constant matrix is mass-weighted before diagonalization, the eigenvectors are the vibrational normal modes. It is commonly assumed that the direction of the low-frequency normal modes leads to low-energy TSs, and this is used for example in the eigenvector-following method for locating saddle points.³⁷ In the following, we will denote the eigenvectors from diagonalization of the force constant matrix as *f*-vectors and the eigenvectors from diagonalization of the mass-weighted force constant matrix as *g*-vectors.

While vibrational analysis traditionally is performed in Cartesian coordinates, it is for the present application more convenient to use internal coordinates²⁴ since the conformational space is effectively spanned only by the torsional coordinates. The *f*-vectors in internal coordinates are orthogonal, but this is not the case for the *g*-vectors. In order to facilitate the analysis, we

have orthogonalized the *g*-vectors by a frequency-weighted Löwdin procedure, where the orthogonalization is carried out such that the low-frequency normal modes are perturbed as little as possible.²⁶

The reaction path can be approximated either as a difference vector in internal coordinates between the two minima (ΔR_{EQ}) or as a difference vector between the minimum and the TS (ΔR_{TS}). For each system, we have calculated the overlap between these two reaction paths and the normal modes, both *f*- and *g*-vectors, for each of the two minima. The normal modes can be ordered either according to energy (frequency) or by the largest overlap with the reaction path. The average number of modes required to obtain an 80% overlap with the reaction path for the four test systems is given in Table 3. Transitions corresponding to methyl rotation have, as previously mentioned, been neglected, and all overlaps with modes corresponding to methyl rotation have been set to 0.

Table 3 shows that 5–6 of the lowest energy *f*-vectors are required to represent 80% of the reaction path, while only 2–3 vectors are required if the vectors are arranged according to overlap. This is understandable, as two vectors representing terminal methyl group rotations are among the low energy ones, and these make no contributions to the reaction path. The *g*-vectors, which are the vibrational normal modes, show the same trend, but significantly more modes are required to represent 80% of the reaction path. These results suggest that using the direction of *f*-vectors as a search bias will generally be more efficient than using the *g*-vectors, at least for the present small systems.

To probe whether low energy modes point in the direction of low energy TSs, Figure 4 shows the correlation between the number of modes needed to obtain at least an 80% overlap with ΔR_{EQ} and the activation energy. The *f*-vectors provide a reasonable correlation,

Table 3. Average Number of Modes Required to Obtain at Least 80% Overlap with the Transition Vector ΔR_{EQ} or ΔR_{TS}

	ΔR_{EQ}				ΔR_{TS}			
	sorted by energy		sorted by overlap		sorted by overlap		sorted by energy	
	f	g	f	g	f	g	f	g
Gly	5.1	11.0	2.3	5.2	5.0	10.8	2.6	5.8
Ala	5.3	11.0	2.4	5.4	6.0	12.4	3.2	6.6
Ser	5.5	12.5	2.3	5.9	6.9	13.9	3.8	7.3
Cys	5.6	12.4	2.3	5.9	6.6	12.8	3.4	6.8

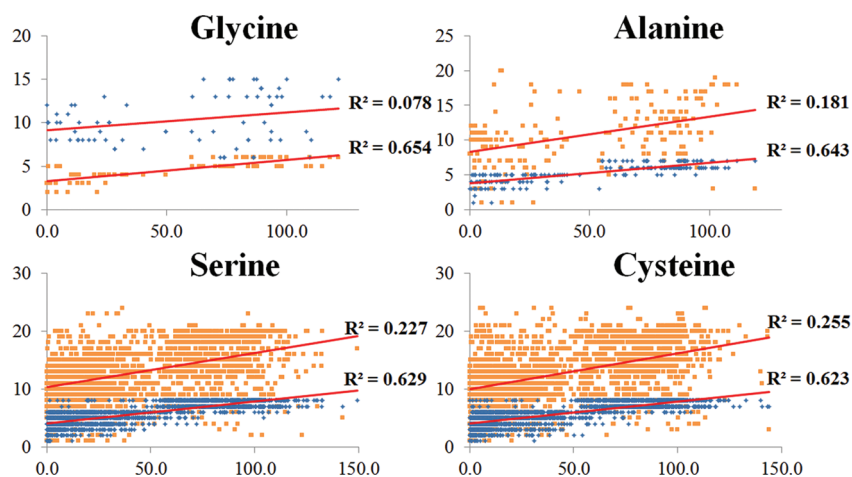


Figure 4. Correlation between the activation energy for a transition (kJ/mol) and the number of modes required to represent at least 80% of the reaction vector.

Table 4. MD Simulations Starting from EQ1 Biased with the Six Lowest Normal Modes in Form of f- and g-Vectors^a

	no bias	f-vectors						g-vectors					
		1	2	3	4	5	6	1	2	3	4	5	6
EQ1*	5.9	6.4	6.3	43.5	68.6	5.5		41.0	5.6	18.7	7.3	6.7	7.1
EQ2	43.5	41.7	42.1	8.1	31.1	36.3	97.5	7.2	42.2	33.0	40.3	42.0	40.7
EQ4						7.7							
EQ5						48.4							
no change	51.1	51.9	51.6	48.3		1.3	2.5	52.0	52.2	48.2	52.4	52.0	52.2
time (ps)	4.8	4.8	4.9	4.3	1.4	1.0	1.2	4.3	4.9	4.9	4.6	4.7	4.8

^aThe numbers refer to the percentage of simulations where a conformational change from EQ1 to EQ_i is observed. Transitions that occur in less than 1% of the simulations are not included. The time is the average time before a transition occurs. EQ1* indicates the mirror image of EQ1.

with correlation coefficients of ~ 0.64 , while a much lower correlation is found for the g-vectors. This suggests that using non-mass-weighted normal modes (Hessian eigenvectors) may be more efficient than using vibrational normal modes to guide a search for low energy TSs.

Using Normal Modes to Bias MD Simulations. Isin et al. have recently used vibrational normal modes to bias MD simulations in order to simulate conformational transitions that otherwise would be too slow to be computationally feasible.³⁸ The correlation between geometry changes and normal modes in Table 3, and the corresponding correlation with activation energies in Figure 4, suggests that eigenvectors from diagonalization of the force constant matrix may have advantages over vibrational normal modes for biasing MD simulations for the

present systems. In order to test this, we have performed a series of MD simulations on the glycine system with bias forces along the six lowest normal modes. Starting from the global minimum, we run 1000 simulations for 10 ps each and analyze the trajectories as described in the Computational Details to obtain statistics for which other minima the molecule escapes to during the simulation. The potential energy surface around EQ1 in terms of the φ and ψ angles is depicted in Figure 5, with the directions of f-vectors 3 and 4 and g-vectors 1 and 3 indicated.

The results of MD simulations starting from EQ1 can be seen in Table 4, where the percentage of changes to a given minimum is listed along with the average time for the transition. When no bias is applied, the majority of conformational changes is from EQ1 to EQ2, while a smaller fraction of the transitions are from

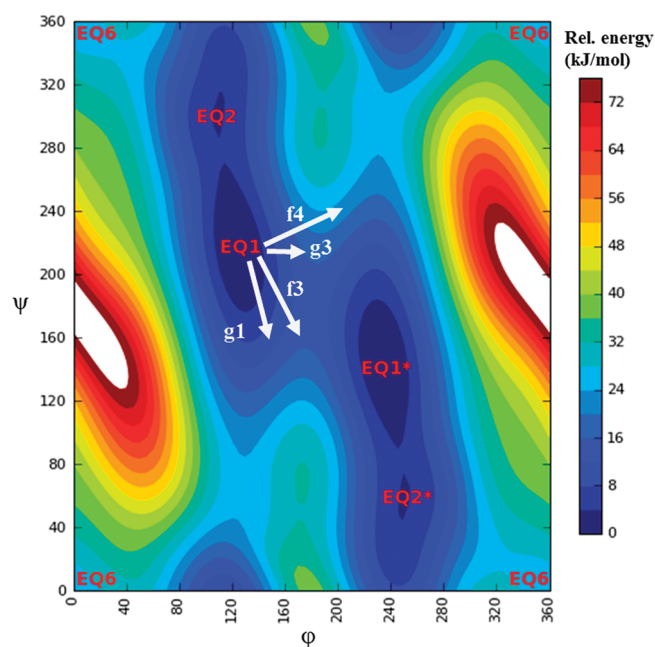


Figure 5. Two-dimensional cut of the PES for glycine showing the three minima (EQ1, EQ2, and EQ6) for the TT class. EQ1* and EQ2* denote mirror images of EQ1 and EQ2.

EQ1 to the mirror image of EQ1 (denoted as EQ1*). This is in line with activation energies of 3.9 and 13.5 kJ/mol for the two transitions (Table S1, Supporting Information). The use of either of the two *f*-vectors with lowest frequencies as a bias does not change this distribution significantly, which is not a surprising since these two vectors mainly correspond to the rotation of the terminal methyl groups. When *f*-vector 3 or 4 is used as a bias, the result is a better sampling of the EQ1 to EQ1* transition, whereas using *f*-vector 6 as a bias almost exclusively induces EQ1 to EQ2 transitions. The use of *f*-vector 5 leads to sampling of two new transitions, namely, EQ1 to EQ4 and EQ1 to EQ5, i.e. transitions corresponding to a rotation of one of the amide bonds. Using *f*-vectors 4, 5, and 6 as bias reduce the percentage of simulations where no conformational change is observed to $\leq 2.5\%$. This is also reflected in the average transition times shown in the last row of Table 4. Without an applied bias, the average time before a conformational change occurs is ~ 5 ps, which is reduced to ~ 1 ps when *f*-vectors 4, 5, or 6 are applied as a bias. The *f*-vectors 3, 4, and 5 all have reasonable overlaps (27–77%) with ΔR_{EQ} for the transitions that they enhance. For *f*-vector 6, however, the overlap with ΔR_{EQ} between EQ1 and EQ2 is almost 0%. The observed effect of using this vector as a bias is therefore most likely due to the increase in system energy. Of the six *g*-vectors used as a bias in this test, only the lowest normal mode leads to significant changes and increases the sampling of the EQ1 to EQ1* transition. None of the *g*-vectors reduce the percentage of simulations where no conformational change is observed significantly. These results thus support the conclusion from Figure 4 that *f*-vectors have advantages over *g*-vectors for biasing MD simulations for these systems.

SUMMARY

The present study has performed a near exhaustive search for conformational minima and transition structures for four small

peptide systems using a force field energy function. Analysis of the results suggests that large structural changes rarely occur in a single step, and if they do, they are associated with a relatively large energy barrier. This indicates that a systematic search for low energy conformational transition structures should focus on pairs of minima that are structurally similar, for example, quantified by their torsional angles. None of the three employed algorithms are able to selectively locate low energy transition structures. The number of possible transition structures increases quadratically with the number of minima, but for the present systems, the actual relationship is close to linear, with typically 5 times as many transition structures as minima.

An analysis of overlaps with geometry vectors describing structural changes and molecular dynamics simulations indicates that eigenvectors obtained by diagonalization of the force constant matrix for minima are better at describing directions for low-energy conformational transitions than vibrational normal modes for these systems. Most of the conformational changes correspond to rotation around one or a few torsional angles, and the superiority of the force constant eigenvectors can be rationalized by the observation that these vectors primarily correspond to pure rotation around only one or two torsional angles. Vibrational normal modes, on the other hand, are spread out over more atoms and often involve both rotation and bending degrees of freedom. Large-scale conformational changes in proteins are often global domain movements, which typically require rotation around several torsions, and vibrational normal modes may here be better descriptors.

ASSOCIATED CONTENT

S Supporting Information. Tables with structural and energetic information for minima and TSs for glycine, alanine, serine, and cysteine. The material is available free of charge via the Internet at <http://pubs.acs.org>.

AUTHOR INFORMATION

Corresponding Author

*E-mail: frj@chem.au.dk

ACKNOWLEDGMENT

This work was supported by grants from the Danish Natural Science Research Council, the Danish Center for Scientific Computing, and the Novo Scholarship program. We thank Prof. K. Ohno for help with the GRRM program used for the SHS optimizations.

REFERENCES

- (1) Schlick, T. *Molecular modeling and simulation*; Springer: New York, 2002.
- (2) Allinger, N. L. *J. Am. Chem. Soc.* **1977**, *99*, 8127.
- (3) Allinger, N. L.; Yan, L. *J. Am. Chem. Soc.* **1993**, *115*, 11918.
- (4) Halgren, T. A. *J. Comput. Chem.* **1996**, *17*, 490.
- (5) Weiner, S. J.; Kollman, P. A.; Case, D. A.; Singh, U. C.; Ghio, C.; Alagona, G.; Profeta, S.; Weiner, P. *J. Am. Chem. Soc.* **1984**, *106*, 765.
- (6) Wang, J.; Cieplak, P.; Kollman, P. A. *J. Comput. Chem.* **2000**, *21*, 1049.
- (7) Jorgensen, W. L.; Tirado-Rives, J. *J. Am. Chem. Soc.* **1988**, *110*, 1657.
- (8) Foloppe, N.; MacKerell, A. D. *J. Comput. Chem.* **2000**, *21*, 86.

- (9) Gundertofte, K.; Liljefors, T.; Norrby, P. O.; Pettersson, I. *J. Comput. Chem.* **1996**, *17*, 429. Mackerell, A. D., Jr.; Feig, M.; Brooks, C. L., III. *J. Am. Chem. Soc.* **2004**, *126*, 698. Buck, M.; Bouguet-Bonnet, S.; Pastor, R. W.; Mackerell, A. D., Jr. *Biophys. J.* **2006**, *90*, L36. Wang, Z.-X.; Zhang, W.; Wu, C.; Lei, H.; Cieplak, P.; Duan, Y. *J. Comput. Chem.* **2006**, *27*, 781.
- (10) Kaminsky, J.; Jensen, F. *J. Chem. Theory Comput.* **2007**, *3*, 1774.
- (11) Gresh, N.; Tiraboschi, G.; Salahub, D. R. *Biopolymers* **1998**, *45*, 405.
- (12) Gould, I. R.; Kollman, P. A. *J. Phys. Chem.* **1992**, *96*, 9255.
- (13) Möhle, K.; Hofmann, H.-J. *J. Mol. Struct.* **1995**, *339*, 57.
- (14) Hermida-Ramón, J. M.; Brdarski, S.; Karlström, G.; Berg, U. *J. Comput. Chem.* **2003**, *24*, 161.
- (15) Yang, Z. Z.; Zhang, Q. *J. Comput. Chem.* **2006**, *27*, 1.
- (16) Chang, G.; Guida, W. C.; Still, W. C. *J. Am. Chem. Soc.* **1989**, *111*, 4379. Chandrasekhar, J.; Saunders, M.; Jorgensen, W. L. *J. Comput. Chem.* **2001**, *22*, 1646.
- (17) Kolossvári, I.; Guida, W. C. *J. Am. Chem. Soc.* **1996**, *118*, 5011.
- (18) Noé, F.; Fischer, S. *Curr. Opin. Struct. Biol.* **2008**, *18*, 154. Wales, D. J. *Curr. Opin. Struct. Biol.* **2010**, *20*, 3. Krivov, S. V.; Karplus, M. *Proc. Natl. Acad. Sci. U.S.A.* **2004**, *101*, 14766. Carr, J. M.; Trygubenko, S. A.; Wales, D. J. *J. Chem. Phys.* **2005**, *122*, 234903.
- (19) Mortenson, P. N.; Wales, D. J. *J. Chem. Phys.* **2001**, *114*, 6443. Mortenson, P. N.; Evans, D. A.; Wales, D. J. *J. Chem. Phys.* **2002**, *117*, 1363. Wei, G.; Mousseau, N.; Derreumaux, P. *J. Chem. Phys.* **2002**, *117*, 11379. Wei, G.; Derreumaux, P.; Mousseau, N. *J. Chem. Phys.* **2003**, *119*, 6403. Yun, M.; Mousseau, N.; Derreumaux, P. *J. Chem. Phys.* **2007**, *126*, 105101. St-Pierre, J.; Mousseau, N.; Derreumaux, P. *J. Chem. Phys.* **2008**, *128*, 045101.
- (20) Evans, D. A.; Wales, D. J. *J. Chem. Phys.* **2003**, *119*, 9947. Evans, D. A.; Wales, D. J. *J. Chem. Phys.* **2004**, *121*, 1080. Carr, J. M.; Wales, D. J. *J. Chem. Phys.* **2005**, *123*, 234901.
- (21) Ponder, J. W. *Tinker*, version 5.1; Washington University School of Medicine: St. Louis, MO. <http://dasher.wustl.edu/tinker/> (accessed 1/1/2010).
- (22) *MacroModel*, version 9.7; Schrödinger, LLC: New York, 2009.
- (23) Jorgensen, W. L.; Maxwell, D. S.; Tirado-Rives, J. *J. Am. Chem. Soc.* **1996**, *118*, 11225. Kaminski, G. A.; Friesner, R. A.; Tirado-Rives, J.; Jorgensen, W. L. *J. Phys. Chem. B* **2001**, *105*, 6474.
- (24) Jensen, F.; Palmer, D. S. *J. Chem. Theory Comput.* **2011**, *7*, 223. Fogarasi, G.; Zhou, X.; Taylor, P. W.; Pulay, P. *J. Am. Chem. Soc.* **1992**, *114*, 8191.
- (25) Schmidt, M. W.; Baldrige, K. K.; Boatz, J. A.; Elbert, S. T.; Gordon, M. S.; Jensen, J. J.; Koseki, S.; Matsunaga, N.; Nguyen, K. A.; Su, S.; Windus, T. L.; Dupuis, M.; Montgomery, J. A. *J. Comput. Chem.* **1993**, *14*, 1347.
- (26) Reed, A. E.; Weinstock, R. B.; Weinhold, F. *J. Chem. Phys.* **1985**, *83*, 735.
- (27) The saddle option in the Tinker program is an implementation of the ideas in: Halgren, T. A.; Lipscomb, W. N. *Chem. Phys. Lett.* **1977**, *49*, 225. Bell, S.; Crighton, J. S. *J. Chem. Phys.* **1984**, *80*, 2464.
- (28) Peters, B.; Heyden, A.; Bell, A. T.; Chakraborty, A. *J. Chem. Phys.* **2004**, *120*, 7877.
- (29) Henkelman, G.; Jónsson, H. *J. Chem. Phys.* **2000**, *113*, 9978.
- (30) Trygubenko, S. A.; Wales, D. J. *J. Chem. Phys.* **2004**, *120*, 2082. Munro, L. J.; Wales, D. J. *Phys. Rev. B* **1999**, *59*, 3969.
- (31) Bauer, M. S.; Strodel, B.; Fejer, S. N.; Koslover, E. F.; Wales, D. J. *J. Chem. Phys.* **2010**, *132*, 054101.
- (32) Ohno, K.; Maeda, S. *Chem. Phys. Lett.* **2004**, *384*, 277. Maeda, S.; Ohno, K. *J. Phys. Chem. A* **2005**, *109*, 5742. The SHS method as implemented in the GRRM program developed by K. Ohno and co-workers has been used.
- (33) Ohno, K.; Maeda, S. *J. Phys. Chem. A* **2006**, *110*, 8933. Yang, X.; Maeda, S.; Ohno, K. *J. Phys. Chem. A* **2007**, *111*, 5099. Watanabe, Y.; Maeda, S.; Ohno, K. *Chem. Phys. Lett.* **2007**, *447*, 21.
- (34) Phillips, J. C.; Braun, R.; Wang, W.; Gumbart, J.; Tajkhorshid, E.; Villa, E.; Chipot, C.; Skeel, R. D.; Kale, L.; Schulten, K. *J. Comput. Chem.* **2005**, *26*, 1781.
- (35) Liu, Z.; Ensing, B.; Moore, P. B. *J. Chem. Theory Comput.* **2011**, *7*, 402.
- (36) Westerberg and Floudas found 10 minima and 38 TSs for the TT-subclass with the ECEPP/3 force field: Westerberg, K. M.; Floudas, C. A. *J. Chem. Phys.* **1999**, *110*, 9259.
- (37) Banerjee, A.; Adams, N.; Simons, J.; Shepard, R. *J. Phys. Chem.* **1985**, *89*, S2. Culot, P.; Dive, G.; Nguyen, V. H.; Ghuysen, J. M. *Theor. Chem. Acc.* **1992**, *82*, 189. Cerjan, C. J.; Miller, W. H. *J. Chem. Phys.* **1981**, *75*, 2800. Baker, J. *J. Comput. Chem.* **1986**, *7*, 385. Baker, J. *J. Comput. Chem.* **1987**, *8*, 563. Baker, J. *J. Comput. Chem.* **1992**, *13*, 240.
- (38) Isin, B.; Schulten, K.; Tajkhorshid, E.; Bahar, I. *Biophys. J.* **2008**, *95*, 789.

Accurate Intermolecular Potentials with Physically Grounded Electrostatics

Maxim Tafipolsky* and Bernd Engels*

Institut für Physikalische und Theoretische Chemie, Universität Würzburg, Am Hubland, D-97074 Würzburg, Germany

ABSTRACT: A strategy is proposed to include the missing charge penetration energy term directly into a force field using a sum over pairwise electrostatic energies between spherical atoms as originally suggested by Spackman. This important contribution to the intermolecular potential can be further refined to reproduce the accurate electrostatic energy between monomers in a dimer by allowing for the radial contraction–expansion of atomic charge densities. The other components of a force field (exchange-repulsion and dispersion) are parametrized to reproduce the accurate data calculated by symmetry-adapted perturbation theory (SAPT). As a proof-of-concept, we have derived the force field parameters suitable for modeling intermolecular interactions between polycyclic aromatic hydrocarbons (PAH). It is shown that it is possible to have a balanced force field suitable for molecular simulations of large molecules avoiding error cancellation to a large extent.

1. INTRODUCTION

Constructing a reliable potential energy surface, which describes the energy of an assembly of molecules as a function of the atomic positions, is still a challenging problem. In particular, the intermolecular forces are primarily responsible for aggregation of molecules in the condensed phase.^{1–3} Due to the size of the system, however, high-quality fully ab initio calculations are computationally very demanding, even more so when dynamics is to be studied (see, for example, refs 4 and 5). The force field methods are therefore indispensable for elucidating the properties of large aggregates of molecules. To be useful, parametrized force fields should be able to treat both intra- and intermolecular interactions accurately and reliably.

Large conjugated π systems, such as polycyclic aromatic hydrocarbons (PAH) and their derivatives (used as dyes), present notorious difficulties for modelers. A particular arrangement of monomers in an aggregate is ruled by a subtle interplay between electrostatic forces and dispersion interactions between extended aromatic π systems. Furthermore, the accurate structure and dynamics of this class of molecules within their crystalline environment are of primary importance for their optoelectronic properties (absorption, energy, and charge transport), needed for use in, for example, organic solar cells.⁶ Due to the extensive π -conjugation with highly anisotropic charge distribution, the accurate description of intermolecular energies is extremely difficult, and literature force fields are too generic to be useful.

Quantum mechanical electronic structure calculations are helping to improve upon our understanding of the forces acting between molecules. The theory of intermolecular interactions^{7,8} is now widely used to shed light on the particular forces responsible for aggregation of molecules in the condensed phase. Energy decomposition analysis (EDA) pioneered by Morokuma has been refined to such an extent (for a review, see ref 9) that it can be used as a reference for deriving all necessary contributions to the intermolecular interaction energy assuming additivity of the force field terms, such as electrostatic, exchange-repulsion, induction, and dispersion (see, for example, ref 10). On the other

hand, intermolecular perturbation theory has emerged as a very powerful tool for the developing of model potentials.¹¹ Recent developments within the Symmetry Adapted Perturbation Theory (SAPT) enable highly accurate studies of intermolecular interactions at a level comparable to state-of-the-art methods such as coupled-cluster theory, CCSD(T), but with much reduced computational effort.^{12–21} The efficient implementations^{22,23,18} of this theory²⁴ allow for a deeper understanding of different contributions to the intermolecular interactions, thus giving a more detailed picture in comparison with the supermolecular approach, where only the total interaction energy is available as reference data. There exist several attempts in the literature to parametrize the intermolecular force fields on the basis of intermolecular perturbation theory (including SAPT) data.^{25–28,12,29–33}

The reliability of a force field is based on its ability to reproduce some reference total intermolecular potential with good accuracy. In other words, it should describe the repulsion–attraction forces in a broad range of intermolecular distances and orientations in a balanced way. That this is not always the case for standard force fields can be illustrated with the help of the benzene dimer. With the highly accurate data calculated by SAPT for this dimer at hand, the interaction energy, being a sum of physically significant contributions, can be directly compared with the corresponding force field terms. This comparison indicates that standard force fields do not always capture the subtle balance between the two important contributions, namely, electrostatic and van der Waals terms (for some recent studies, see refs 16, 33–42). This is mainly due to the fact that the parameters of the majority of (empirical) force fields were optimized to reproduce the total interaction energy and/or thermodynamic data in the condensed phase. To make this point even more clear, we have calculated separate contributions to the total intermolecular potential for the benzene dimers using two

Received: March 17, 2011

Published: May 16, 2011

different orientations (sandwich and T-shaped), as depicted in Figure 1. The results are shown graphically in Figures 2 and 3.

We have chosen three different force fields where the electrostatic interactions are described by point charges (OPLS-AA⁴³), bond dipoles (MM3^{44,45}), or atomic multipoles up to quadrupoles (AMOEBA⁴⁶), as implemented in the TINKER program package.⁴⁷ van der Waals interactions are represented in these force fields with three different functional forms as well: Lennard-Jones (OPLS-AA), modified Buckingham (MM3), and Buffered-14-7 (AMOEBA). We note that, in contrast to OPLS-AA and MM3, the AMOEBA force field is a polarizable one capable of including nonpairwise-additive many body effects in the force field via induced dipoles. The reference energies are taken from ab initio SAPT(DFT) calculations.⁴⁸ An examination of Figures 2 and 3 shows that for both configurations of the benzene dimer the electrostatic energy is substantially underestimated (below 4 and 5 Å for the sandwich and T-shape dimers, respectively), which is entirely due to a neglect of the charge penetration effects not accounted for by the force field. At the same time, van der Waals interactions are underestimated for the sandwich dimer in

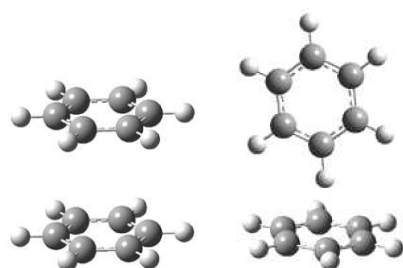


Figure 1. Sandwich (left) and T-shaped (right) configurations of the benzene dimer (carbon and hydrogen atoms are shown in black and white, respectively).

all three types of force fields (below 4 Å), whereas for the T-shaped dimer, the reference data, calculated as a sum of exchange–repulsion and dispersion contributions (see below), closely match the values from the OPLS-AA force field where the corresponding points (see Figure 3, center) almost coincide with their reference counterparts. If we look now at the total energy, it is evident that none of these force fields is able to describe both configurations equally well. As can be seen, OPLS-AA and MM3 are the best choices for treating sandwich and T-shaped dimers, respectively. They show poor results, however, for the other configuration, which is of course an unpleasant situation.

In this contribution, we seek a force field for PAHs which can treat all configurations equally well. Moreover, it is our objective to include more physics in the force field and not just simply reoptimize the parameters on the basis of the calculated overall intermolecular energy. Our preliminary tests using highly accurate total intermolecular interaction energies available in the literature for the benzene dimer⁴⁹ clearly indicate that it is not sufficient to reparameterize the van der Waals parameters utilizing simple functional forms used in current force fields, but incorporating the right physics of the electrostatic interactions is essential for simulations in the condensed phase (see below). To accomplish this task in a balanced way, both the electrostatic and van der Waals terms should be improved simultaneously. In contrast to some previous studies, our approach is based on the explicit inclusion of the short-range term due to charge penetration. In the present work, this term is treated separately from other short-range contributions (exchange–repulsion), as suggested recently by Spackman.⁵⁰ It also differs from other approaches, such as damping the long-range (multipolar) part of the electrostatic energy.^{51,52} It mimics to some extent a more computationally expensive representation of electrostatic interactions with the Gaussian Multipole Model^{53,54} and is similar in spirit to a recent work from Wang and Truhlar.³² The importance

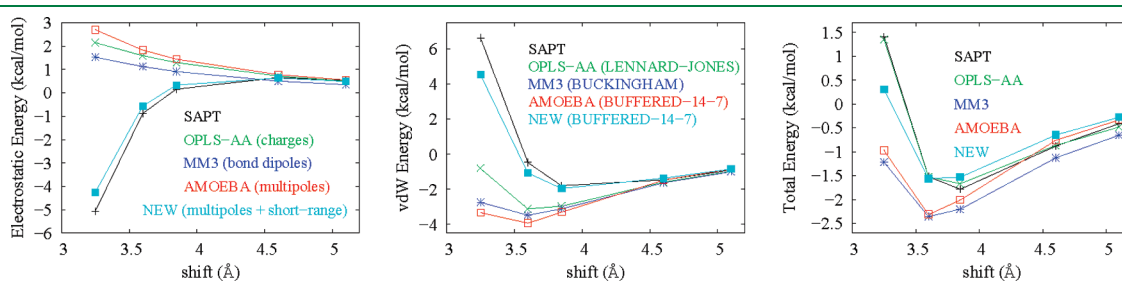


Figure 2. Electrostatic (left), van der Waals (center), and the total interaction energy (right) for the sandwich configuration of the benzene dimer (in kcal/mol). Shift is the distance (in Å) between the two benzene rings (see Figure 1). The reference data are taken from van der Avoird et al.⁴⁸ Lines are drawn to guide the eye.

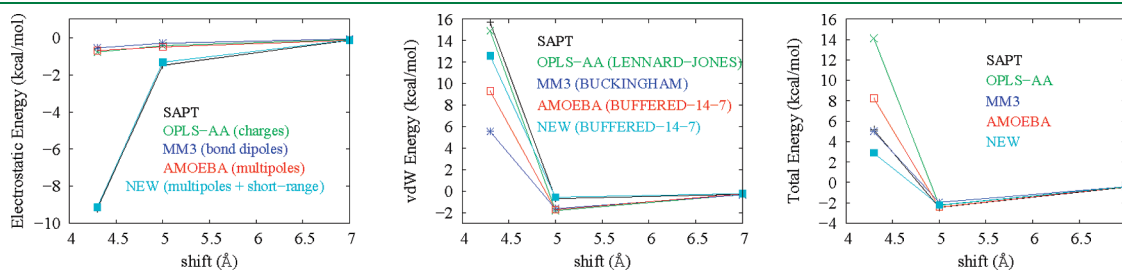


Figure 3. Electrostatic (left), van der Waals (center), and the total interaction energy (right) for the T-shaped configuration of the benzene dimer (in kcal/mol). Shift is the distance (in Å) between the center-of-mass of the two benzene rings (see Figure 1). The reference data are taken from van der Avoird et al.⁴⁸ Lines are drawn to guide the eye.

of charge penetration effects has been recognized in many previous studies, and various approaches have been proposed to include these effects with varying degrees of success (see, for example, refs 53, 55, and 56).

As a reference, we will use highly accurate results from SAPT calculated for a number of small aromatic dimers (benzene, naphthalene, anthracene) to develop the intermolecular force field suitable for molecular simulation of PAHs.

2. FORCE FIELD DEFINITION

In the present work, we use as a reference the results calculated with SAPT utilizing a density-functional theory (DFT) representation of the monomers taken from the work of van der Avoird et al.⁴⁸ (benzene), Podeszwa and Szalewicz⁵⁷ (naphthalene, anthracene, and pyrene), and Podeszwa (coronene).⁵⁸ Within the SAPT methodology, the total interaction energy is represented as a sum of several terms: electrostatic and exchange–repulsion (first-order), induction (polarization), exchange–induction, dispersion, and exchange–dispersion (second order) together with induction and exchange–induction terms of the third and higher orders. As a counterpart of van der Waals interactions in the force field, we use the sum of three terms calculated by SAPT: exchange–repulsion, dispersion, and exchange–dispersion terms, whereas the sum of induction and exchange–induction (second order) energies is used to represent the induction energy to be compared with the induction (polarization) energy from a polarizable force field.

It has been established that an anisotropic charge distribution is difficult (if not impossible) to describe with the widely used point charge models but should include higher multipoles as well (see, for example, refs 11, 59, 60). In this work, we represent the long-range part of the electrostatic energy with atom-centered multipoles up to quadrupoles as implemented in the TINKER program package (AMOEB force field).⁴⁷ Atomic multipoles were calculated with the Distributed Multipole Analysis (GDMA) program^{61,62} from wave functions calculated using the Gaussian program package.⁶³ The hybrid density functional, B3LYP,^{64–66} together with the augmented correlation consistent basis sets, aug-cc-pVXZ (X = D, T),⁶⁷ was employed for all atoms if not stated otherwise. The monomers were kept rigid at the geometries used in the SAPT calculations (see above). If not available, the electrostatic interaction energies between monomers (perylene) were calculated with the SPDF program.⁶⁸ Since distributed multipoles in TINKER are restricted to quadrupoles, we use a locally modified version of the program written by Kisiel⁶⁹ to include all contributions up to hexadecapole–hexadecapole interactions for testing and validation purposes.

In this work, charge penetration is explicitly included in order to account for short-range quantum effects that are not accounted for by the classical multipolar expansion valid only at long range. Recently, Spackman⁵⁰ showed that it is possible to estimate this short-range contribution to the exact electrostatic energy by using a sum of classical Coulomb interaction between spherical atomic charge densities (so-called promolecular densities). In this case, the Coulombic energy between any two atoms separated by a distance R is calculated by the formula

$$E_{ab}(R) = \frac{Z_a Z_b}{R} - \int_{-\infty}^{\infty} \frac{Z_a \rho_b(r_2)}{|R_a - r_2|} dr_2 - \int_{-\infty}^{\infty} \frac{Z_b \rho_a(r_1)}{|R_b - r_1|} dr_1 + \int \int_{-\infty}^{\infty} \frac{\rho_a(r_1) \rho_b(r_2)}{|r_1 - r_2|} dr_1 dr_2 \quad (1)$$

It can be readily shown⁵⁰ that for spherical charge distributions, $\rho(r)$, this expression can be reduced to a one-dimensional integration in reciprocal space (in atomic units):

$$E_{ab}(R) = \frac{2}{\pi} \int_0^{\infty} [Z_a - f_a(s)][Z_b - f_b(s)] \frac{\sin(sR)}{sR} ds \quad (2)$$

where Z_a is the nuclear charge of atom a , $f_a(s)$ is the atomic scattering factor for atom a as a function of the scattering vector s ($= 4\pi \sin \theta/\lambda$) defined in terms of the spherical atomic electron density, $\rho(r)$, by the expression (e.g., for atom a)

$$f_a(s) = 4\pi \int_0^{\infty} \rho_a(r) \frac{\sin(sr)}{sr} dr \quad (3)$$

The atomic scattering factors are obtained analytically from the atomic ground-state wave functions usually expanded with a linear combination of Slater-type functions. Several compilations of the atomic ground-state wave functions are available in the literature from Clementi and Roetti,⁷⁰ Bunge et al.,⁷¹ and Su and Coppens.⁷² In our work, we used closed-form expressions for the Fourier–Bessel transform of Slater-type functions developed by Su and Coppens.⁷³ For a recent implementation of Spackman's original ideas, see ref 74. As Spackman has noted, a contraction of the charge density of the hydrogen atom (Slater exponent) is needed to reproduce the reference electrostatic energies of a number of dimers with hydrogen bonds. The question now remains: how can one estimate the value of this contraction (or expansion)? It turns out that it can be done rather straightforwardly by rewriting the last equation in the following form:⁷⁵

$$E_{ab}(R) = \frac{2}{\pi} \int_0^{\infty} [Z_a - f_a(s/\kappa_a)][Z_b - f_b(s/\kappa_b)] \frac{\sin(sR)}{sR} ds \quad (4)$$

where the radial dependence of the spherical charge densities of atoms a and b is modified by expansion–contraction parameters (“kappa”), κ_a and κ_b , respectively. A similar approach has been used in the refinement of the spherical pseudoatom charge densities based on accurate X-ray diffraction data.⁷⁵ Therefore, we extend the approach of Spackman by allowing for the radial contraction ($\kappa > 1$) or expansion ($\kappa < 1$) for spherical atomic densities. The integral in eq 4 was evaluated numerically as suggested by Spackman⁵⁰ (see also refs 22 and 24 therein) using routines from ref 76.

For the pairwise additive van der Waals (vdW) interactions, we have adopted the buffered 14–7 functional form⁷⁷ used in the AMOEBA force field (for details, see ref 46). It is, however, necessary to adjust the vdW parameters appropriately,⁵⁰ since the electrostatic part of the force field is modified by adding the short-range interactions as described above. In this work, we reoptimize the vdW parameters (two for each atom class) using this particular function, but in principle, any functional form can be used instead.

Induction (polarization) is the interaction of an induced dipole on one fragment with the permanent dipole on another fragment, expressed in terms of the dipole polarizability. The efficacy of truncating the polarizability expansion at the first (dipole) term is due to the treatment of this term in a distributed manner. In the AMOEBA force field, the molecular polarizability is expressed as a sum over atomic isotropic dipole polarizabilities. Iterating the dipole-induced dipole interaction to self-consistency captures many body effects. We adopted the parameters (atomic isotropic polarizabilities and damping factor) from the AMOEBA force field,⁴⁶ i.e., 1.750 for carbon and 0.696 Å³ for

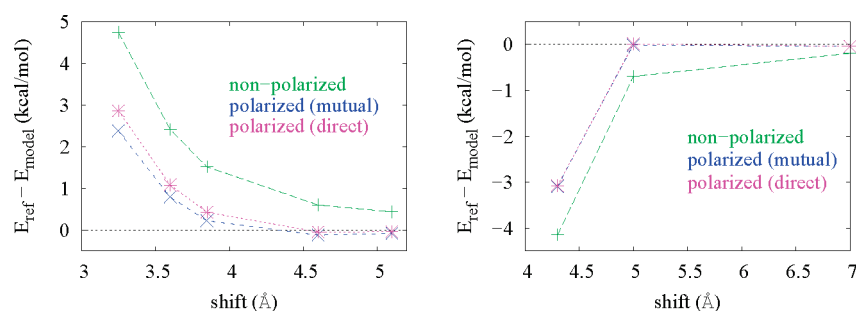


Figure 4. The difference in the total interaction energy for the sandwich (left) and T-shaped (right) configurations of the benzene dimer (in kcal/mol) with and without the polarization term included. Shift is the distance (in Å) between the two benzene rings (see Figure 1). The “direct” dipole polarization avoids an iterative calculation by using only the permanent electric field in computation of induced dipoles, whereas in the “mutual” polarization one iterates the induced dipoles to self-consistency. The reference data are taken from van der Avoird et al.⁴⁸ Dashed lines are drawn to guide the eye.

hydrogen in aromatic rings. There is an indication, however, that the aromatic carbon bridging two aromatic rings (i.e., all its neighbors are carbons) should have a somewhat larger polarizability.⁷⁸ In principle, all parameters for the dipole induction model used in AMOEBA can be reoptimized to reproduce the induction energy (quenched by the exchange-induction contribution) calculated by SAPT as well. Furthermore, the static molecular polarizability tensors calculated with the default parameters for a number of polycyclic aromatic molecules are in accord with the exact values (see below), confirming the results from ref 46. The influence of the polarization energy for the benzene dimers can be appreciated from Figure 4, where the total energies calculated with and without (switched off) the polarization term are compared with their reference counterparts.⁴⁸ In TINKER, two options for the incorporation of the polarization term in the force field are available so that one can select between the use of direct and mutual dipole polarization. In the former approach (“direct”), an iterative calculation is avoided by using only the permanent electric field in computation of induced dipoles, whereas in the latter (“mutual”) one an iteration of the induced dipoles to self-consistency is performed.

Despite the limited number of dimer configurations used, Figure 4 clearly shows that for benzene dimers the noniterative approach to the dipole polarization (“direct”) can be a good approximation of a more elaborate iterative one (“mutual”). It can be seen that at shorter intermonomer distances the deviation from the SAPT calculated total intermolecular energies (E_{ref}) can be quite large. We also note that the simulated (AMOEBA) total energy underestimates (overestimates) their reference counterparts for the sandwich (T-shaped) configuration, regardless of the polarization model used in the force field.

3. PARAMETRIZATION STRATEGY

To fit the various parameters, we have implemented the short-range contribution to the electrostatic energy as described by Spackman⁵⁰ within the TINKER program package.⁴⁷ The expansion-contraction parameters for all symmetrically nonequivalent atoms (eq 4) were optimized with the genetic algorithm PIKAIA,⁷⁹ used successfully by one of the present authors (M.T.) to parametrize the intramolecular force field for metal–organic frameworks (for details, see ref 80). As a fitness function, we use the root-mean-square deviation ($\text{rmsd} = ((\sum_{i=1}^N (E_{\text{ref}}^i - E_{\text{model}}^i)^2) / N)^{1/2}$, where N is the number of dimer configurations) between the exact electrostatic energies calculated by SAPT for the dimer configurations and the sum of the long-range part (distributed

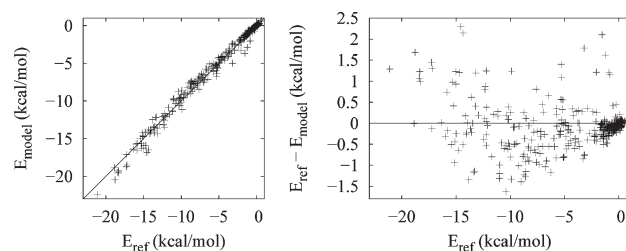


Figure 5. Scatter plots of electrostatic energies (left) and their differences (right) calculated for 500 benzene dimer configurations (in kcal/mol). The reference data are taken from van der Avoird et al.⁴⁸

multipoles) and the short-range part represented by a sum of Coulombic interactions between spherical atoms. For comparison, the atomic scattering factors in eq 4 are calculated from the analytic atomic wave functions taken from three different sources mentioned above.^{70–72} Since the results are very similar for all three compilations, only the results based on the data from Su and Coppens,⁷² obtained using a nonlinear least-squares fitting of numerical relativistic atomic wave functions by a linear combination of Slater-type functions, will be discussed. The atomic multipoles are calculated from wave functions obtained at the B3LYP/aug-cc-pVDZ level of theory. This level of theory is found to be adequate for our purposes, confirming the results of Volkov et al.⁸¹ However, to be consistent with the large basis set used in the SAPT calculations,^{48,57} we employed here a larger aug-cc-pVTZ basis set for benzene, naphthalene, and anthracene as well. To get meaningful expansion–contraction parameters, the dimer configurations were selected with some care. For example, the T-shaped dimer configurations are found to be important for the refinement of the κ parameter for hydrogen in benzene and polycyclic aromatics.

For the vdW part of the force field, we reparametrize the values of the atom size (in Å) and homoatomic well depth (in kcal/mol), whereas a reduction factor for hydrogen atoms was kept unchanged. As a fitness function for the genetic algorithm, the RMSD between the SAPT data (as a sum of exchange–repulsion, dispersion, and exchange–dispersion terms) and the vdW part of the force field is used. In principle, the exchange–repulsion and dispersion (quenched by the exchange–dispersion term) contributions can be refined independently, but this would require a more substantial modification of the TINKER code.

The reference energies for naphthalene (35 configurations), anthracene (32 configurations), and pyrene (44 configurations)

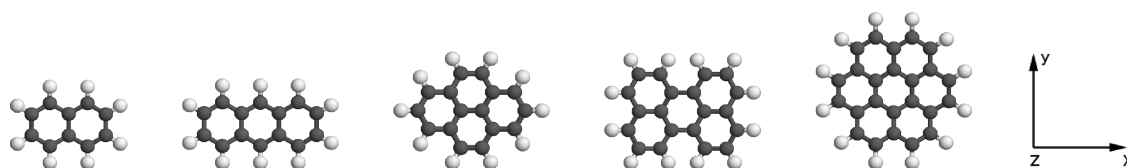


Figure 6. Molecular structure of selected PAHs (from left to right): naphthalene, anthracene, pyrene, perylene, and coronene (carbon and hydrogen atoms are shown in black and white, respectively).

Table 1. Expansion–Contraction (κ) Parameters for Carbon and Hydrogen in Several PAHs

	κ (C)	κ (H)	RMSD (kcal/mol)
naphthalene (35 config.)			
Spackman	1.0	1.24	1.8
benzene	1.002	1.45	0.7
opt	1.012	1.42	0.3
anthracene (32 config.)			
Spackman	1.0	1.24	3.1
benzene	1.002	1.45	1.5
opt	1.018	1.41	0.4
pyrene (44 config.)			
Spackman	1.0	1.24	5.0
benzene	1.002	1.45	4.1
opt	1.024	1.4 (fixed)	0.6
coronene (56 config.)			
Spackman	1.0	1.24	4.4
benzene	1.002	1.45	3.7
opt	1.022	1.4 (fixed)	1.4

dimers are taken from ref 57. The coronene dimer is probably the largest system calculated with SAPT (56 configurations).⁵⁸ In addition, highly accurate correlated calculations of the intermolecular potential surface in the coronene dimer have been published recently by Janowski et al.⁴ For pyrene and coronene dimers, no T-shaped configurations were calculated using SAPT despite the recent finding that this arrangement for coronene might energetically compete with the stacked parallel orientations.^{82,4}

The geometries of the monomers (see Figure 6) were optimized by Podeszwa et al.^{57,58} using the B3LYP/6-31G(d) level of theory and were kept fixed in their dimer calculations.

4. RESULTS AND DISCUSSION

Electrostatic Energy. First, we turn to the benzene dimer. van der Avoird et al.⁴⁸ have calculated SAPT interaction energies and the corresponding physically meaningful contributions for a large number of dimer configurations (~ 500), which we use here as our reference. The scatter plot shown in Figure 5 compares the electrostatic energies calculated by the force field with the optimized expansion–contraction parameters for the carbon and hydrogen atoms (E_{model}) against the reference SAPT data (E_{ref}). During the refinement, all reference energy values are weighted equally (unit weights). The optimized κ value for the carbon atom (1.002) is very close to 1. The value of 1.45 obtained for the hydrogen atom is somewhat larger than that used by Spackman (1.24). The indicated contraction of the electron density of the hydrogen atom makes sense since, being attached

to an aromatic carbon atom, it is positively charged. Interestingly, our value is very close to an average value (1.40) recommended by Coppens et al.⁷⁵ for the radial contraction of H in their spherical-atom X-ray refinements. The RMS deviation for the whole set of benzene dimers is only 0.47 kcal/mol. An examination of Figure 5 shows that the differences between the reference electrostatic energies and their force field counterparts are within 1 kcal/mol for the majority of dimer configurations. This validates the present approach used for the electrostatics. The mean difference ($= 1/N \sum_{i=1}^N [E_{\text{ref}}^i - E_{\text{model}}^i]$) of -0.07 kcal/mol signals that the simulated (force field) energies reproduce the reference data without a systematic error. It follows from Figures 2 and 3 that for the sandwich and T-shaped benzene dimer the new force field is in considerably closer agreement with the SAPT reference data as compared to the other force fields, reproducing the right physics of the electrostatic interactions especially at shorter intermolecular distances.

The κ values optimized for the benzene dimer are readily transferable to other PAHs. This is evident from the data presented in Table 1. It can be seen that the overall reproduction (measured by RMSD) of the electrostatic interaction energies for dimers of larger PAHs is quite satisfactory when the values optimized for the benzene dimer (labeled as “benzene”) are used and that even small changes in the κ parameters (mainly for carbon) can improve the fit significantly (labeled as “opt”). We note that for larger PAHs one can refine the κ parameters for all symmetrically nonequivalent carbon atoms, which would definitely improve the fit even further, and we found that this is indeed the case. But to keep our model as simple as possible (with less parameters), we decided to optimize only one κ parameter for all aromatic carbons. The values used by Spackman are given for comparison. Figure 7 shows scatter plots of electrostatic energies for naphthalene, anthracene, pyrene, and coronene dimers calculated using the optimized κ parameters (labeled as “opt” in Table 1) against the SAPT reference data. Remarkably, with only two expansion–contraction parameters (for C and H), the agreement between the calculated electrostatic energies and their reference counterparts is fairly good over a wide range of energy values.

The significance of the short-range contributions to the electrostatic interaction energy even for relatively nonpolar PAHs can be appreciated from the data in Table 2 below. As an example, we took the perylene dimer (sandwich configuration) and calculated the accurate electrostatic energy by integration over the unperturbed charge densities of the monomers⁶⁸ (labeled as “true”) as a function of the intermonomer distance (see Figure 8). The geometry of the perylene molecule was taken from the database of PAHs⁸³ (optimized at the B3LYP/6-31+G(d) level of theory). The point charges (labeled as “charges”) were obtained by the fit to the electrostatic potential (ESP), as is usually routinely done. To this end, we use the Merz–Kollman sampling scheme⁸⁴ with ca. 2100 grid points

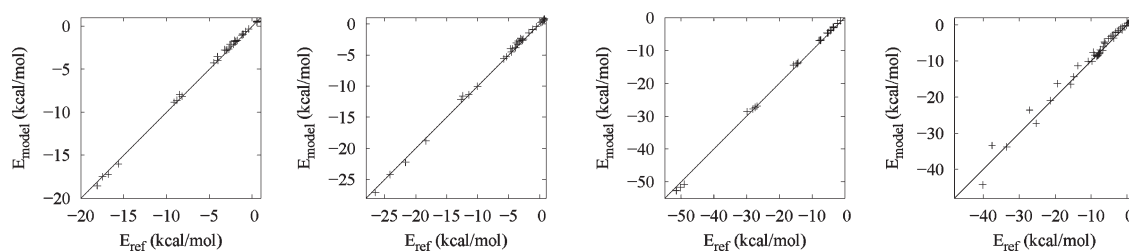


Figure 7. Scatter plots of electrostatic energies for selected dimers of PAHs (in kcal/mol). From left to right: naphthalene (35 configurations), anthracene (32 configurations), pyrene (44 configurations), and coronene (56 configurations). The reference data are taken from Podeszwa et al.^{57,58}

Table 2. Short- and Long-Range Contributions to the Total Electrostatic Interaction Energy for the Perylene Dimer (in kcal/mol)^a

distance, Å	charges ^b	DMA ^c			kappa model ^d	"true" ^e
		quadrupole	octupole	hexadecapole		
3.0	5.02	7.88	6.07	7.70	-49.84	-42.16
3.2	4.10	5.78	4.60	5.49	-26.93	-20.83
3.4	3.39	4.42	3.61	4.13	-14.57	-9.87
3.6	2.84	3.50	2.93	3.24	-7.69	-4.35
3.8	2.41	2.85	2.43	2.63	-4.02	-1.62
4.0	2.06	2.38	2.06	2.19	-2.17	-0.30
4.5	1.44	1.63	1.44	1.50	-0.42	0.66
5.0	1.06	1.19	1.07	1.10	0.03	0.72
5.5	0.80	0.90	0.82	0.84	-0.05	0.64
6.0	0.62	0.71	0.64	0.66	0.004	0.53

^a B3LYP/aug-cc-pVDZ//B3LYP/6-31+G(d). The geometry of the monomer is taken from ref 83. ^b From ESP fit: Merz–Kollman sampling (~2100 points per atom); RMS = 0.71 kcal/mol. ^c Distributed multipole analysis using three different ranks of multipoles. ^d Sum over spherical atomic density Coulomb interactions using $\kappa(C) = 1.01$ and $\kappa(H) = 1.4$. ^e Numerical evaluation of the exact Coulomb integral over unperturbed charge densities of monomers.

per atom with a RMS deviation of 0.71 kcal/mol.⁶³ The long-range contribution to the electrostatic energy is then represented either with these point charges or with the atomically distributed multipoles⁶² (labeled as "DMA") at three different levels (quadrupole, octupole, and hexadecapole). For example, at the hexadecapole level, all interactions up to hexadecapole–hexadecapole ones between all atoms belonging to the two different monomers are included. It should be also noted that the ESP calculated for the same set of grid points as used in the fit of point charges above is reproduced by distributed multipoles truncated at the quadrupolar level with a RMS deviation of 0.85 kcal/mol. Both the point charges from the fit and the atomic multipoles systematically overestimate (more negative on average) the reference ESP data (B3LYP/aug-cc-pVDZ//B3LYP/6-31+G(d)) with the mean difference of 0.2 kcal/mol.

A number of important conclusions can be drawn from these data. First, it can be clearly seen that at the intermonomer distances below 4 Å, both the point charge model and the atomic multipole model severely underestimate the electrostatic interaction in the dimer (compare with the last column of Table 2). We note that the average intermonomer distance in the crystal structure of the so-called α -form of perylene (the four perylene

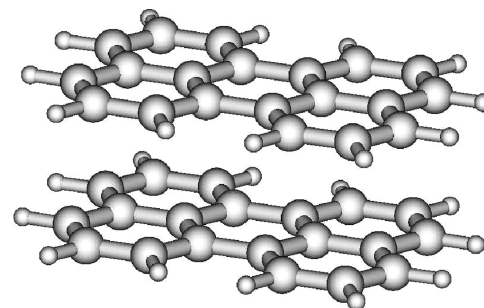


Figure 8. Sandwich configuration of the perylene dimer.

molecules in the unit cell are grouped in pairs about centers of symmetry) is found to be around 3.46 Å.⁸⁵ Thus, an approximation of the electrostatic energy either with point charges or with multipoles is inadequate. These models become valid above ca. 5 Å (see three last rows in Table 2). It can be seen that the charge penetration contribution to the electrostatic interaction for the perylene dimer is significant especially at intermonomer distances < 3.5 Å. This short-range contribution evaluated recently by Jenness et al.⁸⁶ for the water–acene series is much smaller in magnitude and is comparable with the long-range contribution due to atomic multipoles (up to quadrupoles on all carbon atoms). Second, we note that the multipole model truncated at the quadrupolar level would already do a good job in describing the long-range contribution to the electrostatic energy (in comparison with a much more computationally demanding hexadecapolar level). Finally, we see that the missing part (labeled as the " κ model"), calculated as the sum over spherical atomic density interactions using the optimized expansion–contraction (κ) parameters, is quite substantial. Combined with the multipole approximation for the long-range part (represented by the atomic multipoles up to and including quadrupoles), it recovers the total intermolecular electrostatic energy in the perylene dimers (10 sandwich configurations) with an RMS deviation of only 0.36 kcal/mol and a mean difference of -0.2 kcal/mol. Thus, with the optimized κ parameters at hand and assuming their transferability between chemically similar atoms, we can now estimate quite accurately the intermolecular electrostatic energy in the clusters of larger PAH molecules within seconds. For comparison, the numerical evaluation of the exact Coulomb integral for the perylene dimer (wave functions from B3LYP/aug-cc-pVDZ) using a serial version of the SPDF program⁸¹ used here takes ca. 10 h on 1 CPU (Linux OS, x86_64 AMD, 2.933 GHz, 4 GB RAM).

Induction Energy. In principle, the quality of the polarization energy component of the AMOEBA force field⁴⁶ used here can

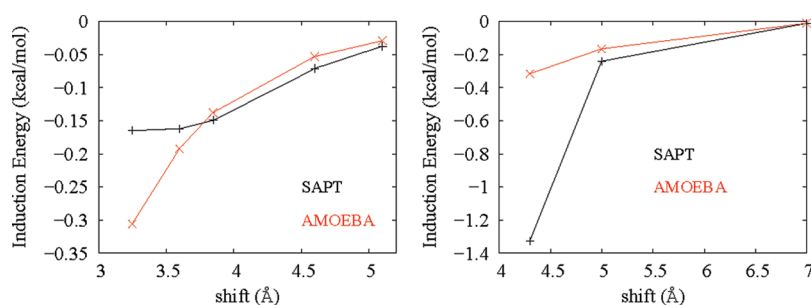


Figure 9. The induction energy for the sandwich (left) and T-shaped (right) configurations of the benzene dimer (in kcal/mol). Shift is the distance (in Å) between the two benzene rings (see Figure 1). The reference data are taken from ref 48. Lines are drawn to guide the eye.

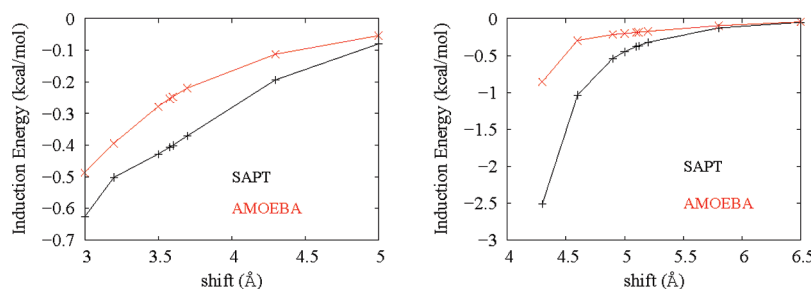


Figure 10. The induction energy for the graphite (left) and T-shaped (right) configuration of the naphthalene dimer (in kcal/mol). Shift is the distance (in Å) between the two naphthalene molecules. The reference data are taken from ref 57. Lines are drawn to guide the eye.

be judged from a direct comparison with the sum of induction and exchange—induction energies calculated using SAPT. However, this particular component is very difficult to obtain accurately in SAPT since third and higher order contributions might be significant as well (see, for example, refs 87–89). The reference data for the benzene dimer we used included third order contributions to the induction energy, and in Figure 9 we compare this data with the induction energy obtained with the standard AMOEBA parameters for a number of sandwich and T-shaped configurations. Overall, for nonpolar molecules, we expect the induction energy to be small in absolute terms compared to other contributions. We note that for the benzene dimer configurations shown in Figure 9, the AMOEBA overestimates (underestimates) the reference values of induction energy at smaller intermonomer separations for the sandwich (T-shaped) dimer configurations. For naphthalene, only second order contributions were included in the SAPT calculations.⁵⁷ As can be seen from Figure 10, the AMOEBA force field systematically underestimates the induction energy for some representative configurations, especially so for the T-shaped ones.

To check the reliability of the AMOEBA parameters, we can, in addition, compare the static molecular polarizability tensors (α) calculated at different levels of theory with those obtained from the AMOEBA force field by iterating the induced dipoles to self-consistency, as implemented in TINKER. Table 3 presents the results (see Figure 6 for the axes definition), where experimental data are also given for comparison. Due to the high symmetry of the molecules, only diagonal elements of the polarizability tensors are nonzero. An examination of Table 3 shows that the components of the static molecular polarizability tensor calculated in this work at the DFT level (B3LYP/aug-cc-pVDZ) match closely their counterparts obtained using the

linear response coupled cluster approach (CCSD) by Hammond et al.⁹⁰ We also note that the calculated molecular polarizabilities (DFT/CCSD) are well reproduced by the force field, especially for the less polarizable perpendicular direction (Z axis). At the same time, it can be seen that for larger PAHs, the agreement is less perfect for the long molecular axis (X), where the polarizability is underestimated by the AMOEBA force field. Despite the fact that refining the atomic polarizability parameters would improve the agreement, it is our belief that some degree of anisotropy should be included in the model⁹¹ to get more accurate results (compared to the “exact” values)³³ for the induction energy.

van der Waals Energy. As already mentioned above, we adopted the functional form for the vdW energy (repulsion—dispersion) used in the AMOEBA force field and reoptimized the two parameters for each atom class (atom size, r , and well depth, ϵ) based on the sum of the three separate contributions calculated using SAPT, namely, exchange—repulsion, dispersion, and exchange—dispersion. Table 4 compares the old and the new values for aromatic carbon and hydrogen atoms taken as an average from the refinements on the naphthalene and anthracene dimers.⁵⁷

With the new vdW parameters, we can reproduce the SAPT reference data with RMS deviations (the mean difference in parentheses) of 0.5 (0.17), 0.5 (–0.18), and 0.9 (0.05) kcal/mol for naphthalene (35 configurations), anthracene (32 configurations), and pyrene (41 configurations) dimers, respectively. For pyrene, we excluded three dimer configurations with the shortest intermonomer distance (2.8 Å) from the reference data set. Figure 11 displays the scatter plots for these three PAH dimers. It can be seen from this figure that with the reoptimized vdW parameters from Table 4 (“new”), we can reproduce the reference data over a wide range of energy values. Even the

Table 3. Molecular Polarizability Tensors (in Å³) for Benzene and Several PAHs

method	α_{xx}	α_{yy}	α_{zz}	α_{iso}^a
benzene				
DFT ^b	12.17	12.17	6.64	10.33
TDDFT ⁹³	12.26	12.26	6.61	10.38
CCSD ⁹⁰	11.89	11.89	6.60	10.13
CCSD ⁹²	12.06	12.06	6.37	10.16
AMOEBA ^c	12.24	12.24	6.64	10.37
exp ⁹³	12.20	12.20	7.28	10.56
naphthalene				
DFT	25.58	18.60	9.80	17.99
TDDFT ⁹⁴	26	19	10	18
CCSD ⁹⁰	24.69	18.28	9.84	17.60
AMOEBA	21.89	18.50	9.77	16.72
exp ⁹⁵	24.39	18.20	9.60	17.40
anthracene				
DFT	44.06	25.09	12.89	27.35
TDDFT ⁹⁴	46	26	13	28
CCSD ⁹⁰	41.73	24.60	12.98	26.44
AMOEBA	32.62	24.56	12.93	23.37
exp ⁹⁶	35.90	24.46	15.88	25.41
pyrene				
DFT	44.17	31.87	13.92	29.98
TDDFT ⁹⁴	45	32	14	30
CCSD ⁹⁰	42.37	31.14	na	na
AMOEBA	33.70	29.81	13.75	25.75
exp ⁹⁷	34.2	34.2	16.3	28.2
perylene				
DFT	55.97	44.01	16.82	38.94
TDDFT ⁹⁴	56	44	16	39
AMOEBA	42.90	38.16	16.95	32.67
exp ⁹⁸	57	46	16	40
coronene				
DFT	59.12	59.12	18.96	45.73
TDDFT ⁹⁴	61	61	19	47
AMOEBA	47.51	47.51	19.14	38.05
exp ⁹⁹	56.8	56.8	20.7	44.8

^aIsotropic polarizability taken as $1/3(\alpha_{xx} + \alpha_{yy} + \alpha_{zz})$. ^bAt the B3LYP/aug-cc-pVDZ//B3LYP/6-31G(d) level. ^cInteractive molecular polarizability.

energies in a very “repulsive” region of the PAH dimers are accurately modeled. For both configurations of the benzene dimer, the agreement with the SAPT reference data is also improved compared to the other force fields (see Figures 2 and 3).

Total Intermolecular Energy. We calculate the total intermolecular interaction energy by summing up the electrostatic (both short- and long-range components), vdW, and induction contributions. We reproduce the total reference energies from SAPT with RMS deviations (the mean difference in parentheses) of 0.64 (−0.45), 0.9 (−0.7), and 0.5 (−0.13) kcal/mol for naphthalene, anthracene, and pyrene dimers, respectively. For PAHs, we recommend using values for the expansion–contraction parameters of 1.02 and 1.4 for carbon and hydrogen atoms,

Table 4. van der Waals Parameters for Carbon and Hydrogen Atom Classes for the AMOEBA Force Field

atom class	old		new	
	$r, \text{Å}$	$\epsilon, \text{kcal/mol}$	$r, \text{Å}$	$\epsilon, \text{kcal/mol}$
C	3.800	0.089	4.285	0.050
H	2.980	0.026	2.560	0.0075

respectively, together with the new vdW parameters listed in Table 4. Examination of Figure 12 and of the mean differences shows that some systematic bias is present, especially for the naphthalene and anthracene dimers, which is probably due to inaccuracies in the induction term (underestimated by the force field) that warrant further investigation. By comparison, with the unmodified AMOEBA force field, the RMS deviations are 2.9 (naphthalene), 4.0 (anthracene), and 2.6 (pyrene) kcal/mol.

To further validate our new force field, we performed a full crystal energy minimization by optimizing over fractional atomic coordinates and the lattice parameters for benzene, naphthalene, anthracene, pyrene, and coronene. To make the comparison with the experimental crystal structures meaningful, the internal flexibilities of the molecules are taken into account using the standard AMOEBA parameters (atom classes 85 and 86 for the aromatic carbon and hydrogen atoms from the amoeba09.prm compilation, respectively). Table 5 presents the results.

Examination of this table shows that the AMOEBA force field poorly reproduces the orthorhombic lattice of the benzene crystal (space group *Pbca*), whereas the unit cell edges based on our new force field (labeled as “new” in Table 5) closely match the experimental data. Ab initio calculations of van der Waals bonded molecular crystals, such as solid benzene, are notoriously difficult to perform accurately. That this is still a challenge is evident from the comparison of the lattice parameters fully optimized by Bucko et al. (ref 100 and references therein) with the VASP program. A closer examination of the unit cell of the solid benzene, in which the four molecules are arranged in an edge-to-face manner at 87° angles pairwise,¹⁰¹ reveals the dominant contribution of this type of tilted T-shaped configuration, shown in Figure 1. We note that this particular configuration is found to be one of the most stable in the gas phase benzene dimer (see, for example, ref 48), and it persists in the solid benzene even under high pressure.¹¹⁰ As is evident from Figure 3 above, the total intermolecular interaction energies for this configuration at a center-of-mass distance of around 5.0 Å, as found in the crystal, are poorly reproduced by the AMOEBA force field as compared to the reference (SAPT) data. Our new force field, on the other hand, nicely reproduces the experimentally observed mutual arrangement of the four molecules in the unit cell, which is not the case with the AMOEBA force field. To investigate the importance of this short-range electrostatic contribution in more detail, we tested two other models, where (1) we reoptimized the four vdW parameters (two for both carbon and hydrogen) of the AMOEBA force field based on the total interaction energies for 500 configurations of the benzene dimer used before without adding the short-range electrostatic contribution and where (2) we included the short-range term without reoptimizing the vdW parameters. Despite the relatively small RMS deviation of ca. 1 kcal/mol for the whole set of benzene dimers, the model (1) was not capable of reproducing either the cell edges or the mutual arrangement of the four

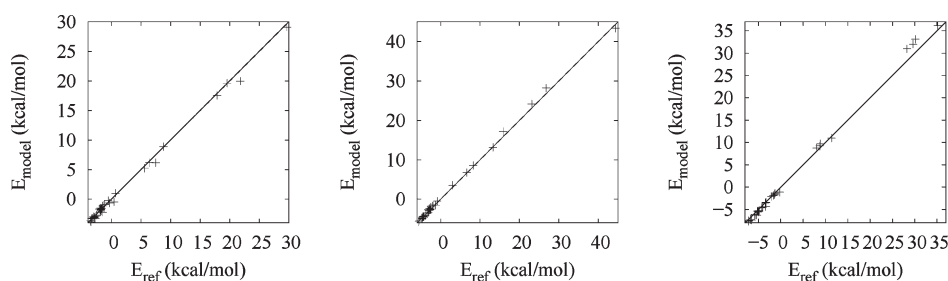


Figure 11. Scatter plots of van der Waals energies for selected dimers of PAHs (in kcal/mol). From left to right: naphthalene (35 configurations), anthracene (32 configurations), and pyrene (41 configurations). The reference data are taken from Podeszwa et al.⁵⁷

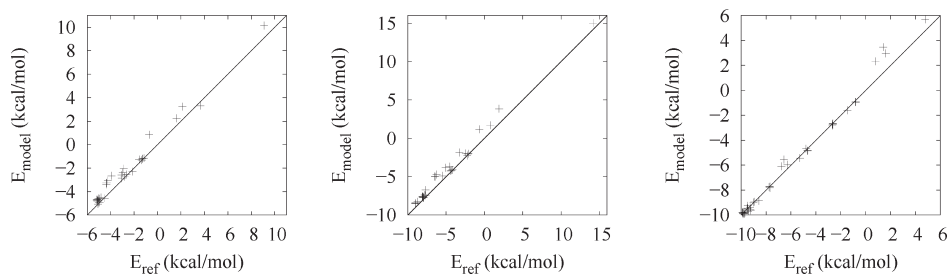


Figure 12. Scatter plots of total intermolecular energies for selected dimers of PAHs (in kcal/mol). From left to right: naphthalene (35 configurations), anthracene (32 configurations), and pyrene (41 configurations). The reference data are taken from Podeszwa et al.⁵⁷

benzene molecules in the unit cell, the results being close to those obtained with the standard AMOEBA force field. Our second model, on the other hand, was found to be in much better agreement with our new force field model, qualitatively reproducing the mutual arrangement of the benzene molecules observed in the experimental crystal structure. This indicates that the short-range electrostatic contribution seems to be particularly important for the intermolecular interaction for a T-shaped configuration in π -conjugated systems (for a discussion, see also refs 111 and 112). It would be interesting to see whether our new force field is able to reproduce (or even predict) high-pressure polymorphs of the solid benzene.¹¹³ For PAHs, the situation is different in a sense that the π - π stacking interactions are now competitive with those found in (more electrostatically controlled) T-shaped configurations.¹¹² From Table 5, it can be seen that the experimental monoclinic lattices (space group $P2_1/a$) of selected PAHs are reproduced by the force fields. Recently, Sanchez-Carrera et al.¹⁰³ optimized the unit cell parameters for a number of oligocenes from naphthalene to pentacene using a different program (DMAREL) and a different force field (Buckingham exp-6 for vdW interactions along with ESP-fitted point charges for electrostatics) within the framework of the rigid-molecule approximation (experimental molecular geometries were used). Despite the markedly different approaches used, their results are in agreement both with ours and with the experiment. Interestingly, our new force field somewhat overestimates the length of the a axis of the unit cell for naphthalene and anthracene. At the same time, the lengths of the other two lattice axes (b and c) for naphthalene are closer to the experimental data than those obtained with the standard AMOEBA force field. It should be also noted that for pyrene the standard AMOEBA force field gave the optimized lattice parameters observed for the low-temperature ($T = 93$ K) metastable phase (II), regardless of the starting values, whereas our new force field recovers the parameters for both solid phases. It is well-known

that lattice energies are important for assessing the quality of a force field. Our values for naphthalene (-12.0 kcal/mol) and anthracene (-16.6 kcal/mol) underestimated the experimental values¹¹⁴ of -17.8 (naphthalene) and -23.9 (anthracene) kcal/mol mainly due to somewhat larger a axis of the unit cell.

Overall, in contrast to the standard AMOEBA and other empirical force fields,¹⁰³ our proposed intermolecular force field parameters are based solely on the properties of monomers calculated from first principles. Indeed, the atomic multipoles come from the distributed multipole analysis (GDMA) based on the monomer wave function, whereas the short-range electrostatic contribution and the vdW parameters were fitted to reproduce the corresponding terms of the SAPT interaction energy, the latter being calculated directly as a sum of physically meaningful contributions. The reason we use the data calculated by SAPT as a reference is that in this type of rigorous perturbation theory the physically meaningful components (first-order electrostatic and exchange contributions and second-order induction and dispersion terms) can be nicely correlated with the terms usually included in current empirical force fields. This would be, however, not so straightforward with some other decomposition schemes, such as the ones described in Khaliullin et al.¹¹⁵ or in Wu et al.,¹¹⁶ where the electrostatic and exchange contributions are not separated (named as the frozen density component there). It would be interesting to try to parametrize a force field using this latter (variational) decomposition scheme as well. It is also worth remarking that the quality of our new force field cannot be better than the quality of the reference data it is based upon, so that our parameters will definitely benefit from further improvement of the reference data. Furthermore, we are confident that the notoriously difficult task of crystal structure prediction can benefit from the force field development strategy presented in this work.¹¹⁷ We also hope that our contribution can help better understand the shortcomings and failures of the currently used force fields and will ultimately lead to an

Table 5. Unit Cell Parameters for Benzene and Selected PAHs

	<i>a</i> (Å)	<i>b</i> (Å)	<i>c</i> (Å)	α (deg)	β (deg)	γ (deg)
benzene						
AMOEBA	7.744	7.750	7.750	90.0	90.0	90.0
new	7.567	9.269	7.142	90.0	90.0	90.0
VASP ¹⁰¹	7.09	9.07	6.54	90.0	90.0	90.0
exp (138 K) ¹⁰²	7.39	9.42	6.81	90.0	90.0	90.0
exp (4.2 K) ¹⁰²	7.3551	9.3712	6.6994	90.0	90.0	90.0
naphthalene						
AMOEBA	8.206	5.512	9.143	90.0	125.2	90.0
new	8.539	5.884	8.954	90.0	122.6	90.0
DMAREL ¹⁰³	8.146	6.033	8.716	90.0	122.5	90.0
exp ¹⁰⁴	8.108	5.940	8.647	90.0	124.4	90.0
anthracene						
AMOEBA	8.361	6.080	11.070	90.0	127.0	90.0
new	8.896	6.121	11.184	90.0	124.6	90.0
DMAREL ¹⁰³	8.361	6.116	11.167	90.0	123.5	90.0
exp ¹⁰⁵	8.414	5.990	11.095	90.0	125.3	90.0
pyrene (I)						
AMOEBA	12.513	9.799	8.104	90.0	94.7	90.0
new	13.637	9.435	8.528	90.0	100.2	90.0
exp ¹⁰⁶	13.532	9.159	8.387	90.0	100.2	90.0
pyrene (II)						
AMOEBA	12.510	9.800	8.105	90.0	94.7	90.0
new	12.635	10.177	8.468	90.0	98.1	90.0
exp ^{107,108}	12.358	10.020	8.260	90.0	96.5	90.0
coronene						
AMOEBA	16.156	4.484	9.934	90.0	110.2	90.0
new	16.186	5.047	9.904	90.0	110.8	90.0
exp ¹⁰⁹	16.119	4.702	10.102	90.0	110.9	90.0

improvement in the quality of future force fields for molecular simulations. Curiously, in a very recent study on the development of polarizable models for calculating interactions between atomic charges and induced point dipoles, Wang et al.¹¹⁸ pointed out the difficulty in reproducing interaction energies (at the MP2/aug-cc-pVTZ level) for molecules possessing aromatic groups (even after reoptimization of the van der Waals parameters). They found out that all MM models investigated (including nonpolarizable or fixed-charge ones) have a tendency to underestimate the attractive force between the aromatic moieties. Even if it is known that the MP2 method (corrected for basis set superposition error) overestimates the binding energy for π stacks (see, for example, ref 119), we believe that a further improvement can be achieved by including more physically grounded electrostatics in a force field, which is the main topic of our work. There is a hint in a recent work of Watanabe et al.¹²⁰ that an accurate treatment of electrostatic interactions between adsorbates and a host framework would necessitate the inclusion of charge penetration effects as well.

One final note is appropriate at this point. Since accurate reference data based on the intermolecular perturbation theory (such as SAPT) are still relatively scarce, a viable strategy using the total intermolecular energy from highly accurate supermolecule

calculations can be used for the parametrization (see, for example, refs 121–123). In this case, first, the short-range electrostatic contribution can be parametrized using a much cheaper method (e.g., B3LYP/aug-cc-pVXZ, X = D or T), as is done here for the perylene dimer, and, second, when an appropriate model for the induction (polarization) contribution is at hand, the vdW parameters for a chosen functional form can be optimized to reproduce the repulsion–dispersion contribution taken as the difference between the total interaction energy (as reference) and the sum of the electrostatic (including both the short- and long-range terms) and induction contributions. As an example, we took the data published recently by Sherrill and co-workers⁴⁹ for the benzene dimer (~ 90 configurations including sandwich, T-shaped, and parallel-displaced ones) calculated with the coupled-cluster theory through perturbative triples, CCSD(T), extrapolated to the complete basis set limit. Having parametrized the short-range part of the electrostatic energy (see Table 1 for expansion–contraction parameters) and utilizing the induced point dipoles method (AMOEBA) to treat polarization, the reoptimized vdW parameters ($r = 4.239$ Å and $\epsilon = 0.0726$ kcal/mol for carbon and $r = 2.553$ Å and $\epsilon = 0.0043$ kcal/mol for hydrogen) turned out to be similar to the values (labeled “new”) shown in Table 4. With these force field parameters at hand, we can reproduce perfectly both the lattice parameters of the orthorhombic phase of solid benzene ($a = 7.391$ Å, $b = 9.356$ Å, and $c = 6.891$ Å) and the mutual arrangement of the four molecules in the unit cell as before using the SAPT data as a reference. In addition, the calculated lattice energy of -10.2 kcal/mol (at $T = 0$ K and without zero-point energy correction), which is known to be notoriously difficult to evaluate reliably, is in very good agreement with the values estimated from first-principles methods^{124–126,100} (see also refs 127–129) and the experimental value (-11.3 kcal/mol).¹¹⁴

5. CONCLUSIONS

Motivated by the need for a force field that can capture the right physics of intermolecular interactions, we incorporated an extra pairwise-additive energy term, which describes the short-range contribution to the electrostatic energy due to charge penetration, into the AMOEBA polarizable force field.⁴⁶ Following the original ideas of Spackman,⁵⁰ the expansion–contraction parameters are proposed to modify the radial dependence of the spherical atomic charge densities. For a series of PAHs, we were able to show that with a limited number of these parameters, the intermolecular electrostatic energies estimated by the force field match nicely the reference data based on SAPT interaction energy calculations. Taken together with the reoptimized van der Waals contribution, a balanced force field can be readily constructed which avoids to a large extent the error cancellation between different terms in the force field. Having implemented the gradients of this new term, we are now in a position to perform static geometry optimizations as well as molecular dynamics simulations on the aggregation of PAH clusters, the outcome of which being relevant for a number of fields such as soot formation in combustion,¹³⁰ interstellar radiation,¹³¹ optoelectronic devices,⁶ supramolecular chemistry (as exemplified by molecular tweezers¹³²), and host–guest systems,¹³³ to name a few. Moreover, we can anticipate that incorporating realistic electrostatic effects into a force field would allow the development of much more accurate QM/MM embedding schemes. Polycyclic aromatic hydrocarbons and their derivatives

are seen as a promising class of materials for optoelectronics and organic solar cells. Understanding the charge and energy transport through these materials is very important in tuning their properties for a particular application. We hope that physically realistic force fields would be indispensable for that purpose, and work along these lines is in progress.

AUTHOR INFORMATION

Corresponding Author

*E-mail: bernd.engels@mail.uni-wuerzburg.de; maxim.tafipolski@uni-wuerzburg.de.

ACKNOWLEDGMENT

We are grateful to the Deutsche Forschungsgemeinschaft (GRK1221, SFB 630) and the Volkswagen Stiftung for financial support. M.T. would like to thank Professor Rafał Podeszwa, Professor Krzysztof Szalewicz, and Dr. Konrad Patkowski for very fruitful discussions and data provided relating to work reported in ref 57 and Dr. Anatoliy Volkov for providing the SPDF program and many useful suggestions.

REFERENCES

- (1) Engkvist, O.; Astrand, P. O.; Karlstrom, G. *Chem. Rev.* **2000**, *100*, 4087.
- (2) Chipot, C.; Angyan, J. G. *New J. Chem.* **2005**, *29*, 411.
- (3) Stone, A. J. *Science* **2008**, *321*, 787.
- (4) Janowski, T.; Ford, A. R.; Pulay, P. *Mol. Phys.* **2010**, *108*, 249.
- (5) Sherrill, C. D. In *Rev. Comput. Chem.*; Lipkowitz, K. B., Cundari, T. R., Eds.; Wiley: New York, 2009; Vol. 26, Chapter 1, pp 1–38.
- (6) Bredas, J. L.; Beljonne, D.; Coropceanu, V.; Cornil, J. *Chem. Rev.* **2004**, *104*, 4971.
- (7) Stone, A. J. *The Theory of Intermolecular Forces*; Oxford University Press: Oxford, U.K., 1996.
- (8) Kaplan, I. G. *Intermolecular Interactions*; John Wiley & Sons, Inc.: New York, 2006.
- (9) Chen, W.; Gordon, M. S. *J. Phys. Chem.* **1996**, *100*, 14316.
- (10) Piquemal, J.-P.; Chevreaux, H.; Gresh, N. *J. Chem. Theory Comput.* **2007**, *3*, 824.
- (11) Stone, A. J.; Misquitta, A. J. *Int. Rev. Phys. Chem.* **2007**, *26*, 193.
- (12) Podeszwa, R.; Bukowski, R.; Szalewicz, K. *J. Phys. Chem. A* **2006**, *110*, 10345.
- (13) Tekin, A.; Jansen, G. *Phys. Chem. Chem. Phys.* **2007**, *9*, 1680.
- (14) Fiethen, A.; Jansen, G.; Hesselmann, A.; Schuetz, M. *J. Am. Chem. Soc.* **2008**, *130*, 1802.
- (15) Pitonak, M.; Riley, K. E.; Neogrady, P.; Hobza, P. *ChemPhysChem* **2008**, *9*, 1636.
- (16) Cybulski, H.; Sadlej, J. *J. Chem. Theory Comput.* **2008**, *4*, 892.
- (17) Geng, Y.; Takatani, T.; Hohenstein, E. G.; Sherrill, C. D. *J. Phys. Chem. A* **2010**, *114*, 3576.
- (18) Hohenstein, E. G.; Sherrill, C. D. *J. Chem. Phys.* **2010**, *133*, 014101.
- (19) Hesselmann, A.; Korona, T. *Phys. Chem. Chem. Phys.* **2011**, *13*, 732.
- (20) Riley, K. E.; Pitonak, M.; Jurecka, P.; Hobza, P. *Chem. Rev.* **2010**, *110*, 5023.
- (21) Hohenstein, E. G.; Sherrill, C. D. *J. Chem. Phys.* **2010**, *132*, 184111.
- (22) Misquitta, A. J.; Szalewicz, K. *J. Chem. Phys.* **2005**, *122*, 214109.
- (23) Hesselmann, A.; Jansen, G.; Schutz, M. *J. Chem. Phys.* **2005**, *122*, 014103.
- (24) Jeziorski, B.; Moszynski, R.; Szalewicz, K. *Chem. Rev.* **1994**, *94*, 1887.
- (25) Mooij, W. T. M.; van Duijneveldt, F. B.; van Duijneveldt-van de Rijdt, J. G. C. M.; van Eijck, B. P. *J. Phys. Chem. A* **1999**, *103*, 9872.
- (26) Mitchell, J. B. O.; Price, S. L. *J. Phys. Chem. A* **2000**, *104*, 10958.
- (27) Hloucha, M.; Sum, A. K.; Sandler, S. I. *J. Chem. Phys.* **2000**, *113*, 5401.
- (28) Torheyden, M.; Jansen, G. *Mol. Phys.* **2006**, *104*, 2101.
- (29) Li, X.; Volkov, A. V.; Szalewicz, K.; Coppens, P. *Acta Crystallogr., Sect. D* **2006**, *62*, 639.
- (30) Szalewicz, K.; Leforestier, C.; van der Avoird, A. *Chem. Phys. Lett.* **2009**, *482*, 1.
- (31) Archambault, F.; Chipot, C.; Soteras, I.; Javier Luque, F.; Schulten, K.; Dehez, F. *J. Chem. Theory Comput.* **2009**, *5*, 3022.
- (32) Wang, B.; Truhlar, D. G. *J. Chem. Theory Comput.* **2010**, *6*, 3330.
- (33) Totton, T. S.; Misquitta, A. J.; Kraft, M. *J. Chem. Theory Comput.* **2010**, *6*, 683.
- (34) Sherrill, C. D.; Sumpter, B. G.; Sinnokrot, M. O.; Marshall, M. S.; Hohenstein, E. G.; Walker, R. C.; Gould, I. R. *J. Comput. Chem.* **2009**, *30*, 2187.
- (35) Paton, R. S.; Goodman, J. M. *J. Chem. Inf. Model.* **2009**, *49*, 944.
- (36) Morgado, C. A.; Jurecka, P.; Svozil, D.; Hobza, P.; Sponer, J. *J. Chem. Theory Comput.* **2009**, *5*, 1524.
- (37) Morgado, C. A.; Jurecka, P.; Svozil, D.; Hobza, P.; Sponer, J. *Phys. Chem. Chem. Phys.* **2010**, *12*, 3522.
- (38) Zgarbova, M.; Otyepka, M.; Sponer, J.; Hobza, P.; P., J. *Phys. Chem. Chem. Phys.* **2010**, *12*, 10476.
- (39) Kolar, M.; Berka, K.; Jurecka, P.; Hobza, P. *ChemPhysChem* **2010**, *11*, 2399.
- (40) Nemkevich, A.; Buergi, H.-B.; Spackman, M. A.; Corry, B. *Phys. Chem. Chem. Phys.* **2010**, *12*, 14916.
- (41) Rutledge, L. R.; Wetmore, S. D. *Can. J. Chem.* **2010**, *88*, 815.
- (42) Tateno, M.; Hagiwara, Y. *J. Phys.: Condens. Matter* **2009**, *21*, 064243.
- (43) Jorgensen, W. L.; Tirado-Rives, J. *J. Am. Chem. Soc.* **1988**, *110*, 1657.
- (44) Allinger, N. L.; Yuh, Y. H.; Lii, J.-H. *J. Am. Chem. Soc.* **1989**, *111*, 8551.
- (45) Allinger, N. L.; Li, F. B.; Yan, L. Q.; Tai, J. C. *J. Comput. Chem.* **1990**, *11*, 868.
- (46) Ponder, J. W.; Wu, C.-J.; Ren, P.-Y.; Pande, V. S.; Chodera, J. D.; Schnieders, M. J.; Haque, I.; Mobley, D. L.; Lambrecht, D. S.; DiStasio, R. A., Jr.; Head-Gordon, M.; Clark, G. N. I.; Johnson, M. E.; Head-Gordon, T. *J. Phys. Chem. B* **2010**, *114*, 2549.
- (47) Tinker software tools for molecular design: Ponder, J. W.; Ren, P.; Pappu, R. V.; Hart, R. K.; Hodgson, M. E.; Cistola, D. P.; Kundrot, C. E.; Richards, F. M. *Tinker*, version 5.1; Washington University School of Medicine: St. Louis, MO, 2010. <http://dasher.wustl.edu/tinker/> (accessed 02/27/2011).
- (48) van der Avoird, A.; Podeszwa, R.; Szalewicz, K.; Leforestier, C.; van Harrevelt, R.; Bunker, P. R.; Schnell, M.; von Helden, G.; Meijer, G. *Phys. Chem. Chem. Phys.* **2010**, *12*, 8219.
- (49) Sherrill, C. D.; Takatani, T.; Hohenstein, E. G. *J. Phys. Chem. A* **2009**, *113*, 10146.
- (50) Spackman, M. A. *Chem. Phys. Lett.* **2006**, *418*, 158.
- (51) Slipchenko, L. V.; Gordon, M. S. *Mol. Phys.* **2009**, *107*, 999.
- (52) Cisneros, G. A.; Tholander, S. N.-I.; Parisel, O.; Darden, T. A.; Elking, D.; Perera, L.; Piquemal, J. P. *Int. J. Quantum Chem.* **2008**, *108*, 1905.
- (53) Wheatley, R. J. *Mol. Phys.* **1993**, *79*, 597.
- (54) Elking, D. M.; Cisneros, G. A.; Piquemal, J.-P.; Darden, T. A.; Pedersen, L. G. *J. Chem. Theory Comput.* **2010**, *6*, 190.
- (55) Stone, A. J.; Price, S. L. *J. Phys. Chem.* **1988**, *92*, 3325.
- (56) Freitag, M. A.; Gordon, M. S.; Jensen, J. H.; Stevens, W. J. *J. Chem. Phys.* **2000**, *112*, 7300.
- (57) Podeszwa, R.; Szalewicz, K. *Phys. Chem. Chem. Phys.* **2008**, *10*, 2735.
- (58) Podeszwa, R. *J. Chem. Phys.* **2010**, *132*, 044704.
- (59) Price, S. L.; Leslie, M.; Welch, G. W. A.; Habgood, M.; Price, L. S.; Karamertzanis, P. G.; Day, G. M. *Phys. Chem. Chem. Phys.* **2010**, *12*, 8478.

- (60) Shaik, M. S.; Devereux, M.; Popelier, P. L. A. *Mol. Phys.* **2008**, *106*, 1495.
- (61) Stone, A. J.; Alderton, M. *Mol. Phys.* **1985**, *56*, 1047.
- (62) Stone, A. J. *J. Chem. Theory Comput.* **2005**, *1*, 1128. GDMA 2.2.04 at <http://www-stone.ch.cam.ac.uk/programs.html> (accessed 02/27/2011).
- (63) Frisch, M. J.; Trucks, G. W.; Schlegel, H. B.; Scuseria, G. E.; Robb, M. A.; Cheeseman, J. R.; Montgomery, J. A., Jr.; Vreven, T.; Kudin, K. N.; Burant, J. C.; Millam, J. M.; Iyengar, S. S.; Tomasi, J.; Barone, V.; Mennucci, B.; Cossi, M.; Scalmani, G.; Rega, N.; Petersson, G. A.; Nakatsuji, H.; Hada, M.; Ehara, M.; Toyota, K.; Fukuda, R.; Hasegawa, J.; Ishida, M.; Nakajima, T.; Honda, Y.; Kitao, O.; Nakai, H.; Klene, M.; Li, X.; Knox, J. E.; Hratchian, H. P.; Cross, J. B.; Adamo, C.; Jaramillo, J.; Gomperts, R.; Stratmann, R. E.; Yazyev, O.; Austin, A. J.; Cammi, R.; Pomelli, C.; Ochterski, J. W.; Ayala, P. Y.; Morokuma, K.; Voth, G. A.; Salvador, P.; Dannenberg, J. J.; Zakrzewski, V. G.; Dapprich, S.; Daniels, A. D.; Strain, M. C.; Farkas, O.; Malick, D. K.; Rabuck, A. D.; Raghavachari, K.; Foresman, J. B.; Ortiz, J. V.; Cui, Q.; Baboul, A. G.; Clifford, S.; Cioslowski, J.; Stefanov, B. B.; Liu, G.; Liashenko, A.; Piskorz, P.; Komaromi, I.; Martin, R. L.; Fox, D. J.; Keith, T.; Al-Laham, M. A.; Peng, C. Y.; Nanayakkara, A.; Challacombe, M.; Gill, P. M. W.; Johnson, B.; Chen, W.; Wong, M. W.; Gonzalez, C.; Pople, J. A. *Gaussian 03*, Revision C.02; Gaussian, Inc.: Wallingford, CT, 2004.
- (64) Becke, A. D. *Phys. Rev. A* **1988**, *38*, 3098.
- (65) Becke, A. D. *J. Chem. Phys.* **1993**, *98*, 5648.
- (66) Lee, C.; Yang, W.; Parr, R. G. *Phys. Rev. B* **1988**, *37*, 785.
- (67) Dunning, T. H. *J. Chem. Phys.* **1989**, *90*, 1007.
- (68) Volkov, A.; Coppens, P. *J. Comput. Chem.* **2004**, *25*, 921.
- (69) Kisiel, Z. *MIN16*; Institute of Physics, Polish Academy of Sciences: Warszawa, Poland. <http://info.ifpan.edu.pl/~kisiel/model/model.htm> (accessed 02/27/2011).
- (70) Clementi, E.; Roetti, C. *At. Data Nucl. Data Tables* **1974**, *14*, 177.
- (71) Bunge, C. F.; Barrientos, J. A.; Bunge, A. V. *At. Data Nucl. Data Tables* **1993**, *53*, 113.
- (72) Su, Z. W.; Coppens, P. *Acta Crystallogr., Sect. A* **1998**, *54*, 646. Available at <http://harker.chem.buffalo.edu/group/wavtable.html> (accessed 02/27/2011).
- (73) Su, Z.; Coppens, P. *J. Appl. Crystallogr.* **1990**, *23*, 71.
- (74) Destro, R.; Soave, R.; Barzaghi, M. *J. Phys. Chem. B* **2008**, *112*, 5163.
- (75) Coppens, P.; Guru Row, T. N.; Leung, P.; Stevens, E. D.; Becker, P. J.; Yang, Y. W. *Acta Crystallogr., Sect. A* **1979**, *35*, 63.
- (76) Press, W. H.; Teukolsky, S.; Vetterling, W.; Flannery, B. *Numerical Recipes in Fortran 77. The Art of Scientific Computing*, 2nd ed.; Cambridge University Press: Cambridge, U. K., 1992; p 136.
- (77) Halgren, T. A. *J. Am. Chem. Soc.* **1992**, *114*, 7827.
- (78) Mkadmh, A. M.; Hinchliffe, A.; Abu-Awwad, F. M. *THEO-CHEM* **2009**, *901*, 9.
- (79) Charbonneau, P. *Astrophys. J. Suppl. S* **1995**, *101*, 309. PIKAIA 1.2 at <http://www.hao.ucar.edu/modeling/pikaia/pikaia.php> (accessed 02/27/2011).
- (80) Tafipolsky, M.; Schmid, R. *J. Phys. Chem. B* **2009**, *113*, 1341.
- (81) Volkov, A.; King, H.; Coppens, P. *J. Chem. Theory Comput.* **2006**, *2*, 81.
- (82) Obolensky, O. I.; Semenikhina, V. V.; Solov'yov, A. V.; Greiner, W. *Int. J. Quantum Chem.* **2007**, *107*, 1335.
- (83) Mallocci, G.; Joblin, C.; Mulas, G. *Chem. Phys.* **2007**, *332*, 353. See also <http://astrochemistry.ca.astro.it/database/pahs.html> (accessed 02/27/2011).
- (84) Besler, B. H.; Merz, K. M.; Kollman, P. A. *J. Comput. Chem.* **1990**, *11*, 431.
- (85) Camerman, A.; Trotter, J. *Proc. R. Soc. London, Ser. A* **1964**, *279*, 129.
- (86) Jenness, G. R.; Karalti, O.; Jordan, K. D. *Phys. Chem. Chem. Phys.* **2010**, *12*, 6375.
- (87) Misquitta, A. J.; Stone, A. J. *J. Chem. Theory Comput.* **2008**, *4*, 7.
- (88) Misquitta, A. J.; Stone, A. J.; Price, S. L. *J. Chem. Theory Comput.* **2008**, *4*, 19.
- (89) Patkowski, K.; Szalewicz, K.; Jeziorski, B. *Theor. Chem. Acc.* **2010**, *127*, 211.
- (90) Hammond, J. R.; Kowalski, K.; deJong, W. A. *J. Chem. Phys.* **2007**, *127*, 144105.
- (91) Mayer, A.; Astrand, P.-O. *J. Phys. Chem. A* **2008**, *112*, 1277.
- (92) Jiemchooraj, A.; Norman, P.; Sernelius, B. E. *J. Chem. Phys.* **2005**, *123*, 124312.
- (93) Ritchie, G. L. D.; Watson, J. N. *Chem. Phys. Lett.* **2000**, *322*, 143.
- (94) Marques, M. A. L.; Castro, A.; Mallocci, G.; Mulas, G.; Botti, S. *J. Chem. Phys.* **2007**, *127*, 014107.
- (95) Vuks, M. F. *Opt. Spectrosc.* **1966**, *20*, 361.
- (96) LeFevre, R. J. W.; Radom, L.; Ritchie, G. L. D. *J. Chem. Soc. B* **1968**, 775.
- (97) Cheng, C. L.; Murthy, D. S. N.; Ritchie, G. L. D. *Aust. J. Chem.* **1972**, *25*, 1301.
- (98) Liptay, W. Z. *Naturforsch.* **1972**, *A 27*, 1336.
- (99) LeFevre, R. J. W.; Sundaram, K. M. *J. Chem. Soc.* **1963**, 4442.
- (100) Bucko, T.; Hafner, J.; Lebegue, S.; Angyan, J. G. *J. Phys. Chem. A* **2010**, *114*, 11814.
- (101) Bacon, G. E.; Curry, N. A.; Wilson, S. A. *Proc. R. Soc. London, Ser. A* **1964**, *279*, 98.
- (102) David, W. I. F.; Ibberson, R. M.; Jeffrey, G. A.; Ruble, J. R. *Physica B* **1992**, *180*, 597.
- (103) Sanchez-Carrera, R. S.; Paramonov, P.; Day, G. M.; Coropceanu, V.; Bredas, J.-L. *J. Am. Chem. Soc.* **2010**, *132*, 14437.
- (104) Brock, C. P.; Dunitz, J. D. *Acta Crystallogr., Sect. B* **1982**, *38*, 2218.
- (105) Brock, C. P.; Dunitz, J. D. *Acta Crystallogr., Sect. B* **1990**, *46*, 795.
- (106) Kai, Y.; Hama, F.; Yasuoka, N.; Kasai, N. *Acta Crystallogr., Sect. B* **1978**, *34*, 1263.
- (107) Frampton, C. S.; Knight, K. S.; Shankland, N.; Shankland, K. *J. Mol. Struct.* **2000**, *520*, 29.
- (108) Allen, F. H. *Acta Crystallogr., Sect. B* **2002**, *58*, 380.
- (109) Fawcett, J. K.; Trotter, J. *Proc. R. Soc. London, Ser. A* **1966**, *289*, 366.
- (110) Budzianowski, A.; Katrusiak, A. *Acta Crystallogr., Sect. B* **2006**, *62*, 94.
- (111) Price, S. L.; Stone, A. J. *J. Chem. Phys.* **1987**, *86*, 2859.
- (112) Williams, D. E.; Xiao, Y. L. *Acta Crystallogr., Sect. A* **1993**, *49*, 1.
- (113) Raiteri, P.; Martonak, R.; Parrinello, M. *Angew. Chem., Int. Ed.* **2005**, *44*, 3769.
- (114) Chickos, J. S.; Acree, W. E. *J. Phys. Chem. Ref. Data* **2002**, *31*, 537-698.
- (115) Khaliullin, R. Z.; Cobar, E. A.; Lochan, R. C.; Bell, A. T.; Head-Gordon, M. *J. Phys. Chem. A* **2007**, *111*, 8753.
- (116) Wu, Q.; Ayers, P. W.; Zhang, Y. K. *J. Chem. Phys.* **2009**, *131*, 164112.
- (117) Day, G. M. *Crystallogr. Rev.* **2011**, *17*, 3.
- (118) Wang, J. M.; Cieplak, P.; Li, J.; Wang, J.; Cai, Q.; Hsieh, M. J.; Lei, H.; Luo, R.; Duan, Y. *J. Phys. Chem. B* **2011**, *115*, 3100.
- (119) Hobza, P.; Selzle, H. L.; Schlag, E. W. *J. Phys. Chem.* **1996**, *100*, 18790.
- (120) Watanabe, T.; Manz, T. A.; Sholl, D. S. *J. Phys. Chem. C* **2011**, *115*, 4824.
- (121) Rezak, J.; Jurecka, P.; Riley, K. E.; Cerny, J.; Valdes, H.; Pluhackova, K.; Berka, K.; Rezac, T.; Pitonak, M.; Vondrasek, J.; Hobza, P. *Collect. Czech. Chem. Commun.* **2008**, *73*, 1261.
- (122) Podeszwa, R.; Patkowski, K.; Szalewicz, K. *Phys. Chem. Chem. Phys.* **2010**, *12*, 5974.
- (123) Takatani, T.; Hohenstein, E. G.; Malagoli, M.; Marshall, M. S.; Sherrill, C. D. *J. Chem. Phys.* **2010**, *132*, 144104.
- (124) Ringer, A. L.; Sherrill, C. D. *Chem.—Eur. J.* **2008**, *14*, 2542.
- (125) Podeszwa, R.; Rice, B. M.; Szalewicz, K. *Phys. Rev. Lett.* **2008**, *101*, 115503.
- (126) Li, Y.; Lu, D.; Nguyen, H.-V.; Galli, G. *J. Phys. Chem. A* **2010**, *114*, 1944.
- (127) Bludsky, O.; Rubes, M.; Soldan, P. *Phys. Rev. B* **2008**, *77*, 092103.

- (128) Liu, Y.; Goddard, W. A., III. *J. Phys. Chem. Lett.* **2010**, *1*, 2550.
- (129) Beran, G. J. O.; Nanda, K. *J. Phys. Chem. Lett.* **2010**, *1*, 3480.
- (130) Sabbah, H.; Biennier, L.; Klippenstein, S. J.; Sims, I. R.; Rowe, B. R. *J. Phys. Chem. Lett.* **2010**, *1*, 2962.
- (131) Tielens, A. G. G. M. *Annu. Rev. Astron. Astrophys.* **2008**, *46*, 289.
- (132) Petitjean, A.; Khoury, R. G.; Kyritsakas, N.; Lehn, J. M. *J. Am. Chem. Soc.* **2004**, *126*, 6637.
- (133) Greathouse, J. A.; Ockwig, N. W.; Criscenti, L. J.; Guilinger, T. R.; Pohl, P.; Allendorf, M. D. *Phys. Chem. Chem. Phys.* **2010**, *12*, 12621.

Exploring Anharmonic Nuclear Dynamics and Spectroscopy Using the Kratzer Oscillator

Mohamad Toutounji

Department of Chemistry, College of Science, United Arab Emirates University, Al-Ain, United Arab Emirates

ABSTRACT: The Kratzer oscillator is useful in modeling anharmonic molecular vibrations; therefore, its underlying theory is briefly explored in this study. The linear dipole moment time correlation function, within the Condon approximation, is analytically evaluated, and linear absorption lineshapes are calculated at different temperatures. An important integral formula of Landau and Lifshitz is, for the first time, utilized to evaluate the anharmonic Franck–Condon factor (FCF) resulting from modeling the initial and final states by Kratzer potentials. In addition, an exact closed-form expression of the FCF for the linearly displaced and shape-distorted final state energy curve, with respect to the ground state, is reported. Within the context of Mukamel formalism, nonlinear spectral/temporal lineshapes, such as hole-burning, photon echo, and pump–probe signals, may not be calculated without nonlinear response theory using the so-called “four-point dipole moment time correlation function”. The above FCFs will be employed to calculate optical linear and nonlinear spectra at different temperatures utilizing a previously developed formula [Toutounji, *M. J. Phys. Chem. C* **2010**, in press], whereby a hole-burned absorption lineshape may be found using a linear dipole moment time correlation function.

I. INTRODUCTION

Molecular vibrations are more realistically modeled by anharmonic oscillators such as Morse, Kratzer, or Rosen-Morse¹ oscillators, all of which render sound treatment of anharmonic molecules. Recently, the Morse potential has been used for modeling diatomic molecules, or local modes,^{2,3} because it has been proven to render qualified results, accounting for important quantum mechanical properties of molecules.⁴ While considerable attention has been given to calculating Franck–Condon factors (FCFs) and linear and nonlinear absorption lineshapes of the Morse oscillator,^{2,3,5–9} little attention has been devoted to that of Kratzer.^{10–12} Various techniques have been employed at different levels of rigor, approximation, and applicability to deal with the Morse oscillator and its consequent dynamics.^{13,14}

Although the Morse oscillator has been at the forefront in modeling anharmonic dynamics, utilizing the Kratzer oscillator has not been as common in chemistry^{10–12} as has it been in physics^{15–17} and mathematics,^{18–22} in an effort to solve the corresponding Schrodinger equation using a Laplace transform approach. Recently, the Kratzer oscillator has been drawing some attention in physics; for example, constructing ladder operators and coherent states of the Kratzer oscillator²³ has been established, employing properties of the corresponding eigenfunctions. It has been noted that the Kratzer oscillator has few advantages over that of the Morse oscillator. For example, the latter has a finite number of bound states, whereas the former has an infinite number of them. The Kratzer potential energy curve has been reported, in the works of Van Hooydonk,^{12,24–26} to be superior to that of the Morse potential energy curve in fitting the energies of ~ 300 diatomic molecules. While the Kratzer oscillator outperforms the Morse oscillator in some molecules, it certainly outperforms harmonic oscillators in all molecules. In addition, a molecular hydrogen (H_2) potential energy curve does not follow the Morse potential: 90%–95% of it comes from that

of Kratzer, and the remaining 5%–10% is attributed to quartic potential behavior. An excellent nonmathematical treatment of H_2 and its vibrational levels using Kratzer potential analysis is provided in ref 26. The H_2 experimental vibrational ground-state energy is 2170.08 cm^{-1} and that calculated using the Kratzer ground-state eigenvalue yields 2170.12 cm^{-1} . The roto-vibrational Schrodinger equation with the Kratzer potential can be solved exactly when rotation (repulsive centrifugal potential) is included, which cannot be done with the Morse potential. (This property, in its own right, is a plus for a Kratzer roto-vibrator. The Morse oscillator Schrodinger equation can only be solved exactly if the vibrator is rotationless.) Another motivation for exploring Kratzer oscillator anharmonic dynamics is that its eigenfunctions have been used previously as a basis set for diatomic molecules, rendering sound results.¹¹ In addition, important matrix elements that were evaluated by Secret¹¹ have rendered finite values for *all* rotational states (finite angular momentum), whereas those values are finite *only* for the zero-rotation state in the case of the Morse oscillator. Needless to mention, the Kratzer oscillator eigenfunctions are easier to deal with than those of the Morse oscillator.

In light of the above, the consequent linear and nonlinear lineshapes and spectral dynamics of employing the Kratzer oscillator have not yet been explored. Therefore, carrying out this exploration in this study is deemed necessary and should prove useful in this study. As such, this article is organized as follows. Section II presents the foundations needed for understanding the underlying theory of the Kratzer oscillator. Section III briefly draws the similarities and differences between the Kratzer and Morse oscillators. A methodology is developed in section IV, to account for both vibrational coherences and

Received: December 13, 2010

Published: May 06, 2011

broadening due to pure electronic dephasing. Section V calculates the hole-burning absorption lineshape using the Kratzer oscillator. Results and discussion are provided in section VI. Concluding remarks and prospects are provided in section VII.

II. BACKGROUND ON THE KRATZER OSCILLATOR

While the Morse potential is a three-parameter potential, the Kratzer oscillator is only a two-parameter potential. The parameters of the former are the Kratzer well depth (D_e), the equilibrium internuclear distance (r_e), and the potential width/shape (a ; this is often known as the Morse parameter), whereas the latter can only accommodate the bond strength (D_e) and length (r_e). The Kratzer potential assumes this form:

$$V(r) = D_e \left[\left(\frac{r - r_e}{r} \right)^2 - 1 \right] \quad (1)$$

where D_e is the well depth and r_e is the equilibrium internuclear distance. A generic shape of the Kratzer potential function is displayed in Figure 1, in which the similarity between the Kratzer potential and that of Morse is readily observed. (The numbers on the abscissa are arbitrary and do not reflect any physicality.) The m th vibrational eigenfunction of the Kratzer oscillator, in coordinate representation, reads as follows:¹⁶

$$\Psi_m(q) = A_m q^\lambda e^{-\eta_m q} {}_1F_1 \left(\lambda - \frac{\Omega^2}{\eta_m} \middle| 2\eta_m q \right) \quad (2)$$

where ${}_1F_1(\cdot)$ is the confluent hypergeometric function, and the nuclear coordinate q is defined over the range of $0 < q < \infty$. The parameters λ , η_m , and the normalization constant A_m are given by

$$\lambda = \frac{1}{2} + \sqrt{\Omega^2 + \frac{1}{4}} \quad (2a)$$

$$\eta_m^2 = \frac{2\mu r_e^2 (D_e - E_m)}{\hbar^2} \quad (2b)$$

and

$$A_m = \frac{1}{\sqrt{r_e(m + \lambda)}} \sqrt{\frac{\Gamma(2\lambda + m)}{2m! \Gamma^2(2\lambda)}} \left(\frac{2\lambda(\lambda - 1)}{\lambda + m} \right)^{\lambda + (1/2)} \quad (2c)$$

with $\Gamma(\cdot)$ being the Gamma function, $\Omega^2 = 2\mu r_e^2 D_e / \hbar^2$, and $q = r/r_e$. E_m in eq 2b are the eigenenergies of the Kratzer oscillator and are given by¹⁶

$$E_m = D_e \left[1 - \frac{\Omega^2}{(m + \lambda)^2} \right] \quad m = 0, 1, 2, \dots \quad (3)$$

This nonstandard integral is needed for evaluating the normalization constant, A_m :

$$\int_0^\infty q^{2\lambda} e^{-2\eta_m q} \left[{}_1F_1 \left(\frac{-m}{2\lambda} \middle| 2\eta_m q \right) \right]^2 dq = \frac{2(\lambda + m)m! \Gamma(2\lambda)}{(2\eta_m)^{2\lambda + 1} (2\lambda)_m}$$

Kratzer oscillator eigenfunctions are most often reported unnormalized, and, in cases where the normalization constant was reported, it was inaccurate, because it did not yield a value of unity when numerically evaluated; therefore, the above challenging integral had to be evaluated. One can define the Kratzer

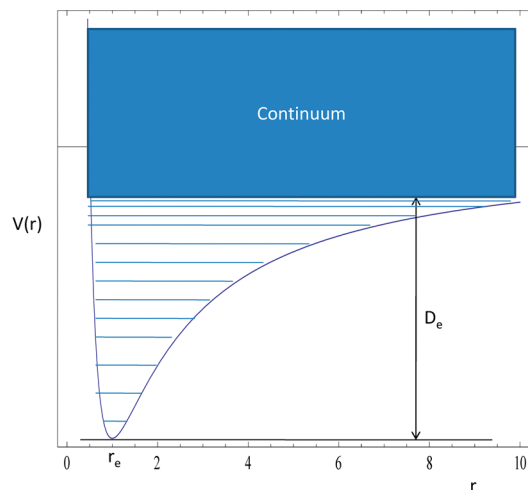


Figure 1. Kratzer potential displaying bound/quantized and continuum/scattering states. It looks very similar to the Morse potential, which has three parameters—namely, well depth (D_e), width (a), and bond length (r_e)—whereas the Kratzer potential lacks the width parameter a .

coordinate, analogous to that of the Morse oscillator (*vide infra*),² as $z = 2\eta_m q$; as such,

$$\Psi_m(z) = A_m (2\eta_m)^{-\lambda} z^\lambda e^{-z/2} {}_1F_1 \left(\frac{-m}{2\lambda} \middle| z \right) \quad (4)$$

An important quantity of the Kratzer oscillator is the dissociation energy (D_0), which is related to the force constant (which can be defined as $k_e = \mu\omega^2$). However, the Kratzer force constant (k_e) is given by¹⁸

$$k_e = \left. \frac{d^2 V(r)}{dr^2} \right|_{r_e} = \frac{2D_e}{r_e^2} \quad (5)$$

III. CONNECTION TO THE MORSE OSCILLATOR AND THE HYDROGEN ATOM (COULOMB POTENTIAL)

The Morse oscillator has been explored extensively by different groups.^{2–9,14} As noted earlier, one can interestingly observe that the Morse and Kratzer potentials seem to have similar sets of eigenfunctions: both sets are products of a power function, an exponential function, and associated Laguerre polynomials. The vibrational Morse oscillator Hamiltonian for the excited state reads

$$H = \frac{P^2}{2\mu} + D_e \left\{ \exp[-2a(q - q_0)] - [2\exp - a(q - q_0)] \right\} \quad (6)$$

defined over a range of $-\infty < q < \infty$, with P and q being the momentum and position, respectively. The eigenfunctions of the Morse oscillator are expressed in terms of the generalized Laguerre polynomials:

$$\Phi_n(q) = B_n \left\{ 2\nu \exp[-a(q - q_0)] \right\}^s \exp\{-\nu \exp[-a(q - q_0)]\} L_n^{2s} 2\nu \exp[-a(q - q_0)] \quad (7)$$

where

$$B_n = \sqrt{\frac{a\Gamma(n+1)2s}{\Gamma(2\nu-n)}} \quad (7a)$$

where $\nu \equiv (2\mu D_e)^{1/2}/(\hbar a)$ and $2s = 2\nu - 2n - 1$. One readily observes that the variable y , which is often called the *Morse coordinate* (defined as $y \equiv 2\nu \exp[-a(q-q_0)]$) can serve as an independent variable in eq 7 and the parameter s is directly related to the number of bound states. Hence, the Morse eigenfunctions, expressed in terms of the Morse coordinate, read as

$$\Phi_n(y) = B_n y^s \exp\left(-\frac{y}{2}\right) L_n^{2s}(y) \quad (8)$$

One can employ this relationship,

$$L_i^\lambda(x) = \frac{\Gamma(\lambda+i+1)}{i!\Gamma(\lambda+1)} {}_1F_1\left(\begin{matrix} -\mu \\ \lambda+1 \end{matrix} \middle| x\right) \quad (9)$$

to express Laguerre polynomials in terms of confluent hypergeometric functions, so that Morse oscillator eigenfunctions can be compared to those of the Kratzer oscillator. Therefore, Morse bound states may be recast as

$$\Phi_n(y) = B_n C_n y^s \exp\left(-\frac{y}{2}\right) {}_1F_1\left(\begin{matrix} -n \\ 2s+1 \end{matrix} \middle| y\right) \quad (10)$$

where

$$C_n = \frac{\Gamma(2s+n+1)}{n!\Gamma(n+1)} \quad (10a)$$

As such, casting Morse eigenfunctions in terms of confluent hypergeometric functions, as in eq 10, will help pinpoint the similarities and differences between the two anharmonic oscillators in modeling molecular vibrations. One may readily notice that both the Kratzer and Morse oscillators stationary states $\Psi_m(z)$ and $\Phi_n(y)$ are made of power functions (z^λ and y^s), exponential functions ($\exp(-z/2)$ and $\exp(-y/2)$), and confluent hypergeometric functions, both of which are linear in nuclear coordinates.

Other important quantities, such as the potential width parameter a ($a \equiv (k_e^{\text{MO}}/2D_e)^{1/2}$, with k_e^{MO} being the force constant at the minimum of the Morse potential, potential depth D_e and anharmonicity constant χ governed by the number of bound states: $\chi = 1/(2\nu)$. (Pollak reported dynamical calculations with two- and five-state Morse oscillators in order to probe very large anharmonic effects.⁴) While the Kratzer force constant k_e is given in eq 5, that of Morse is $k_e^{\text{MO}} = 2aD_e^2$, which will give rise to some spectroscopic and dynamical disparities rendered by both oscillators, as the following discussion will demonstrate.

A fundamental feature of the Kratzer oscillator is that it has an infinite number of vibrational bound states, thereby placing restriction on its anharmonicity nature, as opposed to the Morse oscillator, whose anharmonic character increases as the number of its finite states goes down, whereas that of Kratzer has no adjustable anharmonicity parameter. One can appreciate this by examining the force constants (curvature) of the two oscillators: the Morse oscillator curvature is dependent on its width parameter (bond strength), whereas the Kratzer

curvature lacks any width-related parameter and, hence, is independent of it (leading to an infinite number of bound states) and, thus, is dependent only on frequency. As such, as much as the Kratzer and Morse oscillators eigenfunctions resemble each other, the above-cited differences will render slightly different spectra and dynamics, as will be discussed in the following sections.

Close examination of the hydrogen atom stationary states shows that not only these states,

$$\begin{aligned} R_{n\ell}(\xi) &= M_{n\ell} \xi^\ell \exp\left(-\frac{\xi}{2}\right) L_{n+\ell}^{2\ell+1}(\xi) \\ &= M_{n\ell} \xi^\ell \exp\left(-\frac{\xi}{2}\right) {}_1F_1\left(\begin{matrix} -(n+\ell) \\ 2(\ell+1) \end{matrix} \middle| \xi\right) \end{aligned} \quad (11)$$

resemble those of Kratzer and Morse but also the energies of these states can be recovered from the Kratzer oscillator eigenenergies, as well-elucidated in ref 18. $M_{n\ell}$ in eq 11 is a normalization constant that has no relevance here.

IV. ANHARMONIC LINEAR SPECTROSCOPY VIA KRATZER POTENTIAL

Suppose a quantum system is excited from an electronic ground state $|g\rangle$ to an excited state $|e\rangle$. The adiabatic electronic Hamiltonian of the system is

$$\hat{H} = H_g |g\rangle\langle g| + H_e |e\rangle\langle e| \quad (12)$$

where the nuclear Hamiltonians are

$$H_g = \sum_{j=1}^{\infty} \frac{P_j^2}{2\mu_j} + D''_{ej} \left[\left(\frac{1}{q_j}\right)^2 - 2\frac{1}{q_j} \right] \quad (12a)$$

and

$$H_e = \sum_{j=1}^{\infty} \frac{P_j^2}{2\mu_j} + D'_{ej} \left[\left(\frac{1}{q_j}\right)^2 - 2\frac{1}{q_j} \right] \quad (12b)$$

Henceforth, the formal theory will be carried out over one mode, without any loss of generality, where confusion is unlikely to arise. Here, we follow the conventional notation in spectroscopy whereby the initial state is denoted by double-primed quantities, whereas the final state is denoted by single-primed ones. The linear dipole moment time correlation function (DMTCF) is given by

$$J(t) = \frac{\text{Tr}(\exp(i\hat{H}t/\hbar) d \exp(-i\hat{H}t/\hbar) d \exp(-\beta\hat{H}))}{\text{Tr}(d^2 \exp(-\beta\hat{H}))} \quad (13)$$

where β is the inverse temperature, $\text{Tr}(\cdot)$ denotes the trace over the entire system, and d is the electronic transition dipole moment operator:

$$d = d_{eg} |e\rangle\langle g| + d_{ge} |g\rangle\langle e| \quad (14)$$

While the nuclear transition dipole moment operator d_{eg} , under the Born–Oppenheimer approximation, is a matrix element in the electronic subspace, it acts as an operator in the nuclear subspace. Expanding eq 13 in the electronic

two-dimensional basis set, assuming the electronic adiabatic gap is much greater than kT and invoking the Condon approximation, yields

$$J(t) = \frac{\text{Tr}_{\tilde{N}}(\exp(iH_g t/\hbar) \exp(-iH_e t/\hbar) \exp(-\beta H_g))}{Q} \quad (15)$$

where the partition function Q is

$$Q = \text{Tr}_{\tilde{N}}(\exp(-\beta H_g)) \quad (15a)$$

where $\text{Tr}_{\tilde{N}}(\cdot)$ denotes the trace over the nuclear degrees of freedom. In light of the above, one can assume that the equilibrium density operator of the entire system is

$$\rho = \frac{\exp(-\beta H_g) |g\rangle\langle g|}{Q} \quad (16)$$

That is, the entire system is in thermal equilibrium with the electronic ground state. Once the DMTCF is determined, the linear electronic absorption lineshape function may be calculated using

$$I(\omega) = \frac{1}{2\pi} \int_{-\infty}^{\infty} dt J(t) \exp(i\omega t) \quad (17)$$

In the foregoing sections, one-mode excitation is assumed, while the rest of the modes remain in the ground state, and a similarity of normal coordinates in the ground and excited electronic states is assumed.

While the eigenfunctions of H_g , for one mode, are given as

$$\Psi_n''(q'') = A_n'' q''^{\lambda''} \exp(-\eta_n'' q'') {}_1F_1\left(\frac{-n}{2\lambda''} \middle| 2\eta_n'' q''\right) \quad (18)$$

and those of H_e are given as

$$\Psi_m'(q') = A_m' q'^{\lambda'} \exp(-\eta_m' q') {}_1F_1\left(\frac{-m}{2\lambda'} \middle| 2\eta_m' q'\right) \quad (19)$$

The ground-state quantities are

$$\lambda'' = \frac{1}{2} + \sqrt{\Omega''^2 + \frac{1}{4}} \quad (20a)$$

$$\eta_n'' 2 = \frac{2\mu r_e'' 2(D_e'' - E_n'')}{\hbar^2} \quad (20b)$$

with $\Omega''^2 = 2\mu r_e''^2 D_e''/\hbar^2$ and $q'' = r/r_e''$, whereas those of the excited state are

$$\lambda' = \frac{1}{2} + \sqrt{\Omega'^2 + \frac{1}{4}} \quad (20c)$$

$$\eta_m' 2 = \frac{2\mu r_e' 2(D_e' - E_m')}{\hbar^2} \quad (20c)$$

with $\Omega'^2 = 2\mu r_e'^2 D_e'/\hbar^2$ and $q' = r/r_e'$. Upon expanding the nuclear trace, in terms of anharmonic number states, and using trace

invariance, $\{|\Psi_n''\rangle\}_{n=0}$, eq 15 reads

$$J(t) = Q^{-1} \sum_{n=0}^{\infty} \exp(-\beta E_n'') \exp\left(\frac{iE_n'' t}{\hbar}\right) \langle \Psi_n'' | \exp\left(-\frac{iH_e t}{\hbar}\right) | \Psi_n'' \rangle \quad (21)$$

In order to proceed forward, one would need to surmount the dilemma of $\{|\Psi_n''\rangle\}_{n=0}$ not being eigenstates of $\exp(-iH_e t/\hbar)$. One may expand the ket $|\Psi_n''\rangle$, in terms of the eigenbasis set of the excited state nuclear Hamiltonian H_e , *vide supra*, which will involve some formidable integrals.

$$\langle r | \Psi_n'' \rangle = \sum_{m=0}^{\infty} c_{mn} \langle r | \Psi_m' \rangle \quad (22)$$

where the expansion coefficient c_{mn} is given by

$$c_{mn} = \int_0^{\infty} \Psi_m'^*(r) \Psi_n''(r) dr \quad (23)$$

Equation 21 thus reads

$$J(t) = Q^{-1} \sum_{n=0}^{\infty} \exp(-\beta E_n'') \exp\left(\frac{iE_n'' t}{\hbar}\right) \sum_{m=0}^{\infty} \exp\left(-\frac{iE_m' t}{\hbar}\right) |c_{mn}|^2 \quad (24)$$

$$c_{mn} = A_n'' A_m' \int_0^{\infty} \left(\frac{r}{r_e''}\right)^{\lambda''} \left(\frac{r}{r_e'}\right)^{\lambda'} \exp[-\kappa r] {}_1F_1\left(\frac{-m}{2\lambda'} \middle| \alpha_2 r\right) {}_1F_1\left(\frac{-n}{2\lambda''} \middle| \alpha_1 r\right) dr \quad (24a)$$

where $\alpha_1 = 2\eta_n''/r_e''$, $\kappa = (\eta_n''/r_e'') + (\eta_m'/r_e')$, $\alpha_2 = 2\eta_m'/r_e'$, and the partition function Q is given by

$$Q = \sum_{n=0}^{\infty} \exp(-\beta E_n) \quad (25)$$

Using the Landau and Lifshitz integral formula,^{19,20}

$$\int_0^{\infty} x^{\alpha-1} \exp[-hx] {}_1F_1\left(\frac{a}{b} \middle| kx\right) {}_1F_1\left(\frac{a'}{b'} \middle| k'x\right) dx = h^{-\alpha} \Gamma(\alpha) F_2\left(\alpha; a, a'; b, b'; \frac{k}{h}, \frac{k'}{h}\right) \quad (26)$$

where $F_2(\cdot)$ is Appell's hypergeometric function,^{21,27} which yields

$$c_{mn} = A_n'' A_m' (r_e'')^{-\lambda''} (r_e')^{-\lambda'} (\kappa)^{-(\lambda'' + \lambda' + 1)} \Gamma(\lambda'' + \lambda' + 1) \times F_2\left(\lambda'' + \lambda' + 1; -m, -n; 2\lambda', 2\lambda''; \frac{\alpha_2}{\kappa}, \frac{\alpha_1}{\kappa}\right) \quad (27)$$

$|c_{mn}|^2$ acts as a FCF for the corresponding anharmonic transition $m \leftarrow n$. Using eq 24 in eq 17 yields the homogeneous (single-site) absorption lineshape:

$$I(\omega) = \frac{\gamma Q^{-1}}{2\pi} \sum_{n=0}^{\infty} \sum_{m=0}^{\infty} \frac{|c_{mn}|^2 \exp(-\beta E_n'')}{(\omega + E_n'' - E_m')^2 + (\gamma/2)^2} \quad (28)$$

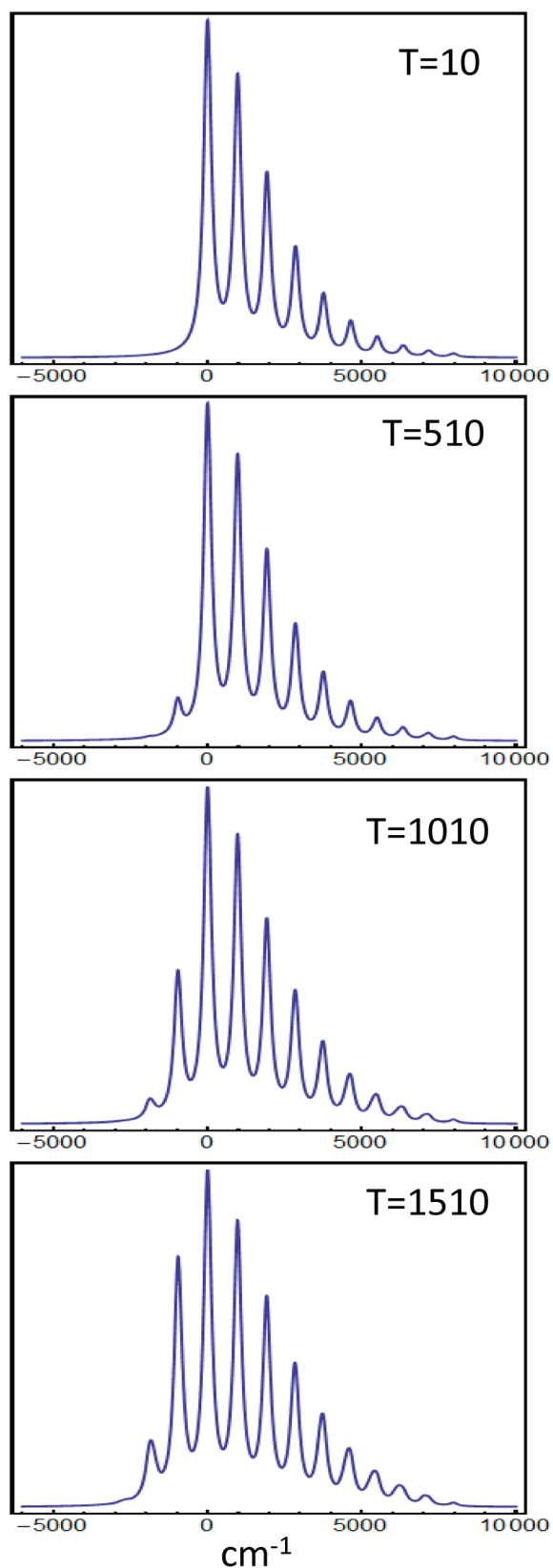


Figure 2. Linear homogeneous absorption spectra calculated with eqs 24–28, using $\omega'' = 1000 \text{ cm}^{-1}$ and $r_e'' - r_e' = 1.5325$ at different temperatures. Note that the electronic bands appear at $\Delta E = E_m' - E_n'' = D_e' \{1 - (2\mu D_e' r_e'^2) / [\hbar^2 (m + \lambda')^2]\} - D_e'' \{1 - (2\mu D_e'' r_e''^2) / [\hbar^2 (n + \lambda'')^2]\}$.

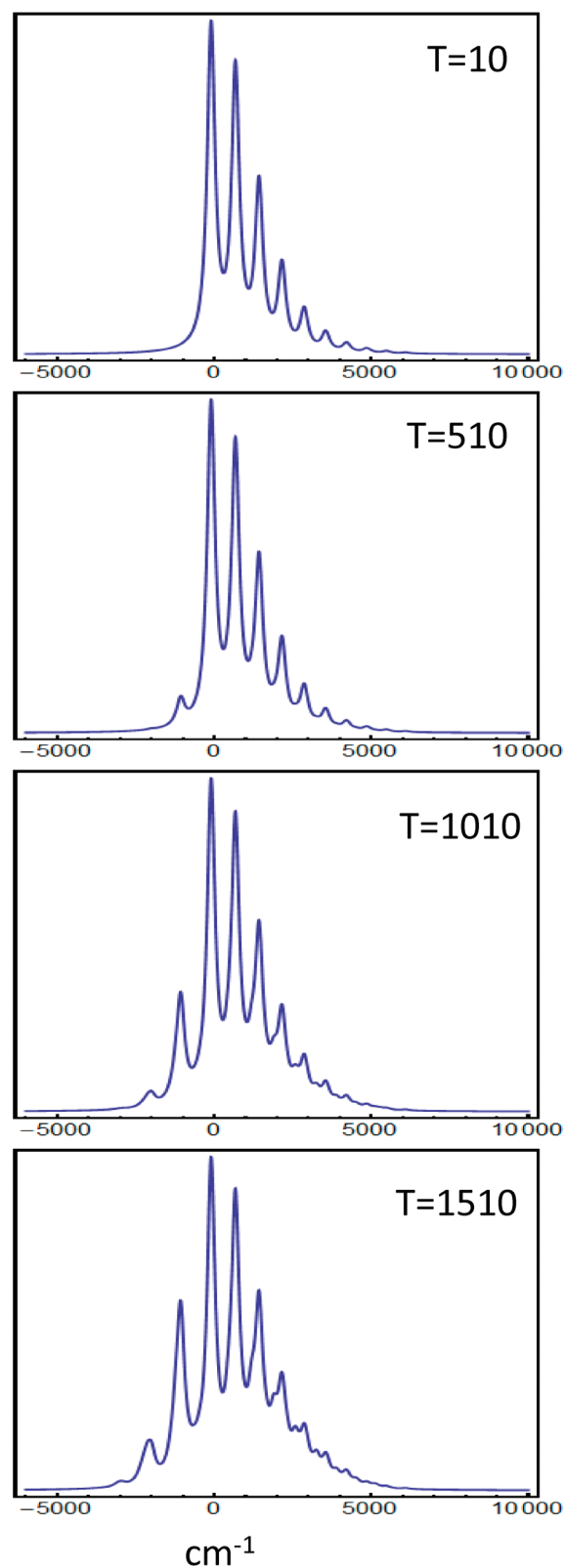


Figure 3. Linear homogeneous absorption spectra calculated with eqs 24–28 using $\omega'' = 1000 \text{ cm}^{-1}$, $\omega' = 800 \text{ cm}^{-1}$, and $r_e'' - r_e' = 1.5325$ at different temperatures.

where γ is the homogeneous line width. As well-elucidated in ref 3 and refs 28–30, eq 28 generates a lineshape of which all bands

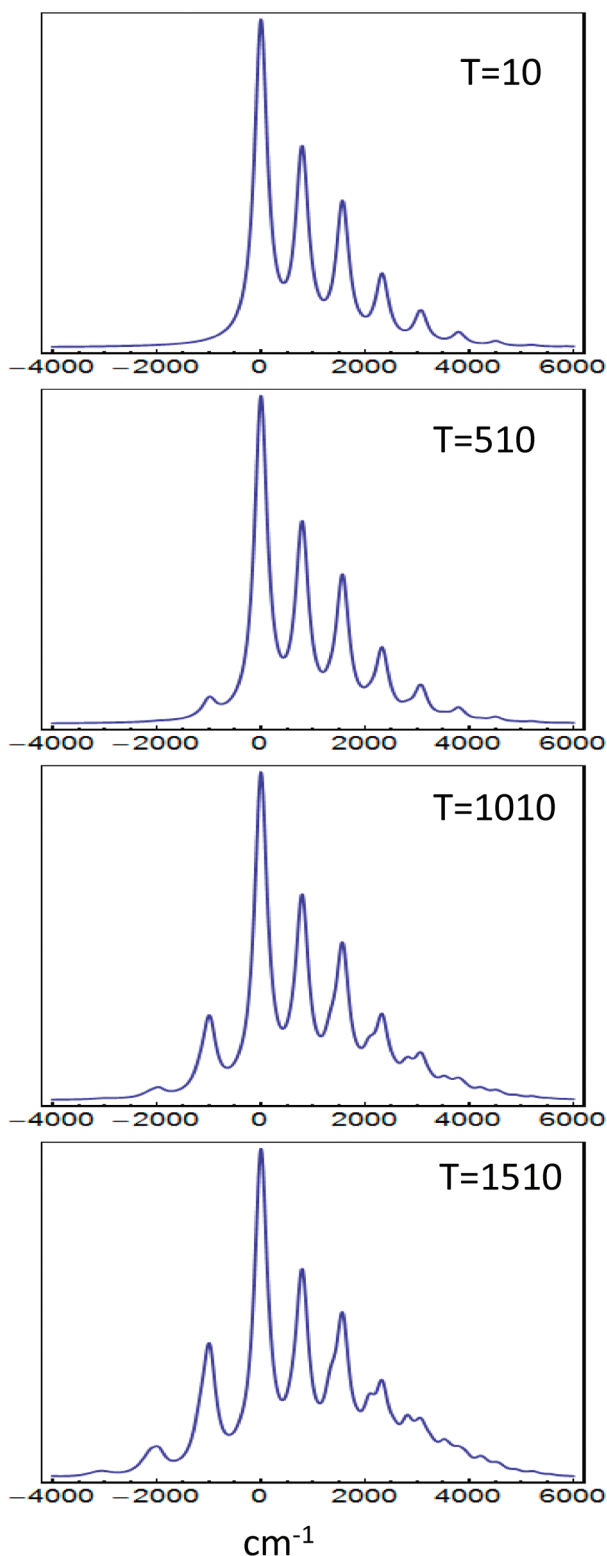


Figure 4. Linear homogeneous absorption spectra calculated, using the Morse oscillator DMTCF and the lineshape function developed in ref 2, with $\omega'' = 1000 \text{ cm}^{-1}$, $\omega' = 800 \text{ cm}^{-1}$, and $r_e'' - r_e' = 1.5325$ at different temperatures. Although this figure and Figure 3 are plotted on different wavenumber scales, one can easily see the similarity of the spectra calculated using the Kratzer and Morse oscillators.

have the same homogeneous width. For example, at low temperatures, one would find that the zero-phonon line (ZPL) and

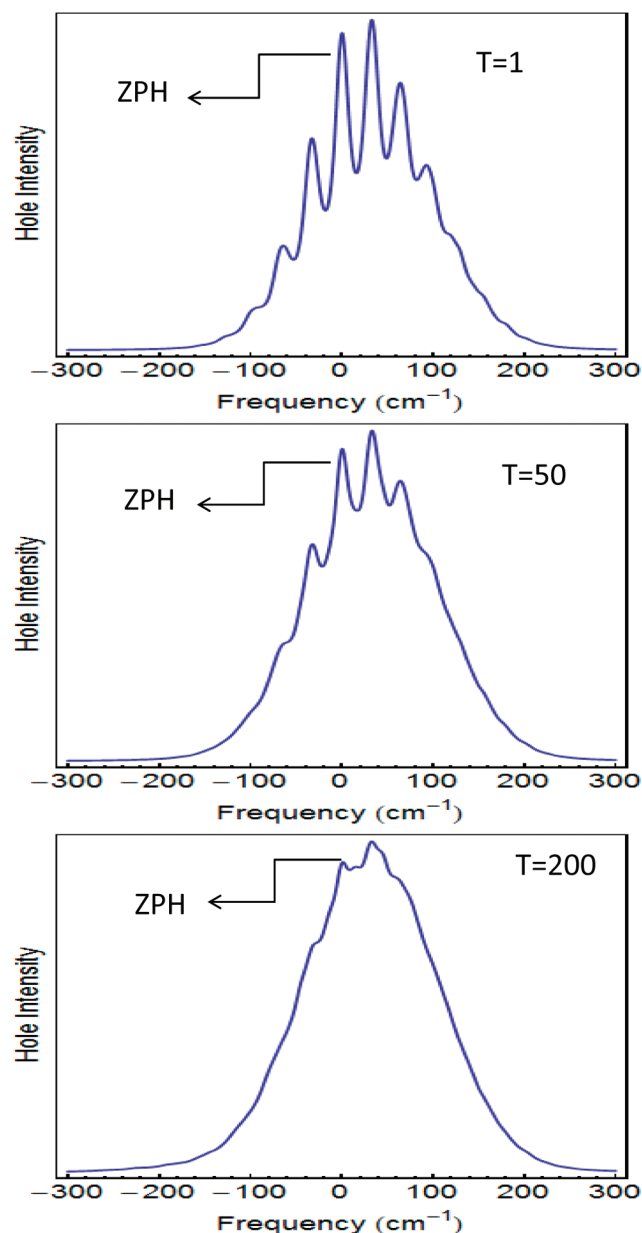


Figure 5. Hole-burned absorption lineshape with parameters of $\omega'' = 50 \text{ cm}^{-1}$, $\omega' = 40 \text{ cm}^{-1}$, $r_e'' - r_e' = 0.910$, $\omega_B = 0$, and $\Delta = 64.4 \text{ cm}^{-1}$ at different temperatures, showing the zero-phonon hole (ZPH) profile tapering off at higher temperatures. These calculations yield $\gamma_{\text{ZPH}} = 2\gamma_{\text{eb}}$ as expected.

progression members have the same relaxation time constant, $1/\gamma$, which is unphysical.^{3,28–30}

For an N -mode system, the total DMTCF can be expressed as follows, where the Duschinsky mixing effect is assumed to be negligible:

$$J(t) = \prod_{j=1}^N J_j(t) \quad (29)$$

where $J_j(t)$ is the individual DMTCF for the j th mode provided in eq 24. In the case of exciting all the modes of this system, the absorption spectrum is then given by combining all of the

individual mode spectra:

$$I(\omega) = \int d\omega_1 \int d\omega_2 \cdots \int d\omega_{N-1} I_1(\omega - \omega_1) I_2(\omega_1 - \omega_2) \cdots I_N(\omega_{N-1}) \quad (30)$$

where $I_j(\omega)$ is the homogeneous absorption spectrum for mode j given by eq 28. To this end, one can identify the ZPL width, to probe the electronic pure dephasing, as illustrated in the next section.

A direct application of utilizing herein the DMTCF $J(t)$ and the corresponding absorption lineshape in eqs 24 and 28 is shown in Figure 2. Figure 2 uses a typical vibrational frequency of diatomic molecules, e.g., $\omega'' = 1000 \text{ cm}^{-1}$, $r'_e - r''_e = 1.5325$ (dimensionless unit). Figure 3 shows the same spectra but with a frequency change upon excitation (curvature change) to $\omega' = 800 \text{ cm}^{-1}$. Figure 4 shows the same spectra as those shown in Figure 3 but calculated using the Morse oscillator absorption lineshape.^{2,3} Spectra in Figures 3 and 4, which have been calculated using the Kratzer and Morse oscillator models, are comparable, showing clear similarities with a light difference in the hot band $0 \leftarrow 1$ transition.

V. PURE DEPHASING AND LINEAR ABSORPTION SPECTRA

If the system of interest consists of several anharmonic modes, the total DMTCF reads

$$F(t) = J_{\text{el}}(t) J_{\text{anh}}(t) \quad (31)$$

$$J_{\text{el}}(t) = \exp\left[-\frac{\gamma_{\text{el}}|t|}{2}\right] \quad (31a)$$

results from integrating the product of the vibronic ground-state wave functions, with

$$\sigma'' = \sqrt{\frac{2\mu r''_e 2(D''_e - E''_0)}{\hbar^2}} \quad (32b)$$

$$\sigma' = \sqrt{\frac{2\mu r'_e 2(D'_e - E'_0)}{\hbar^2}} \quad (32c)$$

The above description is very similar to the treatment of the Morse oscillator dephasing problem given in ref 3. Fourier transforming equations 31 and 32 will produce absorption spectra in which the ZPL has zero width in the low-temperature limit and starts to gain some width as the temperature increases, causing the ZPL to broaden and eventually diminish in the high-temperature limit.

$$J_{\text{anh}}(t) = \prod_j^N J_{\text{anh},j}(t) \quad (31b)$$

where $J_{\text{anh},j}(t)$ is given by

$$J_{\text{anh},j}(t) = \frac{1}{Q} \left\{ |c_{00}|^2 \exp\left[-\beta\left(D''_e - \frac{2D''_e 2r''_e 2\mu}{\hbar^2 \lambda''_e{}^2}\right) + i\Xi t/\hbar\right] + \sum_{n=1}^{\infty} \sum_{m=1}^{\infty} |c_{nm}|^2 \exp\left[-\beta E''_n + \frac{it(E''_n - E'_m)}{\hbar} - \frac{\gamma_j |t|}{2}\right] \right\} \quad (31c)$$

where

$$\Xi = D''_e - D'_e + \frac{2D''_e 2r''_e 2\mu}{\hbar^2 \lambda''_e{}^2} - \frac{2D'_e 2r'_e 2\mu}{\hbar^2 \lambda'_e{}^2} \quad (31d)$$

The set of equations presnted as in eq 31 will lead to an electronic dephasing time equal to $1/\gamma_{\text{el}}$ and a vibrational relaxation time equal to $(\gamma_{\text{el}} + \gamma_j)^{-1}$. Of course, the dependence of γ_{el} on temperature is determined by the nature of the ensuing dephasing mechanism dictated by the guest–host relationship.^{3,28–30} If one was to look *only* at the 0–0 transition (ZPL) rendered by eq 31c (before multiplying it by $J_{\text{el}}(t)$), it will have a delta function-like profile with a zero width and an intensity equal to

$$Q^{-1} |c_{00}|^2 \exp\left[-\beta\left(D''_e - \frac{2D''_e 2r''_e 2\mu}{\hbar^2 \lambda''_e{}^2}\right)\right] \quad (32)$$

where the overlap integral,

$$c_{00} = \frac{2^{\lambda'' + \lambda'} (r'')^{-\lambda''} (r')^{-\lambda'} \Gamma(1 + \lambda'' + \lambda') \sigma^{\lambda'' + (1/2)} \sigma'^{\lambda' + (1/2)} \left(\frac{\sigma''}{r''} + \frac{\sigma'}{r'}\right)^{-(1 + \lambda'' + \lambda')}}{\sqrt{\lambda'' \lambda' r'' r' \Gamma(2\lambda'') \Gamma(2\lambda')}} \quad (32a)$$

VI. ANHARMONIC HOLE-BURNING SPECTROSCOPY VIA THE KRATZER POTENTIAL

As elucidated in ref 3, although hole burning is a nonlinear technique, one may still calculate its lineshapes, using the linear correlation function $J(t)$, by calculating the absorption spectrum following a burn time η :

$$I_{\eta}(\omega, \omega_B) = \int_{-\infty}^{\infty} d\Omega \chi(\Omega - \nu_m) J(\omega - \Omega) \exp[-\theta J(\omega_B - \Omega)\eta] \quad (33)$$

where Ω is the variable frequency of the ZPL of a single absorber and ω_B is the burn frequency. The absorption spectrum before burning is $I_0(\omega)$, which is obtained by setting the burning time as $\eta = 0$. Thus, the hole-burned spectrum is given by

$$S_{\text{HB}}(\omega, \omega_B) = I_{\eta}(\omega) - I_0(\omega) \quad (34)$$

$\chi(\Omega - \nu_m)$ is a Gaussian function, with variance Δ^2 centered at ν_m , which governs the distribution of ZPL frequencies, because of structural heterogeneity. θ is the product of three terms: the

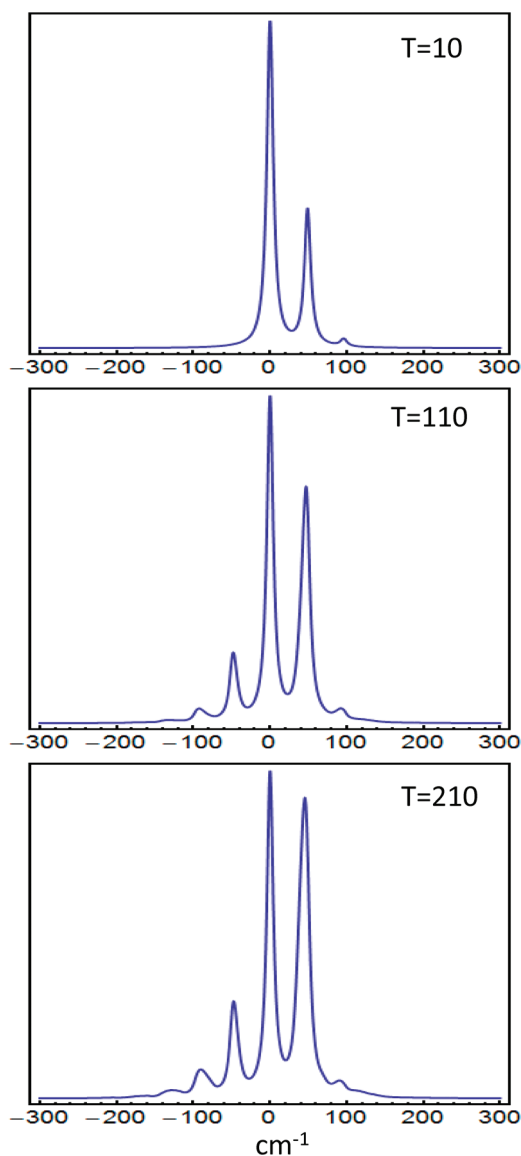


Figure 6. Linear homogeneous absorption spectra calculated using the Morse oscillator model with $\chi'' = 0.02$, $\omega'' = 50 \text{ cm}^{-1}$, $\chi' = 0.01$, $\omega' = 50 \text{ cm}^{-1}$, and $r'_e - r''_e = 0.910$.

absorption cross section, the laser burn flux, and the quantum yield for hole burning. Toutounji showed, using the theory of Bessel functions, that, in the case of a large inhomogeneous broadening, the hole-burning lineshape may be expressed in terms of the linear DMTCF:³

$$S_{\text{HB}}(\omega, \omega_{\text{B}}) = \frac{1}{2\pi} \theta \eta \int_{-\infty}^{+\infty} dt |J(t)|^2 \exp(-i\omega t) \exp(i\omega_{\text{B}} t) \quad (35)$$

The correctness and applicability of eq 35 was evidently ratified in ref 3. Figure 5 shows a model calculation of hole-burned absorption lineshapes with parameters of $\omega'' = 50 \text{ cm}^{-1}$, $\omega' = 40 \text{ cm}^{-1}$, $r'_e - r''_e = 0.910$, and inhomogeneous broadening $\Delta = 64.4 \text{ cm}^{-1}$ at different temperatures, showing the zero-phonon hole (ZPH) and phonon-sideband hole in the burned spectra at $\omega_{\text{B}} = 0$. These parameters are similar to those used in ref 3 to

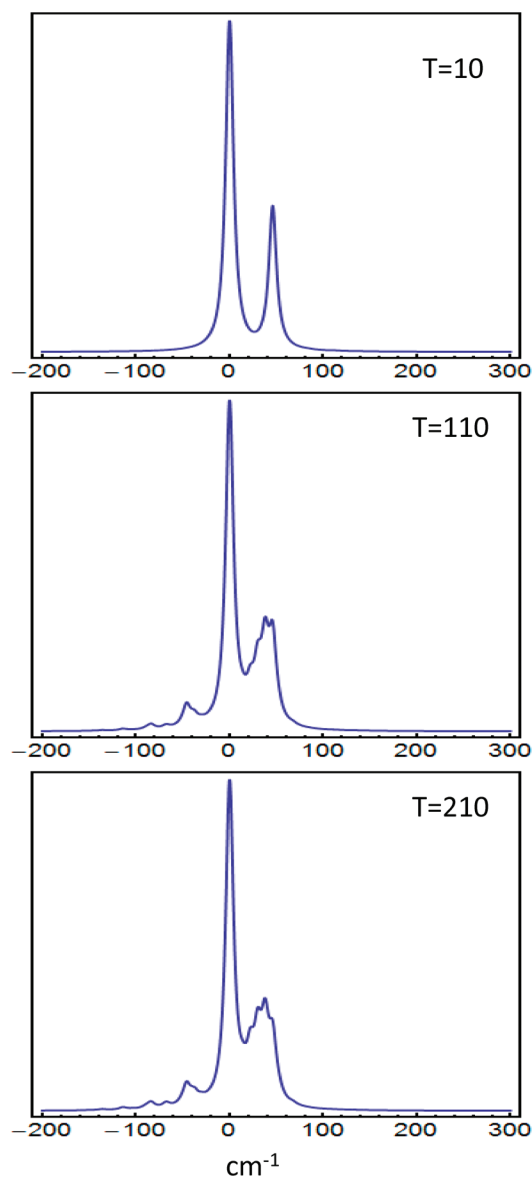


Figure 7. Same as in Figure 6, but with much higher anharmonicity (and, hence, much less vibrational bound states), to contrast the resulting spectra with those in Figure 6; see text for details.

simulate hole-burned spectra of APT in glassy ethanol.^{31,32} In these spectra, the ZPH width is given as $\gamma_{\text{ZPH}} = 2\gamma_{\text{el}}$.

VII. CALCULATIONS AND DISCUSSION

Utilizing the Kratzer potential for modeling molecular vibrations can be fruitful, because the Morse and harmonic oscillators fail to reproduce the experimental vibrational ground-state energy (2170.08 cm^{-1}) of the hydrogen molecule (H_2), whereas that of the Kratzer oscillator, using eq 3, successfully renders a value of 2170.12 cm^{-1} . (The Morse and harmonic oscillators yield values of 2201.6 and 2233.24 cm^{-1} for the vibrational ground-state energy of H_2 , respectively.)

Figure 6 shows different absorption spectra calculated at various temperatures using the Morse potential to describe the initial and final states. The parameters used in Figure 6 are close to those reported for CS_2 molecule in refs 7–9. Figure 6 was

calculated with $\chi'' = 0.02$, $\omega'' = 50 \text{ cm}^{-1}$, $\chi' = 0.01$, $\omega' = 50 \text{ cm}^{-1}$, and $r_e - r_e'' = 0.910$. Figure 7, on the other hand, illustrates single-site absorption spectra with steep anharmonicity; it is calculated using values of $\chi'' = \chi' = 0.08$, $\omega'' = \omega' = 50 \text{ cm}^{-1}$, and $r_e - r_e'' = 0.910$ at the indicated temperatures. Figure 7 uses a largely anharmonic system with only six vibrational bound states in the upper and lower electronic states. Although the parameters in Figures 6 and 7 are the same, except for the anharmonicity constant, one can see how much of a critical role the potential anharmonicity may play in describing the spectra at hand. Although both figures were calculated using the Morse oscillator model, one can see how the disparity between the two sets of spectra starts to develop at higher temperatures, because of anharmonicity differences. Significant differences in the spectra in both figures are observed at high temperatures, and those differences are attributed to the differences in FCFs, which are governed by χ^2 .

It is worth noting, in light of Figures 6 and 7, that making a comparison between two Morse oscillators can sometimes be pointless, which is very unlike comparing two harmonic oscillators. This is because the number of bound states in a Morse potential is intimately dependent on the extent of its anharmonicity; for example, a largely anharmonic Morse oscillator can have as few as two bound states, whereas a Morse potential with a small anharmonicity (typically found to be ~ 0.02 in diatomics) can confine as many as 100 bound states. Comparing these two Morse oscillators would yield dissimilar results. Similarly, one must be cautious when comparing Kratzer and Morse oscillators. While the former has two parameters, namely, the bond length (r_e) and strength (D_e), the latter has r_e , D_e , and anharmonicity constants, which can influence the shape and, therefore, the spectral dynamics, of the Morse potential upon optical excitation. Thus, the anharmonicity constant may dramatically affect the lineshape, depending on its value. In contrast, the shape of the Kratzer potential does not vary upon excitation, because it lacks a potential width parameter (anharmonicity constant). However, under a carefully designed set of conditions, one may make the comparison.

VIII. CONCLUDING REMARKS

The motivation for this work is 2-fold: first, the report by Van Hooydonk¹² on the superiority of the Kratzer potential over the Morse potential in modeling ~ 300 diatomic molecules, and second, our calculation, which shows that the former potential gives much better vibrational ground-state energy for molecular hydrogen (H_2) than both Morse and harmonic oscillators (see section VII). The Kratzer oscillator features several advantages, which the Morse oscillator does not have, two of which are the ability to exactly solve the Schrodinger equation after including the centrifugal term, and the ability to obtain finite matrix elements in case of finite angular momenta, as noted in section I. It should be kept in mind that the Morse potential is a three-parameter potential, which will always have this “extra third parameter” as a merit over that of Kratzer, which will often make it outperform the Kratzer oscillator. However, as noted earlier, that extra parameter was not as helpful in calculating the vibrational ground-state energy of H_2 : only the Kratzer oscillator can reasonably match its observed value in the laboratory, and not that of the Morse oscillator.

The dynamics of the Morse and Kratzer oscillators can be challenging under some conditions. Prezdho¹⁴ and Cao³³ studied the dynamics of the Morse oscillator, where divergence

problems arose. Therefore, as a maneuvering tactic, one may attempt to employ wavelets, because they have proven to be robust tools in treating divergence- and singularity-related problems. Also, it turns out that the Morse oscillator can readily be mapped onto the rotating Kratzer oscillator, as carried out by Stanek,¹⁵ which, in turn, allows for the latter oscillator Wigner distribution function to be obtained.³⁴ This is important, because one can then work in phase space to probe mixed quantum-classical dynamics (MQCD), using an anharmonic Wigner distribution function, since MQCD formalism relies heavily on Wigner transforms and their properties for calculating cross- and autocorrelation functions in the mixed quantum-classical limit.^{35–38}

In addition, Cooper¹⁷ also presented a unified, and extremely useful, approach for utilizing Kratzer and Morse oscillators harmonically, using a combination of nonlinear coordinate transformation and similarity transformation. This transformation should allow for development of the time-Green's function of the Kratzer oscillator, whereby more efficient and accurate spectroscopy of complex systems may be probed. Finally, as an additional method to test the consistency with experiments, one may consider evaluating Franck–Condon factors (FCFs) upon making a transition from a Kratzer potential to that of Morse, to better suit the experimental conditions, *vide supra*, of the system of interest. However, the integrals that arise are challenging, because they tend to be of a two-center integral nature, and the best way to handle such a case is through the use of elliptical coordinates.

■ AUTHOR INFORMATION

Corresponding Author

E-mail: Mtoutounji@uaeu.ac.ae.

■ ACKNOWLEDGMENT

The author would like to thank Professors G. Van Hooydonk and M. Molski for useful discussions.

■ REFERENCES

- (1) Toutounji, M. *Int. J. Quantum Chem.* **2010**, in press.
- (2) Toutounji, M. *J. Phys. Chem. B* **2010**, DOI: 10.1021/jp104731s, and references therein.
- (3) Toutounji, M. *J. Phys. Chem. C* **2010**, *114* (48), 20764–20774, and references therein.
- (4) Moix, J. M.; Pollak, E. *J. Chem. Phys.* **2008**, *129*, 064515.
- (5) Grad, J.; Yan, Y.; Mukamel, S. *J. Chem. Phys.* **1986**, *86*, 3441.
- (6) Yan, Y.; Mukamel, S. *J. Chem. Phys.* **1988**, *88*, 5735.
- (7) Tanimura, Y.; Ishaizaki, A. *Acc. Chem. Res.* **2009**, *42*, 1270 and references therein.
- (8) Suzuki, Y.; Tanimura, Y. *Phys. Rev. E* **1999**, *59*, 1475 and references therein.
- (9) Tanimura, Y.; Maruyama, Y. *J. Chem. Phys.* **1997**, *107*, 1779.
- (10) Waldenstrom, S.; Razi, N. K. *J. Chem. Phys.* **1987**, *87*, 3563.
- (11) Secrest, D. *J. Chem. Phys.* **1988**, *89*, 1017.
- (12) Van Hooydonk, G. *Eur. J. Inorg. Chem.* **1999**, 1617.
- (13) Wang, Z.; Heller, E. *J. Phys. A: Math. Theor.* **2009**, *42*, 285304.
- (14) Heatwole, E. M.; Prezdho, O. V. *J. Chem. Phys.* **2009**, *130*, 244111.
- (15) Stanek, J. *Int. J. Quantum Chem.* **2009**, *110*, 1615.
- (16) Molski, M. *Phys. Rev. A* **2007**, *76*, 022107.
- (17) Cooper, I. *Chem. Phys.* **1988**, *121*, 343.
- (18) Fernández, F. M.; Castro, E. A. *Three-Dimensional Lie Algebras and Some of Their Realizations in Quantum Mechanics*. Chapter 5

in *Algebraic Methods in Quantum Chemistry and Physics*; Klein, D., Randic, M., Eds.; CRC Press: Boca Raton, FL, 1996; p 71.

(19) Saad, N.; Hall, R.; Katabeh, D., Q. *J. Math. Phys.* **2005**, *46*, 022104.

(20) Saad, N.; Hall, R. *J. Phys. A: Math. Gen.* **2003**, *36*, 7771.

(21) Murley, J.; Saad, N. *Tables of the Appell Hypergeometric Functions ${}_2F_2$* ; arXiv:0809.5203v1 [math-ph], 2008. (Accessible via the Internet at <http://arxiv.org/abs/0809.5203v1>.)

(22) Matamala, A. *Int. J. Quantum Chem.* **2002**, *89*, 129.

(23) Setare, M. R.; Karimi, E. *Phys. Scr.* **2007**, *75*, 90.

(24) Van Hooydonk, G. *Spectrochim. Acta, Part A* **2000**, *56*, 2273.

(25) Van Hooydonk, G. *Phys. Rev. Lett.* **2008**, *100*, 159301.

(26) Van Hooydonk, G. *Z. Naturforsch.* **2009**, *64a*, 801.

(27) Opps, S; Saad, N.; Srivastava, H., M. *J. Math. Anal. Appl.* **2005**, *302*, 180.

(28) Toutounji, M.; Small, G. J.; Mukamel, S. *J. Chem. Phys.* **1998**, *109*, 7949.

(29) Toutounji, M.; Small, G. J. *J. Chem. Phys.* **2002**, *117*, 3848.

(30) Hays, J.; Lyle, P. A.; Small, G. J. *J. Phys. Chem.* **1994**, *98*, 7337 and references therein.

(31) Reinot, T.; Kim, W.-H.; Hayes, J. M.; Small, G. J. *J. Chem. Phys.* **1996**, *104*, 793.

(32) Reinot, T.; Kim, W.-H.; Hayes, J. M.; Small, G. J. *J. Chem. Phys.* **1997**, *106*, 457.

(33) Wu, J.; Cao, J. *J. Chem. Phys.* **2001**, *115*, 5381.

(34) Bund, G., W.; Tijero, M. C. *J. Phys. A: Math. Gen.* **2004**, *37*, 3687.

(35) Toutounji, M.; Kapral, R. *Chem. Phys.* **2001**, *268*, 279.

(36) Toutounji, M. *Chem. Phys.* **2003**, *293*, 311.

(37) Toutounji, M. *J. Chem. Phys.* **2005**, *123*, 244102.

(38) Toutounji, M. *J. Chem. Phys.* **2006**, *125*, 194520.

Excited-State Electronic Structure with Configuration Interaction Singles and Tamm–Dancoff Time-Dependent Density Functional Theory on Graphical Processing Units

Christine M. Isborn,^{†,‡} Nathan Luehr,^{†,‡} Ivan S. Ufimtsev,^{†,‡} and Todd J. Martínez^{*,†,‡}

[†]PULSE Institute and Department of Chemistry, Stanford University, Stanford, California 94305, United States

[‡]SLAC National Accelerator Laboratory, Menlo Park, California 94025, United States

 Supporting Information

ABSTRACT: Excited-state calculations are implemented in a development version of the GPU-based TeraChem software package using the configuration interaction singles (CIS) and adiabatic linear response Tamm–Dancoff time-dependent density functional theory (TDA-TDDFT) methods. The speedup of the CIS and TDDFT methods using GPU-based electron repulsion integrals and density functional quadrature integration allows full ab initio excited-state calculations on molecules of unprecedented size. CIS/6-31G and TD-BLYP/6-31G benchmark timings are presented for a range of systems, including four generations of oligothiophene dendrimers, photoactive yellow protein (PYP), and the PYP chromophore solvated with 900 quantum mechanical water molecules. The effects of double and single precision integration are discussed, and mixed precision GPU integration is shown to give extremely good numerical accuracy for both CIS and TDDFT excitation energies (excitation energies within 0.0005 eV of extended double precision CPU results).

INTRODUCTION

Single excitation configuration interaction (CIS),¹ time-dependent Hartree–Fock (TDHF), and linear response time-dependent density functional theory (TDDFT)^{2–6} are widely used for ab initio calculations of electronic excited states of large molecules (more than 50 atoms, thousands of basis functions) because these single-reference methods are computationally efficient and straightforward to apply.^{7–9} Although highly correlated and/or multireference methods, such as multireference configuration interaction (MRCI),¹⁰ multireference perturbation theory (MRMP¹¹ and CASPT2),¹² and equation-of-motion coupled cluster methods (SAC-CI¹³ and EOM-CC),^{14,15} allow for more reliably accurate treatment of excited states, including those with double excitation character, these are generally too computationally demanding for large molecules.

CIS/TDHF is essentially the excited-state corollary of the ground-state Hartree–Fock (HF) method and thus similarly suffers from a lack of electron correlation. Because of this, CIS/TDHF excitation energies are consistently overestimated, often by ~ 1 eV.⁸ The TDDFT method includes dynamic correlation through the exchange–correlation functional, but standard nonhybrid TDDFT exchange–correlation functionals generally underestimate excitation energies, particularly for Rydberg and charge-transfer states.⁵ The problem in charge-transfer excitation energies is due to the lack of the correct $1/r$ Coulombic attraction between the separated charges of the excited electron and hole.¹⁶ Charge-transfer excitation energies are generally improved with hybrid functionals and also with range separated functionals that separate the exchange portion of the DFT functional into long- and short-range contributions.^{17–21} Neither CIS nor TDDFT (with present-day functionals) properly includes the effects of

dispersion but promising results have been obtained with an empirical correction to standard DFT functionals,^{22,23} and there are continued efforts to include dispersion directly in the exchange–correlation functional.^{24,25} Both the CIS and TDDFT²⁶ single reference methods lack double excitations and are unable to model conical intersections or excitations in molecules that have multireference character.^{27,28} In spite of these limitations, the CIS and TDDFT methods can be generally expected to reproduce trends for one-electron valence excitations, which are a majority of the transitions of photochemical interest. TDDFT using hybrid density functionals, which include some percentage of HF exact exchange, has been particularly successful in modeling the optical absorption of large molecules. Furthermore, the development of new DFT functionals and methods is an avid area of research, with many new functionals introduced each year. Thus it is a virtual certainty that the quality of the results available from TDDFT will continue to increase. A summary of the accuracy currently available for vertical excitation energies is available in a recent study by Jacquemin et al. which compares TDDFT results using 29 functionals for ~ 500 molecules.²⁹

Although CIS and TDDFT are the most tractable methods for excited states of large molecules, their computational cost still prevents application to many systems of photochemical interest. Thus, there is considerable interest in extending the capabilities of CIS/TDDFT to even larger molecules, beyond hundreds of atoms.

Quantum mechanics/molecular mechanics (QM/MM) schemes provide a way to model the environment of a

Received: January 14, 2011

Published: May 12, 2011

photophysically interesting molecule by treating the molecule with QM and the surrounding environment with MM force fields.^{30–34} However, it is difficult to know when the MM approximations break down and when a fully QM approach is necessary. With fast, large-scale CIS/TDDFT calculations, all residues of a photoactive protein could be treated quantum mechanically to explore the origin of spectral tuning, for example. Explicit effects of solvent–chromophore interactions, including hydrogen bonding, charge transfer, and polarization, could be fully included at the ab initio level in order to model solvatochromic shifts.

One potential route to large scale CIS and TDDFT calculations is through exploitation of the stream processing architectures³⁵ now widely available in the form of graphical processing units (GPUs). The introduction of the compute unified device architecture³⁶ (CUDA) as an extension to the C language has greatly simplified GPU programming, making it more easily accessible for scientific programming. GPUs have already been applied to achieve speed-ups of orders of magnitude in ground-state electronic structure,^{37–40} ab initio molecular dynamics⁴¹ and empirical force field-based molecular dynamics calculations.^{42–45}

In this article we extend our implementation of GPU quantum chemistry in the newly developed TeraChem program⁴⁶ beyond our previous two-electron integral evaluation⁴⁷ and ground-state self-consistent field,^{39,48,49} geometry optimization, and dynamics calculations⁴¹ to also include the calculation of excited electronic states. We use GPUs to accelerate both the matrix multiplications within the CIS/TDDFT procedure and also the integral evaluation (these steps comprise most of the effort in the calculation). The computational efficiency that arises from the use of redesigned quantum chemistry algorithms on GPU hardware to evaluate electron repulsion integrals (ERIs) allows full QM treatment of the excited states of very large systems—both large chromophores and chromophores in which the environment plays a critical role and should be treated with QM. We herein present the results of implementing CIS and TDDFT within the Tamm–Dancoff approximation using GPUs to drastically speed up the bottleneck two-electron integral evaluation, density functional quadrature, and matrix multiplication steps. This results in CIS calculations over 400 times faster than those achieved running on a comparable CPU platform. Benchmark CIS/TDDFT timings are presented for a variety of systems.

■ CIS/TDDFT IMPLEMENTATION USING GPUS

The linear response formalism of TDHF and TDDFT has been thoroughly presented in review articles.^{4,7,8,50} Only the equations relevant for this work are presented here, and real orbitals are assumed throughout. The TDHF/TDDFT working equation for determining the excitation energies ω and corresponding X and Y transition amplitudes is

$$\begin{pmatrix} A & B \\ B & A \end{pmatrix} \begin{pmatrix} X \\ Y \end{pmatrix} = \omega \begin{pmatrix} 1 & 0 \\ 0 & -1 \end{pmatrix} \begin{pmatrix} X \\ Y \end{pmatrix} \quad (1)$$

where for TDHF (neglecting spin indices for simplicity):

$$A_{ai,bj} = \delta_{ij}\delta_{ab}(\varepsilon_a - \varepsilon_i) + (ia|jb) - (ij|ab) \quad (2)$$

$$B_{ai,bj} = (ia|bj) - (ib|aj) \quad (3)$$

and for TDDFT:

$$A_{ai,bj} = \delta_{ij}\delta_{ab}(\varepsilon_a - \varepsilon_i) + (ia|jb) + (ij|f_{xc}|ab) \quad (4)$$

$$B_{ai,bj} = (ia|bj) + (ib|f_{xc}|aj) \quad (5)$$

The two electron integrals (ERIs) are defined as

$$(ia|jb) = \iint \frac{\phi_i(r_1)\phi_a(r_1)\phi_j(r_2)\phi_b(r_2)}{|r_1 - r_2|} dr_1 dr_2 \quad (6)$$

and within the adiabatic approximation of density functional theory, in which the explicit time dependence of the exchange–correlation functional is neglected:

$$(ia|f_{xc}|jb) = \iint \phi_i(r_1)\phi_a(r_1) \frac{\delta^2 E_{xc}}{\delta\rho(r_1)\delta\rho(r_2)} \phi_j(r_2)\phi_b(r_2) dr_1 dr_2 \quad (7)$$

The ij and ab indices represent occupied and virtual molecular orbitals (MOs), respectively, in the HF/Kohn–Sham (KS) ground-state determinant.

Setting the B matrix to zero within TDHF results in the CIS equation, while in TDDFT this same neglect yields the equation known as the Tamm–Dancoff approximation (TDA):

$$AX = \omega X \quad (8)$$

In part because DFT virtual orbitals provide a better starting approximation to the excited state than HF orbitals, the TDA generally gives results that are very close to the full linear response TDDFT results for nonhybrid DFT functionals at equilibrium geometries.^{7,8,51} Furthermore, previous work has shown that a large contribution from the B matrix in TDDFT (and to a lesser extent also in TDHF) is often indicative of a poor description of the ground state, either due to singlet–triplet instabilities or multireference character.⁵² Casida and co-workers have examined the breakdown of TDDFT in modeling photochemical pathways⁵² and have come to the conclusion that “the TDA gives better results than does conventional TDDFT when it comes to excited-state potential energy surfaces in situations where bond breaking occurs.” Thus, if there is substantial deviation between the full TDDFT and TDA-TDDFT excitation energies, then the TDA results will often be more accurate.

A standard iterative Davidson algorithm⁵³ has been implemented to solve the CIS/TDA-TDDFT equations. As each AX matrix–vector product is formed, the required two-electron integrals are calculated over primitive basis functions within the atomic orbital (AO) basis directly on the GPU. Within CIS, the AX matrix–vector product is calculated as

$$(A^{\text{CIS}}X)_{bj} = \sum_{ia} [\delta_{ij}\delta_{ab}(\varepsilon_a - \varepsilon_i) + (ia|jb) - (ij|ab)] X_{ia} \quad (9)$$

$$\sum_{ia} [(ia|jb) - (ij|ab)] X_{ia} = \sum_{\mu\nu} C_{\mu j} C_{\nu b} F_{\mu\nu} \quad (10)$$

$$F_{\mu\nu} = \sum_{\lambda\theta} T_{\lambda\theta} \{(\mu\nu|\lambda\theta) - (\mu\lambda|\nu\theta)\} \quad (11)$$

$$T_{\lambda\theta} = \sum_{ia} X_{ia} C_{\lambda i} C_{\theta a} \quad (12)$$

Here Greek indices represent AO basis functions, $C_{\lambda i}$ is the ground-state MO coefficient of the HF/KS determinant, and $T_{\lambda\theta}$

is a nonsymmetric transition density matrix. For very small matrices, there is no time savings with GPU computation of the matrix multiplication steps in eqs 10 and 12. For matrices of dimension less than 300, we thus perform the linear algebra on the CPU. For larger matrices, the linear algebra is performed on the GPU using calls to the NVIDIA CUBLAS library, a CUDA implementation of the BLAS library.⁵⁴

In quantum chemistry the AO basis functions are generally a linear combination of primitive atom-centered Gaussian basis functions. For a linear combination of M primitive basis functions χ centered at a nucleus, the contracted AO basis function ϕ_μ is

$$\phi_\mu(\mathbf{r}) = \sum_{m=1}^M c_{\mu m} \chi_m(\mathbf{r}) \quad (13)$$

Thus the two-electron integrals in the contracted AO basis that need to be evaluated for eq 11 above are given by

$$(\mu\nu|\lambda\theta) = \sum_{m_1}^{M_\mu} \sum_{m_2}^{M_\nu} \sum_{m_3}^{M_\lambda} \sum_{m_4}^{M_\theta} c_{\mu m_1} c_{\nu m_2} c_{\lambda m_3} c_{\theta m_4} [\chi_{m_1} \chi_{m_2} | \chi_{m_3} \chi_{m_4}] \quad (14)$$

where parentheses indicate integrals over contracted basis functions and square brackets indicate integrals over primitive functions.

While transfer of matrix multiplication from the CPU to the GPU provides some speedup, the GPU acceleration of the computation of the ERIs delivers a much more significant reduction in computer time. Details of our GPU algorithms for two-electron integrals in the \mathbf{J} and \mathbf{K} matrices (Coulomb and exchange operators, respectively) have been previously published,^{39,47} so we only briefly highlight information relevant to our excited-state implementation, which uses these algorithms. Both J and K algorithms employ extensive screening and presorting on the CPU. The GPU evaluates the \mathbf{J} and \mathbf{K} matrices over primitives, and these are contracted on the CPU. Initially pairs of primitive atomic orbital functions are combined using the Gaussian product rule into a set of bra- and ket- pairs. A prescreening threshold is used to remove negligible pairs, and the remaining pairs are sorted by angular momentum class and by their [bra] or [ket] contribution to the total [bra|ket] Schwarz bounds, respectively.⁵⁵ All data needed to calculate the [bra|ket] integrals (e.g., exponents, contraction coefficients, atomic coordinates, etc.) are then distributed among the GPUs. The Coulomb \mathbf{J} matrix and exchange \mathbf{K} matrix are calculated separately, with both algorithms designed to minimize interthread communication by ensuring that each GPU has all necessary data for its share of integrals. The [bra] and [ket] pairs are processed in order of decreasing bound, and execution is terminated once the combined [bra|ket] bound falls below a predetermined threshold. Because the ground-state density matrix is symmetric, both the ground-state \mathbf{J} and \mathbf{K} matrices are also symmetric, and thus only the upper triangle of each needs to be computed.

The Coulomb \mathbf{J} matrix elements are given by

$$J_{\mu\nu} = \sum_{\lambda\theta} P_{\lambda\theta}(\mu\nu|\lambda\theta) \quad (15)$$

Within our \mathbf{J} matrix algorithm, one GPU thread evaluates one primitive two-electron integral using the Hermite Gaussian formulation as in the McMurchie–Davidson algorithm,^{56,57} which then must be contracted into the final \mathbf{J} matrix element as given in eq 15. \mathbf{J} matrix computation uses the $\mu\nu \leftrightarrow \nu\mu$ and $\lambda\theta \leftrightarrow \theta\lambda$ symmetry and eliminates duplicates within the bra and ket

primitive Hermite product lists, reducing the number of integrals calculated from $O(N^4)$ to $O(N^4/4)$. A different GPU subroutine (or GPU kernel) is called for each angular momentum class, leading to nine GPU kernel calls for all s - and p - combinations: $[ss|ss]$, $[ss|sp]$, $[ss|pp]$, $[sp|ss]$, $[sp|sp]$, $[sp|pp]$, $[pp|ss]$, $[pp|sp]$, and $[pp|pp]$. Many integrals are calculated twice because [bra|ket] \leftrightarrow [ket|bra] symmetry is not taken into account. This is intentional—it is often faster to carry out more (but simpler) computations on the GPU (compared to an algorithm that minimizes the number of floating point operations) in order to avoid bookkeeping overhead and/or memory access bottlenecks. This may be viewed as a continuation of a trend that began already on CPUs and has been discussed in that context previously.⁵⁸

The maximum density matrix element of all angular momentum components weights the ket contribution to the Schwarz upper bound. This allows the \mathbf{J} matrix algorithm to take complete advantage of sparsity in the density matrix, since there is a one-to-one mapping between ket pairs and density matrix elements. Also, because density matrix elements are packed together with the \mathbf{J} matrix ket integral data, its memory access pattern is contiguous, i.e., neighboring threads access neighboring memory addresses. In general, noncontiguous access patterns increase the number of executed memory operations, hampering GPU performance.

The exchange \mathbf{K} matrix elements are given by

$$K_{\mu\nu} = \sum_{\lambda\theta} P_{\lambda\theta}(\mu\lambda|\nu\theta) \quad (16)$$

Within our \mathbf{K} matrix algorithm, one block of GPU threads evaluates one \mathbf{K} matrix element and thereby avoids any communication with other thread blocks. Because the integrals (bra| $\nu\theta$) and (bra| $\theta\nu$) are paired with different density matrix elements, the \mathbf{K} matrix algorithm does not take into account the $\mu\lambda \leftrightarrow \lambda\mu$ and $\nu\theta \leftrightarrow \theta\nu$ symmetry. On the other hand, [bra|ket] \leftrightarrow [ket|bra] symmetry is used, leading to $O(N^4/2)$ integrals computed to form the final \mathbf{K} matrix.

In addition to having to compute more integrals than is required for the \mathbf{J} matrix computation, the \mathbf{K} matrix computation is slowed relative to \mathbf{J} matrix computation by two additional issues. The first is that unlike the \mathbf{J} matrix GPU implementation, the \mathbf{K} matrix algorithm cannot map the density matrix elements onto the ket integral data, since the density index now spans both bra and ket indices. Instead each thread must load an independent density matrix element noncontiguously. The second issue facing \mathbf{K} matrix computation is that because the sparsity of the density cannot be included in the presorting of ket pairs, the sorted integral bounds cannot be guaranteed to be strictly decreasing, and a more stringent cutoff threshold (still based on the product of the density matrix element and the Schwarz upper bound) must be applied for \mathbf{K} kernels, meaning that \mathbf{K} computation does not take as much advantage of density matrix sparsity as \mathbf{J} computation. As a result of these drawbacks, the exchange matrix takes longer to calculate than its Coulomb counterpart. Based solely on the number of integrals required, the \mathbf{K}/\mathbf{J} timing ratio for ground-state SCF calculations should be ~ 2 . In practice, with the memory access and the thresholding issues, values of 3–5 are more common.

In our excited-state calculations, we use the same \mathbf{J} and \mathbf{K} matrix GPU algorithms, adjusted for the fact that the nonsymmetric transition density matrix \mathbf{T} replaces the symmetric ground-state density matrix \mathbf{P} . The portion of the \mathbf{F} matrix from

the product of $T_{\lambda\theta}$ with the first integral in eq 11 is computed with the **J** matrix algorithm. The portion of the **F** matrix from the product of $T_{\lambda\theta}$ with the second integral in eq 11 is computed with the **K** matrix algorithm. While the **J** matrix remains symmetric even with a nonsymmetric transition density matrix, the **K** matrix does not. We must thus calculate both the upper and lower triangle contributions for the CIS/TDDFT **K** matrix, resulting in two calls to the **K** matrix algorithm and computation of up to $O(N^4)$ integrals. In addition to an increased number of integrals in the excited state, the **K**/**J** timing discrepancy (comparing CIS/TDDFT to ground-state SCF calculations) is also increased due to the sparseness of the transition density compared to the ground-state density.

Evaluation of the exchange–correlation functional contribution from eq 7 needed for TDDFT excited states⁷ is performed using numerical quadrature on a three-dimensional grid, which

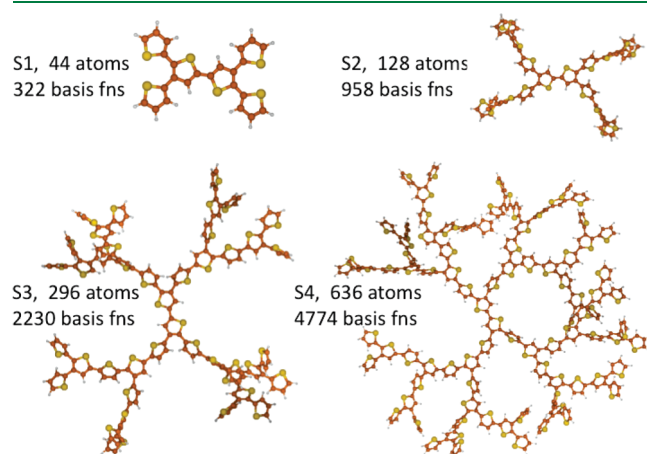


Figure 1. Structures, number of atoms, and basis functions (fns) using the 6-31G basis set for four generations of oligothiophene dendrimers, S1–S4. Carbon atoms are orange, and sulfur atoms are yellow.

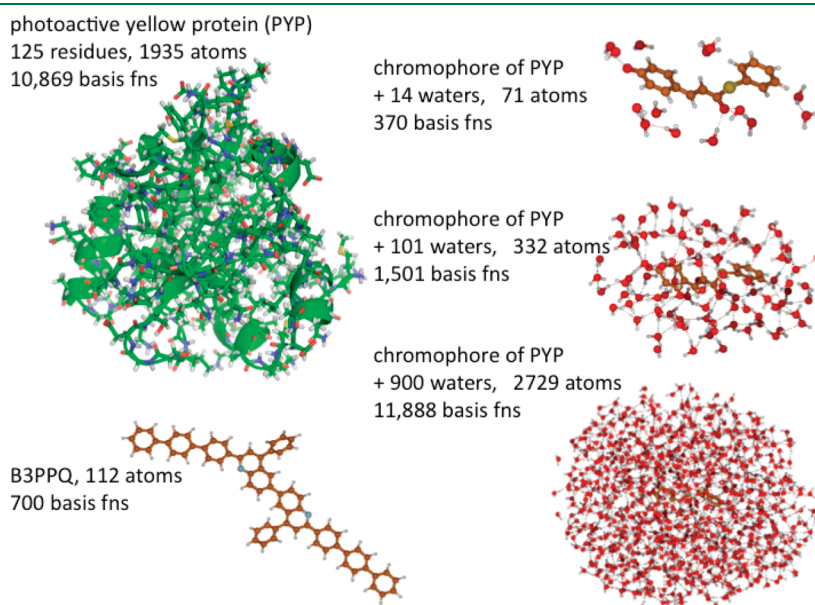


Figure 2. Structures, number of atoms, and basis functions (fns) for the 6-31G basis for benchmark systems photoactive yellow protein (PYP), the solvated PYP chromophore, and oligoquinoline B3PPQ. For PYP, carbon, nitrogen, oxygen, and sulfur atoms are green, blue, red, and yellow, respectively. For the other molecules, atom coloration is as given in Figure 1, with additional red and blue coloration for oxygen and nitrogen atoms, respectively.

maps efficiently onto massively parallel architectures, such as the GPU. This was recently demonstrated for ground-state DFT, for both GPU^{38,41} and related⁵⁹ architectures. The expensive steps are evaluating the electron density/gradient at the grid quadrature points to numerically determine the necessary functional derivatives and summing the values on the grid to assemble the matrix elements of eq 7. We use a Becke-type quadrature scheme⁶⁰ with Lebedev angular⁶¹ and Euler–Maclaurin radial⁶² quadrature grids. For the excited-state calculations, we generate the second functional derivative of the exchange–correlation functional only once, saving its value at each quadrature point in memory. Then, for each Davidson iteration, the appropriate integrals are evaluated, paired with the saved functional derivative values, and summed into matrix elements.

RESULTS AND DISCUSSION

We evaluate the performance of our GPU-based CIS/TDDFT algorithm on a variety of test systems: 6,6'-bis(2-(1-triphenyl)-4-phenylquinoline) (B3PPQ), an oligoquinoline recently synthesized and characterized by the Jenekhe group for use in OLED devices⁶³ and characterized theoretically by Tao and Tretiak;⁶⁴ four generations of oligothiophene dendrimers that are being studied for their interesting photophysical properties;^{65–67} the entire photoactive yellow protein (PYP)⁶⁸ solvated by TIP3P⁶⁹ water molecules; and deprotonated *trans*-thiophenyl-*p*-coumarate, an analogue of the PYP chromophore⁷⁰ that takes into account the covalent cysteine linkage, solvated with an increasing number of QM waters. We use the 6-31G basis set for all computations, since we do not yet have GPU integral routines implemented for *d*-functions. This limits the quality of the excited-state energies, as polarization functions can give improved accuracy relative to experimental values and are often necessary for metals and hypervalent atoms, such as sulfur and phosphorus. Benchmark structures are shown in Figures 1 and 2 along with the number of atoms and basis functions for a 6-31G

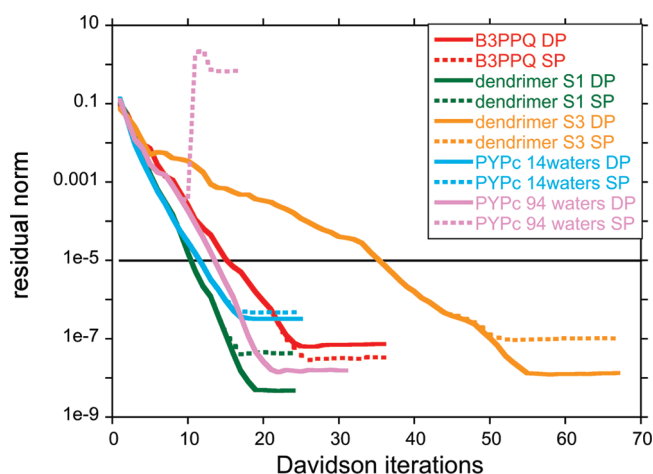


Figure 3. Plot of single and double precision (SP and DP) convergence behavior for the first CIS/6-31G excited state of five of the benchmark systems. The convergence threshold of 10^{-5} (norm of residual vector) is indicated with a straight black line. In most cases, convergence behavior is identical for single and double precision integration until very small residual values well below the convergence threshold. A very small percentage of calculations require double precision for convergence. One such example is shown here for a snapshot of the PYP chromophore (PYPc) surrounded by 94 waters.

basis set. For the solvated PYP chromophore, only three structures are shown in Figure 2, but benchmark calculations are presented for 15 systems with increasing solvation, starting from the chromophore in vacuum and adding water molecules up to a 16 Å solvation shell, which corresponds to 900 water molecules. Cartesian coordinates and geometry details for all structures are provided in the Supporting Information.

For our benchmark TDDFT calculations, we use the generalized gradient approximation with Becke's exchange functional⁷¹ combined with the Lee, Yang, and Parr correlation functional⁷² (BLYP), as well as the hybrid B3LYP functional. During the SCF procedure for the ground-state wave function, we use two different DFT grids. A sparse grid of ~ 1000 grid points/atom is used to converge the wave function until the DIIS error reaches a value of 0.01, followed by a more dense grid of ~ 3000 grid points/atom until the ground-state wave function is fully converged. This denser grid is also used for the excited-state TDDFT timings reported herein, unless otherwise noted.

An integral screening threshold value of 1×10^{-11} atomic units is used by default unless otherwise noted. Within TeraChem, this means that Coulomb integrals with products of the density element and Schwarz bound below the integral screening threshold are not computed, and exchange integrals with products of the density element and Schwarz bound below the threshold value times a guard factor of 0.001 are not computed. The initial N^2 pair quantities list is also pruned, with a default pruning value of 10^{-15} for removing pairs from integral computation. The pair quantity pruning value is set to the smaller of 10^{-15} and $0.01 \times$ the integral screening threshold. The timings reported herein were obtained on a desktop workstation using dual quad-core Intel Xeon X5570 CPUs, 72 GB RAM, and 8 Tesla C1060 GPUs.

All CPU operations are performed in full double precision arithmetic, including one-electron integral evaluation, integral postprocessing and contraction, and diagonalization of the subspace matrix of **A**. To minimize numerical error, integral

accumulation also uses double precision. Calculations carried out on the GPU (Coulomb and exchange operator construction and DFT quadrature) use mixed precision unless otherwise noted. The mixed precision integral evaluation is a hybrid of 32- and 64-bit arithmetic. In this case, integrals with Schwarz bounds larger than 0.001 au are computed in full double precision, and all others are computed in single precision. The potential advantages of mixed precision arithmetic in quantum chemistry have been discussed in the context of GPU architectures by several groups^{47,73,74} and stem in part from the fact that there are often fewer double precision floating point units on a GPU than single precision floating point units. To study the effects of using single precision on excited-state calculations, we have run the same CIS calculations using both single and double precision integral evaluation for many of our benchmark systems.

In general we find that mixed (and often even single) precision arithmetic on the GPU is more than adequate for CIS/TDDFT. In most cases we find that the convergence behavior is nearly identical for single and double precision until the residual vector is quite small. Figure 3 shows the typical single and double precision convergence behavior as represented by the CIS residual vector norm convergence for B3PPQ, the first and third generations of oligothiophene dendrimers S1 and S3, and a snapshot of the PYP chromophore surrounded by 14 waters. The convergence criterion of the residual norm, which is 10^{-5} au, is shown with a straight black line. Note that for the examples in Figure 3, we are not using mixed precision—all two-electron integrals on the GPU are done in single precision (with double precision accumulation as described previously).³⁹ This is therefore an extreme example (other calculations detailed in this paper used mixed precision where large integrals and quadrature contributions are calculated in double precision) and serves to show that CIS and TDDFT are generally quite robust, irrespective of the precision used in the calculation. Nevertheless, a few problematic cases have been found in which single precision integral evaluation is not adequate and where double precision is needed to achieve convergence.⁷⁵ During the course of hundreds of CIS calculations performed on snapshots of the dynamics of the PYP chromophore solvated by various numbers of water molecules, a small number (<1%) of cases yield ill-conditioned Davidson convergence when single precision is used for the GPU-computed ERIs and quadrature contributions. For illustration, the single and double precision convergence behavior for one of these rare cases, here the PYP chromophore with 94 waters, is shown in Figure 3. In practice, this is not a problem since one can always switch to double precision, and this can be done automatically when convergence problems are detected. Recent work in our group⁷⁶ shows a speedup of 2–4 times for an RHF ground-state calculation in going from full double precision to mixed or single precision for our GPU ERI algorithms. Similar speedups are observed here for excited-state calculations.

Timings and CIS excitation energies (from the ground-state S_0 to the lowest singlet excited state S_1) for some of the test systems are given in Table 1 and compared to the GAMESS quantum chemistry package version 12 Jan 2009 (R3). The GAMESS timings are obtained using the same Intel Xeon X5570 eight-core machine as for the GPU calculations (where GAMESS is running in parallel over all eight cores). We compare to GAMESS because it is a freely available and mature quantum chemistry code and provides a reasonable benchmark of the expected speed of the algorithms on a CPU. GAMESS may not represent the absolute best performance that can be achieved using the implemented

Table 1. Time for CIS computation, relative speedups of SCF and CIS computation for GPU-based TeraChem compared to CPU-based GAMESS, and first excited-state energies ($\Delta E_{S_0/S_1}$)^a

molecule (atoms; basis functions)	CIS timings (s)		speedup		$\Delta E_{S_0/S_1}$ (eV)	
	GPU	GAMESS	SCF	CIS	GPU	GAMESS
B3PPQ oligoquinoline (112; 700)	41.9	371.5	11	9	4.7056398	4.7056482
S2 oligothiophene dendrimer (128; 958)	97.1	755.9	13	8	4.1130572	4.1130275
PYP chromophore + 101 waters (332; 1501)	133.2	3032.7	48	23	3.6409681	3.6409411
PYP chromophore + 146 waters (467; 2086)	217.5	8654.9	84	40	3.6394478	3.6394222
PYP chromophore + 192 waters (605; 2684)	318.1	20546.8	131	65	3.6425942	3.6425632
PYP chromophore + 261 waters (812; 3581)	493.2	57800.5	218	117	3.6454079	3.6453773
PYP chromophore + 397 waters (1220; 5349)	894.0	243975.7	426	273	3.6496150	3.6495829
PYP chromophore + 487 waters (1490; 6519)	1221.2	562606.6	547	461	3.6549966	3.6549636

^a Calculations were performed on a dual Intel Xeon X5570 (8 CPU cores) with 72 GB RAM. GPU calculations use 8 Tesla C1060 GPU cards.

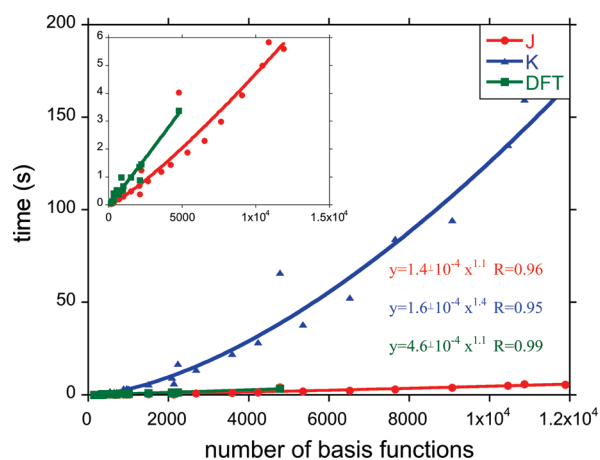


Figure 4. Contributions to the time for building an initial **AX** vector in CIS and TD-BLYP. Ten initial **X** vectors are created based on the MO energy gap, and the timing reported is the average time for building **AX** for those 10 vectors. The timings are obtained on a dual Intel Xeon X5570 platform with 72 GB RAM using 8 Tesla C1060 GPUs. Data (symbols) are fit to power law (solid line, fitting parameters in inset). Fewer points are included for the TD-BLYP timings because the SCF procedure does not converge for the solvated PYP chromophore with a large number of waters or for the full PYP protein.

algorithms on a CPU.⁴⁰ Coordinates of all the geometries used in the tests are provided in Supporting Information, so the interested reader can determine timings for other codes and architectures if further comparisons are desired. Unfortunately, it is not possible to compare our own code against itself, running on the CPU or GPU, since there does not presently exist a compiler that can generate a CPU executable from CUDA code.

Comparing the values for the CIS first excited-state energy ($\Delta E_{S_0/S_1}$) given in Table 1, we find that the numerical accuracy of the excitation energies for mixed precision GPU integral evaluation is excellent for all systems studied. The largest discrepancy in the reported excitation energies between GAMESS and our GPU implementation in TeraChem is less than 0.00004 eV. We also report the CIS times and speedups for GAMESS and GPU accelerated CIS in TeraChem (note that the times reported refer to the entire CIS calculation from the completion of the ground-state SCF to the end of program execution). Since CIS is necessarily preceded by a ground-state SCF calculation, we also report the SCF speedups to give a

complete picture. We leave out the absolute SCF times, since the efficiency of the GPU-based SCF algorithm has been discussed for other test molecules previously.^{39,41,76} We find a large increase in performance is obtained using the GPU for both ground- and excited-state methods. The speedups increase as system size increases, with SCF speedups outperforming CIS speedups. For the largest system compared with GAMESS, which is the 29 atom chromophore of PYP surrounded by 487 QM water molecules, the speedup is well over 500 times for SCF and 400 times for CIS. Some possible reasons for the differing speedups in ground- and excited-state calculations are discussed below.

In the Supporting Information, we also include a table giving the absolute TeraChem SCF and CIS times for four of the test systems, along with the corresponding SCF and CIS energies, for both mixed and double precision computation and for three different integral screening threshold values. While the timings increase considerably in switching from mixed precision to double precision and in tightening the integral screening thresholds, the CIS excitation energies remain nearly identical, suggesting that the CIS algorithm is quite robust with respect to thresholding.

The dominant computational parts in building the CIS/TDDFT **AX** vector can be divided into Coulomb **J** matrix, exchange **K** matrix, and DFT contributions. Figure 4 plots the CPU + GPU time consumed by each of these three contributions (both CPU and GPU times are included here, although the CPU time is a very small fraction of the total), in which **J** and **K** timings are taken from an average of the 10 initial guess **AX** builds for a CIS calculation, and the DFT timings are from an average of the initial guess **AX** builds for a TD-BLYP calculation. The initial guess transition densities are very sparse, and thus this test highlights the differing efficiency of screening and thresholding in these three contributions. The **J** timings for CIS and BLYP are similar, and only those for CIS are reported. Power law fits are shown as solid lines and demonstrate near-linear scaling behavior of all three contributions to the **AX** build. The **J** matrix and DFT quadrature steps are closest to linear scaling, with observed scaling of $N^{1.1}$ for both contributions, where N is the number of basis functions. The **K** matrix contribution scales as $N^{1.4}$ because it is least able to exploit the sparsity of the transition density matrix. These empirical scaling data demonstrate that with proper sorting and integral screening, the **AX** build in CIS and TDDFT scales much better than quadratic, with no loss of accuracy in excitation energies.

Table 2. TD-BLYP Timings and First Excitation Energies Using Increasingly Dense Quadrature Grids^a

grid	points	points/atom ^b	time (s) ^c	ΔE (eV)
PYP Chromophore (29 atoms)				
0	29497	1017	0.12	2.31734131
1	81461	2809	0.21	2.31743628
2	182872	6305	0.39	2.31742594
3	330208	11386	0.68	2.31736989
4	841347	29011	1.53	2.31737016
5	2126775	73337	3.77	2.31737016
NWChem/medium		21655	n/a	2.31751053
S2 Dendrimer (128 atoms)				
0	141684	1106	0.70	2.28428601
1	382576	2988	1.41	2.28429445
2	848918	6632	2.73	2.28429363
3	1506502	11769	4.54	2.28429472
4	3770640	29458	10.57	2.28429472
5	9472331	74002	25.48	2.284299472
NWChem/medium		25061	n/a	2.28445412

^aTD-BLYP timings (average time for the DFT quadrature in one AX build for the initial 10 AX vectors). For comparison, NWChem excitation energies are also given using the default 'medium' grid.

^bNumber of points/atom refers to the pruned grid for TeraChem and the unpruned grid for NWChem. ^cNWChem was run on a different architecture, so timings are not comparable.

Of the three integral contributions (J , K , and DFT quadrature), the computation of the K matrix is clearly the bottleneck. This is due to the three issues with exchange computation previously discussed: (1) the J matrix takes full advantage of density sparsity because of efficient density screening that is not possible for our K matrix implementation, (2) exchange kernels access the density in memory noncontiguously, and (3) exchange requires the evaluation of 4 times more integrals than J both because it lacks the $\mu\lambda \leftrightarrow \lambda\mu$ and $\nu\theta \leftrightarrow \theta\nu$ symmetry and because it needs to be called twice to account for the nonsymmetric excited-state transition density matrix. It is useful to compare the time required to calculate the K matrix contribution to the first ground-state SCF iteration (which is the most expensive iteration due to the use of Fock matrix updating⁷⁷) and to the AX vector build for CIS (or TD-B3LYP). We find that for the systems studied herein the K matrix contribution is on average almost 2 times faster in CIS compared to the first iteration of the ground-state SCF. One might have expected the excited-state computation to be 2 times slower because of the two K matrix calls, but the algorithm efficiently exploits the greater sparsity of the transition density matrix (compared to the ground-state density matrix).

Due to efficient prescreening of the density and integral contributions to the Schwarz bound before the GPU Coulomb kernels are launched, the J matrix computation also exploits the greater sparseness of the transition density and therefore is 3.5 times faster than the ground-state first iteration J matrix computation. Since J matrix computation profits more from transition density sparsity than K matrix computation, the current implementation of the J matrix computation scales better with system size than the implementation of the K matrix computation ($N^{1.1}$ vs $N^{1.4}$ for the excited-state benchmarks presented here).

As can be seen in Figure 4,⁷⁸ the DFT integration usually takes more time than the J matrix contribution. This is because of the larger prefactor for DFT integration, which is related to the density of the quadrature grids used. It has previously been noted⁷⁹ that very sparse grids can be more than adequate for TDDFT. We further support this claim with the data presented in Table 2, where we compare the lowest excitation energies and the average TD-BLYP integration times for the initial guess vectors for six different grids on two of the test systems. For both molecules, the excitation energies from the sparsest grid agree well with those of the more dense grids but with a substantial reduction in integration time, suggesting that a change to an ultra sparse grid for the TDDFT portion of the calculation could result in considerable time savings with little to no loss of accuracy. The TD-BLYP values computed with NWChem⁸⁰ using the default 'medium' grid are also given to show the accuracy of our implementation. The small (<0.0002 eV) differences in excitation energies between our GPU-based TD-BLYP and the CPU-based NWChem are likely due to slightly differing ground-state densities, which differ in energy by 7 microhartrees for the chromophore and 1.9 millihartrees for the S2 dendrimer.

While successive ground-state SCF iterations take less computation time than the first (because of the use of Fock matrix updating), all iterations in the excited-state calculations take roughly the same amount of time. This is the dominant reason for the discrepancy in the speedups for ground-state SCF and excited-state CIS shown in Table 1. An additional reason that the SCF speedup is greater than the CIS speedup is decreased parallel efficiency because the ground-state density is less sparse than the transition density (all of the reported calculations are running on eight GPU cards in parallel).

GPU-accelerated CIS and TDDFT computation provides the excited states of much larger compounds than can be currently studied with ab initio methods. For the well-behaved valence transitions in the PYP systems, CIS convergence requires very few Davidson iterations. The total wall time (SCF + CIS) required to calculate the first CIS/6-31G excited state of the entire PYP protein (10869 basis functions) is less than 6 h, with ~ 4.7 h devoted to the SCF procedure and ~ 1.2 h to the CIS procedure. We can thus treat the protein with full QM and study how mutation within PYP will affect the absorbance. For any meaningful comparison with the experimental absorption energy of PYP at 2.78 eV,⁷⁰ many geometrical configurations need to be taken into account. For this single configuration, the CIS excitation energy of 3.69 eV is much higher than the experimental value, as expected with CIS. The TD-B3LYP bright state (S_5) is closer to the experimental value but still too high at 3.33 eV.

Solvatochromic studies in explicit water are problematic for standard DFT methods, including hybrid functionals, due to the well-known difficulty in treating charge-transfer excitations.^{16,81} In calculating the timings for the first excited state of the PYP chromophore with increasing numbers of waters, we found that the energy of the CIS first excited state quickly leveled off and stabilized, while that for TD-BLYP and TD-B3LYP generally decreased to unphysical values, at which point the ground-state SCF convergence was also problematic. This behavior of the first excitation energies for the PYP chromophore with increasing numbers of waters is shown in Figure 5 for CIS, TD-BLYP, and TD-B3LYP. While the 20% HF exchange in the hybrid TD-B3LYP method does improve the excitation energies over TD-BLYP, the energies are clearly incorrect for both methods, and a higher level of theory or a range-separated hybrid functional^{19,21}

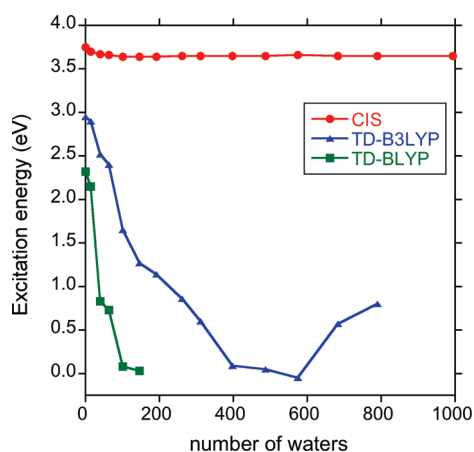


Figure 5. The first excitation energy (eV) of the PYP chromophore with increasing numbers of surrounding water molecules. Both TD-BLYP and TD-B3LYP exhibit spurious low-lying charge-transfer states. The geometry is taken from a single AMBER dynamics snapshot.

Table 3. Experimental and Calculated Vertical Transition Energies (eV) and Transition Dipole Moments (Debye) for the Lowest-Energy Bright State

	Expt ^a	TDA-TD-B3LYP ^b		TD-B3LYP ^c	
	ΔE	ΔE	μ_{ge}	ΔE	μ_{ge}
S1	3.25	3.13	9.2	3.00	8.0
S2	3.25	2.98	10.6	2.92	10.1
S3	3.20	2.93	12.0	2.89	11.9
S4	3.19	2.83	13.3		

^a Experimental results from refs 65 and 67. ^b GPU accelerated TD-B3LYP computed within the Tamm–Dancoff approximation. ^c TD-B3LYP results from ref 67.

is certainly necessary for studying excitations involving explicit QM waters.

The recent theoretical work by Badaeva et al. examining the one and two photon absorbance of oligothiophene dendrimers was limited to results for the first three generations S1–S3, even though experimental results were available for S4.^{65–67} In Table 3, we compare our GPU accelerated results on the first bright excited state (oscillator strength >1.0) using TD-B3LYP within the TDA to the full TD-B3LYP and experimental results. Results within the TDA are comparable to those from full TD-B3LYP, for both energies and transition dipole moments. Our results for S4 show the continuing trend of decreasing excitation energy and increasing transition dipole moment with increasing dendrimer generation.

CONCLUSIONS

We have implemented ab initio CIS and TDDFT calculations within the TeraChem software package, designed from inception for execution on GPUs. This allows full QM calculation of the excited states of large systems. The numerical accuracy of the excitation energies is shown to be excellent using mixed precision integral evaluation. A small percentage of cases require full double precision integration. For these occasional issues, we can easily switch to full double precision to achieve the desired convergence. The ability to use lower precision in much of the

CIS and TDDFT calculation is reminiscent of the ability to use coarse grids when calculating correlation energies, as shown previously for pseudospectral methods.^{79,82–85} Recently, it has also been shown⁸⁶ that single precision can be adequate for computing correlation energies with Cholesky decomposition methods which are closely related to pseudospectral methods.⁸⁷ Both quadrature and precision errors generally behave as relative errors, while chemical accuracy is an absolute standard (often taken to be 1 kcal/mol). Thus, coarser grids and/or lower precision can be safely used when the quantity being evaluated is itself small (and therefore less relative accuracy is required), as is the case for correlation and/or excitation energies.

For some of the smaller benchmark systems, we present speedups as compared to the GAMESS quantum chemistry package running over eight processor cores. The speedups obtained for CIS calculations range from 9 to 461 times, with increasing speedups with increasing system size. These speedup figures are not necessarily normative (other quantum chemistry packages might be more efficient), but we feel they give a good sense of the degree to which redesign of quantum algorithms for GPUs may be useful.

The increased size of the molecules that can be treated using our GPU-based algorithms exposes some failings of DFT and TDDFT. Specifically, the charge-transfer problem¹⁶ of TDDFT and the delocalization problem⁸⁸ of DFT both seem to become more severe as the molecules become larger, especially for the case of hydrated chromophores with large numbers of surrounding quantum mechanical water molecules. It remains to be seen whether range-separated hybrid functionals^{19,21} can solve these problems for large molecules, and we are currently working to implement these.

ASSOCIATED CONTENT

S Supporting Information. CIS, BLYP, and B3LYP excitation energies, oscillator strengths, timings, number of CIS/TD iterations, geometry details, and Cartesian coordinates for the 22 structures used in this text. This material is available free of charge via the Internet at <http://pubs.acs.org>.

AUTHOR INFORMATION

Corresponding Author

*E-mail: todd.martinez@stanford.edu.

ACKNOWLEDGMENT

This work was supported by NSF (CHE-06-26354) and the Department of Defense (Office of the Director of Defense Research and Engineering) through a National Security Science and Engineering Faculty Fellowship. C.M.I. is supported by an NIH Ruth L. Kirschstein NRSA fellowship. I.S.U. is an NVIDIA Fellow. Partial support has been provided by PetaChem, LLC, and through an AFOSR STTR grant administered by Spectral Sciences. T.J.M. and I.S.U. are part owners of PetaChem, LLC. The authors thank Ekaterina Badaeva for providing coordinates of the oligothiophene dendrimers and John Chodera for help with the AMBER⁸⁹ calculations of PYP.

REFERENCES

- (1) Foresman, J. B.; Head-Gordon, M.; Pople, J. A.; Frisch, M. J. *J. Phys. Chem.* **1992**, *96*, 135.

- (2) Runge, E.; Gross, E. K. U. *Phys. Rev. Lett.* **1984**, *52*, 997.
- (3) Gross, E. K. U.; Kohn, W. *Phys. Rev. Lett.* **1985**, *55*, 2850.
- (4) Casida, M. E. Time Dependent Density Functional Response Theory for Molecules. In *Recent Advances in Density Functional Methods*; Chong, D. P., Ed.; World Scientific: Singapore, 1995; pp 155.
- (5) Casida, M. E.; Jamorski, C.; Casida, K. C.; Salahub, D. R. *J. Chem. Phys.* **1998**, *108*, 4439.
- (6) Appel, H.; Gross, E. K. U.; Burke, K. *Phys. Rev. Lett.* **2003**, *90*, 043005.
- (7) Hirata, S.; Head-Gordon, M.; Bartlett, R. J. *J. Chem. Phys.* **1999**, *111*, 10774.
- (8) Dreuw, A.; Head-Gordon, M. *Chem. Rev.* **2005**, *105*, 4009.
- (9) Burke, K.; Werschnik, J.; Gross, E. K. U. *J. Chem. Phys.* **2005**, *123*, 062206.
- (10) Dallos, M.; Lischka, H.; Shepard, R.; Yarkony, D. R.; Szalay, P. G. *J. Chem. Phys.* **2004**, *120*, 7330.
- (11) Kobayashi, Y.; Nakano, H.; Hirao, K. *Chem. Phys. Lett.* **2001**, *336*, 529.
- (12) Roos, B. O. *Acc. Chem. Res.* **1999**, *32*, 137.
- (13) Tokita, Y.; Nakatsuji, H. *J. Phys. Chem. B* **1997**, *101*, 3281.
- (14) Krylov, A. I. *Annu. Rev. Phys. Chem.* **2008**, *59*, 433.
- (15) Stanton, J. F.; Bartlett, R. J. *J. Chem. Phys.* **1993**, *98*, 7029.
- (16) Dreuw, A.; Weisman, J. L.; Head-Gordon, M. *J. Chem. Phys.* **2003**, *119*, 2943.
- (17) Iikura, H.; Tsuneda, T.; Yanai, T.; Hirao, K. *J. Chem. Phys.* **2001**, *115*, 3540.
- (18) Heyd, J.; Scuseria, G. E.; Ernzerhof, M. *J. Chem. Phys.* **2003**, *118*, 8207.
- (19) Tawada, Y.; Tsuneda, T.; Yanagisawa, S.; Yanai, T.; Hirao, K. *J. Chem. Phys.* **2004**, *120*, 8425.
- (20) Rohrdanz, M. A.; Herbert, J. M. *J. Chem. Phys.* **2008**, *129*, 034107.
- (21) Rohrdanz, M. A.; Martins, K. M.; Herbert, J. M. *J. Chem. Phys.* **2009**, *130*, 054112.
- (22) Grimme, S. *J. Comput. Chem.* **2004**, *25*, 1463.
- (23) Grimme, S. *J. Comput. Chem.* **2006**, *27*, 1787.
- (24) Vydrov, O. A.; Van Voorhis, T. *J. Chem. Phys.* **2010**, *132*, 164113.
- (25) Dion, M.; Rydberg, H.; Schroder, E.; Langreth, D. C.; Lundqvist, B. I. *Phys. Rev. Lett.* **2004**, *92*, 246401.
- (26) For TDDFT, we are here referring to the adiabatic linear response formalism with presently available functionals.
- (27) Maitra, N. T.; Zhang, F.; Cave, R. J.; Burke, K. *J. Chem. Phys.* **2004**, *120*, 5932.
- (28) Levine, B. G.; Ko, C.; Quenneville, J.; Martinez, T. J. *Mol. Phys.* **2006**, *104*, 1039.
- (29) Jacquemin, D.; Wathelot, V.; Perpeate, E. A.; Adamo, C. *J. Chem. Theory Comput.* **2009**, *5*, 2420.
- (30) Warshel, A.; Levitt, M. *J. Mol. Biol.* **1976**, *103*, 227.
- (31) Virshup, A. M.; Punwong, C.; Pogorelov, T. V.; Lindquist, B. A.; Ko, C.; Martinez, T. J. *J. Phys. Chem. B* **2009**, *113*, 3280.
- (32) Ruckebauer, M.; Barbatti, M.; Muller, T.; Lischka, H. *J. Phys. Chem. A* **2010**, *114*, 6757.
- (33) Polli, D.; Altoe, P.; Weingart, O.; Spillane, K. M.; Manzoni, C.; Brida, D.; Tomasello, G.; Orlandi, G.; Kukura, P.; Mathies, R. A.; Garavelli, M.; Cerullo, G. *Nature* **2010**, *467*, 440.
- (34) Schafer, L.; Groenhof, G.; Boggio-Pasqua, M.; Robb, M. A.; Grubmuller, H. *PLoS Comp. Bio.* **2008**, *4*, e1000034.
- (35) Kapasi, U. J.; Rixner, S.; Dally, W. J.; Khailany, B.; Ahn, J. H.; Mattson, P.; Owens, J. D. *Computer* **2003**, *36*, 54.
- (36) Compute Unified Device Architecture Programming Guide. NVIDIA CUDA, version 2.0; NVIDIA: Santa Clara, CA; http://developer.download.nvidia.com/compute/cuda/2_0/docs/NVIDIA_CUDA_Programming_Guide_2.0.pdf. Accessed August 1, 2010.
- (37) Vogt, L.; Olivares-Amaya, R.; Kermes, S.; Shao, Y.; Amador-Bedolla, C.; Aspuru-Guzik, A. *J. Phys. Chem. A* **2008**, *112*, 2049.
- (38) Yasuda, K. *J. Chem. Theory Comput.* **2008**, *4*, 1230.
- (39) Ufimtsev, I. S.; Martinez, T. J. *J. Chem. Theory Comput.* **2009**, *5*, 1004.
- (40) Asadchev, A.; Allada, V.; Felder, J.; Bode, B. M.; Gordon, M. S.; Windus, T. L. *J. Chem. Theory Comput.* **2010**, *6*, 696.
- (41) Ufimtsev, I. S.; Martinez, T. J. *J. Chem. Theory Comput.* **2009**, *5*, 2619.
- (42) Stone, J. E.; Phillips, J. C.; Freddolino, P. L.; Hardy, D. J.; Trabuco, L. G.; Schulten, K. *J. Comput. Chem.* **2007**, *28*, 2618.
- (43) Anderson, J. A.; Lorenz, C. D.; Travestet, A. *J. Comput. Phys.* **2008**, *227*, 5342.
- (44) Liu, W.; Schmidt, B.; Voss, G.; Muller-Wittig, W. *Comput. Phys. Commun.* **2008**, *179*, 634.
- (45) Friedrichs, M. S.; Eastman, P.; Vaidyanathan, V.; Houston, M.; Legrand, S.; Beberg, A. L.; Ensign, D. L.; Bruns, C. M.; Pande, V. S. *J. Comput. Chem.* **2009**, *30*, 864.
- (46) PetaChem, LLC; PetaChem, LLC: Los Altos, CA; <http://www.petachem.com>.
- (47) Ufimtsev, I. S.; Martinez, T. J. *J. Chem. Theory Comput.* **2008**, *4*, 222.
- (48) Ufimtsev, I. S.; Martinez, T. J. *Comput. Sci. Eng.* **2008**, *10*, 26.
- (49) Shi, G.; Kindratenko, V.; Ufimtsev, I. S.; Martinez, T. J. Proceedings of the IEEE International Parallel and Distributed Processing Symposium (IPDPS), Atlanta, GA, April 19–23, 2010; IEEE: New York, 2010; p 1
- (50) Grabo, T.; Petersilka, M.; Gross, E. K. U. *J. Mol. Struct. (THEOCHEM)* **2000**, *501–502*, 353.
- (51) Hirata, S.; Head-Gordon, M. *Chem. Phys. Lett.* **1999**, *314*, 291.
- (52) Cordova, F.; Doriol, L. J.; Ipatov, A.; Casida, M. E.; Filippi, C.; Vela, A. *J. Chem. Phys.* **2007**, *127*, 164111.
- (53) Davidson, E. R. *J. Comput. Phys.* **1975**, *17*, 87.
- (54) CUBLAS Library; NVIDIA: Santa Clara, CA; http://developer.download.nvidia.com/compute/cuda/2_0/docs/CUBLAS_Library_2.0.pdf. Accessed August 1, 2010.
- (55) Whitten, J. L. *J. Chem. Phys.* **1973**, *58*, 4496.
- (56) McMurchie, L. E.; Davidson, E. R. *J. Comput. Phys.* **1978**, *26*, 218.
- (57) Ahmadi, G. R.; Almlöf, J. *Chem. Phys. Lett.* **1995**, *246*, 364.
- (58) Frisch, M. J.; Johnson, B.; Gill, P. M. W.; Fox, D.; Nobes, R. *Chem. Phys. Lett.* **1993**, *206*, 225.
- (59) Brown, P.; Woods, C.; McIntosh-Smith, S.; Manby, F. R. *J. Chem. Theory Comput.* **2008**, *4*, 1620.
- (60) Becke, A. D. *J. Chem. Phys.* **1988**, *88*, 2547.
- (61) Lebedev, V. I.; Laikov, D. N. *Dokl. Akad. Nauk* **1999**, *366*, 741.
- (62) Murray, C. W.; Handy, N. C.; Laming, G. J. *Mol. Phys.* **1993**, *78*, 997.
- (63) Hancock, J. M.; Gifford, A. P.; Tonzola, C. J.; Jenekhe, S. A. *J. Phys. Chem. C* **2007**, *111*, 6875.
- (64) Tao, J.; Tretiak, S. *J. Chem. Theo. Comp.* **2009**, *5*, 866.
- (65) Ramakrishna, G.; Bhaskar, A.; Bauerle, P.; Goodson, T. *J. Phys. Chem. A* **2007**, *112*, 2018.
- (66) Harpham, M. R.; Suzer, O.; Ma, C.-Q.; Bauerle, P.; Goodson, T. *J. Am. Chem. Soc.* **2009**, *131*, 973.
- (67) Badaeva, E.; Harpham, M. R.; Guda, R.; Suzer, O.; Ma, C.-Q.; Bauerle, P.; Goodson, T.; Tretiak, S. *J. Phys. Chem. B* **2010**, *114*, 15808.
- (68) Yamaguchi, S.; Kamikubo, H.; Kurihara, K.; Kuroki, R.; Niimura, N.; Shimizu, N.; Yamazaki, Y.; Kataoka, M. *Proc. Natl. Acad. Sci. U.S.A.* **2009**, *106*, 440.
- (69) Jorgensen, W. L.; Chandrasekhar, J.; Madura, J. D.; Impey, R. W.; Klein, M. L. *J. Chem. Phys.* **1983**, *79*, 926.
- (70) Nielsen, I. B.; Boye-Peronne, S.; El Ghazaly, M. O. A.; Kristensen, M. B.; Brondsted Nielsen, S.; Andersen, L. H. *Biophys. J.* **2005**, *89*, 2597.
- (71) Becke, A. D. *Phys. Rev. A* **1988**, *38*, 3098.
- (72) Lee, C.; Yang, W.; Parr, R. G. *Phys. Rev. B* **1988**, *37*, 785.
- (73) Olivares-Amaya, R.; Watson, M. A.; Edgar, R. G.; Vogt, L.; Shao, Y.; Aspuru-Guzik, A. *J. Chem. Theory Comput.* **2010**, *6*, 135.
- (74) Yasuda, K. *J. Comput. Chem.* **2008**, *29*, 334.
- (75) Of course, if the convergence threshold was made sufficiently small, all calculations would require double (or better) precision throughout.

- (76) Luehr, N.; Ufimtsev, I. S.; Martinez, T. J. *J. Chem. Theory Comput.* **2011**, *7*, 949.
- (77) Almlöf, J.; Faegri, K.; Korsell, K. *J. Comput. Chem.* **1982**, *3*, 385.
- (78) Fewer points are included for the TD-BLYP timings in Figure 4 because the SCF procedure does not converge for the solvated PYP chromophore with a large number of waters or for the full PYP protein. This is due to the well-known problem with nonhybrid DFT functionals having erroneously low-lying charge-transfer states that can prevent SCF convergence.
- (79) Ko, C.; Malick, D. K.; Braden, D. A.; Friesner, R. A.; Martinez, T. J. *J. Chem. Phys.* **2008**, *128*, 104103.
- (80) Valiev, M.; Bylaska, E. J.; Govind, N.; Kowalski, K.; Straatsma, T. P.; VanDam, H. J. J.; Wang, D.; Nieplocha, J.; Apra, E.; Windus, T. L.; deJong, W. A. *Comput. Phys. Commun.* **2010**, *181*, 1477.
- (81) Grimme, S.; Parac, M. *ChemPhysChem* **2003**, *4*, 292.
- (82) Martinez, T. J.; Carter, E. A. *J. Chem. Phys.* **1993**, *98*, 7081.
- (83) Martinez, T. J.; Carter, E. A. *J. Chem. Phys.* **1994**, *100*, 3631.
- (84) Martinez, T. J.; Carter, E. A. *J. Chem. Phys.* **1995**, *102*, 7564.
- (85) Martinez, T. J.; Mehta, A.; Carter, E. A. *J. Chem. Phys.* **1992**, *97*, 1876.
- (86) Vysotskiy, V. P.; Cederbaum, L. S. *J. Chem. Theory Comput.* **2010**, *7*, 320.
- (87) Martinez, T. J.; Carter, E. A. Pseudospectral Methods Applied to the Electron Correlation Problem. In *Modern Electronic Structure Theory, Part II*; Yarkony, D. R., Ed.; World Scientific: Singapore, 1995; p 1132.
- (88) Cohen, A. J.; Mori-Sanchez, P.; Yang, W. *Science* **2008**, *321*, 792.
- (89) Case, D. A.; Cheatham, T. E., III; Darden, T.; Gohlke, H.; Luo, R.; Merz, K. M., Jr.; Onufriev, A.; Simmerling, C.; Wang, B.; Woods, R. J. *J. Comput. Chem.* **2005**, *26*, 1668.

Effective Time-Independent Calculations of Vibrational Resonance Raman Spectra of Isolated and Solvated Molecules Including Duschinsky and Herzberg–Teller Effects

Fabrizio Santoro,^{*,†} Chiara Cappelli,^{*,†,‡} and Vincenzo Barone^{†,§}

[†]CNR—Consiglio Nazionale delle Ricerche, Istituto di Chimica dei Composti Organo Metallici (ICCOM-CNR), UOS di Pisa, Area della Ricerca, via G. Moruzzi 1, I-56124 Pisa, Italy

[‡]Dipartimento di Chimica e Chimica Industriale, Università di Pisa, via Risorgimento, 35 I-56126 Pisa, Italy

[§]Scuola Normale Superiore, Piazza dei Cavalieri, 7 I-56126 Pisa, Italy

S Supporting Information

ABSTRACT: We present a method of modeling vibrational resonance Raman scattering (RRS) spectra of isolated and solvated systems with the inclusion of Franck–Condon (FC) and Herzberg–Teller (HT) effects and a full account for possible differences between the harmonic potential energy surfaces of the initial and resonant electronic states. It describes fundamentals, overtones, and combination bands and computes the RRS spectrum as a two-dimensional function of the incident and scattered frequencies. The theoretical foundations of the method are described and the differences with other currently available methodologies are outlined. Applications to the phenoxyl radical in the gas phase and indolinedimethine–malononitrile (IDMN) in acetonitrile and cyclohexane solution are reported, as well as comparisons with available experimental data.

I. INTRODUCTION

Resonance Raman scattering (RRS) refers to Raman scattering at wavelengths close to an electronic excitation of the molecule¹ (see Figure 1 for a pictorial view). Because of this peculiarity, RRS is able to provide information on electronically excited state properties and structure,² which is an outcome that only rarely is obtained through other experimental techniques, and for which the formulation of modern quantum mechanical (QM) models has instead reached a well-recognized maturity.³

The sensitivity of experimental RRS has largely improved recently,⁴ so it is becoming a very valuable technique for the study of the structure and dynamics of biosystems and materials. However, the calculation of RRS spectral parameters is far from being common in the literature; some aspects of such a subject still remain unexplored. Most of the RRS calculations reported until now are based on the so-called Transform Theory (TT)⁵ or on the short-time dynamics (STD) approach.^{6,7} TT is rooted in the Kramers–Kronig relationship between the polarizability and the absorption spectrum and, in its most common version, derives relative resonance Raman intensities from the differences in the equilibrium structures between the ground and the resonant excited states and a lineshape function Φ attainable from the absorption spectrum. The STD method originates from the pioneering work by Heller and co-workers, and it is based on a time-dependent redefinition of the energy-frame Kramers, Heisenberg, and Dirac (KHD) expression for the polarizability tensor,^{8,9} in terms of the dynamics of a wave packet. Although this approach is quite general, most of its practical applications actually use the STD expressions, which are valid when only the

STD of the system is reflected in the RRS spectra, and, therefore, are well-suited for preresonance regimes.^{6,7} In this limit, relative RRS intensities are expressed in terms of the resonant-state energy gradient at the ground equilibrium geometry; therefore, they do not require explicit time-dependent calculations. Because of that, STD is also generally known as the “gradient method”. The time-independent analysis of Warshel and Dauber allows one to bridge the TT and STD approaches in the harmonic limit,¹⁰ where simple relations hold between excited-state gradients and equilibrium geometry displacements. Recently, a computationally different approach has been reported.¹¹ There, RRS is obtained from the geometrical derivatives of the frequency-dependent resonance polarizabilities, calculated by including a finite lifetime of the electronic excited states, using time-dependent density functional theory (TD-DFT). Such a method still relies on a short-time approximation and is similar to the simple excited-state gradient approximation method if only one electronic excited state is important.

Most of the previous methods for the calculation of RRS focus on the calculation of the so-called “Albrecht A^{VI} term”,^{1,12} which implies that Herzberg–Teller (HT) vibronic couplings are completely discarded, so that only Franck–Condon (FC)-type scattering is considered in the theoretical formalism. Also, it is assumed that only one electronic excited state is relevant in the process, and that the potential energy surfaces (PES) of the ground and excited state are harmonic. In addition, ground and excited state normal modes and their frequencies are assumed to

Received: January 24, 2011

Published: April 29, 2011

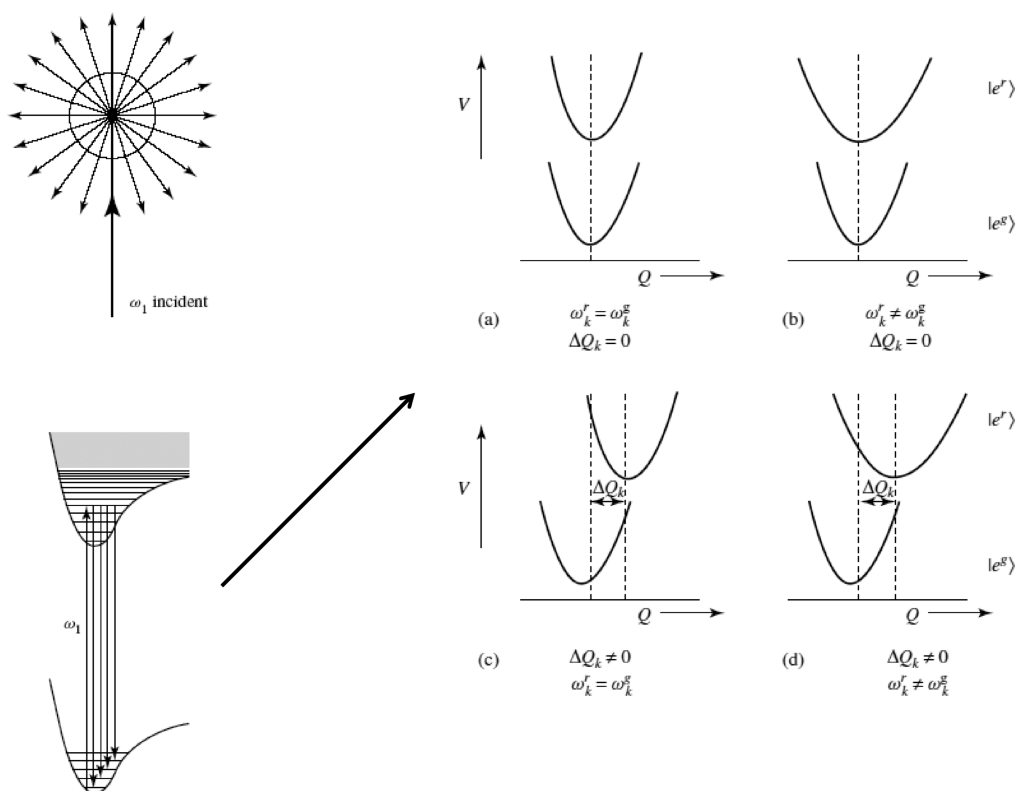


Figure 1. Pictorial view of the resonance Raman effect, along with a graphical representation of the various levels of treatment (a–d) of the ground (*g*) and excited (*r*) states potential energy surfaces: (a) $\omega_k^r = \omega_k^g$, $\Delta Q_k = 0$; (b) $\omega_k^r \neq \omega_k^g$, $\Delta Q_k = 0$; (c) $\omega_k^r = \omega_k^g$, $\Delta Q_k \neq 0$; and (d) $\omega_k^r \neq \omega_k^g$, $\Delta Q_k \neq 0$. *Q* stands for a normal coordinate, ΔQ_k is the displacement along that coordinate, and the ω terms are the vibrational frequencies associated with the *Q* values in the ground and excited states.

be identical (“independent mode, displaced harmonic oscillator model” (IMDHO)¹³) and excited- and ground-state normal coordinates are assumed to differ only in their equilibrium positions, so that Duschinsky rotations are not important. Finally, in most cases, only fundamental $0 \rightarrow 1$ transitions are considered, and the dependence on the incident frequency is not explicitly considered (although this is actually possible using both the TT theory⁵ and the STD method^{6,7}).

Within the above frameworks, several contributions have been presented in the literature, such as extensions to address anti-resonance contributions,¹⁴ methods for the selective calculation of high-intensity modes,¹⁵ computations of the lineshape function Φ entering in the TT expressions from sum over states approaches (and not from the experimental data),¹⁶ corrections for the contributions of more than one resonant state,¹⁷ extensions to resonance Raman optical activity,¹⁸ as well as applications to interesting systems such as uracil,¹⁹ pyrenes,²⁰ rhodamine,^{21,22} julonidinemalononitrile chromophores,²³ and large ruthenium complexes.^{24,25}

In this paper, we intend to present a general method rooted in the harmonic approximation that overcomes the approximations of the methods described above, using a time-independent sum-over-states (SOS) approach. We focus on vibrational RRS from the ground vibrational state $|0^g\rangle$ (only Stokes bands), with the aim of describing both FC and HT effects (the so-called “Albrecht B^{VI}–D^{VI} terms”) and to fully account for any possible difference between the harmonic PES of the initial and resonant electronic states. In addition, the SOS approach, by explicitly computing the polarizability tensor, allows one to provide RRS

spectra as a function of two frequency coordinates (two-dimensional (2D) RRS spectra)—the incident coordinate and scattered coordinate—and to account for interferential features arising from the contribution of more than one quasi-resonant electronic state. Recall that formal expressions to include Duschinsky and HT effects in the TT approach²⁶ and along the time-correlator formalism^{27–29} have been derived in the past, and that the effect of HT³⁰ and Duschinsky mixings³¹ has been addressed in simplified models for specific systems. However, a general tool for computing RRS spectra at the harmonic level is still lacking.

The basic ingredients to perform SOS RRS calculations, including Duschinsky and HT effects, are very similar to those required to compute absorption spectra. Namely, accurate formulas are needed to compute multidimensional FC integrals and, in large systems, effective prescreening methods must be able to select the relevant transitions among the very large number of possible quasi-resonant vibronic states (easily exceeding 10^{20}). While easily implemented recurrence formulas to compute FC integrals were derived a long time ago, through a generating function approach,^{32–34} or a coherent state approach,^{35,36} only recently effective selection schemes have been worked out (see ref 37 for a comprehensive review). They include specific partition in “levels” of the possible transitions³⁸ and selections through block factorization of the Duschinsky matrix,^{39,40} or through analytical sum rules.⁴¹

We recently worked out a method based on partition of the possible transitions in classes C_m depending on the number (*n*) of simultaneously excited modes in the final state, and a

prescreening method for high-order ($n > 2$) classes based on the analysis of C_1 and C_2 classes.⁴² The method, which was originally worked out for FC 0 K one-photon absorption (OPA) and emission spectra, has been generalized to include temperature effects⁴³ and HT effects,⁴⁴ and to deal with one-photon circular dichroism (ECD)⁴⁵ and two-photon absorption and circular dichroism.⁴⁶ It has been recently implemented^{47,48} for OPA and ECD in a optimized routine in the Gaussian 09 package.⁴⁹ Here, we present its further extension to 2D RRS spectra, exploiting the protocols developed for dealing with vibrationally excited initial states in finite temperature spectra⁴³ and including additional prescreening recipes on the final vibronic states of the ground electronic states, together with a generalization of analytical sum rules to check SOS calculation convergence.

It has been recognized that a very important role in RRS is played by the presence of a solvent,^{4,21,50} because of the fact that the solute–solvent interactions can largely affect the electronic excited states, both by modifying their nature (the charge-transfer character is usually increased in polar solvents) and by inducing structural deformations, which can lead to very different relaxed excited states, with respect to their counterparts in the gas phase. In recent years, a method to couple TT and STD to continuum solvation models has been proposed.^{51,52} In this paper, its further extension is reported, by also including the solvent effects on excited-state normal modes and transition dipoles, by exploiting the Polarizable Continuum Model (PCM).^{53,54}

The paper is organized as follows. In the next section (section II), the theoretical background is summarized. After a brief section on computational details (section III), application of the methodologies to few selected systems in the gas phase or in solution is reported (section IV). Concluding remarks (in section V) end the presentation.

II. THEORETICAL FRAMEWORK

A. General Expression for Vibrational Resonance Raman Cross Section. We consider a monochromatic incident (I) radiation with angular frequency ω_I propagating in the direction of the unit vector \mathbf{n}_0^I , impinging on the sample, and we analyze the scattered radiation (s) of frequency ω_s in the propagation direction \mathbf{n}_0^s . The terms \mathbf{n}_0^I and \mathbf{n}_0^s define the so-called “scattering plane”, and θ is the scattering angle ($\theta = \cos^{-1}(\mathbf{n}_0^I \cdot \mathbf{n}_0^s)$). Two possible polarizations for the incident and scattered light are, respectively, perpendicular (\perp) and parallel (\parallel) to the scattered plane. The scattered intensity at an angle of $\theta = 90^\circ$ for any polarization ($\perp^s + \parallel^s$) for incident light with perpendicular polarization (\perp^I) is given as^{1,55}

$$I\left(\frac{\pi}{2}; \perp^s + \parallel^s, \perp^I\right) = \frac{\omega_s^4 \mathcal{I}}{16\epsilon_0^2 c_0^4 \pi^2} \frac{45a^2 + 7g^2 + 5d^2}{45} \quad (1)$$

where \mathcal{I} is the incident field irradiance, c_0 the speed of light, and ϵ_0 the electric permittivity in a vacuum. The orientational average has been taken into account by considering freely rotating molecules. The a , g , and d terms are functions of the molecular polarizability tensor and, therefore, are dependent on ω_I and ω_s , as well as on molecular parameters; they are the so-called “mean polarizability”, “symmetric anisotropy”, and “antisymmetric anisotropy”, respectively, and their explicit expressions are given below. Removing the dependence on

\mathcal{I} , a differential cross section (with respect to a scattering solid angle Ω) is defined:

$$\sigma'(\omega_I, \omega_s) = \frac{\partial \sigma}{\partial \Omega} = \frac{I(\pi/2; \perp^s + \parallel^s, \perp^I)}{\mathcal{I}} \quad (2)$$

Note that an alternative definition of $\sigma'(\omega_I, \omega_s)$ is reported by some authors, not in terms of unit incident irradiance (\mathcal{I}), but per unit of incident photon flux ($\mathcal{I}/\hbar\omega_I$). In this case, the second differential cross section $\sigma''(\omega_I, \omega_s)$ (where $\sigma''(\omega_I, \omega_s) = \partial^2 \sigma / \partial \Omega \partial \omega_s$), which is dependent on $\omega_s^3 \omega_I$ rather than ω_s^4 (see eq 2), is reported.

We now introduce the polarizability tensor for a transition $|i\rangle \rightarrow |f\rangle$. Its $\rho\sigma$ th element ($\rho, \sigma = x, y, z$) is

$$\alpha_{\rho\sigma}^{fi} = \frac{1}{\hbar} \sum_m \frac{\langle f | \mu_\rho | m \rangle \langle m | \mu_\sigma | i \rangle}{\omega_{mi} - \omega_I - i\gamma_m} + \frac{1}{\hbar} \sum_m \frac{\langle f | \mu_\rho | m \rangle \langle m | \mu_\sigma | i \rangle}{\omega_{mi} + \omega_I + i\gamma_m} \quad (3)$$

where μ_ρ is the ρ -Cartesian component of the electric dipole. The sum is taken over all possible intermediate states $|m\rangle$, $\omega_{mi} = \omega_m - \omega_i$; $\hbar\omega_i$ and $\hbar\omega_m$ are the energies of states $|i\rangle$ and $|m\rangle$, respectively; and, finally, γ_m is the lifetime of excited state $|m\rangle$. In the framework of the Born–Oppenheimer approximation (BO) and by considering, in eq 1, rotational states to be factorized out and summation over all possible orientations, we must address the vibronic states, which can be written as a product

$$|e_k; v_i^k\rangle = |e_k\rangle \otimes |v_i^k\rangle$$

where $|e_k\rangle$ is the electronic state and $|v_i^k\rangle$ the associated vibrational state. The previously introduced a , g^2 , and d^2 quantities are given as¹

$$a = \frac{1}{3} (\alpha_{xx}^{fi} + \alpha_{yy}^{fi} + \alpha_{zz}^{fi}) \quad (4)$$

$$g^2 = \frac{1}{2} [|\alpha_{xx}^{fi} - \alpha_{yy}^{fi}|^2 + |\alpha_{xx}^{fi} - \alpha_{zz}^{fi}|^2 + |\alpha_{yy}^{fi} - \alpha_{zz}^{fi}|^2 + \frac{3}{2} (|\alpha_{xy}^{fi} + \alpha_{yx}^{fi}|^2 + |\alpha_{xz}^{fi} + \alpha_{zx}^{fi}|^2 + |\alpha_{yz}^{fi} + \alpha_{zy}^{fi}|^2)] \quad (5)$$

$$d^2 = \frac{3}{4} (|\alpha_{xy}^{fi} - \alpha_{yx}^{fi}|^2 + |\alpha_{xz}^{fi} - \alpha_{zx}^{fi}|^2 + |\alpha_{yz}^{fi} - \alpha_{zy}^{fi}|^2) \quad (6)$$

When the incident frequency is close to resonance with the transition energy ω_{mi} , the first resonant term in eq 3 dominates over the second off-resonant term, which can be safely neglected. Moreover, if both the initial and final states belong to the ground electronic state $|e_g\rangle$ (vibrational resonance Raman), by integrating over the electronic degrees of freedom, the following equation is obtained:

$$\alpha_{\rho\sigma}^{fi} = \sum_{k,m} \frac{\langle v_f^g | \mu_\rho^{gk} | v_m^k \rangle \langle v_m^k | \mu_\sigma^{kg} | v_i^g \rangle}{\omega_{km,gi} - \omega_I - i\gamma_k} \quad (7)$$

where $\mu_\beta^{gk} = \langle e_g | \mu_\beta | e_k \rangle$, $\omega_{km,gi} = \omega_{e_k} + \omega_{v_m^k} - (\omega_{e_g} + \omega_{v_i^g})$, and the lifetime γ_{km} of the intermediate states $|e_k; v_m^k\rangle$ is assumed to be independent from the vibrational state $|v_m^k\rangle$, so that it is possible to drop the m subscript out (γ_k). As shown by eq 2, the transition probability is dependent on the square of polarizability tensor elements. Therefore, when the exciting frequency is in near-resonance with the transitions to more than one excited electronic state $|e_k\rangle$, the sum in eq 7 must be carried out over all the

intermediate states, which can give rise to interferential features. Nonetheless, in this case, it also is possible to compute a polarizability tensor $\alpha_{\rho\sigma}^{gk}$ for each intermediate state $|e_k\rangle$ and obtain the total polarizability tensor by summing them up. Without any loss of generality, it is therefore possible, in the following, to refer to a single intermediate state $|e_k\rangle$, so that the summation over k will drop out.

B. The RR Cross Section in the Harmonic Approximation: Franck–Condon and Herzberg–Teller Terms. The discussion of the previous section has been carried out in very general terms. This section will focus the theory on the special cases where the PES of both the initial $|e^g\rangle$ and intermediate $|e^k\rangle$ electronic states can be treated within the harmonic approximation. In this case, vibrational states $|v_m^l\rangle$ of a given electronic state $|e_l\rangle$ are direct products of one-dimensional (1D) states $|m_j^l\rangle$ for each mode j , and $|v_m^k\rangle = |\mathbf{m}^k\rangle = |m_1^k\rangle \otimes |m_2^k\rangle \dots \otimes |m_N^k\rangle$, with N being the number of normal coordinates and m_j^k the quantum number of mode j .

According to Duschinsky,⁵⁶ the sets of mass-weighted normal coordinates \mathbf{Q}^g and \mathbf{Q}^k of electronic states $|e^g\rangle$ and $|e^k\rangle$ are related through a linear transformation:

$$\mathbf{Q}^g = \mathbf{J}\mathbf{Q}^k + \mathbf{K} \quad (8)$$

where \mathbf{J} is the Duschinsky matrix and \mathbf{K} is a column vector collecting the displacements between the equilibrium geometries of the two electronic PES.

The transition electric dipole $\vec{\mu}^{gk}$ generally is an unknown function of the normal coordinates. Its ρ Cartesian component can be written in terms of a Taylor expansion of the normal coordinates of the initial (ground) electronic state, \mathbf{Q}^g :

$$\mu_{\rho}^{gk} = \mu_{\rho}^{gk}(0) + \sum_j \mu_{\rho}^{gk}(j) Q_j^g + \sum_{j,l} \mu_{\rho}^{gk}(j,l) Q_j^g Q_l^g + \dots \quad (9)$$

By restricting the expansion to the first order and substituting into eq 7, it follows that

$$\begin{aligned} \alpha_{\rho\sigma}^{fi} &= \frac{1}{\hbar} \sum_{\mathbf{m}} \frac{\langle \mathbf{n}^{f,g} | \mu_{\rho}^{gk}(0) | \mathbf{m}^k \rangle \langle \mathbf{m}^k | \mu_{\sigma}^{kg}(0) | \mathbf{n}^{i,g} \rangle}{\omega_{km,gi} - \omega_I - i\gamma_k} \\ &+ \frac{1}{\hbar} \sum_{\mathbf{m}} \frac{\langle \mathbf{n}^{f,g} | \sum_l \mu_{\rho}^{gk}(l) Q_l^g | \mathbf{m}^k \rangle \langle \mathbf{m}^k | \mu_{\sigma}^{kg}(0) | \mathbf{n}^{i,g} \rangle}{\omega_{km,gi} - \omega_I - i\gamma_k} \\ &+ \frac{1}{\hbar} \sum_{\mathbf{m}} \frac{\langle \mathbf{n}^{f,g} | \mu_{\rho}^{gk}(0) | \mathbf{m}^k \rangle \langle \mathbf{m}^k | \sum_j \mu_{\sigma}^{kg}(j) Q_j^g | \mathbf{n}^{i,g} \rangle}{\omega_{km,gi} - \omega_I - i\gamma_k} \\ &+ \frac{1}{\hbar} \sum_{\mathbf{m}} \frac{\langle \mathbf{n}^{f,g} | \sum_l \mu_{\rho}^{gk}(l) Q_l^g | \mathbf{m}^k \rangle \langle \mathbf{m}^k | \sum_j \mu_{\sigma}^{kg}(j) Q_j^g | \mathbf{n}^{i,g} \rangle}{\omega_{km,gi} - \omega_I - i\gamma_k} \end{aligned} \quad (10)$$

The first term of eq 10 is the FC term, while the remaining terms arise from the HT borrowing mechanism of electronic transitions. By inspection of eq 10, it is apparent that the antisymmetric anisotropy d (eq 6) vanishes for pure FC transitions but is generally different from zero when the HT effect is considered. Adopting a second quantization,

$$\hat{Q}_i^g = \sqrt{\frac{\hbar}{2\omega_i}} (\hat{a}_i^{g,+} + \hat{a}_i^g)$$

we have

$$\begin{aligned} \hat{Q}_i^g | \mathbf{n}^{f,g} \rangle &= \sqrt{n_i^{f,g} + 1} | \mathbf{n}^{f,g} + 1_i \rangle \\ &+ \sqrt{n_i^{f,g}} | \mathbf{n}^{f,g} - 1_i \rangle \end{aligned} \quad (11)$$

where $| \mathbf{n}^{f,g} + p_i \rangle$ is a vibrational state characterized by the same quantum numbers of $| \mathbf{n}^{f,g} \rangle$ for all modes except mode i , for which there are p_i additional quanta. Therefore, both FC and HT contributions can be computed if the generic FC overlap integrals $\langle \mathbf{n}^g | \mathbf{m}^k \rangle$ can be evaluated. Such integrals can be computed starting from the FC integrals between the ground vibrational states $\langle \mathbf{0}^g | \mathbf{0}^k \rangle$, according to the well-known recurrence formulas:^{33,34,57}

$$\begin{aligned} \langle \mathbf{0}^g | \mathbf{m}^k \rangle &= \left(\frac{1}{2m_j^k} \right)^{1/2} A_j \langle \mathbf{0}^g | \mathbf{m}^k - 1_j \rangle + \left(\frac{m_j^k - 1}{m_j^k} \right)^{1/2} D_{jj} \langle \mathbf{0}^g | \mathbf{m}^k - 2_j \rangle \\ &+ \sum_{l, (l \neq j)} \left(\frac{m_l^k}{m_j^k} \right)^{1/2} D_{jl} \langle \mathbf{0}^g | \mathbf{m}^k - 1_j - 1_l \rangle \end{aligned} \quad (12)$$

$$\begin{aligned} \langle \mathbf{n}^g | \mathbf{m}^k \rangle &= \left(\frac{1}{2n_j} \right)^{1/2} B_j \langle \mathbf{n}^g - 1_j | \mathbf{m}^k \rangle + \left(\frac{n_j^g - 1}{n_j^g} \right)^{1/2} E_{jj} \langle \mathbf{n}^g - 2_j | \mathbf{m}^k \rangle \\ &+ \sum_{l, (l \neq j)} \left(\frac{n_l^g}{n_j^g} \right)^{1/2} E_{jl} \langle \mathbf{n}^g - 1_j - 1_l | \mathbf{m}^k \rangle \\ &+ \sum_l \left(\frac{m_l^k}{n_j^g} \right)^{1/2} F_{jl} \langle \mathbf{n}^g - 1_j | \mathbf{m}^k - 1_l \rangle \end{aligned} \quad (13)$$

where

$$\begin{aligned} \mathbf{Y} &= \mathbf{J}^\dagger \mathbf{\Gamma}^g \mathbf{K} \\ \mathbf{X} &= \mathbf{J}^\dagger \mathbf{\Gamma}^g \mathbf{J} + \mathbf{\Gamma}^k \\ \mathbf{A} &= -2\mathbf{K}^\dagger \mathbf{\Gamma}^g \mathbf{X}^{-1} (\mathbf{\Gamma}^k)^{1/2} \\ \mathbf{D} &= 2(\mathbf{\Gamma}^k)^{1/2} \mathbf{X}^{-1} (\mathbf{\Gamma}^k)^{1/2} - \mathbf{I} \\ \mathbf{B} &= 2\mathbf{K}^\dagger (\mathbf{\Gamma}^g)^{1/2} (\mathbf{I} - (\mathbf{\Gamma}^g)^{1/2} \mathbf{J} \mathbf{X}^{-1} \mathbf{J}^\dagger (\mathbf{\Gamma}^g)^{1/2}) \\ \mathbf{E} &= 2(\mathbf{\Gamma}^g)^{1/2} \mathbf{J} \mathbf{X}^{-1} \mathbf{J}^\dagger (\mathbf{\Gamma}^g)^{1/2} - \mathbf{I} \\ \mathbf{F} &= 2(\mathbf{\Gamma}^g)^{1/2} \mathbf{J} \mathbf{X}^{-1} (\mathbf{\Gamma}^k)^{1/2} \end{aligned} \quad (14)$$

and $\mathbf{\Gamma}^g$ and $\mathbf{\Gamma}^k$ are diagonal matrices collecting the reduced frequencies ω_j^g/\hbar and ω_j^k/\hbar , respectively, whereas \mathbf{I} is the identity matrix. The FC integral between the ground states is⁵⁷

$$\begin{aligned} \langle \mathbf{0}^g | \mathbf{0}^k \rangle &= (\det \mathbf{\Gamma}^g \det \mathbf{\Gamma}^k)^{1/4} \left(\frac{2^N \det \mathbf{J}}{\det \mathbf{X}} \right)^{1/2} \\ &\times \exp \left[-\frac{1}{2} \mathbf{K}^\dagger \mathbf{\Gamma}^g \mathbf{K} + \frac{1}{2} \mathbf{Y}^\dagger \mathbf{X}^{-1} \mathbf{Y} \right] \end{aligned} \quad (15)$$

Equations 10–13 are our working expressions. In the following, the treatment will be restricted to transitions from the ground vibrational state $|\mathbf{0}^g\rangle$, i.e., by definition to Stokes transitions $\omega_s < \omega_I$.

C. Comparison with Alternative Approaches. Limiting the discussion to time-independent methods only, as already reported in the Introduction, two main approaches have been

employed so far for the evaluation of RRS. The first one is based on the so-called “transform theory” (TT),⁵ while the other is commonly known as the “short-time dynamics” (STD) method or the “gradient method”.^{6,7} For harmonic models, both approaches can be seen as particular cases of eq 10, and most of the reported calculations rely on the IMDHO model, where, as previously mentioned, the ground and excited PES share the same set of normal modes (i.e., for the Duschinsky matrix $\mathbf{J} = \mathbf{I}$) and there are no frequency changes (i.e., $\mathbf{\Gamma}^k = \mathbf{\Gamma}^g$).

In this case, the recurrence formulas in eqs 12 and 13 are drastically simplified, because the FC integrals can be written as products of one-dimensional (1D) integrals, and in eq 14, all the matrices except \mathbf{F} vanish. Furthermore, $\mathbf{F} = \mathbf{I}$ and $\mathbf{A} = -\mathbf{B}$, with

$$A_j = -B_j = -K_j(\Gamma_j^g)^{1/2} = -\Delta_j \quad (16)$$

Note that $\Delta_j = K_j(\omega_j^g/\hbar)^{1/2}$ is the so-called “dimensionless displacement”. Therefore, one simply obtains

$$\langle 0_j^g | m_j^k \rangle = -\frac{\Delta_j}{\sqrt{2m_j^k}} \langle 0_j^g | m_j^k - 1_j \rangle \quad (17)$$

$$\langle n_j^g | m_j^k \rangle = \frac{\Delta_j}{\sqrt{2n_j^g}} \langle n_j^g - 1_j | m_j^k \rangle + \sqrt{m_j^k/n_j^g} \langle n_j^g - 1_j | m_j^k - 1_j \rangle \quad (18)$$

In addition, the most popular and simplified approaches assume that HT contributions are negligible, and in eq 10, they only consider fundamental transitions $0_j \rightarrow 1_j$ for each mode j .

1. *The Transform Theory.* Let us start from a well-known relationship, which holds between the absorption cross section (Lorentzian broadening) and the polarizability tensor ($T = 0$ K is assumed):

$$\begin{aligned} \sigma_{\text{abs}}(\omega_l) &= C\omega_l \sum_{\mathbf{m}^k} |\langle 0^g | \mu^{g,k} | \mathbf{m}^k \rangle|^2 \frac{\gamma_k}{\pi[\omega_{kg} + \sum_j \omega_j^k m_j^k - \omega_l]^2 + \gamma_k^2} \\ &= \frac{C}{\pi} \omega_l \text{Im}[\alpha_{xx}^{0,0} + \alpha_{xx}^{0,0} + \alpha_{xx}^{0,0}] \quad (19) \end{aligned}$$

where C is a proportionality factor and ω_{kg} is the energy difference between the ground vibrational states associated to the two electronic states k and g . The explicit definition of such a factor has been previously reported in the literature⁴⁸ and is dependent on universal constants. By expressing all the parameters in atomic units, $\varepsilon(\omega_l)$ (given in $\text{dm}^3 \text{mol}^{-1} \text{cm}^{-1}$) is obtained (for a Lorentzian broadening). Let us further define a normalized cross section $\bar{\sigma}_{\text{abs}}(\omega_l) = \sigma_{\text{abs}}(\omega_l)/(\omega_l \int \sigma_{\text{abs}}(\omega_l)/\omega_l d\omega_l)$. By focusing on a FC case and considering a specific oscillator l , one can write

$$\bar{\sigma}_{\text{abs}}(\omega_l) = \sum_{m_l} |\langle 0_l^g | m_l^k \rangle|^2 S(\omega_l - m_l^k \omega_l^k) \quad (20)$$

where, according to ref 19, we define

$$\begin{aligned} S(\omega_l - m_l^k \omega_l^k) &= \sum_{m_j^k, \forall j \neq l} \frac{\prod_{j \neq l} |\langle 0_j^g | m_j^k \rangle|^2}{\pi[(\omega_{kg} + \sum_{j \neq l} \omega_j^k m_j^k) - (\omega_l - m_l^k \omega_l^k)]^2 + \gamma_k^2} \end{aligned}$$

$$\begin{aligned} T(\omega_l - m_l^k \omega_l^k) &= \sum_{m_j^k, \forall j \neq l} \frac{\prod_{j \neq l} \gamma_k |\langle 0_j^g | m_j^k \rangle|^2 [(\omega_{kg} + \sum_{j \neq l} \omega_j^k m_j^k) - (\omega_l - m_l^k \omega_l^k)]}{\pi[(\omega_{kg} + \sum_{j \neq l} \omega_j^k m_j^k) - (\omega_l - m_l^k \omega_l^k)]^2 + \gamma_k^2} \\ \Phi(\omega_l) &= \sum_{m_l} |\langle 0_l^g | m_l^k \rangle|^2 [T(\omega_l - m_l^k \omega_l^k) + iS(\omega_l - m_l^k \omega_l^k)] \quad (21) \end{aligned}$$

Application of eq 18 gives

$$\begin{aligned} \langle 1_l^g | m_l^k \rangle &= \frac{\Delta_l}{\sqrt{2}} \langle 0_l^g | m_l^k \rangle + \sqrt{m_l^k} \langle 0_l^g | m_l^k - 1_l \rangle \\ \langle m_l^k | 0_l^g \rangle &= -\frac{\Delta_l}{\sqrt{2m_l^k}} \langle 0_l^g | m_l^k - 1_l \rangle = \frac{\Delta_l^2}{2\sqrt{m_l^k(m_l^k - 1)}} \langle 0_l^g | m_l^k - 2_l \rangle \\ \langle 1_l^g | m_l^k \rangle \langle m_l^k | 0_l^g \rangle &= \frac{\Delta_l}{\sqrt{2}} [|\langle 0_l^g | m_l^k \rangle|^2 - |\langle 0_l^g | m_l^k - 1_l \rangle|^2] \\ \langle 2_l^g | m_l^k \rangle \langle m_l^k | 0_l^g \rangle &= \frac{\Delta_l^2}{2\sqrt{2}} [|\langle 0_l^g | m_l^k \rangle|^2 - 2|\langle 0_l^g | m_l^k - 1_l \rangle|^2 \\ &\quad + |\langle 0_l^g | m_l^k - 2_l \rangle|^2] \\ \langle 1_l^g 1_l^g | m_j^k m_l^k \rangle \langle m_j^k m_l^k | 0_j^g 0_l^g \rangle &= \frac{\Delta_j \Delta_l}{2} [|\langle 0_j^g | m_j^k \rangle|^2 - |\langle 0_j^g | m_j^k - 1_j \rangle|^2] \\ &\quad \times [|\langle 0_l^g | m_l^k \rangle|^2 - |\langle 0_l^g | m_l^k - 1_l \rangle|^2] \quad (22) \end{aligned}$$

Such expressions are equivalent to those given by Neugebauer and Hess¹⁹ in the case of $|0_l^g\rangle \rightarrow |1_l^g\rangle$ fundamental transitions and also extend them to the treatment of overtones $|0_l^g\rangle \rightarrow |2_l^g\rangle$ and combination bands $|0_j^g 0_l^g\rangle \rightarrow |1_j^g 1_l^g\rangle$. By further following Neugebauer and Hess,¹⁹ one finally gets the following, for fundamentals:

$$\alpha_{\rho\sigma}^{0_l \rightarrow 1_l} = \mu_{\rho}^{gk}(0) \mu_{\sigma}^{gk}(0) \frac{\Delta_l}{\sqrt{2}} [\Phi(\omega_l) - \Phi(\omega_l - \omega_l)] \quad (23)$$

where $\Phi(\omega_l)$ is related to the normalized spectrum $\bar{\sigma}_{\text{abs}}(\omega_l)$ through the following equation (\mathcal{P} indicates the Cauchy principal-value integral):

$$\Phi(\omega_l) = i\pi \bar{\sigma}_{\text{abs}}(\omega_l) + \mathcal{P} \int d\omega \frac{\bar{\sigma}_{\text{abs}}(\omega)}{(\omega - \omega_l)} \quad (24)$$

For the first overtone band, one similarly obtains

$$\alpha_{\rho\sigma}^{0_l \rightarrow 2_l} = \mu_{\rho}^{gk}(0) \mu_{\sigma}^{gk}(0) \frac{\Delta_l^2}{2\sqrt{2}} [\Phi(\omega_l) - 2\Phi(\omega_l - \omega_l) + \Phi(\omega_l - 2\omega_l)] \quad (25)$$

and, for the two-mode combination bands,

$$\begin{aligned} \alpha_{\rho\sigma}^{0,0_l \rightarrow 1,1_l} &= \mu_{\rho}^{gk}(0) \mu_{\sigma}^{gk}(0) \frac{\Delta_j \Delta_l}{2} \\ &\quad \times [\Phi(\omega_l) - \Phi(\omega_l - \omega_j) - \Phi(\omega_l - \omega_l) \\ &\quad + \Phi(\omega_l - \omega_j - \omega_l)] \quad (26) \end{aligned}$$

Note that eqs 23 and 25 hold whenever mode l is not mixed (i.e., $J_{ll} = 1$) and its frequency is unchanged in the two electronic states ($\mathbf{\Gamma}_{ll}^g = \mathbf{\Gamma}_{ll}^k$), and, therefore, also when Duschinsky mixing and frequency

changes take place for other modes (i.e., $\mathbf{J} \neq \mathbf{I}$ and/or $\mathbf{I}^g \neq \mathbf{I}^k$). The same also holds for eq 26 if both modes j and l fulfill these requirements. Therefore, eqs 23–26 can be utilized to estimate the intensities *a priori* for the modes that almost meet the conditions reported above. For instance, when Δ_l (and Δ_j) are small (i.e., $\ll 1$), fundamental transitions are expected to be the strongest ones.

2. The Gradient Approximation. Let us consider only FC terms in the polarizability tensor and only the fundamental transitions $0_j \rightarrow 1_j$ for each mode j . If $\Delta_j \ll 1$, as already noticed by Long¹ and by Warshel and Dauber,¹⁰ it follows that $\langle 0_j^g | 0_j^k \rangle \approx \langle 1_j^g | 1_j^k \rangle \approx 1$ and $\langle 0_j^g | 1_j^k \rangle = -\langle 1_j^g | 0_j^k \rangle = -\Delta_j / \sqrt{2}$, while all the other integrals are zero. By neglecting all the terms beyond the first order in the displacements Δ_b , the polarizability tensor simply becomes

$$\alpha_{\rho\sigma}^{0_j \rightarrow 1_j} = \mu_{\rho}^{gk}(0) \mu_{\sigma}^{kg}(0) \left[\frac{\langle 0_j^g | 0_j^k \rangle \langle 0_j^k | 1_j^g \rangle}{\omega_{kg} - \omega_l - i\gamma_k} + \frac{\langle 0_j^g | 1_j^k \rangle \langle 1_j^g | 1_j^k \rangle}{\omega_{kg} + \omega_j - \omega_l - i\gamma_k} \right] \quad (27)$$

$$\alpha_{\rho\sigma}^{0_j \rightarrow 1_j} = \mu_{\rho}^{gk}(0) \mu_{\sigma}^{kg}(0) \frac{\omega_j \Delta_j}{\sqrt{2}(\omega_{kg} - \omega_l - i\gamma_k)(\omega_{kg} + \omega_j - \omega_l - i\gamma_k)} \quad (28)$$

where ω_{kg} is the electronic adiabatic energy difference. When $\omega_{kg} - \omega_l \gg \omega_j$, the denominator of last equation can be considered constant for different ω_j ; therefore, the approximate relationships hold for the polarizability tensor component $\alpha_{\rho\sigma}^{0_j \rightarrow 1_j} \propto \Delta_j \omega_j$, and for the differential cross section $\sigma^{0_j \rightarrow 1_j} \propto (\Delta_j \omega_j)^2$. Note that, in the limit of validity of the IMDHO model, Δ_j can be obtained avoiding geometry optimization of the excited state, by simply computing the derivative of the excited-state energy, with respect to the normal coordinate Q_j at the ground equilibrium geometry (the so-called “vertical gradient”):

$$\left(\frac{\partial E^k}{\partial Q_j} \right)_0 = E_j^k = -\omega_j^2 K_j = -\frac{\omega_j^{3/2} \Delta_j}{\hbar^{1/2}} \quad (29)$$

Therefore, it is possible to write that the ratio between the RRS intensities of the two modes j and l is

$$\frac{I_j^{0 \rightarrow 1}}{I_l^{0 \rightarrow 1}} = \left(\frac{E_j^k}{E_l^k} \right)^2 \frac{\omega_l}{\omega_j} = \frac{\omega_j^2 \Delta_j^2}{\omega_l^2 \Delta_l^2} \quad (30)$$

To complete this section, it is worth recalling that, in a series of seminal papers,^{6,7} Heller and co-workers showed, using a time-dependent approach, that, under preresonance conditions, when only the very short time dynamics on the excited state is to be considered, the first equality of eq 30 is still fulfilled; also, in case the IMDHO model is not valid and the second equality of eq 30 does not hold. In true resonance cases, even when the harmonic approximation is valid, eq 30 does not hold and Duschinsky mixing and frequency changes must be considered; this can be done via direct application of eq 10, thus also allowing for a detailed analysis of these effects.

III. COMPUTATIONAL METHOD: A DOUBLE-LAYER SELECTION SCHEME

As already stated in the Introduction, our aim is to focus on vibrational RR transitions from the ground vibrational state $|0^g\rangle$ (only Stokes bands), to describe both Franck–Condon (FC) and Herzberg–Teller (HT) effects, and to fully account for any

possible difference between the harmonic PES of the initial and intermediate electronic states. Our working expressions for intensity are eqs 1–6, while the polarizability tensor for each intermediate electronic state $|e^k\rangle$ is computed according to eq 10.

As reported above, the necessary integrals on the vibrational coordinates can be computed according to recurrence formulas (see eqs 12 and 13). However, such a treatment can be very cumbersome from the computational point of view, for two main reasons. The first one is that the explicit calculation of the polarizability tensor, in terms of a brute-force SOS expression, is generally unfeasible, because the number of vibrational states of the intermediate electronic state in a sizable molecule is huge (can easily exceed 10^{20}). Note that, in fact, if one wants to compute the RRS spectra as a function of the excitation frequency, all the vibronic transitions relevant for the absorption spectrum of the resonant state must be taken into account. The second reason is that the number of possible final vibrational states (i.e., those belonging to the ground electronic state) also is extremely large. Thus, in order to make the calculation feasible, it is necessary to work out effective prescreening techniques that are able to select only the relevant contributions *a priori*. Here, we will propose a way to overcome such difficulties using a two-layer strategy, by keeping in mind the fact that, although a too-strict selection of the final states may result in the absence of some bands in the simulated RR spectrum, an incomplete inclusion of the intermediate states may lead to inaccuracies in the predicted bands, which cannot easily be controlled.

A. Selection of the Intermediate States. Upon inspection of eq 10, it can be realized that, by resorting to an SOS time-independent perspective, the computation of the polarizability tensor for a given final state $|f^g\rangle$ (the initial state is always the ground state $|0^g\rangle$) is equivalent to the computation of two absorption spectra (possibly including HT effects) for the electronic transition $|e^g\rangle \rightarrow |e^k\rangle$. The first one arises from the ground vibrational state $|0^g\rangle$ (for $T = 0$ K), and the second arises from a selected hot-vibrational state $|f^g\rangle$. If more than one intermediate electronic state $|e^k\rangle$ is to be considered, the calculation should be repeated for each state and the polarizability tensors summarized before computing the square contributions to eq 2. An effective method to compute absorption spectra including Duschinsky and HT effects both for $T = 0$ K and finite temperature spectra has been proposed previously by some of us.^{42–44} It is intuitive that the machinery that permits the computation of spectra at finite temperature also allows, in a straightforward manner, the computation of the spectrum from a single hot state $|f^g\rangle$.

In brief, our method is based on a partition of the manifold of vibrational states $|m^k\rangle$ of the resonant state $|e^k\rangle$ (and of the corresponding transitions) in different classes C_n , each depending on the number n of oscillators, whose quantum number is different from zero. For instance, $\langle n^g | 3, 0, \dots \rangle$ is a C_1 transition, and $\langle n^g | 0, 3, 0, 5, 4, 0, \dots \rangle$ is a C_3 transition. For each C_n , a maximum-allowed excitation vector $\mathbf{W}_n^{\max}(n^g)$ is defined, so that all the integrals $\langle n^g | m^k \rangle$ to states $|m^k\rangle$ with larger quantum numbers can be considered as negligible. In the general case of a finite-temperature spectrum with HT effects, the determination of $\mathbf{W}_n^{\max}(n^g)$ is based on the analysis of the C_1 and C_2 FC transitions (which involve a low computational cost), both from the ground and from the excited initial states (in our case, $|0^g\rangle$ and $|f^g\rangle$), with the addition of the HT contribution to the C_1 class.⁴⁴ For further details, the interested reader is directed to the cited references.

Because of the recursive nature of the formulas in eqs 12 and 13, the calculation of the spectrum from the $|f^g\rangle$ state automatically provides all the data that are required for the computation of the spectrum from any state $|f^g\rangle$, as far as $f_j^g \leq f_j^g$ for $\forall j$. In the cited references, such a feature was exploited in the computation of the finite temperature spectra, by grouping the Boltzmann-populated initial states into “mother states”, which are used for the calculation of the spectra for all the initial states that share the same set of initially excited normal modes.

Here, we will exploit the recursive properties of the method by performing separate calculations for the overtones of each normal mode j , up to a given quantum f_j (i.e., by adopting the initial state $|f^g\rangle = |0^g + f_j^g\rangle$), and also by collecting, in this way, the information for lower overtones and fundamentals. In an analogous way, for combination bands, a separate calculation for each couple (j, l) up to quanta f_j and f_l can be performed (i.e., selecting the initial state $|f^g\rangle = |0^g + f_j^g + f_l^g\rangle$), to gather the information needed for any less-excited combination band of the same couple j and l .

B. Selection of the Final Vibrational States of the Ground Electronic State. In principle, the number of the possible final states of the ground electronic states populated upon RRS is not limited by any strict selection rule. However, experimental RRS spectra are usually measured in a rather narrow energy window, only encompassing fundamentals and low-excited overtones and combination bands. Concerning theoretical simulations, most of those reported in the literature so far consider only fundamental bands.

Here, we will focus on fundamentals, overtones, and combination bands of two modes, and we will adopt simple selection schemes, based on the analysis of the TT predictions within the IMDHO model. In practice, we exclude from the calculation all of the modes that are essentially not mixed by Duschinsky couplings and that show displacements and frequency changes that are below a given threshold. For all the other modes, fundamentals and overtones are computed up to the same maximum quantum number. The analysis of the fundamentals and overtones is used to guess the most important combination bands of two modes, by sorting the modes in decreasing order of RRS intensities for fundamentals and by further selecting the first N_r modes for which combination bands are actually computed, that, in order to keep the number of initial states for combination bands $N_r^*(N_r - 1)/2$ below a given maximum number. This very simple selection is based on the observation that, in the limit of validity of the IMDHO model, according to TT predictions (see eqs 23–26), fundamental intensities are dependent on dimensionless displacements and $(1 + 1)$ combination bands on their product; therefore, the combination bands of two modes showing negligible fundamentals is expected to be negligible (unless very strong Duschinsky mixings take place). More-refined selections are obviously possible, but the investigation of such a matter will be postponed to future work.

C. Analytical Sums and Convergence Checks. It is worthy to note that, when the transition is off-resonant $\omega_I \ll \omega_{km,gi}$ the denominator in eq 10 can be considered constant and equal to $\omega_{kg} - \omega_I$ for each intermediate electronic state $|e_k\rangle$. Therefore, it is possible to sum over the vibrational \mathbf{m}^k states and, by exploiting the closure relationship $\sum_{v_m^k} |v_m^k\rangle\langle v_m^k| = 1$, one can easily prove that the FC term vanishes. In those particular cases, the dominant terms in the polarizability tensor that determine the transition intensity are the HT terms (i.e., those depending linearly on the normal coordinates Q^g). Obviously, when $\omega_I \ll \omega_{km,gi}$ the

second term in the right-hand side (rhs) of eq 3 cannot be considered negligible in comparison with the first term, however, its FC contribution also vanishes, thus making the FC contribution to Raman scattering null. In the resonant case, both FC and higher-order terms may contribute to the polarizability tensor and FC terms are expected to dominate for strongly allowed transitions, i.e., when $|\bar{\mu}^{gk}(0)| \gg |\sum_i \bar{\mu}^{gk}(l)\Delta Q_l|$, where now $\bar{\mu}$ is the vector (μ_x, μ_y, μ_z) and ΔQ_l represents the displacements of the equilibrium structures caused by the electronic transition along mode l .

To compute the RRS intensities through the SOS expression in eq 10, the number of intermediate vibronic states to be considered is, in principle, infinite, and clearly the sum must be truncated. Moreover, Duschinsky effects prevent easy routes to accelerate the calculations. Therefore, it is useful to work out analytical sum rules in order to check the convergence of the results. As already discussed, the calculation of RRS intensities can be reduced to the calculation of two absorption spectra, and, therefore, the same analytical sums that have been derived in previous papers⁴⁴ also can be useful for RRS.

In addition, the off-resonant limit of the polarizability tensor provides a suitable route to obtain new and specific sum rules for RRS. In fact, by skipping the denominators in eq 10, we obtain

$$\begin{aligned} \bar{\alpha}_{\rho\sigma}^{f_0} = & \sum_{\mathbf{m}} \langle 0^g | \mu_{\rho}^{gk}(0) | \mathbf{m}^k \rangle \langle \mathbf{m}^k | \mu_{\sigma}^{kg}(0) | f^g \rangle \\ & + \sum_{\mathbf{m}} \langle 0^g | \sum_l \mu_{\rho}^{gk}(l) Q_l^g | \mathbf{m}^k \rangle \langle \mathbf{m}^k | \mu_{\sigma}^{kg}(0) | f^g \rangle \\ & + \sum_{\mathbf{m}} \langle 0^g | \mu_{\rho}^{gk}(0) | \mathbf{m}^k \rangle \langle \mathbf{m}^k | \sum_j \mu_{\sigma}^{kg}(j) Q_j^g | f^g \rangle \\ & + \sum_{\mathbf{m}} \langle 0^g | \sum_l \mu_{\rho}^{gk}(l) Q_l^g | \mathbf{m}^k \rangle \langle \mathbf{m}^k | \sum_j \mu_{\sigma}^{kg}(j) Q_j^g | f^g \rangle \quad (31) \end{aligned}$$

and by summing over the intermediate vibrational states, we get

$$\begin{aligned} \bar{\alpha}_{\rho\sigma}^{f_0} = & \mu_{\rho}^{gk}(0) \mu_{\sigma}^{kg}(0) \langle 0^g | f^g \rangle + \mu_{\sigma}^{kg}(0) \sum_l \mu_{\rho}^{gk}(l) \langle 0^g | Q_l^g | f^g \rangle \\ & + \mu_{\rho}^{gk}(0) \sum_j \mu_{\sigma}^{kg}(j) \langle 0^g | Q_j^g | f^g \rangle \\ & + \sum_{l,j} \mu_{\rho}^{gk}(l) \mu_{\sigma}^{kg}(j) \langle 0^g | Q_l^g Q_j^g | f^g \rangle \quad (32) \end{aligned}$$

The above integrals are easily evaluated (for example, switching to a second quantization), giving

$$\bar{\alpha}_{\rho\sigma}^{f_0} = \left\{ \begin{array}{ll} \mu_{\rho}^{gk}(0) \mu_{\sigma}^{kg}(0) + \sum_l \mu_{\rho}^{gk}(l) \mu_{\sigma}^{kg}(l) \frac{\hbar}{2\omega_l^g} & \text{if } |f^g\rangle \equiv |0^g\rangle \\ (\mu_{\rho}^{gk}(0) \mu_{\sigma}^{kg}(l) + \mu_{\rho}^{gk}(l) \mu_{\sigma}^{kg}(0)) \sqrt{\frac{\hbar}{2\omega_l^g}} & \text{if } |f^g\rangle \equiv |0^g + 1_l\rangle \\ (\mu_{\rho}^{gk}(l) \mu_{\sigma}^{kg}(j) + \mu_{\rho}^{gk}(j) \mu_{\sigma}^{kg}(l)) \frac{\hbar}{2\sqrt{\omega_l^g \omega_j^g}} & \text{if } |f^g\rangle \equiv |0^g + 1_l + 1_j\rangle \\ \mu_{\rho}^{gk}(l) \mu_{\sigma}^{kg}(l) \frac{\sqrt{2}\hbar}{2\omega_l^g} & \text{if } |f^g\rangle \equiv |0^g + 2_l\rangle \\ 0 & \text{for all other final states} \end{array} \right\} \quad (33)$$

When performing the SOS calculation of the RRS intensity for a given final state $|f^g\rangle$, it is thus possible to compute numerical quantities $\bar{\alpha}_{\rho\sigma}^{num}$, analogous to the analytical $\bar{\alpha}_{\rho\sigma}$ ones, by adding all the contributions for each different intermediate state

considered, $|\mathbf{m}^k\rangle$. Comparison of numerical and analytical sums permits one to check the convergence of the calculations.

IV. APPLICATIONS

Here, the methodology described in the previous sections to evaluate RRS is applied to selected systems, i.e., the phenoxyl radical in the gas phase, and indolinedimethine–malononitrile (IDMN) in an acetonitrile and cyclohexane solution. These two cases were chosen because of the availability of experimental data in the literature that allow for a critical comparison of the accuracy of our computations and a detailed analysis of performance of the various levels of approximation. Although our approach, in principle, is applicable to any electronic structure method that can locate equilibrium structures of ground and excited states and their Hessian matrices, in the following, we will refer to TD-DFT calculations for mere computational convenience.

In parallel to the presentation of RRS spectra, we also report and discuss absorption spectra of the various systems, in order to evaluate the overall performance of TD-DFT in reproducing excitation energies, vibronic band profiles, and states hierarchy, and to identify the electronic states that are in resonance with a certain excitation frequency exploited in the RRS spectra.

A necessary starting point for the simulation is to locate the equilibrium geometry of the ground electronic state and to perform a normal-mode analysis in order to establish a harmonic model of the ground PES (V_g). In addition, both RRS and absorption spectra calculation rely on the specific model of the excited (resonant) state PES (V_k). Vertical (V) and adiabatic (A) approaches can be exploited, depending whether the excited PES is expanded in a Taylor series of the nuclear coordinates around its own equilibrium geometry (“A” approach) or around the ground-state geometry (“V” approach). Moreover, when only constant and linear terms are retained in the Taylor expansion of the difference $V_k - V_g$, the model implicitly assumes that normal modes and frequencies are the same in the two states and only the equilibrium geometries are displaced (IMDHO model). In this framework, if displacements are obtained from the excited-state gradient at the ground-state geometry, we have the so-called “Vertical Gradient” (VG) model; alternatively, if they are directly obtained as the difference in the equilibrium geometries, a different model—which we call the “Adiabatic Shift” (AS) model—is obtained.

In order to account not only for displacements, but also for frequency changes and Duschinsky mixings, it is necessary to compute the excited-state Hessian, thus obtaining the Vertical Hessian (VH) or Adiabatic Hessian (AH) models, depending on the reference geometry. The model for the computation is complete if the approximation for the transition electric dipole is specified, namely, if only the constant (FC) terms, the linear (HT) terms, or both (FC + HT) terms are considered in the expansion (see eq 9).

In the following, we will compare the results obtained from SOS expressions for absorption and RRS spectra (see eqs 20 and 10), according to FC|AS, FC|AH, and (FC + HT)|AH models (for the sake of brevity, “FC + HT” will be abbreviated hereafter as HT; this generates no confusion, since we never show the pure HT contributions alone). In the case of RRS spectra, in order to highlight the differences between our method and the ones mostly exploited in the literature so far, we will also report the FC results obtained according to the gradient (VG)

approximation (TT spectra are usually computed by skipping the Φ factor and, therefore, are assimilable to VG results).

All the electronic calculations that will be reported were performed by exploiting the Gaussian09⁴⁹ package. Vibronic FC⁴² and HT⁴⁴ calculations were done using a modified version of the \mathcal{FC} classes code;⁵⁸ in the latter, the convergence of the results is ruled by a user-defined parameter N^{\max} , which limits the number of possible transitions to be computed for each excitation class n . Increasing N^{\max} results in a better convergence (hence, better quality of the results) but also increases the computational burden; therefore, a compromise must be chosen. Convergence of absorption and RRS was checked according to the analytical sums given in eq 33, as well as by direct comparison of the spectra obtained with different choices of N^{\max} . RRS spectra appeared to converge much faster than the analytical sums, which is a favorable feature that was already observed for absorption spectra.⁴²

When required, solvent effects were taken into account using the PCM,^{53,54} by setting cavity parameters as well as the proper static and optical dielectric constant values according to Gaussian09⁴⁹ default values.

A. The Phenoxyl Radical in the Gas Phase. 1. *Absorption Spectrum.* In Figure 2, calculated excitation energies from the doublet 2B_1 ground state D_0 to the first five OPA allowed electronic excited states of the phenoxyl radical in the gas phase are reported (C_{2v} symmetry). Following ref 40, the uB3LYP/TZVP level was selected, among others. As can be seen from the results reported in the figure, such a level performs in a manner pretty similar to that of the uB3LYP/cc-PVTZ level (which was already proposed for this molecule by Radziszewski et al.⁵⁹) and to the 6-31+G(d,p), 6-31++G(d,p) and 6-311+G(d,p) basis sets. The level of reproduction of the experimental excitation energies is almost independent of the choice of the basis set, and it is pretty good overall, with the maximum deviation being of the order of 0.4 eV. Because of this fact, the following discussion will be limited to the uB3LYP/TZVP results.

Figure 3 sketches the calculated absorption spectrum of the phenoxyl radical, and the FC|AS, FC|AH, and HT|AH approaches are compared by focusing on the transitions to states D_2 (2B_2) and D_3 (2A_1), since the transition to D_1 is extremely weak. In order to simulate inhomogeneous broadening, stick spectra have been convoluted with a Gaussian lineshape, whose width is indicated in the figure caption. As is evident upon inspection of the calculated spectra, the role of HT is quite marginal for the D_2 spectrum (panel a), whereas a more substantial effect is noticed on relative intensities of the various vibronic peaks of the D_3 transition (panel b). One dominant progression can be singled out in the $D_0 \rightarrow D_2$ absorption spectrum, along mode $\nu_6^{(2)}$ (the number in parentheses specifies the electronic state, $0 \equiv g$), whose frequency is 522 cm^{-1} ; this mode is projected for more than 99% on ground-state mode $\nu_3^{(0)}$, and it corresponds to a 1,4 elongation of the phenyl ring; secondary progressions involve three modes in the $1550\text{--}1600 \text{ cm}^{-1}$ range. The main vibrational progressions in the D_3 spectrum are due to $\nu_{23}^{(3)}$ (1499 cm^{-1}), $\nu_{13}^{(3)}$ (1278 cm^{-1}) and $\nu_{14}^{(3)}$ (927 cm^{-1}). Notice that $\nu_{23}^{(3)}$ and $\nu_{19}^{(3)}$ show the largest derivatives of $\bar{\mu}^{-0.5}$; however, interestingly, HT leads to a decrease of their vibronic intensities (as they become lower than the fundamental of $\nu_{14}^{(3)}$), because of partial destructive interference. The approximations of the AS model, with respect to the AH model, manifest themselves in a general blueshift of the spectrum, because of neglect of the zero-point energy differences in the ground and resonant electronic states, and in some redistribution

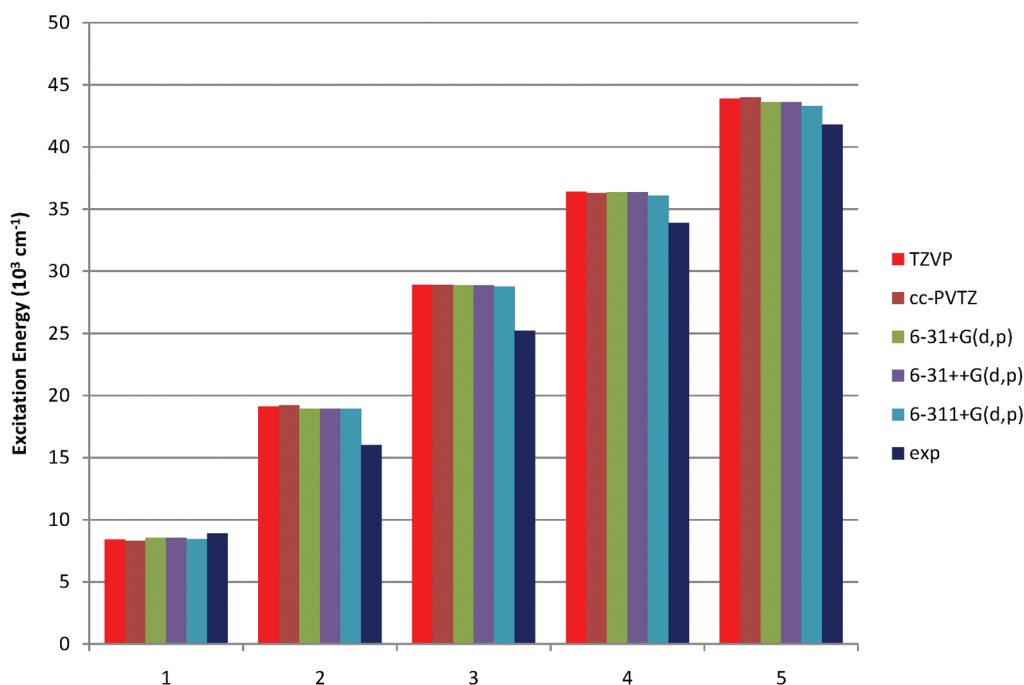


Figure 2. Calculated excitation energies of the first five OPA allowed electronic states of phenoxyl radical in the gas phase, as obtained using the B3LYP functional and different basis sets. Symmetry assignments are done according to the orientation reported in Figure 3 and are as follows: (1) 2A_2 , (2) 2B_2 , (3) 2A_1 , (4) 2B_2 , and (5) 2A_1 . For comparison, experimental excitation energies taken from ref 59 are also reported.

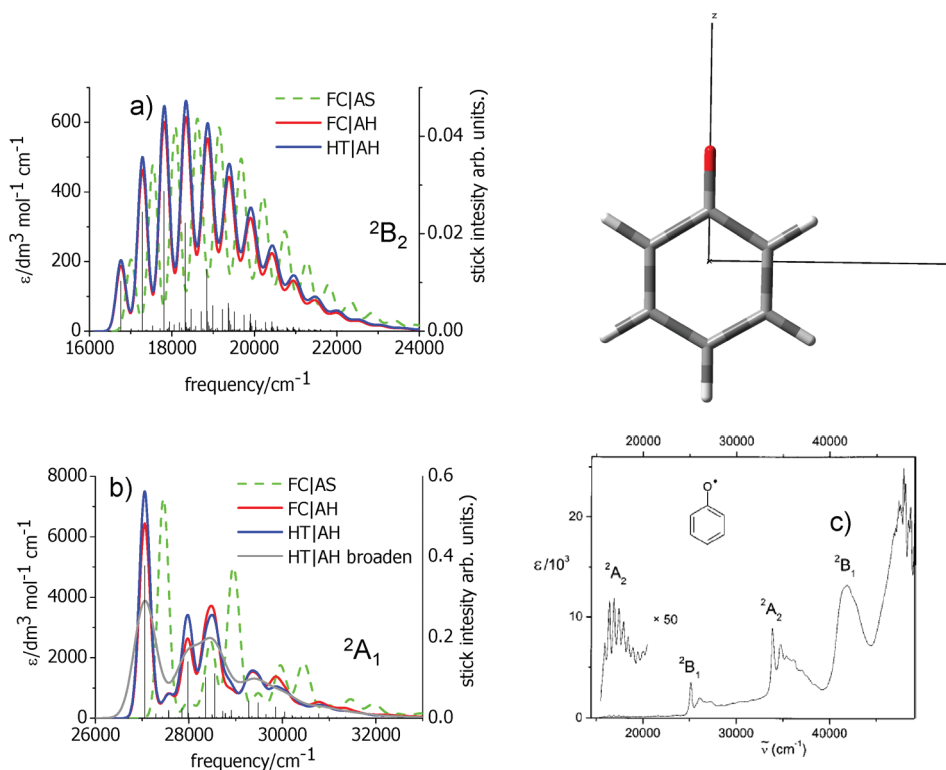


Figure 3. Absorption spectrum for the (a) $D_0 \rightarrow D_2$ (labeled 2A_2 in panel c) and (b) $D_0 \rightarrow D_3$ (labeled 2B_1 in panel c) transitions of phenoxyl radical, computed according to different models, convoluted with a Gaussian lineshape with HWHM = 0.033 eV. For $D_0 \rightarrow D_3$, a spectrum convoluted with a Gaussian lineshape with HWHM = 0.066 eV (labeled as “broaden” in the inset) also is reported. Stick spectra refer to the HT|AH calculation. (c) The experimental spectrum is also reported, for comparison (reprinted with permission from ref 59, Copyright 2001, American Institute of Physics).

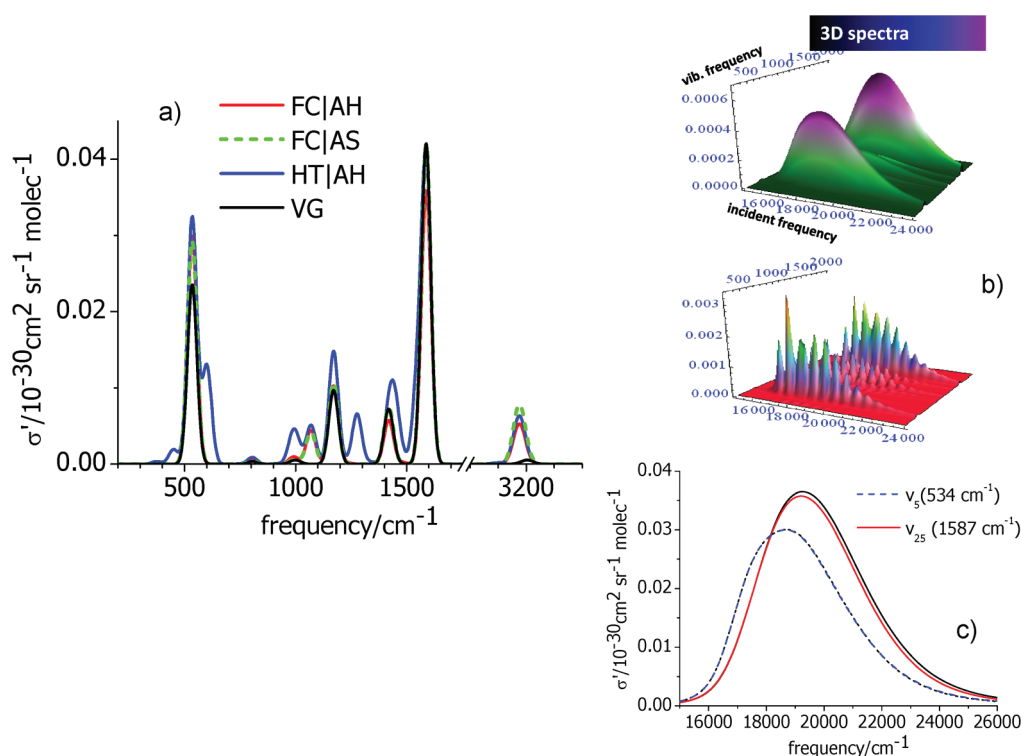


Figure 4. (a) Comparison of the RRS spectrum resonant with the maximum of the $D_0 \rightarrow D_2$ transition, computed according to different models ($\gamma = 0.1$ eV). (b) FC resonance Raman 2D spectrum for the $D_0 \rightarrow D_2$ transition for $\gamma = 0.1$ eV (upper panel) and 0.02 eV (lower panel). (c) FC Raman excitation profile resonant with the $D_0 \rightarrow D_2$ transition for two different vibrational modes for a $\gamma = 0.1$ eV. A convergence test is also shown in the case of $\nu_{25}^{(0)}$ (the accuracy parameter N^{\max} is varied from 10^5 to 10^7 , see red and black straight lines). The vibrational stick RRS bands have been convoluted with a Gaussian lineshape, with $\text{HWHM} = 25 \text{ cm}^{-1}$ (not normalized, i.e., its maximum is 1).

of the peak intensities, which are more pronounced for the D_3 state.

Overall, the reproduction of the experimental absorption spectrum (which was recorded in an argon matrix at a temperature of 7 K, see ref 59), shown in Figure 3c, is good, thus showing the reliability of the combination of TD-DFT with our approach to calculate vibronic progressions.

2. RR Scattering for the $D_0 \rightarrow D_2$ Transition: Fundamentals and Overtones. Moving to RRS, in Figure 4, the spectrum obtained for the $D_0 \rightarrow D_2$ transition is reported (Figure 4a) as a function of the level of description of the RR phenomenon. All the spectra have been computed assuming an excitation at the vertical transition energy and, if not differently stated, an excited-state lifetime of $\gamma = 0.1$ eV, apart from those computed according to the gradient approximation, which are not explicitly dependent on these parameters and are thus given in arbitrary units. Note that, in the present manuscript, γ is used as a purely phenomenological parameter: the dependence of the description of RR spectra and Raman excitation profiles on γ will be underlined for selected cases (*vide infra*). Calculated vertical transition energies (and not estimated experimental ones) have been used (see Figure 2 for their values). Note further that, here and afterward, in order to be free of possible anharmonic effects that would complicate the comparison of the different harmonic models, the excited-state energy gradient values are actually retrieved, by invoking the harmonic approximation, from the displacements of the equilibrium structures, according to the relations given in eq 29.

The convergence of the reported spectra is very good. As shown in the Supporting Information, spectra evaluated with

$N^{\max} = 10^5$ are exactly superimposable to the more accurate ones computed with $N^{\max} = 10^7$, even if, in the first case, a maximum error of 7% still remains, as far as the convergence to the analytical sums for fundamentals is concerned.

A general overview of the spectra reported in Figure 4 indicates remarkable differences in the predictions obtained by the different models all over the spectrum, and that mostly involve vibrations in the $400\text{--}700 \text{ cm}^{-1}$ and $1000\text{--}1500$ ranges (out-of-plane and in-plane ring bending and C–O stretching modes). By analyzing the spectra in more detail, two dominant lines can be seen at the FC level, corresponding to the fundamentals of the $\nu_5^{(0)}$ and $\nu_{25}^{(0)}$ modes (a combination of ring CC stretchings). It is remarkable that these lines are strictly correlated to the progressions observed in the absorption spectrum, but also that, at the same time, noticeable differences arise. In fact, the $\nu_5^{(0)}$ mode gives rise to the main progression in the absorption spectrum, and the progressions at $\sim 1550\text{--}1600 \text{ cm}^{-1}$ (although more than one mode is involved, because of Duschinsky effects) are mainly correlated with a remarkable displacement along the $\nu_{25}^{(0)}$ mode. Nonetheless, while the progression along the $\nu_5^{(0)}$ mode is, by far, the dominant one in the absorption spectrum, the RRS intensity along this mode is overcome by that along the $\nu_{25}^{(0)}$ mode. Moreover, the difference between the various computational approaches is more evident in the RRS spectrum than in the absorption spectrum. In particular, the introduction of HT effects causes a markedly different intensity pattern, leading to the appearance of new bands that are not predicted by the other models. This is the case, for example, of the bands at 600 cm^{-1} and 1276 cm^{-1} , which are respectively assigned to the fundamentals of the $\nu_6^{(0)}$ and $\nu_{19}^{(0)}$ modes, which, in fact, exhibit large

derivatives of the transition dipole moment $\vec{\mu}^{02}$. Despite this fact, these two modes (or, better, the corresponding D_2 modes) do not appear to give appreciable signatures in the absorption spectrum.

It is also worth highlighting some marked differences between the VG and FC|AS spectra. In fact, while, for small displacements, the two models are expected to give similar results, differences arise when the displacements are relevant. The two peaks at 1068 and 3175 cm^{-1} are overtones (2 quanta) of the dominant fundamental bands along the $\nu_5^{(0)}$ and $\nu_{25}^{(0)}$ modes, which have remarkable intensity but are not described within the gradient approach (at least in its standard implementation). Finally, the differences among the FC|AS and FC|AH models are only marginal (see, for example, the overtone band at 3175 cm^{-1}), thus indicating that Duschinsky effects play only a minor role in the present case.

2D RRS Spectra and Raman Excitation Profiles. Figure 4b reports the RRS 2D spectrum as a function of the incident frequency and the difference between the frequencies of the incident and scattered light (indicated as vibrational frequency, i.e., the same coordinate already adopted in Figure 4a). Because of some arbitrariness in the choice of the γ parameter, two possibilities are compared, corresponding to a short lifetime ($\gamma = 0.1$ eV) and a long lifetime ($\gamma = 0.01$ eV). As expected, the 2D spectra appear very different for the two values of γ and are much more resolved for a long lifetime. A more-detailed analysis is possible by examining cuts of the 2D spectra obtained by fixing the vibrational frequency (i.e., the so-called Raman excitation profiles). Figure 4c reports such spectra for the two dominant bands: the fundamentals of the $\nu_5^{(0)}$ and $\nu_{25}^{(0)}$ modes. For the $\nu_{25}^{(0)}$ mode, the results of two different calculations are reported, performed with $N^{\text{max}} = 10^5$ and $N^{\text{max}} = 10^7$ (black and red straight lines), to show that the method permits to reach a very good convergence, even with respect to the excitation profile. Focusing on the interpretative aspects, it is worth noting that the relative RR intensities of the two modes are dependent on the frequency of the exciting light, and, in particular, because of the shape of the curves, the band at 534 cm^{-1} may or may not overtake that at 1587 cm^{-1} , depending on the exciting radiation.

At this point of the discussion, a general comment is appropriate. Given the current state of the art, the γ value is not easily computable *ab initio*, so it is commonly treated as a phenomenological parameter. Moreover, the computational prediction of the absolute position of the excited states is always affected by some error, so it may not be easy to establish a one-to-one correspondence between the experimental incident frequency and the vertical frequency at which the RRS spectrum is simulated. Therefore, it is very encouraging that the method presented here can efficiently compute spectra, as a function of these parameters. In fact, this may allow for a careful check of the sensitivity of the predictions on these parameters, in order to provide a robust interpretation, which is possibly not biased by particular and possibly inappropriate choices of such values.

3. RR Scattering for the $D_0 \rightarrow D_3$ Transition: Fundamentals and Overtones. Figure 5 shows calculated RRS spectra of the $D_0 \rightarrow D_3$ transition, as a function of the choice of the computational model. Similar to that observed for the $D_0 \rightarrow D_2$ transition, in this case, the predicted spectral shape also changes remarkably as the computational model varies with the appearance/disappearance of some peaks, the most evident differences being those introduced by HT effects (the HT|AH model). Comparison with the experiment (taken from ref 60) documents a good overall

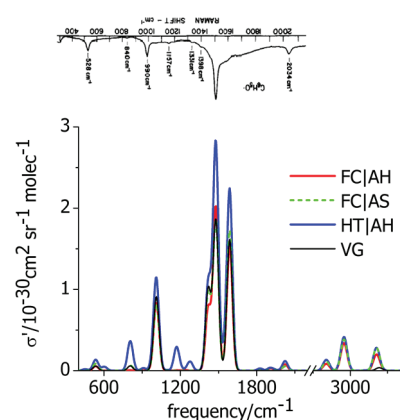


Figure 5. RRS spectrum resonant with the maximum of the $D_0 \rightarrow D_3$ transition, computed according to different models. VG calculation only includes fundamental transitions and is reported in arbitrary units. The experimental spectrum is reported for comparison (reprinted with permission from ref 60, Copyright 1984, American Institute of Physics). Vibrational stick RRS bands have been convoluted with a Gaussian lineshape, with HWHM = 25 cm^{-1} (not normalized, i.e., its maximum is 1).

agreement, especially if the low resolution of the experimental data is considered. In more detail, our calculation correctly predicts the dominant band to be observed at ~ 1500 cm^{-1} (assigned to the fundamental of the $\nu_{23}^{(0)}$ mode with a frequency of 1478 cm^{-1}), and that such a band is accompanied by a second blue-shifted peak, assigned to the $\nu_{25}^{(0)}$ mode at a frequency of 1587 cm^{-1} , whose intensity, however, is significantly overestimated in our calculations when compared with the experiment, where it simply appears as a shoulder. The positions of minor peaks at ~ 1200 , 1000, 800, and 600 cm^{-1} are also nicely predicted, as well as, in most cases, the relative order of their intensities. The strongest band at 1011 cm^{-1} is assigned to the fundamental of the $\nu_{15}^{(0)}$ mode. Note that, similar to that observed in the $D_0 \rightarrow D_2$ spectrum, in the region above 3000 cm^{-1} , some small but non-negligible peaks arise. These latter might be erroneously assigned to CH stretchings, whereas they are actually due to overtones of the fundamental bands in the 1500 cm^{-1} region. This can be easily recognized by noticing that they are absent in VG calculations, which only account for fundamentals.

Raman Excitation Profiles. In Figure 6, Raman excitation profiles resonant with the $D_0 \rightarrow D_3$ transition are reported for two selected normal modes. FC|AH and HT|AH results are compared in Figure 6a, where absorption spectra, obtained using the same broadening (0.1 eV), also are given, for comparison. The difference between FC and HT is not relevant for the band at 1011 cm^{-1} (only a shift in the intensity), whereas the difference is more substantial for the mode at 1478 cm^{-1} . Both FC and HT models, however, predict a larger RR intensity for this last band. Figure 6b only reports FC results, computed with a much narrower linewidth ($\gamma = 0.02$ eV), documenting that the shape of the profile is hugely dependent on the chosen linewidth, and that, for small values, the relative intensity of the two peaks may become drastically dependent on the incident frequency. Specifically, while the intensity of the 1011 cm^{-1} peak is higher than that of the 1478 cm^{-1} one when the exciting frequency is in resonance with the 0–0 transition at ~ 27000 cm^{-1} , in two different regions—namely, at ~ 28800 and 30000 cm^{-1} —the 1011 cm^{-1} peak is almost completely quenched and it is overcome by the 1478 cm^{-1} peak, by more than 1 order of magnitude.

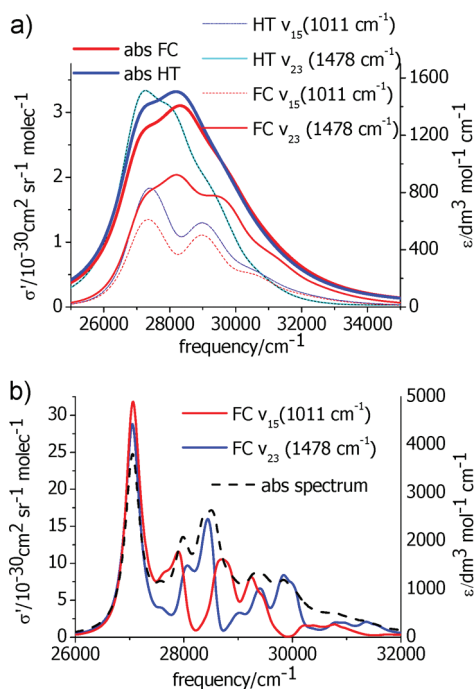


Figure 6. (a) FC and HT Raman excitation profiles resonant with the $D_0 \rightarrow D_3$ transition for two different vibrational modes and for $\gamma = 0.1$ eV. For HT computations, a convergence test also is reported by giving the results obtained by setting the accuracy parameter as $N^{\max} = 10^6$ and 10^7 . RR profiles are compared with the corresponding absorption spectra computed with a Lorentzian broadening, with the same linewidth and $\gamma = 0.1$ eV. (b) FC Raman excitation profile resonant with the $D_0 \rightarrow D_3$ transition for two different vibrational modes and a small linewidth and $\gamma = 0.02$ eV (solid lines). The RR profiles are compared with the corresponding absorption spectrum, computed with the same Lorentzian broadening.

4. *RR Scattering for the $D_0 \rightarrow D_3$ Transition: Combination Bands.* The unusually high-frequency experimental peak at 2034 cm^{-1} (see Figure 5) is not reproduced in our calculations, which do predict a band in that region (2022 cm^{-1}), assigned to the first overtone of $\nu_{15}^{(0)}$, but its intensity is much smaller than its experimental counterpart. Based on the position of the strongest experimental band slightly above 1500 cm^{-1} and the secondary band at 528 cm^{-1} , it may be suggested that the peak at 2034 cm^{-1} corresponds to a combination band of the two modes, giving rise to these fundamentals.

A brute-force SOS calculation of all of the possible combinations of two bands (435 pairs) would require a very expensive calculation. Analysis of the TT expression for combination bands in eq 26 indicates that, apart the frequency-dependent Φ factors, their RRS intensities are expected to be dependent on the product of the displacements along the two modes, in the same way as fundamentals and overtones are dependent on such displacements and their powers. Here, based on these considerations, we have selected the combination bands of pairs of modes corresponding to the eight most-intense fundamentals (namely, $\nu_5^{(0)}$, $\nu_{10}^{(0)}$, $\nu_{15}^{(0)}$, $\nu_{17}^{(0)}$, $\nu_{19}^{(0)}$, $\nu_{21}^{(0)}$, $\nu_{23}^{(0)}$, $\nu_{25}^{(0)}$). The RRS spectra obtained including either only fundamentals and overtones (up to the quantum number $n = 3$) for each mode or also the two-mode combination bands (quantum numbers $1 + 1$) of the eight selected modes are compared in Figure 7. Here, for an easier individuation, the fundamentals and overtones of mode n with quantum number q are labeled as n^q and the combination bands

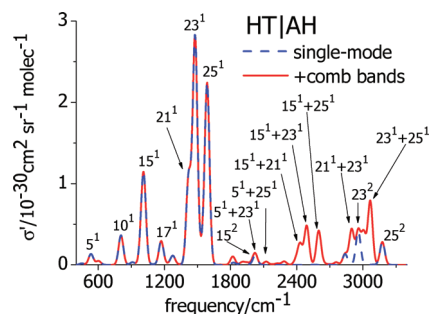


Figure 7. RRS spectrum resonant with the maximum of the $D_0 \rightarrow D_3$ transition, computed according to the HT|AH model, including only fundamentals and overtones (blue dashed line, the same data reported in blue in Figure 5, here denoted by the label “single-mode”) or also the main combination bands of two modes (red solid line). The vibrational stick RRS bands have been convoluted with a Gaussian, with HWHM = 25 cm^{-1} (not normalized, i.e., its maximum is 1).

of modes n and m with quantum numbers q and r are labeled as $n^q + m^r$. It is interesting to note that combination bands strongly modify the spectral shape at $\sim 2500 \text{ cm}^{-1}$ and $\sim 3000 \text{ cm}^{-1}$, creating new features in a region otherwise totally flat ($\sim 2500 \text{ cm}^{-1}$), or dominating the close-lying overtones of the modes involved in the combination ($\sim 3000 \text{ cm}^{-1}$). As an example, the combination band $23^1 + 25^1$, of the $\nu_{23}^{(0)}$ and $\nu_{25}^{(0)}$ modes, is more intense than the overtone 25^2 , even if the fundamental 23^1 is more intense than 25^1 . In agreement with what we speculated at the beginning of this section, in the region of $2000\text{--}2100 \text{ cm}^{-1}$, two combination bands arise— $5^1 + 23^1$ and $5^1 + 25^1$ respectively—at frequencies of 2013 cm^{-1} (enforcing the 15^2 band at 2022 cm^{-1}) and 2122 cm^{-1} , but their intensities (relative to the spectrum maximum at $\sim 1500 \text{ cm}^{-1}$) are underestimated, with respect to the experimental band at 2034 cm^{-1} ; this feature was expected, since the computed fundamental 5^1 is actually sensibly weaker than the experimental band at 528 cm^{-1} . As a last remark, it is interesting to note that the band $5^1 + 25^1$ is $\sim 25\%$ higher than $5^1 + 23^1$, even if the fundamental 23^1 is more intense than 25^1 , showing that the exact intensities of combination bands cannot be trivially deduced from the intensities of the fundamentals of the involved modes.

B. IDMN in Acetonitrile and Cyclohexane Solutions. In this section, we present results for IDMN in a cyclohexane and acetonitrile solution. IDMN has 96 normal modes and, therefore, is a much larger system than that of a phenoxyl radical (30 normal modes). Based on the results of a previous study performed in ref 52 on IDMN RRS spectra in solution, calculations were performed by adopting CAMB3LYP and the 6-311G(d,p) basis sets. In the Supporting Information, we checked that the dependence of the computed spectra on the basis set is very weak, using calculations with the smaller 6-31G(d) basis set.

1. *Absorption Spectra.* Figure 8 sketches the calculated absorption spectra in the two solvents, according to different computational models. In this case, only the first singlet excited state is relevant to the spectrum. Apart from a general blue-shift in all the spectrum, because of the particular choice of the combination of DFT functional and basis set, the comparison between calculations and experimental findings, given in Figure 8b and taken from ref 61, shows generally good agreement. In both solvents, the relative intensity of the bluest peak appears slightly too small, thus indicating a slight underestimation of geometry displacements or Duschinsky mixings.

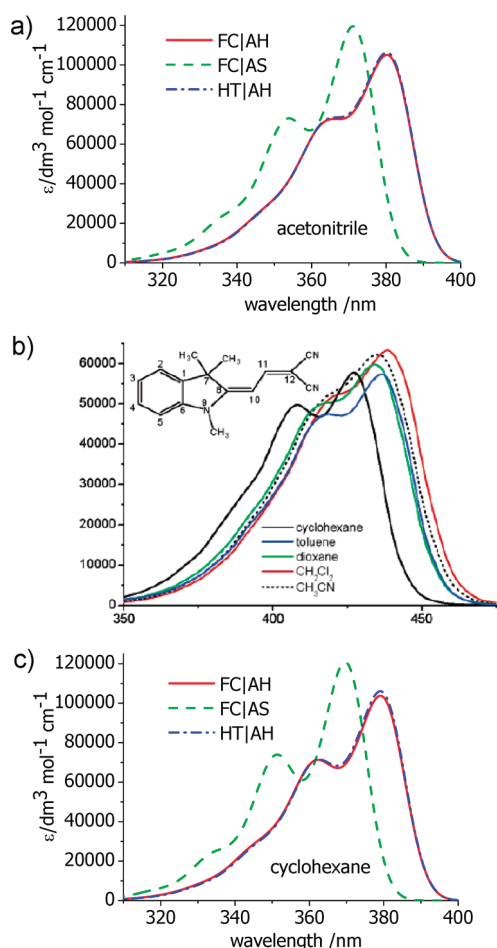


Figure 8. Calculated absorption spectrum of IDMN in (a) acetonitrile and (c) cyclohexane, computed according to different models and convoluted with a Gaussian lineshape, with HWHM = 0.05 eV. (b) For comparison, the experimental spectrum taken from ref 61 also is reported.

Inhomogeneous broadening is larger in acetonitrile than in cyclohexane, because of their different polarities. This is the main reason why, in the experimental spectrum, the two peaks almost coalesce in acetonitrile while they are better distinguished in cyclohexane. *A priori* estimate of the electrostatic contribution to the broadening is becoming feasible and is the subject of work we currently have in progress, while the treatment of the non-electrostatic (dispersion, repulsion, and cavitation) contributions might be addressed by a recent approach presented in the literature.⁶² At the state of the art, the broadening is usually treated as a phenomenological parameter; therefore, for the scope of the present article, we decided to avoid a proliferation of parameters, convoluting the stick spectra in the two solvents by the same Gaussian lineshape (fwhm = 0.1 eV). Nonetheless, the two peaks in acetonitrile still appear to coalesce slightly more than those in cyclohexane, highlighting an interesting pure vibronic contribution to broadening, even if it is clearly of secondary importance, with respect to the effect of solvent fluctuations.

The inclusion of HT terms causes only negligible effects, whereas more-substantial differences are observed by varying the model to approximate the excited state PES (compare the AS and AH results). In both solvents, the AH results, which include the

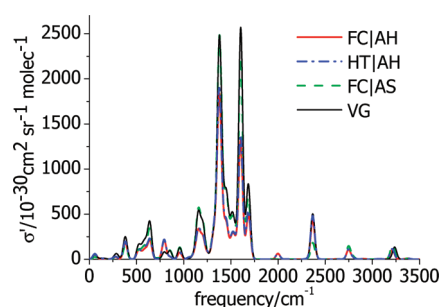


Figure 9. Calculated RRS spectrum of IDMN in acetonitrile excited at the band maximum, assuming $\gamma = 0.1$ eV, and obtained by exploiting different computational models. The vibrational stick RRS bands have been convoluted with a Gaussian lineshape, with HWHM = 25 cm^{-1} (not normalized, i.e., its maximum is 1).

effect of frequency changes and Duschinsky mixings, outperform the AS results, as far as the ratio of the intensity of the peaks is concerned.

2. Resonance Raman Scattering. The calculated RRS spectrum of IDMN in acetonitrile is reported in Figure 9, as a function of the different models used to treat the vibronic coupling. The spectrum obtained by exploiting the VG model is also shown. The vibrational modes giving rise to the most intense peaks involve the motion of the π -system (in the 1200–1700 cm^{-1} range) and the nitrile groups stretching (at ~ 2350 cm^{-1}). As already seen for the absorption spectrum, HT effects on the transition dipoles are negligible for RRS, whereas changing the level of accuracy of the description of the PES of the resonant state has a remarkable impact on the relative intensities of the various peaks, which is clear via comparison of the AS and VG results with those provided by the full AH model. This highlights the possible importance of the effect of frequency changes and Duschinsky mixings in resonance Raman spectra. It is worthy to note, for example, that the relative intensities of the two major peaks at ~ 1400 and 1600 cm^{-1} are remarkably dependent on the introduction of Duschinsky effects. Actually, these two peaks arise from fundamentals of the 62 and 77 modes, respectively, and these two modes are affected by strong Duschinsky mixings. In fact, respectively, 9 and 10 excited-state normal modes are needed to project them by more than 95%. Therefore, it is not surprising that, as shown in the Supporting Information, the calculation of overtones along these modes is more challenging for the computational method. Figure 10 compares the FC|AH RRS spectra in acetonitrile (Figure 10a) and cyclohexane (Figure 10c) with the experimental spectra (Figure 10b). Both theoretical stick spectra, and spectra obtained by their Gaussian convolution, with HWHM = 15 cm^{-1} , are given. All the most intense lines correspond to fundamental transitions and are labeled by the number (in order of increasing frequency) of the involved normal mode. Overall, the theoretical results are in very good agreement with their experimental counterparts and nicely reproduce the main structure characterized by three multiplets lying at ~ 1150 , ~ 1350 and ~ 1550 cm^{-1} , both in terms of their positions (apart from a slight blueshift, expected since no scaling factor has been applied on the frequencies), and in terms of their relative intensities. Also, the agreement in the relative intensities is satisfactory. Focusing on the results in acetonitrile, comparison of the relative heights of the FC|AH multiplets at ~ 1350 and ~ 1550 cm^{-1} with those predicted by the simpler FC|AS and VG models indicates that the inclusion of

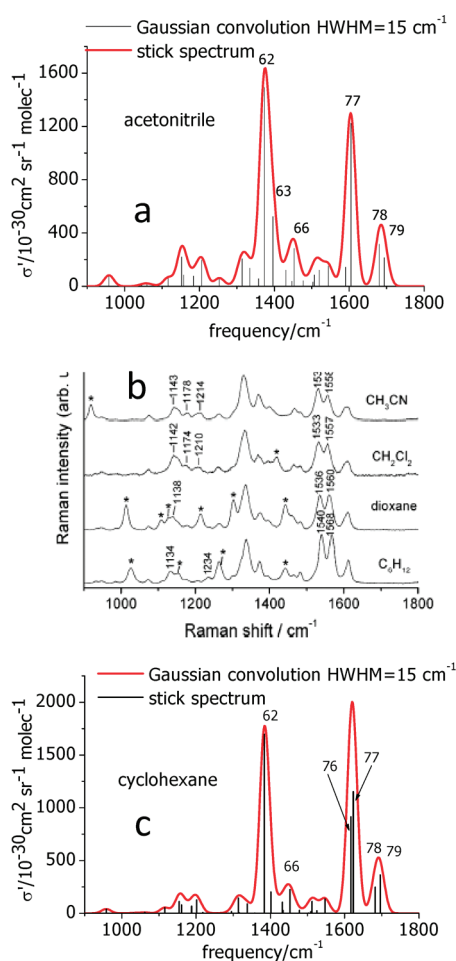


Figure 10. Stick and Gaussian convoluted (HWHM = 15 cm^{-1}) RRS spectra of IDMN in (a) acetonitrile and (c) cyclohexane, computed according to the FC|AH model for an excitation at the band maximum. (b) Experimental RR spectrum for an excitation at 391 nm, taken from ref 61.

Duschinsky effects and frequency changes significantly improves the agreement with the experiment (see Figure 10).

As far as the solvent effect is concerned, comparison of the theoretical and experimental spectra shows that the combination of the PCM with our approach is able to account for the peculiarities in the spectrum introduced by the nature of the medium. In particular, the presence of the solvent and its polarity characteristics do not simply cause a shift in the bands and/or an homogeneous increase/decrease of band intensities, but the relative intensities of the peaks remarkably change, as a result of the nature of the solute–solvent interactions, thus causing an overall different intensity pattern in the spectrum. Major differences in the computed spectra in the two solvents arise in the relative heights of the multiplet at ~ 1350 and ~ 1550 cm^{-1} (the blue one is enhanced in cyclohexane, in very good agreement with the experimental findings). Also, the inner structure of each multiplets can be analyzed. While the two-peak structure of the multiplet at ~ 1350 cm^{-1} is perfectly reproduced in our calculations, the three-peak structure of the bluest multiplet is apparently not reproduced in the convoluted spectrum, where only two peaks appear (with the middle peak being apparently missing). Nonetheless, analysis of the stick spectra shows that two different transitions contribute to the major peak at ~ 1600 cm^{-1} , in agreement with the experiment, but they are too

close to each other, so they coalesce in a single peak after convolution. Finally, the experimental multiplet at ~ 1150 cm^{-1} shows a richer and more asymmetric structure in acetonitrile than in cyclohexane; even this feature is nicely reproduced by our calculations.

It is also worth noting that computed spectra in Figures 9 and 10 assume an excitation at the vertical transition, while experimental spectra were recorded at 391 nm, which is an excitation blue-shifted by more than 2000 cm^{-1} , with respect to the band maximum (estimated for an infinite broadening) both in acetonitrile and cyclohexane. By taking into account such a blue-shift, the computed RRS spectra change only slightly for the chosen γ value (see the Supporting Information).

To end this section, it is worth noting that the noticeable improvement of the use of our full FC|AH model, with respect to other methodologies, is further evidenced in comparison with previous calculated spectra reported in the literature.⁵²

V. SUMMARY, CONCLUSIONS, AND PERSPECTIVES

We have presented a time-independent method, grounded in the harmonic approximation, and based on a sum-over-states (SOS) calculation of the polarizability tensor that provides several improvements, with respect to the commonly adopted models for the computation of vibrational resonance Raman scattering (RRS) spectra. In particular, our method is able to include Duschinsky and Herzberg–Teller (HT) effects, and to consider not only fundamental transitions but also overtones and combination bands. In addition, its computational effectiveness allows one to compute two-dimensional (2D) RRS spectra, as a function of both the incident and the scattered frequencies, and to explore the dependence of the spectra on the excited-state lifetime, which is a parameter that is usually treated phenomenologically. Moreover, the present method paves the way for analysis of the interferential features that occur when more than one excited state is in quasi-resonance with the excitation frequency. Beyond that, it is worthwhile to note that the approach presented here can be extended rather straightforwardly to the description of other spectroscopic phenomena related to RRS, such as resonance Raman optical activity or resonance hyper-Raman, by also including, for these spectroscopies, Duschinsky and HT effects.

The computational burden of RRS calculations increases significantly with respect to absorption spectra. In this respect, the numerical evidence that the convergence of RRS spectra does not require the full convergence to the analytical sums (either the RRS ones or the absorption ones) is very encouraging, because it allows one to strongly decrease the computational cost. Nonetheless, although, in principle, the method also can be adopted for extensive exploration of the intensities of combination bands involving two or more modes, computational efficiency would probably require refinement and further optimization of the selection schemes. In this respect, in future work, we plan to explore different computational strategies, based on the time-dependent formalism introduced by Heller and collaborators.^{6,7}

■ ASSOCIATED CONTENT

S Supporting Information. Convergence tests of the results for the phenoxyl radical in the gas phase and for FC|AH spectra of IDMN in acetonitrile; FC|AH RRS spectra and RR excitation profiles for IDMN in acetonitrile at different excitation

frequencies; comparison of the absorption and RRS spectra of IDMN computed with the 6-311G(d,p) and 6-31G(d) basis sets. (PDF) This material is available free of charge via the Internet at <http://pubs.acs.org>.

AUTHOR INFORMATION

Corresponding Author

*E-mail addresses: fabrizio.santoro@iccom.cnr.it (F.S.), chiara@dcc.uniipi.it (C.C.).

ACKNOWLEDGMENT

The computational resources for this work have been provided through the CNR-Village Network (<http://village.pi.iccom.cnr.it>). F.S. acknowledges the support of Italian MIUR (PRIN 2008) and IIT (Project IIT-Seed "Helyos").

REFERENCES

- (1) Long, D. A. *The Raman Effect*; Wiley: Chichester, U.K., 2002.
- (2) Myers, A. B. Resonance Raman Intensities and Charge-Transfer Reorganization Energies. *Chem. Rev.* **1996**, *96*, 911.
- (3) Barone, V.; Imbrota, R.; Rega, N. Quantum Mechanical Computations and Spectroscopy: From Small Rigid Molecules in the Gas Phase to Large Flexible Molecules in Solution. *Acc. Chem. Res.* **2008**, *41*, 605–616.
- (4) Kelley, A. M. Resonance Raman and Resonance Hyper-Raman Intensities: Structure and Dynamics of Molecular Excited States in Solution. *J. Phys. Chem. A* **2008**, *112*, 11975.
- (5) Peticolas, L.; Rush, T., III. Ab Initio Calculations of the Ultraviolet Resonance Raman Spectrum of Uracil. *J. Comput. Chem.* **1995**, *16*, 1261–1270.
- (6) Heller, E. J.; Lee, S.-Y. Time Dependent Theory of Raman Scattering. *J. Chem. Phys.* **1979**, *71*, 4777–4788.
- (7) Heller, E. J.; Sundberg, R. L.; Tannor, D. Simple aspects of Raman scattering. *J. Phys. Chem.* **1982**, *86*, 1822–1833.
- (8) Kramers, K. A.; Heisenberg, W. Uber die Streuung von Strahlung durch Atome. *Z. Phys.* **1925**, *31*, 681.
- (9) Dirac, P. A. M. The Quantum Theory of Dispersion. *Proc. R. Soc. London, Ser. A* **1927**, *114*, 710.
- (10) Warshel, A.; Dauber, P. Calculations of Resonance Raman Spectra of Conjugated Molecules. *J. Chem. Phys.* **1977**, *66*, 5477–5488.
- (11) Jensen, L.; Zhao, L. L.; Autschbach, J.; Schatz, G. C. Theory and method for calculating resonance Raman scattering from resonance polarizability derivatives. *J. Chem. Phys.* **2005**, *123*, 174110.
- (12) Albrecht, A. C. On the Theory of Raman Intensities. *J. Chem. Phys.* **1961**, *34*, 1476.
- (13) Blazej, D. C.; Peticolas, W. L. J. Ultraviolet resonance Raman excitation profiles of pyrimidine nucleotides. *J. Chem. Phys.* **1980**, *72*, 3134–3142.
- (14) Zheng, R.-H.; Wei, W.-M. Density Functional Theory Study on Anti-resonance in Preresonance Raman Scattering for Naphthalene Molecules. *J. Phys. Chem. A* **2007**, *111*, 3652–3660.
- (15) Kiewisch, J.; Neugebauer, K.; Reiher, M. Selective calculation of high-intensity vibrations in molecular resonance Raman spectra. *J. Chem. Phys.* **2008**, *129*, 204103.
- (16) Kane, A. K.; Jensen, L. Calculation of Absolute Resonance Raman Intensities: Vibronic Theory vs Short-Time Approximation. *J. Phys. Chem. C* **2010**, *114*, 5540–5546.
- (17) Jarzecki, A. A. Quantum-Mechanical Calculations of Resonance Raman Intensities: The Weighted-Gradient Approximation. *J. Phys. Chem. A* **2009**, *113*, 2926–2934.
- (18) Lubber, S.; Neugebauer, J.; Reiher, M. Enhancement and de-enhancement effects in vibrational resonance Raman optical activity. *J. Chem. Phys.* **2010**, *132*, 044113.
- (19) Neugebauer, J.; Hess, B. A. Resonance Raman spectra of uracil based on Kramers–Kronig relations using time-dependent density functional calculations and multireference perturbation theory. *J. Chem. Phys.* **2004**, *120*, 11564.
- (20) Neugebauer, J.; Baerends, E. J.; Efremov, E. V.; Ariese, F.; Gooijer, C. Combined Theoretical and Experimental Deep-UV Resonance Raman Studies of Substituted Pyrenes. *J. Phys. Chem. A* **2005**, *109*, 2100.
- (21) Guthmuller, J.; Champagne, B. Resonance Raman Scattering of Rhodamine 6G as Calculated by Time-Dependent Density Functional Theory: Vibronic and Solvent Effects. *J. Phys. Chem. A* **2008**, *112*, 3215–3223.
- (22) Jensen, L.; Schatz, G. C. Resonance Raman Scattering of Rhodamine 6G as Calculated Using Time-Dependent Density Functional Theory. *J. Phys. Chem. A* **2006**, *110*, 5973–5977.
- (23) Guthmuller, J.; Champagne, B. Time dependent density functional theory investigation of the resonance Raman properties of the julolidinemalononitrile push-pull chromophore in various solvents. *J. Chem. Phys.* **2007**, *127*, 164507.
- (24) Guthmuller, J.; Champagne, B.; Moucheron, C.; Kirsch-De Mesmaeker, A. Investigation of the Resonance Raman Spectra and Excitation Profiles of a Monometallic Ruthenium(II) [Ru(bpy)₂(HAT)]²⁺ Complex by Time-Dependent Density Functional Theory. *J. Phys. Chem. B* **2010**, *114*, 511–520.
- (25) Herrmann, C.; Neugebauer, J.; Presselt, M.; Uhlemann, U.; Schmitt, M.; Rau, S.; Popp, J.; Reiher, M. The First Photoexcitation Step of Ruthenium-Based Models for Artificial Photosynthesis Highlighted by Resonance Raman Spectroscopy. *J. Phys. Chem. B* **2007**, *111*, 6078–6087.
- (26) Hizhnyakov, V.; Tehver, I. Transform Method in Resonance Raman Scattering with quadratic Franck-Condon and Herzberg-Teller Interactions. *J. Raman Spectrosc.* **1988**, *19*, 383–388.
- (27) Chan, C. K.; B., P. J. Temperature Effects in the time correlator theory of Resonance Raman Scattering. *J. Chem. Phys.* **1983**, *79*, 5234.
- (28) Tonks, D. L.; B., P. J. Diagrammatic Theory of temperature-dependent resonance Raman scattering from polyatomic systems with general harmonic potential surfaces. *J. Chem. Phys.* **1988**, *88*, 738.
- (29) Lu, H. M.; Page, J. B. General transform technique including mode mixing and non-Condon coupling in resonance Raman scattering. *J. Chem. Phys.* **1990**, *90*, 5315.
- (30) Priyutov, M. V.; Burova, T. G. *Opt. Spectrosc. (USSR)* **1988**, *64*, 108.
- (31) Priyutov, M. V.; Burova, T. G. *Opt. Spectrosc. (USSR)* **1991**, *71*, 37.
- (32) Sharp, T. E.; Rosenstock, H. M. Franck–Condon Factors for Polyatomic Molecules. *J. Chem. Phys.* **1963**, *41*, 3453–3463.
- (33) Kupka, H.; Cribb, P. H. Multidimensional Franck–Condon integrals and Duschinsky mixing effects. *J. Chem. Phys.* **1986**, *85*, 1303.
- (34) Ruhoff, P. T. Recursion relations for multi-dimensional Franck–Condon overlap integrals. *Chem. Phys.* **1994**, *186*, 355–374.
- (35) Doktorov, E. V.; Malkin, I. A.; Man'ko, V. I. Dynamical symmetry of vibronic transitions in polyatomic molecules and the Franck–Condon principle. *J. Mol. Spectrosc.* **1977**, *64*, 302–326.
- (36) Doktorov, E. V.; Malkin, I. A.; Man'ko, V. I. Dynamical symmetry of vibronic transitions in polyatomic molecules and the Franck–Condon principle. *J. Mol. Spectrosc.* **1975**, *56*, 1–20.
- (37) Biczysko, M.; Bloino, J.; Santoro, F.; Barone, V. In *Computational Strategies for Spectroscopy: From Small Molecules to Nano Systems*; Barone, V., Ed.; Wiley: Chichester, U.K., 2011; pp 300–386.
- (38) Hazra, A.; Nooijen, M. Derivation and efficient implementation of a recursion formula to calculate harmonic Franck–Condon factors for polyatomic molecules. *Int. J. Quantum Chem.* **2003**, *95*, 643–657.
- (39) Dierksen, M.; Grimme, S. An efficient approach for the calculation of Franck–Condon integrals of large molecules. *J. Chem. Phys.* **2005**, *122*, 244101/1–9.
- (40) Dierksen, M.; Grimme, S. The Vibronic Structure of Electronic Absorption Spectra of Large Molecules: A Time-Dependent Density Functional Study on the Influence of "Exact" Hartree–Fock Exchange. *J. Phys. Chem. A* **2004**, *108*, 10225–10237.
- (41) Jankowiak, H.-C.; Stuber, J. L.; Berger, R. Vibronic transitions in large molecular systems: Rigorous prescreening conditions for Franck–Condon factors. *J. Chem. Phys.* **2007**, *127*, 234101/1–23.

- (42) Santoro, F.; Improta, R.; Lami, A.; Bloino, J.; Barone, V. Effective method to compute Franck–Condon integrals for optical spectra of large molecules in solution. *J. Chem. Phys.* **2007**, *126*, 084509/1–13.
- (43) Santoro, F.; Lami, A.; Improta, R.; Barone, V. Effective method to compute vibrationally resolved optical spectra of large molecules at finite temperature in the gas phase and in solution. *J. Chem. Phys.* **2007**, *126*, 184102/1–11.
- (44) Santoro, F.; Lami, A.; Improta, R.; Bloino, J.; Barone, V. Effective method for the computation of optical spectra of large molecules at finite temperature including the Duschinsky and Herzberg-Teller effect: The Q_x band of porphyrin as a case study. *J. Chem. Phys.* **2008**, *128*, 224311/1–17.
- (45) Santoro, F.; Barone, V. Computational approach to the study of the lineshape of absorption and electronic circular dichroism spectra. *Int. J. Quantum Chem.* **2010**, *110*, 476–486.
- (46) Lin, N.; Santoro, F.; Luo, Y.; Zhao, X.; Barone, V. Theory for Vibrationally Resolved Two-Photon Circular Dichroism Spectra. Application to (R)-(+)-3-Methylcyclopentanone. *J. Phys. Chem. A* **2002**, *113*, 4198–4207.
- (47) Barone, V.; Bloino, J.; Biczysko, M.; Santoro, F. Fully Integrated Approach to Compute Vibrationally Resolved Optical Spectra: From Small Molecules to Macrosystems. *J. Chem. Theory Comput.* **2009**, *5*, 540–554.
- (48) Bloino, J.; Biczysko, M.; Santoro, F.; Barone, V. General Approach to Compute Vibrationally Resolved One-Photon Electronic Spectra. *J. Chem. Theory Comput.* **2010**, *6*, 1256.
- (49) Frisch, M. J.; Trucks, G. W.; Schlegel, H. B.; Scuseria, G. E.; Robb, M. A.; Cheeseman, J. R.; Scalmani, G.; Barone, V.; Mennucci, B.; Petersson, G. A.; Nakatsuji, H.; Caricato, M.; Li, X.; Hratchian, H. P.; Izmaylov, A. F.; Bloino, J.; Zheng, G.; Sonnenberg, J. L.; Hada, M.; Ehara, M.; Toyota, K.; Fukuda, R.; Hasegawa, J.; Ishida, M.; Nakajima, T.; Honda, Y.; Kitao, O.; Nakai, H.; Vreven, T.; Montgomery, Jr., J. A.; Peralta, J. E.; Ogliaro, F.; Bearpark, M.; Heyd, J. J.; Brothers, E.; Kudin, K. N.; Staroverov, V. N.; Kobayashi, R.; Normand, J.; Raghavachari, K.; Rendell, A.; Burant, J. C.; Iyengar, S. S.; Tomasi, J.; Cossi, M.; Rega, N.; Millam, N. J.; Klene, M.; Knox, J. E.; Cross, J. B.; Bakken, V.; Adamo, C.; Jaramillo, J.; Gomperts, R.; Stratmann, R. E.; Yazyev, O.; Austin, A. J.; Cammi, R.; Pomelli, C.; Ochterski, J. W.; Martin, R. L.; Morokuma, K.; Zakrzewski, V. G.; Voth, G. A.; Salvador, P.; Dannenberg, J. J.; Dapprich, S.; Daniels, A. D.; Farkas, Ö.; Foresman, J. B.; Ortiz, J. V.; Cioslowski, J.; Fox, D. J. Gaussian 09, Revision A.02. Gaussian, Inc., Wallingford, CT, 2009.
- (50) Guthmuller, J.; Champagne, B. Time dependent density functional theory investigation of the resonance Raman properties of the julolidinmalononitrile push-pull chromophore in various solvents. *J. Chem. Phys.* **2007**, *127*, 164507.
- (51) Mennucci, B.; Cappelli, C.; Cammi, R.; Tomasi, J. A quantum mechanical polarizable continuum model for the calculation of resonance Raman spectra in condensed phase. *Theor. Chem. Acc.* **2007**, *117*, 1029.
- (52) Mennucci, B.; Cappelli, C.; Guido, C. A.; Cammi, R.; Tomasi, J. Structures and Properties of Electronically Excited Chromophores in Solution from the Polarizable Continuum Model Coupled to the Time-Dependent Density Functional Theory. *J. Phys. Chem. A* **2009**, *113*, 3009.
- (53) Miertus, S.; Scrocco, E.; Tomasi, J. Electrostatic interaction of a solute with a continuum. A direct utilization of ab initio molecular potentials for the prevision of solvent effects. *Chem. Phys.* **1981**, *55*, 117–129.
- (54) Tomasi, J.; Mennucci, B.; Cammi, R. Quantum Mechanical Continuum Solvation Models. *Chem. Rev.* **2005**, *105*, 2999–3093.
- (55) Califano, S. *Vibrational States*; Wiley, London, 1976.
- (56) Duschinsky, F. *Acta Physicochim. URSS* **1937**, *7*, 551.
- (57) Peluso, A.; Santoro, F.; Del Re, G. Vibronic coupling in electronic transitions with significant Duschinsky effect. *Int. J. Quantum Chem.* **1997**, *63*, 233.
- (58) Santoro, F. *FCclasses: A Fortran 77 Code*; 2008. (Available via the Internet at <http://village.pi.iccom.cnr.it>; last accessed March 23, 2011.)
- (59) Radziszewski, J. G.; Gil, M.; Gorski, A.; Spanget-Larsen, J.; Waluk, J.; Mróz, B. J. Electronic states of the phenoxyl radical. *J. Chem. Phys.* **2001**, *115*, 9733.
- (60) Tripathi, G. N. R.; Schuler, R. H. Electronic states of the phenoxyl radical. *J. Chem. Phys.* **1984**, *81*, 113.
- (61) Leng, W.; Wurthner, F.; Kelley, A. M. Solvent-Dependent Vibrational Frequencies and Reorganization Energies of Two Merocyanine Chromophores. *J. Phys. Chem. A* **2005**, *109*, 1570.
- (62) Weijo, V.; Mennucci, B.; Frediani, L. Toward a General Formulation of Dispersion Effects for Solvation Continuum Models. *J. Chem. Theory Comput.* **2010**, *6*, 3358.

Importance of Polarization and Charge Transfer Effects to Model the Infrared Spectra of Peptides in Solution

Francesca Ingrosso,^{*,†} Gérald Monard,[†] Marwa Hamdi Farag,[‡] Adolfo Bastida,[‡] and Manuel F. Ruiz-López[†]

[†]Equipe de Chimie et Biochimie Théoriques, UMR 7565 SRSMC, CNRS-Nancy Université, BP 70239 Vandœuvre-lès Nancy, France

[‡]Departamento de Química Física, Universidad de Murcia, 30100 Murcia, Spain

 Supporting Information

ABSTRACT: We present a study of the infrared spectrum of N-methyl acetamide (NMA) performed by using molecular dynamics (MD) with a quantum electronic Hamiltonian. A recently developed method, based on the Born–Oppenheimer approximation and on a semiempirical level of quantum chemistry (SEBOMD), is employed. We focus on the solvent effect on the infrared spectrum of the solute, on its geometry, and on its electrostatic properties. We thus run simulations of NMA in the gas phase and in water (64 solvent molecules with periodic boundary conditions), taking into account its two different conformers—cis and trans. The use of a semiempirical electronic Hamiltonian allows us to explore much larger time scales compared to density functional theory based MD for systems of similar size. NMA represents a simple model system for peptide bonds: those infrared bands that are more significant as a signature of the peptide bond (amide I, II, and III and the N–H stretch) are identified, and the solvent shift is evaluated and compared to experiments. We find a satisfying agreement between our model and experimental measurements, not only for the solvent shift but also for the structural and electrostatic properties of the solute. On the other hand, when a molecular mechanics, nonpolarizable force field is used to run MD, very little or nil solvent effect is observed. By analyzing our results, we propose an explanation of this discrepancy by stressing the importance of mutual polarization and charge transfer in an accurate modeling of the solute–solvent interactions.

1. INTRODUCTION

Recent advances in computer simulations of the condensed phase have made possible the investigation of dynamics in large systems at a quantum level.^{1–8} The use of a quantum Hamiltonian and the definition of the wave function of the whole electronic system result in an accurate description of polarization and charge transfer. This is crucial for modeling bond making/breaking, a feature that is lacking in most molecular dynamics (MD) simulations based on molecular mechanics (MM) force fields. The possibility of treating at a quantum level the electronic Hamiltonian of bio-organic systems in their real environment is thus becoming closer, even for molecular dynamics simulations.

In molecular biology studies, infrared spectroscopy often complements the widely employed X-ray diffraction and NMR techniques, in particular to study proteins and peptides. Amide bands are used to probe the secondary structure when exploring the folding dynamics of proteins.^{9,10} A theoretical model of these systems should therefore be able to describe the effect of the environment on the infrared signature of peptide bonds.¹¹ In addition, theoretical investigations at the DFT-molecular dynamics level have stressed the importance of conformational sampling for an accurate description of specific infrared features, such as, for example, the experimental line shape resulting from a mixture between two different conformations of a peptide.^{12,13}

N-methyl acetamide (NMA) has been widely used as a model of the peptide group. It results from a linkage between two residues, a C-terminal (ACE) and a N-terminal (N Met) residue. NMA has two different conformers, corresponding to the cis and trans arrangements of the carbonyl and –NH groups. The trans

form is the most stable in the gas phase and in solution,^{14–17} and an experimental evaluation of the energy difference between the two forms in a rigid matrix gives a value of 2.3 kcal/mol,¹⁸ while NMR measurements in 1,2-dichloroethane gave a difference ranging from 2.8 to 3.4 kcal/mol.¹⁹ The free energy barrier between the two forms has been investigated by means of different computational techniques, and it varies between 15 and 20 kcal/mol, depending on the method.^{16,20–23} The presence of a solvent enhances the barrier height by 2–3 kcal/mol.^{14,20,21}

The literature concerning experimental and theoretical studies of NMA in solution is quite remarkable in size, and it is beyond the scope of this work to provide a full review. We shall only address those works that are closer to our objectives, that is, studies of the IR spectra of NMA in water. The most significant bands in the IR spectrum of a peptide group are the amide I, II, and III bands and the one corresponding to the N–H stretch (Amide A). The amide I mode is mostly related to the C–O stretching motion, which was shown to be coupled with water motions in aqueous solution.²⁴ Amide II arises mostly from the C–N–H bending motion combined with the C–N stretch, whereas a larger contribution of the C–N stretch combined with the C–N–H bend generates amide III.

The IR spectrum of NMA obtained through classical MM simulations has been compared to the one obtained through a QM/MM approach.²⁵ The authors have concluded that reliable

Received: January 26, 2011

Published: April 29, 2011

modeling of IR spectra in solution should include the effect of the time-dependent solvent-induced dipole on the solute. The effect of hydrogen bonding with surrounding water molecules on the vibrational frequencies of NMA has been extensively studied by means of quantum chemistry calculations on NMA–water clusters,²⁶ and it has been described in terms of a spatially inhomogeneous electric field generated by the solvent acting on the solute.²⁷ Quantum chemistry calculations have been performed on NMA–water clusters (8000 structures) extracted from MM simulations.²⁸ The results obtained through this approach for the position and for the shape of amide I–III bands are in good agreement with experiments: solute–solvent hydrogen bonding plays a relevant role in reproducing band profiles.

The importance of hydrogen bonding and nonspecific electrostatic interactions between the solute and solvent has been analyzed in depth by modeling the harmonic frequencies and by including anharmonic effects in a joint quantum chemistry and experimental study.²⁹ Another study based on the interplay between quantum chemistry and experiments has focused on the influence of the environment and the temperature on the amide I band.³⁰ According to this work, the intensity of this band depends strongly on the solvent, and it varies with temperature. Concerning the solvent effect on the band position, the authors have shown that a simple approach based on the Onsager reaction field can reasonably predict both the solvent-induced and the temperature-induced frequency shifts.

Recent work on theoretical modeling of two-dimensional (2D) IR spectroscopy has been carried out by Jeon and Cho and applied to deuterated NMA in a cluster of 16 D₂O molecules, based on a QM/MM scheme.³¹ The approach has been shown to be successful in reproducing the main features of the experimental 2D IR spectrum. The authors have pointed out that a better description of inhomogeneous broadening might be achieved by including more solvent molecules and by describing them at a quantum level.

Most of the work on IR spectra of small peptides in solution points toward the importance of including polarization and of specific solute–solvent interactions (i.e., hydrogen bonding) in the theoretical description of vibrational properties. In particular, we believe that the mutual polarization between solute and solvent should be included, as well as charge transfer, which might be relevant in the case of NMA, due to the presence of a hydrogen bond donor and of a hydrogen bond acceptor within the peptide bond. All of these terms are taken into account if the electronic Hamiltonian of the full system is treated at the quantum level.

The two conformers of NMA immersed in water, as well as more complex examples of peptides, have already been investigated at the DFT molecular dynamics level, in particular by Gageot et al. (see ref 8 for a recent review). However, due to their high computational cost, DFT-based MD simulations are in general limited to simple systems and/or small simulation times. As explained below, the method proposed here is intended to address such limitation by relaxing the level of the quantum chemistry approach used to describe the electronic structure of the solution. This is particularly important when dealing with the calculation of infrared spectra,^{25,32} which requires good statistics³³ (as we shall discuss in section 2).

The method used here is based on a semiempirical Born–Oppenheimer molecular dynamics (SEBOMD) approach.⁷ At each step of the MD simulation, the electronic wave function of the system is computed with a semiempirical quantum method

making use, if necessary, of a linear scaling algorithm, such as the divide and conquer method.^{34,35} Obviously, semiempirical Hamiltonians strongly reduce the computational cost of the simulations compared to ab initio or density functional theory based molecular dynamics. The price to be paid is a lower accuracy in the computed molecular properties, though reasonable results are expected for the IR spectra of isolated molecules^{36–38}

However, in the case of solvated molecules, further tests are necessary. In fact, traditional semiempirical Hamiltonians, which were parametrized mainly on the basis of gas-phase properties of molecules, do not describe intermolecular interactions correctly. For example, a PM3 Hamiltonian³⁹ applied to water dimers gives rise to a few wrong features in the potential energy surface.^{40,41} In addition, unphysical artifacts are obtained for H–H interactions at short distances.⁴² A new parametrization of intermolecular interactions within PM3 has thus been introduced in terms of a parametrizable interaction function (PIF),^{40,43} based on fitting high level ab initio results. This approach has been tested in depth on liquid water,⁷ and though it appears that the average polarizability is slightly underestimated by the semiempirical Hamiltonian, the predicted structure and thermodynamical properties of the liquid (simulation with 216 molecules using periodic boundary conditions, 100 ps time scale) are in good agreement with experimental data. By contrast, the structure of water is not well described by using the standard PM3 Hamiltonian.

The present study illustrates the first application of SEBOMD to study the molecular properties of a solvated solute, and we would like to test the accuracy of this approach to predict the infrared spectrum of biological systems in solution.

This paper is organized as follows. The next section will be devoted to the computational strategies adopted in our study. In section 3, we shall present and illustrate our results, including a comparison with experimental data and other theoretical work in the literature. We shall finally conclude in section 4 by summarizing our findings and by introducing the guidelines of the future developments of our work.

2. COMPUTATIONAL DETAILS

In this section, we shall describe in detail the computational methods and the procedures that were adopted to run molecular dynamics simulations and to compute infrared spectra.

First of all, we introduce our MD simulations carried out with a MM force field. We performed MD simulations by using the Amber code, version 9,⁴⁴ and the Amber03⁴⁵ force field. This force field was recently introduced to overcome some of the shortcomings of previous nonpolarizable force fields in the simulations of proteins in the condensed phase, especially in the prediction of molecular dipole moments and of properties related to the torsional parameters.

Simulations of *cis*- and *trans*-NMA isolated and in cubic boxes containing 64, 125, and 216 SPC/E⁴⁶ water molecules were run at 300 K both in the microcanonical ensemble and at constant temperature. In the latter case, the Anderson method⁴⁷ was used for temperature control, and the frequency for velocity randomization was 1 ps⁻¹. The SPC/E model was used since it gives very similar results to the ones obtained with the semiempirical electronic Hamiltonian and PIF corrections with respect to the structure of liquid water.⁷ In addition, SPC/E is one of the best available MM models to describe the dielectric properties (and thus electrostatic solvation properties) of water.⁴⁸ We do not expect large effects on the infrared spectrum of NMA due to

using a rigid water model, since the solute–solvent correlations are not included in our calculation (see below).

Simulations in the condensed phase were run with periodic boundary conditions. Long-range electrostatics was treated with the Ewald sum scheme.⁴⁹ The size of the boxes was adapted to reproduce the room temperature density of water (0.996 g/mL⁵⁰), by taking into account the volume occupied by the solute.

Equilibration at a constant temperature ($T = 300$ K, Andersen thermostat) was performed for 500 ps, followed by data acquisition over 1 ns for each simulation. We used a time step of 1 fs. The SHAKE procedure^{51,52} was used to keep water molecules rigid, whereas all bonds in the solute molecule were flexible.

Regarding MD simulations with a semiempirical quantum mechanical PM3 Hamiltonian to describe the electronic wave function of the whole system, we compared the results obtained in the gas phase with those obtained in the condensed phase by using the standard PM3 Hamiltonian for intramolecular interactions and the PIF correction for water–water^{40,40} and solute–water⁴² intermolecular interactions.

We remind the reader that a well-known issue with the PM3 method is an artificial tendency toward pyramidal hybridization of the N atom. A specific correction term (PM3-MM) has thus been introduced to keep peptide bonds planar through a harmonic constraint on the H–N–C–O dihedral. In our calculations, we used the Gaussian 03⁵³ implementation of this potential. In order to test the effect of this correction on the vibrational frequencies of NMA, we performed gas phase calculations on both the *cis* and the *trans* conformers by carrying out geometry optimization and normal modes analysis in Gaussian.⁵³ We used both the standard PM3 parameters and the PM3-MM parameters. Other than the different values for the H–N–C–O dihedral and for the molecular dipole moment, no remarkable difference was found in the normal mode frequencies of *cis*- and *trans*-NMA as well as in the interatomic distances.

In water solution, each of the two NMA conformers were dissolved in a box with 64 water molecules, and we ran dynamics on a 300 ps time scale, at the same temperature and using the same time step as in the MM simulations. No SHAKE constraints were applied. Previous equilibration for each MD run was performed over 100 ps starting from a configuration extracted from the molecular mechanics force field MD simulations. The Fock matrix of the system was built at each time step and diagonalized through standard techniques according to the self-consistent field (SCF) scheme. This ensures that the electronic density converges at each step of the simulation, and that the dynamics follows the Born–Oppenheimer potential energy surface.^{54,55}

We would like to stress here that the density matrix of the system can also be obtained by means of the divide and conquer approach. However, in our case, the standard diagonalization techniques are faster than the divide and conquer approach, since the size of the system is below the crossover point.⁵⁶

Simulations in the condensed phase were run with periodic boundary conditions, and long-range electrostatic interactions were taken into account by using the Ewald method.⁵⁷ The full Fock matrix is built using the minimum image convention for all direct interactions inside the periodic box (direct sum). The Ewald reciprocal sum is incorporated as a correction to the Fock matrix in a way similar to the one proposed by Nam et al.:⁵⁷ atomic partial charges computed from the semiempirical wave function define an Ewald field in the reciprocal space that can be incorporated in the core Hamiltonian as long as derivatives of

these atomic charges with respect to the density matrix elements are defined. In our implementation, Ewald summation can be performed by using either Mulliken or CM1⁵⁸ atomic charges to represent the long-range electrostatic field that self-consistently polarizes the semiempirical wave function.

A typical SCF procedure proceeds as follows: from an initial guess for the density matrix, (1) the atomic charges are computed (Mulliken or CM1 charges); (2) the minimum image Fock matrix is perturbed by the Ewald field (i.e., both the minimum image Fock matrix and the Ewald field are derived from the same density matrix); (3) the total Fock matrix is diagonalized to obtain the wave function coefficients; (4) a new density matrix is built from the coefficients of the molecular orbitals; (5) convergence is checked, and back to step 1 if the procedure has not converged yet.

During the MD simulation, the different sets of charges can be derived from the wave function evaluated at each time step. We also evaluated CM2⁵⁹ partial charges. We recall that CM1 and CM2 charges are parametrized to obtain reliable charge-dependent molecular properties, in particular, the molecular dipole moment.

In the case of isolated NMA, we ran simulations in the microcanonical ensemble and at constant temperature (the same conditions as those used for simulations with an MM force field). In all (isolated, condensed phase) simulations, we monitored the O–C–N–H dihedral, in order to make sure that the NMA molecule would stay in the original *cis* or *trans* conformation during the simulation, in agreement with the observation of a high barrier between the two conformers predicted by other calculations.^{20–23}

Let us now give some details on the calculation of infrared spectra. It has been shown that the IR absorption line shape $I(\omega)$ for an isotropic sample is related to the quantum mechanical electrical dipole moment ($\hat{\mu}$) time correlation function (TCF)^{60–62} through a Fourier transform (FT) operation:

$$I(\omega) \sim \int_{-\infty}^{+\infty} dt e^{-i\omega t} \frac{\text{Tr}[e^{-\beta\hat{H}} \hat{\mu}(0) \cdot \hat{\mu}(t)]}{\text{Tr}[e^{-\beta\hat{H}}]} \quad (1)$$

where Tr denotes the trace operator, \hat{H} is the Hamiltonian of the system (under the Born–Oppenheimer approximation), and β is the inverse of the Boltzmann constant times the temperature.

In order to make it possible to extend this theory to classical dynamics, one can approximate the quantum TCF by using its classical analog⁶³ and the quantum electric dipole moment operator by using the classical dipole moment μ :

$$I(\omega) \sim Q(\omega) \int_{-\infty}^{+\infty} dt e^{-i\omega t} \langle \mu(0) \cdot \mu(t) \rangle \quad (2)$$

where the effect of approximating quantum operators with their classical counterparts is compensated by the use of the quantum correction factor Q .

Although different forms for $Q(\omega)$ have been proposed in the literature,⁶⁴ this factor is often omitted, and it has been recently proven that its inclusion does not significantly affect $I(\omega)$.⁶⁵ We calculate IR spectra by omitting the prefactor, and they are thus expressed in arbitrary units. In addition, we do not introduce any scaling factor to rescale our computed frequencies in order to better reproduce the experimental results.

During the SEBOMD simulation in the gas phase, the dipole moment of NMA can be obtained by applying the dipole moment operator to the wave function of the molecule.

However, the same procedure cannot be applied to NMA in water, due to the delocalization of the wave function over the entire system. This issue has already been discussed in a previous paper,⁷ and we adopt here the same approximation proposed there. We evaluate the dipole moment of NMA on the basis of partial atomic charges (instantaneous Mulliken, CM1, and CM2 charges) and instantaneous atomic positions, exactly as it is done for the classical MM simulations. In the gas phase, we compared the SEBOMD results based on partial charges with those obtained from the dipole moment operator. As for the IR spectrum, no differences were observed with respect to the band positions and shape.

In solution, experiments aimed at recording the IR spectrum of a solute use a subtraction method (the spectrum of a blank is subtracted from the spectrum of the full solution). In simulations, this would translate into considering cross-correlations (solute–solvent) to calculate the TCF of the dipole moment as well as solute–solute correlations. However, this approach requires taking into account correlations between solute and solvent motions, and much better statistics are necessary compared to the calculation of self-correlations.^{33,66,67} Following the same approximations proposed by Gaigeot and collaborators,⁶⁶ we restrict our calculation to self-correlations of the NMA dipole moment.

In the quantum calculation, at each time step, NMA interacts with neighboring water molecules; thus its instantaneous charge may differ from zero. We therefore calculated the dipole moment of NMA with respect to its center of mass.

According to eq 2, we should calculate the Fourier transform of the TCF of the dipole moment. In order to obtain reasonable results, one needs very good statistics for the calculation of the TCF, which means quite long NVE simulations. This can be more easily done in the gas phase. However, when switching to simulations in water with periodic boundary conditions using a semiempirical Hamiltonian, temperature control is necessary. In the Andersen approach, this means that we have NVE intervals between two successive velocity randomizations. In our case, we have a collection of 1 ps NVE simulations over a 300 ps simulation time.

We thus tested a procedure to calculate IR spectra on each 1 ps NVE trajectory, averaging over the 300 1 ps blocks. In the gas phase, we had the chance to compare this procedure with the single 300-ps-long NVE simulation.

Another issue that we analyzed is the numerical method to calculate the Fourier transform of a TCF. In the gas phase, we compared IR spectra obtained by using the Wiener–Khinchin theorem⁶⁸ and those obtained by using the maximum entropy method (MEM)⁶⁸ with the result obtained by numerically calculating the integral in eq 2.

We found that the MEM and the procedure based on averaging over the 300 NVE blocks, 1-ps-long each, gave spectra in excellent agreement with the direct evaluation of the FT of the dipole TCF in the microcanonical ensemble. The comparison between the different methodologies is available as Supporting Information (SI).

Peak assignment on IR spectra was carried out by using a decomposition of the total vibrational density of states (VDOS) into atomic contributions. This procedure is often used when dealing with peak assignment in calculated IR spectra.^{66,67} The VDOS is obtained by calculating the FT of the self-correlation function of the atomic velocities of NMA. The same procedure described above to calculate the FT of a time correlation function

Table 1. Geometrical Parameters for Isolated *cis*- and *trans*-NMA^a

atom	Amber03 <i>cis</i>	Amber03 <i>trans</i>	PM3 <i>cis</i>	PM3 <i>trans</i>
C _{ACE} –H _{ACE}	1.09	1.09	1.10	1.10
C _{NMet} –H _{NMet}	1.09	1.09	1.10	1.10
C–O	1.22	1.22	1.22	1.22
N–H	1.01	1.01	1.00	1.00
C _{ACE} –C	1.52	1.52	1.51	1.51
C–N	1.33	1.34	1.43	1.43
N–C _{NMet}	1.46	1.47	1.47	1.47

^a Average values from molecular mechanics MD and from SEBOMD with a PM3 Hamiltonian. Distances are in Å. The standard deviation on distances is 0.03 Å with the exception of the CO and CN distances, for which it is 0.02 Å.

was applied. Additionally, some tests were performed by using internal coordinates to confirm the assignment. Results for the VDOS decomposition are provided as SI.

While more precise methods have been proposed to identify the IR bands when the vibrational modes differ significantly from the zero temperature equilibrium normal modes (ENMs) in the gas phase,^{69,70} it was not necessary to apply them in the present work, since recent studies have shown that the instantaneous normal modes of the NMA molecule in water solution can be identified using the corresponding ENMs as patterns (see refs 71 and 72).

In the next section, we shall discuss and compare the molecular properties that we obtained from our models. Only IR spectra calculated by applying the MEM on data from NVT simulations will be presented.

3. RESULTS

3.1. Results in the Gas Phase. We first analyze the average intramolecular properties calculated from our MD simulations. When considering the equilibrium geometry of NMA, no differences in the average bond distances are observed between the *cis* and the *trans* conformers, and the values that we found by using the PM3 Hamiltonian are similar to those found when using the Amber03 force field, with the exception of the C–N distance. Results are collected in Table 1. We recall that PIF parameters only modify the intermolecular (solvent–solvent and solvent–solute) interactions and therefore do not affect the intramolecular properties of NMA in the gas phase.

In Table 2, we report the results obtained for the molecular dipole moment of *cis*- and *trans*-NMA and a comparison with other results obtained with different levels of calculations and from experiments in the literature. Atomic charge parameters for the Amber03 simulations and the Mulliken, CM1, and CM2 charges for the quantum Hamiltonian are provided as Supporting Information.

On average, our PM3 results are in reasonable agreement with the data in the literature; in particular, the result obtained for *trans*-NMA through CM1 charges is in remarkable agreement with experiments.^{76,77} The Mulliken charges lead to an underestimation of the molecular dipole moment. Higher levels of quantum chemistry predict a more polar *cis* conformer as well as the PM3 calculations both from the electronic structure calculations on the minimum geometry and from the average value of the SEBOMD simulations. This is in agreement with the trend

Table 2. Comparison of NMA Dipole Moment (in Debye) As Obtained from Different Methods in the Gas Phase: Car–Parrinello Molecular Dynamics (CP-MD), Quantum Chemistry Calculations at the B3LYP/6-31G* and HF/6-31G(d) Levels of Theory, Our Results for Quantum Calculations at the PM3 Level (in the Case of Standard PM3 Parameters As Well As PM3 with the Correction for the Peptide Bond (PM3-MM)), Our Results from SEBOMD at the PM3 Level (Average Value of the Molecular Dipole—from the Dipole Moment Operator—and the Corresponding Values from Partial Atomic Charges Using Different Schemes), and Our Results from Simulations with the Amber03 Force Field

method	<i>cis</i> -NMA	<i>trans</i> -NMA
CP-MD ⁶⁶	4.38	3.99
B3LYP/6-31G* ⁷³	4.00	3.81
B3LYP/6-311++G* ⁷⁴	4.31	3.97
HF/6-31G(d) ⁷⁵	4.37	4.22
MP2/6-31G(d) ¹⁴	4.21	4.04
PM3	3.39	3.10
PM3-MM	3.68 (TS) ^a	3.31
PM3-SEBOMD	3.36	3.09
PM3-SEBOMD (Mulliken charges)	3.09	2.64
PM3-SEBOMD (CM1 charges)	3.24	3.79
PM3-SEBOMD (CM2 charges)	3.54	3.54
Amber03 molecular mechanics MD	4.09	4.50
exp. (in benzene) ⁷⁶	3.85	
exp. (vapor) ⁷⁷	3.71–3.73	

^a In this case, geometry optimization of the *cis* conformer led to a transition state (TS).

based on Mulliken charges from SEBOMD simulations. On the other hand, the MM force field Amber03 and CM1 charges at a PM3 level predict the *trans* conformer to be more polar than the *cis*. Finally, no difference in polarity is observed when evaluating the molecular dipole moment through CM2 charges.

We now present our results for the IR spectra of *cis*- and *trans*-NMA. In Figure 1, we show the computed spectra for *cis*- and *trans*-NMA as obtained from MM MD simulations by using the Amber03 force field.⁴⁵

The procedure based on the VDOS decomposition, described in section 2, allows us to deduce the following assignment. The bands between 3200 and 3400 cm⁻¹ are due to the N–H stretch, those between 2800 and 3100 cm⁻¹ to the C–H stretch (both for the ACE and the N Met residues). The positions of such bands are quite similar for *cis*- and *trans*-NMA, though the former is slightly red-shifted in *trans*-NMA compared to *cis*. On the basis of low temperature nitrogen matrices, the infrared spectra of *cis*- and *trans*-NMA were measured.¹⁸ According to this study, the N–H stretch absorption due to the *cis* form has a peak at 3458 cm⁻¹ and the one due to the *trans* form at 3498 cm⁻¹. Experiments in CCl₄ at ambient temperature found a peak at 3476 cm⁻¹, whereas symmetric and antisymmetric C–H stretches fall between 2900 and 3000 cm⁻¹.^{18,78}

The analysis of the VDOS decomposition shows that in the simulated spectrum of *trans*-NMA the H–N–C bending vibration (amide II) occurs at 1780 cm⁻¹ and the C–O stretch (amide I) occurs at 1680 cm⁻¹, whereas in *cis*-NMA, these two bands superimpose in a broader absorption around 1800 cm⁻¹.

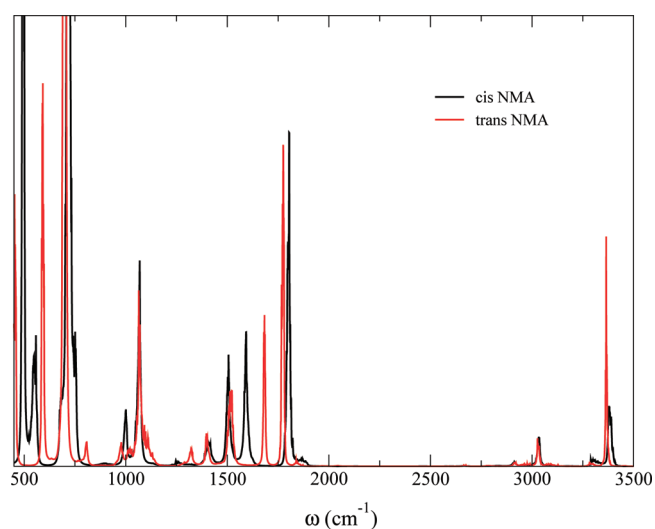


Figure 1. Isolated NMA. Calculated infrared spectrum from molecular dynamics simulations with an MM force field. The infrared intensity is arbitrary units.

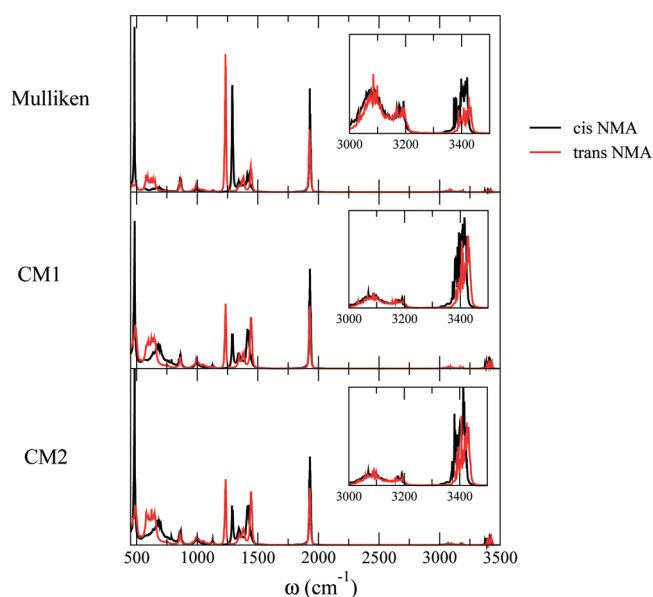


Figure 2. Isolated NMA. Calculated infrared spectrum from SEBOMD simulations with a PM3 Hamiltonian. The infrared intensity is arbitrary units.

Experimental measurements of the IR spectrum (see ref 78 and references therein for the *trans* conformer) assign absorption between 1714 and 1731 cm⁻¹ to amide I and between 1497 and 1500 cm⁻¹ to amide II. As for the experimental spectrum of the less stable *cis* conformer,¹⁸ the amide I mode occurs in the same frequency range as for the *trans* conformer, while the amide II mode is found at lower frequencies (by about 40 cm⁻¹) than in *trans*. In any case, the molecular mechanics force field employed does not give the correct trend between amide I and amide II absorption. It has been pointed out that pyramidalization at the peptide group N atom needs to be taken into account along an MD simulation,^{79,80} since the CN torsion and the N–H out-of-plane bending give an important contribution to the NMA IR

Table 3. Collection of Results for the Infrared Frequencies Which Are Characteristic of the Peptide Bond of NMA in the Gas Phase and in Water: Amide I (AI), Amide II (AII), Amide III (AIII), and N–H Stretch (δ_{NH})^a

mode	Amber03			SEBOMD			experiment ^{18,78}		
	GP	sol.	Δ	GP	sol.	Δ	GP	sol.	Δ
AI	1680, ^b 1800 ^c	1680, ^b 1800 ^c	0	1920 ^{b,c}	1800 ^{b,c}	−120	1714–1731	1625–1646	−90
AII	1780, ^b 1800 ^c	1780, ^b 1800 ^c	0	1420, ^b 1440 ^c	1485, ^b 1522 ^c	75	1497,1500	1565–1585	80
AIII	1250, ^b 1320 ^c	1250, ^b 1330 ^c	5	1290, ^b 1230 ^c	1340, ^b 1370 ^c	95	1255–1259	1314–1317	60
δ_{NH}	3380, ^b 3370 ^c	3380, ^b 3370 ^c	0	3405, ^b 3410 ^c	3370, ^b 3300 ^c	−110 ^c	3476 ^d	3300	−130

^a All data in the gas phase (GP), in water (sol.), and the average shift of the condensed phase results with respect to the gas phase (Δ) are reported in cm^{-1} . ^b *cis*-NMA. ^c *trans*-NMA. ^d In CCl_4 solution.

Table 4. Geometrical Parameters for *cis*- and *trans*-NMA in Water^a

atom	Amber03		PM3-PIF	
	Amber03 <i>cis</i>	<i>trans</i>	PM3-PIF <i>cis</i>	<i>trans</i>
$\text{C}_{\text{ACE}}-\text{H}_{\text{ACE}}$	1.09 (0.00)	1.09 (0.00)	1.11 (+0.01)	1.11 (+0.01)
$\text{C}_{\text{NMet}}-\text{H}_{\text{NMet}}$	1.09 (0.00)	1.09 (0.00)	1.11 (+0.01)	1.11 (+0.01)
C–O	1.23 (0.00)	1.23 (0.00)	1.25 (+0.03)	1.25 (+0.03)
N–H	1.01 (0.00)	1.01 (0.00)	1.00 (0.00)	1.01 (−0.01)
$\text{C}_{\text{ACE}}-\text{C}$	1.52 (0.00)	1.52 (0.00)	1.50 (−0.01)	1.51 (0.00)
C–N	1.33 (0.00)	1.33 (−0.01)	1.39 (−0.04)	1.39 (−0.04)
$\text{N}-\text{C}_{\text{NMet}}$	1.46 (0.00)	1.46 (−0.01)	1.48 (+0.01)	1.47 (0.00)

^a Average values from molecular mechanics MD and from SEBOMD with a PM3 Hamiltonian and PIF corrections. [The standard deviation on distances is 0.03 Å with the exception of the CO and CN distances, for which it is 0.02 Å.] Distances are in Å. In parentheses, we report the shifts with respect to the gas phase.

spectrum. Krimm and collaborators have performed extensive studies showing that including geometry-dependent charges may be more important than developing a polarizable MM force field.^{81,82} An alternative approach has been proposed, generally improving the agreement with experiments compared to the classical MM-based evaluation of the vibrational properties of biological systems.⁸³ This method is based on including additional terms in the potential energy function of the MM force field.

Another band in the IR spectrum from MD simulations, located around 1590 cm^{-1} in *cis*-NMA, was assigned to the $\text{H}_{\text{ACE}}-\text{C}_{\text{ACE}}-\text{C}$ bend. This band is red-shifted to about 1510 cm^{-1} in *trans*-NMA. Between 1320 and 1510 cm^{-1} , in *trans*-NMA we find the amide III bend and the H–C–C and H–C–N bending motions. As for *cis*-NMA, the same bands fall between 1380 and 1590 cm^{-1} . The amide III band position varies between 1255 and 1259 cm^{-1} in experiments, and backbone motions absorb at lower frequencies, where the pattern becomes more and more complicated for both conformers.

In Figure 2, we show the results obtained from SEBOMD simulations by using the PM3 Hamiltonian. We recall that we have different results according to the different scheme for partial atomic charges.

The band positions and their width do not seem to depend on the charge type, which however affects slightly the peak intensities. Results are collected in Table 3.

The two regions in the high frequency portion of the spectrum (between 3000 and 3200 cm^{-1} and around 3420 cm^{-1}) are very similar for *cis*- and *trans*-NMA, the latter being blue-shifted by

20 cm^{-1} compared to the *cis*. This finding is in agreement with the experiment in ref 18.

The amide I band is located for both conformers around 1920 cm^{-1} . The result is overestimated compared to the average experimental data. The amide II and amide III bands are spread over the 1230 – 1480 cm^{-1} region for *trans*-NMA, and in a less extended region (between 1290 and 1480 cm^{-1} region) for *cis*-NMA. The amide II peak in *cis*-NMA is red-shifted by 20 cm^{-1} compared to the *trans*, again in agreement with the results in ref 18 (red shift of about 40 cm^{-1}). The positions of the amide II and amide III bands in the gas phase seem in quite good agreement with experiments. MD simulations within the Car–Parrinello scheme⁶⁶ have provided the following results: the frequency for amide I is 1609 cm^{-1} in *trans*-NMA and 1606 cm^{-1} in *cis*-NMA. The frequency calculated for amide II is 1458 cm^{-1} in *trans*- and 1369 cm^{-1} in *cis*-NMA. Finally, The frequency for amide III is 1189 cm^{-1} in *trans*- and 1259 cm^{-1} in *cis*-NMA. Our results are in general agreement with the CPMD results. In particular, the amide I frequency is the same in *cis*- and *trans*-NMA, and the amide II peak in *cis*-NMA is red-shifted compared to *trans*-NMA. However, it seems that the latter approach leads to a better agreement with experiments for the amide I band and to a worse agreement for amide II. In addition, no bands in the N–H stretch region are observed on the basis of CPMD simulations.

In summary, though the amide I experimental band position is not accurately reproduced by our SEBOMD, we obtain a general reasonable agreement with experiments. On the other hand, MD with the Amber03 force field does not reproduce the correct ordering between amide I and II, predicting a lower frequency amide I mode compared to amide II.

3.2. Results in Water. First of all, we examine solvent effects on the solute geometry. Compared to the results in the gas phase, few or no differences are observed when using the MM force field, whereas quite a few interesting conclusions can be drawn from an analysis of the results obtained with a quantum electronic Hamiltonian. In the latter case, we used PM3 parameters with PIF corrections, as described in section 2. Results obtained on the intramolecular distances are collected in Table 4.

When going from the gas phase to a solution in water, the C–O bond is elongated. The distance between the C and the N atoms is quite shortened. This is in agreement with the results observed in the literature.⁶⁶

To interpret this result, we recall the two possible resonance structures of NMA in Figure 3.

In a polar solvent, the zwitterionic form is stabilized by electrostatic interactions between the solute and the solvent, and accordingly, the C–O distance elongates and the C–N bond shortens. This effect cannot be reproduced by MM force

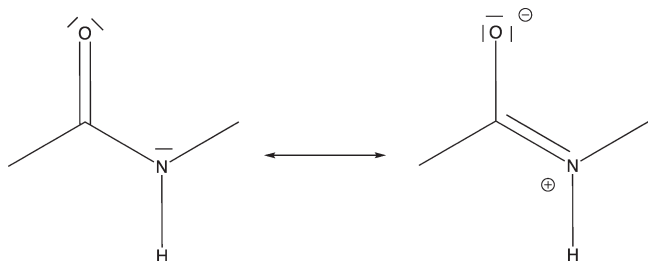


Figure 3. Resonance structures for NMA.

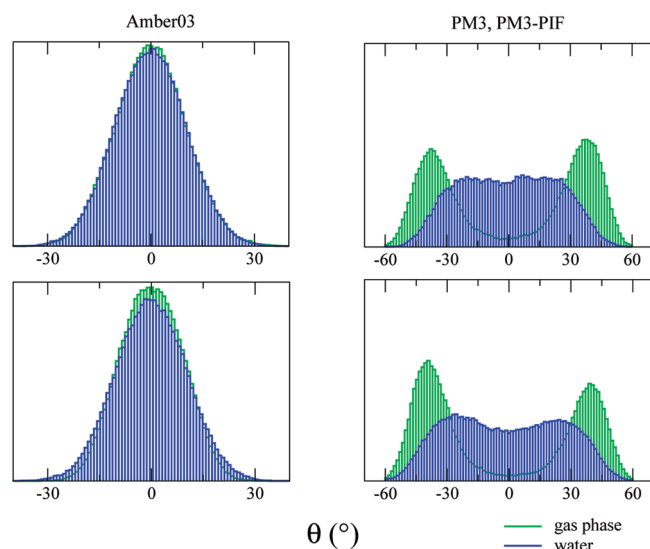


Figure 4. Distribution of the angle formed by the N–H bond with the plane instantaneously identified by N and the two C atoms from molecular dynamics with the Amber 03 force field (left side) and from SEBOMD (right side). Top panels: *cis*-NMA (gas phase and solution). Bottom panels: *trans*-NMA (gas phase and solution).

fields and, not surprisingly, in this case, MD simulations of NMA in water do not predict significant changes in NMA geometry with respect to the gas phase.

As for the out-of-plane position of the N–H bond in the case of simulations with a quantum Hamiltonian, we find distributions corresponding to a pyramidal N atom (see Figure 4).

The distribution is much broader in solution than in the gas phase, and the out-of-plane angle is smaller ($\pm 16^\circ$ for *cis*- and $\pm 25^\circ$ for *trans*-NMA). This is consistent with a larger contribution of the zwitterionic resonance structure in a polar solvent.

When analyzing CM1 and CM2 atomic charges (tables collecting all results are available as SI), we observe a displacement of electrons from the –NH group toward the –CO group, again in agreement with a larger contribution of the zwitterionic form. Charges on the O atom decrease, whereas those on the N and the H atoms increase on going from the gas phase to solution. The C atom is less affected. On average, about $-0.1e$ is transferred from –NH to –CO. We can therefore expect to observe a strong increase of the molecular dipole moment in solution. We collect our results for the molecular dipole moment together with other values obtained at different levels of theory in Table 5.

As in the gas phase, some methods (Car–Parrinello MD, density functional theory with a B3LYP functional and a

Table 5. Comparison of NMA Dipole Moment (in Debye) As Obtained from Different Methods in Aqueous Solution^a

method	<i>cis</i> -NMA	<i>trans</i> -NMA
CP-MD ⁶⁶	7.33 (+2.95)	6.96 (+2.97)
B3LYP/6-31G*-SCRF ⁷³	4.95 (+0.95)	4.86 (+1.05)
HF/6-31G(d)-RISM ⁷⁵	5.79 (+1.42)	5.93 (+1.71)
PM3,PIF(Mulliken)	5.94 (+2.85)	5.41 (+2.77)
PM3,PIF(CM1)	6.26 (+3.02)	6.63 (+2.94)
PM3,PIF(CM2)	6.26 (+2.52)	6.22 (+2.68)
Amber03 MM MD	4.14 (+0.05)	4.54 (+0.04)

^a Car–Parrinello molecular dynamics (CP-MD), quantum chemistry calculations (B3LYP/6-31G* in a continuum solvent and HF/6-31G(d) coupled with RISM), our results from SEBOMD at the PM3 and PIF levels (average molecular dipole from partial atomic charges using different schemes), and from simulations with the Amber03 force field. In parentheses, we report the shifts with respect to the gas phase.

6-31G(d) basis set coupled with a continuum solvent, or our PM3 calculation with Mulliken and CM2 charges) predict a more polar *cis* conformer, while others (Hartree–Fock calculations with a 6-31G(d) basis set coupled with a reference interaction site model (RISM) to describe the solvent, molecular mechanics MD with the Amber03 force field, or our PM3 calculation with CM1 charges) predict the *trans* conformer to be the most polar in water.

Not surprisingly, very small induced dipole moments are calculated when running MD simulation with an MM force field. On the contrary, a very large change in the dipole moment on the order of 3 D is calculated from CP-MD and in our simulations when using CM1 charges. The effect is similar when using CM2 charges (about 2.7 D) and Mulliken charges (about 2.7–2.8 D), but much smaller with HF/RISM (1.4–1.7 D) and B3LYP/continuum (about 1 D). Since the two latter methods take into account the solvent as a bulk, specific interactions between solute and solvent are not described explicitly, in particular, the formation of hydrogen bonds with water molecules.

The final part of this section will be devoted to the analysis of the IR spectra in water, and to a comparison with the gas phase results.

The results obtained for the IR spectrum of *cis*- and *trans*-NMA in water when running MD simulations with an MM force field (see Figure 5) show no remarkable differences both in band positions and shapes compared to the gas phase (compare with Figure 1—peak positions are collected in Table 3).

The only perceivable difference in band position involves those modes which are located at lower frequencies (under 1000 cm^{-1}), where one can observe some line broadening both for *trans*- and *cis*-NMA.

In addition to the wrong frequency ordering of amide I and amide II bands, the Amber03 force field is thus not able to describe the differences in the IR spectrum of peptides going from the gas phase to aqueous solution.

On the other hand, the results obtained with the SEBOMD approach display significant differences in the condensed phase compared to the gas phase. This finding is in agreement with the CPMD results from ref 66. The effect of the dipole induced by water molecules on the solute has been shown to significantly affect the spectral profile of amide I–III bands.²⁵ In this work, the authors have compared the relative intensity and the band shape of amide I–III with experiments. An agreement with

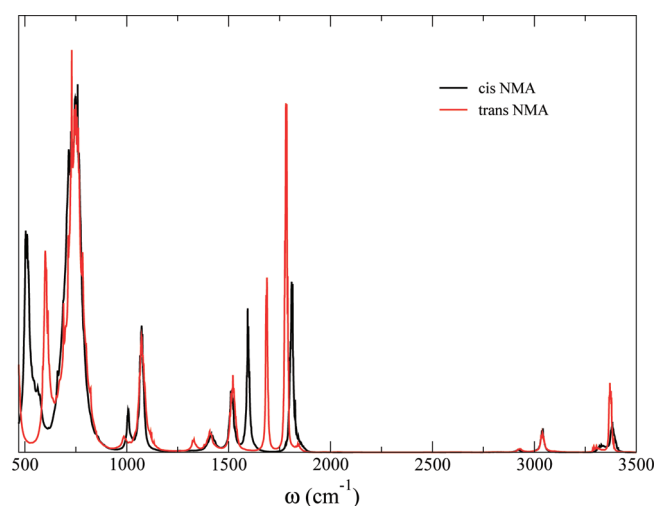


Figure 5. NMA in water. Calculated infrared spectrum from MD simulations with an MM force field. The infrared intensity is arbitrary units.

experimental features of these bands is achieved only if the solute is treated at a quantum level by means of a semiempirical electronic Hamiltonian.

In Figure 6, we collect the IR obtained from the three different charge schemes used in this work. When comparing Figure 6 with Figure 2, the IR bands in solution are broadened with respect to gas phase spectra. In addition, differences between spectra for the *cis* and *trans* conformers are enhanced in the condensed phase. A more detailed analysis of solvent effects for each vibrational mode is presented below and summarized in Table 3.

SEBOMD simulations predict the N–H stretch to be red-shifted in both conformers. The *trans* conformer of NMA (band around 3300 cm^{-1}) undergoes a larger effect (red shift of about 110 cm^{-1}) compared to the *cis* one (band around 3370 cm^{-1} , shift of about 35 cm^{-1}). Experimentally, the frequency of the N–H stretch was measured in CCl_4 to be 3476 cm^{-1} and 3300 cm^{-1} in water.⁸⁴ One should point out that this band is very sensitive to temperature and concentration. A large red shift is observed in experiments, the magnitude of which is compatible with our calculated result based on the most stable conformer *trans* NMA.

The band related to the C–H stretch (between 2900 and 3200 cm^{-1}) is similar for *cis*- and *trans*-NMA. Compared to the gas phase, this band is quite broadened but not shifted. To our knowledge, no experimental data are available for the frequencies of the C–H stretching motions in aqueous solution.

The amide I band is located around 1800 cm^{-1} , and the *cis*- and *trans*-NMA conformers are predicted to absorb at the same frequency. In this case, solvent effects lead to a red shift of about 120 cm^{-1} . Results in the literature for amide I absorption band position vary from 1625 to 1646 cm^{-1} in aqueous solution.⁷⁸ An average red shift of about 90 cm^{-1} is thus observed, in good agreement with our results.

In the *cis*-NMA spectra, the peak centered at 1485 cm^{-1} is assigned to the amide II mode. A similar assignment is made in the case of *trans*-NMA for the peak at 1522 cm^{-1} . Compared to gas phase data, we predict a blue shift of 80 cm^{-1} in *cis*-NMA and 75 cm^{-1} in *trans*-NMA. Experimental results for this band in water vary between 1565 and 1585 cm^{-1} .⁷⁸ The average blue shift is thus about 80 cm^{-1} , again in quite good agreement with our calculated shift.

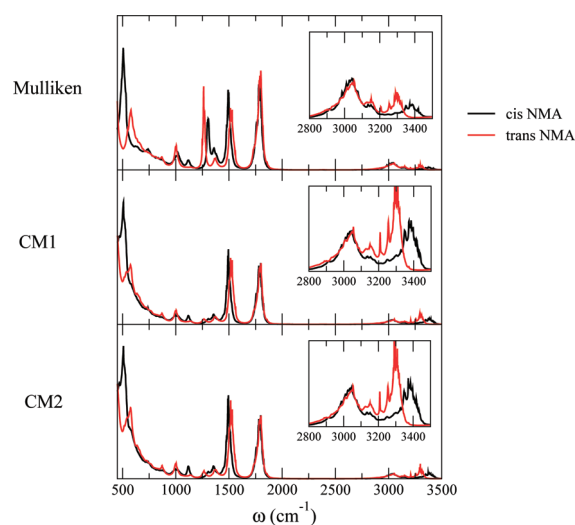


Figure 6. NMA in water. Calculated infrared spectrum from SEBOMD simulations with a PM3 Hamiltonian with PIF corrections. The infrared intensity is arbitrary units.

Bands between 1260 and 1370 cm^{-1} are quite broadened in solution. In this region, we observe the amide III motion. However, some other modes are active too, and it is not easy to quantitatively extract their position. The *cis* absorption appears at slightly lower frequencies compared to the *trans* form. On average, we can estimate a solvent blue shift effect of about 95 cm^{-1} . The experimental results for amide III absorption vary between 1314 and 1317 cm^{-1} , with an average blue shift of 60 cm^{-1} compared to the gas phase.⁷⁸

The results obtained with Car–Parrinello MD in ref 66 predict an average blue shift of 110 cm^{-1} for amide I, an average red shift 20 of cm^{-1} for amide II, and of 40 cm^{-1} for amide III. The solvent effect obtained at this level of theory is again in fairly good agreement with our description. A comparison with the AM1/MM method used by Cho and collaborators²⁵ can only be carried out on the absolute values of the IR frequencies, since the corresponding results in the gas phase are not available. In addition, only the most stable (*trans*) conformer was considered. Amides I, II, and III and the N–H stretch are reported to occur at 1896 , 1721 , 1444 , and 3332 cm^{-1} , respectively. With the exception of the last band, it seems as if the AM1/MM combined strategy tends to overestimate the frequencies which are characteristic of the peptide bond.

The IR spectrum of *trans* deuterated NMA in a $16\text{ D}_2\text{O}$ molecule cluster has been calculated on the basis of a PM3/MM approach.³¹ If we compare the results obtained in this work with the experimental measurements^{78,85} on the amide I' band (the band corresponding to amide I in the deuterated system), we obtain an underestimated blue shift (30 cm^{-1} in the simulations vs 90 cm^{-1} in the experiment). Although not conclusive, this comparison suggests that the solvent effect on the position of the solute IR bands is better described when the full system is treated at the quantum level, thus including mutual polarization and charge transfer.

Finally, broad absorption around 1000 cm^{-1} is related to backbone motion, but it becomes more and more complicated to analyze in depth the lower frequency regions of the spectrum, since many different modes are active there.

Overall, solvent effects are well reproduced by our SEBOMD simulations, although the absolute values of the frequencies are

not predicted with high accuracy. Specifically, when considering the frequency of the amide I, II, and III modes, the calculated frequencies are overestimated, the error being relatively large for amide I but smaller and similar for amides II and III. As a consequence, the gap between the amide I and II frequencies is too high, while the amide II–amide III gap is in reasonable agreement with experiments, both in the gas phase and in solution.

4. CONCLUDING REMARKS

In this paper, we have reported the first analysis of infrared spectra of solvated compounds using molecular dynamics simulations in which the electronic Hamiltonian of the whole solute–solvent system is described by a semiempirical quantum mechanical method. The PM3 Hamiltonian was used to obtain the electronic wave function of the system, and PIF corrections for the core–core interaction terms were considered in order to improve the description of intermolecular interactions. The main scope of this study was to assess the validity of this SEBOMD approach to predict solvent effects on the vibrational frequency of amide bonds. This is an important objective in the perspective of the application of this model to larger systems such as peptides, and eventually proteins.

Overall, our results are quite encouraging. Indeed, a remarkably good agreement was obtained with available experimental data and other calculations in the literature. Interestingly, the same study conducted by using a molecular mechanics, non-polarizable force field showed no remarkable difference in the infrared bands that are more significant signatures of a peptide bond when going from the gas phase to aqueous solution. This finding stresses the importance of a correct description of electronic properties (polarization, charge transfer, etc.) for an adequate molecular modeling of absorption spectra in solution. This is particularly crucial in the case of amide (peptide) bonds since the relative weight of neutral vs zwitterionic tautomeric structures is extremely sensitive to electrostatic interactions with the environment and needs to be accounted for.

As far as the absolute position of the bands is concerned, and not surprisingly, our study shows the usual limitations connected to the use of semiempirical methods, namely on the position of the amide I band. In addition, predicted IR intensities are not quantitative. However, several improvements of the present approach can be envisaged. For instance, including the prefactor in eq 2 might lead to more accurate band shapes,^{63,64,86} although a strong effect should not be expected on the bands' intensity.⁶⁵ In addition, exploiting the possibility offered by the SEBOMD approach to run long time scale simulations (i.e., compared to ab initio MD) should allow one to unravel the role of the solute–solvent cross-correlation term mentioned in section 2⁶⁶ and thus the contribution of intermolecular coupling on the solute vibrations.

Finally, it is worth noting that this approach would be suitable for studying energy transfer in solution. In a recent work, a novel formulation of the instantaneous normal modes (INM) approach was proposed and applied to energy reorganization after the excitation of the amide I⁷¹ and the C–H stretching⁷² modes of NMA in solution using an MM, nonpolarizable force field. The relevance of this kind of investigation stems from the importance of energy transfer along peptide chains in biological systems, where polarization and charge transfer effects are expected to play a role in the mechanism of energy redistribution through

intra- and intermolecular modes. Accordingly, coupling the SEBOMD method to the INM analysis is a very promising technique in this domain that will be evaluated in forthcoming work with model peptides.

■ ASSOCIATED CONTENT

Supporting Information. Atomic charges for *cis*- and *trans*-NMA in the gas phase and in solution, a comparison between different methods to calculate the IR spectrum of NMA, a comparison between the results obtained for the NVE and the NVT ensembles, and finally the VDOS for *cis* and *trans* NMA in the gas phase and in solution are given. This information is available free of charge via the Internet at <http://pubs.acs.org>.

■ AUTHOR INFORMATION

Corresponding Author

*E-mail: Francesca.Ingrosso@cbt.uhp-nancy.fr.

■ ACKNOWLEDGMENT

This work was partially supported by the Ministerio de Educación y Ciencia of Spain under Projects CTQ2007-66528/BQU and CONSOLIDER CSD2009-00038 and by the Fundación Séneca del Centro de Coordinación de la Investigación de la Región de Murcia under Project 08735/PI/08. M.H.F. gratefully acknowledges a fellowship from the Ministerio de Educación y Ciencia of Spain. F.L., G.M., and M.F.R.L. thank CINES (Montpellier, France) for generous access to their computational facilities.

■ REFERENCES

- (1) Car, R.; Parrinello, M. *Chem. Phys. Lett.* **1985**, *55*, 2471.
- (2) Laasonen, K.; Sprik, M.; Parrinello, M.; Car, R. *J. Chem. Phys.* **1993**, *99*, 9080.
- (3) Carloni, P.; Rothlisberger, U.; Parrinello, M. *Acc. Chem. Res.* **2002**, *35*, 455.
- (4) Silvestrelli, P. L.; Bernasconi, M.; Parrinello, M. *Chem. Phys. Lett.* **1997**, *277*, 478.
- (5) Silvestrelli, P. L.; Parrinello, M. *Phys. Rev. Lett.* **1998**, *81*, 1235.
- (6) Iftimie, R.; Minary, P.; Tuckerman, M. E. *Proc. Natl. Acad. Sci. U.S.A.* **2005**, *102*, 6654.
- (7) Monard, G.; Bernal-Uruchurtu, M. I.; van des Vaart, A.; Merz, K. M., Jr.; Ruiz-López, M. F. *J. Phys. Chem. A* **2005**, *109*, 3425.
- (8) Gaigeot, M. P. *Phys. Chem. Chem. Phys.* **2010**, *12*, 3336.
- (9) Montalvo, G.; Waegle, M. M.; Shandler, S.; Gai, F.; De Grado, W. F. *J. Am. Chem. Soc.* **2010**, *132*, 5616.
- (10) Gilman, R.; Williams, S.; Callender, R. H.; Woodruff, W. H.; Dyer, R. B. *Biochemistry* **1997**, *36*, 15006.
- (11) Schultheis, V.; Reichold, R.; Schropp, B.; Tavan, P. *J. Phys. Chem. B* **2008**, *112*, 12217.
- (12) Gaigeot, M. P. *Phys. Chem. Chem. Phys.* **2010**, *12*, 10198.
- (13) Gaigeot, M. P. *J. Phys. Chem. B* **2009**, *113*, 10059.
- (14) Jorgensen, W. L.; Gao, J. *J. Am. Chem. Soc.* **1988**, *110*, 4212.
- (15) Gao, J.; Freindorf, M. *J. Phys. Chem. A* **1997**, *101*, 3182.
- (16) Villani, V.; Alagona, G.; Ghio, C. *Mol. Eng.* **1999**, *8*, 135.
- (17) Cuevas, G.; Renugopalakrishnan, V.; Madrid, G.; Hagler, A. T. *Phys. Chem. Chem. Phys.* **2002**, *4*, 1490.
- (18) Ataka, S.; Takeuchi, H.; Tasumi, M. *J. Mol. Struct.* **1984**, *113*, 147.
- (19) Drakenberg, T.; Forsen, S. *J. Chem. Soc., Chem. Commun.* **1971**, 1404.
- (20) Luque, F. J.; Orozco, M. *J. Org. Chem.* **1993**, *58*, 6397.

- (21) Mantz, Y. A.; Gerard, H.; Iftimie, R.; Martyna, G. J. *J. Am. Chem. Soc.* **2004**, *126*, 4080.
- (22) Mantz, Y. A.; Gerard, H.; Iftimie, R.; Martyna, G. J. *J. Phys. Chem. B* **2006**, *110*, 13523.
- (23) Mantz, Y. A.; Branduardi, D.; Bussi, G.; Parrinello, M. *J. Phys. Chem. B* **2009**, *113*, 12521.
- (24) Chen, X. C.; Schweitzer-Stenner, R.; Krimm, S.; Mirkin, N. G.; Asher, S. A. *J. Am. Chem. Soc.* **1994**, *116*, 11141.
- (25) Yang, S.; Cho, M. *J. Chem. Phys.* **2005**, *123*, 134503.
- (26) Mennucci, B.; Martinez, J. M. *J. Phys. Chem. B* **2005**, *109*, 9818.
- (27) Hayashi, T.; Zhuang, W.; Mukamel, S. *J. Phys. Chem. A* **2005**, *109*, 9747.
- (28) Besley, N. A. *J. Phys. Chem. A* **2004**, *108*, 10794.
- (29) Andrushchenko, V.; Matějka, P.; Anderson, D. T.; Kaminský, J.; Horncek, J.; Paulson, L. O.; Bouř, P. *J. Phys. Chem. A* **2009**, *113*, 9727.
- (30) Ackels, L.; Stawski, P.; Amunson, K. E.; Kubelka, J. *Vib. Spectrosc.* **2009**, *50*, 2.
- (31) Jeon, J.; Cho, M. *New J. Phys.* **2010**, *12*, 065001.
- (32) Kinnaman, C. S.; Cremeens, M. E.; Romesberg, F. E.; Corcelli, S. A. *J. Am. Chem. Soc.* **2005**, *128*, 13334.
- (33) Richardi, J.; Fries, P.; Millot, C. *J. Mol. Liq.* **2005**, *117*, 3.
- (34) Yang, W.; Lee, T.-S. *J. Chem. Phys.* **1995**, *103*, 5674.
- (35) Dixon, S. L.; Merz, K. M., Jr. *J. Chem. Phys.* **1996**, *104*, 6643.
- (36) Mokrane, A.; Friant-Michel, P.; Cartier, A.; Rivail, J.-L. *THEO-CHEM* **1997**, *395*, 71.
- (37) Li, S.; Schmidt, J. R.; Corcelli, S. A.; Lawrence, C. P.; Skinner, J. L. *J. Chem. Phys.* **2006**, *124*, 2041.
- (38) Garcia-Viloca, M.; Nam, K.; Alhambra, C.; Gao, J. L. *J. Phys. Chem. B* **2004**, *108*, 13501.
- (39) Stewart, J. J. P. *J. Comput. Chem.* **1989**, *10*, 209.
- (40) Bernal-Uruchurtu, M. I.; Martins-Costa, M. T. C.; Millot, C.; Ruiz-López, M. F. *J. Comput. Chem.* **2000**, *21*, 572.
- (41) Csonka, G. I.; Angyan, J. G. *THEOCHEM* **1997**, *393*, 31.
- (42) Harb, W.; Bernal-Uruchurtu, M. I.; Ruiz-López, M. F. *Theor. Chem. Acc.* **2004**, *112*, 204.
- (43) Bernal-Uruchurtu, M. I.; Ruiz-López, M. F. *Chem. Phys. Lett.* **2000**, *330*, 118.
- (44) Case, D. A.; Darden, T. A.; Cheatham, T. E., III; Simmerling, C. L.; Wang, J.; Duke, R. E.; Luo, R.; Merz, J. M. K.; Pearlman, D. A.; Crowley, M.; Walker, R. C.; Zhang, W.; Wang, B.; Hayik, S.; Roitberg, A.; Seabra, G.; Wong, K. F.; Paesani, F.; Wu, X.; Brozell, S.; Tsui, V.; Gohlke, H.; Yang, L.; Tan, C.; Mongan, J.; Hornak, V.; Cui, G.; Beroza, P.; Mathews, D. H.; Schafmeister, C.; Ross, W. S.; Kollman, P. A. *AMBER9*; University of California: San Francisco, 2006.
- (45) Duan, Y.; Wu, C.; Chowdhury, S.; Lee, M. C.; Xiong, G.; Zhang, W.; Yang, R.; Cieplak, P.; Luo, R.; Lee, T.; Caldwell, J.; Wang, J.; Kollman, P. *J. Comput. Chem.* **2003**, *24*, 1999.
- (46) Berendsen, H. J. C.; Grigera, J. R.; Straatsma, T. P. *J. Phys. Chem.* **1987**, *91*, 6269.
- (47) Andersen, H. C. *J. Chem. Phys.* **1980**, *72*, 2384.
- (48) Rami Reddy, M.; Berkowitz, M. *Chem. Phys. Lett.* **1989**, *155*, 173.
- (49) Allen, M. P.; Tildesley, D. J. *Computer Simulation of Liquids*; Oxford University Press: Oxford, U. K., 1987.
- (50) Lemmon, E.; McLinden, M.; Friend, D. Thermophysical Properties of Fluid Systems. In *NIST Chemistry WebBook, NIST Standard Reference Database Number 69*; Linstrom, P. J., Mallard, W. G., Eds.; National Institute of Standards and Technology: Gaithersburg MD, 2008. <http://webbook.nist.gov> (accessed April 2011).
- (51) Ryckaert, J. P.; Ciccotti, G.; Berendsen, H. J. C. *J. Comput. Phys.* **1977**, *23*, 327.
- (52) Ciccotti, G.; Ryckaert, J. P. *Comp. Phys. Rep.* **1986**, *4*, 345.
- (53) Frisch, M. J.; Trucks, G. W.; Schlegel, H. B.; Scuseria, G. E.; Robb, M. A.; Cheeseman, J. R.; Montgomery, J. A., Jr.; Vreven, T.; Kudin, K. N.; Burant, J. C.; Millam, J. M.; Iyengar, S. S.; Tomasi, J.; Barone, V.; Mennucci, B.; Cossi, M.; Scalmani, G.; Rega, N.; Petersson, G. A.; Nakatsuji, H.; Hada, M.; Ehara, M.; Toyota, K.; Fukuda, R.; Hasegawa, J.; Ishida, M.; Nakajima, T.; Honda, Y.; Kitao, O.; Nakai, H.; Klene, M.; Li, X.; Kno, J. E.; Hratchian, H. P.; Cross, J. B.; Adamo, C.; Jaramillo, J.; Gomperts, R.; Stratmann, R. E.; Yazyev, O.; Austin, A. J.; Cammi, R.; Pomelli, C.; Ochterski, J. W.; Ayala, P. Y.; Morokuma, K.; Voth, G. A.; Salvador, P.; Dannenberg, J. J.; Zakrzewski, V. G.; Dapprich, S.; Daniels, A. D.; Strain, M. C.; Farkas, O.; Malick, D. K.; Rabuck, A. D.; Raghavachari, K.; Foresman, J. B.; Ortiz, J. V.; Cui, Q.; Baboul, A. G.; Clifford, S.; Cioslowski, J.; Stefanov, B. B.; Liu, G.; Liashenko, A.; Piskorz, P.; Komaromi, I.; Martin, R. L.; Fox, D. J.; Keith, T.; Al-Laham, M. A.; Peng, C. Y.; Nanayakkara, A.; Challacombe, M.; Gill, P. M. W.; Johnson, B.; Chen, W.; Wong, M. W.; Gonzalez, C.; Pople, J. A. *Gaussian 03*, revision B.03; Gaussian, Inc.: Pittsburgh, PA, 2003.
- (54) Niklasson, A.; Tymczak, C. J.; Challacombe, M. *Phys. Rev. Lett.* **2006**, *97*, 123000.
- (55) Herbert, J. M.; Head-Gordon, M. *Phys. Chem. Chem. Phys.* **2005**, *7*, 3269.
- (56) Goedecker, S. *Rev. Mod. Phys.* **1999**, *71*, 1085.
- (57) Nam, K.; Gao, J.; York, D. M. *J. Chem. Theory Comput.* **2005**, *1*, 2.
- (58) Storer, J. W.; Giesen, D. J.; Cramer, C. J.; Truhlar, D. G. *J. Comput.-Aided Mol. Des.* **1995**, *9*, 87.
- (59) Li, J.; Zhu, T.; Cramer, C. J.; Truhlar, D. G. *J. Phys. Chem. A* **1998**, *102*, 1820.
- (60) Gordon, R. G. *J. Chem. Phys.* **1965**, *43*, 1307.
- (61) Berens, P. H.; Wilson, K. R. *J. Chem. Phys.* **1981**, *74*, 4872.
- (62) McQuarrie, D. A. *Statistical Mechanics*; University Science Books: Sausalito, CA, 2000.
- (63) Schmidt, J. R.; Corcelli, S. A. *J. Chem. Phys.* **2008**, *128*, 184504.
- (64) Egorov, S. A.; Everitt, K. F.; Skinner, J. L. *J. Phys. Chem. A* **1999**, *103*, 9494.
- (65) Lawrence, C. P.; Skinner, J. L. *Proc. Natl. Acad. Sci. U. S. A.* **2005**, *102*, 6720.
- (66) Gaigeot, M. P.; Vuilleumier, R.; Sprik, M.; Borgis, D. *J. Chem. Theory Comput.* **2005**, *1*, 772.
- (67) Gaigeot, M. P.; Sprik, M. *J. Phys. Chem. B* **2003**, *107*, 10344.
- (68) Press, W. H.; Teukolsky, S. A.; Vetterling, W. R.; Flannery, B. P. *Numerical Recipes in Fortran*; Cambridge University Press: Cambridge, U.K., 1992.
- (69) Gaigeot, M. P.; Martinez, M.; Vuilleumier, R. *Mol. Phys.* **2007**, *105*, 2857.
- (70) Martinez, M.; Gaigeot, M. P.; Borgis, D.; Vuilleumier, R. *J. Chem. Phys.* **2006**, *125*, 144106.
- (71) Bastida, A.; Soler, M. A.; Zúñiga, J.; Requena, A.; Kalstein, A.; Fernández-Alberti, S. *J. Chem. Phys.* **2010**, *132*, 224501.
- (72) Bastida, A.; Soler, M. A.; Zúñiga, J.; Requena, A.; Kalstein, A.; Fernández-Alberti, S. *J. Phys. Chem. A* **2010**, *114*, 11450.
- (73) Garcia-Martinez, A.; Teso-Vilar, E.; Garcia-Fraile, A.; Martinez-Ruiz, P. *J. Phys. Chem. A* **2002**, *106*, 4942.
- (74) Han, W. G.; Suhai, S. *J. Phys. Chem.* **1996**, *100*, 3942.
- (75) Du, Q.; Wei, D. *J. Phys. Chem. B* **2003**, *107*, 13463.
- (76) Rodrigo, M. M.; Tarazona, M. P.; Saiz, E. *J. Phys. Chem.* **1986**, *90*, 2236.
- (77) Meighan, R. M.; Cole, R. H. *J. Phys. Chem.* **1964**, *68*, 503.
- (78) Kubelka, J.; Keidel, T. A. *J. Phys. Chem. A* **2001**, *105*, 10922.
- (79) Mannfors, B. E.; Mirkin, N. M.; Palmo, K.; Krimm, S. *J. Phys. Chem. A* **2003**, *207*, 207.
- (80) Mirkin, N. G.; Krimm, S. *J. Phys. Chem. A* **2004**, *108*, 5438.
- (81) Palmo, K.; Krimm, S. *J. Chem. Theory Comput.* **2007**, *3*, 2120.
- (82) Palmo, K.; Mirkin, N. M.; Krimm, S. *Biopolymers*. **2003**, *68*, 383.
- (83) Lagant, P.; Nolde, D.; Stote, R.; Vergoten, G.; Karplus, M. *J. Phys. Chem. A* **2004**, *108*, 4019.
- (84) Herrebout, W. A.; Clou, K.; Desseyn, H. O. *J. Phys. Chem. A* **2001**, *105*, 4865.
- (85) Chen, X. G.; Schweitzer-Stenner, R.; Asher, S. A.; Mirkin, N. G.; Krimm, S. *J. Phys. Chem.* **1995**, *99*, 3074.
- (86) Bakker, H. J.; Skinner, J. L. *Chem. Rev.* **2010**, *110*, 1498.

Solvent Effects on the Structure and Spectroscopy of the Emitting States of 1-Phenylpyrrole

Ignacio Fdez. Galván,* M. Elena Martín, Aurora Muñoz-Losa, M. Luz Sánchez, and Manuel A. Aguilar

Química Física, Edif. José María Viguera Lobo, Universidad de Extremadura, Avda. de Elvas s/n, 06071 Badajoz, Spain

ABSTRACT: Theoretical calculations of absorption and fluorescence properties of 1-phenylpyrrole have been performed, at the CASPT2//CASCF level, in the gas phase and in acetonitrile solution, using in the latter case the ASEP/MD method. In addition to a locally excited state, it was also possible to identify a candidate intramolecular charge transfer state that could explain the second red-shifted fluorescence band that appears in polar solvents. In the gas phase, the charge transfer state is found to lie higher in energy than the locally excited state and the Franck–Condon absorption state, making it unlikely to be reached under these conditions. In acetonitrile solution, the charge transfer state is stabilized and lies much closer to the locally excited state, becoming accessible after absorption. The results indicate that the free-energy surface of the charge transfer state is very flat in solution, and several geometries are possible, ranging from almost planar to twisted and bent. Solvent caging and transition probabilities favor emission from structures with a small twist angle between the rings and without a pyramidal atom.

1. INTRODUCTION

A significant number of organic molecules combining electron donor and acceptor groups exhibit the so-called dual fluorescence in polar solvents. In nonpolar solvents, the fluorescence spectrum features a single “normal” band, which suffers only a slight shift when the solvent polarity is increased. In polar solvents, a second “anomalous” band appears in the spectrum; this second band’s position and intensity is much more affected by the solvent polarity, being strongly red-shifted and intensified (at the expense of the “normal” band) in highly polar solvents. The phenomenon of dual fluorescence has been widely studied in the literature since its discovery 50 years ago.^{1–8} It was suggested early on that the “anomalous” fluorescence band is due to the existence of an intramolecular charge transfer (ICT) state that can be stabilized in polar solvents, while in nonpolar solvents only the state responsible for the “normal” band, usually called local excitation (LE), is stable enough to be observed.

This picture is still generally accepted as a valid explanation for the dual fluorescence. However, there is a continuing controversy between different groups regarding the nature and geometry of the ICT state, the possible existence of other intermediate states, the mechanism through which the LE and ICT states are formed, and practically every other detail of the dual fluorescence phenomenon.

Perhaps the most successful models for the dual fluorescence in the prototype molecule 4-(N,N-dimethylamino)benzonitrile (DMABN) and its derivatives are the ones known as TICT (twisted ICT) and PICT (planar ICT). These models propose, respectively, a perpendicular and coplanar relative configuration of the donor and acceptor groups. Experimental evidence in favor of one model or the other is usually derived from comparison of the properties of various compounds with different geometric constraints and substituents. For example, compounds like 3,5-dimethyl-4-(N,N-dimethylamino)benzonitrile, where the dimethylamino group is forced to be twisted, display only the ICT band in fluorescence, suggesting a TICT is responsible for the

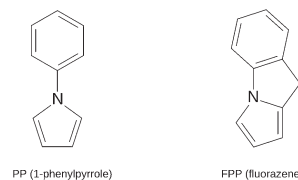


Figure 1. Two similar compounds with dual fluorescence.

band. Other compounds where the twisting is hindered (like 6-cyano-1,2,3,4-tetrahydroquinoline, NTC6) can present dual fluorescence, which points to a PICT state. These apparently conflicting conclusions probably indicate that the two models can be valid, and each particular system will favor one of them.

In recent years, a pair of closely related molecules has been studied for their dual fluorescence properties, see Figure 1. The two rings in 1-phenylpyrrole (PP) can freely rotate around the middle bond, while fluorazene (FPP) has a methylene bridge that effectively locks the rings in an almost planar conformation. Interestingly, both molecules have very similar photophysical properties, and in particular, both show dual fluorescence in polar solvents. Moreover, the planar FPP has been found to have enhanced ICT emission compared to PP (it appears in less polar solvents and has a higher quantum yield), which naturally leads to the conclusion that the PICT model applies better to these molecules.^{9,10} However, most theoretical calculations predict a twisted structure for the ICT state of PP,^{11–15} which seems unsatisfactory.

In this work, we have carried out a theoretical study on the absorption and fluorescence properties of the PP molecule, both in the gas phase and in acetonitrile solution. The electronic states of PP are described with a multiconfigurational quantum method, and we used an explicit model of atomic detail for the solvent. By examining

Received: February 18, 2011

Published: April 29, 2011

the relative energies, geometries, and emission energies of the different electronic states, we hope to cast further light on the nature of the emitting ICT state of this interesting system.

Early during this research, it became evident that we were not getting “ideal” TICT or PICT structures, and that this nomenclature would not be adequate to describe the results. Therefore, in the rest of this paper, we have avoided the use of these two terms, preferring other descriptive terms for the ICT state and its geometries.

2. METHODS AND DETAILS

Solvent effects on the PP UV/vis spectra were calculated with the ASEP/MD (Average Solvent Electrostatic Potential from Molecular Dynamics) method. This is a sequential quantum mechanics/molecular mechanics (QM/MM) method implementing the mean field approximation. It combines, alternately, a high-level quantum mechanics (QM) description of the solute with a classical molecular mechanics (MM) description of the solvent. One of its main features is the fact that the solvent effect is introduced into the solute’s wave function as an average perturbation. Details of the method have been described in previous papers,^{16–18} so here we will only present a brief outline.

As mentioned above, ASEP/MD is a method combining QM and MM techniques, with the particularity that full QM and MD (molecular dynamics) calculations are alternated and not simultaneous. During the MD simulations, the intramolecular geometry and charge distribution of all molecules, and particularly the solute, is considered fixed. From the resulting simulation data, the average electrostatic potential generated by the solvent molecules on the solute (ASEP) is obtained. This potential is introduced as a perturbation into the solute’s quantum mechanical Hamiltonian, and by solving the associated Schrödinger equation, one gets a new charge distribution for the solute, which is used in the next MD simulation. This iterative process is repeated until the electron distribution of the solute and the solvent structure around it are mutually equilibrated.

The ASEP/MD framework can also be used to optimize the geometry of the solute molecule.¹⁹ At each step of the ASEP/MD procedure, the gradient and Hessian on the system’s free-energy surface (including the van der Waals contribution) can be obtained, and thus they can be used to search for stationary points on this surface by some optimization method. In the computation of the gradient and Hessian, the free-energy gradient method²⁰ is used, with the incorporation of the mean field approximation to reduce the number of quantum calculations needed. In this way, after each MD simulation, the solute geometry is optimized within the fixed “average” solvent structure by using the free-energy derivatives. In the next MD simulation, the new solute geometry and charge distribution are used. This approach allows the optimization of the solute geometry in parallel with the solvent structure.

For calculating transition energies, the iterative process is performed on the initial state of the transition (the ground state for absorption, the excited state for emission); i.e., the atomic charges for the MD and the energy derivatives for the geometry optimization of the solute are calculated with the initial state’s wave function. Then, with a frozen solvent model, the transition energies between the different states are obtained.

Once the different solute electronic states and the solvent structure around them have been optimized and equilibrated, the free energy differences between those states can be calculated,

within the ASEP/MD framework, making use of the free energy perturbation method.^{21,22} The expression we use to calculate the free energy difference between two species in equilibrium in solution, ΔG , is

$$\Delta G = \Delta E + \Delta G_{\text{int}} + \Delta V \quad (1)$$

where ΔE is the difference in the internal quantum energy of the solute between the two species, ΔG_{int} is the difference in the solute–solvent interaction energy, which is calculated classically with the free energy perturbation method, and ΔV is a term that includes the difference in the zero-point energy (ZPE) and entropic contributions of the solute. The last term, ΔV , is normally evaluated by applying the harmonic approximation to the vibrational modes of the solute in solution, and it needs the information provided by the Hessian matrix. In this work, obtaining an accurate enough Hessian matrix required computational resources that were too large, and we decided to approximate the results by neglecting this term. It must be noted that this ΔV term refers only to the internal nuclear degrees of freedom of the solute; free energy contributions from the solvent around the solute are properly accounted for in the ΔG_{int} term.

2.1. Computational Details. The quantum calculations on the solute molecule were done with the complete active space self-consistent field (CASSCF) method,²³ using the 6-31G* basis set. In some cases, single-point calculations with the cc-pVTZ basis set were also performed. The active orbitals were the six π and π^* orbitals of the phenyl ring, plus the five π and π^* orbitals of the pyrrole ring, and 12 electrons were included in these orbitals, for a (12,11) total active space. All calculations were performed using a state-average (SA) of the first five singlet states, with equal weights. It is known that, in order to obtain accurate transition energies, it is necessary to include the dynamic electron correlation in the quantum calculations, which we did with the complete active space second order perturbation (CASPT2) method,^{24,25} using the SA(5)-CASSCF(12,11) wave functions as a reference. An IPEA-shifted (ionization potential–electron affinity) zeroth-order Hamiltonian has been proposed for CASPT2 calculations,²⁶ which is supposed to reduce systematic overestabilization errors in open-shell systems (as is the case of the excited states studied here). We did all CASPT2 with the proposed IPEA shift of $0.25 E_h$ (CASPT2(0.25)) as well as with no IPEA shift (CASPT2(0.00)). To minimize the appearance of intruder states, an additional imaginary shift of $0.1 i E_h$ was used. No symmetry was imposed or assumed in any case.

The MD simulations were carried out with rigid molecules, with acetonitrile (CH₃CN) as a solvent. Lennard-Jones parameters and solvent atomic charges were taken from the OPLS-AA (Optimized Potentials for Liquid Simulations, all atoms) force field,²⁷ solute atomic charges were computed from the quantum calculations through a least-squares fit to the electrostatic potential obtained at the points where the solvent charges are located. The geometry of acetonitrile was optimized with the Becke’s three-parameter Lee–Yang–Parr density functional (B3LYP) and the 6-311G** basis set. A total of 375 CH₃CN molecules and the solute were included at the experimental solvent density (779.3 kg/m³). Periodic boundary conditions were applied, and spherical cutoffs were used to truncate the interatomic interactions at 12.75 Å. Long-range interactions were calculated using the Ewald sum technique. The temperature was fixed at 298.15 K by using the Nosé–Hoover thermostat. A time step of 0.5 fs was

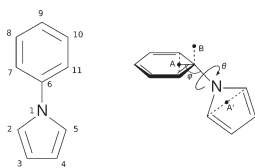


Figure 2. Atom numbering of the PP molecule and illustration of the two angles ϕ and θ .

Table 1. Definition of Geometric Parameters for the PP Molecule^a

$$\begin{aligned} \overline{\text{Ph}} &= 1/6(d(\text{C}_6\text{C}_7) + d(\text{C}_7\text{C}_8) + d(\text{C}_8\text{C}_9) + d(\text{C}_9\text{C}_{10}) + d(\text{C}_{10}\text{C}_{11}) \\ &\quad + d(\text{C}_{11}\text{C}_6)) \\ \overline{\text{Py}} &= 1/5(d(\text{N}_1\text{C}_2) + d(\text{C}_2\text{C}_3) + d(\text{C}_3\text{C}_4) + d(\text{C}_4\text{C}_5) + d(\text{C}_5\text{N}_1)) \\ Q(\text{Ph}) &= 1/4(d(\text{C}_6\text{C}_7) + d(\text{C}_8\text{C}_9) + d(\text{C}_9\text{C}_{10}) + d(\text{C}_{11}\text{C}_6) \\ &\quad - 1/2(d(\text{C}_7\text{C}_8) + d(\text{C}_{10}\text{C}_{11}))) \\ Q(\text{Py}) &= 1/3(d(\text{N}_1\text{C}_2) + d(\text{C}_3\text{C}_4) + d(\text{C}_5\text{N}_1)) - 1/2(d(\text{C}_2\text{C}_3) \\ &\quad + d(\text{C}_4\text{C}_5)) \\ \text{Ph-Py} &= d(\text{N}_1\text{C}_6) \\ \phi &= a(\text{AC}_6\text{N}_1) \\ \psi &= a(\text{C}_6\text{N}_1\text{A}') \\ \theta &= D(\text{BC}_6\text{N}_1\text{B}') \end{aligned}$$

^a d is a bond length, a a bond angle, and D a dihedral angle. Point A is the midpoint between C_7 and C_{11} ; point B is 1 Å away from C_6 , in the normal direction of the $\text{C}_6\text{C}_7\text{C}_{11}$ plane. Points A' and B' are equivalent for the pyrrole ring. The angle ψ is always very close to 180°.

used during the simulations; each of them was run for 50 ps after 25 ps of equilibration.

At each step of the ASEP/MD procedure, 500 configurations evenly distributed from the MD run were used to calculate the ASEP. The charges from each solvent molecule were kept explicitly whenever the molecule's center of mass was closer than $9 a_0$ to any solute nucleus; the effect of the farther molecules was included in an additional shell of fitted charges. Each ASEP/MD run was continued until the energies and solute geometry and charges were stabilized for at least five iterations; results are reported as the average of these last five iterations, being an effective average of 250 ps dynamics.

For in solution calculations, a development version of the ASEP/MD software¹⁷ was used. All quantum calculations were performed with Molcas 6.4 and Molcas 7.4.²⁸ All MD simulations were performed using Moldy.²⁹ The electrostatic potential generated by the solute was calculated with Molden.³⁰

3. RESULTS AND DISCUSSION

3.1. Gas Phase. *3.1.1. Optimized Geometries.* The PP geometry was optimized in the gas phase at the SA(5)-CASSCF-(12,11)/6-31G* level for the electronic ground state and different excited states. For comparing and describing the structures, we use some geometric parameters, such as the average bond length of the phenyl ring ($\overline{\text{Ph}}$), the average bond length of the pyrrole ring ($\overline{\text{Py}}$), the phenyl–pyrrole bond length (Ph–Py), or the phenyl–pyrrole twist angle (θ). See Figure 2 and Table 1 for the atom numbering and parameter definitions.

The optimized ground state (GS) structure features the usual aromatic bond lengths in benzene and pyrrole ($\overline{\text{Ph}} = 1.397$ Å, $\overline{\text{Py}} = 1.385$ Å) and a similar Ph–Py length of 1.400 Å. The N_1 – C_6 bond is coplanar with both rings, and the twist angle θ takes a

value of 29.7°. Similar geometries are found in the literature for theoretical calculations,^{11–13,15,31,32} the θ angle ranging from 28° with AM1 to 42.7° with CASSCF(12,11)/6-31G*. The experimental determination of the twist angle in the gas phase yielded values of 32°³³ and 38.7°.³⁴ The pyrrole moiety is more electron-withdrawing than the phenyl, resulting in a slightly polarized electron density for the PP molecule, with a small global dipole moment of 1.48D.

At the ground state geometry, the first excited state corresponds to a $\pi \rightarrow \pi^*$ transition in the phenyl ring. When the geometry is optimized for this state, the LE (local excitation) geometry is reached. The rings in this geometry are also linear and slightly twisted. Ph–Py is shorter than for the GS (1.385 Å), and the θ angle is smaller too (20.9°). Reflecting the local excitation character of the state, $\overline{\text{Ph}}$ increases significantly to 1.432 Å. These features agree with other theoretical calculations, where the θ angle ranges from 1.95° with CIS/6-31+G** to 29.5° with CASSCF(12,11)/6-31G*,^{15,32} although Zilberg and Haas reported a planar structure with $\theta = 0.0^\circ$.¹³ The experimental data indicate that the optimum angle is 19.8°, but the rotation barrier is on the order of 0.3 kcal/mol.³⁴ The electron distribution in this state is similar to that of the ground state, and the dipole moment decreases to 0.40D.

In the higher excited states at the GS geometry, there is an intramolecular charge transfer. The electron density polarization is inverted with respect to the ground state, and the negative charge is displaced toward the phenyl ring (see below, in section 3.1.2), which we indicate in the tables with a negative sign in the dipole moment. When the geometry of a charge transfer state is optimized in the gas phase, at least two different structures can be found. The lowest energy structure we could get has a pyramidalized C_6 atom, which is also slightly out of the main phenyl plane. The angle ϕ , which measures this pyramidalization of C_6 , is 134.3°, while the twist angle θ is almost 90°. The deformation of the two rings is measured by their “quinoidality”, defined in Table 1 as $Q(\text{Ph})$ and $Q(\text{Py})$, indicating the extent to which the C_7 – C_8 and C_{10} – C_{11} bonds are shorter (or longer, for negative Q) than the other bonds in the phenyl ring, and similarly for the pyrrole. In this case, $Q(\text{Ph})$ is 0.050 Å and $Q(\text{Py})$ is -0.085 Å, meaning that the C_7 – C_8 and C_{10} – C_{11} bonds become shorter while the C_2 – C_3 and C_4 – C_5 bonds become longer. The Ph–Py bond is longer than for the GS structure, 1.486 Å. At this geometry, the charge transfer state is the first excited singlet, S_1 , and has a dipole moment of 8.21D. This bent twisted structure, which we will denote with PQ (perpendicular quinoidal), is also reported by Xu et al.,¹⁵ and is found as well in calculations for the DMABN molecule.^{35,36}

In the other structure, we find for the ICT state, the two rings remain almost linear, with a ϕ angle close to 180°, and the twist angle θ , instead of becoming perpendicular, decreases from the GS structure to 16.1°. In general, this structure, which we will call LQ (linear quinoidal), is similar to the GS and LE structures, with a shorter Ph–Py length (1.373 Å) and quinoidal and antiquinoidal phenyl and pyrrole rings, respectively ($Q(\text{Ph}) = 0.074$ Å, $Q(\text{Py}) = -0.093$ Å). At this geometry, the ICT state is not the first but the second excited state, S_2 (although very close to S_1), and its dipole moment is lower than for the PQ, 4.67D, but in the same direction. A similar structure is reported by Zilberg and Haas,¹³ although they use planar symmetry and give a very low dipole moment for it, 0.75D; this smaller value may be due to the presence of the S_1 state very close in energy, and to a different

Table 2. Geometrical Parameters and Dipole Moments of the Different Optimized Structures of PP in the Gas Phase^a

	GS (S_0)	LE (S_1)	PQ (S_1)	LQ (S_2)
$\overline{\text{Ph}}$ (Å)	1.397	1.432	1.417	1.420
$\overline{\text{Py}}$ (Å)	1.385	1.387	1.389	1.405
$Q(\text{Ph})$ (Å)	0.004	-0.003	0.050	0.074
$Q(\text{Py})$ (Å)	0.025	0.035	-0.085	-0.093
Ph-Py (Å)	1.400	1.385	1.486	1.373
$180 - \phi$ (Å)	0.0	0.0	45.7	3.1
θ (deg)	29.7	20.9	89.6	16.1
μ (D)	1.48	0.40	-8.21	-4.67

^aGeometries optimized at the SA-CASSCF level, dipoles calculated at the CASPT2(0.25) level. The negative sign in the dipole indicates the negative charge is displaced towards the phenyl ring.

Table 3. Vertical Absorption Energies (in eV), Dipole Moments (in D), and Oscillator Strengths for the PP Molecule in Gas Phase at the GS Geometry^a

	vertical energies			μ	f
	CASSCF	CASPT2(0.25)	CASPT2(0.00) exp. ³⁹		
S_0				1.48	
S_1	4.77	4.85	4.51	0.59	0.004
S_2	6.04	5.48	5.03	-3.43	0.436
S_3	6.13	5.84	5.53	-7.15	0.012
S_4	6.61	6.20	5.92	-10.09	0.037

^aDipole moments and oscillator strengths calculated at the CASPT2(0.25) level. The negative sign in the dipole indicates the negative charge is displaced towards the phenyl ring.

state-averaging in their calculations. A summary of the different structures optimized in the gas phase is provided in Table 2.

Other authors have reported antiquinoidal structures for a charge transfer state,^{13,14,37} where the C_7-C_8 and $C_{10}-C_{11}$ bonds are longer than other phenyl ring bonds, and therefore $Q(\text{Ph})$ is negative. We have, however, been unable to obtain such structures, all trials reverting to one of the quinoidal or LE geometries.

3.1.2. Absorption. The vertical absorption properties of PP at the optimized ground state geometry are summarized in Table 3. We report the CASSCF transition energies for comparison, but it is known that only transition energies calculated with dynamic electron correlation are reliable. Therefore, we will only discuss CASPT2 energies in the rest of the article. By comparing the CASPT2(0.25) and CASPT2(0.00) columns, it is ascertained that the former values are always 0.3–0.4 eV larger; this difference has been found in previous works.^{35,38} Other properties like dipole moments or oscillator strengths are much more similar between the two CASPT2 variants, and only CASPT2(0.25) values are reported. Of the four transitions studied, only $S_0 \rightarrow S_2$ has a relatively large oscillator strength and is therefore predicted to be the active transition in the absorption spectrum. The experimental spectrum shows a broad band at 5.03 eV,³⁹ and in some solvents a weak shoulder appears in the red end, indicating the presence of a hidden band. Thus, the experimental absorption can be safely assigned to the $S_0 \rightarrow S_2$ transition.

As previously found, the CASPT2(0.00) values with the 6-31G* basis set tend to agree very well with the experiment,

Table 4. Same as Table 3, with the cc-pVTZ//6-31G* Basis Set

	vertical energies			μ	f
	CASSCF	CASPT2(0.25)	CASPT2(0.00)		
S_0				1.50	
S_1	4.72	4.71	4.28	0.42	0.004
S_2	5.89	5.20	4.71	-3.83	0.449
S_3	5.96	5.57	5.21	-7.41	0.012
S_4	6.37	5.85	5.49	-10.08	0.061

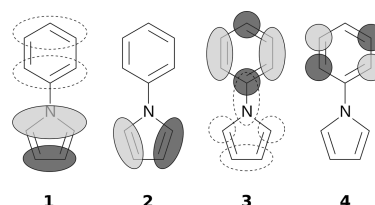


Figure 3. Main active molecular π orbitals of PP (simplified). Dashed contributions appear in more planar structures (lower θ). In the dominant ground state configuration, orbitals 1 and 2 are doubly occupied, while 3 and 4 are empty ($1^2 2^2 3^0 4^0$).

while CASPT2(0.25) values are overestimated. This has been attributed to an error cancellation in the case of CASPT2(0.00), since in general, when increasing the basis set quality, transition energies decrease, and then, with larger basis sets, the CASPT2(0.25) results are closer to experimental results and CASPT2(0.00) results are underestimated. This can be confirmed in Table 4, where we show the results of calculations performed with the cc-pVTZ basis set on the same geometries obtained with 6-31G*. Other authors have also found that CASPT2(0.25) results are more robust and in better agreement with other comparable methods.⁴⁰ In view of these facts, we will generally report CASPT2(0.25) values, bearing in mind that transition energies are probably overestimated by around 0.4 eV due to the limited basis set employed. One should also be cautious when comparing with CASPT2 results reported in the bibliography, for many of them use the CASPT2(0.00) or similar variant.

When the electron configurations of the states are examined, it is clear that states S_3 and S_4 correspond mainly to single excitations from the pyrrole to the phenyl ring. In terms of the simplified molecular orbitals pictured in Figure 3, S_3 is a $2 \rightarrow 3$ transition, and S_4 is $2 \rightarrow 4$. S_1 has a significant contribution from other orbitals, resulting in a $\pi \rightarrow \pi^*$ transition local to the phenyl ring, while S_2 has the larger contribution from $1 \rightarrow 3$, but there is significant mixture of other transitions. It is interesting to note that, although the absorption to the S_2 state is the active one and this state has an evident charge transfer character, the optimized ICT structures detailed above (PQ and LQ) correspond to the electron configuration of S_3 ($2 \rightarrow 3$), as suggested by the values of $Q(\text{Ph})$ and $Q(\text{Py})$.

The energies and electron configurations of the states at the GS geometry are in good agreement with previous calculations by other groups,^{11,12,14,15} although the DFT/MRCI method gives relatively lower energies for the S_3 and S_4 states.

3.1.3. Fluorescence. Experimentally, a single fluorescence band, assigned to the LE state, is observed in the gas phase or

Table 5. Vertical Emission Energies (Transitions to S_0 , in eV), Dipole Moments (in D), and Oscillator Strengths for the PP Molecule in the Gas Phase^a

	vertical energies		μ	f	ΔE
	CASPT2(0.25)	CASPT2(0.00)			
LE (S_1)	4.45	4.12	0.40	0.005	4.67
PQ (S_1)	3.80	3.55	-8.21	0.001	5.12
LQ (S_2)	4.71	4.41	-4.67	0.011	5.42

^a ΔE is the relative energy (in eV) with respect to S_0 at the ground state minimum, GS. Dipole moments, oscillator strengths, and ΔE calculated at the CASPT2(0.25) level. The negative sign in the dipole indicates the negative charge is displaced towards the phenyl ring.

nonpolar solvents,^{10,34,39,41,42} with a maximum at around 4.10–4.15 eV. In Table 5, we have summarized the calculated emission properties from the three excited-state structures obtained. The predicted LE fluorescence agrees very well with the experimental value, as does the Stokes shift, and the low oscillator strength is in accord with the findings of Belau et al.,⁴³ who conclude that the observed fluorescence occurs from a state different from that populated at excitation. The two charge transfer geometries have very different fluorescence properties: emission from the charge transfer state in PQ is around 0.9 eV lower in energy than in LQ, and its oscillator strength is significantly weaker. The ΔE values indicate that, while all three states are below the Franck–Condon absorption to S_2 (5.48 eV, see Table 3), only LE has a lower energy than S_1 at the GS structure (4.85 eV). This may explain why a single fluorescence band, corresponding to LE, is observed in the gas phase. The ΔE value for the LE structure, 4.67 eV, can be compared with the experimental 0–0 transition which is found at around 4.40 eV.³⁴ A scheme of the relative energies of the states at the different geometries is presented in Figure 4.

As happened in the case of absorption, calculations with the cc-pVTZ basis set yield lower transition energies by around 0.2 eV and make the CASPT2(0.00) values underestimated with respect to the experimental results. For comparison, cc-pVTZ result are given in Table 6.

3.2. Acetonitrile Solution. **3.2.1. Optimized Geometries.** The same structures obtained in the gas phase for the PP molecule were also optimized in acetonitrile solution, using the ASEP/MD method^{16–18} to model the solvation. The resulting geometries are given in Table 7. In the case of the LQ structure, it was not found to be a minimum but yielded the BQ structure when fully optimized (see below). The reported LQ geometry in solution corresponds to an optimization with the $C_8-C_7-C_6-N_1$ and $C_{10}-C_{11}-C_6-N_1$ dihedrals fixed to the ground state geometry values (an unconstrained optimization from the Franck–Condon point proceeds first to LQ and then to BQ).

The GS and LE geometries are hardly affected by the solvent, and only a small increase in the dipole moment is observed. The charge transfer structures PQ and LQ, as expected, suffer more significant changes. The ϕ angle in PQ becomes more linear, and the θ angle in LQ becomes more planar. The bond lengths are more similar between both structures than in the gas phase. The dipole moments are also quite similar and greatly enhanced from the gas phase values. These findings are in agreement with results obtained with the PCM method.⁵

In solution, we found another optimized structure for a charge transfer state, characterized by pyramidal C_6 , like PQ, but with a

Table 6. Same as Table 5, with the cc-pVTZ//6-31G* Basis Set

	vertical energies			f	ΔE
	CASPT2(0.25)	CASPT2(0.00)			
LE (S_1)	4.32	3.90		0.005	4.56
PQ (S_1)	3.64	3.34		0.001	5.04
LQ (S_2)	4.52 ^a	4.15		0.010	5.22

^a At this level, the charge transfer state is S_1 .

Table 7. Geometrical Parameters and Dipole Moments of the Different Optimized Structures of PP in Acetonitrile Solution^a

	GS (S_0)	LE (S_1)	PQ (S_1)	LQ (S_1) ^b	BQ (S_1)
$\overline{\text{Ph}}$ (Å)	1.397	1.432	1.415	1.415	1.415
$\overline{\text{Py}}$ (Å)	1.385	1.387	1.388	1.393	1.391
Q(Ph) (Å)	0.004	-0.003	0.056	0.063	0.061
Q(Py) (Å)	0.023	0.034	-0.092	-0.095	-0.096
Ph-Py (Å)	1.404	1.386	1.468	1.417	1.446
$180 - \phi$ (°)	0.1	0.1	36.5	1.3	32.0
θ (°)	29.4	19.0	87.0	32.7	41.7
μ (D)	1.96	0.56	-11.92	-10.79	-10.91

^a Geometries optimized at the SA-CASSCF level; dipoles calculated at CASPT2(0.25) level. The negative sign in the dipole indicates the negative charge is displaced towards the phenyl ring. ^b Not a fully optimized minimum, see the text.

nonperpendicular θ ; this structure will be called BQ (bent quinoidal). In Table 7, it can be seen that the bond lengths and dipole moment are rather similar to PQ and LQ. The optimized charge transfer state in all three quinoidal structures obtained (PQ, LQ, and BQ) is dominated by the single excitation $2 \rightarrow 3$ (see Figure 3), suggesting that they belong to the same electronic energy surface. As in the gas phase calculations, we could not obtain an optimized geometry of antiquinoidal (negative Q(Ph)) character.

3.2.2. Absorption. The results for ground state absorption properties of PP in CH_3CN are summarized in Table 8. The values obtained are very similar to those in the gas phase, with a small blue shift in the transition energies. The dipole moments of the S_0 and S_1 states are slightly increased, while the dipoles decrease for the other states due to their opposite direction. The calculated solvatochromic shift, 0.07 eV, contrasts with the experimental shift, -0.12 eV. A similar discrepancy was found in DMA (N,N-dimethylaniline) and DMABN,^{35,38} and we attribute it to the neglect of the dispersion component in the electron transition energies. The dispersion component is expected to be quite uniform among solvents of similar refractive indexes, such as hexane ($n = 1.375$) and acetonitrile ($n = 1.342$). By comparing the transition energies in the gas phase (5.03 eV) and in hexane (4.87 eV),¹⁰ we can get an estimation for the dispersion contribution to the solvatochromic shift. If this estimation (-0.16 eV) is added to the calculated gas–acetonitrile shift, an almost perfect agreement with experimental results is obtained. Otherwise, the blue shift in a vertical transition can be expected, in view of the opposite direction of the dipole moments in the S_0 and S_2 states.

3.2.3. Fluorescence. The calculated emission energies from the different optimized excited states in solution are shown in Table 9.

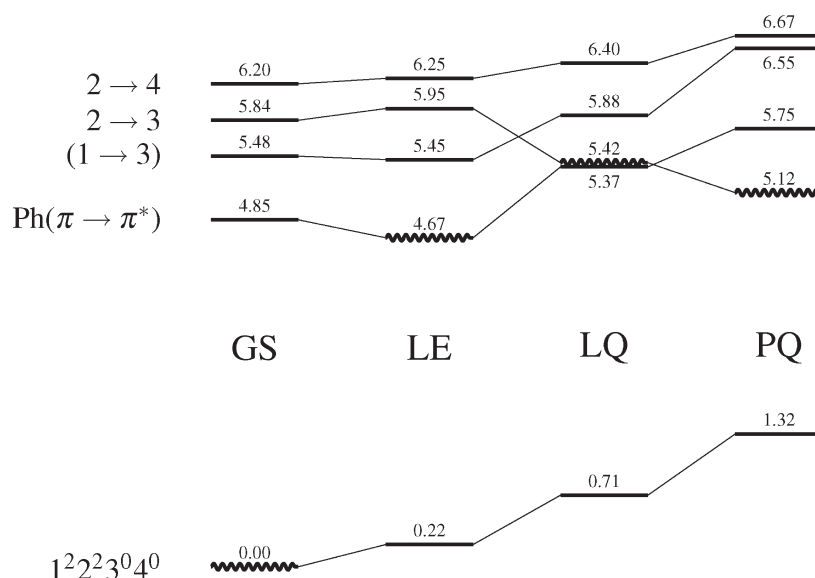


Figure 4. Relative energies (CASPT2(0.25), in eV) of the calculated electronic states of PP in the gas phase at the optimized geometries. The state for which each geometry is optimized is drawn as a wavy line. States of equivalent electron configuration are joined by lines. For the nature of the different states, labeled on the left, refer to Table 3, Figure 3, and the corresponding text.

Table 8. Vertical Absorption Energies (in eV), Dipole Moments (in D), and Oscillator Strengths for the PP Molecule in Acetonitrile at the GS Geometry^a

	vertical energies		μ	f
	CASPT2(0.25)	exp. ¹⁰		
S_0			1.96	
S_1	4.89		1.22	0.003
S_2	5.55	4.91	-2.41	0.413
S_3	5.96		-6.26	0.014
S_4	6.38		-9.48	0.037

^aThe negative sign in the dipole indicates the negative charge is displaced towards the phenyl ring.

As with the absorption, there is very little change in the emission at the LE geometry, something that is also observed experimentally for the LE band (4.05 eV in CH_3CN ,¹⁰ 4.10 eV in the gas phase).

The most interesting results are obtained by comparing the emissions from the ICT structures. There is a large variation in the transition energies for PQ, LQ, and BQ, of almost 1 eV, and the oscillator strength ranges from practically zero (less than 3×10^{-5}) to approximately the same value as for the LE emission, both quantities increasing in the order $\text{PQ} < \text{BQ} < \text{LQ}$. The band maximum for the experimentally observed CT band in acetonitrile is located at 3.48 eV; this would agree (considering the overestimation of the transition energies with CASPT2(0.25) already discussed) with the LQ emission, the emissions for PQ and BQ being too low.

The relative free energy of the states at their respective structures is listed in the ΔG column. A scheme of the energies of the first five states for each structure is shown in Figure 5. The three ICT structures have a similar energy, well below S_2 at GS and comparable to S_1 , and are therefore accessible from the initial excitation of the molecule; they are also very close to the energy of the fluorescing LE state.

Table 9. Vertical Emission Energies (Transitions to S_0 , in eV), Dipole Moments (in D), and Oscillator Strengths for the PP Molecule in Acetonitrile^a

	vertical energies			ΔG
	CASPT2(0.25)	μ	f	
LE (S_1)	4.47	0.56	0.005	4.68
PQ (S_1)	3.02	-11.92	0.000	4.86
LQ (S_1)	3.95	-10.79	0.004	5.03
BQ (S_1)	3.31	-10.91	0.002	4.86

^a ΔG is the relative free energy (in eV) with respect to S_0 at the ground state minimum, GS. The negative sign in the dipole indicates the negative charge is displaced towards the phenyl ring.

The almost constant energy from LQ to BQ and PQ indicates that the free energy surface is probably very flat between these structures, and fluorescence would be more likely wherever the oscillator strength for the $S_1 \rightarrow S_0$ transition is larger. This would favor emission at LQ and BQ, while the PQ geometry, although energetically available, would give rise to almost no fluorescence.

Druzhinin et al.¹⁰ have estimated some thermodynamic quantities for the PP system from the fluorescence properties; in particular, they conclude the free energy difference between the emitting LE and ICT states is lower than 1 kcal/mol in acetonitrile at room temperature. Our results yield an ICT state about 4 kcal/mol (0.18 eV) higher in energy than the LE state; considering the errors, approximations and assumptions in the experiments, interpretations, and calculations, there is qualitative agreement with the recent experimental findings.

It is interesting that the best accord with the experimental fluorescence is obtained for the LQ structure, which is not a true minimum in our calculations. This could be due to a limitation in the calculation level used in this work, and it is possible that by including a more complete description in the quantum calculations a true minimum with lower relative energy would be

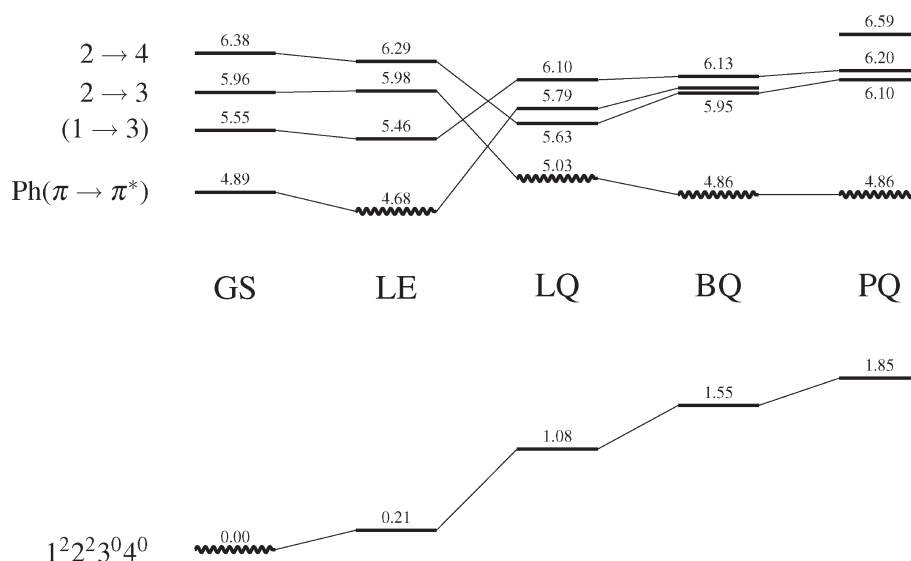


Figure 5. Relative free energies (CASPT2(0.25), in eV) of the calculated electronic states of PP in acetonitrile solution at the optimized geometries. The state for which each geometry is optimized is marked as a wavy line; this is also the state with which the solvent is in equilibrium. States of equivalent electron configuration are joined by lines. For the nature of the different states, labeled on the left, refer to Table 8 and Figure 3.

obtained. On the other hand, the experimental fluorescence band maximum need not correspond to a minimum in the excited state surface, and other elements such as the system's dynamics and the Franck–Condon factors should be included. Some of these considerations favor the fluorescence at an LQ-like structure. First, as pointed out above, the oscillator strength for the electron transition is higher at LQ than at BQ or PQ. Also, the overall molecular shape in LQ is more similar to GS and LE; this means that the structure can be reached with less important solvent reorganization around the solute, while for reaching BQ or PQ more significant solvent changes are needed.

To investigate this suggestion, we optimized the ICT state keeping the solvent frozen in equilibrium with the ground state. The result was a geometry practically identical to LQ in the gas phase, and the transition energy was very similar as well (4.80 eV). It indicates, nevertheless, that the frozen solvent does not pose significant electrostatic or steric impediments to the solute's attaining a geometry close to LQ. When afterward the solvent geometry is relaxed and the solute and solvent are mutually equilibrated, as we mentioned above, the solute geometry proceeds by first keeping the ϕ angle around 180° , and only later is the molecule bent.

In another calculation, the solute geometry was fixed at GS, and the solvent was equilibrated with the active absorption state (identified by its large oscillator strength, initially S_2). In this situation, S_0 and S_1 are destabilized by 0.33 eV and 0.20 eV, respectively, while S_3 and S_4 are stabilized by 0.36 eV and 0.61 eV. This is expected given the orientation and magnitude of the dipole moments of the states. The result is that the S_2 and S_3 states become almost degenerate, but the S_1 state still corresponds to a local excitation.

Considering the above two calculations together, it can be concluded that the solvent's direct influence alone is not sufficient to stabilize the ICT state below the LE one, and a change in the solute geometry is needed. This change, however, is not necessarily a twist of the two rings (θ angle), the modification of the rings' bond lengths, combined with the solvent equilibration, being enough to ensure the ICT state becomes the first excited state, S_1 .

Xu et al.,¹⁵ in a theoretical study of PP and FPP with a similar computational level to the present work, but using the PCM solvent model, arrived to different conclusions. They report, as we do, a considerably flat energy surface for the ICT state. On this surface, they locate a minimum ICT structure comparable to our PQ and two other structures with linear ϕ angle, planar and twisted (PICT and TICT), with θ equal to 0° and 90° , respectively (these two with symmetry constraints). The solvatochromic shift they obtain with PCM for PQ is about half of what we get (0.30 eV vs 0.78 eV), which may be due to the absence of specific interactions in PCM, or to the different active space used in both calculations. The lower solvent shift in their calculations led Xu et al. to discard the linear structures as responsible for the observed “anomalous” band and to accept the PQ structure as the source of the band, in spite of its fluorescence energy being underestimated and the computed oscillator strength being very small.

4. CONCLUSIONS

We have studied the ground and excited singlet states of 1-phenylpyrrole in the gas phase and in acetonitrile solution, using a high-level quantum method for the electronic structure and an explicit MM model for the solvent. The optimized ground state, GS, and locally excited state, LE, structures provide good agreement with the observed absorption bands and the higher-energy fluorescence band. These states have very low dipole moments and are very weakly affected by the solvent; consequently, the absorption and emission properties show little change between the gas phase and solution.

The case is different for the internal charge transfer state, ICT. We could optimize different geometries for an ICT state, all of them belonging apparently to the same electronic surface (corresponding to a $2 \rightarrow 3$ single excitation, see Figure 3) and featuring a quinoidal deformation in the phenyl ring. In gas phase, the lowest-energy structure has perpendicular rings and a pyramidal C_6 atom, and another minimum was found for a structure more similar to GS, with a small θ angle and a linear ϕ

angle. Both ICT structures are significantly higher in energy than the LE minimum and higher than the Franck–Condon point on absorption too, explaining why no fluorescence from this state is observed in the gas phase.

In acetonitrile solution, the ICT state is stabilized, and its energy becomes similar to the LE minimum. The free energy surface seems very flat from the LQ (linear) to the PQ (perpendicular and bent) structure, which makes emission possible from any point of the path. In this direction of geometry change, the emission energy decreases, but so does the oscillator strength, which gives a measure of the probability of transition. Thus, fluorescence is more likely in earlier structures, closer to LQ, where the solute molecule remains linear and with a low twist, and without requiring a large reorganization of the solvent.

Our proposal for the dual fluorescence in 1-phenylpyrrole is therefore that there are several ICT geometries accessible in polar solvents. The twist between the two rings is not necessary to stabilize the ICT state; the needed changes are the quinoidal deformation of the phenyl and the solvent equilibration with the charge transfer state. The fact that ICT fluorescence is more likely in geometries near LQ can explain why this fluorescence is relatively more intense in the planar and rigidized fluorazene: part of the ICT population of PP can change the geometry and relax through other paths, something that cannot happen in fluorazene.

AUTHOR INFORMATION

Corresponding Author

*E-mail: jellby@unex.es.

ACKNOWLEDGMENT

This work was supported by the CTQ2008-06224/BQU Project from the Ministerio de Ciencia e Innovación of Spain and the PRI08A056 Project from the Consejería de Economía, Comercio e Innovación of the Junta de Extremadura. I.F.G. acknowledges the Junta de Extremadura and the European Social Fund for financial support; A.M.-L. acknowledges financial support from the Juan de la Cierva subprogramme of the Ministerio de Ciencia e Innovación of Spain. The authors also thank the Fundación Computación y Tecnologías Avanzadas de Extremadura (COMPUTAEX) for additional computational resources.

REFERENCES

- (1) Lippert, E.; Lüder, W.; Moll, F.; Nägele, W.; Boos, H.; Prigge, H.; Seibold-Blankenstein, I. *Angew. Chem.* **1961**, *73*, 695–706.
- (2) Grabowski, Z. R.; Rotkiewicz, K.; Rettig, W. *Chem. Rev.* **2003**, *103*, 3899–4032.
- (3) Kato, S.; Amatatsu, Y. *J. Chem. Phys.* **1990**, *92*, 7241–7257.
- (4) Hayashi, S.; Ando, K.; Kato, S. *J. Phys. Chem.* **1995**, *99*, 955–964.
- (5) Serrano-Andrés, L.; Merchán, M.; Roos, B. O.; Lindh, R. *J. Am. Chem. Soc.* **1995**, *117*, 3189–3204.
- (6) Sudholt, W.; Arnulf Staib, A. L. S.; Domcke, W. *Phys. Chem. Chem. Phys.* **2000**, *2*, 4341–4353.
- (7) Mennucci, B.; Toniolo, A.; Tomasi, J. *J. Am. Chem. Soc.* **2000**, *122*, 10621–10630.
- (8) Minezawa, N.; Kato, S. *J. Phys. Chem. A* **2005**, *109*, 5445–5453.
- (9) Yoshihara, T.; Druzhinin, S. I.; Zachariasse, K. A. *J. Am. Chem. Soc.* **2004**, *126*, 8535–8539.
- (10) Druzhinin, S. I.; Kovalenko, S. A.; Senyushkina, T. A.; Demeter, A.; Zachariasse, K. A. *J. Phys. Chem. A* **2010**, *114*, 1621–1632.

- (11) Parusel, A. B. *J. Phys. Chem. Chem. Phys.* **2000**, *2*, 5545–5552.
- (12) Proppe, B.; Merchán, M.; Serrano-Andrés, L. *J. Phys. Chem. A* **2000**, *104*, 1608–1616.
- (13) Zilberg, S.; Haas, Y. *J. Phys. Chem. A* **2002**, *106*, 1–11.
- (14) Schweke, D.; Baumgarten, H.; Haas, Y.; Rettig, W.; Dick, B. *J. Phys. Chem. A* **2005**, *109*, 576–585.
- (15) Xu, X.; Cao, Z.; Zhang, Q. *J. Phys. Chem. A* **2006**, *110*, 1740–1748.
- (16) Sánchez, M. L.; Aguilar, M. A.; Olivares del Valle, F. J. *J. Comput. Chem.* **1997**, *18*, 313–322.
- (17) Fdez. Galván, I.; Sánchez, M. L.; Martín, M. E.; Olivares del Valle, F. J.; Aguilar, M. A. *Comput. Phys. Commun.* **2003**, *155*, 244–259.
- (18) Aguilar, M. A.; Sánchez, M. L.; Martín, M. E.; Fdez. Galván, I. An Effective Hamiltonian Method from Simulations: ASEP/MD. In *Continuum Solvation Models in Chemical Physics*, 1st ed.; Mennucci, B., Cammi, R., Eds.; Wiley: New York, 2007; Chapter 4.5, pp 580–592.
- (19) Fdez. Galván, I.; Sánchez, M. L.; Martín, M. E.; Olivares del Valle, F. J.; Aguilar, M. A. *J. Chem. Phys.* **2003**, *118*, 255–263.
- (20) Okuyama-Yoshida, N.; Nagaoka, M.; Yamabe, T. *Int. J. Quantum Chem.* **1998**, *70*, 95–103.
- (21) Zwanzig, R. W. *J. Chem. Phys.* **1954**, *22*, 1420–1426.
- (22) Fdez. Galván, I.; Aguilar, M. A.; Ruiz-López, M. F. *J. Phys. Chem. B* **2005**, *109*, 23024–23030.
- (23) Roos, B. O.; Taylor, P. R.; Siegbahn, P. E. M. *Chem. Phys.* **1980**, *48*, 157–173.
- (24) Andersson, K.; Malmqvist, P.-Å.; Roos, B. O.; Sadlej, A. J.; Wolinski, K. *J. Phys. Chem.* **1990**, *94*, 5483–5488.
- (25) Andersson, K.; Malmqvist, P.-Å.; Roos, B. O. *J. Chem. Phys.* **1992**, *96*, 1218–1226.
- (26) Ghigo, G.; Roos, B. O.; Malmqvist, P.-Å. *Chem. Phys. Lett.* **2004**, *396*, 142–149.
- (27) Jorgensen, W. L.; Maxwell, D. S.; Tirado-Rives, J. *J. Am. Chem. Soc.* **1996**, *118*, 11225–11236.
- (28) Karlström, G.; Lindh, R.; Malmqvist, P.-Å.; Roos, B. O.; Ryde, U.; Varyazov, V.; Widmark, P.-O.; Cossi, M.; Schimmelpfennig, B.; Neogrady, P.; Seijo, L. *Comput. Mater. Sci.* **2003**, *28*, 222–239.
- (29) Refson, K. *Comput. Phys. Commun.* **2000**, *126*, 310–329.
- (30) Schaftenaar, G.; Noordik, J. H. *J. Comput.-Aided Mol. Des.* **2000**, *14*, 123–134.
- (31) Fabian, W. M. F. *J. Comput. Chem.* **1988**, *9*, 369–377.
- (32) He, R.-X.; Li, X.-Y. *Chem. Phys.* **2007**, *332*, 325–335.
- (33) Rettig, W.; Marschner, F. *Nouv. J. Chim.* **1983**, *7*, 425.
- (34) Okuyama, K.; Numata, Y.; Odawara, S.; Suzuka, I. *J. Chem. Phys.* **1998**, *109*, 7185–7196.
- (35) Fdez. Galván, I.; Martín, M. E.; Aguilar, M. A. *J. Chem. Theory Comput.* **2010**, *6*, 2445–2454.
- (36) Köhn, A.; Hättig, C. *J. Am. Chem. Soc.* **2004**, *126*, 7399–7410.
- (37) Schweke, D.; Haas, Y.; Dick, B. *J. Phys. Chem. A* **2005**, *109*, 3830–3842.
- (38) Fdez. Galván, I.; Martín, M. E.; Muñoz-Losa, A.; Aguilar, M. A. *J. Chem. Theory Comput.* **2009**, *5*, 341–349.
- (39) Sarkar, A.; Chakravorti, S. *Chem. Phys. Lett.* **1995**, *235*, 195–201.
- (40) Valsson, O.; Filippi, C. *J. Chem. Theory Comput.* **2010**, *6*, 1275–1292.
- (41) Schweke, D.; Haas, Y. *J. Phys. Chem. A* **2003**, *107*, 9554–9560.
- (42) Yoshihara, T.; Druzhinin, S. I.; Demeter, A.; Kocher, N.; Stalke, D.; Zachariasse, K. A. *J. Phys. Chem. A* **2005**, *109*, 1497–1509.
- (43) Belau, L.; Haas, Y.; Rettig, W. *Chem. Phys. Lett.* **2002**, *364*, 157–163.

Introduction of a New Theory for the Calculation of Magnetic Coupling Based on Spin–Flip Constricted Variational Density Functional Theory. Application to Trinuclear Copper Complexes which Model the Native Intermediate in Multicopper Oxidases

Hristina Zhekova, Michel Seth, and Tom Ziegler*

Department of Chemistry, University of Calgary, Calgary, Alberta Canada T2N 1N4

ABSTRACT: We have introduced a new method for the calculation of spin–exchange between weakly interacting electron spins on different metal centers. The method is based on spin–flip constricted variational density functional theory (SF-CV-DFT). The application of SF-CV-DFT to two trinuclear systems $[\text{Cu}_3(\text{L})(\mu_3\text{-O})]^{4+}$ and $[(\text{L}')_3\text{Cu}_3(\mu\text{-OH})_3]^{3+}$ revealed that SF-CV-DFT affords exchange coupling constants that are similar to the values obtained by the traditional broken-symmetry (BS) scheme for the same functional. The BHandHLYP functional affords for both systems the best fit to experiment and results from high-level theory in the case of BS-DFT as well as SF-CV(2)-DFT. All methods and functionals predict $[\text{Cu}_3(\text{L})(\mu_3\text{-O})]^{4+}$ to be ferromagnetic and the $[(\text{L}')_3\text{Cu}_3(\mu\text{-OH})_3]^{3+}$ system to be antiferromagnetic. The SF-CV(2)-DFT method is not only able to evaluate exchange coupling constants, it can in addition calculate the full multiplet spectrum with complete use of spatial symmetry. Further, in its restricted formulation, calculations can be carried out with use of full spin–symmetry without spin–contamination.

1. INTRODUCTION

The two trinuclear copper complexes of the present study, $[\text{Cu}(\text{L})(\mu_3\text{-O})]^{4+}$ (where L is a complex dodecaza macrotetraycle)¹ and $[(\text{DBED})_3\text{Cu}_3(\mu\text{-OH})_3]^{3+}$ (where DBED stands for N,N' -ditert-butyl-ethylenediamine),² have attracted considerable attention as synthetic analogues of the native intermediate (NI) occurring during the catalytic reactions at the active sites of the multicopper oxidases.^{3–5} The latter is a metalloenzyme found in some plants, fungi and animals and involved in the four e^- reduction of O_2 to H_2O .^{6–8} The reduction process is coupled with four one-electron oxidations of a substrate and leads to the synthesis of key metabolite substances of vital importance. Some of the most studied multicopper oxidases are laccase,⁹ ascorbate oxidase,¹⁰ ceruloplasmin,¹¹ and Fet3p.¹²

Two potential models of NI,^{1,2} $[\text{Cu}_3(\text{L})(\mu_3\text{-O})]^{4+}$ and $[(\text{DBED})_3\text{Cu}_3(\mu\text{-OH})_3]^{3+}$, were synthesized and studied extensively with X-ray diffraction, magnetic susceptibility, absorption spectroscopy, electron paramagnetic resonance (EPR), and conventional and ariable-temperature, variable-fieldmagnetic circular dichroism (VTVH MCD).^{1–5} $[\text{Cu}_3(\text{L})(\mu_3\text{-O})]^{4+}$ was found to be ferromagnetic with a quartet ^4A ground state and a low-lying doublet ^2E excited state situated 163.5 cm^{-1} above the ground state.^{1,3} The second structure, $[(\text{DBED})_3\text{Cu}_3(\mu\text{-OH})_3]^{3+}$ is antiferromagnetic^{2,4} and has a doublet ^2E ground state and a quartet $^4\text{A}_1$ excited state with a $^2\text{E} - ^4\text{A}_1$ energy gap of 315 cm^{-1} . The VTVH MCD studies^{5,13} point to the $[\text{Cu}_3(\text{L})(\mu_3\text{-O})]^{4+}$ model as the one that best reproduces the observed MCD spectrum of NI.

The ground and the lowest excited states of the two synthetic models were analyzed theoretically with density functional theory (DFT)^{3–5,13} and multireference complete active space second-order perturbation theory/complete active space self-consistent field (CASPT2/CASSCF) and multireference

difference dedicated CI 2-degrees of freedom (MRDDCI2) methods.^{14–17} The DFT calculations employed the broken symmetry approach¹⁸ for the simulation of the doublet states in C_3 and D_3 symmetry for $[\text{Cu}_3(\text{L})(\mu_3\text{-O})]^{4+}$ and $[(\text{DBED})_3\text{Cu}_3(\mu\text{-OH})_3]^{3+}$, respectively. CASPT2/CASSCF calculations with and without spin–orbit coupling corrections were done¹⁶ in order to estimate the quartet–doublet splitting for $[\text{Cu}_3(\text{L})(\mu_3\text{-O})]^{4+}$ and $[(\text{DBED})_3\text{Cu}_3(\mu\text{-OH})_3]^{3+}$ in C_s and C_2 symmetry, respectively. These results were then correlated to the structures in their original symmetry (C_3 and D_3 , respectively). The CASPT2/CASSCF studies afford good agreement with the experimental data with regard to spin multiplicity and the relative energy of the ground and low-lying excited states.^{16,17}

The multireference methods, albeit more accurate than DFT, are computationally expensive and difficult to apply for systems larger than 40 atoms. On the other hand, conventional DFT, which is a good compromise between accuracy and model size, has problems in describing some of the open shell spin states encountered in the two model systems discussed here. The difficulties arise from the fact that conventional DFT as a single determinantal method has problems with the description of spin states that even to zero order must be represented by a multi-determinantal wave function.^{18,19}

This problem is partially circumvented within the conventional DFT formalism by the broken symmetry method,¹⁸ where use is made of a simple Heisenberg Hamiltonian.²⁰ The single determinantal broken symmetry state is represented as a weighted average of the pure spin states of a system. The difference of the energy of the broken symmetry states and the

Received: February 25, 2011

Published: May 05, 2011

pure symmetry state of highest spin (which can be described easily by a single determinant) can be related directly to the exchange coupling constants J_{ij} of the Heisenberg Hamiltonian¹⁸ and hence to the difference in energy of the various spin states. This approach is straightforward and computationally feasible. However it does not provide detailed separate information about each individual spin state aside from their relative energies.

Time-dependent density functional theory (TDDFT)^{21,22} is in contrast to conventional DFT and is able to describe states of a multideterminantal nature as “excited states” relative to a single determinantal reference. In conventional TDDFT this reference is the ground state. However based on the constricted variational DFT (CV-DFT) formulation²³ of the reference can be any state. We shall in the following demonstrate that we can describe the different spin states in our two model compounds with the help of CV-DFT using the pure symmetry state of highest spin as a reference. As some of the spin states are related to the reference by spin-flip, we will make use of spin-flip theory²⁴ based on our noncollinear exchange–correlation potential formulation^{25–27} as implemented into the Amsterdam Density Functional (ADF) package.^{28,29} It is the objective of the present investigation to apply the novel spin-flip CV-DFT scheme²³ to the difference in energy of the various spin states encountered in the two model systems $[\text{Cu}_3(\text{L})(\mu_3\text{-O})]^{4+}$ and $[(\text{DBED})_3\text{Cu}_3(\mu\text{-OH})_3]^{3+}$. We hope in addition to provide the first test of the novel spin-flip CV-DFT scheme as an alternative to the broken symmetry method¹⁸ in DFT-based studies of magnetic coupling between weakly interacting metal centers.

2. COMPUTATIONAL METHODS AND DETAILS

Formulation of the CV-DFT to Second Order. We shall in accordance with Kohn–Sham (KS) theory¹⁹ describe our reference state by a single Slater determinant:

$$\Psi^0 = |\psi_1\psi_2, \dots, \psi_i\psi_j, \dots, \psi_n| \quad (1)$$

constructed from a set of occupied spin-orbitals $\{\psi_i(1); i = 1, \text{occ}\}$. The related density matrix¹⁹ is given by

$$\rho(1, 1') = \sum_i^{\text{occ}} \psi_i^*(1')\psi_i(1) \quad (2)$$

The energy of the reference system corresponding to the density matrix in eq 2 can be expressed as

$$\begin{aligned} E_{\text{KS}} &= E_{T+V_{\text{Ne}}} + E_C + E_{\text{XC,KS}} \\ &= \int [\hat{h}^0(1')\rho(1, 1')]_{(1=1')} d\tau_1 + \frac{1}{2} \int \rho(1, 1) \frac{1}{r_{12}} \rho(2, 2) d\tau_1 d\tau_2 \\ &\quad + \int E_{\text{XC,KS}}[\rho(1, 1)] d\tau_1 \end{aligned} \quad (3)$$

The one-electron Hamiltonian \hat{h}^0 includes the kinetic energy operator (\hat{T}) for a single electron and the potential (V_{Ne}) from the nuclear-electron interactions. E_C represents the coulomb interactions of the molecular electron density with itself. $E_{\text{XC,KS}}$ is the exchange–correlation energy, defined as a functional of the electron density $\rho(1, 1)$.

The spin-orbitals $\{\psi_i(1); i = 1, \text{occ}\}$ of eq 1 that afford the minimum energy according to eq 3, satisfy the one-electron KS equation:

$$\hat{F}^{\text{KS}}(1)\psi_i(1) = \varepsilon_i\psi_i(1) \quad (4)$$

with the KS operator \hat{F}^{KS} defined as

$$\hat{F}^{\text{KS}}(1) = \hat{h}^0 + \int \rho(2, 2) \frac{1}{r_{12}} d\tau_2 + V_{\text{XC}}(1) \quad (5)$$

Here

$$V_{\text{XC}}[\rho] = \frac{\delta E_{\text{XC}}}{\delta \rho} \quad (6)$$

is the exchange–correlation potential expressed as the functional derivative of the exchange–correlation energy with respect to the density.

The solution of eq 4 yields a set of optimized occupied $\{\psi_i(1); i = 1, \text{occ}\}$ and virtual $\{\psi_a(1); a = 1, \text{vir}\}$ spin orbitals. Given that the complete set of spin orbitals $\{\psi_p(1); p = 1, \text{occ} + \text{vir}\}$ are solutions to eq 4, we can write

$$F_{rs}^{\text{KS}} = \int \psi_r^*(1)\hat{F}^{\text{KS}}(1)\psi_s(1)d\tau_1 = \delta_{rs}\varepsilon_r \quad (7)$$

In CV-DFT²³ we seek new determinantal wave functions:

$$\Psi' = |\psi'_1\psi'_2, \dots, \psi'_i\psi'_j, \dots, \psi'_n| \quad (8)$$

that ultimately will represent excited states. Here the orbital set $\{\psi'_i(1); i = 1, \text{occ}\}$ in eq 8 is constructed by mixing into each of the occupied reference orbitals $\{\psi_i(1); i = 1, \text{occ}\}$ a fraction of the virtual reference orbitals $\{\psi_a(1); a = 1, \text{vir}\}$:

$$\delta\psi_i = \sum_a^{\text{vir}} U_{ai}\psi_a \quad (9)$$

where the mixing coefficient U_{ai} shall serve as a variational parameter that minimizes the energy associated with the excited state that is represented by Ψ' .

After orthonormalization to second order in U , we can write the new set of occupied orbitals as

$$\psi'_i(1) = \psi_i(1) + \sum_a^{\text{vir}} U_{ai}\psi_a(1) - \frac{1}{2} \sum_a^{\text{vir}} \sum_k^{\text{occ}} U_{ai}U_{ak}^*\psi_k(1) + O^{(3)}[U] \quad (10)$$

The density matrix corresponding to ψ' of eq 8 now reads to second order in U :

$$\begin{aligned} \rho'(1, 1') &= \rho(1, 1') + \Delta\rho'(1, 1') = \rho(1, 1') \\ &\quad + \sum_i^{\text{occ}} \sum_a^{\text{vir}} U_{ai}^*\psi_{ai}^*(1)\psi_a(1') + \sum_i^{\text{occ}} \sum_a^{\text{vir}} U_{ai}^*\psi_{ai}^*(1)\psi_i(1') \\ &\quad + \sum_a^{\text{vir}} \sum_b^{\text{vir}} \sum_i^{\text{occ}} U_{ai}^*U_{bi}\psi_a^*(1)\psi_b(1') \\ &\quad - \sum_i^{\text{occ}} \sum_k^{\text{occ}} \sum_a^{\text{vir}} U_{ak}^*U_{ai}\psi_i^*(1)\psi_k(1') + O^{(3)}[U] \end{aligned} \quad (11)$$

A substitution of eq 11 into eq 3 affords²³ the energy of Ψ' to second order in U as

$$\begin{aligned} E_{\text{KS}}[\rho^0 + \Delta\rho'] - E_{\text{KS}}[\rho^0] &= \Delta E_{\text{KS}}[\Delta\rho'] + O^{(3)}[U] \\ &= \frac{1}{2}(U^* U) \begin{pmatrix} \mathbf{A}^{\text{KS}} & \mathbf{B}^{\text{KS}} \\ \mathbf{B}^{\text{KS}} & \mathbf{A}^{\text{KS}} \end{pmatrix} \begin{pmatrix} U \\ U^* \end{pmatrix} + O^{(3)}[U] \end{aligned} \quad (12)$$

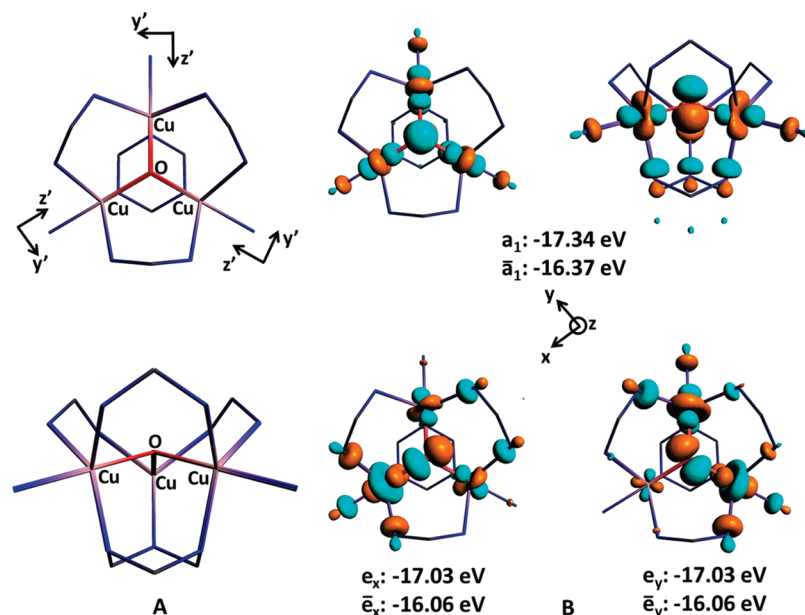


Figure 1. (A) The $\mu_3\text{O}$ model in C_{3v} symmetry: front view (up) and side view (down). Included are the copper centered coordinate systems x', y', z' . (B) Frontier SUMO orbitals of $(\mu_3\text{O})_{C_{3v}}$. Up: Front and side view of \bar{a}_1 , along with the values of the orbital energies. Down: Front view of the \bar{e}_x and \bar{e}_y orbitals with the orbital energies and the orientation of the molecular coordinate system x, y, z . The SOMO orbitals a_1 , e_x and e_y are not shown, since they have similar spatial distribution as their SUMO counterparts.

The 2×2 supermatrix in eq 12 is also known as the electronic ground-state Hessian. Its matrix elements $A_{ai,bj}^{\text{KS}}$ and $B_{ai,bj}^{\text{KS}}$ of A^{KS} and B^{KS} , respectively, are given by

$$A_{ai,bj}^{\text{KS}} = \delta_{ab}\delta_{ij}(\epsilon_a - \epsilon_i) + K_{ai,bj}^{\text{KS}}; B_{ai,bj}^{\text{KS}} = K_{ai,jb}^{\text{KS}} \quad (13)$$

where

$$\begin{aligned} K_{rs,tq}^{\text{KS}} &= K_{rs,tq}^{\text{KS}} + K_{rs,tq}^{\text{KS,XC}} \\ &= \int \psi_r^*(1)\psi_s(1)\frac{1}{r_{12}}\psi_t^*(2)\psi_q(2)d\tau_1d\tau_2 \\ &\quad + \int \psi_r^*(1)\psi_s(1)f_{\text{XC}}[\rho^0, s^0]\psi_t^*(1)\psi_q(1)d\tau_1 \quad (14) \end{aligned}$$

In eq 14 $f_{\text{XC}}[\rho^0, s^0]$ represents the exchange–correlation kernel evaluated at the reference state with density ρ^0 and spin density s^0 . It can be expressed^{21,22} in terms of the functional derivatives of the exchange–correlation potential V_{XC} given in eq 6 with respect to the density ρ and spin s .

The CV-DFT²³ method considers an excitation as a perturbation of the reference system in which a single electron is moved from the space of the occupied orbitals, represented by $\Delta\rho_{\text{occ}} = -\sum_i^{\text{occ}}\sum_k^{\text{occ}}\sum_a^{\text{vir}}U_{ak}^*U_{ai}\psi_k^*(1)\psi_i(1')$ in eq 11, to the virtual space, represented by $\Delta\rho_{\text{vir}} = \sum_a^{\text{vir}}\sum_b^{\text{vir}}\sum_i^{\text{occ}}U_{ai}^*U_{bi}\psi_a^*(1)\psi_b(1')$ of eq 11. The total charge of $\Delta\rho_{\text{occ}}$ is readily found by integration to be $-\sum_i^{\text{occ}}\sum_a^{\text{vir}}U_{ai}^*U_{ai}$ whereas the total charge of $\Delta\rho_{\text{vir}}$ is $\sum_a^{\text{vir}}\sum_i^{\text{occ}}U_{ai}^*U_{ai}$. We now identify excited states with stationary points on $E_{\text{KS}}[\rho^0 + \Delta\rho'] - E_{\text{KS}}[\rho^0]$ for which $\sum_a^{\text{vir}}\sum_i^{\text{occ}}U_{ai}^*U_{ai} = U^t \cdot U = 1$.

An optimization of $E_{\text{KS}}[\rho^0 + \Delta\rho'] - E_{\text{KS}}[\rho^0]$ from eq 12 with respect to U under the constraint $U^t \cdot U = 1$ affords²³ the eigenvalue equation:

$$(A^{\text{KS}} + B^{\text{KS}})U^{(I)} = \lambda^{(I)}U^{(I)} \quad (15)$$

Here $\lambda^{(I)}$ is the transition energy for the excited state I and $U^{(I)}$ is the corresponding optimized set of U_{ai} coefficients. Within the

Tamm–Dancoff approximation³⁰ $B_{ai,bj}^{\text{KS}} = 0$ so that eq 15 can be rewritten as

$$A^{\text{KS}}U^{(I)} = \lambda^{(I)}U^{(I)} \quad (16)$$

The eigenvalue eq 16 is identical to that obtained from TDDFT^{21,22} in the adiabatic formulation after invoking the Tamm–Dancoff approximation.³⁰ However, in TDDFT the reference Ψ^0 must be^{21,22} the ground state, whereas Ψ^0 in CV-DFT²³ can be any state that can be represented to zeroth order by a single Slater determinant. In deriving eqs 15 and 16 it was assumed that the set of spin orbitals $\{\psi_p(1); p = 1, \text{occ} + \text{vir}\}$ are solutions to eq 4. However this condition does not need to be satisfied. If the condition is not satisfied, then

$$A_{ai,bj}^{\text{KS}} = -\delta_{ab}F_{ij}^{\text{KS}} + \delta_{ij}F_{ab}^{\text{KS}} + F_{ai,bj}^{\text{KS}}; B_{ai,bj}^{\text{KS}} = K_{ai,jb}^{\text{KS}} \quad (17)$$

Here F_{rs}^{KS} was defined in eq 7. Note that the operator $\hat{F}^{\text{KS}}(1)$ is defined with respect to the density ρ^0 and spin density S^0 evaluated from Ψ^0 using the unoptimized orbital set $\{\psi_i(1); i = 1, \text{occ}\}$ that defines the determinant. As the energy in eq 12 is evaluated only to second order in U we refer²³ to our scheme as second-order CV-DFT [CV(2)-DFT]. We shall shortly return to the application of CV(2)-DFT to our two model systems.

Computational Parameters. The two models used in the present study are shown in Figures 1a and 2a, respectively. They were derived from the X-ray structures^{1,2} of $[\text{Cu}_3(\text{L})(\mu_3\text{-O})]^{4+}$ and $[(\text{DBED})_3\text{Cu}_3(\mu\text{-OH})_3]^{3+}$. We shall refer to them as $\mu_3\text{O}$ and TrisOH , respectively, for consistency with other available experimental and theoretical studies on these systems.^{3–5,13} Each copper atom in $\mu_3\text{O}$ is coordinated to five ligands in a distorted trigonal bipyramidal geometry.^{1,3} The three copper atoms are bridged through a central oxygen atom. The initial X-ray structure has C_3 symmetry. TrisOH features three copper atoms, each coordinated with four ligands in a distorted tetrahedral configuration.^{2,4} The connection between the copper atoms is

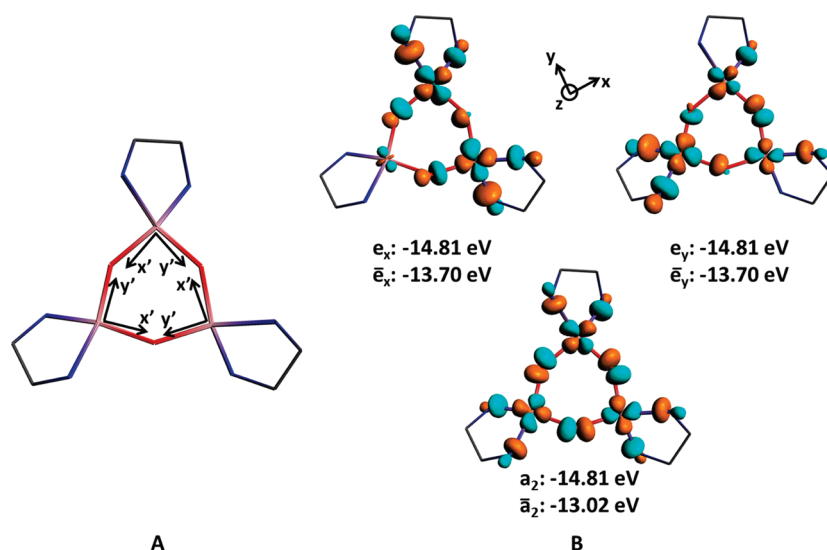


Figure 2. (A) Side view of the TrisOH model in D_3 symmetry. Included are the copper centered coordinate systems x', y', z' . (B) Frontier SUMO orbitals of $(\text{TrisOH})_{D_3}$. Up: Front view of the \bar{e}_x and \bar{e}_y orbitals with the orbital energies and the orientation of the molecular coordinate system x, y, z . Down: Front and side view of \bar{a}_2 , along with the values of the orbital energies. The SOMO orbitals a_2 , e_x and e_y are not shown, since they have similar spatial distribution as their SUMO counterparts.

made through three OH bridges which results in a planar hexagonal Cu_3O_3 structure. The ethylene bridges between the equatorial and axial N atoms in the $\mu_3\text{O}$ structure were truncated with H atoms reducing the size of the model to 58 atoms. In the TrisOH structure, a 45 atom model was created by replacement of the bulky tert-butyl groups by H atoms. The models on Figures 1a and 2a were optimized in C_{3v} and D_3 symmetry (see below) for $\mu_3\text{O}$ and TrisOH, respectively, with the C_3 axis perpendicular to the plane of the three copper atoms.

All calculations were based on the KS formalism,¹⁹ as implemented in ADF (version 2009)^{28,29} employing an all-electron TZ2P basis set. Geometry optimizations of the quartet reference states (see below for more details) were done in C_{3v} for $\mu_3\text{O}$ (configurations $a_1^1 e_x^1 e_y^1$) and D_3 for TrisOH (configurations $e_x^1 e_y^1 a_2^1$) using the regular unrestricted KS formalism.¹⁹ Additional restricted KS-DFT calculations were carried out for a given geometry on the quartet reference states with occupation of 0.5 electrons assigned to the six orbitals which are in the original quartet reference state, the highest-occupied α - and the lowest-unoccupied β -molecular orbitals.

The calculations presented here made use of the following functionals: local density approximation Vosko–Wilk–Nusair (LDA-VWN),³¹ BP86,^{32,33} Becke–Lee–Yang–Parr (BLYP),^{32–34} Perdew, Burke and Ernzerhof (PBE)³⁵ B3LYP,³⁶ and BHandHLYP.³⁶ The microstates for the two models in the different symmetries were generated with the clebschgordan.exe program, written by M. A. Buijse.³⁷

3. RESULTS AND DISCUSSION

Electronic Structure of $\mu_3\text{O}$. Figures 1b and 2b display the frontier orbitals of $\mu_3\text{O}$ and TrisOH with their respective energies based on unrestricted DFT calculations using the LDA-VWN³¹ functional. The quartet reference state has three unpaired electrons of α -spin in the a_1 and e orbitals for $(\mu_3\text{O})_{C_{3v}}$ and in the a_2 and e orbitals for $(\text{TrisOH})_{D_3}$. We shall refer to these orbitals as singly occupied molecular orbitals (SOMO's). The three lowest vacant orbitals have β -spin, and we shall refer to

them as singly unoccupied molecular orbitals (SUMO's). The SUMO's have roughly the same composition as their SOMO counterparts but are higher in energy as the smaller number of β -electrons leads to fewer stabilizing exchange interactions for electrons of β -spin. In the description of the orbitals we shall make use of the local copper-centered coordinate axes x', y', z' (Figures 1a and 2a) introduced in ref 5.

The lowest SOMO and SUMO of $(\mu_3\text{O})_{C_{3v}}$ are of a_1 symmetry. They feature a pseudo σ -antibonding interaction between the copper d_{z^2} orbitals and the p_z orbital of the central oxygen atom. This interaction appears upon a displacement of the oxygen atom above the plane of the three copper atoms. If the oxygen lies in the Cu_3 plane, then the overlap between these two sets of orbitals ceases. The position of the oxygen with respect to the plane of the metal atoms has been previously discussed in connection with the magnetic behavior of the $\mu_3\text{O}$ complex.^{1,3,5} The vanishing overlap between the metal d_{z^2} orbitals and the oxygen p_z orbital when the O atom is positioned in the Cu_3 plane leads to a decrease of the energy of the a_1 orbital, which increases the e – a_1 energy gap. As a consequence the out-of-plane conformation might be ferromagnetic with a $a_1^1 e^2$ configuration (see below), whereas the in-plane conformation potentially could be antiferromagnetic with a $a_1^2 e^1$ configuration.^{1,3,5}

The doubly degenerate SOMO and SUMO of e symmetry are of higher energy than the corresponding a_1 orbitals due to the larger σ -antibonding overlap between the d_{z^2} orbitals of three or two copper atoms and the p_x or p_y orbitals of the oxygen. The motion of the O atom into the Cu_3 plane increases the antibonding interactions between the metal and oxygen orbitals leading to a higher energy of the e orbitals and a larger e – a_1 energy gap.

The three unpaired electrons in $(\mu_3\text{O})_{C_{3v}}$ can be distributed within the six frontier spin orbitals to afford three possible electron configurations: $a_1^2 e^1$, $a_1^1 e^2$, and e^3 . In addition, each of these configurations can give rise to microstates of different multiplicity and symmetry.

The construction of the symmetrized microstates is done with the clebschgordan.exe program.³⁷ The number of the

Table 1. Doublet Microstates for $\mu_2\text{O}$ in C_{2v} Symmetry

C_{3v} microstates	M_s	C_{3v} symmetrized microstate functions
(a_1) ² e ¹ Configuration ^{a,b}		
$a(^2E_x)$	1/2	$ a_1\bar{a}_1e_x\rangle$
	-1/2	$ a_1\bar{a}_1\bar{e}_x\rangle$
$a(^2E_y)$	1/2	$ a_1\bar{a}_1e_y\rangle$
	-1/2	$ a_1\bar{a}_1\bar{e}_y\rangle$
(a_1) ¹ e ² Configuration		
$a(^2A_1)$	1/2	$1/\sqrt{2}(a_1e_x\bar{e}_x\rangle + a_1e_y\bar{e}_y\rangle)$
	-1/2	$1/\sqrt{2}(\bar{a}_1e_x\bar{e}_x\rangle + \bar{a}_1e_y\bar{e}_y\rangle)$
$a(^2A_2)$	1/2	$1/\sqrt{6}(-2 \bar{a}_1e_xe_y\rangle + a_1\bar{e}_xe_y\rangle + a_1e_x\bar{e}_y\rangle)$
	-1/2	$1/\sqrt{6}(2 \bar{a}_1e_x\bar{e}_y\rangle - \bar{a}_1\bar{e}_xe_y\rangle - \bar{a}_1e_x\bar{e}_y\rangle)$
$b(^2E_x)$	1/2	$1/\sqrt{2}(a_1e_x\bar{e}_x\rangle - a_1e_y\bar{e}_y\rangle)$
	-1/2	$1/\sqrt{2}(\bar{a}_1e_x\bar{e}_x\rangle - \bar{a}_1e_y\bar{e}_y\rangle)$
$b(^2E_y)$	1/2	$1/\sqrt{2}(- a_1e_x\bar{e}_y\rangle + a_1\bar{e}_xe_y\rangle)$
	-1/2	$1/\sqrt{2}(- \bar{a}_1e_y\bar{e}_y\rangle + \bar{a}_1\bar{e}_xe_y\rangle)$
e ³ Configuration		
$c(^2E_x)$	1/2	$ e_xe_y\bar{e}_y\rangle$
	-1/2	$ \bar{e}_xe_y\bar{e}_y\rangle$
$c(^2E_y)$	1/2	$ e_x\bar{e}_xe_y\rangle$
	-1/2	$ e_x\bar{e}_y\bar{e}_y\rangle$

^a Electron configuration. ^b a_1, e_x, e_y are the frontier orbitals of α -spin, whereas $\bar{a}_1, \bar{e}_x, \bar{e}_y$ are the frontier orbitals of β -spin.

microstates is calculated from combinatorics to be 20 of which many are degenerate. Tables 1 and 2 display all 20 doublet and quartet microstates which can be built with the 3 unpaired electrons and the 6 frontier SOMO and SUMO of $(\mu_3\text{O})_{C_{3v}}$. The overall symmetry of the microstates can be evaluated from group theory.³⁸

Detailed Description of Spin–Flip CV-DFT as Applied to $(\mu_3\text{O})_{C_{3v}}$. The high-spin quartet reference state which is a starting point in most of our SF-CV(2)-DFT calculations arises from the $a_1^1e^2$ configuration. It is labeled as $a(^4A_2)_{3/2}$ and has $M_s = 3/2$ (Table 2). All other microstates can be obtained from the reference state by replacing one or more of the orbitals a_1, e_x or e_y with \bar{a}_1, \bar{e}_x or \bar{e}_y , where a_1, e_x and e_y refer to the α -orbitals, while \bar{a}_1, \bar{e}_x and \bar{e}_y refer to the β -orbitals.

The energy of a certain basic single determinantal microstate $\Psi_{i \rightarrow a}$ relative to the reference Ψ^0 can by analogy to single excitation configuration interaction (CIS)³⁹ in wave function mechanics be identified in CV(2)-DFT (or TDDFT) with the diagonal elements of the **A** matrix in eqs 13 and 17 according to

$$A_{ai, ai} = \langle \Psi_{i \rightarrow a} | H^{\text{KS}} | \Psi_{i \rightarrow a} \rangle = \varepsilon_a - \varepsilon_i + K_{ai, ai}^{\text{KS}} \quad (18)$$

Here $\Psi_{i \rightarrow a}$ is a single determinantal wave function obtained from Ψ^0 after a promotion of an electron from one of the occupied reference orbitals (including the SOMO's) with energy ε_i to one of the unoccupied reference orbitals (including the SUMO's) with energy ε_a . Further $K_{ai, ai}^{\text{KS}}$ is the combination of two-electron coulomb and exchange–correlation integrals defined in eq 14.

It is possible in general³⁷ to make symmetrized microstates of all the basic determinants $\Psi_{i \rightarrow a}$ that span the irreducible representation of the point group for the molecule under investigation as it was done specifically for the first 20 states in Tables 1 and 2. In order to evaluate the energy of each symmetrized microstate, one needs the diagonal elements of

Table 2. Quartet microstates for $\mu_3\text{O}$ in C_{3v} symmetry

C_{3v} microstates	M_s	C_{3v} symmetrized microstate functions
(a_1) ¹ e ² Configuration ^{a,b}		
$a(^4A_2)$	3/2	$ a_1e_xe_y\rangle$
	1/2	$1/\sqrt{3}(a_1e_x\bar{e}_y\rangle + a_1\bar{e}_xe_y\rangle + \bar{a}_1e_xe_y\rangle)$
	-1/2	$1/\sqrt{3}(a_1\bar{e}_x\bar{e}_y\rangle + 1e_x\bar{e}_y\rangle + \bar{a}_1\bar{e}_xe_y\rangle)$
	-3/2	$ \bar{a}_1\bar{e}_x\bar{e}_y\rangle$

^a Electron configuration. ^b a_1, e_x, e_y are the frontier orbitals of α -spin, whereas $\bar{a}_1, \bar{e}_x, \bar{e}_y$ are the frontier orbitals of β -spin.

eq 18 as well as the off-diagonal elements given by

$$A_{aij} = \langle \Psi_{i \rightarrow a} | H^{\text{KS}} | \Psi_{j \rightarrow b} \rangle = K_{ai, bj}^{\text{KS}} \quad (19)$$

in analogy to the single excitation CIS³⁹ in wave function mechanics.

It is now possible to determine the energy of all the doublet states with $M_s = 1/2$ within the $a_1^2e^1$, $a_1^1e^2$, and e^3 configurations relative to the $(^4A_2)_{3/2}$ reference by solving an eigenvalue equation $AU = \lambda U$ similar to that of eq 16. Here

$$A_{IJ} = \langle \Psi_I | H^{\text{KS}} | \Psi_J \rangle \quad (20)$$

are matrix elements between symmetrized microstates of the same representation. These states (I, J) include not only those doublet states with $M_s = 1/2$ within the $a_1^2e^1$, $a_1^1e^2$, and e^3 configurations, but all other $M_s = 1/2$ doublets generated by a spin–flip replacement of an occupied $(^4A_2)_{3/2}$ reference orbital ψ_i with a virtual reference orbital ψ_a . The elements in eq 20 can all be calculated based on eqs 18 and 19. The construction of A_{IJ} in eq 20 corresponds to a symmetry blocking⁴⁰ in space and spin of $A_{ai, bj}$ over all basic microstates.

It should be noted that a and i , as well as b and j , in eqs 18 and 19 are of different spins as all $M_s = 3/2$ doublets are generated from $(^4A_2)_{1/2}$ by a spin–flip ($i \rightarrow \bar{a}$), where i is of α -spin and \bar{a} is of β -spin. The formulas for $K_{ai, bj}^{\text{KS}}$ required to evaluate eqs 18 and 19 were first derived in 2004 by Wang and Ziegler^{25–27} based on a noncollinear exchange–correlation expression, see also refs 41 and 42. The same integrals would be zero in the collinear exchange–correlation formulation. We have

$$K_{ai, bj}^{\text{KS}, \text{XC}} = \int [\bar{\psi}_a^*(\vec{r}_1)\psi_i(\vec{r}_1)\bar{\psi}_b(\vec{r}_1)\psi_j^*(\vec{r}_1)] \left[\frac{1}{s^0} \left(\frac{\partial E_{\text{XC}}^{\text{KS}}}{\partial \rho\alpha} - \frac{\partial E_{\text{XC}}^{\text{KS}}}{\partial \rho\beta} \right) \right]_{(\rho^0, s^0)} d\vec{r}_1 \quad (21)$$

where integration over spin already has taken place so that $\bar{\psi}_a^*(\vec{r}_1)$ and $\bar{\psi}_b(\vec{r}_1)$ represent the spatial part of the two virtual orbitals of β -spin. The evaluation of $K_{ai, bj}^{\text{KS}, \text{XC}}$ by numerical integration might lead to numerical instabilities if $s^0 = \rho^\alpha - \rho^\beta \approx 0$. We can in that case carry out a Taylor expansion of $\partial E_{\text{XC}}^{\text{KS}}/\partial \rho\alpha$ and $\partial E_{\text{XC}}^{\text{KS}}/\partial \rho\beta$ from $\rho = \rho^\alpha + \rho^\beta = \rho^0$ and $s = 0$. Thus

$$K_{ai, bj}^{\text{KS}, \text{XC}} = \int [\bar{\psi}_a^*(\vec{r}_1)\psi_i(\vec{r}_1)\bar{\psi}_b(\vec{r}_1)\psi_j^*(\vec{r}_1)] \approx \left[\left(\frac{\partial^2 E_{\text{XC}}^{\text{KS}}}{\partial \rho\alpha^2} + \frac{\partial^2 E_{\text{XC}}^{\text{KS}}}{\partial \rho\beta^2} - 2 \frac{\partial^2 E_{\text{XC}}^{\text{KS}}}{\partial \rho\alpha \partial \rho\beta} \right) \right]_{(\rho^0, s=0)} d\vec{r}_1 = K_{ai, bj}^{\text{KS}, \text{XC}} - K_{ab, \bar{ij}}^{\text{KS}, \text{XC}} \quad (22)$$

Table 3. Lower Excited States for $\mu_3\text{O}$ of C_{3v} Symmetry Based on SF-CV(2)-DFT Calculations^a

C_{3v} symmetry ^b			
state	E_i , cm ⁻¹	contributing microstates ^c	%
$1(^2E_{xy})$	863 ^d (645) ^e	$a(^2E_{xy})$	70 (69) ^e
		$b(^2E_{xy})$	18 (18) ^e
$2(^2E_{xy})$	4630 ^d (4533) ^e	$b(^2E_{xy})$	74 (74) ^e
		$a(^2E_{xy})$	23 (24) ^e
$1(^2A_1)$	5275 ^d (5167) ^e	$a(^2A_2)$	100 (100) ^e
$1(^2A_2)$	6525 ^d (6462) ^e	$a(^2A_1)$	100 (100) ^e
$3(^2E_{xy})$	7985 ^d (7929) ^e	$c(^2E_{xy})$	87 (87) ^e

^aLDA calculations. ^bLDA SF-CV(2)-DFT calculations carried out with C_{3v} symmetry and based on a $(\mu_3\text{O})_{C_{3v}}$ geometry optimized for the $a(^4A_2)_{3/2}$ microstate using unrestricted KS-DFT. ^cMicrostates defined in Tables 1 and 2. ^dUnrestricted calculations ($E[(\text{State})] - E[(^4A_2)_{3/2}]$) with orbitals optimized for $(^4A_2)_{3/2}$, relative to $(^4A_2)_{3/2}$ reference. ^eRestricted calculations ($E[(\text{State})] - E[(^4A_2)_{1/2}]$) with orbitals optimized from average configuration with 0.5 electrons in e_{xy} , a_1 , \bar{e}_{xy} , \bar{e}_y , \bar{a}_1 , relative to $(^4A_2)_{3/2}$ reference.

where $K_{ai,bj}^{KS,XC}$, $K_{ab,ij}^{KS,XC}$ are well-defined integrals from regular TDDFT.^{21,22} The expression in eq 22 is correct to $(s^0)^3$ and has no singularities for $s^0 \approx 0$. It can thus be used for small values of s^0 where eq 21 becomes singular. In practice we have found that eq 21 can be used for the LDA-VWN³¹ functional. For functionals based on the generalized gradient approximation (GGA), such as BP86,^{32,33} BLYP,^{32–34} and PBE,³⁵ where we can write the exchange–correlation energy as $E_{XC}^{GGA} = E_{XC}^{LDA} + \Delta E_{XC}^{GGA}$, we calculate the contribution from E_{XC}^{LDA} according to eq 21 and the contribution from ΔE_{XC}^{GGA} according to eq 22. For the hybrid functionals B3LYP³⁶ and BHandHLYP³⁶ we need in addition to calculate the regular exchange integrals

$$K_{\bar{a}_i, \bar{b}_j}^{HF, XC} = \iint \bar{\psi}_a^*(\vec{r}_1) \psi_i(\vec{r}_2) (1/r_{12}) \bar{\psi}_b(\vec{r}_1) \psi_j^*(\vec{r}_2) d\vec{r}_1 d\vec{r}_2$$

already implemented in ADF.⁴³

Results from SF-CV(2)-DFT Calculations on $(\mu_3\text{O})_{C_{3v}}$. By solving the eigenvalue equation $A_\Gamma U_\Gamma^{(I)} = \lambda_\Gamma^{(I)} U_\Gamma^{(I)}$ for each symmetry representation Γ , where A_Γ is defined in eq 20, we obtain the state functions:

$$\Phi_\Gamma^{(I)} = \sum_q U_{\Gamma,q}^{(I)} \Psi_{\Gamma,q} \quad (23)$$

as a linear combination of symmetrized microstates summed over q as well as the energies $\lambda_\Gamma^{(I)}$ relative to $(^4A_2)_{3/2}$. Table 3 presents $\lambda_\Gamma^{(I)}$ for the lowest doublet states with $M_s = 1/2$ based on SF-CV(2)-DFT calculations. In Table 3 is included also for each excited state I the participating microstates $\Psi_{\Gamma,q}$ with their percent contribution to $\Phi_\Gamma^{(I)}$ of eq 23. Some of the contributions are close to 100% which is indicative of a predominance of a certain symmetrized microstate in each excited state. However, in principle $\Phi_\Gamma^{(I)}$ can have contributions from the microstates of Table 1 and from all the microstates used to construct A_Γ of eq 20.

Table 3 displays results from restricted and unrestricted LDA SF-CV(2)-DFT calculations based on the unrestricted LDA KS-DFT geometries of the reference states $a(^4A_2)_{3/2}$ optimized with C_{3v} constraints. Here the unrestricted calculations make use of orbitals optimized for $a(^4A_2)_{3/2}$, whereas the restricted calculations employ orbitals from a SCF calculations in which a_1 , e_{xy} , \bar{a}_1 , \bar{e}_{xy} and \bar{e}_y each are assigned half an electron. The first real

excited doublet is the doubly degenerate $1(^2E_{xy})$ state. It is due to coupling of the $a(^2E_{xy})$ and $b(^2E_{xy})$ microstates with significant predominance of $a(^2E_{xy})$. The complementary coupling with predominance of the $b(^2E_{xy})$ microstates from the $a_1^1e^2$ configuration gives rise to excited state $2(^2E_{xy})$ which is of higher energy. This result corresponds to the qualitative conclusions drawn for the microstates on the basis of the orbital energies (eq 18) with $a_1^2e^1$ below $a_1^1e^2$, with the exception of the ground state $(^4A_2)_{3/2}$ which also belongs to the electron configuration $a_1^1e^2$.

The following two excited states $1(^2A_1)$ and $1(^2A_2)$ are based solely on the $a(^2A_2)$ and $a(^2A_1)$ microstates, respectively. They originate from the same $a_1^1e^2$ configuration as $2(^2E_{xy})$. The last spin–flip excitation of Table 3 yields a doublet degenerate $3(^2E_{xy})$ state with a large contribution from the $c(^2E_{xy})$ microstate, consistent with the analysis based on the orbital energies.

The positive values in Table 3 for the energies $\lambda_\Gamma^{(I)}$ of the $M_s = 1/2$ doublets mean that these states are all above the $(^4A_2)_{3/2}$ reference. This is in line with experiment^{1,3} that finds $(\mu_3\text{O})_{C_{3v}}$ to have a 4A ground state. The $(\mu_3\text{O})_{C_{3v}}$ system is seen to favor for its ground state the high-spin quartet configuration $a_1^1e^2$ stabilized by extra exchange interaction integrals K^{KS} but having two electrons in e of high energy, instead of the low-spin doublet configuration $a_1^2e^1$ with two electrons paired on a_1 of low energy.

It is also in agreement with experiment that our calculations find a low lying $1(^2E_{xy})$ excited state for $(\mu_3\text{O})_{C_{3v}}$. This state is (based on magnetization experiments)^{1,3} situated at $\Delta E = 163.5$ cm⁻¹ above 4A_2 . We find ΔE from our LDA SF-TDDFT calculations to be somewhat higher with $\Delta E = 863$ cm⁻¹ for the unrestricted case (where $\Delta E = E[(^2E_{xy})] - E[(^4A_2)_{3/2}]$, see below) and $\Delta E = 645$ cm⁻¹ for the restricted case (where $\Delta E = E[(^2E_{xy})] - E[(^4A_2)_{1/2}]$). In general the $\lambda_\Gamma^{(I)}$ values of Table 3 are slightly larger for the unrestricted results compared to the restricted SF-TDDFT numbers. This is understandable since the orbitals for the unrestricted calculations are optimized with respect to the $(^4A_2)_{3/2}$ reference with three electrons in a_1 , e_{xy} and e_y , respectively, whereas the restricted calculations make use of orbitals from an averaged configuration with 1/2 electron in each of the orbitals a_1 , e_{xy} , \bar{a}_1 , \bar{e}_{xy} and \bar{e}_y .

The energies in Table 3 were all based on the simple LDA³¹ functional. We shall next examine how the energy difference ΔE between the lowest 4A_2 and $1(^2E_{xy})$ states depends on the choice of functional. The difference ΔE is a key parameter and, as mentioned already, has been measured. It can be related directly to the exchange coupling constants J of the Heisenberg Hamiltonian^{5,18,44} as $\Delta E = 3J$. Here $|J|$ is a measure of the strength of the coupling between spins of weakly interacting electrons on different metal centers. Further, $J < 0$ indicates antiferromagnetic coupling with a low-spin ground state, whereas $J > 0$ correspond to ferromagnetic coupling with a high-spin ground state.

We shall in the following determine ΔE as

$$\Delta E = E[(^2E_{xy})] - E[(^4A_2)_{1/2}] \quad (24)$$

where both $E[(^2E_{xy})]$ and $E[(^4A_2)_{1/2}]$ are found from SF-CV(2)-DFT calculations with $(^4A_2)_{3/2}$ as the reference. We have adopted eq 24 as it gives a more balanced description where both states are described on the same footing as opposed to the definition $\Delta E = E[(^2E_{xy})] - E[(^4A_2)_{3/2}]$, where one state $(^4A_2)_{3/2}$ is described by a single determinant and the other $(^2E_{xy})$ by SF-CV(2)-DFT (Table 3). Such a practice is common in studies based on multiconfiguration wave function theory.⁴⁵

Table 4. Calculated^a Energy Difference $\Delta E^{b,c}$ in $(\mu_3\text{O})_{\text{C}3v}$ between Lowest Quartet State (${}^4\text{A}_2$)_{1/2} and Doublet State (${}^2\text{E}_{x,y}$)_{1/2} for Different Functionals and Methods

functionals	broken ^d symmetry	unrestricted ^{e,g} SF-CV(2)-DFT		restricted ^{f,g} SF-CV(2)-DFT
	ΔE^d	ΔE^b		ΔE^b
LDA	879	664		645
BP86	617	468		365
BLYP	561	414		334
PBE	613	465		363
B3LYP	471	385		318
BHandHLYP	134	142		152

^a Based on geometry optimized for (${}^4\text{A}_2$)_{3/2}. ^b $E[({}^2\text{E}_{x,y})] - E[({}^4\text{A}_2)_{1/2}]$. ^c In cm^{-1} . ^d Calculated according to ref 5 as $\Delta E = E(\text{LS}) - E[({}^4\text{A}_1)_{3/2}] = 3J = (3/2)\{E(\text{BS}) - E[({}^4\text{A}_1)_{3/2}]\}$, where $E(\text{BS})$ is the energy from a broken symmetry calculation.^{5,18,44} ^e Unrestricted calculations with orbitals optimized for (${}^4\text{A}_2$)_{3/2}. ^f Restricted calculations with orbitals optimized from average configuration with 0.5 electrons in e_x , e_y , a_1 , \bar{e}_x , \bar{e}_y , \bar{a}_1 . ^g Relative to (${}^4\text{A}_2$)_{3/2} reference.

Table 5. Doublet Microstates for TrisOH in D_3 Symmetry

D_3 microstates	M_s	D_3 symmetrized microstate functions
e^3 Configuration ^{a,b}		
$a({}^2\text{E}_x)$	1/2	$ e_x e_y \bar{e}_y $
	-1/2	$ \bar{e}_x e_y \bar{e}_y $
$a({}^2\text{E}_y)$	1/2	$ e_x \bar{e}_x e_y $
	-1/2	$ e_x \bar{e}_x \bar{e}_y $
$e^2(a_2)^1$ Configuration		
$a({}^2\text{A}_2)$	1/2	$1/\sqrt{2}(e_x \bar{e}_x a_2 + e_y \bar{e}_y a_2)$
	-1/2	$1/\sqrt{2}(e_x \bar{e}_x \bar{a}_2 + e_y \bar{e}_y \bar{a}_2)$
$a({}^2\text{A}_1)$	1/2	$1/\sqrt{6}(2 e_x e_y \bar{a}_2 - e_y \bar{e}_y a_2 - \bar{e}_x e_x a_2)$
	-1/2	$1/\sqrt{6}(-2 \bar{e}_x \bar{e}_x a_2 + e_y \bar{e}_y \bar{a}_2 + \bar{e}_x e_x \bar{a}_2)$
$b({}^2\text{E}_x)$	1/2	$1/\sqrt{2}(\bar{e}_x e_x a_2 - e_x \bar{e}_x a_2)$
	-1/2	$1/\sqrt{2}(\bar{e}_x e_x \bar{a}_2 - e_x \bar{e}_x \bar{a}_2)$
$b({}^2\text{E}_y)$	1/2	$1/\sqrt{2}(e_y \bar{e}_y a_2 - e_x \bar{e}_x a_2)$
	-1/2	$1/\sqrt{2}(e_y \bar{e}_y \bar{a}_2 - e_x \bar{e}_x \bar{a}_2)$
$e^1(a_2)^2$ Configuration		
$c({}^2\text{E}_x)$	1/2	$ e_x a_2 \bar{a}_2 $
	-1/2	$ \bar{e}_x a_2 \bar{a}_2 $
$c({}^2\text{E}_y)$	1/2	$ e_y a_2 \bar{a}_2 $
	-1/2	$ \bar{e}_y a_2 \bar{a}_2 $

^a Electron configuration. ^b $a_2, e_{xy} e_y$ are the frontier orbitals of α -spin, whereas $\bar{a}_2, \bar{e}_x, \bar{e}_y$ are the frontier orbitals of β -spin.

It is also possible^{5,18,44} to estimate ΔE within DFT by the “broken-symmetry approach” (BS), where one performs one high-spin calculation on $a_1^1 e^2$ followed by one low-spin calculation in which the symmetry of a_1 , e_x and e_y is allowed to break by letting each of the orbitals localize on a different Cu center. It is possible to relate ΔE to the energy difference between the high- and low-spin calculations. We compare in Table 4 ΔE from BS calculations with those obtained by employing either the unrestricted or restricted SF-CV(2)-DFT method for different functionals.

We see in Table 4 that the calculated ΔE values have the same large dependence on the functionals for all three methods. Thus LDA³¹ affords the largest estimate whereas the GGA (BP86,^{32,33} BLYP,^{32–34} PBE³⁵) values for ΔE are close and intermediate. The two hybrids (B3LYP³⁶ and BHandHLYP)³⁶ give rise to the smallest values with $\Delta E(\text{BHandHLYP}) < \Delta E(\text{B3LYP})$. For LDA, the GGA's and B3LYP the ΔE values for the same

Table 6. Quartet Microstates for TrisOH in D_3 Symmetry

D_3 microstates	M_s	D_3 symmetrized microstate functions
$e^2(a_2)^{1a,b}$		
$a({}^4\text{A}_1)$	3/2	$ e_x e_y a_2 $
	1/2	$1/\sqrt{3}(e_x e_y \bar{a}_2 + e_x \bar{e}_y a_2 + \bar{e}_x e_y a_2)$
	-1/2	$1/\sqrt{3}(e_x \bar{e}_y \bar{a}_2 + \bar{e}_x \bar{e}_y a_2 + \bar{e}_x e_y \bar{a}_2)$
	-3/2	$ \bar{e}_x \bar{e}_y \bar{a}_2 $

^a Electron configuration. ^b $a_2, e_{xy} e_y$ are the frontier orbitals of α -spin, whereas $\bar{a}_2, \bar{e}_x, \bar{e}_y$ are the frontier orbitals of β -spin.

functional tend to be somewhat larger (100–150 cm^{-1}) for the BS scheme than the SF-CV(2)-DFT methods. This gap might close somewhat if use is made of the more refined BS formulation due to Yamaguchi et al.⁴⁶ in which the overlap between the broken symmetry orbitals is taken into account. For LDA, the GGA's and B3LYP we find further that the restricted SF-CV(2)-DFT method affords ΔE values that on average are some 50 cm^{-1} smaller than the unrestricted estimates. The trend is what one would expect for reasons already mentioned. The margin is also an indication of the possible error for spin contamination present in the unrestricted scheme but not in the restricted method. We recommend the restricted SF-CV(2)-DFT method as the more accurate of the two SF-CV(2)-DFT schemes as it is free of spin contamination.

Chalupsky et al.¹⁶ have in a recent high-level CASPT2 calculation obtained an estimate for ΔE of 165 cm^{-1} in very good agreement with the experimental value of 163.5 cm^{-1} . We obtain the best agreement for the BHandHLYP functional with values of 134 cm^{-1} (BS), 142 cm^{-1} (unrestricted SF-CV(2)-DFT), and 152 cm^{-1} (restricted SF-CV(2)-DFT), respectively. It is interesting to note that the BS scheme and the SF-CV(2)-DFT method, which appear very different, afford quite similar results especially for the BHandHLYP functional.

Electronic Structure and Ground-State Geometry of TrisOH. The frontier orbitals of TrisOH (Figure 2b) feature σ -antibonding interactions between the copper $d_{x^2-y^2}$ orbitals and p_x, p_y on oxygen. The a_2 orbital is the highest in energy since all six atoms of the planar Cu_3O_3 cycle are involved in the σ -antibonding overlap. The antibonding interaction is reduced in the e-set as it can be seen for e_x where it is confined to two copper and three oxygen atoms.

Similarly to $(\mu_3\text{O})_{C_{3v}}$, $(\text{TrisOH})_{D_3}$ has three different low-energy electron configurations, e^3 , $e^2a_2^2$, and $e^1a_2^2$. The microstates corresponding to these configurations are shown in Tables 5 and 6. Their relative energies can be evaluated qualitatively from the orbital energies (eq 18). Microstates $a(^2E_x)$ and $a(^2E_y)$ arise from configuration e^3 . They should be the doublet microstates of lowest energy. Configuration $e^2a_2^2$ contains the doublets $a(^2A_1)$, $a(^2A_2)$, and $b(^2E_{xy})$, which are the microstates of intermediate energy. The sole quartet microstate $a(^4A_1)$ belongs to configuration $e^2a_2^2$ as well. The last electron configuration $e^1a_2^2$ affords the microstates $c(^2E_{xy})$ of highest energy.

Results from SF-CV(2)-DFT Calculations on TrisOH. Table 7 displays the “restricted” and “unrestricted” LDA SF-TDDFT excitation energies for $(\text{TrisOH})_{D_3}$ relative to the $(^4A_1)_{3/2}$ reference. Here the energy of $(^4A_1)_{3/2}$ has been obtained by optimizing both the orbitals and the geometry from high-spin unrestricted KS calculations based on the $a(^4A_1)_{3/2}$ microstate of Table 6. Further, all the LDA excited-state energies given in Table 7 are based on the optimized structure for $a(^4A_1)_{3/2}$. The lowest doubly degenerate excited state [$1(^2E_{xy})$] features coupling of microstates $a(^2E_{xy})$ and $b(^2E_{xy})$ with a significant predominance

Table 7. Lower Excited States for TrisOH in D_3 Symmetry Based on SF-TDDFT Calculations^a

D_3 symmetry ^b			
state	E , cm^{-1}	contributing microstates ^c	%
$1(^2E_{xy})$	-2315^d (-2333^e)	$a(^2E_{xy})$ $b(^2E_{xy})$	86(85) ^e 8(9) ^e
$2(^2E_{xy})$	4815^d (4790^e)	$b(^2E_{xy})$ $a(^2E_{xy})$	86(84) ^e 11(12) ^e
$1(^2A_1)$	6686^d (6733^e)	$a(^2A_1)$	100(100) ^e
$1(^2A_2)$	6791^d (6868^e)	$a(^2A_2)$	100(100) ^e
$4(^2E_{xy})$	$11\,042^d$ ($11\,061^e$)	$c(^2E_y)$	87(79) ^e

^aLDA calculations. ^bLDA SF-TDDFT calculations carried out with D_3 symmetry and based on a $(\text{TrisOH})_{D_3}$ geometry optimized for the $a(^4A_1)_{3/2}$ microstate. ^cMicrostates defined in Tables 5 and 6. ^dUnrestricted calculations ($E[(\text{State})] - E[(^4A_1)_{3/2}]$) with orbitals optimized for $(^4A_1)_{3/2}$ relative to $(^4A_1)_{3/2}$ reference. ^eRestricted calculations ($E[(\text{State})] - E[(^4A_1)_{1/2}]$) with orbitals optimized from average configuration with 0.5 electrons in $e_x, e_y, a_2, \bar{e}_x, \bar{e}_y, \bar{a}_2$ relative to $(^4A_1)_{3/2}$ reference.

of $a(^2E_{xy})$. The negative excitation energy in Table 7 is an indication that $1(^2E_{xy})$ has in fact a lower energy than the reference quartet $a(^4A_1)_{3/2}$. It can thus be regarded as the ground state of the $(\text{TrisOH})_{D_3}$ model. This is consistent with the experimental results according to which TrisOH has a 2E ground state and a low-lying quartet excited state situated 315 cm^{-1} ($\Delta E = -315\text{ cm}^{-1}$) above the ground state.^{2,4} Our doublet–quartet splitting is however overestimated with $\Delta E = -2351\text{ cm}^{-1}$ for the unrestricted SF-CV(2)-DFT LDA calculation and $\Delta E = -2333\text{ cm}^{-1}$ for the restricted SF-CV(2)-DFT LDA calculation. The BS-DFT approach yields $\Delta E = -2783\text{ cm}^{-1}$ (Table 8).

The three states based on the $e^2a_2^2$ configuration [$2(^2E_{xy})$, $1(^2A_1)$, and $1(^2A_2)$] are as expected of higher energy than $1(^2E_{xy})$. The state $2(^2E_{xy})$ is a product of the coupling of microstates $b(^2E_{xy})$ and $a(^2E_{xy})$ with predominance of $b(^2E_{xy})$, and $1(^2A_1)$ and $1(^2A_2)$ arise from microstates $a(^2A_1)$ and $a(^2A_2)$, respectively. A few states due to transitions between the SOMO's and virtual orbitals closely above the SUMO's or from occupied orbitals below the SOMO's to the SUMO's are found after $1(^2A_2)$ and are not presented in Table 7, since they do not belong to the discussed electron configurations. The last SOMO to SUMO excitation gives rise to state $4(^2E_{xy})$ originating from the $e^1a_2^2$ electron configuration and microstates $c(^2E_{xy})$.

We present in Table 8 values for $\Delta E = E[(^2E_{xy})] - E[(^4A_1)_{1/2}]$ based on different functionals. The gap ΔE was calculated with both the unrestricted and restricted SF-CV(2)-DFT schemes using the same procedure as the one outlined earlier for $\mu_3\text{O}$. Also shown are estimates due to the BS method. We find for LDA and the GGA's that ΔE in absolute terms is somewhat larger for the BS scheme compared to the unrestricted SF-CV(2)-DFT method. Most likely some of the discrepancy can be reduced by the Yamaguchi correction⁴⁶ not available in the ADF program. In going from the unrestricted to the restricted estimates for ΔE we encounter as expected for LDA, the GGA's and B3LYP a reduction in the gap. The CASPT2 method¹⁶ affords for $(\text{TrisOH})_{D_3}$ a value of -196 cm^{-1} for ΔE compared to the experimental estimate^{2,4} of $\Delta E = -315\text{ cm}^{-1}$. Our BHandHLYP results come close to the experimental value with -249 cm^{-1} (BS), -239 cm^{-1} (unrestricted), and -284 cm^{-1} (restricted). Thus as for $\mu_3\text{O}$, BHandHLYP affords for all three methods the closest fit with experiment in the case of TrisOH.

Table 8. Calculated^a Energy Difference $\Delta E^{b,c}$ in TrisOH between Lowest Quartet State $(^4A_1)_{1/2}$ and Doublet State $(^2E_{xy})_{1/2}$ for Different Functionals and Methods

functionals	Broken ^d Symmetry	Unrestricted ^{e,g} SF-CV(2)-DFT	Restricted ^{f,g} SF-CV(2)-DFT
	ΔE^d	ΔE^b	ΔE^b
LDA	-2783	-2463	-2333
BP86	-2074	-1951	-1826
BLYP	-2082	-1948	-1824
PBE	-2094	-1968	-1840
B3LYP	-720	-721	-572
BHandHLYP	-249	-239	-284

^aBased on geometry optimized for $(^4A_1)_{3/2}$. ^b $E[(^2E_{xy})] - E[(^4A_1)_{1/2}]$. ^cIn cm^{-1} . ^dCalculated according to ref 5 as $\Delta E = E(\text{LS}) - E[(^4A_1)_{3/2}] = 3J = (3/2)\{E(\text{BS}) - E[(^4A_1)_{3/2}]\}$, where $E(\text{BS})$ is the energy from a broken symmetry calculation.^{5,18,44} ^eUnrestricted calculations with orbitals optimized for $(^4A_1)_{3/2}$. ^fRestricted calculations with orbitals optimized from average configuration with 0.5 electrons in $e_x, e_y, a_2, \bar{e}_x, \bar{e}_y, \bar{a}_2$. ^gRelative to $(^4A_1)_{3/2}$ reference.

4. CONCLUDING REMARKS

We have here applied the spin–flip formalism²⁴ in conjunction with the noncollinear exchange–correlation formulation^{25–27,41,42} of CV(2)-DFT²³ to study spin–exchange and multiplet splittings in the two model systems $[\text{Cu}_3(\text{L})(\mu_3\text{-O})]^{4+}$ and $[(\text{DBED})_3\text{Cu}_3(\mu\text{-OH})_3]^{3+}$. We have shown that SF-CV(2)-DFT affords exchange coupling constants (J) that are similar to the values obtained by the broken-symmetry scheme due to Noodleman^{18,44} and Yamaguchi⁴⁶ for a given functional. For the two systems at hand both BS-DFT and SF-CV(2)-DFT predict correctly that $[\text{Cu}_3(\text{L})(\mu_3\text{-O})]^{4+}$ is ferromagnetic, whereas the $[(\text{DBED})_3\text{Cu}_3(\mu\text{-OH})_3]^{3+}$ system is antiferromagnetic for all functionals. Both LDA and the GGA's overestimate in absolute terms the exchange coupling constants (J). On the other hand, the BHandHLYP functional affords estimates for both $[\text{Cu}_3(\text{L})(\mu_3\text{-O})]^{4+}$ and $[(\text{DBED})_3\text{Cu}_3(\mu\text{-OH})_3]^{3+}$ that are in good agreement with experiment^{1–4} and high-level theory¹⁶ in the case of BS-DFT as well as SF-CV(2)-DFT. More work has to be done to establish SF-CV(2)-DFT as an alternative to BS-DFT in the calculation of exchange coupling constants.

The SF-CV(2)-DFT method is not only able to evaluate exchange coupling constants, it can in addition calculate the full multiplet spectrum with complete use of spatial symmetry. Further, in its restricted formulation calculations can be carried out with use of full spin symmetry without spin contamination. Finally, SF-CV(2)-DFT can also be used to optimize⁴⁷ the geometry of each individual spin state, an option we plan to pursue in the near future. Our study adds to the increasing body of work based on DFT (or TDDFT) directed toward the study of spin multiplets^{48,49} and weakly interacting spin systems.^{50,51}

AUTHOR INFORMATION

Corresponding Author

*E-mail: ziegler@ucalgary.ca.

ACKNOWLEDGMENT

This work was supported by NSERC as well as a scholarship (H.Z.) from the University of Calgary. T.Z. thanks the Canadian Government for a Canada Research Chair.

REFERENCES

- (1) Suh, M. P.; Han, M. Y.; Lee, J. H.; Min, S. K.; Hyeon, C. *J. Am. Chem. Soc.* **1998**, *120*, 3819–3820.
- (2) Mirica, L. M.; Stack, T. D. P. *Inorg. Chem.* **2005**, *44*, 2131–2133.
- (3) Yoon, J.; Solomon, E. I. *Inorg. Chem.* **2005**, *44*, 8076–8086.
- (4) Yoon, J.; Mirica, L. M.; Stack, T. D. P.; Solomon, E. I. *J. Am. Chem. Soc.* **2004**, *126*, 12586–12595.
- (5) Yoon, J.; Mirica, L. M.; Stack, T. D. P.; Solomon, E. I. *J. Am. Chem. Soc.* **2005**, *127*, 13680–13693.
- (6) Solomon, E. I.; Augustine, A. J.; Yoon, J. *Dalton. Trans.* **2008**, 3921–3932.
- (7) Solomon, E. I.; Sundaram, U. M.; Machonkin, T. E. *Chem. Rev.* **1996**, *96*, 2563–2605.
- (8) Solomon, E. I.; Chen, P.; Metz, M.; Lee, S.-K.; Palmer, A. E. *Angew. Chem., Int. Ed.* **2001**, *40*, 4570–4590.
- (9) Davies, G. J.; Ducros, V. In *Handbook of Metalloproteins*; Messerschmidt, A., Huber, R., Wieghardt, K., Poulos, T., Eds.; Wiley: New York, 2001; pp 1359.
- (10) Malkin, R.; Malmström, B. G. *Adv. Enzymol.* **1970**, *33*, 177–&.
- (11) Crichton, R. R.; Pierre, J.-L. *BioMetals* **2001**, *14*, 99–112.
- (12) deSilva, D. M.; Askwith, C. C.; Eide, D.; Kaplan, J. J. *Biol. Chem.* **1995**, *270*, 1098–1101.
- (13) Yoon, J.; Solomon, E. I. *Coord. Chem. Rev.* **2007**, *251*, 379–400.
- (14) Andersson, K.; Malmqvist, P. A.; Roos, B. O.; Sadlej, A. J.; Wolinski, K. *J. Phys. Chem.* **1990**, *94*, 5483–5488.
- (15) Roos, B. O.; Andersson, K.; Fulscher, M. P.; Malmqvist, P. A.; Serrano-Andres, L.; Pierloot, K.; Merchan, M. In *Advances in Chemical Physics: New Methods in Computational Quantum Mechanics*; Prigogine, I., Rice, S. A., Eds.; John Wiley & Sons: New York, 1996; Vol. XCIII, p 219.
- (16) Chalupský, J.; Neese, F.; Solomon, E. I.; Ryde, U.; Rulišek, L. *Inorg. Chem.* **2006**, *45*, 11051–11069.
- (17) Vancoillie, S.; Chalupský, J.; Ryde, U.; Solomon, E. I.; Pierloot, K.; Neese, F.; Rulišek, L. *J. Phys. Chem. B* **2010**, *114*, 7692–7702.
- (18) Noodleman, L.; Case, D. A.; Aizman, A. *J. Am. Chem. Soc.* **1988**, *110*, 1001–1005.
- (19) Koch, W.; Holthausen, M. C. *A Chemist's Guide to Density Functional Theory*, Wiley-VCH: New York, 2001.
- (20) Sinn, E. *Coord. Chem. Rev.* **1970**, *5*, 313–347.
- (21) Runge, E.; Gross, E. K. U. *Phys. Rev. Lett.* **1984**, *52*, 997–1000.
- (22) Casida, M. E. In *Recent Advances in Density Functional Methods*; D. E. Chong, Ed.; World Scientific: Singapore, 1995; p 155.
- (23) Ziegler, T.; Seth, M.; Krykunov, M.; Autschbach, J.; Wang, F. *J. Chem. Phys.* **2009**, *130*, 154102–(1–8).
- (24) Krylov, A. *Acc. Chem. Res.* **2006**, *39*, 83–91.
- (25) Wang, F.; Ziegler, T. *J. Chem. Phys.* **2004**, *121*, 12191–12196.
- (26) Wang, F.; Ziegler, T. *J. Chem. Phys.* **2005**, *122*, 074109–(1–9).
- (27) Wang, F.; Ziegler, T. *Int. J. Quantum Chem.* **2006**, *106*, 2545–2550.
- (28) te Velde, G.; Bickelhaupt, F. M.; Baerends, E. J.; van Gisbergen, S. J. A.; Fonseca Guerra, C.; Snijders, J. G.; Ziegler, T. *J. Comput. Chem.* **2001**, *22*, 931–967.
- (29) *ADF2009.01, SCM, Theoretical Chemistry*; Vrije Universiteit: Amsterdam, The Netherlands; <http://www.scm.com>.
- (30) Hirata, S.; Head-Gordon, M. *Chem. Phys. Lett.* **1999**, *314*, 291–299.
- (31) Vosko, S. H.; Wilk, L.; Nusair, M. *Can. J. Phys.* **1980**, *58*, 1200–1211.
- (32) Becke, A. D. *Phys. Rev. A* **1988**, *38*, 3098–3100.
- (33) Perdew, J. P.; Wang, Y. *Phys. Rev. B* **1986**, *33*, 8822–8824.
- (34) Lee, C.; Yang, W.; Parr, R. G. *Phys. Rev. B* **1988**, *37*, 785–789.
- (35) Perdew, J. P.; Burke, K.; Ernzerhof, M. *Phys. Rev. Lett.* **1996**, *77*, 3865–3868. **1997**, *78*, 1396–1396 (E).
- (36) Becke, A. D. *J. Chem. Phys.* **1993**, *98*, 1372–1377.
- (37) *Clebschgordan.exe*; Buijse, M. A., University de Boelelaan: Amsterdam, The Netherlands, 1991.
- (38) Kostler, F. G.; Dimmock, J. O.; Wheeler, R. G.; Statz, H. *Properties of the Thirty-Two Point Groups*; M.I.T. Press: Cambridge, Massachusetts, 1963.
- (39) Foresman, J. B.; Head-Gordon, M.; Pople, J. A.; Frisch, M. J. *J. Phys. Chem.* **1992**, *96*, 135–149.
- (40) van Gisbergen, S. J. A.; Snijders, J. G.; Baerends, E. J. *Comput. Phys. Commun.* **1999**, *118*, 119–138.
- (41) Wang, F.; Liu, W. *J. Chin. Chem. Soc. (Taipei)* **2003**, *50*, 597–606.
- (42) Gao, J.; Liy, W.; Song, B.; Liu, C. *J. Chem. Phys.* **2004**, *121*, 6658–6666.
- (43) Krykunov, M.; Ziegler, T.; van Lenthe, E. *J. Phys. Chem. A* **2009**, *113*, 11495–11500.
- (44) Noodleman, L. *J. Chem. Phys.* **1981**, *74*, 5737–5743.
- (45) Shavitt, I. In *Methods of Electronic Structure Theory*; Schaefer, H. F., III, Ed.; Plenum: New York, 1977; pp 189–275.
- (46) Yamaguchi, K.; Jensen, F.; Dorigo, A.; Houk, K. N. *Chem. Phys. Lett.* **1988**, *149*, 537–542.
- (47) Seth, M.; Mazur, G.; Ziegler, T. *Theor. Chem. Acc.* **2010** ASAP.
- (48) Vahtras, O.; Rinkevicius, Z. *J. Chem. Phys.* **2007**, *126* (11), 114101–114111).
- (49) Li, Z.; Liu, W. *J. Chem. Phys.* **2010**, *133* (06), 064106–064128).
- (50) Rinkevicius, Z.; Ågren, H. *Chem. Phys. Lett.* **2010**, *491*, 132–135.
- (51) Moreira, I. P. R.; Sosta, R.; Filatov, M.; Illas, F. *J. Chem. Theory Comput.* **2007**, *3*, 764–774.

Analysis of the Cartesian Tensor Transfer Method for Calculating Vibrational Spectra of Polypeptides

Noah S. Bieler,[†] Moritz P. Haag,[†] Christoph R. Jacob,^{*,‡} and Markus Reiher^{*,†}

[†]ETH Zurich, Laboratorium für Physikalische Chemie, Wolfgang-Pauli-Strasse 10, 8093 Zurich, Switzerland

[‡]Karlsruhe Institute of Technology (KIT), Center for Functional Nanostructures, Wolfgang-Gaede-Str. 1a, 76131 Karlsruhe, Germany

 Supporting Information

ABSTRACT: The Cartesian Tensor Transfer Method (CTTM) was proposed as an efficient way to calculate infrared, Raman, and Raman Optical Activity (ROA) spectra for large molecules from the Hessian matrix and property tensor derivatives calculated for smaller molecular fragments. Although this approach has been widely used, its reliability has not been analyzed in depth yet. Especially for ROA spectra, such an analysis became only recently possible because of methodological advances that allow for the calculation of full ROA spectra of fairly large molecules with large basis sets. In this work, we investigate an α -helical polypeptide of 20 alanine amino acids, for which we reported the full ROA spectra earlier, in order to study the CTTM for protein subunits. By comparing the full first-principles calculation of the vibrational spectra with spectra reconstructed with the CTTM from different fragment sizes, we find that infrared and Raman spectra are mostly well reproduced. However, this is not the case for the ROA spectrum. This might have implications for peptide and protein CTTM ROA spectra that have already been published in the literature.

1. INTRODUCTION

Vibrational spectra are a widely used tool to study biomolecules, in particular, polypeptides and proteins. Conventional infrared (IR) and Raman spectroscopy,^{1–4} their chiral variants, vibrational circular dichroism (VCD)^{5–8} and Raman optical activity (ROA),^{9–14} as well as other specialized techniques such as resonance Raman spectroscopy^{15–18} or multidimensional IR spectroscopy^{19–21} can provide detailed insight into the structure and dynamics of biomolecules in solution. Biomolecules in the gas phase can be investigated using infrared multiple-photon dissociation (IR-MPD) spectroscopy^{22–24} and IR-UV double resonance spectroscopy.^{25,26}

However, the interpretation of experimental vibrational spectra is hampered by the difficulty of establishing a direct relationship between observed spectra and the molecular structure. Therefore, first-principles calculations of the vibrational spectra (for a review, see ref 27) are often necessary to unambiguously assign vibrational spectra. Such calculations can provide information that is not available from experimental results alone, such as the precise atomic displacements corresponding to each of the observed vibrational transitions. In combination with appropriate analysis tools,^{28–30} this can be utilized to understand the relationship between molecular structure and vibrational spectra in detail.^{31–34}

The computational cost for such first-principles calculations is very high because of the higher derivatives of the total electronic energy and of molecular property tensors that are required for the vibrational frequencies and intensities, respectively. Hence, more efficient approaches for the calculation of vibrational spectra have been developed. For instance, the mode-tracking^{35–37} and intensity-tracking^{38–41} methods allow for the direct calculation of particular normal modes or of only the intense modes. For

the targeted modes, these approaches give results identical to those of a full calculation.

In addition, methods that introduce further approximations have been investigated.^{42,43} An interesting and popular approximation is the so-called Cartesian Tensor Transfer Method (CTTM) proposed by Bouř et al. in 1997.⁴⁴ The CTTM constructs the second derivatives of the electronic energy (i.e., the Hessian matrix) and the intensities of a large molecule from the Hessian matrices and molecular property tensor derivatives calculated for smaller molecular fragments. Obviously, depending on the size of these fragments, this approximation neglects long-range interactions between atoms in the large molecule, which are further apart from one another so that they do not belong to the same fragment. Since information about these long-range interactions is not contained in the properties of the smaller fragments, it cannot be accounted for. In terms of the underlying Hessian matrix, this means that the far-off diagonal elements are set to zero. Similarly, the use of small fragments might significantly alter the electronic structure and in turn the property tensor derivatives determining the vibrational intensities.

The CTTM has been applied in numerous studies to calculate IR^{45–49} and Raman^{45,50} spectra of biomolecules. Also for the corresponding chiral analogues VCD^{7,8,51–66} and ROA,^{50,67–74} the CTTM has been applied extensively. An example is a study by Kapitan et al., who employed the CTTM for β -peptides,⁷⁰ where both the force field (i.e., the Hessian matrix) and the polarizability tensors' derivatives were constructed with the CTTM. In that work, the β -peptide under study was decomposed into fragments separately representing the backbone and the side

Received: February 28, 2011

Published: May 06, 2011

chain, and the backbone was further decomposed into two fragments. In another study,⁶⁷ Kapitan et al. calculated Raman and ROA spectra of poly-L-proline with the CTTM from HCO-(L-Pro)₃-NH₂ fragments.

Despite its wide use, the CTTM has never been analyzed in detail for such large biomolecules by performing a comparison to full calculations. Mostly, this is because full calculations for such large systems have only become possible in recent years. In particular, for ROA spectroscopy, full calculations are now possible for rather large polypeptides^{31,75,76} and even for small proteins⁷⁷ by using efficient density-fitting techniques for the calculation of the required polarizability tensors.⁷⁸ In the future, analytical derivative methods developed for Raman^{79,80} and ROA spectroscopy^{81–84} will push the limits even further.

In this work, we intend to close this gap by investigating the accuracy and reliability of the CTTM in detail. As a test system, we chose an α -helical polypeptide consisting of 20 alanine residues. To allow for a direct comparison, all calculations for the large molecules and the corresponding smaller fragments are carried out with the same basis set and exchange-correlation functional. Only the fragment size was varied in order to assess its influence. As a consequence, we should be able to determine the limits of this method and the reliability of the spectra of polypeptides calculated with the CTTM.

This work is organized as follows. In section 2, we review the theory of calculating vibrational spectra as well as the CTTM and outline our CTTM implementation, before explaining the computational details in section 3. This is followed in section 4 by two tests on small molecules in order to validate our implementation of the CTTM before we proceed to a detailed analysis of the CTTM for an α -helical polypeptide in section 5. Finally, conclusions are presented in section 6.

2. METHODOLOGY

Within the harmonic approximation, the vibrational frequencies ν_p and the normal modes \mathbf{Q}_p can be obtained by diagonalizing the mass-weighted molecular Hessian matrix $\mathbf{H}^{(m)}$ with the elements

$$H_{i\alpha,j\beta}^{(m)} = \frac{1}{\sqrt{m_i m_j}} \left(\frac{\partial^2 E}{\partial R_{i\alpha} \partial R_{j\beta}} \right)_0 \quad (1)$$

where E is the total energy, $R_{i\alpha}$ is the $\alpha = x, y, z$ Cartesian component of the position of nucleus i , m_i is the atomic mass of nucleus i , and the subscript “0” indicates that the derivative is taken at the molecular equilibrium structure R_0 . Here and in the following, we will use Greek indices $\alpha, \beta, \gamma, \delta$, etc. to refer to the Cartesian components x, y, z of a vector or tensor and indices i, j, k , etc. for nuclei.

The intensities for infrared, Raman, and ROA spectroscopy corresponding to each vibrational transition can be expressed as

$$I_p \propto \sum_l c_l \left(\frac{\partial P_l^{(i)}}{\partial \mathbf{Q}_p} \right)_0 \left(\frac{\partial P_l^{(i)}}{\partial \mathbf{Q}_p} \right)_0 \quad (2)$$

where c_l are coefficients depending on the type of spectroscopy as well as the experimental setup and $P_l^{(i)}$ are components of the appropriate property tensors. In the case of infrared spectroscopy, these are the components of the dipole moment μ , and for Raman spectroscopy, those of the electric-dipole–electric-dipole polarizability tensor α . For ROA spectroscopy, the electric-dipole–magnetic-dipole polarizability tensor \mathbf{G} and the electric-dipole–electric-quadrupole polarizability tensor \mathbf{A} are also

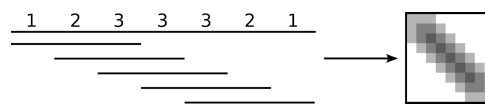


Figure 1. An abstract example for defining the overlaps: A large polymer (heptamer) is reconstructed from a fragment (trimer). The numbers above the bar show how many overlaps exist for one unit of the large polymer. An approximation of the Hessian matrix of the large molecule is then constructed with the ones of the fragments as illustrated on the right.

required. For explicit intensity expressions of these different types of vibrational spectroscopy, see, e.g., Appendix D in ref 29. The derivatives with respect to normal modes in eq 2 can be obtained from the derivatives of the property tensors with respect to Cartesian displacements $(\partial P_l^{(i)} / \partial R_{i\alpha})_0$.

For large molecular systems, such as polypeptides, the calculation of the second energy derivatives in eq 1 and of the property tensor derivatives becomes a very expensive step, in particular for calculations of ROA spectra. Therefore, in the CTTM of Bouř et al., these derivatives are approximated by those calculated for smaller fragments. In the following, we briefly outline the CTTM as well as the details of our implementation.

In the simplest case, one considers a molecule constituted of several identical monomers such as, for instance, an alanine polypeptide. In this case, a smaller fragment of only a few monomers is used to perform the actual calculations of the Hessian matrix and the property tensor derivatives, and these results are then transferred to the larger molecule. A schematic example is illustrated in Figure 1. The large molecule is in this case a heptamer, and as a small fragment a trimer is used. The small fragment can then be moved along the large fragment, and for each position, a mapping between atoms of the small fragment and atoms of the large molecule can be defined (following the terminology of ref 44, this mapping will be called an *overlap*). As shown in the figure, the atoms in the central part of the large molecule can be mapped to the smaller fragment in several different ways; i.e., different overlaps are possible. Of course, by using several different small fragments, such a procedure can be generalized to polymers consisting of different monomers and to entirely general large molecules.

The Hessian matrix is then calculated in the following way: For each pair of atoms i and j , one finds those overlaps that map both atoms to the same small fragment. If no such overlap is found, the corresponding elements of the Hessian are set to zero. If one or more overlaps are found, the corresponding elements of the Hessian of the small fragment are transferred to the large molecule (see below for details). This results in a band-diagonal Hessian matrix, as is illustrated in Figure 1. Initially, Bouř et al. suggested to fill the gaps where the Hessian has been set to zero with entries of a semiempirical or empirical force field.⁴⁴ However, since in most of the published papers so far this possibility was not used, we will only investigate the generic method here as a true *ab initio* method without any empirical contributions.

To transfer the Hessian matrix elements from the small fragment to the large molecule, one has to determine a rotation matrix $\mathbf{U}^{(ij)}$ that maps the relevant atoms of the small fragment to the corresponding atoms of the large molecule. For this, one considers the atoms i and j as well as their next neighbors (as defined by a connectivity table). If this results in less than three atoms, another set of next neighbors is included. Then, both sets of atoms $\{\mathbf{R}_k^{(\text{large})}\}$ and $\{\mathbf{R}_k^{(\text{small})}\}$ are translated to their

geometric centers ($\bar{\mathbf{R}}_{\text{large}}^{(ij)} = 1/N \sum_k \mathbf{R}_k^{(\text{large})}$ and $\bar{\mathbf{R}}_{\text{small}}^{(ij)} = 1/N \sum_k \mathbf{R}_k^{(\text{small})}$, respectively, where the index k runs over the N relevant atoms). Subsequently, the rotation matrix $\mathbf{U}^{(ij)}$ is determined such that the mean square error

$$\delta(\mathbf{U}^{(ij)}) = \sum_k |(\mathbf{R}_k^{(\text{large})} - \bar{\mathbf{R}}_{\text{large}}^{(ij)}) - \mathbf{U}^{(ij)}(\mathbf{R}_k^{(\text{small})} - \bar{\mathbf{R}}_{\text{small}}^{(ij)})|^2 \quad (3)$$

is minimized, where the index k runs over the relevant atoms. For this minimization, one can apply different methods. Some methods employ a Euler angle parametrization, which can raise different problems such as the Gimbal lock;^{85,86} others employ a quaternion parametrization.^{85,86} The latter has the advantage that it allows one to apply algebraic methods to solve the minimization problem, which is then turned into an eigenvalue problem, rather than to deal with trigonometric functions. For these reasons, an algorithm based on quaternions, similar to the one described in ref 87, is employed in this work.

It is important to note that a different rotation matrix \mathbf{U} is determined for each pair of atoms i and j , which is indicated by the superscript index “ (ij) ”. Alternatively, it would also be possible to apply a common rotation matrix for each overlap of a small fragment with the larger molecule. However, by readjusting the rotation such that the agreement is optimal for the atoms i and j and their neighbors, a more accurate Hessian (and property tensor derivatives) should be obtained. Finally, if there are several overlaps that contain the atom pair i and j , one has to decide which of them (i.e., which small fragment) is used. The papers of Bouř and co-workers mention that there are several possibilities for handling such cases⁴⁴ (e.g., always choosing the fragment for which the geometry matches best or performing a, possibly weighted, average). However, they are not very clear in explaining which option has actually been used in their calculations. On the basis of our own tests, we chose to always use the overlap for which the smallest error $\delta(\mathbf{U}^{(ij)})$ is obtained.

Given the rotation matrix \mathbf{U} , the entries of the Hessian matrix for the atom pair i and j can be transformed with⁴⁴

$$\frac{\partial^2 E^{(\text{large})}}{\partial R_{i\alpha} \partial R_{j\beta}} = U_{\alpha\gamma}^{(ij)} U_{\beta\delta}^{(ij)} \frac{\partial^2 E^{(\text{small})}}{\partial R_{i\gamma} \partial R_{j\delta}} \quad (4)$$

The usual sum convention is used throughout (i.e., a Greek index occurring more than once on the right-hand side is summed over all Cartesian components) if no explicit sum sign is used.

For the spectral intensities, one has to obtain the different derivatives of electric property tensors (i.e., the electric-dipole polarizability μ , the electric-dipole–electric-dipole polarizability tensor α , the electric-quadrupole–electric-dipole polarizability \mathbf{A} , and the electric-dipole–magnetic-dipole polarizability \mathbf{G}') with respect to Cartesian coordinates. These are also obtained by transferring the property tensor derivatives from the small fragments to the large molecule. However, since these derivatives only depend on one atom i (in contrast to the elements of the Hessian, which depend on two atoms), the rotation matrices $\mathbf{U}^{(ii)}$ found for the diagonal elements of the Hessian can be used.

The dipole moment μ and the electric-dipole–electric-dipole polarizability α of an uncharged molecule are not origin-dependent and transform as⁴⁴

$$\frac{\partial \mu_{\alpha}^{(\text{large})}}{\partial R_{i\epsilon}} = U_{\epsilon\eta}^{(ii)} U_{\alpha\pi}^{(ii)} \frac{\partial \mu_{\pi}^{(\text{small})}}{\partial R_{i\eta}} \quad (5)$$

$$\frac{\partial \alpha_{\alpha\beta}^{(\text{large})}}{\partial R_{i\epsilon}} = U_{\epsilon\eta}^{(ii)} U_{\alpha\tau}^{(ii)} U_{\beta\rho}^{(ii)} \frac{\partial \alpha_{\tau\rho}^{(\text{small})}}{\partial R_{i\eta}} \quad (6)$$

The electric-dipole–magnetic-dipole polarizability \mathbf{G}' and the electric-quadrupole–electric-dipole polarizability \mathbf{A} change under a gauge transformation (i.e., a shift of the origin).^{9,78} Therefore, for transferring their derivatives from the small fragments to the large molecule, it is not sufficient to transform them with the rotation matrix $\mathbf{U}^{(ii)}$, but the translation by $-\bar{\mathbf{R}}_{\text{small}}^{(ii)}$ applied before the rotation and the translation by $\bar{\mathbf{R}}_{\text{large}}^{(ii)}$ applied after the rotation have also to be considered. This way, it is ensured that the property tensor derivatives for the large molecule all refer to the same common origin. This is only relevant for the calculation of ROA spectra, but (as long as neutral molecules are studied) not for IR or Raman spectra.

The first step is a translation of the small fragment to its geometric center, i.e., by the vector $-\bar{\mathbf{R}}_{\text{small}}^{(ii)}$. This corresponds to shifting the origin \mathbf{O} to $\mathbf{O} + \bar{\mathbf{R}}_{\text{small}}^{(ii)}$. Under this transformation, the Cartesian derivatives of \mathbf{G}' and \mathbf{A} change as^{9,44,78}

$$\begin{aligned} \frac{\partial}{\partial R_{i\epsilon}} G'_{\alpha\beta}^{(\text{small})}(\mathbf{O} + \bar{\mathbf{R}}_{\text{small}}^{(ii)}) &= \frac{\partial}{\partial R_{i\epsilon}} G'_{\alpha\beta}^{(\text{small})}(\mathbf{O}) \\ &+ \frac{1}{2} \omega \epsilon_{\beta\gamma\delta} \bar{R}_{\text{small},\gamma}^{(ii)} \frac{\partial}{\partial R_{i\epsilon}} \alpha_{\alpha\delta}^{(\text{small})} \end{aligned} \quad (7)$$

$$\begin{aligned} \frac{\partial}{\partial R_{i\epsilon}} A_{\alpha,\beta\gamma}^{(\text{small})}(\mathbf{O} + \bar{\mathbf{R}}_{\text{small}}^{(ii)}) &= \frac{\partial}{\partial R_{i\epsilon}} A_{\alpha,\beta\gamma}^{(\text{small})}(\mathbf{O}) \\ &- \frac{3}{2} \bar{R}_{\text{small},\beta}^{(ii)} \frac{\partial}{\partial R_{i\epsilon}} \alpha_{\alpha\gamma}^{(\text{small})} - \frac{3}{2} \bar{R}_{\text{small},\gamma}^{(ii)} \frac{\partial}{\partial R_{i\epsilon}} \alpha_{\alpha\beta}^{(\text{small})} \\ &+ \delta_{\beta\gamma} \bar{R}_{\text{small},\delta}^{(ii)} \frac{\partial}{\partial R_{i\epsilon}} \alpha_{\alpha\delta}^{(\text{small})} \end{aligned} \quad (8)$$

where ω is the angular frequency of the incident light, $\delta_{\beta\gamma}$ is the Kronecker delta, and $\epsilon_{\beta\gamma\delta}$ is the Levi–Civita symbol. After this transformation, the rotation $\mathbf{U}^{(ii)}$ has to be applied:

$$\frac{\partial}{\partial R_{i\epsilon}} G'_{\alpha\beta}^{(\text{large})}(\mathbf{O} + \bar{\mathbf{R}}_{\text{large}}^{(ii)}) = U_{\epsilon\eta}^{(ii)} U_{\alpha\tau}^{(ii)} U_{\beta\rho}^{(ii)} \frac{\partial}{\partial R_{i\eta}} G'_{\tau\rho}^{(\text{small})}(\mathbf{O} + \bar{\mathbf{R}}_{\text{small}}^{(ii)}) \quad (9)$$

$$\frac{\partial}{\partial R_{i\epsilon}} A_{\alpha,\beta\gamma}^{(\text{large})}(\mathbf{O} + \bar{\mathbf{R}}_{\text{large}}^{(ii)}) = U_{\epsilon\eta}^{(ii)} U_{\alpha\tau}^{(ii)} U_{\beta\rho}^{(ii)} U_{\gamma\sigma}^{(ii)} \frac{\partial}{\partial R_{i\eta}} A_{\tau,\rho\sigma}^{(\text{small})}(\mathbf{O} + \bar{\mathbf{R}}_{\text{small}}^{(ii)}) \quad (10)$$

Following this rotation around the origin, the polarizability tensor derivatives refer to the large fragment that has been shifted such that its geometric center is at the origin, i.e., by $-\bar{\mathbf{R}}_{\text{large}}^{(ii)}$. Thus, the \mathbf{G}' tensor and the \mathbf{A} tensor have to be translated back to the original position of the large molecule. This corresponds to shifting the origin from $\mathbf{O} + \bar{\mathbf{R}}_{\text{large}}^{(ii)}$ to \mathbf{O} and therefore,

$$\begin{aligned} \frac{\partial}{\partial R_{i\epsilon}} G'_{\alpha\beta}^{(\text{large})}(\mathbf{O}) &= \frac{\partial}{\partial R_{i\epsilon}} G'_{\alpha\beta}^{(\text{large})}(\mathbf{O} + \bar{\mathbf{R}}_{\text{large}}^{(ii)}) \\ &- \frac{1}{2} \omega \epsilon_{\beta\gamma\delta} \bar{R}_{\text{large},\gamma}^{(ii)} \frac{\partial}{\partial R_{i\epsilon}} \alpha_{\alpha\delta}^{(\text{large})} \end{aligned} \quad (11)$$

$$\begin{aligned} \frac{\partial}{\partial R_{i\epsilon}} A_{\alpha,\beta\gamma}^{(\text{large})}(\mathbf{O}) &= \frac{\partial}{\partial R_{i\epsilon}} A_{\alpha,\beta\gamma}^{(\text{large})}(\mathbf{O} + \bar{\mathbf{R}}_{\text{large}}^{(ii)}) \\ &+ \frac{3}{2} \bar{R}_{\text{large},\beta}^{(ii)} \frac{\partial}{\partial R_{i\epsilon}} \alpha_{\alpha\gamma}^{(\text{large})} + \frac{3}{2} \bar{R}_{\text{large},\gamma}^{(ii)} \frac{\partial}{\partial R_{i\epsilon}} \alpha_{\alpha\beta}^{(\text{small})} \\ &- \delta_{\beta\gamma} \bar{R}_{\text{large},\delta}^{(ii)} \frac{\partial}{\partial R_{i\epsilon}} \alpha_{\alpha\delta}^{(\text{large})} \end{aligned} \quad (12)$$

calculate Hessians and property tensor derivatives for all small fragments

for all atoms i in large molecule:

for all atoms j in large molecule:

find the relevant atoms

[i , j , and their neighbors, at least three atoms]

for all overlaps (i.e., small fragments):

if atoms i and j are mapped to this small fragment:

find relevant atoms in small fragment

determine translation vectors $\bar{R}_{\text{large}}^{(ij)}$ and $\bar{R}_{\text{small}}^{(ij)}$

determine rotation matrix $U^{(ii)}$

calculate mean-square error $\delta(U^{(ii)})$

find best overlap [with smallest $\delta(U^{(ii)})$]

if no overlap found :

set $H_{i\alpha,j\beta}^{(\text{large})} = 0$

else :

calculate $H_{ij}^{(\text{large})}$ with eq 4

if $i == j$:

calculate dipole derivatives $\frac{\partial \mu}{\partial R_{i\alpha}}$ with eq 5

calculate polarizability derivatives $\frac{\partial \alpha}{\partial R_{i\alpha}}$ with eq 6

calculate G-tensor derivatives $\frac{\partial G'}{\partial R_{i\alpha}}$ with eqs 7, 9, 11

calculate A-tensor derivatives $\frac{\partial A}{\partial R_{i\alpha}}$ with eqs 8, 10, 12

calculate vib. frequencies and normal modes of large molecule from $H^{(\text{large})}$

calculate IR, Raman, and ROA intensities from property tensor derivatives

Figure 2. Pseudocode for the calculation of vibrational spectra of large molecules according to the CTTM.

Once all (pairs of) atoms of the large molecule have been considered, the IR, Raman, and ROA spectra can be computed from the final Hessian matrix and property tensor derivatives using the usual procedure.

3. COMPUTATIONAL DETAILS

All calculations of Hessians and property tensor derivatives have been performed using the SNF program.^{88,89} The Hessian matrix is calculated by numerical differentiation of analytical gradients calculated with density-functional theory in the Turbomole program package.⁹⁰ For the calculation of the property tensor derivatives, the dipole moment as well as the electric-dipole–electric-dipole, electric-dipole–magnetic-dipole, and the electric-dipole–electric-quadrupole polarizability tensors calculated with Turbomole are differentiated numerically. The polarizability tensors are obtained with time-dependent density-functional theory from a modified version of Turbomole’s *escf* program.⁷⁸ The electric-dipole–electric-dipole polarizability α is calculated both in the length and in the velocity representation, the electric-dipole–magnetic-dipole polarizability G' is calculated in the velocity representation, and the electric-dipole–electric-quadrupole polarizability A is calculated in the length representation. All Turbomole calculations employ the BP86 exchange-correlation functional^{91,92} and Ahlrichs’ valence triple- ζ basis with one set of polarization functions (def-TZVP)^{93,94} and the corresponding auxiliary basis sets.^{95,96}

The CTTM method as described in the previous section has been implemented in an add-on package to SNF written in the Python programming language. A pseudocode representation of the calculation of vibrational spectra with our implementation of the CTTM is shown in Figure 2. This add-on reads the Hessian matrices and property tensor derivatives calculated by SNF for the small fragments and assembles the Hessian matrix and property

tensor derivatives of the large molecule. For determining the rotation matrix U , a quaternion-based algorithm^{86,87} is used. For this step, our program makes use of the routines provided by the PyVib2 library of Fedorovsky.⁹⁷

The Hessian matrix and the property tensor derivatives constructed using the CTTM are then read back into the SNF program, so that the usual routines can be employed for calculating the vibrational frequencies and normal modes, as well as IR, Raman, and ROA intensities. When calculating the ROA intensity differences, the $\beta(G')^2$ invariant is calculated in the velocity representation to ensure gauge invariance, whereas the $\beta(A)^2$ invariant, which is always gauge invariant, is calculated in the length representation.⁷⁸ All Raman scattering factors are calculated for linearly polarized incident light and for the scattered light detected at 90° , ROA intensity differences are for 180° backscattering. Both the Raman and the ROA spectra use an excitation wavelength of 799 nm. In all plotted spectra, the calculated transitions have been broadened using a Lorentzian line shape with a full-width at half-maximum of 15 cm^{-1} . If included in the plots, the line spectrum has been scaled by 0.05 compared to the broadened spectrum.

4. VERIFYING THE CTTM IMPLEMENTATION

First, we carefully tested that our implementation of the CTTM is correct. As a simple test case to verify that the various transformation steps have been implemented correctly, we study the L-alanine molecule. The IR, Raman, and ROA spectra calculated for L-alanine are shown in Figure 3 as “Original” at the bottom of each plot. The molecule is then rotated by 120° in the xy plane and afterward translated by 1.0 bohr in the x and y directions. The spectra calculated for this rotated and translated molecule are shown in Figure 3 as “Rotated & Translated” at the top of each plot. The Hessian and the property tensor derivatives calculated for the rotated and translated L-alanine molecule are then transformed back to the coordinates of the original molecule. The resulting spectra are shown in Figure 3 in the middle of each plot as “Transferred”. The IR, Raman, and ROA spectra are identical in all three cases, which demonstrates that the implementation is working correctly. For a more detailed comparison, the IR intensities as well as the Raman and ROA invariants for all normal modes are listed in the Supporting Information. From the calculation for the translated and rotated molecule and from the CTTM identical values are obtained. For the original L-alanine molecule, very small deviations are observed. These are due to the numerical integration grid in the DFT calculations, which depends on the orientation of the molecule.

However, since the origin dependence of the G' tensor and the A tensor drops out when the ROA invariants are calculated, one still has to verify that the translation of the molecule (eqs 7–8, 11, and 12) is performed correctly. Therefore, in the Supporting Information, also the elements of derivatives of the G' tensor and the A tensor with respect to some of the nuclei are given. Again, a close agreement between all three calculations is found. This validates our implementation of the CTTM.

As a first test of the CTTM itself, we consider a simple case where the CTTM gives correct results. To this end, we chose two L-alanine molecules which are located far apart from each other, separated by approximately 10.5 \AA . The IR, Raman, and ROA spectra calculated for these two L-alanine molecules in a full calculation are shown in Figure 4 as “Original” at the bottom of

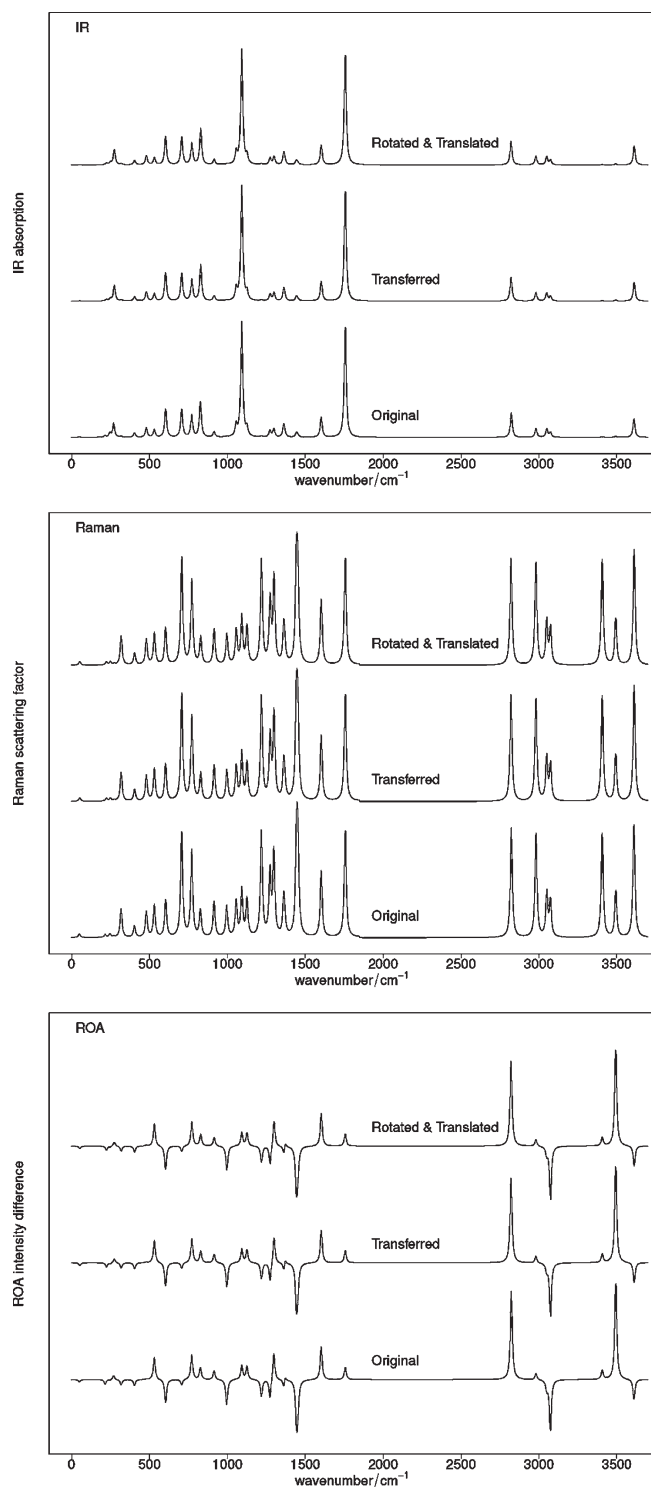


Figure 3. Test case for the implementation of the Cartesian Tensor Transfer Method: Reconstruction of the spectrum of *L*-alanine from an *L*-alanine molecule translated and rotated in space.

each plot. The “Reconstructed” spectra are obtained by merging two separately calculated *L*-alanine molecules with exactly the same structure as in the full calculation with the CTTM. The IR, Raman, and ROA spectra show no differences between the result of the full calculation and of the CTTM, which also demonstrates that our implementation is correct.

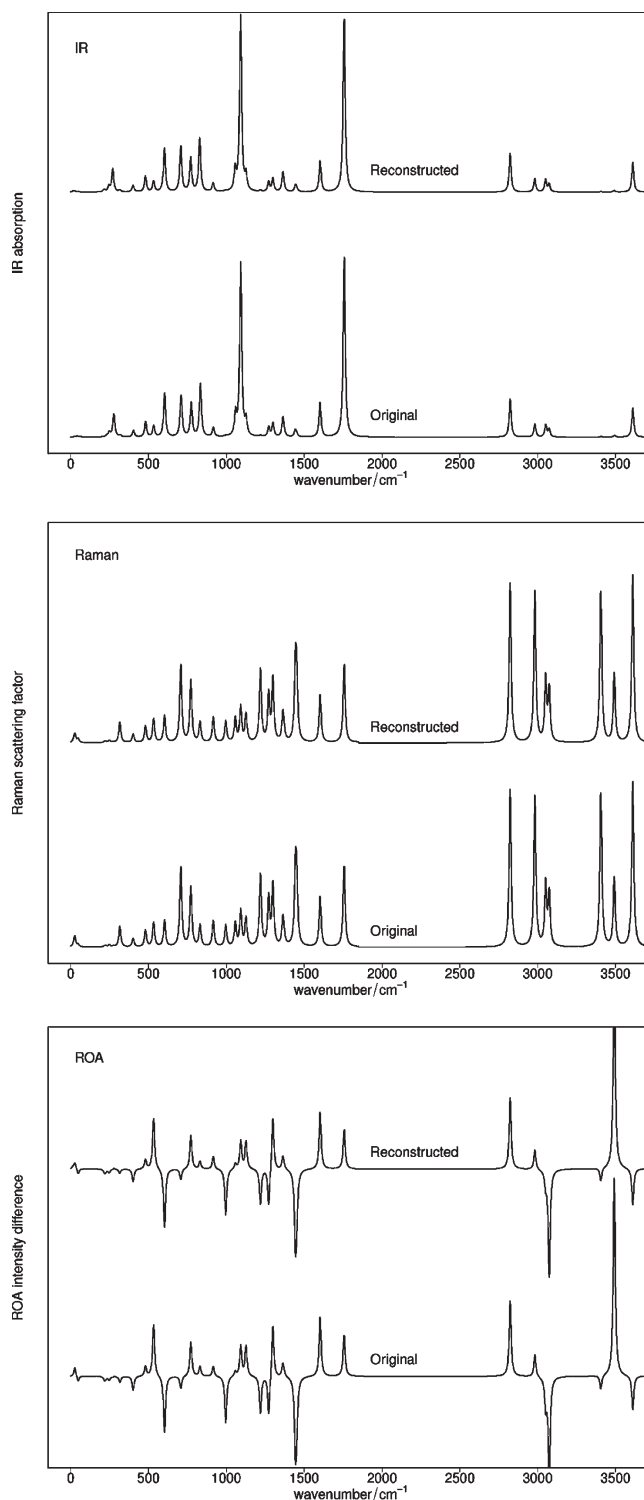


Figure 4. Test case for our implementation of the Cartesian Tensor Transfer Method: Reconstruction of the spectrum of two distant *L*-alanine molecules from two separately calculated *L*-alanine molecules.

In an additional test, we consider a *N*-methyl-acetamide (NMA) trimer. A similar test case was already used by Bouř et al.⁴⁴ The structure of the trimer is fully optimized, and as a reference, the full IR, Raman, and ROA spectra are calculated. From the trimer structure, we then constructed two NMA dimers, one by taking the two *N*-terminal NMA units and

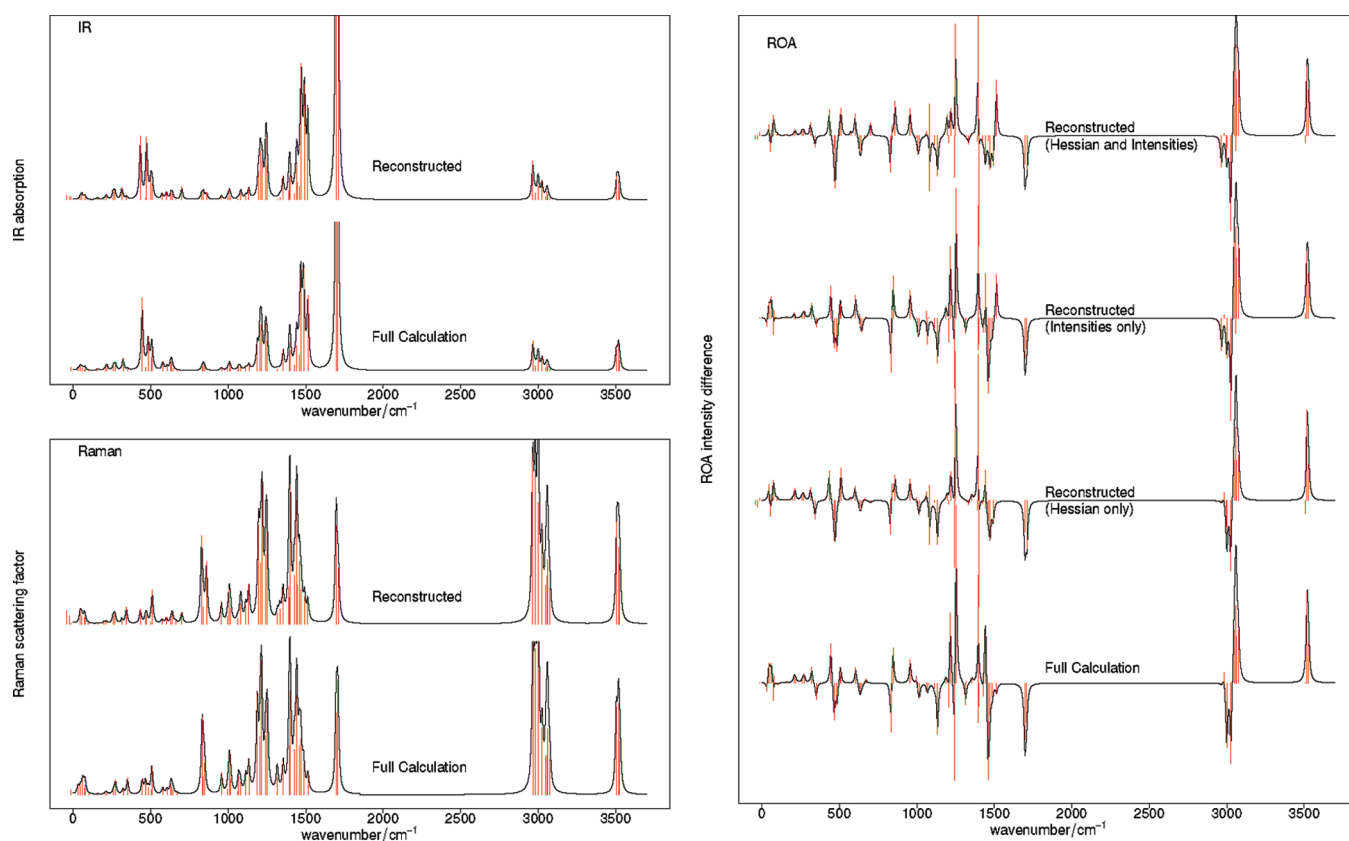


Figure 5. Vibrational spectra of an N-methyl-acetamide trimer reconstructed from two dimer calculations with the CTTM (IR, top left; Raman, bottom left; ROA, right). In the Raman spectra, the region below 2000 cm^{-1} has been magnified by a factor of 8.

another one by considering the two C-terminal NMA units. For these dimers, the atomic coordinates are fixed to those in the trimer, and only the positions of the additional terminal hydrogen atoms are optimized. The IR, Raman, and ROA spectra of the trimer are then reconstructed by transferring the Hessians and property tensor derivatives from the two dimers to the trimer. Note that since the atomic coordinates of the dimers match those of the trimer, a rotation or translation is actually not required in this case, and the Hessian matrix elements and property tensor derivatives calculated for the dimers could be used directly.

The comparison of the IR and Raman spectra from the full calculation and from the CTTM are compared in the plots in the left column of Figure 5. Even though there are some slight differences (e.g., the peak at about 850 cm^{-1} in the Raman spectrum from the full calculation is split into two peaks in the reconstructed Raman spectrum), the agreement is very good. Also for the ROA spectra, shown in the right column of Figure 5, the full calculation (bottom spectrum) and the reconstructed spectrum from the CTTM (top spectrum) match closely in most regions. However, there are also some clear deviations: For instance, around 1500 cm^{-1} (where combinations of amide II and side chain CH_3 bending vibrations appear), the spectrum from the full calculation shows a couplet, while in the reconstructed spectrum, there are only negative peaks. Similarly, there are deviations in the amide III region between 1200 and 1300 cm^{-1} .

To shed light on the origin of these deviations, Figure 5 also includes the spectra obtained if only the Hessian matrix is transferred and the property tensor derivatives from the full calculation are used (labeled “Hessian only”) and if only the

property tensor derivatives are transferred but the Hessian from the full calculation is used (labeled “Intensities only”). In both cases, there are still differences in the full calculation, but if the Hessian from the full calculation is used, the spectrum agrees more closely with the reference. Therefore, it appears that the ROA spectrum is, in contrast to the IR and Raman spectra, rather sensitive to (small) changes in the normal modes.

5. ANALYSIS OF THE CTTM FOR AN $(\text{ALA})_{20}$ POLYPEPTIDE

Since the CTTM has extensively been applied to calculate vibrational spectra of biomolecules, in particular polypeptides, it is crucial to assess its accuracy for such systems. As a typical test case, we choose a polypeptide of 20 alanine residues $(\text{Ala})_{20}$ in an α -helical conformation. Full DFT calculations of the IR and Raman spectra as well as the ROA spectrum of this model system have previously been performed in our group and were analyzed in detail.^{29,31,32} The structure of this $(\text{Ala})_{20}$ α -helix is shown in Figure 6a. Even though these calculations might only partly agree with experimental spectra because of limitations of the computational methodology (i.e., the approximations applied for the exchange-correlation functional as well as the neglect of anharmonic effects) and the neglect of solvent effects, these full calculations can serve as a reference for the CTTM. Since the calculations for the small fragments are based on the very same approximations, any deviations of the reconstructed vibrational spectra from the full calculations are caused solely by the CTTM.

Of course, the accuracy of the CTTM will strongly depend on the size of the small fragments employed. The structure of the

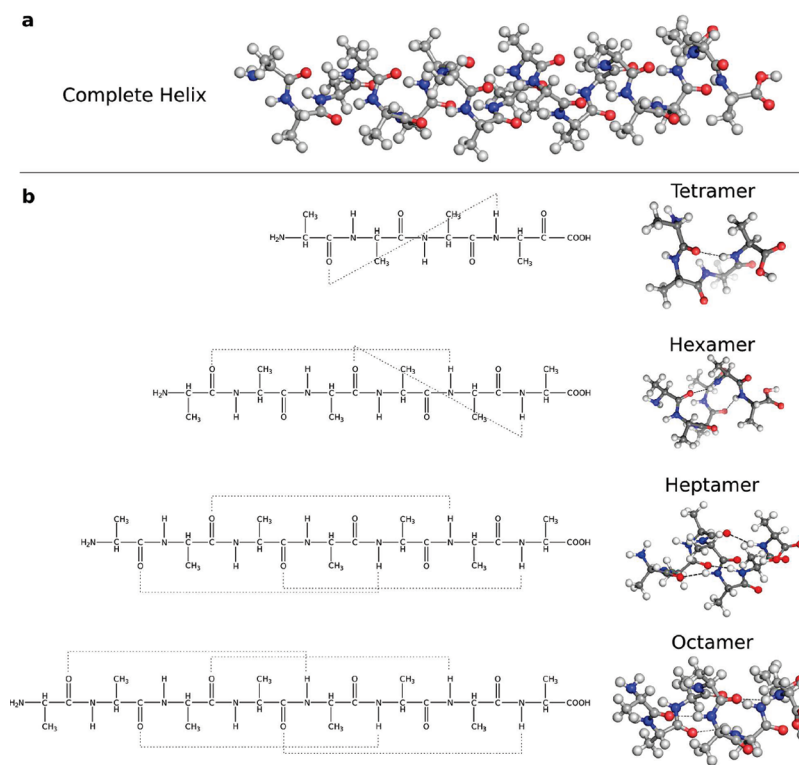


Figure 6. (a) Molecular structure of the $(Ala)_{20}$ α -helix. (b) Molecular structures of the different fragments used to reconstruct the vibrational spectra with the CTTM. In the octamer, there is one peptide bond, which has one H bond in both directions.

α -helix is stabilized by hydrogen bonds, which could strongly affect the vibrational frequencies as well as the property tensor derivatives. In too small fragments, these hydrogen bonds are not present. Furthermore, the size of the fragments determines the number of off-diagonal elements of the Hessian that are included in the CTTM.

To test the sensitivity of the CTTM to the size of the small fragments, four different sizes are compared. As the smallest fragment, an alanine tetramer $(Ala)_4$ is used. This fragment is cut from the C-terminal end of the α -helix and contains only one internal hydrogen bond. Next, a hexamer $(Ala)_6$, also taken from the C-terminal end of the α -helix, has been employed. In this hexamer, there are two hydrogen bonds. Additionally, a heptamer $(Ala)_7$ and an octamer $(Ala)_8$ have been considered. The structures of these larger fragments have been cut from the central part of the $(Ala)_{20}$ (starting from the eighth and from the second amino acid counting from the C-terminus for the heptamer and the octamer, respectively) and thus have an mostly undistorted α -helical structure. The octamer is the smallest possible fragment in which the central peptide group is involved in hydrogen bonds both at the N–H and at the C=O group. The structures of these four different small fragments are shown in Figure 6b. For all of these small fragments, all molecular coordinates, except for the ones of the terminal NH_2 group, have been fixed in order to keep their structures as close to the full helix as possible. Therefore, the small fragments are no minimum structures with respect to the energy anymore, and the Hessians calculated for these fragments have negative eigenvalues.

The IR and Raman spectra obtained for the $(Ala)_{20}$ α -helix with the CTTM are compared to the full calculation in Figure 7. In general, a good agreement between the full calculation and the CTTM is found already for the spectra reconstructed from the

alanine tetramer. When going to a larger fragment size, the spectra only change slightly. There are only a few exceptions where the agreement is worse. First, in the region between 3300 and 3600 cm^{-1} , where the N–H stretching (amide A) vibrations appear, the CTTM cannot reproduce the full calculations. Since the hydrogen bonds in the α -helix are formed between the N–H and the C=O groups of the backbone, these N–H stretching vibrations are especially sensitive to the (partial) neglect of these hydrogen bonds in the CTTM. Only for the octamer, the shape of the amide A band resembles the full calculation, but its intensity is still underestimated, both in the IR and in the Raman spectrum. The peak at 3309 cm^{-1} in the full calculation (slightly below the amide A band), which stems from the N–H stretch vibration of the terminal NH_2 group, is missing in all CTTM spectra. Since we took the structure of our fragments from the central parts or from the C-terminal end of the helix, the structure and chemical environment of the terminal NH_2 are not well described.

Second, the IR and Raman spectra from the CTTM do not agree with the full calculation in the extended amide III region between 1100 and 1350 cm^{-1} (i.e., for the amide III and the C_α –H bending vibrations). While the positions of most of the bands in this region agree in all cases, their relative intensities change significantly between the different fragment sizes. It is known that the extended amide III region is particularly sensitive to structural changes because of the coupling between the classical amide III and the C_α –H bending vibrations.^{98,99,34} Finally, there are also deviations in the lower wavenumber region, for instance, around 500 cm^{-1} in the IR spectra or between 650 and 700 cm^{-1} in the Raman spectra. For these features, one can observe that the agreement of the CTTM with the full calculation improves if larger fragments are used.

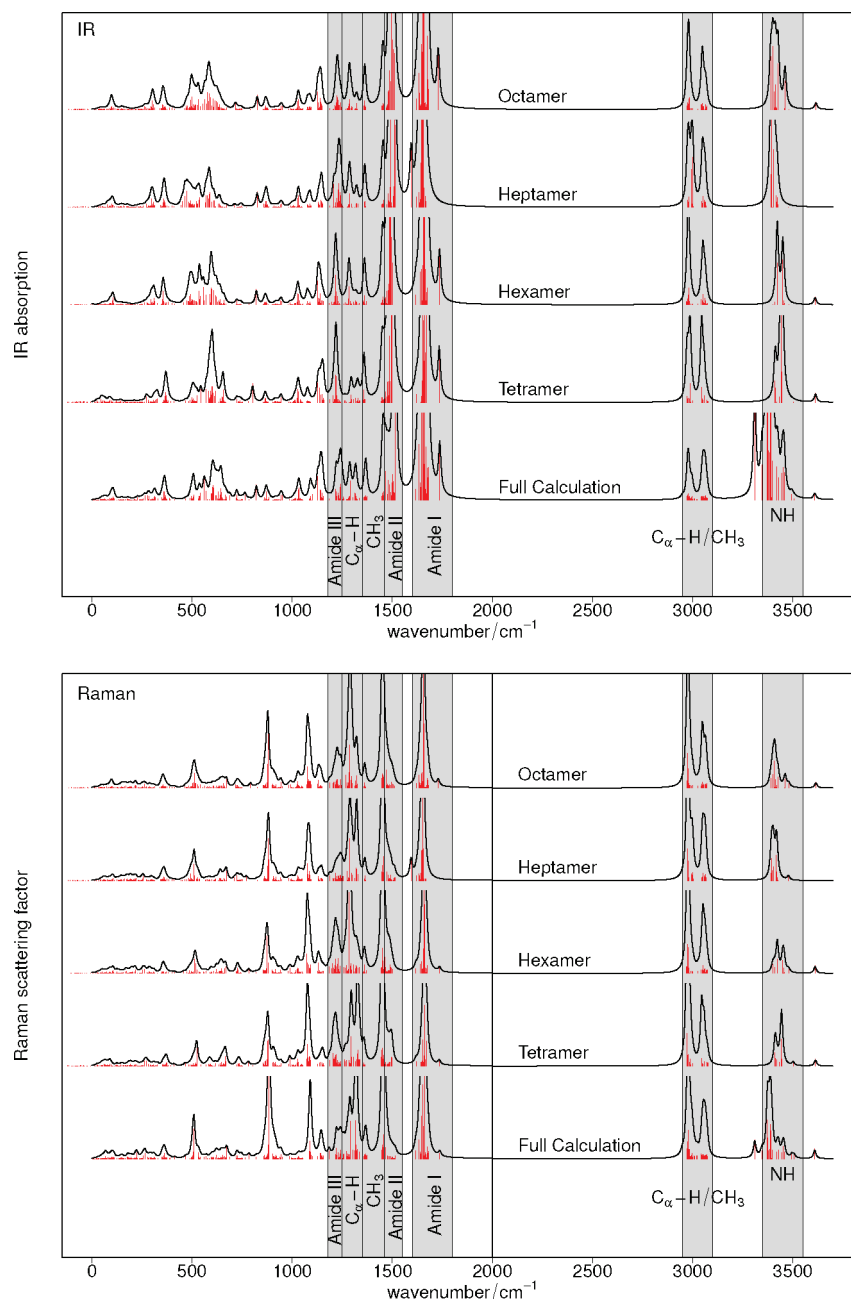


Figure 7. Comparison of the IR and Raman spectra from the full calculation on an $(\text{Ala})_{20}$ α -helix and the spectra obtained with the CTTM by using an alanine tetramer, hexamer, heptamer, and octamer as small fragments. In the Raman spectra, the region up to 2000 cm^{-1} is enlarged by a factor of 20.

A more quantitative comparison can be obtained by looking at the differences in the vibrational frequencies of each individual transition. For such a comparison, we identify the normal modes corresponding to the same transition in the full and CTTM calculations by identifying those pairs of normal modes that have the largest overlap (as defined, for instance, in ref 30). For the CTTM calculations starting from the different fragment sizes, Figure 8 highlights the error in the wavenumber for each of the normal modes. The comparison shows quite significant errors in the vibrational frequencies. For each of the bands, the errors in the individual vibrational frequencies are not systematic but scatter (usually around zero) by about 20 to 50 cm^{-1} . When ignoring the low-frequency vibrations (below about 300 cm^{-1}), the largest errors of up to 80 cm^{-1} are found for the N–H

stretching (amide A) vibrations. Also, for the extended amide III region, larger deviations are observed. Nevertheless, it appears that for most of the other regions the errors in the vibrational frequencies—even though they are considerable—do not affect the overall IR and Raman spectra significantly.

For the ROA spectrum, the comparison of the CTTM with the full calculation is shown in the upper part of Figure 9. Some features found in the ROA spectrum from the full calculation can (at least qualitatively) also be found in all the spectra, e.g., the negative peak for the skeletal stretch vibrations at about 1150 cm^{-1} , the strong positive peak at the lower-wavenumber end of the $\text{C}_{\alpha}\text{–H}$ stretching region, or the small positive peak for the symmetric CH_3 bending vibrations. Other features, such as the negative peak at the lower-wavenumber end of the amide III

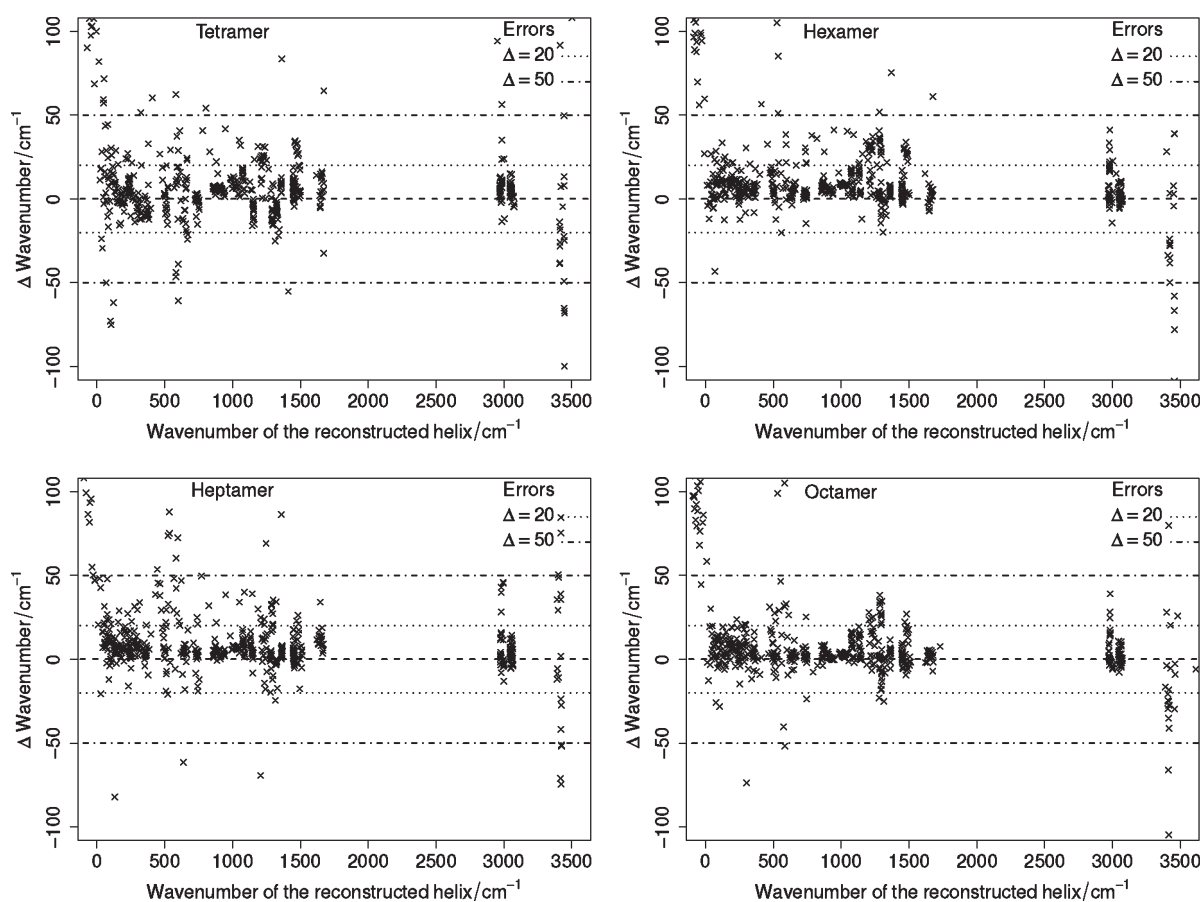


Figure 8. Comparison of the vibrational frequencies obtained with the CTTM starting from a tetramer, hexamer, heptamer, and octamer to those obtained in a full calculation. For each normal mode in the reconstructed spectrum, the corresponding normal mode in the full calculation is identified by considering the overlap between the modes.

region or the couplet for the asymmetric CH_3 stretching vibrations at 1450 cm^{-1} appear with the CTTM only for the heptamer and the octamer. In general, one notices that there is a much stronger dependence on the size of the fragments used in the CTTM, and in some regions, the spectrum changes significantly with fragment size. An example is the amide I region: While there is a negative–positive couplet in the full calculation,³¹ a positive peak is found with the CTTM using the tetramer; a couplet is found for the hexamer, and negative peaks are found for the octamer. It is important to point out that, while in some regions the CTTM is able to approach the full calculation if large enough fragments are used, this is not true in general. Even with the octamer, the CTTM produces—in contrast to the full calculation—a strong negative amide II band, an additional negative peak in the amide III region, and an additional positive peak at about 1000 cm^{-1} . Moreover, there are significant deviations from the full calculation in the extended amide III (i.e., amide III and $\text{C}_\alpha\text{—H}$ bending) region.

One reason for the dissatisfying performance of the CTTM for ROA spectra could be the influence of the terminal residues in the small fragments. These have a different electronic structure than the central residues, which will affect both the Hessian and the property tensor derivatives but are still considered in the reconstruction of the Hessian and property tensor derivatives of the central parts of the full helix. To test their influence on the reconstructed ROA spectra, we repeated the CTTM calculations, but this time the terminal residues are excluded when mapping

the atoms of the small fragment to the full α -helix (except for the “ends” of the helix). For the tetramer, the two central peptide groups; for the hexamer, the three central peptide units; and for the heptamer and octamer, the four and three central peptide groups, respectively, are included. The spectra obtained with these smaller overlaps in the CTTM are shown in the lower part of Figure 9. However, while the ROA spectra change in some parts, the disagreement between the CTTM and the full calculation remains.

To better understand why the CTTM is in disagreement with the full calculation of the ROA spectra, we also performed calculations where the CTTM is applied only to the property tensor derivatives, but where the Hessian from the full calculation is used (“Intensities only”), as well as calculations where the CTTM is applied only for the Hessian, but where the property tensor derivatives from the full calculation are used (“Hessian only”). The results are shown in Figure 10. For the “Intensities only” spectra (shown in the upper part), there are still large deviations from the full calculation, and in some parts, the ROA spectrum changes completely when the fragment size is increased. On the other hand, for the “Hessian only” CTTM calculations, the ROA spectra agree rather well with the full calculation. Nevertheless, there are still some smaller differences, for instance, in the extended amide III region or for the amide II band. Therefore, the dissatisfying performance of the CTTM for ROA calculations is mainly caused by the transfer of the property tensors, not by approximations introduced for the Hessian.

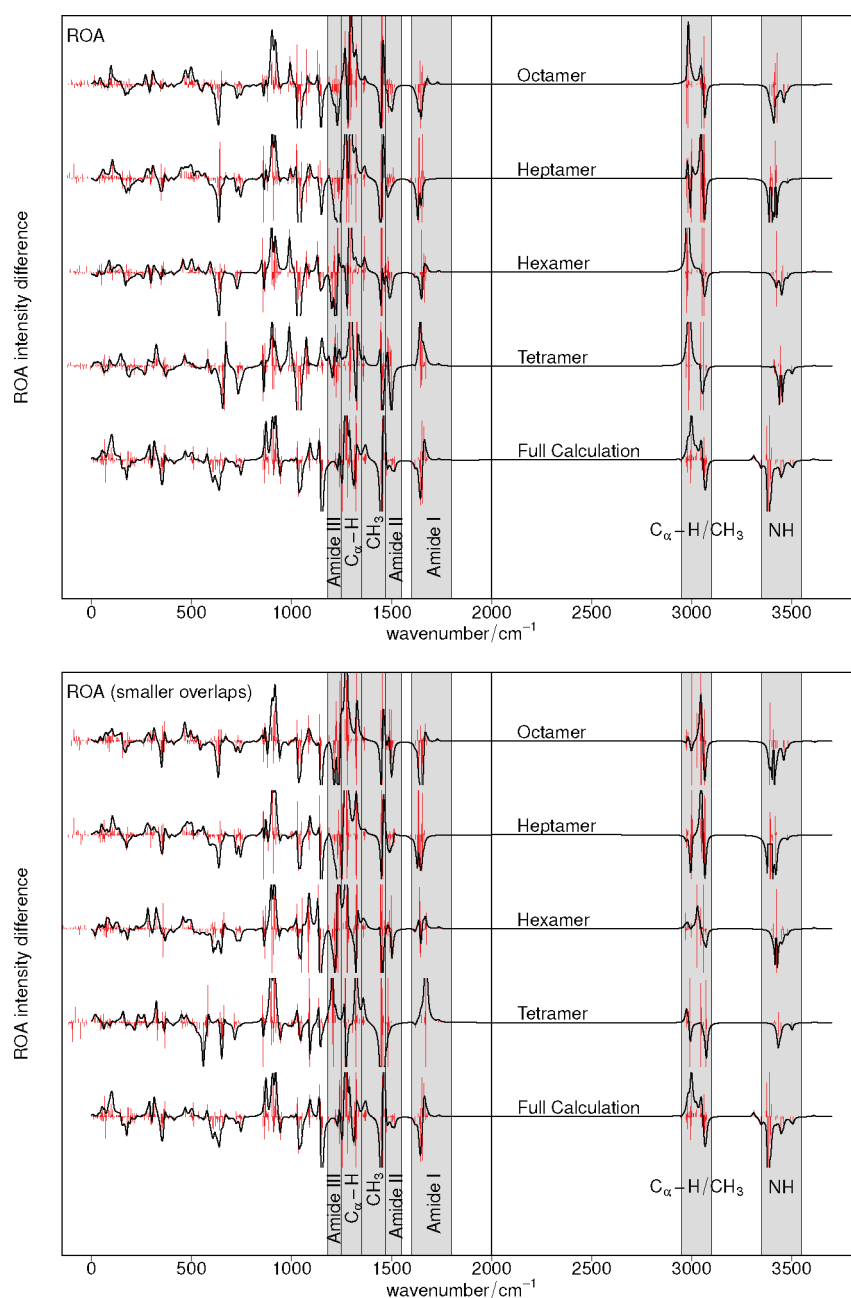


Figure 9. Comparison of the ROA spectra from the full calculation on an (Ala)₂₀ α -helix and the spectra obtained with the CTTM by using an alanine tetramer, hexamer, heptamer, and octamer as small fragments. In the top part, all atoms of the small fragments are included for the CTTM calculation, while in the bottom part, the terminal residues of the small fragments are not considered. In all spectra, the region up to 2000 cm^{-1} is enlarged by a factor of 20.

As the ROA intensities depend on the derivatives of three different property tensors (the electric-dipole–electric-dipole polarizability tensor α , the electric-dipole–magnetic-dipole tensor \mathbf{G}' , and the electric-dipole–magnetic-quadrupole polarizability tensor \mathbf{A}),⁹ it is instructive to investigate the degree to which the individual tensors are affected by the CTTM. The α tensor cannot be the reason for the disagreement with the full calculation because good results were obtained for the Raman intensities. To determine which one of the other two tensors is responsible for the errors, pseudospectra treating the two ROA invariants $\beta(\mathbf{G}')^2$ and $\beta(\mathbf{A})^2$ separately are plotted in Figure 11. In these pseudospectra, only the property tensor derivatives have

been reconstructed with the CTTM, whereas the Hessian from the full calculation has been used. From the plots, it is evident that the derivatives of the \mathbf{A} tensor are less affected by the CTTM than the \mathbf{G}' tensor derivatives. In addition, the invariants $\beta(\mathbf{G}')^2$ and $\beta(\mathbf{A})^2$ enter the ROA intensity expression in a 3:1 ratio (the pseudospectra in Figure 11 have been scaled accordingly). Keeping in mind that the \mathbf{A} tensor hardly contributes to the full ROA spectrum,¹⁰⁰ it is obvious that the error in the CTTM-constructed ROA spectrum stems from the \mathbf{G}' tensor derivatives when compared to the full ROA calculation.

To further understand the origin of the errors in the ROA intensities introduced by the CTTM, an analysis in terms of local

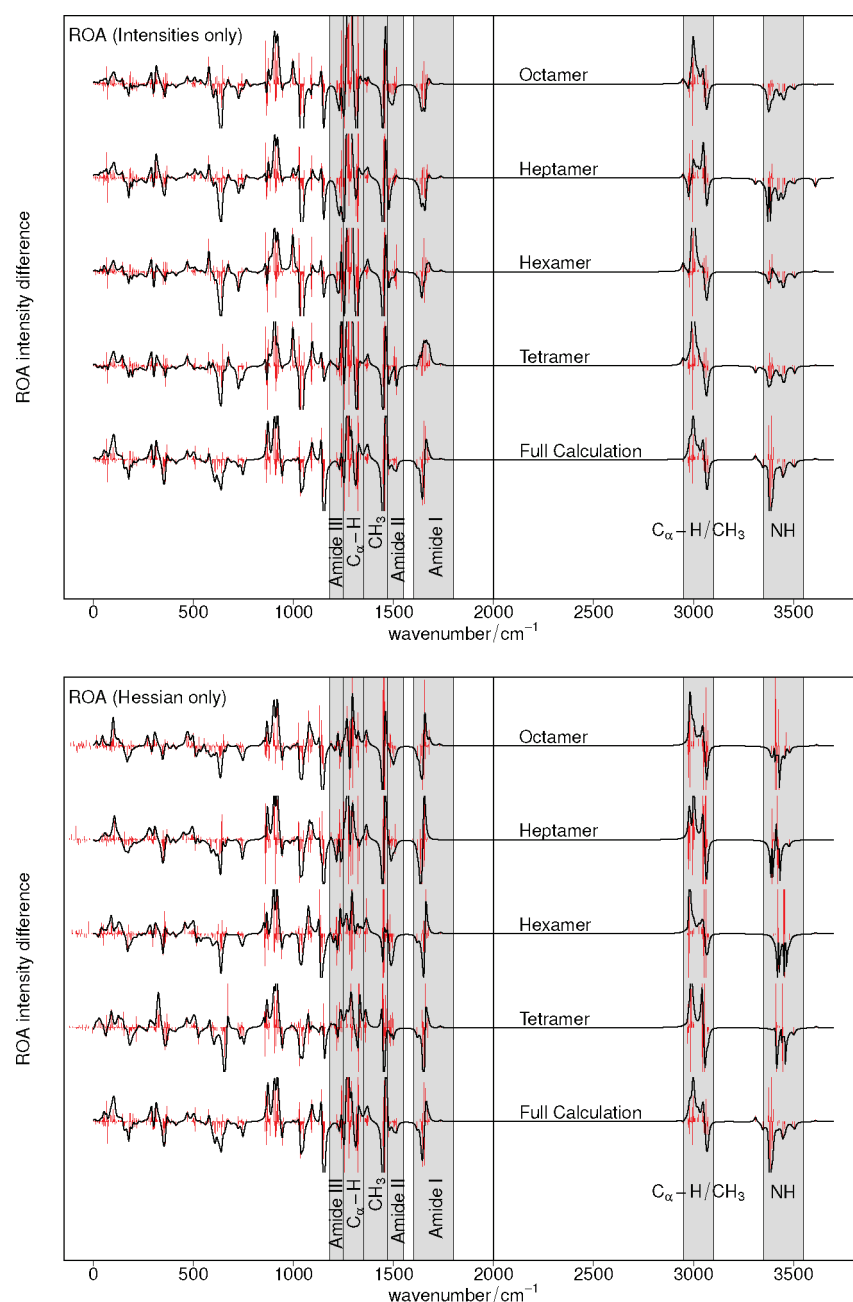


Figure 10. Comparison of the ROA spectra from the full calculation on an $(\text{Ala})_{20}$ α -helix and the spectra obtained with the CTTM applied only for the intensities (top part) or only for the Hessian (bottom part). In all spectra, the region up to 2000 cm^{-1} is enlarged by a factor of 20.

modes²⁹ can provide additional insight. In such an analysis, the delocalized normal modes contributing to one band are unitarily transformed to a set of localized modes. In general, these localized modes are vibrations of a single amino acid residue or peptide group. Even though they do not correspond to the transitions observed in the experiment, a wavenumber and a ROA intensity can be assigned to each localized mode, and the total intensity of a specific band is invariant under the transformation from normal modes to localized modes. For more details, we refer to refs 29 and 32. For the ROA spectrum of $(\text{Ala})_{20}$, such an analysis has previously been performed in our group for the full ROA calculation,³¹ to which we may compare here.

As an example, we consider the amide III band between ca. 1200 and 1260 cm^{-1} . For this band, the full ROA calculation yields

a rather small negative peak, while a much stronger negative peak is obtained in the CTTM calculation, even when using the large octamer fragment. The ROA intensities of the amide III localized modes are listed in Table 1 for both the full calculation and the intensities-only CTTM calculation employing the octamer fragment. Note that because the CTTM is applied for the property tensor derivatives only, the normal modes and also the localized modes are identical in both cases. For the terminal residues, the localized-mode intensities from the CTTM qualitatively agree with the full calculation. However, for the central residues, there are larger differences. While in the full calculations, the ROA intensities of the localized modes are approximately $-10 \times 10^{-3}\text{ \AA}^4/\text{amu}$, those obtained when applying the CTTM are about twice as large. This is then reflected by the sum of the intensities for the

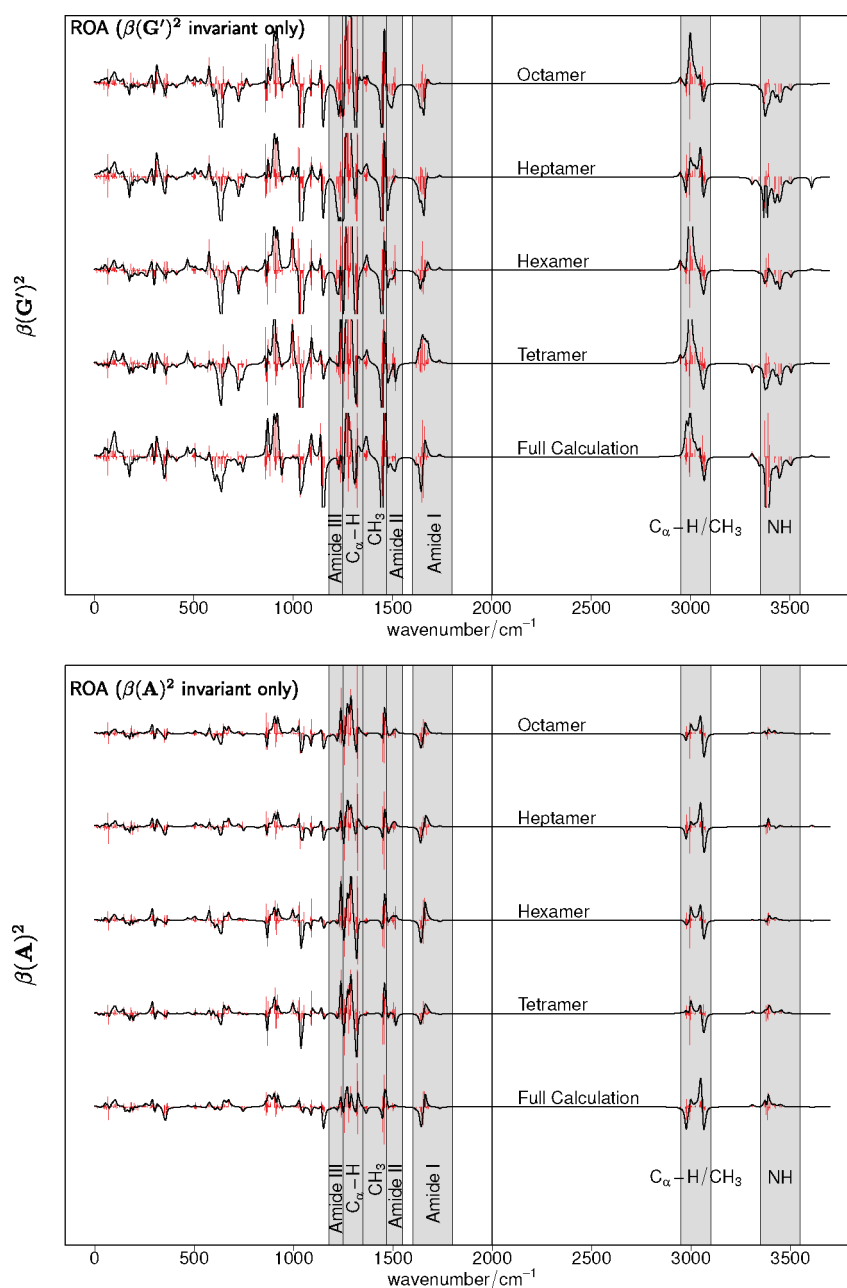


Figure 11. Comparison of the pseudospectra showing only the $\beta(G')^2$ and $\beta(A)^2$ invariants from the full calculation on an $(Ala)_{20}$ α -helix and from the CTTM. The pseudospectra are scaled such that their sum corresponds to the total ROA intensity, as shown in the upper part of Figure 10. In all spectra, the region up to 2000 cm^{-1} is enlarged by a factor of 20.

amide III band, resulting in a much stronger negative peak in the CTTM calculation. In addition, the ROA intensities of the octamer fragment can also be analyzed in terms of local modes. The resulting wavenumbers and ROA intensities of the localized modes are included in Table 1. A comparison shows that the localized mode intensities of the $(Ala)_{20}$ CTTM calculation are similar to the ones of the octamer fragment calculation. This is not surprising, since the property tensors of the fragment were used to reconstruct the corresponding property tensor derivatives of the complete helix. In conclusion, one would obtain correct ROA intensities if the localized mode intensities of the fragment and the large molecule were similar. However, our analysis shows that, even with the relatively large octamer fragment, this is not the case, in

particular for the central residues. Finally, we note that for the other bands in the ROA spectrum, similar observations could be made.

6. DISCUSSION AND CONCLUSION

By comparing the vibrational spectra reconstructed from small fragments to those from a full calculation, the accuracy of the CTTM has been investigated. For IR and Raman spectra, we find that the CTTM yields spectra which are generally in good agreement with the full calculation. However, we also find that for the vibrational frequencies of the individual normal modes, there are rather large deviations of 20 to 50 cm^{-1} , and in some

Table 1. Wavenumbers Ω_{ii} (in cm^{-1}) and ROA Intensities (in $10^{-3} \text{ \AA}^4/\text{amu}$) for the Amide III Localized Modes of the Full Calculation and the Intensity-Only CTTM Calculation on the $(\text{Ala})_{20}$ Helix and for the Amide III Localized Modes Obtained for the Octamer Fragment Used in the CTTM

residue	$(\text{Ala})_{20}$ helix			octamer	
	Ω_{ii}	ROA int. (full)	ROA int. (CTTM)	Ω_{ii}	ROA int. (full)
1	1225.7	1.87	9.84	1215.0	14.32
2	1198.6	-26.20	-26.58	1217.2	-23.43
3	1219.6	-18.22	-20.24	1218.9	-32.55
4	1250.0	-8.07	-19.30	1228.4	-23.94
5	1235.7	-5.41	-15.42	1239.5	-30.21
6	1228.5	10.71	3.16	1222.0	15.08
7	1237.0	-9.64	-9.27	1237.5	-27.05
8	1242.6	-10.42	-20.61	1225.0	44.62
9	1242.0	-6.85	-22.02		
10	1243.2	-12.93	-18.01		
11	1243.4	-12.62	-20.89		
12	1244.1	-13.95	-19.73		
13	1243.8	-18.18	-20.07		
14	1238.7	-19.76	-41.18		
15	1246.0	-20.44	-43.80		
16	1240.3	-20.43	-32.27		
17	1224.4	16.59	20.09		
18	1239.6	-14.72	-17.43		
19	1223.2	58.46	51.84		
20	1254.3	-14.38	-5.73		
20	1221.7	33.75	32.51		
sum		-110.86	-235.10		-63.16

problematic cases (such as the N–H stretching vibrations), even larger errors are found. The observation that these errors hardly affect the overall IR and Raman spectra can be understood through an analysis in terms of local modes: As was discussed in ref 32, the positions and total intensities of the bands observed in the IR and Raman spectra of polypeptides are determined by local properties (i.e., vibrational frequencies and intensities of localized modes). These local properties can be described adequately by small fragments. On the other hand, the coupling between local modes determines the observed band shapes. Some of these couplings (i.e., off-diagonal elements of the Hessian) are neglected in the CTTM, which affects the individual normal modes but leaves the overall band shapes unchanged, particularly if the nearest-neighbor couplings are included. However, for bands where the local mode properties are very dependent on the environment, such as the N–H stretching vibrations, or in regions that are very sensitive to changes in the coupling between different modes, such as the extended amide III region,³⁴ the approximations introduced by the CTTM show up as errors in the IR and Raman spectra.

For ROA spectroscopy, a different picture emerges. The CTTM spectra are strongly dependent on the size of the fragments. Even with the largest fragment used here, an octamer, the agreement of the CTTM ROA spectra with the full calculation is not satisfying. However, if the CTTM is applied only to the Hessian and not to the property tensor derivatives, a much better agreement with the full calculation is found. Thus, the

poor performance of the CTTM for ROA is due to the approximations introduced when calculating property tensor derivatives for smaller fragments. On the other hand, applying the CTTM to the Hessian and neglecting the vibrational coupling between some residues only has a minor effect. Revisiting the analysis of the ROA spectrum of $(\text{Ala})_{20}$ in terms of local modes³¹ helps to understand these errors. The comparison of the localized mode intensities from the CTTM to those from the full calculation clearly shows the reason for these errors. The localized ROA intensities of the octamer fragment are quite different compared to those of the larger $(\text{Ala})_{20}$ α -helix. Already in ref 31, it was found that the ROA intensities of the localized modes are very different for the terminal residues than for the central ones (see Tables in the Supporting Information of ref 31). Thus, because of the neglect of hydrogen bonding in the smaller fragments, the “local” ROA intensities can change significantly. Because this fragment is then used to reconstruct the complete $(\text{Ala})_{20}$ α -helix, wrong ROA intensities are obtained, and since the ROA intensities can even change sign, the effect on the overall spectra is more dramatic than in the case of CTTM-constructed IR and Raman spectra.

Of course, there are several details of our implementation of the CTTM and of its application that could be changed in order to attempt to improve on the present results. Most important, other choices would be possible for the small fragments. Instead of extracting their geometry from the full calculation, the small fragments could be constructed to resemble an idealized α -helix. Moreover, instead of fixing their geometry, the small fragments could be (at least partly) optimized. In their applications of the CTTM method, Bouř, Keiderling and co-workers mostly employed a geometry optimization in normal coordinates for the small fragments, in which the low frequency modes are kept fixed.¹⁰¹ Furthermore, our calculations used a single small fragment for reconstructing the whole α -helix. Instead, it would be possible to employ different small fragments for different parts of the helix. However, because the small fragments have to overlap, the additional computational cost for the calculations on the small fragments might then render the CTTM more expensive than a full calculation.

Another issue is the definition of the mapping between the atoms of the small fragment and the large molecule. For this, we tested two different options, either to include all atoms of the small fragment or to consider only those of the central residues (i.e., those where hydrogen bonding is accounted for and the electronic structure should be most similar to the one of the large molecule). Finally, if different small fragments (or different parts of the same fragment) can be employed in the reconstruction, there are different ways to decide which one is used. Here, we always choose the one that has the structure most similar to the large molecule. An average of all matching small fragments or a weighted average that prefers the central parts of the small fragment could be employed instead.

Carefully testing these different options might improve the agreement of the CTTM with the full calculations for ROA spectra. Nevertheless, this would also imply that the CTTM applied to ROA spectroscopy is very sensitive to the choice of these parameters. In conclusion, our analysis indicates that applying the CTTM for ROA spectra is strongly dependent on the details of how the CTTM is applied, most importantly on the size and structure of the small fragments. Therefore, many ROA results obtained previously with the CTTM will have to be re-evaluated carefully. It is particularly puzzling that the CTTM was

found to work well in direct comparison to the experiment (see references provided in the Introduction), which might point to a fortunate error compensation. If this is not the case, it might even be necessary to revise the conclusions previously drawn from such calculations. Moreover, it appears to be necessary to also investigate the reliability of the CTTM for the calculation of VCD spectra.

One solution to these problems could be to perform the calculations on the small fragments not for the isolated molecules but for embedded structures which feature an appropriate environment. A first step is to apply a continuum solvation model that could partly account for the effect of hydrogen bonding, as has already been done in applications of the CTTM (whether this is the reason for the high reliability previously reported remains to be shown). More accurate environment models, such as combined quantum mechanics/molecular mechanics (QM/MM) methods,^{102,103} have already been adopted for use in computational vibrational spectroscopy, for instance, in the mobile block Hessian method.^{42,43} Additionally, more advanced embedding approaches based on a subsystem formulation of DFT have been shown to provide an accurate description of the effect of hydrogen bonds.^{104,105} Combining the generalization of such methods to polypeptides and proteins¹⁰⁶ and to the subsystem calculation of polarizabilities^{107,108} could lead to accurate and efficient methods for the calculation of ROA spectra that go beyond the CTTM.

■ ASSOCIATED CONTENT

S Supporting Information. Detailed results of the validation of our CTTM implementation for L-alanine, coordinates of all considered molecules as well as the corresponding fragments, and further details of the CTTM calculations for (Ala)₂₀. This information is available free of charge via the Internet at <http://pubs.acs.org/>.

■ AUTHOR INFORMATION

Corresponding Author

*E-mail: christoph.jacob@kit.edu, markus.reiher@phys.chem.ethz.ch.

■ ACKNOWLEDGMENT

Financial support by the Swiss National Science Foundation (project no. 200020-132542/1) for the Zurich group and from the DFG-Center for Functional Nanostructures at KIT for C.R.J. is gratefully acknowledged. We also would like to acknowledge correspondence with Petr Bouř on the implementation of the CTTM and on the accuracy of CTTM ROA spectra when we discovered the discrepancies reported in this paper in 2010.

■ REFERENCES

- (1) Vass, E.; Hollosi, M.; Besson, F.; Buchet, R. *Chem. Rev.* **2003**, *103*, 1917–1954.
- (2) Barth, A. *Biochim. Biophys. Acta, Bioenerg.* **2007**, *1767*, 1073–1101.
- (3) Carey, P. R. *J. Biol. Chem.* **1999**, *274*, 26625–26628.
- (4) Thomas, G. J., Jr. *Biopolymers* **2002**, *67*, 214–225.
- (5) Holzwarth, G.; Hsu, E. C.; Mosher, H. S.; Faulkner, T. R.; Moscovitz, A. *J. Am. Chem. Soc.* **1974**, *96*, 251–252.
- (6) Keiderling, T. A. In *Circular Dichroism: Principles and Applications*, 2nd ed.; Berova, N.; Nakanishi, K.; Woody, R. W., Eds.; Wiley-VCH: New York, 2000; pp 621–666.

- (7) Silva, R. A. G. D.; Kubelka, J.; Bouř, P.; Decatur, S. M.; Keiderling, T. A. *Proc. Natl. Acad. Sci. U. S. A.* **2000**, *97*, 8318–8323.
- (8) Kubelka, J.; Silva, R. A. G. D.; Keiderling, T. A. *J. Am. Chem. Soc.* **2002**, *124*, 5325–5332.
- (9) Barron, L. D. *Molecular Light Scattering and Optical Activity*, 2nd ed.; Cambridge University Press: Cambridge, U. K., 2004; pp 327–381.
- (10) Barron, L. D.; Bogaard, M. P.; Buckingham, A. D. *J. Am. Chem. Soc.* **1973**, *95*, 603–605.
- (11) Hug, W.; Kint, S.; Bailey, G. F.; Scherer, J. R. *J. Am. Chem. Soc.* **1975**, *97*, 5589–5590.
- (12) Barron, L. D.; Hecht, L.; McColl, I. H.; Blanch, E. W. *Mol. Phys.* **2004**, *102*, 731–744.
- (13) Zhu, F.; Isaacs, N. W.; Hecht, L.; Tranter, G. E.; Barron, L. D. *Chirality* **2006**, *18*, 103–115.
- (14) Barron, L. D.; Buckingham, A. D. *Chem. Phys. Lett.* **2010**, *492*, 199–213.
- (15) Schweitzer-Stenner, R. *J. Raman Spectrosc.* **2001**, *32*, 711–732.
- (16) Asher, S. A.; Ianoul, A.; Mix, G.; Boyden, M. N.; Karnoup, A.; Diem, M.; Schweitzer-Stenner, R. *J. Am. Chem. Soc.* **2001**, *123*, 11775–11781.
- (17) Schweitzer-Stenner, R. *J. Raman Spectrosc.* **2005**, *36*, 276–278.
- (18) Huang, C.-Y.; Balakrishnan, G.; Spiro, T. G. *J. Raman Spectrosc.* **2006**, *37*, 277–282.
- (19) Hamm, P.; Lim, M.; Hochstrasser, R. M. *J. Phys. Chem. B* **1998**, *102*, 6123–6138.
- (20) Ganim, Z.; Chung, H. S.; Smith, A. W.; DeFlores, L. P.; Jones, K. C.; Tokmakoff, A. *Acc. Chem. Res.* **2008**, *41*, 432–441.
- (21) Zhuang, W.; Hayashi, T.; Mukamel, S. *Angew. Chem., Int. Ed.* **2009**, *48*, 3750–3781.
- (22) Polfer, N. C.; Oomens, J.; Suhai, S.; Paizs, B. *J. Am. Chem. Soc.* **2007**, *129*, 5887–5897.
- (23) Lagutschenkov, A.; Langer, J.; Berden, G.; Oomens, J.; Dopfer, O. *J. Phys. Chem. A* **2010**, *114*, 13268–13276.
- (24) Rossi, M.; Blum, V.; Kupser, P.; von Helden, G.; Bierau, F.; Pagel, K.; Meijer, G.; Scheffler, M. *J. Phys. Chem. Lett.* **2010**, *1*, 3465–3470.
- (25) Rizzo, T. R.; Stearns, J. A.; Boyarkin, O. V. *Int. Rev. Phys. Chem.* **2009**, *28*, 481.
- (26) Nagornova, N. S.; Rizzo, T. R.; Boyarkin, O. V. *J. Am. Chem. Soc.* **2010**, *132*, 4040–4041.
- (27) Herrmann, C.; Reiher, M. *Top. Curr. Chem.* **2007**, *268*, 85–132.
- (28) Hug, W. *Chem. Phys.* **2001**, *264*, 53–69.
- (29) Jacob, Ch. R.; Reiher, M. *J. Chem. Phys.* **2009**, *130*, 084106.
- (30) Hug, W.; Fedorovsky, M. *Theor. Chem. Acc.* **2008**, *119*, 113–131.
- (31) Jacob, Ch. R.; Luber, S.; Reiher, M. *Chem.—Eur. J.* **2009**, *15*, 13491–13508.
- (32) Jacob, Ch. R.; Luber, S.; Reiher, M. *J. Phys. Chem. B* **2009**, *113*, 6558–6573.
- (33) Liégeois, V.; Jacob, Ch. R.; Champagne, B.; Reiher, M. *J. Phys. Chem. A* **2010**, *114*, 7198–7212.
- (34) Weymuth, T.; Jacob, Ch. R.; Reiher, M. *J. Phys. Chem. B* **2010**, *114*, 10649–10660.
- (35) Reiher, M.; Neugebauer, J. *J. Chem. Phys.* **2003**, *118*, 1634–1641.
- (36) Reiher, M.; Neugebauer, J. *Phys. Chem. Chem. Phys.* **2004**, *6*, 4621–4629.
- (37) Herrmann, C.; Neugebauer, J.; Reiher, M. *New J. Chem.* **2007**, *31*, 818–831.
- (38) Kiewisch, K.; Neugebauer, J.; Reiher, M. *J. Chem. Phys.* **2008**, *129*, 204103.
- (39) Kiewisch, K.; Luber, S.; Neugebauer, J.; Reiher, M. *Chimia* **2009**, *63*, 270–274.
- (40) Luber, S.; Neugebauer, J.; Reiher, M. *J. Chem. Phys.* **2009**, *130*, 064105.
- (41) Luber, S.; Reiher, M. *ChemPhysChem* **2009**, *10*, 2049–2057.
- (42) Ghysels, A.; Van Neck, D.; Van Speybroeck, V.; Verstraelen, T.; Waroquier, M. *J. Chem. Phys.* **2007**, *126*, 224102.
- (43) Ghysels, A.; Van Neck, D.; Brooks, B. R.; Van Speybroeck, V.; Waroquier, M. *J. Chem. Phys.* **2009**, *130*, 084107.

- (44) Bouř, P.; Sopková, J.; Bednářová, L.; Maloň, P.; Keiderling, T. A. *J. Comput. Chem.* **1997**, *18* (5), 646–659.
- (45) Bouř, P.; Zaruba, K.; Urbanova, M.; Setnicka, V.; Matejka, P.; Fiedler, Z.; Kral, V.; Volka, K. *Chirality* **2000**, *12*, 191–198.
- (46) Kubelka, J.; Keiderling, T. *J. Am. Chem. Soc.* **2001**, *123*, 6142–6150.
- (47) Mazaleyrat, J.; Wright, K.; Gaucher, A.; Wakselman, M.; Oancea, S.; Formaggio, F.; Toniolo, C.; Setnicka, V.; Kapitan, J.; Keiderling, T. *Tetrahedron: Asymmetry* **2003**, *14*, 1879–1893.
- (48) Huang, R.; Setnicka, V.; Etienne, M. A.; Kim, J.; Kubelka, J.; Hammer, R. P.; Keiderling, T. A. *J. Am. Chem. Soc.* **2007**, *129*, 13592–13603.
- (49) Grahnen, J. A.; Amunson, K. E.; Kubelka, J. *J. Phys. Chem. B* **2010**, *114*, 13011–13020.
- (50) Bouř, P.; Kapitan, J.; Baumruk, V. *J. Phys. Chem. A* **2001**, *105*, 6362–6368.
- (51) Bouř, P.; McCann, J.; Wieser, H. *J. Phys. Chem. A* **1997**, *101*, 9783–9790.
- (52) Bouř, P.; McCann, J.; Wieser, H. *J. Phys. Chem. A* **1998**, *102*, 102–110.
- (53) Bouř, P.; Kubelka, J.; Keiderling, T. *Biopolymers* **2000**, *53*, 380–395.
- (54) Kubelka, J.; Keiderling, T. *J. Am. Chem. Soc.* **2001**, *123*, 12048–12058.
- (55) Hilaro, J.; Kubelka, J.; Syud, F.; Gellman, S.; Keiderling, T. *Biopolymers* **2002**, *67*, 233–236.
- (56) Andrushchenko, V.; Wieser, H.; Bouř, P. *J. Phys. Chem. B* **2002**, *106*, 12623–12634.
- (57) Hilaro, J.; Kubelka, J.; Keiderling, T. *J. Am. Chem. Soc.* **2003**, *125*, 7562–7574.
- (58) Huang, R.; Kubelka, J.; Barber-Armstrong, W.; Silva, R.; Decatur, S.; Keiderling, T. *J. Am. Chem. Soc.* **2004**, *126*, 2346–2354.
- (59) Andrushchenko, V.; Wieser, H.; Bouř, P. *J. Phys. Chem. B* **2004**, *108*, 3899–3911.
- (60) Bouř, P.; Keiderling, T. *J. Phys. Chem. B* **2005**, *109*, 5348–5357.
- (61) Setnicka, V.; Huang, R.; Thomas, C.; Etienne, M.; Kubelka, J.; Hammer, R.; Keiderling, T. *J. Am. Chem. Soc.* **2005**, *127*, 4992–4993.
- (62) Kubelka, J.; Huang, R.; Keiderling, T. *J. Phys. Chem. B* **2005**, *109*, 8231–8243.
- (63) Bouř, P.; Andrushchenko, V.; Kabelac, M.; Maharaj, V.; Maharaj, V. *J. Phys. Chem. B* **2005**, *109*, 20579–20587.
- (64) Bouř, P.; Keiderling, T. *J. Phys. Chem. B* **2005**, *109*, 23687–23697.
- (65) Kim, J.; Huang, R.; Kubelka, J.; Bouř, P.; Keiderling, T. A. *J. Phys. Chem. B* **2006**, *110*, 23590–23602.
- (66) Turner, D. R.; Kubelka, J. *J. Phys. Chem. B* **2007**, *111*, 1834–1845.
- (67) Kapitan, J.; Baumruk, V.; Bouř, P. *J. Am. Chem. Soc.* **2006**, *128* (7), 2438–2443.
- (68) Zhu, F.; Kapitan, J.; Tranter, G. E.; Pudney, P. D. A.; Isaacs, N. W.; Hecht, L.; Barron, L. D. *Proteins* **2008**, *70*, 823–833.
- (69) Budesinsky, M.; Sebestik, J.; Bednarova, L.; Baumruk, V.; Safarik, M.; Bouř, P. *J. Org. Chem.* **2008**, *73*, 1481–1489.
- (70) Kapitan, J.; Zhu, F.; Hecht, L.; Gardiner, J.; Seebach, D.; Barron, L. D. *Angew. Chem., Int. Ed.* **2008**, *47*, 6392–6394.
- (71) Budesinsky, M.; Danecek, P.; Bednarova, L.; Kapitan, J.; Baumruk, V.; Bouř, P. *J. Phys. Chem. A* **2008**, *112*, 8633–8640.
- (72) Sebek, J.; Kapitan, J.; Sebestik, J.; Baumruk, V.; Bouř, P. *J. Phys. Chem. A* **2009**, *113* (27), 7760–7768.
- (73) Hudcová, J.; Kapitan, J.; Baumruk, V.; Hammer, R. P.; Keiderling, T. A.; Bouř, P. *J. Phys. Chem. A* **2010**, *114*, 7642–7651.
- (74) Yamamoto, S.; Straka, M.; Watarai, H.; Bouř, P. *Phys. Chem. Chem. Phys.* **2010**, *12*, 11021–11032.
- (75) Herrmann, C.; Ruud, K.; Reiher, M. *ChemPhysChem* **2006**, *7*, 2189–2196.
- (76) Jacob, Ch. R.; Lubner, S.; Reiher, M. *ChemPhysChem* **2008**, *9*, 2177–2180.
- (77) Lubner, S.; Reiher, M. *J. Phys. Chem. B* **2010**, *114*, 1057–1063.
- (78) Lubner, S.; Reiher, M. *Chem. Phys.* **2008**, *346*, 212–223.
- (79) Quinet, O.; Champagne, B. *J. Chem. Phys.* **2001**, *115*, 6293–6299.
- (80) Rappoport, D.; Furche, F. *J. Chem. Phys.* **2005**, *122*, 064105.
- (81) Quinet, O.; Liegeois, V.; Champagne, B. *J. Chem. Theory Comput.* **2005**, *1*, 444–452.
- (82) Liegeois, V.; Ruud, K.; Champagne, B. *J. Chem. Phys.* **2007**, *127*, 204105.
- (83) Ruud, K.; Thorvaldsen, A. J. *Chirality* **2009**, *21*, E54–E67.
- (84) Bast, R.; Ekström, U.; Gao, B.; Helgaker, T.; Ruud, K.; Thorvaldsen, A. J. *Phys. Chem. Chem. Phys.* **2011**, *13*, 2627.
- (85) Altmann, S. L. *Rotations, Quaternions and Double Groups*; Oxford University Press: New York, 1986; pp 201–223.
- (86) Kearsly, S. K. *J. Comput. Chem.* **1990**, *11* (10), 1187–1192.
- (87) Kneller, G. R. *Mol. Simul.* **1991**, *7*, 113–119.
- (88) Neugebauer, J.; Reiher, M.; Kind, C.; Hess, B. A. *J. Comput. Chem.* **2002**, *23*, 895–910.
- (89) SNF 4.0.0 program for the quantum chemical calculation of vibrational spectra. Neugebauer, J.; Herrmann, C.; Lubner, S.; Reiher, M. www.reiher.ethz.ch/software/snf (accessed Apr 04, 2011).
- (90) Turbomole. Ahlrichs, R. <http://www.turbomole.com> (accessed Apr 04, 2011).
- (91) Perdew, J. P. *Phys. Rev. B* **1986**, *33*, 8822–8824.
- (92) Becke, A. D. *Phys. Rev. A* **1988**, *38*, 3098–3100.
- (93) Schäfer, A.; Huber, C.; Ahlrichs, R. *J. Chem. Phys.* **1994**, *100*, 5829–5835.
- (94) Turbomole basis set library. <ftp://ftp.chemie.uni-karlsruhe.de/pub/basen> (accessed Apr 04, 2011).
- (95) Turbomole auxiliary basis sets. <ftp://ftp.chemie.uni-karlsruhe.de/pub/jbasen> (accessed Apr 04, 2011).
- (96) Eichkorn, K.; Treutler, O.; Öhm, H.; Häser, M.; Ahlrichs, R. *Chem. Phys. Lett.* **1995**, *240*, 283–289.
- (97) PyVib2, a program for analyzing vibrational motion and vibrational spectra. Fedorovsky, M. <http://pyvib2.sourceforge.net> (accessed Apr 04, 2011).
- (98) Oboodi, M. R.; Alva, C.; Diem, M. *J. Phys. Chem.* **1984**, *88*, 501–505.
- (99) Diem, M.; Lee, O.; Roberts, G. M. *J. Phys. Chem.* **1992**, *96*, 548–554.
- (100) Lubner, S.; Herrmann, C.; Reiher, M. *J. Phys. Chem. B* **2008**, *112*, 2218–2232.
- (101) Bouř, P.; Keiderling, T. A. *J. Chem. Phys.* **2002**, *117*, 4126–4132.
- (102) Senn, H.-M.; Thiel, W. *Top. Curr. Chem.* **2007**, *268*, 173–290.
- (103) Senn, H. M.; Thiel, W. *Angew. Chem., Int. Ed.* **2009**, *48*, 1198–1229.
- (104) Jacob, Ch. R.; Neugebauer, J.; Jensen, L.; Visscher, L. *Phys. Chem. Chem. Phys.* **2006**, *8*, 2349–2359.
- (105) Kiewisch, K.; Eickerling, G.; Reiher, M.; Neugebauer, J. *J. Chem. Phys.* **2008**, *128*, 044114.
- (106) Jacob, Ch. R.; Visscher, L. *J. Chem. Phys.* **2008**, *128*, 155102.
- (107) Neugebauer, J. *J. Chem. Phys.* **2009**, *131*, 084104.
- (108) Neugebauer, J.; Curutchet, C.; Munoz-Losa, A.; Mennucci, B. *J. Chem. Theory Comput.* **2010**, *6*, 1843–1851.

TD-DFT Vibronic Couplings in Anthraquinones: From Basis Set and Functional Benchmarks to Applications for Industrial Dyes

Denis Jacquemin,^{*,†} Eric Brémond,[‡] Aurélien Planchat,[†] Ilaria Ciofini,[‡] and Carlo Adamo^{*,‡}

[†]Laboratoire CEISAM - UMR CNR 6230, Université de Nantes, 2 Rue de la Houssinière, BP 92208, 44322 Nantes Cedex 3, France

[‡]Ecole Nationale Supérieure de Chimie de Paris, Laboratoire LECIME, UMR CNRS-ENSCP no. 7575, 11, rue Pierre et Marie Curie, F-75321 Paris Cedex 05, France

 Supporting Information

ABSTRACT: Vibrationally resolved absorption spectra of a series of anthraquinoidic dyes have been obtained with a polarizable continuum model time-dependent density functional theory approach. Firstly, we assessed the impact of the atomic basis set on both the transition energies and the vibronic shapes of 1,4-NH₂-anthraquinone using a large panel of Pople's basis sets, up to the 6-311++G(3df,3pd). In a second stage, an extensive functional benchmark has been performed to determine an adequate approach for the same compound. In the third step, a complete analysis of the origin of the band shape was performed for the same derivative. In the fourth stage, a set of functionals has been applied to investigate the position isomers in the dihydroxy anthraquinone series. Finally, in a last phase, the methodology has been used for three dyes of technological interest. It turns out that the chosen basis set has a relatively limited impact on the computed transition energies as well as the topology of the vibronic shape, but both are significantly influenced by the selected functional. In the present case, no single functional simultaneously provides highly accurate positions and intensities of the different bands, but ω B97XD appears to be a good compromise. This analysis allows to rationalize the difference in shapes experimentally noticed for the visible band of apparently similar anthraquinones.

1. INTRODUCTION

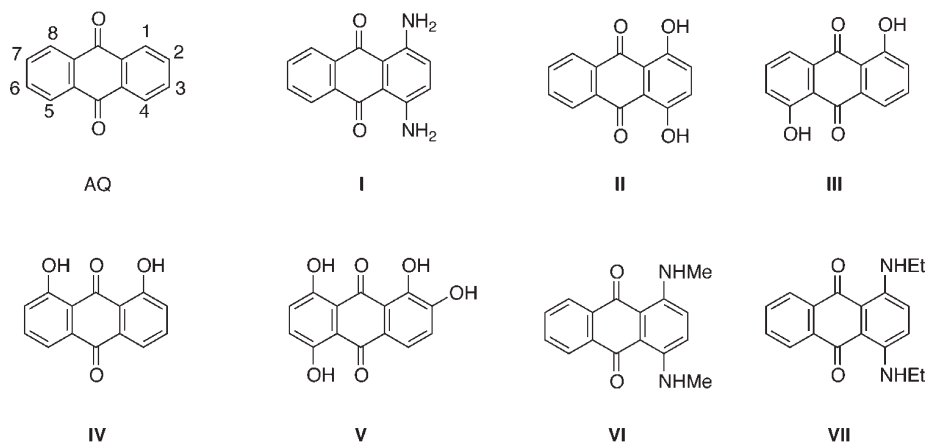
Commonly referred to as anthraquinone (AQ), 9,10-anthraquinone is composed of three fused aromatic rings, the central entity bearing two carbonyl groups (see Scheme 1). AQ derivatives are essential building blocks in several fields,^{1–4} but the most common application of AQ compounds remains the dyeing of both natural and synthetic fibers. Indeed, substituted AQ may provide a complete and tunable panel of vivid colors if the auxochroms placed in positions 1–8 of the central core (see Scheme 1) are adequately selected.^{5–10} Together with the existence of straightforward synthetic pathways and their thermal stability, the broad color palette explains why AQ dyes represent about one-fourth of today's organic world production of dyes.^{6,8,11–18} The most simple anthraquinoidic dyes present an intense bell-shaped and structureless visible band, and the typical structure–property relationships used in color chemistry can be applied to adequately predict their absorption wavelength.⁵ However, if two or more hydrogen-bond donors (typically alcohols or amines) are grafted in positions 1, 4, 5, or 8, strong interactions with the carbonyl groups play a key role and modify the properties of both the ground and the excited states. Consequently, the visible band of these AQ derivatives often features a characteristic multipeak structure.^{5,7,8,13,19} The origin of multiple absorption maxima in quinoidic dyes is not necessarily unique, and proposals to explain this effect include aggregation,²⁰ tautomeric equilibrium,^{21–23} and vibrational effects.^{24,25} As we will demonstrate in this contribution, the latter explanation is by far the most appropriate for neutral AQ.

While there are numerous specific theoretical investigations aiming to simulate the absorption spectra of AQ dyes, only a few

have focused on a large set of compounds in a way to obtain statistically relevant conclusions.^{26–33} Without performing a detailed description of these previous studies, it turns out that time-dependent density functional theory (TD-DFT), within the popular vertical approximation is generally a (very) adequate tool to predict the λ_{\max} of AQ derivatives but is obviously less accurate for the dyes presenting multiple absorption bands, e.g., the TD-DFT errors are larger for 1,4-NH₂-AQ (I in Scheme 1) than for 2-OH-AQ.²⁸ In this contribution, we aim to accurately simulate the absorption spectra of I as well as other challenging amino- and hydroxy-AQ presenting a structured visible band. To this end, we have to evaluate the vibronic couplings, in order to pinpoint one or more vibrational modes that hook up with the electronic transition and induce the experimentally observed specific shape of the visible band. To perform such task, one needs to calculate the Hessian of both the ground state and relevant (generally first) singlet excited state. While the first task is straightforward for molecules including a few dozen of atoms, the second job remains extremely challenging as the only available analytic method is the gas-phase configuration interaction singles (CIS) approach.³⁴ It is well-known that the quality of the CIS geometries for well-behaved excited states is comparable to its HF counterpart for the ground state, i.e., CIS is only sufficient if a qualitative picture is sought for.³⁵ In addition, CIS presents drawbacks to evaluate solvatochromic shifts.³⁶ To improve the accuracy of the simulations, one needs to include electron correlation. In practice, this can be done with TD-DFT. The first TD-DFT derivatives (gradients) allowing to

Received: April 15, 2011

Published: May 10, 2011

Scheme 1. Representation of the Systems Investigated Herein^a

^aFor the generic anthraquinone (AQ), the numbering of substitution positions is also given.

Table 1. Basis Set Effects on the Ground and Excited-state of I.^a

basis set	ground state						excited state						vibronic			
	PG	$d_{C=O}$	d_{C-N}	d_{Hbond}	λ_{vert} (f)	ZPVE	PG	$d_{C=O}$	d_{C-N}	d_{Hbond}	λ_{vert} (f)	ZPVE	ΔG	P_1^{conv} (I_r)	P_2^{conv} (I_r)	P_3^{conv} (I_r)
STO-3G	C_{2v}	1.312	1.360	1.280	527 (0.23)	6.10	C_s	1.310	1.397	1.372	667 (0.11)	6.08	2.12	517 (1.00)	429 (0.34)	367 (0.20)
6-31G	C_{2v}	1.273	1.356	1.791	520 (0.27)	5.97	C_{2v}	1.279	1.354	1.746	578 (0.26)	5.90	2.17	561 (1.00)	524 (0.61)	
6-31G(d)	C_s	1.242	1.354	1.822	516 (0.24)	5.87	C_s	1.249	1.348	1.761	590 (0.24)	5.80	2.13	561 (1.00)	527 (0.78)	
6-31+G(d)	C_s	1.245	1.353	1.828	521 (0.26)	5.83	C_{2v}	1.251	1.348	1.769	587 (0.26)	5.78	2.23	550 (0.92)	523 (1.00)	
6-31++G(d,p)	C_{2v}	1.245	1.352	1.813	521 (0.26)	5.83	C_{2v}	1.252	1.347	1.749	587 (0.26)	5.77	2.17	559 (1.00)	527 (0.88)	
6-31++G(2d,2p)	C_s	1.240	1.352	1.808	521 (0.25)	5.83	C_s	1.247	1.345	1.739	592 (0.24)	5.76	2.13	564 (1.00)	530 (0.79)	
6-311G(d)	C_s	1.237	1.351	1.844	520 (0.25)	5.84	C_{2v}	1.243	1.345	1.785	591 (0.24)	5.78	2.14	561 (1.00)	528 (0.85)	464 (0.18)
6-311+G(d)	C_s	1.238	1.352	1.845	518 (0.26)	5.83	C_s	1.245	1.347	1.786	589 (0.25)	5.77	2.12	561 (1.00)	527 (0.81)	
6-311++G(d,p)	C_s	1.238	1.352	1.823	519 (0.26)	5.81	C_s	1.246	1.347	1.758	592 (0.25)	5.75	2.15	562 (1.00)	528 (0.81)	
6-311+G(2d,p)	C_s	1.238	1.351	1.811	519 (0.25)	5.82	C_s	1.246	1.344	1.742	596 (0.24)	5.76	2.14	563 (1.00)	529 (0.82)	
6-311++G(2d,2p)	C_s	1.238	1.352	1.815	518 (0.25)	5.83	C_s	1.245	1.344	1.746	595 (0.24)	5.76	2.13	563 (1.00)	529 (0.82)	
6-311++G(2df,2pd)	C_{2v}	1.237	1.348	1.812	520 (0.25)	5.82	C_s	1.244	1.342	1.739	590 (0.25)	5.76	2.17	556 (1.00)	526 (0.97)	
6-311++G(3df,3pd)	C_{2v}	1.236	1.348	1.810	521 (0.25)	5.79	C_s	1.243	1.342	1.738	591 (0.24)	5.74	2.13	558 (1.00)	528 (0.94)	

^aPoint group (PG), selected distances (in Å), vertical transition energies (in nm) and zero-point vibrational energies (ZPVE in eV) are reported. The positions and relative intensities of the vibronic peaks (P_i^{conv}) obtained after convolution with a 0.05 eV fwhm Gaussian as well as the difference of Gibbs energies (ΔG , in eV) are also given. All results use a PCM(cyclohexane)-PBE0 approach.

optimize the excited-state geometries are available since the seminal work of van Caillie and Amos³⁷ and the subsequent extensions and improvements.^{38–40} An extra advantage of TD-DFT, compared to more refined electron correlated wave function theories is the possibility to include bulk solvation effects during excited-state force minimizations, through the use of dielectric approximations, typically the polarizable continuum model (PCM).^{40,41} Though PCM-TD-DFT vibronic simulations are becoming more and more popular,^{25,42–50} they remain at the border of today's computational possibilities, as a numerical differentiation of the gradients is a prerequisite to obtain the excited-state Hessian, and therefore to simulate the vibronic spectrum. Therefore, PCM-TD-DFT calculations are generally applied to relatively compact (or symmetric) molecules using a predefined approach (basis set/functional) in order to limit the computational burden. For the first time, we tackle the vibronic spectra of AQ dyes, and we start with a complete benchmark work. In this framework, we have to highlight the key work of Dierksen and Grimme,³⁹ who computed (in the gas phase)

the structured bands of a large set of molecules, principally fused aromatic, using three functionals. To the best of our knowledge, this 2004 paper that concluded that ca. 30–50% of exact exchange was optimal to reproduce experimental band shapes stands as the most complete vibronic benchmark to date.

This paper is organized as follows. In Section 2, we describe our computational protocol. In Sections 3.1 and 3.2, we investigate the basis set and functionals effects for I. Section 3.3 provides an in-depth analysis for this specific dye, whereas Section 3.4 gives the vibronic spectra of three dihydroxy AQ. In Section 3.5, we report vibrationally resolved spectra for selected “real-life” dyes, and eventually, we conclude.

2. METHOD

All our calculations have been performed with the Gaussian09⁵¹ program, using default thresholds and algorithms except when noted. We have selected a large set of atomic basis

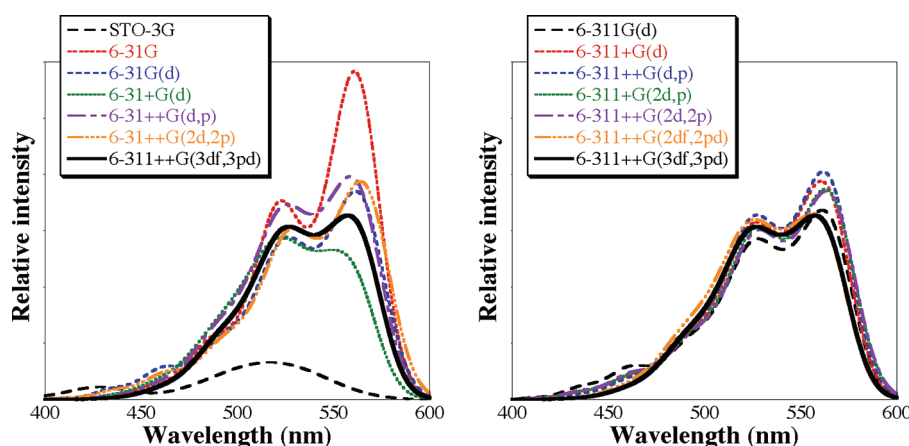


Figure 1. Comparison of the obtained vibronic shapes for system I using double- ζ (left) and triple- ζ (right) basis sets. In both cases, the reference 6-311++G(3df,3pd) black curve appears in bold.

sets (ABS) and DFT functionals: SVWN5,^{52,53} BLYP,^{54,55} PBE,⁵⁶ τ -HCTH,⁵⁷ O3LYP,⁵⁸ B3LYP,^{59,60} X3LYP,⁶¹ PBE0,^{62,63} M06,⁶⁴ BMK,⁶⁵ BHHLYP,⁶⁶ M06-2X,⁶⁷ M06-HF,⁶⁴ CAM-B3LYP,⁶⁸ LC-PBE,^{69,70} ω B97,⁷¹ ω B97X,⁷¹ and ω B97XD⁷² to perform benchmarks for I, and we redirect the reader to these original references for complete description of these functionals. Though we have used the popular Pople's ABS in this paper, other possibilities, such as Jensen $pc-n$ ⁷³ ABS could have been selected as well. The ground-state (excited-state) geometries have first been optimized with DFT (TD-DFT) until the residual mean square forces are smaller than 1×10^{-5} au (tight threshold). Next, the vibrational frequencies have been computed analytically (numerically) for the S_0 (S_1) state. They confirmed the presence of minima characterized by the absence of imaginary modes (and transition states characterized by a single imaginary mode). In several cases, we have performed both force and frequency calculations using two or three point groups (PG) in order to ascertain the symmetry of all states. During all calculation steps, we have included bulk solvent effects by using the PCM⁴¹ that correctly models the major solvent effects as long as no specific solute–solvent interactions are implied. Several solvents have been used (see below), but we have mainly selected an aprotic apolar solvent, so that the selection of the PCM model is fully legitimate. Vibrationally resolved spectra within the harmonic approximation were computed using the FCclasses program.^{42,44,45} The reported spectra have been simulated at 298.15 K using a convoluting Gaussian functions presenting a full width at half-maximum (fwhm) of 0.05 eV during benchmark investigations. In other cases, the fwhm was adjusted according to the available experimental data as in ref 39. A maximal number of 25 overtones for each mode and 20 combination bands on each pair of modes were included in the calculation. The maximum number of integrals to be computed for each class was set to 1×10^6 .

3. RESULTS AND DISCUSSION

3.1. Basis Set Investigation. For I, the results of the ABS investigation can be found in Table 1, whereas Figure 1 compares the corresponding vibronic shapes.⁷⁴ Separate representations of the stick and convoluted spectra, using a tighter Gaussian for convolution, can be found in the Supporting Information. We have used an uniform PCM-PBE0 method since global hybrids, and more specifically B3LYP and PBE0, have been found

efficient within the vertical PCM-TD-DFT approximation for AQ dyes.^{27,28} To the best of our knowledge, there are no previous investigations aiming at assessing the influence of the size of the chosen ABS on the shape of the vibronic bands of real-life molecules. This is certainly understandable, because computing numerically the vibrational TD-DFT spectrum is a very demanding task (several months of CPU for the largest ABS used here). Therefore, most TD-DFT benchmarks available in the literature^{31–33,75–83} have been performed in the vertical model, whereas the studies also optimizing the excited-state geometries performed by Grimme and co-workers used a given basis set,^{39,78,82} typically TZVP, a diffuseless triple- ζ ABS to determine the geometrical and vibrational parameters.

As can be seen in Table 1, the point groups of the ground and excited states are affected by the chosen ABS, the amino groups being perfectly coplanar to the AQ core (C_{2v}) or not (C_s). In the X-ray diffraction (XRD) structure⁸⁴ available for the dihydrate form of I, the amine groups are almost fully flat (torsion angles of ca. $2-3^\circ$), but they interact with water molecules, making straightforward comparisons with our cyclohexane simulations uneasy. In the XRD structure we obtained (see the cif file in Supporting Information and discussion below), the deviation of the amino groups is also trifling (ca. 4°). The energetic variations related to this change of PG are however limited, e.g., for 6-31G(d), the C_{2v} structures are, respectively, only 0.2 and 1.0 kcal·mol⁻¹ less stable than the true C_s minima for the S_0 and S_1 states. In that sense, the obtained PG is probably not the most important discriminating factor. For I, it is striking that the ABS effects on the spectral properties are quite limited, as all selected Pople's basis leads to similar results, except for the two smallest that lack polarization functions. Even the compact 6-31G(d) provides vertical transition wavelengths and positions of the vibronic bands within 5 nm of the results obtained with 6-311++G(3df,3pd). The zero-point vibrational energy (ZPVE) computed for the ground and excited states are also nearly ABS independent, and the same holds for the small ZPVE decrease (ca. 0.05 eV) related to the $S_0 \rightarrow S_1$ transition. These findings may probably be quite specific to AQ dyes,²⁷ and we do not advocate to systematically use 6-31G(d) for TD-DFT calculations. As expected, the most sensitive geometrical parameter is the hydrogen bond (H-bond) distance between the carbonyl and the amine, that is significantly shortened when diffuse functions are added on both carbon and hydrogen atoms.

Table 2. Functional Benchmarks Obtained Using System I^a

functional	ground state						excited state						vibronic			
	PG	$d_{C=O}$	d_{C-N}	d_{Hbond}	λ_{vert} (f)	ZPVE	PG	$d_{C=O}$	d_{C-N}	d_{Hbond}	λ_{vert} (f)	ZPVE	ΔG	P_1^{conv} (I_r)	P_2^{conv} (I_r)	P_3^{conv} (I_r)
SVWNS	C_{2v}	1.264	1.343	1.630	611 (0.21)	5.65	C_s	1.267	1.346	1.602	670 (0.18)	5.57	1.85	650 (1.00)	520 (0.09)	449 (0.00)
BLYP	C_{2v}	1.271	1.369	1.813	617 (0.20)	5.59	C_s	1.273	1.375	1.790	698 (0.17)	5.53	1.85	653 (1.00)	524 (0.21)	439 (0.01)
PBE	C_{2v}	1.267	1.360	1.769	614 (0.20)	5.62	C_s	1.270	1.367	1.741	692 (0.17)	5.56	1.87	647 (1.00)	518 (0.21)	439 (0.01)
τ -HCTH	C_{2v}	1.257	1.353	1.770	605 (0.21)	5.68	C_{2v}	1.260	1.359	1.743	681 (0.18)	5.63	1.92	638 (1.00)	511 (0.25)	428 (0.02)
O3LYP	C_s	1.250	1.357	1.836	561 (0.22)	5.76	C_s	1.254	1.359	1.803	646 (0.20)	5.71	2.06	592 (1.00)		
B3LYP	C_{2v}	1.251	1.360	1.835	536 (0.25)	5.77	C_{2v}	1.257	1.356	1.781	603 (0.25)	5.71	2.12	573 (1.00)	543 (0.95)	
X3LYP	C_{2v}	1.250	1.359	1.834	531 (0.25)	5.78	C_{2v}	1.257	1.354	1.778	598 (0.25)	5.73	2.14	568 (1.00)	537 (0.95)	
PBE0	C_{2v}	1.245	1.352	1.813	521 (0.26)	5.83	C_{2v}	1.252	1.347	1.749	587 (0.26)	5.77	2.17	559 (1.00)	527 (0.88)	
M06	C_s	1.242	1.357	1.850	514 (0.26)	5.78	C_{2v}	1.250	1.351	1.793	584 (0.26)	5.73	2.23	548 (0.98)	520 (1.00)	
BMK	C_{2v}	1.236	1.358	1.884	482 (0.29)	5.85	C_{2v}	1.246	1.348	1.801	558 (0.28)	5.79	2.37	491 (1.00)		
BHHLYP	C_s	1.230	1.356	1.870	445 (0.32)	6.02	C_{2v}	1.244	1.339	1.773	529 (0.31)	5.96	2.48	487 (0.84)	461 (1.00)	
M06-2X	C_s	1.236	1.360	1.888	465 (0.29)	5.84	C_{2v}	1.250	1.345	1.782	548 (0.29)	5.77	2.36	508 (0.89)	482 (1.00)	
M06-HF	C_{2v}	1.227	1.358	1.881	415 (0.34)	5.87	C_{2v}	1.252	1.331	1.669	538 (0.32)	5.77	2.56	443 (1.00)		
CAM-B3LYP	C_{2v}	1.241	1.357	1.844	470 (0.31)	5.85	C_{2v}	1.254	1.345	1.749	549 (0.30)	5.81	2.43	477 (1.00)		
ω B97	C_s	1.239	1.367	1.891	421 (0.34)	5.89	C_{2v}	1.256	1.345	1.771	520 (0.32)	5.83	2.57	441 (1.00)		
ω B97X	C_s	1.238	1.362	1.876	438 (0.33)	5.89	C_{2v}	1.253	1.344	1.764	527 (0.32)	5.83	2.52	454 (1.00)		
ω B97XD	C_s	1.240	1.359	1.856	467 (0.31)	5.86	C_{2v}	1.252	1.346	1.758	546 (0.30)	5.81	2.39	505 (0.90)	479 (1.00)	
LC-PBE	C_{2v}	1.229	1.347	1.817	415 (0.36)	5.97	C_{2v}	1.246	1.328	1.673	514 (0.34)	5.93	2.65	431 (1.00)		

^a All results use a PCM(cyclohexane)-(TD-)DFT/6-31++G(d,p) level of theory, see Table 1 for more details.

For the carbonyl bond, going from a double- ζ to a triple- ζ ABS decreases its length by ca. 0.01 Å, but this effect is constant for both S_0 and S_1 states. At the exception of the 6-31+G(d), all double- ζ and triple- ζ basis sets predict that the longest wavelength peak is slightly more intense than its short-wavelength counterpart. As a compromise ABS in the following, we have selected 6-31++G(d,p) that presents both polarization and diffuse orbitals on all atoms and delivers relative intensities for the vibronic bands relatively close to the 6-311++G(3df,3pd) reference. Of course other basis sets, e.g., 6-311+G(d), could have been reasonable choices.

3.2. Functional Benchmark. The results obtained for 18 functionals are summarized in Table 2, whereas representations of the vibronic shapes may be found in Figure 2 as well as in the Supporting Information. Obviously, the selected functional impacts significantly on the computed $S_0 \rightarrow S_1$ ΔG and the corresponding transition energies, that tend to increase when more exact exchange is plugged in an expected trend for $\pi-\pi^*$ transitions (see previous benchmarks).^{31,32,39,77,82} The predicted elongation of the carbonyl group upon electronic transition is also dependent on the DFT/HF blend, as it tends to increase when larger shares of exact exchange are applied. Even more striking are the evolutions of the C–N and H-bond distances induced by photon absorption. The former lengthens with the four pure functionals and O3LYP but shortens with all other functionals, an effect that is much larger with M06-HF (–0.027 Å) or LC-PBE (–0.019 Å) than with B3LYP (–0.004 Å). The H-bond distance is smaller in the S_1 than S_0 state but with a variation that is not a simple function of the exact exchange mixing parameter(s).

In ref 82, the authors have computed the geometries (and hence the ZPVE energies) at the PBE/TZVP level but selected a much larger basis set and a wide panel of functionals for determining the vertical transition energies. It is indeed common to use a given geometry and to benchmark the transition

energies, a procedure that we have also used several times,^{32,33,83,85} as the geometry optimization process may be time-consuming. For the ZPVE, the results listed in Table 2 justify such an approach: the PBE $S_0 \rightarrow S_1$ ZPVE shift is –0.08 eV, whereas B3LYP and ω B97XD estimates are relatively close, –0.06 and –0.05 eV, respectively. Therefore the implied error is negligible. For the vertical transitions, the impact of using a given geometry is apparently larger. Indeed, the vertical B3LYP and ω B97XD absorption wavelengths computed using the PBE ground-state structure are 554 and 502 nm, respectively, implying variations of –0.08 and –0.19 eV compared to the corresponding data calculated with a consistent structure (536 and 467 nm, see Table 2). The ω B97XD λ_{vert} computed on the B3LYP geometry is 482 nm, closer to the 467 nm reference value, but still implying a –0.08 eV deviation, that we recently neglected.⁸³ This is just one more illustration that the exact benchmark procedure could slightly tune the results and that such an outcome is inherent to all computationally tractable processes.

In the most recent experimental measurements,¹³ the visible absorption band has been found to present three peaks in cyclohexane: 578.4, 567.2, and 537.6 nm with a shoulder (sh) at ~500 nm.¹³ The relative intensities are estimated to be 0.82, 0.82, 1.00, and 0.61 for the three peaks and the shoulder, respectively.¹³ In dioxan, the first two bands are not distinguishable, and Perkampus reports in his famous book: 585 (0.92), 547 (1.00), and 510 nm (sh, 0.59).⁹ The same holds in the protic and more polar solvent, ethanol: 592 (1.00), 551 (1.00) and 522 nm (sh, 0.81).⁸⁶ Obviously, the visible spectra provided by pure functionals (SVWNS, BLYP, PBE, and τ -HCTH) and by approaches including a very large ratio of exact exchange (M06-HF, ω B97, and LC-PBE) are not satisfying neither for the predicted shapes nor for the transition energies. Hybrids including 15–30% of exact exchange yield accurate positions for the different bands but incorrectly predict a more

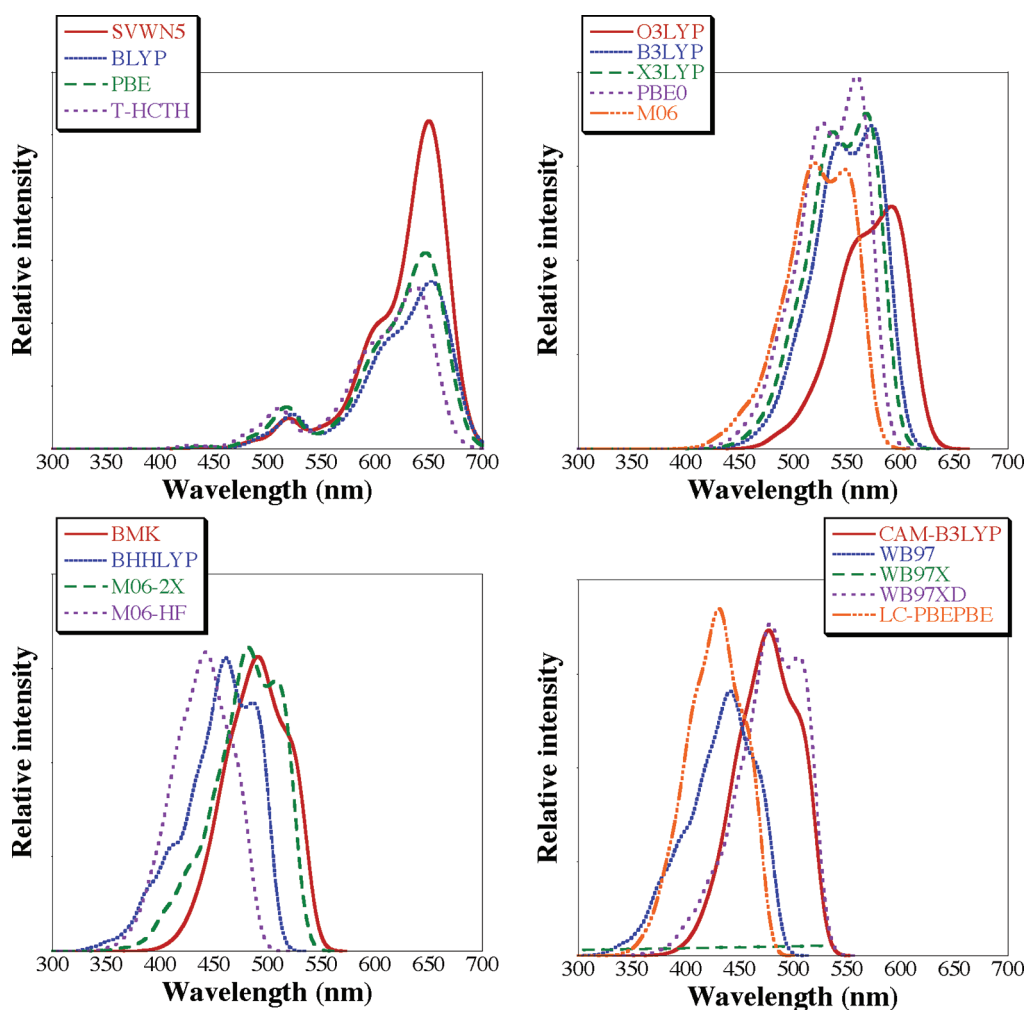


Figure 2. Comparison of the obtained vibronic shapes for system I using different DFT functionals and a PCM-TD-DFT/6-31++G(d,p) level. Top left: pure functionals; top right: global hybrids with less than 30% of exact exchange; bottom left: other global hybrids; and bottom right: range-separated hybrids.

intense first band, whereas global hybrids including 40–60% of exact exchange as well as range-separated approaches relying on a relatively small damping parameter give the opposite trends: too short wavelengths but accurate intensities and topology. For these reasons, we have chosen to use five functionals in Section 3.4: the popular B3LYP and PBE0 that provide wavelengths on the experimental spot (573 and 543 nm, for the former) but incorrect relative intensities; M06-2X, a global hybrid including a large share of HF exchange, that overestimates the transition energy but gives a correct topology (see Supporting Information and ref 13); as well as CAM-B3LYP and ω B97XD, two range-separated hybrids providing an interesting compromise between wavelengths and intensities.

3.3. Analysis for 1,4-NH₂-AQ. Figure 3 compares the experimental and theoretical (ω B97XD) shapes of the visible band of I in cyclohexane. This figure also provides the main vibronic contributions through a stick spectrum. The agreement between the measured and the predicted topologies is obvious, though the selected functional locates the maximal absorption at 512.9, 508.8, and 479.8 nm and therefore undershoots the experimental wavelengths,¹³ as already discussed in the previous section. However, the separation between the first and second (third) peaks attains 274 (1345) cm⁻¹ with PCM-TD- ω B97XD, in very

good match with the measurement 341 (1312) cm⁻¹, thus substantiating the predictive power of the selected approach. As expected, the first maximum principally originates from the 0–0 line. Although a blend of several vibrational modes contribute to the second and third peaks, one can mainly ascribe the bands to modes 14 (408 cm⁻¹) and 18 (479 cm⁻¹), 56 (1421 cm⁻¹) and 58 (1491 cm⁻¹) of the excited state, respectively (see Figure 3). Representations of these modes can be found in Supporting Information. Modes 14 and 18 correspond to bending of the amino groups and breathing of the aromatic ring bearing the two amines. On the other hand, the high-intensity band is related to stretchings of the same ring and displacements of the hydrogen atoms of the amines. Therefore, the substituents play a key role in the experimental shape, though the main coupling mode does not correspond to very intense IR C–N elongation (computed at an higher 1604 cm⁻¹ for S₁) as historically proposed for amino-AQ.²⁴ We have also simulated the spectra of I in dioxane. Convoluting the spectrum with a 0.04 eV fwhm Gaussian, we obtain two maxima at 510 and 481 (579 and 543) nm with relative intensities of 0.89 and 1.00 (1.00 and 0.94) applying ω B97XD (B3LYP), and this nicely fits the relative experimental intensities (positions of the bands): 585 (0.92) and 547 (1.00) nm.⁹

For **I**, these results seem to confirm the experimental analysis²⁴ that the shape of the visible absorption band is related to vibronic interactions. Let us nevertheless assess the possibility to form “conventional” tautomers corresponding to the transfer of one or two protons between the carbonyl and the amine (Figure 4). Using ω B97XD, a functional accurate for electronic spectra, H-bond and other weak interactions,^{83,87,88} we computed λ_{vert} of 467, 496, and 447 nm for the canonical structure, the tautomer

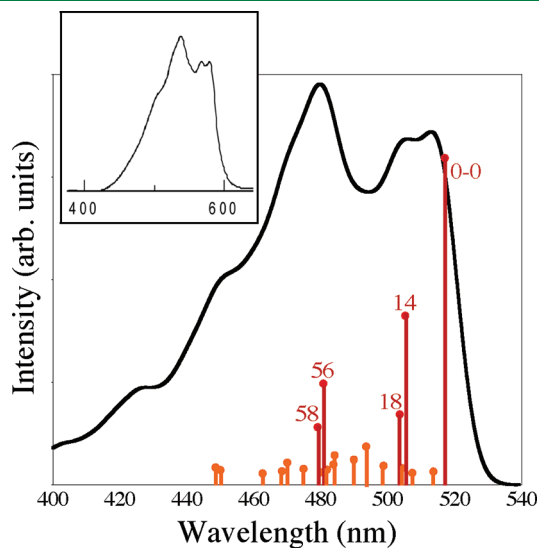


Figure 3. Computed ω B97XD spectra of **I**, using a convoluting Gaussian with fwhm 0.03 eV. The main contributions to the stick spectrum are shown, with numbers corresponding to the vibrational modes for the four largest contributions. The top panel is the experimental graph reprinted with permission from Khan, M. S. and Khan, Z. H. Electronic absorption spectra of amino-substituted anthraquinones and their interpretation using the ZINDO/S and AM1 methods. *Spectrochim. Acta, Part A* **2003**, *59*, 1409–1426. Copyright 2003, Elsevier.

corresponding to a first proton transfer between the amine and carbonyl groups and the double tautomer, respectively (see Figure 4). Such results may apparently fit the two peaks and shoulder topology found in polar environments.^{9,86} However, by analyzing the relative energies of all species as well as the corresponding transition states, one clearly notes that the apparent agreement is purely fortuitous. Indeed, on the ground-state potential energy surface, the first proton transfer not only requires an energy more than 20 times the thermal energy ($13.6 \text{ kcal}\cdot\text{mol}^{-1}$) but also yields a product very close to the transition state. This implies that even if the transfer occurs (a very unlikely event), the back reaction will be instantaneous; the computed back reaction barrier is $<0.05 \text{ kcal}\cdot\text{mol}^{-1}$. For the second proton transfer, the situation is quite similar and leads to a very unstable product. Of course, one has also to probe the S_1 potential energy surface, as a more complex process (absorption of the canonical form, excited-state proton transfer, relaxation to the ground-state tautomer, and photon absorption of this tautomer) may also occur. To test this hypothesis, we have tried to optimize the S_1 geometries of both tautomers, but they systematically converged to the canonical form. This can be explained by examining Figure 4 that indicates that there is no minimum on the excited-state surface for the tautomers. Fain and co-workers have recently proposed that the multiple bands of **I** correspond to the presence of several more exotic species (see refs 22 and 23 as well as references therein) corresponding to tautomers of 4,9-diamino-1,10-anthraquinone (see central molecule in Figure 5), itself obtained by exchanging of one carbonyl and one amine in **I**. These authors did not propose a chemical path to obtain their structure (and there is, to the best of our knowledge, no experimental proof of their existence), but they justify this choice with the correlation between the λ_{max} computed with a semiempirical approach for the different tautomers and the measured positions for the maxima.²² This 4,9-diamino-1,10-anthraquinone derivative is less stable than **I** by $6.3 \text{ kcal}\cdot\text{mol}^{-1}$ and presents a S_0 dipole moment of 1.7 D at the PCM-(cyclohexane)- ω B97XD/6-31++G(d,p) level. This value can

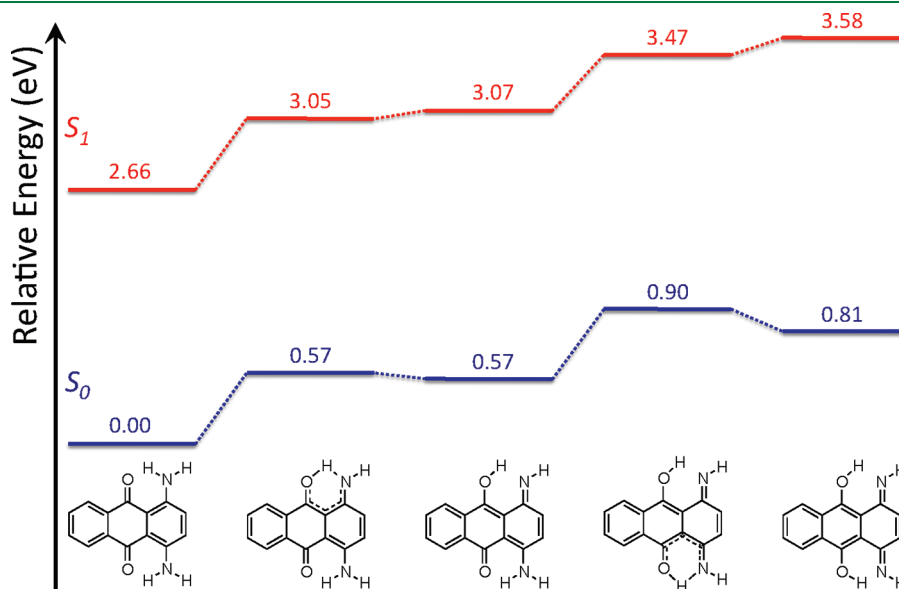


Figure 4. Representation of the relative total energies of the tautomers of **I** together with the transition states. All values are in eV. The S_1 energies are computed within the vertical approximation (PCM-(TD)- ω B97XD/6-31++G(d,p)). Representation of the imaginary modes characteristics of the transition states can be found in Supporting Information.

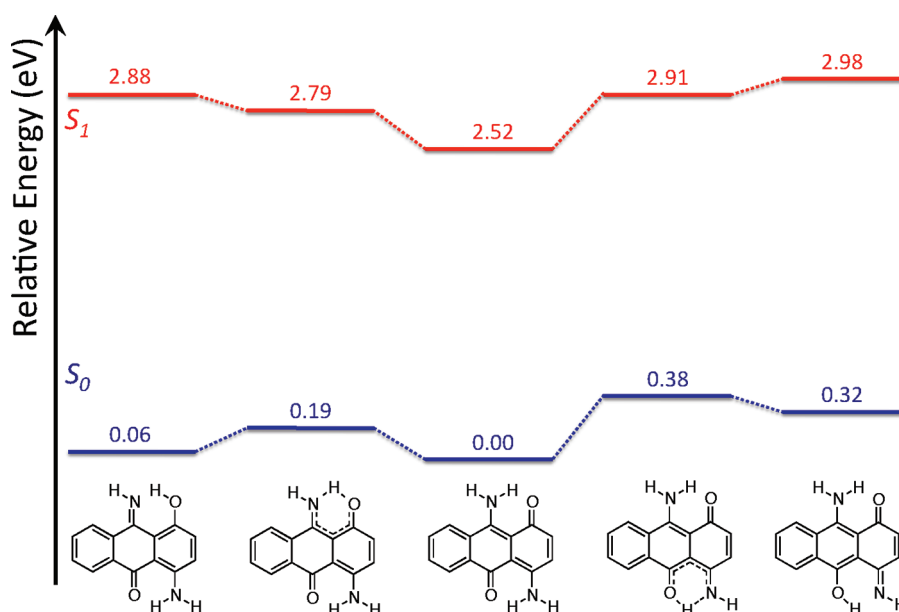


Figure 5. Representation of the relative total energies of the tautomers of 4,9-diamino-1,10-anthraquinone obtained at the PCM-(TD-) ω B97XD/6-31++G(d,p) level of theory.

be compared to the 3.6 D value obtained for **I**, with the same method and, to the 3.1 D figure obtained by the most recent experimental measurements.⁸⁹ Likewise, the excited-state dipole moment is estimated to be larger than its ground-state counterpart by 0.6–1.8 D (depending on the selected experimental method, see ref 89), and we compute a variation of -0.4 D for 4,9-diamino-1,10-anthraquinone and $+2.3$ D for 1,4-diamino-9,10-anthraquinone. Clearly, these values are not in favor of a significant contribution of the former “exotic” structure. Nevertheless, we have investigated its tautomers and the corresponding transition states (see Figure 5). First let us note that a stable “double” tautomer could not be located on the ground-state surface despite several attempts. It systematically reverts to one of the two possible “single” tautomeric forms, hinting that it is risky to attribute one band to such compound. For the most stable tautomer, we find a reaction barrier of $4.4 \text{ kcal}\cdot\text{mol}^{-1}$. If one uses classical Boltzmann and transition-state theories, one obtains only 9% of this tautomer (that presents a smaller oscillator strength than both **I** and 4,9-diamino-1,10-anthraquinone) and a back reaction 10 times faster than the forward reaction. The second tautomer is too high in energy to impact significantly. In short, our analysis rules out any significant proportion of conventional or exotic tautomers in solution.

We have also tested the possible presence of aggregates in solution. For **I**, the only available XRD structure corresponds to a dihydrate with inter-AQ interactions mostly proceeding through water-assisted H-bonds.⁸⁴ In the course of defining reasonable starting points for our geometry optimizations, we have therefore decided to recrystallize **I**⁹⁰ and actually obtained a new XRD structure (see cif files and Supporting Information). This water-free structure has a completely different packing than the previously reported one, with AQ arranged in a slipped antiparallel orientation along the first axis, bonded through intermolecular H-bonds between the amine and the carbonyl for the second and displaying a weaker π - π stacking along the third direction. The data from both XRD structures as well as chemical intuition have been used to define the initial coordinates for our geometry

Table 3. Relative Free Energies ($\text{kcal}\cdot\text{mol}^{-1}$) and Vertical Transition Wavelengths (nm) for Four Dimers of **I**^a

		ΔG	λ_{max}
A	π - π + H-bond	0.00	474 (0.35)
B	π - π + H-bond	2.47	455 (0.51)
C	H-bonded	9.16	468 (0.51)
D	H-bonded	8.94	478 (0.52) and 469 (0.16)

^a See Supporting Information. All calculations performed at the PCM-(TD-) ω B97XD/6-31++G(d,p) level.

optimizations of the dimers of **I**. We have reached four different structures that are represented in Supporting Information: two, **A** and **B** presents cofacial head-to-tail **I** with H-bonds between both carbonyl and amino groups, and two, **C** and **D**, are characterized by H-bonded side-by-side (but not coplanar) AQ. Their spectral features are listed in Table 3. At the PCM- ω B97XD/6-31++G(d,p) level, only the two first aggregates are characterized by a stabilizing interaction energy compared to the monomer: $-3.51 \text{ kcal}\cdot\text{mol}^{-1}$ for **A** and $-1.04 \text{ kcal}\cdot\text{mol}^{-1}$ for **B**. Their spectra display small bathochromic (**A**) and hypsochromic (**B**) shifts compared to the isolated case but only possess a major absorption band. In a naive view, one could imagine that the first experimental band at 578.4 nm corresponds to the most stable dimer, the 567.2 nm absorption to the monomer, and the most intense band 537.6 nm to the **B** dimer. However, with these assignments, the energetic separation between the first and the most intense band would be 0.11 eV, in poor agreement with experiment (0.16 eV) and with vibronic simulations (0.17 eV). Consistently with experimental investigations carried out for different concentration of dyes,²⁴ this analysis therefore hints that aggregation falls short to provide a convincing explanation to the experimental findings.

3.4. The Dihydroxy Series. The results obtained with five functionals for three dihydroxy-AQ are listed in Table 4. Though

Table 4. Predicted Values in the Dihydroxy Series.^a

dye	functional	ground state				excited state				vibronic							
		PG	$d_{C=O}$	d_{H-bond}	$\lambda_{vert}(f)$	ZPVE	PG	$d_{C=O}$	d_{H-bond}	$\lambda_{vert}(f)$	ZPVE	ΔG	$P_1^{conv}(I_r)$	$P_2^{conv}(I_r)$	$P_3^{conv}(I_r)$		
II	B3LYP	C_{2v}	1.251	1.341	1.658	475 (0.22)	5.15	C_{2v}	1.264	1.330	1.573	551 (0.22)	5.06	531 (1.00)	495 (0.83)	464 (0.41)	
	PBE0	C_{2v}	1.246	1.331	1.633	461 (0.24)	5.18	C_{2v}	1.259	1.319	1.535	535 (0.24)	5.10	516 (1.00)	482 (0.85)	453 (0.45)	
	M06-2X	C_{2v}	1.236	1.338	1.715	401 (0.27)	5.20	C_{2v}	1.260	1.312	1.505	501 (0.28)	5.09	427 (1.00)			
	CAM-B3LYP	C_{2v}	1.241	1.337	1.666	413 (0.28)	5.22	C_{2v}	1.262	1.316	1.523	497 (0.28)	5.12	469 (0.73)	460 (0.74)	440 (1.00)	
	ω B97XD	C_{2v}	1.240	1.336	1.690	409 (0.29)	5.22	C_{2v}	1.260	1.315	1.552	490 (0.28)	5.12	462 (0.74)	453 (0.76)	434 (1.00)	
III	B3LYP	C_{2h}	1.249	1.341	1.669	438 (0.29)	5.15	C_s	1.274/1.268	1.341/1.317	1.636/1.456	514 (0.23)	5.03	477 (0.87)	455 (1.00)		
	PBE0	C_{2h}	1.243	1.331	1.643	420 (0.31)	5.20	C_s	1.271/1.262	1.330/1.305	1.602/1.385	499 (0.26)	5.06	461 (0.90)	440 (1.00)		
	M06-2X	C_{2h}	1.234	1.337	1.721	357 (0.38)	5.20	C_s	1.306/1.250	1.334/1.268	1.679/1.037	518 (0.35)	5.09	2.92			
	CAM-B3LYP	C_{2h}	1.239	1.336	1.674	371 (0.38)	5.22	C_s	1.309/1.256	1.334/1.272	1.633/1.035	521 (0.37)	5.12	2.91			
	ω B97XD	C_{2h}	1.237	1.335	1.700	367 (0.39)	5.22	C_s	1.274/1.259	1.332/1.302	1.637/1.403	439 (0.34)	5.07	3.00	405 (0.99)	386 (1.00)	
IV	B3LYP	C_{2v}	1.229/1.267	1.343	1.686	439 (0.29)	5.15	C_s	1.246/1.295	1.321/1.342	1.677/1.510	507 (0.23)	5.04	2.53	483 (0.94)	473 (0.94)	454 (1.00)
	PBE0	C_{2v}	1.223/1.261	1.333	1.665	421 (0.31)	5.20	C_s	1.240/1.291	1.310/1.331	1.649/1.469	487 (0.26)	5.08	2.62	464 (0.92)	456 (1.00)	437 (1.00)
	M06-2X	C_{2v}	1.218/1.250	1.338	1.729	362 (0.37)	5.20	C_s	1.233/1.298	1.299/1.331	1.686/1.387	441 (0.34)	5.05	2.94	383 (1.00)		
	CAM-B3LYP	C_{2v}	1.221/1.257	1.338	1.687	376 (0.37)	5.23	C_{2v}	1.238/1.298	1.318	1.541	433 (0.38)	5.08	2.92	413 (0.93)	395 (1.00)	
	ω B97XD	C_{2v}	1.220/1.254	1.336	1.707	373 (0.36)	5.22	C_{2v}	1.238/1.294	1.317	1.565	429 (0.38)	5.09	2.95	408 (0.96)	391 (1.00)	

^a All calculation with the PCM(pentane)-(TD)-DFT/6-31++G(d,p) approach. The vibronic maxima have been obtained with a fwhm Gaussian of 0.05 eV. See caption of Table 1 for more details.

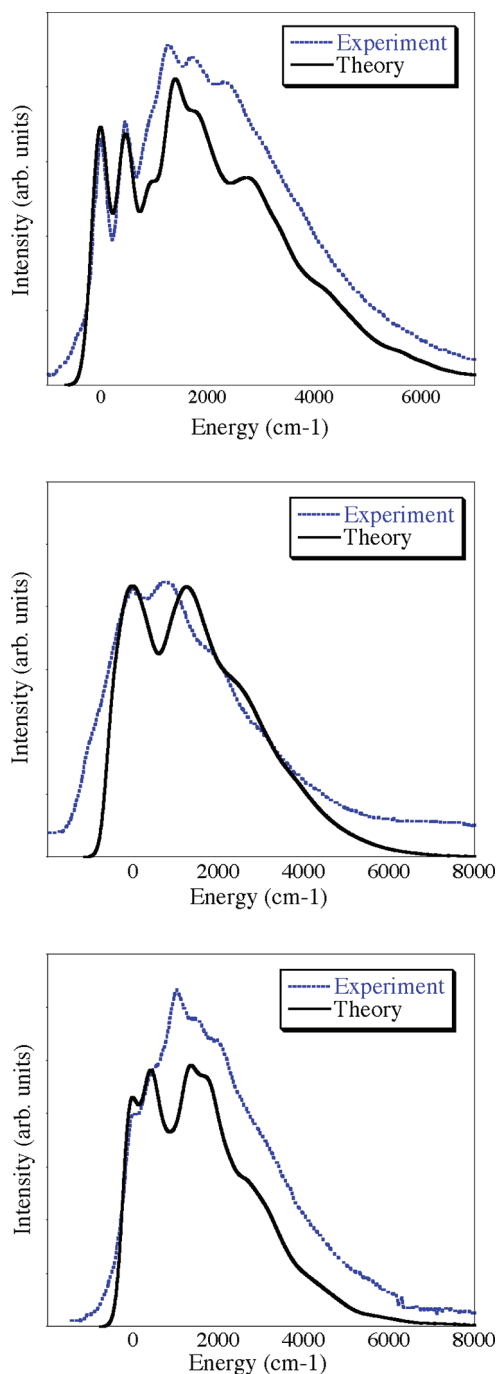


Figure 6. Comparison between the experimental and theoretical shapes for the visible absorption band of (from top to bottom) II–IV taking the first maximum as reference. The measured data have been extracted from ref 19 and recast on the energy scale, whereas theoretical values have been obtained at the PCM-TD- ω B97XD/6-31++G(d,p) level of theory, using a convoluting sum of Gaussian functions with a fwhm of 0.023 eV for all cases.

II–IV are all characterized by two H-bonds between carbonyl and alcohol groups, they differ by their symmetry. Recent experimental data in *n*-pentane show a significant variations of the position for the characteristic visible band, each band possessing a specific vibronic signature.¹⁹ The ZPVE computed with all functionals is similar for the three dyes and shows only a

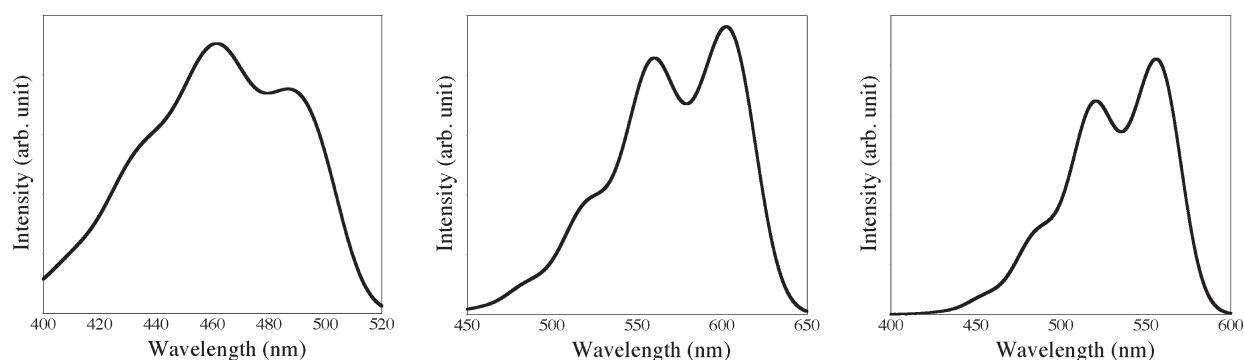


Figure 7. PCM-TD- ω B97XD/6-31++G(d,p) spectra computed for **V** (left, methanol), **VI** (central, ethanol), and **VII** (right, cyclohexane) using a convoluting sum of Gaussian functions with fwhm of 0.50 eV in all cases.

ca. -0.1 eV shift when going from the ground state to the excited state, confirming that the ZPVE variation may be rapidly estimated with any functional. As noted in Section 3.2, the predicted vertical wavelengths increase with the amount of *exact* exchange included in the hybrid.

For **II**, Table 4 shows the same trends as for its amino counterpart, **I**: photon absorption yields an extension of the carbonyls and a concomitant shortening of both the single C–O bonds and the H-bond intervals. Nevertheless, for the latter the variation accompanying the electronic transition is much more pronounced than in **I**, a phenomenon related to the symmetric/asymmetric nature of the H-bond. The vibronic spectra obtained with a fwhm of 0.03 eV are shown in Supporting Information, and they follow the same qualitative evolution as for **I** when modifying the functional. B3LYP and PBE0 not only provide a first absorption at 531 and 516 nm, respectively, the latter being on the experimental spot (517 nm),¹⁹ but also predict a dominant 0–0 band, which is inconsistent with measurements.¹⁹ In terms of shape, it turns out that the best theory/experiment match is reached with CAM-B3LYP or ω B97XD, as illustrated in Figure 6, but at the price of less accurate positions for the first band: 469 and 461 nm, respectively. This corresponds to a ca. 0.25 eV error, which is in the line of average TD-DFT accuracy but remains sizable for a well-behaved low-lying π – π^* transition (see the Introduction Section for reference benchmarks). As can be seen in Figure 6, following the 0–0 band, one notices a second absorption of equal intensity at ca. 470 cm^{-1} , followed by a dominating band peaking at ca. 1440 cm^{-1} . The two main S_1 vibrational modes responsible for these vibronic effects are 16 (479 cm^{-1}) and 49 (1311 cm^{-1}), respectively. The first corresponds to an extension of the phenyl ring bearing the hydroxyl groups, whereas the second is related to stretching of the phenyl rings and bending of the hydrogen atoms of the alcohols (animations may be found in the Supporting Information).

For **III**, the ground-state carbonyl bonds are slightly shorter than for **II**, and the transition energies are larger, which agrees with experiment. The S_0 inversion symmetry is lost at the excited state and it is quite clear from Table 4 that one hydroxyl group is strongly affected transition. This is a marked difference with respect to **II** that presented the same kinds of intramolecular interactions in S_0 and S_1 , indicating that the ground-state geometries and vertical transition energies may not provide a complete picture of the chemical differences between these two dyes. With B3LYP, PBE0 and ω B97XD, one H-bond of **III** is significantly shorten (ca. 0.25 Å) by photon absorption, whereas for M06-2X and CAM-B3LYP, the S_1 optimization actually yield

to a tautomeric form, with one alcohol function at the center of the AQ. In other words, with these latter hybrids, the ground- and excited-state geometries are not simple variations, and it becomes obvious that a “conventional” approximation cannot be applied to calculate the vibrationally resolved band. Consequently, in the Supporting Information, we report the vibronic (stick and convoluted) spectra for B3LYP, PBE0, and ω B97XD only. The best qualitative agreement is again reached with ω B97XD (see Figure 6) with two maxima of nearly equal intensities. For **III**, theory reproduces the camel-back shape of the experimental spectrum, though the separation between the two maxima is clearly overshoot by the model. We attribute this error to the application of an harmonic approximation that is obviously becoming less suitable for strongly distorted O–H bonds. Indeed, the most important coupling mode, responsible for the first extremum, corresponds to proton transfer between the two oxygen atoms, whereas the second maximum originates to a large panel of modes implying both alcohols. It is also worth noting that the first peak (406 nm) does not exactly correspond to the 0–0 band (413 nm), making comparisons between experimental and theoretical λ_{max} a nontrivial task.

For **IV**, the highest PG is only systematically conserved with the two range-separated functionals, all three global hybrids providing an asymmetric excited state, with one long and one short H-bond, although contrary to **III**, we found no clear-cut tautomer. Once again, B3LYP and PBE0 yield transition energies in good agreement with experiment with deviations of ca. 20 nm. No functional is fully satisfying in terms of shape (Figure 6 and Supporting Information), and as for **III**, this effect is related to anharmonicities as the O–H bond are strongly elongated for **IV** (see Table 4). This induces a too large separation in the stick spectrum (overestimates frequencies), and subsequently, a clear-cut minimum in the convoluted spectrum that is not found in the experiment.

3.5. Application to Other AQ Dyes. We have used ω B97XD to compare the experimental and theoretical spectra of three dyes of industrial interest: quinalizarin (**V**) a tetra-hydroxy-AQ, disperse blue 14 (**VI**), and solvent blue 59 (**VII**), two amino-substituted AQ presenting large extinction coefficients. All three dyes present well-structured absorption bands,^{7,9,91} the latter containing 40 atoms and represents a computational challenge at this level of theory. The simulated spectra can be found in Figure 7. For **V**, the spectrum measured in methanol is very broad and presents two maxima reported at 512 and 490 nm by Green⁷ and at 517 and 495 nm by Perkampus.⁹ The simulation provides 486 and 462 nm, a 0.13 eV separation

that apparently fits experiment (0.11 eV) though we do not obtain exactly the same topology. The computed spectra of VI and VII are similar, and this outcome fits experiment.^{7,91} For VII, one can estimate the experimental wavelengths (relative intensities) to be 643 nm (1.00), 600 nm (0.84), and 560 nm (sh, 0.39) in cyclohexane,⁹¹ whereas TD-DFT yields 556 nm (1.00), 521 nm (0.83), and 490 nm (sh, 0.35), in obvious qualitative agreement but for the too large transition energies. Nevertheless, the shift of the main band compared to I in the same solvent is -0.19 eV in theory and -0.22 eV in the experiment, illustrating the accuracy of auxochromic displacements. Note that there is also an inversion of relative intensities of the two first peaks compared to I, and this effect is perfectly reproduced by ω B97XD. For disperse blue 14, experiment yields 640 nm (1.00), 594 nm (0.83), and 550 nm (sh, 0.43) in methanol,⁷ whereas TD-DFT gives: 603 nm (1.00), 560 nm (0.89), and 522 nm (sh, 0.41), again in good qualitative agreement. As the solvent used for this latter AQ is polar and protic, the auxochromic displacement wrt I and VII cannot be compared directly due to the application of a continuum model.

4. CONCLUSIONS

We have computed vibrationally resolved absorption spectra of a series of amino and hydroxy anthraquinone dyes, using a time-dependent density functional approach accounting for bulk environmental effects. It turned out that the selected atomic basis set has a relatively modest impact on the properties, provided polarization functions are used. On the contrary, the selected DFT functional strongly affects the computed transition wavelengths, the geometries as well as the topology of the vibronic envelope, although it does not modify significantly the ZPVE energy differences computed for the ground and excited states. As no functional delivers fully consistent values, pinpointing the most adequate approach is not straightforward. Nevertheless, one can discard both pure functionals and hybrids including a very large share of exact exchange. In the present case, B3LYP and PBE0 provide accurate positions (wavelengths) for the absorption peaks but are less efficient than two range-separated hybrids, namely CAM-B3LYP and ω B97XD, to determine the shapes of the absorption bands (that is relative intensities). For 1,4-NH₂-AQ, our calculations show that the experimental spectrum cannot be easily explained by the presence of tautomers nor aggregates, but that it results from four major coupling modes implying the amino groups. For 1,4-OH-AQ, 1,4-NHMe-AQ, and 1,4-NHEt-AQ, the agreement between simulated and measured electronic spectra is also rather astonishing. This is an essential fact, as most AQ industrial dyes used today rely on a 1,4 pattern with strong H-bond donors. On the contrary, for 1,5-OH-AQ and 1,8-OH-AQ, the positions of the hydrogen atoms implied in intramolecular H-bonds are strongly modified following photon absorption, and the theory/experiment match is less satisfying. This is probably related to the harmonic approximation that becomes unsuitable to evaluate vibrations related to distorted bonds. Therefore, efforts to include anharmonicity are of primary importance to further improve the description of the visible bands of hydroxy-AQ. Besides, this work illustrates the limitations of the available functionals and the developments that are still necessary to obtain new approaches able to correctly restore the experimental features typical of electronically excited states.

■ ASSOCIATED CONTENT

S Supporting Information. Representation of all stick spectra for the benchmark study of I, these graphs use a Gaussian with a fwhm of 0.03 eV. Four principal vibrational modes of I related to Figure 3. Movies of the imaginary modes for the TS of Figures 4 and 5. Description of the XRD structure and cif file, deposited at the Cambridge Crystallographic Data Centre under number CCDC 819514. Representation of optimized dimers. Representation of all stick spectra for II–IV convoluted using a Gaussian with a fwhm of 0.03 eV. This material is available free of charge via the Internet at <http://pubs.acs.org>.

■ AUTHOR INFORMATION

Corresponding Author

*E-mail: denis.jacquemin@univ-nantes.fr; carlo-adamo@chimie-paristech.fr.

■ ACKNOWLEDGMENT

The authors thank Dr. C. Peltier (Paris) and Dr. J. Ceron (Nantes) for fruitful discussions and their help. D.J. is indebted to the Région des Pays de la Loire for financial support in the framework of a recrutement sur poste stratégique. The authors are indebted to the COST program CODECS and its members for support and many helpful discussions, respectively. This research used resources of: (1) the Interuniversity Scientific Computing Facility located at the University of Namur, Belgium, which is supported by the F.R.S.-FNRS under convention no. 2.4617.07; (2) the GENCI-CINES/IDRIS (grant c2011085117); and (3) the CCIPL (Centre de Calcul Intensif des Pays de Loire).

■ REFERENCES

- (1) Iwanaga, H.; Aiga, F. *Liq. Cryst.* **2011**, *38*, 135–148.
- (2) Palaniappan, S.; Manisankar, P. J. *Polym. Res.* **2011**, *18*, 311–317.
- (3) Werner, S. J.; Linz, G. M.; Carlson, J. C.; Pettit, S. E.; Tupper, S. K.; Santer, M. M. *Appl. Anim. Behav. Sci.* **2011**, *129*, 162–169.
- (4) Zhang, J.; Redman, N.; Litke, A. P.; Zeng, J.; Zhan, J.; Chan, K. Y.; Chang, C.-W. T. *Bioorg. Med. Chem.* **2011**, *19*, 498–503.
- (5) Labhart, H. *Helv. Chim. Acta* **1957**, *40*, 1410–1421.
- (6) Griffiths, J. *Colour and Constitution of Organic Molecules*; Academic Press: London, 1976.
- (7) Green, F. J. *The Sigma-Aldrich Handbook of Stains, Dyes and Indicators*; Aldrich Chemical Company, Inc: Milwaukee, WI, 1990.
- (8) Christie, R. M. *Colour Chemistry*; The Royal Society of Chemistry: Cambridge, U.K., 1991; p 228.
- (9) Perkampus, H. H. *UV/Vis. Atlas of Organic Compounds*, 2nd ed.; VCH: Weinheim, Germany, 1992.
- (10) Hunger, K. *Industrial Dyes*; Wiley-VCH: Weinheim, Germany, 2003.
- (11) Fabian, J.; Hartmann, H. *Light Absorption of Organic Colorants*; Springer-Verlag: Berlin, Germany, 1980; Vol. 12 of Reactivity and Structure Concepts in Organic Chemistry.
- (12) Zollinger, H. *Color Chemistry, Syntheses, Properties and Applications of Organic Dyes and Pigments*, 3rd ed.; Wiley-VCH: Weinheim, Germany, 2003; p 647.
- (13) Khan, M. S.; Khan, Z. H. *Spectrochim. Acta A* **2003**, *59*, 1409–1426.
- (14) Dahiya, P.; Choudhury, S. D.; Maity, D. K.; Mukherjee, T.; Pal, H. *Spectrochim. Acta A* **2008**, *69*, 134–141.
- (15) Siddlingeshwar, B.; Hanagodimath, S. M. *Spectrochim. Acta A* **2009**, *72*, 490–495.
- (16) Yoon, C.; Choi, J.-H.; Kim, J. P. *Mol. Cryst. Liq. Cryst.* **2010**, *533*, 102–112.

- (17) Jung, J.; Park, Y.; Jaung, J.-Y.; Park, J. *Mol. Cryst. Liq. Cryst.* **2010**, *529*, 88–94.
- (18) Sezer, B.; Sener, M. K.; Koca, A.; Erdogmus, A.; Avciata, U. *Synth. Met.* **2010**, *160*, 2155–2166.
- (19) Khan, M. S.; Khan, Z. H. *Can. J. Anal. Sci. Spectrosc.* **2002**, *47*, 146–156.
- (20) Giles, C. H.; Shah, C. D. *Trans. Faraday Soc.* **1969**, *65*, 2508–2515.
- (21) Wegerle, D. J. *Soc. Dyers Colour* **1973**, *89*, 54–55.
- (22) Fain, V. Y.; Zaitsev, B. E.; Ryabov, M. A. *Russ. J. Org. Chem.* **2009**, *45*, 374–382.
- (23) Fain, V. Y.; Zaitsev, B. E.; Ryabov, M. A.; Strashnov, P. V. *Russ. J. Gen. Chem.* **2010**, *80*, 1986–1995.
- (24) Sinclair, R. S.; Mc Alpine, E. J. *Soc. Dyers Colour* **1975**, *91*, 399–405.
- (25) Jacquemin, D.; Peltier, C.; Ciofini, I. *Chem. Phys. Lett.* **2010**, *493*, 67–71.
- (26) Guillaumont, D.; Nakamura, S. *Dyes Pigm.* **2000**, *46*, 85–92.
- (27) Jacquemin, D.; André, J. M.; Perpète, E. A. *J. Chem. Phys.* **2004**, *121*, 4389–4396.
- (28) Perpète, E. A.; Wathélet, V.; Preat, J.; Lambert, C.; Jacquemin, D. *J. Chem. Theory Comput.* **2006**, *2*, 434–440.
- (29) Jacquemin, D.; Wathélet, V.; Preat, J.; Perpète, E. A. *Spectrochim. Acta A* **2007**, *67*, 334–341.
- (30) Matsuura, M.; Sato, H.; Sotoyama, W.; Takahashi, A.; Sakurai, M. *J. Mol. Struct. (THEOCHEM)* **2008**, *860*, 119–127.
- (31) Jacquemin, D.; Perpète, E. A.; Scuseria, G. E.; Ciofini, I.; Adamo, C. *J. Chem. Theory Comput.* **2008**, *4*, 123–135.
- (32) Jacquemin, D.; Wathélet, V.; Perpète, E. A.; Adamo, C. *J. Chem. Theory Comput.* **2009**, *5*, 2420–2435.
- (33) Jacquemin, D.; Perpète, E. A.; Ciofini, I.; Adamo, C.; Valero, R.; Zhao, Y.; Truhlar, D. G. *J. Chem. Theory Comput.* **2010**, *6*, 2071–2085.
- (34) Foresman, J. B.; Head-Gordon, M.; Pople, J. A.; Frisch, M. J. *J. Phys. Chem.* **1992**, *96*, 135–149.
- (35) Guido, C. A.; Mennucci, B.; Jacquemin, D.; Adamo, C. *Phys. Chem. Chem. Phys.* **2010**, *12*, 8016–8023.
- (36) Jacquemin, D.; Perpète, E. A.; Assfeld, X.; Scalmani, G.; Frisch, M. J.; Adamo, C. *Chem. Phys. Lett.* **2007**, *438*, 208–212.
- (37) van Caillie, C.; Amos, R. D. *Chem. Phys. Lett.* **1999**, *308*, 249–255.
- (38) Furche, F.; Ahlrichs, R. *J. Chem. Phys.* **2002**, *117*, 7433–7447.
- (39) Dierksen, M.; Grimme, S. *J. Phys. Chem. A* **2004**, *108*, 10225–10237.
- (40) Scalmani, G.; Frisch, M. J.; Mennucci, B.; Tomasi, J.; Cammi, R.; Barone, V. *J. Chem. Phys.* **2006**, *124*, 094107.
- (41) Tomasi, J.; Mennucci, B.; Cammi, R. *Chem. Rev.* **2005**, *105*, 2999–3094.
- (42) Santoro, F.; Improta, R.; Lami, A.; Bloino, J.; Barone, V. *J. Chem. Phys.* **2007**, *126*, 084509.
- (43) Improta, R.; Scalmani, G.; Frisch, M. J.; Barone, V. *J. Chem. Phys.* **2007**, *127*, 074504.
- (44) Santoro, F.; Improta, R.; Lami, A.; Bloino, J.; Barone, V. *J. Chem. Phys.* **2007**, *126*, 184102.
- (45) Santoro, F.; Lami, A.; Improta, R.; Bloino, J.; Barone, V. *J. Chem. Phys.* **2008**, *128*, 224311.
- (46) Improta, R.; Santoro, F.; Barone, V.; Lami, A. *J. Phys. Chem. A* **2009**, *113*, 15346–15354.
- (47) Peltier, C.; Laine, P. P.; Scalmani, G.; Frisch, M. J.; Adarno, C.; Ciofini, I. *J. Mol. Struct. (THEOCHEM)* **2009**, *914*, 94–99.
- (48) Jacquemin, D.; Peltier, C.; Ciofini, I. *J. Phys. Chem. A* **2010**, *114*, 9579–9582.
- (49) Klaumuenzer, B.; Kroener, D.; Saalfrank, P. *J. Phys. Chem. B* **2010**, *114*, 10826–10834.
- (50) Jacquemin, D.; Perpète, E. A.; Scalmani, G.; Ciofini, I.; Peltier, C.; Adamo, C. *Chem. Phys.* **2010**, *372*, 61–66.
- (51) Friedländer, P. *Ber. Dtsch. Chem. Ges.* **1909**, *42*, 765–770.
- (52) Slater, J. C. *Quantum Theory of Molecular and Solids*; McGraw-Hill: New York, 1974; Vol. 4.
- (53) Vosko, S. J.; Wilk, L.; Nusair, M. *Can. J. Phys.* **1980**, *58*, 1200–1211.
- (54) Becke, A. D. *Phys. Rev. A* **1988**, *38*, 3098–3100.
- (55) Lee, C.; Yang, W.; Parr, R. G. *Phys. Rev. B* **1988**, *37*, 785–789.
- (56) Perdew, J. P.; Burke, K.; Ernzerhof, M. *Phys. Rev. Lett.* **1996**, *77*, 3865–3868.
- (57) Boese, A. D.; Handy, N. C. *J. Chem. Phys.* **2002**, *116*, 9559–9569.
- (58) Baker, J.; Pulay, P. *J. Chem. Phys.* **2002**, *117*, 1441–1449.
- (59) Becke, A. D. *J. Chem. Phys.* **1993**, *98*, 5648–5652.
- (60) Stephens, P. J.; Devlin, F. J.; Chabalowski, C. F.; Frisch, M. J. *J. Phys. Chem.* **1994**, *98*, 11623–11627.
- (61) Xu, X.; Goddard, W. A., III *Proc. Natl. Acad. Sci. U.S.A.* **2004**, *101*, 2673–2677.
- (62) Adamo, C.; Barone, V. *J. Chem. Phys.* **1999**, *110*, 6158–6170.
- (63) Ernzerhof, M.; Scuseria, G. E. *J. Chem. Phys.* **1999**, *110*, 5029–5036.
- (64) Zhao, Y.; Truhlar, D. G. *Theor. Chem. Acc.* **2008**, *120*, 215–241.
- (65) Boese, A. D.; Martin, J. M. L. *J. Chem. Phys.* **2004**, *121*, 3405–3416.
- (66) Becke, A. D. *J. Chem. Phys.* **1993**, *98*, 1372–1377.
- (67) Zhao, Y.; Truhlar, D. G. *J. Phys. Chem. A* **2006**, *110*, 5121–5129.
- (68) Yanai, T.; Tew, D. P.; Handy, N. C. *Chem. Phys. Lett.* **2004**, *393*, 51–56.
- (69) Tawada, T.; Tsuneda, T.; Yanagisawa, S.; Yanai, T.; Hirao, K. *J. Chem. Phys.* **2004**, *120*, 8425–8433.
- (70) Iikura, H.; Tsuneda, T.; Yanai, T.; Hirao, K. *J. Chem. Phys.* **2001**, *115*, 3540–3544.
- (71) Chai, J. D.; Head-Gordon, M. *J. Chem. Phys.* **2008**, *128*, 084106.
- (72) Chai, J. D.; Head-Gordon, M. *Phys. Chem. Chem. Phys.* **2008**, *10*, 6615–6620.
- (73) Jensen, F. *Chem. Phys. Lett.* **2005**, *402*, 510–513.
- (74) Note that the vertical transitions reported in Table 1 have been determined using a nonequilibrium PCM model for the ground state and an equilibrium PCM approach for the excited state. The latter cannot therefore be straightforwardly compared to fluorescence wavelengths, but this is not the focus of the present contribution.
- (75) Jacquemin, D.; Perpète, E. A.; Vydrov, O. A.; Scuseria, G. E.; Adamo, C. *J. Chem. Phys.* **2007**, *127*, 094102.
- (76) Peach, M. J. G.; Benfield, P.; Helgaker, T.; Tozer, D. J. *J. Chem. Phys.* **2008**, *128*, 044118.
- (77) Silva-Junior, M. R.; Schreiber, M.; Sauer, S. P. A.; Thiel, W. *J. Chem. Phys.* **2008**, *129*, 104103.
- (78) Goerigk, L.; Moellmann, J.; Grimme, S. *Phys. Chem. Chem. Phys.* **2009**, *11*, 4611–4620.
- (79) Caricato, M.; Trucks, G. W.; Frisch, M. J.; Wiberg, K. B. *J. Chem. Theory Comput.* **2010**, *6*, 370–383.
- (80) Jacquemin, D.; Perpète, E. A.; Ciofini, I.; Adamo, C. *J. Chem. Theory Comput.* **2010**, *6*, 1532–1537.
- (81) Fabian, J. *Dyes Pigm.* **2010**, *84*, 36–53.
- (82) Goerigk, L.; Grimme, S. *J. Chem. Phys.* **2010**, *132*, 184103.
- (83) Jacquemin, D.; Perpète, E. A.; Ciofini, I.; Adamo, C. *Theor. Chem. Acc.* **2011**, *128*, 127–136.
- (84) Kahino, S.; K., S.; Haisa, M. *Acta Cryst. C* **1988**, *44*, 1044–1046.
- (85) Jacquemin, D.; Perpète, E. A.; Scuseria, G. E.; Ciofini, I.; Adamo, C. *Chem. Phys. Lett.* **2008**, *465*, 226–229.
- (86) Weast, R. C. *Handbook of Chemistry and Physics*, 60th ed.; The Chemical Rubber Company: Cleveland, OH, 1979.
- (87) Thanthiruwatte, K. S.; Hohenstein, E. G.; Burns, L. A.; Sherrill, C. D. *J. Chem. Theory Comput.* **2011**, *7*, 88–96.
- (88) Burns, L. A.; Vazquez-Mayagoitia, A.; Sumpter, B. G.; Sherrill, C. D. *J. Chem. Phys.* **2011**, *134*, 084107.
- (89) Siddlingeshwar, B.; Hanagodimath, S. M. *Spectrochim. Acta A* **2010**, *75*, 1203–1210.
- (90) Crystals grown by slow diffusion of cyclohexane into a solution of 1,4-diaminoanthraquinone in dichloromethane.
- (91) Zakerhamidi, M. S.; Ghanadzadeh, A.; Moghadam, M. *Spectrochim. Acta A* **2011**, *79*, 74–81.

Absolute Entropy and Energy of Carbon Dioxide Using the Two-Phase Thermodynamic Model

Shao-Nung Huang,[†] Tod A. Pascal,^{‡,§} William A. Goddard, III,^{‡,§} Prabal K. Maiti,^{||} and Shiang-Tai Lin^{*,†}

[†]Department of Chemical Engineering, National Taiwan University, Taipei 10617, Taiwan

[‡]Materials and Process Simulation Center, Beckman Institute, California Institute of Technology, Pasadena, California 91125, United States

[§]Graduate School of EEWS (WCU), Korea Advanced Institute of Science and Technology, Daejeon 305-701, Republic of Korea

^{||}Centre for Condensed Matter Theory, Department of Physics, Indian Institute of Science, Bangalore 560012, India

ABSTRACT: The two-phase thermodynamic (2PT) model is used to determine the absolute entropy and energy of carbon dioxide over a wide range of conditions from molecular dynamics trajectories. The 2PT method determines the thermodynamic properties by applying the proper statistical mechanical partition function to the normal modes of a fluid. The vibrational density of state (DoS), obtained from the Fourier transform of the velocity autocorrelation function, converges quickly, allowing the free energy, entropy, and other thermodynamic properties to be determined from short 20-ps MD trajectories. The anharmonic effects in the vibrations are accounted for by the broadening of the normal modes into bands from sampling the velocities over the trajectory. The low frequency diffusive modes, which lead to finite DoS at zero frequency, are accounted for by considering the DoS as a superposition of gas-phase and solid-phase components (two phases). The analytical decomposition of the DoS allows for an evaluation of properties contributed by different types of molecular motions. We show that this 2PT analysis leads to accurate predictions of entropy and energy of CO₂ over a wide range of conditions (from the triple point to the critical point of both the vapor and the liquid phases along the saturation line). This allows the equation of state of CO₂ to be determined, which is limited only by the accuracy of the force field. We also validated that the 2PT entropy agrees with that determined from thermodynamic integration, but 2PT requires only a fraction of the time. A complication for CO₂ is that its equilibrium configuration is linear, which would have only two rotational modes, but during the dynamics it is never exactly linear, so that there is a third mode from rotational about the axis. In this work, we show how to treat such linear molecules in the 2PT framework.

1. INTRODUCTION

Carbon dioxide (CO₂) is an important chemical in the biosphere. It is the source of carbon for photosynthetic generation development of plants and the product of respiration in animals. Industrial societies produce a great deal of CO₂ from combustion and other chemical processes, and it is a popular solvent for supercritical extraction. Above its critical pressure (72.9 atm) and temperature (304.2 K), carbon dioxide behaves as a supercritical fluid: it has the diffusion constant of a gas, while maintaining the density of a liquid. This behavior facilitates the use of supercritical CO₂ (scCO₂) in a wide range of industrial processes, from chemical extraction^{1,2} to petroleum recovery.^{3,4} Recent studies have focused on utilizing liquid and scCO₂ as a cost-effective “green” solvent⁵ for chemical reactions, owing to low toxicity, high availability, and catalytic ability.^{6,7} More recently there is great concern that CO₂ is responsible for anthropomorphic climate change, responsible for global warming, which is stimulating many efforts to capture and sequester CO₂.^{8–10} The knowledge of thermodynamic properties of CO₂ under various conditions and with various additional components is important for studying such CO₂ related problems.

Computer simulations (molecular dynamics, Monte Carlo, quantum mechanics) are powerful tools used to estimate physical properties of CO₂. Of particular interest are the vapor–liquid coexistence curve,^{11–16} supercritical behavior

(thermodynamics,^{15,16} transport properties,^{11,16–18} structural properties,^{11,15,16,19,20} other properties^{20–22}), and properties of solid CO₂.²³ The CO₂ molecule is unique due to its linear structure, zero dipole moment, and large quadrupole moment.²⁴ However, in a dynamics collection of CO₂ molecules, it is essentially always nonlinear.^{15,19–21} This change in character contributes to the special properties of CO₂, particularly in the supercritical state, and challenges the prediction of its properties using molecular simulations. A thermodynamic property of particular interest is the absolute entropy. Recently, some theory and methods have been developed to estimate the absolute entropy and/or solvation free energy. However, most focus on water,^{25–27} aqueous solutions,^{28–30} or glass-like systems.^{25,31} There is no report on the performance of such methods for linear molecules such as CO₂.

The two-phase thermodynamic (2PT) method is an efficient way to estimate thermodynamic properties (energy, entropy, and heat capacity) of a system. This method has been shown to provide accurate properties using a short (about 20 ps) MD trajectory for systems such as Lennard-Jones fluids,³² liquid–vapor water along the coexistence curve,³³ and many common organic liquids under standard conditions.³⁴ The 2PT

Received: March 27, 2011

Published: May 16, 2011

method has also been successfully used in calculating the entropy of water in different regions such as the dendrimer,³⁵ lipid bilayer,³⁶ and carbon nanotube.³⁷ The method is also reasonably accurate in describing the entropic penalty of DNA while binding to dendrimer³⁸ as well as describing the role of counterion release entropy in macromolecular complexation.^{39,40} In this work, we present the use of 2PT in the property determination of CO₂. We validate the 2PT determined entropy by comparing it to those determined from thermodynamic integration (TI).

2. THEORY

2.1. Density of State Function and Its Decomposition. The density of state function, $S(v)$, which is defined as the sum of mass-weighted atomic spectral densities, can be obtained from the Fourier transform of velocity autocorrelation function (VACF),^{32,33} or equivalently the velocity spectrum⁴¹

$$S(v) = \frac{1}{k_B T} \sum_{l=1}^N \sum_{k=1}^3 \lim_{\tau \rightarrow \infty} \frac{m_l}{\tau} \left| \int_{-\tau}^{\tau} v_l^k(t) e^{-i2\pi vt} dt \right|^2 \quad (1)$$

where N is the total number of atoms in the system, m_l is the mass of atom l , and v_l^k is the velocity of atom l in the k direction ($k = 1-3$ represents $x, y,$ and z directions, respectively). The function $S(v)$ is the distribution of normal modes of the system, i.e., $S(v) dv$ represents the number of normal modes with frequencies from v to $v + dv$. The integration $S(v)$ gives the total degrees of freedom (DF) $3N$; i.e.

$$\int_0^{\infty} S(v) dv = 3N \quad (2)$$

(Note that in MD simulations the translational degrees of freedom are removed for the conservation of linear momentum; therefore, the integration gives $3N - 3$ instead.) For a pure monatomic system, the zero-frequency density of state is associated with the diffusion coefficient of particles^{32,33}

$$D = \frac{k_B T}{12mN} S(0) \quad (3)$$

where T is the temperature and k_B is the Boltzmann constant.

For systems of polyatomic molecules, Lin et al.³³ suggested that the $S(v)$ be decomposed into three components: translation (trn), rotation (rot), and intramolecular vibration motions (imv):

$$S(v) = S_{\text{trn}}(v) + S_{\text{rot}}(v) + S_{\text{imv}}(v) \quad (4)$$

where the translation component is obtained from the center of mass velocity of the molecules

$$S_{\text{trn}}(v) = \frac{1}{k_B T} \sum_{j=1}^M \sum_{k=1}^3 \lim_{\tau \rightarrow \infty} \frac{m_j}{\tau} \left| \int_{-\tau}^{\tau} v_j^{*k}(t) e^{-i2\pi vt} dt \right|^2 \quad (5)$$

where M is the total number of molecules in the system, m_j is the mass of molecule j , and v_j^{*k} is the center of mass velocity of molecule j in the k direction. The rotational density of state function is determined by using the following equations:

$$S_{\text{rot}}(v) = \frac{1}{k_B T} \sum_{j=1}^M \sum_{k=1}^{3(2)} \lim_{\tau \rightarrow \infty} \frac{I_j^k}{\tau} \left| \int_{-\tau}^{\tau} \omega_j^k(t) e^{-i2\pi vt} dt \right|^2 \quad (6)$$

where ω_j^k and I_j^k are the angular velocity and moment of inertia of molecule j along the k th principal axis, respectively. For nonlinear

molecules (e.g., water), there are three nonzero principle moments of inertia. For linear molecules (e.g., nitrogen and carbon dioxide), there are only two nonzero principle moments of inertia, and the value of k runs from 1 to 2.

The intramolecular velocity can be determined by subtracting the center of mass translation and rotation velocities

$$\vec{v}_l^{\text{imv}} = \vec{v}_l - \vec{v}_j^* - \vec{\omega}_j \times \vec{r}_{lj} \quad (7)$$

where \vec{r}_{lj} is the position vector of atom l from the center of mass of molecule j . Using the intramolecular velocity in eq 1 leads to the corresponding component of the density of state function.

2.2. Thermodynamic Properties from Two-Phase Thermodynamic (2PT) Model. The thermodynamic properties (absolute entropy, energy, and heat capacity) are determined from the sum of translation, rotation, and intramolecular vibration contributions³³

$$E = E_0 + E_{\text{trn}} + E_{\text{rot}} + E_{\text{imv}} \quad (8)$$

$$S = S_{\text{trn}} + S_{\text{rot}} + S_{\text{imv}} \quad (9)$$

$$C_v = \frac{dE_0}{dT} + C_{v_{\text{trn}}} + C_{v_{\text{rot}}} + C_{v_{\text{imv}}} \quad (10)$$

where E_0 is the reference energy.³³ For a system containing only harmonic motions (e.g., crystals), its thermodynamic properties can be calculated exactly from the density of state $S(v)$ based on statistical mechanics for harmonic oscillators. For fluids, such a harmonic approximation is no longer valid because of the significant anharmonic nature of the low frequency modes. In particular, the zero-frequency (diffusive) modes would lead to diverged properties. In the two-phase thermodynamic (2PT) model, the anharmonic effects are treated by dividing the density of state distribution into solid-like and gas-like components, i.e.

$$S_m(v) = S_m^s(v) + S_m^g(v) \quad (11)$$

where the subscript m denotes the translation (trn) or rotation (rot) component. The gas component is determined accordingly based on the DoS at zero frequency and the fluidicity factor f_m

$$S_m^g(v) = \frac{S_m(0)}{1 + \left[\frac{\pi v S_m(0)}{6 f_m M} \right]^2} \quad (12)$$

and the fluidicity factor f_m is determined from the dimensionless diffusivity constant Δ_m as

$$2\Delta_m^{-9/2} f_m^{15/2} - 6\Delta_m^{-3} f_m^5 - \Delta_m^{-3/2} f_m^{7/2} + 6\Delta_m^{-3/2} f_m^{5/2} + 2f_m - 2 = 0 \quad (13)$$

with

$$\Delta_m(T, V, M, m, S_m(0)) = \frac{2S_m(0)}{9M} \left(\frac{\pi k_B T}{m} \right)^{1/2} \left(\frac{N}{V} \right)^{1/3} \left(\frac{6}{\pi} \right)^{2/3} \quad (14)$$

Equation 12 ensures that all of the diffusive modes are included in the gas-like component, i.e., $S(0) = S^g(0)$. The integration of eq 12 over frequency gives the degrees of freedom of the gas-like component, $3Mf_m$. Once the gas-like component is determined, the solid-like component can be obtained from the difference between the total DoS and the gas-like DoS from eq 11.

Once the DoS are available, the thermodynamic properties can be expressed as the integral of the density of state function weighed by the corresponding weighting functions for the j component of different motions $W_{i,m}^j(v)$ ($i = E, S$, or Cv ; $j = s$ or g ; $m = \text{trn, rot, or imv}$)

$$E_m = \beta^{-1} \left[\int_0^\infty dv S_m^s(v) W_{E,m}^s(v) + \int_0^\infty dv S_m^g(v) W_{E,m}^g(v) \right] \quad (15)$$

$$S_m = k_B \left[\int_0^\infty dv S_m^s(v) W_{S,m}^s(v) + \int_0^\infty dv S_m^g(v) W_{S,m}^g(v) \right] \quad (16)$$

$$Cv_m = k_B \left[\int_0^\infty dv S_m^s(v) W_{Cv,m}^s(v) + \int_0^\infty dv S_m^g(v) W_{Cv,m}^g(v) \right] \quad (17)$$

where $\beta = (k_B T)^{-1}$. The weighing functions are

$$W_E^s(v) = \frac{\beta h v}{2} + \frac{\beta h v}{\exp(\beta h v) - 1} \quad (18)$$

$$W_S^s(v) = \frac{\beta h v}{\exp(\beta h v) - 1} - \ln[1 - \exp(-\beta h v)] \quad (19)$$

$$W_{Cv}^s(v) = \frac{(\beta h v)^2 \exp(\beta h v)}{[\exp(\beta h v) - 1]^2} \quad (20)$$

$$W_{E,\text{trn}}^g(v) = W_{E,\text{rot}}^g(v) = W_{Cv,\text{trn}}^g(v) = W_{Cv,\text{rot}}^g(v) = 0.5 \quad (21)$$

$$W_{S,\text{trn}}^g(v) = \frac{1}{3} \frac{S^{\text{HS}}}{k_B} \quad (22)$$

$$W_{S,\text{rot}}^g(v) = \frac{1}{3} \frac{S^{\text{R}}}{k_B} \quad (23)$$

where S^{HS} and S^{R} are the hard-sphere entropy and rotational entropy of molecules (rigid rotor) at the ideal gas state, respectively:

$$\frac{S^{\text{HS}}}{k} = \frac{5}{2} + \ln \left[\left(\frac{2\pi m k T}{h^2} \right)^{3/2} \frac{V}{f_{\text{trn}} N} z(y) \right] + \frac{y(3y-4)}{(1-y)^2} \quad (24)$$

$$\frac{S^{\text{R}}}{k} = 1 + \ln \left[\frac{T}{\sigma \Theta_r} \right] \quad (25)$$

where $y = f_{\text{trn}}^{5/2} / \Delta_{\text{trn}}^{3/2}$ and $z(y)$ is the compressibility factor of hard sphere gases from the Carnahan–Starling equation of state,⁴² $\Theta_r = h^2 / (8\pi^2 I_r k)$ is the rotation temperature, and σ is the symmetry number. It is noteworthy that the 2PT method includes quantum correction by applying the harmonic oscillator (HO) approximation for the canonical partition function Q , which is included in the weighting function of the solid-like components.^{32,33} The reference energy is obtained by comparing the MD potential energy to the 2PT energy based on classical harmonic oscillators³³

Table 1. FEPM2 Force Field Parameters for CO₂^a

element	ε/k_b (K)	σ (Å)	q (e)
O	80.507	3.033	-0.3256
C	28.129	2.757	0.6512
l_0 (Å)	1.149	K_b (kcal/mol/Å ²) ^b	1283.38
θ_0 (deg)	180	K_θ (kcal/mol/rad ²) ^b	56.53

^a ε and σ are the Lennard-Jones parameters in the LJ-12-6 potential $E^{\text{vdw}}(r) = 4\varepsilon[(\sigma/r)^{12} - (\sigma/r)^6]$. q is the atomic charge for calculation of electrostatic energy. The valence energy for CO₂ is $E^{\text{valence}} = E^{\text{bond}} + E^{\text{angle}} = K_b(l - l_0)^2 + K_\theta(\theta - \theta_0)^2$, where l_0 is the equilibrium C=O bond length, θ_0 is the equilibrium OCO angle, and K_b and K_θ are the stretching and bending force constants, respectively. ^b The value of K_b and K_θ are taken from refs 17 and 21, respectively; all other parameters are from ref 14.

$$E_0 = E_{\text{MD}} - \beta^{-1} 3N(1 - 0.5f_{\text{trn}} - 0.5f_{\text{rot}}) \quad (26)$$

where E_{MD} is the total energy of the system from the same MD simulation.

3. COMPUTATIONAL DETAILS

The open-source LAMMPS⁴³ package is used for the molecular dynamic simulations. The absolute entropy and energy of CO₂ fluid are determined along the experimental vapor–liquid equilibrium (VLE) conditions and compared to the experimental data. The experimental VLE data are taken from the steam table.⁴⁴ Three-dimensional periodic models of 256 molecules at desired densities are created for the subsequent molecular dynamic simulations.

The flexible version of the EPM2 force field (FEPM2; original EPM2¹⁴ with the stretching force constant by Nieto-Draghi et al.¹⁷ and bending force constant by Anderson et al.;²¹ parameters are listed in Table 1) is used to describe the interactions in the system. The two force constants were fitted to the vibration frequencies of symmetric stretching and angle bending, respectively. We compare the vibration frequencies of CO₂ with the experimental data⁴⁵ in Table 2.

Energy minimization is performed on the initial structure. A long 4 ns MD simulation at constant volume and temperature (NVT) follows to equilibrate the system. To facilitate thermal equilibration between different types of motion (translation, rotation, and vibration), the three temperatures associated with each motion type are rescaled to the system temperature by rescaling the velocities of the corresponding motions at a time interval of 1 ps. We will show that such a velocity rescaling is critical for obtaining thermal equilibration in CO₂. The system is further equilibrated using an additional 1 ns NVT simulation without such a velocity rescaling. An additional 20 ps simulation for sampling is performed with the trajectory saved at every 4 fs for the 2PT property analysis. We have examined and confirmed that thermodynamic properties of CO₂ from 2PT analysis converge within 20 ps, which is consistent with previous findings.^{33,34}

The integration time step is set to 1 fs. The time constants for the Nose-Hoover thermostat⁴⁶ and velocity rescaling are set to 0.1 and 1 ps, respectively. The long-range electrostatic interaction is estimated by the particle–particle particle–mesh Ewald method⁴⁷ (pppm) with an accuracy of 4.18×10^{-5} kJ/mol. The cutoff radii for the ppm and van der Waals interaction are 8.5 Å

Table 2. Comparison of Intramolecular Vibration Frequencies of CO₂ from the Experiment and MD Simulations

vibration modes	NIST data ⁴⁵	this work	this work
	(gas phase)	(220 K, sat'd liquid)	(220 K, sat'd vapor)
symmetric stretching	1285.40 (Raman)	1326	1324
	1388.15 (Raman)	1418	1416
angle bending	667.38 (IR)	679	681
asymmetric stretching	2349.16 (IR)	2659	2658

and 9.5 Å for liquid-phase simulations. For vapor phase simulations, we use a cutoff radius of 17.0 Å for more efficient pppm calculations.⁴⁸

To validate the accuracy of the entropy from the 2PT model, we compared it to the results from thermodynamic integration (TI) for CO₂ from 220 K to 600 K. Since TI leads only to an entropy difference between two state points, whereas 2PT leads to absolute entropies, we take the difference between the absolute 2PT entropies.

The way to determine the density-of-state function for translation, rotation, and intramolecular vibration has been detailed elsewhere.³³ Briefly, the center of mass velocity (\vec{v}^*), the angular momentum (\vec{L}), and the inertia tensor (\vec{I}) are determined for every molecule at each time instant. The principle moments of inertia (I_1 , I_2 , and I_3) and the principal axis (\vec{p}_1 , \vec{p}_2 , and \vec{p}_3) are then obtained by solving the eigenvalue and eigenvector of the inertia tensor. The angular velocity along the principal axis can be calculated by $\omega_i = (\vec{L} \cdot \vec{p}_i / I_i) \vec{p}_i$. The velocity component due to intramolecular vibration (\vec{v}^{imv}) can then be determined from eq 7. These velocity components allow for the determination of the corresponding DoS using eqs 5 (trn), 6 (rot), and 1 (vib). It should be noted that while carbon dioxide is regarded as a linear molecule, it is almost never linear in the molecular dynamic simulations. For example, Saharay and Balasubramanian¹⁹ reported the average value of the angle OCO to be 174.2° on the basis of the Car–Parrinello molecular dynamic simulations. In practice, CO₂ has two large principle moments of inertia ($I_1 = I_2 = 43.4$ g/mol Å²) and a third one that fluctuates around zero ($I_3 \sim 0.01$ g/mol Å²). Therefore, we have set I_3 and ω_3 to zero and therefore attribute such motions as part of the intramolecular vibration.

4. RESULTS AND DISCUSSION

4.1. The Density of State of Carbon Dioxide. Figure 1 shows the DoS spectrum of liquid FEPM2 CO₂ at $T = 220$ K. The decomposition of $S(v)$ to translation, rotation, and internal vibration is also presented. The broad band between 0 and 200 cm⁻¹ represents the modes corresponding to librations. Intramolecular vibrations are observed in the higher frequency region: angle bending at 679 cm⁻¹, symmetric stretching at 1326 and 1418 cm⁻¹, and asymmetric stretching at 2660 cm⁻¹ (also listed in Table 2). The splitting peaks of symmetric stretching is a result of the Fermi resonance.^{49,50} Both the translation and rotation motions contribute to the zero-frequency density of state function $S(0)$, indicating translational and rotational diffusion in the system.

Figure 1b and c illustrate the decomposition of translation DoS, $S_{\text{trn}}(v)$, and rotational DoS, $S_{\text{rot}}(v)$, to gas-like and solid-like contributions. It can be seen that the 2PT method nicely

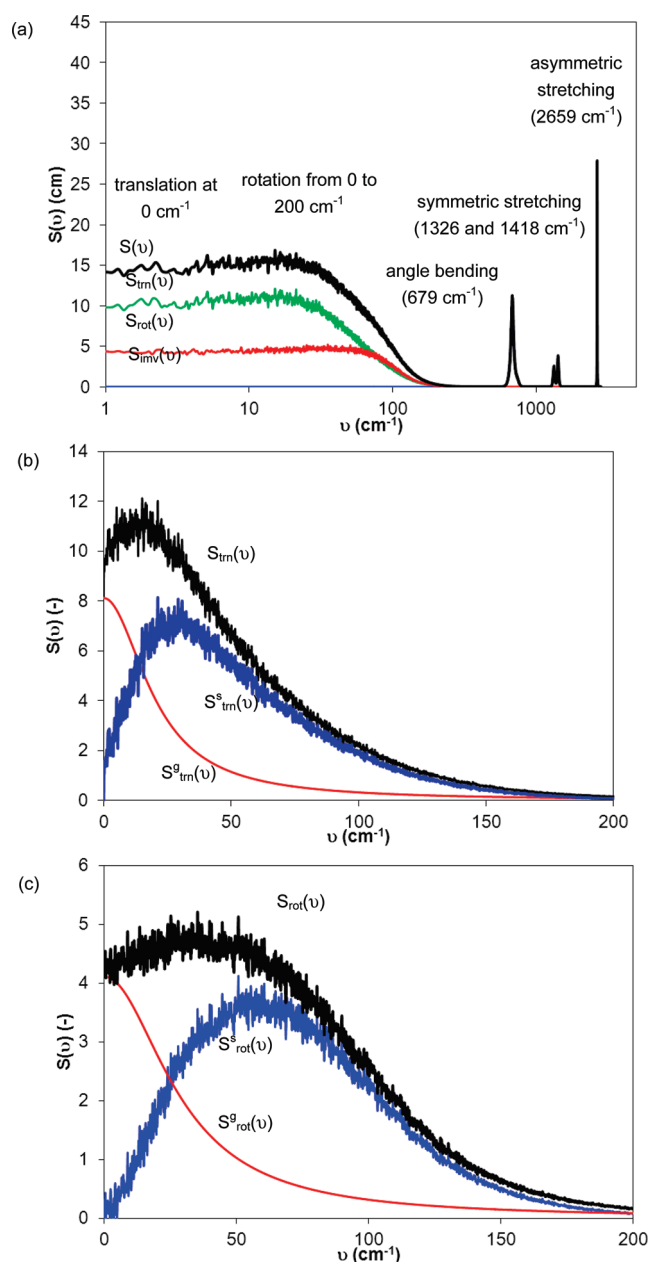


Figure 1. (a) Density of state spectrum of liquid CO₂ at 220 K and 1.1663 g/cm³ from 200-ps sampling. (b) Translation density of state and its components. (c) Rotation density of state and its components. This illustrates the various DoS components used in the 2PT analysis.

separates the DoS to an exponentially decaying gas-like component and a solid-like component with its intensity approaching zero at zero frequency.

4.2. Thermodynamic Properties of CO₂. To illustrate the applicability of 2PT over a wide range of state conditions, the entropy and energy of CO₂ are determined at temperatures and densities⁴⁴ along the vapor–liquid coexistence curve. Table 3 summarizes the calculation results of the temperatures of the molecular motions, internal energy, and absolute entropy and compares the 2PT calculations with the experimental data.⁴⁴ The fluidicity factors increase from 0.36 (translation) and 0.25 (rotation) for the liquid at 220 K to 0.70 and 0.48 at the critical point (304 K), and to 0.89 and 0.81 for the vapor at 220 K. The

Table 3. Comparison between 2PT Properties of FEPM2 CO₂ and the Experimental Data^{44a}

state of aggregation	<i>d</i>	<i>T</i>	<i>S</i> _{2PT}	<i>S</i> _{exp}	<i>E</i> _{2PT}	<i>E</i> _{md}	<i>E</i> _{exp}	<i>f</i> _{trn}	<i>f</i> _{rot}
saturated liquid	1.1663	220	111.82	118.12	18.91	17.71	17.25	0.36	0.25
	1.1292	230	116.56	121.59	19.16	18.85	18.06	0.40	0.26
	1.0896	240	119.38	125.07	19.90	20.04	18.88	0.42	0.28
	1.0467	250	123.68	128.64	21.04	21.18	19.74	0.44	0.29
	1.0000	260	127.50	132.24	21.30	22.39	20.65	0.47	0.31
	0.9470	270	131.35	135.94	22.34	23.65	21.61	0.51	0.33
	0.8850	280	136.79	139.77	22.91	24.88	22.64	0.53	0.35
	0.8058	290	141.66	143.95	24.76	26.27	23.81	0.57	0.39
	0.6803	300	147.53	149.32	26.50	28.18	25.33	0.63	0.43
	critical point	0.4662	304	156.09	156.58	27.52	30.36	27.32	0.70
saturated vapor	0.2703	300	163.86	164.68	29.76	31.99	29.28	0.78	0.58
	0.1724	290	169.50	169.61	30.03	32.53	30.19	0.82	0.64
	0.1220	280	171.63	172.73	30.12	32.65	30.59	0.85	0.69
	0.0885	270	175.25	175.20	29.93	32.36	30.78	0.87	0.71
	0.0645	260	177.07	177.44	30.57	32.26	30.86	0.88	0.73
	0.0467	250	179.85	179.51	30.78	31.77	30.87	0.89	0.77
	0.0333	240	182.56	181.67	30.81	31.45	30.82	0.90	0.79
	0.0234	230	184.35	183.87	30.66	31.06	30.74	0.89	0.80
	0.0160	220	186.71	186.24	30.62	30.62	30.62	0.89	0.81

^a Reference state of energy: saturated vapor at 220 K. Units: *T* in K, *E* in kJ/mol, *S* in J/mol/K, and *d* in g/cm³.

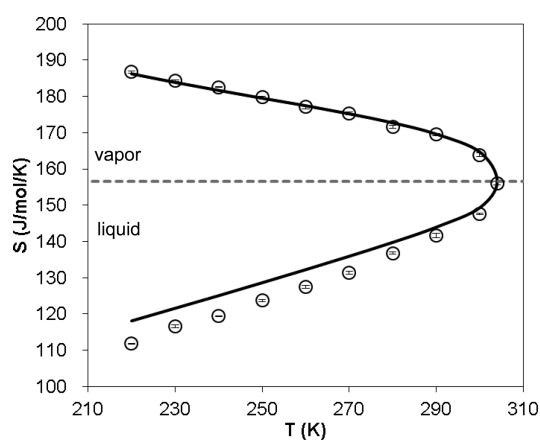


Figure 2. The absolute entropy of CO₂ along the vapor–liquid coexistence curve (for CO₂, *T*_{tp} = 216.6 K and *T*_c = 304.2 K) calculated by the 2PT model (open circle) from 20-ps MD trajectories. The results are compared with the experimental data⁴⁴ (black solid line). The gray dashed line indicates the entropy at the critical state. This shows that 2PT can provide a reliable entropy of CO₂ vapor and liquid over a wide range of conditions.

increase of the fluidicity factor implies the increasing gas-like nature of the fluid as its density decreases along the coexistence curve. Figures 2 and 3 illustrate the absolute entropy *S*(2PT) and its components (*S*_{trn}, *S*_{rot}, and *S*_{inv}) along the vapor–liquid coexistence curve. The 2PT entropies are in excellent agreement with experimental results in the vapor phase. The discrepancy between 2PT entropy and experimental results increases with increasing density, with the largest error observed for the saturated liquid at 220 K (5.3%). Furthermore, the

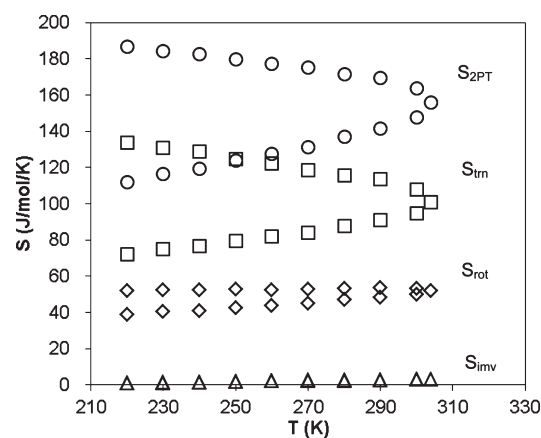


Figure 3. The absolute entropy (*S*_{2PT}) its components (*S*_{trn}, *S*_{rot}, *S*_{inv}) of CO₂ along the vapor–liquid coexistence curve. This shows that the entropy of CO₂ is dominated by contributions from translation and rotational motions.

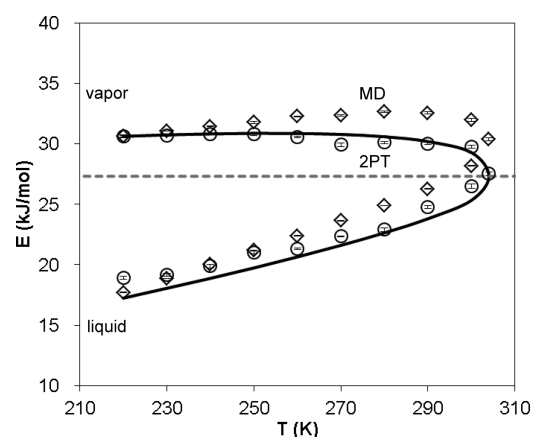


Figure 4. The internal energy of CO₂ along the vapor–liquid coexistence curve calculated by the 2PT model (open circle) from 20-ps MD trajectories. The results are compared with classical energy from MD simulations (open diamond) and the experimental data⁴⁴ (black solid line). The gray dashed line indicates the energy at the critical state. This shows that while MD energy difference between the vapor and liquid phases (energy of vaporization) may be consistent with experimental data, the value in each individual phase is incorrect. The 2PT energies are in better agreement with the experimental data for both phases.

intramolecular vibration entropy *S*_{inv} is negligible compared to the other two components (*S*_{trn} and *S*_{rot}) in all cases (see Figure 3). The change of entropy along the coexistence curve is dominated by *S*_{trn}, meaning that the change of density and temperature affects the translational motion most. *S*_{rot} is about constant in the vapor phase, whereas it increases in the liquid phase with increasing temperature and decreasing density. That is, under high-density conditions, the rotational motion of CO₂ molecules is hindered by the surrounding molecules, while the molecular rotation hindrance is insignificant at low density because of the weaker intermolecular interaction.

Figure 4 shows the energy along the vapor–liquid coexistence curve. It is interesting to note that the total energy *E*_{md} from MD (sum of kinetic and potential energies, shown in open diamonds) is overestimated in both phases, especially near the critical point, when compared to the experimental data (solid curve). This

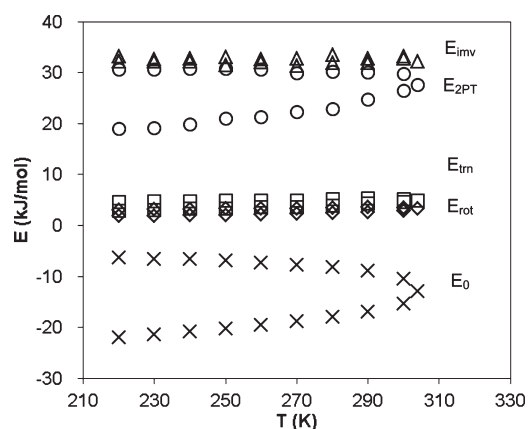


Figure 5. The internal energy (E_{2PT}) and its components (E_0 , E_{tm} , E_{rot} , E_{imv}) of CO_2 along the vapor–liquid coexistence curve. This shows that the total energy E_{2PT} is dominated by the reference energy E_0 .

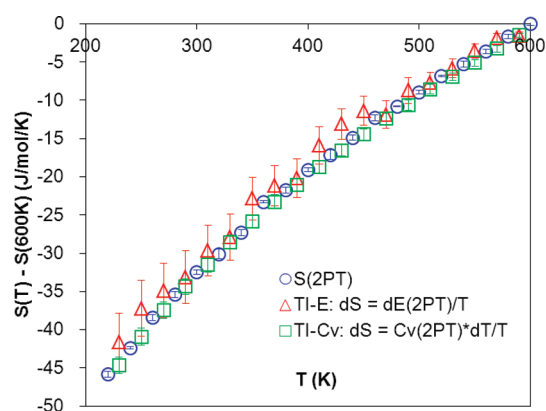


Figure 6. The relative entropy of CO_2 ($d = 1.1663 \text{ g/cm}^3$, the saturated liquid density at 220 K) from $T = 600$ to 220 K using the 2PT method and thermodynamic integration calculations. This shows that the 2PT entropies are consistent with those determined from TI.

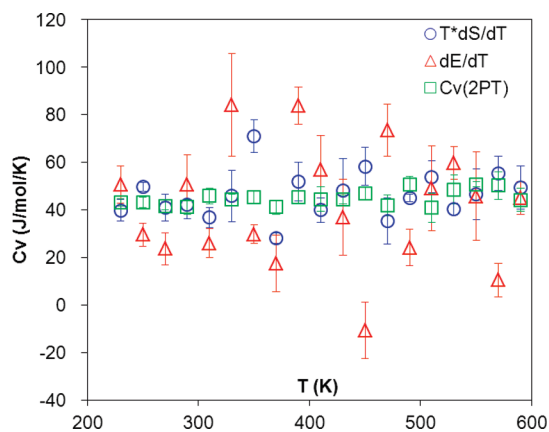


Figure 7. The constant volume heat capacity of liquid CO_2 ($d = 1.1663 \text{ g/cm}^3$, the saturated liquid density at 220 K) from $T = 600$ to 220 K. Triangle, calculated from $Cv = dE_{2PT}/dT$; square, heat capacity directly from 2PT method (eq 17); circle, from TdS_{2PT}/dT . This shows that the direct calculation of the specific heat from the 2PT DoS is much more accurate than deriving it from the changes in the calculated properties of other variables.

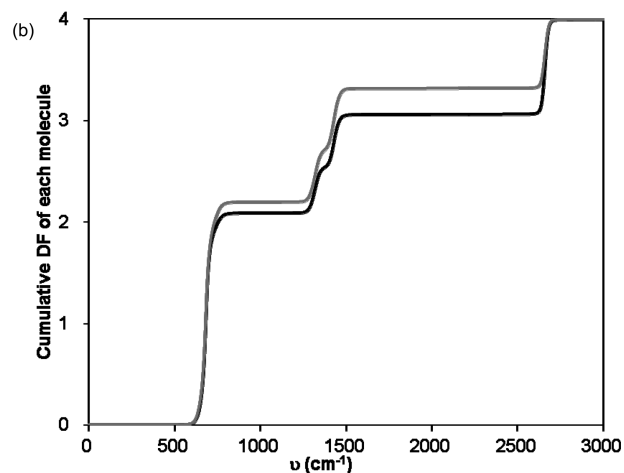
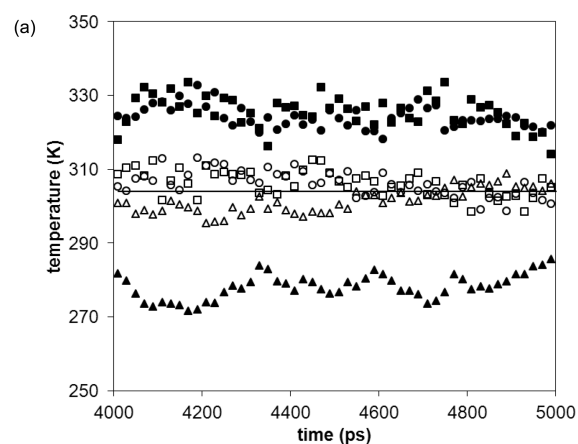


Figure 8. (a) The temperature components (circles for translation T_{trn} , squares for rotation T_{rot} , and triangles for intramolecular vibration T_{imv}) from the simulations of CO_2 at the critical point. The closed symbols indicate temperatures in the 5th ns from a regular NVT simulation. The open symbols represent results if the first 4 ns are subjected to velocity rescaling. (b) Cumulative vibration degrees of freedom of the intramolecular vibrations from simulations with (solid line) and without (gray line) velocity rescaling. This shows that velocity rescaling provides effective means for energy exchange between different modes of motions in CO_2 .

indicates that, while the heat of vaporization obtained from E_{md} may be consistent with experimental data over a wide range of temperatures, the (dynamic and thermodynamic) properties may be in error in both the vapor and liquid phases. In contrast, the 2PT energies, which take the quantum correction into consideration, are in good agreement with the experiment. The components of the total energy E_{2PT} are illustrated in Figure 5. In both phases, E_{tm} and E_{rot} slightly increase with the increasing temperature, whereas E_{imv} is nearly constant. The change of the reference energy (E_0) dominates the temperature and density dependence of E_{2PT} . It is noteworthy that the fluctuations observed in E_{2PT} are a result of the fluctuation in E_{imv} , which is affected by the energy equilibration between different vibrational modes.

4.3. Comparison of Entropy from 2PT and Thermodynamic Integration. Here, we validate the entropy change of CO_2 between two thermodynamic states from 2PT with that from thermodynamic integration (TI). The entropy change by

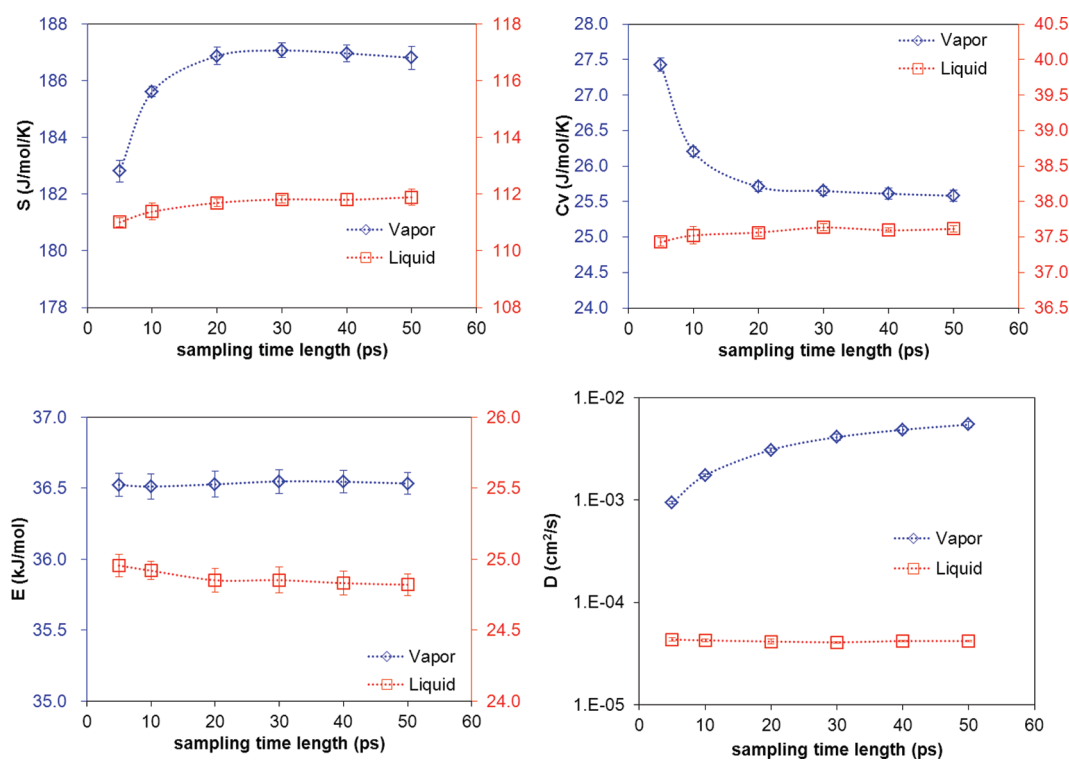


Figure 9. The 2PT thermodynamic (S , E , and C_v) and transport (diffusivity D) properties evaluated using different lengths of trajectories for saturated vapor (open diamonds) and liquid (open squares) CO_2 at 220 K. The error bars (of all the figures presented in this paper) indicate the standard deviations from four samplings. This shows that the 2PT thermodynamic properties converge within 20 ps.

heating a fluid from T_1 to T_2 under constant volume can be obtained from the temperature integration of the energy (referred to as TI-E) or constant volume heat capacity (TI-Cv) as follows:

$$S(T_2, d) - S(T_1, d) = \int_{T_1}^{T_2} \frac{dE_{2PT}(T', d)}{T' dT'} dT' \quad (27)$$

$$S(T_2, d) - S(T_1, d) = \int_{T_1}^{T_2} \frac{C_{V, 2PT}(T', d)}{T'} dT' \quad (28)$$

where d is the density of the system. Figure 6 shows the calculated entropy change of CO_2 from a saturated liquid at $T_1 = 220$ K ($d = 1.17$ g/cm³) to a higher temperature (up to 600 K) under constant density. Twenty sets of simulations were performed at a temperature interval of 20 K between 220 and 600 K. The parameters and settings for the simulations are the same as the previous cases. Note that temperature 600 K is well above the critical temperature of CO_2 (at 304.2 K), so the fluid behaves like a system of hard spheres. The integrations in eq 27 and 28 are calculated numerically on the basis of the midpoint trapezoidal rule. It can be seen that the entropy changes calculated from 2PT (open sphere) and TI (open triangle for TI-E and open square for TI-Cv) are identical within statistical uncertainty.

It should be noted that the relatively large standard deviation seen in TI-E is a result of the energy fluctuations, mainly due to intramolecular vibrations. Figure 7 compares the heat capacity from the numerical derivative of energy ($C_v = (\partial E(2PT))/(\partial T)|_d$), entropy ($C_v = (T\partial S(2PT))/(\partial T)|_d$), and the value directly obtained from eq 17. The 2PT heat capacity (open squares) is nearly constant with the increasing of

temperature, whereas the temperature derivative of either the energy (open triangles) or the entropy (open spheres) shows significant fluctuations. The fluctuation in the DoS distribution (especially in the high frequency region, i.e., internal vibrations) causes about 0.5–1 kJ/mol fluctuations in energy, resulting in $10^1 \sim 10^2$ J/mol K fluctuations in heat capacity from the numerical derivative of E . While such fluctuations may be reduced by longer simulations, the 2PT is capable of providing converged properties (e.g., C_v) without the use of exhaustive samplings.

4.4. Thermal Equilibration in CO_2 Simulations. We notice that there is a weak coupling of internal vibrational and libration modes with collisions for molecules like CO_2 with no net dipole. As a result, there is a poor thermal equilibration between different types of motions (translation, rotation, and vibration) in the system. Figure 8a illustrates the temperatures determined from the corresponding kinetic energies of a simulation at the critical point (304.2 K and 0.47 g/cm³). The temperatures are calculated from the last 1 ns of a 5 ns NVT simulation. It is seen that the translation and rotational temperatures (closed circles and squares) fluctuate around 325 K, while the intramolecular vibration temperature (closed triangles) fluctuates around 275 K over a time period of 1 ns. The slow convergence of these temperatures indicates a poor energy exchange between different types of motions in CO_2 . Also shown in Figure 8a are the temperature components (open symbols) from a simulation that has been subjected to velocity rescaling (as described in the Computational Details) in the first 4 ns of simulation. It is seen that the velocity rescaling effectively equilibrates the kinetic energies of different types of motions. The system remains in good thermal equilibration even without the velocity rescaling in the fifth ns. The velocity rescaling is also important for obtaining

the correct distribution of the degrees of freedom for the internal vibrations (two angle bending, one symmetric, and one asymmetric stretching). Figure 8b shows that the DFs of angle bending and symmetric stretching are overestimated (by 0.2 and 0.1, respectively) if the temperatures associated with different motions are not fully equilibrated (the gray line). When a good equilibration is reached, a proper DF distribution is obtained (black line). The distribution of DF has a significant impact on the energy associated with vibrations (especially the zero point energy). We note that if the DF of angle bending of CO₂ is 3% higher than the expected value (2), E_{imv} will be about 0.5 kJ/mol too low.

4.5. Convergence of Thermodynamic Properties. Figure 9 shows the thermodynamic and transport properties of saturated vapor and liquid CO₂ at 220 K evaluated using different lengths of MD trajectory. It can be seen that thermodynamic properties (E , S , and C_v) are converged within 20 ps for both phases, even though the diffusivity is not fully converged. Similar results have been reported for other organic solvents.³⁴ While the gas–solid decomposition in 2PT relies on the value of diffusivity, there seems to be a good balance between the calculated properties in from the solid and gas components such that the total property is not sensitive to the accuracy of diffusivity. We regard this merit of 2PT which allows for obtaining accurate thermodynamic properties using a very short MD trajectory.

5. CONCLUSION

The two-phase thermodynamic (2PT) method is extended to obtain the thermodynamic properties of fluids of linear molecules such as CO₂. In 2PT, the properties are calculated on the basis of proper statistical mechanical weighting to the normal modes, or density of state (DoS) distribution, of a fluid. The DoS can be analytically decomposed to contributions from molecular translation, rotation, and intramolecular vibrational motions. In molecular dynamic simulations, CO₂ molecules are almost never linear, and therefore, attention is required for the evaluation of the rotational DoS and the rotational weighting functions. We show that with proper treatment, both the energy (with quantum corrections) and the absolute entropy of CO₂ can be obtained from a short, 20 ps MD trajectory (when the system is equilibrated). We have examined the calculations over a wide range of conditions along the vapor–liquid coexistence curve. It is found that both the 2PT entropy and energy obtained from the FEPM2 force field are in good agreement with the experiment. The agreement in energy of vaporization between classical MD energy and experimental data is a cancellation of errors in the energy of both the vapor and the liquid phase. The 2PT energy, however, properly captures the experimental energy variations along the coexistence curve. Our results suggests that the classical force field may be refined on the basis of the 2PT properties. Finally, we also validate the 2PT entropy with those obtained from thermodynamic integration.

AUTHOR INFORMATION

Corresponding Author

*E-mail stlin@ntu.edu.tw.

ACKNOWLEDGMENT

This research was partially supported by the National Science Council of Taiwan (NSC 98-2221-E-002-087-MY3) and the

Ministry of Economic Affairs of Taiwan (99-5226904000-04-04). The computation resources from the National Center for High-Performance Computing of Taiwan and the Computing and Information Networking Center of the National Taiwan University are acknowledged. W.A.G. acknowledges support from the WCU (World Class University) program through the National Research Foundation of Korea funded by the Ministry of Education, Science and Technology (R31-2008-000-10055-0). W.A.G. and T.A.P. acknowledge support from DOE (DE-FE0002057, DE-AC26-07NT42677, and DE-FE0003032).

REFERENCES


- (1) Penninger, J. M. L. *Supercritical fluid technology*; Elsevier Science: Amsterdam, 1985.
- (2) Roberts, C. B.; Chateaneuf, J. E.; Brennecke, J. F. *J. Am. Chem. Soc.* **1992**, *114*, 8455–8463.
- (3) Lee, C. T.; Ryoo, W.; Smith, P. G.; Arellano, J.; Mitchell, D. R.; Lagow, R. J.; Webber, S. E.; Johnston, K. P. *J. Am. Chem. Soc.* **2003**, *125*, 3181–3189.
- (4) Schievelbein, V. H. *Method for decreasing mobility of dense carbon dioxide in subterranean formations*; Texaco Inc.: White Plains, NY, 1991.
- (5) Leitner, W.; Poliakoff, M. *Green Chem.* **2008**, *10*, 730–730.
- (6) Beckman, E. J. *J. Supercrit. Fluid* **2004**, *28*, 121–191.
- (7) Baiker, A. *Chem. Rev.* **1999**, *99*, 453–473.
- (8) Jung, J. W.; Espinoza, D. N.; Santamarina, J. C. *J. Geophys. Res., Solid Earth* **2010**, *115*, B10102.
- (9) Zhou, X. T.; Fan, S. S.; Liang, D. Q.; Du, J. W. *Energy Convers. Manage.* **2008**, *49*, 2124–2129.
- (10) Yezdimer, E. M.; Cummings, P. T.; Chialvo, A. A. *J. Phys. Chem. A* **2002**, *106*, 7982–7987.
- (11) Merker, T.; Engin, C.; Vrabc, J.; Hasse, H. *J. Chem. Phys.* **2010**, *132*.
- (12) Vrabc, J.; Stoll, J.; Hasse, H. *J. Phys. Chem. B* **2001**, *105*, 12126–12133.
- (13) Potoff, J. J.; Siepmann, J. I. *AIChE J.* **2001**, *47*, 1676–1682.
- (14) Harris, J. G.; Yung, K. H. *J. Phys. Chem.* **1995**, *99*, 12021–12024.
- (15) Zhu, A. M.; Zhang, X. B.; Liu, Q. L.; Zhang, Q. G. *Chin. J. Chem. Eng.* **2009**, *17*, 268–272.
- (16) Zhang, Z. G.; Duan, Z. H. *J. Chem. Phys.* **2005**, *122*.
- (17) Nieto-Draghi, C.; de Bruin, T.; Perez-Pellitero, J.; Avalos, J. B.; Mackie, A. D. *J. Chem. Phys.* **2007**, *126*, 8.
- (18) Galliero, G.; Nieto-Draghi, C.; Boned, C.; Avalos, J. B.; Mackie, A. D.; Baylaucq, A.; Montel, F. *Ind. Eng. Chem. Res.* **2007**, *46*, 5238–5244.
- (19) Saharay, M.; Balasubramanian, S. *J. Chem. Phys.* **2004**, *120*, 9694–9702.
- (20) Zhang, Y.; Yang, J. C.; Yu, Y. X. *J. Phys. Chem. B* **2005**, *109*, 13375–13382.
- (21) Anderson, K. E.; Mielke, S. L.; Siepmann, J. I.; Truhlar, D. G. *J. Phys. Chem. A* **2009**, *113*, 2053–2059.
- (22) Inomata, H.; Saito, S.; Debenedetti, P. G. *Fluid Phase Equilib.* **1996**, *116*, 282–288.
- (23) Murthy, C. S.; Singer, K.; McDonald, I. R. *Mol. Phys.* **1981**, *44*, 135–143.
- (24) Graham, C.; Pierrus, J.; Raab, R. E. *Mol. Phys.* **1989**, *67*, 939–955.
- (25) Sharma, R.; Agarwal, M.; Chakravarty, C. *Mol. Phys.* **2008**, *106*, 1925–1938.
- (26) Henchman, R. H. *J. Chem. Phys.* **2007**, *126*.
- (27) Wang, L.; Abel, R.; Friesner, R. A.; Berne, B. J. *J. Chem. Theory Comput.* **2009**, *5*, 1462–1473.
- (28) Irudayam, S. J.; Plumb, R. D.; Henchman, R. H. *Faraday Discuss.* **2010**, *145*, 467–485.
- (29) Shirts, M. R.; Pande, V. S. *J. Chem. Phys.* **2005**, *122*.
- (30) Garrido, N. M.; Jorge, M.; Queimada, A. J.; Economou, I. G.; Macedo, E. A. *Fluid Phase Equilib.* **2010**, *289*, 148–155.

- (31) Scala, A.; Starr, F. W.; La Nave, E.; Sciortino, F.; Stanley, H. E. *Nature* **2000**, *406*, 166–169.
- (32) Lin, S. T.; Blanco, M.; Goddard, W. A. *J. Chem. Phys.* **2003**, *119*, 11792–11805.
- (33) Lin, S. T.; Maiti, P. K.; Goddard, W. A. *J. Phys. Chem. B* **2010**, *114*, 8191–8198.
- (34) Pascal, T. A.; Lin, S. T.; Goddard, W. A. *Phys. Chem. Chem. Phys.* **2010**, *13*, 169–181.
- (35) Lin, S. T.; Maiti, P. K.; Goddard, W. A. *J. Phys. Chem. B* **2005**, *109*, 8663–8672.
- (36) Debnath, A.; Mukherjee, B.; Ayappa, K. G.; Maiti, P. K.; Lin, S. T. *J. Chem. Phys.* **2010**, 133.
- (37) Kumar, H.; Mukherjee, B.; Lin, S.-T.; Dasgupta, C.; Sood, A. K.; Maiti, P. K. *J. Chem. Phys.* **2011**, *134*, 124105.
- (38) Maiti, P. K.; Bagchi, B. *Nano Lett.* **2006**, *6*, 2478–2485.
- (39) Nandy, B.; Maiti, P. K. *J. Phys. Chem. B* **2011**, *115*, 217–230.
- (40) Vasumathi, V.; Maiti, P. K. *Macromolecules* **2010**, *43*, 8264–8274.
- (41) Berens, P. H.; Mackay, D. H. J.; White, G. M.; Wilson, K. R. *J. Chem. Phys.* **1983**, *79*, 2375–2389.
- (42) Carnahan, N. F.; Starling, K. E. *J. Chem. Phys.* **1970**, *53*, 600–603.
- (43) Plimpton, S. J. *Comput. Phys.* **1995**, *117*, 1–19.
- (44) Perry, R. H.; Green, D. W.; Maloney, J. O. *Perry's Chemical Engineers' Handbook*, 7th ed.; McGraw-Hill: New York, 1997.
- (45) NIST Chemistry WebBook, Reference Database Number 69; National Institute of Standards and Technology: Gaithersburg, MD, 2000. <http://webbook.nist.gov/chemistry/> (accessed May 2011).
- (46) Hoover, W. G. *Phys. Rev. A* **1985**, *31*, 1695–1697.
- (47) Hockney, R. W.; Eastwood, J. W. *Computer Simulation Using Particles*; Taylor & Francis: New York, 1989.
- (48) Karasawa, N.; Goddard, W. A. *J. Phys. Chem.* **1989**, *93*, 7320–7327.
- (49) Arakawa, M.; Yamamoto, J.; Kagi, H. *Chem. Lett.* **2008**, *37*, 280–281.
- (50) Olijnyk, H.; Jephcoat, A. P. *Physica B* **1999**, *265*, 54–59.

Development of a Polarizable Force Field for Molecular Dynamics Simulations of Poly (Ethylene Oxide) in Aqueous Solution

Oleg N. Starovoytov, Oleg Borodin, Dmitry Bedrov, and Grant D. Smith*

Department of Materials Science and Engineering, University of Utah, 122 S. Campus Drive, Salt Lake City, Utah 84112, United States

 Supporting Information

ABSTRACT: We have developed a quantum chemistry-based polarizable potential for poly(ethylene oxide) (PEO) in aqueous solution based on the APPLE&P polarizable ether and the SWM4-DP polarizable water models. Ether–water interactions were parametrized to reproduce the binding energy of water with 1,2-dimethoxyethane (DME) determined from high-level quantum chemistry calculations. Simulations of DME–water and PEO–water solutions at room temperature using the new polarizable potentials yielded thermodynamic properties in good agreement with experimental results. The predicted miscibility of PEO and water as a function of the temperature was found to be strongly correlated with the predicted free energy of solvation of DME. The developed nonbonded force field parameters were found to be transferrable to poly(propylene oxide) (PPO), as confirmed by capturing, at least qualitatively, the miscibility of PPO in water as a function of the molecular weight.

I. INTRODUCTION

Poly(ethylene oxide), or PEO, also referred to as poly(ethylene glycol) or PEG, is a water-soluble polymer used in a wide variety of applications ranging from biomedical to viscosity modifications.^{1–4} PEO is consoluble with water for low molecular weights (less than 2000 Da) but exhibits lower critical solution temperature (LCST) behavior for higher molecular weights.^{5–7} The conformations,^{8–11} hydration,^{12,13} hydrogen bonding,^{14–17} and phase behavior^{18–20} of PEO–water solutions have been the subject of extensive molecular dynamics (MD) simulations and theoretical studies, which have provided valuable insight into the behavior and properties of this important polymer solution.

The phase behavior of numerous block copolymers of water-soluble PEO and various hydrophobic polymers, including poly(propylene oxide) or PPO, in aqueous solutions has also been investigated.¹ Chemical structures of PEO and PPO as well as their shortest oligomers are shown in Figure 1. Many of these amphiphilic block copolymers utilize PEO as a soluble block and PPO as an insoluble block in diblock, triblock, or other architectures.^{1–3} The well-known PEO–PPO–PEO triblock architectures as produced by BASF are referred to as Pluronic. At low concentrations and temperatures, Pluronic typically exist as fully solubilized, isolated chains or unimers. Transition from the unimer to micelle state occurs with an increase in concentration or temperature when the critical micelle concentration (CMC) or critical micelle temperature (CMT) is reached.²¹ As a result, spherical micelles are formed with external PEO coronas, and central PPO cores are often observed.^{22,23} Other structures are achievable with particular length ratios of hydrophilic and hydrophobic blocks.^{23,24}

The self-assembly of PEO–PPO–PEO triblock polymers in water into micelles with increasing temperature is thought to be due to the increasing hydrophobicity of the central PPO block while PEO remains soluble. In this context, the phase behavior of PPO and PEO in aqueous solution is quite relevant. PPO with –OH

termination groups and various molecular weights ($M_w = 280–2179$ Da) in water has been studied as a function of the temperature.^{7,25–30} It was determined that the solubility of PPO ($M_w = 400$ Da) has a strong temperature dependence, being insoluble in water above ~ 328 K. The position of the LCST for other molecular weight PPOs shifts to lower temperatures as the molecular weight of the polymer is increased.²⁶ However, PEO, while soluble with water in the temperature range of interest for applications of Pluronic micellar solutions (273–373 K), does exhibit LCST behavior at higher temperatures, as mentioned above, indicating that water becomes a poorer solvent for PEO with increasing temperature. Hence, it is likely that the changing quality of water as a solvent for both PPO and PEO with increasing temperature plays an important role in determining the phase behavior of PEO–PPO–PEO aqueous solutions.

In previous works, we have utilized atomistic molecular dynamics simulations to gain insight into the behavior of PEO in aqueous solutions.^{8,12,15,17} While these studies have provided valuable insight into PEO–water solutions, including the temperature dependence of solution properties, they suffer from the shortcomings of the TIP4P water potential,³¹ which was employed in these simulations. Specifically, it is well-known that the TIP4P water potential, while reproducing the density and self-diffusion coefficient of pure water at and near room temperature with reasonable accuracy,³² does a poor job in reproducing these and other properties at high temperatures.³³ As discussed below, the temperature dependence of thermodynamic and transport properties of water can be much better reproduced utilizing water models that include atomic dipole polarizability.

In order to utilize high-quality polarizable potentials for water in simulations of PEO–water solutions, it is necessary to develop polarizable potentials for the polymers and for the polymer–water interactions. In this study, an existing, validated polarizable

Received: January 27, 2011

Published: April 29, 2011

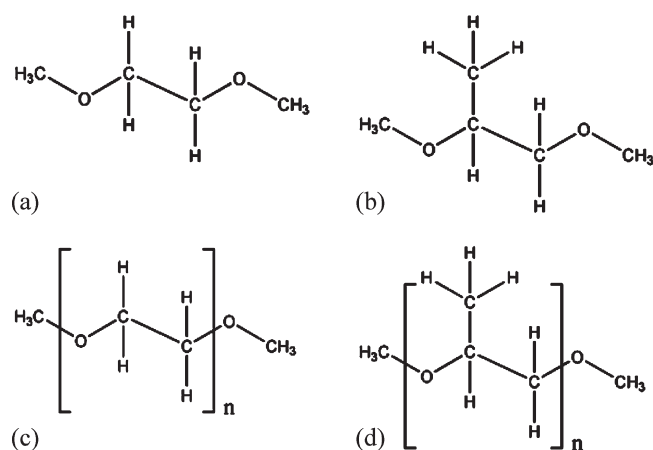


Figure 1. Chemical structures of 1,2-dimethoxyethane (a), 1,2-dimethoxypropane (b), poly(ethylene oxide) (c), and poly(propylene oxide) (d) compounds, where n is the number of repeat units.

potential was used for water, ethers and poly(ethers), while force field parameters for ether–water interactions were obtained on the basis of high-level quantum chemistry data. Thermodynamic and structural properties from simulations were compared with available experimental data and with simulations using our previous TIP4P-based nonpolarizable force field. We investigate the transferability of developed nonbonded force field parameters for PEO–water interactions to PPO and related ethers.

II. FORCE FIELD DEVELOPMENT

In order to develop an accurate potential for atomistic MD simulations of PEO aqueous solutions, we (a) selected an appropriate polarizable water model, (b) parametrized electrostatic interactions for the ether on the basis of quantum chemistry calculations of electrostatic potential around model PEO compounds, and (c) parametrized water–ether van der Waals interactions on the basis of a quantum chemistry study of interactions of the model ether compound with water. In the latter step, we generated two sets of nonbonded parameters as discussed below.

A. Selection of Water Model. We have considered the COS/B2³⁴ and COS/G2,³⁵ TIP4P/FQ,^{36,37} POL5/TZ,³⁸ and SWM4-DP³⁹ models as candidate polarizable water models. We also show results for the nonpolarizable TIP4P³¹ model for comparison. Model simplicity and accuracy in reproducing thermodynamic, dynamic, and dielectric properties were the main criteria for the selection. Specifically, the liquid density ρ , enthalpy of vaporization ΔH_{vap} , and self-diffusion coefficient D_w were considered functions of the temperature. For all models except SWM4-DP, the reported properties were obtained from the available literature.^{31–41} Since the liquid state properties of water as a function of the temperature have not been reported for the SWM4-DP model, properties of interest for this model were determined by performing a series of MD simulations implementing this water model with modification of the polarization mechanism, as described in the next section. The modified water model is referred to as the SWM4-AD model, where AD stands for isotropic atomic dipole polarizability. Simulations of pure water were performed on an ensemble of 500 molecules utilizing a version of the MD simulation package Lucretius that includes isotropic atom dipole polarizability. Initially, equilibration for

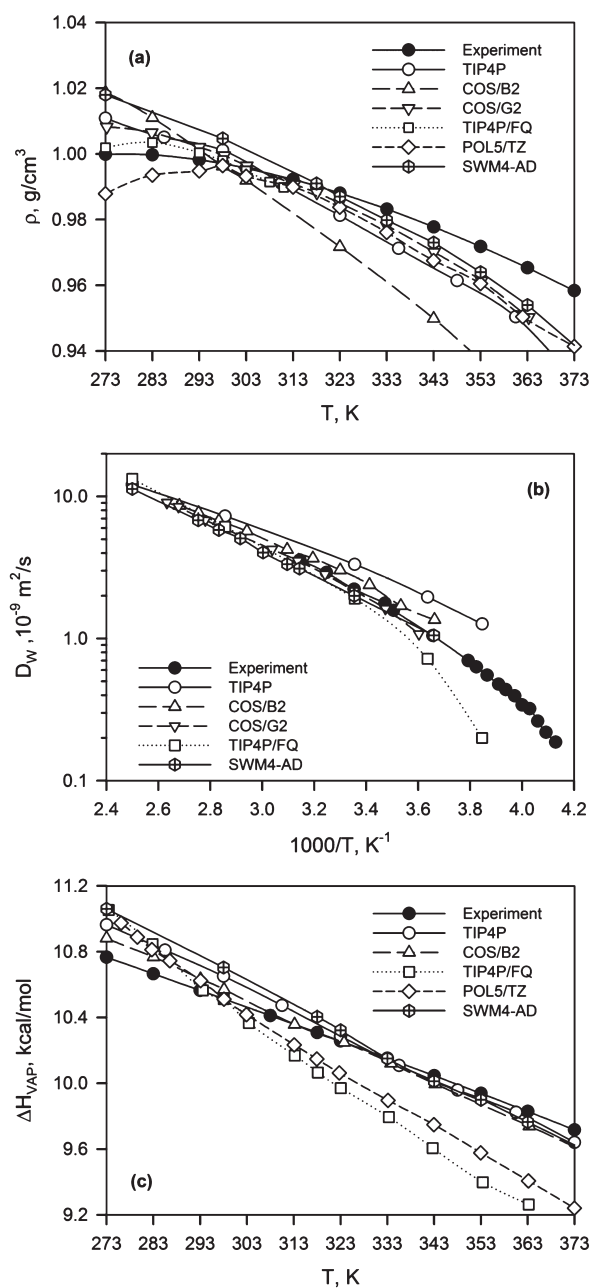


Figure 2. Water densities ρ (a), water self-diffusion coefficients D_w (b), and enthalpies of vaporization ΔH_{vap} (c) are summarized as a function of the temperature for the various models investigated. Experimental data were taken from refs 62, 80, and 91.

1 ns was performed followed by sampling trajectories of 4 ns. Isobaric–isothermal (NPT) ensemble simulations were performed at 1 atm and 298–363 K. All bond lengths were constrained during the simulation using the Shake algorithm.⁴² The Ewald summation method⁴³ with $\alpha = 0.232$ and $k = 6$ parameters was used to treat long-range electrostatic interactions. A multiple time step reversible propagator algorithm⁴⁴ was implemented to solve the equations of motion with a time step of 0.5 fs for valence interactions (bonds, bends, and torsions), 2 fs for nonbonded interactions within a cutoff radius of $R_{\text{cutoff}} = 6.0 \text{ \AA}$, and 4 fs for nonbonded interactions within the range of 6.0 and 10.5 \AA and the reciprocal part of the electrostatic interactions.

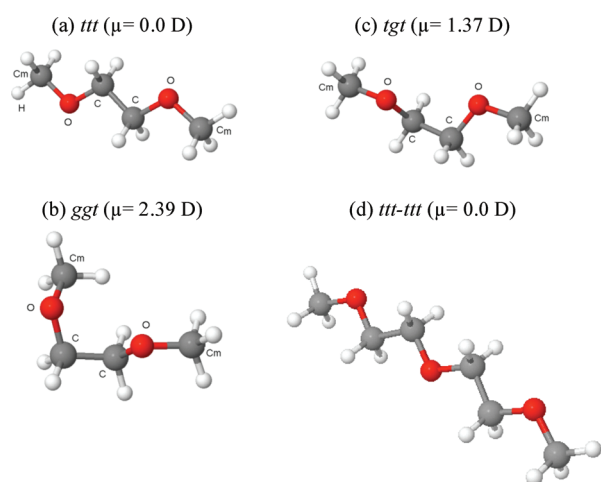


Figure 3. Hydrophilic and hydrophobic conformations of DME and diglyme are given that were used in the fitting of partial charges. Atomic labels: C_m , methoxy carbon; C, methylene carbon; and O, oxygen of ether.

Figure 2a–c show water density, enthalpy of vaporization, and the water self-diffusion coefficient as a function of the temperature for the various models investigated. Most of the water potentials do a reasonable job in reproducing experimental data at 298 K, as the potentials are typically adjusted to reproduce density at room temperature. Among the tested models, the best agreement with experiment for water density above room temperature is observed for the SWM4-AD model. The TIP4P, SWM4-AD, and COS/B2 models all reproduce experimental data for the enthalpy of vaporization reasonably well above room temperature. Therefore, these models give a reasonable estimation of the strength of intermolecular water–water interactions and its temperature dependence. All polarizable potentials were found to reproduce the water self-diffusion coefficient reasonably well while the nonpolarizable TIP4P exhibits too fast water dynamics over the entire temperature range. On the basis of these results and the fact that the SWM4-DP water model yields a dielectric constant^{39,40} and surface tension⁴⁵ in good agreement with experimental results at room temperature, we have selected the SWM4-AD water model.

B. Modification of the SWM4-DP Model. The SWM4-DP polarizable water model consists of four interaction sites and Drude polarizability.³⁹ The latter involves a massless charge on a spring attached to the oxygen of water. In the SWM4-AD model, we have replaced Drude polarizability with an induced point dipole model. The water geometry in the SWM4-AD model was adopted unchanged from the SWM4-DP model, with an O–H bond length of 0.9572 Å and an H–O–H angle of 104.52°. The fourth (massless) site was attached to the oxygen of water by a rigid bond at a distance of 0.238 Å along the H–O–H bisector. An isotropic atomic polarizability of 1.043 Å³ was assigned to the oxygen atom. Partial atomic charges were assigned to the massless particle ($-1.1074e$) and hydrogen atoms ($+0.5537e$) in accord with the original SWM4-DP model. No partial charge was allocated on the oxygen atom of water. Lennard-Jones (12–6) repulsion and dispersion parameters were taken without any adjustments ($\epsilon_{O-O} = 0.20568$ kcal/mol and $\sigma_{O-O} = 3.18030$ Å). Excellent agreement was found using the SWM4-AD model with published data for the SWM4-DP model for liquid density, enthalpy of vaporization, and self-diffusion coefficient at 298 K.

Table 1. Partial Atomic Charges for DME (PEO) and DMP (PPO) (See Figure 3 for Atom Labels)

atom type	DME (PEO)	DMP (PPO)
O (C–O–C) (polymer)	0.4296	0.4068
O(C_m –O–C)	0.4348	0.4949
C_m	−0.3507	−0.4042
H_m	0.1169	0.1290
C	−0.1100	−0.2997
H	0.0576	0.0951
Lp	−0.2200	−0.2200

C. Parameterization of PEO Partial Atomic Charges. Density functional calculations were performed on 1,2-dimethoxyethane (DME) and diglyme molecules, illustrated in Figure 3, for the calculation of electrostatic potentials that were used to fit partial atomic charges. These oligomers have essentially the same local conformations as PEO in aqueous solution and similar dependence on solution composition;^{8,9,46} hence, these molecules are good model compounds for PEO. The Gaussian 03 software package⁴⁷ was used for all quantum chemistry calculations. The B3LYP density functional^{48–51} in combination with the aug-cc-pvDz basis set⁵² was utilized on the basis of our previous studies.¹² Geometry optimization was performed for isolated DME molecule in hydrophobic *ttt* and hydrophilic *tgt* and *ggt* conformations and isolated diglyme molecule in the hydrophobic *ttt* conformation, as listed in Figure 3. Quantum chemistry calculation of the electrostatic potential for both oligomers was performed on a grid of 80 000 evenly distributed points for each single conformation. Partial atomic charges were determined using a charge fitting approach described elsewhere^{53–56} that uses least-squares minimization of the objective function $\chi^2 = \sum_i^N 1/N(\phi_i^{QC} - \phi_i^{FF})^2$ relative to the electrostatic potential ϕ_i^{QC} obtained from quantum chemistry calculations. A square value of the objective function $\chi^2 = 1.7$ was obtained. This value is much higher than the values typically obtained using such an approach (0.5–0.8). In order to improve the description of the electrostatic potentials, an additional pair of massless charges (labeled Lp) connected to ether oxygen atoms was introduced. Optimal positions and angles associated with the additional charges as well as the optimal value of the atom-based partial charges were determined simultaneously using the charge fitting approach mentioned above. The electrostatic potential ϕ_i^{FF} was calculated as a function of the angle Lp–O–Lp and distance O–Lp from the oxygen of ether. The best description of the electrostatic potential $\chi^2 = 0.7$ was obtained for an Lp–O–Lp angle of 96°, an Lp–O separation of 0.7 Å, and an extended charge magnitude of $q_{Lp} = -0.2200e$. However, the minimum of the objective function was found to be very shallow, showing little dependence of quality of the fit in the range of $\pm 10^\circ$ for the Lp–O–Lp angle and ± 0.1 for the Lp–O distance from the optimal values. Therefore, in the final version of the force field, we used an Lp–O–Lp angle of 102° and an Lp–O distance of 0.65 Å that allowed us to obtain an improved fit of DME–water binding energies (see below) and electrostatic potential around DME. The resulting assignment of partial charges for DME molecule is given in Table 1. Torsional parameters for DME/PEO were refitted to reproduce conformational energies of DME obtained from *ab initio* calculations at the MP2/aug-cc-pvDz//B3LYP/aug-cc-pvDz level. A comparison of conformational energies obtained from *ab initio* calculations and molecular mechanics calculations using PFF are given in

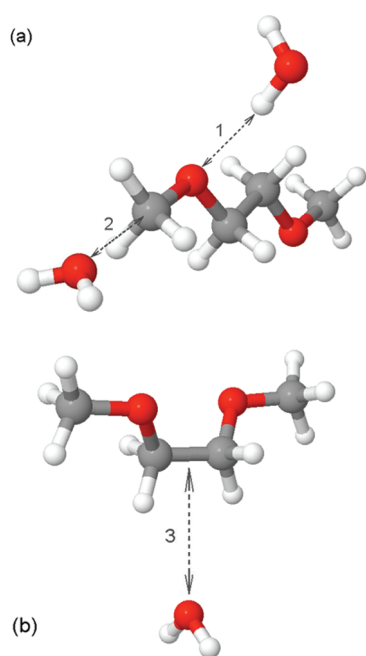


Figure 4. Schematic representations of the testing configurations are given for the calculation of DME–water binding energies in a and b, respectively. DME is in hydrophobic *ttt* (a) and hydrophilic *tgt* (b) conformations. Gray atoms represent carbons, white are hydrogens, and red are oxygen atoms. Dashed arrows indicate the directions along which the water molecule is shifted.

the Supporting Information for the most important conformers. Conformational energies predicted by PFF are in very good agreement with ab initio data and provide similar quality descriptions as our previous nonpolarizable force field and CHARMM⁵⁷ polarizable force field.

D. Parameterization of PEO–Water Interactions. Parameters for all valence (bond, bend, and dihedral) interactions, atomic polarizabilities, and dispersion/repulsion parameters for PEO–PEO interactions were taken from the APPLE&P force field^{55,58} that was found to provide a consistent description of density ρ , heat of vaporization ΔH_{vap} , and transport properties for a wide variety of liquids. The polarizable water model is described above in sections A and B, while the ether partial charges are described in section C. In order to complete our description of PEO–water systems within the atomistic polarizable force field framework, dispersion/repulsion parameters for intermolecular interactions between the ether and water need to be determined. For this purpose, extensive quantum chemistry calculations of binding energies between DME and a single water molecule were conducted. MP2/aug-cc-pvDz level calculations with basis set superposition error (BSSE) were performed using the counterpoise correction approach⁵⁹ for a number of ether–water geometries, as described below.

Water–Ether Quantum Chemistry Paths. The interactions of a water molecule with the hydrophobic *ttt* and hydrophilic *tgt* conformers of DME have been investigated along various water–ether paths designed to provide information about the interaction of water with ether oxygen atoms and methylene and methoxy groups. The paths are illustrated in Figure 4a and b. Path 1, which involves hydrogen bonding between a water hydrogen atom and an ether oxygen atom, was investigated for the DME in *ttt* conformation as well as for dimethyl ether. In the

ttt conformer, the ether oxygen atoms of DME are on opposite sides of the molecule, facilitating investigation of hydrogen bonding between water and a single ether oxygen atom. Path 2, which involves the interaction of water with the methyl group of the methoxy group, was also investigated for the *ttt* conformer of DME. Path 3 involves the interaction of water with the “hydrophobic” side of DME, i.e., the methylene groups as opposed to the ether oxygen atoms. For all paths, initially, a locally optimized geometry was obtained at the MP2/aug-cc-pvDz level. Subsequently, the energy of the ether–water complex was determined at this level with fixed water and ether geometries, with the distance between the water oxygen being systematically increased or decreased along the water oxygen–ether oxygen vector (path 1), the water oxygen–carbon vector (paths 2), and the vector between the water oxygen and the midpoint of the carbon–carbon bond (path 3). Binding energies are reported as the difference between the BSSE (counterpoise method) corrected water–ether complex energy and that of the geometry optimized ether and water at infinite separation.

Determination of Water–Ether Dispersion/Repulsion Parameters. Dispersion/repulsion interactions between water and ether atoms were described using the Buckingham (exp-6) function for all pairs:

$$U^{\text{exp-6}}(r_{ij}) = A_{ij} \exp(-B_{ij}r_{ij}) - \frac{C_{ij}}{r_{ij}^6} \quad (1)$$

where $i = \text{O}_w$ or H_w and $j = \text{C}, \text{H}, \text{O}$, and C_m . A_{ij} and B_{ij} are repulsion parameters, while C_{ij} is the dispersion parameter. Atom labels are shown in Figure 3. The term $D(12/B_{ij}r_{ij})^{12}$ is applied with $D = 5 \times 10^{-5}$ kcal/mol for all pair interactions and is essentially zero at typical nonbonded atomic separations but becomes the dominant term at $r_{ij} < 1 \text{ \AA}$, ensuring that $U^{\text{exp-6}}(r)$ is repulsive at distances much smaller than the size of an atom. However, this term is not applied when the A parameter is negative (see below). Dispersion C_{ij} parameters for $i = \text{O}_w$ and $j = \text{C}, \text{H}, \text{O}$, and C_m were determined using the Waldman–Hagler (WH) combining rule⁶⁰ and hence were not adjustable parameters. Dispersion parameters for $i = \text{H}_w$ and $j = \text{C}, \text{H}$, and C_m were set to zero with the exception of the $i = \text{H}_w$ and $j = \text{O}$ atomic pair, where the dispersion parameter was treated as adjustable.

The adjustable water–ether nonbonded parameters were determined by optimization of the objective function

$$\chi^2 = \sum_{\text{path}(k)} \sum_{\text{geometry}(l)} w_{kl} (\Delta U_{kl}^{\text{FF}} - \Delta U_{kl}^{\text{QC}})^2 \quad (2)$$

where $\Delta U_{kl}^{\text{FF}}$ is the binding energy for geometry l of path k predicted by the force field, while $\Delta U_{kl}^{\text{QC}}$ is the same quantity from quantum chemistry calculations. All three DME–water binding paths (paths 1–3) were fit simultaneously. The weighting factor w_{kl} is given as

$$w_{kl} = \exp \left[-\frac{\Delta U_{kl}^{\text{QC}} - \Delta U_{kl}^{\text{EL}}}{k_b T} \right] \quad (3)$$

where $T = 298 \text{ K}$ and $\Delta U_{kl}^{\text{EL}}$ is the electrostatic (polarization and Coulomb) contribution to the water–DME binding energy for each water–ether pair geometry, as determined from already established atomic polarizabilities and partial atomic charges. The subtraction of the electrostatic contribution to the binding energy from the total in determining the weight factor assures that each water–DME geometry is weighted in the

Table 2. Nonbonded Repulsion Parameters for Ether–Water Interactions

ether–water interaction pair	PFF-1		PFF-2		PFF-1,2 ^a
	A_{ij} , kcal/mol	B_{ij} , Å ⁻¹	A_{ij} , kcal/mol	B_{ij} , Å ⁻¹	C_{ij} , kcal/mol Å ⁶
C _m –O _w	14500.76	3.28913	24893.76	3.32675	690.76
C _m –H _w	35764.40	4.85465	45764.40	4.83499	0.00
O–O _w	341418.22	3.94109	787505.34	4.17895	451.12
O–H _w ^b	–21.60				355.75
	–20.0 (PFF-3)	1.38137	1841.85	3.12997	330.0 (PFF-4)
	–16.5 (PFF-5)				310.0 (PFF-6)
C–O _w	29589.70	3.55272	79674.89	3.58426	665.24
C–H _w	34242.45	4.73729	43297.32	4.81314	0.00
H–O _w	11934.82	3.67285	5445.07	3.50718	138.67
H–H _w	2361.00	3.98266	2506.97	4.08434	0.00

^a Dispersion parameters C_{ij} are the same for all force fields with the exception of O–H_w interactions. For PFF-1,3,5, $C_{ij}(\text{O–H}_w) = 0.0$; for PFF-2,4,6, it varies as indicated in the table. ^b Only parameters for O–H_w interactions were adjusted to obtain PFF-3–6. To obtain PFF-3,5, the repulsion parameter A_{ij} was the only the adjustable parameter, while to obtain PFF-4,6, the dispersion parameter C_{ij} was changed.

determination of the nonbonded parameters according to the dispersion/repulsion contribution to the binding energy of that particular geometry. In determining the molecular mechanics energy along each path, a molecular mechanics geometry optimization was first performed, and the path was determined by systematically changing the ether–water separation for the fixed ether and water geometries, analogous to the procedure used for determining the quantum chemistry paths.

The fitted force field parameters are shown in Table 2. There are two sets of fitted parameters for the water hydrogen–ether oxygen interaction. For the first, labeled PFF-1 (polarizable force field 1), the C (dispersion) parameter for the O–H_w interaction, was constrained to be zero, resulting in a negative value of A , while in the second (PFF-2), both the A and C parameters for the O–H_w interaction were treated as adjustable. Ether–water binding energies for paths 1, 2, and 3 for PFF-1 and PFF-2 as well as our previously parametrized nonpolarizable ether force field¹² (NPPF) employing the TIP4P³¹ water model are compared with quantum chemistry values in Figure 5a–c. Figure 5 reveals that our PFF-1 and PFF-2 force fields provide an excellent description of the water–ether interactions and are a noticeable improvement over the NPPF. Specifically, the NPPF resulted in an underestimation of binding energies for the “hydrophilic” path 1 at separations larger than the equilibrium distance and an overestimation of binding energies of water with the methoxy carbon (path 2) and methylene carbons (path 3). These deficiencies are corrected in the PFF-1 and PFF-2 force fields.

III. MOLECULAR DYNAMICS SIMULATIONS OF ETHER-WATER SOLUTIONS

Molecular dynamics (MD) simulations of ether and poly(ether) aqueous solutions were performed in order to (1) validate the polarizable force fields by comparison of thermodynamic and transport properties with available experimental data, (2) empirically adjust PFF-1 and PFF-2 to improve agreement with experimental results, and (3) conduct initial studies of the phase behavior of PEO–water and PPO–water solutions as a function of the temperature using the newly developed polarizable potentials. Obtaining an accurate representation of PEO–water solutions as a function of the temperature was our primary motivation for the development of the polarizable force fields.

A. Simulation Methodology. MD simulations of DME, 1,2-dimethoxypropane (DMP), 12 repeat unit PEO (PEO12, with CH₃ terminal groups, 530 Da), and six repeat unit PPO (PPO6, with CH₃ terminal groups, 395 Da) in aqueous solution have been performed in the composition range (ether weight fraction) $w_p = 0.01–0.93$. Aqueous solutions were comprised of 1–72 solute molecules and 1200–100 water molecules depending upon the composition. The polarizable version of the Lucretius⁶¹ simulation package was used to carry out MD simulations using a cubic simulation cell with periodic boundary conditions. The standard Shake algorithm⁴² was employed to constrain the bond lengths and water geometry. Charge–charge long-range electrostatic interactions were computed employing Ewald⁶³ summation. The reaction field scheme⁴³ was implemented to handle long-range induced dipole–induced dipole calculations. The cutoff radius was 10.5 Å for nonbonded and electrostatic interactions in real space. A reversible multiple time step propagator algorithm⁴⁴ was implemented to solve the equations of motion with the parameters as specified in section A of the force field development. Simulations for $T < 373$ K were conducted at atmospheric pressure, while at elevated temperatures, simulations were conducted at pressures close to water saturation conditions at these temperatures to prevent potential system instability due to water evaporation. The dielectric constant ϵ of the solvent, which is used in reaction field calculations, was adjusted from 79 to 30 according to the experimental temperature dependence of the water dielectric constant.⁶² All systems were initially equilibrated in the isothermal–isobaric ensemble until satisfactory steady state conditions (such as density of the solutions) were reached. Sampling trajectories were performed over 10 ns.

B. Free Energy of DME Solvation. The free energy of DME solvation in water, ΔG_{solv} , was determined for PFF-1 and PFF-2 using the interface transit method (IT), as described in detail in the Appendix. Briefly, a film of water comprised of 500 molecules was created in the center of an orthorhombic cell with dimensions of 24.6 Å × 24.6 Å × 84.6 Å in the x , y , and z directions, respectively. The water film is periodic in the x and y directions and has a thickness of approximately 29 Å in the z direction. The Ewald summation method⁴³ with $\alpha = 0.232$ and k_{limit} in x , y , $z = 6, 6, 11$ was used to treat long-range electrostatic interactions. Otherwise, the simulation methodology and parameters were identical to those employed in the bulk solution simulations described above except

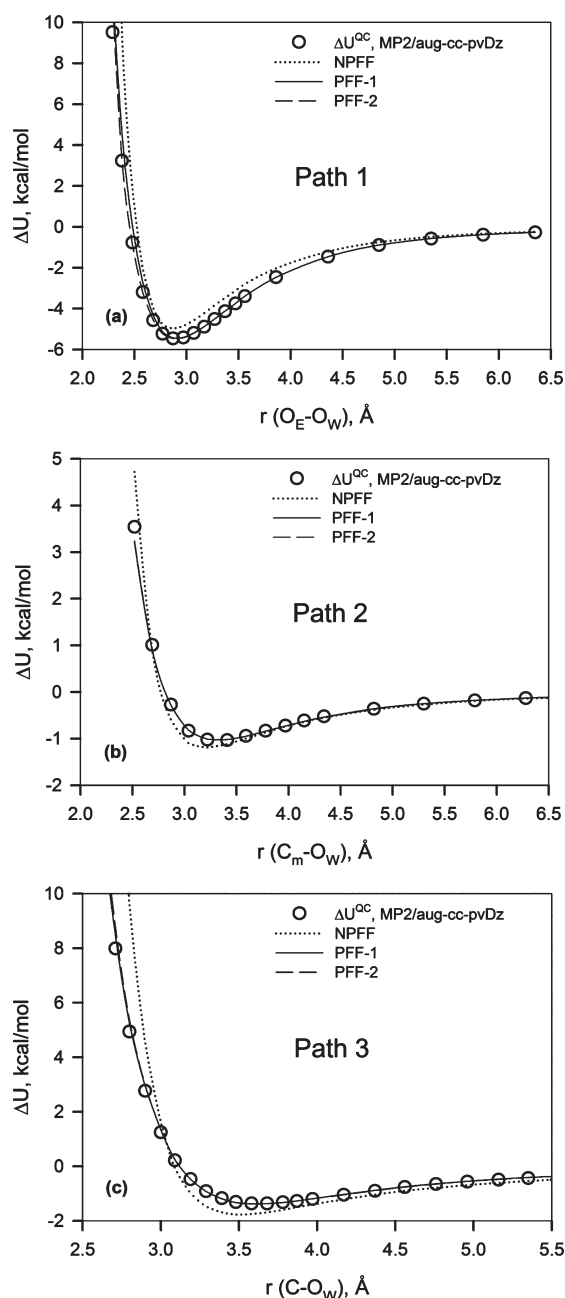


Figure 5. DME–water binding energies as obtained from quantum chemistry calculations and force field predictions for various ether–water paths.

that a single time step algorithm with a time step of 1 fs was employed instead of the multiple time step algorithm. In order to adequately thermalize the single gas-phase molecule, the solute was subjected to additional Brownian forces⁶³ with a friction coefficient of $\gamma = 0.002 \text{ fs}^{-1}$. The average force required to constrain the center-of-mass of the DME molecule to a given Δz , $\langle F(\Delta z) \rangle$, was determined from 4 ns trajectories and 57 Δz windows ranging from 0 (in the middle of the water film) to 30 Å (middle of the vacuum phase). The free energy of transfer of the solute from the vacuum phase to the liquid phase (center of the film) is given as

$$\Delta G_{\text{solv}} = - \int_{\text{max}}^0 \langle F(\Delta z) \rangle d(\Delta z) \quad (4)$$

Table 3. Free Energy, Enthalpy, and Entropy of Solvation of DME in Aqueous Solution from MD Simulations and Experiment at 298 K^a

FF	ΔG_{solv} , kcal/mol	ΔH_{solv} , kcal/mol	$T\Delta S$, kcal/mol
PFF-1	−5.7	−15.6	−9.9
PFF-2	−6.6	−16.8	−10.2
PFF-3	−4.9	−14.4	−9.5
PFF-4	−4.7	−14.6	−9.9
PFF-5	−3.7	−13.4	−9.7
PFF-6	−3.8	−13.5	−9.7
NFFF ^b	−5.6	−17.1	−11.5
CHARMM ^c	−3.8		
	−5.6 ^c		
experiment	−4.8 ^d	−14.0 ^e , −14.2 ^f	−9.4

^a For simulations using PFF-1 through PFF-6, the uncertainty in ΔG_{solv} is 0.6 kcal/mol and for ΔH_{solv} is 0.4 kcal/mol. ^b Nonpolarizable force field of refs 12 and 87. We note that values for the free energy and enthalpy of solvation reported in ref 87 differ from those reported here by $k_B T$ (0.6 kcal/mol), as the previously reported values did not employ the same gas-phase and solution-phase reference states as were utilized in determining the experimental values. ^c Polarizable potential from refs 13 and 85. The values are taken from those works. ^d Ref 88. ^e Ref 89. ^f Ref 90.

Here, $\Delta z = \text{max}$ corresponds to the center of the vacuum region. The direct equating of the free energy of transfer with the Gibbs free energy of solvation ΔG_{solv} is a consequence of the reference states used in defining ΔG_{solv} .^{64,65} We note that although the IT method simulations are carried out in the NVE ensemble, the film is able to adjust dimensions upon insertion of the solute so as to maintain negligible normal stress in the z direction. Consequently, the free energy change determined from integration of the mean force (eq 4) is the Gibbs free energy and not the Helmholtz free energy. Validation of the IT method was carried out by testing the method to determine ΔG_{solv} for the TIP4P water model. The IT method yielded a value of $\Delta G_{\text{solv}} = -5.9 \pm 0.6$ kcal/mol, which is in excellent agreement with Monte Carlo simulation results of $\Delta G_{\text{solv}} = -6.1 \pm 0.3$ kcal/mol.⁶⁶ We also estimated the uncertainty of the free energy calculations as described in previous publications.^{67,68} The IT method yields ΔG_{solv} (DME in water) = -5.7 ± 0.6 kcal/mol for PFF-1 and $\Delta G_{\text{solv}} = -6.6 \pm 0.6$ kcal/mol PFF-2, as summarized in Table 3.

C. Empirical Adjustment of the Polarizable Potentials. A comparison of ΔG_{solv} for PFF-1 and PFF-2 with experimental results (Table 3) reveals that these quantum-chemistry-fitted potentials yield water–ether interactions that are too hydrophilic. In order to improve agreement with experimental results for ΔG_{solv} , the repulsion parameter $A_{\text{O-H}_w}$ of PFF-1 was empirically adjusted to yield force field PFF-3, and the dispersion parameter $C_{\text{O-H}_w}$ of PFF-2 was adjusted to yield force field PFF-4. The resulting parameters are given in Table 2. All other nonbonded parameters were kept unchanged. In order to determine the new values of $A_{\text{O-H}_w}$ and $C_{\text{O-H}_w}$, a thermodynamic perturbation method⁶⁹ was employed to obtain the free energy of solvation as a function of these parameters using trajectories of a single DME molecule in water using the PFF-1 and PFF-2 force fields as reference states. The resulting ΔG_{solv} values for PFF-3 and PFF-4 are in good agreement with experimental results, as shown in Table 3.

To match the experimental free energy of DME solvation, the A parameter in PFF-1 has to be reduced by about 7%

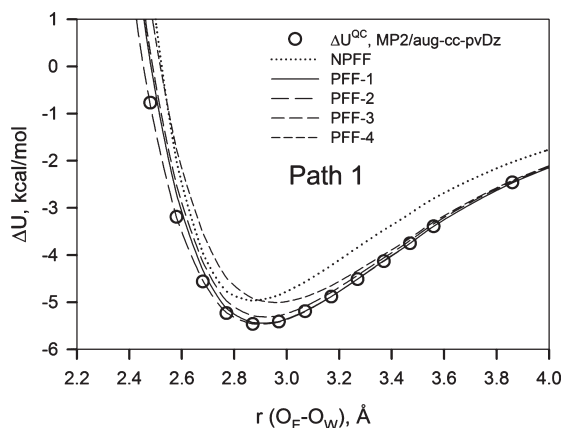


Figure 6. DME–water binding energies for path 1 as predicted by various force fields and quantum chemistry calculations.

(from -21.6 to -20.0 kcal/mol). The force field with this adjusted parameter was labeled as PFF-3. To achieve the same for PFF-2, a similar reduction by $\sim 7\%$ of the dispersion parameter C_{O-H_w} was necessary (see Table 2), yielding the PFF-4 force field. To examine how these empirical adjustments of nonbonded parameters influence the description of quantum chemistry data for DME–water binding energies, we have compared the PFF-3 and PFF-4 descriptions of binding energies along paths 1–3 described above. In Figure 6, we show this comparison for the hydrophilic path 1, which shows that while description of quantum chemistry data by PFF-3 and PFF-4 is worse (compared to PFF-1 and PFF-2), it is still very good. For hydrophobic paths 2 and 3, no degradation of the description of quantum chemistry data was observed, which is expected since empirical adjustment of the $O-H_w$ interactions should not have a significant influence on hydrophobic interactions such as interactions of water with methylene and methoxy segments of DME.

D. Enthalpy, Free Energy, and Entropy of Solvation of DME. The enthalpy of solvation of DME in water, which corresponds to the energy of the transfer of a single molecule from the gas phase to the solution at constant pressure,^{64,65} was determined at 298 K and 1 atm as

$$n\Delta H_{\text{solv}}(w_{\text{DME}}) = E_{\text{H}_2\text{O} + \text{DME}}^{\text{l}}(P, T, w_{\text{DME}}) - [E_{\text{H}_2\text{O}}^{\text{l}}(P, T) - nE_{\text{DME}}^{\text{g}}(P, T)] \quad (5)$$

where the superscript l or g indicates the liquid or gas phase, E is the internal energy, and the subscripts H_2O , $\text{H}_2\text{O} + \text{DME}$, and DME indicate a system of 500 water molecules; a system of 500 water molecules plus n DME molecules required to yield the weight fraction of DME, w_{DME} ; or a single DME molecule. We assumed that in the gas phase DME at 298 K and 1 atm behaves as an ideal gas. The internal energy of the gas phase of the DME molecule was determined from Brownian dynamics⁶³ simulations of 125 noninteracting DME molecules performed at 298 K. The enthalpy of solvation for DME as a function of solution composition using all four sets of nonbonded parameters (PFF-1 through PFF-4) is compared with experimental results in Table 3. The dilute solution value of ΔH_{solv} was obtained by linear extrapolation of eq 5 to infinite dilution. The entropy of solvation, calculated as $T\Delta S_{\text{solv}} = \Delta H_{\text{solv}} - \Delta G_{\text{solv}}$ is given as well.

Examination of Table 3 reveals that MD simulations using PFF-1 and PFF-2 have resulted in $\Delta H_{\text{solv}} = -15.6$ kcal/mol and $\Delta H_{\text{solv}} = -16.8$ kcal/mol, respectively, which are noticeably more than experimental values of about -14.0 kcal/mol. Interestingly, both force fields provide a basically identical description of the quantum chemistry data for paths 1–3, yet both the free energy and the enthalpy of solvation obtained using PFF-2 are about 1.0 kcal/mol more negative than for PFF-1. This difference perhaps can be attributed to different partitionings of short- and long-range nonbonded interactions between these force fields due to variation in the functional form of the $O-H_w$ potential. Such redistribution of short- and long-range interactions, while not influencing the description of selected paths in the gas phase, clearly has a noticeable effect in the condensed phase, indicating that selection of the functional form for nonbonded interactions is important.

For the empirically adjusted (to match experimental free energy of solvation) PFF-3 and PFF-4 force fields, the enthalpy of solvation was found to be in a very good agreement with experimental results as well. Interestingly, the entropy of solvation was not affected much by empirical adjustments and, taking into account the accuracy of our calculations, is in good agreement with experimental values for all force fields (PFF-1 through PFF-4). This indicates that (a) overestimation of the free energy of DME solvation by PFF-1 and PFF-2 is primarily energetic in nature and (b) the hydration structure of DME is likely captured well by our polarizable force field and is not sensitive to variations in the functional form of nonbonded interactions.

E. Conformational Populations of DME in Water. The local conformational properties of PEO and its oligomers in water have been a subject of extensive discussions regarding key characteristics that define the unique behavior of PEO in aqueous solution. Detailed analysis and discussion of these issues can be found in our previous works. Here, we only focus on the influence of the force field on local conformations and compare predictions with available experimental data. For this purpose, we analyzed DME triad populations as a function of the composition in DME/water mixtures. In our previous simulations using NPPF, we showed that *tgt* and *tgg* conformers are hydrophilic (their population increases with increasing water content compared to the gas phase), while all other conformers, including the highly polar tg^+g^- , are hydrophobic.⁸ Those results were in good agreement with previous spectroscopic studies,^{70–74} with the exception of trends and populations predicted for the *tgg* and tg^+g^- conformers, which were not well resolved in the initial analysis of spectroscopic data. Subsequent to publication of our simulation results, experimental spectra were reanalyzed taking into account the potential importance of the *tgg* conformer, and the trends observed in simulations were confirmed.⁷⁵ Later, more detailed measurements and an analysis of Raman spectra were conducted by Goutev et al.⁷⁶ to obtain triad populations of DME in water as a function of the concentration. In Figure 7a, we compare total populations of hydrophilic (*tgt* + *tgg*) and major hydrophobic (tg^+g^- + *ttt* + *tgg*) conformers, as obtained from our simulations using different force fields and Raman analysis. Data for individual triad conformers are given in the Supporting Information.

Figure 7a shows very good qualitative agreement between simulation and experimental data for all concentrations. A comparison of different force fields shows very weak dependence of conformational populations on the force field, indicating insensitivity of conformations to force field parameters varied

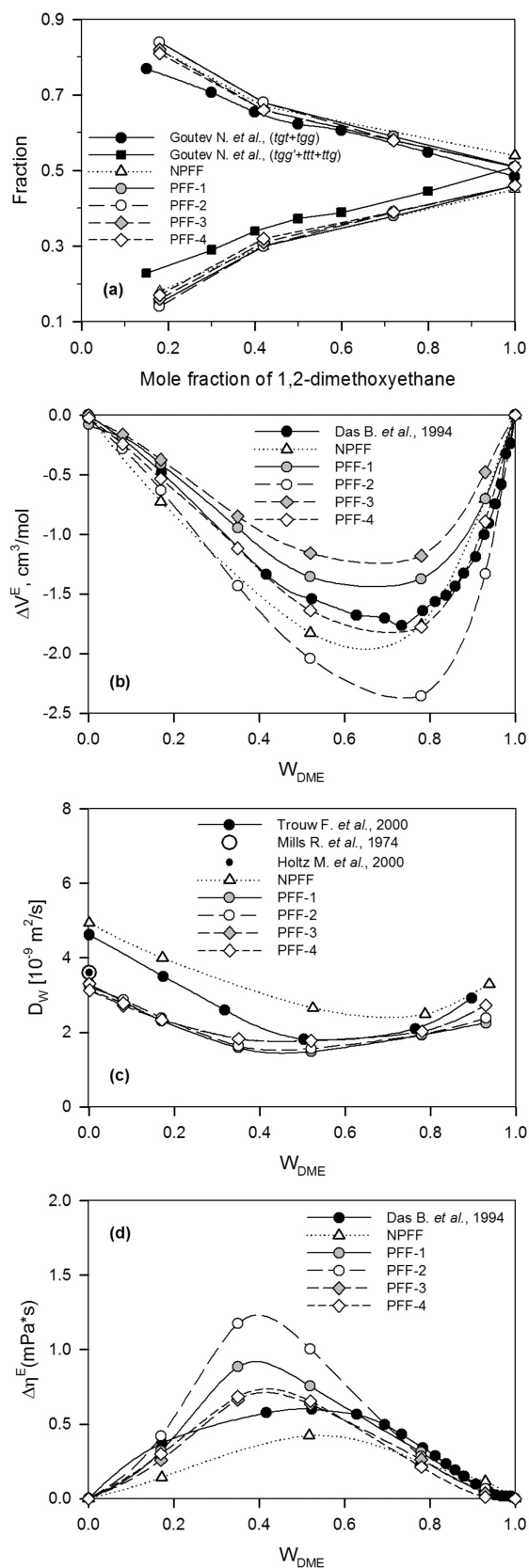


Figure 7. Comparison of conformer populations of DME in water (a), excess volume ΔV^E (b), water self-diffusion coefficient D_w (c), and excess viscosity $\Delta\eta^E$ (d) as obtained from MD simulations and experiments at 318 K for DME–water solutions. Experimental data were taken from refs 76–78, 80, and 81.

in this work despite the fact that those variations noticeably influence the free energy of solvation of DME. These observations are in agreement with our previous studies where the influence of DME conformation on solvation thermodynamics was shown to be relatively small.¹⁰

F. Excess Volume of DME–Water Solutions. Excess volume is often considered to be a sensitive measure of the effects of a solvation (mixing) process for two or more compounds. It can be negative or positive depending upon the strength of the solute/solvent intermolecular interactions, the difference in solute/solvent molecular sizes, and the solute/solvent solvation structures.⁷⁷ Positive excess volume usually indicates weak, unfavorable solute/solvent intermolecular interactions, while negative excess volume is an indicator of strong favorable interactions. Here, the DME–water intermolecular interactions are studied by calculating the excess volume as a function of the DME concentration. The excess molar volume ΔV^E of ether–water solutions was determined as indicated by

$$\Delta V^E = V_{\text{mixture}} - (x_{\text{solvent}} V_{\text{solvent}} + x_{\text{solute}} V_{\text{solute}}) \quad (6)$$

where $V_{\text{mixture}} = (M_{\text{solvent}} x_{\text{solvent}} + M_{\text{solute}} x_{\text{solute}}) / \rho_{\text{mixture}}$ is the molar volume of the mixture, $V_i = (M_i x_i) / \rho_i$ is the molarity of the pure components (solvent and solute), M_i is the molecular weights of the pure components, x_i is the mole fraction of the solvent or solute in the mixture, and ρ is the density. The excess molar volume for DME in 318 K aqueous solutions obtained using the four developed sets of nonbonded parameters and NPF are compared with experimental results⁷⁷ in Figure 7b.

Examination of Figure 7b shows that simulations using PFF-1 and PFF-2 result in excess volumes in qualitative agreement with experimental results. However, simulations with PFF-1 resulted in underestimation of the excess volume, while those employing PFF-2 resulted in noticeable overestimation of the excess volume. Both force fields predict minimum weight fractions of DME between 0.6 and 0.8. A similar quality agreement for excess volume is obtained at 298 K (not shown). While for PFF-2 the more negative (than experiment) values of the excess volume are consistent with overestimation of the free energy and enthalpy of solvation, the underestimation of the excess volume by PFF-1 seems contrary to the trends observed in solvation thermodynamic properties. Despite a clear overestimation (compared to experimental results) of hydration enthalpy and free energy of solvation by PFF-1, in simulations with this force field, DME and water molecules are not able to pack efficiently enough to achieve the excess volumes observed in experimental results.

Since empirical adjustments made to PFF-1 and PFF-2 to yield PFF-3 and PFF-4 reduced the strength of DME–water interactions (as evidenced by the less favorable free energy and enthalpy of solvation as well as binding energies along path 1), it is not surprising that a significant shift to less negative values of excess volume was obtained for PFF-3 and PFF-4 force fields. While this resulted in excellent agreement between PFF-4 and experimental results, simulations using PFF-3 resulted in excess volumes in even worse agreement with experimental results than PFF-1. These data show two interesting points: (a) despite the fact that PFF-3 and PFF-4 force fields predict a similar free energy and enthalpy of solvation, the predicted excess volumes are very different, and (b) excess volume is strongly sensitive to details of O–H_w potential and, hence, the partitioning of short- and long-range nonbonded interactions. Therefore, when empirical adjustments to the force fields are made to match the free energy

(or enthalpy of solvation) of the solute, it does not necessarily guarantee accurate prediction of the excess volume.

G. Water Self-Diffusion Coefficient and Excess Viscosity in DME–Water Solutions. The self-diffusion of water is another solution property that is sensitive to the quality of the description of solute–water interactions. The mobility of water molecules near the solute can be affected by hydrogen bonding or by hydrophobic hydration. It is also well-known that water dynamics at the interface are much different from those of bulk water, including protein–water, polymer–water, and other interfaces.⁷⁸ Here, the influence of solute concentration on water dynamics is studied by obtaining the self-diffusion coefficient of water for various concentrations of DME.

The concentration dependence of the self-diffusion coefficient of water in DME–water solutions was calculated from MD simulations using PFF-1 through -4 force fields. The self-diffusion coefficient of water in DME–water solutions was determined using the Einstein relation:⁴³

$$D_w = \lim_{t \rightarrow \infty} \frac{\langle (r(t) - r(0))^2 \rangle}{6t} \quad (7)$$

where $r(t)$ is the center of mass position of a molecule at time t , $\langle \dots \rangle$ indicates an ensemble average, and $\langle (r(t) - r(0))^2 \rangle$ corresponds to the mean square displacement of a molecule's center of mass. Water self-diffusion coefficients were further corrected to account for the finite size effects in molecular dynamics simulations as suggested by Yeh and Hummer.⁷⁹ The viscosity η of pure SWM4-AD water was calculated at 318 K using eq 8, which is necessary for calculations of correction coefficients. The value of 0.0054P was obtained, which is in a good agreement with the experimental value of 0.0060P.⁶² Corrected self-diffusion coefficients of water were 2–3% higher than initially calculated using eq 7.

The water self-diffusion coefficients obtained from MD simulations as a function of the concentration are compared with experimental results in Figure 7c. We are aware only one experimental work, by Trouw et al., using the QENS (quasi-elastic neutron scattering) technique, which reports water self-diffusion coefficients for the entire range of concentrations in DME–water solutions.⁷⁸ However, the diffusion coefficient for the pure water reported in this work is too high ($D_w = 4.6 \times 10^{-9} \text{ m}^2 \text{ s}^{-1}$) compared to other experimental data obtained using the isotopic method ($D_w = 3.6 \times 10^{-9} \text{ m}^2 \text{ s}^{-1}$)⁸⁰ and pulsed magnetic field gradient NMR method ($D_w = 3.6 \times 10^{-9} \text{ m}^2 \text{ s}^{-1}$),⁸¹ which are also shown in Figure 7c. This mismatch might be due to the inadequacy of some assumptions of the jump diffusion model that was used to fit QENS data as discussed in ref 78. Therefore, the self-diffusion coefficient of water as a function of DME concentration reported in ref 78 is likely overestimated, particularly in dilute solutions, where it was shown that the jump diffusion model for translational motion is inconsistent with MD simulations.

Figure 7c shows that the diffusion coefficient of pure SWM4-DP water ($W_{\text{DME}} = 0$) is in good agreement with experimental results determined by isotopic and NMR methods. It is also clear that the water self-diffusion coefficient is not sensitive to variations in nonbonded parameters between polarizable force fields PFF-1 through -4 in the entire concentration range. Concentration dependences of the water self-diffusion coefficient obtained using polarizable force fields PFF-1 through -4 are in qualitative agreement with QENS data, showing a minimum weight fraction

of DME at around 0.55. At higher concentrations (>0.5 DME weight fraction), simulation data are also in good quantitative agreement with QENS data. Taking into account the mismatch of experimental data in pure water, we believe that the concentration dependence of water self-diffusion using MD simulations with the polarizable force fields is quite reasonable and is certainly more accurate than previously obtained data for the nonpolarizable force field (NPFF), which are also shown in Figure 7c and noticeably overestimate water self-diffusion in the entire range of concentrations. The latter is consistent with the general trend of polarizable water models having lower diffusion coefficients compared to nonpolarizable force fields due to explicit polarization effects.³²

Excess viscosity is another transport property useful for the validation of force field accuracy. The viscosity of DME–water solutions, pure water, and pure DME were determined using the Einstein⁴³ relation accounting for diagonal and nondiagonal elements as previously described.^{58,82}

$$\eta = \lim_{t \rightarrow \infty} \frac{V}{20k_B T t} \langle \sum (L_{\alpha\beta}(t) - L_{\alpha\beta}(0))^2 \rangle \quad (8)$$

where $L_{\alpha\beta}(t) = \int_0^t P_{\alpha\beta}(t') dt'$, $P_{\alpha\beta}$ is the symmetrized stress tensor, $\alpha\beta$ are the components of the stress tensor, k_B is the Boltzmann constant, T is the temperature, V is the volume of the simulation cell, and $\langle \dots \rangle$ indicates an ensemble average. Here, $P_{\alpha\beta}$ is the stress tensor defined as $P_{\alpha\beta} = (\sigma_{\alpha\beta} + \sigma_{\beta\alpha})/2 - (\delta_{\alpha\beta})/3 \times tr(\sigma)$, where $\sigma_{\alpha\beta}$ is a stress tensor, $\delta_{\alpha\beta} = 1$ for $\alpha = \beta$, and $\delta_{\alpha\beta} = 0$ for $\alpha \neq \beta$. The excess viscosity is given by the following relationship:

$$\Delta\eta^E = \eta_{\text{mixture}} - (x_{\text{solvent}}\eta_{\text{solvent}} + x_{\text{solute}}\eta_{\text{solute}}) \quad (9)$$

where $\Delta\eta^E$ is the excess viscosity, η_{mixture} is the viscosity of the binary solution, η_i is the viscosity of the pure component (solvent or solute), and x_i is the molar fraction of the solvent or solute in the mixture. The excess viscosities using four sets of parameters are compared with experimental results as a function of the solution composition at 318 K in Figure 7d.

Figure 7d shows that experimental data for excess viscosity have a maximum at a weight fraction of DME of about 0.5. Simulations using PFF-1 and PFF-2 qualitatively show the same trend as experiments for excess viscosity; however, the position of the maximum appears to be shifted to a weight fraction of about 0.4, and the value at the maximum is about a factor of 2 larger than the experimental value. At dilute concentrations ($W_{\text{DME}} = 0.17$) and high concentrations ($W_{\text{DME}} > 0.7$), simulation results are in a very good agreement with experimental data. Simulations using empirically adjusted PFF-3 and PFF-4 force fields provide significantly better descriptions of the maximum value for excess viscosity, although the position of the peak is still slightly shifted to lower concentrations compared to the experimental location of the maximum. Interestingly, unlike the self-diffusion coefficient, which showed very little dependence on the version of polarizable force field, excess viscosity is much more sensitive, both to the choice of the force field (PFF-1 vs PFF-2) and to empirical adjustments of these force fields (PFF-3 and PFF-4). Finally, MD simulations using PFF-3 and PFF-4 provide a better description of excess viscosity compared to NPFF.

H. Extension of the Force Fields to Poly(Propylene Oxide)–Water Solutions. As with PEO, all bonded parameters for DMP and PPO were taken from APPLE&P.^{55,58} All nonbonded

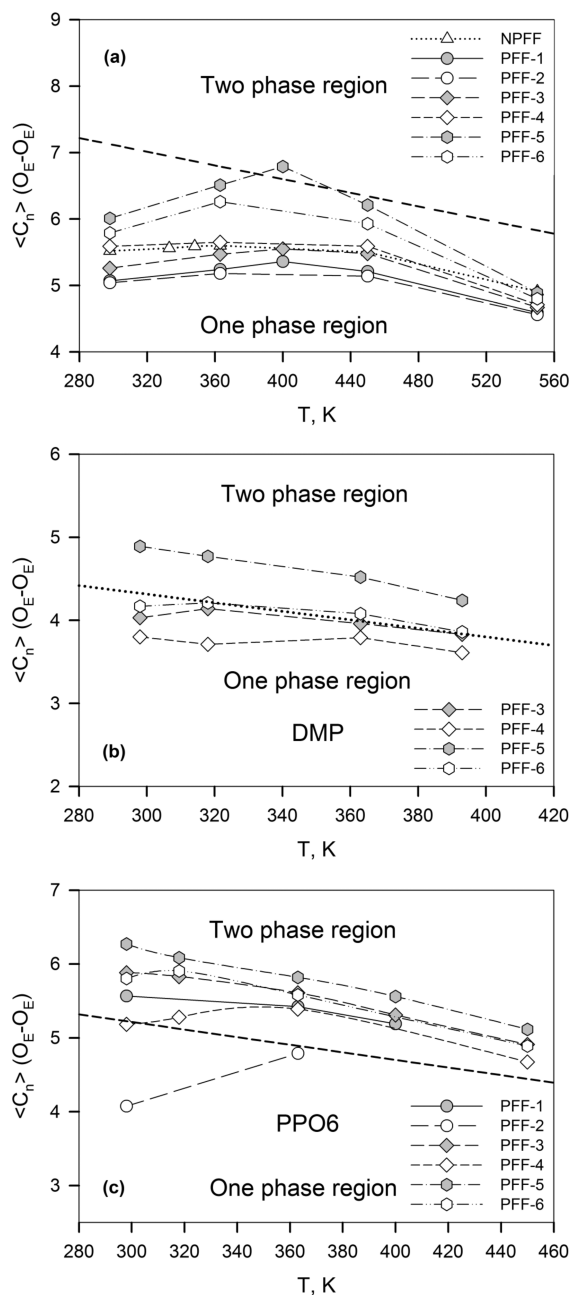


Figure 8. Ether oxygen coordination numbers and approximate phase boundaries (short double-dashed line) for PEO (a), (dotted line) for DMP (b), and (short dashed line) for PPO (c) aqueous solutions as a function of the temperature, obtained from MD simulations for various force fields investigated.

parameters for ether–water interactions were transferred as obtained for DME/PEO (see Table 2) without any additional empirical adjustments. The nonbonded parameters for the methyl–water interactions of DMP/PPO were taken as parameters for methoxy–water interactions of DME/PEO. The partial atomic charges for DMP/PPO were obtained in a similar way to that discussed in the parametrization of partial charges section, employing the most populous hydrophilic and hydrophobic conformations of DMP and 3,6-dimethyl diglyme (DMD) that could be found in a previous publication.⁸³ These charges are also given in Table 1.

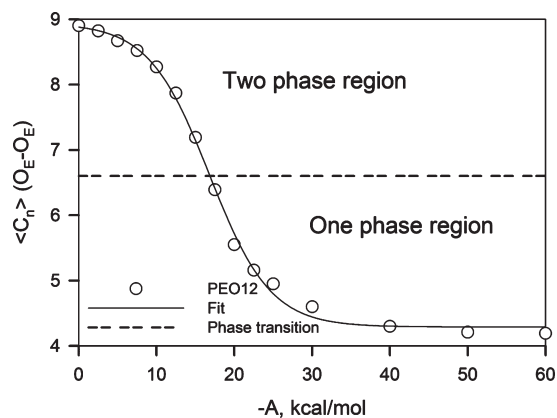


Figure 9. Ether oxygen coordination number as a function of the ether oxygen–water hydrogen intermolecular interaction parameter A at 400 K for PEO12–water solutions. Open circles indicate values obtained from MD simulations, and the solid line indicates a sigmoidal fit. The short double-dashed line indicates the approximate phase transition (inflection point).

I. Preliminary Investigation of the Phase Behavior of PEO and PPO in Aqueous Solutions. One of the goals of this work is to gain a better understanding of the correlation between the ΔG_{soln} of DME in water predicted by a force field and the predicted phase behavior of PEO and PPO in aqueous solution. For this purpose, we introduce two additional force fields, PFF-5 and PFF-6, which are variations of PFF-1,3 and PFF-2,4, respectively, with parameters given in Table 2. These force fields are more “hydrophobic” than PFF-3 and PFF-4 and have correspondingly smaller (by about 1.0 kcal/mol) ΔG_{soln} values of DME in water, as shown in Table 3.

The phase behavior of PEO–water and PPO–water was investigated as follows. Systems of 0.35 weight fractions of PEO12, DMP, and PPO6 were simulated over the temperature range of 298 to 550 K (PEO12). We used ether oxygen–ether oxygen (O_E-O_E) correlations as an order parameter to quantify the homogeneity/heterogeneity of systems. Specifically, the average O_E-O_E coordination number C_n was determined by counting the number of intra- and intermolecular O_E 's within 6 Å of a given O_E . This coordination number is plotted as a function of the temperature for PEO12, DMP, and PPO6 solutions in Figure 8a–c, respectively.

PEO–Water Solutions. Figure 8a shows that initially O_E-O_E correlation increases for PEO12–water solutions with increasing temperature for all of the force fields investigated. It is reasonable to associate increased ether–ether correlation with decreasing solvent quality, which is expected for PEO–water solutions since they exhibit LCST behavior at sufficiently high molecular weights, as discussed in the Introduction. At even higher temperatures, Figure 8 reveals that ether–ether correlation decreases, consistent with the UCST behavior exhibited by PEO–water solutions. Furthermore, it can be seen that the most hydrophilic force fields (PFF-1 and PFF-2), with the largest ΔG_{soln} of DME in water, show the least ether–ether coordination, while the most hydrophobic force fields with the smallest ΔG_{soln} of DME in water (PFF-5 and PFF-6) exhibit the greatest extent of ether–ether correlation.

The relationship between the extent of O_E-O_E correlation and phase behavior is illustrated in Figure 9. Here, the O_E-O_E coordination number is plotted as a function of the “ A ”

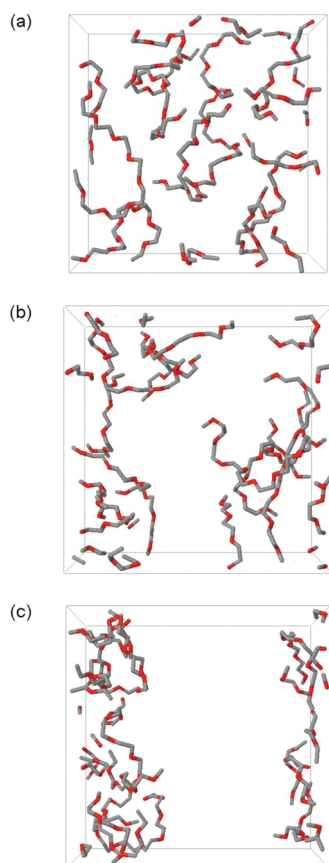


Figure 10. Snapshots for PEO12–water solutions are given as obtained from MD simulations scaling the repulsion interaction parameter A . Hydrogen atoms and solvent are omitted for clarity. Homogeneous solution is obtained for $A = -30$ kcal/mol (a) and $A = -17.50$ kcal/mol (b). The phase separated system is illustrated as obtained for $A = -5$ kcal/mol (c).

parameter in the O_E-H_w nonbonded energy function (eq 1) at 400 K. Here, $A = -21.6$ kcal/mol, -20.0 kcal/mol, and -16.5 kcal/mol corresponds to PFF-1, -3, and -5, respectively (see Table 2). It can be seen that ether–ether coordination increases with decreasing O_E-H_w nonbonded attraction. Also shown in Figure 10a–c are snapshots from trajectories with $A = -30.0$ kcal/mol, -17.5 kcal/mol, and -5.0 kcal/mol. Clearly $A = -5.0$ kcal/mol is phase separate, while $A = -17.5$ kcal/mol appears to be in transition and $A = -30.0$ kcal/mol corresponds to a miscible system. On the basis of this, we associate a value of $C_n(O_E-O_E) \approx 6.7$ (which corresponds to the inflection point in the $C_n(A)$ curve) with a phase separation in the 0.35 weight fraction PEO12–water solutions at this temperature. This value is temperature dependent due to thermal expansion of the system. To establish this temperature dependence, a similar $C_n(A)$ curve was obtained for 318 K, and linear extrapolation was assumed using inflection points at two temperatures to obtain the approximate phase boundary shown in Figure 8a. On the basis of theoretical predictions, PEO12 even with methyl termination is too low in molecular weight to exhibit phase separation, i.e., to exhibit LCST behavior.²⁰ Hence, force fields PFF-1, PFF-2, PFF-3, and PFF-4 exhibit expected behavior for the PEO12–water solutions, while PFF-5 and PFF-6 appear to be too hydrophobic in the description of ether–water interactions, as expected.

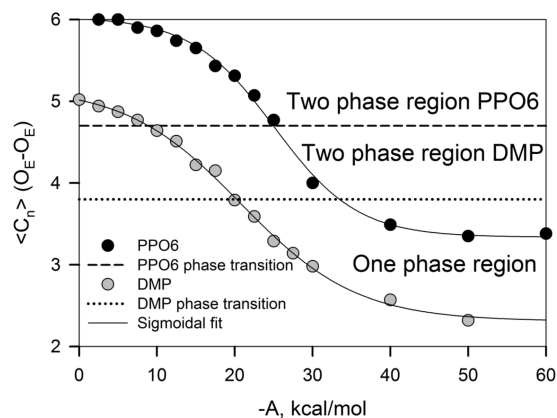


Figure 11. Ether oxygen coordination number as a function of the ether oxygen–water hydrogen intermolecular interaction parameter A at 400 K for DMP and PPO6. Black circles correspond to PPO6 values, and gray circles correspond to DMP values as obtained from MD simulations. Solid lines illustrate a sigmoidal fit. A short dashed line indicates the approximate phase transition for PPO6, and a dotted line indicates the approximate phase transition for DMP.

DMP–Water and PPO–Water Solutions. It has been shown experimentally that DMP is consoluble in water at least to temperatures up to 368 K.⁸⁴ We also have found experimental results for PPO–water mixtures as discussed in the Introduction. Those experimental results provide us with a position of the LCST for hydroxyl terminated PPO6 which is more hydrophilic than the methoxy terminated PPO6 simulated here. No experimental data on solvation of methoxy terminated PPO in water were found in the literature. Therefore, the position of the LCST for methoxy terminated PPO is uncertain but, on the basis of the behavior of PEO–water solutions, is likely to be significantly lower than that for hydroxyl terminated PPO. Therefore, we anticipate that 298 K is already above the LCST for PPO6–water solutions. Figure 11 shows $C_n(O_E-O_E)$ as a function of the “ A ” parameter in the O_E-H_w nonbonded potential for the 0.35 weight fraction DMP–water and PPO6–water solutions, respectively. As with PEO12–water solutions, more ether–ether clustering is observed with decreasing of the ether–water interaction strength. Similarly, the values of C_n corresponding to phase transition (inflection points) for PPO6 and DMP were obtained at two temperatures and were used to obtain approximate phase boundaries shown in Figure 8b and c. Figure 8b indicates that the DMP–water solution does not show signs of phase separation for PFF-1,2 (not shown) and PFF-4. Simulations using PFF-3 and -6 are very close or slightly above the phase boundary, while C_n obtained from simulations using PFF-5 is clearly above the phase boundary, indicating a potential phase transition for this force field. For the PPO6–water solution, where phase separation is anticipated, PFF-2 appears to provide a too hydrophilic description of ether–water interactions, while all other force fields predict phase separation at all temperatures. These results indicate that simulations using PFF-1 and -4 are the most consistent with what one can expect on the basis of existing experimental data. They predict the solubility of DMP in water yet at the same time result in phase separation for PPO6.

IV. PFF-3 VS PFF-4

Table 3 reveals that PFF-3 and PFF-4 both provide a good description of $\Delta G_{\text{sol}}^{\text{DME}}$ of DME in water (as they were empirically

adjusted to do so). Furthermore, both force fields accurately describe the ΔH of solvation for DME in water. In accord with the free energy of DME solvation, PFF-3 and PFF-4 reproduce the water self-diffusion and excess viscosity of DME–water solutions at 318 K well. However, PFF-4 provides a noticeably better description of the excess volume of mixing (Figure 7b) and hence appears to be the superior force field. This is despite the fact that PFF-3 actually provides a better description of DME–water interactions along path 1, as shown in Figure 6. From these observations, we conclude that in the parametrization of polymer–water potentials

- (1) parametrizing the potential to match gas phase small molecule–water interactions as obtained from high-level QC calculations is a good starting point for a potential, but empirical adjustments are likely to be required
- (2) empirically adjusting the potential to reproduce the free energy of solvation of small molecules in water provides an improved description of other small molecule–water solution properties as well as polymer–water solution properties
- (3) unfortunately, there is no unique way to carry out such an empirical adjustment, and variations that provide equally good descriptions of the free energy of solvation of the small molecule(s) in water can provide significantly different descriptions of other important properties
- (4) point three reveals the danger of empirical adjustment of potentials to match a single solution property. The ability of the empirically adjusted potential to describe an array of solution properties should be investigated.

V. CONCLUSIONS

The ability of MD simulations to accurately reproduce the properties of PEO–water and PPO–water solutions as a function of the temperature requires a high-quality water potential and an accurate description of the interaction of ether–ether and ether–water interactions. A strong indicator of the quality of the potential is the ability of the potential to accurately describe the free energy and energy of solvation of DME in water. Our new empirically adjusted polarizable potential PFF-4 provides a good description of DME–water interactions in the gas phase as provided by high-level QC calculations while at the same time accurately reproducing the thermodynamic properties of DME–water solutions. The PFF-4 potential was found to provide a description of PEO–water, DMP–water, and PPO–water solutions consistent with experimental observations based upon preliminary simulation studies. We are currently conducting studies of higher molecular weight PEO–water solutions where LCST behavior is expected to further investigate the ability of our polarizable ether–water potential to describe PEO–water phase behavior.

The observed correlation between DME–water thermodynamic properties and the phase behavior of poly(ether)–water solutions with ΔG_{solv} for DME–water solutions provides a readily accessible method for initially evaluating the quality of an ether–water potential. For example, our previously published nonpolarizable ether–water potential¹² yields $\Delta G_{\text{solv}} = -5.6$ kcal/mol, significantly greater than the experimental value, and hence we anticipate that this potential predicts too hydrophilic interactions between PEO and water and PPO and water. Similarly, the polarizable CHARMM potential¹³ yields $\Delta G_{\text{solv}} = -3.8$ kcal/mol (similar to our PFF-5 and PFF-6 potentials), which is

apparently too hydrophobic in the description of ether–water interactions. A more recently published polarizable CHARMM potential⁸⁵ yields $\Delta G_{\text{solv}} = -5.6$ kcal/mol, and we anticipate that this potential will yield PEO–water and PPO–water interactions that are too favorable.

APPENDIX

The interface transit method (IT) is based on the constrained force approach⁸⁶ to estimate the free energy of solvation ΔG_{solv} . In this method, a simulation cell with a film of solvent and a vacuum is set up. In order to sharpen the solvent/vacuum interface, two artificial walls parallel to the solvent/vacuum interface are applied (x – y plane) on the left ZL and on the right ZR sides of the film. The biasing force from the walls $F_i^{\text{wall}}(z_i)$ acting on each atom is defined as

$$F_i^{\text{wall}}(z_i) = \begin{cases} +k(z_i - z_l)^2 & z_i < z_l \\ -k(z_i - z_r)^2 & z_i > z_r \\ 0 & z_l \leq z_i \leq z_r \end{cases} \quad (\text{A1})$$

where z_i is the position of an atom i , Å; $k = 5$ kcal/mol·Å² is a force constant, and z_l and z_r are the positions for the left or right walls relative to the center of mass of the water film, Å. To ensure that the net external force (from the walls) on the film is zero at each time step, the total force from both walls was determined, and then a counter force was evenly distributed between all atoms in the film. Therefore, the effective force experienced by each atom in the film is

$$F_i^{\text{eff}}(z_i) = F_i^{\text{wall}}(z_i) - \sum_{i=1}^N \frac{F_i^{\text{wall}}(z_i)}{N} \quad (\text{A2})$$

where N is the total number of atoms in the water film. As can be seen in Figure A1, application of this force sharpens the water–vacuum interface without significantly perturbing the density at the center of the film.

A single solute molecule is introduced into the system at various positions ranging from the center of the solvent film (representing a bulk-like environment) to the vacuum phase away from the film (corresponding to the ideal gas phase). The center of mass of the solute is kept at a fixed separation distance Δz from the center of mass of the film, and the force required to

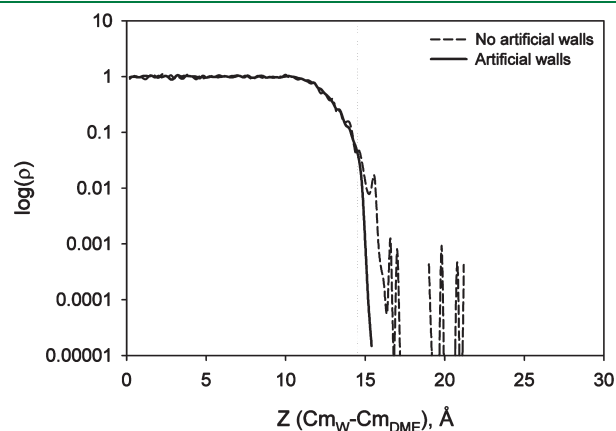


Figure A1. Water bulk distribution densities shown without constraints (no artificial walls) and with additional constraints (artificial walls applied) at the water/vacuum interface.

maintain this constraint is determined every time step and then is averaged over the entire simulation. Simulations of multiple systems with regular separation step Δz_i between the solute and center of mass of the film are conducted. In order to adequately thermalize the solute molecule in the vacuum, the solute was subjected to additional Brownian forces.

■ ASSOCIATED CONTENT

S Supporting Information. Conformational energy paths for tXt , gXt , Xtt , and Xgt and populations of tgt , tgg , tgg' , ttt , and ttg conformers of DME as a function of the concentration at 318 K. This material is available free of charge via the Internet at <http://pubs.acs.org>.

■ AUTHOR INFORMATION

Corresponding Author

*E-mail: gds8@utah.edu, gsmith2@cluster2.mse.utah.edu.

■ ACKNOWLEDGMENT

We would like to acknowledge the support from the National Science Foundation through Grants CBET-0708368 and MRSEC (University of Colorado) DME-0213918.

■ REFERENCES

- (1) Hamley, I. W. *The Physics of Block Copolymers*; Oxford University Press, Inc.: New York, 1998; p 295.
- (2) Hadjichristidis, N.; Pispas, S.; Floudas, G. A. In *Block Copolymers: Synthetic Strategies, Physical Properties, and Applications*; Hadjichristidis, N., Ed.; John Wiley & Sons, Inc.: New York, 2003; p 290.
- (3) Yallapu, M. M.; Reddy, M. K.; Labhasetwar, V. In *Biomedical Applications of Nanotechnology*; Labhasetwar, V., Leslie-Pelecky, D. L., Eds.; John Wiley & Sons, Inc.: New York, 2007; p 131.
- (4) Batrakova, E. V.; Kabanov, A. V. *J. Controlled Release* **2008**, *130*, 98.
- (5) Bae, Y. C.; Lambert, S. M.; Soane, D. S.; Prausnitz, J. M. *Macromolecules* **1991**, *24*, 4403.
- (6) Saeki, S.; Kuwahara, N.; Nakata, M.; Kaneko, M. *Polymer* **1976**, *17*, 685.
- (7) Malcolm, G. N.; Rowlinson, J. S. *J. Chem. Soc., Faraday Trans.* **1957**, *53*, 921.
- (8) Bedrov, D.; Borodin, O.; Smith, G. D. *J. Phys. Chem. B* **1998**, *102*, 5683.
- (9) Smith, G. D.; Bedrov, D.; Borodin, O. *J. Am. Chem. Soc.* **2000**, *122*, 9548.
- (10) Smith, G. D.; Bedrov, D. *J. Phys. Chem. A* **2001**, *105*, 1283.
- (11) Anderson, P. M.; Wilson, M. R. *Mol. Phys.* **2005**, *103*, 89.
- (12) Smith, G. D.; Borodin, O.; Bedrov, D. *J. Comput. Chem.* **2002**, *23*, 1480.
- (13) Vorobyov, I.; Anisimov, V. M.; Greene, S.; Venable, R. M.; Moser, A.; Pastor, R. W.; MacKerell, A. D. *J. Chem. Theory Comput.* **2007**, *3*, 1120.
- (14) Bekiranov, S.; Bruinsma, R.; Pincus, P. *Phys. Rev. E* **1997**, *55*, 577.
- (15) Smith, G. D.; Bedrov, D.; Borodin, O. *Phys. Rev. Lett.* **2000**, *85*, 5583.
- (16) Dormidontova, E. E. *Macromolecules* **2002**, *35*, 987.
- (17) Smith, G. D.; Bedrov, D. *Macromolecules* **2002**, *35*, 5712.
- (18) Matsuyama, A.; Tanaka, F. *Phys. Rev. Lett.* **1990**, *65*, 341.
- (19) Karlström, G. *J. Phys. Chem.* **1984**, *89*, 4962.
- (20) Dormidontova, E. E. *Macromolecules* **2004**, *37*, 7747.
- (21) Goldmints, I.; Holzwarth, J. F.; Smith, K. A.; Hatton, T. A. *Langmuir* **1997**, *13*, 6130.
- (22) Goldmints, I.; vonGottberg, F. K.; Smith, K. A.; Hatton, T. A. *Langmuir* **1997**, *13*, 3659.
- (23) Mortensen, K. *J. Phys. Cond. Matter* **1996**, *8*, A103.
- (24) Mortensen, K.; Brown, W. *Macromolecules* **1993**, *26*, 4128.
- (25) Sandell, L. S.; Goring, D. A. I. *Makromol. Chem.* **1970**, *138*, 77.
- (26) Bilimova, Y. S.; Gladkovskii, G. A.; Golubev, V. M.; Medved, Z. N. *Polym. Sci. U.S.S.R.* **1980**, *22*, 2456.
- (27) Medved, Z. N.; Pencel, Y.; Denisova, T. A.; Lebedev, B. C. *Vysokomol. Soedin. Ser. B* **1981**, *23*, 276.
- (28) Medved, Z. N.; Petrova, N. I.; Tarakanov, O. G. *Vysokomol. Soedin. Ser. B* **1982**, *24*, 674.
- (29) Carlsson, M.; Hallén, D.; Linse, P. *J. Chem. Soc., Faraday Trans.* **1995**, *91*, 2081.
- (30) Crowther, N. J.; Eagland, D. *J. Chem. Soc., Faraday Trans.* **1996**, *92*, 1859.
- (31) Jorgensen, W. L.; Chandrasekar, J.; Madura, J. D.; Impey, R. W.; Klein, M. L. *J. Chem. Phys.* **1983**, *79*, 926.
- (32) Guillot, B. *J. Mol. Liq.* **2002**, *101*, 219.
- (33) Jorgensen, W. L.; Jenson, C. J. *Comput. Chem.* **1998**, *19*, 1179.
- (34) Yu, H.; Hansson, T.; van Gunsteren, W. F. *J. Chem. Phys.* **2003**, *118*, 221.
- (35) Yu, H.; van Gunsteren, W. F. *J. Chem. Phys.* **2004**, *121*, 9549.
- (36) Rick, S. W.; Stuart, S. J.; Berne, B. J. *J. Chem. Phys.* **1994**, *101*, 6141.
- (37) Rick, S. W. *J. Chem. Phys.* **2001**, *114*, 2276.
- (38) Stern, H. A.; Rittner, F.; Berne, B. J.; Friesner, R. A. *J. Chem. Phys.* **2001**, *115*, 2237.
- (39) Lamoureux, G.; MacKerell, A. D.; Roux, B. *J. Chem. Phys.* **2003**, *119*, 5185.
- (40) Lamoureux, G.; Harder, E.; Vorobyov, I. V.; Roux, B.; MacKerell, A. D. *Chem. Phys. Lett.* **2006**, *418*, 245.
- (41) English, N. J. *Mol. Phys.* **2005**, *103*, 1945.
- (42) Rycckaert, J. P.; Ciccotti, G.; Berendsen, H. J. C. *J. Comput. Phys.* **1977**, *23*, 327.
- (43) Allen, M. P.; Tildesley, D. J. *Computer Simulation of Liquids*; Oxford University Press: New York, 1987; p 33.
- (44) Martyna, G. J.; Tuckerman, M. E.; Tobias, D. J.; Klein, M. L. *Mol. Phys.* **1996**, *87*, 1117.
- (45) Ismail, A. E.; Grest, G. S.; Stevens, M. J. *J. Chem. Phys.* **2006**, *125*, 014702(1).
- (46) Smith, G. D.; Bedrov, D. *Macromolecules* **2002**, *35*, 5712.
- (47) Frisch, M. J.; Trucks, G. W.; Schlegel, H. B.; Scuseria, G. E.; Robb, M. A.; Cheeseman, J. R.; Montgomery, J. A., Jr.; Vreven, T.; Kudin, K. N.; Burant, J. C.; Millam, J. M.; Iyengar, S. S.; Tomasi, J.; Barone, V.; Mennucci, B.; Cossi, M.; Scalmani, G.; Rega, N.; Petersson, G. A.; Nakatsuji, H.; Hada, M.; Ehara, M.; Toyota, K.; Fukuda, R.; Hasegawa, J.; Ishida, M.; Nakajima, T.; Honda, Y.; Kitao, O.; Nakai, H.; Klene, M.; Li, X.; Knox, J. E.; Hratchian, H. P.; Cross, J. B.; Bakken, V.; Adamo, C.; Jaramillo, J.; Gomperts, R.; Stratmann, R. E.; Yazayev, O.; Austin, A. J.; Cammi, R.; Pomelli, C.; Ochterski, J. W.; Ayala, P. Y.; Morokuma, K.; Voth, G. A.; Salvador, P.; Dannenberg, J. J.; Zakrzewski, V. G.; Dapprich, S.; Daniels, A. D.; Strain, M. C.; Farkas, O.; Malick, D. K.; Rabuck, A. D.; Raghavachari, K.; Foresman, J. B.; Ortiz, J. V.; Cui, Q.; Baboul, A. G.; Clifford, S.; Cioslowski, J.; Stefanov, B. B.; Liu, G.; Liashenko, A.; Piskorz, P.; Komaromi, I. M.; Fox, D. J.; Keith, T.; Al-Laham, M. A.; Peng, C. Y.; Nanayakkara, A.; Challacombe, M.; Gill, P. M. W.; Johnson, B.; Chen, W.; Wong, M. W.; Gonzalez, C.; Pople, J. A. *Gaussian 03*, Revision E.01; Gaussian, Inc.: Wallingford, CT, 2004.
- (48) Lee, C.; Yang, W.; Parr, R. G. *Phys. Rev. B* **1988**, *37*, 785.
- (49) Becke, A. D. *Phys. Rev. A* **1988**, *38*, 3098.
- (50) Becke, A. D. *J. Chem. Phys.* **1992**, *98*, 1372.
- (51) Becke, A. D. *J. Chem. Phys.* **1992**, *98*, 5648.
- (52) Kendall, R. A.; Dunning, T. H. *J. Chem. Phys.* **1992**, *96*, 6796.
- (53) Borodin, O.; Smith, G. D. *J. Phys. Chem. B* **2003**, *107*, 6801.
- (54) Smith, G. D.; Borodin, O. In *Molecular Simulation Methods for Predicting Polymer Properties*; Galiatsatos, V., Ed.; John Wiley & Sons Inc: New York, 2005; p 47.
- (55) Borodin, O.; Smith, G. D. *J. Phys. Chem. B* **2006**, *110*, 6279.

- (56) Borodin, O.; Smith, G. D. *J. Phys. Chem. B* **2009**, *113*, 1763.
- (57) Lee, H.; Venable, R. M.; MacKerell, A. D.; Pastor, R. W. *Biophys. J.* **2008**, *95*, 1590.
- (58) Borodin, O. *J. Phys. Chem. B* **2009**, *113*, 11463.
- (59) Boys, S. F.; Bernardi, F. *Mol. Phys.* **1970**, *19*, 553.
- (60) Waldman, M.; Hagler, A. T. *J. Comput. Chem.* **1993**, *14*, 1077.
- (61) <http://www.eng.utah.edu/~gdsmith/lucretius.html> (accessed April 2011).
- (62) *CRC Handbook of Chemistry and Physics*; Lide, D. R., Ed.; CRC Press: Boca Raton, FL, 2006.
- (63) Gunsteren, W. F.; Berendsen, H. J. C. *Mol. Phys.* **1982**, *45*, 637.
- (64) Ben-Naim, A.; Marcus, Y. *J. Chem. Phys.* **1984**, *81*, 2016.
- (65) Ben-Naim, A. *Statistical Thermodynamics for Chemists and Biochemists*; Plenum Press: New York, 1992; p 459.
- (66) Jorgensen, W. L.; Blake, J. F.; Buckner, J. K. *Chem. Phys.* **1989**, *129*, 193.
- (67) Li, L. W.; Davande, H.; Bedrov, D.; Smith, G. D. *J. Phys. Chem. B* **2007**, *111*, 4067.
- (68) Bedrov, D.; Smith, G. D.; Davande, H.; Li, L. W. *J. Phys. Chem. B* **2008**, *112*, 2078.
- (69) Simkin, B. Y.; Sheikhet, I. I. In *Quantum Chemical and Statistical Theory of Solutions: A Computational Approach*; Kemp, T. J., Ed.; Ellis Horwood Limited: New York, 1995; p 155.
- (70) Yoshida, H.; Takikawa, K.; Kaneko, I.; Matsuura, H. *J. Mol. Struct.* **1993**, *311*, 205.
- (71) Matsuura, H.; Sagawa, T. *J. Mol. Liq.* **1995**, *65/66*, 313.
- (72) Masatoki, S.; Takamura, M.; Matsuura, H.; Kamogawa, K.; Kitagawa, T. *Chem. Lett.* **1995**, 991.
- (73) Yoshida, H.; Tanaka, T.; Matsuura, H. *Chem. Lett.* **1996**, 637.
- (74) Begum, R.; Matsuura, H. *J. Chem. Soc., Faraday Trans.* **1997**, *93*, 3839.
- (75) Yoshida, H.; Matsuura, H. *J. Phys. Chem. A* **1998**, *102*, 2691.
- (76) Goutev, N.; Ohno, K.; Matsuura, H. *J. Phys. Chem. A* **2000**, *104*, 9226.
- (77) Das, B.; Roy, M. N.; Hazra, D. K. *Indian J. Chem. Technol.* **1994**, *1*, 93.
- (78) Trouw, F.; Bedrov, D.; Borodin, O.; Smith, G. D. *J. Chem. Phys.* **2000**, 01.
- (79) Yeh, I.-C.; Hummer, G. *J. Phys. Chem. B* **2004**, *108*, 15873.
- (80) Mills, R. *Mol. Motions Liq.* **1974**, 391.
- (81) Holtz, M.; Heil, S. R.; Sacco, A. *Phys. Chem. Chem. Phys.* **2000**, *2*, 4740.
- (82) Daivis, P. J.; Evans, D. J. *J. Chem. Phys.* **1994**, *100*, 541.
- (83) Smith, G. D.; Borodin, O.; Bedrov, D. *J. Phys. Chem. A* **1998**, *102*, 10318.
- (84) Stephenson, R. M. *J. Chem. Eng. Data* **1993**, *38*, 134.
- (85) Baker, C. M.; MacKerell, A. D. *J. Mol. Model.* **2009**, *16*, 567.
- (86) Mülders, T.; Krüger, P.; Swegat, W.; Schlitter, J. *J. Chem. Phys.* **1996**, *104*, 4869.
- (87) Smith, G. D.; Bedrov, D. *J. Phys. Chem. B* **2003**, *107*, 3095.
- (88) Cabani, S.; Mollica, V. *J. Chem. Soc., Faraday Trans.* **1978**, *74*, 2667.
- (89) Dohnal, V.; Roux, A. H.; Hynek, V. *J. Solution Chem.* **1994**, *23*, 889.
- (90) Kustov, A. V.; Antonova, O. A.; Korolev, V. P. *J. Solution Chem.* **2002**, *31*, 671.
- (91) Gillen, K. T.; Douglass, D. C.; Hoch, M. J. *J. Chem. Phys.* **1972**, *57*, 5117.

Transferability of Coarse Grained Potentials: Implicit Solvent Models for Hydrated Ions

Jia-Wei Shen,[†] Chunli Li,[‡] Nico F.A. van der Vegt,[‡] and Christine Peter^{*,†}

[†]Max Planck Institute for Polymer Research, Ackermannweg 10, D-55128 Mainz, Germany

[‡]Center of Smart Interfaces, Technische Universität Darmstadt, Petersenstrasse 32, D-64287 Darmstadt, Germany

 Supporting Information

ABSTRACT: Understanding the relation between structural and thermodynamic quantities obtained with simplified—e.g., coarse-grained (CG) or implicit-solvent—models is an ongoing challenge in the field of multiscale simulation. Assessing the transferability of such models to state points that differ from the one where the model was parametrized is important if one wants to apply these models to complex systems, which, for example, exhibit spatially varying compositions. Here, we investigate the transferability of CG (in this case implicit-solvent) ion models with effective pair potentials derived at very low concentrations to different ion concentrations in aqueous solution. We evaluate both thermodynamic and structural properties of systems of NaCl in aqueous solution both in atomistic explicit-solvent and CG simulations. For the explicit solvent simulations, osmotic coefficients have been calculated at a wide range of salt concentrations and agree very well with experimental data. It had been shown previously that a concentration-dependent dielectric permittivity can be used to make effective implicit-solvent pair potentials transferable since it accounts for the effect of ion concentration on solvent properties, resulting in very good osmotic properties of these models for a certain range of salt concentrations. We investigate the explicit and implicit solvent models also in terms of structural properties, where we can show how with a concentration-dependent dielectric constant one obtains very good structural agreement at low and intermediate salt concentrations, while for larger salt concentrations, multibody ion–ion correlations put a limit to straightforward transferability. We show how—guided by this structural analysis—the transferability of the implicit-solvent model can be improved for high ion concentrations. Doing so, we obtain transferable implicit-solvent effective pair potentials which are both structurally and thermodynamically consistent with an explicit solvent reference model.

1. INTRODUCTION

In simulations of complex molecular systems, reduced-resolution models have come to play a more and more important role due to the fact that highly detailed simulation methods (i.e., quantum or atomistic level simulations) can hardly handle the broad range of time and length scales involved. In most cases, coarse grained (CG) models are designed to merge groups of atoms into “superatoms”, i.e., CG beads, and the effective CG interaction potentials are derived by averaging over the microscopic details of models at higher resolution. In this way, CG methods reduce the number of degrees of freedom of the system and thus can speed up the simulations. In recent years, various approaches have been proposed to develop CG effective potentials,^{1–6} targeting thermodynamic properties^{7–11} or properties obtained from atomistic simulations of a reference system, the latter being either structural properties^{12–16} or mean forces.^{17–19} Unfortunately, CG models are dependent on the state point and system composition, and on most occasions, the transferability of these CG models to different state points (temperature, pressure, system composition, chemical environment, etc.) is poorly understood. Transferability of CG models is vitally important to the simulation of complex systems, where various complicated multibody interactions are involved due to spatially biased structures and fluctuations. Yet, the construction of transferable CG models which accurately reproduce both structural and thermodynamic properties is an extremely challenging task, and the relation

between structural and thermodynamic properties of a CG model is central to many studies.^{20–22} Most often, effective pairwise potentials are used to describe the interactions in CG models. Since those effective pair potentials account for multibody effects, for example, three body interactions, they are only to a limited extent additive, and this sets limits to the transferability of the potentials. Understanding the physical nature of nonadditivity in the system of interest can help to make a CG model transferable. Many CG models presented in the literature were developed by constructing effective potentials in such a way that predominantly either structure or thermodynamic properties are reproduced, and then attempts were made to make the potentials transferable to similar systems (e.g., different concentration,²³ chain length,²⁴ component fraction,²⁵ etc.). In principle, transferability of effective pair potentials can be achieved in several ways: (i) One applies a model derived at/optimized for a given state point unaltered to a range of state points “nearby”; in that case, one has to carefully investigate the range in which this is permissible.¹⁵ (ii) One creates a new set of potentials for each state point one wants to investigate (e.g., density or temperature-dependent potentials).^{20,21,25,26} (iii) One specifically designs a single CG model with the aim to be transferable,^{19,27} or (iv) one uses a model derived at one state point and (analytically) modifies it to be applicable to different

Received: February 24, 2011

Published: April 27, 2011

conditions. (A simple example of the last case is the rescaling of potentials which one wants to apply to a different temperature.)

Recently, Villa et al. proposed a CG model for benzene/water.²² The CG benzene–benzene potential had been parametrized on the basis of the benzene–benzene potential of mean force of two benzene molecules in aqueous solution, i.e., at “infinite” dilution. By applying Kirkwood–Buff theory, they illustrate that this CG model can reproduce the changes in the benzene chemical potential and the activity coefficients of the mixtures over a range of mixture compositions (up to concentrations where benzene and water demix in the atomistic reference simulation). An explanation is that hydrophobic interactions between benzene solutes are short-ranged, and the multibody correlations involved in hydrophobic associations can be described by pairwise additive effective potentials (category i of the above list).

A different situation is found in the case of ion–ion interactions in aqueous solution. Due to long-range electrostatic interactions, the ions affect the behavior of water increasingly with increasing ion concentration. More specifically, the presence of many ions reduces the orientational fluctuations of the water molecules and thus the dielectric permittivity of the solvent. Therefore, effective ion–ion potentials parametrized at infinite dilution are not directly transferable to higher salt concentrations. Hess et al. developed a reduced-resolution (in this case implicit-solvent) potential for aqueous electrolyte solutions where an ion-concentration-dependent Coulomb term was added to the (ion-specific) pair interaction. Thus, by using a concentration-dependent dielectric permittivity of water, part of the multibody effects in the system were accounted for in the ion–ion pairwise interaction in the implicit solvent model.^{28–30} Their approach reproduced the NaCl solution osmotic properties and the ion coordination up to a concentration of 2.8 M (mol/L).

While in the case of the CG model of benzene–water mixtures²² the short-range hydrophobic interactions parametrized at infinite dilution were directly transferable to higher benzene concentrations, in the case of aqueous ion solutions, the ion–ion interactions determined at infinite dilution had to be split into a short ranged ion-specific and a long-range electrostatic part. The interactions were then made transferable by keeping the short-ranged part constant and analytically modifying the long-ranged electrostatic part (category iv of the above list).

On the basis of the work of Hess et al.,^{28,29} we revisit in this study the implicit solvent ion model with a concentration-dependent dielectric permittivity and investigate it in the context of transferability and structural and thermodynamic consistency of reduced-resolution models which are parametrized on the basis of an atomistic simulation model. To this end, we study osmotic coefficients and the structure of aqueous NaCl solutions over a wide range of concentrations. Osmotic properties of aqueous ion solutions have been investigated by several research groups on the basis of effective ion potentials and pair correlation functions.^{28–31} Luo and Roux³² presented a direct method to calculate the osmotic pressure of ion solutions by performing explicit-solvent atomistic simulations making use of a semipermeable wall. We employ this method by Luo and Roux to obtain osmotic coefficients of atomistic reference simulations of NaCl solutions. Thus, we can easily compare implicit and explicit solvent simulation results and evaluate our implicit solvent model. In addition, we also compare both atomistic and implicit solvent models with experimental measurements over a wide range of salt concentrations.

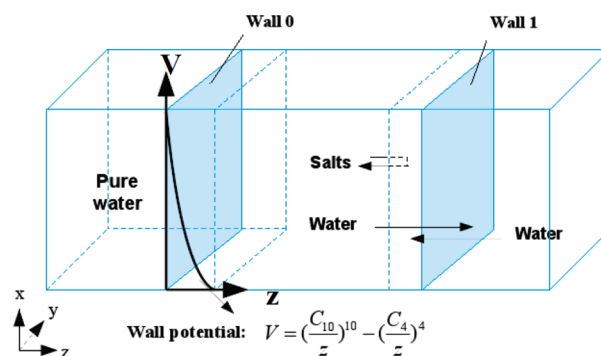


Figure 1. Setup of simulation systems to calculate the osmotic pressure of NaCl solutions using an explicit solvent model.

2. METHODS

2.1. Osmotic Pressure Calculation. Osmotic pressures of sodium chloride solutions were calculated at seven different concentrations, i.e., 0.5 m, 0.7 m, 1 m, 2 m, 3 m, 4 m, and 5 m (molality, mol/kg). Note that at the highest concentration of 5 m, this corresponds to only about 11 water molecules per ion pair. The atomic systems were set up in a similar way to Luo and Roux’s paper.³² In an orthorhombic simulation box, two semi-permeable walls were imposed along the long axis z direction to restrict the ions within the central region of the box, while water molecules can go freely through the walls. The virtual walls were set up by modifying the wall functions built in GROMACS. Particularly, a 10–4 potential was shifted with a cutoff value in such a way that only repulsive forces can be felt by the ions as they start to diffuse out of the central region. The setup of the system with the NaCl solution and a pure water region is depicted in Figure 1. The entire system was subjected to NpT dynamics. The simulation box was set to be semi-isotropic, with the side lengths x and y fixed, and only the side length z was allowed to change. However, the distance between the two walls was fixed to ensure the volume of restricted ions to be constant. Therefore, the osmotic pressure of the salt solutions can be obtained by calculating the average forces exerted by the walls on the ions divided by the surface areas of the two walls.³² All of the atomistic systems were initially constructed using the program packmol,³³ by randomly placing a certain number of ions in the central region, while water molecules were distributed in the whole region of the orthorhombic box. In our osmotic pressure calculations, 11 112 water molecules were placed in the simulation box at each concentration. The number of ion pairs was chosen according to the concentration; i.e., 50, 70, 100, 200, 300, 400, and 500 ion pairs were put into the central region (see Figure 2) for concentrations of 0.5 m, 0.7 m, 1 m, 2 m, 3 m, 4 m, and 5 m, respectively. Then, a short minimization was performed, followed by an NpT simulation as long as 30 ns. The last 10 ns was block averaged and used to calculate the osmotic pressure. Figure 2 shows a snapshot of equilibrated structure using explicit solvent simulations to calculate the osmotic pressure of NaCl solutions at 4 m.

For each concentration, an independent NpT simulation of NaCl solution was performed for 20 ns before the calculation of osmotic pressure. This simulation includes a cubic periodic box filled with 5556 water molecules and an appropriate number of ion pairs according to the concentrations. One objective of this simulation is to calculate the volume of the central region

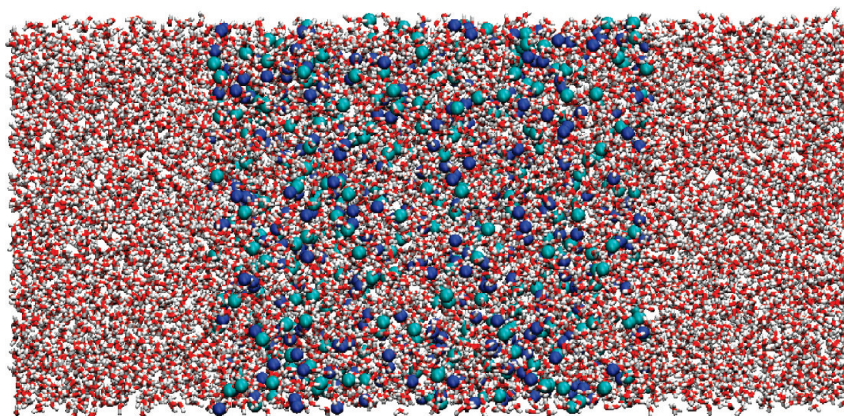


Figure 2. A snapshot of equilibrated structure using explicit solvent simulations to calculate the osmotic pressure of NaCl solutions at 4 m.

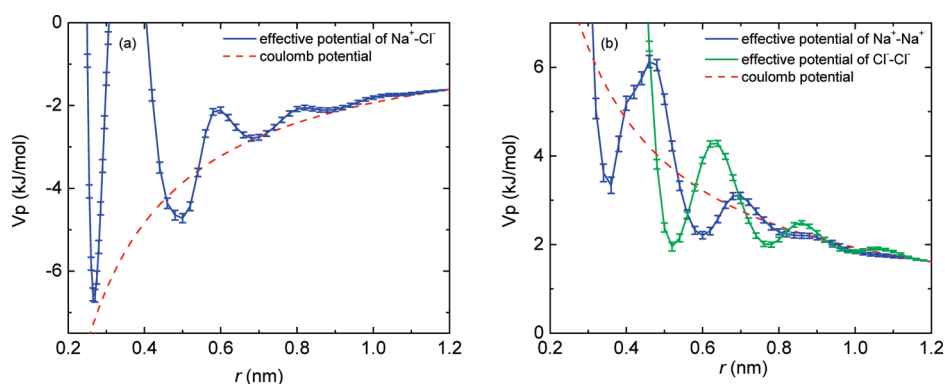


Figure 3. Effective potentials of (a) $\text{Na}^+ - \text{Cl}^-$ as well as (b) $\text{Na}^+ - \text{Na}^+$ and $\text{Cl}^- - \text{Cl}^-$ at infinite dilution derived from explicit solvent simulations. The red dashed line shows the Coulomb potential for $\epsilon_r = 71.9$ corresponding to SPC/E water. The (cumulative) errors in the PMF that originate from the errors of constraint force are also displayed.

restricting the ions in the following osmotic pressure calculations. Another is to derive the concentration-dependent dielectric permittivity $\epsilon_E(c)$, which will be mentioned in section 2.3.

2.2. Potentials of Mean Force and Effective Pair Potentials. Effective (implicit solvent/coarse grained) ion–ion pair potentials were derived as described in a previous study.^{28,29} Potentials of mean force (PMF) for all ion pairs ($\text{Na}^+ - \text{Cl}^-$, $\text{Na}^+ - \text{Na}^+$, and $\text{Cl}^- - \text{Cl}^-$) were computed using distance constraints, where the linear constraint solver (LINCS) algorithm³⁴ was used to keep two ions at a fixed distance. The free energy difference is then obtained by integrating the average constraint force f_c :

$$V(r_2) - V(r_1) = \int_{r_1}^{r_2} \langle f_c \rangle_r dr \quad (1)$$

In our simulations, we are limited to finite distances and therefore integrate backward starting from a distance $r_m = 1.2$ nm. Since the effective potential is very close to a Coulomb interaction between 1.0 and 1.2 nm,^{28,29} the total effective potential can be expressed as

$$V_p(r) = \begin{cases} \int_{r_m}^r \left[\langle f_c \rangle_s + \frac{2k_B T}{s} \right] ds + \frac{q_1 q_2}{4\pi\epsilon_0\epsilon_r r_m} & r < r_m \\ \frac{q_1 q_2}{4\pi\epsilon_0\epsilon_r r} & r \geq r_m \end{cases} \quad (2)$$

where $(2k_B T)/s$ is an entropic term, k_B is the Boltzmann

constant, and T is the temperature. ϵ_0 and ϵ_r are the dielectric permittivity of the vacuum and of the SPC/E water model, respectively. If one subtracts the (long-range) Coulombic interactions between different ions from $V_p(r)$ in eq 2 one obtains the short-range (non-Coulombic) contribution to the interaction between these ions:

$$V_{\text{short}}(r) = V_p(r) - V_{\text{coul}}(r) = V_p(r) - \frac{q_1 q_2}{4\pi\epsilon_0\epsilon_r r} \quad (3)$$

This short-range contribution $V_{\text{short}}(r)$ is used as tabulated ion-specific pair interaction in combination with Coulomb interactions (which are typically computed using Particle Mesh Ewald summation or similar) in implicit solvent/coarse grained ion simulations.

A series of independent constrained simulations for the $\text{Na}^+ - \text{Cl}^-$, $\text{Na}^+ - \text{Na}^+$, and $\text{Cl}^- - \text{Cl}^-$ ion pairs were carried out at distances up to 1.2 nm. For like-ion pairs, intervals of 0.02 nm between constraint distances were used. For the $\text{Na}^+ - \text{Cl}^-$ pair, intervals of 0.005 nm were used between 0.2 and 0.4 nm to get sufficient sampling around the first minimum of the potential, and intervals of 0.02 nm were used above 0.4 nm. All systems contained two ions and 1000 water molecules in a dodecahedron box. Figure 3 shows the effective potentials of $\text{Na}^+ - \text{Cl}^-$ (left panel) as well as $\text{Na}^+ - \text{Na}^+$ and $\text{Cl}^- - \text{Cl}^-$ (right panel) at infinite dilution and, for comparison, the Coulomb

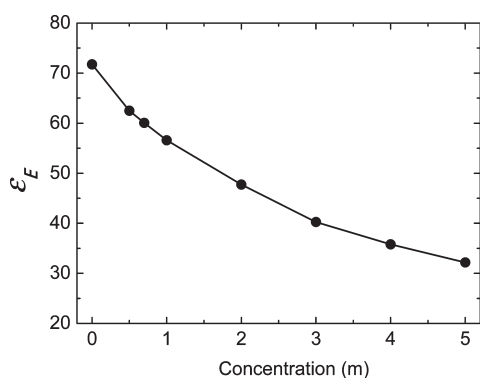


Figure 4. The equilibrium concentration dependent dielectric permittivity ϵ_E as a function of NaCl concentrations, calculated from explicit solvent simulation of SPC/E water model.

interaction for a dielectric constant of $\epsilon_r = 71.9$ (SPC/E water model).

2.3. Concentration-Dependent Dielectric Constants. The potentials of mean force determined as described in the above paragraph—which by construction include the effect of the solvent on the ion–ion interactions—can be used as effective pair potentials for ions in implicit solvent simulations. However, at finite concentrations of aqueous NaCl solutions, water molecules will feel the fields of several ion pairs at the same time, and their orientational fluctuations will be suppressed. It has been found that this effect becomes important for NaCl solutions with a concentration above 0.5 M,^{28,30} and it would lead to a breakdown of additivity of effective ion potential based on the potentials of mean force (an additional effect of multi-ion correlations will be discussed later in the paper). The effect of the ion concentration on the water molecules can be accounted for with an ion-concentration-dependent dielectric permittivity $\epsilon_E(c)$.^{28,29} We determined $\epsilon_E(c)$ (of the water molecules) at concentrations of 0.5 m, 0.7 m, 1 m, 2 m, 3 m, 4 m, and 5 m via explicit solvent simulations from the fluctuations of the total dipole moment of the solvent molecules.³⁵ Simulations at 1 m, 2 m, 3 m, 4 m, and 5 m were performed for 20 ns. For the concentrations of 0.5 m and 0.7 m, simulations were performed for 40 ns. ϵ_E as a function of salt concentration is displayed in Figure 4. It is not surprising that ϵ_E decreases with the increasing salt concentration because the orientational fluctuations of water become smaller at higher salt concentrations. Our results agree well with previous simulations by Hess et al.²⁹ and Kalcher and Dzubiella.³⁰ For all concentrations, the atomistic simulations slightly overestimate the effect of adding salt to the solutions; i.e., compared to experimental results, the dielectric constant is slightly too low, with a maximum deviation of 13%.

The concentration-dependent dielectric permittivity can be used to correct the effective ion–ion interaction potentials over the whole range for the dependence on the salt molality c :²⁸

$$\begin{aligned} V_{\text{total}}(r, c) &= V_{\text{short}}(r) + V_{\text{coul}}(r, c) \\ &= V_{\text{short}}(r) + \frac{q_1 q_2}{4\pi\epsilon_0\epsilon_E(c)r} \end{aligned} \quad (4)$$

The dielectric permittivity dependent effective potentials in eq 4 were applied to the implicit solvent simulations, with the $\epsilon_E(c)$ calculated from explicit solvent simulations.

3. COMPUTATIONAL DETAILS

3.1. Explicit Solvent Simulations. All explicit solvent simulations were carried out using molecular dynamics simulation package GROMACS 4.0.7.³⁶ Simulations were performed under constant temperature T (298 K) and pressure P (1 bar) conditions using a Berendsen thermostat and a Berendsen barostat³⁷ with a coupling time of 0.1 ps. Particle Mesh Ewald (PME)³⁸ was applied to treat the electrostatic interactions with a grid spacing of 0.12 nm, a PME order of 4, and a real space cutoff of 0.9 nm. On the other hand, the cutoff distance of Lennard-Jones interactions was set as 0.9 nm. In addition, long-range dispersion correction was applied for energy and pressure. The integration time step was set as 4 fs, and the neighbor list was updated every five steps.

The SPC/E model was used for water molecules in all explicit solvent simulations, with bond lengths and angles constrained using the SETTLE algorithm.³⁹ On the other hand, the parameters of Lennard-Jones potentials for Na^+ and Cl^- were taken from the Kirkwood–Buff force field (KBFF) presented in the paper of Weerasinghe and Smith.⁴⁰ The geometric combination rule was used for van der Waals interactions between different types of atoms in the system. However, a scaling factor of 0.75 was added to the interactions between the cations and oxygen atoms in water molecules, as presented in the paper of Weerasinghe and Smith.

3.2. Implicit Solvent Simulations. In all implicit solvent simulations, stochastic dynamics with a friction coefficient of 1.0 ps^{-1} was used, and these simulations were performed in the NVT ensemble with the average volume of corresponding explicit solvent simulations. The initial structures of the implicit simulation at various concentrations were derived from the final structure of the corresponding explicit solvent simulations. By using the effective potentials between ions in the implicit solvent simulation, the solvent degrees of freedom are averaged, and the osmotic coefficient of NaCl solution at various concentrations could be calculated:

$$\phi = \frac{P}{P_{\text{ideal}}} = \frac{K - \Xi}{K} \quad (5)$$

where K is the kinetic energy and Ξ is the virial of the ions.²⁹

3. RESULTS AND DISCUSSION

In the present work, we evaluate the transferability of the implicit solvent ion (NaCl) model from parametrization at infinite dilution to a wide range of concentrations, from 0.5 m to 5 m. To this end, we study the correspondence with atomistic reference simulations in terms of both structural as well as thermodynamic properties, in this case, the osmotic coefficient, a thermodynamic quantity which is sensitively related to the structure of the solution. It is a measure of the strength of the effective interactions between ions in solution and depends sensitively on the ion–ion coordination. At first, we compare osmotic coefficients of NaCl solutions obtained from explicit-solvent atomistic simulations (converting osmotic pressures to osmotic coefficients via $\Phi = P/P_{\text{ideal}}$; see eq 5) and from implicit solvent simulations with experimental data,⁴¹ as shown in Figure 5. One can see that the force field parameters we used in explicit solvent simulations are able to reproduce the experimental osmotic coefficient accurately over a wide range of salt concentrations, especially below 4 m. This is consistent with the

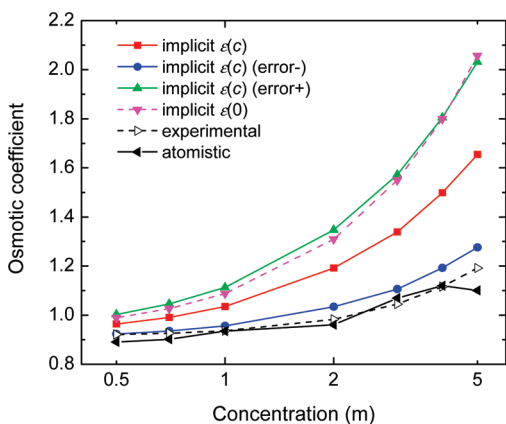


Figure 5. Osmotic coefficients of NaCl solutions from the explicit solvent model (black full triangles), from the implicit solvent model with a concentration-dependent dielectric constant (red full squares, label “implicit $\epsilon(c)$ ”), the implicit solvent with a pure water dielectric constant (pink full triangles, dashed line, label “implicit $\epsilon(0)$ ”), as well as experimental data (empty black triangles).⁴¹ The osmotic coefficients computed with effective potentials using error estimation (as discussed in the text; green and blue symbols, denoted as “implicit $\epsilon(c)$ (error+)” and “implicit $\epsilon(c)$ (error-)”, respectively) are also displayed.

previous study^{28,42} that this force field could reproduce the experimental results^{41,43} for osmotic coefficients and activity coefficients. The concentration-dependent implicit solvent model reproduces the general behavior of the osmotic coefficient compared with the atomistic simulations, although we should note that with increasing ion concentration the deviation becomes larger—and between ~ 0.75 m and ~ 3 m one finds a qualitative disagreement. Here, the implicit-solvent osmotic coefficient is greater than 1, whereas it is less than 1 in the atomistic simulations; i.e., the osmotic pressure of the implicit solvent system is greater than that of an ideal solution, while the atomistic/experimental osmotic pressures are smaller than that of an ideal solution. We will discuss the correspondence between implicit solvent and explicit solvent osmotic pressures again later in this paper, where we will show that these implicit solvent osmotic coefficients are extremely sensitive to tiny changes in the ion–ion interaction potential. The results of the implicit solvent ion model agree well with the work of Kalcher and Dzubiella,³⁰ where osmotic coefficients of atomistic simulations were computed with ion potentials of mean force and concentration dependent dielectric constant via a virial route. To illustrate the effect of the concentration dependent $\epsilon_E(c)$ on the implicit solvent model, the osmotic coefficients of uncorrected (with permittivity of pure SPC/E water) implicit solvent simulations are also displayed in Figure 5 (dashed pink line). For these simulations with the dielectric constant of SPC/E water, we will from now on use the label “implicit $\epsilon(0)$ ” while we will label the model with concentration-dependent dielectric constant “implicit $\epsilon(c)$ ”. At all concentrations, the “implicit $\epsilon(0)$ ” model predicts substantially larger osmotic coefficients than the “implicit $\epsilon(c)$ ” model, with the difference growing with increasing ion concentration.

One might argue that the increasing deviation between the “implicit $\epsilon(c)$ ” model and the atomistic simulations mainly results from multi-ion effects which should become more prominent with increasing ion concentration and which are not captured by a concentration dependent $\epsilon_E(c)$. To investigate this more closely, we estimated the magnitude of various sources for

errors in the osmotic coefficients in the implicit solvent simulations. We first estimate the error in the kinetic energy and the virial which enter eq 5—including the influence of the thermostat settings on the kinetic energy. The accuracy of the osmotic coefficient computation is 0.002 for 0.7 m and 0.001 for the remaining concentrations. The accuracy is much higher than the osmotic coefficient differences between atomistic and CG levels of resolution. A more important source of error is the accuracy of the PMF calculation. The PMF for all ion pairs ($\text{Na}^+ - \text{Cl}^-$, $\text{Na}^+ - \text{Na}^+$, and $\text{Cl}^- - \text{Cl}^-$) were obtained by integrating the average constraint force at a large number of ion distances. The error in the average constraint force accumulates to an error in the resulting PMF indicated in Figure 3. As the osmotic coefficient is very sensitive to the ion parameters or the effective potentials, the cumulative errors in the PMF may have remarkable influence on the osmotic coefficient of the implicit solvent model. To estimate the magnitude of this, we computed two limiting cases, a PMF– (PMF minus the error at each point) and a PMF+ (PMF plus the error at each point) for each of the three ions pairs ($\text{Na}^+ - \text{Cl}^-$, $\text{Na}^+ - \text{Na}^+$, and $\text{Cl}^- - \text{Cl}^-$) and determined the respective short-range (tabulated) potentials (V_{short} , eq 3). With these “error estimated” effective potentials, we performed implicit solvent simulations (again with concentration-dependent dielectric constant) and determined the osmotic coefficients. The results are shown in Figure 5 (indicated as “implicit $\epsilon(c)$ (error+)” and “implicit $\epsilon(c)$ (error-)”). We are aware that this procedure is not a stringent estimation of the error of the osmotic coefficients; nevertheless, it nicely illustrates that even a small error (the PMF calculations had been carried out very accurately) in the pair potentials of mean force between the two ions may have a very big effect on the osmotic behavior of the implicit solvent model. The “implicit $\epsilon(c)$ (error+)” and “implicit $\epsilon(c)$ (error-)” models are slight variations (within the error bars of the underlying potentials of mean force) of the “implicit $\epsilon(c)$ ” model which are slightly less or more attractive over the entire range of the short-range potential V_{short} . It is interesting that the osmotic coefficients obtained from the “implicit $\epsilon(c)$ (error-)” simulations are very close to the atomistic and experimental results at all concentrations up to 4 m, while the osmotic coefficients of the “implicit $\epsilon(c)$ (error+)” simulations are very close to those obtained with the uncorrected “implicit $\epsilon(0)$ ” model. This finding shows that the osmotic coefficient is a highly sensitive thermodynamic property, and in implicit-solvent ion models it strongly depends on the ion–ion effective potentials. It also shows that it is difficult to assess the quality of a CG ion model on the basis of osmotic behavior alone, since for example the “implicit $\epsilon(c)$ (error+)” and the uncorrected “implicit $\epsilon(0)$ ” models exhibit almost the same osmotic behavior but for completely different reasons and with very different consequences on structural properties, as we will show below. Here, we would like to point out that even though the osmotic coefficient alone might not be a good measure to assess the agreement with the underlying atomistic model, it is nevertheless a crucial property in force field parametrization. The osmotic behavior strongly depends on the ion types, and ion specific force fields (both with explicit and implicit solvent) should reproduce these differences between the ions.

The osmotic coefficient is closely linked to the structure of the ion solution (see, e.g. ref 30); thus we compared the structural properties obtained in the explicit and implicit solvent (“implicit $\epsilon(c)$ ” and “implicit $\epsilon(0)$ ”) simulations. Figure 6 shows the radial distribution functions (RDFs) between Na^+ and Cl^- in these

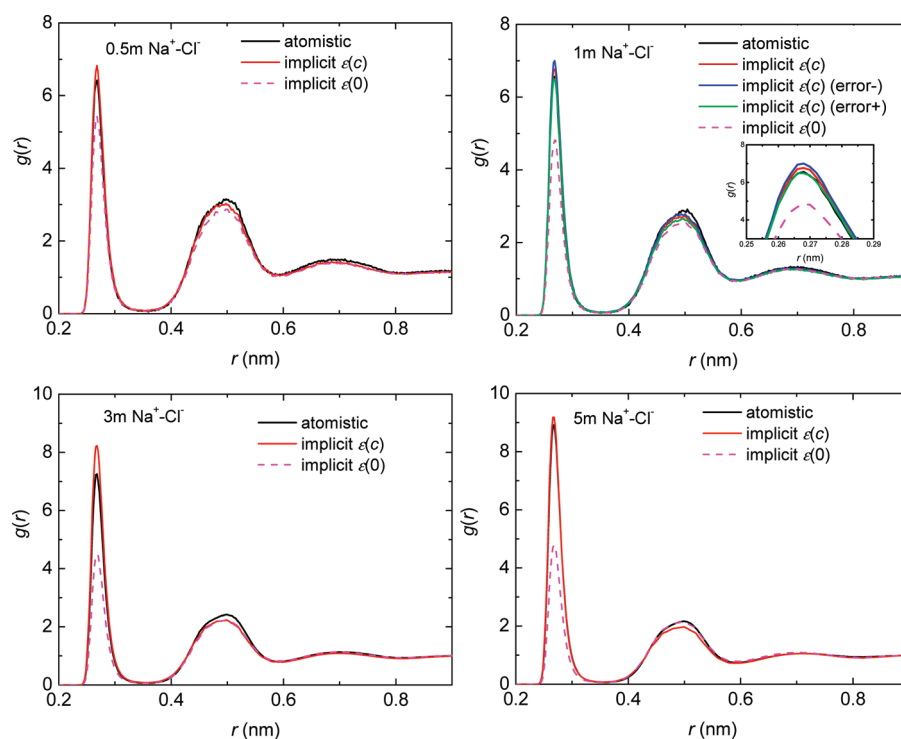


Figure 6. The radial distribution functions (RDFs) of $\text{Na}^+ - \text{Cl}^-$ in explicit, implicit and uncorrected implicit solvent simulations at different concentrations. The RDF of $\text{Na}^+ - \text{Cl}^-$ from computation with effective potentials using the error estimate of the potentials of mean force (denoted as “implicit $\epsilon(c)$ (error–)” and “implicit $\epsilon(c)$ (error+)”; see text) for 1 m is also displayed.

Table 1. The $\text{Na}^+ - \text{Cl}^-$ Coordination Numbers in the Contact Minimum (0–0.35 nm) and the Solvent Shared Minimum (0.35–0.59 nm) for Explicit Solvent Simulations and Simulations with the “implicit $\epsilon(c)$ ” and “implicit $\epsilon(0)$ ” Models

	0.00–0.35 nm					0.35–0.59 nm				
	explicit	implicit $\epsilon(c)$	relative difference (%)	implicit $\epsilon(0)$	relative difference (%)	explicit	implicit $\epsilon(c)$	relative difference (%)	implicit $\epsilon(0)$	relative difference (%)
0.5 m	0.053	0.056	5.7	0.045	15.1	0.359	0.349	2.8	0.329	8.4
0.7 m	0.079	0.079	0.0	0.060	24.1	0.489	0.461	5.7	0.435	11.0
1 m	0.106	0.111	4.7	0.080	24.5	0.648	0.622	4.0	0.584	9.9
2 m	0.212	0.233	9.9	0.148	30.2	1.149	1.094	4.8	1.051	8.5
3 m	0.337	0.382	13.4	0.217	35.6	1.580	1.499	5.1	1.488	5.8
4 m	0.492	0.528	7.3	0.291	40.9	1.950	1.823	6.5	1.897	2.7
5 m	0.656	0.669	2.0	0.367	44.1	2.262	2.111	6.7	2.280	0.8

simulations at concentrations of 0.5 m, 1 m, 3 m, and 5 m. At relatively low concentrations of 0.5 m and 1 m, the first peaks (contact ion pairs) of the “implicit $\epsilon(c)$ ” $\text{Na}^+ - \text{Cl}^-$ RDFs agree very well with explicit solvent simulations, while the second peaks (solvent shared ion pairs) are slightly lower compared to explicit solvent simulations. The effect of the concentration dependent permittivity can be best seen by comparing to the implicit solvent simulations with the permittivity of pure SPC/E water (“implicit $\epsilon(0)$ ” model), shown by the dashed magenta lines in Figure 6, which severely underestimate the first peaks of the $\text{Na}^+ - \text{Cl}^-$ RDFs.

In Table 1, we show the $\text{Na}^+ - \text{Cl}^-$ coordination numbers in the contact minimum (0–0.35 nm) and the solvent shared minimum (0.35–0.59 nm) for explicit, corrected, and uncorrected implicit solvent simulations, which give a quantitative description of the structure information of NaCl solution at

different concentrations. These numbers quantify the qualitative observation made above, that the structural agreement between the explicit solvent and implicit solvent models is good after using a concentration-dependent dielectric constant. The uncorrected “implicit $\epsilon(0)$ ” model, where the larger dielectric permittivity weakens the interaction between Na^+ and Cl^- ions, severely underestimates the coordination numbers of the first peak at all concentrations, and this effect becomes stronger with an increase in concentration. For the second peak in the RDF, these effects are much weaker. Overall, these results confirm that the use of a concentration-dependent dielectric constant $\epsilon_E(c)$ makes the implicit solvent model which had been parametrized at infinite dilution transferable to a wide range of concentrations.

Figure 6 (for 1 m concentration) and Figure S1 in the Supporting Information show the $\text{Na}^+ - \text{Cl}^-$ RDFs obtained with the “implicit $\epsilon(c)$ (error+)” and “implicit $\epsilon(c)$ (error–)”

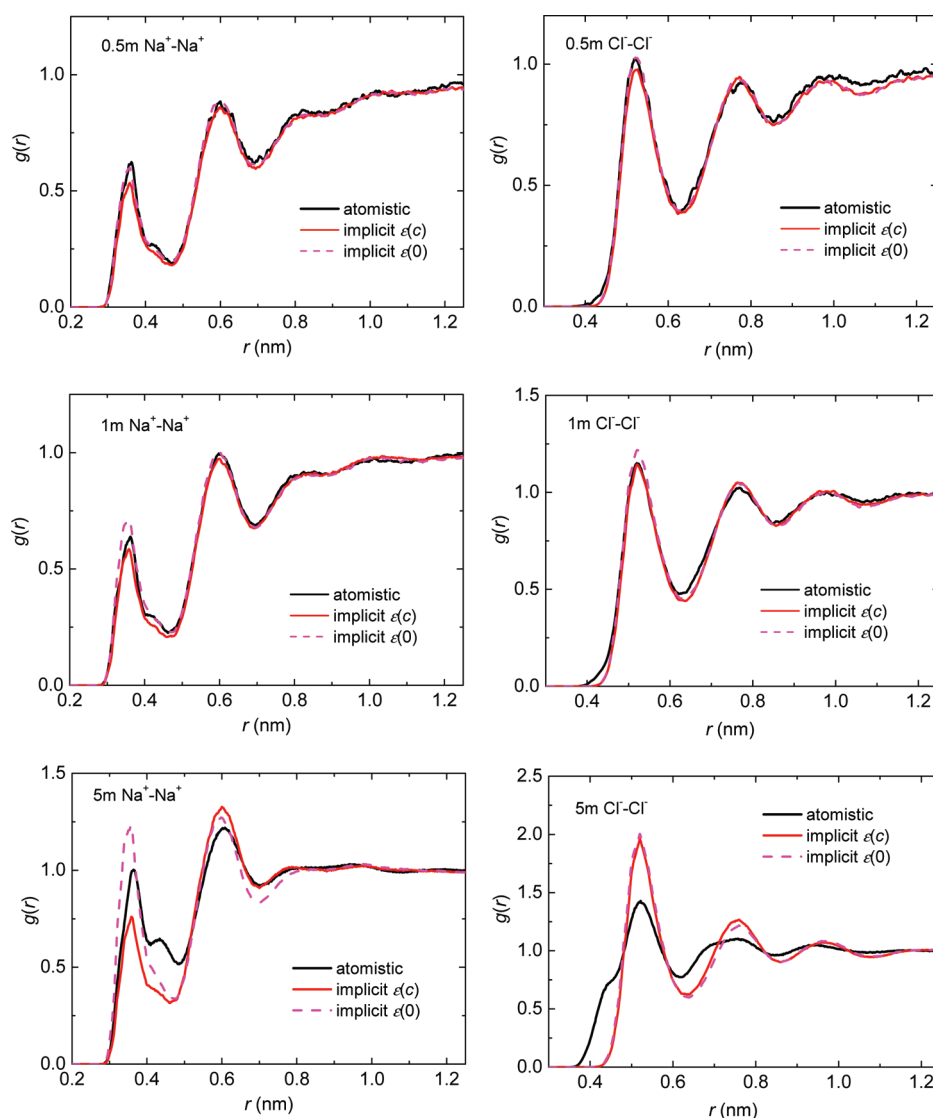


Figure 7. The radial distribution functions of $\text{Na}^+ - \text{Na}^+$ and $\text{Cl}^- - \text{Cl}^-$ in explicit, implicit, and uncorrected implicit solvent simulations at 0.5 m, 1 m, and 5 m concentrations of NaCl solutions (labels and line colors as in previous figures).

models. Note that despite the fact that the osmotic coefficients from these models are drastically different (see Figure 5), the structure appears to be hardly affected while the uncorrected “implicit $\epsilon(0)$ ” (which leads to similar osmotic coefficients as “implicit $\epsilon(c)$ (error+)”) gives a rather different structure, especially in the first coordination shell. These observations show that even though the osmotic coefficient is intimately linked to the electrolyte structure (see Kalcher and Dzubiella³⁰) and can be reproduced by a structure-based (i.e., pair-PMF based) implicit solvent model, it is very sensitive to errors in the PMF. In our particular example, we have mimicked a systematic error by generating—within the error bars of the PMF calculation—slightly more attractive (model “implicit $\epsilon(c)$ (error-)”) or slightly more repulsive (model “implicit $\epsilon(c)$ (error+)”) interaction potentials. The simulations with these modified interaction potentials show that reproducing electrolyte structure and a related thermodynamic property such as the osmotic coefficient may depend differently on different aspects of the interaction potential, namely, the short-ranged attraction in the different minima of V_{short} versus the overall attraction which is dominated

by the tail of the potentials (mainly electrostatic interaction). This is confirmed if one looks at the Kirkwood–Buff integral, i.e., the integrated ion–ion radial distribution function (with all ions treated as indistinguishable)—a property that establishes the link between osmotic behavior, association, and structure (data shown and in more detail discussed in the Supporting Information). For this property, we see a correspondence between the different implicit solvent electrolyte models and the atomistic simulations, which is very similar to the osmotic coefficient.

The above results also show that it is possible to obtain equally good structural agreement, in this case, a good representation of the electrolyte structure, with different potentials—even though they lead to different thermodynamic behaviors. This is an important observation in the context of transferability of reduced resolution models since the aim of a well transferable model is often not in perfect agreement with a reference at a single state point but rather in reasonable agreement (both structurally and thermodynamically) for a range of state points. The results in the “implicit $\epsilon(c)$ (error \pm)” models show that this can in principle be achieved without entirely sacrificing structural agreement.

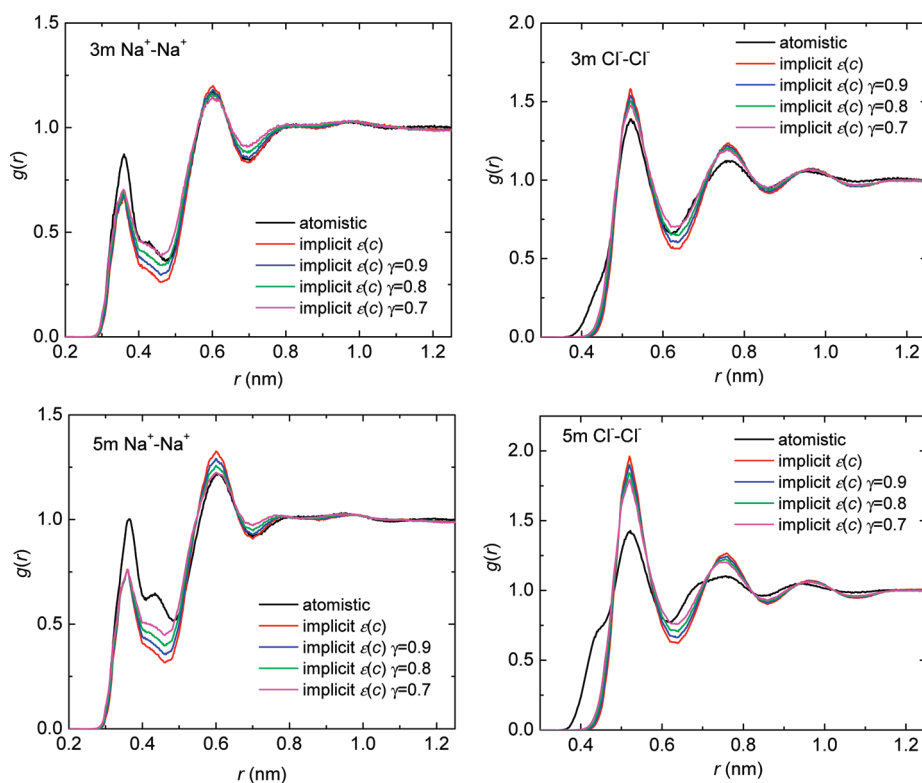


Figure 8. Radial distribution functions of $\text{Na}^+ - \text{Na}^+$ and $\text{Cl}^- - \text{Cl}^-$ in explicit, “implicit $\epsilon(c)$ ”, and PMF-scaled implicit solvent simulations at 3 m and 5 m concentrations of NaCl solutions. Scaling factors γ of 0.9, 0.8, and 0.7 were used.

As discussed above, the deviations of the osmotic coefficient obtained by the implicit solvent model from the explicit solvent reference keeps increasing with the increasing concentration (even for the “implicit $\epsilon(c)$ (error-)” set of potentials which reproduces the atomistic osmotic coefficients at low concentrations very well). They are most likely due to higher order ion–ion correlations which are not captured by a concentration-dependent $\epsilon_E(c)$, which only accounts for the changes in the solvent behavior with increasing ion concentration. To better understand this, we investigated the structure of like-charged ion pairs, i.e., $\text{Na}^+ - \text{Na}^+$ and $\text{Cl}^- - \text{Cl}^-$ RDFs, in explicit and all implicit solvent models, which are displayed in Figure 7 and Figure S2 (in the Supporting Information) for selected concentrations. It is not surprising that at the relatively low concentrations of 0.5 m and 1 m, both $\text{Na}^+ - \text{Na}^+$ and $\text{Cl}^- - \text{Cl}^-$ RDFs show good agreement between explicit and implicit solvent simulations. At higher concentrations (see, for example, the 5 m case), the implicit solvent model (“implicit $\epsilon(c)$ ”) underestimates the first peak and overestimates the second peak of the $\text{Na}^+ - \text{Na}^+$ RDF, and the $\text{Cl}^- - \text{Cl}^-$ RDF is overstructured compared to the explicit solvent reference. In the explicit solvent reference, the $\text{Cl}^- - \text{Cl}^-$ RDF exhibits a shoulder before the first peak at 5 m, which indicated that at these high concentrations, special configurations (most probably involving more than two ions) start to play an important role. Since these configurations had not been accounted for in the parametrization of the implicit solvent model, they can hardly be reproduced and set a limit to what we can expect in terms of transferability of the model to higher concentrations. Figure 7 also displays the like-ion RDFs for implicit solvent simulations with the permittivity of pure water, which shows that the transition from $\epsilon_E(0)$ to $\epsilon_E(c)$ has a different effect on the $\text{Na}^+ - \text{Na}^+$ and $\text{Cl}^- - \text{Cl}^-$ structures (also

compared to the $\text{Na}^+ - \text{Cl}^-$ structure). The $\text{Cl}^- - \text{Cl}^-$ structure is hardly affected by the change in dielectric constant, while the first peak of the $\text{Na}^+ - \text{Na}^+$ structure is strongly affected (we provide tables with the corresponding coordination numbers in the Supporting Information). Since we know already that the dielectric constant has a strong effect on $\text{Na}^+ - \text{Cl}^-$ (contact) pairs, these results indicate that for higher concentrations the $\text{Na}^+ - \text{Na}^+$ structure is influenced by higher order ion correlations involving more than two ions, possibly including Cl^- ions.

The RDF of like ions reflects the fact that reducing the dielectric permittivity accounts for the change in solvent properties; i.e., the long-range attractive interactions need to be adapted accounting for the reduced dielectric screening by the water. At low ion concentrations, this is sufficient, and the effective ion–ion potentials are perfectly additive and transferable. The biggest effect of the reduced screening will be on the close (oppositely charged) contact ion pairs, i.e., the first peak in the $\text{Na}^+ - \text{Cl}^-$ RDFs (as observed in Figure 6). One could however argue that for like-charged ion pairs one would rather expect a reduced repulsion at higher concentrations because of multi-ion correlations (mediated interactions through nearby counterions, for example). When these multibody effects between the ions start to play a role, direct pairwise additivity of the effective potentials breaks down. The reduced ion–ion repulsion at short distances would be an effect that counteracts the reduced dielectric screening when using $\epsilon(c)$, which explains why the “implicit $\epsilon(0)$ ” shows a different behavior for the first peak of the $\text{Na}^+ - \text{Na}^+$ RDF compared to the “implicit $\epsilon(c)$ ” (see Figure 7). Therefore, the explicit hydration effects of ions within short range at high concentrations cannot be simply described by only applying a concentration-dependent dielectric constant

$\epsilon_E(c)$, and we probably need a second parameter to take effects on Na^+-Na^+ and Cl^--Cl^- interactions into account.

In the following, we will describe two possible approaches (which we will label “PMF-scaled” and “RDF-refined”) to improve the transferability of the implicit solvent electrolyte model to very

Table 2. Osmotic Coefficients of NaCl Solutions at 3 m and 5 m Concentrations Calculated from Explicit Solvent and Different Implicit Solvent Simulations (“implicit $\epsilon(c)$ ”, “PMF-scaled” ($\gamma = 0.8$), and “RDF-refined” as Described in the Text)

	explicit	implicit	PMF-scaled	RDF-refined
0.5 m	0.890	0.964		0.939
1 m	0.935	1.035		0.988
3 m	1.069	1.339	1.060	1.204
5 m	1.101	1.654	1.190	1.427

high concentrations. In the first approach, denoted as “PMF-scaled”, we made an attempt to adapt the (short-range) interaction between Na^+-Na^+ and Cl^--Cl^- pairs since—as discussed above—the repulsion between like ions at short distances in solutions at high concentration is possibly reduced (compared to lower concentrations). This we did by scaling (down) the PMF that is the basis of the effective pair potential by a factor γ (we will discuss other possibilities to reduce the like-ion repulsion below). Figure 8 displays the RDF of Na^+-Na^+ and Cl^--Cl^- pairs in explicit, normal “implicit $\epsilon(c)$ ”, and PMF-scaled implicit solvent simulations at concentrations of 3 m and 5 m. Scaling factors γ for both Na^+-Na^+ and Cl^--Cl^- PMFs in the range of 0.9 to 0.7 were used. This new model with reduced short-range repulsion between like-charged ion pairs shows only a slightly better agreement of the Na^+-Na^+ and Cl^--Cl^- RDFs with the explicit solvent simulations (see Figure 8).

The Na^+-Cl^- RDFs are not affected at all by the change (data not shown). More importantly, these modifications have a

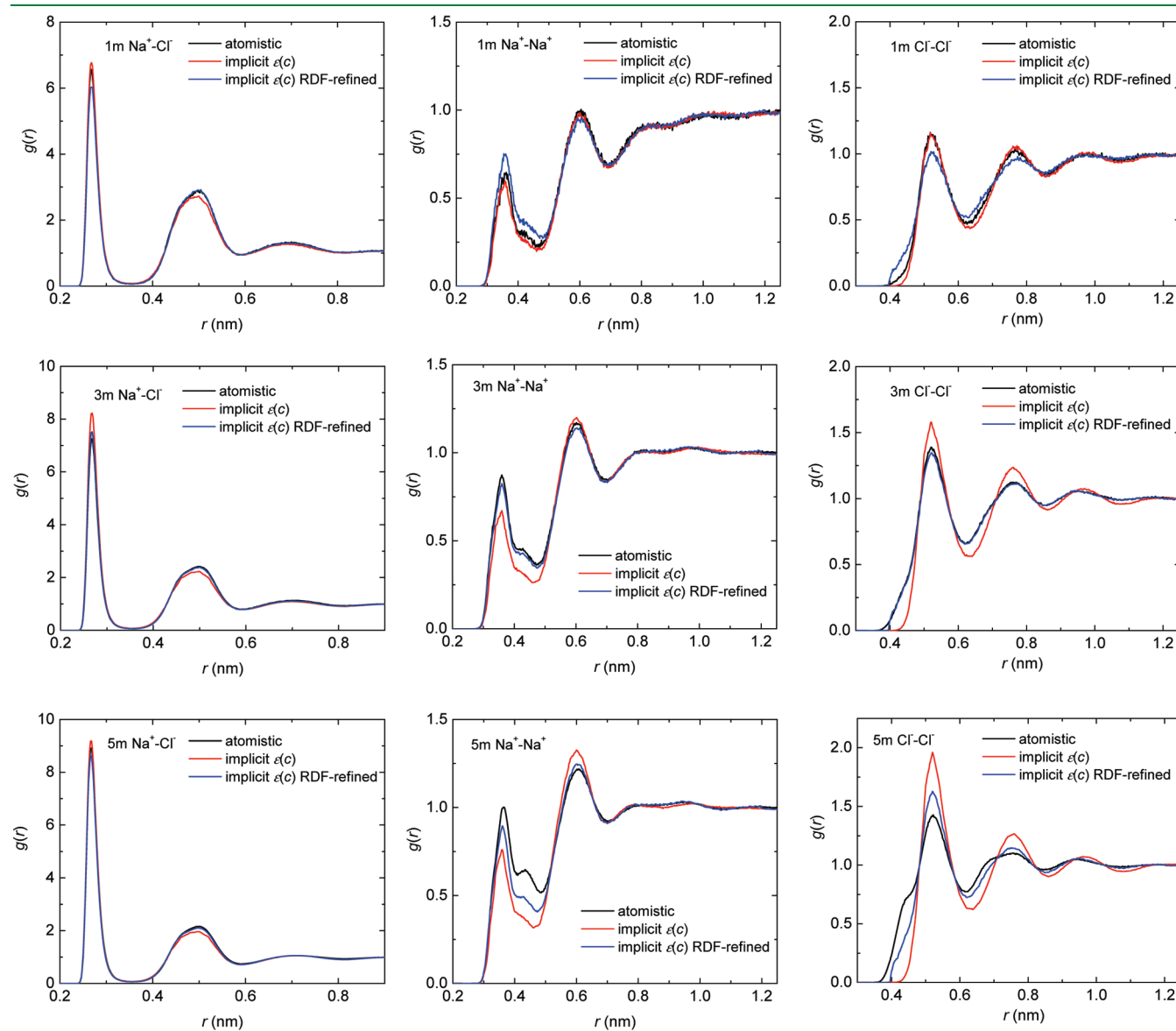


Figure 9. Radial distribution functions of Na^+-Cl^- , Na^+-Na^+ , and Cl^--Cl^- in explicit, “implicit $\epsilon(c)$ ”, and “RDF-refined” implicit solvent simulations at 1 m, 3 m, and 5 m concentrations of NaCl.

large effect on the osmotic behavior of the system, reducing the osmotic coefficient and bringing it much closer to the values of the atomistic simulations, as can be seen in Table 2. In fact, the osmotic coefficient can be used to determine the optimal choice for the exact value of the scaling parameter γ . In our case, $\gamma = 0.8$ gives the best fit of atomistic osmotic coefficient at 3 m and 5 m. By rescaling the entire PMF before splitting the interaction into a short-range and a long-range electrostatic part (eq 3), we have reduced the overall repulsion in the range of the short distances (while the long-range Coulomb interactions beyond the cutoff remain as before). This appears to be a quite ad hoc approach to account for multi-ion correlation, and we are aware that we showed already that the osmotic coefficient alone is a weak criterion for a good model. Nevertheless, we show that we can employ this ad hoc but physically justifiable additional parameter to improve the osmotic behavior at high ion concentrations without corrupting the structural properties of the model. Alternative to the above approach, we tried two other scaling methods, thus providing three possible ways of modifying the ion–ion repulsion of like ion pairs: (i) We have reduced only the short-range interaction V_{short} (scaled the tabulated potential). (ii) We have reduced only the Coulombic contribution (repulsion) to the interaction between like ions. (iii) We have reduced the short-range total interaction. The latter is done by scaling the PMF as described above. It appears that the PMF scaling gives the best results among these attempts, both structure-wise and in terms of osmotic coefficient. With this additional (rather arbitrary but physically justifiable) scaling factor, the implicit solvent ion potentials could be made transferable over the entire range of concentrations, giving a good correspondence between atomistic reference and implicit solvent simulations both in terms of structure and osmotic coefficient.

One might argue that with these scaling parameters one ends up reparameterizing the implicit solvent model for higher concentrations. However, as opposed to generating a series of independent models for each state point, this approach uses in principle the same potentials as before, which consist of a short-range/ion-specific part and (concentration dependent) long-range Coulomb interactions, and just modifies the strength of these interactions accordingly to account for multibody effects.

In a second approach to make the “implicit $\epsilon(c)$ ” model transferable to very high concentrations, we focus on the structure of the like-charged ion pairs since these RDFs appear to be most affected by the limited transferability of the model (see Figure 7), even for models with correct osmotic behavior (see Figure 8). Following the “structure-based” coarse graining methodology,^{12,44} we refine the ion–ion interactions by taking the electrolyte structure from atomistic simulations as a reference. Iterative methods such as iterative Boltzmann inversion (IBI) or inverse Monte Carlo (IMC) are methods that refine CG potentials such that radial distribution functions of the reference system are reproduced.^{12,44} Here, we do not iteratively refine the $\text{Na}^+ - \text{Cl}^-$, $\text{Na}^+ - \text{Na}^+$, and $\text{Cl}^- - \text{Cl}^-$ potentials until the respective radial distribution functions are exactly reproduced. Instead, we employ a single refinement step where we adjust the concentration-dependent implicit solvent model at 3 m to better reproduce the corresponding RDFs. That means we add a correction term to V_{short} that accounts for the difference in the RDF obtained with the implicit solvent model ($g_{\text{implicit } \epsilon(c)}(r)$) compared to the reference RDF ($g_{\text{ref}}(r)$). This correction term is $kT \ln(g_{\text{implicit } \epsilon(c)}(r)/g_{\text{ref}}(r))$. This new set of potentials, from now on labeled as “RDF-refined”, which is based on the pair

PMFs at infinite dilution and refined at 3 m concentration, is now applied to simulations at a wide range of NaCl concentrations from 0.5 m to 5 m. Figure 9 shows the radial distribution functions of $\text{Na}^+ - \text{Cl}^-$, $\text{Na}^+ - \text{Na}^+$, and $\text{Cl}^- - \text{Cl}^-$ in explicit, “implicit $\epsilon(c)$ ”, and “RDF-refined” implicit solvent simulations at 1 m, 3 m, and 5 m. It shows that at 3 m, all of the ion–ion RDFs in the “RDF-refined” model reproduce the corresponding RDF at the atomistic explicit solvent level very well. At 5 m, the “RDF-refined” model still underestimates the first peak of the $\text{Na}^+ - \text{Na}^+$ RDF and overestimates the first peak of the $\text{Cl}^- - \text{Cl}^-$ RDF, but the electrolyte structure has improved a lot. However, at 1 m, the first peak of the $\text{Na}^+ - \text{Na}^+$ RDF is now overestimated. The first peak of the $\text{Cl}^- - \text{Cl}^-$ RDF is also underestimated, and the agreement with the explicit solvent reference has become worse compared to that with the “implicit $\epsilon(c)$ ” model. This means that by enforcing structural agreement at a specific high ion concentration, we have “lost” transferability to low concentrations. Table 2 also shows the osmotic coefficients obtained with the “RDF-refined” model at 0.5, 1, 3, and 5 m. With great improvement of the electrolyte structure at 3 m, the osmotic coefficient also improves considerably at 3 m. In general, the osmotic coefficients of the “RDF-refined” model are lower than the one of the “implicit $\epsilon(c)$ ” model, thus in better agreement with atomistic reference data. However, we see in Figure 9 that this does not imply better structural agreement at all concentrations. These results show that in our electrolyte systems the effective potentials optimized with one iteration at one specific concentration/state point are not very well transferable to other concentrations/state points. Thus, if one aims at a well-structured electrolyte solution at a very high concentration obtained with an implicit solvent model, one has to apply the correction (possibly with more than one iteration step) at each concentration individually. Even though this contradicts the initial intention to have one model that is transferable to the entire range of concentrations this approach nevertheless has one advantage compared to “traditional” iterative Boltzmann inversion: instead of starting the iterative process individually at each concentration, here all potentials are based on the same set of pair PMFs obtained at infinite dilution and thus systematically related. The iterations apply just a minor correction to these effective potentials. This could be an advantage in complex systems with many different interactions where in principle structure-based methods should converge to a unique solution.⁴⁵ In practice, however, convergence problems are quite common, and the initial guess and the exact method used can influence the set of potentials obtained finally.^{5,20,46}

4. CONCLUSIONS

Transferability to different state points remains an ongoing challenge in the development of reduced-resolution (coarse grained or implicit solvent) simulation models. While effective potentials for hydrophobic entities in aqueous solution parameterized at “infinite” dilution are transferable over a wide range of mixture compositions,²² interactions between charged molecules cannot be immediately transferred to higher concentrations since the ion concentration affects the solvent, leading to different dielectric properties. In the present paper, we have investigated how effective implicit solvent potentials for ions in aqueous solution can be made transferable to a wide range of ion concentrations in a way that both the osmotic behavior and

the electrolyte structure of atomistic, explicit solvent reference simulations are reproduced.

We have studied concentration-dependent effective ion potentials parametrized on the basis of ion–ion pair potentials of mean force at infinite dilution in explicit solvent simulations which are split into a short range (ion-specific, not concentration-dependent) and a long range (electrostatic, with a concentration-dependent dielectric permittivity).^{28,29} As shown previously by Hess et al., these potentials are transferable over a certain range of concentrations and reproduce experimental osmotic coefficients well. In the present paper, we studied more closely the contributions of long-range and short-range parts of the effective interactions to osmotic behavior and electrolyte structure to gain a better understanding between thermodynamic and structural properties obtained with these effective potentials and their transferability within an even wider range of concentrations, up to 5 m.

We observe that the use of a concentration-dependent dielectric constant drastically improves the correspondence of the pair structure in the implicit solvent model with the explicit solvent reference compared to using the higher dielectric permittivity of pure water (at the same time also bringing the osmotic coefficients closer). By making small “artificial” variations to the effective potentials (within the error bars of the initial potential of mean force calculation), we could also show that, even though the osmotic coefficient is intimately linked to the electrolyte structure and can be reproduced by a structure-based (i.e., pair-PMF based) implicit solvent model, it is very sensitive to variations in the PMF, making it difficult to judge the quality of a reduced resolution model solely on the basis of this thermodynamic property. It is even possible to generate three (or more) implicit solvent models out of which two show essentially the same osmotic behavior for very different reasons (and with different electrolyte structures), while two others more or less exhibit the same structure (in good agreement with the explicit solvent reference) but a large variation in osmotic coefficients. This shows that reproducing electrolyte structure and a related thermodynamic property such as the osmotic coefficient may depend differently on different aspects of the interaction potential, namely, the short-ranged attraction in the different minima of V_{short} versus the overall attraction, which is dominated by the tail of the potentials (mainly electrostatic interaction). This is an important observation in the context of transferability of reduced resolution models since the aim of a well transferable model is often not in perfect agreement with a reference at a single state point but in rather reasonable agreement (both structurally and thermodynamically) for a range of state points. Our results show that this can in principle be achieved without entirely sacrificing structural agreement.

At very high concentrations, multi-ion correlations start to play a role in addition to the changed solvent behavior. These effects are by construction not accounted for by the infinite dilution pair potential (based on two ions) and the concentration-dependent dielectric permittivity (which only covers the concentration effect on solvent properties). After analyzing the explicit-solvent electrolyte structure at high ion concentrations, we employed two methods to make the effective ion potentials even further transferable: in a first approach, we reduced the repulsion between like-charged ion pairs at high concentrations (“PMF scaling”). The need to do this can be explained from the fact that the first peak of like-charged ion pair correlation functions in explicit solvent simulations is higher than one

would expect due to electrostatic repulsion in water with reduced dielectric screening. Thus, electrostatic repulsion is counterbalanced by other effects in the system (for example, bridging by additional counterions or specific water molecules), which need to be at least approximately accounted for. The model with reduced dielectric repulsion can be parametrized to reproduce atomistic osmotic coefficients and gives a reasonable representation of electrolyte structure also at very high ion concentrations. Contrasting this rather “thermodynamic property-based” route, we also followed a “structure-based” approach where we apply a single refinement step of the implicit solvent ion potentials targeting the electrolyte structure at one concentration (e.g., 3 m). Such a procedure results in a set of interaction functions for all ion pairs which give a very good representation of the electrolyte structure at this particular concentration and also yield a better agreement in the osmotic coefficient. However, these structurally refined potentials are not highly transferable (only to very small variations in the concentration). That means one would have to apply the refining procedure individually at different concentrations and would obtain a family of interaction potentials which are related since they rely on the same initial infinite dilution pair PMFs.

The present paper illustrates the difficulty to parametrize a transferable reduced resolution model for aqueous electrolyte solutions, especially if one aims at both good structural and good thermodynamic agreement with an explicit solvent reference system up to very high salt concentrations. It, however, also shows that it is possible to obtain a well transferable model by not adhering to a strictly “thermodynamics-based” or “structure-based” route but instead employing elements of both approaches— basing the interactions on the pair structure at infinite dilution and making it transferable to higher concentrations with thermodynamically justified scaling constants.

■ ASSOCIATED CONTENT

S Supporting Information. Additional data are shown concerning (i) the radial distribution functions (RDFs) of all ion pairs computed with effective potentials using the error estimate of the potentials of mean force, (ii) the coordination numbers of the like-charged ion pairs, and (iii) the Kirkwood–Buff integrals of the system. This material is available free of charge via the Internet at <http://pubs.acs.org>.

■ AUTHOR INFORMATION

Corresponding Author

*E-mail: peter@mpip-mainz.mpg.de.

■ ACKNOWLEDGMENT

We would like to thank Biswaroop Mukherjee, Christoph Junghans, and Kurt Kremer for many helpful discussions and Pim Schravendijk for helping to implement the explicit solvent osmotic coefficient calculations. This project has been carried out as part of the priority program SPP 1420 by the German Science Foundation. C.P. gratefully acknowledges financial support by the German Science Foundation within the Emmy Noether program (grant PE 1625/1-1).

REFERENCES

- (1) *Coarse-Graining of Condensed Phase and Biomolecular Systems*; Voth, G., Ed.; Chapman and Hall/CRC Press, Taylor and Francis Group: New York, 2008.
- (2) Tschop, W.; Kremer, K.; Batoulis, J.; Burger, T.; Hahn, O. *Acta Polym.* **1998**, *49*, 61–74.
- (3) Müller-Plathe, F. *ChemPhysChem* **2002**, *3*, 754–769.
- (4) Murtola, T.; Bunker, A.; Vattulainen, I.; Deserno, M.; Karttunen, M. *Chem. Chem. Phys.* **2009**, *11*, 1869–1892.
- (5) Rühle, V.; Junghans, C.; Lukyanov, A.; Kremer, K.; Andrienko, D. *J. Chem. Theory Comput.* **2009**, *5*, 3211–3223.
- (6) Peter, C.; Kremer, K. *Faraday Discuss.* **2010**, *144*, 9–24.
- (7) Nielsen, S. O.; Lopez, C. F.; Srinivas, G.; Klein, M. L. *J. Chem. Phys.* **2003**, *119*, 7043–7049.
- (8) Marrink, S. J.; de Vries, A. H.; Mark, A. E. *J. Phys. Chem. B* **2004**, *108*, 750–760.
- (9) Bond, P. J.; Sansom, M. S. P. *J. Am. Chem. Soc.* **2006**, *128*, 2697–2704.
- (10) Shinoda, W.; Devane, R.; Klein, M. L. *Mol. Simul.* **2007**, *33*, 27–36.
- (11) Michel, J.; Orsi, M.; Essex, J. W. *J. Phys. Chem B* **2008**, *112*, 657–660.
- (12) Lyubartsev, A. P.; Laaksonen, A. *Phys. Rev. E* **1995**, *52*, 3730–3737.
- (13) Harmandaris, V. A.; Reith, D.; van der Vegt, N. F. A.; Kremer, K. *Macromol. Chem. Phys.* **2007**, *208*, 2109–2120.
- (14) Peter, C.; Delle Site, L.; Kremer, K. *Soft Matter* **2008**, *4*, 859–869.
- (15) Fritz, D.; Harmandaris, V. A.; Kremer, K.; van der Vegt, N. F. A. *Macromolecules* **2009**, *42*, 7579–7588.
- (16) Villa, A.; Peter, C.; van der Vegt, N. F. A. *Phys. Chem. Chem. Phys.* **2009**, *11*, 2077–2086.
- (17) Izvekov, S.; Voth, G. A. *J. Phys. Chem. B* **2005**, *109*, 2469–2473.
- (18) Zhou, J.; Thorpe, I. F.; Izvekov, S.; Voth, G. A. *Biophys. J.* **2007**, *92*, 4289–4303.
- (19) Mullinax, J.; Noid, W. G. *J. Chem. Phys.* **2009**, *131*, 104110.
- (20) Johnson, M. E.; Head-Gordon, T.; Louis, A. A. *J. Chem. Phys.* **2007**, *126*, 144509.
- (21) Allen, E. C.; Rutledge, G. C. *J. Chem. Phys.* **2008**, *128*, 154115.
- (22) Villa, A.; Peter, C.; van der Vegt, N. F. A. *J. Chem. Theory Comput.* **2010**, *6*, 2434–2444.
- (23) Silbermann, J.; Klapp, S. H. L.; Schoen, M.; Chennamsetty, N.; Bock, H.; Gubbins, K. E. *J. Chem. Phys.* **2006**, *124*, 074105.
- (24) Fischer, J.; Paschek, D.; Geiger, A.; Sadowski, G. *J. Phys. Chem. B* **2008**, *112*, 13561–13571.
- (25) Allen, E. C.; Rutledge, G. C. *J. Chem. Phys.* **2009**, *130*, 034904.
- (26) Ghosh, J.; Faller, R. *Mol. Simul.* **2007**, *33*, 759–767.
- (27) Mognetti, B. M.; Virnau, P.; Yelash, L.; Paul, W.; Binder, K.; Müller, M.; MacDowell, L. G. *J. Chem. Phys.* **2009**, *130*, 044101.
- (28) Hess, B.; Holm, C.; van der Vegt, N. F. A. *Phys. Rev. Lett.* **2006**, *96*, 147801.
- (29) Hess, B.; Holm, C.; van der Vegt, N. F. A. *J. Chem. Phys.* **2006**, *124*, 164509.
- (30) Kalcher, I.; Dzubiella, J. *J. Chem. Phys.* **2009**, *130*, 134507.
- (31) Lyubartsev, A. P.; Laaksonen, A. *Phys. Rev. E* **1997**, *55*, 5689–5696.
- (32) Luo, Y.; Roux, B. *J. Phys. Chem. Lett.* **2010**, *1*, 183–189.
- (33) Martínez, L.; Andrade, R.; Birgin, E. G.; Martínez, J. M. *J. Comput. Chem.* **2009**, *30*, 2157–2164.
- (34) Hess, B.; Bekker, H.; Berendsen, H. J. C.; Fraaije, J. G. E. M. *J. Comput. Chem.* **1997**, *18*, 1463–1472.
- (35) Neumann, M. *Mol. Phys.* **1983**, *50*, 841–845.
- (36) van der Spoel, D.; Lindahl, E.; Hess, B.; Groenhof, G.; Mark, A. E.; Berendsen, H. J. C. *J. Comput. Chem.* **2005**, *26*, 1701–1718.
- (37) Berendsen, H. J. C.; Postma, J. P. M.; van Gunsteren, W. F.; DiNola, A.; Haak, J. R. *J. Chem. Phys.* **1984**, *81*, 3684–3690.
- (38) Essmann, U.; Perera, L.; Berkowitz, M. L.; Darden, T.; Lee, H.; Pedersen, L. G. *J. Chem. Phys.* **1995**, *103*, 8577–8593.
- (39) Miyamoto, S.; Kollman, P. A. *J. Comput. Chem.* **1992**, *13*, 952–962.
- (40) Weerasinghe, S.; Smith, P. E. *J. Chem. Phys.* **2003**, *119*, 11342–11349.
- (41) Robinson, R. A.; Stokes, R. H. *Trans. Faraday Soc.* **1949**, *45*, 612–624.
- (42) Hess, B.; van der Vegt, N. F. A. *Proc. Natl. Acad. Sci. U. S. A.* **2009**, *106*, 13296–13300.
- (43) Pitzer, K. S.; Mayorga, G. *J. Phys. Chem.* **1973**, *77*, 2300–2308.
- (44) Reith, D.; Pütz, M.; Müller-Plathe, F. *J. Comput. Chem.* **2003**, *24*, 1624–1636.
- (45) Henderson, R. L. *Physics Lett. A* **1974**, *49*, 197–198.
- (46) Rzepliela, A. J.; Louhivuori, M.; Peter, C.; Marrink, S. J. *Phys. Chem. Chem. Phys.* [Online] DOI: 10.1039/c0cp02981e.

Assessing the Quality of the OPEP Coarse-Grained Force Field

Alessandro Barducci,^{†,¶} Massimiliano Bonomi,^{†,¶} and Philippe Derreumaux^{*,‡}[†]Computational Science, Department of Chemistry and Applied Biosciences, ETH Zurich, c/o USI Campus, via Buffi 13, CH-6900 Lugano, Switzerland[‡]Laboratoire de Biochimie Théorique, UPR 9080 CNRS, Institut de Biologie Physico-Chimique and Université Paris Diderot, Paris 7, Institut Universitaire de France, 13 rue Pierre et Marie Curie, 75005 Paris, France**S** Supporting Information

ABSTRACT: A coarse-grained potential that could accurately describe the overall conformational landscape of proteins would be extremely valuable not only for structure prediction but also for studying protein dynamics, large conformational motions, and intrinsically disordered systems. Here, we assessed the quality of the OPEP coarse-grained potential by comparing the reconstructed free-energy surfaces (FESs) of two prototypical β -hairpin and α -helix peptides to all-atom calculations in explicit solvent. We found remarkable agreement between the OPEP FES and those obtained using atomistic models, despite a general over-stabilization of α - and β -structures by the coarse-grained potential. The use of advanced sampling techniques based on metadynamics and parallel tempering guaranteed a thorough exploration of the conformational space accessible to the two peptides studied.

1. INTRODUCTION

Computer simulations have been proven over the years to be a powerful instrument for getting valuable insight into many biological, physical, and chemical processes. However, many interesting phenomena in these fields of science occur in a time scale—and involve systems with a dimension—that is still not easily treatable in a simulation at atomistic resolution. To bridge the gap between simulation and reality, many different advanced computational techniques have been proposed.¹ Among these is the development of coarse-grained (CG) force fields. This approach consists in representing a configuration of the system in terms of beads at lower resolution and developing an effective interaction between the CG sites that preserves as much as possible the underlying physics. The reduced number of degrees of freedom and a smoother, more-efficient potential allow for systems of bigger size to be simulated for a much longer time scale.

A variety of recipes for coarse-graining a system and building an effective potential have been proposed with the aim of studying protein structure and dynamics, lipid bilayers, nucleic acids, surfactants or polyelectrolytes. Providing an exhaustive review of the many existing CG force fields is beyond the scope of this paper (see refs 2 and 3 for a comprehensive treatment of this topic). In some cases, CG potentials have been parametrized using thermodynamics data from simulations carried out with higher-resolution models, either using force matching or inverse Boltzmann techniques. In the realm of proteins, another class of CG potentials has been developed by fitting analytical functions on a dataset of protein structures resolved by NMR spectroscopy or X-ray crystallography. This type of model can be extremely effective in predicting the native form of those proteins whose three-dimensional structure is unknown. However, since these potentials were parametrized using information about the global free-energy minimum alone, their capability of correctly reproducing the thermodynamics of the overall conformational landscape of a protein is arguable.

A CG potential with such an ability would indeed have a much greater value, because it could be used not only for structure prediction but also for studying protein dynamics, large conformational changes, and systems that are intrinsically disordered. In this respect, a practical way of validating a CG potential is to quantitatively compare it with all-atom (AA) explicit-solvent force fields. In fact, these models have been proven to accurately describe protein conformational landscapes and to reproduce experimental observables.^{4,5} In doing this type of comparison, advanced sampling techniques should be used to guarantee a thorough exploration of all the relevant configurations of the proteins chosen as test subjects.

Here, we have focused on OPEP,⁶ which is a CG potential that has been developed for proteins. In this model, an amino acid is represented by six beads and the energy function has been fitted to maximize the energy of the native structure and an ensemble of non-native states for a large training set including peptides and proteins.^{6,7} OPEP combined with a greedy algorithm and a structural alphabet was able to locate using a benchmark of 25 peptides with 9–23 amino acids, lowest-energy conformations differing by 2.6 Å C α root-mean-square deviation from the full NMR structures.⁸ OPEP has also been applied to the amyloid peptide A β 16-22 and provided structural information on the aggregates consistent with or later confirmed by other computational studies and experimental studies.⁹ Finally, OPEP was also able to reproduce the two NMR conformations of the A β 21-30 peptide in solution.¹⁰

We assessed the quality of this potential with the help of two peptides that are prototypical examples of β - and α -structures: the C-terminal β -hairpin of protein GB1 and the C-peptide corresponding to the N-terminal residues of RNase A. In particular, we compared the conformational landscape sampled by a

Received: November 10, 2010

Published: May 19, 2011

combined metadynamics and parallel tempering algorithm^{11–13} using the OPEP potential and two popular AA force fields in explicit solvent, AMBER99SB¹⁴ and OPLS-AA.¹⁵ For both the peptides, the OPEP force field could properly reproduce the features of the atomistic free-energy landscape, despite a general overstabilization of the β - and α -structures, compared to the AA models.

2. METHODS

2.1. The OPEP Potential. OPEP is based on a six-bead representation of an amino acid, namely, the N, H, C α , CO, O atoms and one bead or centroid for the side chain. Unlike other CG force fields, which group heavy backbone atoms into interaction centers,^{16,17} OPEP is basically an AA backbone with CG side chains. This choice was motivated by a tradeoff between structural resolution, CPU speed, and accuracy of the potential energy function, and, notably, for hydrogen-bond (H-bond) interactions.⁶

The OPEP energy function is defined as a sum of local, nonbonded, and hydrogen-bonded terms. The local term includes the potential energy associated with bond stretching, bending, and torsional angles. These parameters were modeled on the AMBER force field¹⁸ with an additional term in the torsional potential for the Φ and Ψ dihedral angles, which renders realistic Ramachandran plots. The nonbonded potential term is expressed as a sum of van der Waals interactions between a pair of beads. This interaction can be repulsive or attractive, depending on the specific pair of beads. The hydrogen-bond potential has a two-body contribution and a four-body contribution. The latter represents the cooperativity of hydrogen-bond formation and accounts for the propensity of forming different secondary structure as a function of the amino-acid sequence. All the OPEP potential parameters were recently refitted using a training set of 11 protein experimental structures. This version of the potential has been proven to correctly identify 24 native or native-like states for 29 proteins.⁷ In this work, we use the OPEP molecular dynamics (MD) code (OPEP-MD), which allows one to efficiently perform both single-replica and replica exchange MD simulations using the OPEP potential.^{19,20}

2.2. Metadynamics and Parallel Tempering. Metadynamics is an advanced sampling algorithm that relies on the introduction of a history-dependent potential acting on a selected number of slow degrees of freedom, dubbed collective variables (CVs).¹¹ If properly applied, metadynamics can both accelerate sampling and reconstruct the free-energy surface (FES) as a function of the CVs. In the well-tempered variant,²¹ the FES is obtained by exploiting the relation

$$V(s, t \rightarrow \infty) = -\frac{T + \Delta T}{\Delta T} F(s) + C \quad (1)$$

where s represents the CVs, $V(s, t)$ denotes the bias potential at time t , C is an irrelevant additive constant, T is the temperature of the system, and ΔT denotes an input parameter representing an effective sampling temperature of the CV space.²¹ Furthermore, information about the degrees of freedom, other than the CVs, can be easily recovered from a well-tempered metadynamics simulation. In fact, the unbiased probability distribution of a generic function of the microscopic coordinates of the system can be reconstructed using a recently developed reweighting algorithm.²² This algorithm is particularly helpful whenever one

Table 1. Details of the PTMetaD Simulations of GB1 β -hairpin (HPIN) and RNase C-peptide (CPEP) Using the OPEP CG Potential and the AA Force Fields AMBER99SB and OPLS-AA^a

	force field	length (ns)	N_{atom}	N_{solv}	N_{rep}	$T_{\text{min}} - T_{\text{max}}$ (K)
HPIN	AMBER99SB	70	5758	5502	64	270–695
	OPLS-AA	51	5758	5502	64	270–695
	OPEP	660	95	0	16	300–600
CPEP	AMBER99SB	17	3777	3570	64	270–650
	OPLS-AA	22	3777	3570	64	270–650
	OPEP	300	84	0	16	300–600

^aDetails include the length of the PTMetaD run (per replica), the total number of atoms (N_{atom}), the number of solvent atoms (N_{solv}), the number of replicas (N_{rep}), and the temperature range ($T_{\text{min}} - T_{\text{max}}$).

wants to quantitatively compare a simulation with experimental observables.⁵

The capabilities of metadynamics can be further enhanced by combining it with parallel tempering (PT).¹² In the combined method (PTMetaD), several independent metadynamics calculations are performed using the same set of CVs at different temperatures. As in standard PT, configurations are swapped from time to time, following (modified) Metropolis criteria. PTMetaD greatly improves the performance of both PT and single-replica metadynamics.¹³

2.3. Simulation Details. We simulated both the GB1 β -hairpin (GEWTYDDATKTPVTTE) and the RNase C-peptide (AETAAAKFLRNHA) using two AA force-fields (AMBER99SB and OPLS-AA) and the OPEP potential for a total of six independent PTMetaD runs.

In the AA simulations, the system was explicitly solvated using TIP3P water molecules²³ in a rhombic dodecahedron box with periodic boundary conditions. The basic details of the simulations are reported in Table 1. Additional technical details can be found in the Supporting Information.

In the AA PTMetaD runs, exchanges were attempted every 0.2 ps, whereas in the OPEP simulations the stride used was 4 ps. Note that, in all simulations, the average probability of accepting an exchange was ~ 0.3 – 0.4 across the temperature range.

In the case of GB1 β -hairpin, the metadynamics bias was applied to two CVs that describe, respectively, the formation of the hydrophobic core and the population of the backbone–backbone hydrogen bonds associated with the β -sheet formation. In the AA simulations, the first CV was defined as the radius of gyration of all the heavy atoms of the backbone and side chain of residues Trp3, Tyr5, Phe12, and Val14. In the OPEP simulation, we included in the definition the backbone atoms plus the beads that represent the side chains of these residues. The second CV was defined in the same way in both the AA and OPEP simulations as

$$S_{\beta} = \sum_{i,j} \frac{1 - (d(O_i, HN_j)/d_0)^6}{1 - (d(O_i, HN_j)/d_0)^{12}} \quad (2)$$

where $d(O_i, HN_j)$ is the distance between the backbone oxygen atom of residue i and the backbone amide hydrogen of residue j , $d_0 = 3 \text{ \AA}$, and the summation runs over all of the pairs of residues whose separation in sequence is greater than 4.

The two metadynamics CVs chosen for the C-peptide were the C α radius of gyration and the population of the α -helical

hydrogen bonds. This latter CV was defined similarly to S_β , following the example of ref 5:

$$S_\alpha = \sum_{i=1}^9 \frac{1 - (d(O_i, HN_{i+4})/d_0)^6}{1 - (d(O_i, HN_{i+4})/d_0)^{12}} \quad (3)$$

where $d(O_i, HN_{i+4})$ is the distance between the backbone oxygen atom of residue i and the backbone amide hydrogen of residue $i + 4$ and $d_0 = 3 \text{ \AA}$. Since, for this peptide, both CVs are a function of the backbone atoms alone, the same definition was used, regardless of the force field.

All the AA PTMetaD simulations were performed with GROMACS 4²⁴ equipped with PLUMED,²⁵ and metadynamics was coded in OPEP-MD¹⁹ in order to run PTMetaD CG simulations. The metadynamics bias potential was stored on a grid and updated every time a new Gaussian was added, using the implementation available in PLUMED. This computational trick keeps the (additional) cost of metadynamics constant during the simulation and it is particularly convenient whenever the OPEP potential is used. In fact, the cost of computing the CG forces is so small that it would become negligible, compared to the exploding cost of summing, at every MD step, the ever-growing number of Gaussians deposited by metadynamics.

3. RESULTS AND DISCUSSION

3.1. GB1 β -hairpin. The C-terminal domain of the GB1 immunoglobulin binding protein corresponding to residues 41–56 is a prototypical example of β -hairpin structure. It is one of the smallest peptides, displaying two-state behavior with a marginally stable fold at room conditions and a fast folding time of $6 \mu\text{s}$.²⁶ For these reasons, this β -hairpin has attracted the interest of both the experimental community^{26–30} and the computational community.^{31–53}

Although the details of the folding mechanism are still under debate, it is well-established that folding is a two-state process, in which the turn plays a central role, the secondary structure is formed cooperatively, and both interstrand hydrophobic side-chain–side-chain interactions and backbone hydrogen bonds contribute to the β -hairpin stability. Furthermore, in a recent study,⁵⁴ the nature of the configurations belonging to the unfolded ensemble has been investigated and these have been found to be rather compact and dominated by non-native, misfolded β -hairpin structures.

Despite its small size, the conformational ensemble of this peptide appeared to be extremely heterogeneous. Capturing this complexity by projecting the conformations on a low-dimensional set of descriptors is a difficult task. Here, we chose two order parameters that have often been used for studying this β -hairpin:^{13,35,41,49} the number of backbone hydrogen bonds and the radius of gyration of few hydrophobic residues (see the Methods section for details). A coordinate similar to the number of hydrogen bonds used here has been recently used to model a stochastic dynamics on it and calculate the folding time distribution of this very same β -hairpin from all-atom replica-exchange simulations.⁵⁵

In Figure 1, we show the FES as a function of these CVs, which were obtained with PTMetaD using the OPEP CG force field and the two AA force fields in explicit solvent (AMBER99SB and OPLS-AA).

The free-energy landscape obtained with the OPEP potential looked qualitatively similar to the AA profiles. The region around five hydrogen bonds and with a radius of gyration equal to 5 \AA

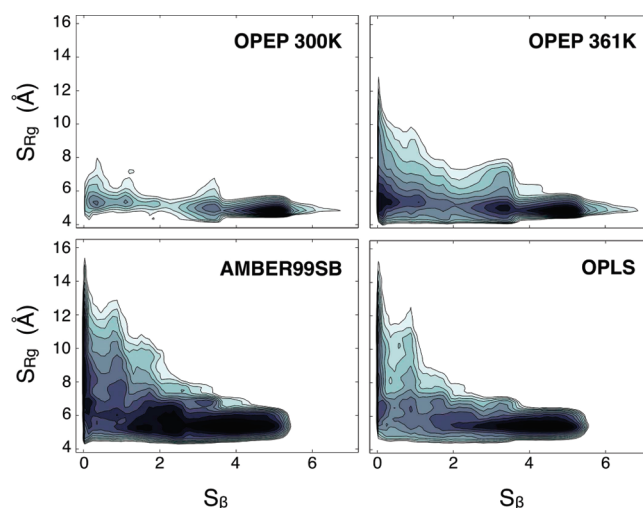


Figure 1. GB1 β -hairpin FES as a function of the number of hydrogen bonds (S_β) and the radius of gyration of the hydrophobic residues (S_{Rg}). The top panels show the OPEP FES at 300 K (left) and 361 K (right), and the bottom panels show the FES from AA simulations in explicit solvent at 300 K using AMBER99SB (left) and OPLS-AA (right) force fields. Isoenergy lines are drawn every $1.5k_B T$.

corresponded to the native states of the β -hairpin (see Figure 2, basin A). A cluster analysis of the structures that populate this basin resulted in a single cluster whose central configuration had a root-mean-square deviation (rmsd) of 0.8 \AA from the crystallographic structure of the C-terminal of protein GB1.

Basin B contained two main clusters. The former was populated by configurations where the two hydrogen bonds at the termini were broken (Figure 2, basin B₁), the latter by misfolded structures with a shifted pattern of hydrogen bonds (Figure 2, basin B₂). The folded state predicted by the AA potentials more closely resembled the configuration of type B₁. In fact, it is well-known that, in explicit-solvent simulations, the most stable conformation is often a “fried state”, in which the terminal hydrogen bonds are not formed. In OPEP, the 4-body term describing the cooperativity of the hydrogen-bond formation and the implicit description of the solvent effects might overstabilize the “full” β -hairpin state.

The unfolded basin corresponded to compact states ($S_{Rg} \approx 5 \text{ \AA}$) with no hydrogen bonds formed (Figure 2, basin C₁). Part of the structures that belong to this basin presented a single α -helix loop in the central region of the peptide (see Figure 2, basin C₂).

Despite a remarkable, yet qualitative, agreement between the OPEP and the AA FES, it is clear that the native basin in the OPEP landscape at 300 K is overpopulated with respect to the unfolded region. This contrasts both with the recent AA simulations in explicit solvent and with the experimental data which suggested that this peptide was only marginally stable at room temperature.^{26,53} To make our comparison more quantitative, we further coarse-grained our description of the β -hairpin by defining those conformations with more than one hydrogen bond formed as being “folded” and those conformations with less than one hydrogen bond formed as being “unfolded”. Note that, based on our definition, we included in the “folded” basin not only native-like structures but also misfolded configurations. From the monodimensional FES $F(S_\beta)$, we calculated the free-energy difference ΔF_{FU} between folded (F) and unfolded (U) states for AMBER99SB, OPLS-AA, and OPEP (see the Supporting

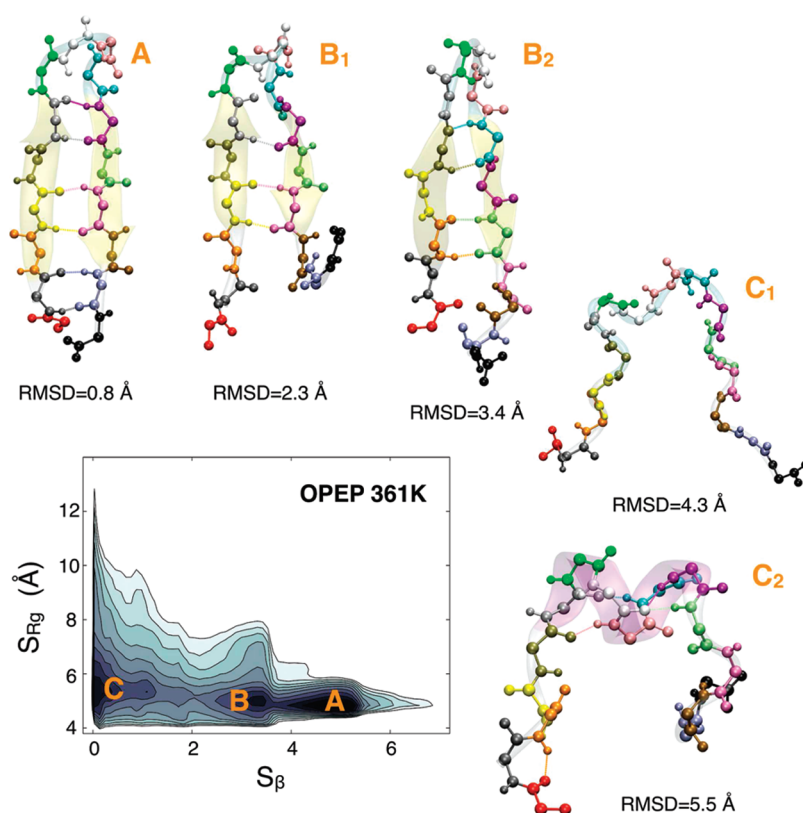


Figure 2. Characterization of the OPEP GB1 β -hairpin FES at 361 K. For each basin, the structure(s) of the most populated cluster(s) is represented. The cluster analysis has been performed using the *g_cluster* tool included in the GROMACS 4 package. The method of Daura and Van Gunsteren⁵⁶ was used for clustering, with a cutoff of 1.5 Å on the backbone atoms. The root-mean-square deviation (rmsd) from the crystallographic structure of the C-terminal of protein GB1 (PDB code: 1GB1) was calculated on the backbone.

Table 2. Free-Energy Difference between Folded (F) and Unfolded (U) States of GB1 β -hairpin (ΔF_{FU}) and Unfolding Barrier (ΔF_{TF}) from PTMetaD Calculations Using AMBER99SB, OPLS-AA, and OPEP Force Fields

force field	T (K)	ΔF_{FU} (kcal/mol)	ΔF_{TF} (kcal/mol)
AMBER99SB	300	-2.1	2.5
OPLS-AA	300	-3.4	4.7
OPEP	300	-4.5	7.9
	345	-2.3	6.1
	361	-1.2	5.2

Information for details). The results reported in Table 2 show that the estimates of ΔF_{FU} obtained with two AA models significantly differ and that the AMBER99SB data are more similar to the experimental value.

From $F(S_\beta)$, we also calculated the free-energy difference ΔF_{TF} between the transition state (T) and the folded state (F). This would correspond to the real kinetic barrier that the system must overcome during the unfolding, assuming that S_β is the ideal reaction coordinate of this process. The discrepancy between the values predicted by the two AA models for ΔF_{TF} was even greater than for ΔF_{FU} .

As expected, the overstability observed with the OPEP potential at 300 K could be alleviated by increasing the temperature (see Figure 3). In the temperature range of 345–361 K, the deviation from AA data in terms of both ΔF_{FU} and ΔF_{TF} was minimized.

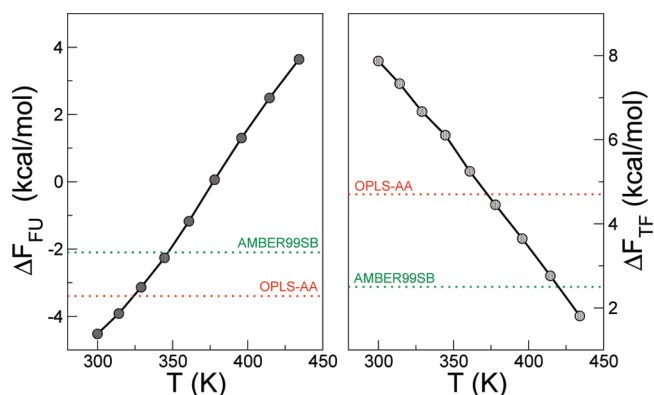


Figure 3. Free-energy difference between folded (F) and unfolded (U) states of GB1 β -hairpin (left panel) and unfolding barrier (right panel), as a function of temperature from the OPEP PTMetaD calculations. Dashed lines indicate the results from the AA simulations at 300 K, using AMBER99SB (green) and OPLS-AA (red).

3.2. RNase C-peptide. The C-peptide corresponding to the first 13 N-terminal residues of Ribonuclease A has a remarkable α -helical propensity for a system of such a small size. In particular, according to circular dichroism experiments, the average helicity is dependent on both temperature and pH and exhibits a maximum at $T = 276$ K and pH 5.25.⁵⁷ NMR experiments⁵⁸ and AA MD simulations in explicit solvent on a mutant sequence^{5,59} showed that the conformational landscape

of the C-peptide is characterized by an equilibrium among different conformers. These include a set of extended coil conformations, a set of complete α -helical configurations, and a set of partially formed α -helical structures with a salt bridge between the side chains of Glu2 and Arg10.

Here, we reconstructed the FES as a function of the number of α -helical hydrogen bonds (S_α) and the radius of gyration calculated on the C α atoms (see the Methods section for details). The FES obtained with PTMetaD, using OPEP, AMBER99SB, and OPLS-AA potentials, are reported in Figure 4.

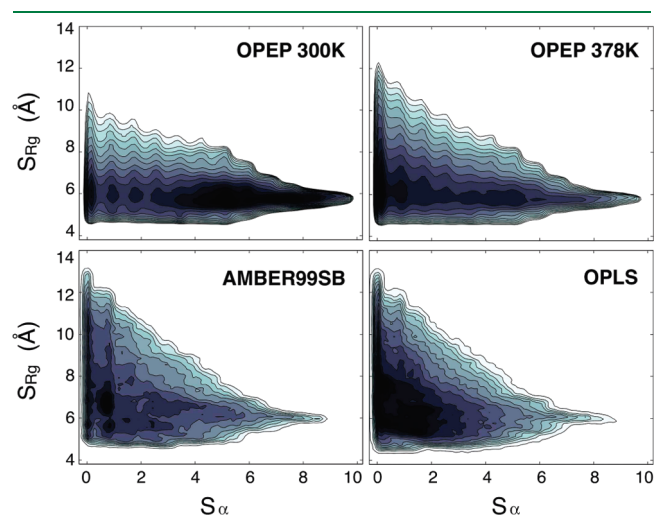


Figure 4. RNase A C-peptide FES, as a function of the number of α -helical hydrogen bonds (S_α) and the C α radius of gyration (S_{Rg}). The top panels show the OPEP FES at 300 K (left) and 378 K (right), and the bottom panels show the FES from AA simulations in explicit solvent at 300 K using AMBER99SB (left) and OPLS-AA (right) force fields. Isoenergy lines are drawn every $1.5k_B T$.

As for the case of β -hairpin, it is clear from Figure 4 that the OPEP potential overstabilized α -helical conformers at 300 K. This affected both the extended α -helix structure (Figure 5, basin A) and the partially helical conformation that most resembled the crystallographic structure of the N-terminal fragment of Ribonuclease A (Figure 5, basin B).

At higher temperatures, the FES obtained with OPEP looked qualitatively similar to the AA force field landscapes. However, a more quantitative comparison among the FES became problematic, since a two-state (or multistates) behavior was not well-defined as the temperature increased. We decided on a different approach and calculated the propensity of each residue of the C-peptide to form an α -helix. This was defined as the free-energy

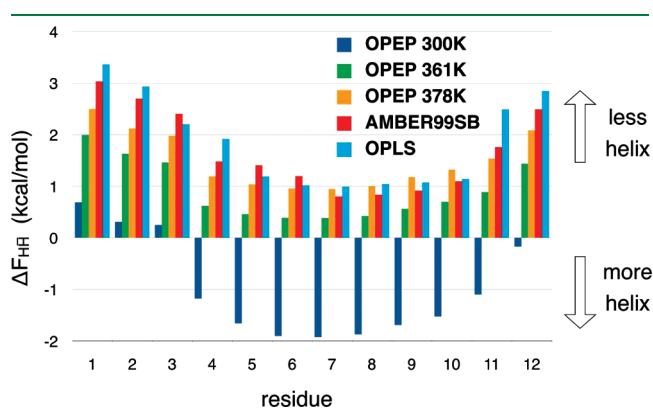


Figure 6. C-peptide helical propensity profile defined as the free-energy difference between helical (H) and nonhelical (\bar{H}) states at residue level. The secondary structure was assigned by the STRIDE algorithm. Data were obtained by reweighting the configurations sampled during the PTMetaD run with OPEP at 300 K (blue), 361 K (green), and 378 K (yellow); AMBER99SB at 300 K (red); and OPLS-AA at 300 K (light blue).

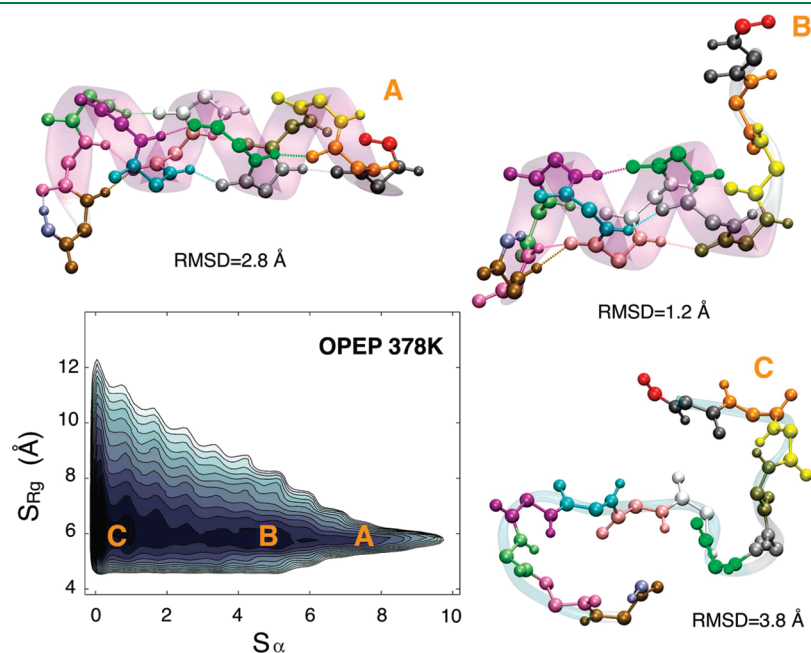


Figure 5. Characterization of the OPEP C-peptide FES at 378 K. The basins that are more clearly recognizable at 300 K become more shallow as temperature increases. (Details of the cluster analysis are reported in the caption of Figure 2.) The rmsd from the crystallographic structure of N-terminal fragment of Ribonuclease A (PDB code: 2AAS) was calculated on the backbone.

Table 3. RMSD of OPEP $\Delta F_{\text{H}\bar{\text{H}}}$ Data from AA Data at 300 K, as a Function of the OPEP Temperature

T (K)	AMBER99SB (kcal/mol)	OPLS (kcal/mol)
300	2.7	2.9
314	2.3	2.5
329	1.9	2.1
345	1.4	1.6
361	0.8	1.0
378	0.3	0.5
396	0.4	0.5
415	0.7	0.6
434	1.0	0.9

difference $\Delta F_{\text{H}\bar{\text{H}}}$ between the α -helix state (H) and the states characterized by any other type of secondary structure ($\bar{\text{H}}$). We used the STRIDE algorithm⁶⁰ to assign the secondary structure to the conformations sampled by the PTMetaD run, and, for each residue, we calculated $\Delta F_{\text{H}\bar{\text{H}}}$ by reweighting²² the statistics accumulated during this biased simulation. Results are reported in Figure 6.

At 300 K, the AA force fields predicted a very similar $\Delta F_{\text{H}\bar{\text{H}}}$ for each residue, with an RMSD of 0.3 kcal/mol between the two sets of data. In contrast, at this temperature, the OPEP potential significantly overstabilized helicity. However, the trend along the peptide sequence was correctly reproduced, with the central residues being the most prone to form α -helix. Also in this case, at higher temperatures, OPEP results became quantitatively comparable to AA data at room temperature (see Table 3). In particular, considering OPEP $\Delta F_{\text{H}\bar{\text{H}}}$ data at 361 and 378 K, the rmsd values were 1.0 and 0.5 kcal/mol, with respect to OPLS-AA at 300 K, and 0.8 and 0.3 kcal/mol, with respect to AMBER99SB at 300 K.

4. CONCLUSIONS

In this paper, we used an advanced sampling algorithm to describe the conformational landscape of two peptides that are prototypical examples of β -hairpin and α -helical structures. We used three different models for the force field: two with atomistic details (AMBER99SB and OPLS-AA), and one coarse-grained (CG) potential (OPEP). This CG force field was fitted on a dataset of protein structures, in order to maximize the energy of the native configuration and of an ensemble of non-native states.

Our results showed that the OPEP potential could properly reproduce the features of the free-energy landscape obtained with the AA explicit-solvent force fields. However, an over-stabilization of both α - and β -structures was observed with OPEP at 300 K. To determine the optimal OPEP temperature that minimized the deviation from AA data at 300 K, we analyzed the temperature dependence of the OPEP folding free-energy difference and unfolding barrier in the case of the β -hairpin and of the α -helical propensity profile in the case of the C-peptide. Our results showed that the optimal temperatures were similar for both peptides and reside in the interval of 345–360 K for the former system and 360–378 K for the latter system. By choosing the OPEP simulation temperature in these regions, the agreement with the AA results at room temperature was of the same quality as that obtained between the two explicit-solvent AA models. Furthermore, it must be pointed out that, if implicit solvation models were added in the comparison, the discrepancies

among the AA results would be even greater, at least in the case of the β -hairpin.⁶¹ This information, along with other more-extensive tests, will be used to improve the model in future versions of the OPEP potential.

A key feature of the OPEP potential is the detailed description of the protein backbone and the introduction of specific potential terms accounting for backbone–backbone hydrogen bonding. Several studies showed that the introduction of backbone directional contacts intrinsically stabilized secondary structure elements.^{62–64} In order to check the validity of our results in the case of unstructured peptides, we performed OPEP PTMetaD simulation of an intrinsically disordered glycine-serine block copolypeptide (GS)₈. This peptide has been recently characterized by means of MD simulations with umbrella sampling, using the OPLS potential in explicit solvent.⁶⁵ Even in this case, the results of the OPEP simulations in the temperature range of 360–378 K were comparable with the room-temperature AA data reported in Figure 3 of ref 65 (see the Supporting Information).

In conclusion, here, using advanced sampling techniques, we have shown that simulations carried out with OPEP potential at a universal temperature close to 360 K could properly reproduce the results obtained with atomistic models for a variety of different systems, including ordered and disordered peptides. It must also be noted that, thanks to the reduced representation of the system, OPEP significantly outperforms AA simulations, in terms of computational efficiency. This computational advantage further increases in PT and PTMetaD simulations, because of the fact that fewer replicas are needed to cover the same temperature range.⁶⁶ For all these reasons, the combination of the OPEP potential with the PTMetaD sampling algorithm, introduced and tested here for small peptides, paves the way for extending the capabilities of molecular simulations to the study of complex biomolecular processes such as the folding of large proteins and protein–protein interactions.

■ ASSOCIATED CONTENT

S Supporting Information. Supporting Information contains additional details of the well-tempered metadynamics algorithm and technical details of the AA and OPEP simulations of the GB1 β -hairpin and RNase C-peptide. General details of the molecular dynamics simulations and specific parameters of the PTMetaD algorithm are given. The convergence of the PTMetaD simulations is discussed in details. The OPEP free-energy landscape of (GS)₈, as a function of the radius of gyration, is reported. (PDF) This material is available free of charge via the Internet at <http://pubs.acs.org>.

■ AUTHOR INFORMATION

Corresponding Author

*E-mail: philippe.derreumaux@ibpc.fr.

Author Contributions

[†]These authors contributed equally to this work.

■ ACKNOWLEDGMENT

Calculations were performed on the Brutus cluster at ETH Zurich.

REFERENCES

- (1) Frenkel, D.; Smit, B. *Understanding Molecular Simulation*; Academic Press: New York, 2002; pp 1–617.
- (2) Voth, G. A. *Coarse-Graining of Condensed Phase and Biomolecular Systems*; CRC Press: Boca Raton, FL, 2009.
- (3) Tozzini, V. Q. *Rev. Biophys.* **2010**, *43*, 333–371.
- (4) Best, R. B.; Hummer, G. *J. Phys. Chem. B* **2009**, *113*, 9004–9015.
- (5) Barducci, A.; Bonomi, M.; Parrinello, M. *Biophys. J.* **2010**, *98*, L44–L46.
- (6) Derreumaux, P. *J. Chem. Phys.* **1999**, *111*, 2301–2310.
- (7) Maupetit, J.; Tuffery, P.; Derreumaux, P. *Proteins* **2007**, *69*, 394–408.
- (8) Maupetit, J.; Derreumaux, P.; Tuffery, P. *Nucleic Acids Res.* **2009**, *37*, W498–W503.
- (9) Santini, A.; Mousseau, N.; Derreumaux, P. *J. Am. Chem. Soc.* **2004**, *126*, 11509–11516.
- (10) Chen, W.; Mousseau, N.; Derreumaux, P. *J. Chem. Phys.* **2006**, *125*, 084911.
- (11) Laio, A.; Parrinello, M. *Proc. Natl. Acad. Sci. U.S.A.* **2002**, *99*, 12562–12566.
- (12) Hansmann, U. H. E. *Chem. Phys. Lett.* **1997**, *281*, 140–150.
- (13) Bussi, G.; Gervasio, F. L.; Laio, A.; Parrinello, M. *J. Am. Chem. Soc.* **2006**, *128*, 13435–13441.
- (14) Hornak, V.; Abel, R.; Okur, A.; Strockbine, B.; Roitberg, A.; Simmerling, C. *Proteins* **2006**, *65*, 712–725.
- (15) Kaminsky, G. A.; T-R., J.; Friesner, R. A.; Jorgensen, W. L. *J. Phys. Chem. B* **2001**, *105*, 6474–6487.
- (16) Monticelli, L.; Kandasamy, S. K.; Periole, X.; Larson, R. G.; Tieleman, P. D.; Marrink, S. J. *Chem. Theory Comput.* **2008**, *4*, 819–834.
- (17) DeVane, R.; Shinoda, W.; Moore, P. B.; Klein, M. L. *J. Chem. Theory Comput.* **2009**, *5*, 2115–2124.
- (18) Cornell, W. D.; Cieplak, P.; Bayly, C. I.; Gould, I. R.; Merz, K. M.; Ferguson, D. M.; Spellmeyer, D. C.; Fox, T.; Caldwell, J.; Kollman, P. J. *J. Am. Chem. Soc.* **1995**, *117*, 5179–5197.
- (19) Derreumaux, P.; Mousseau, N. *J. Chem. Phys.* **2007**, *126*, 025101.
- (20) Chebaro, Y.; Dong, X.; Laghaei, R.; Derreumaux, P.; Mousseau, N. *J. Phys. Chem. B* **2009**, *113*, 267–274.
- (21) Barducci, A.; Bussi, G.; Parrinello, M. *Phys. Rev. Lett.* **2008**, *100*, 020603.
- (22) Bonomi, M.; Barducci, A.; Parrinello, M. *J. Comput. Chem.* **2009**, *30*, 1615–1621.
- (23) Jorgensen, W. L.; Chandrasekhar, J.; Madura, J. D.; Impey, R. W.; Klein, M. L. *J. Chem. Phys.* **1983**, *79*, 926–935.
- (24) Hess, B.; Kutzner, C.; van der Spoel, D.; Lindahl, E. *J. Chem. Theory Comput.* **2008**, *4*, 435–447.
- (25) Bonomi, M.; Branduardi, D.; Bussi, G.; Camilloni, C.; Provasi, D.; Raiteri, P.; Donadio, D.; Marinelli, F.; Pietrucci, F.; Broglia, R. A.; Parrinello, M. *Comput. Phys. Commun.* **2009**, *180*, 1961–1972.
- (26) Muñoz, V.; Thompson, P. A.; Hofrichter, J.; Eaton, W. A. *Nature* **1997**, *390*, 196–199.
- (27) Blanco, F. J.; Rivas, G.; Serrano, L. *Nat. Struct. Biol.* **1994**, *1*, 584–590.
- (28) Honda, S.; Kobayashi, N.; Munekata, E. *J. Mol. Biol.* **2000**, *295*, 269–278.
- (29) Du, D.; Zhu, Y.; Huang, C.; Gai, F. *Proc. Natl. Acad. Sci. U.S.A.* **2004**, *101*, 15915–15920.
- (30) Muñoz, V.; Ghirlando, R.; Blanco, F. J.; Jas, G. S.; Hofrichter, J.; Eaton, W. A. *Biochemistry* **2006**, *45*, 7023–7035.
- (31) Muñoz, V.; Henry, E. R.; Hofrichter, J.; Eaton, E. A. *Proc. Natl. Acad. Sci. U.S.A.* **1998**, *95*, 5872–5879.
- (32) Kolinski, A.; Ilkowski, B.; Skolnick, J. *Biophys. J.* **1999**, *77*, 2942–2952.
- (33) Dinner, A. R.; Lazaridis, T.; Karplus, M. *Proc. Natl. Acad. Sci. U.S.A.* **1999**, *96*, 9068–9073.
- (34) Wang, H.; Sung, S. S. *Biopolymers* **1999**, *50*, 763–776.
- (35) Pande, V. S.; Rokhsar, D. S. *Proc. Natl. Acad. Sci. U.S.A.* **1999**, *96*, 9062–9067.
- (36) Roccatano, D.; Amadei, A.; Nola, A. D.; Berendsen, H. J. C. *Protein Sci.* **1999**, *8*, 2130–2143.
- (37) Klimov, D. K.; Thirumalai, D. *Proc. Natl. Acad. Sci. U.S.A.* **2000**, *97*, 2544–2549.
- (38) Ma, B. Y.; Nussinov, R. *J. Mol. Biol.* **2000**, *296*, 1091–1104.
- (39) Lee, J.; Shin, S. *Biophys. J.* **2001**, *81*, 2507–2516.
- (40) García, A. E.; Sanbonmatsu, K. Y. *Proteins: Struct., Funct., Genet.* **2001**, *42*, 345–354.
- (41) Zhou, R.; Berne, B. J.; Germain, R. *Proc. Natl. Acad. Sci. U.S.A.* **2001**, *98*, 14931–14936.
- (42) Bolhuis, P. G. *Proc. Natl. Acad. Sci. U.S.A.* **2003**, *100*, 12129–12134.
- (43) Ma, B.; Nussinov, R. *Protein Sci.* **2003**, *12*, 1882–1893.
- (44) Colombo, G.; DeMori, G. M. S.; Roccatano, D. *Protein Sci.* **2003**, *12*, 538–550.
- (45) Krivov, S. V.; Karplus, M. *Proc. Natl. Acad. Sci. U.S.A.* **2004**, *101*, 14766–14770.
- (46) Evans, D. A.; Wales, D. J. *J. Chem. Phys.* **2004**, *121*, 1080–1090.
- (47) Wei, G.; Mousseau, N.; Derreumaux, P. *Proteins* **2004**, *56*, 464–474.
- (48) Andrec, M.; Felts, A. K.; Gallicchio, E.; Levy, R. M. *Proc. Natl. Acad. Sci. U.S.A.* **2005**, *102*, 6801–6806.
- (49) Nguyen, P.; Stock, G.; Mittag, E.; Hu, C.; Li, M. S. *Proteins* **2005**, *61*, 795–808.
- (50) Yoda, T.; Sugita, Y.; Okamoto, Y. *Proteins: Struct., Funct., Bioinf.* **2007**, *66*, 846–859.
- (51) Thukral, L.; Smith, J. C.; Daidone, I. *J. Am. Chem. Soc.* **2009**, *131*, 18147–18152.
- (52) Juraszek, J.; Bolhuis, P. G. *J. Phys. Chem. B* **2009**, *113*, 16184–16196.
- (53) Best, R. B.; Mittal, J. *J. Phys. Chem. B* **2010**, *114*, 8790–8798.
- (54) Bonomi, M.; Branduardi, D.; Gervasio, F. L.; Parrinello, M. *J. Am. Chem. Soc.* **2008**, *130*, 13938–13944.
- (55) Yang, S.; Onuchic, J. N.; Garcia, A. E.; Levine, H. *J. Mol. Biol.* **2007**, *372*, 756–763.
- (56) Daura, X.; Gademann, K.; Jaun, B.; Seebach, D.; van Gunsteren, W. F.; Mark, A. E. *Angew. Chem., Int. Ed.* **1999**, *38*, 236–240.
- (57) Shoemaker, K. R.; Kim, P. S.; York, E. J.; Stewart, J. M.; Baldwin, R. L. *Nature* **1987**, *326*, 563–567.
- (58) Osterhout, J. J.; Baldwin, R. L.; York, E. J.; Stewart, J. M.; Dyson, H. J.; Wright, P. E. *Biochemistry* **1989**, *28*, 7059–7064.
- (59) Caballero-Herrera, A.; Nordstrand, K.; Berndt, K. D.; Nilsson, L. *Biophys. J.* **2005**, *89*, 842–857.
- (60) Frishman, D.; Argos, P. *Proteins* **1995**, *23*, 566–579.
- (61) Lwin, T. Z.; Luo, R. *Protein Sci.* **2006**, *15*, 2642–2655.
- (62) Hoang, T. X.; Trovato, A.; Seno, F.; Banavar, J. R.; Maritan, A. *Proc. Natl. Acad. Sci. U.S.A.* **2004**, *101*, 7960–7964.
- (63) Yap, E. H.; Fawzi, N. L.; Head-Gordon, T. *Proteins* **2008**, *70*, 626–638.
- (64) Alemani, D.; Collu, F.; Cascella, M.; Peraro, M. D. *J. Chem. Theory Comput.* **2010**, *6*, 315–324.
- (65) Tran, H. T.; Mao, A.; Pappu, R. V. *J. Am. Chem. Soc.* **2008**, *130*, 7380–7392.
- (66) Earl, D. J.; Deem, M. W. *Phys. Chem. Chem. Phys.* **2005**, *7*, 3910–3916.

Analysis of Mammalian Histidine Decarboxylase Dimerization Interface Reveals an Electrostatic Hotspot Important for Catalytic Site Topology and Function

Aurelio A. Moya-García,^{†,‡,||} Daniel Rodríguez-Agudo,^{†,||,⊥} Hideyuki Hayashi,[§] Miguel Angel Medina,^{†,‡} José Luis Urdiales,^{†,‡} and Francisca Sánchez-Jiménez^{*,†,‡}

[†]Departamento de Biología Molecular y Bioquímica, Facultad de Ciencias, Campus de Teatinos, Universidad de Málaga, Málaga, Spain

[‡]CIBER de Enfermedades Raras (CIBERER), Málaga, Spain

[§]Department of Biochemistry, Osaka Medical College, Takatsuki, Osaka 569-8686, Japan

ABSTRACT: Selective intervention of mammalian histidine decarboxylase (EC 4.1.1.22) could provide a useful antihistaminic strategy against many different pathologies. It is known that global conformational changes must occur during reaction that involves the monomer–monomer interface of the enzyme. Thus, the dimerization surface is a promising target for histidine decarboxylase inhibition. In this work, a rat apoenzyme structural model is used to analyze the interface of the dimeric active HDC. The dimerization surface mainly involves the fragments 1–213 and 308–371 from both subunits. Part of the overlapping surfaces conforms each catalytic site entrance and the substrate-binding sites. In addition, a cluster of charged residues is located in each overlapping surface, so that both electrostatic hotspots mediate in the interaction between the catalytic sites of the dimeric enzyme. It is experimentally demonstrated that the carboxyl group of aspartate 315 is critical for the proper conformation of the holoenzyme and the progression of the reaction. Comparison to the available information on other evolutionary related enzymes also provides new insights for characterization and intervention of homologous l-amino acid decarboxylases.

1. INTRODUCTION

Mammalian histidine decarboxylase (HDC) is a pyridoxal 5'-phosphate (PLP)-dependent enzyme that is responsible for the biosynthesis of histamine. This biogenic amine is involved in several physiological responses (e.g., immune responses, gastric acid secretion, neurotransmission, etc.), and consequently, it has been implicated in many different human pathologies such as anaphylaxis, peptic ulcers and other inflammatory responses, basophilic leukemias, osteoporosis, schizophrenia, rare diseases such as histidinemia (ORPHA2157), and mast cell related rare diseases such as the different mastocytoses (ORPHA98292, ORPHA66646, ORPHA2467, ORPHA98848, ORPHA98849, and ORPHA98850). In spite of the importance of these diseases, HDC has not been fully characterized. Thus, most of the current antihistaminic strategies tend to interfere with histamine reception by target cells (i.e., histamine receptors) rather than with histamine synthesis in histamine-producing cells. However, the recent development of HDC knock-out animals suggests that HDC activity is itself important for the development and proliferation of the cells that produce it,¹ indicating that selective intervention of histamine synthesis could be a straightforward pharmacological strategy for some of the histamine-related pathologies.

Mature histidine decarboxylase purified from mammalian tissues has been reported as a dimer where each monomer (53–58 kDa) is processed from a carboxy-elongated 74 kDa precursor.^{1,2} It has been demonstrated that the first 476 residues of the protein can support the enzymic activity.³ We have characterized the catalytic mechanism of a recombinant version of a carboxy-truncated form of the rat enzyme (fragment 1–512, also named HDC 1/512),⁴ which has kinetic constants similar to the mature enzyme purified from rodent

tissues.² We studied the rate-limiting step with atomic detail.⁵ We have observed that the Stokes radius of the protein is modified during catalysis, indicating that local changes in the catalytic site of mammalian histidine decarboxylase affect its global conformation by a rearrangement of the dimerization surface.⁶ A flexible region (within residues 330–360) has been proven to participate^{7–10} in the conformational changes of the catalytic site neighborhood after substrate binding, and we have established the role of this region in the increased stability of the enzyme on substrate uptake.¹¹ These results have highlighted the importance of dimerization for the enzymic activity of this protein and consequently implicate dimerization as a potential target for selective inhibition of this mammalian enzyme. Thus, we focus on the characterization and analysis of the intermonomer interaction surface of this enzyme.

The computational analysis in the present work revealed that an electrostatic hotspot, with contributions of the same cationic and anionic residues from both monomers, is located between the two catalytic sites of the homodimer. Residue D315 plays an important role in the stabilization of the electrostatic hotspot and the right active site conformation. This hypothesis was experimentally tested by direct mutagenesis strategies, biophysical measurements, and enzymic activity determinations.

2. MATERIALS AND METHODS

2.1. Structure Preparation. In order to investigate the hotspot contribution to both the electrostatic properties and monomer

Received: December 1, 2010

Published: May 13, 2011

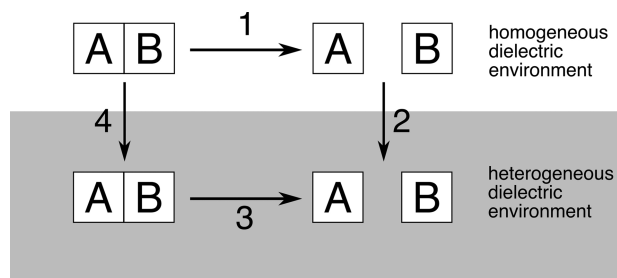


Figure 1. Thermodynamic cycle for calculation of binding free energy. The binding free energy is calculated from the transfer free energies of the protein from a homogeneous dielectric environment to a heterogeneous dielectric environment.

binding, we generated structural models for several mutations of rat HDC (rHDC). Taking our previous homology-based model⁵ as the wild type enzyme, mutations of selected hotspot residues were performed with PyMOL¹² on each monomer of the homodimeric enzyme.

To define the monomer–monomer interactions surface, water accessibilities of the residues were calculated with the DSSP program,¹³ and the proper protonation state at physiological pH and atomic charges were established using the PDB2PQR and PROPKA server and software^{14,15} in order to obtain a suitable input structure for electrostatics calculations.

The initial geometry of each system was relaxed using the Steepest Descent algorithm (10 000 energy minimization steps) and the OPLS force field implemented in the DYNAMO library.¹⁶ Each mutated structure was solvated in a 41.8 Å radius sphere of TIP3P explicit water molecules and subjected to Molecular Dynamics (MD) simulations with NAMD¹⁷ and the CHARMM22 protein force field.¹⁸ The systems were heated to 310 K followed by equilibration without restraints using Langevin dynamics to control the temperature. Once equilibrated, coordinates were saved every 10 ps to obtain 20 ns MD trajectories.

2.2. Energy Calculations. Electrostatics binding free energies for the formation of the homodimeric rHDC complex (ΔG^{elec}) were calculated by combining several hypothetical processes in the thermodynamic cycle,¹⁹ depicted in Figure 1. The electrostatic binding free energy is then given by:

$$\Delta G^{\text{elec}} = -\Delta G_3 = \Delta G_4 - \Delta G_2 - \Delta G_1$$

Our framework essentially decomposes ΔG^{elec} in terms of transfer free energies from a homogeneous dielectric environment (in which a dielectric constant of 4 is applied to the protein and the solvent) to a heterogeneous dielectric environment with different internal and external dielectric constants (namely, 4 for the protein and 80 for the solvent). In other words, we compute the electrostatic contribution to the binding free energy in terms of solvation and Coulombic electrostatic interaction free energies. The Adaptive Poisson–Boltzmann Solver (APBS)²⁰ was used to compute the contribution of solvation to ΔG^{elec} by solving the Poisson–Boltzmann equation for the complex and for each component, in both the homogeneous and the heterogeneous dielectric environments. Intermolecular Coulombic contributions to ΔG^{elec} (ΔG_{coul}) are considered in our simulations by computing the change in Coulombic electrostatic energy upon complex formation in a homogeneous dielectric environment (with a

dielectric constant of 4), ΔG_1 depicted in Figure 1. Thus

$$\Delta G_{\text{coul}} = -\Delta G_1 = \Delta G^{\text{AB}} - \Delta G^{\text{A}} - \Delta G^{\text{B}}$$

Each term in this equation is the sum of pairwise Coulombic interactions among all atoms in the two rHDC monomers or in the rHDC dimer. These terms were calculated with the accessory program Coulomb, from the APBS software. The temperature was 298 K, and the ionic strength equaled 0.15 M in all cases.

Due to the strong dependence of the calculated free energies on the value taken for the protein dielectric constant and the discussion and controversy regarding the most appropriate value of this parameter,^{21–23} it is difficult to know whether the calculated ΔG^{elec} accurately represents experimental energies. Therefore, the calculated values for ΔG^{elec} are meaningful only for the comparison of relative complex formations among the wild type enzyme and the mutants studied, so we offer relative binding affinities in terms of $\Delta\Delta G^{\text{elec}} = \Delta G^{\text{elec}}(\text{mutant}) - \Delta G^{\text{elec}}(\text{wt})$, where positive values indicate a decreased binding affinity and negative values indicate an affinity increase caused by the mutation.

2.3. Electrostatic Potential Maps. Electrostatic potential maps were calculated using APBS to solve the Poisson–Boltzmann equation. The protein is centered in a $193 \times 193 \times 161$ grid. A solvent dielectric constant of 80 and a protein dielectric constant of 4 were used for the electrostatic potential map calculations, as they are standard values used by other authors.²⁴

2.4. Recombinant HDC Expression and Purification. Direct mutants were generated using the Quickchange system (Promega). The previously reported recombinant pBluescript SK-II plasmid encoding for fragment 1–512 of rat HDC (namely, p1/512.rHDC) was used as the template.²⁵ The primers used for the different substitutions were the following: D315V, 5'-GGATGATGGTGCACTTTGTTTGCACCTGGGTTCTGGG-3' (sense) and its antisense counterpart (the mutated codon is in italic lettering); D315N, equal to the previous ones but AAT and its antisense counterpart are in the respective primers as the mutated codon; and C316A, 5'-GGATGATGGTGCACCTTTGACGCCACTGGTTCTGGG-3' (sense) and its antisense counterpart. All mutants were tested using full double-strand sequencing after each subcloning step. Different expression systems have been used throughout this work for the wild-type and the mutant versions. The in vitro expression system was previously described.²⁵ The purified preparations of the recombinant versions were obtained as described elsewhere.⁴ For rapid screening of activities, the mutant enzymes were expressed and purified from recombinant pGEX6P-1 plasmids as mutant versions of the pGEX6P-1/HDC1/512 product, as reported previously.⁴ The mutant versions were released from the glutathione S-transferase fusions by treatment with the Pre-Scission TM protease supplied with the kit. The HDC activity assay was carried out by following ¹⁴C₂ release from [U-¹⁴C₂]-labeled L-histidine (American Radiolabeled Chemicals, U. S. A.), as reported elsewhere.²⁵ Spectroscopic measurements were carried out with the expression product of a recombinant pET11a plasmid encoding for mutant D315N. It was expressed and purified as reported elsewhere for the wild-type enzyme, following three chromatographic steps (Phenyl-Sepharose CL-4B, DEAE interchange, and hydroxyapatite).^{4,6} Purity of the final preparations was assessed by Coomassie blue staining and Western blotting. All preparations used in this work had greater than 90% purity. When required, the enzyme was concentrated in different Amycon ultrafiltration systems (cutoff between 10 and 30 kDa) depending on the initial volume. To

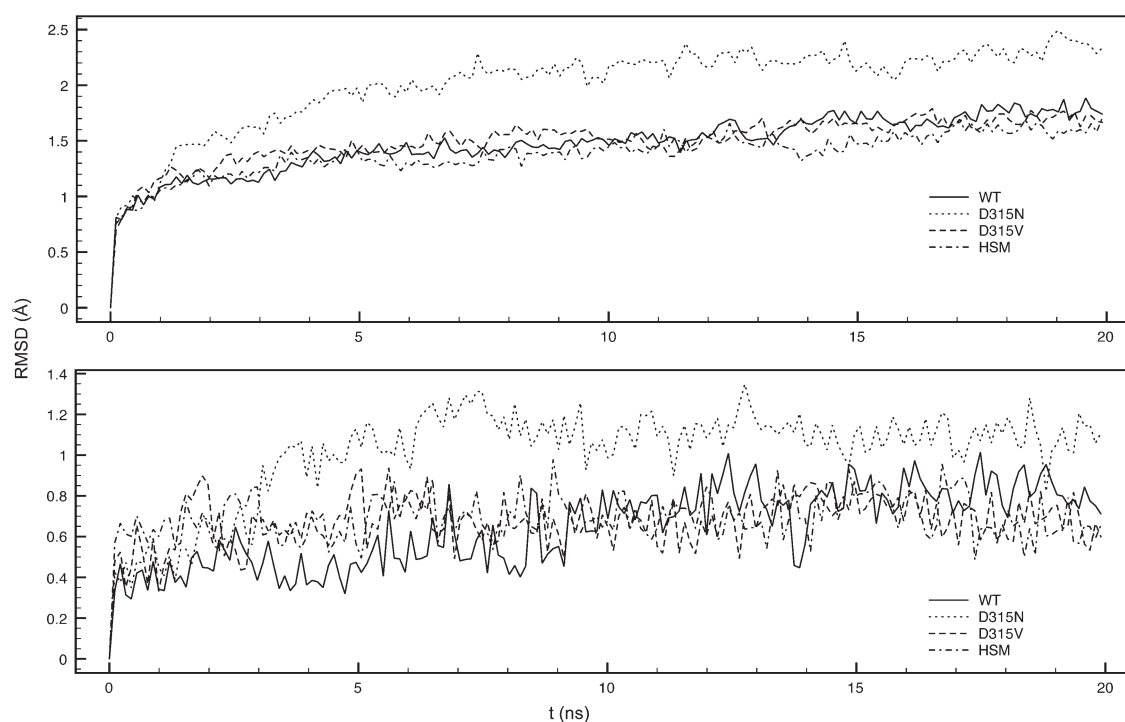


Figure 2. Root-mean-square deviations from the first structure of the MD trajectory for each system studied, for the backbone (upper graph) and hotspot residues (lower graph). WT, wild-type HDC; HSM, hotspot mutant.

avoid interferences with free PLP, the final preparation was gel filtrated in a Sephadex G25 immediately before starting spectroscopic measurements. For the experiments shown in Figures 3 and 4, purified HDC preparations were incubated at room temperature in either the presence or absence of histidine methyl ester (HisOMe) for 60 min. HisOMe and histidine were provided by Sigma-Aldrich (Spain).

2.5. Spectroscopic Measurements. Absorption spectra were measured using a HP8452A diode array spectrophotometer (Hewlett-Packard, U. S. A.). Fluorescence spectra were obtained with a QuantaMaster SE spectrofluorimeter (Photon Technology International Inc., U. S. A.). All spectroscopic measurements were carried out at RT under the same conditions as those described previously.⁴

3. RESULTS AND DISCUSSION

3.1. General Description of the Dimer Interface. Our previous work indicates that the dimerization surface must be involved in conformational changes occurring during catalysis,⁶ so we focused our attention on this part of the enzyme. In a close examination of the dimerization surface, we found a cluster of charged residues in each monomer between both catalytic sites. Dimerization and active site conformations were explained previously.³¹ This led us to hypothesize that the electrostatic properties of this hotspot would be important in maintaining a proper environment in each active site.

To check putative dramatic reorganizations in the molecular structures after the mutations, we built molecular models for mutations in the hotspot of HDC, and we made molecular dynamics simulations with these versions. Results showed that no major changes or structural reorganization occur in the enzyme as a consequence of the mutations (Figure 2). In fact, backbone

root-mean-square deviations from the initial structure are below 2.5 Å during the 20 ns MD trajectory, and root-mean-square deviations in the hotspot are below 1.4 Å for the wild type and deviant models. Thus, the mutations do not seem to cause important rearrangements in the enzymatic structure.

We computed changes in the electrostatic properties of the monomer–monomer interface to address the importance of surface complementarity in enzymatic activity using our homology model of mammalian HDC structure. The major features of the predicted quaternary structure of the mammalian enzyme are (Figure 3) as follows: the dimer presents a 2-fold axial symmetry; the first 100 residues of both polypeptides are intertwined; two catalytic sites are conformed within the dimer interface, involving mainly random coiled fragments of the central polypeptide sequence of both monomers.

Residues taking part in the dimer interface were predicted by calculating the differences in the water accessibility scores of each residue when comparing the monomeric and the dimeric models. Water accessibility values decreasing by more than 12 Å² after dimerization are the following: S5, Y7, Y10, Q11, K15, M17, V18, Y20, I21, Y24, L25, R31, P35, V37-R43, I46, S48, A50, P54, D55, W57, I60, I64, I68, M69, G71-Q76, Y83, Y84, A86, T88, L93, L94, D96-L98, D100-L105, F107-S111, P113, E117, L118, M120, N121, D124, W125, K128, D134, H139-P141, R151, T152, S154, E155, T157, L158, L161, L162, R165, D180, E181, S182, N185, A186, A190, A192, H197, S198, V200-F213, E225, F243, T251, K308, H313-D315, F331-V333, P335-Y337, R339, H340, N342, V345, T347, M350, I354-R359, W366, F367, R370, S371, E424, K428, F437, I439, P440, and T442. They map the dimerization surface. From these data, it can be deduced that dimerization mainly involves residues of the amino-terminus, up to residue 213, and those between positions 308 and 371 of each monomer. The dimerization surface and the location of the active

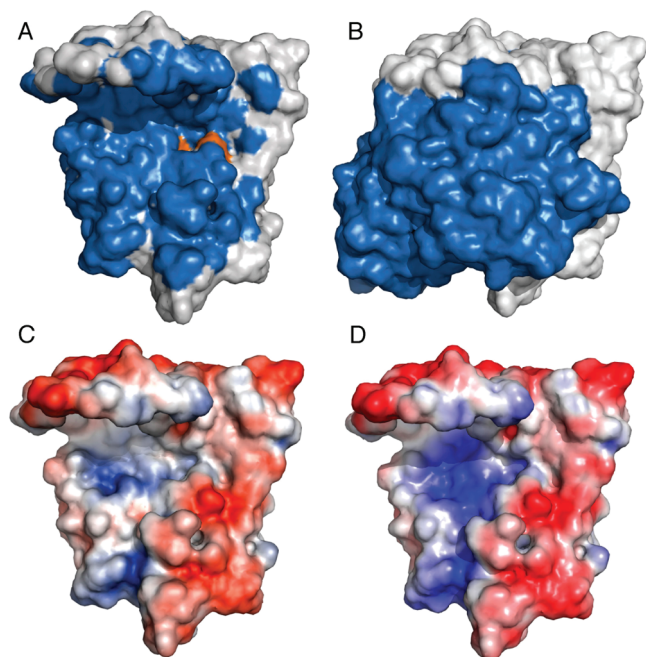


Figure 3. Dimerization surface and electrostatic potential maps. The dimerization surface is shown in dark blue, and the active site is colored in orange, mapped by K308 and H197 (A). Quaternary structure of rHDC: one subunit is colored in dark blue, and the other is colored in white (B). The lower panels show the surface representations of the electric potential, for the wild-type (C) and the hotspot mutant (D). Color range from deep red to deep blue corresponds to the range in values of electrostatic potential from -3.1 to $+3.1$ kT/e , where k is the Boltzmann constant, T is the absolute temperature, and e is a proton's charge.

site (mapped by K308 and H197) are shown in panel A of Figure 3. K308 is the residue responsible for the covalent PLP binding during internal aldimine formation, and H197 seems to stabilize the pyridine ring of the cofactor, not only in HDC but also in other homologous enzymes.^{26–28} Both residues, colored in orange in Figure 3A, indicate the position of the PLP-binding site.

Protein–protein interaction surfaces are geometrically complementary. In nonpermanent complexes, where each component can exist in solution, electrostatic contacts direct protein–protein interaction, while in permanent complexes hydrophobic contacts are dominant.²⁹ Electrostatic complementarity between interacting proteins is also generally assumed³⁰ despite the generally low and often unfavorable contribution of electrostatics to the assembly of a complex.²²

Mammalian HDC is proposed as a homodimer,^{31,32} and as can be seen in Figure 3, there is important shape complementarity. Most of the hydrophobic surface of each monomer is quenched during dimerization. Thus, as expected for a permanent complex, hydrophobic contacts direct monomer–monomer interactions. There is only one electrostatic patch on the dimerization surface of each monomer; it is located next to the PLP binding site of the contrary monomer. This electrostatic hotspot is formed by side chains of residues D96, D100, R151, E155, D315, and R359, all of them exposed to the dimer interface and delineating an area of positive potential (Figure 3C), suggesting a way to stabilize negatively charged PLPs in the active sites.

Because both monomers have an identical patch, they must influence the dimer conformation by minimizing direct contact

between these areas. We checked the role of this patch in stabilizing the quaternary structure, comparing the electrostatic potential in the dimerization surface of the wild-type enzyme and a mutant in which every residue of the electrostatic hotspot was replaced with valine residues. Results are shown in Figure 3C and D. In the hotspot mutant HDC, the positive electrostatic potential patch is considerably larger than that of the wild type enzyme, in accordance with the net elimination of two negative charges. The hotspot mutant HDC cannot avoid the overlapping of these two electropositive regions. Consequently, the relative binding affinity of the hotspot mutant HDC is $\Delta\Delta G^{\text{elec}} = 371.518$ kcal/mol. This large dimer destabilization indicates that the electrostatic patch contributes to stabilizing the dimeric quaternary structure in mammalian HDC.

3.2. Aspartate 315 is Predicted to Play an Important Structural Role. The fact that the enzyme minimizes an unfavorable monomer–monomer electrostatic interaction, provided that it can maintain a polar environment between the two active sites, points to the idea that the enzyme needs these charges. We focused our attention on residue D315 due to the following observations. This negatively charged residue holds a central position in the electrostatic hotspot, and it is located close to the essential residue K308 (10 Å between both α -carbons). Both K308 and D315 take part in the same random-coiled loop (residues 305–317). In spite of their opposite charges, these two residues could not establish a direct interaction because the aromatic group of F314 (of the same polypeptide) prevents such interactions. Consequently, the orientation of the D315 γ -carboxylate group does not seem to be determined by the secondary structure of the fragment but by polarity of the residues in its surroundings. Only four residues, namely, F314 (monomer A), D315 (monomer A), D315 (monomer B), and F314 (monomer B), separate the two K308 residues of the homodimer. Altogether, these considerations allow us to hypothesize an essential role for the carboxylate group of this residue as a stabilizer of the electrostatic hotspot at its closest part to both catalytic centers. Besides its effect on the electrostatic potential, removal of D315 could also disturb the optimal topology of the catalytic site (mainly K308 orientation) and consequently the PLP-binding to the apoenzyme and subsequently the HDC activity.

3.3. Aspartate 315 is Proven to Be Essential for HDC Activity. We generated computationally and experimentally two different substituted mutants called D315V and D315N. In the former, the acid group moiety was substituted by an uncharged group with a similar volume. The second substitution nullified the positive charge of the group. Both versions, together with the wild 1/512 version, were expressed *in vitro* and in *E. coli* and were further purified. In all cases, no enzymatic activity was detectable for both D315 mutants by following decarboxylation of radiolabeled histidine, even when both concentrations of the purified dimeric enzyme were higher than 7 μM and 3.2 mM histidine was used.

In order to test whether D315N contributes to establishing a proper quaternary structure, binding free energies were computed for the four systems (Table 1) as described in the Materials and Methods section.

These results indicate that removal, or even amidation, of the carboxylate group at this position has dramatic consequences on the catalytic site structure.

It was necessary to check whether this effect on the active site could be reproduced by mutation of any other residue as close to the catalytic site as D315. This was tested with a C316A mutant. In addition, this residue is one of the most conserved residues in the 308–316 fragment (apart from the essential K308), not only

Table 1. Electrostatic Binding Free Energies of Wild Type and Mutants HDC^a

	WT	D315N	D315 V	C316 V
ΔG^{elec}	-294.942	-134.669	-161.871	-289.761
$\Delta\Delta G^{\text{elec}}$		160.273	133.071	5.181

^aReported values (kcal/mol) are calculated as described in the Materials and Methods section: $\Delta\Delta G^{\text{elec}} = \Delta G^{\text{elec}}(\text{mutant}) - \Delta G^{\text{elec}}(\text{wt})$. Positive values indicate a dimer stability decrease, whereas negative values indicate a complex stability increase.

among mammalian HDCs but also in other evolutionarily related enzymes. In contrast to D315 mutants, the C/A substitution, which abolishes any polar interaction of this residue, gave rise to an active HDC with a $66 \pm 5\%$ (mean \pm SD, $n = 3$) reduction in activity compared to the wild-type 1/512 version. The calculated relative affinity for C316V (Table 1) together with those calculated for the D315 mutants show a direct relationship between electrostatic binding free energy and enzyme activity. We conclude that a proper electrostatic complementarity between both HDC monomers is essential for a proper quaternary structure of the enzyme and thus for the activity. In addition, D315 plays a fundamental role in stabilizing the electrostatic patch that directs monomer–monomer interactions, and it establishes an electropositive environment in the PLP interaction region of each active site.

3.4. Amidation of the D315 Carboxylate Group Is Enough to Alter Catalytic Site Conformation and PLP Binding.

Because enzymic activity was followed by CO₂ decarboxylation, the D315 mutants seem to lack the ability to release CO₂ (one of the final products). However, we wanted to further check whether the reaction could at least proceed during its first steps (Michaelis complex and/or external aldimine formation). For PLP-dependent enzymes, this kind of information can be obtained from spectroscopic approaches by analyzing absorption and fluorescence spectra of the cofactor during Michaelis complex and PLP–substrate or PLP–product complex formation.^{27,33} In fact, this approach has been used previously for the recombinant wild-type 1/512 version.^{4,6} The substrate analog histidine methyl ester (HisOMe) acts as the substrate during the initial steps and reproduces the spectral changes observed with histidine but blocks the reaction in the external aldimine state (PLP–substrate complex). Thus, any HDC enzyme that could accept the substrate (or the analogue) and proceed along any of these steps would change the shape of its spectrum.

Absorption spectra of wild-type HDC (Figure 4) reproduced those reported previously.⁴ They reveal a major enolimine tautomeric form for the holoenzyme (maximum at 335 nm) and a low percentage of the complex in the ketoenamine tautomeric form (maximum at 420 nm). However, the spectra of the analogue-untreated mutant enzyme were very different to those of the free wild-type holoenzyme and HisOMe could induce no major shift when added up to the final 5 mM concentration. The main absorption bands of D315N are those centered at 360–370 nm and at 470–480 nm. Unusual spike peaks are also found at 380 and 450 nm. Additionally, the shallow valley between the two peaks suggests the presence of absorption peak(s) in this region (around 430 nm). At a glance, the overall shape of the absorption spectrum of D315N suggests that the two main bands correspond to those of the wild-type enzyme. If this is the case, the 360 and 480 nm absorption bands could reflect the enolimine and ketoenamine structures of the Schiff

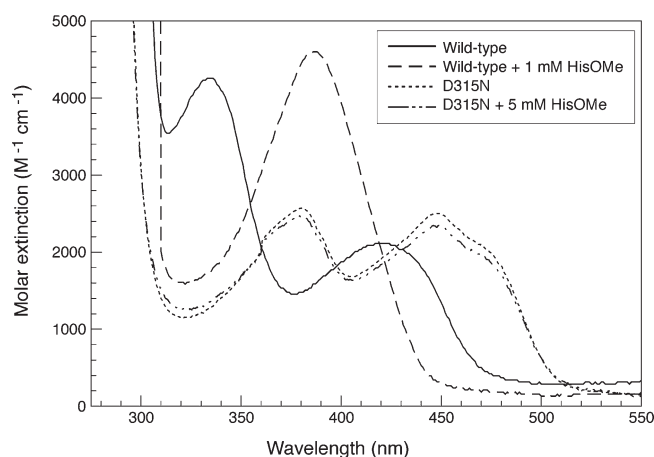


Figure 4. Absorption spectra of the HDC 1/512 wild-type and its mutant D315N in the absence or the presence of the substrate analog histidine methyl ester (HisOMe). Spectra of purified and gel-filtered wild-type 1/512 and D315N HDC were recorded before and 1 h after HisOMe addition.

base, which are 30–50 nm red-shifted by some conformational or environmental factors. As an approach to identify the components of these absorption peaks, we measured the fluorescence (Figure 5A) and excitation (Figure 5B) spectra because different structures of PLP Schiff bases show distinctive fluorescence spectra.^{27,33}

With excitation at 360, 380, 430, 450, and 480 nm, fluorescence was observed with maximum emission wavelengths at 434, 454, 507, 527, and 556 nm, respectively. That is, the emission wavelengths were generally 74–77 nm longer than the excitation wavelength. The observed fluorescence spectra with variable maximum emission wavelengths indicate that the two main absorption bands are each composed of multiple absorption transitions. These transitions may correspond to distinct species. Alternatively, they may be considered to come from similar species with different conformations or placed in different environments.

The 480 nm absorption could initially be considered to correspond to the quinonoid structure that usually absorbs at around 500 nm. However, the fluorescence excitation spectrum for this band showed a broad band ranging between 450 and 500 nm (Figure 5B) and is different from the narrow peak typical for the quinonoid structure. Therefore, we consider that the 480 nm absorption is not the quinonoid intermediate and may be related to the 430 nm absorption, which is thought to be the ketoenamine tautomeric species.

The absorption at 360–380 nm is generally ascribed to the deprotonated Schiff base. The absorption spectrum of D315N, however, does not essentially change with pH. This indicates that the 360–380 nm absorption band of D315N does not come from the deprotonated Schiff base. Again, we consider that this species may be related to the 340 nm absorption, which is interpreted to be the enolimine tautomeric species. That the fluorescence excitation spectra (Figure 5B) showed smooth curves and had no spikes observed for the absorption spectra (Figure 4) indicates that these spikes arise from minor impurities that are difficult to remove and that the absorption bands are largely those of PLP derivatives. From these considerations, we adopt the interpretation that the multiple absorption bands arise from a limited number of PLP species placed at different environments.

For many PLP enzymes, excitation of the enolimine species of the Schiff base results in emission at around 500 nm, identical to that of the emission caused by the excitation of the ketoenamine species, in addition to the emission around 390 nm. The ~ 500 nm emission comes from a species generated by the migration of the proton from O3' (enolimine) to the imine N (ketoenamine) in the excited state, and the ~ 390 nm emission is the direct emission of the enolimine in the excited state before migration of the proton.³⁴ The wild-type HDC shows little emission at 500 nm on excitation of the enolimine species.⁴ In the D315N mutant, however, no emission at around 500 nm was seen upon excitation of the 360 nm absorption species, although the ~ 500 nm emission is clearly seen upon excitation of the 430 and/or 480 nm absorption bands.

In summary, the results obtained with this mutant allow us to suggest that the D315N mutation could strongly alter the status of the PLP Schiff base in the active site, as indicated by the possible existence of ketoenamine and enolimine species placed in multiple microenvironments, lack of the large Stokes shift on

excitation of the enolimine species caused by the proton migration in the excited state, and the shift in tautomeric equilibrium toward the ketoenamine form reflecting a decrease in polarity in its microenvironment. Altogether, we consider that the mutation of the D315 residue should indeed distort the optimum conformation of K308 and the polarity of its environment, thereby decreasing the efficiency of the initial Schiff base formation, as well as the following steps necessary to further the reaction and release the products.

3.5. Comparison among Homologous PLP-Dependent Decarboxylases Allows Us to Suggest New Applications for the Present Findings. To investigate the putative existence of a similar ionic arrangement in other evolutionary enzymes, we initially carried out multiple sequence alignments, including HDCs and DDCs from different living organisms and mammalian GADs. An alignment of representative sequences is shown in Figure 6. Curiously, in mammalian GADs, the D315 homologous position is occupied by a Q residue. As mentioned before, an amide group at this position caused the inactivation of mammalian HDC. Following our hypothesis on the role of the electrostatic hotspot interaction as one of the major structural determinants of mammalian HDC dimerization, the differences observed in the alignment should be accompanied by important differences in the quaternary structural organization of Gram-negative HDCs and GADs with respect to mammalian HDCs and DDCs. In fact, some of the bacterial HDCs have been described as tetrameric enzymes.^{35,36} Some GAD enzymes have been found to be hexameric enzymes.³⁷ To avoid speculation, we do not do any further structural comparison with bacterial and plant PLP-dependent HDCs, or with GADs. However, the present data should provide valuable information for those groups working on the structural characterization of these other related enzymes, which control biogenic amine and alkaloid synthesis in many different organisms where they also play important physiological roles.

In any case, it is tempting to think that synthesis of specific ligands of this ionic motif could constitute a novel possibility for selective intervention of PLP-dependent HDC activities because dimerization (more specifically, the negative charge of the D315 carboxylate group) is critical for the proper conformation of the catalytic site of animal HDC. For instance, this strategy could allow us to inhibit, in a selective manner, animal HDC versus the same enzyme from other sources. This possibility would be relevant, as such a selective inhibition cannot yet be reached by using other previously characterized inhibitors that have the PLP-dependent HDC catalytic center as the target. In fact, HDC from both Gram-negative bacteria and animal sources can coexist

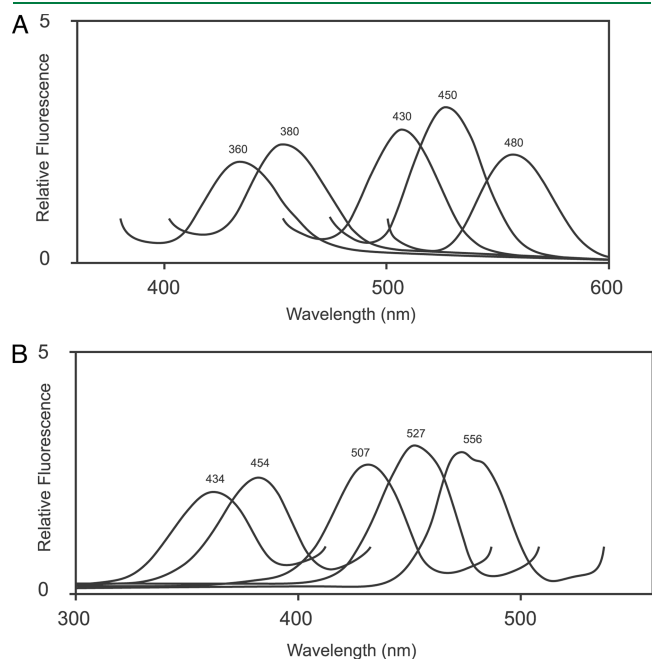


Figure 5. Fluorescence spectra of the mutant version D315N. (A) Fluorescence emission spectra. Excitation wavelengths are indicated on the different peaks. (B) Fluorescence excitation spectra of the peaks shown in panel A. Emission values are indicated on the respective excitation peaks.

rat HDC	96	DMLAD	151	RTVSE	308	KWMMVHFDC	358	RRFRSIK
human HDC	93	DMLAD	148	STVSE	305	KWMMVHFDC	355	RRFRSVK
rat DDC	92	DMLCG	146	GSASE	303	KWLLVNFDC	355	RRFRSLK
pig DDC	92	DMLCG	146	GSASE	303	KWLLVNFDC	355	RRFRSLK
<i>Drosophila</i> HDC	92	DMLAD	147	TTASE	304	KWLMVHFDA	354	RRFRALK
<i>Lycopersicon</i> HDC	49	PLLQF	95	SGGTE	222	KFLGCPMSC	281	NGFTPIF
<i>Enterobacter</i> HDC	40	RFLRF	90	NGGTE	232	KMIGSPIPC	272	NGHTPLM
rat GAD1	202	EWLTS	249	PGGAI	404	KMMGVLLQC	456	RHVDIFK
rat GAD2	194	DWLTG	241	PGGAI	396	KMMGVPLQC	448	RHVDVFK
<i>E. coli</i> GAD	129	ACMLG	161	P---	276	KFGLAPLGC	323	---QVIA

Figure 6. Alignment of fragments homologous to those of rat HDC that contain the ionic residues mentioned in the text. In boxes, the most relevant rat HDC residues mentioned in the text and their identical counterparts in other homologous L-aADCs are highlighted. The first residues of each homologous fragment are numbered for each protein.

in the same physiological system (for instance, in the gastrointestinal track).

On the other hand, it is noteworthy that a similar but larger electrostatic hotspot is also observed in the X-ray structure of pig DDC. This electrostatic hotspot involves the following ionic residues of both DDC monomers: D92, E150, D310, R356, and R358, which are exactly the counterparts of D96, E155, R359, and R361 in rat HDC (Figure 6). Therefore, HDC and DDC also seem to share this dimerization motif, as occurs with other structural and functional characteristics. It has been suggested that the side chain of D310 of DDC could establish hydrogen bonds important for the right conformation of the K303-containing loop.³⁸ The occurrence of these hydrogen bonds is indeed supported by our work. Nevertheless, the present work shows that the role of D315, or its counterparts in the other homologous enzymes, is more drastic than a simple local structural distortion of weak electrostatic interactions, as the lack of these carboxylate groups could also affect the whole arrangement of the dimerization interface and the dynamics of these surfaces, which has been demonstrated to occur, at least during HDC reaction.

The electrostatic hotspot studied here adds to other structural and functional parallelisms between mammalian HDC and DDC, including sequence identity, tautomeric forms of the holoenzyme, and quaternary structure. But there are also slight structural differences that lead finally to important functional differences between both enzymes. These include the higher catalytic efficiency and less stringent substrate specificity of the latter when compared to mammalian HDCs. The slight differences between them could be responsible for any functional differences, and testing this hypothesis would need further work. In any case, the present results should also be of interest for groups working on the molecular bases of dopamine and serotonin synthesis. As far as we know, this structural characteristic of DDC has not been mentioned so far.

4. CONCLUDING REMARKS

The present work was designed to analyze the dimer interface of mammalian HDC. The enzyme prevents direct interaction between the electrostatic hotspots of both monomers because they are in a mainly hydrophobic dimerization surface and show electrostatic repulsion. Some of the ionic residues participating in the hotspot (especially D315) are located just in between the two catalytic sites, establishing an electropositive environment that can anchor PLP to each active site. In addition to the most exposed charged moieties, other thiol and hydroxyl groups and charged residues can contribute to the stabilization of the polar patch. It is tempting to hypothesize that this part of the protein could suffer rearrangements during the different stages of the reactions, thereby contributing to the conformational change that has been previously observed from biophysical approaches. These findings can provide valuable information for the full characterization of this poorly understood mammalian enzyme and also for DDC, an enzyme producing other biogenic amines that also has physiological and pharmacological importance. This ionic motif does not seem to be shared by other PLP-dependent L-aADCs, such as the bacterial PLP-dependent HDC, providing insight for developing selective inhibitors that are able to distinguish between these two enzymes sharing both substrates and cofactors.

AUTHOR INFORMATION

Corresponding Author

*Phone: +34-952131674. Fax: +34-952132000. E-mail: kika@uma.es.

Present Addresses

[†]Department of Medicine, Veterans Affairs McGuire Medical Center/Virginia Commonwealth University, Richmond, Virginia 23249, United States.

Author Contributions

[‡]Both authors have contributed equally to the present work.

ACKNOWLEDGMENT

The authors thank Dr. Ignacio Tuñón and Dr. Javier Ruiz-Pernía from Universitat de València and Dr. Sergio Martí from Universitat Jaume I for their valuable advice and computational support. This work was supported by Grant SAF2008-2522 (Ministerio de Ciencia e Innovación, Spain), Grant BIO-267 from Junta de Andalucía, and funds from Fundación Ramón-Areces. CIBERER is an initiative of the ISCIII.

ABBREVIATIONS

3D, three-dimensional; DDC, aromatic L-amino acid decarboxylase or DOPA decarboxylase (EC 4.1.1.28); DOPA, L-3,4-dihydroxyphenylalanine; GAD, glutamate decarboxylase (EC 4.1.1.15); HDC, histidine decarboxylase (EC 4.1.1.22); HisOMe, histidine methyl ester; L-aADCs, L-amino acid decarboxylases; MD, molecular dynamics; PLP, pyridoxal 5'-phosphate; rms, root-mean-square deviations; UV/vis, ultraviolet/visible

REFERENCES

- (1) Ohmori, E.; Fukui, T.; Imanishi, N.; Yatsunami, K.; Ichikawa, A. *J. Biochem. (Tokyo)* **1990**, *107*, 834–9.
- (2) Taguchi, Y.; Watanabe, T.; Kubota, H.; Hayashi, H.; Wada, H. *J. Biol. Chem.* **1984**, *259*, 5214–21.
- (3) Fleming, J. V.; Wang, T. C. *J. Biol. Chem.* **2003**, *278*, 686–94.
- (4) Olmo, M. T.; Sanchez-Jimenez, F.; Medina, M. A.; Hayashi, H. *J. Biochem. (Tokyo)* **2002**, *132*, 433–9.
- (5) Moya-Garcia, A. A.; Ruiz-Pernia, J.; Marti, S.; Sanchez-Jimenez, F.; Tunon, I. *J. Biol. Chem.* **2008**, *283*, 12393–401.
- (6) Rodriguez-Caso, C.; Rodriguez-Agudo, D.; Moya-Garcia, A. A.; Fajardo, I.; Medina, M. A.; Subramaniam, V.; Sanchez-Jimenez, F. *Eur. J. Biochem.* **2003**, *270*, 4376–87.
- (7) Ghosh, A. K.; Hirasawa, N.; Ohtsu, H.; Watanabe, T.; Ohuchi, K. *J. Exp. Med.* **2002**, *195*, 973–82.
- (8) Graff, L.; Frungieri, M.; Zanner, R.; Pohlner, A.; Prinz, C.; Gratzl, M. *Am. J. Pathol.* **2002**, *160*, 1561–5.
- (9) Nathan, C. *Nature* **2002**, *420*, 846–52.
- (10) Medina, M. A.; Urdiales, J. L.; Rodriguez-Caso, C.; Ramirez, F. J.; Sanchez-Jimenez, F. *Crit. Rev. Biochem. Mol. Biol.* **2003**, *38*, 23–59.
- (11) Pino-Angeles, A.; Morreale, A.; Negri, A.; Sanchez-Jimenez, F.; Moya-Garcia, A. A. *Proteins* **2010**, *78*, 154–61.
- (12) DeLano, W. L. *The PyMOL Molecular Graphics System*; DeLano Scientific: San Carlos, CA, 2002.
- (13) Kabsch, W.; Sander, C. *Biopolymers* **1983**, *22*, 2577–637.
- (14) Dolinsky, T. J.; Nielsen, J. E.; McCammon, J. A.; Baker, N. A. *Nucleic Acids Res.* **2004**, *32*, W665–7.
- (15) Li, H.; Robertson, A. D.; Jensen, J. H. *Proteins* **2005**, *61*, 704–21.
- (16) Field, M. J. *A Practical Introduction to the Simulation of Molecular Systems*; Cambridge University Press: New York, 1999.

- (17) Phillips, J. C.; Braun, R.; Wang, W.; Gumbart, J.; Tajkhorshid, E.; Villa, E.; Chipot, C.; Skeel, R. D.; Kalé, L.; Schulten, K. *J. Comput. Chem.* **2005**, *26*, 1781–1802.
- (18) MacKerell, A. D.; Bashford, D.; Bellott, D.; Dunbrack, R. L.; Evanseck, J. D.; Field, M. J.; Fischer, S.; Gao, J.; Guo, H.; Ha, S.; Joseph-McCarthy, D.; Kuchnir, L.; Kuczera, K.; Lau, F. T. K.; Mattos, C.; Michnick, S.; Ngo, T.; Nguyen, D. T.; Prodhom, B.; Reiher, W. E.; Roux, B.; Schlenkrich, M.; Smith, J. C.; Stote, R.; Straub, J.; Watanabe, M.; Wiórkiewicz-Kuczera, J.; Yin, D.; Karplus, M. *J. Phys. Chem. B* **1998**, *102*, 3586–3616.
- (19) Fogolari, F.; Brigo, A.; Molinari, H. *J. Mol. Recognit.* **2002**, *15*, 377–92.
- (20) Baker, N. A.; Sept, D.; Joseph, S.; Holst, M. J.; McCammon, J. A. *Proc. Natl. Acad. Sci. U. S. A.* **2001**, *98*, 10037–41.
- (21) Sheinerman, F. B.; Norel, R.; Honig, B. *Curr. Opin. Struct. Biol.* **2000**, *10*, 153–9.
- (22) Schutz, C. N.; Warshel, A. *Proteins* **2001**, *44*, 400–17.
- (23) Karp, D. A.; Gittis, A. G.; Stahley, M. R.; Fitch, C. A.; Stites, W. E.; Garcia-Moreno, E. B. *Biophys. J.* **2007**, *92*, 2041–53.
- (24) Sharp, K. A.; Honig, B. *Annu. Rev. Biophys. Biophys. Chem.* **1990**, *19*, 301–32.
- (25) Engel, N.; Olmo, M. T.; Coleman, C. S.; Medina, M. A.; Pegg, A. E.; Sánchez-Jiménez, F. *Biochem. J.* **1996**, *320*, 365–8.
- (26) Burkhard, P.; Dominici, P.; Borri-Voltattorni, C.; Jansonius, J. N.; Malashkevich, V. N. *Nat. Struct. Biol.* **2001**, *8*, 963–7.
- (27) Hayashi, H.; Mizuguchi, H.; Kagamiyama, H. *Biochemistry* **1993**, *32*, 812–8.
- (28) Nishino, J.; Hayashi, H.; Ishii, S.; Kagamiyama, H. *J. Biochem. (Tokyo)* **1997**, *121*, 604–11.
- (29) Heifetz, A.; Katchalski-Katzir, E.; Eisenstein, M. *Protein Sci.* **2002**, *11*, 571–87 and references therein.
- (30) Jones, S.; Thornton, J. M. *Proc. Natl. Acad. Sci. U. S. A.* **1996**, *93*, 13–20.
- (31) Moya-Garcia, A. A.; Medina, M. A.; Sanchez-Jimenez, F. *Bioessays* **2005**, *27*, 57–63 and references therein.
- (32) Dartsch, C.; Chen, D.; Persson, L. *Regul. Pept.* **1998**, *77*, 33–41.
- (33) Metzler, C. M.; Harris, A. G.; Metzler, D. E. *Biochemistry* **1988**, *27*, 4923–33.
- (34) Zhou, X.; Toney, M. D. *Biochemistry* **1999**, *38*, 311–20.
- (35) Guirard, B. M.; Snell, E. E. *J. Bacteriol.* **1987**, *169*, 3963–8.
- (36) Tahanejad, F. S.; Naderi-Manesh, H.; Habibinejad, B.; Mahmoudian, M. *Eur. J. Med. Chem.* **2000**, *35*, 567–76.
- (37) Capitani, G.; Tramonti, A.; Bossa, F.; Grutter, M. G.; De Biase, D. *FEBS Lett.* **2003**, *554*, 41–4.
- (38) Poupon, A.; Jebai, F.; Labesse, G.; Gros, F.; Thibault, J.; Mormon, J. P.; Krieger, M. *Proteins* **1999**, *37*, 191–203.

A High-Throughput Steered Molecular Dynamics Study on the Free Energy Profile of Ion Permeation through Gramicidin A

Toni Giorgino* and Gianni De Fabritiis*

Computational Biochemistry and Biophysics Laboratory (GRIB-IMIM), Universitat Pompeu Fabra, Barcelona Biomedical Research Park (PRBB), C/Doctor Aiguader 88, 08003 Barcelona, Spain

ABSTRACT: Steered molecular dynamics (SMD) simulations for the calculation of free energies are well suited for high-throughput molecular simulations on a distributed infrastructure due to the simplicity of the setup and parallel granularity of the runs. However, so far, the computational cost limited the estimation of the free energy typically over just a few pullings, thus impeding the evaluation of statistical uncertainties involved. In this work, we performed two thousand pulls for the permeation of a potassium ion in the gramicidin A pore by all-atom molecular dynamics in order to assess the bidirectional SMD protocol with a proper amount of sampling. The estimated free energy profile still shows a statistical error of several kcal/mol, while the work distributions are estimated to be non-Gaussian at pulling speeds of 10 Å/ns. We discuss the methodology and the confidence intervals in relation to increasing amounts of computed trajectories and how different permeation pathways for the potassium ion, knock-on and sideways, affect the sampling and the free energy estimation.

1. INTRODUCTION

Biologically relevant events often take place at time scales far beyond those accessible by fully atomistic simulations, for example, conduction of ions through narrow channels.^{1–3} A successful approach for describing molecular phenomena at longer time scales is to average out all but a few degrees of freedom of the system by selecting a reaction coordinate. The forces affecting the process are then described as an effective potential of mean force (PMF), i.e., the free energy profile along the reaction coordinate.^{4–6} The PMF can, in principle, be computed by sampling the equilibrium statistical distribution of the system. However, the time required for the system to cross high free energy barriers may be long enough to make the computation infeasible.

This problem has been successfully addressed with biasing protocols,^{7,8} such as umbrella sampling (US),⁹ which overcomes this limitation by sampling several biased equilibrium distributions, which are later merged by histogram-based techniques.^{10–13} Jarzynski equation (JE) and Crooks fluctuation theorem (CFT) equalities showed that the PMF can also be recovered from nonequilibrium steered molecular dynamics.^{14,15} Steered molecular dynamics (SMD) is a well-known computational protocol to exploit nonequilibrium sampling, in which the application of time-dependent biasing forces guides the system according to a predefined protocol.^{16,17} In SMD experiments, several pulls are simulated in one (forward)^{15,18} or two (forward and reverse) directions.^{14,19–21}

A number of previous studies have used SMD simulations to compute free energy profiles on realistic biomolecules. The JE applied to one-directional (forward only) SMD experiments has been used by several authors to compute the free energy profile in large biomolecular systems. Among the most recent works, Cuendet et al.²² used two groups of $n \sim 150$ single directional trajectories (total sampled time of approximately 2 μ s) to compute the PMF of the T cell receptor with a major histocompatibility

complex peptide (TCR-pMHC) complex and a mutant. Martin et al.²³ used single directional SMD on a large system to compute the energetics of translocation of a polynucleotide through a nanopore. The pullings were conducted with various parameters, and the PMF curves computed on 2–6 samples. Liu et al.²⁴ studied the permeation of Na⁺ through gramicidin A (gA) with $n \approx 8$ single directional trajectories. Zhang et al.²⁵ used $n \sim 35$ trajectories and four different computational methods based on the JE to compute the unbinding of acetylcholine from the α -7 nicotinic receptor along four different paths. Jensen et al. computed the energetics of sugar permeation through lactose permease²⁶ and glycerol through aquaglyceroporin,²⁷ respectively, via four SMD runs with cumulant expansion. Comparatively, fewer works have discussed the use of bidirectional pulling experiments in large proteins. De Fabritiis et al.²⁸ computed the PMF in gA with 25 pulls in each direction. Forney et al.¹⁹ computed the PMF of gA, as well, with 10 pulls in each direction comparing various ionic strengths and backbone restrain types. Due to limitations in computational resources, most studies could only sample a low number of trajectories and were therefore unable to assess the impact of increased sampling on the precision of the PMF profiles.

Here, we expand the amount of sampling with respect to previous bidirectional SMD studies by almost two orders of magnitude in a realistic system, the gA dimer embedded in a membrane and explicit solvent, to test the methodology in a properly sampled system. Gramicidin A (see Figure 1) is a helical antibacterial dimer (15 amino acids each) which increases permeability of biological membranes to inorganic ions.²⁹ The backbone of the gA dimer forms a narrow pore, allowing a single file of water molecules (or potassium ions) to fill it. Due to the diameter of the pore, the transport of a single ion drags with it a

Received: December 9, 2010

Published: April 27, 2011

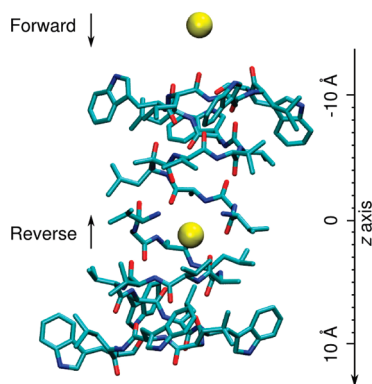


Figure 1. Structure of the gramicidin A dimer, with the starting K^+ ion positions for the forward and reverse steered molecular dynamics runs (yellow). In the former, the cation is pushed from the outside toward the inside of the channel (z increasing from -15 toward 0 Å). In the reverse simulations, the ion is pulled along the time-reversed path. The z axis runs through the center of the pore. Lipid bilayer (117 DMPC molecules), water (8668 molecules), and other solvated ions have been omitted for clarity.

column of six to nine water molecules in a single file, reducing drastically the possibility that water molecules slip past each other.³⁰ The small size and the early availability of its structure made gA a frequently used model for a membrane channel.^{31,32} Despite its simplicity, permeation is not so well reproduced computationally; several studies reported with a barrier to permeation of 10–20 kcal/mol, several kcal/mol higher than the experimental one.^{33,34} The barrier height was recently shown to be much improved with the use of a polarizable force field.³⁵

We performed an extensive set of all-atom molecular dynamics (MD) experiments on the gA channel³⁶ and computed the PMF from bidirectional pulling experiments^{21,37} using 1000 pulls per direction. Confidence bands for an increasing number of pulls, computed with a variable-size bootstrap procedure, are also presented. The importance of sampling effectively the degrees of freedom orthogonal to the reaction coordinate is well illustrated by two permeation pathways shown by the potassium ion in the interface between the two monomers of gA with different free energy profiles.

2. MATERIALS AND METHODS

2.1. The Potential of Mean force. The PMF is a convenient description of the energetics of the system obtained integrating out all of the degrees of freedom with the exception of one reaction coordinate, $z = z(\mathbf{R})$, which should capture the interesting features of the system. The PMF $G(z)$ would then be

$$e^{-\beta\Delta G(z')} = \frac{\int d\mathbf{R}d\mathbf{P}\delta(z(\mathbf{R}) - z') \exp(-\beta H)}{\int d\mathbf{R}d\mathbf{P} \exp(-\beta H)}$$

where $H = H(\mathbf{R}, \mathbf{P})$ is the Hamiltonian of the system, $\mathbf{R} = (\mathbf{r}_1, \dots, \mathbf{r}_N)$, $\mathbf{P} = (\mathbf{p}_1, \dots, \mathbf{p}_N)$ are the positions and momenta of the N atoms, $\delta(\cdot)$ is the Dirac delta function, and $\beta = 1/(k_B T)$, where k_B is the Boltzmann constant and T the temperature of the system.

The Crooks fluctuation relation^{18,38,39} allows one to compute the equilibrium free energy difference ΔG between two states “0”

and “1” described by two Hamiltonians H_0 and H_1 as

$$\frac{P_F(+\beta W)}{P_R(-\beta W)} = \exp(\beta(W - \Delta G)) \quad (1)$$

where W is the external work done on the system by forcing it to change from state 0 to 1, and P_F and P_R are the probability distributions of releasing the work W into the system during a transformation in the forward (F) $0 \rightarrow 1$ and reverse (R) $1 \rightarrow 0$ direction, respectively, in a finite time. The Crooks fluctuation relation is a generalization of the Jarzynski equality (JE):¹⁵

$$\langle \exp(-\beta W) \rangle_F = \exp(-\beta \Delta G)$$

recovered from Crooks fluctuation relation by integrating both sides of eq 1. The Crooks fluctuation relation can be estimated using the optimal Bennett acceptance ratio method.⁴⁰ Interestingly, these two fundamental relations have their equilibrium counterparts obtained for an infinite pulling speed, where CFT resembles an equilibrium relation previously derived by Shing and Gubbins⁴¹ and JE corresponds to Widom’s formula used to compute the chemical potential by test particle insertion⁴² (with well-known poor convergence properties).⁴³ The exponential average of the JE causes few rare low-energy trajectories dominating the estimate of ΔF . When only few trajectories are available, the estimate can be improved using a first-order cumulant expansion, which is exact in the limit when the distribution of W values is Gaussian.^{22,44} The CFT has much better convergence properties than a direct application of JE and was therefore used in a previous study²⁸ and in this study. Both the JE and the CFT have been confirmed experimentally in atomic force and single-molecule pulling experiments.^{18,39}

In this work, we use the estimator for the PMF $G(z)$ proposed by Minh and Adib:²¹

$$e^{-\beta G(z)} = \sum_t \left[\left\langle \frac{n_F \delta(z - z_t) e^{-\beta W_t^a}}{n_F + n_R e^{-\beta(W - \Delta F)}} \right\rangle_F + \left\langle \frac{n_R \delta(z - z_{\tau-t}) e^{\beta W_{\tau-t}^a}}{n_F + n_R e^{\beta(W + \Delta F)}} \right\rangle_R \right] \times \frac{e^{\beta \Delta F_t}}{\sum_t e^{-\beta[V(z;t) - \Delta F_t]}} \quad (2)$$

where n_F and n_R are the number of forward and reverse trajectories, respectively, W_a^b is the partial work performed in the interval between time a and b , τ is the final simulation time, and ΔF_t is the free energy difference between the initial state and the one at time t . In this work we used the implementation of eq 2 provided in the FERBE package.⁴⁵

2.2. Steered MD Protocol. To describe the permeation experiments of one potassium ion through the gA channel, the collective reaction coordinate was assumed to be the z coordinate of one of the cations, which will be called K_{SMD}^+ in the following, i.e., $z(\mathbf{R}) = z_K$. The chosen cation was driven through the channel applying a simple harmonic biasing potential parallel to the z axis producing the force:

$$F_z(z_K, t) = -k(z_K - b(t)) \quad (3)$$

where k is the spring constant, z_K is the instantaneous z coordinate of the ion, and $b(t)$ is the time-dependent equilibrium point for the biasing force. The spring constant $k = 10$ kcal/mol of the biased system was set in order to fulfill the strong spring approximation, $k > \max(2\alpha/\delta z^2, 2U_{\text{max}}/\delta z^2)$, where δz is the spatial resolution that we are seeking for the PMF, U_{max} is the maximum energetic barrier that we expect in δz , and $\alpha \gg 1$. The

biasing position was displaced linearly with time:

$$b(t) = \begin{cases} z_F + vt & (\text{forward}) \\ z_R - vt & (\text{reverse}) \end{cases}$$

The cumulative work profile was obtained by integrating the instantaneous forces over the corresponding interval:

$$W(t) = \int_{t'=0}^t F(t')v dt' \quad (4)$$

with $F(t)$ given by eq 3. For the numerical computation of eq 4, the integral was approximated as a discrete summation over time intervals of length Δt :

$$W_a^b = \sum_{t_j=a}^b -k(z(t_j) - z_0 \mp vt_j)v\Delta t \quad (5)$$

where $t_j = j\Delta t$ is the time corresponding to the j -th interval, z_0 is the starting position of the pull, and the sign is taken according to the pull direction. The z axis was divided in 100 bins, equally spaced over the interval $z = -10, \dots, 0 \text{ \AA}$.

2.3. Preparation of the System. The gA dimer was prepared based on the Protein Data Bank entry PDB:1JNO,⁴⁶ extending the protocol already presented in De Fabritiis et al.²⁸ The structure used in the previous study, comprising the gA dimer and dimyristoylphosphatidylcholine (DMPC) lipid bilayer, was solvated with 8668 TIP3 water molecules and ionized at a ionic strength of 150 mM with 24 pairs of K^+ and Cl^- ions. The final system, comprising 40 410 atoms, was then equilibrated at 1 atm and 305 K with the CHARMM27⁴⁷ force field in the NPT ensemble for approximately 13 ns. The lipid bilayer is oriented in the xy plane, and the z axis goes through the gA pore (see Figure 1). The simulation box resulting from the NPT equilibration was $66.1 \times 65.8 \times 88.9 \text{ \AA}^3$. The preparation runs were performed with the NAMD program,⁴⁸ with particle-mesh Ewald (PME) electrostatics,⁴⁹ rigid bonds, cubic periodic boundary conditions, and a time step of 2 fs.

In order to generate the initial configurations for the forward run, the position of one potassium ion was exchanged with that of a water molecule located close to the entrance of the pore, i.e., approximately at $(0, 0, -15) \text{ \AA}$. For the reverse runs, the ion was exchanged with the water molecule closest to the middle of the channel. The two systems were subject to a further 20 ns of equilibration in the NVT ensemble, while restraining K_{SMD}^+ to its initial position with a spring constant of $10 \text{ kcal/mol/\AA}^2$. After the initial 20 ns of equilibration, the runs were extended further for 20 ns in the same conditions, taking snapshots at 200 ps intervals, thus yielding 100 snapshots for each of the two systems. Each snapshot was used as an initial configuration for 10 SMD runs. Figure 1 shows the ion at the initial positions z_F and z_R for one of the forward and reverse pulls, respectively.

Further analysis on the configurations, e.g., the water occupancy of the pore, and statistics on ion–water–protein relative positions were performed using the scripting facilities of the VMD program.⁵⁰

2.4. Production Runs. We performed 1000 forward and 1000 reverse SMD runs, starting from the 200 distinct initial configurations prepared according to the protocol explained above. The pulling speed and the SMD spring constants were set at $v = \pm 10 \text{ \AA/ns}$ and $k = 10 \text{ kcal/mol/\AA}^2$, respectively. Each SMD run lasted 2 ns, long enough for the pulled ion to reach the starting position for the opposite direction, i.e., until $z < z_R$ for the forward runs and $z > z_F$ for the reverse ones. When the ion was

outside of the channel, a flat bottom potential was applied to keep the ion in line with the pore during the approach (the region $z < 10$ was excluded from the PMF calculation). No constraints were imposed on the ion on the plane orthogonal to z . Only the center of mass of the $C\alpha$ atoms of the pore was restrained to its initial position with a harmonic potential of $100 \text{ kcal/mol/\AA}^2$, to avoid the pore being displaced out of the membrane by the net force applied throughout the simulations. The restrain was just applied to the center of mass, in order not to artificially constrain the local helix radius, interdimer distance, or orientations of the side-chain. The pore was therefore free to expand under the influence of the permeating cation; this flexibility has been shown to play an important role in the permeation energetics.^{19,51,52}

All of the production runs were performed with ACEMD,⁵³ which leverages off-the-shelf accelerated graphic processing units (GPUs) allowing one to achieve approximately 100 ns per day of simulated time on a single GPU for system size of the order of 23 000 atoms, performance decreasing linearly with system size. Production runs have been performed in the constant volume and temperature (NVT) ensemble, Langevin thermostat at 305 K with a relaxation of 0.1/ps, computing the electrostatic interactions with the PME algorithm.⁵⁴ The integration time step was set to 4 fs, enabled by the hydrogen mass repartitioning scheme^{53,55} available in ACEMD. This scheme allows for longer timesteps by using the property that the equilibrium distribution is not affected by individual atom masses provided that the total mass of the system stays the same. Transport properties change by less than 10%, a small amount compared of the errors intrinsic in the TIP3P water model compared to real water.⁵⁵

The runs were performed on a distributed computing grid called GPUGRID.net.⁵⁶ We set up a server based on the Berkeley Open Infrastructure for Network Computing (BOINC) to automatically distribute the runs through the Internet.⁵⁷ In order to be executed remotely, each forward and reverse run was arranged as a separate work unit. As soon as each participating computer finished computing the assigned simulation time, it returned a log file with the trajectory $z(t)$ and the force $F(t)$ exerted on the SMD ion, recorded at intervals of 200 fs. The computational effort used for computing the PMF curves amounted to the generation of $4 \mu\text{s}$ of total simulation data.

2.5. Bootstrapping Procedure. The convergence properties of the PMF were estimated with respect to increased configuration sampling by recomputing the potential curves with a varying sample size bootstrapping technique,⁵⁸ similar to the one employed by Cuendet et al.²² In this procedure we constructed resampled sets of the available bidirectional pulls of increasing cardinality. Each of the available pulling trajectories was randomly taken zero or more times, in order to build a resampled set containing R bidirectional trajectories. A PMF profile was computed considering only the resampled set, and the PMF depth was obtained. The process was iterated until B bootstrapped replicas were obtained, finally yielding the standard deviation of the PMF depth, $\sigma(R)$. The procedure was repeated for resampled sets of sizes $R = 10, 50, 100, 250, 500, 750, n$, with $n = 1000$ being the count of all available pulls. The case $R = 1000$ corresponds to the plain bootstrap procedure, which creates resampled sets as large as the number of trajectories originally available.

3. RESULTS

We computed cumulative work profiles using eq 5 for all of the 2000 pulling experiments. The upper and lower part of Figure 2

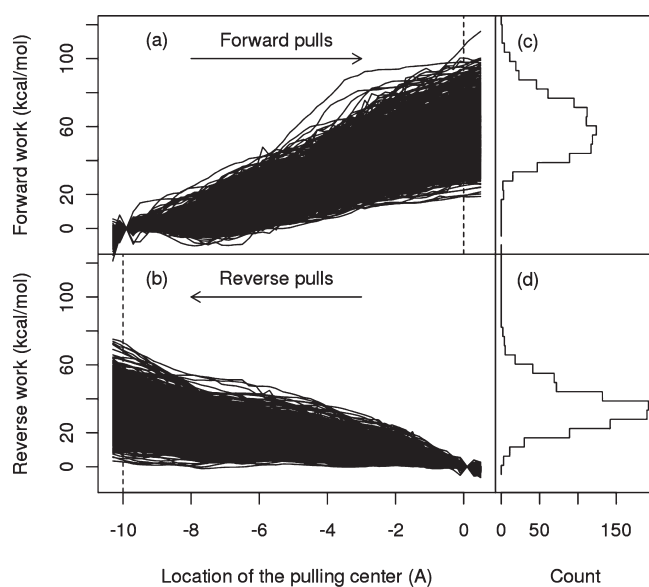


Figure 2. Profiles of the accumulated work $W(z)$ spent to pull the ion inside (a, forward) or outside (b, reverse) the gA channel at 10 Å/ns (1000 pulls per direction). The panels on the right-hand side show the distribution of final work values for the forward (c) and reverse (d) directions, respectively. The mean work performed in the forward direction at the end of the pulls was 55.5 kcal/mol (SD 14.9 kcal/mol); for the reverse direction it was 31.9 kcal/mol (SD 11.2 kcal/mol).

shows the work profiles for the forward (a) and reverse work (b), respectively. For the forward pulls, the work was taken as the one required to push the K_{SMD}^+ ion from $z = -10$ to 0; for the reverse pulls, the end points are reversed. The distributions of final work values for the forward and reverse pulls are shown on the right-hand side of Figure 2, respectively in panels (c) and (d). The mean work performed in the forward direction at the end of the pulls (dashed line) was 55.5 kcal/mol [standard deviation (SD) 14.9 kcal/mol]; for the reverse direction it was 31.9 kcal/mol (SD 11.2 kcal/mol).

3.1. Final Work Distributions. The CFT implies that if the forward work values follow a normal distribution with a variance σ , the reverse work values should also be a Gaussian with the same variance.⁵⁹ To check whether the final work values obtained in the simulations follow a normal distribution, we applied the well-known Shapiro–Wilk normality test.⁶⁰ The test quantifies the probability p that a given set of values could have been taken from a Gaussian distribution (null hypothesis). If the p value computed by the test is smaller than a fixed threshold, usually taken as 0.05, then one concludes that there is strong evidence against normality. The Shapiro–Wilk test rejected the null hypothesis that the final work values follow normal distributions in either direction ($p < 4 \times 10^{-7}$ for both the forward and reverse runs). Given that the pulling speed used here was 10 Å/ns, it is unlikely that the work distribution is Gaussian, at least for a system with enough dissipation like pulling an ion through a pore.

3.2. PMF Profiles. The PMF curves recovered from the bidirectional pulls with the analysis protocol cited above²¹ are shown in Figure 3. For clarity, the potential profile has been symmetrized around the $z = 0$ axis and offset so that the PMF is 0 at $z = -10$ Å. The PMF exhibits a binding site at $z \approx 8.5$ Å and a total barrier height with respect to the bulk of ~ 14 kcal/mol. The

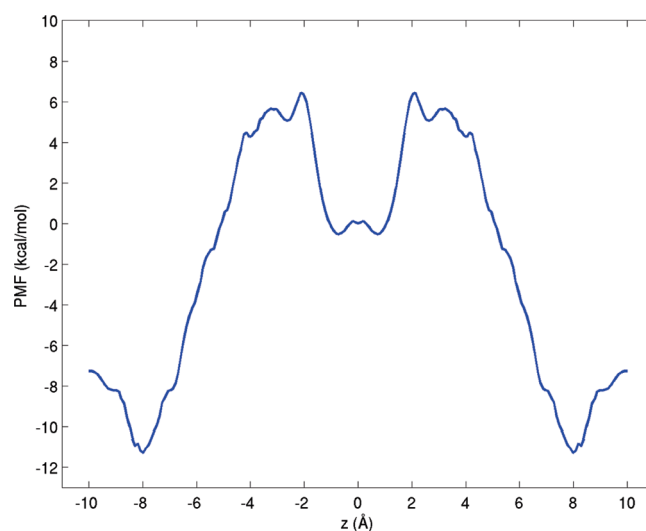


Figure 3. PMF curves for a K^+ atom to cross the gA channel, computed from 1000 steered MD experiments at pulling speed of 10 Å/ns in each direction.

location of the binding site is approximately consistent with the ones reported in the literature.^{19,34,35,61}

The barrier height obtained here is lower with respect to the one computed from the ref 28 data set (19 kcal/mol), obtained from 25 bidirectional pulls. As discussed in the same paper, the induced dipole of the water molecules surrounding the channel provides an important component to the barrier to permeation. In particular, when the K^+ ion is not in the middle of the channel, a large fraction of its electrostatic interaction energy is due to atoms between 6 and 16 Å of distance, i.e., in the second coordination shell. This fact underlines the role played by the water molecules' polarization and the finite time required for their reorientation. Part of the relatively higher barrier to permeation found in this study with respect to others performed with US^{34,61} or SMD¹⁹ may be therefore ascribed to the biological (150 mM) KCl ionic strength employed outside the pore, compared to higher concentrations used in other studies.

Furthermore, the previous study ref 28 sampled only 25 bidirectional pulls and therefore could not provide a measure of the statistical uncertainty. We shall show later that this amount of sampling still incurs a statistical uncertainty of tens of kcal/mol.

3.3. Permeation Pathways. Ion and water permeate through the narrow gA channel as a single file;^{30,61} the sequence of ion and water molecules should therefore be preserved during a pull. However, during some of the reverse (outgoing) pulls, K_{SMD}^+ was observed to exchange places with the preceding water molecule. These trajectories could be distinguished according to the value of the work W cumulated at 300 ps, as shown in Figure 4a. We inspected the structural features of the two groups analyzing a subset of the reverse runs and labeled the trajectories for which $W(300 \text{ ps}) > 10$ kcal/mol as belonging to the “H” group (37% of the trajectories) and “L” otherwise (63%). To analyze the atomistic basis for this difference, we computed 52 additional trajectories recording the state of the system every 10 ps and labeled the pulls in groups H (14 pulls) and L (38 pulls) as above. Inspection of the trajectories in group H revealed that the order in the water file was partially lost around 300 ps after the beginning of the pull (Figure 4b and c). When this event occurred, the K_{SMD}^+ ion overtook the preceding water molecule

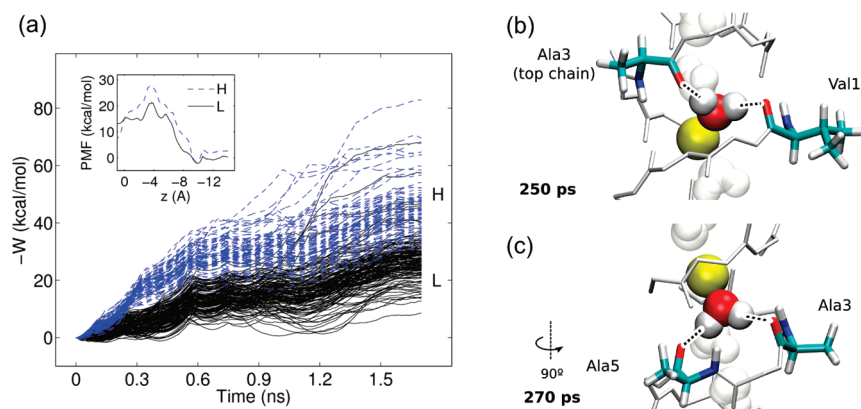


Figure 4. (a) Work profiles for the pulls in groups H (37% of the pulls at $v = 10 \text{ \AA/ns}$) and L (63%), with the distinction drawn at $t = 0.3 \text{ ns}$. Inset: PMF profiles reconstructed considering the pulls of the two groups separately. (b and c) The putative structural explanation of the water file disruption in group H. In these runs the water molecule preceding the pulled ion, W2, formed hydrogen bonds with the carbonyl atoms of the backbone close to the dimer interface. The bonds were most frequently observed with residues Val1 of chain A (about 50% of the runs in group H) and Ala3 of chain B (70%).

(indicated as W2 in Figure 5, left). Conversely, in the pulls in group L, the order of the water file is preserved (Figure 5, right).

The interruption of the water file may be traced back to the formation of hydrogen bonds between W2 and carbonyl atoms in the gA backbone. Figure 4b and c shows the residues whose carbonyl atoms were most often acceptors of a hydrogen atom of W2 at the time when it was overtaken by K_{SMD}^+ . A hydrogen bond was observed with residue Val1 of chain A in about 50% of the runs in group H and with residue Ala3 of chain B in about 70% (chains A and B being the monomer placed at positive and negative z , respectively). Radial and angular cutoffs for hydrogen bonds were taken as 4 \AA and 30° , respectively.

Finally, we performed a control simulation to check the stability of the dimer's embedding in the hydrophobic membrane environment. Specifically, we checked the equilibrium configuration of the dimer when the permeating ion was held close to the dimer interface ($z = 0 \text{ \AA}$) by a constant biasing potential of $k = 10 \text{ kcal/mol/\AA}^2$, analogous to a setup that would be used for a US window in the middle of the channel. A simulation of 50 ns was sufficient to disrupt the pore structure, with water fingering from bulk on the side of the channel in order to balance the ion charge in the middle of the membrane. Thus, the biased equilibrium with the ion forced to stay within the pore is substantially different from the unbiased permeation event, which could imply that SMD is better than US for this system.

3.4. Sampling and Convergence. We characterized the convergence of PMF estimates with respect to increased sampling with two methods. First, the available trajectories were split in nonoverlapping blocks of different sizes, computing the PMF profiles using the data contained in each, assuming $G(0) = 0$. Figure 6a shows the PMF curves obtained using 10 bidirectional trajectories each, i.e., 1–10 (first block), 11–20 (second block), and so on, for a total of 100 profiles. Analogously, Figure 6b shows PMF profiles computed with blocks of 50 bidirectional pulls each (20 profiles), and Figure 6c shows the same using 250 bidirectional pulls at a time (4 profiles). For reference, in panels (a–c) the thick blue line shows the PMF computed with all available data. Increased sampling clearly improves the reproducibility of PMF curves. In particular, it appears that curves obtained with only 10 bidirectional pulls each are affected by a statistical error of the order of 10 kcal/mol, comparable to the PMF depth.

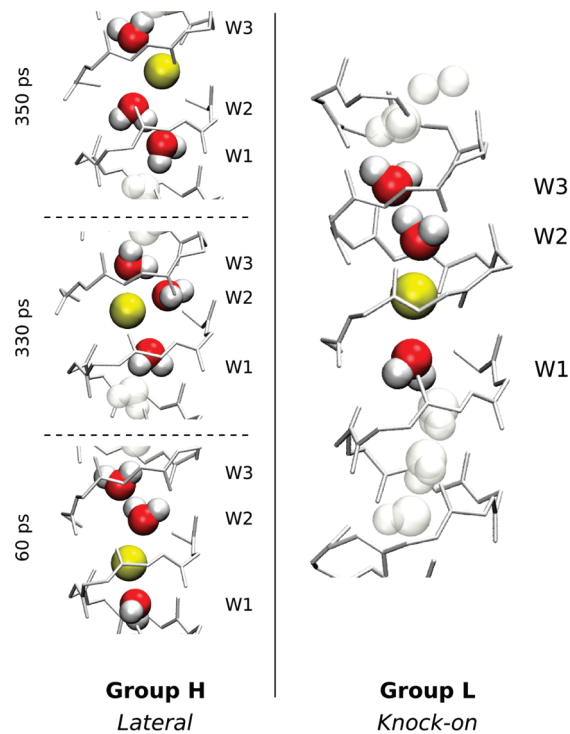


Figure 5. Left: the position of water molecules and K_{SMD}^+ at three snapshots (60, 330, and 350 ps after the beginning of the run) during a representative trajectory of group H. The ion steered upward (yellow) laterally “slips past” the preceding water molecule in the file (W2). The water molecule is held in place by hydrogen bonds with carbonyl oxygens of the backbone and exchanges sides with the ion. Right: during runs in group L, the water filling the channel is displaced together with the ion, preserving the sequence of the file (knock-on).

We used the bootstrapping procedure outlined in Section 2.5 to quantify the effect of increased sampling on the variability of the PMF depth, $G(10) - G(0)$. Figure 6d shows the SD of the PMF depth over the bootstrapped profiles, obtained including different number of trajectories. The results confirm that the SD for $R = 10$ trajectories is of the order of 5 kcal/mol, which decreases to 3 for $R = 50$ and to 2 for $R = 250$. When using all of

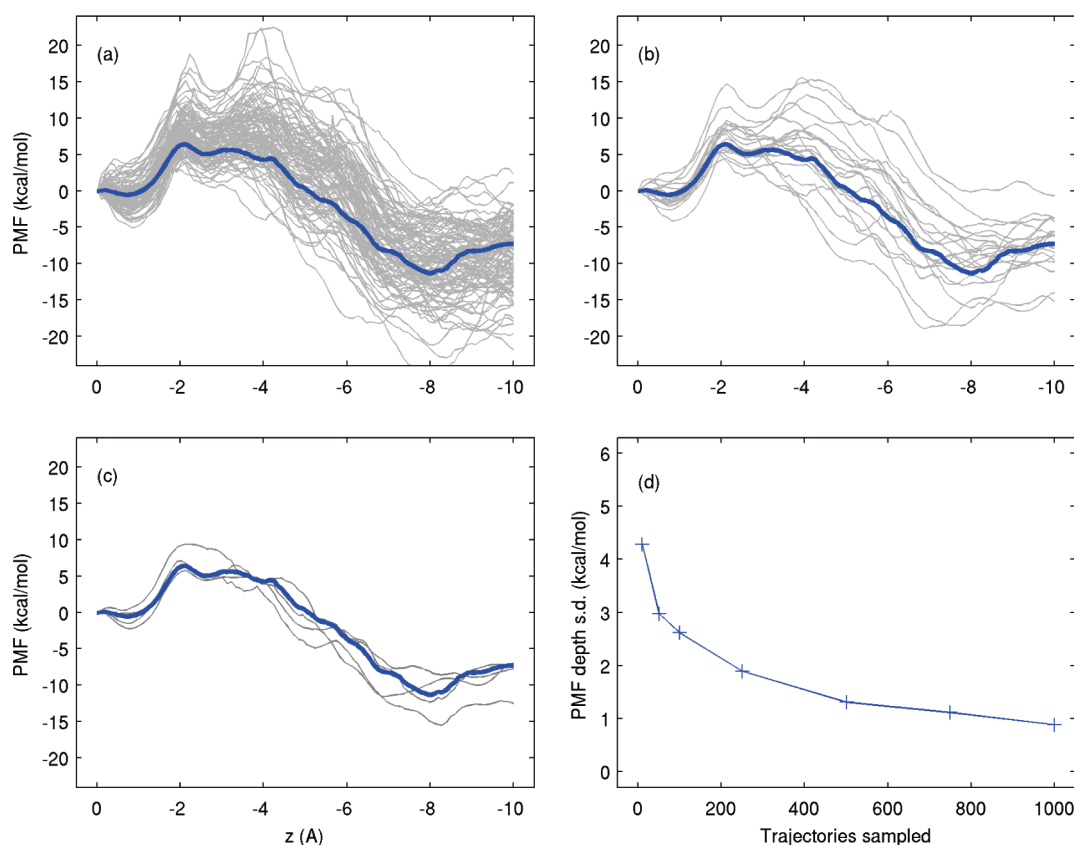


Figure 6. PMF curves computed in nonoverlapping blocks of (a) 10 bidirectional, (b) 50, and (c) 250 pulls. SD of the PMF depth with various amounts of sampled trajectories, obtained by 200-fold bootstrapping (d).

the 1000 available trajectories, the bootstrap analysis estimates a statistical error of 1 kcal/mol.

Finally, we performed two additional simulation sets as controls to check the influence of pulling speed on the PMF depths and profiles. The structures for these runs were taken from the previous study²⁸ and were slightly smaller than the production simulations ($\sim 29\,000$ atoms in total). In the two control sets the ion was pulled at $v = 10$ (221 bidirectional pulls) and 2.5 \AA/ns (171 bipulls), respectively. We used the aforementioned bootstrapping technique to compute the convergence of the PMF depth in the two data sets (Table 1). The final PMF profiles are qualitatively similar with each other and with one obtained from the production simulations. Consistently to what is observed in the production runs, decreasing the statistical error below 2 kcal/mol requires significant computational effort for both pulling speeds. Given that slow pulls require four times as much simulation time as the fast ones, performing SMD at $v = 10 \text{ \AA/ns}$ appears to be more computationally efficient for this system.

4. DISCUSSION AND CONCLUSIONS

In this paper we performed an extensive set of SMD forward–reverse experiments, sampling a simple but realistic biomolecular test system, gA, well beyond the state of the art, to analyze the effect of increased sampling on the precision of the estimate of the PMF of permeation of a potassium ion steered through the channel.

The advent of accelerator processors and codes able to exploit them, like ACEMD for graphical processing units,⁵³ should play

Table 1. Statistical Uncertainty of the PMF Depth Estimate (in kcal/mol), at Ion Pulling Speeds of $v = 10$ and 2.5 \AA/ns , Computed through Bootstrapping for Increasing Number of Pulls^a

pulls	PMF depth CI (kcal/mol)	
	10 \AA/ns	2.5 \AA/ns
10	8.3	8.7
25	5.4	6.9
50	3.9	5.8
100	3.2	4.3
150	2.8	3.9
171	—	3.6
221	2.5	—

^aThe figures show the width of the 68% confidence interval (CI), matching a $1\text{-}\sigma$ interval around the mean. Computation of each of the slower pulls requires four times the computational effort of a fast one.

an important role in reducing sampling limitations to obtain free energy estimates up to the accuracy of the force fields. The SMD protocol is well suited for high-throughput molecular simulations in distributed computing infrastructures, like GPUGRID. Still, considering the particle being steered, the case of ion permeation through gA is a relatively simplistic test case. In particular, a single ion does not have orientational nor conformational degrees of freedom; this is not the case when dealing with generic ligands, whose internal degrees of freedom have to be sampled as well.

The scientist has to prepare two initial systems (forward and reverse) from which many simulations are spawned. Umbrella sampling offers a similar degree of parallelism, as long as several uncorrelated configurations are generated to start each US window or a sufficient equilibration time (100 ns or more) is allowed for each window.⁵⁶ US simulations with stratification of windows showed much less variability than the one reported here for SMD, but the question remains of how much is actually due to poorer sampling. As each US window is starting from a single initial configuration, the US protocol is averaging the effective potential on a small area of the configurational space close to it. If multiple configurations are used, as in ref 56, similar levels of fluctuations in the free energy are obtained. With US, the method used to generate the initial configurations of the biasing windows has a crucial importance, but it is subject to the specific choice of the scientist; the SMD protocol mitigates the problem of generating initial conditions because better sampling is achieved simply by increasing number of trajectories. However, for gA, the US biased equilibrium with the ion forced to stay within the pore was structurally different from the unbiased configuration and thus probably less representative of a permeation event than a SMD pull.

Finally, the choice of the pulling speed influences the amount of pulls for a fixed computational cost: pulling too fast would produce higher energy pathways but allows for more pulls, while slower pulls would be closer to equilibrium but more computationally demanding. Given that the system is in nonequilibrium, however, there may be regions of the phase space that only become accessible after some transient time, like for the two permeation pathways showed for the potassium ion in gA, and faster pulling speeds may prevent some conformational transitions from happening. Therefore, the preference of SMD versus US is probably system dependent, and the biasing methodology that produces the lesser perturbation compared to the unbiased case should be chosen.

In the case studied here, thousands of pulls were required to reach a statistical precision within 1 kcal/mol. Even though the results were obtained on the basis of extensive experiments on a specific, admittedly simple, system, similar considerations may apply to more complex cases.

AUTHOR INFORMATION

Corresponding Author

*E-mail: toni.giorgino@upf.edu, gianni.defabritiis@upf.edu.

ACKNOWLEDGMENT

The authors would like to thank Dr. S. K. Sadiq, I. Buch, and M. J. Harvey for reading the manuscript. We acknowledge Sony Computer Entertainment, Spain. G.D.F. acknowledges support from the Ramon y Cajal scheme and by the Spanish Ministry of Science and Innovation (ref. FIS2008-01040). T.G. acknowledges support from the Programa Beatriu de Pinós from the Generalitat de Catalunya. This work was partially supported by the virtual physiological human EU network of excellence (VPH-NoE). The authors would like to express a special acknowledgment to the volunteers who contribute to GPUGRID (formerly PS3GRID) distributed computing networks.

REFERENCES

- (1) Allen, T. W.; Baştuğ, T.; Kuyucak, S.; Chung, S.-H. *Biophys. J.* **2003**, *84*, 2159.
- (2) Jordan, P. C. *IEEE Trans. Nanobiosci.* **2005**, *4*, 3.
- (3) Allen, T. W.; Andersen, O. S.; Roux, B. *Biophys. J.* **2006**, *90*, 3447.
- (4) Åqvist, J.; Luzhkov, V. *Nature* **2000**, *404*, 881.
- (5) Treptow, W.; Tarek, M. *Biophys. J.* **2006**, *91*, L81–L83.
- (6) Åqvist, J.; Warshel, A. *Biophys. J.* **1989**, *56*, 171.
- (7) Gervasio, F. L.; Laio, A.; Parrinello, M. *J. Am. Chem. Soc.* **2005**, *127*, 2600–2607.
- (8) Zwier, M. C.; Chong, L. T. *Curr. Opin. Pharmacol.* **2010**, *10*, 745–752.
- (9) Torrie, G. M.; Valleau, J. P. *J. Comput. Phys.* **1977**, *23*, 187.
- (10) Bernèche, S.; Roux, B. *Nature* **2001**, *414*, 73.
- (11) Roux, B. *Comput. Phys. Commun.* **1995**, *91*, 275.
- (12) Kumar, S.; Rosenberg, J. M.; Bouzida, D.; Swendsen, R. H.; Kollman, P. A. *J. Comput. Chem.* **1992**, *13*, 1011.
- (13) Kato, M.; Warshel, A. *J. Phys. Chem. B* **2005**, *109*, 19516.
- (14) Crooks, G. E. *Phys. Rev. E* **2000**, *61*, 2361.
- (15) Jarzynski, C. *Phys. Rev. Lett.* **1997**, *78*, 2690.
- (16) Izrailev, S.; Stepaniants, S.; Isralewitz, B.; Kosztin, D.; Lu, H.; Molnar, F.; Wrigger, W.; Schulten, K. *Steered Molecular Dynamics. In Lecture Notes in Computational Science and Engineering 4*; Deuffhard, P., Hermans, J., Leimkuhler, B., Mark, A. E., Reich, S., Skeel, R. D., Eds.; Springer-Verlag: Berlin, Germany, 1998.
- (17) Isralewitz, B.; Baudry, J.; Gullingsrud, J.; Kosztin, D.; Schulten, K. *J. Mol. Graphics Modell.* **2001**, *19*, 13.
- (18) Hummer, G.; Szabo, A. *Proc. Natl. Acad. Sci. U.S.A.* **2001**, *98*, 3658.
- (19) Forney, M. W.; Janosi, L.; Kosztin, I. *Phys. Rev. E* **2008**, *78*, 051913.
- (20) Kosztin, I.; Barz, B.; Janosi, L. *J. Chem. Phys.* **2006**, *124*, 064106.
- (21) Minh, D. D. L.; Adib, A. B. *Phys. Rev. Lett.* **2008**, *100*, 180602.
- (22) Cuendet, M. A.; Michielin, O. *Biophys. J.* **2008**, *95*, 3575.
- (23) Martin, H. S. C.; Jha, S.; Howorka, S.; Coveney, P. V. *J. Chem. Theory Comput.* **2009**, *9*, 2135.
- (24) Liu, Z.; Xu, Y.; Tang, P. *J. Phys. Chem. B* **2006**, *110*, 12789.
- (25) Zhang, D.; Gullingsrud, J.; McCammon, J. A. *J. Am. Chem. Soc.* **2006**, *128*, 3019.
- (26) Jensen, M. O.; Yin, Y.; Tajkhorshid, E.; Schulten, K. *Biophys. J.* **2007**, *93*, 92.
- (27) Jensen, M. O.; Park, S.; Tajkhorshid, E.; Schulten, K. *Proc. Natl. Acad. Sci. U.S.A.* **2002**, *99*, 6731.
- (28) De Fabritiis, G.; Coveney, P. V.; Villà-Freixa, J. *Proteins* **2008**, *73*, 185.
- (29) Miloshevsky, G. *Biophys. J.* **2004**, *86*, 92.
- (30) Hille, B. *Ion Channels of Excitable Membranes*, 2nd ed.; Sinauer Associates, Inc: Sunderland, Massachusetts, 2001; Chapter 11, p 299.
- (31) Chung, S. H.; Kuyucak, S. *Biochim. Biophys. Acta* **2002**, *1565*, 267.
- (32) Mamonov, A. B.; Coalson, R. D.; Nitzan, A.; Kurnikova, M. G. *Biophys. J.* **2003**, *84*, 3646.
- (33) de Groot, B. L.; Tieleman, D. P.; Pohl, P.; Grubmüller, H. *Biophys. J.* **2002**, *82*, 2934.
- (34) Baştuğ, T.; Kuyucak, S. *J. Chem. Phys.* **2007**, *126*, 105103.
- (35) Patel, S.; Davis, J. E.; Bauer, B. A. *J. Am. Chem. Soc.* **2009**, *131*, 13890–13891.
- (36) Andersen, O. S.; Koeppe, R. E., II; Roux, B. *IEEE Trans. Nanobiosci.* **2005**, *4*, 10.
- (37) Ytreberg, F. M.; Swendsen, R. H.; Zuckerman, D. M. *J. Chem. Phys.* **2006**, *125*, 184114.
- (38) Crooks, G. E. *Phys. Rev. E* **1999**, *60*, 2721.
- (39) Collin, D.; Ritort, F.; Jarzynski, C.; Smith, S. B.; Tinoco, I.; Bustamante, C. *Nature* **2005**, *437*, 231.
- (40) Bennett, C. H. *J. Comput. Phys.* **1976**, *22*, 245.
- (41) Shing, K. S.; Gubbins, K. E. *Mol. Phys.* **1982**, *46*, 1109.
- (42) Delgado-Buscalioni, R.; De Fabritiis, G.; Coveney, P. V. *J. Chem. Phys.* **2005**, *123*, 054105.
- (43) Frenkel, D.; Smit, B. *Understanding Molecular Simulation*, 2nd ed.; Academic Press: San Diego, California, 2001.
- (44) Gore, J.; Ritort, F.; Bustamante, C. *Proc. Natl. Acad. Sci. U.S.A.* **2003**, *100*, 12564.

- (45) Minh, D. D. L. *FERBE: Free Energy Reconstruction from Biased Experiments*, version 0.2; <https://simtk.org/home/ferbe/>. Accessed April 18, 2011.
- (46) Townsley, L. E.; Tucker, W. A.; Sham, S.; Hinton, J. F. *Biochemistry* **2001**, *40*, 11676–11686.
- (47) MacKerell, A. D.; Banavali, N.; Foloppe, N. *Biopolymers* **2000**, *56*, 257.
- (48) Phillips, J. C.; Braun, R.; Wang, W.; Gumbart, J.; Tajkhorshid, E.; Villa, E.; Chipot, C.; Skeel, R. D.; Kalé, L.; Schulten, K. *J. Comput. Chem.* **2005**, *26*, 1781.
- (49) Darden, T.; York, D.; Pedersen, L. *J. Chem. Phys.* **1993**, *98*, 10089–10092.
- (50) Humphrey, W.; Dalke, A.; Schulten, K. *J. Mol. Graphics* **1996**, *14*, 33.
- (51) Bastug, T.; Grayweale, A.; Patra, S.; Kuyucak, S. *Biophys. J.* **2006**, *90*, 2285.
- (52) Corry, B.; Chung, S. *Eur. Biophys. J.* **2005**, *34*, 208.
- (53) Harvey, M. J.; Giupponi, G.; De Fabritiis, G. *J. Chem. Theory Comput.* **2009**, *5*, 1632.
- (54) Harvey, M. J.; De Fabritiis, G. *J. Chem. Theory Comput.* **2009**, *5*, 2371.
- (55) Feenstra, K. A.; Hess, B.; Berendsen, H. J. C. *J. Comput. Chem.* **1999**, *20*, 786.
- (56) Buch, I.; Harvey, M. J.; Giorgino, T.; Anderson, D. P.; Fabritiis, G. D. *J. Chem. Inf. Model.* **2010**, *50*, 397.
- (57) Giorgino, T.; Harvey, M.; De Fabritiis, G. *Comput. Phys. Commun.* **2010**, *181*, 1402.
- (58) Efron, B.; Tibshirani, R. *Stat. Sci.* **1986**, *1*, 54.
- (59) Procacci, P.; Marsili, S.; Barducci, A.; Signorini, G. F.; Chelli, R. *J. Chem. Phys.* **2006**, *125*, 164101.
- (60) Shapiro, S. S.; Wilk, M. B. *Biometrika* **1965**, *52*, 591.
- (61) Allen, T. W.; Andersen, O. S.; Roux, B. *Proc. Natl. Acad. Sci. U.S.A.* **2004**, *101*, 117.

Absolute pK_a Values and Solvation Structure of Amino Acids from Density Functional Based Molecular Dynamics Simulation

Martina Mangold,[†] Leslie Rolland,[‡] Francesca Costanzo,[§] Michiel Sprik,[†] Marialore Sulpizi,[†] and Jochen Blumberger^{*||}

[†]Department of Chemistry, University of Cambridge, Lensfield Road, Cambridge CB2 1EW, United Kingdom

[‡]Departement de Chimie, Ecole Normale Supérieure, 24 rue Lhomond, 75231 Paris Cedex 05, France

[§]Dipartimento di Chimica Fisica e Inorganica, Università di Bologna, Viale Risorgimento 4, I-40136 Bologna, Italy

^{||}Department of Physics and Astronomy, University College London, London WC1E 6BT, United Kingdom

S Supporting Information

ABSTRACT: Absolute pK_a values of the amino acid side chains of arginine, aspartate, cysteine, histidine, and tyrosine; the C- and N-terminal group of tyrosine; and the tryptophan radical cation are calculated using a revised density functional based molecular dynamics simulation technique introduced previously [Cheng, J.; Sulpizi, M.; Sprik, M. *J. Chem. Phys.* **2009**, *131*, 154504]. In the revised scheme, acid deprotonation is considered as a dissociation rather than a proton transfer reaction, and a correction term for treating the proton as a hydronium ion is suggested. The acidity constants of the amino acids are obtained from the vertical energy gaps for removal or insertion of the acidic proton and the computed solvation free energy of the proton. The unsigned mean error relative to experimental results is 2.1 pK_a units with a maximum error of 4.0 pK_a units. The estimated mean statistical uncertainty due to the finite length of the trajectories is ± 1.1 pK_a units. The solvation structures of the protonated and deprotonated amino acids are analyzed in terms of radial distribution functions, which can serve as reference data for future force field developments.

1. INTRODUCTION

The prediction of pK_a values of solvated molecules has attracted much attention in the computational chemistry community over many years.^{1–32} This is not very surprising if one takes into consideration that proton transfer is the most frequently occurring reaction in nature, and an often encountered reaction in technological processes. Protons play an important role in energy conversion in living cells and fuel cells, facilitate ion exchange in biological and synthetic membranes, and catalyze chemical reactions at the active site of proteins and in synthetic reactions. Central to a quantitative characterization of such processes is the knowledge of the pK_a values of the molecules involved, as this quantity determines the protonation state of the system at a given pH as well as the energetics for intra- or intermolecular proton transfer. The ability to predict pK_a values from computation is very important, in particular when the system under consideration is not amenable to experimental measurements.

The majority of pK_a calculations of solvated molecules have been carried out by treating the solute at the QM level, while assuming that the interactions with the environment can be modeled by an electric continuum; see refs 1–18 for a selection of papers that have appeared in the past 10 years. Using thermodynamic cycles, the deprotonation free energy is expressed as the sum of the deprotonation free energy of the molecule in the gas phase and the solvation free energy difference of products (deprotonated acid plus proton) and the reactant (protonated acid). The advantage of such a scheme is that high-level *ab initio* methods can be used to describe the chemical deprotonation step. The disadvantage is that short-range

intermolecular interactions with solvent molecules, such as hydrogen bonds and ion–dipole interactions, are not explicitly accounted for, although they are considered to be particularly important to describe solvation free energies.

In a recent study, a number of QM-continuum protocols for calculation of pK_a values of biologically important carbonic acids have been compared.¹⁶ While none of the standard continuum calculations were reported to give a satisfactory overall performance for neutral and charged acids, it was possible to obtain in some cases good agreement with experimental results by either comparing relative pK_a values of iso-Coulombic deprotonation reactions or by adding explicit solvent molecules in the QM calculation. It was concluded that the consideration of the “real” character of the solvent is of major importance in the future development of solvation models beyond the continuum approximation.

An alternative to QM-continuum computations is the density functional based molecular dynamics (DFMD) calculation of pK_a values.^{25–32} In contrast to QM-continuum methods, in the DFMD approach, both the solute and the solvent are treated at the DFT level of theory, and the deprotonation free energy can be obtained from the statistical mechanics formalism of condensed phase simulation. The advantage of DFMD is that solute–solvent interactions are accounted for at the same QM level of theory, albeit at a higher computational cost and a more restricted choice of the electronic structure method. In early applications, proton transfer free energies were obtained from

Received: December 13, 2010

Published: May 04, 2011

the potential of mean force for transfer of a proton from the solvated acid to a neighboring water molecule.^{25,26} Using this method, the pK_a value of an inorganic acid²⁵ could be calculated to a good degree of accuracy as well as the proton transfer free energy in an enzyme active site.²⁶

More recently, some of us have developed an alternative simulation protocol, by combining DFMD with the thermodynamic integration method (DFMD-TI).^{29–32} Here, the pK_a value is obtained in a two-step process. In the first step, the free energy is calculated for the alchemical transformation of the acidic proton into a dummy atom in the condensed phase by sampling the vertical DFT energy gap for this transformation along DFMD trajectories. In the second reaction step, the free energy for the transfer of the dummy atom into the gas phase is calculated. The absolute deprotonation free energy is the sum of the two contributions, and the pK_a value is the difference in the absolute deprotonation free energy for the acid under consideration and the solvated proton (see section 2 for details). Similar simulation approaches have been carried out before with classical^{19–21} or QM/MM^{22–24} potentials. However, application in the framework of all-QM DFMD remains scarce.

The aim of our present study is three-fold. First, we present a scheme for the DFMD-TI computation of pK_a values that is somewhat different from our previous formulation. Here, we consider deprotonation as a dissociation reaction rather than a proton transfer reaction, and we suggest a correction term for treating the solvated proton as a hydronium ion. Second, we investigate the performance of this method for the prediction of absolute pK_a values of naturally occurring amino acids. In particular, we investigate the relative error of this method with respect to experimental results, and how the achieved accuracy compares with that of typical continuum calculations. Third, as the pK_a calculation requires us to run DFMD of the protonated and deprotonated solute, we provide reference data for the solvation structure of the amino acids in both protonation states. Such structural information is important for the future development of QM/MM models for protein pK_a predictions, where aqueous amino acid solutions serve as reference states. The pK_a calculations carried out for tyrosine and the tryptophan cation radical are similar to the ones of ref 33, where proton transfer coupled reduction potentials of these amino acids are reported.

We find that DFMD-TI in the present form can predict absolute acidity constants of amino acids to an accuracy of ± 2.1 pK_a units, which is comparable to the performance of some of the best QM-continuum calculations carried out recently for a set of similar acids.¹⁷

2. THEORY

2.1. Definition of pK_a Value. We consider the dissociation of an acidic molecule AH in aqueous (aq) solution to the solvated proton $H^+(aq)$, and the conjugate base $A^-(aq)$,



The pK_a value of AH(aq) is defined as the negative logarithm of the equilibrium constant K_a of reaction eq 1:

$$pK_a = -\log K_a \quad (2)$$

$$K_a = \frac{a_{A^-} a_{H^+}}{c^\circ a_{AH}} \quad (3)$$

where a_X is the equilibrium activity of species X, which is equal to the equilibrium concentration for dilute solutions, and $c^\circ = 1 \text{ mol dm}^{-3}$ is the standard concentration.

The aim is the computation of the standard reaction free enthalpy of reaction eq 1, $\Delta_{dp}G^\circ$, related to the equilibrium constant by

$$\Delta_a G^\circ = -k_B T \ln K_a \quad (4)$$

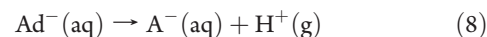
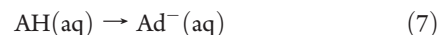
where the subscript “dp” refers to deprotonation. In practice, we neglect the (small) difference between free enthalpies and free energies in condensed phase reactions and formulate a computational scheme for the reaction free energy for deprotonation, $\Delta_a A^\circ$. For this purpose, we split the full reaction eq 1 into two steps. In the first step, the proton is transferred into the gas phase while the conjugate base remains in aqueous solution:



and in the second step the proton is transferred from the gas to the solution phase, the reverse process of the reaction



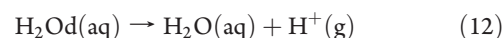
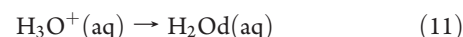
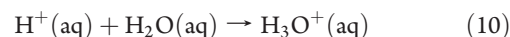
In order to make the reaction eq 5 amenable to DFMD computation, we describe it by a series of two alchemical transformations:



In the reactant state of reaction eq 7, the acidic proton is treated like the rest of the system, at the DFT level of theory. The proton is transformed into a dummy atom in the product state as indicated by the symbol “d”. The dummy atom is connected to A by harmonic spring potentials (see eq 18), but it does not interact with the system otherwise. In reaction eq 8, the artificial spring is removed, and the dummy atom is transferred from the aqueous to the gas phase and transformed back into a proton. The free energy changes of reaction eqs 7 and 8 are denoted as $\Delta_{dp}A_{AH}$ and $-\Delta A_{Ad}$, respectively. When adding a quantum correction for nuclear motion, ΔA_{qc} , one obtains the reaction free energy of reaction eq 5:

$$\Delta_{dp}A_{AH}^\circ = \Delta_{dp}A_{AH} - \Delta A_{Ad} - \Delta A_{qc} \quad (9)$$

The computation of the desolvation free energy of the aqueous proton, reaction eq 6, is complicated by the transient nature of this species. The solvated proton is often modeled as a hydronium ion ($H_3O^+(aq)$), but one should bear in mind that this is only an idealized structure adopted by the proton during its structural diffusion in aqueous solution.³⁴ Thus, we make a clear distinction between the “real” solvated proton $H^+(aq)$ and the idealized hydronium ion. In order to compute the desolvation free energy, we consider the following reaction steps:



In the first step, reaction eq 10, the idealized hydronium ion is “assembled” from the hydrated proton and a water molecule with a reaction free energy of $-\Delta A_{H_3O^+}$. The second and the third

reaction steps, eqs 11 and 12 with reaction free energies $\Delta_{\text{dp}}A_{\text{AH}}$ and $-\Delta A_{\text{H}_2\text{O,d}}$, respectively, are similar to the two reaction steps eqs 7 and 8 with AH replaced by the hydronium ion. The sum of all free energy contributions gives the free energy for desolvation of the aqueous proton:

$$\Delta_{\text{ds}}A_{\text{H}^+}^{\circ} = \Delta_{\text{dp}}A_{\text{H}_3\text{O}^+} - \Delta A_{\text{H}_2\text{O,d}} - \Delta A_{\text{qc}} - \Delta A_{\text{H}_3\text{O}^+} \quad (13)$$

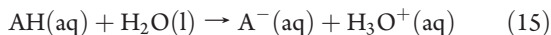
where we have also added a quantum correction term.

Combining eqs 2, 4, 9, and 13, the $\text{p}K_{\text{a}}$ value of AH is given by the difference in the deprotonation free energy of AH and the desolvation free energy of the solvated proton, reaction eqs 5 and 6:

$$\text{p}K_{\text{a}} = \frac{1}{\ln 10 k_{\text{B}} T} (\Delta_{\text{dp}}A_{\text{AH}}^{\circ} - \Delta_{\text{ds}}A_{\text{H}^+}^{\circ}) \quad (14)$$

with $\Delta_{\text{dp}}A_{\text{AH}}^{\circ}$ and $\Delta_{\text{ds}}A_{\text{H}^+}^{\circ}$ computed according to eqs 9 and 13, respectively.

The present definition of $\text{p}K_{\text{a}}$ is somewhat different from the one used previously.^{29–31} Here, we consider acid deprotonation according to Arrhenius as a *dissociation* reaction (eq 1), whereas in previous work we considered it according to Brønsted, as a *proton transfer* reaction:



with equilibrium constant

$$K'_{\text{a}} = \left[\frac{a_{\text{A}^-} a_{\text{H}_3\text{O}^+}}{c^{\circ} a_{\text{AH}}} \right] \quad (16)$$

The subtle difference between the two definitions is that in the Brønsted picture one assumes that the acidic proton is chemically bonded to a solvent molecule forming a solvated hydronium ion, whereas in the Arrhenius picture this assumption is not made. Indeed, the equilibrium constants eqs 3 and 16 differ only by the notation for the proton, a_{H^+} and $a_{\text{H}_3\text{O}^+}$, respectively. While this distinction is of course irrelevant in experiments, it affects the results of computations, where a model for the proton in solution must be chosen. The difference between the two $\text{p}K_{\text{a}}$ definitions is the free energy for assembling the hydronium ion from the solvated proton and a water molecule, $-\Delta A_{\text{H}_3\text{O}^+}$ of reaction eq 10. We will estimate $\Delta A_{\text{H}_3\text{O}^+}$ in section 2.5, after we have described the computation of the other free energy terms that appear in the expressions for $\Delta_{\text{dp}}A_{\text{AH}}^{\circ}$ and $\Delta_{\text{ds}}A_{\text{H}^+}^{\circ}$.

2.2. Free Energy for Alchemical Transformation, $\Delta_{\text{dp}}A_{\text{AH}}$

The free energy for transformation of the proton into a dummy atom, $\Delta_{\text{dp}}A_{\text{AH}}$ of reaction eqs 7 and 11, is computed using Kirkwood's coupling parameter method.³⁵ A mapping potential E_{η} is defined that couples the potential energy surfaces of the reactant and product states.

$$E_{\eta} = (1 - \eta)E_0 + \eta E_1 \quad (17)$$

In eq 17, η is a coupling parameter that takes values from 0 to 1. E_0 is the DFT potential energy surface (PES) of AH(aq) (or $\text{H}_3\text{O}^+(\text{aq})$), and E_1 is the DFT PES of $\text{Ad}^-(\text{aq})$ (or $\text{H}_2\text{O,d}(\text{aq})$) plus the restraining potential V_{r} that keeps the dummy atom attached to A (H_2O).

$$V_{\text{r}} = \sum_{\text{bonds}} \frac{k_{\text{r}}}{2} (r - r_{\text{eq}})^2 + \sum_{\text{angles}} \frac{k_{\theta}}{2} (\theta - \theta_{\text{eq}})^2 + \sum_{\text{dihedrals}} \frac{k_{\varphi}}{2} (\varphi - \varphi_{\text{eq}})^2 \quad (18)$$

The presence of the restraining potential in the product state E_1 allows one to generate positions for insertion of the proton as required for the energy gap calculation according to eq 20. Note that E_0 of the weakly acidic amino acids does not contain the restraining potential V_{r} , whereas E_0 of the hydronium ion does contain V_{r} in order to suppress spontaneous dissociation and proton hopping that would otherwise occur during the DFMD simulation.

The free energy difference between reactant and product described by the PESs E_0 and E_1 , respectively, is the thermodynamic integral:

$$\begin{aligned} \Delta_{\text{dp}}A_{\text{AH}} &= A(\eta = 1) - A(\eta = 0) \\ &= \int_0^1 d\eta \langle \Delta_{\text{dp}}E_{\text{AH}} \rangle_{\eta} \end{aligned} \quad (19)$$

where ΔE is the vertical energy gap

$$\Delta_{\text{dp}}E_{\text{AH}} = E_1 - E_0 \quad (20)$$

and the brackets $\langle \dots \rangle_{\eta}$ denote the usual thermal average on the PES E_{η} . The vertical energy gap eq 20 is sampled along DFMD trajectories on the PES E_{η} . In present calculations, the full thermodynamic integral eq 19 is approximated using Simpson's rule:

$$\begin{aligned} \Delta_{\text{dp}}A_{\text{AH}} &\approx \Delta A_{\text{TP}} \\ &= \frac{1}{6} (\langle \Delta_{\text{dp}}E_{\text{AH}} \rangle_0 + \langle \Delta_{\text{dp}}E_{\text{AH}} \rangle_1) + \frac{2}{3} \langle \Delta_{\text{dp}}E_{\text{AH}} \rangle_{0.5} \end{aligned} \quad (21)$$

and compared to the standard linear response (LR) expression:

$$\Delta_{\text{dp}}A_{\text{AH}} \approx \Delta A_{\text{LR}} = \frac{1}{2} (\langle \Delta_{\text{dp}}E_{\text{AH}} \rangle_0 + \langle \Delta_{\text{dp}}E_{\text{AH}} \rangle_1) \quad (22)$$

The LR approximation is exact if the thermal probability distribution of ΔE is Gaussian, or equivalently, if the root-mean-square fluctuations (rmsf) of the energy gap

$$\sigma_{\eta} = \left(\langle (\Delta_{\text{dp}}E_{\text{AH}} - \langle \Delta_{\text{dp}}E_{\text{AH}} \rangle_{\eta})^2 \rangle_{\eta} \right)^{1/2} \quad (23)$$

are the same for any value of η .

2.3. Free Energy for Dummy Atom Insertion, ΔA_{Ad} . The reaction free energy for the reverse of reactions eq 8 and 12, ΔA_{Ad} , is related to the restraining potential V_{r} by

$$\Delta A_{\text{Ad}} = k_{\text{B}} T \ln \langle \exp(\beta V_{\text{r}}) \rangle_1 \quad (24)$$

Equation 24 is rigorous and can be readily derived from statistical mechanical principles (see the Supporting Information (SI) of this article for a proof). It is the free energy of transforming a free dummy particle confined to the volume $V^{\circ} = 1 \text{ mol}/c^{\circ}$ plus a solvated species A^- at concentration c° and described by the PES $E_1 - V_{\text{r}}$ to the solvated species Ad^- , described by the PES E_1 (that is, with the dummy atom attached to A^- , see eq 12 in the SI). In the derivation of eq 24, the standard concentrations of the aqueous phase and gas phase are assumed to be the same, $c^{\circ} = 1 \text{ mol dm}^{-3}$. A term $k_{\text{B}} T \ln(c^{\circ} RT/p^{\circ})$ has to be added to eq 24 if the conventional standard state of the gas phase is used. The free energy ΔA_{Ad} thus depends on the strength of the dummy potential, and also on the definition of the standard volume V° .

Our previously derived expression for ΔA_{Ad} reads³⁰

$$\Delta A_{\text{Ad}} = -k_{\text{B}} T \ln(c^{\circ} \Lambda_{\text{H}^+}^3 f_{\text{Ad}}) \quad (25)$$

where f_{Ad} is the ratio of the internal gas-phase partition functions of Ad^- and A^- ; $f_{Ad} = q_{Ad}^{int}/q_A^{int}$ with q^{int} the product of electronic, vibrational, and rotational partition functions; and Λ_{H^+} is the thermal wavelength of the proton (1.01 Å at 298 K). In the SI, we show that eq 25 follows from eq 24, if one assumes that the excess chemical potentials of A^- and Ad^- as well as their thermal wavelengths are the same. One can expect that the first approximation is a very good one as long as the presence of the dummy atom does not induce any major changes in the equilibrium structure of the solute. The second approximation is valid if the mass of A is much larger than that of the dummy atom, which is usually the case. As discussed in the SI, we prefer to calculate ΔA_{Ad} according to eq 25, since the MD estimate of the expectation value on the rhs of eq 24 gives very poor results. The ratio of gas-phase partition functions, f_{Ad} , is approximated by the three mode vibrational partition function:³⁰

$$f_{Ad} = \frac{T^3}{\theta_1^{vib} \theta_2^{vib} \theta_3^{vib}} \quad (26)$$

where $\theta_i^{vib} = h\nu_{Ad,i}/k_B$ is the vibrational temperature and $\nu_{Ad,i}$ is the frequency of mode i . The approximation eq 26 is justified when the mass of A is sufficiently large compared to the mass of the dummy atom, so that the vibrations of the latter can be treated as local modes decoupled from the molecular modes of A. The effect of the dummy atom on the inertial tensor used to calculate the rotational partition function is ignored. We have previously shown that under these approximations ΔA_{Ad} is the free energy for confining the free dummy particle from volume V° to the volume $(2\pi)^{3/2} \Delta_1 \Delta_2 \Delta_3$, where $\Delta_i = (k_B T/k_i)^{1/2}$ is the mean square displacement of the local normal mode i of the dummy particle with force constant k_i .³⁰ The same physically appealing picture can be derived from eq 24 (see SI for details). For $f_{H_2O_d}$, eq 26 is not a good approximation. Here, the full classical partition functions of H_2O_d and H_2O have to be calculated. We refer to ref 30 for an explicit expression.

2.4. Quantum Corrections, ΔA_{qc} . The first two terms on the rhs of eqs 9 and 13, $\Delta_{dp} A_{AH} - \Delta A_{Ad}$, are the reaction free energy for the deprotonation reactions eqs 7 and 8 and eqs 11 and 12, if one assumes classical ionic motion. Nuclear quantum effects are expected to be significant, however, because in these reactions three modes of rather high frequency are lost when lifting the proton into the gas phase. We correct for this effect by subtracting the classical vibrational free energy of the acid in the gas phase using the three mode model (ΔA_{cl}^{vib}) and adding the corresponding quantized vibrational free energy (ΔA_{q}^{vib}):

$$\Delta A_{qc}(X) = \Delta A_{q}^{vib}(X) - \Delta A_{cl}^{vib}(X) \quad (27)$$

For $X = AH$,

$$\begin{aligned} \Delta A_{q}^{vib}(AH) &= -k_B T \ln \prod_{i=1}^3 \frac{\exp(-h\nu_{AH,i}/(2k_B T))}{1 - \exp(-h\nu_{AH,i}/(k_B T))} \\ &\approx \sum_{i=1}^3 \frac{1}{2} h\nu_{AH,i} \end{aligned} \quad (28)$$

$$\Delta A_{cl}^{vib}(AH) = -k_B T \ln \prod_{i=1}^3 \frac{k_B T}{h\nu_{AH,i}} \quad (29)$$

where $\nu_{AH,i}$ denotes the three modes of the proton. For the hydronium ion, $X = H_3O^+$, all modes of the solute are taken into account:

$$\Delta A_{q}^{vib}(H_3O^+) = \sum_{i=1}^6 \frac{1}{2} h\nu_{H_3O^+,i} - \sum_{i=1}^3 \frac{1}{2} h\nu_{H_2O,i} \quad (30)$$

$$\Delta A_{cl}^{vib}(H_3O^+) = -k_B T \left(\ln \prod_{i=1}^6 \frac{k_B T}{h\nu_{H_3O^+,i}} - \ln \prod_{i=1}^3 \frac{k_B T}{h\nu_{H_2O,i}} \right) \quad (31)$$

2.5. Dissociation Free Energy of H_3O^+ , $\Delta A_{H_3O^+}$. The free energy for dissociation of the hydronium ion into the solvated proton and a water molecule, the reverse process of reaction eq 10, can be written as follows:

$$\Delta A_{H_3O^+} = k_B T \ln \frac{c^\circ \Lambda_{H^+}^3 \Lambda_{H_2O}^3 q_{H_3O^+}^q}{\Lambda_{H_3O^+}^3 q_{H^+}^q q_{H_2O}^q} \quad (32)$$

where q_X^q is the quantum partition function of the solvated species X after separation of the thermal wavelength Λ_X . The ratio of partition functions on the rhs of eq 32 is difficult to calculate in practice due to the delocalized nature of the solvated proton. To estimate this term, we adopt a mixed quantum-classical scheme, where the hydronium ion is modeled with one quantum proton and two classical protons, $H_2OH_q^+$, interacting with a classical environment. The ratio of partition functions $q_{H_3O^+}^q/q_{H_2O}^q$ is then approximated by an effective quantum vibrational partition function of the single quantum proton, $q_{H^+,eff}^q = q_{H_3O^+}^q/q_{H_2O}^q$:

$$\begin{aligned} \Delta A_{H_3O^+} &= k_B T \ln c^\circ \Lambda_{H^+}^3 \frac{q_{H^+,eff}^q}{q_{H^+}^q} \\ &= k_B T \ln c^\circ \Lambda_{H^+}^3 \frac{q_{H^+,eff}^q}{q_{H^+}^q} - \Delta E_{H^+,eff}^{zp} \end{aligned} \quad (33)$$

where we have neglected the (small) difference in the thermal wavelengths of water and the hydronium ion, similarly as in eq 25. In the last equation, we have separated $q_{H^+,eff}^q$ into the zero-point energy term $\Delta E_{H^+,eff}^{zp}$ and the partition function $q_{H^+,eff}^q$ in which vibrational energies are referred to the vibrational ground state, so that $q_{H^+,eff}^q = 1$ for $T = 0$. Assuming that the zero-point motion for the proton in the hydronium ion and the solvated proton are similar, we obtain

$$\Delta A_{H_3O^+} \approx k_B T \ln c^\circ \Lambda_{H^+}^3 q_{H^+,eff}^q \quad (34)$$

Equation 34 is of course an approximation that could in principle be validated with path-integral DFMD calculations. This equation can be further simplified by noting that the vibrational temperature constant of a proton is significantly higher than room temperature, i.e., $q_{H^+,eff}^q \approx 1$. Thus, under the above assumptions, the dissociation free energy is equal to the translational free energy of the proton

$$\Delta A_{H_3O^+} \approx k_B T \ln c^\circ \Lambda_{H^+}^3 \quad (35)$$

We find that eq 35 compensates for the loss in the translational free energy for dummy atom insertion (eq 25), thereby leaving the

Table 1. Force Constants and Equilibrium Values for Bonds (k_r , r_{eq}), Angles (k_θ , θ_{eq}), and Dihedrals (k_ϕ , ϕ_{eq}) of the Restraining Potential V_r for the Dummy Particle (eq 18)

	k_r (au)	r_{eq} (Å)	k_θ (au)	θ_{eq} (deg)	k_ϕ (au)	ϕ_{eq} (deg)	n (H ₂ O) ^a
Arg _{mod}	0.2	1.03	0.2	122	0.02	13	54
Asp	0.2	1.02	0.2	111	0.20	9	53
Cys	0.2	1.35	0.2	97	0.02	92	55
His	0.2	1.05	0.2	123	0.02	173	54
Trp*	0.2	1.03	0.2	125	0.20	178	48
Tyr	0.2	1.00	0.2	110	0.02	20	53
Tyr _C	0.2	1.03	0.2	112	0.02	166	53
Tyr _N	0.2	1.05	0.2	112	0.02	47	53
H ₃ O ⁺	0.2	1.00	0.2	111			63

^aNumber of solvent water molecules per unit cell.

number of degrees of freedom unchanged. Indeed, this should be the case for the transfer of a proton from the gas to the aqueous phase.

2.6. Final Expression for pK_a . We can now write the pK_a explicitly in terms of the deprotonation integrals and the dummy, quantum, and dissociation corrections. Insertion of eqs 9 and 13 in eq 14 gives

$$pK_a = \frac{1}{\ln 10k_B T} (\Delta_{dp}A_{AH} - \Delta_{dp}A_{H_3O^+} - \Delta A_{Ad} + \Delta A_{H_2Od} - \Delta A_{qc}(AH) + \Delta A_{qc}(H_3O^+) + \Delta A_{H_3O^+}) \quad (36)$$

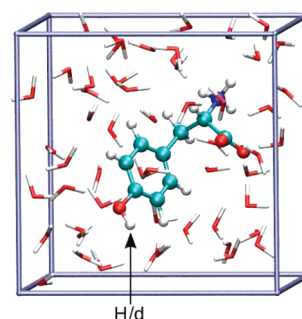
and insertion of eqs 19, 25, and 35 gives

$$pK_a = \frac{1}{\ln 10k_B T} \left(\int_0^1 d\eta \langle \Delta_{dp}E_{AH} \rangle_\eta - \int_0^1 d\eta \langle \Delta_{dp}E_{H_3O^+} \rangle_\eta + k_B T \ln \frac{q_{Ad^-}^{int} q_{H_2O}^{int}}{q_{A^-}^{int} q_{H_2Od}^{int}} - \Delta A_{qc}(AH) + \Delta A_{qc}(H_3O^+) + k_B T \ln c^\circ \Lambda_{H^+}^3 \right) \quad (37)$$

We will see that the vibrational frequencies of the dummy atom in the acid (Ad^-) and in the hydronium (H_2Od) are rather similar. Consequently, the third term on the rhs of eq 37 will be small. The same is true for the proton frequencies in most acids, leading to partial cancellation of the fourth and fifth terms on the rhs of eq 37. Thus, the pK_a of an acid is approximately equal to the difference of the deprotonation integral of the acid and the hydronium ion corrected by the standard translational free energy of the proton.

3. SIMULATION DETAILS

Aqueous solutions of amino acids were simulated under periodic boundary conditions. Each unit cell comprised of one amino acid molecule (modified arginine (Arg_{mod}), aspartic acid (Asp), cysteine (Cys), histidine (His), tryptophan radical cation (Trp*), and tyrosine (Tyr)), and a variable number of water molecules (48–55, see Table 1). A model aqueous solution for the simulation of Tyr is shown in Figure 1. The long side chain of arginine was shortened by two CH₂ groups in order to fit the molecule into the simulation box specified below. We refer to this amino acid as Arg_{mod}. The pK_a calculations are for the side chain ionizable proton, if not specified otherwise, and the N- and C-termini of the amino acids are treated in the ionized form. For pK_a calculation of the C-terminus of tyrosine (Tyr_C), the

**Figure 1.** Aqueous model solution used for calculation of the pK_a value of tyrosine (Tyr). The latter is depicted in ball and stick representation, and the water molecules are depicted in stick representation. Color code: C, cyan; O, red; N, blue; H, white. The arrow indicates the hydrogen atom that is treated quantum mechanically in the protonated state (H) and as a dummy atom in the deprotonated state (d).**Table 2.** Local Normal Mode Frequencies of the Dummy Atom d ($\nu_{Ad,i}$) and of the Quantum Mechanically Treated Proton H ($\nu_{AH,i}$) for the Gas Phase Amino Acids Ad and AH, Respectively, and the Vibrational Temperature θ_i^{vib} Corresponding to $\nu_{Ad,i}$

	$\nu_{Ad,i}$ (cm ⁻¹)	θ_i^{vib} (K)	$\nu_{AH,i}$ (cm ⁻¹)
Arg _{mod}	440, 1182, 2290	633, 1701, 3295	263, 1204, 3340
Asp	1186, 1797, 2290	1706, 2585, 3295	577, 1141, 3446
Cys	284, 893, 2290	409, 1285, 3295	240, 877, 2542
His	433, 1154, 2290	623, 1660, 3295	575, 1165, 3417
Trp*	1182, 1448, 2290	1701, 2083, 3295	503, 1203, 3392
Tyr	1212, 1296, 2290	1744, 1865, 3295	382, 1208, 3566
Tyr _C	396, 1171, 2290	570, 1685, 3295	667, 1131, 3420
Tyr _N	384, 1152, 2290	552, 1657, 3295	1183, 1227, 3173
H ₃ O ⁺ ^a	1450, 1810, 1920	2090, 2600, 2760	1032, 1668, 1692
	3340, 3660, 3760	4810, 5260, 5400	3449, 3523, 3540

^a $\nu_{Ad,i}$ and θ_i^{vib} from ref 30.

N-terminus and the side chain were protonated, and for pK_a calculation of the N-terminus (Tyr_N), the C-terminus was deprotonated and the side chain was protonated. The net charge of the solutions is compensated by the neutralizing background charge included in the Ewald summation of the electrostatic energy. The number of water molecules per unit cell was obtained from classical MD simulation runs of each amino acid, by varying the number of solvent molecules until a box length close to 12.426 Å was obtained. This value was taken as the dimension of the cubic unit cell in all DFMD simulations described below.

A snapshot from an equilibrated classical MD trajectory of the protonated amino acid ($\eta = 0$) was taken as an initial configuration for DFMD. The solution was equilibrated for 5 ps at 330 K, and the following 10–15 ps of dynamics was taken for calculation of thermal averages. A higher temperature than the standard temperature of 298 K is chosen to compensate for the underestimation of dynamical properties due to the approximate nature of the exchange correlation functional used (see below). The MD time step was 0.5 fs. Trajectories for the deprotonated state ($\eta = 1$) and for the midpoint ($\eta = 0.5$) were generated similarly. The thermal averages in eqs 21 and 22 were obtained by calculating the energy gap, eq 20, for about 150 equidistantly spaced snapshots of these trajectories. The calculations for

Table 3. Summary of Vertical Energy Gaps and Root-Mean-Square Fluctuations for Removal and Insertion of an Excess Proton out of or into Aqueous Solutions of Amino Acids, As Obtained from Density Functional Based Molecular Dynamics Simulation^a

AH	$\langle\Delta_{\text{dp}}E_{\text{AH}}\rangle_0^b$	σ_0^c	$\langle\Delta_{\text{dp}}E_{\text{AH}}\rangle_{0.5}^b$	$\sigma_{0.5}^c$	$\langle\Delta_{\text{dp}}E_{\text{AH}}\rangle_1^b$	σ_1^c	ΔA_{LR}^d	ΔA_{TP}^e	ΔA_{Ad}^f	ΔA_{qc}^g
Arg _{mod}	17.75 ± 0.11	0.29	16.48 ± 0.03	0.26	14.08 ± 0.13	0.84	15.92	16.29	0.32	0.17
Asp	17.43 ± 0.02	0.30	15.55 ± 0.10	0.28	13.41 ± 0.10	0.65	15.42	15.50	0.35	0.18
Cys	17.31 ± 0.08	0.26	15.97 ± 0.16	0.27	14.20 ± 0.06	0.49	15.79	15.93	0.33	0.12
His	17.33 ± 0.02	0.20	16.17 ± 0.02	0.21	13.14 ± 0.11	1.15	15.23	15.85	0.31	0.18
Trp*	16.97 ± 0.04	0.21	15.73 ± 0.03	0.19	13.60 ± 0.05	0.98	15.29	15.57	0.35	0.17
Tyr	17.79 ± 0.07	0.25	16.27 ± 0.13	0.33	12.67 ± 0.34	1.76	15.22	15.94	0.34	0.18
Tyr _C	17.40 ± 0.07	0.27	15.72 ± 0.08	0.30	13.61 ± 0.16	0.77	15.50	15.64	0.31	0.18
Tyr _N	17.49 ± 0.07	0.27	16.34 ± 0.10	0.26	13.06 ± 0.19	1.28	15.28	15.98	0.31	0.19
H ₃ O ⁺	17.40 ± 0.03	0.28	15.46 ± 0.00	0.31	11.98 ± 0.07	0.84	14.69	15.20	0.34	0.20

^aEnergies are for protonation/deprotonation of the side chain, except for Tyr_C and Tyr_N, where the C-terminus and N-terminus is protonated/deprotonated. All energies are in eV. ^bThermal average of the energy gap eq 20 for $\eta = 0, 0.5$, and 1. ^cEquation 23 for $\eta = 0, 0.5$, and 1. ^dEquation 22. ^eEquation 21. ^fEquation 25 using the data given in Table 2. ^gEquation 27 using the data given in Table 2.

aqueous H₃O⁺ were carried out in the Eigentype structure of the hydronium ion as described in ref 29. All three O–H bonds were restrained by a harmonic potential with a force constant of 1.0 au and an equilibrium bond length of 1.0 Å to avoid spontaneous proton transfer to a neighboring water molecule. The energy E_0 used to calculate the energy gap, eq 20, does not include these additional potential terms. The parameters defined in eq 18 for the dummy potential are summarized in Table 1. The frequencies used for the calculation of ΔA_{Ad} and ΔA_{qc} are summarized in Table 2.

The exchange-correlation energy was calculated according to Becke³⁶ and Lee, Yang, and Parr.³⁷ Core electrons and the nuclei were described using Goedecker–Teter–Hutter pseudopotentials, and the valence electrons were expanded in the TZV2P atomic basis set. The density cutoff for the auxiliary plane wave basis was 280 Ry. The tryptophan radical cation (Trp*) was treated at the local spin density functional level of theory, enforcing the lowest (doublet) spin state in both protonation states. DFMD simulations were carried out with the CP2k simulation package.³⁸ The initial equilibration of the structures was performed using the AMBER99 force field³⁹ and TIP3P water⁴⁰ as implemented in the NAMD simulation package.⁴¹ Snapshots of the equilibrated systems can be made available on request.

4. RESULTS

4.1. Vertical Energy Gaps. The thermal average of the vertical energy gaps, $\langle\Delta_{\text{dp}}E_{\text{AH}}\rangle_\eta$, and the corresponding root-mean-square fluctuations (rmsf), σ_η , were obtained from DFMD simulation of the aqueous amino acids and are summarized in Table 3. The mean values are reasonably well converged, despite the rather short simulation time of 10–15 ps. The statistical uncertainty, estimated as half the difference of the mean value obtained for the first and the second half of the trajectory, is no more than about 0.1 eV for the initial ($\eta = 0$) and midpoint states ($\eta = 0.5$). The uncertainty for the final state ($\eta = 1$) is in general larger, 0.1–0.3 eV. This trend is paralleled by the rmsf of the energy gap. In the initial state, the rmsf is between 0.2 and 0.3 eV, which, interestingly, is in the same range as the rmsf reported for vertical ionization of aqueous solutes^{42,43} and proteins.⁴⁴ The rmsf in the final state is significantly larger by a factor of 2 (Cys) to 7 (Tyr).

Table 4. Calculated Free Energies of Deprotonation and Comparison of Calculated and Experimental Absolute pK_a Values of Amino Acids

AH	$\Delta_{\text{dp}}A_{\text{AH}}^{\circ a}$ (eV)	$\Delta_{\text{dp}}A_{\text{AH}}^{\circ b}$ (eV)	pK _a (calc) ^c	pK _a (exp) ^d
Arg _{mod}	15.43 ± 0.08	15.80 ± 0.03	16.1 ± 0.6	12.10
Asp	14.89 ± 0.05	14.97 ± 0.07	2.0 ± 1.2	3.71
Cys	15.34 ± 0.05	15.48 ± 0.11	10.7 ± 1.8	8.14
His	14.74 ± 0.06	15.36 ± 0.02	8.6 ± 0.4	6.04
Trp* ^e	14.77 ± 0.03	15.05 ± 0.02	3.4 ± 0.4	4.30 ^f
Tyr ^e	14.70 ± 0.17	15.42 ± 0.11	9.7 ± 1.8	10.10
Tyr _C	15.01 ± 0.09	15.15 ± 0.06	5.1 ± 1.0	2.24
Tyr _N	14.78 ± 0.10	15.48 ± 0.07	10.7 ± 1.2	9.04
H ⁺	14.34 ± 0.04	14.85 ± 0.01		

^aEquation 9 for the amino acids, using the linear response approximation (LR) to $\Delta_{\text{dp}}A_{\text{AH}}$, ΔA_{LR} of eq 22, and eqs 25 and 27 for estimation of ΔA_{Ad} and ΔA_{qc} , respectively. For the solvated proton (H⁺), the computed desolvation free energy is given, $\Delta_{\text{ds}}A_{\text{H}^+}^{\circ}$ of eq 13. $\Delta A_{\text{H}_3\text{O}^+}$ in eq 13 is approximated by eq 35. Data are taken from Table 3. ^bAs in footnote a, but with $\Delta_{\text{dp}}A_{\text{AH}}$ estimated by the three-point approximation ΔA_{TP} of eq 21 (TP). ^cEquation 14 using the TP estimate for $\Delta_{\text{dp}}A_{\text{AH}}$. ^dRef 48 if not specified otherwise. ^eThe numerical values differ somewhat from the values given in ref 33 due to different system composition for Tyr and the neglect of quantum corrections for Tyr and Trp* in ref 33. ^fRef 49.

The large fluctuations in the final state are a consequence of the very small distance between solvent molecules and the inserted proton. The water molecules are oriented so as to solvate the deprotonated acid Ad[−] (note that the dummy atom does not interact with the solvent). Thus, two to three hydrogen atoms of the solvent are within 0.5–1 Å of the dummy atom. This unusually small H–H distance leads to relatively high energies when the dummy atom is transformed into the proton, as required for the calculation of the vertical energy gap, eq 20. As a consequence, the fluctuations of this energy and of the energy gap are large, too. Yet the distance is large enough for the insertion to be feasible; i.e., there is no hard core repulsion problem, which is usually the case in alchemical transformations. In fact, the proton affinities are still positive in the final state. By contrast, in the protonated state AH, the proton is typically solvated by one solvent molecule at a H–O distance of about 2 Å. Transformation of the proton into the dummy atom does not

lead to high energy solvation structures. Hence, the fluctuations are smaller in the initial state.

According to our explanation, one would expect the difference in the rmsf of the gap in the initial and final states to increase with increasing strength of solvation of the deprotonated state (as this would lead to shorter H–H distances in the protonated state). This is indeed the case. For deprotonated Cys, the first peak of the radial distribution function between the S atom and the hydrogen atoms of the solvent (H_w) is at a rather large distance, 2.4 Å, giving the smallest difference in rmsf, whereas for deprotonated Tyr the first peak of the O– H_w radial distribution is at a very small distance, 1.6 Å, giving the largest difference in rmsf.

4.2. Free Energies and Absolute pK_a Values. The free energies $\Delta_{dp}A_{AH}^{\circ}$ of eq 9 and $\Delta_{ds}A_{H^+}^{\circ}$ of eq 13 are summarized in Table 4. They include the deprotonation free energy, the dummy and quantum correction, and, in case of $\Delta_{ds}A_{H^+}^{\circ}$, the thermochemical correction for the hydronium ion. The deprotonation free energy $\Delta_{dp}A_{AH}$ was calculated from the average energy gaps according to the three-point (TP) approximation of the thermodynamic integral, eq 21 (third column in Table 4), and according to the linear response formula (LR), eq 22 (second column in Table 4). It is already clear from the above observations that linear response is not a good approximation in the present calculations. For this approximation to hold, the rmsf's in the initial and final states have to be the same or should at least be similar. Indeed, the LR estimate differs by up to 0.7 eV (Tyr, Tyr_N) from the TP estimate, but also smaller deviations are observed (0.1 eV, Asp). Similar results were found in previous pK_a calculations of ammonia,²⁹ indicating that three points are the absolute minimum for evaluation of the thermodynamic integral, eq 19. An alternative cumulant expansion of the free energy $\Delta_{dp}A_{AH}$ up to second order (which requires the simulation of the two end states only, similarly to LR) does not give an improvement over the linear response estimate.

The deprotonation free energies $\Delta_{dp}A_{AH}^{\circ}$ obtained from the TP approximation of the thermodynamic integral correlate reasonably well with the experimental pK_a values, see Figure 2. The R^2 value for the linear fit is 0.93, and the computed slope of 64 meV is in good agreement with the theoretical slope of $k_B T \ln 10 = 59$ meV. The correlation with experimental results is poor for the linear response estimates, showing again that this approximation cannot be applied for the calculation of pK_a values. The absolute pK_a values are obtained according to eq 14 by subtracting the desolvation free energy of the solvated proton, $\Delta_{ds}A_{H^+}^{\circ}$, from $\Delta_{dp}A_{AH}^{\circ}$. The results are summarized in Table 4. We obtain an unsigned mean error (UME) of 2.1 pK_a units, a signed mean error (SME) of +1.3 pK_a units, and a maximum error of 4.0 pK_a units. The agreement is fairly good if one takes into account the average statistical uncertainty of 1.1 pK_a units, caused by the limited length of the DFMD trajectories.

4.3. Importance of $\Delta A_{H_3O^+}$, ΔA_{Ad} , and ΔA_{qc} . In view of possible simplifications of the computational procedure, it is of particular interest to analyze the importance of the terms $\Delta A_{H_3O^+}$, ΔA_{Ad} , and ΔA_{qc} , which relate the thermodynamic integral (eq 19) to the deprotonation free energies (eq 9) and absolute pK_a values (eq 2). Of the three corrections, the thermochemical correction for the hydronium ion, $\Delta A_{H_3O^+}$, is the most important one, amounting to -0.19 eV according to the approximation eq 35. The effect is a decrease in absolute pK_a by 3.2 units for all amino acids; relative pK_a values remain unchanged.

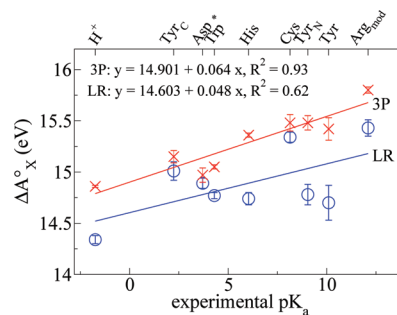


Figure 2. Computed free energies for deprotonation of amino acids in aqueous solution as obtained from density functional based molecular dynamics simulation, versus experimental pK_a values. The free energies $\Delta_{dp}A_{AH}^{\circ}$, defined in eq 9 for amino acids and in eq 13 for the solvated proton, as well as their error bars are taken from Table 4. Best linear fit functions for the free energies obtained from the three-point (\times , TP, eq 21) and linear response (\circ , LR, eq 22) approximation to the thermodynamic integral, eq 19, are shown in red and blue, respectively.

Numerical values for the other terms ΔA_{Ad} and ΔA_{qc} are summarized in Table 3. We find that the dummy correction ΔA_{Ad} obtained from the gas phase partition function formula (eq 25) lies in the interval 0.31–0.35 eV for all amino acids investigated as well as for the hydronium ion. Thus, the effect of this correction is small, leading typically to an increase in absolute pK_a by less than 0.5 units and to a change in relative pK_a by less than 0.7 units. Indeed, we aimed at keeping the variation in ΔA_{Ad} small by choosing the equilibrium geometry of the dummy atom to be close to that of the proton. In this way, one also avoids introducing additional barriers for the transformation of the proton into the dummy atom.

The vibrational quantum correction ΔA_{qc} varies only marginally among amino acids, 0.17–0.19 eV, except for Cys, where a significantly smaller value of 0.12 eV is obtained. This trend is not surprising if one bears in mind that the quantum correction increases with increasing frequencies. While in all amino acids except Cys the proton is bound to a (light) second row atom (O or N), which gives rise to high frequencies in the range 3100–3600 cm^{-1} , in the case of Cys, the proton is bound to the heavier sulfur atom with a maximum frequency of about 2500 cm^{-1} (see Table 2). The hydronium ion has three modes that have a frequency larger than 3400 cm^{-1} . It thus exhibits the largest quantum correction. However, the difference in quantum correction between the amino acids and the hydronium ion (which enters the pK_a calculation) is rather small, 0.01–0.03 eV, but significant for Cys, 0.08 eV. This corresponds to an increase in the absolute pK_a value by 0.2–0.5 and 1.4 units, respectively. Thus, we conclude that the quantum correction for deprotonation from N and O atoms is relatively small, at least according to the simple correction model used, but can be significant if deprotonation from heavier heteroatoms is considered.

4.4. Solvation Structure. The solvation structure of the protonated and deprotonated amino acids is investigated to characterize the response of the solvent to the removal of the acidic proton. For this purpose, we have calculated the radial distribution function between the hydrogen atoms of solvent water molecules (H_w) and the heteroatom of the amino acid (O, N, S) to which the acidic proton is bonded in the protonated state. The distributions are shown in Figure 3 for all amino acids investigated as well as for aqueous hydronium ions. Peak positions and coordination numbers obtained by integration of the

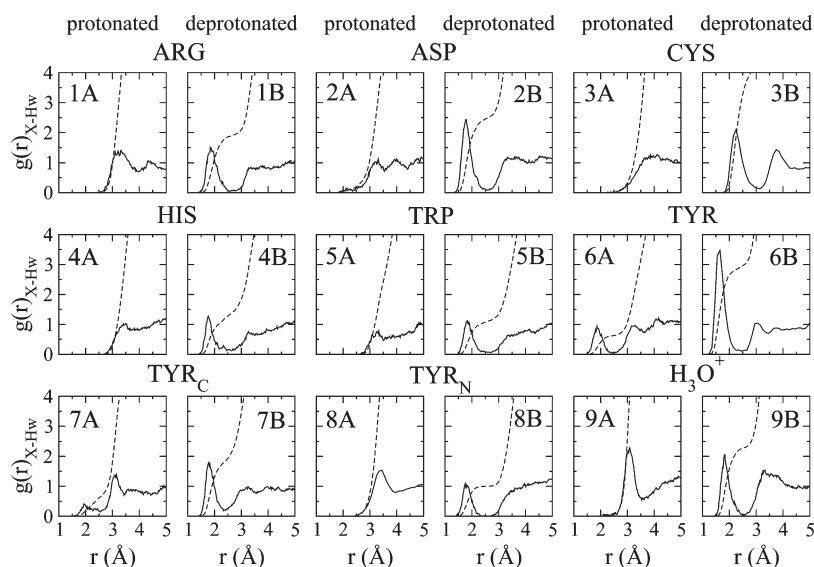


Figure 3. Radial distribution functions $g_{X-HW}(r)$ (solid lines) and coordination numbers (dashed lines) for protonated and deprotonated amino acids. H_W denotes the hydrogen atoms of water molecules (solvent). X denotes the basic N(H) atom of the side chain of Arg_{mod} (1A, 1B), the O(H) atom of the side chain of Asp (2A, 2B), the S(H) atom of the side chain of Cys (3A, 3B), the ϵ N atom of the side chain of His (4A, 4B), the N(H) atom of the side chain of Trp* (5A, 5B), the O atom of the side chain of Tyr (6A, 6B), the O(H) atom of the carboxyl group of Tyr_C (7A, 7B), the N(H₃) atom of Tyr_N (8A, 8B), and the O atom of hydronium/water, respectively (9A, 9B). Coordination numbers are obtained by spherical integration of $g_{X-HW}(r)$. The positions of the first maxima and coordination numbers are given in Table 5.

Table 5. Characterization of the First Solvation Shell of Protonated and Deprotonated Amino Acids, As Obtained from Density Functional Based Molecular Dynamics Simulation

	protonated		deprotonated		Δn^c
	CN ^a	R_0^b (Å)	CN ^a	R_0^b (Å)	
Arg _{mod}	0.0	3.3	1.7	1.8	1.7
Asp	0.1	3.3	2.4	1.7	2.3
Cys	0.3	4.0	4.1	2.3	3.8
His	0.0	3.4	1.2	1.8	1.2
Trp*	0.0	3.3	1.0	1.8	1.0
Tyr	0.6	1.9	2.9	1.6	2.3
Tyr _C	0.5	2.0	1.8	1.8	1.3
Tyr _N	0.0	3.4	1.0	1.8	1.0
H ₃ O ⁺	0.0	3.0	2.2	1.9	2.2

^aCoordination numbers obtained from spherical integration of the radial distribution functions $g_{X-HW}(r)$ shown in Figure 3, up to a distance of 2.4 Å (except for Cys integrated up to 3.0 Å). ^bPosition of the first peak of $g_{X-HW}(r)$ shown in Figure 3. ^c $\Delta n = \text{CN}(\text{deprotonated}) - \text{CN}(\text{protonated})$.

radial distributions up to a distance of 2.4 Å or 3.0 Å for cysteine are summarized in Table 5.

Cysteine exhibits the most significant change in solvation structure upon removal of the acidic proton (see Figure 3 (3A and 3B)). In the protonated state, the side chain forms a hydrophobic cavity, as indicated by the large distance for the first peak at $R_0 = 4.0$ Å (Figure 3 (3A)). Removal of the HS proton and formation of a negative charge on the S atom causes a major reorganization of the solvation shell, which is indicated by the formation of four weak hydrogen bonds with water molecules at an S–H distance of 2.3 Å (see Figure 3 (3B)). Thus, the water

coordination is qualitatively similar to the one reported for aqueous hydroxide.^{34,45,46} However, we observe that an additional hydrogen bond is formed with the ammonium group, giving in total an approximately quadratic pyramidal hydrogen bond network.

A strong reorganization of the hydrogen bond network can also be observed when tyrosine is deprotonated. The coordination number changes from 0.6 (Figure 3 (6A)) to 2.9 (Figure 3 (6B)), concomitant with a significant increase in the strength of the hydrogen bonds, as indicated by the decrease in the peak position from $R_0 = 1.9$ to 1.6 Å. The three water molecules bound to the tyrosinate oxyanion form a tetrahedral coordination, implying that the oxygen atom is better described as sp^3 hybridized rather than sp^2 . Considering the carboxyl group of tyrosine, we find that in the protonated state the oxygen atom OH forms occasionally one weak hydrogen bond and, in the deprotonated state, 1.8 hydrogen bonds. Interestingly, this is less than for aspartate, which forms 2.4 hydrogen bonds, and aqueous formate.²⁸ This can be explained by the fact that the positively charged α -ammonium group of tyrosine is in close proximity to its carboxylate group, thereby replacing the stabilizing effect of an additional hydrogen bond donating water molecule. The second oxygen atom of the carboxylate group of tyrosine points in a direction opposite the ammonium group, with the result that the coordination number (= 2.3) is very similar to the one obtained for aspartate.

Turning to the amino acids Arg_{mod}, His, Trp*, and Tyr_N, we find that in the protonated state the positively charged nitrogen atom does not form any hydrogen bonds with the solvent. Upon deprotonation, the nitrogen atoms of His, Trp*, and Tyr_N form one strong hydrogen bond in accord with expectation. By contrast, for Arg_{mod}, we find a coordination number of 1.7. One hydrogen bond is due to a water molecule strongly bonded to the sp^2 lone pair of the imide nitrogen as well as to the carboxylate group. A second hydrogen bond is formed by water

molecules that penetrate the space perpendicular to the molecular plane and interact with the Π -bonding orbital of the imide. This hydrogen bond is weak and of a temporary nature, thus giving only a fractional contribution of 0.7.

5. DISCUSSION

Our computations reproduce experimental absolute pK_a values of natural amino acids rather well judging from the reasonably small UME of 2.1 pK_a units. A similar accuracy was reported in our previous study on smaller inorganic and organic aqueous acids.³¹ However, the present investigation differs in one important aspect from our previous work.^{30,31} In refs 30 and 31, the aqueous proton was modeled as a hydronium ion in its Eigen-structure, whereas in current work, we treat the proton as a solvated particle that is not attached to a particular water molecule (it is modeled as a hydronium ion only in the intermediate states of the thermodynamic cycle, see eqs 10–12). By assuming that the proton forms a stable hydronium ion in water, one overestimates its free energy by a contribution $\Delta A_{H_3O^+}$, corresponding to the free energy of the reverse process of reaction eq 10. The present approach takes into account $\Delta A_{H_3O^+}$, whereas our previous formulation did not.

An accurate estimation of $\Delta A_{H_3O^+}$ is difficult, however, due to the delocalized nature of the “true” solvated proton, and the limited length of the DFMD trajectories. Adopting a simple quantum-classical model for the hydronium ion, we found that at ambient temperature the free energy difference between the solvated proton and the solvated hydronium is approximately equal to the ideal translational free energy of the proton, see eq 35. The result is that the absolute pK_a values are now shifted down by 0.19 eV with respect to our previous approach.^{30,31} Indeed, a similar down shift of pK_a values by 0.2 eV was obtained previously, by fitting the calculated deprotonation free energies of small acids to the experimental pK_a values.³¹ This gives some credence to our assumption that the reaction free energy of reaction eq 10 is dominated by the standard translational free energy of the proton.

We have recalculated the pK_a values reported in ref 31 according to our revised scheme and combined them with the results obtained herein for the amino acids. This gives in total a set of 18 inorganic and organic acids and natural amino acids for which we obtain a UME of 2.3 pK_a units and a SME of 2.0 pK_a units. The relatively small difference between UME and SME implies that pK_a values are in general overestimated. Though, for the amino acids studied here, the difference between UME and SME (2.1 and 1.3, respectively) is larger, implying a less systematic trend in the errors for this subset of acids. This could be related to the statistical uncertainty of the computed pK_a values, which is on the same order of magnitude as the UME. A breakdown of the UME into groups with the same functional groups reflects the overall trend (hydroxyl, 1.9; carboxylic acid, 2.1; amine/imine, 2.4), except for the thiol group which has a larger UME of 3.4 pK_a units.

There are a number of sources for errors in our pK_a calculations in addition to the modeling of the solvated proton. This becomes evident when the pK_a value differences of amino acids are compared, for which the solvation free energy of the proton drops out. The UME and the SME of the corresponding relative pK_a values are 2.4 and 0.2 when averaged over all possible pairs of amino acids. Since the SME is close to zero, the deviations are evenly spread in both directions and therefore not systematic.

They are likely to be the result of a number of factors. First, the three point approximation of the thermodynamic integral eq 21 may introduce some error. In previous work we have shown that this approximation gives accurate results for aqueous HCl and H₂S, but this may not be the case in general.³¹ Unfortunately, using a finer grid for the integration was computationally not feasible for the relatively large system sizes studied. Second, the amino acids were modeled in their zwitterionic state in accord with their experimental protonation state at the pH where the side chain acidic groups titrate. Thus, the amino acids carry a large and permanent dipole that interacts with the acidic group of the side chain. While the structures were initiated from the minimum energy configuration and were found to be stable on the 10–20 ps time scale of our simulation, it may be that the charged groups forming the molecular dipole undergo fluctuations on a longer time scale, which could lead to shifts of the pK_a value that are not accounted for in the present simulations. Third, the finite number of solvent molecules used may also have some effect. We have used a simulation box large enough to include the first solvation shell of the amino acid. This is sufficient to model the response of the solvent in the vicinity of the acidic group. The effect of higher solvation shells on the energetics of deprotonation is expected to cancel to a good approximation for iso-Coulombic half reactions, i.e., for reactions where reactant and product have the same net charge. In this respect, it is interesting to note that the UME for the subsets of iso-Coulombic reactions is not lower than for the overall UME that includes all amino acid pairs. This indicates that the error is likely to be due to other reasons. Finally, there is also an error due to the approximation of the exchange-correlation functional. While proton affinities are generally very well described by the BLYP functional that was used in DFMD-TI, the UME of this functional for the PA8 set of molecules and atoms is not negligible on the pK_a energy scale, 1.53 kcal/mol or 1.1 pK_a units.⁴⁷ We expect, however, that the DFT error is smaller for proton affinity differences, which is the relevant quantity in pK_a calculations.

A comparison between the present DFMD-TI approach and QM-continuum calculations may be of interest. In ref 17, the performances of a number of QM-continuum calculation protocols with different continuum models were investigated on neutral organic and inorganic acids. It was found that the direct approach was unsuitable for calculation of absolute pK_a values, although reasonable results with UME < 3 and maximum error < 5 pK_a units were possible for alcohols and phenols in combination with the COSMO-RS continuum model. Hybrid approaches performed better with best UMEs of about 2 pK_a units, but the calculations were very sensitive on the number of explicit water molecules included. The proton exchange scheme, which yields pK_a values relative to a reference compound, gave good overall results with UMEs of 1–2 pK_a units for alcohols, phenols, and carboxylic acids. Thus, the error reported here for the DFMD-TI approach is comparable to the error of the proton-exchange scheme. Yet, this comparison can only be of a qualitative nature, since different compounds have been investigated with the two methods.

Finally, a word on the solvation structures obtained in this study. They generally comply with expectations, with a few exceptions. The oxyanion of tyrosinate forms three strong hydrogen bonds in a tetrahedral arrangement, implying that the oxygen atom is best described as sp^3 hybridized. This contrasts the situation in the gas phase, where oxygen is described as sp^2 hybridized, as required for delocalization of

the negative charge over the phenyl ring. Evidently, the polarizing effect of the solvent leads to charge localization and a change in hybridization. We have also shown that in addition to solute–solvent interactions, also intramolecular interactions are important for the stabilization of the deprotonated species. In the cysteine anion, an approximately quadratic pyramidal hydrogen bond network is observed that includes the ammonium group. Similarly, one carboxylate oxygen of tyrosine is stabilized by the positive charge of the nearby ammonium group, whereas in modified arginine a water molecule binding to the imine group is tightly held in place by the nearby carboxylate group.

6. CONCLUSION

In conclusion, we have shown that DFMD-TI can reproduce absolute experimental acidity constants of naturally occurring amino acids to a UME of 2.1 pK_a units with a maximum absolute deviation of 4.0 pK_a units. The errors for absolute and relative pK_a values of the amino acids do not appear to be systematic. This is probably a consequence of the relatively small number of compounds investigated (limited by the high computational cost of DFMD compared to QM/continuum approaches) and the statistical uncertainty of our simulations of 1.1 pK_a units. Extending the set of amino acids with the set of acids studied previously,^{30,31} we find a more systematic correlation in the errors. The computed pK_a values are on average overestimated by about 2 pK_a units. The accuracy reported here is comparable with that reported recently for the best QM/continuum calculations on a series of alcohols, phenols, and carboxylic acids.¹⁷

Our calculation of absolute pK_a values relies on a computational model for the solvated proton. We have used the Eigen-structure of the hydronium ion as in our previous calculations, but now corrected by a free energy term that accounts for the formation of the Eigen-structure from the “real”, delocalized solvated proton. This correction term was estimated to be the standard translational free energy of the proton. It would be interesting and challenging to further investigate the accuracy of this approximation by explicit calculation of the free energy difference between the delocalized proton and the Eigen-structure of the hydronium ion.

The approximation made for the solvated proton is not the only source of errors in our calculations, because the average error in pK_a differences, for which the solvated proton drops out, is just as large. The accuracy of our approach can in principle be systematically improved (i) by carrying out longer simulations to reduce the statistical uncertainty, (ii) by using more integration points for evaluation of the thermodynamic integral, and (iii) by using a larger number of solvent molecules to reduce possible system size effects. With the steady increase in computational power, we remain confident that a more accurate and precise estimation of pK_a values from DFMD should be possible in the near future.

■ ASSOCIATED CONTENT

S Supporting Information. The derivation of eq 24 and the results of the numerical calculation of ΔA_{Ad} using eq 24. This material is available free of charge via the Internet at <http://pubs.acs.org/>.

■ AUTHOR INFORMATION

Corresponding Author

*E-mail: j.blumberger@ucl.ac.uk.

■ ACKNOWLEDGMENT

The authors thank Dr. Harald Oberhofer and Dr. Jun Cheng for helpful discussions, the European Commission for an EST Ph.D. studentship (M.M.), the Royal Society for a University Research Fellowship (J.B.), and the EPSRC for financial support (M.Su., M.Sp.). Calculations were carried out on a computer cluster at the University of Cambridge, Department of Chemistry.

■ REFERENCES

- (1) Silva, C.; Da Silva, E.; Nascimento, M. *J. Phys. Chem. A* **2000**, *104* (11), 2402.
- (2) Liptak, M.; Shields, G. *J. Am. Chem. Soc.* **2001**, *123* (30), 7314.
- (3) Chipman, D. *J. Phys. Chem. A* **2002**, *106* (32), 7413.
- (4) Klicic, J.; Friesner, R.; Liu, S.-Y.; Guida, W. *J. Phys. Chem. A* **2002**, *106* (7), 1327.
- (5) Pliego, J.; Riveros, J. M. *J. Phys. Chem. A* **2002**, *106*, 7434.
- (6) Saracino, G.; Improta, R.; Barone, V. *Chem. Phys. Lett.* **2003**, *373*, 411.
- (7) Kelly, C. P.; Cramer, C. J.; Truhlar, D. G. *J. Phys. Chem. A* **2006**, *110*, 2493.
- (8) Bryantsev, V. S.; Diallo, M. S.; Goddard, W. A. *J. Phys. Chem. A* **2007**, *111*, 4422.
- (9) Lu, H.; Chen, X.; Zhan, C.-G. *J. Phys. Chem. B* **2007**, *111* (35), 10599.
- (10) Jia, Z.; Du, D.; Zhou, Z.; Zhang, A.; Hou, R. *Chem. Phys. Lett.* **2007**, *439* (4–6), 374.
- (11) Sadley-Sosnowska, N. *Theor. Chem. Acc.* **2007**, *118*, 281.
- (12) Verdolino, V.; Cammi, R.; Munk, B. H.; Schlegel, H. B. *J. Phys. Chem. B* **2008**, *112*, 16860.
- (13) Trummel, A.; Rummel, A.; Lippmaa, E.; Burk, P.; Koppel, I. A. *J. Phys. Chem. A* **2009**, *113*, 6206.
- (14) Casanovas, R.; Frau, J.; Ortega-Castro, J.; Salva, A.; Donoso, J.; Munoz, F. *J. Mol. Spectrosc.* **2009**, *912*, 5.
- (15) Khalili, F.; Henni, A.; East, A. L. *J. Mol. Spectrosc.* **2009**, *916*, 1.
- (16) Ho, J. M.; Coote, M. L. *J. Chem. Theory Comput.* **2009**, *5*, 295.
- (17) Ho, J. M.; Coote, M. L. *Theor. Chem. Acc.* **2010**, *125*, 3.
- (18) Eckert, F.; Diedenhofer, M.; Klamt, A. *Mol. Phys.* **2010**, *108*, 229.
- (19) Simonson, T.; Carlsson, J.; Case, D. *J. Am. Chem. Soc.* **2004**, *126* (13), 4167.
- (20) Mongan, J.; Case, D. A. *Curr. Opin. Struct. Biol.* **2005**, *15*, 157.
- (21) Click, T. H.; Kaminski, G. A. *J. Phys. Chem. B* **2009**, *113*, 7844.
- (22) Li, H.; Hains, A.; Everts, J.; Robertson, A.; Jensen, J. H. *J. Phys. Chem. B* **2002**, *106* (13), 3486.
- (23) Riccardi, D.; Schaefer, P.; Cui, Q. *J. Phys. Chem. B* **2005**, *109* (37), 17715.
- (24) Kamerlin, S. C. L.; Haranczyk, M.; Warshel, A. *J. Phys. Chem. B* **2009**, *113*, 1253.
- (25) Davies, J. E.; Doltsinis, N. L.; Kirby, A. J.; Roussev, C. D.; Sprik, M. *J. Am. Chem. Soc.* **2002**, *124*, 6594.
- (26) Ivanov, I.; Chen, B.; Raugei, S.; Klein, M. *J. Phys. Chem. B* **2006**, *110* (12), 6365.
- (27) Simon, C.; Ciccotti, G.; Klein, M. *Chem. Phys. Chem.* **2007**, *8* (14), 2072.
- (28) Maurer, P.; Iftimie, R. *J. Chem. Phys.* **2010**, *132*, 074112.
- (29) Sulpizi, M.; Sprik, M. *Phys. Chem. Chem. Phys.* **2008**, *10*, 5238.
- (30) Cheng, J.; Sulpizi, M.; Sprik, M. *J. Chem. Phys.* **2009**, *131*, 154504.
- (31) Sulpizi, M.; Sprik, M. *J. Phys.: Condens. Matter* **2010**, *22*, 284116.
- (32) Cheng, J.; Sprik, M. *J. Chem. Theory Comput.* **2010**, *6*, 880.
- (33) Costanzo, F.; Della Valle, R. G.; Sulpizi, M.; Sprik, M. Submitted.
- (34) Marx, D. *Chem. Phys. Chem.* **2006**, *7*, 1848.
- (35) Kirkwood, J. G. *J. Chem. Phys.* **1935**, *3*, 300.

- (36) Becke, A. D. *Phys. Rev. A* **1988**, *38*, 3098.
- (37) Lee, C.; Yang, W.; Parr, R. *Phys. Rev. B* **1988**, *37*, 785.
- (38) Quickstep, version 2.0.0, CP2K Developers Group. <http://www.cp2k.berlios.de> (accessed August 2008).
- (39) Case, D. A.; Darden, T. A.; Cheatham, T. E., III; Simmerling, C. L.; Wang, J.; Duke, R. E.; Luo, R.; Merz, K. M.; Pearlman, D. A.; Crowley, M.; Walker, R. C.; Zhang, W.; Wang, B.; Hayik, S.; Roitberg, A.; Seabra, G.; Wong, K. F.; Paesani, F.; Wu, X.; Brozell, S.; Tsui, V.; Gohlke, H.; Yang, L.; Tan, C.; Mongan, J.; Hornak, V.; Cui, G.; Beroza, P.; Mathews, D. H.; Schafmeister, C.; Ross, W. S. Kollman, P. A. *AMBER 9*, University of California: San Francisco, CA, 2006.
- (40) Jorgensen, W. L.; Chandrasekhar, J.; Madura, J. D.; Impey, R. W.; Klein, M. L. *J. Chem. Phys.* **1983**, *79*, 926.
- (41) Phillips, J. C.; Braun, R.; Wang, W.; Gumbart, J.; Tajkhorshid, E.; Villa, E.; Chipot, C.; Skeel, R. D.; Kale, L.; Schulten, K. *J. Comput. Chem.* **2005**, *26*, 1781.
- (42) Seidel, R.; Faubel, M.; Winter, B.; Blumberger, J. *J. Am. Chem. Soc.* **2009**, *131*, 16127.
- (43) Moens, J.; Seidel, R.; Geerlings, P.; Faubel, M.; Winter, B.; Blumberger, J. *J. Phys. Chem. B* **2010**, *114*, 9173.
- (44) Blumberger, J. *Phys. Chem. Chem. Phys.* **2008**, *10*, 5651.
- (45) Blumberger, J.; Ensing, B.; Klein, M. L. *Angew. Chem., Int. Ed.* **2006**, *45*, 2893.
- (46) Blumberger, J.; Klein, M. L. *Chem. Phys. Lett.* **2006**, *422*, 210.
- (47) Zhao, Y.; Truhlar, D. G. *J. Chem. Phys.* **2006**, *125*, 194101.
- (48) Lide, D. R. *CRC Handbook of Chemistry and Physics*, 75th ed.; CRC Press: Boca Roton, FL, 1995.
- (49) Solar, S.; Getoff, N.; Surdhar, P.; Armstrong, D.; Singh, A. *J. Phys. Chem.* **1991**, *95* (9), 3639.

Constant pH Molecular Dynamics in Explicit Solvent with λ -Dynamics

Serena Donnini, Florian Tegeler,[†] Gerrit Groenhof,* and Helmut Grubmüller*

Department of Theoretical and Computational Biophysics, Max Planck Institute for Biophysical Chemistry, Göttingen, Germany

 Supporting Information

ABSTRACT: pH is an important parameter in condensed-phase systems, because it determines the protonation state of titratable groups and thus influences the structure, dynamics, and function of molecules in solution. In most force field simulation protocols, however, the protonation state of a system (rather than its pH) is kept fixed and cannot adapt to changes of the local environment. Here, we present a method, implemented within the MD package GROMACS, for constant pH molecular dynamics simulations in explicit solvent that is based on the λ -dynamics approach. In the latter, the dynamics of the titration coordinate λ , which interpolates between the protonated and deprotonated states, is driven by generalized forces between the protonated and deprotonated states. The hydration free energy, as a function of pH, is included to facilitate constant pH simulations. The protonation states of titratable groups are allowed to change dynamically during a simulation, thus reproducing average protonation probabilities at a certain pH. The accuracy of the method is tested against titration curves of single amino acids and a dipeptide in explicit solvent.

1. INTRODUCTION

Together with temperature, pressure, and ionic strength, pH is one of the key parameters that determine the structure and dynamics of proteins in solution. Most notably, many proteins denature at low pH values,¹ and aggregation, such as formation of amyloid fibrils in Alzheimer's disease² and insulin aggregation,³ is pH-dependent. Because the function of a protein depends on its structure, pH is critical for protein function. Examples of pH-dependent regulation of protein function are the pH-controlled gating of membrane channels,^{4–6} or activation of influenza virus in host cells.⁷

pH affects protein structure, because the protonation state of the ionizable groups of a protein depends on pH, in particular histidine amino acids for which the proton affinity (pK_a) is very close to the physiological pH. Mainly via its charge, the protonation state of each ionizable group influences, in turn, the physicochemical properties of proteins, their structure, and their function.

Despite its relevance to biomolecular structure and function, pH and changes of protonation state of titratable groups of a protein are usually not described in computer simulations. Typically, a structure with fixed protonation states is used, chosen according to the most probable protonation arrangement at a given pH. This choice is often not straightforward, because hydrogens are usually not resolved in X-ray crystallography and the acid dissociation constant (K_a) values of the ionizable groups, in most cases, are not known. Therefore, the protonation state must be inferred from NMR⁸ or spectroscopic data,⁹ or from electrostatic calculations (e.g., Poisson–Boltzmann (PB)^{10,11} or Generalized Born¹² approaches). Furthermore, changes in the protonation state, either due to a change in the environment pH or in the protein conformation, as well as equilibrium protonation fluctuations leading to fractional protonation probabilities, are not taken into account by conventional simulations. As a consequence, the understanding of many biological phenomena, which involve a redistribution of charge, such as ligand binding reactions

inducing a proton redistribution,^{13,14} peptide insertion in membranes (e.g., fusion peptides),^{15,16} and pH-dependent conformational changes,^{2,6} would greatly benefit from a dynamic description of the protonation states.

Several attempts have been made to overcome these limitations. The most-accurate way of modeling (de)protonation events is to describe the system at a quantum mechanics level, where the electronic structure responds to changes in the local environment. However, these calculations are very expensive, in terms of computational cost. This drawback has been partly overcome in mixed quantum mechanics/molecular mechanics approaches,¹⁷ where only the ionizable groups of the protein are treated at the quantum level.

Computationally more affordable approaches to describe proton transfer events are EVB^{18–21} and QHOP²² methods. Here, the potential energy surface on which protons move is parametrized by *ab initio* calculations, whereas the rest of the system is described by a molecular mechanics force field.

A complication common to these approaches is that the equilibrium state is generally reached at time scales that are much slower than those accessible to molecular dynamics (MD) simulations. This is particularly true for protein systems, where typical deprotonation times of ionizable groups in the interior of a protein are microseconds or slower.²³ As a consequence, enhanced sampling of the transitions between the protonated and deprotonated state is particularly relevant for simulations of protein systems. For the aforementioned approaches, however, there is no obvious way how to enhance proton transfer rates.

A further problem concerns the proper description of the pH of a solution. The average hydronium concentration in a typical simulation box can be described by a time average, as well as via an ensemble average. In the case of a time average, because of the fact that the concentrations of hydronium considered are low,

Received: January 26, 2011

Published: April 25, 2011

typically pH 7, it might require very long simulation times to sample the hydronium distribution in the solution. In the case of the ensemble average, however, unpractically large simulation boxes would have to be considered, as, for example, for a typical simulation box of $\sim 30\,000$ water molecules, one hydronium ion already corresponds to a pH of $\sim 2-3$, thus increasing the computational cost of the calculation.

To address these issues in the context of force field simulations, several approaches have been proposed, all of which use a titration coordinate λ , which describes the protonation state of a certain ionizable group. For example, values of $\lambda = 0$ and $\lambda = 1$ correspond to the protonated and deprotonated states of a titratable group, respectively, as will be used in this work. Two main categories of approaches can be distinguished depending on the nature—discrete or continuous—of this titration coordinate.²⁴

A discrete titration coordinate is typically used by methods combining MD and Monte Carlo (MC) simulations for the sampling of the protonation reaction coordinate. At intervals during the MD simulation, a MC step is performed, in which the protonation state of a residue is changed. The acceptance criterion to keep the new protonation state is based on the protonation free energy of the titratable group, which is computed at every MC step. The major differences between the approaches in this category concern the way that this free energy is computed. In the approaches of Baptista and co-workers,²⁵ Dlugosz and Antosiewicz²⁶ and Mongan and Case,¹² the contribution of each protonation state to the protonation partition function is evaluated, and the protonation free energy (and $\text{p}K_{\text{a}}$) is then obtained from the partition function. Because all possible protonation states of the system have to be considered, the computational effort formally scales exponentially (2^N) with the number of titratable sites in the system (N). In practice, however, MC sampling and cutoffs are applied to reduce computational effort. To estimate the free energy of each state, implicit solvent Poisson–Boltzmann (PB)^{25,26} or Generalized Born¹² approaches are used. The use of continuum approximations in the estimation of protonation free energies has the advantage of reducing degrees of freedom of the system. However, to describe more-complex systems, such as membrane proteins, or systems such as channels for which explicit water molecules are crucial, continuum solvent models are of limited use.

In contrast, Bürgi et al. suggested to evaluate the protonation free energy at the MC step by a short thermodynamic integration (TI) simulation.²⁷ However, the cost of the free-energy calculation step can become significant, because it has to be evaluated at each trial. Also, inclusion of interactions between titratable sites is difficult.

In contrast to MD/MC simulations, in the second category of approaches, the titration coordinate λ is allowed to change continuously between the protonated and deprotonated states. Börjesson and Hünenberger^{28,29} developed the “acidostat” method, where the extent of deprotonation is relaxed to equilibrium by weak coupling to a proton bath in a way similar to methods for constant temperature and pressure.³⁰ Equilibrium fluctuations of the protonation states are not described, and each site thus experiences the average effect of the others.

In a different approach, introduced by Merz and Pettitt,³¹ the continuous λ coordinate is treated as an additional particle of the system, which is propagated in time, according to the equations of motion. The potential of the system is coupled to the chemical potential, which is a function of pH, of the reactants and of the

products. Along the same lines, the successive λ -dynamics approach³² and λ -adiabatic free-energy dynamics³³ treat λ as a dynamical variable in the Hamiltonian. In particular, the λ -dynamics approach was applied to constant pH simulations in implicit solvent by Lee et al.³⁴ and Khandogin and Brooks.^{35,36} In their approach, the potential energy landscape, which drives continuous changes of λ , is modulated by the potentials of isolated model titratable groups, and by the pH. Protons are not transferred explicitly to bulk water, forming H_3O^+ ; rather, similar to the acidostat of Börjesson and Hünenberger,^{28,29} the proton-solvation contribution to the force acting on λ is implicitly taken into account. Because this contribution depends on pH, by setting the pH parameter in the simulation, the effect of the proton concentration is included. Coupling between titratable sites, described by multiple λ particles, is implicitly taken into account via the potential energy landscape. In principle, linear scaling of the calculation with the number of protonatable sites is achieved. Because of the continuous character of the titration coordinate, fractional λ values can occur, which correspond to a partially protonated state. To decrease the population of these *unphysical* states, a barrier potential is used.³⁴ This is introduced as a separate parabolic function centered at $\lambda = 0.5$.³⁴ Alternatively, *ad hoc* nonlinear interpolation schemes between the potentials of the end states sampled by λ have been used to decrease the population of intermediate λ values, and thus obtain minima at $\lambda = 0$ and $\lambda = 1$.³³

As seen, most of the approaches for constant pH simulations both in the first and second category rest on an implicit description of the solvent. We are not aware of any fully atomistic description that (i) achieves sampling of the relevant space of the titration coordinate (i.e., the physically meaningful end states) and (ii) allows one to control the protonation/deprotonation rate.

In this work, we develop and test a framework to describe changes in protonation states at constant pH that meets all of these requirements. Our method extends the λ -dynamics approach of Brooks and co-workers^{32,34,35} by introducing a new coupling scheme to describe chemically coupled titratable sites, such as those on the side chain of histidine. Both pH and, via the height of the barrier potential, the protonation rates can be controlled to either reflect experimental proton transfer rates, if available, or to enhance sampling of the protonation space. The method has been implemented within the MD package GROMACS.^{37–39}

To test our method, the titration behavior of simple systems in an explicit solvent was analyzed. First, we considered glutamic acid with neutral termini. To provide a simple example of interactions that can occur in a protein environment, a small dipeptide of sequence Glu-Ala was simulated. Because of its importance in protein systems, imidazole and histidine were chosen as a test case for chemically coupled titratable sites. Finally, the effect of different temperature coupling schemes and different barrier potential heights on deprotonation/protonation rates was assessed.

2. THEORY

To clarify the notation, we will first summarize the thermodynamic integration and λ -dynamics approaches. Subsequently, we will describe and develop the building blocks of our approach. First, we will describe how the interval sampled by the titration coordinate λ is constrained, to describe the protonated and deprotonated states of the system during the constant pH

simulation. We will then specify how λ is coupled to a temperature bath. After introducing the thermodynamic cycle that is used to couple the protonated and deprotonated states to the appropriate reference states, we will develop the constant pH MD method. Finally, we will generalize the λ -dynamics approach for multiple protonation sites in a protein.

2.1. Thermodynamic Integration. Thermodynamic integration (TI)⁴⁰ is used to calculate the free-energy difference (ΔG) between a reactant state R and a product state P:

$$\Delta G_{PR} = \int_{\lambda=0}^{\lambda=1} d\lambda \left\langle \frac{\partial H_{TI}(\lambda)}{\partial \lambda} \right\rangle_{\lambda} \quad (1)$$

Here, H_{TI} is the Hamiltonian of the system, and λ is a coupling parameter that interpolates between the R ($\lambda = 0$) and P ($\lambda = 1$) states, e.g.,

$$H_{TI}(\lambda) = (1 - \lambda)H_0 + \lambda H_1 \quad (2)$$

To calculate ΔG via eq 1, λ is changed from 0 to 1 during the simulation, thus forcing the system from its reactant to its product state. The ensemble average in eq 1 is then taken from the MD ensemble generated from the Hamiltonian $H_{TI}(\lambda)$.

For later use, and following the notation of Kong and Brooks,³² we split the Hamiltonians of the reactant and product in λ -dependent (\tilde{H}_0 and \tilde{H}_1) and λ -independent (H_{Env}) parts:

$$H_{TI}(\lambda) = (1 - \lambda)\tilde{H}_0 + \lambda\tilde{H}_1 + H_{Env} \quad (3)$$

2.2. λ -Dynamics. In the λ -dynamics approach,³² a Hamiltonian similar to eq 3 is used. In contrast to TI, λ is defined as an additional dynamic degree of freedom of the system with mass m , coordinate λ , and velocity $\dot{\lambda}$. Accordingly, the Hamiltonian of the system is now expressed by³²

$$H(\lambda) = (1 - \lambda)\tilde{H}_0 + \lambda\tilde{H}_1 + H_{Env} + \frac{m}{2}\dot{\lambda}^2 + U^*(\lambda) \quad (4)$$

with a force acting on λ ,

$$F_{\lambda} = -\frac{\partial V(\lambda)}{\partial \lambda} \quad (5)$$

where $V(\lambda)$ is the potential energy part of the Hamiltonian in eq 4:

$$V(\lambda) = (1 - \lambda)\tilde{V}_0 + \lambda\tilde{V}_1 + V_{Env} + U^*(\lambda) \quad (6)$$

In eq 4, $(m/2)\dot{\lambda}^2$ is the kinetic energy term associated with the λ "particle". The λ -dependent potential term $U^*(\lambda)$ will serve as a biasing potential to limit the range of λ ; this will be defined further below.

2.3. Constraining the Interval of λ . Because only $\lambda = 0$ and $\lambda = 1$ represent physical states of the system—the protonated and deprotonated states—we require λ to be close to these values for most of the simulation time. More specifically, we require that:

- (1) the λ space is limited to the interval between the two physical states;
- (2) the average values of λ in the protonated and deprotonated states are close to 0 and 1, respectively;
- (3) the time spent at intermediate states by the system is short, i.e., the transitions between the protonated and deprotonated states are fast;
- (4) the residence time at the physical states is sufficiently long to allow conformational sampling of each state; and
- (5) the frequency of transitions can be controlled.

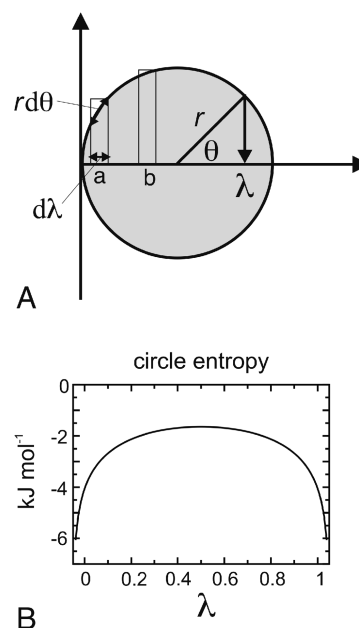


Figure 1. (A) Schematic describing the angular coordinate. λ is defined as a function of the angular θ coordinate, $\lambda = r \cos(\theta) + (1/2)$, with the radius of the circle being defined as $r = (1/2) + \sigma$, and σ a fluctuation size (see main text). The segments of circumference corresponding to the intervals a and b close to the end and center of the λ interval, respectively, are indicated. (B) Entropic free-energy term introduced by the use of an angular coordinate θ .

To address condition 1, a projection of an angular coordinate on the λ space has been proposed in previous applications.^{33,34,41} Here, we will extend this approach to meet also condition 2. Following Lee et al.,³⁴ we will address condition 3 by using a suitably chosen biasing potential. Finally, we will meet conditions 4 and 5 by adjusting the height of the biasing potential, taking into account the entropic part introduced by the use of the angular coordinate.

Note that a similar shape of the λ free-energy profile, which meets conditions 3 and 4, can be achieved also by designing *ad hoc* interpolation schemes between the potentials of the protonated and deprotonated states of λ , as previously proposed in the λ -adiabatic free-energy dynamics approach by Tuckerman and co-workers.³³ By adjusting the temperature of the λ particle, Tuckerman and co-workers,³³ ensured efficient barrier crossing, also meeting the last condition.

2.3.1. Projection of the Angular θ Coordinate on the λ Space. In order to constrain the space sampled by λ , we switch to a new dynamic angular coordinate θ , as shown in Figure 1. By this modification, the actual dynamics takes place in θ space, and λ is redefined as the projection of θ on the abscissa (see Figure 1),

$$\lambda = r \cos(\theta) + \frac{1}{2} \quad (7)$$

The force acting on θ is

$$F_{\theta} = -\frac{\partial V(\lambda(\theta))}{\partial \theta} = r \sin(\theta) \frac{\partial V(\lambda(\theta))}{\partial \lambda} \quad (8)$$

with V being the potential energy of the system, as defined in eq 6.

In contrast to previous approaches,^{33,34,41} where $r = 1/2$, and to meet condition 2, we chose $r = (1/2) + \sigma$, with an appropriate

fluctuation size σ . Several values of σ were tested. We have used a value of $\sigma = 0.05$, because, with this value, the average λ at the physical states was ~ 0 (protonated state) and ~ 1 (deprotonated state).

2.3.2. Biasing Potential. To meet condition 3, a parabolic biasing potential of the form³⁴

$$U^*(\lambda) = 4h\lambda(1 - \lambda) \quad (9)$$

is used. By adjusting its height h , the frequency of the protonation transitions can be controlled, as required by condition 5.

Note that the choice of the above angular coordinate implies an entropic contribution to the effective free energy governing the λ -dynamics. This contribution originates from the higher density of λ states at the end points of the λ interval, with respect to the center of the interval, as indicated by the mapping of the intervals a and b in Figure 1A onto the circumference. The segment length for a given value of λ is

$$d\lambda = d\theta \sqrt{r^2 - \left(\lambda - \frac{1}{2}\right)^2} \quad (10)$$

resulting in a free-energy contribution of

$$\begin{aligned} A(\lambda) = -TS(\lambda) &= RT \ln \left| \frac{d\lambda}{d\theta} \right| \\ &= \frac{1}{2} RT \ln \left[r^2 - \left(\lambda - \frac{1}{2}\right)^2 \right] \end{aligned} \quad (11)$$

where R is the gas constant and T is the temperature. The $A(\lambda)$ term in eq 11 stabilizes the end parts of the λ interval by a barrier of a few kJ mol^{-1} , as shown in Figure 1B. This barrier needs to be taken into account when adjusting the height h of the biasing potential.

Note that the free energy $A(\lambda)$ in Figure 1B, as well as the corresponding probability distribution, diverges for $\lambda = 0$ and $\lambda = 1$. This is, however, not a problem, because, for any finite interval $[\lambda_1 \cdots \lambda_2]$, there is a finite probability for the system to be within this interval. Similarly, the partition function integral

$$Z = \int_{\lambda=0}^{\lambda=1} \exp(-\beta A(\lambda)) d\lambda = \pi \quad (12)$$

with $\beta = 1/(\kappa_B T)$, over every finite λ interval of the free-energy curve is also finite.

2.4. λ -Dynamics Thermostat. The temperature of the λ particle is kept constant by coupling the particle to an external heat bath. We have considered two coupling schemes, the Berendsen,³⁰ or weak coupling thermostat, and the Andersen thermostat.⁴²

It is not clear *a priori* whether to couple the λ particle to (i) the same heat bath as the *real* atoms of the system, or (ii) a separate heat bath. In the first situation, the temperature is computed from the total kinetic energy of the real atoms and the λ particle. In the second, different heat baths are used to couple the λ particle and real atoms separately, and the kinetic energy of the λ particle is used to calculate the temperature of the λ subsystem.

Therefore, we have tested the two coupling schemes. For variant (i), we used the Berendsen thermostat (with a coupling time of 0.10 ps), whereas, for variant (ii), the λ particle was coupled to the Andersen thermostat (with a coupling time of 0.15 ps), and the rest of the system to the Berendsen thermostat.

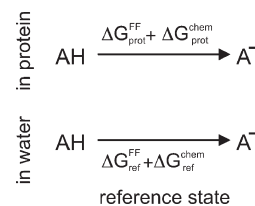


Figure 2. Equilibria between the protonated (AH) and deprotonated (A^-) forms of a titratable site in a protein and in the reference state in water. $\Delta G_{\text{prot}}^{\text{FF}}$ and $\Delta G_{\text{ref}}^{\text{FF}}$ are obtained from a molecular dynamics (MD) simulation, whereas $\Delta G_{\text{prot}}^{\text{chem}}$ and $\Delta G_{\text{ref}}^{\text{chem}}$ include contributions from the environmental pH and from bonded terms, which are missing in the force field. We assume $\Delta G_{\text{prot}}^{\text{chem}} \approx \Delta G_{\text{ref}}^{\text{chem}}$.

We have used the Andersen thermostat, because the Berendsen thermostat is not suitable for low-dimensional systems, such as the λ subsystem.³⁰ At 300 K and with a λ particle mass of 20 u, the latter coupling scheme generated λ -trajectories that were more suitable (i.e., sufficiently long residence time at the physical states, fast transitions) to simulate biomolecular systems (see the Results section).

2.5. Constant pH MD Simulations with λ -Dynamics. To describe protonation and deprotonation events of a titratable site at a given pH, we included, within the Hamiltonian in eq 4, (i) the effect of the external pH bath on protonation and (ii) contributions to the free energy of protonation due to breakage and formation of chemical bonds, which are not described by the force field. These two free-energy contributions will be described by an additional term $V^{\text{chem}}(\lambda)$, which will shift the protonation equilibria by a certain free energy (ΔG^{chem}).

To determine ΔG^{chem} , we considered the equilibrium between a protonated (AH) and a deprotonated acid (A^-), in a (solvated) protein (see Figure 2, top) and in water (see Figure 2, bottom). We will use the latter as a *reference state*. This state is chosen such that a measured deprotonation free energy is available, and the reference compound AH is chemically similar for the reference and protein states, generally a solvated amino acid. Note that no H^+ or H_3O^+ species appears on the right side of the equilibria in Figure 2, since, here, we consider the free-energy difference between the protonated and deprotonated forms of the titratable site. Below, we will describe how the pH dependency of this free energy is taken into account.

The free energies for the top (prot) and bottom (ref) reactions of Figure 2 are split into a contribution ΔG^{FF} (obtained via a force field calculation) and ΔG^{chem} (contributions (i) and (ii) from pH bath and bond breakage and formation, respectively). Because of the choice of the reference state, ΔG^{chem} is not expected to differ significantly between the top and bottom reactions in Figure 2.^{18,43,44} Thus, the dominant contribution to the difference in the free energies of these two reactions is due to the different environment of the titratable site in the protein and in water. This contribution essentially depends on the long-range interactions of the titratable group, which are described by the force-field free-energy terms $\Delta G_{\text{prot}}^{\text{FF}}$ and $\Delta G_{\text{ref}}^{\text{FF}}$.

Accordingly,

$$\Delta G_{\text{prot}}^{\text{chem}} \approx \Delta G_{\text{ref}}^{\text{chem}} = (\ln 10)RT(\text{p}K_{\text{a,ref}} - \text{pH}) - \Delta G_{\text{ref}}^{\text{FF}} \quad (13)$$

where $\text{p}K_{\text{a,ref}}$ is the measured $\text{p}K_{\text{a}}$ of the reference titratable site in the reference state. The pH term describes the pH dependency of

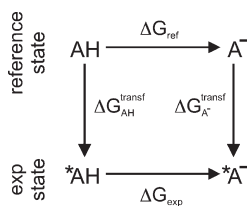


Figure 3. Thermodynamic cycle for the calculation of the reference free-energy difference ΔG_{ref} . AH and A^- are transformed to chemically similar compounds $*AH$ and $*A^-$, respectively, for which the free-energy difference has been experimentally measured (ΔG_{exp}).

the equilibria in Figure 2, thus accounting for the missing proton in Figure 2.

The last contribution in eq 13, $\Delta G_{\text{ref}}^{\text{FF}}$ is obtained from a thermodynamic integration calculation (reference free-energy simulation), which is performed prior to starting the constant pH simulation,

$$\begin{aligned} \Delta G_{\text{ref}}^{\text{FF}} &= G_{\text{ref}}^{\text{FF}}(\lambda = 1) - G_{\text{ref}}^{\text{FF}}(\lambda = 0) \\ &= \int_{\lambda=0}^{\lambda=1} \left\langle \frac{\partial H_{\text{ref}}(\lambda)}{\partial \lambda} \right\rangle_{\lambda} d\lambda \end{aligned} \quad (14)$$

where $H_{\text{ref}}(\lambda)$ is the Hamiltonian of the reference system.

Having determined ΔG^{chem} for the protein state, the following potential $V^{\text{chem}}(\lambda)$ serves to implement the desired free-energy difference in the λ -dynamics calculations:

$$V^{\text{chem}}(\lambda) = \lambda(\ln 10)RT(\text{p}K_{\text{a,ref}} - \text{pH}) - \tilde{\Delta G}_{\text{ref}}^{\text{FF}}(\lambda) \quad (15)$$

with $\tilde{\Delta G}_{\text{ref}}^{\text{FF}}(\lambda)$ as a polynomial fit to $G_{\text{ref}}^{\text{FF}}(\lambda)$, which is typically close to a parabola.^{45,46}

Note the use of $\tilde{\Delta G}_{\text{ref}}^{\text{FF}}(\lambda)$ to describe the $\Delta G_{\text{ref}}^{\text{FF}}(\lambda)$ contribution, instead of a linear function of λ (analogously to the first term in eq 15). By this choice, the free-energy profile of the reference state ($G_{\text{ref}}^{\text{FF}}(\lambda)$) is effectively subtracted (except for fluctuations) from the one of the protein state ($G_{\text{prot}}^{\text{FF}}(\lambda)$). In the simplest case of a constant pH simulation of an amino acid in water, in which case $G_{\text{ref}}^{\text{FF}}(\lambda)$ and $G_{\text{prot}}^{\text{FF}}(\lambda)$ are the same, $\tilde{\Delta G}_{\text{ref}}^{\text{FF}}(\lambda)$ will, therefore, remove the barrier in the energy landscape between the protonated and deprotonated states of the titratable site. Therefore, the barrier is given and controlled directly by the height of the biasing potential, which thus can be adjusted to achieve the desired transition rates. In the less trivial case of a protein simulation, $\tilde{\Delta G}_{\text{ref}}^{\text{FF}}(\lambda)$ will not remove the barrier completely, but still the remaining perturbation can be assumed to be small also in the general case.

2.5.1. Reference Thermodynamic Cycle. If a measured $\text{p}K_{\text{a}}$ is available only for a compound that is similar, but not identical, to that considered in the reference state, a thermodynamic cycle can be used to calculate and correct for the free-energy difference due to this modification. In Figure 3, the free-energy difference of the reference state (ΔG_{ref}) is given by

$$\Delta G_{\text{ref}} = \Delta G_{\text{exp}} + (\Delta G_{\text{AH}}^{\text{transf}} - \Delta G_{\text{A}^-}^{\text{transf}}) \quad (16)$$

where $\Delta G_{\text{AH}}^{\text{transf}}$ and $\Delta G_{\text{A}^-}^{\text{transf}}$ indicate the free-energy differences for the transformation of the protonated and deprotonated forms of the reference state into the corresponding compounds of the experimentally known state (*exp*), respectively. The terms $*AH$ and $*A^-$ in Figure 3 denote compounds chemically similar to those in the reference state.

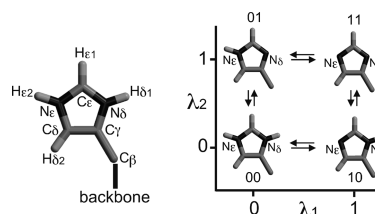


Figure 4. Four protonation states of the histidine side chain: λ_1 and λ_2 are the titration coordinates of the N_{ϵ} and N_{δ} deprotonation sites, respectively. $\lambda_1 = \lambda_2 = 0$ (00) corresponds to the fully protonated and positively charged histidine; $\lambda_1 = 0, \lambda_2 = 1$ (01) and $\lambda_1 = 1, \lambda_2 = 0$ (10) correspond to the neutral histidine; and $\lambda_1 = \lambda_2 = 1$ (11) corresponds to the negatively charged fully deprotonated histidine.

After calculation of $\Delta G_{\text{AH}}^{\text{transf}}$ and $\Delta G_{\text{A}^-}^{\text{transf}}$ by conventional TI, these two free-energy differences are included in eq 4, similar to $V^{\text{chem}}(\lambda)$ in eq 15:

$$V^{\text{transf}}(\lambda) = \lambda(\Delta G_{\text{AH}}^{\text{transf}} - \Delta G_{\text{A}^-}^{\text{transf}}) \quad (17)$$

This approach will be used further below to parametrize the λ -dynamics simulation of histidine.

2.6. Generalization to Multiple Titratable Groups. The above formulation of the λ -dynamics approach for constant pH simulations is extended to multiple titratable groups by assigning a separate λ -coordinate to each titratable group in the protein.^{34,35} In order to illustrate the approach, we first will consider the case of two titratable sites on a protein and derive the Hamiltonian for this system. We will then distinguish the case of two sites, which are (i) chemically *uncoupled* and (ii) chemically *coupled*. In the first case of uncoupled sites, interactions between titratable sites are mainly governed by electrostatics. In terms of the force field, these sites interact only via nonbonded interactions, which are described by the Coulomb and Lennard-Jones potential energies. For this reason, the Hamiltonian for uncoupled sites can be extended in a straightforward manner to any number N of uncoupled titratable sites in a protein,^{34,35} and formally linear scaling with the number of sites is achieved. As this approach will be used later on, we will review it below. For chemically coupled sites, this straightforward approach is not applicable. In this case, the chemical character, which is described in the force field by a set of parameters, such as atomic charges, bonds, and angles, of the titratable sites depends on the protonation states of the respective other coupled sites. Because of this dependency, cross terms occur in the expression for the potential energies, which have to be taken into account explicitly, and the contributions of interacting atoms cannot be rearranged as conveniently as those for uncoupled sites. Therefore, unavoidably, in this case, the number of calculations scales exponentially with the number of sites, rather than linearly. Here, we will discuss the example of histidine, where the two deprotonation sites on the side chain are chemically coupled. Note that, in this case, since only two sites are coupled, the calculations still scale linearly. We will also discuss how this description of histidine differs from the treatment of Khandogin and Brooks.³⁵

2.6.1. Constant pH λ -Dynamics of Two Titratable Sites on a Protein. We start by considering the case of two titratable sites on a protein. Each of the two sites i and j is described by a λ -coordinate, λ_i and λ_j , respectively. At $\lambda = 0$, the site is protonated; at $\lambda = 1$, the site is deprotonated. Independent of whether the two titratable groups are uncoupled or coupled, four protonation states are relevant. In Figure 4, these four states for histidine are denoted as 00 (both sites i and j protonated), 10

(site i deprotonated and site j protonated), 01 (site i protonated and site j deprotonated), and 11 (both sites i and j deprotonated).

Applying eq 4 in a first step to each group i and j separately, and combining the two resulting Hamiltonians again, according to eq 4 in a second step, yields

$$H(\lambda_i, \lambda_j) = (1 - \lambda_i)[(1 - \lambda_j)\tilde{H}_{00} + \lambda_j\tilde{H}_{01}] + \lambda_i[(1 - \lambda_j)\tilde{H}_{10} + \lambda_j\tilde{H}_{11}] + H_{\text{Env}} + \left(\frac{m_i}{2}\right)\dot{\lambda}_i^2 + \left(\frac{m_j}{2}\right)\dot{\lambda}_j^2 + U^*(\lambda_i) + U^*(\lambda_j) \quad (18)$$

where the first four Hamiltonians on the right side of the equation describe the titratable sites of the protein in the four protonation states in Figure 4, and $U^*(\lambda)$ is the biasing potential discussed earlier in section 2.3.2.

Similarly, the potential energy of the system described by the Hamiltonian $H(\lambda_i, \lambda_j)$ in eq 18 is given as

$$V(\lambda_i, \lambda_j) = (1 - \lambda_i)[(1 - \lambda_j)V_{00} + \lambda_jV_{01}] + \lambda_i[(1 - \lambda_j)V_{10} + \lambda_jV_{11}] + V_{\text{Env}} + U^*(\lambda_i) + U^*(\lambda_j) \quad (19)$$

where the first four potential energies V on the right side of the equation describe the interactions of the titratable sites in their respective states (see Figure 4), with forces acting on λ_i and λ_j , respectively:

$$-\frac{\partial V(\lambda_i, \lambda_j)}{\partial \lambda_i} = -[(1 - \lambda_j)(V_{10} - V_{00}) + \lambda_j(V_{11} - V_{01})] - \frac{dU^*(\lambda_i)}{d\lambda_i} \quad (20)$$

and

$$-\frac{\partial V(\lambda_i, \lambda_j)}{\partial \lambda_j} = -[(1 - \lambda_i)(V_{01} - V_{00}) + \lambda_i(V_{11} - V_{10})] - \frac{dU^*(\lambda_j)}{d\lambda_j} \quad (21)$$

As can be seen for the case of two interacting titratable sites, the force acting on each site depends on the protonation state of the respective other site, which also holds true for the general case of N interacting sites. This interdependence entails an exponential scaling.

2.6.2. Chemically Uncoupled Titratable Sites. If the two titratable sites are chemically uncoupled, however, the computational complexity is dramatically reduced. Uncoupled sites interact only via long-range (nonbonded) interactions. Below, we will show how these interactions (Coulombic and van der Waals) are efficiently described, achieving linear scaling of the calculations.

Coulombic Interactions. For two uncoupled titratable sites i and j , the Coulombic potential energy (V^c) for two interacting atoms simplifies (from eq 19) to

$$V^c(\lambda_i, \lambda_j) = \frac{1}{4\pi\epsilon}[(1 - \lambda_i)q_0^i + \lambda_iq_1^i][(1 - \lambda_j)q_0^j + \lambda_jq_1^j] \quad (22)$$

where q_0 and q_1 are the atomic charges in the protonated ($\lambda = 0$) and deprotonated ($\lambda = 1$) states, respectively, of the corresponding atoms, r is the distance between the two atoms, and ϵ is the permittivity. Note that eq 22 involves only two states, compared to the four states of eq 19.

Accordingly, the force acting on λ_i is

$$-\frac{\partial V^c(\lambda_i, \lambda_j)}{\partial \lambda_i} = -[V^c(\lambda_i = 1, \lambda_j) - V^c(\lambda_i = 0, \lambda_j)] \quad (23)$$

where the Coulombic energies $V^c(\lambda_i = 0, \lambda_j) = [1/(4\pi\epsilon)]q_0^i[(1 - \lambda_j)q_0^j + \lambda_jq_1^j]$ and $V^c(\lambda_i = 1, \lambda_j) = [1/(4\pi\epsilon)]q_1^i[(1 - \lambda_j)q_0^j + \lambda_jq_1^j]$ are evaluated at λ_j .

Equation 23 is extended in a straightforward manner to N uncoupled interacting sites:

$$-\frac{\partial V^c(\lambda_1, \dots, \lambda_{i-1}, \lambda_i, \lambda_{i+1}, \dots, \lambda_N)}{\partial \lambda_i} = -[V^c(\lambda_1, \dots, \lambda_{i-1}, \lambda_i = 1, \lambda_{i+1}, \dots, \lambda_N) - V^c(\lambda_1, \dots, \lambda_{i-1}, \lambda_i = 0, \lambda_{i+1}, \dots, \lambda_N)] \quad (24)$$

and linear scaling of the calculation with the number of interacting uncoupled sites is achieved.

van der Waals Interactions. The remaining long-range interactions are somewhat less straightforward. We consider the usual case where the van der Waals energies, together with the Pauli repulsion, are described by a Lennard-Jones potential V_{LJ} :

$$V_{\text{LJ}} = \frac{A}{r^{12}} - \frac{B}{r^6} \quad (25)$$

where r is the distance between the two atoms, and A and B are two parameters, which depend on the pairs of interacting atoms i and j ,

$$A = (A^i A^j)^{1/2} \quad (26)$$

and similarly for B .

For two uncoupled titratable sites i and j , the Lennard-Jones potential energy for two interacting atoms is (here, we treat only the r^{12} part; the r^6 part is very similar)

$$V_{\text{LJ}}^{12}(\lambda_i, \lambda_j) = \frac{(1 - \lambda_i)[(1 - \lambda_j)A_{00} + \lambda_j A_{01}] + \lambda_i[(1 - \lambda_j)A_{10} + \lambda_j A_{11}]}{r^{12}} \quad (27)$$

where the indices of the A parameter indicate the protonation states of the two titratable sites (see Figure 4).

Similar to the Coulombic energy, eq 27 is rearranged in terms of the protonated ($\lambda = 0$) and deprotonated ($\lambda = 1$) values of the A^i and A^j Lennard-Jones parameters,

$$V_{\text{LJ}}^{12}(\lambda_i, \lambda_j) = \frac{[(1 - \lambda_i)(A_0^i)^{1/2} + \lambda_i(A_1^i)^{1/2}][(1 - \lambda_j)(A_0^j)^{1/2} + \lambda_j(A_1^j)^{1/2}]}{r^{12}} \quad (28)$$

with force acting on λ_i

$$-\frac{\partial V_{\text{LJ}}^{12}(\lambda_i, \lambda_j)}{\partial \lambda_i} = -[V_{\text{LJ}}^{12}(\lambda_i = 1, \lambda_j) - V_{\text{LJ}}^{12}(\lambda_i = 0, \lambda_j)] \quad (29)$$

The potentials $V_{\text{LJ}}^{12}(\lambda_i = 1, \lambda_j)$ and $V_{\text{LJ}}^{12}(\lambda_i = 0, \lambda_j)$ are obtained by evaluating the second term in square brackets on the right side of eq 28 prior to starting the force calculation, analogous to the calculation of the Coulombic forces. As a more technical remark, note that, in GROMACS,³⁹ the Lennard-Jones parameters are not accessible in a straightforward manner in the MD source code. Therefore, instead of interpolating linearly between $(A_0^j)^{1/2}$ and $(A_1^j)^{1/2}$, we define the atom type (a) of the j atom, which is

used to determine A_0^j and A_1^j , prior to calculating the force, by

$$a^j(\lambda_j) = \begin{cases} a_0 & \lambda_j \leq 0.5 \\ a_1 & \lambda_j > 0.5 \end{cases} \quad (30)$$

This yields, effectively, an approximation to the second term in square brackets on the right side of eq 28. Note that, in the GROMOS96 force field,⁴⁷ only the A term of the atoms of the carboxylic group changes upon deprotonation. Since, in the Lennard-Jones potential (eq 25), the A (the repulsion) term decays with $1/r^{12}$, the approximation in eq 30 is not expected to introduce significant artifacts.

2.6.3. Chemically Coupled Titratable Sites. We move now to the situation of chemically coupled sites. To illustrate this case, Figure 4 shows the four protonation states of histidine, where λ_1 and λ_2 denote the titration coordinates of the N_ϵ and N_δ sites, respectively. In contrast to the chemically uncoupled situation, here, the protonation state of one site (e.g., N_δ) does affect the charge of the other site (N_ϵ). Depending on the chemistry, other force-field parameters also may be affected. This prevents further simplification of eq 18, which leaves us with four Hamiltonians (\tilde{H}_{00} , \tilde{H}_{01} , \tilde{H}_{10} , and \tilde{H}_{11}) and four states for the atomic charges (q_{00} , q_{01} , q_{10} , and q_{11}). Therefore, the calculations will scale exponentially with the number of coupled sites, as each combination of the protonation states of the sites must be evaluated.

We note that this description of histidine differs from that of Khandogin and Brooks,³⁵ in that each of the two titratable sites on the side chain is described by a titration coordinate, and the coupling between the two sites is taken into account explicitly. Accordingly, our treatment also describes the doubly deprotonated, negatively charged form of histidine, which is not included in the model of Khandogin and Brooks,³⁵ where only three states are considered. Furthermore, our treatment is readily generalized to more than two chemically coupled titratable sites.

Chemically Coupled Reference States. The chemical coupling between titratable sites also must be taken into account for the reference states in a constant pH simulation. For example, when λ_2 changes from 0 to 1 in histidine, the reference deprotonation reaction of the titratable site described by λ_1 changes from the bottom ($00 \rightleftharpoons 10$) to the top ($01 \rightleftharpoons 11$) deprotonation equilibrium in Figure 4.

To account for this dependency, we define $V^{\text{chem}}(\lambda_1, \lambda_2)$ (see for comparison $V^{\text{chem}}(\lambda)$ in eq 15), e.g., for group λ_1 , as

$$V^{\text{chem}}(\lambda_1, \lambda_2) = \lambda_1(\ln 10)RT(\text{p}K_{a,\text{ref}}^*(\lambda_2) - \text{pH}) - \Delta\tilde{G}_{\text{ref}}^{\text{FF}}(\lambda_1, \lambda_2) \quad (31)$$

where

$$\text{p}K_{a,\text{ref}}^*(\lambda_2) = (1 - \lambda_2)\text{p}K_{a,\text{ref}}(00 \rightleftharpoons 10) + \lambda_2\text{p}K_{a,\text{ref}}(01 \rightleftharpoons 11) \quad (32)$$

and $\Delta\tilde{G}_{\text{ref}}^{\text{FF}}(\lambda_1, \lambda_2)$ is a polynomial fit to $G_{\text{ref}}^{\text{FF}}(\lambda_1, \lambda_2)$, which is the force-field free-energy profile for the reference deprotonations. To determine $\Delta\tilde{G}_{\text{ref}}^{\text{FF}}(\lambda_1, \lambda_2)$, several reference free-energy simulations at different values of λ_2 are performed (see the Methods section).

Similarly to the reference state, the reference thermodynamic cycle (in section 2.5.1) of chemically coupled titratable sites will depend on the protonation state of the respective other sites. For

the example of histidine, eq 17 becomes, e.g., for group λ_1 ,

$$V^{\text{transf}}(\lambda_1, \lambda_2) = \lambda_1[(1 - \lambda_2)(\Delta G_{\text{AHH}^+} - \Delta G_{\text{AH}}) + \lambda_2(\Delta G_{\text{AH}} - \Delta G_{\text{A}^-})] \quad (33)$$

with ΔG_{AHH^+} , ΔG_{AH} , and ΔG_{A^-} being the transfer free energies of the double protonated (00), singly protonated (10 or 01), and fully deprotonated (11) forms of histidine (see Figure 4).

3. METHODS

3.1. $\text{p}K_a$ Calculations. To estimate the $\text{p}K_a$ of a titratable compound, constant pH simulations of the compound at different pH values were performed, similar to a titration experiment. From each simulation, the fraction (S) of deprotonated acid was calculated, and the Henderson–Hasselbalch equation was fitted to the obtained titration curve,

$$S^{\text{deprot}} = \frac{1}{10^{(\text{p}K_a - \text{pH})} + 1} \quad (34)$$

which, for N noninteracting titratable sites, takes the form

$$S^{\text{deprot}} = \sum_i^N \frac{1}{10^{(\text{p}K_{a,i} - \text{pH})} + 1} \quad (35)$$

In one case, where the fit was not satisfactory, the Hill equation has been used,

$$S^{\text{deprot}} = \frac{1}{10^{n(\text{p}K_a - \text{pH})} + 1} \quad (36)$$

where n is the Hill coefficient, which accounts for the degree of cooperativity ($n > 1$) or anticooperativity ($n < 1$) of the system.^{48,49}

The fraction of deprotonated acid S in a constant pH simulation was calculated from the titration coordinate λ during the simulation, where all steps with $\lambda < 0.1$ were recorded as protonated and those with $\lambda > 0.9$ as deprotonated. The error in the calculated S was estimated via a Bayesian approach from the number of transitions observed during the simulations between the protonated and deprotonated states (see the Supporting Information).

In contrast to a conventional titration experiment, in a constant pH simulation, the titration coordinates of each titratable site in the compound are accessible. Therefore, both the *macroscopic* (or *apparent*) $\text{p}K_a$ values of the entire compound, and the *microscopic* $\text{p}K_a$ values of each site, can be estimated.

For a compound with two titratable sites, such as histidine, the equilibrium constant for the deprotonation of the first proton ($K_{a,I}$) is related to the equilibrium constants for the deprotonations at sites N_ϵ and N_δ ($K'_{a,1}$ and $K'_{a,2}$, respectively) by

$$K_{a,I} = K'_{a,1} + K'_{a,2} \quad (37)$$

from which follows

$$\text{p}K_{a,I} = -\log_{10}(10^{-\text{p}K'_{a,1}} + 10^{-\text{p}K'_{a,2}}) \quad (38)$$

with $\text{p}K_{a,I}$ the (macroscopic) $\text{p}K_a$ value for the deprotonation of the first proton of histidine, and $\text{p}K'_{a,1}$ and $\text{p}K'_{a,2}$ the (microscopic) $\text{p}K_a$ value for the deprotonation of the first proton of histidine at sites N_ϵ and N_δ , respectively.

Similarly, the equilibrium constant for the deprotonation of the second proton of histidine ($K_{a,II}$) is related to the equilibrium constants for the deprotonations at sites N_ϵ and N_δ ($K''_{a,1}$ and

$K''_{a,2}$, respectively) by

$$K_{a,\text{II}} = \frac{1}{\frac{1}{K''_{a,1}} + \frac{1}{K''_{a,2}}} \quad (39)$$

from which follows

$$\text{p}K_{a,\text{II}} = \log_{10}(10^{\text{p}K''_{a,1}} + 10^{\text{p}K''_{a,2}}) \quad (40)$$

where $\text{p}K_{a,\text{II}}$ is the second macroscopic $\text{p}K_a$ value of histidine, and $\text{p}K''_{a,1}$ and $\text{p}K''_{a,2}$ the microscopic $\text{p}K_a$ values for the deprotonation of the second proton at sites N_ϵ and N_δ , respectively.

In all cases, the error in the calculated $\text{p}K_a$ has been determined from the standard deviation of a set of four or five $\text{p}K_a$ obtained from different fragments of the simulations.

3.2. Constant pH MD Simulations. The constant pH MD simulation method, as described above, was implemented in the GROMACS MD package (version 3.3).^{37–39}

As test cases, constant pH simulations were carried out for four compounds: glutamic acid (Glu) with neutral termini, a dipeptide of sequence glutamic acid-alanine (Glu-Ala), imidazole, and a capped histidine (acetyl-NH-CHR-CO-methylamide with R the side chain of histidine). Glu, Glu-Ala, and histidine (His) were described with the GROMOS96 53A6 force field.⁵⁰ Force-field parameters of imidazole were adapted from histidine (atomic charges are listed in Table s1 in the Supporting Information). For the fully deprotonated form of histidine, no force-field parameters are available in GROMOS96.⁵⁰ Charges for this protonation state were thus taken from imidazole and, therefore, are not very accurate. However, in the pH interval considered here (pH 4–10), the doubly deprotonated state should never be visited, because the $\text{p}K_a$ value for the second deprotonation of histidine is far beyond than the pH interval.¹ Thus, we do not expect a large influence of the charges on the protonation populations.

Each compound was placed in a dodecahedral box, which was subsequently filled with ~ 4200 – 5200 SPC (simple point charge) water molecules.⁵¹ Interactions between atoms within 1.0 nm were evaluated at every step of the simulation, while interactions with atoms beyond 1.0 nm were evaluated every five steps. The Lennard-Jones long-range cutoff was set to 1.6 nm. The Particle Mesh Ewald (PME)^{52,53} was used for the long-range electrostatic interactions, with a grid spacing of 0.12 nm and an interpolation order of 4. Constant pressure and temperature were maintained by weakly coupling the system to an external bath at 1 bar and 300 K, using the Berendsen barostat and thermostat³⁰ with coupling times of 1.0 and 0.1 ps, respectively. A leapfrog integrator was used with an integration time step of 2 fs. The bond distances and bond angles of water were constrained using the SETTLE algorithm.⁵⁴ All other bond distances were constrained using the LINCS algorithm.⁵⁵ Prior to the simulations, the potential energy of each system was minimized using a steepest descent approach. A 50-ps MD simulation with position restraints (with a force constant of $1000 \text{ kJ mol}^{-1} \text{ nm}^{-2}$) on the amino acid/peptide atoms was then performed to relax the water molecules. Finally, a 5-ns simulation was performed to equilibrate each system before starting the constant pH MD simulations.

Deprotonation of a site was achieved by transforming the titratable hydrogen into a dummy atom, which is topologically bound to the acid, but has no interactions with the rest of the system. Charges and atom types of the ionizable groups were changed accordingly, from their force-field values in the

protonated state ($\lambda = 0$) to the deprotonated state ($\lambda = 1$). Bonded terms (bonds, angles, and torsions) were maintained in the protonated state. For glutamic acid and C-terminal, this effectively yields an approximate description of the deprotonated state. For N-terminal, imidazole, and histidine, instead, the bonded terms do not differ in the protonated and deprotonated states of the GROMOS96⁵⁰ force field. For glutamic acid in explicit solvent, the free energy of deprotonation was calculated, as described in the next section for the reference free-energy simulations, with and without change in the bonded terms. The difference was less than 2 kJ mol^{-1} (see Table s2 in the Supporting Information).

To compare constant pH simulations performed with two different force fields, the titration curve of Glu with neutral termini was calculated also with OPLSA⁵⁶ and TIP4P⁵⁷ water molecules, and the titration curves for a tripeptide Ala-Glu-Ala were calculated with GROMOS96⁵⁰ and OPLSA⁵⁷ in SPC⁵¹ water. When OPLSA⁵⁷ was used to describe the system, in addition to the bonded terms, atom types also were maintained in their protonated state.

The temperature of the λ degree of freedom was set to 300 K. Unless indicated otherwise, each λ particle was coupled to a separate heat bath via the Andersen thermostat⁴² with a coupling parameter of 6 ps^{-1} . A fixed barrier height of 3.0 kJ mol^{-1} was used for the biasing potential.

The mass of λ was set to 20 u. With this value of the mass, the calculations yielded suitable λ -trajectories (i.e., small ratio between transition time and residence time) for the simulated systems (see the Results section). At the same time, the mass of λ is in the same range as that for the other atoms in the system.

Finally, we note that during the change of the protonation state in the constant pH simulations, the overall charge of the system is (eventually) changed. In this situation, artifacts can arise due to the use of Ewald and related methods to describe electrostatic interactions. In particular, these artifacts are related to the periodic boundary conditions and the background charge that is used to neutralize the system.^{58,59} However, for small compounds in a high dielectric medium (water), such as those investigated here, these effects are expected to be negligible.^{28,58}

3.3. Reference States and Reference Free-Energy Simulations. Constant pH simulations require a reference state for each of the simulated titratable sites. The measured and calculated (force field) deprotonation free energies of this reference state were used to include the effect of the pH bath, and the effect of the breakage and formation of chemical bonds in the simulation (see eq 13).

Table 1 lists the titratable sites and their reference states, as well as the measured $\text{p}K_a$ values obtained from the literature^{1,60–62} and force-field deprotonation free energies ($\Delta G_{\text{ref}}^{\text{FF}}$). Note that two measured $\text{p}K_a$ values and $\Delta G_{\text{ref}}^{\text{FF}}$ are reported for imidazole. These correspond to the *microscopic* $\text{p}K_a$ values for the first and second deprotonation reaction of imidazole, respectively (the second microscopic $\text{p}K_a$ value is obtained using eq 40, with the second macroscopic $\text{p}K_a$ value being approximated from histidine, for which there are experimental data¹). The first and second microscopic $\text{p}K_a$ values of the N_δ and N_ϵ sites are identical, because of the symmetry of the imidazole molecule.

For the Ala-Glu-Ala tripeptide, which was added to the compounds set to compare the GROMOS96⁵⁰ and OPLSA⁵⁷ force fields, the reference states were chosen as follows: acetyl-Glu-methylamide ($\text{p}K_{a,\text{ref}} = 4.25$,⁶⁰ $\Delta G_{\text{ref}}^{\text{FF(GROMOS)}} = -225.6 \text{ kJ mol}^{-1}$,

Table 1. Reference States, Reference pK_a Values, and $\Delta G_{\text{ref}}^{\text{FF}}$ Values

titratable site	reference state	reference pK_a	$(\ln 10)RT$ ($pK_{a,\text{ref}}$) (kJ mol^{-1})	$\Delta G_{\text{ref}}^{\text{FF}}$ (kJ mol^{-1})
Glu	Glu (neutral termini)	4.25 ⁶⁰	24.4	−220.8
N-terminus	di-Ala (neutral C-terminus)	8.0 ⁶¹	45.9	332.8
C-terminus	di-Ala (neutral N-terminus)	3.5 ⁶¹	20.1	−231.3
imidazole (N_δ) ^a	imidazole (N_δ)	7.28, ⁶² 14.4 ¹	41.8, 82.7	155.4, −211.7

^a For imidazole, only N_δ is reported; values for N_ϵ are the same.

$\Delta G_{\text{ref}}^{\text{FF(OPLSA)}} = -370.5 \text{ kJ mol}^{-1}$, di-Ala-methylamide ($pK_{a,\text{ref}} = 8.0$,⁶¹ $\Delta G_{\text{ref}}^{\text{FF(GROMOS)}} = 331.7 \text{ kJ mol}^{-1}$, $\Delta G_{\text{ref}}^{\text{FF(OPLSA)}} = 219.0 \text{ J mol}^{-1}$), and acetyl-di-Ala ($pK_{a,\text{ref}} = 3.5$,⁶¹ $\Delta G_{\text{ref}}^{\text{FF(GROMOS)}} = -230.7 \text{ kJ mol}^{-1}$, $\Delta G_{\text{ref}}^{\text{FF(OPLSA)}} = -338.2 \text{ kJ mol}^{-1}$), for titratable sites Glu, N-terminus, and C-terminus, respectively.

The force-field deprotonation free energies for the reference states $\Delta G_{\text{ref}}^{\text{FF}}$ were determined via conventional thermodynamic integration (see eq 14) as follows. Each reference compound was placed in a dodecahedral box filled with SPC⁵¹ water molecules. The reference free-energy simulations consisted of 5-ns MD, during which λ was continuously increased from 0 to 1, thus deprotonating the reference compound, as described above for the constant pH simulations. The size and shape of the box in the reference and constant pH simulations was identical. Using the same simulation conditions in the reference and constant pH simulations, differences due to approximations of the force field and of the interaction potentials are minimized.²⁸

$\Delta \tilde{G}_{\text{ref}}^{\text{FF}}(\lambda)$ (eq 15) was derived from a least-squares fit to $\partial H/\partial \lambda$ obtained from the reference free-energy simulation. Since the deprotonation reaction in explicit water showed a nonlinear $\partial H/\partial \lambda$ profile,²⁸ a third-order polynomial was used. Coefficients of these polynomials are given in Table s3 in the Supporting Information.

The two titration coordinates λ_1 and λ_2 of imidazole (Figure 4) are chemically coupled and, therefore, deserved particular attention. Here, the reference state changes as a function of the protonation state of the respective other site. Thus, $\Delta G_{\text{ref}}^{\text{FF}}(\lambda_1, \lambda_2)$, and, accordingly, $\Delta \tilde{G}_{\text{ref}}^{\text{FF}}(\lambda_1, \lambda_2)$, are a function of both, λ_1 and λ_2 (see eq 31). For this reason, reference free-energy simulations of one titratable site (e.g., the site described by λ_1) were carried out for $\lambda_2 = 0, 0.1, \dots, 0.9, 1$. For each of these 11 simulations, a third-order polynomial in λ_1 was fitted to its $\partial H/\partial \lambda_1$ profile, in a manner similar to the case of chemically uncoupled sites. To describe the dependency from λ_2 , third-order polynomials in λ_2 were subsequently fitted to the coefficients of these polynomials, and vice versa for the titratable site described by λ_2 . These two sets of polynomials served to calculate continuous forces for the two degrees of freedom λ_1 and λ_2 .

3.3.1. Histidine Reference State. As the reference state for the constant pH simulations of histidine, we chose imidazole, such that contributions from the backbone to the proton affinities of the side chain N_ϵ and N_δ titratable sites were present in the constant pH simulations, but not in the reference free-energy simulations. Because the force-field parameters of imidazole and histidine differed, imidazole was transformed to a modified imidazole molecule described with histidine force-field parameters, using the thermodynamic cycle in Figure 3. The transfer free energies along the thermodynamic cycle were then used to redefine the reference state, according to eq 16. Since N_ϵ and N_δ are chemically coupled, the transfer potential $V^{\text{transf}}(\lambda_1, \lambda_2)$ was defined according to eq 33, which accounts for the dependency of the transfer free energies from the protonation state of the

respective other site. The transfer free energies were calculated via free-energy simulations (thermodynamic integration, eq 1). In a first step, the bond lengths and angles were changed from their force-field values in imidazole to those in histidine. In a second step, Lennard-Jones parameters, and, in a last step, charges (see Table 1s in the Supporting Information) were modified. Each free-energy simulation consisted of 18 independent simulations with λ values between 0 and 1. At each λ value, 100 ps of equilibration were followed by 300 ps of data collection. The integration was carried out numerically using the trapezoidal method. The error in $\langle \partial H/\partial \lambda \rangle_\lambda$ was estimated using block averaging.^{63,64}

3.4. λ Probability Distribution and Free-Energy Profile. In order to calculate the probability distribution $p(\lambda)$ during the constant pH simulation, the λ interval was divided in 10 bins [$\lambda_1, \dots, \lambda_i, \dots, \lambda_{10}$], and $p(\lambda)$ at bin i was obtained as

$$p(\lambda_i) = \frac{n_i}{N} \quad (41)$$

where n_i is the time of the simulation during which λ visited bin i and N is the total simulation time.

The probability distribution of λ , which is given by the entropic term introduced by the use of the circular coordinate, was calculated as

$$p(\lambda_i) = \int_{\lambda_i}^{\lambda_{i+1}} p(\lambda) d\lambda \quad (42)$$

with

$$p(\lambda) = \frac{\exp[-\beta A(\lambda)]}{Z} \quad (43)$$

and $A(\lambda)$ and Z being obtained from eqs 11 and 12, respectively. $p(\lambda_i)$ was then used to obtain a free-energy profile as a function of the λ titration coordinate, with the free energy $G(\lambda)$ at bin i being given by

$$G(\lambda_i) = -RT \ln p(\lambda_i) \quad (44)$$

4. RESULTS

To test the accuracy of the constant pH MD simulation method described above, we have calculated the titration curves of four compounds: glutamic acid, a Glu-Ala dipeptide, imidazole, and histidine. The effects of the choice of the barrier height of the biasing potential, the temperature coupling scheme, and the force field, on the simulation were also investigated.

4.1. Glutamic Acid. First, we asked if the constant pH MD simulation method is able to accurately reproduce the titration curve of glutamic acid. To this end, glutamic acid with neutral amino and carboxyl termini ($-\text{NH}_2$ and $-\text{COOH}$, respectively) was solvated in water, and four constant pH simulations of 5 ns

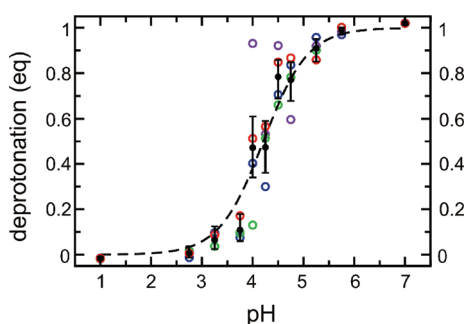


Figure 5. Calculated titration curve of glutamic acid with neutral termini. The deprotonation of glutamic acid (in equivalents, eq) is plotted as a function of pH. At each pH, four simulations of 4.5 ns each were performed. Data from each of these simulations (colored dots), and from the average of the four simulations (black filled dots), are shown. Error bars denote estimates from the statistics of the observed transitions. The dashed line is a Henderson–Hasselbalch fit to the average data.

each (0.5-ns equilibration time and 4.5-ns data collection time) were carried out for 11 pH values between 1.0 and 7.0. Figure 5 shows the fractions of deprotonated acid (in equivalents) as a function of pH (i.e., the titration curve) for each of the four sets of simulations (colored dots), and their average (black dots), the latter together with error bars, which were determined from the statistics of the observed transitions, as described in the Methods section and the Supporting Information. As can be seen, the scatter of the four simulations agrees with the error estimate of the average. Note that, at the end points of the titration curve, values slightly below 0 or above 1 are observed, which is due to the use of a radius of $r = 0.55$ for the circle covered by the angular coordinate θ (see the Theory section). We chose $r = 0.55$ to get 0 and 1, on average, at the protonated ($\lambda < 0.1$) and deprotonated states ($\lambda > 0.9$), respectively. Because of statistical fluctuations, however, slightly negative values and values above 1 occur. However, this is much better than averages of $\langle \lambda \rangle = 0.05$ or $\langle \lambda \rangle = 0.95$ for $r = 0.5$.

From a fit of the Henderson–Hasselbalch equation (eq 34) to the average deprotonation (the dashed line in Figure 5), the pK_a value was estimated to be 4.21 ± 0.14 , which is consistent with the measured pK_a value of 4.25.⁶⁰

For the chemists, we note that, in a titration experiment, the pH is usually measured as a function of the volume of a strong base (or acid) solution added to the analyte solution. In contrast, in the constant pH simulations, pH is a fixed parameter, whereas the equivalents of analyte (i.e., how much of the analyte supplies or reacts with one mole of hydrogen ions) is the quantity to be estimated. Therefore, the titration curves in Figure 5 are to be read as *inverted* titration curves, with respect to a typical experimental titration curve.

Figures 6A–C illustrate the effect of different barrier heights of the biasing potential (see eq 9). As expected, an increase of the barrier height by $1 k_B T$ ($\sim 2.5 \text{ kJ mol}^{-1}$) reduces the number of transitions by a factor of ~ 2.5 – 3 . Therefore, by adjusting the biasing potential, the transition rate can be optimized to ensure sufficient sampling of the physical end states. At the same time, the fraction of intermediate states remains small (between 30% with a barrier of 3 kJ mol^{-1} , and 10% with a barrier of 7.5 kJ mol^{-1}). Overall, by adjusting the barrier, the statistical error of the constant pH simulation can be minimized.

Note that the effective barrier between the protonated and deprotonated states has a contribution from the entropic barrier

introduced by the use of an angular coordinate to perform the actual λ -dynamics (see the Theory section, Figure 1 and eq 11). This can be seen in Figure 7, which shows the free-energy profile as a function of the titration coordinate λ from an 18-ns constant pH simulation of glutamic acid in explicit solvent at pH 4.25 and with the barrier height of the biasing potential 3 kJ mol^{-1} (continuous line). The free energy at $\lambda = 0.5$ is $\sim 7 \text{ kJ mol}^{-1}$ more positive than that at $\lambda = 0$ and $\lambda = 1$. When the biasing potential is subtracted from the simulation free-energy profile, we obtain the dotted line in Figure 1, which shows a residual barrier of $\sim 4 \text{ kJ mol}^{-1}$. This compares with the entropic barrier term introduced by the use of the angular coordinate θ (broken dotted line in Figure 7).

To investigate the effect of the chosen temperature coupling scheme on sampling of the protonation states during the constant pH simulations, the following two variants were considered. In variant (i), the λ particle was coupled to a separate heat bath via the Andersen thermostat,⁴² and the rest of the system was coupled to the Berendsen thermostat, whereas in variant (ii), all degrees of freedom were coupled to a common heat bath via the Berendsen thermostat.³⁰ Figures 6A and 6D compare typical λ -trajectories for the two variants. As can be seen, the number of transitions for the Berendsen variant is ~ 3 – 4 times larger than that for the Andersen method. Accordingly, the average residence time is ~ 3 – 4 times shorter for the Berendsen simulation ($\sim 60 \text{ ps}$), compared to that for the Andersen simulation ($\sim 200 \text{ ps}$). The probability distributions of λ with the two variants of the temperature coupling scheme are very similar (see right plot of Figure 6D). Figure 6E shows typical short-time (50 ps) traces of both simulations, with $\lambda(t)$ shown in the top row, and respective velocities of the underlying angular coordinate ($v\theta$) at the bottom. As can be seen, the λ -trajectories are similar, with the Berendsen variant showing somewhat larger oscillations at the end states. The velocities, in contrast, look very different, with a marked proportion of high-frequency fluctuations for the Andersen thermostat, which are absent for the Berendsen thermostat. Figure 6F quantifies this behavior, in terms of the distribution of angular distances covered by the circular coordinate θ between successive velocity reversals. These distances are, on average, shorter for the Andersen thermostat (0.08 radians), as compared to the Berendsen thermostat (0.57 radians). In particular, the long tail for the Berendsen thermostat (up to 6 radians) shows that inertia-driven full circle motions do occur, which implies correlated transitions. This effect reduces the statistical accuracy and is not seen for the Andersen thermostat.

Overall, the Andersen temperature coupling scheme seems to provide a better tradeoff between residence times and the number of uncorrelated transitions. In particular, the λ -trajectories obtained with the Andersen variant showed a sufficiently long residence time at the physical end states, allowing the system to respond to the new protonation state. Because these features are crucial for constant pH simulations, the Andersen temperature coupling scheme has been used for all subsequent simulations.

4.2. Glu-Ala Dipeptide. The second system that we considered was the dipeptide Glu-Ala. This system has three interacting titratable sites—glutamic acid (Glu), amino terminus (N-terminus), and carboxyl terminus (C-terminus)—and, therefore, was chosen to test if our method is capable of describing pK_a shifts due to these interactions.

Constant pH simulations were carried out for 14 pH values between 1.0 and 11.0. Each trajectory covered a 20-ns simulation

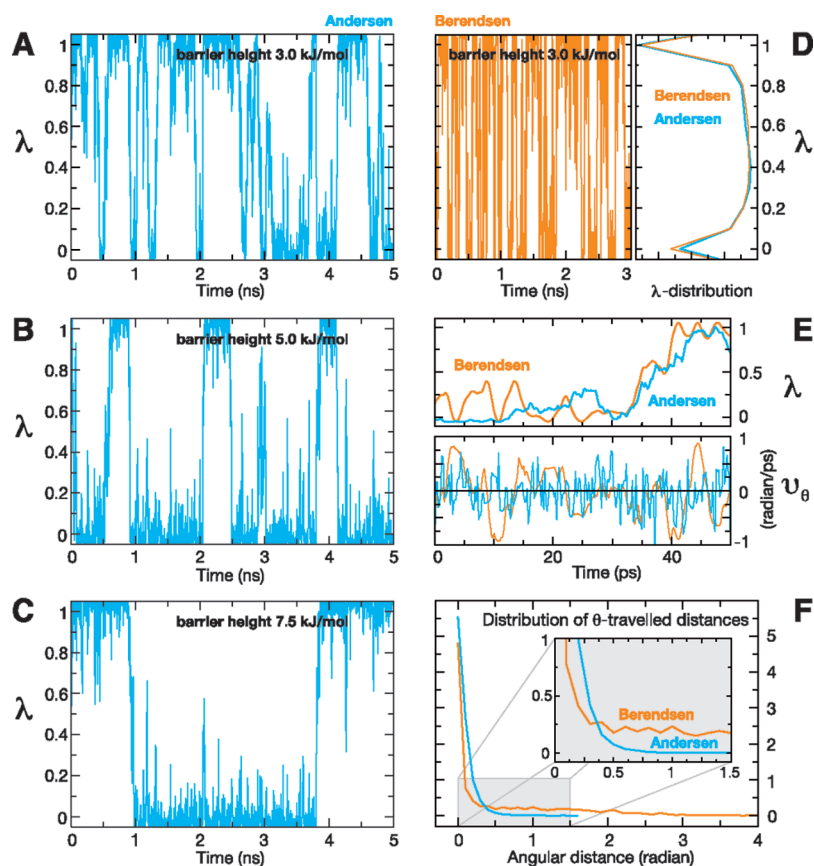


Figure 6. Dynamics of the deprotonation variable λ of glutamic acid for different barrier heights of the biasing potential and different temperature coupling schemes of λ : (A, B, C) λ is plotted over time during constant pH simulations at pH 4.25 for three different barrier heights ((A) 3.0 kJ mol^{-1} , (B) 5.0 kJ mol^{-1} , and (C) 7.5 kJ mol^{-1}) of the biasing potential using the Andersen temperature coupling scheme. (D) In the left-hand side of the panel, λ is shown during a constant pH simulation at pH 4.25 for a barrier height of 3.0 kJ mol^{-1} , using Berendsen temperature coupling; on the right-hand side of the panel, the λ -distributions of this simulation and of simulation (see panel A) are superimposed. (E) Variable λ and respective velocity v_θ (in radians/ps) during 50 ps of simulation with Andersen and Berendsen temperature coupling schemes. (F) Distributions of the angular distances (in radians) covered between velocity reversals by the θ -variable, during the simulations depicted in panels A and D.

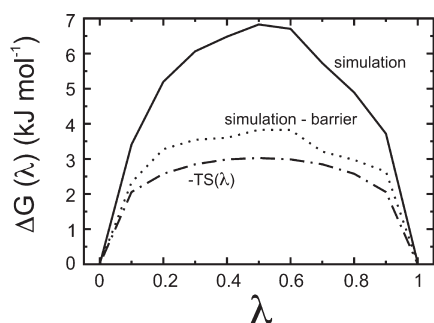


Figure 7. Relative free-energy profile as a function of the titration coordinate λ from the 18-ns constant pH MD simulation of glutamic acid in explicit solvent at pH 4.25 (continuous line). The biasing barrier potential (barrier height = 3 kJ mol^{-1}) is subtracted from the simulation free-energy profile to yield the dotted line. The broken dotted line is the relative free-energy profile that is due to the circle entropy ($-TS(\lambda)$; see text).

time with a 2-ns equilibration time and an 18-ns data collection time. Figure 8 shows the obtained titration curve (left graph), in which the cumulative deprotonation (in equivalents) of all three titratable sites is plotted as a function of pH, together with the individual contributions of the three sites (see right side of Figure 8).

Apparent pK_a values were estimated from a fit of a sum of three Henderson–Hasselbalch equations (eq 35) to the cumulative titration curve (Table 2). Similarly, the pK_a values of each of the titratable sites (site-specific pK_a values) were obtained by fitting the Henderson–Hasselbalch equation to the individual titration curves (see Table 2). Note that the apparent pK_a values are listed in Table 2, next to each titratable site, only for the sake of clarity, because they are defined in terms of deprotonation of the entire dipeptide.

The apparent and site-specific pK_a values are similar for the N-terminus, whereas, for Glu and for the C-terminus, there is a difference of 0.28 and -0.22 pK_a units, respectively (see Table 2). The Henderson–Hasselbalch curve fitted the calculated deprotonation equivalents of the N-terminus and Glu (see top and center right of Figure 8) well, whereas the titration curve of the C-terminus (see bottom right of Figure 8) deviated slightly from the Henderson–Hasselbalch curve. In particular, the slope of the titration curve is shallower, as is indicative of interactions between titratable sites.^{48,49} Since the N-terminus was constantly protonated below pH 7 (see top right in Figure 8), the interacting titratable sites were the C-terminus and Glu, which had similar pK_a values (~ 3). A fit of the Hill equation (eq 36) to the C-terminus titration curve (dashed magenta line in Figure 8, lower graph) recovers the pK_a value of 2.98 already obtained for the Henderson–Hasselbalch fit, and

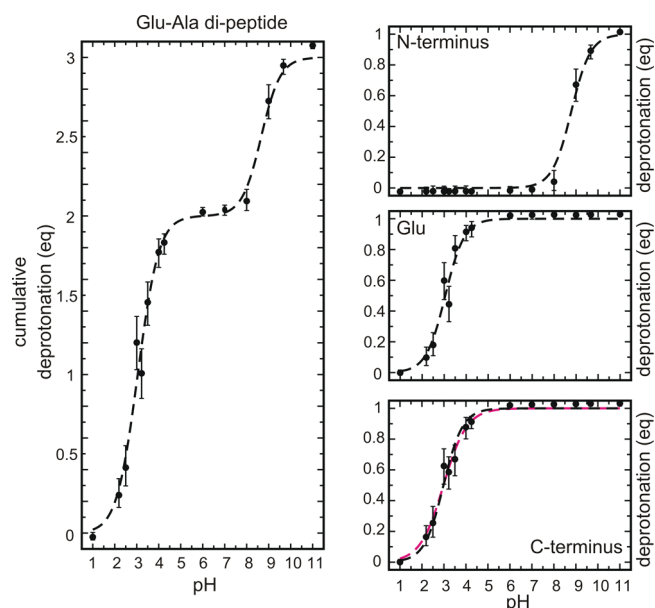


Figure 8. Calculated titration curves of a Glu-Ala dipeptide: (left) titration curve of the dipeptide and (right) site-specific titration curves of the N-terminus, Glu, and C-terminus. The fitted Henderson–Hasselbalch curve (dashed line) and, for the C-terminus, the fitted Hill curve (dashed magenta line) are also shown. Error bars denote estimates from the statistics of the observed transitions.

Table 2. Calculated pK_a values of the Glu-Ala di-peptide

titratable site	apparent pK_a	site-specific pK_a	reference pK_a^a
N-terminus	8.66 ± 0.13	8.79 ± 0.10	8.0^{61}
Glu	3.33 ± 0.08	3.05 ± 0.08	4.25^{60}
C-terminus	2.76 ± 0.07	2.98 ± 0.07	3.5^{61}

^a Measured pK_a values of the isolated titratable sites (reference pK_a values) are listed for the sake of comparison.

it provides a better description of the titration behavior. The obtained Hill coefficient of $n = 0.82$ indicates a certain degree of anticooperativity in the binding/unbinding of the proton. This is expected, as both the deprotonated C-terminus and Glu are negatively charged, and the release of a proton from one site will increase the affinity of the respective other site.

To quantify the interaction between the C-terminus and Glu in terms of a free energy, we determined the shift in the pK_a values of these two groups, which is due to the change in the protonation state of the respective other group. For that purpose, we selected, for each titratable site from the trajectories, those frames where the respective other site (C-terminus or Glu) was protonated or deprotonated. In the former case (trajectories where the opposite site was always protonated), we obtained the titration curve for the deprotonation of a site given the respective other was protonated (first *microscopic* titration curve), whereas in the latter (trajectories where the opposite site was always deprotonated), we obtained the titration curve given the other site was deprotonated (second *microscopic* titration curve). From a fit of the Henderson–Hasselbalch equation to the first and second *microscopic* titration curves, we obtained the *microscopic* pK_a values (pK_a^I and pK_a^{II} , respectively). For the C-terminus, $pK_a^I = 2.89$ and $pK_a^{II} = 3.05$, and for Glu, $pK_a^I = 2.95$ and $pK_a^{II} = 3.11$, which show a difference of $0.16 pK_a$ units between

the first and second *microscopic* pK_a values for both the C-terminus and the Glu. Thus, the affinity of the two titratable sites for the proton increased upon deprotonation of the other site by $\sim 1 kJ mol^{-1}$, which is of the same order as a simple estimate of the interaction energy (at the average distance of $0.6 nm$, see below) from the Coulombic law ($\sim 3 kJ mol^{-1}$).

As the C-terminus and Glu became charged, the average distance between these two groups increased. In particular, this distance changed gradually from $0.55 nm$ to $0.60 nm$ between pH 1 (when both groups were protonated) and pH 6 (when both groups were negatively charged), and then more markedly from 0.60 to $0.74 nm$ between pH 8 and pH 11, when the N-terminus was mostly deprotonated, and the system had a net charge of -2 .

As can be seen from Table 2 when comparing the site-specific and reference pK_a values, in all three cases, a shift in the pK_a value was observed, favoring the charged form of the titratable sites in the dipeptide. In particular, the pK_a of the N-terminus increased by almost $1 pK_a$ unit, whereas the pK_a of the Glu and C-terminus decreased by 1.2 and $0.5 pK_a$ units, respectively. The more-pronounced shifts in the pK_a value of the N-terminus and Glu suggest that these two groups interact favorably in their charged states. The average distance between the nitrogen of the N-terminus and the oxygens of the carboxyl group of Glu decreased from $0.47 nm$ to $0.43 nm$ between pH 2 and pH 6 and, beyond pH 8, increased again to $0.47 nm$. The N-terminus and Glu were at the closest distance of $0.43 nm$ between pH 6 and pH 8, when both groups were mainly in their charged states. No significant salt-bridge formation was observed between these two groups ($<15\%$ of simulation time). On average, the distance between the C-terminus and N-terminus was larger, and almost constant, between pH 1 and pH 8 (between $0.58 nm$ and $0.59 nm$).

4.3. Force-Field Comparison: GROMOS96 and OPLSA. To assess the sensitivity of the constant pH MD approach to the chosen force field, we calculated the titration curve and pK_a value of glutamic acid (with neutral termini) with a second force field. In particular, the OPLSA⁵⁶ and TIP4P⁵⁷ explicit water model was used. In addition, we calculated titration curves and pK_a values for a tripeptide of sequence Ala-Glu-Ala with GROMOS96⁵⁰ and OPLSA,⁵⁶ both with an SPC⁵¹ explicit water model.

For glutamic acid with neutral termini, both force fields yielded very similar titration curves, with pK_a values very close to the reference pK_a value, as can be seen in Table 3 and in Figure s1 in the Supporting Information. This is expected, because the constant pH simulation is parametrized via the measured pK_a value of the reference state, which, in these simulations, was glutamic acid, such that any possible force-field bias should cancel.

For the Ala-Glu-Ala tripeptide, at each of 15 pH values between 1 and 11, four constant pH simulations were performed for a total of 30 ns per pH value. Slight differences between the titration curves obtained with the two force fields are seen. In particular, the Glu and C-terminus titration curves differed most significantly (see Figure s2 in the Supporting Information). As can be seen in Table 3, the site-specific pK_a of the C-terminus is shifted by $-0.4 pK_a$ units, with respect to the reference pK_a value in the GROMOS96 simulations, whereas it is shifted slightly by $0.1 pK_a$ unit in the OPLSA simulations. For Glu, the site-specific pK_a value is shifted by 0.2 , with respect to the reference state, in the GROMOS96 constant pH simulations, whereas it is shifted by $-0.2 pK_a$ units in the OPLSA simulations. Overall, the force-field sensitivity seems to be small.

4.4. Imidazole. The titratable sites considered above in the dipeptide simulations interacted only via electrostatics. The

Table 3. Calculated pK_a Values of a Single Glutamic Amino Acid with Neutral Termini ($\text{NH}_2\text{-Glu-COOH}$), and Ala-Glu-Ala Tripeptide with GROMOS96⁵⁰ and OPLSA,⁵⁶ in Combination with TIP4P⁵⁷ and SPC⁵¹ Water Molecules

$\text{NH}_2\text{-Glu-COOH}$					
titratable site	GROMOS96 + SPC		OPLSA + TIP4P		reference pK_a^a
	pK_a		pK_a		
Glu	4.21 ± 0.14		4.14 ± 0.07		4.25 ⁶⁰
Ala-Glu-Ala					
titratable site	GROMOS96 + SPC		OPLSA + SPC		reference pK_a^a
	apparent pK_a	site-specific pK_a	apparent pK_a	site-specific pK_a	
N-terminus	7.93 ± 0.08	8.05 ± 0.08	8.01 ± 0.10	8.15 ± 0.09	8.0 ⁶¹
Glu	4.48 ± 0.13	4.46 ± 0.07	4.09 ± 0.18	4.04 ± 0.06	4.25 ⁶⁰
C-terminus	3.14 ± 0.12	3.12 ± 0.11	3.55 ± 0.18	3.59 ± 0.07	3.5 ⁶¹

^a Measured pK_a values of the isolated titratable sites (reference pK_a values) are listed for the sake of comparison.

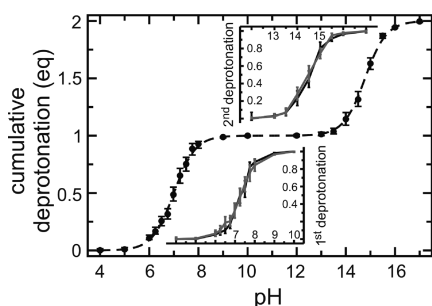


Figure 9. Titration curve of imidazole. The cumulative deprotonation (in equivalents, eq) of the two titratable sites (N_ϵ and N_δ) is plotted as a function of pH. The dashed line is a fitted Henderson–Hasselbalch curve. The insets show the microscopic titration curves of sites N_ϵ (black line) and N_δ (gray line) for the first (bottom graph) and second (top graph) deprotonation reaction of imidazole. Error bars were determined from the statistics of the observed transitions.

chemical character of each site of the dipeptide (technically, its force-field parameters) was independent of the protonation state of the other sites, and the free energy of deprotonation of one site was affected only via Coulombic interactions with the other sites. Now, in contrast, we focus on two examples of “chemical coupling”, where two titratable sites interact also via chemical bonds. In this case, the chemical character, and, thus, the pK_a value of a site, is affected by any change in the protonation state of the respective *coupled* site. As a first example, we consider the two chemically coupled titratable sites N_ϵ and N_δ of imidazole (Figure 4). A second example, histidine, is discussed further below.

Constant pH simulations of imidazole were carried out for 22 pH values between pH 4 and pH 17. Each trajectory covered 20 ns, with 2 ns of equilibration and 18 ns of data collection. At pH values of 8–13, a barrier height of 0 kJ mol⁻¹ was used, as discussed further below. Figure 9 shows the titration curve of imidazole, in which the cumulative deprotonation of both N_ϵ and N_δ titratable sites is plotted as a function of pH. The first and second apparent pK_a values of imidazole were estimated by a Henderson–Hasselbalch fit as described above, and are listed as Im($N_\epsilon + N_\delta$) in Table 4. The obtained apparent pK_a values of 7.00 ± 0.12 and

Table 4. Calculated and Measured pK_a Values of Imidazole (Im) and Histidine (His)

titratable site	calculated pK_a	measured pK_a
Imidazole		
Im($N_\epsilon + N_\delta$)	7.00 ± 0.12, 14.78 ± 0.08	6.98, ⁶² 14.7 ¹
Im(N_ϵ)	7.29 ± 0.08, 14.51 ± 0.16	7.28, ⁶² 14.4 ¹
Im(N_δ)	7.28 ± 0.18, 14.46 ± 0.18	7.28, ⁶² 14.4 ¹
Histidine ^a		
His($N_\epsilon + N_\delta$)	6.56 ± 0.21	6.42 ⁶²
His(N_ϵ)	7.18 ± 0.23	6.92 ⁶²
His(N_δ)	6.70 ± 0.23	6.53 ⁶²

^a For histidine, only the first deprotonation reaction was investigated.

14.78 ± 0.08 agree with the measured pK_a values of 6.98 (from ref 62) and 14.7 (from ref 1). Note that the measured value for the imidazole second apparent pK_a value, which was also used for the reference state, is replaced by the one of the chemically similar histidine, for which there are experimental data.¹

The microscopic pK_a values of the N_ϵ and N_δ sites (see Table 4) were estimated from the microscopic titration curves. These were obtained, similar to the C-terminus and Glu of the dipeptide, by plotting the fraction of deprotonated acid at one site, given that the other site was protonated (bottom inset in Figure 9; black for N_ϵ , gray for N_δ), or deprotonated (top inset in Figure 9; black for N_ϵ , gray for N_δ). The first and second microscopic pK_a values were similar for N_ϵ (7.29 ± 0.08 and 14.51 ± 0.16) and N_δ (7.28 ± 0.18 and 14.46 ± 0.18). This is expected, because the two titratable sites of imidazole are equivalent by symmetry. Consistently, the difference between the apparent and microscopic pK_a values is approximately $-(\log_{10} 2)$ and $+(\log_{10} 2)$ for the first and second deprotonation reaction, respectively (see eqs 38 and 40, for the case where $pK_{a,1} = pK_{a,2}$). This follows from the fact that the probability of deprotonating either two of the sites is twice the probability of deprotonating one of the sites.

Since the affinities of the N_ϵ and N_δ titratable sites are identical, one expects to observe, at every pH value, similar corresponding

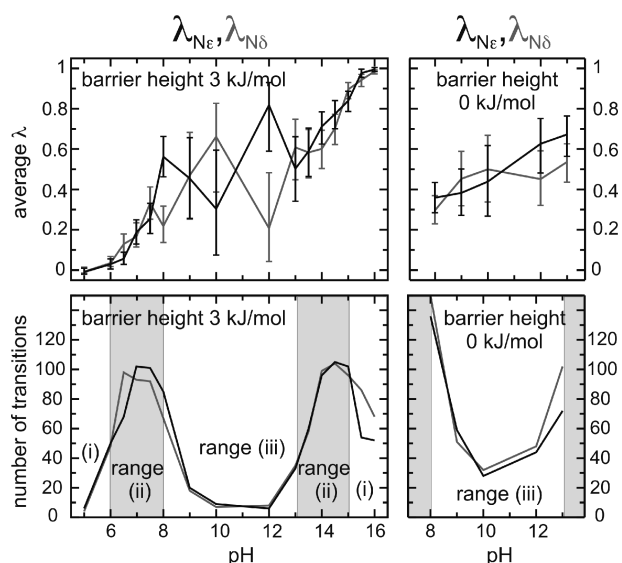


Figure 10. Average values (top) and number of transitions (bottom) of imidazole titration coordinates $\lambda_{N_{\epsilon}}$ (for site N_{ϵ} , black) and $\lambda_{N_{\delta}}$ (for site N_{δ} , gray). Constant pH simulations (of 20 ns) were carried out at each pH at barrier heights as indicated. Error bars denote estimates from the statistics of the observed transitions. Ranges (i), (ii), and (iii) are as referenced in the main text.

average deprotonation levels, which provides an independent test of the statistical accuracy of the calculations. Accordingly, Figure 10 shows the average deprotonation $\langle \lambda \rangle$ (top left), and the number of transitions (bottom left) for N_{ϵ} and N_{δ} , in black and gray, respectively, as a function of pH. Three ranges can be distinguished: (i) pH values close to 5 and 16, with similar $\langle \lambda \rangle$ of the two sites, and few transitions; (ii) pH values close to 7 and 14, with $\langle \lambda \rangle$ of N_{ϵ} and N_{δ} also similar, but many transitions; and (iii) pH between 8 and 13, with marked differences for the average deprotonation between the two sites, and again few transitions. To enhance sampling in this last regime, and, thus, statistical accuracy, we lowered the barrier height of the biasing potential from 3 kJ mol^{-1} to 0 kJ mol^{-1} , which is expected to increase the observed transitions, and repeated the calculations. As can be seen in the right side of Figure 10, the difference in average deprotonation is now significantly smaller, as, indeed, more transitions are observed. This example demonstrates how, by adjusting the barrier height, the transition frequency can be controlled and, thus, the accuracy can be enhanced.

Note that, in range (i), close to pH 5 and 16, also few transitions occur, but the accuracy is much higher than for range (iii) at pH 8–13. This is due to the fact that, in range (iii), statistical fluctuations can favor one of the singly deprotonated forms over the other, whereas in range (i), only one form of imidazole is (mainly) sampled, fully protonated at pH close to 5, and fully deprotonated at pH close to 16. Therefore, insufficient sampling can result in a large inaccuracy in range (iii), as compared to the more straightforward case of range (i), where only one form is sampled.

Similar to range (iii), in range (ii), more than one form of imidazole is significantly sampled (fully protonated and neutral forms, and fully deprotonated and neutral forms, at pH close to 7 and 14, respectively). In this range, the inaccuracy is also larger than that observed in range (i). However, in contrast to range (iii), many more transitions are observed and, thus, sampling is

Table 5. Free Energies of Transfer (ΔG^{transf}) of Each Imidazole Protonation State (see Figure 4) to the Corresponding Histidine State

protonation state	ΔG^{transf} (kJ mol^{-1})
00 (+)	-12.59 ± 0.54
10 ($N_{\delta}+$)	-0.04 ± 0.61
01 ($N_{\epsilon}+$)	-13.68 ± 0.55
11 (-)	-14.36 ± 0.59

enhanced. This is due to the fact that the free-energy difference between the protonated and deprotonated states of λ is small at pH values close to the pK_a value, and the transition barrier is lower, implying more-frequent transitions.

4.4.1. Histidine. As a second example of chemical coupling, we considered histidine, which plays a crucial role in many biological processes, because its pK_a value is close to the physiological pH. Accordingly, its protonation state changes with its local electrostatic environment. Here, we considered only biologically relevant pH values ($\text{pH} < 10$), because no accurate force-field parameters for the negatively charged, fully deprotonated form of histidine at $\text{pH} > 10$ are available.⁴⁷

In the previous section, we have studied imidazole, which is the chemical moiety of the histidine side chain. The difference in the measured pK_a values of histidine and imidazole is $\sim 0.5 \text{ pK}_a$ units,⁶² with histidine having lower affinity for the proton (see Table 4). Moreover, in histidine, the affinities of the two sites are not identical, as in imidazole, but differ with respect to each other, also by $\sim 0.5 \text{ pK}_a$ units.⁶² This situation enabled us to address the question of whether the constant pH simulation method is capable of quantitatively describing these differences (i.e., the effect of the presence of the backbone on the affinities for the proton of N_{ϵ} and N_{δ}).

For this purpose, we parametrized the constant pH simulation, such that contributions to the proton affinities from the histidine backbone were not present in the reference state simulation, for which we used imidazole. Because of these contributions, the calculated pK_a value is expected to be equal to the measured pK_a value of histidine, and is expected to differ from the measured pK_a value of the reference imidazole compound. Prior to starting the constant pH simulations, however, the contribution to the affinities from the different force-field parameters of imidazole and histidine were calculated. The thermodynamic cycle in Figure 3 served this purpose (i.e., to compute the free energies of transferring imidazole parameters to histidine parameters for each of the protonation states). Table 5 shows the free energies that have been obtained. As can be seen, these are similar to each other (between $-12.59 \text{ kJ mol}^{-1}$ and $-14.36 \text{ kJ mol}^{-1}$), except for the neutral form (01). In this form, N_{ϵ} is protonated, whereas N_{δ} , which is two bonds away from the backbone C_{β} , is deprotonated. The free energies in Table 5 were then used to redefine the reference state (see eq 33) prior to starting the simulations.

Constant pH simulations of histidine were carried out for 15 pH values between pH 4 and pH 10. Each trajectory covered 20 ns of simulation time with 2 ns of equilibration time and 18 ns of data collection time. Similar to imidazole, for pH values between 8 and 10, a barrier height of 0 kJ mol^{-1} was used. Figure 11 shows the obtained titration curve. The calculated pK_a value of 6.56 ± 0.21 , estimated via a Henderson–Hasselbalch fit (dashed line), agrees with the measured pK_a value of 6.42 (see Table 4). Thus,

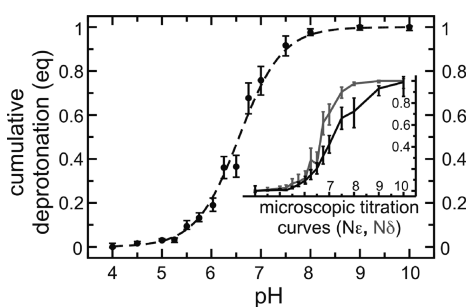


Figure 11. Titration curve of histidine. The cumulative deprotonation (in equivalents, eq) of the two titratable sites (N_ϵ and N_δ) is plotted as a function of pH. The dashed line is the fitted Henderson–Hasselbalch curve. The inset shows the microscopic titration curves of the N_ϵ and N_δ (in black and gray, respectively). Error bars were determined from the statistics of the observed transitions.

the ~ 0.5 pK_a units downward shift in the pK_a value of histidine, with respect to the reference compound (imidazole), was calculated within the statistical error (see Table 4).

The inset of Figure 11 shows the microscopic titration curves, which were obtained as described above for imidazole and Glu-Ala. Henderson–Hasselbalch fits to these curves yielded microscopic pK_a curves of 7.18 ± 0.23 for N_ϵ and 6.70 ± 0.23 for N_δ , which is consistent with a macroscopic pK_a value of 6.56 (see eq 38). The difference of 0.48 pK_a units between the two microscopic pK_a values agrees with the measured value of 0.39 pK_a units (see Table 4). Thus, in addition to decreasing the affinity of the two sites, the effect of the histidine backbone manifests itself with a shift in the pK_a of the two titratable sites with respect to each other, with N_ϵ having a higher affinity than N_δ .

5. DISCUSSION AND CONCLUSIONS

We have developed a framework to describe changes in protonation states at constant pH, where the requirements of (i) sampling of the relevant λ configurational space, with conformations being the protonated ($\lambda = 0$) and deprotonated ($\lambda = 1$) states, (ii) control of the rate of transition between the two states, and (iii) fully atomistic description of the system are fulfilled. The method, which was implemented within the molecular dynamics (MD) package GROMACS,^{37–39} is based on the λ -dynamics approach of Kong and Brooks,³² and it follows, in the main lines, the constant pH simulation method by Brooks and co-workers.^{32,34,35} A new general approach was developed to treat chemically coupled sites, and it was applied to describe the proton tautomerism of imidazole and histidine. In proteins, other examples of chemical coupling are coordinating residues around metal ions, such as that observed in copper binding sites⁶⁵ or zinc binding sites.⁶⁶

In order to test whether, and under which conditions, the above-mentioned requirements are actually fulfilled by our method, constant pH simulations of four systems, glutamic acid, Glu-Ala dipeptide, imidazole, and histidine, were carried out. In the following, we will briefly discuss these results in light of the aforementioned requirements, and then we will address the questions of how accurately the calculated average protonation agreed with the measured pK_a values, and whether the method is capable of describing interacting titratable sites. In particular, two types of interactions were considered: those between chemically uncoupled sites, which interact only via electrostatics, and those

between chemically coupled sites, for which a new coupling scheme was developed.

During the constant pH simulations, the average λ in the protonated and deprotonated states was found to be very close to values of 0 or 1, respectively, as required to describe the system in a physically realistic way. This was achieved by appropriately increasing the radius that defines the circular degree of freedom that is used. Similarly, sampling of the intermediate unphysical states was minimized by introducing suitable biasing potentials, in addition to the entropic barrier (of a few kJ mol^{-1}) implied by the angular degree of freedom. It was shown that, for a 3 kJ mol^{-1} biasing potential barrier height, more than 70% of the simulation time was spent close to physical states ($\lambda < 0.1$ and $\lambda > 0.9$).

Adjusting the barrier of the biasing potential also allowed us to control the transition rate, as demonstrated for glutamic acid and imidazole. In particular, for imidazole, it was shown how the accuracy of the calculations at pH values between 8 and 13 was significantly enhanced by increasing the transition rate, thus achieving fast sampling of different protonation states.

In all systems investigated, a fully atomistic description was used, including an explicit solvent. Interestingly, we found that the average residence time at the protonated and deprotonated states is more than 2 orders of magnitude larger than that for comparable systems simulated with the λ -dynamics constant pH approach developed by Brooks and co-workers^{34,35} with an implicit solvent. The choice of the thermostat is critical, as shown in Figure 6, where the average residence time is three times larger for the Andersen thermostat, compared to the Berendsen thermostat. Note that the transitions observed in the simulations with the Berendsen thermostat were partially correlated, which reduced the statistical accuracy. However, the thermostat alone does not seem to explain the differences between simulations in implicit and explicit solvents. Thus, the explicit description of water is likely to be crucial as well. We note that the fluctuations in the effective barrier for a transition are quite large due to the water dipoles. These effects, which are important for the kinetics of proton transfer, are not described in implicit water. It would certainly be interesting to study these in more detail.

For the first test system (glutamic acid), the calculated titration curve agreed very well with the measured one. Although this result may seem trivial, as the constant pH simulation was parametrized via the measured pK_a value of glutamic acid (the reference state), it nevertheless shows that the effect of pH is taken into account correctly. As expected, an increase of the total simulation time from 4.5 ns to 18 ns significantly improved accuracy. By increasing the length of the simulation, on one hand, the number of transitions increases, and, on the other hand, a more extensive sampling of the configurational space of the side chain at a certain protonation state is achieved. Both factors enhanced the accuracy of the simulation. Note that adjusting the barrier height of the biasing potential allows one to study the relaxation effects that are due to the change in protonation state.

To study the interaction between titratable sites, we further considered the dipeptide Glu-Ala as a test case. Here, we expected the interactions in the dipeptide to shift the calculated pK_a values, with respect to the values of the individual titratable sites (the reference states). Indeed, the calculated pK_a values were all shifted to favor the charge states of the titratable sites. This was more evident for Glu and N-terminus, which moved closer to each other in the pH range at which they were mainly in their charged states. The C-terminus and Glu had rather similar pK_a values (~ 3), and the individual contributions of these two

groups to the deprotonation of the dipeptide were distinguishable only in the site-specific titration curves. By analyzing the microscopic pK_a values, the interaction between these two titratable sites was estimated as $\sim 1 \text{ kJ mol}^{-1}$. The Hill coefficient of 0.82 for the titration curve of the C-terminus indicated anticooperativity in the system, in agreement with the microscopic pK_a values. We note that, by calculating the microscopic pK_a values, this anticooperativity was quantified here, in terms of free energy.

For Glu-Ala, the titratable sites interacted only via electrostatics. In contrast, in imidazole, which was the third system considered, the titratable sites N_ϵ and N_δ interacted *chemically*, because the affinity for the proton of one site is a function of the protonation state of the respective other site. To describe this type of interaction, a general approach was developed, in which each site is described by a titration coordinate λ , and coupling between the sites is explicitly taken into account. Note that this approach was applied here to describe the tautomerism of imidazole and histidine, but it can be used to describe chemical coupling between any two or more sites. Moreover, we showed that our general approach simplifies to the case of chemically uncoupled sites when interactions occur only via electrostatics. The approach of describing each site of a tautomer as a separate titratable site (or pseudo-site) is not new.⁶⁷ However, to avoid the occurrence of the double deprotonated state at pH 7, we do not introduce an arbitrary energy penalty.⁶⁷ Instead, the reference states of the pseudo-sites are coupled, such that they are a function of the protonation state of the titratable site. For example, in histidine, the reference pK_a value of one of the sites on the side chain increases from ~ 6 to ~ 14 as the respective other site deprotonates. Therefore, at pH 7, a second deprotonation is highly improbable. Alternatively, in the constant pH approach of Khandogin and Brooks,³⁵ tautomerism of titratable amino acids is described by considering three states only. In practice, only one titration coordinate is used, whereas an additional continuous coordinate controls the interconversion between the two tautomeric forms.³⁵ We note that, by appropriately choosing the protonation states, a three-state description also is obtained within our approach.

We did not use a tautomeric model for Glu in this work. However, it is straightforward to apply such a model to Glu as well, to allow for deprotonation/protonation of both oxygens on the carboxylic group. In particular, such a description is required in protein simulations, in which specific intramolecular interactions can significantly increase the barrier for rotation of the carboxylic group.

The obtained titration curve of imidazole agreed well with the measured one. To test the model, we simulated over a large pH range, to also observe the doubly deprotonated state. Although, at physiological pH, this form is quite unlikely to occur, it cannot be excluded that, in the presence of particular interactions, it plays a role as well.

Histidine was considered as a second example of chemically interacting sites. Here, we investigated the shift of the calculated proton affinity, with respect to the reference one, because of the presence of the backbone. For these simulations, the reference state was *transformed* to a similar one by means of the thermodynamic cycle shown in Figure 3. In general, the reference state is chosen such that the chemical character of the titratable site is similar in the reference and simulated states²⁸ (i.e., that all differences are described via electrostatics). This implies that one is restricted to those states for which experimental data are

available. Now we have proposed an approach that allows one to use a less similar state, therefore, broadening the range of accessible systems.

Finally, we would like to note that our constant pH approach will also be useful for determining protonation states from X-ray structures. A constant pH MD simulation is performed before the production run is started. During this equilibration phase, position restraints can be applied to the protein backbone, or heavy atoms, to keep the atomic coordinates close to the X-ray data. This procedure might be particularly useful for proteins, in which internal water molecules play a role in stabilizing protonation states.⁶⁸

■ ASSOCIATED CONTENT

S Supporting Information. In the Supporting Information, Tables s1, s2, and s3 list the side-chain atomic charges of histidine and imidazole, the contribution of bonded terms to the deprotonation free energy of glutamic acid, and the coefficients of polynomial fits for the reference states, respectively. Figures s1 and s2 show the titration curves calculated with GROMOS96⁵⁰ and OPLSA⁵⁶ force fields, of Glu with neutral termini, and of the tripeptide Ala-Glu-Ala, respectively. The error estimate for the average protonation state via bayesian approach is also presented. This information is available free of charge via the Internet at <http://pubs.acs.org/>.

■ AUTHOR INFORMATION

Corresponding Author

*Tel.: +49-551-2012300. Fax: +49-551-2012302. E-mail addresses: hgrubmu@gwdg.de (H.G.), ggroenh@gwdg.de (G.G.).

Present Addresses

[†]Institute of Computer Science, Georg August University, Göttingen, Germany.

■ ACKNOWLEDGMENT

The authors thank Berk Hess from the University of Stockholm, Sweden, for helpful discussions and Ulrike Gerischer for proofreading the manuscript.

■ REFERENCES

- (1) Creighton, T. E. *Proteins: Structures and Molecular Properties*; W. H. Freeman and Company: New York, 1993.
- (2) Dobson, C. M. *Nature* **2003**, *426*, 884–890.
- (3) Haas, J.; Vöhringer-Martinez, E.; Bögehold, A.; Matthes, D.; Hensen, U.; Pelah, A.; Abel, B.; Grubmüller, H. *Chem. Biol. Chem.* **2009**, *10*, 1816–1822.
- (4) Stouffer, A. L.; Acharya, R.; Salom, D.; Levine, A. S.; Costanzo, L. D.; Soto, C. S.; Tereshko, V.; Nanda, V.; Stayrook, S.; DeGrado, W. F. *Nature* **2008**, *451*, 596–599.
- (5) Schnell, J. R.; Chou, J. J. *Nature* **2008**, *451*, 591–595.
- (6) Tournaire-Roux, C.; Sutka, M.; Javot, H.; Gout, E.; Gerbeau, P.; Luu, D.-T.; Bligny, R.; Maure, C. *Nature* **2003**, *425*, 393–397.
- (7) Wiley, D. C.; Skehel, J. J. *Annu. Rev. Biochem.* **1987**, *56*, 365–394.
- (8) Popov, K.; Ronkkomaki, H.; Lajunen, L. H. J. *Pure Appl. Chem.* **2006**, *78*, 663–675.
- (9) Allen, R. I.; Box, K. J.; Comer, J. E. A.; Peake, C.; Tam, K. Y. *J. Pharm. Biomed. Anal.* **1998**, *17*, 669–741.
- (10) Bashford, D.; Karplus, M. *Biochemistry* **1990**, *29*, 10219–10225.
- (11) Ullmann, G. M.; Knapp, E.-W. *Eur. Biophys. J.* **1999**, *28*, 533–551.

- (12) Mongan, J.; Case, D. A.; McCammon, J. A. *J. Comput. Chem.* **2004**, *25*, 2038–2048.
- (13) Lolis, E.; Petsko, G. A. *Biochemistry* **1990**, *29*, 6619–6625.
- (14) Kozlov, A. G.; Lohman, T. M. *Proteins: Struct. Funct. Bioinf.* **2000**, *41*, 8–22.
- (15) Tamm, L. K.; Han, X. *Biosci. Rep.* **2000**, *20*, 501–518.
- (16) Cohen, F. S.; Melikyan, G. B. *Nat. Struct. Biol.* **2001**, *8*, 653–655.
- (17) Warshel, A.; Levitt, M. *J. Mol. Biol.* **1976**, *103*, 227–249.
- (18) Warshel, A.; Weiss, R. M. *J. Am. Chem. Soc.* **1980**, *102*, 6218–6226.
- (19) Day, T. J. F.; Soudackov, A. V.; Cuma, M.; Schmitt, U. W.; Voth, G. A. *J. Chem. Phys.* **2002**, *117*, 5839–5849.
- (20) Brancato, G.; Tuckerman, M. E. *J. Chem. Phys.* **2005**, *122*, 224507.
- (21) Maupin, C. M.; Wong, K. F.; Soudackov, A. V.; Kim, S.; Voth, G. A. *J. Phys. Chem. A* **2006**, *110*, 631–639.
- (22) Lill, M. A.; Helms, V. *J. Chem. Phys.* **2001**, *114*, 1125–1132.
- (23) Cymes, G. D.; Ni, Y.; Grosman, C. *Nature* **2005**, *438*, 975–980.
- (24) Mongan, J.; Case, D. A. *Curr. Opin. Struct. Biol.* **2005**, *15*, 1–7.
- (25) Baptista, A. M.; Teixeira, V. H.; Soares, C. M. *J. Chem. Phys.* **2002**, *117*, 4184–4200.
- (26) Dlugosz, M.; Antosiewicz, M. *Chem. Phys.* **2004**, *302*, 161–170.
- (27) Bürgi, R.; Kollman, P. A.; van Gunsteren, W. F. *Proteins: Struct. Funct. Bioinf.* **2002**, *47*, 469–480.
- (28) Börjesson, U.; Hünenberger, P. H. *J. Chem. Phys.* **2001**, *114*, 9706–9719.
- (29) Baptista, A. M. *J. Chem. Phys.* **2002**, *116*, 7766–7768.
- (30) Berendsen, H. J. C.; Postma, J. P. M.; van Gunsteren, W. F.; Nola, A. D. *J. Chem. Phys.* **1984**, *81*, 3684–3690.
- (31) Mertz, J. E.; Pettitt, B. M. *Int. J. Supercomput. Appl. High Perform. Eng.* **1994**, *8*, 47–53.
- (32) Kong, X.; Brooks III, C. L. *J. Chem. Phys.* **1996**, *105*, 2414–2423.
- (33) Abrams, J. B.; Rosso, L.; Tuckerman, M. E. *J. Chem. Phys.* **2006**, *125*.
- (34) Lee, M. S.; Salsbury, J. F. R.; Brooks III, C. L. *Proteins: Struct. Funct. Bioinf.* **2004**, *56*, 738–752.
- (35) Khandogin, J.; Brooks III, C. L. *Biophys. J.* **2005**, *89*, 141–157.
- (36) Wallace, J. A.; Shen, J. K. *Methods Enzymol.* **2009**, *466*, 455–475.
- (37) Berendsen, H. J. C.; van der Spoel, D.; van Drunen, R. *Comput. Phys. Commun.* **1995**, *91*, 43–56.
- (38) Lindahl, E.; Hess, B.; van der Spoel, D. *J. Mol. Model.* **2001**, *7*, 306–317.
- (39) van der Spoel, D.; Lindahl, E.; Hess, B.; Groenhof, G.; Mark, A.; Berendsen, H. J. *Comput. Chem.* **2005**, *26*, 1701–1718.
- (40) Kirkwood, J. G. *J. Chem. Phys.* **1935**, *3*, 300–313.
- (41) van der Vegt, N. F. A.; Briels, W. J. *J. Chem. Phys.* **1998**, *109*, 7578–7582.
- (42) Andersen, H. C. *J. Chem. Phys.* **1980**, *72*, 2384–2393.
- (43) Warshel, A.; Sussman, F.; King, G. *Biophysics* **1985**, *25*, 8368–8372.
- (44) Kollman, P. A. *Chem. Rev.* **1993**, *93*, 2395–2417.
- (45) Hwang, J.-K.; Warshel, A. *J. Am. Chem. Soc.* **1987**, *109*, 715–720.
- (46) Simonson, T.; Archontis, G.; Karplus, M. *Acc. Chem. Res.* **2002**, *35*, 430–437.
- (47) van Gunsteren, W. F.; Billeter, S. R.; Eising, A. A.; Hünenberger, P. H.; Krüger, P.; Mark, A. E.; Scott, W. R. P.; Tironi, I. G. *Biomolecular Simulation: GROMOS96 Manual and User Guide*; BIOMOS b.v.: Zürich, Switzerland, and Groningen, The Netherlands, 1996.
- (48) Onufriev, A.; Case, D. A.; Ullmann, G. M. *Biochemistry* **2001**, *40*, 3413–3419.
- (49) Klingen, A. R.; Bombarda, E.; Ullmann, G. M. *Photochem. Photobiol. Sci.* **2006**, *5*, 588–596.
- (50) Oostenbrink, C.; Villa, A.; Mark, A. E.; van Gunsteren, W. F. *J. Comput. Chem.* **2004**, *25*, 1656–1676.
- (51) Berendsen, H. J. C.; Postma, J. P. M.; van Gunsteren, W. F.; Hermans, J. Interaction models for water in relation to protein hydration. In *Intermolecular Forces*; Pullman, B., Ed.; D. Reidel: Dordrecht, The Netherlands, 1981; pp 331–342.
- (52) Darden, T.; York, D.; Pedersen, L. *J. Chem. Phys.* **1993**, *98*, 10089–10092.
- (53) Essmann, U.; Perera, L.; Berkowitz, M. L.; Darden, T.; Lee, H.; Pedersen, L. G. *J. Chem. Phys.* **1995**, *103*, 8577–8592.
- (54) Miyamoto, S.; Kollman, P. A. *J. Comput. Chem.* **1992**, *13*, 952–962.
- (55) Hess, B.; Bekker, H.; Berendsen, H. J. C.; Fraaije, J. G. E. M. *J. Comput. Chem.* **1997**, *18*, 1463–1472.
- (56) Jorgensen, W. L.; Maxwell, S.; Tirado-Rives, J. *J. Am. Chem. Soc.* **1996**, *118*, 11225–11236.
- (57) Jorgensen, W. L.; Chandrasekhar, J.; Madura, J. D.; Impey, R. W.; Klein, M. L. *J. Chem. Phys.* **1983**, *79*, 926–935.
- (58) Hünenberger, P. H.; McCammon, J. A. *J. Chem. Phys.* **1999**, *110*, 1856–1872.
- (59) Hummer, G.; Pratt, L. R.; Garcia, A. E. *J. Phys. Chem.* **1996**, *100*, 1206–1215.
- (60) Bundi, A.; Wüthrich, K. *Biopolymers* **1979**, *18*, 285–297.
- (61) Thurlkill, R. L.; Grimsley, G. R.; Scholtz, J. M.; Pace, C. M. *Protein Sci.* **2006**, *15*, 1214–1218.
- (62) Tanokura, M. *Biochim. Biophys. Acta* **1983**, *742*, 576–585.
- (63) Flyvbjerg, H.; Petersen, H. G. *J. Chem. Phys.* **1989**, *91*, 461–466.
- (64) Hess, B. *J. Chem. Phys.* **2002**, *116*, 209–217.
- (65) Xie, Y.; Inoue, T.; Miyamoto, Y.; Matsumura, H.; Kataoka, K.; Yamaguchi, K.; Nojima, M.; Suzuki, S.; Kai, Y. *J. Biochem.* **2005**, *137*, 455–461.
- (66) Mehle, A.; Thomas, E. R.; Rajendran, K. S.; Gabuzda, D. *J. Biol. Chem.* **2006**, *281*, 17259–17265.
- (67) Baptista, A. M.; Soares, C. M. *J. Phys. Chem. B* **2001**, *105*, 293–309.
- (68) Damjanovic, A.; Brooks, B. R.; Garcia-Moreno, B. *J. Phys. Chem. A* **2011**, *115*, 4042–4053.

CafeMol: A Coarse-Grained Biomolecular Simulator for Simulating Proteins at Work

Hiroo Kenzaki,[†] Nobuyasu Koga,[†] Naoto Hori,[†] Ryo Kanada,[†] Wenfei Li,^{†,‡} Kei-ichi Okazaki,[§] Xin-Qiu Yao,[†] and Shoji Takada^{*,†,||}

[†]Department of Biophysics, Graduate School of Science, Kyoto University, Kyoto 606-8502, Japan

[‡]Department of Physics, Nanjing University, Nanjing 210093, China

[§]Department of Physics, School of Advanced Science and Engineering, Waseda University, Tokyo 169-8555, Japan

^{||}Advanced Center for Computing and Communication, RIKEN, Wako Saitama 351-0198, Japan

S Supporting Information

ABSTRACT: For simulating proteins at work in millisecond time scale or longer, we develop a coarse-grained (CG) molecular dynamics (MD) method and software, CafeMol. At the resolution of one-particle-per-residue, CafeMol equips four structure-based protein models: (1) the off-lattice Go model, (2) the atomic interaction based CG model for native state and folding dynamics, (3) the multiple-basin model for conformational change dynamics, and (4) the elastic network model for quasiharmonic fluctuations around the native structure. Ligands can be treated either explicitly or implicitly. For mimicking functional motions of proteins driven by some external force, CafeMol has various and flexible means to “switch” the energy functions that induce active motions of the proteins. CafeMol can do parallel computation with modest sized PC clusters. We describe CafeMol methods and illustrate it with several examples, such as rotary motions of F₁-ATPase and drug exports from a transporter. The CafeMol source code is available at www.cafemol.org.

1. INTRODUCTION

Proteins work with their characteristic sequences, structures, and dynamics. For example, enzymatic activity relies on well-designed structural arrangement of several key residues at catalytic sites, and the enzymatic activity is often allosterically regulated by structural change dynamics upon binding to their regulatory molecules. Thus, interplay among sequences, structures, dynamics, and functions is the focus of our studies. Unfortunately, however, no single experiment is powerful to simultaneously address all these aspects. Structural biology methods, such as X-ray crystallography, are the most powerful for addressing sequence–structure relation in high spatial resolution, but their primacy is on static structure, and the dynamic information is limited. A broad range of biochemical experiments is the most useful for addressing overall functions and their relations to sequences. They, however, do not provide direct evidence in structure and dynamics. Single-molecule observations and laser chemistry experiments are the most direct to see protein motions and dynamics, but their spatial resolution is unavoidably low.

In this context, molecular dynamics (MD) simulations are candidates to fill the gap among these and other various experiments providing much of the time-dependent structural information. The conventional fully atomistic MD simulations^{1–4} have high spatial and temporal resolution, but currently they suffer from the time-range problem: Time scales reachable by these MD simulations are typically on the order of microseconds, which is orders of magnitude shorter than the typical time scales of most biological processes. Thus, as a complementary approach, coarse-grained (CG) molecular models have been

used for simulating much longer time scales of biomolecular systems. Naturally, CG MDs are popular in studying long time behaviors,^{5–10} such as folding of proteins,^{11–13} work of protein machines,^{10,14–18} and lipid membrane self-assembly and morphology change.^{19–22} We have recently been developing such CG models of proteins and applying them to various protein systems.^{13–15,18,23–25} In doing so, we developed a software, CafeMol. This paper presents the CafeMol methods and the software for simulating proteins at work with various CG models.

2. METHODS

2.1. CG Strategy. Coarse-graining is not a unique procedure at all, and each CG model is, to some extent, based on the developers' own perspectives. CafeMol is based on the energy landscape theory developed in protein folding study,^{26,27} although the range of its applicability is not limited to the folding. Proteins have evolved to have ability of folding to their own native structures. At the native structures of proteins, overall, most side-chains are extremely well-packed in their cores. Whenever one finds a charge in the core, it is either paired with its counter charge or it is functionally essential. Thus, except for functional reasons, the interactions at the native structures are highly consistent, as pointed out many years ago by Go.²⁸ Proteins gained through evolution, the foldability by minimizing the frustration at their native structures, which was termed

Received: February 13, 2011

Published: May 10, 2011

“principle of the minimum frustration” by Bryngelson and Wolynes.²⁶ The effective energy takes the minimal value at the native, and as the conformation deviates from the native, the effective energy, on average, increases, which leads to an overall funnel-like energy landscape, first coined by Onuchic et al.²⁹ Completeness of the side-chains packing at the native structure may resemble to the high-density packing in crystal. On the other hand, the denatured state is characterized with low-level side-chain packing and larger fluctuation, and thus it resembles fluid.

Coarse-graining is relatively easy for the fluid-like denatured state because we primarily need to approximate the statistical average over the ensemble. Conversely, the native state is more difficult to be described by CG models because of the high level of side-chain packing, which is a very specific and a non-self-averaging property. If the side-chain architecture is lost by coarse-graining, then very surely we lose those specific interactions, to some extent.³⁰ Thus purely physicochemical coarse-graining is not effective for approximating the native state. Instead, an evolutionary perspective in the minimal frustration principle can be used as a guiding principle for coarse-graining. Namely, we assume, as an extreme, that all the interactions found at the native structure are attractive. Simultaneously, we require that the protein can take nearly random coil at sufficiently high temperature. These two requirements led to the so-called Go model, first developed in the lattice representation of proteins.³¹ However, of course, protein dynamics near the native is not well approximated by the lattice representation but is well-approximated by a quasiharmonic potential, such as the elastic network model (ENM).^{32,33} The ENM model is good only near the native. A model that is similar to the ENM near the native structure and simultaneously that shares the concept of the lattice Go model was developed and called the off-lattice Go model or the perfect funnel model.¹² The off-lattice Go model represents quasiharmonic fluctuations near the native structure and simultaneously realizes the perfect funnel energy landscape in global conformational space. CafeMol employs the off-lattice Go model developed by Clementi, Nyemyer, and Onuchic^{12,13} and its derivative as a basic CG model of proteins.

For applying CG MD to protein functional dynamics, however, the standard Go model is not sufficient because we often need to simulate conformational change of proteins, which is beyond the range of standard Go model. To simulate conformational change, many extensions of the Go model to multiple-basin cases have been proposed.^{18,23,34,35} CafeMol equips Okazaki et al’s version of the multiple-basin potential,²³ which is an important feature of CafeMol since the multiple-basin model simulation is not easily fit with standard MD codes.

We note that the Go model and its derivative, as well as ENM, explicitly depend on the native structure. Thus, these models are often called the structure-based model or the native-centric model. The “structure-based MD” is quite different in concept from the conventional fully atomistic MD because the latter uses a physicochemically derived force field and thus the Hamiltonian does not explicitly depend on the native structure. Structure-based model, by design, says that the native structure is the most stable state, and this design implicitly and indirectly takes into account chemical interactions in a very crude sense. In addition, CafeMol has a new model that combines the structure-based Go model and the fully atomistic force field by using a multiscale protocol, which we term the atomic

interaction based CG (AICG) model.³⁶ In the AICG model, we can take into account chemical feature of interactions observed at the native state, without significant increase in computational time.

By CG MD, we can easily simulate protein dynamics in time scales comparable to milliseconds or longer, but the long-time simulation alone is not sufficient to simulate “proteins at work”. In cells, many proteins work as “machines”. For the machines to work lively, some free energy source is necessary. Many protein machines use chemical energy as the free energy source, such as energy from ATP hydrolysis and that by ion passage through membrane. These chemical events cannot be well represented by CG models, and thus we need to mimic them in some ways. For the purpose, we proposed to “switch” the energy function at a certain time.¹⁴ By switching, we put some energy into the protein systems, and proteins start to “work” as machines. Switching MD has some similarity, in concept, to the Brownian ratchet model studied in modeling molecular motors.³⁷ One of the key advantages of CafeMol, in comparison with other MD packages, is to equip various means to conduct dynamic “switching” simulations, which try to mimic roles of the energy source given to the system and turn on the active motion of the machines. Simulations of molecular motors, such as F₁-ATPase,¹⁴ AAA+ motor,²⁴ kinesin (Kanada et al unpublished), and a multidrug transporter²⁵ are examples of these functions.

The CafeMol employs a simplified representation of proteins where one particle is assigned to each amino acid most often placed at C_α atoms (can be at C_β or at the geometric center of amino acids, though). Four models are included: (1) the off-lattice Go model,¹² (2) the AICG model,³⁶ which is a chemically tuned extension to the Go model in which residue–pairwise interactions are modeled by their atom-based interaction derived from an all-atom force field, (3) the multiple-basin model,²³ which is a minimal model that represents energy landscape with more than one basins, and (4) the ENM.³² The Go model and the AICG model can simulate global and local folding/unfolding of proteins as well as native-state fluctuations. The multiple-basin model can be used to simulate conformational change dynamics. As such, the model assumes knowledge of (at-least) two structures corresponding to end-points of the conformational change. The ENM is to represent quasiharmonic fluctuation around the native structure. In addition, one can optionally turn on ligand models, generic electrostatic interactions, and empirical forms of hydrophobic interactions. The CafeMol implements various simulation protocols: (1) The constant temperature MD by Newtonian dynamics with Berendsen thermostat³⁸ and by Langevin dynamics. Based on the constant temperature MD, many higher order protocols are available. (2) One can automatically estimate the folding transition temperature by iterative folding/unfolding simulations in different temperatures. (3) Simulated annealing simulations can be done. (4) The one- and two-dimensional replica exchange MD can be run. (5) During MD simulations, one can switch (suddenly change) the native structure information. This is a simple way to mimic proteins at work driven by some external forces, such as ATP hydrolysis free energy or proton motive force. (6) During MD simulations, one can switch the relative stability in the multiple-basin model. This is another and somewhat more sophisticated way to mimic activation by some driving force. The protocols 5 and 6 are the major advantages of CafeMol over other methods and packages.

It may be convenient to compare CafeMol software with other publicly available means for CG MDs of proteins. Standard and some extended Go models can be run by GROMACS with the SMOG tool³⁹ and by Charmm with the Go-model-builder tool.⁴⁰ They are convenient since they can run on common MD packages, which are familiar to many people, although some extensions, such as multiple-basin potentials, may be more difficult because of the framework given by the packages. The ENM and its extensions are simpler models and thus can be run conveniently by many ways including a software RedMD,¹⁰ another software REACH,⁴¹ and web servers iGNM/oGNM/oANM.⁴² These tools, by themselves, cannot handle large-scale deviations from the native structure that include complete or partial unfolding. More flexible ways to realize CG MD may be to use general tools, such as a CG-builder of VMD/NAMD packages^{3,43} and some modules of LAMMPS.⁴⁴ They are flexible and thus may require more adaptation to particular applications. No publicly available method, other than CafeMol, can run conformational change dynamics between two (or more than two) given structures, to our knowledge. Also, internal framework for switching the potential is a unique feature of CafeMol.

CafeMol is a standalone software written in Fortran90 with MPI and C preprocessing directives. Thus, it can run in virtually any computer that has a Fortran90 compiler. The CafeMol source code, together with the parameter set and sample input files, is freely available to anyone at the web page, <http://www.cafemol.org>. A summary on the structure of the code and used file formats are given in Supporting Information.

2.2. Models and Energy Functions. *2.2.1. Off-Lattice Go Model.* CafeMol implements the off-lattice Go model developed by Clementi, Nyemyer, and Onuchic.¹² For a protein with the number of amino acids n_{aa} , the Go model potential $V_{Go}(\mathbf{R}|\mathbf{R}_0)$ is defined by

$$\begin{aligned}
 V_{Go}(\mathbf{R}|\mathbf{R}_0) = & \sum_i K_b (b_i - b_{i,0})^2 + \sum_i K_\theta (\theta_i - \theta_{i,0})^2 \\
 & + \sum_i \{K_\phi^{(1)} [1 - \cos(\phi_i - \phi_{i,0})] + K_\phi^{(3)} [1 - \cos 3(\phi_i - \phi_{i,0})]\} \\
 & + \sum_{i < j - 3}^{\text{nat contact}} \varepsilon_{go} \left[5 \left(\frac{r_{ij0}}{r_{ij}} \right)^{12} - 6 \left(\frac{r_{ij0}}{r_{ij}} \right)^{10} \right] + \sum_{i < j - 3}^{\text{non-native}} \varepsilon_{ev} \left(\frac{d}{r_{ij}} \right)^{12}
 \end{aligned} \quad (1)$$

Here, \mathbf{R} is the Cartesian coordinates of the simulated protein as a $3n_{aa}$ -dimensional vector, b_i is the i -th virtual bond length defined as $|\mathbf{r}_{i+1} - \mathbf{r}_i|$ ($1 \leq i \leq n_{aa} - 1$), where \mathbf{r}_i stands for the Cartesian coordinate of the i -th amino acid (= CG particle), θ_i is the i -th bond angle between two consecutive virtual bond vectors, $\mathbf{r}_{i+1} - \mathbf{r}_i$ and $\mathbf{r}_{i+2} - \mathbf{r}_{i+1}$ ($1 \leq i \leq n_{aa} - 2$), ϕ_i is the i -th dihedral angle around the $i + 1$ -th virtual bond $\mathbf{r}_{i+2} - \mathbf{r}_{i+1}$ ($1 \leq i \leq n_{aa} - 3$), and r_{ij} is the distance between i -th and j -th amino acids. All parameters with the subscript 0 are the constants which have the values of the corresponding variables at the native structure \mathbf{R}_0 , which corresponds to the structure at the bottom of the folding funnel. K_b , K_θ , $K_\phi^{(1)}$, $K_\phi^{(3)}$, ε_{go} , ε_{ev} , and d are the parameters. For the former six parameters, Clementi et al's original model uses homogeneous setting, i.e., for each parameter, the same value is used for the entire systems. In CafeMol one can optionally use site-specific parameters, i.e., the parameter values that depend on residues, which allow one to model flexible loops, for example. The summation $\sum_{i < j - 3}^{\text{nat contact}}$

is over the "native contact pairs", pairs of amino acids that are physically close to each other at the native (or the reference) structure. If one of the nonhydrogen atoms in the i -th amino acid is within a threshold distance (which is 6.5 Å by default) from a nonhydrogen atom in the j -th amino acid, then we define the pair of the i -th and the j -th amino acids as being the native contact. Only nonlocal pairs with $i < j - 3$ are taken into account. We note that, even though CafeMol uses one bead (most often located at C_α atom) per amino acid as the dynamic variable in MD simulations, the native contacts are defined by using all-atom information at the native (reference) structure. Thus, the PDB structure given for the native structure must contain all-atom coordinates. The summation $\sum_{i < j - 3}^{\text{non-native}}$ is over pairs that are not in the native contact pair set. Only nonlocal pairs with $i < j - 3$ are taken into account.

2.2.2. Atomic Interaction Based CG Model. In the Go model, by default, the parameters K_b , K_θ , $K_\phi^{(1)}$, $K_\phi^{(3)}$, and ε_{go} are independent of the residue number i and of secondary structures, which implies that all the information coded by amino acid sequence of a protein is represented by the protein native structure. For better chemical specificity, one may want to use sequence-dependent parameters. Indeed, it was found that in some cases, such a chemical specificity can be crucial for the protein folding and other functional dynamics. Undoubtedly, appropriately implementing the interaction specificity into the Go model can improve the description of the protein dynamics. In CafeMol, based on the work of Li, Wolynes, and Takada,³⁶ we provide a way to implement such a kind of Go model with sequence-specific interactions, of which parameters were determined based on all-atom AMBER energy with an implicit solvent model by using a multiscale approach. This new model is called atomic interaction based CG (AICG) model.

In the AICG model, the interaction strength between the natively interacting residues i and j depends on i and j and is written as $\varepsilon_{go,ij} = \varepsilon_{go} w_{ij}$, with w_{ij} and ε_{go} being the relative weight of the interactions for each pair of contacting residues and the average of the nonlocal native interactions, respectively. The w_{ij} controls the heterogeneity of the nonlocal native interactions. In a simple version of AICG models, CafeMol provides an automatic estimate of w_{ij} via a linear regression to AMBER energy in terms of some atomic details of the residue contacts (see the Supporting Information of ref 36). Alternatively, CafeMol allows the user to provide AMBER-based residue-contact energy pre-calculated by the user.

In the AICG model, the residues with different secondary structures have different interaction parameters for bond and dihedral angles. Residues are assigned to one of the four major secondary structures, i.e., α -helix, β -strand, turn, and random coil, by the define secondary structure of protein (DSSP) method.⁴⁵ We also assign an independent parameter for the bond and dihedral angles which contain glycine. The nonlocal parameter ε_{go} and all the local parameters are generic and optimized by using the fluctuation matching method for a set of proteins.

2.2.3. Multiple-Basin Model. CafeMol employs the multiple-basin potential of Okazaki et al,²³ which, based on the Clementi et al's off-lattice Go model, represents the energy landscape that has more than one energy basin. We here write the equation of the potential for the two-basin case since this is most often used in real application, although CafeMol can treat the cases with more than two basins.

The multiple-basin potential energy function V_{MB} is defined by the (smaller) eigenvalue of the characteristic equation:

$$\begin{pmatrix} V_{\text{Go}+}(\mathbf{R}|\mathbf{R}_1) & \Delta \\ \Delta & V_{\text{Go}+}(\mathbf{R}|\mathbf{R}_2) + \Delta V \end{pmatrix} \begin{pmatrix} c_1 \\ c_2 \end{pmatrix} = V_{\text{MB}} \begin{pmatrix} c_1 \\ c_2 \end{pmatrix} \quad (2)$$

where $V_{\text{Go}+}(\mathbf{R}|\mathbf{R}_\nu)$ is essentially the Clementi's off-lattice Go potential $V_{\text{Go}}(\mathbf{R}|\mathbf{R}_\nu)$ but is modified in two respects, as described later. The condition that a nontrivial solution exists leads to a secular equation of which the explicit solution is given as

$$V_{\text{MB}}(\mathbf{R}|\mathbf{R}_1\mathbf{R}_2) = \frac{1}{2}[V_{\text{Go}+}(\mathbf{R}|\mathbf{R}_1) + V_{\text{Go}+}(\mathbf{R}|\mathbf{R}_2) + \Delta V] - \sqrt{\left(\frac{V_{\text{Go}+}(\mathbf{R}|\mathbf{R}_1) - V_{\text{Go}+}(\mathbf{R}|\mathbf{R}_2) - \Delta V}{2}\right)^2 + \Delta^2} \quad (3)$$

Here, Δ is a coupling constant, which smoothed the connection between two Go models (the larger Δ leads to smaller barrier height between two basins), and ΔV is to modulate the relative energies of the two basins. A convenient reaction coordinate that monitors the conformational change is $\chi = \ln(c_2/c_1)$, where (c_1, c_2) are the eigenvector corresponding to V_{MB} .

$V_{\text{Go}+}(\mathbf{R}|\mathbf{R}_\nu)$ is, as was noted, conceptually the same as $V_{\text{Go}}(\mathbf{R}|\mathbf{R}_\nu)$ of Clementi et al. Purely for technical reasons, we need to introduce two modifications. We write the $V_{\text{Go}+}(\mathbf{R}|\mathbf{R}_\nu)$ in the sum of three terms:

$$V_{\text{Go}+}(\mathbf{R}|\mathbf{R}_\nu) = V_{\text{local}}(\mathbf{R}|\mathbf{R}_\nu) + V_{\text{native-attract}}(\mathbf{R}|\mathbf{R}_\nu) + V_{\text{repul}}(\mathbf{R}|\mathbf{R}_\nu) \quad (4)$$

where the first term is

$$V_{\text{local}}(\mathbf{R}|\mathbf{R}_\nu) = \sum_i K_{b,i}(b_i - b_{i,\nu})^2 + \sum_i K_{\theta,i}(\theta_i - \theta_{i,\nu})^2 + \sum_i \{K_{\phi,i}^{(1)}[1 - \cos(\phi_i - \phi_{i,\nu})] + K_{\phi,i}^{(3)}[1 - \cos 3(\phi_i - \phi_{i,\nu})]\} \quad (5)$$

This local potential is slightly different from that of $V_{\text{Go}}(\mathbf{R}|\mathbf{R}_\nu)$: Namely, all of the K 's are now dependent on i in the following ways:

$$K_{b_i}/K_b = \min \left[1, \frac{\varepsilon_{b,\max}}{K_b(b_{i1} - b_{i2})^2} \right] \quad (6)$$

$$K_{\theta_i}/K_\theta = \min \left[1, \frac{\varepsilon_{\theta,\max}}{K_\theta(\theta_{i1} - \theta_{i2})^2} \right] \quad (7)$$

and

$$K_{\phi_i}^{(1)}/K_\phi^{(1)} = K_{\phi_i}^{(3)}/K_\phi^{(3)} = \min \left[1, \frac{\varepsilon_{\phi,\max}}{K_\phi^{(1)}[1 - \cos(\phi_{i,1} - \phi_{i,2})] + K_\phi^{(3)}[1 - \cos 3(\phi_{i,1} - \phi_{i,2})]} \right] \quad (8)$$

This is introduced so that the spring constant is weakened where too large local changes are observed between the two reference structures. The thresholds $\varepsilon_{b,\max}$, $\varepsilon_{\theta,\max}$, and $\varepsilon_{\phi,\max}$ define the "large local change". We note that because of this, $V_{\text{local}}(\mathbf{R}|\{\mathbf{R}_\nu\})$

is not just a function of the reference structure \mathbf{R}_ν , but it also depends on other reference structures.

Nonlocal potentials are divided into attractive terms $V_{\text{native-attract}}$ and repulsive terms V_{repul} , and the former is given as

$$V_{\text{native-attract}}(\mathbf{R}|\mathbf{R}_\nu) = \varepsilon_{\text{go}} \sum_{i < j - 3}^{\text{nat contact}} \min \left[1, 5 \left(\frac{r_{ij,\nu}}{r_{ij}} \right)^{12} - 6 \left(\frac{r_{ij,\nu}}{r_{ij}} \right)^{10} + 1 \right] \quad (10)$$

where the summation is over the native contact pairs in the same way as that of the single Go model. The repulsive part V_{repul} is further divided into two terms $V_{\text{repul-1}}(\mathbf{R}|\mathbf{R}_\nu)$ and $V_{\text{repul-2}}(\mathbf{R})$:

$$V_{\text{repul}}(\mathbf{R}|\mathbf{R}_\nu) = V_{\text{repul-1}}(\mathbf{R}|\mathbf{R}_\nu) + V_{\text{repul-2}}(\mathbf{R}) \quad (11)$$

where

$$V_{\text{repul-1}}(\mathbf{R}|\mathbf{R}_\nu) = \varepsilon_{\text{go}} \sum_{i < j - 3}^{\text{nat-related}} \max \left[0, 5 \left(\frac{r_{ij,\nu}^{\min}}{r_{ij}} \right)^{12} - 6 \left(\frac{r_{ij,\nu}^{\min}}{r_{ij}} \right)^{10} \right] \quad (12)$$

and

$$V_{\text{repul-2}}(\mathbf{R}) = \varepsilon_{\text{ev}} \sum_{i < j - 3}^{\text{purely non-nat}} \left(\frac{d}{r_{ij}} \right)^{12} \quad (13)$$

where

$$r_{ij,\nu}^{\min} = \min_{\nu}^{\text{nat contact}} [r_{ij,\nu}] \quad (14)$$

Here, the repulsive-1 term is used for the pairs for which the native contact is formed at least in one of the reference structures ("type 1" and "type 2" pairs in the original paper of Okazaki et al). We termed it as "native-related pairs". For a particular pair ij , if the pair is in native contact in the state ν (state corresponds to basin), then this is a (true) native contact for this state. If the pair is not in the native contact in the state ν , but it makes contact in another state, then we call this pair in the "dummy contact" in the state ν . For the state ν , the "native-related pairs" include both the true native and the dummy contact sets. The repulsive-2 term is for the pairs for which native contact is never formed in any of the reference structures ("type 3" pairs in the original paper). $V_{\text{repul-2}}(\mathbf{R})$ is the same form as that of Clementi et al's Go model.

We note that the attractive part has the same shape as that of Clementi et al but the repulsive part of the Lennard-Jones-like potential is modified for the native-related pairs. Between the two (or all the) states, the repulsive part is identical. The $r_{ij,\nu}^{\min}$ is the smallest distance between i and j among all the states ν for which this pair ij is in native contact. We note that because of this, $V_{\text{repul-1}}(\mathbf{R}|\mathbf{R}_\nu)$ is not just a function of the reference structure \mathbf{R}_ν , but also depends on other reference structures.

2.2.4. Elastic Network Model. The ENM was first proposed by Tirion in all-atom representation.³² CafeMol uses it in one-bead-per-amino-acid CG level. Simply, all the native contact pairs are connected by elastic bonds with their natural lengths $r_{ij,0}$ being equal to those at the native structure. The spring constant K is the same for all the elastic bonds. The same definition of the native contact as that of the off-lattice Go model

is used here:

$$V_{\text{ENM}} = K \sum_{i < j}^{\text{nat contact}} (r_{ij} - r_{ij,0})^2 \quad (15)$$

2.2.5. Electrostatic and Hydrophobic Interactions. In addition to the above four models, we can optionally turn on other interactions that include the electrostatic interaction, a hydrophobic interaction, a pulling force for steering, and others. The electrostatic interaction is expressed as the Debye–Hückel form. The hydrophobic interaction defined below is an empirical form and is qualitatively similar to the accessible surface area model.

The hydrophobic (HP) interaction is modeled by a many-body energy function,²⁵ which has a similar functional form to that was used in Fujitsuka et al.:^{46,47}

$$V_{\text{HP}} = -c_{\text{HP}} \sum_{i \in \text{HP}} \varepsilon_{\text{HP},A(i)} S_{\text{HP}}(\rho_i) \quad (16)$$

Here, the coefficient c_{HP} is to scale the overall strength of the hydrophobic interactions. $A(i)$ stands for the type of the particle i ; 21 types are considered: $A(i) = 1, 2, \dots, 20$ means the 20 types of amino acids and $A(i) = 21$ simply represents all nonamino acid particles. The particle-type-specific parameter that reflects the hydrophobicity of particles is $\varepsilon_{\text{HP},A}$. The “buriedness” $S_{\text{HP}}(\rho_i)$ of the particle i is defined by

$$S_{\text{HP}}(\rho) = \begin{cases} c_{\text{linear}}\rho & \rho \leq \rho_{\text{min}} \\ c_{\text{linear}}\rho + 0.5(1 - c_{\text{linear}}) \left[1 + \cos \frac{\pi(1 - \rho)}{1 - \rho_{\text{min}}} \right] & \rho_{\text{min}} < \rho < 1 \\ 1 & \rho \geq 1 \end{cases} \quad (17)$$

Here, c_{linear} defines the contribution of the linear term, and ρ_{min} is the threshold to introduce nonlinear form. The local density ρ_i for particle i is calculated by

$$\rho_i = \frac{\sum_{j \in \text{HP}, j \neq i} n_{A(j)} u_{\text{HP}}(r_{ij}, r_{\text{min},A(i),A(j)}, r_{\text{max},A(i),A(j)})}{n_{\text{max},A(i)}} \quad (18)$$

where n_A is the number of atoms that the particle type A represents, and $n_{\text{max},A}$ is the maximum coordination number for particle type A . The function u_{HP} represents the degree of the contact between particles i and j and is defined as

$$u_{\text{HP}}(r, r_{\text{min}}, r_{\text{max}}) = \begin{cases} 1 & r \leq r_{\text{min}} \\ 0.5 \left(1 + \cos \frac{\pi(r - r_{\text{min}})}{r_{\text{max}} - r_{\text{min}}} \right) & r_{\text{min}} < r < r_{\text{max}} \\ 0 & r \geq r_{\text{max}} \end{cases} \quad (19)$$

where r_{min} (r_{max}) is to define the cutoff for the minimal (maximal) distance, which depends on the particle types $A(i)$ and $A(j)$.

In real applications, the target system may contain more than one protein molecule. In such a case, the total energy function is the sum of intrachain and interchain interactions. For the former, CafeMol allows us to mix the models; it is possible, for example, that one chain is represented by the Go model, and another chain by the multiple-basin model. Interactions between chains may be modeled by a combination of the few interactions, such as the

contact energy (the same way as the Go model), the electrostatic interaction, the hydrophobic interaction, and the simple repulsion.

We also mention that we can realize a frustrated system even in the framework of the Go model. For example, in modeling a flexible docking of two proteins, one can represent the intrachain interactions of two individual proteins by the Go model using their unbound structures as references, while the interactions between two proteins may be modeled by the native contact taken from the bound complex structure. Even though all the interactions are of Go-type, their reference structures are not the same, thus introducing frustrations. CafeMol has flexible interfaces which allow one to realize such a mixed-reference simulation very easily.

2.2.6. Explicit and Implicit Ligand Models. Protein conformational change is coupled with a ligand binding, and one may want to take into account the ligand binding dynamics into CG simulations. CafeMol has two ways to include ligands: the explicit and implicit ligand models. Explicitly including CG ligands is a straightforward method, whereas the implicit ligand model is a computationally faster alternative proposed in Okazaki and Takada, 2008.¹⁸

In the explicit ligand model, small ligand molecules are modeled as a rigid linear chain, in which the sequence of ligand beads is defined in the input PDB file of the ligand. The energy function for explicit ligands is essentially the same as the local potential term in the Go model, in which the spring constants are set as sufficiently large values to make the ligand rigid. Between the ligand and proteins, we can use the same interactions as those for interprotein interactions.

On the other hand, in the implicit ligand model, we describe that ligand binding in the “two-state” manner. Namely, the ligand is either bound (B) or unbound (U) to a protein. In the unbound state, the protein has just its intraenergy, represented typically by the multiple-basin model, whereas the protein in the bound state has the energy which is the sum of its intraenergy and the ligand binding energy, $V_{\text{imp-lig}}$. This ligand binding energy $V_{\text{imp-lig}}$ does not contain the explicit coordinates of the ligand atoms but is a function of the Cartesian coordinates of ligand-mediated sites of the protein. It takes the negative and large absolute value when the local environment around the binding pocket is close to that of the reference conformation. Concretely, the $V_{\text{imp-lig}}$ is normally defined as

$$V_{\text{imp-lig}} = - \sum_{\substack{\text{ligand-mediated} \\ \text{contact pairs}}} c_{\text{lig}} \varepsilon_{\text{go}} \exp \left[- \frac{(r_{ij}/r_{0ij} - 1)^2}{2(\sigma/r_{0ij})^2} \right]$$

where the “ligand-mediated contact pairs” means the amino acid pairs that satisfy the following three conditions: (a) Both of amino acids in the pair are involved in the binding-sites, which are provided in the input file. (b) The pair is not involved in the native contact. (c) At least one non-hydrogen atom in one amino acid is within 10 Å from at least one non-hydrogen atom in the other amino acid. In time propagation, the protein conformation is moved by the standard MD simulation (described below), whereas the ligand binding state (B or U) is stochastically changed by the rates k_b (binding) and k_u (unbinding) implemented as the metropolis Monte Carlo (MC) scheme in the following way. While in the unbound (U) state, a ligand molecule

reaches the binding pocket at every Δt_b time with probability $p = k_b \Delta t_b$. With this probability, the state changes to the bound (B) one. Here k_b is the apparent first-order rate for binding and thus is proportional to the ligand concentration. While in the bound state, at every Δt_u time, the bound ligand has chance to dissociate at a probability $\exp(-|V_{\text{imp-lig}}|/k_B T)$. The mixed MD–MC scheme thus described here is a convenient way of simulating protein conformational dynamics coupled with ligand binding.

2.3. Simulation Methods. *2.3.1. Units.* CafeMol uses a specific unit. The length unit is Å. The energy unit is kcal/mol. For temperature, we use Kelvin, $1 K = 1.987 \times 10^{-3} \text{kcal/mol}$. The mass unit is our own one. We set that each amino acid has the mass of 10, which we call 10 cafe-mu (cafemol mass unit). Since average mass of 20 amino acids is 137 amu (atomic mass unit), we thus define 1 cafe-mu = 13.7 amu. From these, we can directly obtain the unit time of CafeMol to be 1 cafe-time = $1.809 \times 10^{-13} \text{s} \sim 200 \text{fs}$. We need to be cautious in interpreting this time scale. Since intrinsic dynamics is accelerated by coarse graining the energy landscape, this apparent mapping in time scale does not necessarily give a good estimate of the real time.

2.3.2. Constant Temperature MD. The constant temperature MD is the most basic simulation protocol in CafeMol. Currently, one can use either constant-temperature “Newtonian” or Langevin dynamics. The underdamped Langevin dynamics is integrated by the scheme developed by Honeycutt, Guo, and Thirumalai.^{48,49} For the constant-temperature Newtonian dynamics, we employed the velocity-type Verlet algorithm for updating protein structure with the Berendsen thermostat for controlling temperature.³⁸

2.3.3. Searching T_F . CafeMol can automatically estimate T_F , at which the protein is folded (or denatured) with 50% probability, by using the bisection method. Namely, we first specify, in the input file, the lower and the upper bounds of T_F . CafeMol first simulates the protein at the midpoint temperature of the two bounds and sees if the protein is near native conformation for more than half of the simulation time. If yes, then this temperature is set as the new lower bound of T_F . Otherwise, the simulated temperature was set as the new upper bound of T_F . With the new set of the lower and the upper bounds, CafeMol repeats the simulation at their midpoint. This iteration lasts for the required times to narrow the temperature range. For an accurate estimate of T_F , the MD step number needs to be much larger than the folding and unfolding time scale near T_F . Typically, the condition is easily satisfied for proteins with less than 100 amino acids but for proteins with more than 200 residues

2.3.4. Simulated Annealing. The simulated annealing is to search lower (possibly the lowest) energy structure in the simulated system. It uses the constant-temperature MD routine, and the temperature in the routine is decreased at a certain rate.

2.3.5. Replica Exchange Method. CafeMol can run one- and two-dimensional replica exchange method (REM).^{50–52} The standard replica-specifying parameters are the temperature and the ionic strength, although one can easily adapt it for other replica-specifying parameters. In addition, CafeMol equips the feedback-optimized REM,⁵³ by which the replica temperatures can automatically be optimized.

2.3.6. Switching Go Model. Many proteins work by changing their conformations depending on their interactions with their partner molecules. For example, proteins change their conformation upon binding to ligands. How binding and conformational change are coupled in proteins is in itself a subject to be studied. However, for studying more complex biological phenomena, we

may want to enforce such a conformational change by design. The switching Go model is proposed for this type of simulations.

In the switching Go model, we first simulate a protein by the Go model $V_{\text{Go}}(\mathbf{R}|\mathbf{R}_A)$ with a structure A being the reference (i.e., native) structure. At room temperature, the protein usually resides nearby the structure A, $\mathbf{R} \sim \mathbf{R}_A$. At a certain time, we suddenly change the reference structure of the Go model to another structure B, resulting in a new Go potential $V_{\text{Go}}(\mathbf{R}|\mathbf{R}_B)$. The protein jumps from the bottom of the Go model $V_{\text{Go}}(\mathbf{R}|\mathbf{R}_A)$ to the downhill slope of the new Go potential $V_{\text{Go}}(\mathbf{R}|\mathbf{R}_B)$. Note that the simulated structure \mathbf{R} does not change suddenly but changes continuously. Right after the switch, the protein starts to relax its conformation from $\mathbf{R} \sim \mathbf{R}_A$ to $\mathbf{R} \sim \mathbf{R}_B$. This mimics the conformational change from the structure A to the structure B, in a simple and crude way. CafeMol is ready to switch Go models in any fixed times.

2.3.7. Switching Bias in Multiple-Basin Potential. The switching Go model is perhaps the simplest way to realize some large-scale conformational change in biomolecules. However, in switching Go models, the protein is “excited” to the new potential, and the resulting procedure is nothing but the relaxation on the new Go potential surface. This resembles to the photoactivated process. Biologically, however, many events are thermally activated, and thus overcoming the energy barrier by thermal fluctuation may be of essential importance, in some cases. To realize this thermally activated conformational transition, CafeMol uses the multiple-basin model. We first simulate a protein with the multiple-basin model setting the structures A and B as reference structures of the two basins, i.e., $V_{\text{MB}}(\mathbf{R}|\mathbf{R}_A, \mathbf{R}_B, \Delta V)$, where ΔV is positive and sufficiently large so that the basin A is more stable. The protein mostly resides in the basin A, i.e., $\mathbf{R} \sim \mathbf{R}_A$. At a certain time, we suddenly change the bias ΔV to a negative and sufficiently large absolute value so that the basin B is now more stable. Soon after the switch, the protein would still fluctuate in the basin A, but after a while, it overcomes the barrier to reach the more stable basin B, through thermal fluctuations. We can also couple the switch bias in multiple-basin potential and switch the reference structure as in the case of switching Go model.

3. RESULTS

Here, after investigating parallel performance we illustrate prototypical simulations by CafeMol. Six basic examples are followed by simulations of two protein machines at work. Technical details on how to write input files are described in the Supporting Information and in Tables S1–S4.

3.1. Parallel Performance. The CafeMol code is parallelized by MPI and OpenMP commands. The parallel efficiency strongly depends on the simulated system. As in all other MD simulations, the bottleneck in computation is the force calculation and thus parallelization in the force calculations determines the overall parallel performance. For simple Go model simulations without additional interactions, forces from the native contact and excluded volume interactions are dominant. When the electrostatic interaction is turned on, the computational bottleneck shifts to the force calculation of the electrostatic interaction, as in normal MD simulations. This is because the native contact is relatively short ranged, while the electrostatic interactions are long ranged.

Here, we show benchmark tests of parallel efficiency up to 64 cores for 2 viral capsid protein complexes using the Go model

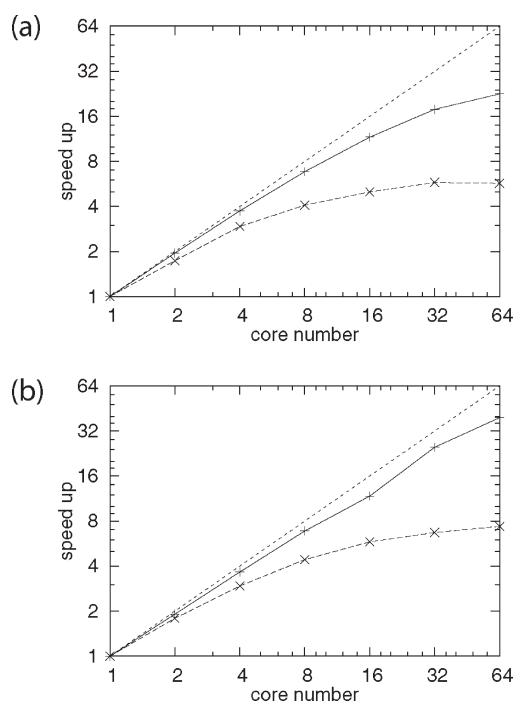


Figure 1. Performance of parallel computation of Go model simulations with (solid curves) and without (dashed curves) electrostatic interactions. (A) STMV capsid proteins containing 8820 residues. (B) Norwalk viral capsid proteins containing 89700 residues. The acceleration rate is plotted against core numbers in the log–log scale. The dotted line indicates the ideal linear scaling.

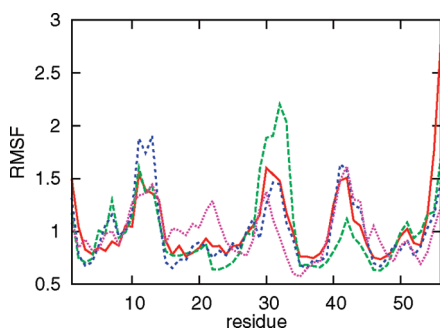


Figure 2. The RMSF of src SH3 domain in its native state at 300 K. Results by Go model (the red solid line), by all-atom MD with an implicit solvent model (the green long-dashed line), and by all atom MD with explicit water solvent (the blue short-dashed line) together with the estimate from the X-ray B-factors (the pink dotted line) are compared. All the curves are scaled so that their averages become unity.

with and without electrostatic interactions. We used a standard PC cluster with infiniband networks. OpenMP is used up to four cores, whereas the MPI/OpenMP hybrid is employed beyond four cores, in which OpenMP always deals with four cores. A smaller system, satellite tobacco mosaic virus (STMV) capsid protein complex (the pdb code 1A34), is made of 60 identical proteins of 147 amino acids (excluding unstructured terminus), containing 8820 CG particles. A larger system, capsid protein complex of Norwalk virus (the pdb code 1ihm), contains 180 subunits of about 500 residue proteins which results in 89700 CG particles (about 10 times as large as STMV). For each of the two protein complexes, we measured the parallel performance of

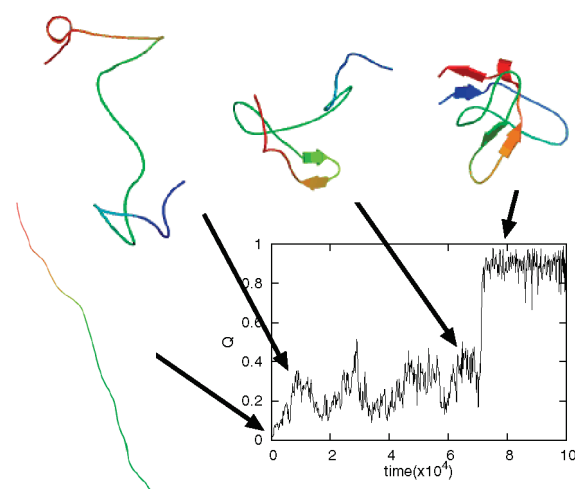


Figure 3. Time course of src SH3 domain folding simulated by the Go model. The nativeness is quantified by the Q score, the fraction of the formed native contacts. Some representative snapshot structures are illustrated. The molecular images in this article were created with PyMOL⁵⁸ and VMD.⁴³

constant temperature MD simulations of the Go model with and without the electrostatic interactions (Figure 1). Without electrostatic interactions, the parallel performance saturated at around 8 cores and the asymptotic speed-up was about 6- and 7- fold for STMV and for the Norwalk virus, respectively (dashed curves). When the electrostatic interactions were turned on, parallel efficiency was markedly improved (solid curves); 24- and 40- fold speeds-up for STMV and for the Norwalk virus, respectively, with 64 cores. Thus, as expected, for larger molecular systems with electrostatic interactions, the parallel performance is more pronounced.

In addition, the replica exchange MD is parallelized naturally by MPI. Namely, different replicas are dealt with different nodes. One can combine the force parallelization and the parallel treatment of replicas, resulting in two-dimensional parallelization.

3.2. Near-Native Dynamics. We start with the constant temperature MD simulation of src SH3 domain protein by the Go model to calculate fluctuations in the native state. We perform a 1×10^6 step MD simulation with the time step 0.2 cafe-time. See Supporting Information, Table S1 for technical details.

Figure 2 represents the root-mean-square fluctuation (RMSF) of every amino acids in src SH3 domain protein calculated by the Go model together with the results obtained by some standard all-atom MD simulations. They contained the 10 ns MD result by all-atom protein model of the AMBER ff99SB⁵⁴ with the modified generalized Born implicit solvent model⁵⁵ as well as those by the same all-atom model with explicit water molecules of TIP3P.⁵⁶ Apparently in Figure 2, the agreement among the three methods is overall quite good. Not surprisingly, both N- and C-termini residues are intrinsically flexible with quite a large RMSF, and they can differ, to more extent, among three results. Ignoring 3 residues in each terminus, we obtained the correlation coefficient between the RMSFs by the Go model and those by the all-atom MD (explicit water) to be 0.88. In contrast, the correlation coefficient between the RMSFs by all-atom MD with explicit waters and those with the implicit water model was 0.65 for this protein.

3.3. Protein Folding. The second example is a folding simulation of src SH3 domain protein by the Go model at 300 K.

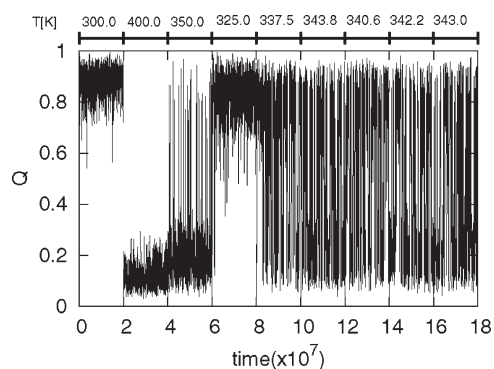


Figure 4. The automatic T_F search by the bisection method for src SH3 domain. The constant temperature MD is performed at each temperature (specified at the top of the figure) for 2×10^7 cafe-time, and the time series of the Q score is plotted.

Figure 3 shows time series of an overall folding reaction coordinate, i.e., Q -score, the fraction of the formed native contacts. We see that the folding occurs quite cooperatively, and the folding nucleus is found in the so-called distal β -hairpin (light-green to orange segments in the cartoon of Figure 4), which agrees quite well with the results of experimental ϕ -value analysis.⁵⁷

3.4. Automatic T_F Search. As described above, CafeMol has a function to automatically estimate T_F for modest size proteins. Here, we exemplify it for src SH3 domain protein. Figure 4 shows the result. Since the upper and the lower temperature bounds are 500 and 100 K, the initial midpoint temperature is 300 K where the first MD simulation is conducted for 2×10^7 cafe-time. This results in the native state for almost the entire time. Then, 300 K is set as the lower bound. In the second round, the new midpoint temperature is 400 K. The same procedure continues nine times. The employed temperatures in every step are shown at the top of the figure. See Supporting Information, Table S2, for technical details.

3.5. Conformational Change by Multiple-Basin Potential. We then illustrate a conformational change simulation of the glutamine binding protein by the multiple-basin potential. The glutamine binding protein is a typical molecule that exhibits close/open conformational changes upon ligand binding/dissociation, and both the open and the closed structures are available. The multiple-basin potential has two empirical and important parameters, ΔV and Δ , which we tuned by a trial-and-error approach so that the resulting MD produces reversible transitions between the open and the closed structures and that the residential time in each state is nearly 0.5. Here, we chose $\Delta V = -8$ and $\Delta = 55$. The result of a MD simulation is shown in Figure 5 where the reaction coordinate χ (defined above) is plotted as a function of time. The χ is negative (positive) when the protein is in the basin of open (closed) state. Here, we observed quite abrupt and reversible conformational transitions between the two states, thus showing that the two states separated by a low free energy barrier are in near equilibrium. See Supporting Information, Table S3, for technical details.

3.6. Conformational Change by Switching Go Model. Although we can realize reversible conformational transitions between two structures for small proteins by the multiple-basin model, as was described in the previous subsection, this may not easily be realized for a very large-amplitude conformational change in very large proteins. For such cases, we can induce

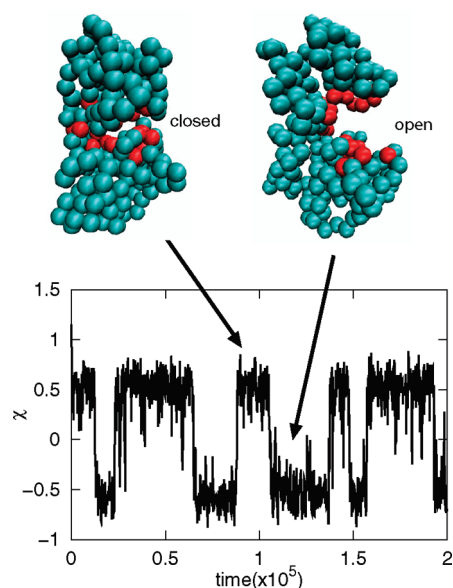


Figure 5. Reversible conformational transitions of glutamine binding protein by the multiple-basin model. The parameters are tuned so that the open and closed states are almost equally stable and the conformational changes are sufficiently frequent. The χ monitors the conformational change and takes the positive (negative) value when it is in the closed (open) state. The representative snapshots are drawn where the binding site residues are in red.

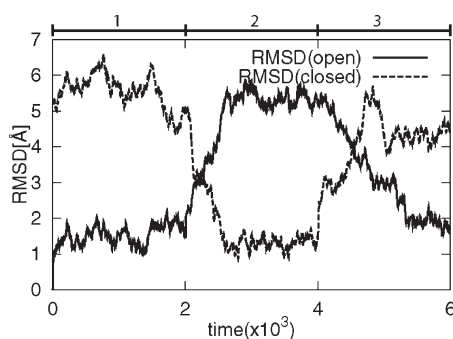


Figure 6. Conformational changes of glutamine binding protein by the switching Go model. The y-axis is the rmsd from the open (solid) and the closed (dashed) states. The potential is switched every 2×10^3 time.

such large-scale conformational changes by switching the Go model, although this is less sophisticated than the multiple-basin model. Here, we exemplify it for the glutamine binding protein. First, the protein is simulated with the Go model with the reference structure being the open structure. At $t = 2 \times 10^3$, we switch the reference structure of the Go model to the closed structure, which immediately initiates a closing motion. Later, we switch the native structure back to the open structure inducing the opening conformational change. See Supporting Information, Table S4, for technical details.

Figure 6 depicts the result, where the y-axis monitors the root-mean-square deviation (rmsd) from two reference structures. We clearly observe here that, after switching, the protein gradually makes conformational change to the new native structures

3.7. Replica Exchange MD. The next example is a simple folding and unfolding simulation of protein G (61 residue small

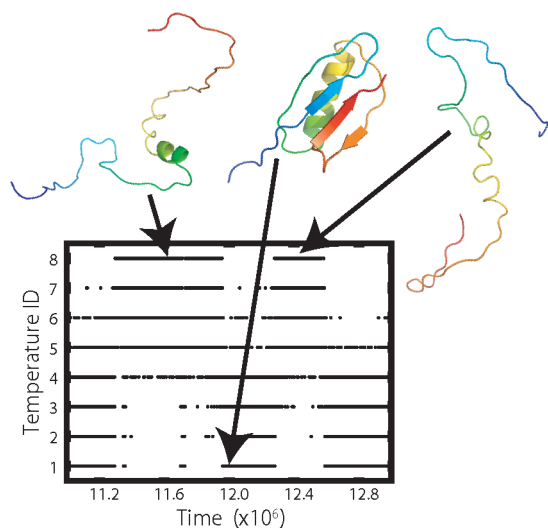


Figure 7. Itinerary of replica 1 in the replica MD simulations of protein G with 8 replicas. The temperature ID of the replica 1 is plotted as a function of time. Some representative snapshot structures are illustrated.

protein, pdb id 2igd) by the REM. Although the automatic T_F search work well for this small protein, the REM is the only one available method in CafeMol one can use to determine the transition temperature T_F for larger proteins. Here, we use 8 replicas of which temperatures are distributed exponentially with the lower and the upper bound temperatures being 300 and 380 K, respectively.

Figure 7 shows temperature id itinerancy of the replica 1 showing that the replica travels all the temperature id's in quite high frequency. Some representative structures are shown in the figure.

3.8. Molecular Motor at Work. The last two examples are simulations of protein machines at work. Here, we illustrate a simulation of a rotary motor F_1 -ATPase. F_1 -ATPase, a half portion of ATP synthase, hydrolyzes ATP to rotate its central stalk. The X-ray structure of the minimal catalytic complex, $\alpha_3\beta_3\gamma$ was first solved by Walker's group.⁵⁹ In the complex, the central stalk, γ -subunit, is surrounded by the hexameric ring $\alpha_3\beta_3$ where the α - and β -subunits are arranged alternatively. The ATP hydrolysis reaction is catalyzed at each interface between the α - and β -subunits, with the catalytic residues primarily in β -subunits. In the Walker's structure, three $\alpha\beta$'s differ in their nucleotide-bound states as well as their structures: one $\alpha\beta$ binds ATP (called $\alpha\beta_{TP}$), another $\alpha\beta$ binds ADP (called $\alpha\beta_{DP}$), and the last $\alpha\beta$ does not bind any nucleotide (called $\alpha\beta_E$, where E stands for "empty"). Sequential and coordinated chemical and structural changes in three $\alpha\beta$'s suggested a 120° rotation of the central γ -subunit. This rotary mechanism, first proposed by Boyer,⁶⁰ was finally proved by the direct observation of the γ rotation by a single-molecule experiment.⁶¹ Based on the structural and single-molecule experiments, we have previously conducted CG MD simulations of the rotary motion using an ancestor program of CafeMol.¹⁴ Our trial-and-error computer experiments ended up with a prediction of a particular mechanochemical coupling scheme, the always bisite model, which is consistent with several experimental results published beforehand as well as afterward.^{62–64}

Here, we present a simple simulation of the rotation of γ in $\alpha_3\beta_3\gamma$ complex by the switching Go model (Figure 8) (We note

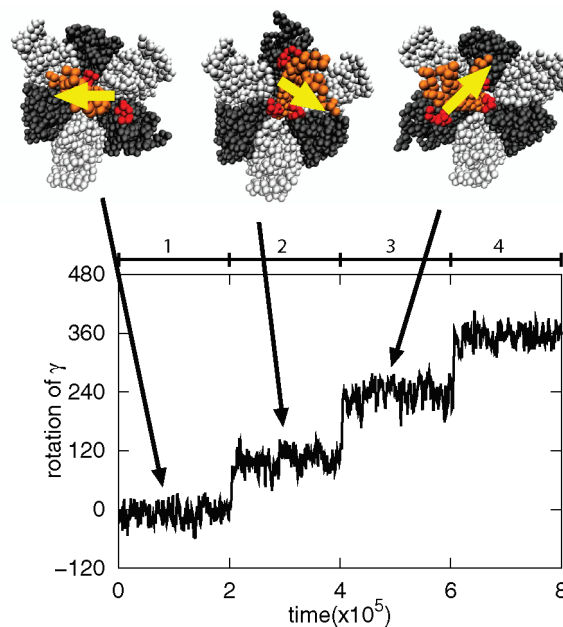


Figure 8. Rotary motion of F_1 -ATPase studied by the switching Go model. The rotation angle of γ -subunit is plotted as a function of time. The potential is switched every 2×10^5 cafe-time when the reference structures of all three $\alpha\beta$'s are cyclically changed. The representative snapshots are shown where the three β 's are drawn in dark gray, the three α 's are in light gray, the central γ is in orange. The yellow arrow is the vector that monitors the rotary angle of γ . In β 's, segments that make large conformational changes are marked in red.

that the simulation here is much simpler one than in ref 14, and it is only for illustration of the utility of CafeMol). We start the CG MD with the Walker's complex structure, where both intrasubunit and intersubunit interactions in $\alpha_3\beta_3$ rings are modeled by the Go model, the central stalk γ is also represented by the Go model, and the interactions between $\alpha_3\beta_3$ and γ are modeled by the simple repulsion. At $t = 2 \times 10^5$, we switch the reference structures of the $\alpha_3\beta_3$ ring so that each $\alpha\beta$ changes its structure one step ahead, i.e., in a site $\alpha\beta_{TP}$ is induced to change to $\alpha\beta_{DP}$, in another site $\alpha\beta_{DP}$ is changed to $\alpha\beta_E$, and in the third site, $\alpha\beta_E$ is changed to $\alpha\beta_{TP}$. After the switch, the three $\alpha\beta$'s indeed made the corresponding conformational changes, which further induced rotary motion of γ by 120° (Figure 8). At $t = 4 \times 10^5$ and 6×10^5 , we further switched the reference structures in the same way, observing totally the 360° rotation of γ -subunit.

3.9. Transporter at Work. As the final example, we show a simulation of a transporter at work. Here, we use a multidrug transporter that exports a drug molecule. Specifically, the simulated system is the bacterial multidrug transporter AcrB together with an antibiotic, minocycline. We note that the simulation here is based on, but is not identical to, our earlier work.²⁵

AcrB is a bacterial multidrug transporter that exports a broad range of hydrophobic drug molecules from cytoplasmic side to the cell outside driven by the proton motive force across the inner membrane. It was experimentally clarified that AcrB forms a homotrimer, and the trimeric complex takes asymmetric structures, where each subunit has different conformation:⁶⁵ one subunit takes the state B as the drug-bound state, another subunit takes the state E as the drug extrusion state, and the third subunit takes the state A as the drug access state. It has been postulated that the cyclic conformational change from state A, to

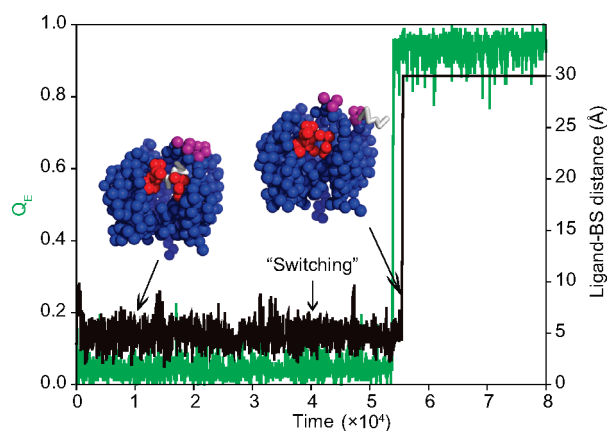


Figure 9. Simulation of multidrug transporter AcrB monomer with a drug molecule. The conformational change of AcrB is quantified as Q_E score (green curve with the scale on the left axis), which is defined as the fraction of native contacts that are observed in the E state but do not exist in the B or A state. Simultaneously, motion of the drug molecule is monitored by the distance between the geometric centers of drug and binding sites (BS) (black curve with the scale on the right axis). The simulation started in the B state and then at $t = 4 \times 10^4$ the potential function is switched to induce conformational change to the E state. The two snapshot structures are illustrated where AcrB is viewed from the side (some residues are not drawn to make the protein interior visible). The red spots in the middle are the drug binding site, whereas the purple spots at the top shows the drug exit point. The drug is drawn by white stick representation, which is near the binding pocket in the left cartoon and is near the exit point in the right cartoon.

state B, and to state E in each subunit can transport one drug molecule from the cytoplasmic side of the membrane to the cell outside per subunit and that, as the homotrimer, it proceeds from the asymmetric complex ABE to BEA, to EAB, and to ABE, which is called the functional rotation mechanism. This is analogous to the rotary motion of the $\alpha_3\beta_3$ ring in F_1 -ATPase.

Here, only for an illustration of a simulation with a small explicit ligand, we use one subunit of the drug binding domain, called the porter domain, of AcrB (see cartoon in Figure 9). We use the multiple-basin model with three states for AcrB and the hydrophobic interaction and the excluded volume terms for the interactions between AcrB and the drug. The simulation starts with the B state, and the drug (shown by the stick representation in Figure 9) is bound near the binding pocket (the left cartoon in Figure 9). Initially, the parameters are set so that the three states are equally probable. The energy function is switched at $t = 4 \times 10^4$ to stabilize the E state. Somewhat after the switching, AcrB makes the transition from the B to E state at around $t = 5.4 \times 10^4$ (monitored by the Q score shown in the green curve), which soon induces the drug export toward the outside of the cell at $t = 5.5 - 5.6 \times 10^4$ (the black curve).

4. DISCUSSIONS AND CONCLUSION

We have described the CafeMol method and software, which is characteristic, among many existing MD packages, in several aspects. First, it provides the MD code specific to the structure-based CG MD. In particular, the multiple-basin model is able to simulate conformational change of proteins when the two end structures are given, which is not easily realized by standard MD packages. Second, CafeMol provides various flexible and convenient means to mimic protein motions driven by external

energy source. Third, CafeMol equips the AICG model that takes into account atomic interactions in the framework of CG models, thus making it much more accurate without much of extra computational cost.

Yet, in the current version, some parameters in the energy functions were determined in a heuristic way. In particular, the parameters in the multiple-basin models are quite heuristic. It is highly desired that these parameters are derived systematically, for example, based on all-atom simulations.

Many more functions are currently under development in CafeMol. First, we are implementing CG models of DNA, RNA, and lipid membrane. Once realized, we can simulate all the macromolecular components of the cell in an integrated way. For better description of rotation and translation of macromolecules, the hydrodynamic interaction is crucial. We are working on implementing methods that take into account it.

■ ASSOCIATED CONTENT

S Supporting Information. Summary on the structure of the code and used file formats. Technical details on how to write input files. This material is available free of charge via the Internet at <http://pubs.acs.org>.

■ AUTHOR INFORMATION

Corresponding Author

*E-mail: takada@biophys.kyoto-u.ac.jp

■ ACKNOWLEDGMENT

This work is supported by Research and Development of the Next-Generation Integrated Simulation of Living Matter, a part of the Development and Use of the Next-Generation Supercomputer Project of the Ministry of Education, Culture, Sports, Science, and Technology. Some of the simulations were performed in RIKEN Integrated Cluster of Clusters.

■ REFERENCES

- (1) Brooks, B.; Bruccoleri, R.; Olafson, B.; States, D.; Swaminathan, S.; Karplus, M. *J. Comput. Chem.* **1983**, *4*, 187–217.
- (2) Pearlman, D.; Case, D.; Caldwell, J.; Ross, W.; Cheatham, T.; DeBolt, S.; Ferguson, D.; Seibel, G.; Kollman, P. *Comput. Phys. Commun.* **1995**, *91*, 1–41.
- (3) Phillips, J.; Braun, R.; Wang, W.; Gumbart, J.; Tajkhorshid, E.; Villa, E.; Chipot, C.; Skeel, R.; Kale, L.; Schulten, K. *J. Comput. Chem.* **2005**, *26*, 1781–1802.
- (4) Lindahl, E.; Hess, B.; van der Spoel, D. *J. Mol. Model.* **2001**, *7*, 306–317.
- (5) Izvekov, S.; Voth, G. *J. Phys. Chem. B* **2005**, *109*, 2469–2473.
- (6) Tozzini, V. *Curr. Opin. Struct. Biol.* **2005**, *15*, 144–150.
- (7) Tan, R.; Petrov, A.; Harvey, S. *J. Chem. Theory Comput.* **2006**, *2*, 529–540.
- (8) Ayton, G.; Noid, W.; Voth, G. *Curr. Opin. Struct. Biol.* **2007**, *17*, 192–198.
- (9) Clementi, C. *Curr. Opin. Struct. Biol.* **2008**, *18*, 10–15.
- (10) Gorecki, A.; Szymowski, M.; Dlugosz, M.; Trylska, J. *J. Comput. Chem.* **2009**, *30*, 2364–2373.
- (11) Levitt, M.; Warshel, A. *Nature* **1975**, *253*, 694–698.
- (12) Clementi, C.; Nymeyer, H.; Onuchic, J. *J. Mol. Biol.* **2000**, *298*, 937–953.
- (13) Koga, N.; Takada, S. *J. Mol. Biol.* **2001**, *313*, 171–180.
- (14) Koga, N.; Takada, S. *Proc. Natl. Acad. Sci. U.S.A.* **2006**, *103*, 5367–5372.

- (15) Takagi, F.; Koga, N.; Takada, S. *Proc. Natl. Acad. Sci. U.S.A.* **2003**, *100*, 11367–11372.
- (16) Hyeon, C.; Lorimer, G.; Thirumalai, D. *Proc. Natl. Acad. Sci. U.S.A.* **2006**, *103*, 18939–18944.
- (17) Hyeon, C.; Onuchic, J. *Proc. Natl. Acad. Sci. U.S.A.* **2007**, *104*, 2175–2180.
- (18) Okazaki, K.; Takada, S. *Proc. Natl. Acad. Sci. U.S.A.* **2008**, *105*, 11182–11187.
- (19) Noguchi, H.; Takasu, M. *Phys. Rev. E* **2001**, *64*, 041913.
- (20) Shelley, J.; Shelley, M.; Reeder, R.; Bandyopadhyay, S.; Moore, P.; Klein, M. *J. Phys. Chem. B* **2001**, *105*, 9785–9792.
- (21) Marrink, S.; de Vries, A.; Mark, A. *J. Phys. Chem. B* **2004**, *108*, 750–760.
- (22) Marrink, S.; Risselada, H.; Yefimov, S.; Tieleman, D.; de Vries, A. *J. Phys. Chem. B* **2007**, *111*, 7812–7824.
- (23) Okazaki, K.; Koga, N.; Takada, S.; Onuchic, J.; Wolynes, P. *Proc. Natl. Acad. Sci. U.S.A.* **2006**, *103*, 11844–11849.
- (24) Koga, N.; Kameda, T.; Okazaki, K.; Takada, S. *Proc. Natl. Acad. Sci. U.S.A.* **2009**, *106*, 18237–18342.
- (25) Yao, X.; Kenzaki, H.; Murakami, S.; Takada, S. *Nat. Commun.* **2010**, *1*, 117.
- (26) Bryngelson, J.; Wolynes, P. *Proc. Natl. Acad. Sci. U.S.A.* **1987**, *84*, 7524–7528.
- (27) Bryngelson, J.; Onuchic, J.; Socci, N.; Wolynes, P. *Proteins* **1995**, *21*, 167–195.
- (28) Go, N. *Annu. Rev. Biophys. Bioeng.* **1983**, *12*, 183–210.
- (29) Leopold, P.; Montal, M.; Onuchic, J. *Proc. Natl. Acad. Sci. U.S.A.* **1992**, *89*, 8721–8725.
- (30) Takada, S. *Proc. Natl. Acad. Sci. U.S.A.* **1999**, *96*, 11698–11700.
- (31) Taketomi, H.; Ueda, Y.; Go, N. *Int. J. Pept. Res.* **1975**, *7*, 445–459.
- (32) Tirion, M. *Phys. Rev. Lett.* **1996**, *77*, 1905–1908.
- (33) Haliloglu, T.; Bahar, I.; Erman, B. *Phys. Rev. Lett.* **1997**, *79*, 3090–3093.
- (34) Best, R.; Chen, Y.; Hummer, G. *Structure* **2005**, *13*, 1755–1763.
- (35) Lu, Q.; Wang, J. *J. Am. Chem. Soc.* **2008**, *130*, 4772–4783.
- (36) Li, W.; Wolynes, P.; Takada, S. *Proc. Natl. Acad. Sci. U.S.A.* **2011**, *108*, 3504–3509.
- (37) Magnasco, M. *Phys. Rev. Lett.* **1993**, *71*, 1477–1481.
- (38) Berendsen, H.; Postma, J.; Van Gunsteren, W.; DiNola, A.; Haak, J. *J. Chem. Phys.* **1984**, *81*, 3684–3690.
- (39) Noel, J.; Whitford, P.; Sanbonmatsu, K.; Onuchic, J. *Nucleic Acids Res.* **2010**, *38*, W657–W661.
- (40) Karanicolas, J.; Brooks, C. *Protein Sci.* **2002**, *11*, 2351–2361.
- (41) Moritsugu, K.; Smith, J. *Comput. Phys. Commun.* **2009**, *180*, 1188–1195.
- (42) Yang, L.-W.; Rader, A.; Liu, X.; Jursa, C.; Chen, S.; Karimi, H.; Bahar, I. *Nucleic Acids Res.* **2006**, *34*, W24–W31.
- (43) Humphrey, W.; Dalke, A.; Schulten, K. *J. Mol. Graphics* **1996**, *14*, 33–38.
- (44) Plimpton, S. *J. Comput. Phys.* **1995**, *117*, 1–19.
- (45) Kabsch, W.; Sander, C. *Biopolymers* **1983**, *22*, 2577–2637.
- (46) Fujitsuka, Y.; Takada, S.; Luthey-Schulten, Z.; Wolynes, P. *Proteins* **2004**, *54*, 88–103.
- (47) Fujitsuka, Y.; Chikenji, G.; Takada, S. *Proteins* **2006**, *62*, 381–398.
- (48) Honeycutt, J.; Thirumalai, D. *Biopolymers* **1992**, *32*, 695–709.
- (49) Guo, Z.; Thirumalai, D. *Biopolymers* **1995**, *36*, 83–102.
- (50) Sugita, Y.; Okamoto, Y. *Chem. Phys. Lett.* **1999**, *314*, 141–151.
- (51) Sugita, Y.; Kitao, A.; Okamoto, Y. *J. Chem. Phys.* **2000**, *113*, 6042–6051.
- (52) Fukunishi, H.; Watanabe, O.; Takada, S. *J. Chem. Phys.* **2002**, *116*, 9058–9067.
- (53) Katzgraber, H.; Trebst, S.; Huse, D.; Troyer, M. *J. Stat. Mech.: Theory Exp.* **2006**, *2006*, P03018.
- (54) Hornak, V.; Abel, R.; Okur, A.; Strockbine, B.; Roitberg, A.; Simmerling, C. *Proteins* **2006**, *65*, 712–725.
- (55) Onufriev, A.; Bashford, D.; Case, D. *J. Phys. Chem. B* **2000**, *104*, 3712–3720.
- (56) Jorgensen, W.; Chandrasekhar, J.; Madura, J.; Impey, R.; Klein, M. *J. Chem. Phys.* **1983**, *79*, 926–935.
- (57) Riddle, D.; Grantcharova, V.; Santiago, J.; Alm, E.; Ruczinski, I.; Baker, D. *Nat. Struct. Biol.* **1999**, *6*, 1016–1024.
- (58) *The PyMOL Molecular Graphics System*, version 1.2; Schrödinger, LLC: New York, 2008.
- (59) Abrahams, J.; Leslie, A.; Lutter, R.; Walker, J. *Nature* **1994**, *370*, 621–628.
- (60) Boyer, P. *BBA Libr.* **1993**, *1140*, 215–250.
- (61) Noji, H.; Yasuda, R.; Yoshida, M.; Kinosita, K., Jr. *Nature* **1997**, *386*, 299–302.
- (62) Adachi, K.; Oiwa, K.; Nishizaka, T.; Furuike, S.; Noji, H.; Itoh, H.; Yoshida, M.; Kinosita, K. *Cell* **2007**, *130*, 309–321.
- (63) Okuno, D.; Fujisawa, R.; Iino, R.; Hirono-Hara, Y.; Imamura, H.; Noji, H. *Proc. Natl. Acad. Sci. U.S.A.* **2008**, *105*, 20722–20727.
- (64) Masaike, T.; Koyama-Horibe, F.; Oiwa, K.; Yoshida, M.; Nishizaka, T. *Nat. Struct. Mol. Biol.* **2008**, *15*, 1326–1333.
- (65) Murakami, S.; Nakashima, R.; Yamashita, E.; Matsumoto, T.; Yamaguchi, A. *Nature* **2006**, *443*, 173–179.

Excited State Dynamics of the Green Fluorescent Protein on the Nanosecond Time Scale

Gabriella Jonasson,^{*,†} Jean-Marie Teuler,[†] Germain Vallverdu,[‡] Fabienne Mérola,[†] Jacqueline Ridard,[†] Bernard Lévy,[†] and Isabelle Demachy,^{*,†}

[†]Laboratoire de Chimie-Physique, UMR8000, CNRS, Université Paris-Sud 11, 91405 Orsay Cedex, France

[‡]Equipe de Chimie-Physique, IPREM, UMR5254, Université de Pau et des Pays de l'Adour, 64000 Pau, France

 Supporting Information

ABSTRACT: We have introduced a new algorithm in the parallel processing PMEMD module of the AMBER suite that allows MD simulations with a potential involving two coupled torsions. We have used this modified module to study the green fluorescent protein. A coupled torsional potential was adjusted on high accuracy quantum chemical calculations of the anionic chromophore in the first excited state, and several 15-ns-long MD simulations were performed. We have obtained an estimate of the fluorescence lifetime (2.2 ns) to be compared to the experimental value (3 ns), which is, to the best of our knowledge, the first theoretical estimate of that lifetime.

1. INTRODUCTION

Fluorescent proteins (FPs) of the green fluorescent protein (GFP) family are invaluable fluorescent markers in cell biology.^{1–5} There is a huge number of mutants and homologues which all share the same overall structure (Figure 1) and general photo-physical characteristics. Most of the brightly fluorescent FPs exhibit fluorescence emission on the nanosecond time scale while in solution or in denaturated (unfolded) proteins; the quantum yield of the chromophore is low (10^3 times smaller than in folded protein) and the fluorescence decay very fast (0.2–1.1 ps for the GFP anionic chromophore in water⁶). Besides, the diversity of fluorescence quantum yields exhibited by proteins carrying identical chromophores in the GFP superfamily⁷ points to the decisive role of the protein architecture in controlling the chromophore radiationless decay.

Classical dynamics simulations based on a semiempirical Hamiltonian⁸ or quantum dynamics studies^{9,10} of the GFP excited S_1 chromophore in vacuo have established that fluorescence quenching occurs through torsion around the two central bonds linking the methylene group to each aromatic ring (τ and φ angles, see Figure 1) and that these torsions take place within a few picoseconds after excitation. It implies that the order of magnitude of the fluorescence lifetime (ns) observed in the folded proteins results from a hindrance of the torsion motions by the protein matrix. Obviously, this hindrance is not a massive steric locking of the motions since in most FPs the volume of the cavity around the chromophore may accommodate twisted geometries.^{11,12} In fact, the constraints exerted by the protein have been scarcely studied.^{9,11–14}

A thorough description of the chromophore–protein interaction is challenging because

- (i) It requires a molecular dynamics (MD) calculation significantly longer than a nanosecond with the chromophore in the excited state. Quantum-mechanics/molecular-dynamics (QM/MD) methods would be ideal for such

studies, and they have already been used to study the radiationless decay of dark states in photoswitchable proteins like asFP595¹⁵ or Dronpa,¹⁶ for which a much smaller simulation time is needed (1 and 20 ps). However, these methods are heavily computer-time-demanding and cannot be used presently to run simulations on the nanosecond time scale.

- (ii) If one turns to classical force field MD simulations, nanosecond simulations become feasible, but one is then faced with a difficulty related to the interplay between the τ and φ torsions. Standard MD programs assume additive potentials, which, in that case, imply an energy minimum in the geometry where the two angles are twisted (the so-called “hula twist” geometry¹⁷) in complete contradiction with *ab initio* calculations.¹⁸

The aim of this work is to enable nanosecond-long MD simulations with a force field accounting for the interaction between the two torsions (2D force field). To that end, we need an analytical 2D potential. Such a potential has already been proposed,¹⁹ but it is based on only a few *ab initio* energy values. Thus, we have first performed accurate *ab initio* calculations of the first excited state of the GFP chromophore on a tight grid of geometries. We have then fitted the energies using an algebraic expression depending on τ and φ , and finally we have introduced a new algorithm in the parallel processing PMEMD module in the AMBER suite²⁰ that allows MD simulations using a 2D force field. In section 2, we first describe the development of the coupled torsional potential $V(\tau, \varphi)$ (*ab initio* calculations, fitting procedure, and implementation in the AMBER suite); we then discuss the resulting 2D potential energy surface (PES) and the results obtained by MD simulations in vacuo using the 2D potential and finally analyze the accuracy and sensibility of this

Received: March 1, 2011

Published: April 28, 2011

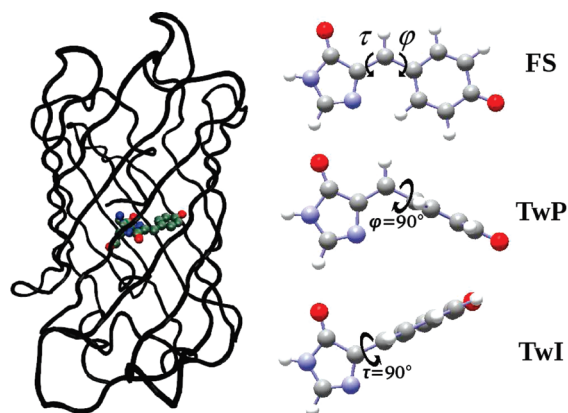


Figure 1. Left: GFP with the chromophore covalently bound to the central α -helix. Right: the anionic GFP *cis* chromophore model p-hydroxybenzylidene-imidazolinone (HBI) in three different geometries: the planar fluorescent state (FS) minimum ($\tau = \varphi = 0^\circ$), the TwP geometry — twisted 90° around the phenol bridge bond — and the TwI geometry — twisted 90° around the imidazolinone bridge bond.

potential. In section 3, we report results from several 15-ns-long MD simulations of GFP and present a theoretical estimate of the fluorescence lifetime. All calculations were performed on the anionic chromophore—the species responsible for the green fluorescence.

2. COUPLED TORSIONAL POTENTIAL $V(\tau, \varphi)$

2.1. Quantum Chemical Method. We have determined the energy of the S_1 excited state of the anionic chromophore in different geometries at the SA2-CAS(4,3) (two state average-complete active space multiconfiguration self-consistent field²¹ with a four electrons-three orbitals active space) level of theory with the 6-31G* basis set for geometry optimizations, followed by a single point PT2 (second-order perturbation theory) computation. The CASSCF and CASPT2 calculations have been performed here using the Gaussian²² and Molpro²³ program packages, respectively. The anionic chromophore has been represented by the p-hydroxybenzylidene—imidazolinone (HBI) motif (Figure 1).

The CASSCF method is today a common choice for determining excited-state geometries of biological chromophores,^{8,18,25,26} but some comments seem necessary on the specific choices of an active space with three orbitals and four electrons and of a two state average. In fact, it has been demonstrated¹⁹ that an appropriate mesomeric description of the electronic wave function of molecules like the anionic GFP chromophore involves at least three structures: two structures P and I with a double bond either on CA2—CB2 or on CB2—CG2 (see Figure 6 in Appendix A for atom names) and a third structure B with an unpaired electron on CA2 and a second unpaired electron on CG2. Such mesomeric structures are found in systems with three orbitals and four electrons²⁷ or in bigger compounds like Brooker dyes.²⁸ Unless one of the bonds is lengthened,²⁷ the third structure B has a lower weight in the first two electronic states S_0 and S_1 compared to the weights of structures P and I (ref 19, Tables V, VI, VII); yet, structure B is required in order to couple P and I.

These three structures are properly taken into account in a CI with four electrons and three orbitals. Now, if one is interested in the first excited state S_1 , one cannot just minimize the second root of the CI because then the energy of the ground state S_0 ,

Table 1. Energy Differences (in kcal/mol) between Critical Geometries on the S_1 Potential Energy Surface of the Anionic Chromophore (HBI or the Dimethyl Derivative (HBDI) Depending of the Reference) and the Planar *cis* Fluorescent State (FS) Minimum^a

	TwP	barrier to TwP	TwI	barrier to TwI	hula-twist
SA2-CAS(4,3) ^b	−14.7		−18.9		−9.2
SA2-CAS(4,3)-PT2 ^b	−6.0		−9.7		4.8
Fit $V(\tau, \varphi)$ ^b	−6.1	0	−9.8	1	4.8
SA2-CAS(12,11) ^c	−8.6	0	−11.3	0	0.1
SA2-CAS(12,11)-PT2 ^c	−7	0	−9	2	4.9
SA2-CAS(2,2)-PT2 ^d	−8.8		−5.5		
SA3-CAS(4,3) ^e	−21.5		−28.2		
SA3-CAS(4,3)-PT2 ^e	0		−7.2		
SA2-CAS(12,11) ^f	−7	<2	−13	<2	

^a Definitions of TwP and TwI can be found in Figure 1. $V(\tau, \varphi)$ is the fitting function described in section 2.1. ^b This work. ^c Martin et al.¹⁸ ^d Toniolo et al.⁸ ^e Olsen et al.²⁴ ^f Polyakov et al.²⁵

constructed with the same orbitals as S_1 , increases, giving rise to a flip-flop between the two states. A more efficient approach consists of first minimizing the average of the energies of the two states and then performing a PT2 calculation in order to (partly) recover the effect of not using the actual optimal orbitals of each state. The PT2 step also provides an estimate of the dynamical correlation. In fact, it has been shown that the PT2 step provides torsional profiles for the excited state GFP chromophore that differ significantly from those obtained when it is discarded.^{8,18,24}

On the other hand, using a three states average (between S_0 , S_1 , and a third state S_2 involving mainly structure B and, possibly, some Rydberg orbitals) would not be an improvement because the orbitals giving a proper coupling of P and I are not necessarily the same as the orbitals minimizing the energy of S_2 . Therefore, the SA2-CAS(4,3)-PT2 method is the best minimal approach.

Energy values from the present quantum calculations (CASSCF and CASPT2 levels) and from other works are given in Table 1 for three critical geometries: TwP, twisted 90° around the phenolic bridge bond (Figure 1); TwI, twisted 90° around the imidazolinone bridge bond; and the hula-twist geometry, twisted 90° around both bonds. Our CASPT2 results are in good agreement with other results at the same level of theory^{8,18} (difference smaller than 1 kcal/mol from the highest accuracy results) and differ strongly from our CASSCF results (up to 14 kcal/mol).

2.2. Fitting Procedure. In the first step of the fitting procedure, before carrying out any parameter optimization, one has to choose a precise definition of the τ and φ variables and their connection with the remaining geometrical variables. It requires to consider several details, and it is presented in Appendix A.

Furthermore, one has to take account of the fact that the τ/φ dependence of the energy in the MD program comes not only from specific dihedral terms but also from van der Waals and electrostatic interactions. We have chosen to adjust the fitting function directly on the CASPT2 energies and to remove the van der Waals and electrostatic interactions that depend on τ and φ when running the MD program (see section 2.3).

In the second step, one has to define a grid of geometries where *ab initio* calculations will be performed. Here, we have used a grid that explores the PES along the two bridge torsion

coordinates with τ and φ frozen at regularly increasing values. Steps of 30° were first used to create a two-dimensional grid of 72 points that covers the complete periods of τ (360°) and φ (180°), and thus the two isomers *cis* ($\tau = 0^\circ$) and *trans* ($\tau = 180^\circ$). We then improved the description of the PES around the planar geometries with a tighter grid of 46 additional calculations for each isomer. Finally, we developed two separate potentials that both cover the complete 2D surface but that have a higher precision for the planar geometry in either the *cis* or the *trans* conformation. In this work, we discuss the dynamics of the *cis* chromophore in GFP and will only detail the *cis* potential.

The 2D grid of CASPT2 energies was interpolated by a sum of products of sine and cosine functions of multiples of τ and φ . The periodicity of 180° for φ was ensured by taking exclusively even multiples of this coordinate ($2\varphi, 4\varphi, \dots$). The analytical expression was developed using an iterative procedure that starts with an initial sum of two terms, $\cos(2\varphi)$ and $\cos(2\varphi)\cos(\tau)$, and progressively adds new terms that improve the fit. The new terms are taken from a list of 200 different terms with multiples of τ and φ ranging from 1 to 10. At each iteration, the new terms are tested in order to find the best candidate to add; the relative root-mean-square deviation (rrmsd) of each possible addition is calculated, and the candidate term giving the best improvement of the fit, i.e., resulting in the smallest rrmsd, gets added to the fitting expression. When several terms result in nearly the same value, the term causing the least surface oscillation (evaluated numerically on a tight grid of points) gets selected.

The resulting fitting function $V(\tau, \varphi)$ comprises 30 terms (see the Supporting Information) and reproduces our CASPT2 energy values of the specific geometries, TwI, TwP, and hula-twist, with very good accuracy (differences within 0.1 kcal/mol; Table 1). Heights of the barriers to TwI and TwP are in good agreement with those of other works (differences within 1 kcal/mol). The rrmsd of the fit is 7%.

2.3. Implementation. A new algorithm has been introduced in the Sander module and in the parallel processing PMEMD module of the AMBER program package, allowing the use of a force field including a coupling between two torsion coordinates. A completely new program module was written for the calculation of energies and forces depending on τ and φ . New subroutines were then required for the input and broadcast of (1) potential parameters of $V(\tau, \varphi)$, (2) atom numbers involved in the definitions of the two torsions, and (3) a list of atom pairs whose nonbonded interactions depend on τ and φ .

van der Waals interactions between the atom pairs in this last list were removed by a test function that cross-checks each atom pair treated by the program with this list. A similar test function was used to remove the electrostatic energies between the point charges of atom pairs. Concerning electrostatic interactions, some care has to be exercised to the use of Ewald sums techniques,²⁹ which consists in evaluating first the electrostatic potential due to all charges of the system and then the energy of each charge in that potential. But, removing the intrachromophore electrostatic energies changes nothing in the potential, and the final electrostatic energy does include all electrostatic interactions between the chromophore and the protein atoms.

2.4. PES Landscape and MD Simulation in vacuo. A two-dimensional representation of $V(\tau, \varphi)$ is shown in Figure 2. It should be emphasized that $V(\tau, \varphi)$ has been obtained via a geometry optimization. It means that all internal coordinates (with the only exception of τ and φ) have been optimized in the excited state. These coordinates include the possible sp^3

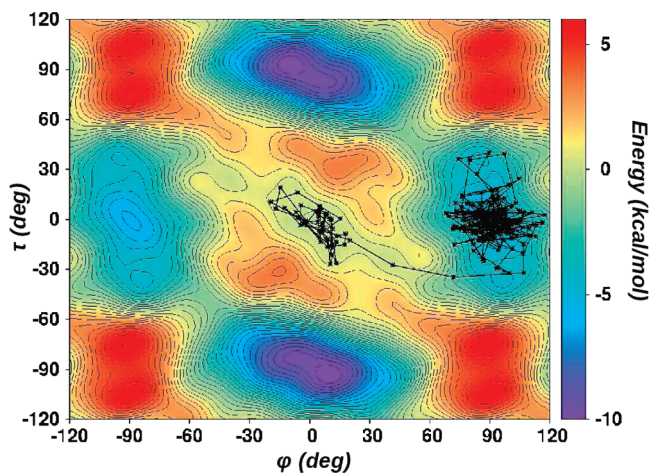


Figure 2. The excited state potential energy surface with a 20 ps trajectory of the anionic chromophore in a vacuum, starting at the planar fluorescent state (FS) minimum ($\tau = \varphi = 0^\circ$). The time step is 1 fs, and coordinates are written out every 0.1 ps.

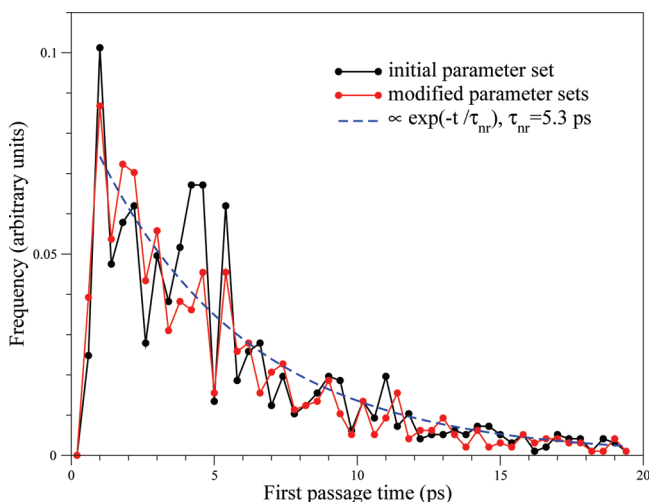


Figure 3. Distributions of first passage times (FPT) at the single-twisted geometries TwP or TwI. A comparison between 1000 simulations with the initial parameter set (solid black line) and 1000 simulations with modified parameter sets (solid red line), see section 2.5. The FPT decay of the initial parameter set is fitted by an exponential (dashed blue line).

hybridization of the imidazolinone bridge bond⁸ as well as the Franck–Condon active modes described recently.³⁰ From the point of view of the fluorescence process, it means that the $\varphi \approx \tau \approx 0$ region described by the present potential energy function $V(\tau, \varphi)$ does not correspond to the Franck–Condon (FC) region resulting from the vertical transition $S_0 \rightarrow S_1$ but to a region which is reached a very short time after the photon absorption by relaxing internal coordinates, and that is usually called the fluorescent state (FS) [ref 18, Figure 3]. It turns out that indeed one has $\varphi \approx \tau \approx 0$ in that region.

The planar FS minimum ($\tau = \varphi = 0^\circ$) lies in the middle of a low-energy valley that comes to a bottleneck at both ends. These narrow exits are reached by a concerted rotation of the bridge bond torsions, $\tau \approx 30^\circ$ and $\varphi \approx -30^\circ$ or $\tau \approx -30^\circ$ and $\varphi \approx 30^\circ$. In these geometries, the chromophore is at the edge of two

potential wells, one that leads to the TwP minimum and one that leads to the TwI minimum, located about 6 and 10 kcal/mol below the FS, respectively. Thus, the minimum energy path involves first concerted variations of φ and τ with opposite signs until $\tau \approx \pm 30^\circ$ and $\varphi \approx \mp 30^\circ$ and then a direct downhill motion toward TwP.

All other types of motion are less favorable. A pure φ -twist passes over a 1 kcal/mol barrier and a pure τ -twist over a 2 kcal/mol barrier. In the same way, the path to TwI can be lowered from 2 to 1 kcal/mol by a concerted twist of φ and τ . The geometries where the two rings are perpendicular to each other ($\tau \approx \pm 45^\circ$, $\varphi \approx \mp 45^\circ$) lie also about 1 kcal/mol above the FS geometry. The hula-twist maxima (τ and φ close to $\pm 90^\circ$) are located about 5 kcal/mol above FS. The path connecting the planar and these last geometries pass along sharp ridges with steeply sloping sides, leading either to the TwP or to the TwI minima. This result implies that the probability of reaching the hula-twist maxima is low. In addition, it might explain the difficulties reported¹⁸ of finding the MEP between the hula-twist and FS.

Further insight into the PES landscape can be obtained by means of MD simulations of the excited chromophore in vacuo using the torsional potential. We have performed 1000 10-ps-long MD simulations, all starting from a unique planar chromophore structure with randomly generated initial velocities, giving a mean initial kinetic energy of 7.2 ± 1.2 kcal/mol. The anionic chromophore model 4-hydroxybenzylidene-1,2-dimethylimidazolinone (HBDI) was used in these simulations. Details of the force field can be found in Appendix B.

We observed a φ -twist in 90% of the simulations and a τ -twist in the remaining fraction. The preference for the φ -twist is consistent with the barrierless character of this movement. We obtained an exponential distribution of joint first passage times (FPT) at TwP and TwI with a mean value of 5.3 ps. These data are well described by the nonradiative decay $A \exp(-t/\tau_{nr})$, with a nonradiative lifetime of $\tau_{nr} = 5.3$ ps (Figure 3, dashed blue line).

Concerning experimental results on fluorescence in vacuo, a recent work³¹ mentions that no fluorescence was detected, and the only quantitative results we can compare to ours come from *ab initio* dynamics¹⁰ using a CASSCF potential that leads to FPT values around 0.5 ps. In the present simulations, less than 1% of the trajectories resulted in a twist within 0.5 ps. The small number of FPTs observed here within the first picosecond is due to the bottleneck profile of the FS valley. The chromophore can only slip through the small exit and reach TwP or TwI in a short period of time if the direction of the randomly generated initial velocities leads directly through the passage. Otherwise, the chromophore will wander within the valley in a random manner until its trajectory finally crosses the exit, and the chromophore can leave the FS valley (Figure 2).

2.5. Assessment and Sensibility of the Fit. In order to assess the fit parameters, we have calculated a new value of the relative root-mean-square deviation, *rmsd*, between $V(\tau, \varphi)$ and the CASPT2 values, where the grid point energies were weighted by their visitation frequency in the MD simulations of the chromophore in vacuo. No significant effect was found; the weighted *rmsd* was found to be 10% compared to the initial 7%. Thus, it seems that the present fit procedure allows one to reach about the same quality level as what would be obtained by performing the *ab initio* calculations on the fly along dynamics while retaining a systematic and computer-time-saving character.

In addition, the accuracy of the predictions obtained by MD simulations was tested by evaluating their dependence on small

variations of the parameters. To that end, the distribution of FPTs obtained with the initial parameters was compared to a distribution resulting from 1000 new simulations obtained by randomly modified parameters. The modifications were chosen in order to reflect the uncertainty of the parameters corresponding to the uncertainty of the fit. They were obtained according to normal distributions whose centers are on the initial parameter values, and the standard deviation σ_k of parameter k is given by (ref 34, eq 15.6.4)

$$\sigma_k^2 = \frac{\chi^2}{C_{kk}}$$

where C_{kk} is the diagonal element of the covariant matrix of the fit functions and χ is the root-mean-square deviation. This expression makes sense only if the covariant matrix is diagonal, and we applied it to unitary combinations of parameters that diagonalize that matrix. In addition, we applied two constraints that locate a minimum at the planar geometry in the potentials resulting from the varied parameters.

The two resulting FPT distributions, either from the initial parameter set or from the 1000 modified parameter sets can be seen in Figure 3. The shift in the median, caused by the parameter modifications, is small (0.4 ps) and not significant compared to the width of the 50% confidence interval (centered on the median) of the two distributions (5 ps). We conclude that the present fit can be used safely to evaluate the fluorescent lifetime.

3. MD SIMULATIONS AND FLUORESCENCE LIFETIME OF GFP

In the present MD simulations, we have chosen to neglect the polarization of the electronic wave function of the chromophore by the protein environment. The polarization effect has been shown to be important in water^{8,9,35} and to significantly accelerate the torsion dynamics compared to the isolated chromophore.^{8,9} However, the proteic environment is generally less polar than bulk water and would not influence the chromophore behavior as much. Indeed, the experimental absorption maximum wavelength of the anionic chromophore in water,³⁶ in vacuo,³⁷ and in wt-GFP³⁸ is found at 426 nm, ~ 475 nm, and 475 nm, respectively. It suggests a weak influence of the protein matrix in near-planar geometries, but one cannot rule out a larger effect on twisted geometries like the hula-twist. Nevertheless, the method used here is a reasonable compromise between accuracy and feasibility. It allows one to carry out nanoseconds-long MD of the protein with a simple force field that captures the main features of the torsional landscape of the excited chromophore.

We have performed 24 MD simulations of the excited state of the S65T mutant of green fluorescent protein (S65T-GFP) in which the chromophore is known to be essentially in its anionic form.³⁹ All excited state simulations started from structures randomly extracted from a ground state simulation of the protein and had a total time duration of 15 ns; further details are given in Appendices B and C. We observed a 90° twist around φ within a few nanoseconds (0.2–12.9 ns) in all simulations, but no 90° twist around τ , a result that can be related to the larger sweep of the conformational space than the one involved in other rotations. The mean first passage time (MFPT) at TwP was 4.0 ns. Concerning the hula-twist geometry, it is not visited in any of the 24 trajectories, consistently with its high energy (5 kcal/mol above FS).

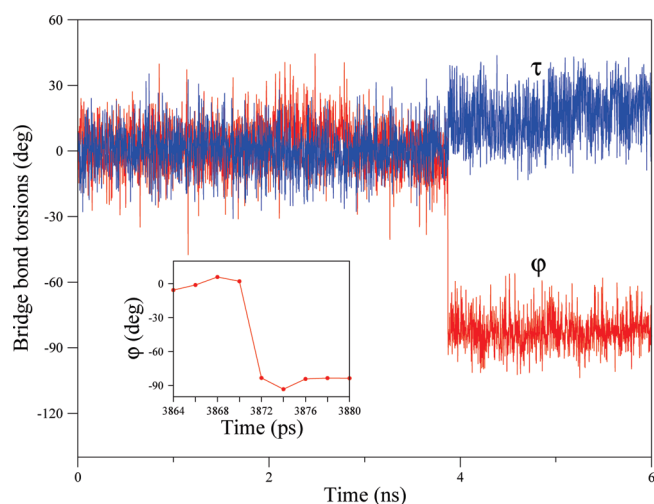


Figure 4. Bridge bond torsions (τ and ϕ) from an excited state MD simulation of the solvated GFP with the anionic chromophore. Snapshots were taken every 2 ps. The inset presents a zoom on the time window where the ϕ twist occurs.

A striking aspect of the observed twist is that, in all cases, it occurs suddenly: the values of ϕ and τ oscillate around 0° for a while, and then, at a given time, the value of ϕ switches from about 0° to about -90° within a time interval shorter than 5 ps, while τ slightly increases. This behavior of ϕ is illustrated in Figure 4 for one of the simulations. The time of 5 ps required by the ϕ -twist is to be compared to the MFPT found in vacuo (5.3 ps). The sudden character of the rotation and the time it requires suggest a description of the interplay between the chromophore and the protein dynamics: in the excited state, the chromophore twists within a few picoseconds in vacuo, but, in the protein, the pocket surrounding the chromophore is too small and the twist is hindered most of the time. However, there are some collective motions of the protein with a long periodicity (several nanoseconds) which modify the pocket and relax the constraint: in such cases, the chromophore dynamics becomes the same as that in vacuo, and the twist occurs within a few picoseconds.

For the time being, this description is just a hypothesis, and in order to verify it, it would be useful to identify the very low frequency motion of the protein in the microwave domain responsible for the constraint removal. That hypothesis suggests that the fluorescence properties of the FPs depend not only on the type and strength of the anchoring of the chromophore in its pocket but also on the nature of the low frequency collective motions (which might be related to the β -barrel structure).

We now look for an evaluation of the nonradiative decay rate of S65T-GFP arising from our results. To that end, we need quantitative information about the link between the twist movement of the excited chromophore and the fluorescence quenching. The process usually invoked for fluorescence quenching of GFP's chromophores is a nonradiative relaxation to the ground state by internal conversion or through a conical intersection, occurring *via* the twisted geometries. But, in fact, the oscillator strengths of the transition S_0-S_1 have been found to be totally cancelled (ref 24, Table 1) in the twisted geometries TwP and TwI. Thus, whatever the fate of the chromophore once it reaches the TwP geometry, the fluorescence emission is immediately quenched.

Table 2. Theoretical versus Experimental Lifetimes (ns) and Quantum Yield of S65T-GFP^a

	this work	experiment
fluorescence lifetime τ_{fluo}	2.20	3.01 ^b
radiative lifetime τ_r		4.7
non radiative lifetime τ_{nr}	4.0	8.3
quantum yield ϕ	0.46	0.64 ^c

^aThe theoretical τ_{nr} is obtained directly from the MD simulations; the experimental τ_r and τ_{nr} are deduced from the experimental τ_{fluo} and ϕ , according to eq 1; the theoretical τ_{fluo} is deduced from the theoretical τ_{nr} and the experimental τ_r using eqs 2. ^bVolkmer et al. ⁴⁰ ^cPatterson et al. ³⁸

Consequently, the fluorescence lifetime τ_{fluo} has to be distinguished here from the excited state lifetime τ_{S_1} . The latter has been evaluated by multiple spawning AIMS (ref 10, Supporting Information, Figure S1.7): it has been found that the fluorescence is quenched by a 90° ϕ -twist within 0.3 ps but that only 2% of the ground state population is recovered within the total simulation time of 0.5 ps (average over 15 trajectories), giving rise to an excited state lifetime on the order of 25 ps. The experimentally observable quantity τ_{fluo} is thus different from τ_{S_1} . The two lifetimes are identical only if all excited state geometries can deactivate by green fluorescence emission. Therefore, the observed quantum yield should be written here as

$$\phi = \frac{\tau_{\text{fluo}}}{\tau_r} \quad (1)$$

(where τ_r is the radiative lifetime) instead of the usual $\phi = \tau_{S_1}/\tau_r$ (see, for instance, ref 32, eq 3.11; ref 33, eq 1.5).

Similarly, one has to use

$$\frac{1}{\tau_{\text{fluo}}} = \frac{1}{\tau_r} + \frac{1}{\tau_{\text{nr}}} \quad (2)$$

instead of the usual $1/\tau_{S_1} = 1/\tau_r + 1/\tau_{\text{nr}}$ (ref 32, eq 3.3).

When substituting the experimental values of ϕ and of τ_{fluo} into eqs 1 and 2, one gets an estimate of the experimental value of τ_{nr} . According to the analysis above, that value should be compared with the MFPT resulting from the MD simulations rather than with the excited state lifetime.

Results are shown in Table 2. It appears that our MD simulations underestimate τ_{nr} by approximately 4 ns (50%). Theoretical values of τ_{fluo} and ϕ can be evaluated by combining the theoretical nonradiative lifetime and the experimental radiative lifetime. One obtains 2.2 ns for τ_{fluo} and 0.46 for ϕ , in qualitative agreement with experimental values (3.0 ns and 0.64, respectively). To the best of our knowledge, this is the first theoretical evaluation of the fluorescence lifetime and quantum yield of a fluorescent protein. The radiative lifetime is a characteristic property of a given chromophore, that is only weakly dependent on the environment.⁴¹ As it should remain rather similar for GFP variants differing only by a few mutations, the methods developed here may help in predicting their relative brightness through MD simulations.

We conclude that our method is able to predict the right order of magnitude of the fluorescent lifetime. Yet, it is useful to investigate the origin of the difference between our result and the experimental values. In this respect, one first points out the small number (24) of FPTs that are used for deducing the MFPT. Could we expect a better agreement by using more FPT values?

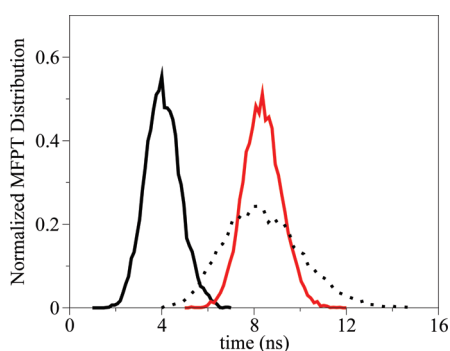


Figure 5. MFPT distribution F_{sim} from Bootstrap-treated MD results (solid black line). MFPT distribution F_{exp} ($n = 100$) from random draws of 100 FPT values extracted from the nonradiative decay distribution ($\exp(-t/\tau_{nr})$ with $\tau_{nr} = 8.3$ ns; solid red line). MFPT distribution F_{exp} ($n = 24$) from random draws of 24 FPT values from the nonradiative decay distribution (dotted black line).

In order to tackle that question, we have assumed that our 24 FPTs can be considered as 24 draws of a random variable with an exponential probability distribution f_{sim} and an unknown decay constant. One can then try to compare the resulting MFPT with what would be obtained using the distribution deduced from experimental results: $f_{exp}(FPT) = \exp(-FPT/\tau_{nr})$ with $\tau_{nr} = 8.3$ ns (Table 2). That comparison can be made indirectly by first resampling our 24 values using the bootstrap techniques,⁴² giving a distribution F_{sim} of MFPTs: that distribution F_{sim} mimics what would be obtained if more than 24 simulations were available and distributed into N bundles of 24 simulations each in order to get a distribution of N values of MFPT. Thus, F_{sim} can be compared with the distribution F_{exp} obtained by using a large number N ($= 1000$) of sets of $n = 24$ draws according to f_{exp} , each set giving a value of MFPT. In fact, we have determined two distributions F_{exp} , one distribution using $n = 24$ and the other using $n = 100$. The results are shown in Figure 5.

We first observe in Figure 5 that the two F_{exp} distributions are centered close to the exact limit value, 8.3 ns. It means that 24 draws of FPT from an exponential distribution like f_{sim} also should result in a distribution of MFPT centered close to the exact limit value obtained if $n \rightarrow \infty$. Therefore, that limit is closer to 4.0 ns than to 8.3 ns, and one has to look for another origin of this difference between the theoretical and experimental τ_{nr} than the small number of FPTs available here.

A possible reason might come from the force field parameters used here: if the protein is too flexible and/or the anchoring of the chromophore is too weak, one probably gets a MFPT which is too short, as found here. Another possible origin can lie in the choice of the 24 initial geometries for the simulations of the excited state. They have been extracted from a 5-ns-long simulation of the ground state, which could be too short to trigger all of the appropriate modes of the protein that can relax or hinder the chromophore twist.

These tracks will be pursued in future works. Despite these limitations, this work offers the first precise representation of the excited chromophore PES and gives access to realistic and unbiased dynamics of excited FPs on a long time scale.

4. CONCLUSION

We have determined a coupled torsional potential $V(\tau, \varphi)$ for the S_1 state of the anionic chromophore of the green fluorescent

protein (GFP), by fitting a grid of SA2-CAS(4,3)-PT2 energy values, and implemented this potential in the parallel module PMEMD of the AMBER package. Using this new program, we have run 24 long trajectories (15-ns-long each) of the brightly fluorescent S65T-GFP. It is the first time to our knowledge that such long free simulations have been carried out for a fluorescent protein with the chromophore in the excited state. We observed a mean first passage time at the φ twisted geometry of 4 ns, which corresponds to a fluorescence lifetime around 2 ns and a quantum yield around 0.5, in qualitative agreement with the experimental data. It appears from these trajectories that the twist movement is very fast once the chromophore leaves the fluorescent state valley, suggesting that it happens when collective motions of the protein allow the chromophore to move in its pocket.

The new tool presented in this work is complementary to the already existing QM/MD methods applied for the study of chromophores in a vacuum or solution, or in weakly fluorescent proteins with a fluorescence lifetime on the picosecond time scale. It is likely to suffer from limitations inherent in the use of classical force fields, which does not take into account the polarization effect between the chromophore and the proteic environment. However, it captures the main features of the torsional behavior of the S_1 state and leads to satisfactory results for S65T-GFP. Applied to other FPs it should be able to provide the right order of magnitude of the nonradiative lifetime τ_{nr} . Since quantum yield values such as 0.6, 0.1, and 0.001 correspond to different orders of magnitude of τ_{nr} ($\approx 7, 0.5$, and 0.005 ns, respectively), it should allow one to unambiguously distinguish proteins with bright, moderate, or very weak fluorescence and to provide analyses of the structural and dynamical factors responsible for these differences.

APPENDICES

Appendix A. Choice of Coordinates. There are two technical difficulties in defining and using the two variables τ and φ of the present 2D potential.

First, each torsion coordinate τ and φ can be described by four dihedral angles, and these angles usually have different values after geometry optimization as well as along the MD calculation.

Second, the equilibrium angles along the bridge depend on τ and φ . Particularly, they take larger values near planar geometries than for twisted geometries, to avoid a close approach of O2 or N2 (on the imidazolinone ring) to HD1 (the H atom linked to CD1 on the phenolate ring); see Figure 6.

We have adopted the following protocol in order to fix these two types of problems:

In geometry optimizations of the S_1 state, the points of the grid (τ, φ) have been defined by fixing the values of two dihedral angles, $\tau_C = C2-CA2-CB2-CG2$ and $\varphi_1 = CA2-CB2-CG2-CD1$; the other dihedral angles around the CA2-CB2 and CB2-CG2 bonds were let free. The resulting geometry is then labeled by τ and φ values defined through the following expressions: $\tau = (\tau_c + \tau_N - 180^\circ)/2$ with $\tau_N = N2-CA2-CB2-CG2$ and $\varphi = (\varphi_1 + \varphi_2 - 180^\circ)/2$ with $\varphi_2 = CA2-CB2-CG2-CD2$. The energy of the optimized geometry is ascribed to the resulting τ and φ values in the fit procedure. Then, in MD simulation, we have calculated $V(\tau, \varphi)$ and the torsional forces using the values of the dihedral angles (τ_N or τ_C , φ_1 or φ_2) as torsion τ/φ coordinates. The four values $V(\tau, \varphi)$ obtained in this way are usually different, and the average is finally used.

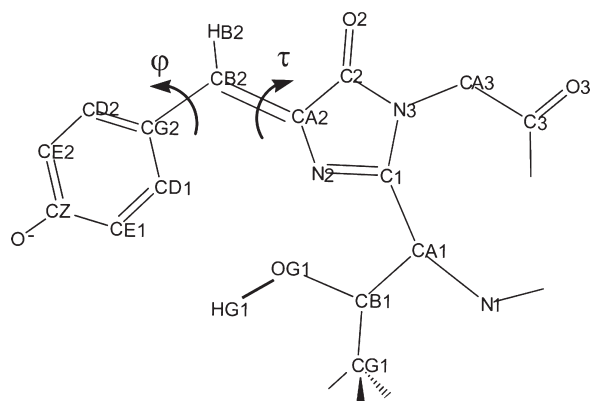


Figure 6. Anionic chromophore of S65T-GFP including the links to the α helix. Atom labels are taken from the Protein Data Bank (entry 1EMA) with the exception of the phenolate oxygen.

Concerning the bridge angles, we use an average of the planar and twisted optimized values.

Appendix B. Force Field. The AMBER 1999 force field, “ff99”, was used for all standard amino acids.

Concerning the chromophore, atomic charges were derived from the *ab initio* molecular potential calculated at the RHF/6-31G* level for the electronic ground state and CIS/6-31G* for the excited state, in the corresponding optimized planar *cis* geometries. Concerning the simulations of GFP, the chromophore model used for these calculations includes the two peptide links to the protein. Several constraints were imposed in the fitting procedure, using a program developed by two of us:⁴³ the total charge of the atoms capping the chromophore was constrained to zero and the charges of those involved in the two peptide bonds were constrained to their values in the AMBER force field. Harmonic constraints were set on the atoms of the Thr65 and Gly67 parts, with target values taken from the AMBER force field. Weak harmonic constraints with target values set to zero were applied to all other atoms in order to avoid large unphysical values. The resulting values are shown in the Supporting Information.

As concerns the τ, φ torsional potential, the coupled potential developed in this work was used for the excited state simulations. Concerning the ground state simulation, where the chromophore never explores strongly twisted geometries, we have assumed that the coupling between the two torsions could be neglected and used the independent τ and φ potentials of Reuter et al.⁴⁴ Concerning the other bonded terms, equilibrium values involved in the bridge and the imidazolinone ring were taken from the *ab initio* optimized planar *cis* geometries. The remaining equilibrium values and all force constant values were chosen by analogy with similar chemical situations in the AMBER force field. An exception concerns the bond angles involving the bridging bonds in the excited state, which were taken as the average of the planar and twisted geometries values (see Appendix A).

Appendix C. Molecular Dynamics Details. The starting coordinates were taken from the crystal structure of S65T-GFP, in which the chromophore is known to be essentially in its anionic form (Protein Data Bank entry 1EMA).³⁹ The protonation states of the histidine residues were assigned as described in the work of Helms et al.⁴⁵ Glu222 was taken in its protonated (neutral) form.⁴⁶ Molecular dynamics (MD) simulations were

carried out using the AMBER 10 suite.²⁰ Hydrogen atoms, water molecules, and neutralizing ions were added using the LEaP program. An initial minimization of the energy of the system was followed by an equilibration procedure consisting of a constant-volume simulation where the temperature was raised gradually from 100 to 300 K and then by a constant-pressure simulation. In order to avoid large conformational changes, the protein was constrained by weak harmonic forces (force constant = 5 kcal mol⁻¹ Å⁻¹) during equilibration. The constraints were then gradually removed, and the equilibration procedure was completed by an unconstrained MD simulation of 1 ns. Periodic boundary conditions were used, and the particle-mesh Ewald method²⁹ was used to handle the electrostatic interactions. The cutoff for the van der Waals interactions and for the direct part of the electrostatic interactions was set to 10 Å.

A 5-ns-long MD simulation, with the chromophore in its electronic ground state, was then run in order to obtain initial coordinates for the excited state simulations. Finally, several 15-ns-long MD simulations, with the chromophore in its electronic excited state, were run with starting coordinates taken among these snapshots. The MD simulations were run in the NPT ensemble, using a time step of 2 fs and with snapshots saved every 2 ps.

■ ASSOCIATED CONTENT

S Supporting Information. Three pages containing the complete analytical expression of the 2D potential and atomic point charges used in MD simulations. This information is available free of charge via the Internet at <http://pubs.acs.org>.

■ AUTHOR INFORMATION

Corresponding Author

*E-mail: gabriella.jonasson@u-psud.fr, isabelle.demachy@u-psud.fr.

■ ACKNOWLEDGMENT

We thank Pascal Pernot and H el ene Pasquier for helpful discussions. We are also grateful to all members of the experimental-theoretical collaboration in the photophysics of fluorescent proteins at Laboratoire de Chimie Physique. This work was granted access to the HPC resources of CINES under the allocation 2010-[c2010086318] made by GENCI (Grand Equipement National de Calcul Intensif). We also acknowledge the use of the cluster computing facility available at Laboratoire de Chimie Physique.

■ REFERENCES

- (1) Tsien, R. Y. *Annu. Rev. Biochem.* **1998**, *67*, 509–544.
- (2) Zimmer, M. *Chem. Rev.* **2002**, *102*, 759–781.
- (3) Chudakov, D. M.; Lukyanov, S.; Lukyanov, K. A. *Trends Biotechnology* **2005**, *23*, 605–613.
- (4) Wachter, R. M. *Photochem. Photobiol.* **2006**, *82*, 339–344.
- (5) Day, R. D.; Davidson, M. W. *Chem. Soc. Rev.* **2009**, *38*, 2887–2921.
- (6) Mandal, D.; Tahara, T.; Meech, S. R. *J. Phys. Chem. B* **2004**, *108*, 1102–1108.
- (7) Merola, F.; Levy, B.; Demachy, I.; Pasquier, H. Photophysics and Spectroscopy of Fluorophores in the Green Fluorescent Protein Family. In *Advanced Fluorescence Reporters in Chemistry and Biology I: Fundamentals and Molecular Design*, Springer Series on Fluorescence, 1st ed.; Demchenko, A. P., Ed.; Springer: Berlin, 2010; Vol. 8, pp 347–383.

- (8) Toniolo, A.; Olsen, S.; Manohar, L.; Martinez, T. J. *Faraday Discuss.* **2004**, *127*, 149–163.
- (9) Virshup, A. M.; Punwong, C.; Pogorelov, T. V.; Lindquist, B. A.; Ko, C.; Martinez, T. J. *J. Phys. Chem. B* **2009**, *113*, 3280–3291.
- (10) Olsen, S.; Lamothe, K.; Martinez, T. J. *J. Am. Chem. Soc.* **2010**, *132*, 1192–1193.
- (11) Maddalo, S. L.; Zimmer, M. *Photochem. Photobiol.* **2006**, *82*, 367–372.
- (12) Megley, C. M.; Dickson, L. A.; Maddalo, S. L.; Chandler, G. J.; Zimmer, M. *J. Phys. Chem. B* **2009**, *113*, 302–308.
- (13) Moors, S. L. C.; Michielssens, S.; Flors, C.; Dedecker, P.; Hofkens, J.; Ceulemans, A. *J. Chem. Theory Comput.* **2008**, *6*, 1012–1020.
- (14) Vallverdu, G.; Demachy, I.; Ridard, J.; Lévy, B. *THEOCHEM* **2009**, *898*, 73–83.
- (15) Schäfer, L. V.; Groenhof, G.; Boggio-Pasqua, M.; Robb, M. A.; Grubmüller, H. *PLoS Comput. Biol.* **2008**, *4*, e1000034.
- (16) Li, X.; Chung, L. W.; Mizuno, H.; Miyawaki, A.; Morokuma, K. *J. Phys. Chem. Lett.* **2010**, *1*, 3328–3333.
- (17) Liu, R. S. H.; Browne, D. T. *Acc. Chem. Res.* **1986**, *19*, 42–48.
- (18) Martin, M. E.; Negri, F.; Olivucci, M. *J. Am. Chem. Soc.* **2004**, *126*, 5452–5464.
- (19) Olsen, S.; McKenzie, R. J. *Chem. Phys.* **2009**, *130*, 184302.
- (20) Case, D. A.; Darden, T. A.; Cheatham, T. E., III; Simmerling, C. L.; Wang, J.; Duke, R. E.; Luo, R.; Crowley, M.; Walker, R. C.; Zhang, W.; Merz, K. M.; Wang, B.; Hayik, S.; Roitberg, A.; Seabra, G. Kolossváry, I.; Wong, K. F.; Paesani, F.; Vanicek, J.; Wu, X.; Brozell, S. R.; Steinbrecher, T.; Gohlke, H.; Yang, L.; Tan, C.; Mongan, J.; Hornak, V.; Cui, G.; Mathews, D. H.; Seetin, M. G.; Sagui, C.; Babin, V.; Kollman, P. A. *AMBER 10*; University of California: San Francisco, CA, 2008.
- (21) Roos, B. O.; Taylor, P. R.; Siegbahn, P. E. M. *Chem. Phys.* **1980**, *48*, 157.
- (22) Frisch, M. J.; Trucks, G. W.; Schlegel, H. B.; Scuseria, G. E.; Robb, M. A.; Cheeseman, J. R.; Montgomery, J. A., Jr.; Vreven, T.; Kudin, K. N.; Burant, J. C.; Millam, J. M.; Iyengar, S. S.; Tomasi, J.; Barone, V.; Mennucci, B.; Cossi, M.; Scalmani, G.; Rega, N.; Petersson, G. A.; Nakatsuji, H.; Hada, M.; Ehara, M.; Toyota, K.; Fukuda, R.; Hasegawa, J.; Ishida, M.; Nakajima, T.; Honda, Y.; Kitao, O.; Nakai, H.; Klene, M.; Li, X.; Knox, J. E.; Hratchian, H. P.; Cross, J. B.; Bakken, V.; Adamo, C.; Jaramillo, J.; Gomperts, R.; Stratmann, R. E.; Yazyev, O.; Austin, A. J.; Cammi, R.; Pomelli, C.; Ochterski, J. W.; Ayala, P. Y.; Morokuma, K.; Voth, G. A.; Salvador, P.; Dannenberg, J. J.; Zakrzewski, V. G.; Dapprich, S.; Daniels, A. D.; Strain, M. C.; Farkas, O.; Malick, D. K.; Rabuck, A. D.; Raghavachari, K.; Foresman, J. B.; Ortiz, J. V.; Cui, Q.; Baboul, A. G.; Clifford, S.; Cioslowski, J.; Stefanov, B. B.; Liu, G.; Liashenko, A.; Piskorz, P.; Komaromi, I.; Martin, R. L.; Fox, D. J.; Keith, T.; Al-Laham, M. A.; Peng, C. Y.; Nanayakkara, A.; Challacombe, M.; Gill, P. M. W.; Johnson, B.; Chen, W.; Wong, M. W.; Gonzalez, C.; Pople, J. A. *Gaussian 03*, Revision C.02; Gaussian, Inc.: Wallingford, CT, 2004.
- (23) Werner, H.-J.; Knowles, P. J.; Manby, F. R.; Schütz, M.; Celani, P.; Knizia, G.; Korona, T.; Lindh, R.; Mitrushenkov, A.; Rauhut, G.; Adler, T. B.; Amos, R. D.; Bernhardsson, A.; Berning, A.; Cooper, D. L.; Deegan, M. J. O.; Dobbyn, A. J.; Eckert, F.; Goll, E.; Hampel, C.; Hesselmann, A.; Hetzer, G.; Hrenar, T.; Jansen, G.; Koppl, C.; Liu, Y.; Lloyd, A. W.; Mata, R. A.; May, A. J.; McNicholas, S. J.; Meyer, W.; Mura, M. E.; Nicklass, A.; Palmieri, P.; Pflüger, K.; Pitzer, R.; Reiher, M.; Shiozaki, T.; Stoll, H.; Stone, A. J.; Tarroni, R.; Thorsteinsson, T.; Wang, M.; Wolf, A. *MOLPRO*, version 2006.1; University College Cardiff Consultants Limited: Cardiff, Wales, 2010.
- (24) Olsen, S.; Smith, S. C. *J. Am. Chem. Soc.* **2008**, *130*, 8677–8689.
- (25) Polyakov, I. V.; Grigorenko, B. L.; Epifanovsky, E. M.; Krylov, A. I.; Nemukhin, A. V. *J. Chem. Theory Comput.* **2010**, *6*, 2377–2387.
- (26) Shapiro, I.; Ryazantsev, M. N.; Ding, W. J.; Huntress, M. M.; Melaccio, F.; Andruniow, T.; Olivucci, M. *Aust. J. Chem.* **2010**, *63*, 413–429.
- (27) Braid, B.; Walter, C.; Engels, B.; Hiberty, P. C. *J. Am. Chem. Soc.* **2010**, *132*, 7631–7637.
- (28) Olsen, S. *J. Chem. Theory Comput.* **2010**, *6*, 1089–1103.
- (29) Darden, T.; York, D.; Pedersen, L. *J. Chem. Phys.* **1993**, *98*, 10089–10092.
- (30) Kamarchik, E.; Krylov, A. I. *J. Phys. Chem. Lett.* **2011**, *2*, 488–492.
- (31) Forbes, M. W.; Joskusch, R. A. *J. Am. Chem. Soc.* **2009**, *131*, 17038–17039.
- (32) Valeur, B. Characteristics of fluorescence emission. In *Molecular Fluorescence*, 1st ed.; Valeur, B., Ed.; Wiley-VCH: Weinheim, Germany, 2002; pp 46–47.
- (33) Lakowitz, J. R. Introduction to fluorescence. In *Principles of Fluorescence Spectroscopy*, 2nd ed.; Lakowitz, J. R., Ed.; Kluwer Academic/Plenum Publishers, New York, 1999; pp 10–11.
- (34) Press, W. H.; Teukolsky, S. A.; Vetterling, W. T.; Flannery, B. P. Modeling of Data. In *Numerical Recipes in FORTRAN: The Art of Scientific Computing*, 2nd ed.; Press, W. H., Teukolsky, S. A., Vetterling, W. T., Flannery, B. P., Eds.; Cambridge University Press: New York, 1992; pp 690–691.
- (35) Altoe, P.; Bernardi, F.; Garavelli, M.; Orlandi, G.; Negri, F. *J. Am. Chem. Soc.* **2005**, *127*, 3952–3963.
- (36) Dong, J.; Solntsev, K. M.; Tolbert, L. M. *J. Am. Chem. Soc.* **2006**, *128*, 12038–12039.
- (37) Nielsen, S. B.; Lapierre, A.; Andersen, J. U.; Pedersen, U. V.; Tomita, S.; Andersen, L. H. *Phys. Rev. Lett.* **2001**, *87*, 228102.
- (38) Patterson, G. H.; Knobel, S. M.; Sharif, W. D.; Kain, S. R.; Piston, D. W. *Biophys. J.* **1997**, *73*, 2782–2790.
- (39) Ormö, M.; Cubitt, A. B.; Kallio, K.; Gross, L. A.; Tsien, R. Y.; Remington, S. J. *Science* **1996**, *273*, 1392–1395.
- (40) Volkmer, A.; Subramaniam, V.; Birch, D. J. S.; Jovin, T. M. *Biophys. J.* **2000**, *78*, 1589–1598.
- (41) Strickler, S. J.; Berg, R. A. *J. Chem. Phys.* **1962**, *37*, 814–822.
- (42) Efron, B. *Ann. Stat.* **1979**, *7*, 1–26.
- (43) Ridard, J.; Lévy, B. *J. Comput. Chem.* **1999**, *20*, 473–482.
- (44) Reuter, N.; Lin, H.; Thiel, W. *J. Phys. Chem. B* **2002**, *106*, 6310–6321.
- (45) Helms, V.; Straatsma, T. P.; McCammon, J. A. *J. Phys. Chem. B* **1999**, *103*, 3263–3269.
- (46) Nifosi, R.; Tozzini, V. *Proteins: Struct., Funct. Genet.* **2003**, *51*, 378–389.

Efficient Handling of Molecular Flexibility in Lattice Energy Minimization of Organic Crystals

A. V. Kazantsev, P. G. Karamertzanis, C. S. Adjiman, and C. C. Pantelides*

Centre for Process Systems Engineering, Department of Chemical Engineering, Imperial College London, South Kensington Campus, London SW7 2AZ, United Kingdom

ABSTRACT: This paper presents a novel algorithm, CrystalOptimizer, for the minimization of the lattice energy of crystals formed by flexible molecules. The algorithm employs isolated-molecule quantum mechanical (QM) calculations of the intramolecular energy and conformation-dependent atomic multipoles in the course of the lattice energy minimization. The algorithm eliminates the need to perform QM calculations at each iteration of the minimization by using Local Approximate Models (LAMs), with a minimal impact on accuracy. Additional computational efficiencies are achieved by storing QM-derived components of the lattice energy model in a database and reusing them in subsequent calculations whenever possible. This makes the approach particularly well suited to applications that involve a sequence of lattice energy evaluations, such as crystal structure prediction. The algorithm is capable of handling efficiently complex systems with considerable conformational flexibility. The paper presents examples of the algorithm's application ranging from single-component crystals to cocrystals and salts of flexible molecules with tens of intramolecular degrees of freedom whose optimal values are determined by the interplay of conformational strain and packing forces. For any given molecule, the degree of flexibility to be considered can vary from a few torsional angles to relaxation of the entire set of torsion angles, bond angles, and bond lengths present in the molecule.

1. INTRODUCTION

The knowledge of the three-dimensional atomic structure of a crystal is the basis toward understanding and predicting the physical properties of the material (color, density, solubility, dissolution rate, etc.).¹ Hence, the development of computational algorithms to predict the structure and the thermodynamic stability of single and multicomponent crystals is of significant practical importance. Prediction of thermodynamic stability requires the minimization of the Gibbs free energy with respect to the unit cell dimensions and the positions of all atoms in the unit cell:

$$\min G = \min(U + PV - TS) \quad (1)$$

where U is the internal energy (which includes the zero-point energy contributions²), V the volume, and S the entropy. The PV term only becomes significant at very high pressures (typically above 1 GPa) and is usually neglected. Furthermore, the thermal, entropic, and zero-point contributions to the Gibbs free energy of flexible molecules cannot, at present, be readily and accurately computed. There is also emerging evidence that most minima on the free energy surface are also minima on the lattice energy surface.³ Consequently, most of the existing computational approaches for crystal structure prediction focus on the minimization of lattice energy.⁴ The lattice energy, E^{latt} , refers to the internal energy, U , at 0 K and 0 Pa (ignoring the zero-point energy) and can be partitioned into the intramolecular and intermolecular contributions. The intramolecular energy, ΔE^{intra} , is the energy required to deform the molecular conformation from its gas-phase geometry. The intermolecular contributions, U^{inter} , consist primarily of the repulsion–dispersion and electrostatic interactions, although intermolecular induction models are also currently being developed.⁵

The assumption underpinning crystal structure prediction is that crystal structures that occur in nature correspond to low-lying minima in the crystal energy landscape, which is usually approximated as the lattice energy. Crystal structure prediction methodologies, such as the ones that have been used in the series of blind tests organized by the Cambridge Crystallographic Data Centre (e.g., Day et al.⁴), generally consist of a structure generation step, in which many possible crystal geometries are constructed, and a refinement step, in which the most promising structures are optimized further with more elaborate models. In the most recent approaches, hundreds of thousands of structures are generated, while only hundreds to thousands of distinct structures are retained in the refinement stage. As many hypothetical crystals have very similar lattice energies,⁶ their reliable ranking requires an accurate representation of all components of the lattice energy. A prerequisite for crystal structure prediction is therefore the availability of reliable local lattice energy minimization methodologies that have a reasonable computational cost. Such an approach, the CrystalOptimizer algorithm, is presented in this paper.

Ideally, the lattice energy of a crystal structure would be evaluated by modeling the entire crystal quantum mechanically. Significant progress toward this goal has been made through the development of the GRACE method,⁷ which combines full crystal QM calculations with an empirical dispersion correction. This, however, remains computationally expensive for many molecules of interest. Instead, an accurate intermolecular potential can be obtained by modeling the electrostatic interactions with distributed multipoles^{8,9} derived directly from the isolated-molecule charge density.^{10,11} In order to avoid unphysical

Received: October 18, 2010

Published: May 09, 2011

distortions of the molecular geometry in the crystal,¹² this anisotropic intermolecular energy model needs to be coupled with an accurate and well-balanced representation of the intramolecular energy.¹³ Electronic structure calculations can generally provide the accuracy required for modeling the deformations of the molecular structure within the crystal. However, the use of quantum mechanics (QM) in the computation of the lattice energy is expensive especially for large and flexible molecules, as the intramolecular energy and atomic multipoles need to be recalculated after any conformational change. Albeit computationally demanding, this approach has been successfully embedded in several lattice energy minimization methodologies described below.

One of the first accurate algorithms to take into account molecular flexibility in lattice energy minimization is UPACK.^{2,14–16} In this approach, the intramolecular energy is calculated using a quadratic approximation constructed from the results of an *ab initio* molecular geometry optimization. The intermolecular potential is fitted to high-level quantum mechanical calculations of alkanes, alcohols, and ethers¹⁷ and involves terms for atomic multipole moments, dipole polarizabilities, and repulsion–dispersion contributions. In order to model the conformational dependence of the electrostatic model, the atomic multipole moments are defined in terms of their local-axis system and rotated with the local environment. Following a significant change in conformation during lattice energy minimization, the intramolecular potential and the electrostatic model are recalculated to maintain accuracy. A feature of this approach is that the use of Cartesian coordinates for the representation of the molecular structure during lattice energy minimization forces the user either to neglect flexibility altogether (rigid-body approach) or to account for full flexibility (atomistic representation). In the latter case, the computational cost becomes prohibitive for any molecule of nontrivial size (more than 20 atoms).

An algorithm that allows the optimization of crystal structures with user-defined flexibility is DMAFlex.¹³ However, in order to calculate the lattice energy accurately, the method incorporates a full isolated-molecule quantum mechanical molecular geometry optimization and charge density calculation at every iteration, which results in very high computational cost. The computational burden is further compounded by the use of a gradient-free (simplex) minimization algorithm¹⁸ that limits the extent of molecular flexibility that can be practically handled to a small number (fewer than 10) of torsional angles.

The CrystalOptimizer algorithm presented in this paper is a local lattice energy minimization scheme for crystal structures containing flexible molecules. It is designed to reduce the computational cost associated with quantum mechanical evaluations without compromising accuracy. It is applicable to molecules of the size, complexity, and flexibility typically encountered in pharmaceutical development. The main novelty of the approach is the use of local approximate models (LAMs) to represent the intramolecular energy and conformationally dependent charge density. These models are practically as accurate as explicit QM calculations but carry a much smaller computational burden. They are presented in section 2. This is followed by the formulation of the lattice energy minimization problem (section 3.1) and a description of the structure of the CrystalOptimizer algorithm (section 3.2). The computational performance and the accuracy of the algorithm are critically assessed by its ability to reproduce the lattice geometry and conformational degrees of freedom for a set of experimentally determined

crystal structures (sections 4.4 and 4.5). Finally, the applicability of CrystalOptimizer to the refinement of hypothetical crystal structures in crystal structure prediction is discussed (section 4.6).

2. LOCAL APPROXIMATE MODELS (LAMs)

2.1. Molecular Flexibility. The geometry of a flexible molecule can be completely defined by its *Z*-matrix consisting of $3N - 6$ intramolecular degrees of freedom θ (torsion angles, bond angles, and bond lengths), where N is the number of atoms in the molecule. In molecular crystals, the intermolecular forces are significantly weaker than the energy of typical covalent interactions. Consequently, only a subset of the intramolecular degrees of freedom, θ , is expected to deviate significantly from their gas-phase values. These flexible degrees of freedom, θ^f (such as torsions around single bonds), are often sufficient in capturing the effect of molecular flexibility and thus need to be explicitly modeled during lattice energy minimization. However, as the values of θ^f for a given molecule change significantly, the rest of the intramolecular degrees of freedom adjust so as to minimize the intramolecular energy. Hence, these remaining, more rigid degrees of freedom, θ^r (such as torsions in aromatic ring systems, most bond angles and bond lengths), and the intramolecular energy, ΔE^{intra} , can be approximated as functions of the flexible degrees of freedom, θ^f , in the solution of a constrained isolated-molecule quantum mechanical geometry optimization:

$$\Delta E^{\text{intra}}(\theta^f) = \min_{\theta^r} [E^{\text{intra}}(\theta^r; \theta^f)] - E^{\text{vac}} \quad (2)$$

where E^{vac} is the global (or at least a local) minimum gas-phase molecular energy used as a correction and needs to be computed only once. Because the evaluation of ΔE^{intra} requires a minimization with respect to the “rigid” degrees of freedom, θ^r , these are not truly constant. The change θ^r in response to changes in the flexible degrees of freedom, θ^f , can be seen explicitly in the following equation:

$$\theta^r(\theta^f) = \arg \min_{\theta^r} [E^{\text{intra}}(\theta^r; \theta^f)] \quad (3)$$

where “arg min” denotes the value of the optimization variables in the solution of the minimization problem shown in eq 2. These changes, however small, will have an effect on the intramolecular energy, molecular geometry, and final structure reproduction (especially for large molecules) and therefore cannot be ignored by keeping θ^r fixed at some nominal values, such as those in the gas-phase conformational minimum. The validity of this partitioning of intramolecular degrees of freedom will be examined in sections 4.4 and 4.5 by comparing the results obtained with different sets of θ^f . The main benefit of considering “rigid” degrees of freedom is a reduction in computational cost with little loss of accuracy. However, the approach presented is also valid when the vector θ^r is empty, i.e., when all intramolecular variables are treated as flexible, as shown in section 4.4.

2.2. Intramolecular Energy LAM. The intramolecular energy for a given conformation in close proximity to a reference conformation, $\theta_{\text{ref}} \equiv (\theta_{\text{ref}}^f, \theta_{\text{ref}}^r)$, can be estimated using a local approximate model (LAM) based on a quadratic Taylor

expansion:

$$\begin{aligned} \Delta E^{\text{intra}}(\theta^f, \theta^r) = & \Delta E^{\text{intra}}(\theta_{\text{ref}}) + \left[\frac{\partial E^{\text{intra}}}{\partial \theta^f} \right]_{\theta_{\text{ref}}}^T (\theta^f - \theta_{\text{ref}}^f) \\ & + \left[\frac{\partial E^{\text{intra}}}{\partial \theta^f} \right]_{\theta_{\text{ref}}}^T (\theta^r - \theta_{\text{ref}}^r) \\ & + \frac{1}{2} (\theta^f - \theta_{\text{ref}}^f)^T \left[\frac{\partial^2 E^{\text{intra}}}{\partial \theta^{f2}} \right]_{\theta_{\text{ref}}} (\theta^f - \theta_{\text{ref}}^f) \\ & + (\theta^r - \theta_{\text{ref}}^r)^T \left[\frac{\partial^2 E^{\text{intra}}}{\partial \theta^f \partial \theta^r} \right]_{\theta_{\text{ref}}}^T (\theta^f - \theta_{\text{ref}}^f) \\ & + \frac{1}{2} (\theta^r - \theta_{\text{ref}}^r)^T \left[\frac{\partial^2 E^{\text{intra}}}{\partial \theta^{r2}} \right]_{\theta_{\text{ref}}} (\theta^r - \theta_{\text{ref}}^r) \quad (4) \end{aligned}$$

The above equation is valid for *any* reference point $\theta_{\text{ref}} \equiv (\theta_{\text{ref}}^f, \theta_{\text{ref}}^r)$ in the coordinate space. Throughout this paper, the subscript “ref” denotes the point around which the Taylor expansion is constructed. The values of θ_{ref}^f at the reference point are obtained via an isolated-molecule quantum-mechanical constrained optimization (eq 2) for the fixed values $\theta^f = \theta_{\text{ref}}^f$. This calculation also yields the minimum molecular deformation energy, $\Delta E^{\text{intra}}(\theta_{\text{ref}})$, and the first- and second-order derivatives of ΔE^{intra} with respect to all intramolecular degrees of freedom, θ_{ref} , necessary to construct the LAM. Since θ_{ref}^f is obtained by minimizing ΔE^{intra} , it must satisfy the first-order optimality condition:

$$\left[\frac{\partial E^{\text{intra}}}{\partial \theta^r} \right]_{\theta_{\text{ref}}^r, \theta_{\text{ref}}^f} = 0 \quad (5)$$

We require that eq 5 also apply to the intramolecular energy LAM. Hence, if θ^f is changed by a small amount $\delta\theta^f$ from the reference value, then θ^r needs to change so that the intramolecular energy remains at a minimum. This can be enforced by ensuring that the first-order optimality conditions continue to be satisfied at $(\theta^r + \delta\theta^r, \theta^f + \delta\theta^f)$, i.e.:

$$\left[\frac{\partial E^{\text{intra}}}{\partial \theta^r} \right]_{\theta_{\text{ref}}^r + \delta\theta^r, \theta_{\text{ref}}^f + \delta\theta^f} = 0 \quad (6)$$

where $\delta\theta^r$ is the corresponding change in θ^r . Performing a first-order Taylor expansion, subtracting eq 5 from eq 6 and solving for $\delta\theta^r$ yields the approximate expression:

$$\delta\theta^r = - \left[\frac{\partial^2 E^{\text{intra}}}{\partial \theta^{r2}} \right]_{\theta_{\text{ref}}^r}^{-1} \left[\frac{\partial^2 E^{\text{intra}}}{\partial \theta^f \partial \theta^r} \right]_{\theta_{\text{ref}}}^T \delta\theta^f \quad (7)$$

which then allows us to approximate θ^r via an explicit linear function of θ^f :

$$\theta^r(\theta^f) = \theta_{\text{ref}}^r + \mathbf{A}(\theta_{\text{ref}})(\theta^f - \theta_{\text{ref}}^f) \quad (8)$$

where the matrix $\mathbf{A}(\theta_{\text{ref}})$ is defined as

$$\mathbf{A}(\theta_{\text{ref}}) \equiv \frac{\partial \theta^r}{\partial \theta^f} = - \left[\frac{\partial^2 E^{\text{intra}}}{\partial \theta^{r2}} \right]_{\theta_{\text{ref}}}^{-1} \left[\frac{\partial^2 E^{\text{intra}}}{\partial \theta^f \partial \theta^r} \right]_{\theta_{\text{ref}}}^T \quad (9)$$

By substituting eq 8 into eq 4 and also taking account of eq 5, an estimate for the intramolecular energy as a quadratic function solely of the flexible degrees of freedom is obtained:

$$\begin{aligned} \Delta E^{\text{intra}}(\theta^f) = & \Delta E^{\text{intra}}(\theta_{\text{ref}}^f) + \mathbf{b}(\theta_{\text{ref}})^T (\theta^f - \theta_{\text{ref}}^f) \\ & + \frac{1}{2} (\theta^f - \theta_{\text{ref}}^f)^T \mathbf{C}(\theta_{\text{ref}}) (\theta^f - \theta_{\text{ref}}^f) \quad (10) \end{aligned}$$

where the vector $\mathbf{b}(\theta_{\text{ref}})$ and matrix $\mathbf{C}(\theta_{\text{ref}})$ are defined as

$$\mathbf{b}(\theta_{\text{ref}}) \equiv \left[\frac{\partial^2 E^{\text{intra}}}{\partial \theta^f} \right]_{\theta_{\text{ref}}} \quad (11)$$

$$\mathbf{C}(\theta_{\text{ref}}) \equiv \left[\frac{\partial^2 E^{\text{intra}}}{\partial \theta^{f2}} \right]_{\theta_{\text{ref}}} - \left[\frac{\partial^2 E^{\text{intra}}}{\partial \theta^f \partial \theta^r} \right]_{\theta_{\text{ref}}} \left[\frac{\partial^2 E^{\text{intra}}}{\partial \theta^{r2}} \right]_{\theta_{\text{ref}}}^{-1} \left[\frac{\partial^2 E^{\text{intra}}}{\partial \theta^f \partial \theta^r} \right]_{\theta_{\text{ref}}}^T \quad (12)$$

Equations 8 and 10 allow the explicit and fast calculation of the values of θ^r and ΔE^{intra} for any given values of θ^f without performing new quantum mechanical calculations; the values obtained are accurate in the proximity of a reference point θ_{ref} . If a molecule is optimized atomistically, i.e., all intramolecular degrees of freedom are treated as flexible, then eq 10 reduces to the standard quadratic Taylor expansion in UPACK.¹⁶

2.3. Electrostatic Model LAM. For limited conformational changes, the conformational dependence of the intermolecular electrostatic model can be captured by rotating the multipole moments with their local environment.^{16,19} Once the distributed multipole moments (Ω) have been computed⁹ (up to the hexadecapole level) for a reference molecular conformation, θ_{ref} , each atom is assigned a local axis system using two directly connected atoms (or first and second bonded atoms for the case of terminal atoms). The calculated multipole moments are then converted to their Cartesian form and rotated to the local axis system of each atom. The locally expressed multipoles are kept constant for small conformational changes during lattice energy minimization. The conformational variability of the electrostatic model is limited to the analytical rotation (using Cartesian tensors) of the local atomic multipoles to the molecular axis system of each newly generated conformation:

$$\begin{aligned} \Omega_{k_1 k_2 \dots k_n}^i(\theta^f, \theta^r(\theta^f)) \\ \approx \sum_{k'_1} \sum_{k'_2} \dots \sum_{k'_n} \text{Rot}_{k_1 k'_1}^i(\theta^f, \theta^r(\theta^f)) \text{Rot}_{k_2 k'_2}^i(\theta^f, \theta^r(\theta^f)) \dots \text{Rot}_{k_n k'_n}^i(\theta^f, \theta^r(\theta^f)) \\ \times \Omega_{k'_1 k'_2 \dots k'_n}^i(\theta_{\text{ref}}^f, \theta_{\text{ref}}^r(\theta_{\text{ref}}^f)) \quad (13) \end{aligned}$$

where the multipole moment of rank n for atom i is calculated using the rotation matrix $\text{Rot}(\theta^f, \theta^r(\theta^f))$ that transforms the local axis system of each atom to the molecular axis system and $\theta^r(\theta^f)$ denotes the LAM-based estimate of the rigid degrees of freedom θ^r using eq 8. After each conformational rotation, the multipoles expressed in the molecular axis system are used to compute the intermolecular electrostatic contribution to lattice energy.

The conformational transferability of multipole moments varies from one molecule to another. For certain functional groups, it cannot be assumed that the localized multipole moments remain

constant even for small conformational changes.²⁰ For instance, the pyramidalization of the $-\text{NH}_2$ group has a direct influence on the position of the electron lone pair on the nitrogen atom that cannot be captured by the analytical rotation of the atomic multipole moments. In such cases, improved accuracy may be obtained by applying a linear correction to the result of eq 13 based on a first-order Taylor expansion:

$$\Omega(\theta^f) = \Omega(\theta^f, \theta^r(\theta^f)) + \left[\frac{\partial \Omega}{\partial \theta^f} \right]_{\theta_{\text{ref}}^f} (\theta^f - \theta_{\text{ref}}^f) \quad (14)$$

The partial derivatives on the right-hand side cannot be obtained in a straightforward manner from currently available QM codes, and consequently the derivatives in the current version of CrystalOptimizer are approximated using finite differences. This requires one additional QM charge density calculation for each flexible degree of freedom being perturbed if one-sided first order finite differences are used.

We note that the correction of eq 14 may not be necessary for all flexible degrees of freedom under consideration, as in many cases the computationally cheaper LAM of eq 13 will already lead to the required accuracy. More research is needed to establish the functional groups for which the application of 14 is necessary.

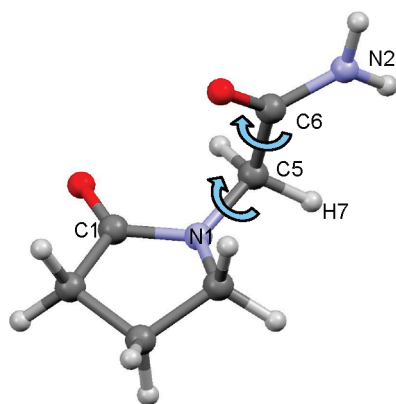


Figure 1. Molecular diagram and atom labeling for piracetam (2-oxo-pyrrolidine-acetamide).

Our preliminary analysis indicates that it is advisable to apply the correction in the case of torsional angles involving nitrogen atoms (e.g. $-\text{NH}_2$ group) or $-\text{OH}$ groups.

2.4. Range of LAM Validity. The range of validity of the proposed LAMs for the estimation of the intramolecular energy and the rigid degrees of freedom (eqs 10 and 8) has been tested against *ab initio* calculations using the GAUSSIAN²¹ suite of programs. The tests were carried out for piracetam (2-oxo-pyrrolidine-acetamide, Figure 1), a molecule comprising 20 atoms (54 intramolecular degrees of freedom). For the purpose of illustration, the two most important torsional angles, $\text{N2}-\text{C6}-\text{C5}-\text{N1}$ and $\text{C6}-\text{C5}-\text{N1}-\text{C1}$, shown as blue arrows in Figure 1, have been considered as the only flexible degrees of freedom.

The *ab initio* intramolecular energy surface, ΔE^{intra} (relative to the energy at the global conformational minimum), is shown in Figure 2a as a function of the two flexible degrees of freedom. The results shown were computed using a total of 64 points on an 8×8 grid. At each point, the two flexible degrees of freedom were fixed at the corresponding grid values, and the remaining rigid degrees of freedom were determined via a quantum mechanical, constrained, isolated-molecule geometry optimization.

As seen in Figure 2b, the intramolecular energy LAM approximates the QM surface with a maximum error of 0.15 kJ mol^{-1} over a range of 5° around the reference point at 90.8° and 155.6° for $\text{C6}-\text{C5}-\text{N1}-\text{C1}$ and $\text{N2}-\text{C6}-\text{C5}-\text{N1}$ torsions, respectively. This error is less than 3% of the 5 kJ mol^{-1} intramolecular energy variation over the conformational region considered. The maximum error is reduced to 0.07 kJ mol^{-1} within 3° of the reference point and 0.02 kJ mol^{-1} within 2° of the expansion point. Similarly, Figure 3 shows that the LAM provides an excellent approximation for the dependence of the rigid degrees of freedom on the flexible torsions. The maximum errors for the rigid degrees of freedom are less than 0.10° for the torsional angle $\text{H7}-\text{C5}-\text{N1}-\text{C1}$ even though this torsion changes by up to 14.5° as the values of the $\text{C6}-\text{C5}-\text{N1}-\text{C1}$ and $\text{N2}-\text{C6}-\text{C5}-\text{N1}$ torsions are modified. Correspondingly, the maximum error is less than 0.06° for bond angle $\text{C5}-\text{N1}-\text{C1}$ and less than 0.0006 \AA for bond length $\text{C1}-\text{N1}$. As expected, the absolute errors are seen to decrease for rigid degrees of freedom that are less sensitive to changes in the flexible degrees of freedom:

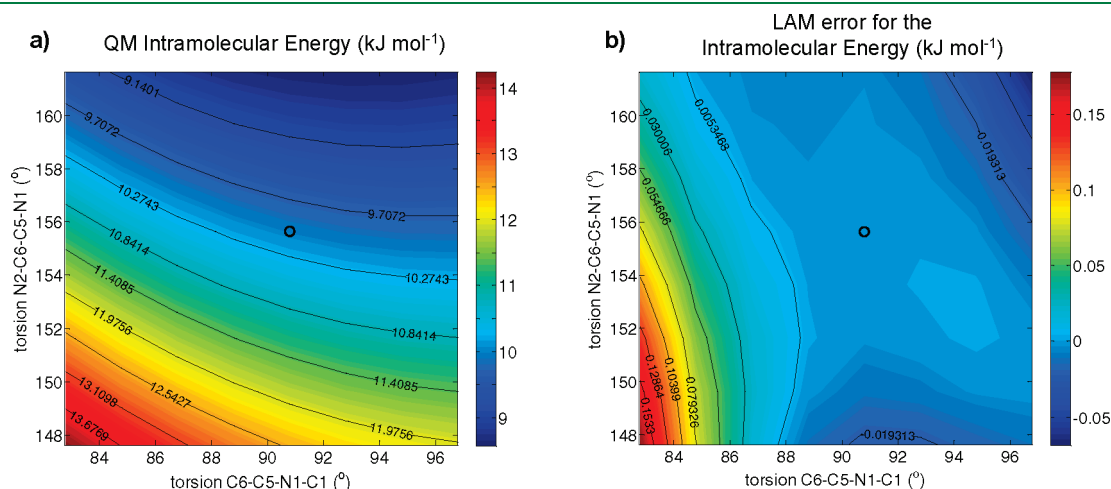


Figure 2. (a) QM intramolecular energy, $\Delta E^{\text{intra, QM}}$ at the HF/6-31G(d,p) level of theory and (b) LAM error for the intramolecular energy defined as $\Delta E^{\text{intra, QM}} - \Delta E^{\text{intra, LAM}}$ as a function of two “flexible” dihedral angles (blue arrows in Figure 1) for piracetam. Open circles correspond to the reference point for the LAM. Reproduced with permission from Adjiman, C. S.; Galindo, A. *Process Systems Engineering: Volume 6: Molecular Systems Engineering*; Wiley-VCH Verlag GmbH & Co. KGaA: New York, 2010; p 15.

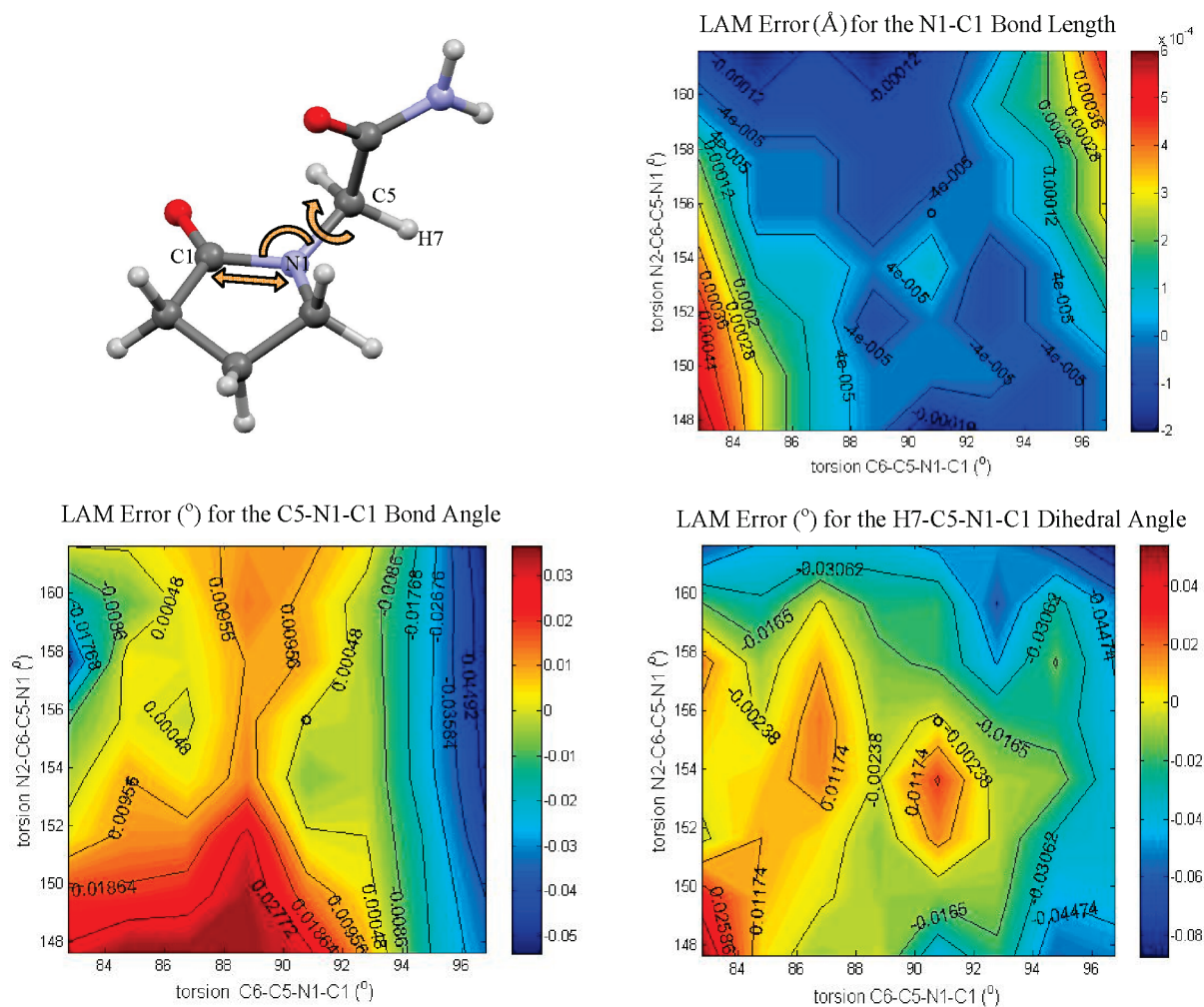


Figure 3. Difference between the quantum mechanical and estimated LAM values for selected “rigid” degrees of freedom (orange arrows, top left) as a function of two “flexible” dihedral angles (blue arrows in Figure 1) for piracetam (2-oxo-pyrrolidine-acetamide). QM calculations performed at the HF/6-31G(d,p) level of theory. Open circles correspond to the reference point for the LAM. Reproduced with permission from Adjiman, C. S.; Galindo, A. *Process Systems Engineering: Volume 6: Molecular Systems Engineering*; Wiley-VCH Verlag GmbH & Co. KGaA: New York, 2010; p 16.

bond angle C5–N1–C1 varies by 1.41° over the region considered and bond length C1–N1 by 0.0094 \AA .

Figure 4 is concerned with the accuracy of the multipole rotation LAM (eq 13) in modeling the electrostatic potential energy of xylitol (1,2,3,4,5-pentapentanol) as a selected torsional angle (H1–O1–C1–C2) deviates from the LAM’s reference point. The latter corresponds to the molecular conformation at the minimized experimental crystal structure²² using nine major torsional angles (all angles involving hydroxyl groups, and four selected backbone torsions, as shown in Table 1). The quantum mechanical electrostatic potential energy of the reference conformation is shown at the center of Figure 4. For the perturbed conformations, the selected hydroxyl torsion (indicated by a blue arrow on the molecule in Figure 4) was varied by up to $\pm 10^\circ$ from its reference value while the other eight flexible degrees of freedom were held constant at their reference values. For each perturbed molecular geometry, the rigid degrees of freedom were computed using a LAM (eq 8) constructed at the PBE/6-31G(d,p) level of theory. The atomic multipole moments and the electrostatic potential were consequently evaluated using both the LAM (eq 13) and explicit quantum mechanical isolated-molecule

calculations at the PBE/6-31G(d,p) level of theory. The maximum error in the electrostatic potential energy increases the further the conformation moves away from the reference molecular geometry but does not exceed 0.03 eV over the entire range $\pm 10^\circ$ of the flexible torsion angle considered. This error is approximately 2% of the electrostatic potential energy range for the reference conformation. The error is reduced to less than 0.02 eV when the LAM is used to model the electrostatic potential energy within $\pm 5^\circ$ of the reference geometry. Of course, what is important for the purposes of crystal structure prediction is not the electrostatic potential energy *per se* but the intermolecular electrostatic contributions to the lattice energy. In section 4.3, we shall return to consider in more detail the accuracy of the multipole LAMs given by eqs 13 and 14.

In conclusion, the error inherent in any LAM increases as one moves further away from the reference point around which the LAM was constructed. It is therefore necessary to reconstruct the LAM after a significant change in the flexible degrees of freedom. What constitutes a significant change is molecule dependent, but in our experience, ranges of $\pm 5^\circ$ for torsional angles, $\pm 5^\circ$ for bond angles, and $\pm 0.1 \text{ \AA}$ for bond lengths leads to reliable results

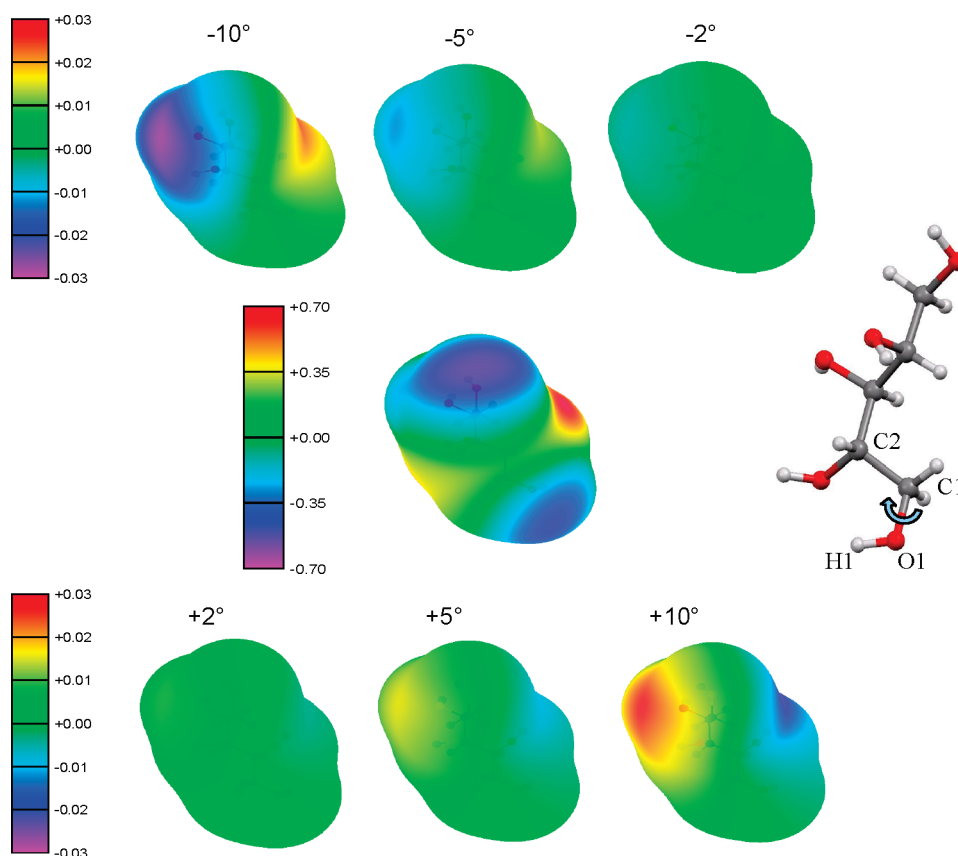


Figure 4. Error in the electrostatic potential energy (in eV; $1 \text{ eV} = 96.5 \text{ kJ mol}^{-1}$) on twice the van der Waals radii surface of xylitol (1,2,3,4,5-pentapentanol) as a function of the H1–O1–C1–C2 torsional angle. LAM used to estimate the rigid degrees of freedom and rotate the atomic multipole moments with their local environment. The quantum mechanical electrostatic potential energy in eV for the reference molecular conformation is also shown for comparison (center). All electrostatic potential energy surfaces were computed with atomic multipoles up to the hexadecapole level, at the PBE/6-31G(d,p) level of theory, using ORIENT.³⁹ The van der Waals radius for hydroxyl hydrogen atoms was set to 1 au; the radii for other atoms were taken from the work of Bondi.⁴⁰ Reproduced with permission from Adjiman, C. S.; Galindo, A. *Process Systems Engineering: Volume 6: Molecular Systems Engineering*; Wiley-VCH Verlag GmbH & Co. KGaA: New York, 2010; p 18.

in the majority of systems. These ranges are comparable to the conformational changes observed during the lattice energy minimization of flexible molecules. Hence, it should be possible to perform such calculations with only a few explicit quantum mechanical optimizations, which provides the motivation for the algorithm presented in this paper.

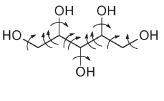
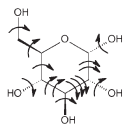
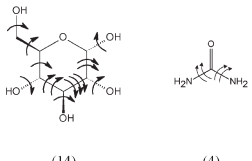
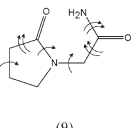
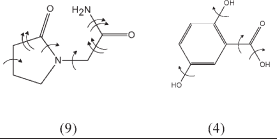
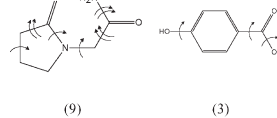
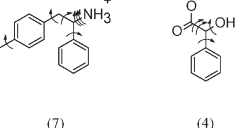
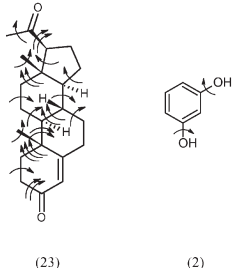
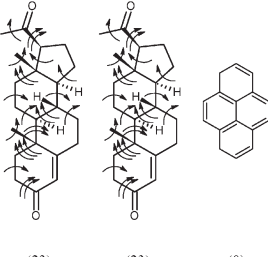
2.5. Reusability of Results of QM Calculations and LAM/QM Databases. For a given molecular species, the local approximate models described above are derived completely from the results of isolated-molecule QM calculations performed at a certain reference point θ_{ref} with a certain level of QM theory. These QM results are independent of the crystalline environment and the physical conditions (e.g., pressure) under which lattice energy minimizations took place. Consequently, they can be reused in repeated calculations involving the same molecule. This is particularly useful in the case of *ab initio* crystal structure prediction studies where it is necessary to perform lattice energy minimizations starting from a large set (possibly hundreds) of candidate structures of a given molecule.

To take advantage of this reusability, all QM-computed quantities (reference conformation, the intramolecular energy, first- and second-intramolecular energy derivatives with respect to all intramolecular degrees of freedom, the localized atomic multipole moments, and their gradients with respect to the flexible degrees of

freedom) used to construct a LAM at any point during a calculation are stored in a database. Torsional angles are allowed to take any value in the course of lattice energy minimization, but are stored only in the $[-180, +180^\circ]$ range in the database. For molecules exhibiting enantiomerism, an entry for the enantiomer of the molecule is also automatically generated from the same *ab initio* calculation, by inverting the values of the torsional angles, intramolecular energy derivatives with respect to the torsional angles, and the relevant components of the multipole moments.

Whenever it is necessary to create LAMs at a new point θ^f in the molecule's conformational space, the corresponding LAM/QM database is searched to identify whether any existing entry θ_{ref} in it can be used to create a LAM that would be valid at θ^f . This would be the case if the differences between the values of the elements of θ^f and the corresponding values in θ_{ref}^f are all within a given tolerance ϵ . If more than one database entry meets these validity criteria, the entry with the lowest root-mean-square deviation from θ^f is chosen. On the other hand, if no database entry satisfies the validity criteria, new QM calculations are performed to construct the required LAMs by solving the constrained minimization problem defined by eq 2 and performing a charge density calculation. The QM results are then used to create a new entry in the database with a reference point $\theta_{\text{ref}} = (\theta^f, \theta^r)$, where θ^r is given by eq 3.

Table 1. Systems Considered for CrystalOptimizer Refinement

Name	Molecular Diagram (number of flexible degrees of freedom)	Space Group	Z'
Xylitol ²²	 (12)	$P2_12_12_1$	1
α -D-glucose ²⁵	 (14)	$P2_12_12_1$	1
α -D-glucose Urea (1:1) co-crystal ²⁶	 (14) (4)	$P2_12_12_1$	1
Piracetam	 (9)	$P2_1/n$	1
		$P\bar{1}$	1
		$P2_1/n$	1
		$P2_1/c$	1
		$P\bar{1}$	1
Piracetam Gentic acid (1:1) co-crystal ³²	 (9) (4)	$C2/c$	2
Piracetam p-Hydroxybenzoic acid (1:1) co-crystal ³²	 (9) (3)	$P2_1/n$	2
(R)-1-phenyl-2-(4-methylphenyl)ethylammonium-(S)-mandelate salt ³³	 (7) (4)	$P2_12_12_1$	2
Progesterone Resorcinol (1:1) co-crystal ³⁴	 (23) (2)	$P2_12_12$	2
Progesterone Pyrene (2:1) co-crystal ³⁵	 (23) (23) (0)	$P1$	3

A LAM/QM database is specific to a particular molecule and level of QM theory. However, it can be reused and, indeed, extended during more than one calculation involving this molecule. For example, a database created during the lattice energy minimization of a given experimentally observed polymorph may be used on a later occasion for the minimization of the same experimental structure under a different pressure, or of a different polymorph, or of a cocrystal that involves the given molecule together with a different one. For this reason, LAM/QM databases are stored as persistent computer files that can be used in any calculation relating to the corresponding molecule, potentially being extended during each such calculation to contain an increasing number of points, thereby becoming more and more useful as an increasing fraction of the molecule's conformational space is covered. An illustrative example of the performance gain that can be achieved due to the use of databases in an *ab initio* crystal structure prediction study is discussed in section 4.6.

Finally, it is worth pointing out that the information being stored in a LAM/QM database entry comprises the results of a QM calculation (i.e., the values of the intramolecular energy and its partial derivatives appearing on the right-hand side of eq 4) and not the LAMs of eqs 8 and 10 (e.g., the matrices $A(\theta_{\text{ref}})$ and $C(\theta_{\text{ref}})$ and the vector $b(\theta_{\text{ref}})$) derived from them. Thus, the LAM/QM database entries are independent of the specific way in which the conformational degrees of freedom θ^f are partitioned between "flexible" θ^f and "rigid" θ^r variables. Consequently, this information may be used for different calculations pertaining to the same molecule under different degrees of flexibility, provided eq 5 still holds. In practice, this means that an existing database can be reused by subsequent calculations considering the same or higher degree of flexibility. It is worth noting that the requirement for nondecreasing flexibility does not apply to the atomic multipole moments; these can be reused across different calculations involving any degree of flexibility as long as the definition of the local axis system for each atom in the molecule remains the same.

3. COMPUTATIONAL METHODOLOGY—CRYSTALOPTIMIZER

3.1. Lattice Energy Minimization. The lattice energy minimization problem can be written as

$$\min_{\mathbf{X}, \theta} E^{\text{latt}} \equiv \min_{\mathbf{X}, \theta} [\Delta E^{\text{intra}}(\theta) + U^{\text{inter}}(\mathbf{X}; \theta, \Omega(\theta))] \quad (15)$$

where ΔE^{intra} is the energy required to deform the molecule from its most stable gas-phase conformation. Stable crystal forms can therefore be identified by minimizing the lattice energy with respect to the intramolecular degrees of freedom, θ (bond lengths, bond angles, and torsional angles), and lattice variables, \mathbf{X} , which include the unit cell geometry and the position and orientation of all crystallographically independent molecules in the lattice. Here, $\Omega(\theta)$ denotes the distributed multipole model⁸ used to represent the dominant electrostatic contributions to the intermolecular energy.

As has already been explained, the dimensionality of the above optimization problem can be reduced by the partitioning of the intramolecular degrees of freedom, θ , into flexible, θ^f , and rigid, θ^r , degrees of freedom, leading to the modified minimization

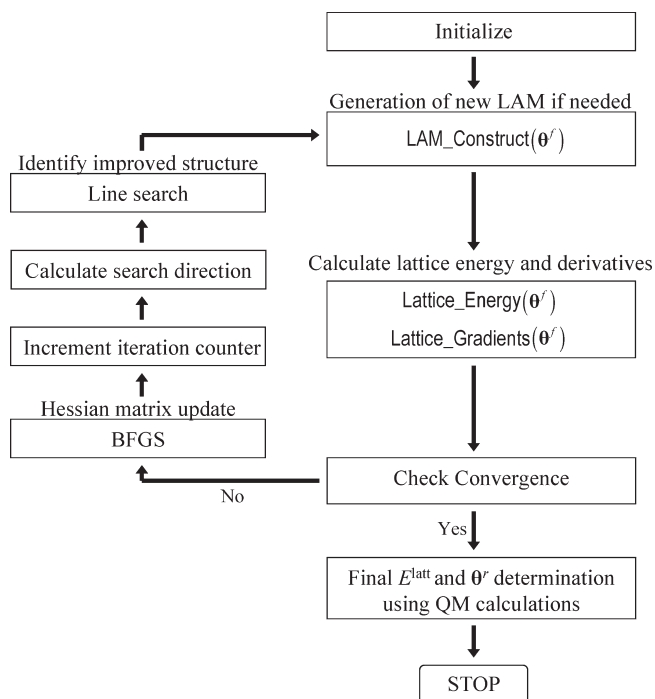


Figure 5. CrystalOptimizer local lattice energy minimization algorithm flowchart. Refer to Figure 6 for procedures for LAM construction (LAM_Construct), lattice energy (Lattice_Energy), and lattice energy derivatives (Lattice_Gradients) calculation.

problem:

$$\min_{\mathbf{X}, \theta^f} E^{\text{latt}} \equiv \min_{\mathbf{X}, \theta^f} [\Delta E^{\text{intra}}(\theta^f) + U^{\text{inter}}(\mathbf{X}; \theta^f, \theta^r(\theta^f), \Omega(\theta^f, \theta^r(\theta^f)))] \quad (16)$$

where $\Delta E^{\text{intra}}(\theta^f)$ and $\theta^r(\theta^f)$ are defined by eqs 2 and 3, respectively, and can be approximated accurately and efficiently via the LAMs shown in eqs 10 and 8, respectively. The multipoles $\Omega(\theta^f, \theta^r(\theta^f))$ can also be approximated via the LAMs defined by eqs 13 and 14.

For a given molecular conformation θ , the minimum intermolecular energy with respect to the lattice variables, \mathbf{X} , can be calculated with existing algorithms such as DMACRYS.⁵ Therefore, in order to use such codes, eq 16 is further reformulated as

$$\min_{\theta^f} E^{\text{latt}} = \min_{\theta^f} [\Delta E^{\text{intra}}(\theta^f) + \bar{U}^{\text{inter}}(\theta^f)] \quad (17)$$

where the second term on the right-hand side is given by the solution of another minimization problem:

$$\bar{U}^{\text{inter}}(\theta^f) \equiv \min_{\mathbf{X}} U^{\text{inter}}(\mathbf{X}; \theta^f, \theta^r(\theta^f), \Omega(\theta^f, \theta^r(\theta^f))) \quad (18)$$

Equations 17 and 18 define a bilevel optimization problem. The inner minimization (eq 18) determines the crystal structure for rigid molecular entities, whose conformation is determined by the outer minimization (eq 17) manipulating the flexible degrees of freedom θ^f . It should be noted that the DMAflex algorithm¹³ solves the same bilevel optimization problem, using DMACRYS⁵ to calculate the intermolecular energy (eq 18).

3.2. The CrystalOptimizer Algorithm. CrystalOptimizer is a local lattice energy minimization algorithm designed to solve the optimization problem given by eq 17 and making use of LAMs in

order to reduce the computational cost associated with quantum mechanical calculations. An overview of the CrystalOptimizer algorithm is shown in Figure 5 and will now be discussed in detail.

In the initialization steps, the algorithm requires the user to specify the starting crystal structure. By representing the molecular geometry in the automatically generated Z-matrix form (that avoids near-linear bond angles), the proposed algorithm allows the user to select the extent of molecular flexibility to be considered during the minimization. This can range from a few selected torsional angles to full atomistic minimization.

Before the optimization is carried out, the user is also required to specify several model parameters such as optimization convergence tolerances, the choice of quantum mechanical methods and basis sets, and the tolerance vector ϵ that defines the range of LAM validity for different types of flexible degrees of freedom. If required, different tolerances may be specified for the LAMs relating, respectively, to intramolecular energy and multipoles. For each flexible degree of freedom, the user also specifies whether or not the linear update to the multiple moments (eq 14) is to be used. Input information relating to DMACRYS, such as the cutoff range for Ewald summation, the type of repulsion-dispersion potential, and the values of parameters within it, must also be specified.

CrystalOptimizer uses a quasi-Newton algorithm coupled with a line-search²³ to solve the outer minimization problem. This approach ensures rapid convergence even when there are many flexible degrees of freedom by using an approximation of the Hessian matrix of the second-order derivatives of the lattice energy with respect to the flexible degrees of freedom. At the start of the lattice energy minimization, this Hessian approximation is normally initialized to the unit matrix; at each subsequent iteration, it is updated via the Broyden–Fletcher–Goldfarb–Shanno (BFGS) method²³. This ensures that the Hessian approximation remains positive-definite, which guarantees the identification of a direction in which to change the flexible degrees of freedom θ^f , which results in a reduction of the lattice energy, thereby avoiding the location of transition states. The use of the BFGS approximation avoids the evaluation of the second-order derivatives of the lattice energy at every outer iteration, instead making use only of values of the lattice energy and its first-order gradients with respect to the flexible degrees of freedom.

As can be seen from the right-hand side of eq 17, the computation of the lattice energy for given θ^f involves two components. The first one, $\Delta E^{\text{intra}}(\theta^f)$, is computed explicitly via the LAM of eq 10. The second component is computed by solving the inner minimization problem (eq 18) using DMACRYS,⁵ with the molecular conformation and distributed multipole moments fixed at the values determined via the LAMs of eqs 8, 13, and 14.

In addition to the value of the lattice energy for given θ^f , the outer optimization algorithm also requires values of its gradients with respect to θ^f . The gradients of its first component, $\Delta E^{\text{intra}}(\theta^f)$, can be computed in a straightforward manner by differentiating the LAM of eq 10:

$$\left. \frac{\partial \Delta E^{\text{intra}}}{\partial \theta^f} \right|_{\theta^f} = \mathbf{b}(\theta_{\text{ref}}) + \mathbf{C}(\theta_{\text{ref}})(\theta^f - \theta_{\text{ref}}^f) \quad (19)$$

The gradients of the second component, \bar{U}^{inter} , of the lattice energy with respect to θ^f cannot be obtained in a closed analytical form. In CrystalOptimizer, they are computed via a centered finite difference scheme. The gradient with respect to the k^{th}

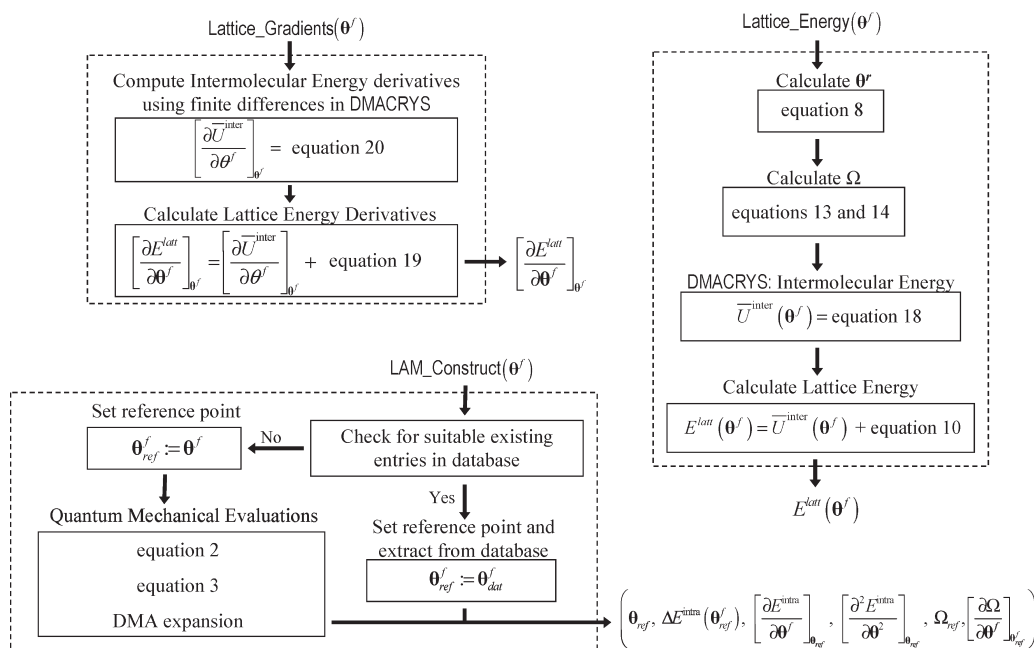


Figure 6. Procedures for lattice energy derivatives (top left), lattice energy (right) calculations, and LAM construction (bottom left) in CrystalOptimizer.

element θ_k^f of the vector θ^f requires a positive and a negative perturbation of magnitude $\delta\theta_k^f$. For each perturbed value, the LAMs of eqs 8, 13, and, where necessary, 14 are used to update the values of the rigid degrees of freedom θ^r and the multipoles Ω , before calling DMACRYS to determine \bar{U}^{inter} via the minimization described by eq 18. The required gradient is then obtained via the finite difference approximation:

$$\left. \frac{\partial \bar{U}^{\text{inter}}}{\partial \theta_k^f} \right|_{\theta^f} \approx \frac{\bar{U}_{k+}^{\text{inter}} - \bar{U}_{k-}^{\text{inter}}}{2\delta\theta_k^f} \quad (20)$$

where $\bar{U}_{k+}^{\text{inter}}$ and $\bar{U}_{k-}^{\text{inter}}$ denote the values of \bar{U}^{inter} returned by DMACRYS for the positive and negative perturbations, respectively.

The required gradients $\partial E^{\text{latt}}/\partial \theta^f$ are then simply computed as the sum of expressions 19 and 20. The procedures for calculating the lattice energy and the gradient of the lattice energy with respect to the flexible degrees of freedom are shown in Figure 6.

On the basis of the value of the lattice energy and the search direction calculated using the lattice energy gradient and the BFGS Hessian matrix approximation, the line-search procedure in the outer minimization algorithm determines a new set of flexible degrees of freedom that results in a sufficiently large reduction of the lattice energy. This involves the evaluation of lattice energy at a sequence of points along the search direction. All but the last of these points do not fulfill the criterion of sufficient reduction in the lattice energy and are immediately discarded from further consideration. As it is not generally worth performing any expensive QM calculations at such points, during the line search part of the algorithm, we relax the LAM validity tolerances ε by a factor n which is typically in the range $1 < n \leq 2$.

After the line search identifies a new improved point in conformational space θ^f , we reset the LAM validity tolerances to their original value ε , before evaluating the new lattice energy

and its gradients with respect to θ^f in the manner detailed above. The BFGS approximation is then used to provide a new estimate of the Hessian matrix, and the algorithm proceeds to the next outer iteration by calculating a new search direction and performing a line search along it.

The optimization terminates successfully when either the changes of all flexible degrees of freedom during the last step or all the lattice energy gradients with respect to θ^f are below specified tolerances. As a final step, CrystalOptimizer uses rigorous QM calculations (eqs 2 and 3) to recompute the lattice energy and molecular conformation at the values of θ^f determined by the optimization, thereby eliminating any small inconsistencies that may have arisen from the use of LAMs. It should be noted, however, that this final calculation does not eliminate any error caused by using LAMs in identifying the true minimum.

CrystalOptimizer returns a failure status if either the line search fails to identify a new set of flexible degrees of freedom that produce a sufficient reduction in the lattice energy along the search direction, or when a predefined maximum number of outer iterations is reached without either of the two convergence criteria having been satisfied.

4. ALGORITHM TESTING, RESULTS AND DISCUSSION

The main question to be answered in validating the CrystalOptimizer algorithm is whether, for a given initial point, the use of the local approximate models leads to the same local energy minimum as when using QM calculations at each minimization iteration. Once this is established, the performance of the algorithm, and particularly the reduction in computational cost for a given number of flexible degrees of freedom can be investigated. The use of additional degrees of freedom can also be studied, and the impact of flexibility on crystal structure can be assessed.

4.1. Systems Studied. The validation of the CrystalOptimizer algorithm was performed on the systems shown in Table 1. These were selected because of their scientific and/or practical

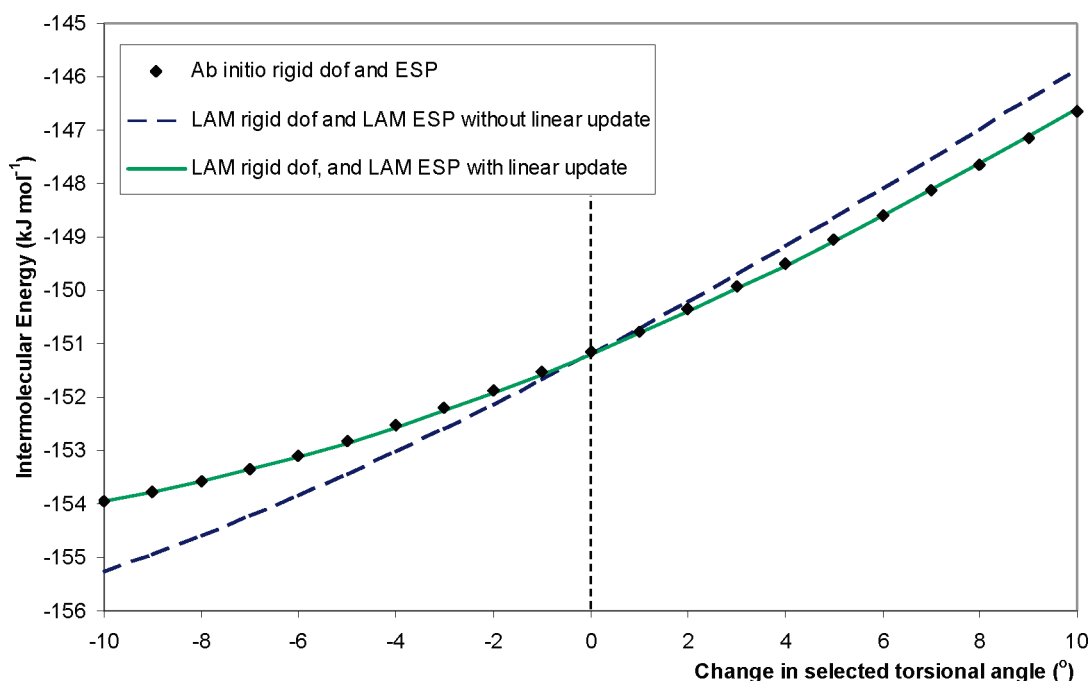


Figure 7. Intermolecular energy as a function of the H1–O1–C1–C2 torsional angle (blue arrow in Figure 4) for three different computational strategies: (1) molecular geometry and the electrostatic potential (ESP) obtained by full quantum mechanical calculations (black diamonds), (2) LAM used to update rigid degrees of freedom (dof) and multipole rotation (blue dashed line), (3) LAMs used to update the rigid degrees of freedom, multipole rotation, and a linear update of the multipole moments (continuous green line).

importance and the fact that they possess sufficient conformational flexibility to present a significant challenge for lattice energy minimization using current techniques.

Xylitol, a naturally occurring sugar alcohol, is a stereoisomer of 1,2,3,4,5-pentapentanol (pentose) for which only one crystal structure has been determined experimentally to date.²² No other organic systems containing xylitol were found in the Cambridge Crystallographic Database²⁴ (CSD).

Our second test system is glucose. We consider the structure of one of its cyclical isomers, α -D-glucose.²⁵ A cocrystal of α -D-glucose with urea²⁶ is also found in the CSD.

Piracetam (2-oxo-pyrrolidine-acetamide) is a pharmaceutical nootropic drug. There are five distinct polymorphs determined experimentally,^{27–31} two of which are observed only at high pressure. Two cocrystals³² of piracetam are also reported in the CSD.

In order to examine the applicability of CrystalOptimizer to a range of systems of practical interest, three additional crystals were considered, namely the salt (*R*)-1-phenyl-2-(4-methylphenyl)ethylammonium-(*S*)-mandelate³³ and the cocrystals of the pharmaceutically important steroid progesterone with resorcinol³⁴ and pyrene.³⁵ These were selected primarily on the basis of posing significant computational challenges in terms of both the molecular size and flexibility.

4.2. Molecular Modeling and Computational Considerations. The quantum mechanical molecular geometry optimizations and the charge density calculations were both evaluated at the PBE/6-31G(d,p) level of theory.

The LAM validity tolerances were set at $\pm 5^\circ$ for torsional and bond angles and ± 0.02 Å for bond lengths. The linear update to the multipole moments (eq 14) was used for all flexible torsional angles that involved the nitrogen atom or the OH groups. Although the extent to which the LAMs are reliable is system-dependent, the above range of validity is expected to provide a

sufficiently small error compared with the other approximations present in the computational model.

The repulsion–dispersion interactions were modeled with an empirical exp-6 potential¹⁰ and were summed in direct space up to a 30 Å cutoff.

CrystalOptimizer was used to perform local lattice energy minimizations starting from the experimental structures for each model system considered. The flexible degrees of freedom that were taken into consideration for each system are marked in the molecular diagrams shown in the second column of Table 1.

Most calculations were performed on a single Intel Xeon 5150 2.66 GHz processor using 1500 MB of memory. In the case of the salt and progesterone cocrystals, the minimizations were performed on four Intel Xeon 5150 2.66 GHz processors with 7 GB of shared memory. The availability of multiple processors was exploited for performing the QM computations using the GAUSSIAN²¹ code.

4.3. Use of Linear Updates for Multipole LAMs. Section 2.4 examined the range of validity of the LAMs for multipoles in terms of their ability to reproduce the electrostatic potential field surrounding an isolated molecule. As noted there, what is more important is the accuracy with which these LAMs can approximate the intermolecular electrostatic contributions to the lattice energy.

We now return to consider this question in more detail using xylitol, with the minimized experimental structure (using nine flexible hydroxyl and backbone torsions) as the reference point. The H1–O1–C1–C2 hydroxyl angle is varied by up to $\pm 10^\circ$ from the reference point while maintaining the remaining flexible degrees of freedom at their reference values; DMACRYS is used to reoptimize the crystal lattice at each different conformation under consideration, and the intermolecular energy contribution to the lattice energy at the optimal structure is recorded.

Figure 7 shows results from three different sets of calculations performed for several values of the selected torsion angle over the range mentioned above.

For each value of the flexible hydroxyl angle, the rigid degrees of freedom were computed explicitly by solving the quantum mechanical constrained optimization in eq 3. The electrostatic potential was also calculated quantum mechanically for each generated conformation. These molecular and electrostatic models were used to compute the intermolecular energy shown as black diamonds in Figure 7.

Next, the LAM of eq 8 was used to approximate the rigid degrees of freedom, and the multipoles were rotated according to eq 13. The results are shown as a blue dashed line in Figure 7. The maximum error in the intermolecular energy is 1.3 kJ mol^{-1} and occurs when the selected flexible torsion angle is 10° from its reference value. The errors for changes of up to $\pm 5^\circ$ and $\pm 2^\circ$ from the reference value are 0.6 kJ mol^{-1} and 0.3 kJ mol^{-1} , respectively.

The intermolecular energy was also calculated using the LAMs for the estimation of the rigid degrees of freedom (eq 8), multipole rotation (eq 13), and a linear update to the multipole moments (eq 14). The results are shown as a continuous green line in Figure 7. The error in the intermolecular energy is within 0.06 kJ mol^{-1} of the *ab initio* value for all values of the selected flexible degree of freedom.

The above results indicate that, for this particular system, the multipole rotation LAM of eq 13 leads to considerable errors in intermolecular energy. However, the subsequent application of the linear correction (eq 14) produces an accurate estimate of the electrostatic potential energy, even for relatively large conformational changes.

4.4. Application of CrystalOptimizer to Single Component Crystals. We start by considering the three model systems which involve single component crystals, namely, xylitol, α -D-glucose, and piracetam form II.

In order to assess the computational performance and the effects of varying molecular flexibility on the performance of the CrystalOptimizer, these systems were studied using different optimization settings and increasingly wider sets of flexible degrees of freedom.

Initially, only the hydroxyl (amide for piracetam form II) and selected backbone dihedrals were treated as flexible degrees of freedom, while the rings in α -D-glucose and piracetam were assumed to be rigid. These simplifications result in nine, six, and four flexible degrees of freedom for xylitol, α -D-glucose, and piracetam, respectively. Although these minimal sets of flexible torsion angles are not sufficient to capture the whole molecular flexibility, they have the advantage of being within the range of applicability of earlier algorithms for lattice energy. Of particular interest in this context is the DMAFlex algorithm,¹³ which has a similar model of inter- and intramolecular interactions as CrystalOptimizer, thereby allowing some validation of the results obtained with our code, and a direct comparison of computational performance. Three different CrystalOptimizer runs were performed with the same number of degrees of freedom:

Case 1. CrystalOptimizer without LAMs or LAM/QM databases was tested. This requires quantum mechanical calculations at every iteration, as with DMAFlex, and shows the effect of using a quasi-Newton algorithm instead of a simplex algorithm.

Case 2. All features of CrystalOptimizer are used. The LAM/QM databases are initially empty and are populated

during these calculations. In fact, for the calculations reported here, no reuse of information stored in the databases has actually occurred. Therefore, only the impact of the LAMs is assessed.

Case 3. All features of CrystalOptimizer are used, including the use of the LAM/QM databases (cf. section 2.5) already populated in case 2.

Following this initial study, additional optimizations were carried out with CrystalOptimizer, by gradually increasing the degree of molecular flexibility under consideration in two further steps.

Case 4. All heavy-atom torsions, and all hydroxyl (H–O–C) and amide (H–N–C) bond angles were additionally treated as flexible, resulting in 17 flexible degrees of freedom for xylitol and 19 for α -D-glucose and piracetam.

Case 5. An atomistic representation corresponding to full molecular flexibility is considered, resulting in 60 flexible degrees of freedom for xylitol, 66 for α -D-glucose, and 54 for piracetam.

Note that in the analysis of the results reported in cases 1, 4, and 5 and also in section 4.5, the LAM/QM database (cf. section 2.5) feature of CrystalOptimizer was disabled. A more detailed analysis of the effects of using these databases is presented in section 4.6.

The detailed results from the above studies are provided in Tables 2, 3, and 4 for xylitol, α -D-glucose, and piracetam form II, respectively. In all cases, agreement between the predicted crystal structures and the experimentally observed ones is assessed on the basis of the root-mean-square deviation of the molecular conformation and the 15-molecule coordination sphere.³⁶

Overall, there is a gain in stability as we widen the set of flexible degrees of freedom considered by CrystalOptimizer, which indicates that the detailed modeling of molecular flexibility is important in order to capture the full extent of conformational distortions by the packing forces. For instance, the inclusion of the selected bond angles (case 4) stabilizes the structures of xylitol, α -D-glucose, and piracetam by roughly 1 kJ mol^{-1} compared to the value obtained by considering the flexibility of only the main torsional angles (cases 1–3). As the number of flexible degrees of freedom increases, small changes are observed in the lattice energy, but the balance between intermolecular and intramolecular energy tends to shift so that the molecule adopts a less stable conformation to reduce the energetic cost of intermolecular interactions. CrystalOptimizer makes it computationally feasible to consider a large number of degrees of freedom but it is up to the user to define the extent of flexibility required for each particular molecule or system.

More generally, explicit consideration of the flexibility of bond angles and stiff torsions, such as those in polyaromatic ring systems, is expected to be especially significant for larger systems and under high pressure. On the other hand, it can be seen by comparing cases 4 and 5 that the additional energy stabilization arising from modeling the bond lengths is more limited (unless proton transfer takes place³⁷). The energy required to perturb a bond length is usually very large, and consequently the modeled bond lengths do not change significantly during lattice energy minimization. Thus, in order to reduce computational cost, the bond lengths can normally be assumed to be rigid with little loss of predictive accuracy.

Figure 8 demonstrates the accuracy of reproduction of the experimental conformation obtained by considering full

Table 2. Lattice Energy Minimization for Xylitol

	CrystalOptimizer				
	DMAFlex ^d	no LAMs, no LAM databases		LAMs and LAM databases	
		case 1	case 2	case 3	case 4
no. of flexible degrees of freedom ^b	9	9	9	17	60
lattice energy (kJ mol ⁻¹)	main torsions -125.32	main torsions -125.15	main torsions -125.16	all torsions, ^c OH angles -127.04	atomistic ^d -127.78
intramolecular energy (kJ mol ⁻¹)	23.31	23.55	23.43	23.18	24.47
intermolecular energy (kJ mol ⁻¹)	-148.62	-149.25	-148.58	-150.22	-152.25
rmsd1 ^e	0.20	0.19	0.19	0.19	0.23
CPU time (hr:min) ^f	35:32	07:30	04:01	12:20	43:55
no. of outer iterations	127	13	13	14	23
no. of QM calculations	127	4	1	5	5
molecular optimization					
molecular Hessian					
charge density	127	10	10	4	4
QM molecular optimization	53.83	19	1	25	25
QM Hessian calculation		4.59	1.07	3.33	0.50
QM charge density, DMA	41.01	23.63	0.00	11.04	2.94
DMACRY5	5.13	49.30	2.82	23.55	6.50
other	0.03	22.37	95.60	61.75	89.58
		0.11	0.51	0.33	0.48

^a Karamertzanis and Price.^{1,3} ^b Linear update to the multipole moments calculated for all torsions involving the OH group. ^c Excluding dihedrals defined as H-C-X-X. ^d All intramolecular degrees of freedom. ^e Root-mean-square deviation in 15-molecule coordination sphere compared with the experimental structure (excluding hydrogen atoms).^{36,f} Single Intel Xeon 5150 2.66 GHz processor using 1500 MB of memory.

Table 3. Lattice Energy Minimization for α -D-Glucose

	CrystalOptimizer				
	DMAFlex ^d	no LAMs, no LAM databases		LAMs and LAM databases	
	case 1	case 2	case 3	case 4	case 5
no. of flexible degrees of freedom ^b	6	6	6	19	66
lattice energy (kJ mol ⁻¹)	main torsions -146.08	main torsions -146.41	main torsions -146.39	all torsions, ^c OH angles -147.86	atomistic ^d -148.62
intramolecular energy (kJ mol ⁻¹)	9.60	10.08	10.05	12.54	12.55
intermolecular energy (kJ mol ⁻¹)	-155.68	-156.49	-156.44	-160.40	-161.16
rmsd1s ^e	0.20	0.20	0.20	0.16	0.14
CPU time (hr:min) ^f	44:13	09:20	02:17	13:22	41:32
no. of outer iterations	118	14	11	16	22
no. of QM calculations	118	5	1	4	4
molecular optimization		4	0	3	3
molecular Hessian		25	1	19	19
charge density	118	8.33	2.71	4.73	0.59
QM molecular optimization	55.47	21.69	0.00	11.20	3.57
QM Hessian calculation	30.89	41.53	6.66	21.91	7.02
QM charge density, DMA	41.14	28.25	89.98	61.71	88.18
DMACRY5	3.37	0.09	0.65	0.45	0.64
other	0.02				

^a Karamertzanis and Price.¹³ ^b Linear update to the multipole moments calculated for all torsions involving the OH group. ^c Excluding dihedrals defined as H-C-X-X. ^d All intramolecular degrees of freedom. ^e Root-mean-square deviation in 15-molecule coordination sphere compared with the experimental structure (excluding hydrogen atoms).³⁶ ^f Single Intel Xeon 5150 2.66 GHz processor using 1500 MB of memory.

Table 4. Lattice Energy Minimization for Piracetam Form II

	CrystalOptimizer								
	DMAFlex ^d	no LAMs, No LAM databases		LAMs, No LAM databases		LAMs and LAM databases		more flexibility, LAMs but no LAM databases	
		case 1	case 2	case 3	case 4	case 5	case 4	case 5	
no. of flexible degrees of freedom ^b	4	4	4	4	4	19	54	54	
lattice energy (kJ mol ⁻¹)	main torsions -93.49	main torsions -93.31	main torsions -93.31	main torsions -93.31	main torsions -93.31	all torsions, ^c all angles ^d -94.18	atomistic ^e -94.33	atomistic ^e -94.33	
intramolecular energy (kJ mol ⁻¹)	15.27	15.47	15.47	15.47	15.47	16.55	17.08	17.08	
intermolecular energy (kJ mol ⁻¹)	-108.76	-108.78	-108.78	-108.78	-108.78	-110.73	-111.41	-111.41	
rmsd ₁₅ ^f	0.25	0.25	0.25	0.25	0.25	0.22	0.21	0.21	
CPU time (hr:min) ^g	11:42	02:11	01:28	01:28	00:17	16:14	58:31	58:31	
no. of outer iterations	55	2	2	2	2	32	54	54	
no. of QM calculations	55	2	2	2	2	7	14	14	
molecular optimization									
molecular Hessian									
charge density	55	10	6	6	6	49	131	131	
QM molecular optimization	57.45	18.18	27.61	27.61	15.48	3.67	1.05	1.05	
QM Hessian calculation		27.04	19.79	19.79	0.00	10.27	6.17	6.17	
QM charge density, DMA	39.97	48.15	43.14	43.14	36.54	31.29	23.29	23.29	
DMACRYS	2.57	6.62	9.43	9.43	47.86	54.64	69.34	69.34	
other	0.01	0.01	0.03	0.03	0.12	0.13	0.15	0.15	

^a Karamertzanis and Price.¹³ ^b Linear update to the multipole moments calculated for all torsions involving the N atom. ^c Excluding dihedrals defined as H-C-X-X. ^d Excluding bond angles defined as H-C-X. ^e All intramolecular degrees of freedom. ^f Root-mean-square deviation in 15-molecule coordination sphere compared with the experimental structure (excluding hydrogen atoms). ^g Single Intel Xeon 5150 2.66 GHz processor using 1500 MB of memory.

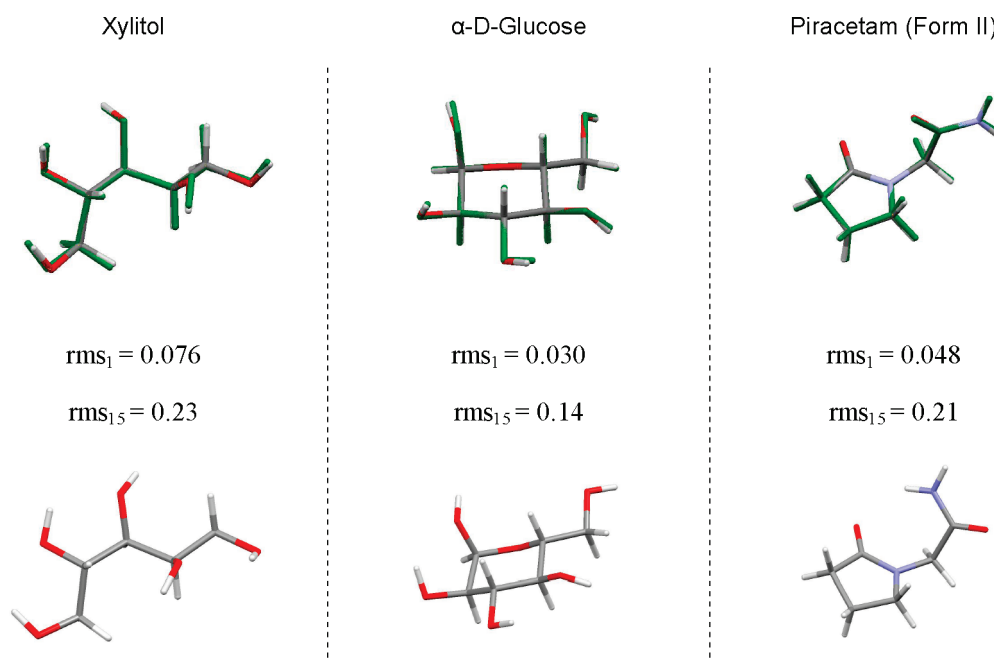


Figure 8. Top row: Overlay of the experimental (colored by element) and minimized (green) structures of xylitol, α -D-glucose, and piracetam when full molecular flexibility is allowed (atomistic representation). The root-mean-square deviations for one molecule (rms_1) and a 15-molecular coordination sphere (rms_{15})³⁶ compared to the experimental structure are shown below. Bottom row: The gas-phase molecular conformations for the three molecules. Reproduced with permission from Adjiman, C. S.; Galindo, A. *Process Systems Engineering: Volume 6: Molecular Systems Engineering*; Wiley-VCH Verlag GmbH & Co. KGaA: New York, 2010; p 36.

molecular flexibility (atomistic representation). Even with the low-quality level of theory used for the QM evaluations, the reproduction of the crystal structures with CrystalOptimizer is acceptable for crystal structure prediction. As shown in Tables 2–4, the maximum error in the root-mean-square deviation of a 15-molecule coordination sphere in all three cases is below 0.3 Å which is less than the 0.4 to 0.5 Å criterion usually taken to indicate a successful prediction in crystal structure blind tests. In general, structure reproduction improves as a larger number of flexible degrees of freedom are being considered. An exception to this trend is observed for xylitol (see the increase in rms_{15} in the last three columns of Table 2), but the overall rms_{15} variation for this molecule is too small to warrant further attention, considering that thermal effects are not taken into account.

Comparisons of the DMAFlex results to those of cases 1–3, as presented in Tables 2–4, indicate that the results obtained from CrystalOptimizer and DMAFlex in terms of energy and structure reproduction are within the errors of the underlying numerical methods, and in particular of the criteria used to determine what constitutes a “converged” solution of the optimization calculations. In the case of CrystalOptimizer, some convergence inaccuracies are introduced by the use of finite differences for the evaluation of the gradients of the intermolecular energy. For DMAFlex, there are convergence issues arising from the use of the gradient-free simplex-based optimization algorithm.

CrystalOptimizer is significantly more computationally efficient than DMAFlex. With all features implemented (case 3), the CPU time is reduced by $\sim 89\%$ for xylitol, $\sim 95\%$ for glucose, and $\sim 97\%$ for piracetam when considering the same degree of molecular flexibility. One reason for this is that CrystalOptimizer’s gradient-based minimization scheme converges in an order of magnitude fewer outer iterations than the simplex algorithm in DMAFlex and scales better with the number of modeled

flexible degrees of freedom, as can be observed by comparing the DMAFlex results and case 1 columns in Tables 2–4. This accounts for an average reduction in CPU time of 63%. A second reason for the much improved computational performance of CrystalOptimizer is that the use of LAMs means that only a small fraction of the outer iterations requires full quantum mechanical calculations. It should be noted, however, that the types of QM calculations required by DMAFlex and CrystalOptimizer are not the same. Each outer iteration in DMAFlex simply requires one constrained geometry optimization and one charge density calculation, the former usually being more computationally expensive. On the other hand, the construction of the LAMs in CrystalOptimizer requires a constrained geometry optimization followed by a (usually much more expensive) analytical evaluation of the intramolecular Hessian matrix (i.e., the second-order partial derivative matrices appearing on the right-hand side of eq 4) and a charge density calculation. Moreover, if the LAM given by eq 14 is used for one or more flexible degrees of freedom, we also need one or two (depending on the finite difference method used for approximating the partial derivatives on the right-hand side of eq 14) additional charge density calculations for each of such flexible degrees of freedom. Nevertheless, despite the additional cost of constructing the LAMs in CrystalOptimizer, the frequency with which this has to be done is small (case 2, Tables 2–4), leading to a further reduction in computational cost of 46%. The poor scaling of the DMAFlex’s simplex optimization algorithm with the number of minimization variables, coupled with the significant cost of the QM calculations, indicates that this approach is unlikely to be practically applicable to systems of even moderate molecular size if they involve more than about 10 flexible degrees of freedom. We believe that any other approach that relies on explicit QM calculations at every iteration would be subject to similar limitations.

Table 5. Lattice Energy Minimization of Additional Crystal Structures Containing α -D-Glucose and Piracetam in the Asymmetric Unit (Refer to Table 1 for Molecular Diagrams)

model system	lattice energy (kJ mol ⁻¹) (pressure) ^a	rmsd ₁₅ ^b (Å)	# outer iterations	# LAM updates ^c	CPU time (hr:min) ^d	
α -D-glucose urea (1:1) cocrystal	-221.62 (0.0 GPa)	0.11	13	2	3	19:08
form I ^e	-91.56 (0.0 GPa)	0.21	5	1		02:58
form II	-93.94 (0.0 GPa)	0.22	9	2		04:28
piracetam	-93.97 (0.0 GPa)	0.13	13	3		07:28
form IV	-52.51 (0.4 GPa)	0.25	9	2		05:10
form V	291.58 (4.0 GPa)	0.30	12	3		06:04
piracetam gentisic acid (1:1) cocrystal	-188.45 (0.0 GPa)	0.26	37	2	1	13:32
piracetam <i>p</i> -hydroxybenzoic acid (1:1) cocrystal	-193.22 (0.0 GPa)	0.28	7	2	1	09:37

^aTwo pressure polymorphs of piracetam, forms IV and V, were minimized at the experimental pressures of 0.4 and 4.0 GPa, respectively. ^bRoot-mean-square deviation in 15-molecule coordination sphere compared with the experimental structure.³⁶ ^cFor each molecule in the asymmetric unit as shown in the model system. ^dSingle Intel Xeon 5150 2.66 GHz processor using 1500 MB of memory. ^eDisordered experimental form with atoms refined over two positions with occupancies 0.657:0.343. Only the most abundant conformer used for the minimization.

Table 6. Lattice Energy Minimization of Selected Crystal Structures of Varying Size and Complexity (Refer to Table 1 for Molecular Diagrams)

model system	lattice energy (kJ mol ⁻¹)	rmsd ₁₅ ^a (Å)	# outer iterations	# LAM updates ^b	CPU time (hr:min) ^c	
(R)-1-phenyl-2-(4-methylphenyl)ethylammonium-(S)-mandelate salt	-596.43	1.34	36	8	8	45:55
progesterone resorcinol (1:1) cocrystal	-221.92	0.15	61	13	4	179:11
progesterone pyrene (2:1) cocrystal	-458.81	0.72	32	3	3	130:53

^aRoot-mean-square deviation in 15-molecule coordination sphere compared with the experimental structure.³⁶ ^bFor each molecule in the asymmetric unit as shown in the model system. ^cFour Intel Xeon 5150 2.66 GHz processors with 7 GB shared memory.

Case 3 in Tables 2–4 indicates the computational cost if all the information required to construct the LAMs was already available in a LAM/QM database, which essentially removes the need to perform QM calculations during the minimization. Note that one QM geometry optimization and one charge density calculation are still necessary for the explicit evaluation of the final lattice energy to remove errors associated with the use of LAMs.

On the basis of cases 2, 4, and 5 in Tables 2–4, the computational cost of the CrystalOptimizer algorithm seems to scale linearly with the number of flexible degrees of freedom and is dominated by two elements, both of them associated with the use of finite difference approximations to partial derivatives. The first element arises from the calculation of the gradients of intermolecular energy with respect to the flexible degrees of freedom (cf. eq 20) by repeated calls to the DMACRYS package; for systems involving more than about 15 flexible degrees of freedom, this calculation accounts for more than 60% of the computational time. The second element is associated with the numerical calculation of multipole derivatives with respect to the specified flexible degrees of freedom (cf. eq 14) and can account for up to 50% of the computational time in cases involving less than 15 flexible degrees of freedom.

4.5. Application of CrystalOptimizer to Cocrystals and Salts. CrystalOptimizer is directly applicable to systems with more than one species in the asymmetric unit, including cocrystals and salts, such as those listed in Table 1. It can also take account of the effects of pressure on crystal structure, via a simple extension of the intermolecular energy (eq 18) to lattice enthalpy. Table 5 presents results for cocrystals involving α -D-glucose and piracetam, and all five known forms of piracetam, two of which (forms IV and V) are studied under elevated

pressures. Table 6 presents further results for a salt and two cocrystals of progesterone.

As in the case of the systems studied in section 4.4, agreement with the experimentally observed crystal structures is generally good, with the rms₁₅ error being below 0.30 Å for all structures other than the salt and the progesterone–pyrene 2:1 cocrystal.

It is worth noting that the reproduction of these larger experimental structures is very sensitive to the selected QM model. Due to the ionic nature of the salt, it is imperative to accurately capture and reproduce the electrostatic interactions in the crystal. If the quality of the charge density calculation is improved to the MP2/6-31G(d,p) level of theory, the rms₁₅ deviation can be reduced from 1.34 Å to 0.84 Å. Similarly, if the hybrid B3LYP/6-31G(d,p) level of theory is used to represent the intramolecular interactions and the multipole model during lattice energy minimization of the progesterone–pyrene (2:1) cocrystal, the error in rms₁₅ is reduced to 0.35 Å.

The selection of the best available computational and flexibility model is therefore integral to the correct reproduction of experimental structures. However, this aspect is beyond the scope of this work.

4.6. Application of CrystalOptimizer to ab initio Crystal Structure Prediction. The main purpose for the development of an accurate local lattice energy minimization algorithm for crystal structures containing flexible molecules is not the reminimization of the experimentally determined crystals but the final refinement of a large set of stable hypothetical structures produced during a crystal structure prediction search. It is in this context that the performance gains through the use of LAM/QM databases (cf. section 2.5) become more relevant.

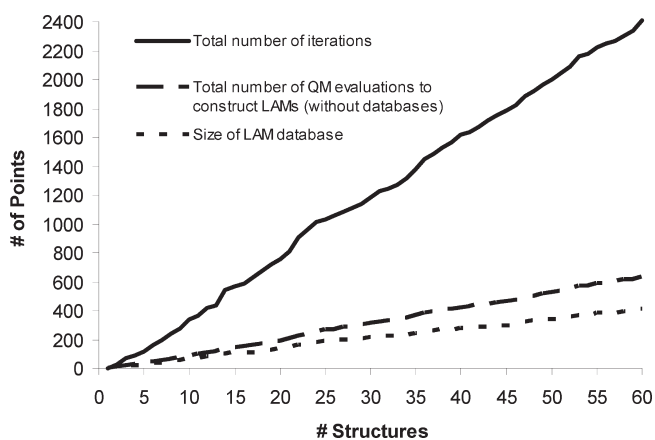


Figure 9. Total number of CrystalOptimizer minimization iterations (solid), number of LAM updates (dashed), and the actual number of QM evaluation sets necessary to construct the LAM/QM database (dotted) as a function of the number of crystal structures minimized in stage 3.

As an illustrative example, we consider the application of CrystalOptimizer to the refinement of 60 distinct crystal structures for xylitol using nine main hydroxyl and backbone torsions as the flexible degrees of freedom (cf. column 3 of Table 2). The 60 structures are typical of those that would be considered in the context of *ab initio* crystal structure prediction; in this example case, they were generated using the CrystalPredictor code³⁸ by treating xylitol as a rigid molecule.

Figure 9 shows three lines:

- The solid line shows the cumulative number of outer minimization iterations against the number of crystal structures analyzed. We can see that a total of 2412 iterations are needed, each effectively corresponding to a different molecular conformation. The computational cost would be prohibitively high if a new QM evaluation of intramolecular energy and charge density were performed at each such iteration. This effectively excludes the use of codes such as DMAFlex for this kind of application.
- The dashed line shows the number of LAMs created if no LAM/QM databases are used. This was obtained by a modified form of the CrystalOptimizer code which, like the standard form, created and used LAMs; however, if an iteration involved a molecular conformation outside the range of validity of the most recently constructed LAM, the latter was simply discarded (i.e., without any information being recorded in the LAM/QM database for possible future use) and a new one created. The total number of LAMs that need to be constructed in this case is 633. Comparing this number with the total number of iterations, we conclude that a LAM is approximately reused over a sequence of, on average, 3.8 successive iterations.
- The dotted line shows the number of LAMs created if the standard CrystalOptimizer code (including LAM/QM databases) is used. In this case, we start the refinement of the first structure using an empty LAM/QM database, and the number of entries in the database potentially increases with the consideration of each new structure. The total number of LAMs created is 408. The difference between this and the dashed line is a measure of the savings achieved via the use of a LAM/QM database.

The savings achieved via the use of a LAM/QM database would be higher if a larger number of crystal structures were refined: as the database is enlarged, there is an increasingly higher probability that a molecular conformation under consideration will be covered by one of the points that are already in the database, thereby obviating the need to perform a new set of QM calculations. This is particularly important since, in typical *ab initio* crystal structure predictions, it is not uncommon to refine many hundreds of candidate structures. These structures are often far from a local minimum, so that additional optimization iterations are needed for convergence. Thus, reducing the cost of each iteration is very important for a thorough search.

In summary, the use of LAM/QM databases is of significant benefit in the context of *ab initio* crystal structure prediction studies involving the refinement of large numbers of candidate crystal structures. It is also advantageous for the computational screening of compounds with different cocrystal formers and for crystal structure calculations under different physical conditions (e.g., a range of different pressures for identification of high-pressure polymorphs).

5. CONCLUSIONS

For the majority of organic crystal structures of practical interest, detailed modeling of molecular flexibility is essential for correct minimization of the lattice energy. In order to obtain balanced models for the intra- and intermolecular energy contributions, it is necessary to use quantum mechanical molecular deformation energies and charge densities, making lattice energy minimization computationally expensive.

An algorithm has been presented that makes it possible to take molecular flexibility into account when identifying crystal structures that minimize the lattice energy. This algorithm, CrystalOptimizer, is a local optimization method that overcomes the large computational cost of treating flexibility through the use of local approximate models (LAMs). This leads to a substantial reduction in the number of quantum mechanical calculations required. In addition, the algorithm is based on a quasi-Newton scheme that ensures rapid convergence even with systems involving many flexible degrees of freedom.

The results presented for a variety of model systems indicate that the implementation of local approximate models can significantly improve the computational efficiency without adversely affecting accuracy. In practice, during the course of an optimization, most iterations rely on previously constructed LAMs (rather than new QM calculations) for the computation of the values of the rigid degrees of freedom, the intramolecular energy and the electrostatic multipole model. Moreover, the use of LAM/QM databases further reduces the computational cost associated with QM calculations allowing the accurate energy minimizations performed by CrystalOptimizer to be coupled directly within the crystal structure prediction techniques. The low-energy structures computed with CrystalOptimizer can also be used as input to the study of kinetic effects⁴¹ and crystal growth,⁴² which play an important role in crystal formation.

Overall, with the CrystalOptimizer code, the computational cost of QM calculations is no longer the limiting factor in accurate lattice energy minimization, and this makes it possible to achieve even higher accuracy by using larger basis sets and/or post-HF levels of theory. The computational cost of the algorithm seems to scale linearly with the number of flexible degrees of freedom and is dominated by the calculation of the multipole

derivatives and of the intermolecular energy derivatives with respect to the flexible degrees of freedom. Both currently require the use of finite difference approximations to partial derivatives. Removing these computational bottlenecks will extend the practical applicability of CrystalOptimizer to even larger molecules.

On a more fundamental level, an important aspect of CrystalOptimizer is its ability to handle systems with more than one molecule or ion in the asymmetric unit, which makes it applicable to the prediction of crystal structures of cocrystals and salts. Our approach to date has been to treat each of these molecules or ions independently for the purposes of QM calculations and then to rely on intermolecular descriptions of the interactions between them. Whether or not this is the most appropriate way of handling such systems, or related ones such as hydrates, requires further investigation.

AUTHOR INFORMATION

Corresponding Author

*E-mail: c.pantelides@imperial.ac.uk.

ACKNOWLEDGMENT

We thank Professor S. L. Price for providing us access to the DMACRYS software. The financial support from the Engineering and Physical Sciences Research Council (EPSRC) under the Molecular Systems Engineering grant (EP/E016340) is gratefully acknowledged. Calculations were performed on the High Performance Computing Cluster at Imperial College London. An earlier version of the algorithm presented in this paper was outlined in Kazantsev et al.,⁴³ we are grateful to Wiley VCH for permission to reproduce some of the material from that publication.

REFERENCES

- (1) Bernstein, J. *Polymorphism in Molecular Crystals*; Clarendon Press: Oxford, U. K., 2002.
- (2) van Eijck, B. P. Ab initio crystal structure predictions for flexible hydrogen-bonded molecules. Part III. Effect of lattice vibrations. *J. Comput. Chem.* **2001**, *22* (8), 816–826.
- (3) Karamertzanis, P. G.; Raiteri, P.; Parrinello, M.; Leslie, M.; Price, S. L. The Thermal Stability of Lattice-Energy Minima of 5-Fluorouracil: Metadynamics as an Aid to Polymorph Prediction. *J. Phys. Chem. B* **2008**, *112*, 4298–4308.
- (4) Day, G. M.; Cooper, T. G.; Cruz Cabeza, A. J.; Hejczyk, K. E.; Ammon, H. L.; Boerrigter, S. X. M.; Tan, J.; Della Valle, R. G.; Venuti, E.; Jose, J.; Gadre, S. R.; Desiraju, G. R.; Thakur, T. S.; van Eijck, B. P.; Facelli, J. C.; Bazterra, V. E.; Ferraro, M. B.; Hofmann, D. W. M.; Neumann, M.; Leusen, F. J. J.; Kendrick, J.; Price, S. L.; Misquitta, A. J.; Karamertzanis, P. G.; Welch, G. W. A.; Scheraga, H. A.; Arnautova, Y. A.; Schmidt, M. U.; van de Streek, J.; Wolf, A.; Schweizer, B. Significant progress in predicting the crystal structures of small organic molecules - a report on the fourth blind test. *Acta Crystallogr., Sect. B* **2009**, *65*, 107–125.
- (5) Price, S. L.; Leslie, M.; Welch, G. W. A.; Habgood, M.; Price, L. S.; Karamertzanis, P. G.; Day, G. M. Modeling organic crystal structures using distributed multipole and polarizability-based model intermolecular potentials. *Phys. Chem. Chem. Phys.* **2010**, *12*, 8478–8490.
- (6) Price, S. L. From crystal structure prediction to polymorph prediction: interpreting the crystal energy landscape. *Phys. Chem. Chem. Phys.* **2008**, *10* (15), 1996–2009.
- (7) Neumann, M. A.; Perrin, M. A. Energy ranking of molecular crystals using density functional theory calculations and an empirical van der Waals correction. *J. Phys. Chem. B* **2005**, *109* (32), 15531–15541.
- (8) Stone, A. J.; Alderton, M. Distributed Multipole Analysis - Methods and Applications. *Mol. Phys.* **1985**, *56* (5), 1047–1064.
- (9) Stone, A. J. Distributed multipole analysis: Stability for large basis sets. *J. Chem. Theory Comput.* **2005**, *1* (6), 1128–1132.
- (10) Coombes, D. S.; Price, S. L.; Willock, D. J.; Leslie, M. Role of Electrostatic Interactions in Determining the Crystal Structures of Polar Organic Molecules. A Distributed Multipole Study. *J. Phys. Chem.* **1996**, *100* (18), 7352–7360.
- (11) Day, G. M.; Motherwell, W. D. S.; Jones, W. Beyond the isotropic atom model in crystal structure prediction of rigid molecules: Atomic multipoles versus point charges. *Cryst. Growth Des.* **2005**, *5* (3), 1023–1033.
- (12) Brodersen, S.; Wilke, S.; Leusen, F. J. J.; Engel, G. A study of different approaches to the electrostatic interaction in force field methods for organic crystals. *Phys. Chem. Chem. Phys.* **2003**, *5* (21), 4923–4931.
- (13) Karamertzanis, P. G.; Price, S. L. Energy Minimization of Crystal Structures Containing Flexible Molecules. *J. Chem. Theory Comput.* **2006**, *2* (4), 1184–1199.
- (14) van Eijck, B. P.; Mooij, W. T. M.; Kroon, J. Attempted Prediction of the Crystal-Structures of 6 Monosaccharides. *Acta Crystallogr., Sect. B* **1995**, *51*, 99–103.
- (15) Mooij, W. T. M.; van Eijck, B. P.; Kroon, J. Ab initio crystal structure predictions for flexible hydrogen-bonded molecules. *J. Am. Chem. Soc.* **2000**, *122* (14), 3500–3505.
- (16) van Eijck, B. P.; Mooij, W. T. M.; Kroon, J. Ab initio crystal structure predictions for flexible hydrogen-bonded molecules. Part II. Accurate energy minimization. *J. Comput. Chem.* **2001**, *22* (8), 805–815.
- (17) Mooij, W. T. M.; van Eijck, B. P.; Kroon, J. Transferable ab initio intermolecular potentials. 2. Validation and application to crystal structure prediction. *J. Phys. Chem. A* **1999**, *103* (48), 9883–9890.
- (18) Nelder, J. A.; Mead, R. A SIMPLEX-method for function minimization. *Comput. J.* **1965**, *7* (4), 308–313.
- (19) Karamertzanis, P. G.; Kazantsev, A. V.; Issa, N.; Welch, G. W. A.; Adjiman, C. S.; Pantelides, C. C.; Price, S. L. Can the Formation of Pharmaceutical Cocrystals Be Computationally Predicted? II. Crystal Structure Prediction. *J. Chem. Theory Comput.* **2009**, *5* (5), 1432–1448.
- (20) Polito, M.; D'Oria, E.; Maini, L.; Karamertzanis, P. G.; Grepioni, F.; Braga, D.; Price, S. L. The Crystal Structures of Chloro and Methyl Ortho-Benzoic Acids and Their Co-crystal: Rationalizing Similarities and Differences. *CrystEngComm* **2008**, *10*, 1848–1854.
- (21) Frisch, M. J.; Trucks, G. W.; Schlegel, H. B.; Scuseria, G. E.; Robb, M. A.; Cheeseman, J. R.; Scalmani, G.; Barone, V.; Mennucci, B.; Petersson, G. A.; Nakatsuji, H.; Caricato, M.; Li, X.; Hratchian, H. P.; Izmaylov, A. F.; Bloino, J.; Zheng, G.; Sonnenberg, J. L.; Hada, M.; Ehara, M.; Toyota, K.; Fukuda, R.; Hasegawa, J.; Ishida, M.; Nakajima, T.; Honda, Y.; Kitao, O.; Nakai, H.; Vreven, T.; Montgomery, J. A.; Peralta, J. E.; Ogliaro, F.; Bearpark, M.; Heyd, J. J.; Brothers, E.; Kudin, K. N.; Staroverov, V. N.; Kobayashi, R.; Normand, J.; Raghavachari, K.; Rendell, A.; Burant, J. C.; Iyengar, S. S.; Tomasi, J.; Cossi, M.; Rega, N.; Millam, J. M.; Klene, M.; Knox, J. E.; Cross, J. B.; Bakken, V.; Adamo, C.; Jaramillo, J.; Gomperts, R.; Stratmann, R. E.; Yazyev, O.; Austin, A. J.; Cammi, R.; Pomelli, C.; Ochterski, J. W.; Martin, R. L.; Morokuma, K.; Zakrzewski, V. G.; Voth, G. A.; Salvador, P.; Dannenberg, J. J.; Dapprich, S.; Daniels, A. D.; Farkas, O.; Foresman, J. B.; Ortiz, J. V.; Cioslowski, J.; Fox, D. J. *Gaussian 09*; Gaussian, Inc.: Wallingford, CT, 2009.
- (22) Kim, H. S.; Jeffrey, G. A. The crystal structure of xylitol. *Acta Crystallogr., Sect. B* **1969**, *25*, 2607–2613.
- (23) Dennis, J. E.; Schnabel, R. B. *Numerical Methods for Unconstrained Optimization and Nonlinear Equations*; Prentice-Hall: London, 1983.
- (24) Allen, F. H. The Cambridge Structural Database: a quarter of a million crystal structures and rising. *Acta Crystallogr., Sect. B* **2002**, *58* (3), 380–388.
- (25) Brown, G. M.; Levy, H. A. alpha-D-Glucose: further refinement based on neutron-diffraction data. *Acta Crystallogr., Sect. B* **1979**, *35*, 656–659.

(26) Snyder, R. L.; Rosenstein, R. D. The crystal and molecular structure of the 1:1 hydrogen bond complex between [alpha]-D-glucose and urea. *Acta Crystallogr., Sect. B* **1971**, *27* (10), 1969–1975.

(27) Admiraal, G.; Eikelenboom, J. C.; Vos, A. Structures of the triclinic and monoclinic modifications of (2-oxo-1-pyrrolidinyl)acetamide. *Acta Crystallogr., Sect. B* **1982**, *38* (10), 2600–2605.

(28) Galdecki, Z.; Glowka, M. L. Crystal-Structure of Nootropic Agent, Piracetam-2-Oxopyrrolidin-1-Ylacetamide. *Pol. J. Chem.* **1983**, *57* (10–1), 1307–1312.

(29) Louer, D.; Louer, M.; Dzyabchenko, A. V.; Agafonov, V.; Ceolin, R. Structure of a Metastable Phase of Piracetam From X-Ray-Powder Diffraction Using Atom-Atom Potential Method. *Acta Crystallogr., Sect. B* **1995**, *51* (Pt2), 182–187.

(30) Fabbiani, F. P. A.; Allan, D. R.; Parsons, S.; Pulham, C. R. An exploration of the polymorphism of piracetam using high pressure. *CrystEngComm* **2005**, *7* (29), 179–186.

(31) Fabbiani, F. P. A.; Allan, D. R.; David, W. I. F.; Davidson, A. J.; Lennie, A. R.; Parsons, S.; Pulham, C. R.; Warren, J. E. High-pressure studies of pharmaceuticals: An exploration of the behavior of piracetam. *Cryst. Growth Des.* **2007**, *7* (6), 1115–1124.

(32) Vishweshwar, P.; McMahon, J. A.; Peterson, M. L.; Hickey, M. B.; Shattock, T. R.; Zaworotko, M. J. Crystal engineering of pharmaceutical co-crystals from polymorphic active pharmaceutical ingredients. *Chem. Commun.* **2005**, *36*, 4601–4603.

(33) Sakai, K.; Sakurai, K.; Nohira, H.; Tanaka, R.; Hirayama, N. Practical resolution of 1-phenyl-2-(4-methylphenyl)ethylamine using a single resolving agent controlled by the dielectric constant of the solvent. *Tetrahedron Asymmetr.* **2004**, *15*, 3495–3500.

(34) Dideberg, O.; Dupont, L.; Campsteyn, H. Structure cristalline et moléculaire du complexe 1:1 progestérone-résorcinol. *Acta Crystallogr., Sect. B* **1975**, *31* (3), 637–640.

(35) Friscic, T.; Lancaster, R. W.; Laszlo, F.; Karamertzanis, P. G. Tunable recognition of the steroid a-face by adjacent p-electron density. *Proc. Natl. Acad. Sci. U.S.A.* **2010**, *107* (30), 13216–13221.

(36) Chisholm, J. A.; Motherwell, S. COMPACT: a program for identifying crystal structure similarity using distances. *J. Appl. Crystallogr.* **2005**, *38*, 228–231.

(37) Mohamed, S.; Tocher, D. A.; Vickers, M.; Karamertzanis, P. G.; Price, S. L. Salt or Cocrystal? A New Series of Crystal Structures Formed from Simple Pyridines and Carboxylic Acids. *Cryst. Growth Des.* **2009**, *9* (6), 2881–2889.

(38) Karamertzanis, P. G.; Pantelides, C. C. Ab initio crystal structure prediction - I. Rigid molecules. *J. Comput. Chem.* **2005**, *26* (3), 304–324.

(39) Stone, A. J.; Dullweber, A.; Engkvist, O.; Fraschini, E.; Hodges, M. P.; Meredith, A. W.; Nutt, D. R.; Popelier, P. L. A.; Wales, D. J. *ORIENT*; University of Cambridge: Cambridge, U. K., 2006.

(40) Bondi, A. van der Waals Volumes and Radii. *J. Phys. Chem.* **1964**, *68* (3), 441–451.

(41) Santiso, E. E.; Trout, B. L. A general set of order parameters for molecular crystals. *J. Chem. Phys.* **2011**, *134*, 064109.

(42) Snyder, R. C.; Doherty, M. J. Predicting crystal growth by spiral motion. *Proc. R. Soc. London, Ser. A* **2009**, *465*, 1145–1171.

(43) Kazantsev, A. V.; Karamertzanis, P. G.; Pantelides, C. C.; Adjiman, C. S. CrystalOptimizer: An Efficient Algorithm for Lattice Energy Minimization of Organic Crystals Using Isolated-Molecule Quantum Mechanical Calculations. In *Process Systems Engineering: Vol. 6: Molecular Systems Engineering*; Adjiman, C. S., Galindo, A., Eds.; Wiley-VCH: Hamburg, Germany, 2010; pp 1–42.